Journal of ASTM International
Selected Technical Papers

STP 1529

Zirconium in the Nuclear Industry

16th International Symposium

JAI Guest Editor
Pierre Barbéris
Magnus Limbäck

Journal of ASTM International
Selected Technical Papers STP1529

Zirconium in the Nuclear Industry: 16th International Symposium

JAI Guest Editors:
Magnus Limbäck
Pierre Barbéris

ASTM International
100 Barr Harbor Drive
PO Box C700
West Conshohocken, PA 19428-2959

Printed in the U.S.A.

ASTM Stock #: STP1529

Library of Congress Cataloging-in-Publication Data

ISBN: 978-0-8031-7515-0
ISSN: 1050-7558

Copyright © 2011 ASTM INTERNATIONAL, West Conshohocken, PA. All rights reserved. This material may not be reproduced or copied, in whole or in part, in any printed, mechanical, electronic, film, or other distribution and storage media, without the written consent of the publisher.

Journal of ASTM International (JAI) Scope

The JAI is a multi-disciplinary forum to serve the international scientific and engineering community through the timely publication of the results of original research and critical review articles in the physical and life sciences and engineering technologies. These peer-reviewed papers cover diverse topics relevant to the science and research that establish the foundation for standards development within ASTM International.

Photocopy Rights

Authorization to photocopy items for internal, personal, or educational classroom use, or the internal, personal, or educational classroom use of specific clients, is granted by ASTM International provided that the appropriate fee is paid to ASTM International, 100 Barr Harbor Drive, P.O. Box C700, West Conshohocken, PA 19428-2959, Tel: 610-832-9634; online: http://www.astm.org/copyright.

The Society is not responsible, as a body, for the statements and opinions expressed in this publication. ASTM International does not endorse any products represented in this publication.

Peer Review Policy

Each paper published in this volume was evaluated by two peer reviewers and at least one editor. The authors addressed all of the reviewers' comments to the satisfaction of both the technical editor(s) and the ASTM International Committee on Publications.

The quality of the papers in this publication reflects not only the obvious efforts of the authors and the technical editor(s), but also the work of the peer reviewers. In keeping with long-standing publication practices, ASTM International maintains the anonymity of the peer reviewers. The ASTM International Committee on Publications acknowledges with appreciation their dedication and contribution of time and effort on behalf of ASTM International.

Citation of Papers

When citing papers from this publication, the appropriate citation includes the paper authors, "paper title", J. ASTM Intl., volume and number, Paper doi, ASTM International, West Conshohocken, PA, Paper, year listed in the footnote of the paper. A citation is provided as a footnote on page one of each paper.

Second Printing, April 2012
Baltimore, MD

Foreword

This publication, *Zirconium in the Nuclear Industry: 16th International Symposium*, contains papers presented at the symposium with the same name held in Chengdu, Sichuan Province, China, May 9-13, 2010. The sponsor of the symposium was ASTM International Committee B10 on Reactive and Refractory Metals and Alloys.

The Symposium Chairman was Magnus Limbäck, Westinghouse Electric Sweden and Co-Chairman Zhao Wenjin, Nuclear Power Institute of China (NPIC), Chengdu, Sichuan Province, China. Serving as Guest Editors of this publication are Magnus Limbäck and Pierre Barbéris, Areva/Cezus Research Centre, Ugine, France. Arthur Motta, Pennsylvania State University, acted as Associate Editor for the publication of these papers in Journal of ASTM International (JAI).

Contents

Overview ix

Kroll Award Papers

Explosion Cladding: An Enabling Technology for Zirconium in the Chemical Process Industry
J. G. Banker 3

Performance of Zirconium Alloys in Light Water Reactors with a Review of Nodular Corrosion
D. G. Franklin 17

The Evolution of Microstructure and Deformation Stability in Zr–Nb–(Sn,Fe) Alloys Under Neutron Irradiation
V. N. Shishov 37

The Development of Zr-2.5Nb Pressure Tubes for CANDU Reactors
B. A. Cheadle 67

Schemel Award Paper

Photoelectrochemical Investigation of Radiation-Enhanced Shadow Corrosion Phenomenon
Y.-J. Kim, R. Rebak, Y.-P. Lin, D. Lutz, D. Crawford, A. Kucuk, and B. Cheng 91

Basic Metallurgy

Dynamic Recrystallization in Zirconium Alloys
J. K. Chakravartty, R. Kapoor, A. Sarkar, and S. Banerjee 121

Measurement and Modeling of Second Phase Precipitation Kinetics in Zirconium Niobium Alloys
M. Ivermark, J. Robson, and M. Preuss 150

Texture Evolution of Zircaloy-2 During Beta Quenching: Effect of Process Variables
J. Romero, M. Preuss, J. Quinta da Fonseca, R. J. Comstock, M. Dahlbäck, and L. Hallstadius 176

In Situ Studies of Variant Selection During the α-β-α Phase Transformation in Zr-2.5Nb
P. Mosbrucker, M. R. Daymond, and R. A. Holt 195

Fabrication and Mechanical Properties

Segregation in Vacuum Arc Remelted Zirconium Alloy Ingots
A. Jardy, F. Leclerc, M. Revil-Baudard, P. Guerin, H. Combeau, and V. Rebeyrolle 219

Damage Build-Up in Zirconium Alloys During Mechanical Processing: Application to Cold Pilgering
A. Gaillac, C. Lemaignan, and P. Barberis 244

Multiscale Analysis of Viscoplastic Behavior of Recrystallized Zircaloy-4 at 400°C
M. Priser, M. Rautenberg, J.-M. Cloué, P. Pilvin, X. Feaugas, and D. Poquillon 269

Polycrystalline Modeling of the Effect of Texture and Dislocation Microstructure on Anisotropic Thermal Creep of Pressurized Zr-2.5Nb Tubes
W. Li, R. A. Holt, and S. Tracy 298

Improved Zr-2.5Nb Pressure Tubes for Reduced Diametral Strain in Advanced CANDU Reactors
G. A. Bickel, M. Griffiths, A. Douchant, S. Douglas, O. T. Woo, and A. Buyers 327

Microstructural Studies of Heat Treated Zr-2.5Nb Alloy for Pressure Tube Applications
N. Saibaba, S. K. Jha, S. Tonpe, K. Vaibhaw, V. Deshmukh, S. V. Ramana Rao, K. V. Mani Krishna, S. Neogy, D. Srivastava, G. K. Dey, R. V. Kulkarni, B. B. Rath, E. Ramadasan, and S. A. Anantharaman 349

Hydriding – Hydrogen Effect

High Temperature Aqueous Corrosion and Deuterium Uptake of Coupons Prepared from the Front and Back Ends of Zr-2.5Nb Pressure Tubes
H. M. Nordin, A. J. Elliot, and S. G. Bergin 373

Hydrogen Absorption Mechanism of Zirconium Alloys Based on Characterization of Oxide Layer
K. Une, K. Sakamoto, M. Aomi, J. Matsunaga, Y. Etoh, I. Takagi, S. Miyamura, T. Kobayashi, and K. Ito 401

In Situ Scanning Electron Microscope Observation and Finite Element Method Analysis of Delayed Hydride Cracking Propagation in Zircaloy-2 Fuel Cladding Tubes
T. Kubo, H. Muta, S. Yamanaka, M. Uno, and K. Ogata 433

Study on the Role of Second Phase Particles in Hydrogen Uptake Behavior of Zirconium Alloys
M. Y. Yao, J. H. Wang, J. C. Peng, B. X. Zhou, and Q. Li 466

Hydride Platelet Reorientation in Zircaloy Studied with Synchrotron Radiation Diffraction
K. B. Colas, A. T. Motta, M. R. Daymond, M. Kerr, and J. D. Almer 496

Statistical Analysis of Hydride Reorientation Properties in Irradiated Zircaloy-2
S. Valance, J. Bertsch, and A. M. Alam 523

The Effect of Microstructure on Delayed Hydride Cracking Behavior of Zircaloy-4 Fuel Cladding—An International Atomic Energy Agency Coordinated Research Programme
C. Coleman, V. Grigoriev, V. Inozemtsev, V. Markelov, M. Roth, V. Makarevicius, Y. S. Kim, K. L. Ali, J. K. Chakravarrty, R. Mizrahi, and R. Lalgudi 544

Neutron Radiography: A Powerful Tool for Fast, Quantitative and Non-Destructive Determination of the Hydrogen Concentration and Distribution in Zirconium Alloys
M. Grosse 575

Corrosion – Oxide Layer Characterization

Detailed Analysis of the Microstructure of the Metal/Oxide Interface Region in Zircaloy-2 after Autoclave Corrosion Testing
P. Tejland, M. Thuvander, H.-O. Andrén, S. Ciurea, T. Andersson, M. Dahlbäck, and L. Hallstadius 595

Study of the Initial Stage and Anisotropic Growth of Oxide Layers Formed on Zircaloy-4
B. X. Zhou, J. C. Peng, M. Y. Yao, Q. Li, S. Xia, C. X. Du, and G. Xu 620

Studies Regarding Corrosion Mechanisms in Zirconium Alloys
M. Preuss, P. Frankel, S. Lozano-Perez, D. Hudson, E. Polatidis, N. Ni , J. Wei, C. English, S. Storer, K. B. Chong, M. Fitzpatrick, P. Wang, J. Smith, C. Grovenor, G. Smith, J. Sykes, B. Cottis, S. Lyon, L. Hallstadius, B. Comstock, A. Ambard, and M. Blat-Yrieix. 649

Understanding Crack Formation at the Metal/Oxide Interface During Corrosion of Zircaloy-4 Using a Simple Mechanical Model
A. Ly, A. Ambard, M. Blat-Yrieix, L. Legras, P. Frankel, M. Preuss, C. Curfs, G. Parry, and Y. Bréchet 682

In Pile Behaviour

Optimization of Zry-2 for High Burnups
F. Garzarolli, B. Cox, and P. Rudling 711

Effects of Secondary Phase Particle Dissolution on the In-Reactor Performance of BWR Cladding
S. Valizadeh, G. Ledergerber, S. Abolhassan, D. Jädernäs, M. Dahlbäck, E. V. Mader, G. Zhou, J. Wright, and L. Hallstadius 729

Hydrogen Solubility and Microstructural Changes in Zircaloy-4 Due to Neutron Irradiation
P. Vizcaíno, A. V. Flores, P. B. Bozzano, A. D. Banchik, R. A. Versaci, and R. O. Ríos 754

Advanced Zirconium Alloy for PWR Application
A. M. Garde, R. J. Comstock, G. Pan, R. Baranwal, L. Hallstadius, T. Cook, and F. Carrera 784

Ultra Low Tin Quaternary Alloys PWR Performance—Impact of Tin Content on Corrosion Resistance, Irradiation Growth, and Mechanical Properties
V. Chabretou, P. B. Hoffmann, S. Trapp-Pritsching, G. Garner, P. Barberis, V. Rebeyrolle, and J. J. Vermoyal 801

Radiation Damage of E635 Alloy Under High Dose Irradiation in the VVER-1000 and BOR-60 Reactors
G. P. Kobylyansky, A. E. Novoselov, A. V. Obukhov, Z. E. Ostrovsky, V. N. Shishov, M. M. Peregud, and V. A. Markelov 827

Creep and Deformation

ZIRLO Irradiation Creep Stress Dependence in Compression and Tension
J. P. Foster and R. Baranwal 853

Experimental Investigation of Irradiation Creep and Growth of Recrystallized Zircaloy-4 Guide Tubes Pre-Irradiated in PWR
M. A. McGrath and S. Yagnik. 875

REFLET Experiment in OSIRIS: Relaxation under Flux as a Method for Determining Creep Behavior of Zircaloy Assembly Components
S. Carassou, C. Duguay, P. Yvon, F. Rozenblum, J. M. Cloué, V. Chabretou, C. Bernaudat, B. Levasseur, A. Maurice, P. Bouffioux, and K. Audic 899

Impact of the Irradiation Damage Recovery During Transportation on the Subsequent Room Temperature Tensile Behavior of Irradiated Zirconium Alloys
B. Bourdiliau, F. Onimus, C. Cappelaere, V. Pivetaud, P. Bouffioux, V. Chabretou, and A. Miquet 929

Shadow Corrosion-Induced Bow of Zircaloy-2 Channels
S. T. Mahmood, P. E. Cantonwine, Y.-P. Lin, D. C. Crawford, E. V. Mader, and K. Edsinger 954

Failure Mechanisms and Transients

Characterization of Oxygen Distribution in LOCA Situations
C. Duriez, S. Guilbert, A. Stern, C. Grandjean, L. Bělovský, and J. Desquines 993

Effect of Hydrides on Mechanical Properties and Failure Morphology of BWR Fuel Cladding at Very High Strain Rate
M. Nakatsuka and S. Yagnik 1021

Simulation of Outside-in Cracking in Boiling Water Reactor Fuel Cladding Tubes under Power Ramp
K. Sakamoto, M. Nakatsuka, and T. Higuchi 1054

RIA Failure of High Burnup Fuel Rod Irradiated the Leibstadt Reactor: Out-of-Pile Mechanical Simulation and Comparison with Pulse Reactor Tests
V. Grigoriev, R. Jakobsson, D. Schrire, G. Ledergerber, T. Sugiyama, F. Nagase, T. Fuketa, L. Hallstadius, and S. Valizadeh 1073

Author Index 1093

Subject Index 1097

Overview

This STP contains the papers presented at the 16th International Symposium on Zirconium in the Nuclear Industry held in in Chengdu, Sichuan Province, China, May 9-13, 2010. The first symposium was held in Philadelphia in 1968, and symposia have been held ever since in two to three year intervals. The proceedings of each symposium in the series have been documented with an STP.

This symposium series remains, after forty years, one of the top presentation and information source for the research in the area of zirconium alloy performance in a nuclear reactor environment. 42 papers and 32 posters were selected for presentation at the 16th Symposium from 130 abstracts submitted. The forty-two papers published in these proceedings were peer reviewed and edited, and are also published in the ASTM online journal, JAI. In addition, the most significant parts of the discussions that followed the oral presentation of each paper at the symposium are included in these proceedings.

Four experts in zirconium area received their Kroll Awards at the 16th Symposium: J. Banker, D. Franklin, V. Shishov and B. Cheadle. Noteworthy is the fact that the first one deals with zirconium outside the nuclear industry. These papers as well as the 26 previous Kroll award papers are now gathered in "The Kroll Medal Papers 1975-2010" published by ASTM, and covering all aspects of zirconium technology.

137 attendants from 19 countries attended the 16th Symposium. North and South America, Europe, and Asia were represented.

The papers were presented during seven sessions, covering the whole spectrum of zirconium metallurgy, from basic metallurgy to accidental conditions and transport, through fabrication, creep and growth, and corrosion and hydriding. Looking back from the beginning of this symposium series, it appears that these topics remained quite constant over the time.

Besides the historical alloys (Zircaloy-2, Zircaloy-4, Zr2.5Nb and Zr-lNb), several studies were devoted to advanced alloys and alloys under development: ZIRLO™, M5™, X5A, VB, N18, N36, NZ2, E635, ZrNbSnFe with low tin content, Ziron. Some optimisation of Zircaloy-2 was proposed.

Modelling appears more and more intricate with the experiments, from precipitation to VAR melting, from the effect of texture and dislocations on creep to the oxygen distribution during LOCA situations or the outside-in cracking in BWR fuel cladding.

As noted in the past few symposia, advanced techniques are more systematically utilised: high temperatures studies of phase transformations using

synchrotron radiation or neutrons diffraction were presented; EBSD allows measuring local texture, studies on corrosion and hydriding benefit from the precise positioning of thin foils with FIB.

Last, it is worth noting that several studies were presented by enthusiastic young searchers or PhD students, which demonstrates the dynamism of the research in the zirconium metallurgy area.

In the field of basic metallurgy, progresses were reported in the following fields:

- plotting the dynamic recrystallisation domain thanks to processing maps, which were shown to depend on the alloy composition.
- experimental quantification of the precipitation of beta Nb second phase particles (SPP) in Zr-Nb alloys, which was investigated by synchrotron radiation and then modelled.
- texture change and variant selection through the α-β-α phase transformation, wich generated some controversial results on the influence of an externally applied stress.

The processing of zirconium was illustrated first by the VAR melting, with modelling of the alloying element segregation allowing efficient control on the ingot chemistry, then by the investigation of the damage mechanism during pilgering, which is alloy dependent through the number and size of the second phase particles. Transmission electron microscopy was used with the aim of investigating the dislocation microstructure of recrystallised Zircaloy-4 after 400°C creep test to develop a model of the anisotropic viscoplastic behaviour.

Three papers were devoted to Zr-2.5Nb tubes. The first one presented a self-consistent modelling of their anisotropic behaviour, which takes into account not only the texture but also the dislocation microstructure resulting from the last cold drawing pass. A second paper showed that the tubes for the future ADC will procure reduced creep variability, owing to a better understanding of its dependence on the microstructure and to an improved extrusion process. A detailed study of the microstructure evolution during annealing and of its relation with texture and mechanical properties of the tubes was also conductive to improvement in the tube fabrication sequence.

The investigation of hydrogen effects and hydriding constituted an important topic of this symposium with eight papers dealing with this topic. Besides a paper showing the capability of neutron radiography to investigate this area, an investigation of Zr-2.5Nb hydriding during autoclave tests showed that the hydrogen pick-up was linked to the sample position in the tube (back end/front end) and correlated to various microstructural parameters. An investigation of autoclave corroded samples from different alloys

by TEM, RAMAN and SIMS led to the hypothesis according to which the rate controlling process for hydrogen absorption was the diffusion of hydrogen ions in the oxide barrier layer, the best alloys having a higher protective layer due to compressive stresses and Fe dissolution from the second phase particles. Another paper confirms that the hydrogen pick up during corrosion is closely related to the size, area fraction, and compositions of the second phase particles.

The hydride dissolution, re-orientation and stress could be followed in situ by synchrotron radiation diffraction during temperature and stress cycles. The hydride re-orientation was the subject of a second paper coupling mechanical tests on irradiated cladding and finite element modelling, showing the importance of the hoop stress, and evidencing some other parameters. Two papers dealt with delayed hydride cracking (DHC). The first one which was derived from an IAEA coordinated research program investigated the effect of the microstructure on DHC, showing its main role is to control the material strength, while the second one presented in situ observation in an SEM of the crack propagation during a DHC experiment and a FEM of the accepted mechanism.

Two papers on the corrosion mechanism and oxide layer characterization showed on the one hand that the delayed oxidation of the SPPs in the oxide layer lead to the formation of small cracks, and on the other hand the influence of the grain substrate orientation on the oxide layer thickness and epitaxy during steam corrosion tests.

The in-pile behaviour was the subject of numerous studies. In the aim of mitigating the accelerated HPUF tendency at high burn up, it was proposed to decrease the nickel content and increase the iron and chromium contents in Zircaloy-2 within the ASTM specification. Zircaloy-2 was also the subject of a detailed study of the SPPs' evolution, showing that Zr(Fe,Cr)2 SPP amorphize while Zr2(Fe,Ni) SPP remain crystalline during irradiation. The shadow corrosion due to galvanic coupling between a zirconium alloy and a more noble metal was investigated by photo-electrochemistry; the alloy influence was evidenced, and it was postulated that a coating on the fuel assembly spacer may mitigate the shadow corrosion.

Annealing and DSC experiments on irradiated Zircaloy-4 enabled the study of the influence of the neutron damage on the hydrogen solubility, while the morphology of hydrides and SPP was investigated by TEM.

The in pile behaviour of advanced alloys were presented: X5A (for PWR) with two different final heat treatments showed improved properties and that the irradiation creep of ZIRLO™ is linear with the (deviatoric hoop) stress. The same phenomenon is observed in tension and compression. The increase in tin content up to 0.3 % in Zr1NbSnFe does not significantly modify the corrosion resistance nor the hydrogen pick-up compared to Zr1Nb

alloy, while ensuring a higher creep resistance and an improved dimensional stability.

Radiation damage of E635 in VVER (SPP evolution, ⟨c⟩-dislocation loop formation) was investigated and found in agreement with the model samples in the BOR-60 reactor.

The creep and deformation during or after irradiation, already evoked in the previous section, was illustrated by four more papers. No effect of commercial reactor irradiation temperature or hydrogen content was found on the Zircaloy-4 guide tube creep. Zircaloy-4 irradiation creep law was deduced from relaxation experiments on bent beam specimens in OSIRIS. Creep deformation of Zr-1%Nb and Zircaloy-4 during transportation was associated to a significant recovery of irradiation damage, preventing the dislocation channelling. Shadow corrosion-induced bow of Zircaloy-2 channels was associated to differential hydrogen concentration on channels sides adjacent to and away from the control blades.

Four papers dealt with accidental conditions. In LOCA conditions, a diffusion model was developed to compute the oxygen distribution, closely related to the mechanical properties, and compared with experiments. An investigation on the effect of hydrides on mechanical properties during RIA concluded that high strain rates did not seem to impact the stress strain behaviour when the hydrogen content is higher than 400ppm, threshold over which the failure elongation at room temperature decreases drastically. When radially oriented hydrides are present in BWR cladding, an outside-in cracking can occur, which was investigated, in isothermal conditions or with a radial thermal gradient: the outside-in cracking during the power ramp seems strongly dependent on the distribution of dissolved hydrogen as a result of thermal diffusion. Finally, a high burn-up BWR fuel rod, subjected to RIA tests in a research reactor, resulted in cladding failure at room temperature, but not at elevated temperature. A mechanical test was developed to reproduce the ramp test and was shown to be predictive.

The John Schemel Award is awarded following each symposium for the best paper presented at the symposium. The selection is based upon the technical content of the paper, the usefulness of the work reported to the worldwide reactor components community, and the technical difficulty in doing the work. This year, a committee of technical experts in several aspects of the zirconium industry selected the paper entitled “Photoelectrochemical Investigation of Radiation Enhanced Shadow Corrosion Phenomenon” by Y.-J. Kim, R. Rebak, Y-P. Lin, D. Lutz, D. Crawford, A. Kucuk and B. Cheng to receive the John Schemel Award.

Pierre Barbéris
Areva/Cezus Research Centre
Guest Editor

KROLL AWARD PAPERS

Reprinted from JAI, Vol. 7, No. 8
doi:10.1520/JAI103050
Available online at www.astm.org/JAI

John G. Banker[1]

Explosion Cladding: An Enabling Technology for Zirconium in the Chemical Process Industry

ABSTRACT: Zirconium is a commonly used material for containment of corrosive media by the chemical process industry (CPI). Zirconium's corrosion resistance is exceptional in a broad range of aggressively corrosive environments. However, zirconium is significantly more expensive than most of the alternative, but often inferior, corrosion resistant alloys. Explosion cladding has enabled CPI companies to cost effectively benefit from the superior performance features of zirconium in heavy-wall pressure vessels and heat exchangers. Explosion cladding is a unique technology that uses the energy of an explosive detonation to produce a metallurgical bond between metal plates. Since its discovery and industrialization in the 1960s, explosion cladding has proven to be a highly reliable, robust manufacturing technology. Zirconium clad has become a broadly accepted material of construction for a significant range of chemical process equipment. Zirconium clad equipment is used in manufacture of an extensive range of chemical products or intermediates including nitric acid, acetic acid, urea, and various organic acids. Zirconium clad and related design, manufacture, and fabrication processes have been shown to be highly reliable and to reduce both capital and operating cost.

KEYWORDS: zirconium, clad, explosion clad, corrosion control, pressure vessels, heat exchangers

Introduction

Zirconium is commonly used as a structural material in the chemical process industry (CPI). The primary driver is zirconium's superior corrosion resistance over a broader range of chemical environments and temperatures than virtually

Manuscript received February 18, 2010; accepted for publication June 23, 2010; published online July 2010.
[1] V. P. Customers and Technology, Dynamic Materials Corporation, Boulder, CO 80301.

Cite as: Banker, J. G., "Explosion Cladding: An Enabling Technology for Zirconium in the Chemical Process Industry," *J. ASTM Intl.*, Vol. 7, No. 8. doi:10.1520/JAI103050.

Copyright © 2011 by ASTM International, 100 Barr Harbor Drive, PO Box C700, West Conshohocken, PA 19428-2959.

TABLE 1—*ASTM B551, zirconium grades commonly used in CPI equipment for corrosion resistance.*

	Composition, wt %	
Grade	R60700	R60700
Zr + Hf, min	99.2	99.2
Hf, max	4.5	4.5
Fe + Cr, max	0.2	0.2
H, max	0.005	0.005
N, max	0.025	0.025
C, max	0.05	0.05
Ox, max	0.16	0.10

any other metal [1–3]. It exhibits excellent resistance to corrosive attack in most organic and inorganic acids, salt solutions, and strong alkalis. Zirconium's ability to withstand alternating acidic and basic environments is unusual. Unlike many of the other corrosion resistant alloys (CRAs), zirconium is considered to be non-toxic. From the technical perspective, zirconium is an exceptional material for construction of chemical process pressure vessels, columns, heat exchangers, piping, and valves. Zirconium alloy R60702 (ASTM B551 Alloy 702) [4], which is essentially chemically pure zirconium, is the most commonly used grade (Table 1). Although R60702 is more expensive than most other CRAs, it continues to be a far better value for some severe corrosion environments. Making direct cost comparisons between R60702 and other CRAs is not simple due to significant variations in corrosion allowances, density, thermal conductivity, mechanical properties, maintenance costs, and failure related costs. Today, R60702 is broadly used for thinner walled construction including tubes, pipes, columns, and similar equipments.

Solid R60702 has traditionally been used much less in construction of heavier equipment (typically driven by environments, which are high temperature and/or high pressure.) This is primarily driven by two factors, cost and design strength. R60702 is relatively expensive compared to many of the other CRAs. Table 2 presents a comparison of the relative cost of several common CRAs after making adjustments for design strength (at ambient temperature) and density. Second, the design strength allowed for R60702 in the ASME Boiler & Pressure

TABLE 2—*Comparative costs of some CRAs.*

Alloy	Price Ratio
S31603 (stainless steel)	1.0
R50400 (titanium)	3.0
N10276 (Hastelloy)	5.0
R60702	8.0
R05400 (tantalum)	20.0

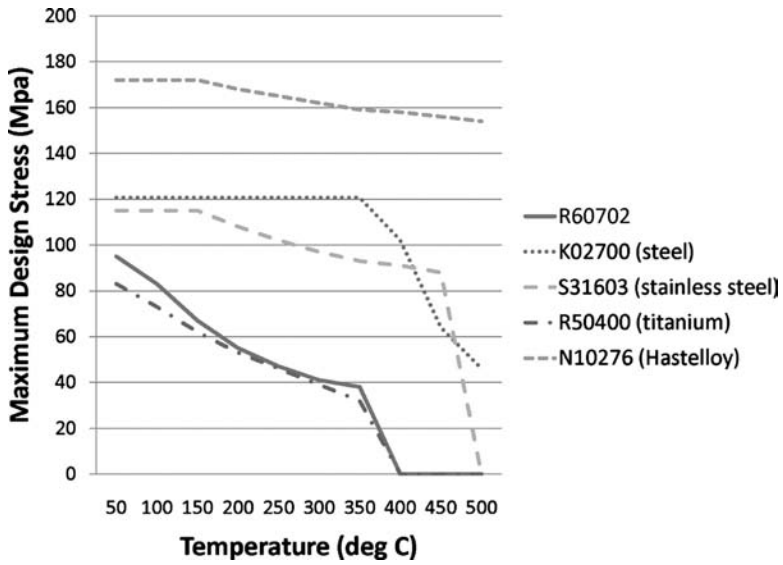


FIG. 1—*Comparative strength R60702 and other alloys.*

Vessel Code [5] is lower than many of the alternative alloys. Further, allowable design strength for R60702 drops off more quickly with increasing temperature than that of stainless steels and nickel alloys (Fig. 1). Consequently, the cost problem is compounded by the need for heavier wall equipment when solid R60702 construction is considered, and even more so when elevated temperature performance is required.

In most chemical process applications, the corrosive media is in contact with only one face of the structural containment material. For reactors and columns, typically the interior surface is exposed to the corrosive contents. The exterior surface sees a much less severe environment, frequently ambient conditions. Costs can be reduced significantly if only a thin layer of zirconium is used in contact with the process media, and a thicker and lower cost metal is used as the structural component. For some applications, loose linings of zirconium inside of a steel containment vessel are suitable. However, in process applications involving elevated temperatures and/or pressures and/or cyclic conditions, loose linings often fail quickly. Loose linings are also inefficient when through-wall heat transfer is important.

Construction using clad plates overcomes the shortcomings of loose-lined equipment. Clad equipment has decades of demonstrated performance in CPI installations. The cost reductions achieved with zirconium clad enable the use of zirconium in many applications where R60702 would otherwise be considered cost prohibitive. Figure 2 shows the cost difference between zirconium clad and solid R60702 over a broad range of thicknesses. The cost benefits are achieved by reducing the amount of zirconium used and further by reducing the overall equipment thickness as a result of the higher allowable design stress of steel. The graph shows two clad thickness combinations. Clad of 3 mm thick

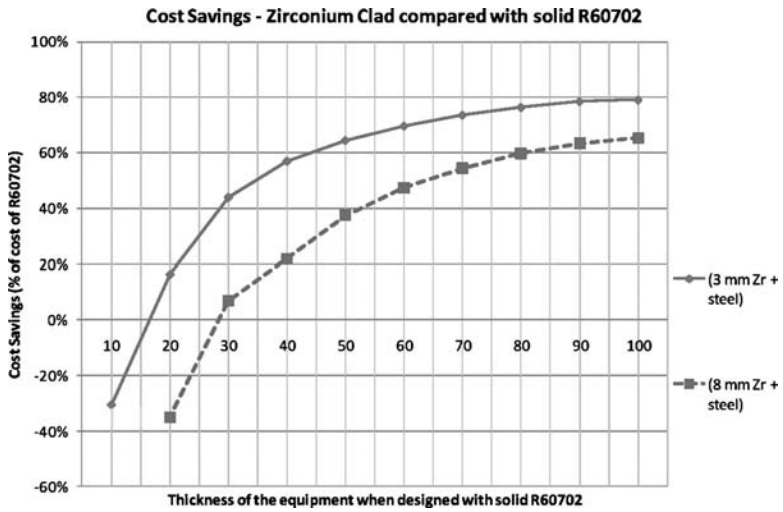


FIG. 2—*Comparative cost of zirconium clad versus solid R60702, including adjustments for design strength. Base metal is SA-516 Gr 70 steel.*

Zr bonded to steel (ASTM A516-70) [6] is commonly used for pressure vessels. A thicker cladding layer, 8 mm, is commonly used for heat exchanger tubesheets. As shown in the graph, clad typically offers cost benefits over solid R60702 construction when the required wall thickness of R60702 exceeds 15 mm. Many of today's pressure vessel and heat exchanger applications that use zirconium clad would not be commercially viable if solid R60702 construction was the only option.

Clad Manufacture

Several industrial processes can be used for making clad steel plates when the CRA alloy is metallurgically compatible with steel at elevated temperatures. These include hot roll bonding, weld overlay, and explosion cladding. CRA alloys that are compatible with steel include the stainless steels and many of the nickel alloys. The clad bond produced during hot roll bonding is very similar to that produced in the coextrusion cladding of Zr and Zircaloy-2 for manufacture of barrier and triclad tubing [7] which is also discussed in the earlier Kroll Medal paper [8].

When the CRA alloy is not metallurgically compatible with steel, explosion cladding is generally the only viable clad manufacturing process. Zirconium is one of these alloys. Efforts to produce zirconium clad using hot rollbonding or weld overlay typically result in a brittle and highly cracked product. The Zr–Fe phase diagram explains this incompatibility [9]. The major problems are the highly stable $ZrFe_2$ intermetallic phase plus the low melting (934°C) Zr rich eutectic (84 % Zr). These two conditions make hot rollbonding and weld overlay

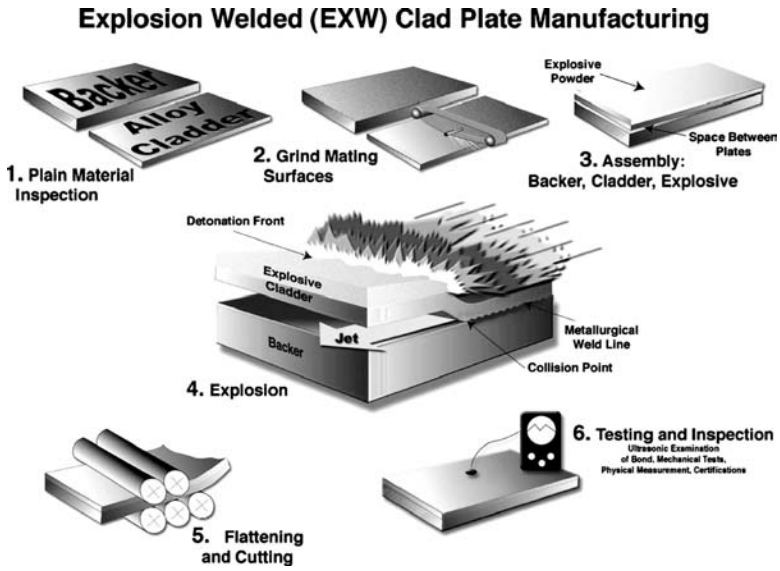


FIG. 3—*DMC's Detaclad explosive cladding process for manufacture of zirconium clad.*

virtually impossible unless interlayer metals, compatible with both Fe and Zr, are inserted. On the other hand, explosion cladding works well for making zirconium clad.

Explosion Cladding

The Detaclad explosion cladding technology was patented and industrialized by the DuPont Chemical Co. in the 1960s [10–13]. Explosion cladding utilizes the energy of an explosive detonation to achieve welding between two metal components. During the explosion cladding event, sheets of the CRA alloy are welded to plates of steel over the full contacting face area. Clad plate sizes can range from a few square centimetres up to around 50 m^2. The explosion clad interface is strong, tough, and highly reliable. Typical bond shear strength of zirconium clad manufactured Dynamic Materials Corporation (DMC) is around 200 MPa. Figure 3 depicts the Detaclad explosion clad manufacturing process. A broader discussion of the technology is presented in the references cited above.

Figure 4 presents a photomicrograph of an explosion clad interface. The wavy bond morphology is typical of the process. Optical microscopy shows no evidence of heating.

- No significant melt layers can be observed.
- There is significant cold work in the waves and no recrystallization is evident.
- Scanning electron microscopy studies show no evidence of diffusion.

Consequently explosion cladding is considered to be a cold welding process. Early researchers referred to it as a "solid state electron sharing bond." The

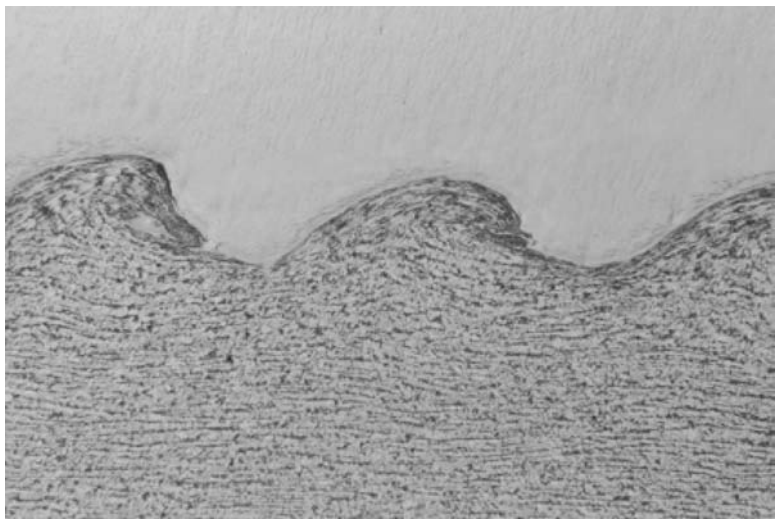


FIG. 4—*Typical explosion clad interface (~50×).*

bond interface was initially assumed to be similar in nature to a high energy grain boundary.

In more recent years, transmission electron microscopy (TEM) studies have provided better insight into the nature of the interface and the bonding mechanism. TEM studies indicate that very significant heating is occurring at the interface but on a scale barely observable with optical microscopy [14–16]. These TEM studies indicate the presence of a thin metallurgical weld, 0.1–0.2 μm thick. Further, they report indications of an amorphous structure of the resolidified weld metal. This suggests that the time at elevated temperature is extremely short and the cooling rates are extremely fast. Other research data indicate that the metals are heated to the welding conditions and returned to well below the melting point in less than 20 microseconds. The result is a metastable metallurgical condition at the interface. The stable and deleterious phases shown in the Zr–Fe phase diagram do not have time to form. Today, the explosion clad interface is frequently referred to as a "very thin, hyper cooled, fusion weld." One needs to be cautious when drawing broad conclusions from these studies. The number of studies of this type has been severely limited by the high cost of TEM work and the relatively small budgets of the explosion cladding companies and research groups. It is estimated that less than 20 specimens were extensively analyzed by TEM prior to 2008. Considering the area analyzed in a single TEM specimen, this is an extremely small sampling ratio.

Modern nano-scale analytical capabilities are beginning to provide further knowledge of the interface. Figure 5 presents TEM data from work performed by Song and others at Max-Planck Institute in 2008 and 2009. Although the work is on titanium-steel samples, we would expect similar results with zirconium clad. Ongoing studies at Max-Planck Institute, Oak Ridge National

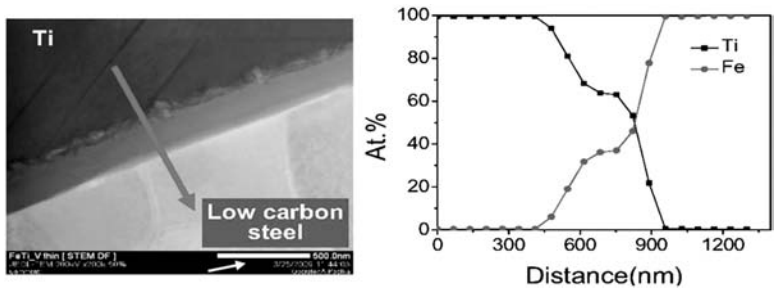


FIG. 5—*TEM analysis of titanium-steel interface (scale of picture at left: 1 cm=250 nm).*

Laboratory, and Colorado School of Mines are beginning to provide significantly more insight and understanding of the product and process.

Zirconium Clad Development and Manufacture

Zirconium-steel clad is generally considered to be the most difficult metal combination to produce by explosion cladding [17,18]. Contributing factors include the limited number of slip planes of the Zr crystal lattice, the high energy of formation of the $ZrFe_2$ intermetallic and the low melting temperature of the Zr–Fe (84–66 wt %) eutectic.

DuPont researchers developed zirconium clad manufacturing parameters in the 1960s. In the initial work, they observed the following.

- It was much easier to clad R60702 to titanium than to clad R60702 direct to steel
- It was relatively easy to clad titanium to steel
- Consequently, the use of a titanium interlayer between R60702 and steel was deemed to greatly simplify the process.

In the 1980s, researchers at the Explosive Fabricators, Inc. (now DMC) developed procedures for reliable industrial manufacture of high quality zirconium-steel clad without an interlayer. This effort involved the development of a number of process variants, which are unique to zirconium. Further, they observed that using zirconium with higher purity and lower strength than that mandated in the ASTM B551 for R60702 was highly beneficial. In support of this effort, ATI Wah Chang agreed to supply a variant of R60702 with reduced oxygen content (1000 ppm maximum), reduced strength, and enhanced ductility. This alloy, which was commonly referred to as "Zr 702 Low Ox" for many years, became the alloy of choice for zirconium clad. In 2003, that higher purity variant was established as R60700 and added to ASTM B551.

Today, clads of both zirconium bonded direct to steel and zirconium bonded to steel using a titanium interlayer can be found in the marketplace. Factors affecting the manufacturing route are cost, material availability, customer preference, and clad manufacturer's know-how. Considerable production data over the past 25 years demonstrate that zirconium clad produced by direct

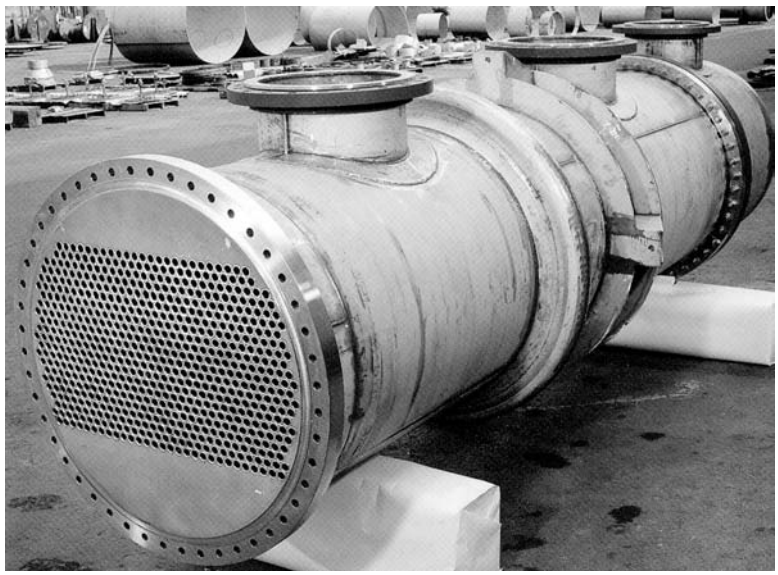


FIG. 6—*Nitric acid cooler condenser, zirconium tubes, zirconium-stainless steel clad tubesheet.*

bonding can be a highly reliable material for construction of process equipment [19].

Zirconium Clad for the Chemical Process Industry

Clad production for the first large CPI zirconium clad project was performed by Explosive Fabricators, Inc., in 1981. The clad plates were used to construct a rotary kiln for a zirconium producer. During the 1980s, zirconium clad pressure vessels and heat exchangers were selected for a number of highly corrosive chemical processes. These included pressure vessels for manufacture of acetic acid and various industrial and specialty chemical products. They also included heat exchangers for manufacture of nitric and numerous other acids. Details regarding the size and operating conditions of several of these units are presented in "Commercial Applications of Explosive Clad" published by ASTM in 1996 [20,21]. Figures 6–11 show several of these units and components of construction.

The pressure vessel for acetic acid manufacture provides a good case study of vessel design options and considerations. This unit was used in a licensed methanol carbonylation process. The process had been developed in the late 1960s and early 1970s and had originally used nickel alloy equipment. The specific nickel alloy being used provided adequate corrosion protection; however, the alloy exhibited a tendency to fail by stress corrosion cracking unless the welded structure was precisely heat treated and water quenched after complete

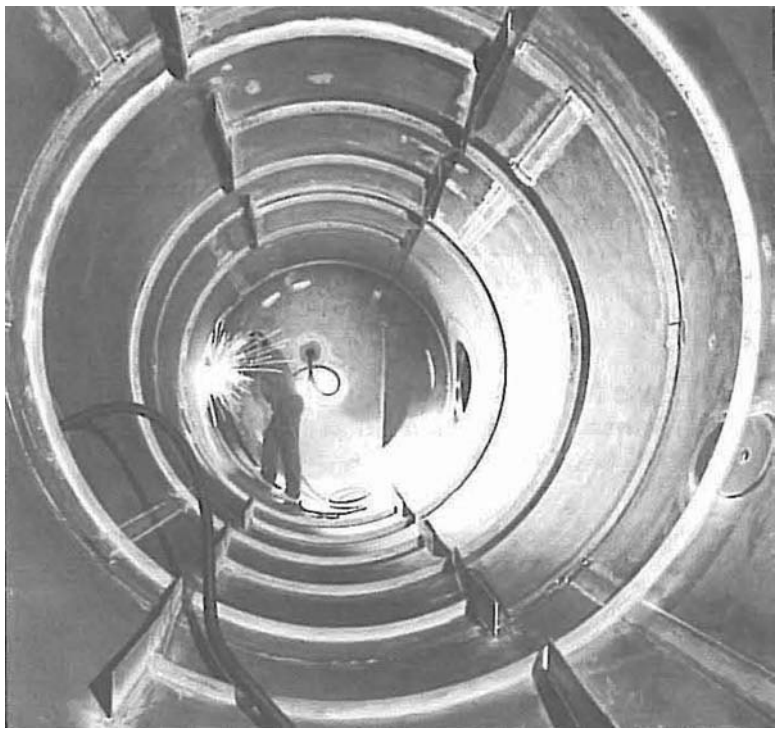


FIG. 7—*Interior view of zirconium clad column during fabrication, 2.5 m diameter.*

fabrication. The reliable manufacturing window was exceptionally narrow. Ongoing fabrication challenges encouraged the process management team to seek a more predictable material. The background of the replacement of nickel alloy with zirconium in this process is presented in Sanders' Kroll Award Paper [22]. Much of the process equipment was relatively light wall and could easily justify a change from nickel alloy to zirconium on cost reduction. On the other hand, the main pressure vessel presented a significant cost challenge. It was $\sim$3.5 m diameter $\times$ 5.0 m tall and operated under conditions that required well over 100 mm wall thickness of R60702. The R60702 design was considerably more expensive than nickel alloy, so sufficiently that the increased performance of zirconium could not alone justify the higher capital cost. In the early 1980s, one of the process licensees chose to proceed with installation of a zirconium clad main pressure vessel. This would be the first heavy-walled zirconium clad vessel ever constructed and required numerous design and fabrication innovations. The zirconium clad pressure vessel had lower cost than the traditional nickel alloy unit. Further, the superior corrosion performance of zirconium allowed the unit to be operated under more aggressive conditions, improving process yields. Subsequently zirconium clad has become the standard for this and similar acetic acid pressure vessels.



FIG. 8—*Zirconium clad heads hot formed after cladding. Largest are 3.7 m diameter.*

Figure 6 shows a typical nitric acid heat exchanger. This unit is a good case study of the benefits of clad in shell-and-tube heat exchanger design. The tubesheet is explosion clad Zr/stainless steel. The clad tubesheet enables the designer to select zirconium for the tube-side components and stainless steel for the shell side components but to still be able to fully weld the tubes to the tubesheet and



FIG. 9—*Zirconium clad reactor with external steel heating jacket. ~3.0 m diameter with wall thickness of 25 mm steel +3 mm Zr.*



FIG. 10—*Zirconium clad tubesheet blanks for a Urea process heat exchanger. Tubesheets are 2750 mm diameter, 500 mm steel thickness, and 10 mm R60700 thickness.*

the tubesheet to the shell, eliminating potential leakage problems. Combining the benefits of Zr tube-to-tubesheet welds, the cost reductions of a steel shell, and the fully-welded shell to tubesheet joint is not possible if solid zirconium tubesheets are used.

The road to broad CPI industry acceptance of zirconium clad involved many efforts in addition to simply learning how to manufacture the clad. These included the development of fabrication techniques [23,24], the development of ASTM B898 for reactive metal clad [25,26], and the development of a zirconium grade specifically designed for explosion cladding, ASTM B551 Alloy 700.



FIG. 11—*Typical large shell-and-tube heat exchanger with reactive metal clad tubesheets.*

Today, zirconium explosion clad is broadly accepted as a reliable material of construction for CPI equipment. The cost reductions of clad construction have enabled the use of zirconium in a number of CPI processes where solid zirconium construction had previously been rejected due to it very high cost. A review of manufacturing records indicates that three zirconium clad pressure vessels were put into service in the 1980s, 12 in the 1990s, and over 30 in the 2000–2009 time period. Over this period, hundreds of zirconium heat exchangers with clad tubesheets were put into service. Virtually all of this equipment has provided highly reliable service and continues in operation. When there have been problems, they have typically been traced to untrained equipment fabricators or engineers duplicating equipment previously designed in stainless steel without making modifications for the differences in basic physical and mechanical properties between stainless steel and zirconium [27].

Conclusion

Zirconium is an exceptional material for containment of corrosive media in CPI processes. The corrosion resistance of zirconium is exceptional in a broad range of aggressively corrosive environments. For heavier wall equipment, it is difficult for the superior benefits of zirconium to justify the increased cost of solid zirconium when compared to alternative but inferior CRAs. Explosion cladding has enabled CPI companies to benefit from the superior performance features of zirconium in heavy-wall pressure vessels and heat exchangers in a cost effective way. Zirconium clad has become a broadly accepted material of

construction for a broad range of chemical process equipment. Zirconium clad design, manufacture, and fabrication process, which have been developed over the past 30 years, are highly reliable, robust, and reduce both capital and operating cost.

References

[1] Hamner, N. E., *Corrosion Data Survey*, NACE, Houston, TX, 1994.

[2] Cox, B., "Oxidation of Zirconium and Its Alloys," *Advances in Corrosion Science and Technology*, M. G. Fontana and R. W. Staehle, Eds., Plenum Press, New York, 1976, Vol. 5, p. 173.

[3] Yau, T. L. and Webster, R. T., "Corrosion of Zirconium and Hafnium," *Corrosion*, ASM Handbook, Vol. 13, 9th ed., ASM International, Metals Park, OH, 1987, p. 707.

[4] ASTM B551, 2007, "Standard Specification for Zirconium and Zirconium Alloy Sheet, Strip and Plate," *Annual Book of ASTM Standards*, Vol. 02.04, ASTM International, West Conshohocken, PA, pp. 510–520.

[5] *ASME Boiler and Pressure Vessel Code*, Section II: Materials, Part D: Properties, American Society of Mechanical Engineers, New York, 1998.

[6] ASTM A516-70, 2010, "Standard Specification for Pressure Vessel Plates, Carbon Steel, for Moderate- and Lower-Temperature Service," *Annual Book of ASTM Standards*, Vol. 01.04, ASTM International, West Conshohocken, PA, pp. 281–284.

[7] Williams, C. D., Marlowe, M. O., Adamson, R. B., Wisner, S. B., Rand, A., and Armijo, J. S., "Zircaloy-2 Lined Zirconium Barrier Fuel Cladding," *Zirconium in the Nuclear Industry: 11th International Symposium, ASTM STP 1295*, Garmisch-Partenkerchen, Germany, 1996, E. R. Bradely and G. P. Sabol, Eds., ASTM International, West Conshohocken, PA, pp. 676–694.

[8] Armijo, J. S., Coffin, L. F., and Rosenbaum, H. S., "Development of Zirconium-Barrier Fuel Cladding," *Zirconium in the Nuclear Industry: Tenth International Symposium, ASTM STP 1245*, Baltimore, MD, 1994, A. M. Garde and E. R. Bradeley, Eds., ASTM International, West Conshohocken, PA, pp. 3–18.

[9] Hansen, M., *Constitution of Binary Alloys*, McGraw-Hill Book Company, New York, 1958, p. 742.

[10] Holtzman, A. H. and Cowan, G. R., "Bonding of Metals with Explosives," *Welding Research Council Bulletin* 104, American Welding Society, New York, April 1965.

[11] Pokolyko, A., "Explosively Clad Metals," *Encyclopedia of Chemical Technology*, Vol. 15, 3rd ed., John Wiley & Sons, New York, 1981, pp. 275–296.

[12] Cowan, G. R., Douglass, J. J., and Holtzman, A. H., "Explosive Bonding," U.S. Patent 3,137,937 (1964).

[13] Banker, J. G. and Reineke, E. G., 1993, "Explosion Welding," *Welding, Brazing, and Soldering*, ASM Handbook, Vol. **6**, ASM International, Metals Park, OH, pp. 303–305.

[14] Hammerschmidt, M. and Kreye, H., "TEM Investigation of the Microstructure Affected by the Bonding Process During Oblique Collision of Metallic Surfaces," *Fifth International Symposium Explosive Working of Metals*, Gottwaldov, Oct. 12–14, 1982, Czechoslovak Scientific and Technical Society, Gottwaldov, Czechoslovakia.

[15] Chiba, A., Minoru, N., and Yasuhiro, M., "Microstructure of Bonding Interface in Explosively-Welded Clads and Bonding Mechanism," Mater. Sci. Forum, Vol. 465–475, 2004, pp. 465–474.

[16] Lafont, M. C., Masri, T., and Nobili, A., "Recent Developments in Characterization of a Titanium-Steel Explosion Bond Interface," *Reactive Metals in Corrosive Applications Conference Proceedings*, Sun River, OR, 1999, J. Haygarth and J. Tosdale, Eds., Wah Chang, Albany, OR, pp. 89–98.
[17] Banker, J. and Winsky, J., "Zirconium Explosion Clad for Cost Effective Process Equipment: Applications, Design, Fabrication," *Proceedings of 1997 Zirconium/Organics Conference*, Gleneden Beach, OR, September 1997, ATI Wah Chang, Albany, OR, pp. 71–78.
[18] Nobili, A. and Banker, J., "Recent Developments in Zirconium-Steel Explosion Clad," *Proceedings 1999 Reactive Metals in Corrosive Applications Conference*, Sun River, OR, September 1999, ATI Wah Chang, Albany, OR, pp. 83–88.
[19] Nobili, A., Banker, J., and Prothe, C., "Continuing Innovation in Zirconium Explosion Clad Manufacturing," *Proceedings Corrosion Solutions Conference*, Sun River, OR, September 2001, ATI Wah Chang, Albany, OR.
[20] Banker, J., "Commercial Applications of Zirconium Explosion Clad," *J. Test. Eval.*, Vol. 24, No. 2, 1996, pp. 91–95.
[21] Banker, J., "Commercial Applications of Zirconium Explosion Clad," Presented at *ASTM Symposium on Industrial Applications of Titanium and Zirconium*, Phoenix, AZ, November 1994, ASTM International, West Conshohocken, PA.
[22] Sanders, B. J., "Zirconium Corrosion Resistance: Key to Success of the Methanol Carbonylation Acetic Acid Process," *The Kroll Medal Papers (1975–2010): Unique and Lasting Contributions to the Technology of Zirconium*, ASTM International, West Conshohocken, PA, 2010.
[23] Banker, J. and Frey, D., "Zirconium Clad Pressure Vessels Offer Cost Savings in Highly Corrosive HCl Service," *Proceedings Corrosion Solutions Conference*, Sun River, OR, September 2001, ATI Wah Chang, Albany, OR.
[24] Prothe, C. E. and Banker, J. G., "Reactive Metal Clad Steel—Hot Working Considerations," *Proceedings Corrosion Solutions Conference*, Park City, OR, September 2009, ATI Wah Chang, Albany, OR.
[25] ASTM B898, 2007, "Standard Specification for Reactive and Refractory Metal Clad Plate," *Annual Book of ASTM Standards*, Vol. 02.04, ASTM International, West Conshohocken, PA, pp. 1112–1118.
[26] Banker, J., "An Introduction to ASTM B898, the Reactive and Refractory Clad Metal Plate Specification," *Proceedings Corrosion Solutions Conference*, Sun River, OR, September 2001, ATI Wah Chang, Albany, OR.
[27] Banker, J. G., Sutherlin, R., and Henry, N., "Study of Two Reactive Metal Heat Exchanger Failures," *Proceedings Corrosion Solutions Conference*, Park City, UT, September 2009, ATI Wah Chang, Albany, OR.

Reprinted from JAI, Vol. 7, No. 6
doi:10.1520/JAI103032
Available online at www.astm.org/JAI

David G. Franklin[1]

Performance of Zirconium Alloys in Light Water Reactors with a Review of Nodular Corrosion

ABSTRACT: This paper provides historical context and future direction on selected contributions to understanding zirconium-alloy deformation and corrosion in light water reactors. More detailed discussion of the relative importance of electrochemical potential and hydrogen pickup on nodular corrosion is provided. Since nodular corrosion was observed about 50 years ago, several explanations have been proposed. None have explained all the observations, especially the sharp transition between nodular-free and nodular-covered regions of some fuel rods, with the transition being reversed between high- and low-power regions. However, the effect of electrochemical potential dominates any effects of hydrogen, other than the effect of hydrogen on electrochemical potential.

KEYWORDS: Zircaloy, corrosion, deformation

Introduction

Concerning the Kroll Medal award, all of the writer's supporting colleagues cannot be mentioned for there are too many, but some must be. At the Bettis Atomic Power Laboratory, the birthplace of the zirconium alloys, the writer benefited greatly from the contributions of other Bettis staff, past and present. Those privileged to work within the Naval Nuclear Propulsion Program benefited from the culture built and left as a legacy by Admiral Rickover, the first Kroll Medal recipient. Pieter Kreyns and Bruce Kammenzind deserve special thanks. While at the Electric Power Research Institute, Albert Machiels, Stephen Gehl, Joseph Santucci, and Rosa Yang provided much support; Professor

Manuscript received February 9, 2010; accepted for publication May 7, 2010; published online July 2010.

[1] Retired from Bettis Atomic Power Laboratory now at 2212 Grier Woods Ct., Las Vegas, NV 89134.

Cite as: Franklin, D. G., "Performance of Zirconium Alloys in Light Water Reactors with a Review of Nodular Corrosion," *J. ASTM Intl.*, Vol. 7, No. 6. doi:10.1520/JAI103032.

Copyright © 2011 by ASTM International, 100 Barr Harbor Drive, PO Box C700, West Conshohocken, PA 19428-2959.

Eugene Lucas at the University of California in Santa Barbara was instrumental in preparation of the monograph on creep of zirconium alloys [1]; and Ronald Adamson contributed greatly to my understanding of deformation phenomena.

Three ongoing or recent developments result in the need for additional understanding about the performance of zirconium alloys in nuclear applications. First, new reactor designs that could result in different operating conditions continue to be developed. Second, the drive to reduce fuel-cycle cost continues and results in additional demand on zirconium-alloy structural materials, especially fuel-element cladding. Third, a change in the U.S. plans to close the fuel cycle may result in much longer spent-fuel storage times prior to disposal, which could increase demand for the zirconium-alloy core structural materials. These developments are considered in reviewing the contributions. One topic, nodular corrosion, is selected for review in detail.

General Aspects of Performance of Zirconium Alloys in Nuclear Applications

Corrosion and deformation continue to be important phenomena for future nuclear applications. Other properties not addressed herein have varying degrees of importance, for example, hydrogen effects remain important, especially at extended exposures, while physical properties like conductivity are relatively well known. Although off-normal conditions, for example, loss-of-coolant conditions, will not be addressed directly, one historical perspective is worth noting because of the reminder it provides. In 1984, several of us concluded that work on high-temperature properties was sufficient and that this area of study should be reviewed and summarized for the next ASTM symposium on Zirconium in the Nuclear Industry with an eye toward reducing resources applied to this area. We asked F.J. Erbacher of the Institut fűr Reaktorbauelemente in Germany to prepare a review paper for the 1985 Strasbourg, France symposium. He and S. Leistikow provided an excellent paper [2], and no sessions on this topic were included for the next five symposia. However, our optimism was not justified, due in part to the industry drive to increase exposures. This topic reappeared as a session at the 13th symposium in 2001. We were reminded that all aspects of performance must be monitored and considered as the industry progresses, conditions change, and knowledge expands.

Concerning deformation, the impacts of mispredicting deformation can be unacceptable. Several of the early and dramatic issues with the use of zirconium alloys as fuel cladding were due to misunderstanding deformation. In 1988, Ron Adamson and the writer provided a review of the effects of creep and growth of Zircaloy-clad fuel rods [3], showing some of the observed effects of not adequately taking into account the effects of creep and growth. Two dramatic examples are (1) cladding creep and collapse into fueled regions vacated by densified fuel and (2) fuel-rod interactions due to growth. For new staff working on in-reactor fuel performance, a review of those dramatic examples is worthwhile, both to understand the past and to realize the importance of their work. Since that time, much work has been done, especially on engineering

aspects of creep and growth, with much of the work reported in the ASTM symposium series on Zirconium in the nuclear industry. These studies extend the basis for predicting behavior to new alloys and increased exposures. Finally, in contrast to the performance of stainless steels in liquid-metal fast breeder reactors, zirconium alloys did not swell significantly from the formation of irradiation-induced voids for light water reactor (LWR) conditions, so an engineering need to model this phenomenon did not develop.

Cladding creep was a concern in the 1960s and 1970s due to its impact on the fuel-to-cladding gap, which, in addition to the example above of cladding collapse, influenced fuel-pellet stored energy, mechanical interactions, including stress corrosion cracking, and fuel-rod growth. In pressure-tube reactors, for example, the Canadian reactors, creep of the pressure tube also was an issue due to the long exposure times. The effects of irradiation, which enhanced creep during irradiation but inhibited creep postirradiation, were surprising and proved to be a challenge to measure and model. During this period, especially before fuel densification was resolved, in-reactor deformation and mechanical properties were considered by many to be more challenging than corrosion. Initially, modeling was fairly simple with some phenomenological aspects in correlations. In the middle 1970s, we attempted to include grain orientation and texture into creep modeling [4], but the general tools were not advanced enough to result in direct applications. As described by Nichols in his Kroll acceptance paper [5], this situation was being remedied by advances both in material-modeling techniques and computing power. Tenckhoff in his Kroll acceptance paper [6] summarized texture aspects.

In the 1970s, the Materials Research Council asked A.L. Bement, G.E. Lucas, and the writer to prepare a monograph on creep of zirconium alloys in nuclear applications, which ASTM published [1]. That effort covered engineering, modeling, and mechanistic studies. Recent models generally are phenomenological incorporations of detailed deformation behavior, for example, by Gelebart et al. [7] and Allen et al. [8]. In parallel, the major Nuclear Steam Supply System providers and some research organizations, for example, the Department of Energy and the Electric Power Research Institute in the United States, developed larger databases. Still, additional benefit can be obtained from the development of data that support more-mechanistic models.

Concerning corrosion, the selection of zirconium by the U.S. Naval Nuclear Propulsion Program as the base metal was, in part, based on the need for corrosion resistance. Therefore, it has been studied and reviewed many times, starting with those who preceded the writer at Bettis, for example Kass [9] and Hillner [10], and continuing through recent reviews by career experts such as Brian Cox. Cox's 2005 review 11 provides a good perspective on nodular corrosion, although the conclusions below are not the same in all respects. Despite the extensive studies on corrosion, the fundamentals are not fully revealed.

The need for additional research on deformation and corrosion is driven by the three changes discussed in the introduction. With new alloys and new conditions associated with either new reactor designs or increased exposures, additional studies will be needed to confirm or revise existing models. An important

recent change is due to the decision in the United States to reconsider the best way to deal with high-level waste. Specifically, the Department of Energy is considering options other than disposal at a Yucca Mountain repository. Some options would result in very-long-term storage of spent-fuel assemblies. The result could be that there is a need to ensure fuel cladding and assembly integrity during very-long-term storage, in part due to the possibility of subsequent handling. Cladding creep, rupture, and handling damage need to be understood for the conditions selected, although those conditions are not known fully. Hydrogen effects may be important due to the effect on mechanical performance. Work is being performed in this area, for example, as reported by Tsai and Billone [12] at the 14th ASTM symposium and by a session with three papers at the 15th symposium [13–15].

For very-long-term storage, inert atmospheres would prevent corrosion and hydrogen pickup. If water or air environments need to be considered in either storage or disposal, Bettis addressed such corrosion for Zircaloy based on 30-year autoclave data [16]. We concluded that the postirradiation corrosion rate returns to or returns close to the nonirradiated corrosion rate, allowing the use of these nonirradiated data. This conclusion was based on in-reactor flux and temperature-shift tests and on two previous postirradiation studies, one by Garzarolli et al. [17] and one by Cheng et al. [18]. Although the latter paper had confusing results for 400°C steam, the more-relevant results for 316°C water were not ambiguous, nor were the results of Garzarolli et al. More recently, Iltis et al. [19] studied postirradiation corrosion effects and the associated causes, especially the effects of irradiation-induced iron dissolution and in-reactor environmental parameters. Their results suggested that iron in solution and its reprecipitation could be controlling the postirradiation results reported previously [17,18]. However, their 400°C postirradiation tests were confusing because there appeared to be irradiation enhancement between 60 and 210 days, but not for the next test period of over 100 days. Since the Cheng et al. [18] results were also mixed at 400°C, model databases may need to be limited to postirradiation testing performed at lower more-prototypical temperatures to obtain unambiguous results. Considering that inert environments may be used for storage and that the corrosion rates can be predicted if water or air is used, the corrosion and hydrogen pickup can be predicted for long storage times for cladding with normal exposures. Some fundamental results that were intended to apply to in-reactor corrosion may help to understand postirradiation performance, especially the memory effects for changing from in-reactor to postirradiation corrosion. For example, studies on the influence of solutes in the oxide on corrosion, as discussed by Cheng and Adamson [20], and the results of Iltis et al. [19] on iron effects, may be a part of the memory effect. For high-exposure cladding, there may be a need for additional postirradiation testing if air environments must be presumed. Some relevant fundamental work is being done on postirradiation corrosion properties, for example, using impedance spectroscopy, which began in the 1950s and became fairly sophisticated by 1980s [21]. Although valuable, these techniques are not as direct as the postirradiation corrosion measurements and the results need to be considered subservient to the direct measurements.

Nodular Corrosion

Nodular corrosion was reported first in the 1960s [22–25]. There was a concern that this accelerated localized corrosion would lead to cladding failures, and much work was initiated to understand nodular corrosion. It was not initially realized that there was a self-limiting aspect to nodular corrosion for most LWR conditions. This phenomenon does not appear only as isolated surface spots. It can appear as accelerated corrosion that covers much or all of a surface. It is distinguished better by the conditions that cause the accelerated corrosion than by its appearance. At reactor temperatures, nodular corrosion requires oxidizing conditions and irradiation, as summarized in many reviews [26,27]. Although dissolved coolant O_2 concentration can be simulated out of reactor, sufficient irradiation is difficult to simulate [28]. Nodule formation in LWRs may be promoted by lower temperatures, which would reduce the rate at which thermal processes remove the effects of irradiation, but such an effect has not been demonstrated conclusively.

At the 1985 ASTM symposium, several papers addressed important aspects of nodular corrosion. Important work at General Electric (GE) was presented and the paper by Cheng and Adamson [20] provided a particularly important contribution, which is discussed later. The most perplexing of the observations of nodular corrosion, and as yet not well explained, is the sharp change in nodular coverage in a boiling-water reactor (BWR) at the blanket-to-fuel transition, which we discussed and correlated with heat flux and other variables [29]. In low-power fuel rods, there was a sharp transition from no nodules to nodules at approximately the axial height of the transition from the lower blanket to the fueled region. High-flux rods had the opposite observation. That paper discussed the possible impact of heat flux and other variables on the observed nodule formation, but no fundamental or mechanistic understanding of these observations was available. Effects of heat flux had been reported earlier, for example, by Urquhart and Vermilyea [30], who reported that more nodules formed on channels with no heat flux than on fuel-rod cladding. Marlowe et al. [31] reported two similar observations on the effects of heat flux: (1) Gd-doped UO_2 rods, which had low-heat-fluxes early in life, had more nodules than UO_2 rods and (2) nonfueled regions of test rods had more nodules than fueled regions. Mishima and Aoki 32 reported grayish-white corrosion at the bottom of fuel rods, which could be full nodular coverage, although they did not describe it as nodular corrosion. Etoh 33 also investigated the effects of heat flux and found a correlation between nodule thickness and heat flux.

The previous evaluation of the nodule coverage change at approximately the enrichment transition [29] was not able to correlate this change with more-fundamental variables than heat flux. Previous studies of nodular corrosion associated nodule formation with electrochemical potential and hydrogen pickup. However, the relative importance of these and other variables, and how they affect nodule formation are not understood fully. Since the roles of hydrogen and electrochemical potential are the primary candidates in the literature for causing nodule formation, they will be the focus of this discussion. The discussion is limited to exposures typical for the occurrence of nodules, which

usually appear in the first reactor cycle [32], well before corrosion in BWRs accelerates after four or five cycles [34]. This limitation on exposure is important because the effects of hydrogen pickup may be different at high exposures and large hydrogen pickup. Etoh et al. [35] demonstrated this limited time period for nodule formation in postirradiation tests on nodular-susceptible Zircaloy-2.

Effect of Hydrogen

Detrimental effects of hydrogen pickup were considered early in the development of zirconium alloys [36]. Several investigators suggested that increasing hydrogen concentration near the metal-to-oxide interface contributed to nodule formation [20,37–39]. However, hydrogen concentration, both in the coolant and in Zircaloys that formed nodules in reactor, did not correlate, and probably correlated inversely with nodule formation. The primary observations were:

- Increasing H_2 concentration in the coolant suppressed nodule formation in LWRs [40,41].
- Hydrogen pickup fraction in Zircaloy in BWRs was low at the exposures where nodules formed [25,32].
- Specialized test-reactor experiments showed no correlation, as shown by Aomi et al. [41] and Takagawa et al. [42] with experiments in the Halden test reactor. Increasing dissolved H_2 in the water to 400 parts per billion (ppb) eliminated nodules, despite an increase in hydrogen concentration in the samples.
- Hydrogen pickup correlation with second-phase particle (SPP) size was inconsistent with the effect of solutes on nodule formation. For instance, Huang et al. [43] and Tagstrom et al. [44] found that the hydrogen pickup increased with increasing solute concentration and with decreasing initial SPP sizes. This observation, when combined with Cheng and Adamson's [20] demonstration that nodule resistance increased with decreasing initial SPP size, suggested that, if anything, nodule formation correlated with low hydrogen pickup.
- The sharp transition in corrosion coverage at the enrichment transition did not support hydrogen being a significant factor because there was no basis for an associated variation in hydrogen concentration at the enrichment transition.

Hydrogen transport through the oxide has been related to the potential across the oxide [45]. However, an increase in the coolant dissolved H_2 content decreases the oxide potential drop, as demonstrated in the section below titled *Electrochemical Potential*. Therefore, increased water H_2 content decreases the driving force of the potential gradient on H^+ diffusion through the oxide. In the end, the sources of each of the drivers for hydrogen diffusion, and oxygen migration for that matter, are the changes in Gibbs free energy from oxidation and reduction reactions, so the individual processes need to not be considered in isolation.

There are suggestions that a greater hydrogen concentration at the base of nodules than away from nodules supports hydrogen as the cause [38]. However, if there is increased hydrogen at the base of nodules, it is likely the result of the

breakdown of the oxide film rather than the cause of the breakdown, given the observations discussed above. In supporting hydrogen as the cause, Rudling and Wikmark [38] referred to pressurized water reactors (PWRs) not forming nodules because PWR temperatures are high enough for hydrogen to diffuse from the base of an SPP before forming a hydride, while this diffusion is slower in BWRs due to the lower BWR temperatures. However, when a PWR operates with low dissolved H_2 in the coolant, nodules do form, as observed in Obrigheim and other reactors, and discussed above. Therefore, the correlating difference in BWR and PWR nodule susceptibility is water chemistry, specifically, water hydrogen concentration and electrochemical potential, and not temperature, with increasing dissolved H_2 suppressing rather than promoting nodule formation. That is not to say that temperature does not affect nodule susceptibility. The rates of recombination of radiolytically produced species and the transport of anion vacancies and electrons through the oxide increase with increasing temperature. The impacts of such changes are discussed below in the section on polarization.

In conclusion, hydrogen concentrations, at least at concentrations observed in BWRs through several cycles, do not contribute to nodule formation. This conclusion does not apply to zirconium alloys at high exposures with high hydrogen concentrations, but this limitation is not important since nodules form early.

Effects of Second-Phase Particles (SPPs)

The nodule-formation requirement for both irradiation flux and low coolant H_2 concentration is related to the concentration of oxidizing species at the oxide barrier-layer interface with the water. This concentration affects the electrochemical potential[2] at that surface. Irradiation produces oxidizing species, which increase the potential at the external surface. Coolant H_2 concentration, recombination, transfer into the steam phase, and transport through the oxide remove oxidizing species, which decreases the external-surface potential.

By 1985, the effects of SPPs on nodular corrosion, especially in autoclave tests, were extensively studied, as evidenced by a number of papers at the seventh ASTM symposium [20,46–51]. It was clear that nodule formation correlated with large SPPs and resistance to nodule formation correlated with small SPPs. The Cheng and Adamson paper [20] suggested a mechanism based on solute concentration in solution, of which most parts have been supported by subsequent studies. Ogata [52] suggested that nodule frequency correlated with regions of low-solute concentration, supporting Cheng and Adamson. In a variation on the Cheng and Adamson model, Etoh [33] suggested that irradiation flux homogenizes solute concentrations, especially Fe and Ni solutes, throughout the matrix. Subsequent reprecipitation creates neighboring regions of low-solute concentration. Etoh still considered nodules to form in regions of low-solute concentrations, but the proposed way these regions formed was different. Although many supported the conclusion that nodules form in matrix devoid of solutes, it is not accepted universally, the above-discussed model by Rudling

[2]When potential is used herein, it refers to the electrochemical potential.

and Wikmark [38] being an example. Based on the preponderance of the information, it is concluded that the Cheng and Adamson model for nodule formation at regions low in solute concentration is likely correct.

Effects of Variables of Lesser Importance

Cox included in his comprehensive review of corrosion [53], which he updated in 2005 [11], a discussion of variables that can impact corrosion. In the present discussion, only a few of the variables presented by Cox will be discussed. Mechanical and structural aspects were suggested early on to contribute to or cause oxide breakdown or nodule formation. The large volume expansion on ZrO_2 formation creates large compressive stresses in the oxide, which promotes deformation and fracture. However, Zhou [54] could not find oxide damage to support it as the cause of nodule formation. He concluded nodules form partially as a result of deformation in the metal, which produces dislocation short circuits for oxygen diffusion into the metal, which increases the anion-vacancy concentration in the oxide and oxygen diffusion through the oxide. Nodule formation may also be influenced by texture [55], grain size, and cold work. Charquet et al. [56] considered the effects of grain size and texture and concluded that they have little effect for nodule-resistant fine-SPP and nodule-susceptible large-SPP materials. However, for intermediate materials, if several favorably oriented grains are located together, he suggested that nodule formation could be promoted.

Oxide dissolution and reprecipitation was shown by Nishino et al. [28] to occur under certain conditions and to increase with gamma irradiation. This phenomenon has also been associated with the transformation from tetragonal to monoclinic zirconia. They suggested that this process produced microcracks in the oxide, which contributed to the oxide breakdown and nodule formation. This process would be promoted by high pH, particularly from LiOH additions. Although this process cannot be excluded from contributing to oxide breakdown, the demonstrated effect of coolant dissolved H_2 concentration to suppress nodule formation and the relatively low pH in BWRs makes it unlikely that this process is a significant contributor to nodule formation.

These and other factors may have some effect, but the results are mixed. A clue to their importance is provided by the observations that we are trying to understand; the sharp transitions in nodular corrosion along the axis of fuel rods [29] at blanket-to-fuel transitions. Material properties such as grain size, texture, and deformation do not vary systematically with such sharp transitions along the axis of the fuel cladding, but the variation in nodular formation does. To be important, these variables would need to be shown to work in concert with a variable that varies axially, which has not been shown, and for which there is no theoretical basis. Therefore, these properties are at most minor contributors to nodule susceptibility.

Phenomena Driving Nodule Formation

The following factors will be evaluated for their contributions to nodular corrosion: Electrochemical potential of the environment, modification of the

potential across the oxide by changes in the controlling reaction or changes in concentration of the oxidizing species at the oxide barrier-layer external surface, and the effect that oxygen potential has on the nodule formation. The effect of each is reviewed and then related to the observed sharp axial changes in nodule formation near enrichment changes [29].

Electrochemical Potential

Early work of researchers like Cox at AECL [57], Urquhart et al. [37,58] at GE, and Rosecrans [21] at the Knolls Atomic Power Laboratory, demonstrated the importance of the electrochemical nature of Zr-alloy corrosion. Urquhart et al. measured 600 mV for nodule-susceptible Zircaloy in 500°C 1500-psi steam. Theoretical calculations for the in-reactor oxygen concentrations associated with the conditions for nodule formation can be used to estimate these potentials. For example, in the International Atomic Energy Agency (IAEA) [27,59] reviews, radiolysis calculations illustrated that the irradiation of nonoxygenated water results in an increase in the O_2 concentration, $\{O_2\}$, by over eight orders of magnitude and $\{O_2^-\}$ by over six orders of magnitude. Hydrogen addition, which changes the water from nodule promoting to nodule resistant, to a system with 200 ppb dissolved $\{O_2\}$ was predicted to decrease $\{O_2\}$ by four orders of magnitude and $\{O_2^-\}$ by even more. Using the Nernst equation one can estimate the effect on potential for such changes in concentration, that is, using $RT\ln(a_1/a_2)/nF$, where R is the gas constant $(8.314\,\mathrm{J/deg \cdot mol})$, T is absolute temperature, a is activity (a_1 and a_2 being the activities for a change between water chemistries 1 and 2), n is the charge transfer, and F is Faraday's constant (96 500 C/eq). With activity taken to be concentration for this application, the increase in potential for concentration changes (a_1/a_2) of 10^5 for $n = 2$ at 300°C is about 280 mV. This simple calculation is only for perspective as it ignores the possibility of changes in the controlling reactions. Still, it demonstrates that there is not an inconsistency between the expected effect of irradiation on potential and the observed potentials that are associated with nodule formation. The effect of the other oxidizing species with large concentration changes is not straightforward, but should promote nodule formation. These results suggest that nodule formation is associated with corrosion potentials of no more than 600 mV. Now we consider when such corrosion potentials (electrochemical potential (ECP)) occur in reactors.

Measurements of ECP in BWRs were made to support programs to reduce the stress corrosion cracking of stainless steels. For example, Cowan [60], Hettiarachchi et al. [61,62] reported ECP as a function of coolant H_2 and O_2 concentrations, with and without the catalyzing effects of noble-metal surfaces. In the absence of noble-metal surfaces, ECP decreased from above 200 mV to about −400 mV (standard hydrogen electrode (SHE)) with increasing H_2 concentration. With noble-metal surfaces, ECP decreased from about −50 to −500 mV, with much less H_2 required for the ECP decrease. In summary, ECP measured in BWR conditions that experienced nodular corrosion are several hundred millivolts without H_2 additions. H_2 additions reduce the ECP by 450–600 mV. Since the interpretation of in-reactor BWR measurements for the effects of

coolant H_2 and O_2 concentrations on ECP is complicated by the effects of boiling, we consider recent measurements without boiling.

Rishel et al. [63], using a special loop in the Halden reactor in Norway to replicate PWR conditions, measured the differences in potential between oxygenated and hydrogenated nonboiling coolant conditions. The reported potentials are not corrected to be referenced to the SHE, but the application here needs only the relative potential differences between conditions with H_2 added (time steps 22 and 23) and with O_2 added (time steps 29 through 37) into the coolant. For the high-flux in-core regions, that is, those regions within the booster rods, the potential for oxygenated conditions was 500–700 mV different from that for hydrogenated conditions and somewhat less for the region outside the booster rods. These experiments provide two relevant results on the effects of irradiation, $\{O_2\}$, and $\{H_2\}$ on corrosion potential at the oxide-to-coolant interface:

(1) The potential differences between (a) the last time periods with H_2 added to the water prior to adding O_2 and (b) subsequent time periods with O_2 addition and no added H_2 were 500–700 mV after allowing several time steps needed to reach equilibrium in the high-flux locations. This change in potential may include both changes in concentrations of oxidizing species and controlling reactions.

(2) In the moderate-flux region above the booster rods, the similar potential difference is 100–200 mV, demonstrating the significant effect of irradiation flux on electrochemical potential for oxygenated conditions, while there is relatively little effect for hydrogenated conditions. Apparently, relatively small changes in irradiation flux in high-flux oxygenated-coolant conditions change significantly the local corrosion potential.

These results must be considered with caution because the reported interpretation was that the addition of O_2 resulted in a measurement of more reducing conditions, which means that there may have been a problem in the interpretation of the results or in the conduction of the tests. Ruiz et al. [64] measured the effect of hydrogen concentration in the plenum of a BWR and found that the potential decreased by about 550 mV as hydrogen concentration increased to about 2.5 parts per million, confirming the effect of coolant hydrogen on potential in BWR oxygenated coolant. In general, the strong effect of $\{O_2\}$ and $\{H_2\}$ on potential and the correlations between potential and nodule susceptibility support potential being a major factor in nodule susceptibility. This importance of potential, which is ascribed above to be highly influenced by the concentration of radiolytic species, is consistent with aspects of Cox's 2005 review third conclusion [11]. Furthermore, the above experiments and calculations demonstrate that the potential difference between hydrogenated and oxygenated conditions in the core coolant environment is at least 600 mV.

These differences in potential need to be related to the effect of potential on nodule formation. Hurst and Tyzack [65] suggested that oxidation potential of the environment played an important role. Urquhart et al. demonstrated that 600 mV more potential drop develops across the oxide of nodule-susceptible alpha-annealed Zircaloy-4 than for nonsusceptible beta-heat-treated Zircaloy-4 in 500°C 1500-psi steam. In the absence of irradiation flux, lower temperatures, even 10°C lower than the required 500°C and certainly by 450°C, eliminate

nodule susceptibility [66]. This result suggests that the required potential for nodule formation is not far below 600 mV for the oxide thicknesses and conditions tested. As a nodule-formation potential, 600 mV is not fixed. However, for a set of conditions, there is a nodule-formation potential. Also, Zircaloy potentiodynamic polarization scans show a fairly sharp breakdown sensitivity with increasing potential [67–69] at about 550 mV, depending on the conditions. These effects of potential changes on the protective nature of the oxide are consistent with the above observed changes in potential with changes in coolant $\{O_2\}$ and $\{H_2\}$ concentrations, which themselves are associated with LWR nodule susceptibility.

The gradient in potential at the transition at the bottom of the enriched portion of a BWR can be estimated to support the evaluation of the effect of potential on the observed transition in nodule coverage at the enrichment transition. The Rishel et al. [63] potential measurements provide a lower bound to the potential gradient by comparing the data from the probes in the booster-rod region to the reference probe above that region. In general, there is a 400 mV difference over 27 cm between the top of the high-flux region and probe #5 during the period of high oxygen in the coolant, resulting in a 15 mV/cm gradient. This estimated sensitivity is a lower bound because the upper probe still is in a relatively high-flux region compared to a blanket region in a BWR. Considering that the flux gradient will be greater compared to those in Rishel's tests, the effect of a flux gradient can produce a significant change in potential in transitioning to the enriched region of a core. This result is significant since the potential can be close to the oxide-breakdown potential.

Above, in estimating the effects of concentrations of oxidizing species, the impact of cations at the oxide surface on the controlling reactions was not considered. The Zircaloy alloying elements Cr, Fe, and Ni have negative ECPs at standard states, that is, E^o values, in the range of −740 mV to −250 mV SHE. These potentials are in the range of the −500 mV ECP that Andresen [70] estimates can occur for the maximum impact of H_2 injection, which is known to suppress nodule formation. Therefore, depending on their concentrations at the oxide surface, their cations may decrease the ECP in a BWR that does not have H_2 injection, and may have a suppressing effect on nodule formation. The contribution of irradiation is to move these elements from the intermetallic SPPs into the ZrO_2 lattice as cations. This result is consistent with the suggested beneficial effects of solute cations in the model of Cheng and Adamson 20. In contrast, Cu cations have positive E^o values relative to H_2 oxidation, and Cu^+/Cu have positive E^o values relative to O_2 reduction as well. The presence of Cu cations raises the ECP and, in sufficient concentration, may counteract the coolant H_2 lowering of the ECP, as observed by Cowan [60]. This effect of Cu on ECP may be in addition to Marlowe's [31] suggested effect of Cu on crud thermal conductivity.

Surface Potential Shifts and Polarization Effects

Cheng and Adamson [20] associated nodule resistance with solute concentration in the oxide matrix, and with the associated effect on oxide anion-vacancy concentration. This finding was adopted by others studying nodule and uniform

corrosion, for example, Beie et al. [71]. Subsequently, Etoh et al. [35] conducted postirradiation corrosion tests on as-irradiated and on irradiated and annealed nodule-susceptible Zircaloy-2. They found that nodular-susceptible Zircaloy did not form nodules when corrosion tested after irradiation. However, when postirradiation annealing was performed to precipitate the solutes into SPPs prior to corrosion testing, nodules formed in subsequent corrosion testing. Their results are consistent with the effects of dissolved oxide solute concentration suggested by Cheng and Adamson. The details of the effect of these aliovalent solutes in the oxide are not settled. Taylor [72] suggested that the conductivity of the oxide is increased while Harding [73] concluded that the effect is to increase the defect population.

Distribution of solutes through the oxide also can change the surface reactions at the oxide-to-water interface. Fe and Ni in the oxide could shift the surface potential, thereby reducing nodule susceptibility. An alternative is associated with the correlation between increased oxide-matrix solute concentration and an increased uniform corrosion rate, as Cheng and Adamson observed. Apparently, an increased oxide-matrix solute concentration increases the flux of oxygen ions by increasing the concentration of anion vacancies. In principle, an increase in the diffusion of oxygen ions through the oxide reduces the concentration of oxidizing species at the interface between the oxide barrier layer and the water in the porous oxide, polarizing the oxide and decreasing the potential at the interface between the oxide barrier layer and the water. However, it is not clear that the flux of anion vacancies is great enough to result in significant polarization. This effect is similar to the effect of increasing the hydrogen concentration at the interface between the oxide barrier layer and the water wherein both increasing oxygen diffusion through the oxide and increasing coolant hydrogen concentration decrease the concentration of oxidizing species at the interface between the oxide barrier layer and the water, which decreases the surface potential. Whichever explanation for the effective polarization is correct, it eliminates an inconsistency with nodule-formation models based on hydrogen pickup effects.

An effective polarization also occurs when the steam phase is created at the interface between the barrier layer and the coolant. The separation of dissolved oxidizing species into the gas phase, as discussed in the original paper [29] based on the suggestions of others, lowers the concentration of these species at the interface between the oxide barrier layer and the water, in effect, polarizing the oxide exterior surface to lower potentials. Therefore, the potential for nodule formation often is not maintained in a two-phase steam-water region. After corrosion transition to thicknesses greater than the barrier-layer thickness, the steam phase may exist in the transitioned oxide at locations in the core below where bulk boiling occurs, as suggested by A.B. Johnson in his thick-film hypothesis [23], which has been discussed by others, as in the IAEA reviews [27,59].

Effect of Oxygen Concentration

Iltis et al. [74] performed experiments that provided insight into the effects of both atomic and molecular $\{O_2\}$ oxygen on oxidation close to the metal-to-oxide

interface. Their use of microwave postdischarge oxidation and thermal oxidation allowed them to correlate oxide oxygen concentration with oxide crystallite size during the formation of oxide films. They concluded that increased oxygen concentration in the early stages of the oxidation process resulted in finer crystallites. Their use of microwave discharge atomic oxygen increased the potential as radiolysis does in reactor. Their results provide a correlation between the formation of small relatively stable oxide crystals and a large concentration of highly oxidizing species at the oxide barrier-layer interface with the water, as well as with the resultant high potential. Petrik et al. [75] correlated oxide crystal size inversely with [60] Co gamma radiolytic decomposition of H_2O,[3] for example, into H_2O_2. That is, smaller oxide grains increase surface area, which increases energy transfer to H_2O, which increases production of radiolytic species. Although the exact nature of the oxidizing species produced during the heterogeneous radiolysis, for example, OH, H_2O_2, O_2, HO_2, etc., is not fully known, it is expected that the oxidizing species increase the local corrosion potential. Therefore, there is an inverse correlation between corrosion potential from radiolysis and oxide crystallite size. This correlation can be combined with the part of the model of Cheng and Adamson [20] that correlates nodule formation with fine oxide crystallites. Then, the picture is that small oxide crystallites are promoted and initiate nodules at Cheng and Adamson's thin low-solute oxide regions. However, the cause of the crystallite formation is different; it is due to the oxidizing species, and the associated potential, rather than to hydrogen.

Others also discussed the effects of high potentials and high breakdown currents. For example, Beie et al. [76] conducted experiments and discussed the effect of potentials and oxygen concentration on oxidation, although they did not focus on nodule formation. In addition, their analysis is based on equilibrium conditions, which do not take into account transport kinetics of anion vacancies, conduction electrons, or holes, and which is needed to complete the application. Anghel et al. [77] suggested that oxygen dissociation may at times control oxidation, which would support the sensitivity of nodule formation to oxygen concentration. Although more-mechanistic studies are needed, for now, it is suggested that the fine oxide crystallites are promoted by large concentrations of oxidizing species, especially radiolytically produced oxidizing species, at the barrier-layer external surface, which then promotes further radiolytic decomposition.

Application to BWR Nodular Observations at Enrichment Transitions

The picture that emerges from the above discussion is one of a critical potential being required to form nodules, with the existing potential being determined greatly by the concentration of oxidizing species and controlling reactions at the interface between the barrier-layer oxide and the water. The concentration of oxidizing species is influenced by solute modifications to surface reactions, oxygen transport rate through the oxide, the availability of a sufficient amount

[3]The radiolytic decomposition of H_2O was inferred from the H_2 production.

of hydrogen to decrease the concentration of oxidizing species, the stripping of oxidizing species by boiling, and temperature. The two observations on the sharp nodular-coverage transition at approximately the locations of the enrichment transitions [29] provide additional support for potential being an important factor wherein potential is a function of core position while other parameters, including hydrogen pickup, vary differently. Then, the proposed explanation for the nodular transitions is as follows:

(1) At the enrichment transition in low-heat-flux rods: The region below the transition has a relatively low irradiation flux at the interface between the barrier-layer oxide and the water, which results in relatively low concentrations of oxidizing species. The result is a potential below the nodule-formation potential. At approximately the enrichment transition, irradiation flux increases sufficiently to increase the potential above the nodule-formation potential, consistent with the results of Rishel et al. [63], which showed the strong sensitivity of potential to irradiation flux. The transition may not be precisely at the enrichment transition, but it is relatively sharp due to the oxide-breakdown sensitivity to potential.

(2) At the enrichment transition in high-heat-flux rods: The region below the enrichment transition has relatively high irradiation flux due to the local core power, and exceeds the nodule-formation potential and is covered by nodules. The region above the enrichment transition increases in temperature and may have some limited nucleate boiling at the oxide surface, reducing the potential to below the nodule-formation potential, due to transport of oxidizing species away from the surface in tiny bubbles.

Another observation [29] that supports this interpretation is the oxide coverage pattern at spacers where the oxide follows the turbulent coolant pattern. Apparently, additional cooling is available to provide enough liquid coolant on the oxide surface to delay the local surface stripping of oxidizing species to the steam phase.

Conclusions

Extending fuel burnups, expanding reactor operating regimes, and changing disposal plans result in the need to expand the understanding of deformation and oxidation. Regarding nodular corrosion, potential across the oxide is a primary contributor to the oxide breakdown. Hydrogen pickup contributes little or not at all to nodule formation. Nodule formation is prevented by polarization that reduces the concentration of oxidizing species at the interface between the oxide barrier layer and the water. Changes in the coolant oxidation potential at the transitions between blanket and enriched BWR core regions contribute to nodule susceptibility.

Acknowledgements

Douglas Rishel, William Moshier, and Bruce Kammenzind provided valuable reviews of the concepts presented in this paper.

References

[1] Franklin, D. G., Lucas, G. E., and Bement, A. L., *Creep of Zirconium Alloys in Nuclear Reactors, ASTM STP 815*, ASTM International, West Conshohocken, PA, 1983.

[2] Erbacher, F. J. and Leistikow, S., "Zircaloy Fuel Cladding Behavior in a Loss-of-Coolant Accident: A Review," *Zirconium in the Nuclear Industry: Seventh International Symposium, ASTM STP 939*, R. B. Adamson and L. F. P. Van Swam, Eds., June 24-27, 1985, Strasbourg, France, ASTM International, West Conshohocken, PA, 1987, pp. 451–488.

[3] Franklin, D. G. and Adamson, R. B., "Implications of Zircaloy Creep and Growth to Light Water Reactor Performance," *J. Nucl. Mater.*, Vol. 159, 1988, pp. 12–21.

[4] Franklin, D. G. and Franz, W. A., "Numerical Model for Anisotropic Creep of Zircaloy," *Zirconium in the Nuclear Industry, ASTM STP 633*, A. L. Lowe Jr. and G. W. Parry, Eds., ASTM International, West Conshohocken, PA, 1977, pp. 365–384.

[5] Nichols, F. A., "Mechanistic Modeling of Zircaloy Deformation and Fracture in Fuel Element Analysis," *Zirconium in the Nuclear Industry: Seventh International Symposium, ASTM STP 939*, R. B. Adamson and L. F. P. Van Swam, Eds., June 24-27, 1985, Strasbourg, France, ASTM International, West Conshohocken, PA, 1987, pp. 5–22.

[6] Tenckhoff, E., "Review of Deformation Mechanisms, Texture, and Mechanical Anisotropy in Zirconium and Zirconium Base Alloys," *Zirconium in the Nuclear Industry: 14th International Symposium, ASTM STP 1467*, P. Rudling and B. Kammenzind, Eds., June 13-17, 2004, Stockholm, Sweden, ASTM International, West Conshohocken, PA, 2005, pp. 25–50.

[7] Gelebart, L., Crepin, J., Dexet, M., Sauzay, M., and Roos, A., "Identification of Crystalline Behavior on Macroscopic Response and Local Strain Field Analysis: Application to Alpha Zirconium Alloys," *Zirconium in the Nuclear Industry: 14th International Symposium, ASTM STP 1467*, P. Rudling and B. Kammenzind, Eds., ASTM International, West Conshohocken, PA, 2005, pp. 585–603.

[8] Allen, V. M., Quinta da Fonseca, J., Preuss, M., Robson, J. D., Daymond, M., and Comstock, R. H., "Determination and Interpretation of Texture Evolution During Deformation of a Zirconium Alloy," *Zirconium in the Nuclear Industry: 15th International Symposium, ASTM STP 1505*, B. Kammenzind and M. Limback, Eds., June 24-28, 2007, Sun River, OR, ASTM International, West Conshohocken, PA, 2009, pp. 550–563.

[9] Kass, S., "The Development of the Zircaloys," *Corrosion of Zirconium Alloys, ASTM STP 368*, ASTM International, West Conshohocken, PA, 1964, pp. 3–27.

[10] Hillner, E., "Corrosion of Zirconium-Base Alloys—An Overview," *Zirconium in the Nuclear Industry, ASTM STP 633*, A. L. Lowe Jr. and G. W. Parry, Eds., ASTM International, West Conshohocken, PA, 1977, pp. 211–235.

[11] Cox, B., "Some Thoughts on the Mechanisms of In-Reactor Corrosion of Zirconium Alloys," *J. Nucl. Mater.*, Vol. 336, 2005, pp. 331–368.

[12] Tsai, H. and Billone, M. C., "Thermal Creep of Irradiated Zircaloy Cladding," *Zirconium in the Nuclear Industry: 14th International Symposium, ASTM STP 1467*, P. Rudling and B. Kammenzind, Eds., June 24-28, 2007, Sun River, OR, ASTM International, West Conshohocken, PA, 2005, pp. 632–650.

[13] Alam, A. M. and Hellwig, C., "Cladding Tube Deformation Test for Stress Reorientation of Hydrides," *Zirconium in the Nuclear Industry: 15th International Symposium, ASTM STP 1505*, B. Kammenzind and M. Limback, Eds., June 24-28, 2007, Sun River, OR, ASTM International, West Conshohocken, PA, 2009, pp. 635–650.

[14] Aomi, M., Baba, T., Miyashita, T., Kamimura, K., Yasuda, T., Shinohara, Y., and Takeda, T., "Evaluation of Hydride Reorientation Behavior and Mechanical Properties for High-Burnup Fuel-Cladding Tubes in Interim Dry Storage," *Zirconium in the Nuclear Industry: 15th International Symposium, ASTM STP 1505*, B. Kammenzind and M. Limback, Eds., June 24-28, 2007, Sun River, OR, ASTM International, West Conshohocken, PA, 2009, pp. 651–673.

[15] Ribis, J., Onimus, F., Bechade, J.-L., Doriont, S., Cappelaere, C., Lemaignan, C., Barbu, A., and Rabouille, O., "Experimental and Modeling Approach of Irradiation Defects Recovery in Zirconium Alloys: Impact of an Applied Stress," *Zirconium in the Nuclear Industry: 15th International Symposium, ASTM STP 1505*, B. Kammenzind and M. Limback, Eds., June 24-28, 2007, Sun River, OR, ASTM International, West Conshohocken, PA, 2009, pp. 674–695.

[16] Hillner, E., Franklin, D. G., and Smee, J. D., "Long-Term Corrosion of Zircaloy Before and After Irradiation," *J. Nucl. Mater.*, Vol. 278, 2000, pp. 334–345.

[17] Garzarolli, F., Jung, W., Schoenfeld, H., Garde, A. M., Parry, G. W., and Smerd, P. G., "Waterside Corrosion of Zircaloy Fuel Rods," *Report No.* EPRI NP-2789, Electric Power Research Institute, Palo Alto, CA, December 1982.

[18] Cheng, B. C., Kruger, R. M., and Adamson, R. B., "Corrosion Behavior of Irradiated Zircaloy," *Zirconium in the Nuclear Industry: 10th International Symposium, ASTM STP 1245*, A. M. Garde and E. R. Bradley, Eds., June 21-24, 1993, Baltimore, MD, ASTM International, West Conshohocken, PA, 1994, pp. 400–418.

[19] Iltis, X., Lefebvre, F., and Lamaignan, C., "Microstructure Evolutions and Iron Redistribution in Zircaloy Oxide Layers: Comparative Effects of Neutron Irradiation Flux and Irradiation Damages," *Zirconium in the Nuclear Industry: 11th International Symposium, ASTM STP 1295*, E. R. Bradley and G. P. Sabol, Eds., September 11–14, 1995, Garmisch-Partenkirchen, Germany, ASTM International, West Conshohocken, PA, 1996, pp. 242–264.

[20] Cheng, B. and Adamson, R. B., "Mechanistic Studies of Zircaloy Nodular Corrosion," *Zirconium in the Nuclear Industry: Seventh International Symposium, ASTM STP 939*, R. B. Adamson and L. F. P. Van Swam, Eds., June 24-27, 1985, Strasbourg, France, ASTM International, West Conshohocken, PA, 1987, pp. 387–416.

[21] Rosecrans, P. M., "Application of Alternating-Current Impedance Measurements to Characterize Zirconium Alloy Oxidation Films," *ASTM STP 824*, ASTM International, West Conshohocken, PA, 1984, pp. 531–553.

[22] Mergerth, F. H., Ruiz, C. P., and Wolff, U. E., "Zircaloy-Clad UO_2 Fuel Rod Evaluation Program," *Report No.* GEAP-10371, U.S. AEC Research and Development, Washington, DC, June 1971.

[23] Johnson, A. B., "Effect of Nuclear Radiation on the Corrosion, Hydriding, and Oxide Properties of Six Zirconium Alloys," *Applications-Related Phenomena for Zirconium and Its Alloys, ASTM STP 458*, ASTM International, West Conshohocken, PA, 1969, pp. 301–324.

[24] Trowse, F. W., Summerling, R., and Garlick, A., "Nodular Corrosion of Zircaloy-2 and Some Other Zirconium Alloys in Steam Generating Heavy Water Reactors and Related Environments," *Zirconium in the Nuclear Industry, ASTM STP 633*, A. L. Lowe Jr. and G. W. Parry, Eds., ASTM International, West Conshohocken, PA, 1977, pp. 236–257.

[25] Garzarolli, F., Diez, W., Francke, K. P., and Fricke, W., "Corrosion and Hydriding of Zircaloy-2 and Other Zirconium Alloys in BWRs," *Effect of Environment on Material Properties in Nuclear Systems*, Institution of Civil Engineers, London, 1971, pp. 15–20.

[26] Cox, B., "Assessment of In-Reactor Corrosion Models and Data for Zircaloys in Water," *Proceedings of the Second International Symposium on Environmental Degradation of Materials in Nuclear Power Systems—Water Reactors*, Monterey, CA, Sept. 9–12, International Atomic Energy Agency, Vienna, Austria, 1985, pp. 219–226.
[27] International Atomic Energy Agency, 1998, "Waterside Corrosion of Zirconium Alloys in Nuclear Poser Plants," *IAEA-TECDOC-996*, Vienna, Austria.
[28] Nishino, Y., Endo, M., Ibe, E., and Yasuda, T., "Formation and Dissolution of Oxide Film on Zirconium Alloys in 288°C Pure Water Under γ-Ray Irradiation," *J. Nucl. Mater.*, Vol. 248, 1997, pp. 292–298.
[29] Franklin, D. G. and Li, C. Y., "Effects of Heat Flux and Irradiation-Induced Changes in Water Chemistry on Zircaloy Nodular Oxidation," *Zirconium in the Nuclear Industry: Seventh International Symposium, ASTM STP 939*, R. B. Adamson and L. F. P. Van Swam, Eds., June 24-27, 1985, Strasbourg, France, ASTM International, West Conshohocken, PA, 1987, pp. 206–223.
[30] Urquhart, A. W. and Vermilyea, D. A., "A Preliminary Correlation Between the Accelerated Corrosion of Zircaloy in BWRs and in High Temperature, High Pressure Steam," *J. Nucl. Mater.*, Vol. 62, 1976, pp. 111–114.
[31] Marlowe, M. O., Armijo, J. S., Cheng, B., and Adamson, R. B., "Nuclear Fuel Cladding Localized Corrosion," *Light Water Reactor Fuel Performance, ANS Topical Meeting*, Vol. 1, Orlando, FL, April 21–24, American Nuclear Society, La Grange Park, IL, 1985, pp. 3-72–3-90.
[32] Mishima, Y. and Aoki, T., "Proving Test on the Reliability of BWR 8×8 Fuel Assemblies in Japan," *Improvements in Water Reactor Fuel Technology and Utilization Symposium*, Stockholm, Sweden, Sept. 15, International Atomic Energy Agency, Vienna, Austria, 1986, pp. 81–99.
[33] Etoh, Y., "Effects of Operational Parameters on Nodular Corrosion Characteristics," *J. Nucl. Sci. Technol.*, Vol. 26(8), 1989, pp. 752–759.
[34] Sell, H.-J., Trapp-Pritsching, S., and Garzarolli, F., "Effect of Alloying Elements and Impurities on In-BSWR Corrosion of Zirconium Alloys," *Zirconium in the Nuclear Industry: 14th International Symposium, ASTM STP 1467*, P. Rudling and B. Kammenzind, Eds., June 13-17, 2004, Stockholm, Sweden, ASTM International, West Conshohocken, PA, 2005, pp. 404–417.
[35] Etoh, Y., Kikuchi, K., Yasuda, T., Koizumi, S., and Oishi, M., "Neutron Irradiation Effects on the Nodular Corrosion of Zircaloy-2," *Proceedings of the ANS International Topical Meeting on LWR Fuel Performance*, Vol. 2, Avignon, France, April 21–24, American Nuclear Society, La Grange Park, IL, 1991, pp. 691–700.
[36] Draley, J. E. and Ruther, W. E., "Some Unusual Effects of Hydrogen in Corrosion Reactions," *J. Electrochem. Soc.*, Vol. 104(6), 1957, pp. 329–333.
[37] Urquhart, A. W., Vermilyea, D. A., and Rocco, W. A., "A Mechanism for the Effect of Heat Treatment on the Accelerated Corrosion of Zircaloy-4 in High Temperature High Pressure Steam," *J. Electrochem. Soc.*, Vol. 125, 1978, pp. 199–204.
[38] Rudling, P. and Wikmark, G., "A Unified Model of Zircaloy BWR Corrosion and Hydriding Mechanisms," J. Nucl. Mater., Vol. 265, 1999, pp. 44–59.
[39] Ramasubramanian, N., "Out-Reactor Nodular Corrosion Behavior of Zircaloys," *J. Nucl. Mater.*, Vol. 119, 1983, pp. 208–218.
[40] Garzarolli, F. and Manzel, R., *Korrosionbestandigkeit von Zircaloy in KWU-Leistungsreaktoren*, Reaktor Tagung, Berlin, 1977.
[41] Aomi, M., Kogai, T., Shimada, S., Ichikawa, N., Ibe, E., Ishii, Y., Cheng, B., and Lutz, D., "Evaluation of Zircaloy Corrosion Under Various Water Chemistries in a BWR Simulation Loop," *Water Chemistry of Nuclear Reactor Systems 7*, BNES, London, England, 1996, pp. 284–286.

[42] Takagawa, Y., Ishimoto, S., Etoh, Y., Kubo, T., Ogata, K., and Kubota, O., "The Correlation Between Microstructures and In-BWR Corrosion Behavior of Highly Irradiated Zr-Based Alloys," *Zirconium in the Nuclear Industry: 14th International Symposium, ASTM STP 1467*, P. Rudling and B. Kammenzind, Eds., June 13-17, 2004, Stockholm, Sweden, ASTM International, West Conshohocken, PA, 2005, pp. 386–403.

[43] Huang, P. Y., Mahmood, T. S., and Adamson, R. B., "Effects of Thermomechanical Processing on In-Reactor Corrosion of Post-Irradiation Mechanical Properties of Zircaloy-2," *Zirconium in the Nuclear Industry: 11th International Symposium, ASTM STP 1295*, E. R. Bradley and G. P. Sabol, Eds., September 11–14, 1995, Garmisch-Partenkirchen, Germany, ASTM International, West Conshohocken, PA, 1996, pp. 726–757.

[44] Tagstrom, P., Limback, M., Dahlback, M., Andersson, T., and Pettersson, H., "Effects of Hydrogen Pickup and Second-Phase Particle Dissolution on the In-Reactor Corrosion Performance of BWR Claddings," *Zirconium in the Nuclear Industry: 13th International Symposium, ASTM STP 1423*, G. D. Moan and P. Rudling, Eds., June 10-14, 2001, Annecy, France, ASTM International, West Conshohocken, PA, 2002, pp. 96–118.

[45] Kakiuchi, K., Itagaki, N., Furuya, T., Miyazaki, A., Ishii, Y., Suzuki, S., Terai, T., and Yamawaki, M., "Role of Iron for Hydrogen Absorption Mechanism in Zirconium Alloys," *Zirconium in the Nuclear Industry: 14th International Symposium, ASTM STP 1467*, P. Rudling and B. Kammenzind, Eds., June 13-17, 2004, Stockholm, Sweden, ASTM International, West Conshohocken, PA, 2005, pp. 349–366.

[46] Rudling, P., Lundblad Vannesjo, K., Vesterlund, G., and Massih, A. R., "Influence of Second-Phase Particles on Zircaloy Corrosion in BWR Environment," *Zirconium in the Nuclear Industry: Seventh International Symposium, ASTM STP 939*, R. B. Adamson and L. F. P. Van Swam, Eds., June 24-27, 1985, Strasbourg, France, ASTM International, West Conshohocken, PA, 1987, pp. 292–306.

[47] Maussner, G., Steinberg, E., and Tenckhoff, E., "Nucleation and Growth of Intermetallic Precipitates in Zircaloy-2 and Zircaloy-4 and Correlation to Nodular Corrosion Behavior," *Zirconium in the Nuclear Industry: Seventh International Symposium, ASTM STP 939*, R. B. Adamson and L. F. P. Van Swam, Eds., June 24-27, 1985, Strasbourg, France, ASTM International, West Conshohocken, PA, 1987, pp. 307–320.

[48] Andersson, T. and Thorvaldsson, T., "Nodular Corrosion Resistance of Zircaloy-2 in Relation to Second-Phase Particle Distribution," *Zirconium in the Nuclear Industry: Seventh International Symposium, ASTM STP 939*, R. B. Adamson and L. F. P. Van Swam, Eds., June 24-27, 1985, Strasbourg, France, ASTM International, West Conshohocken, PA, 1987, pp. 321–337.

[49] Bangaru, N. V., Busch, R. A., and Schemel, J. H., "Effect of Beta Quenching on the Microstructure and Corrosion of Zircaloys," *Zirconium in the Nuclear Industry: Seventh International Symposium, ASTM STP 939*, R. B. Adamson and L. F. P. Van Swam, Eds., June 24-27, 1985, Strasbourg, France, ASTM International, West Conshohocken, PA, 1987, pp. 341–363.

[50] Weidinger, H. G., Garzarolli, F., Euchen, C. M., and Baroch, E. F., "Effect of Chemistry on Elevated Temperature Nodular Corrosion," *Zirconium in the Nuclear Industry: Seventh International Symposium, ASTM STP 939*, R. B. Adamson and L. F. P. Van Swam, Eds., June 24-27, 1985, Strasbourg, France, ASTM International, West Conshohocken, PA, 1987, pp. 364–386.

[51] Garzarolli, F., Stehle, H., Steinberg, E., and Weidinger, H., "Progress in the Knowledge of Nodular Corrosion," *Zirconium in the Nuclear Industry: Seventh*

International Symposium, ASTM STP 939, R. B. Adamson and L. F. P. Van Swam, Eds., June 24-27, 1985, Strasbourg, France, ASTM International, West Conshohocken, PA, 1987, pp. 417–430.

[52] Ogata, K., "Effects of Alloying Element Distribution on the Nodular Corrosion of Zircaloy-2," *Zirconium in the Nuclear Industry: Eighth International Symposium, ASTM STP 1023*, L. F. R. Van Swam and C. M. Eucken, Eds., June 19–23, 1988, San Diego, CA, ASTM International, West Conshohocken, PA, 1989, pp. 346–359.

[53] Cox, B., "Oxidation of Zirconium and Its Alloys," *Advances in Corrosion Science and Technology*, Plenum Press, New York, 1976.

[54] Zhou, B., "Electron Microscopy Study of Oxide Films Formed on Zircaloy-2 in Superheated Steam," *Zirconium in the Nuclear Industry: Eighth International Symposium, ASTM STP 1023*, L. F. R. Van Swam and C. M. Eucken, Eds., June 19–23, 1988, San Diego, CA, ASTM International, West Conshohocken, PA, 1989, pp. 360–373.

[55] Bibb, A. E. and Faxcia, J. R., "Aqueous Corrosion of Zirconium Single Crystals," KAPL-2257, Knolls Atomic Power Laboratory, Schenectady, NY, October 1962.

[56] Charquet, D., Tricot, R., and Wadier, J.-F., "Heterogeneous Scale Growth During Steam Corrosion of Zircaloy-4 and 500°C," *Zirconium in the Nuclear Industry: Eighth International Symposium, ASTM STP 1023*, L. F. R. Van Swam and C. M. Eucken, Eds., ASTM International, West Conshohocken, PA, 1989, pp. 374–391.

[57] Cox, B., "Rate Controlling Processes During the Pre-Transition Oxidation of Zirconium Alloys," *J. Nucl. Mater.*, Vol. 31, 1969, pp. 48–66.

[58] Urquhart, A. W. and Vermilyea, D. A., "Characterization of Zircaloy Oxidation Films," *Zirconium in the Nuclear Industry: ASTM STP 551*, ASTM International, West Conshohocken, PA, 1974, pp. 463–478.

[59] International Atomic Energy Agency, 1993, "Corrosion of Zirconium Alloys in Nuclear Power Plants," *IAEA-TECDOC-684*,Vienna, Austria.

[60] Cowan, R. L., "BWR Water Chemistry…a Delicate Balance," *Water Chemistry of Nuclear Reactor Systems 8*, British Nuclear Engineering Society, London, England, 2000, pp. 97–102.

[61] Hettiarachchi, S., Law, R. J., Diaz, T. P., Miller, W. D., Cowan, R. L., Keith, W., Kriege, L., and Pathania, R. S., "Application of Noble Metal Chemical Addition Technology to an Operating BWR to Mitigate IGSCC of Reactor Internals," *CORROSION 98*, March 22-27, 1998 San Diego, CA, National Association of Corrosion Engineers, Houston, TX, 1998, pp. 142/1–142/15.

[62] Hettiarachchi, S., Law, R. J., Miller, W. D., Diaz, T. P., and Cowan, R. L., "First Application of NOBLECHEM™ to an Operating BWR," *Japan Atomic Industrial Forum Meeting*, Kashiwazaki, Japan, October 13-16, 1998, Japan Atomic Industrial Forum, Tokyo, Japan, 1998.

[63] Rishel, D. M., Eklund, K. L., and Kammenzind, B. F., "In Situ EIS Measurements of Irradiated Zircaloy-4 Post-Transition Corrosion Kinetic Behavior," *Zirconium in the Nuclear Industry: 15th International Symposium, ASTM STP 1505*, B. Kammenzind and M. Limback, Eds., June 24-28, 2007, Sun River, OR, ASTM International, West Conshohocken, PA, 2009, pp. 326–359.

[64] Ruiz, C. P., Lin, C. C., Robinson, R. N., Burns, W. G., Henshaw, J., and Pathania, R., "Model Calculations of Water Radiolysis and Electrochemical Potentials in BWR Primary Coolant II," *Water Chemistry of Nuclear Reactor Systems 6*, BNES, London, 1992, pp. 141–152.

[65] Hurst, P. and Tyzack, C., "The Effect of Environment on the In-Pile Corrosion and Hydrogen Pick-Up of Some Zirconium Alloys," *Effects of Environment on Material*

Properties in Nuclear Systems, Institution of Civil Engineers, London, 1971, pp. 37–49.

[66] Cheng, B., Levin, H. A., Adamson, R. B., Marlowe, M. O., and Monroe, V. L., "Development of a Sensitive and Reproducible Steam Test for Zircaloy Nodular Corrosion," *Zirconium in the Nuclear Industry: Seventh International Symposium, ASTM STP 939*, R. B. Adamson and L. F. P. Van Swam, Eds., June 24-27, 1985, Strasbourg, France, ASTM International, West Conshohocken, PA, 1987, pp. 257–283.

[67] Greene, C. A., Brossia, C. S., Dunn, D. S., and Cragnolino, G. A., "Environmental and Electrochemical Factors on the Localized Corrosion of Zircaloy-4," *Corrosion 2000*, March 26-31, 2000, Orlando, FL, National Association of Corrosion Engineers, Houston, TX, 2000.

[68] Brossia, C. S., Cragnolino, G. A., and Dunn, D. S., "Effect of Oxide Thickness on the Localized Corrosion of Zircaloy," *Corrosion 2002*, April 7–11, 2002, Denver, CO, National Association of Corrosion Engineers, Houston, TX, 2002.

[69] Maguire, M., "The Pitting Susceptibility of Zirconium in Aqueous Cl-, Br-, and I-Solutions," *ASTM STP 850*, ASTM International, West Conshohocken, PA, 1984, pp. 175–189.

[70] Andresen, P. L., "Mitigation of Stress Corrosion Cracking by Underwater Thermal Spray Coating of Noble Metals," *CORROSION 95*, March 26–31, 1995 Orlando, FL, National Association of Corrosion Engineers, Houston, TX, 1995, pp. 412/1–412/30.

[71] Beie, H.-J., Mitwalsky, A., Garzarolli, F., Ruhmann, H., and Sell, H.-J., "Examinations of the Corrosion Mechanism of Zirconium Alloys," *Zirconium in the Nuclear Industry: 10th International Symposium, ASTM STP 1245*, A. M. Garde and E. R. Bradley, Eds., June 21–24, 1993, Baltimore, MD, ASTM International, West Conshohocken, PA, 1994, pp. 615–643.

[72] Taylor, D. F., "An Oxide-Semiconductance Model of Nodular Corrosion and Its Application to Zirconium Alloy Development," *J. Nucl. Mater.*, Vol. 184, 1991, pp. 65–77.

[73] Harding, J. H., "The Effect of Alloying Elements on Zircaloy Corrosion," *J. Nucl. Mater.*, Vol. 202, 1993, pp. 216–221.

[74] Iltis, X., Viennot, M., David, D., Hertz, D., and Michel, H., "Special Kinetic and Microstructural Features Associated with Zircaloy-4 Oxidation Between 520 and 620 K in the Post-Discharge of an Argon-Oxygen Microwave Discharge," *J. Nucl. Mater.*, Vol. 209, 1994, pp. 180–190.

[75] Petrik, N. G., Alexandrov, A. B., and Vall, A. I., "Interfacial Energy Transfer During Gamma Radiolysis of Water on the Surface of ZrO_2 and Some Other Oxides," *J. Phys. Chem. B*, Vol. 105, 2001, pp. 5935–5944.

[76] Beie, H.-J., Mitwalsky, A., Garzarolli, F., Ruhmann, H., and Sell, H.-J., "Examinations of the Corrosion Mechanism of Zirconium Alloys," *Zirconium in the Nuclear Industry: 10th International Symposium, ASTM STP 1245*, A. M. Garde and E. R. Bradley, Eds., ASTM International, West Conshohocken, PA, 1994, pp. 6615–6643.

[77] Anghel, C., Hulquist, G., Limback, M., and Szakalos, P., "Effects of Pt Surface Coverage on Oxidation of Zr and Other Materials," *Zirconium in the Nuclear Industry: 15th International Symposium, ASTM STP 1505*, B. Kammenzind and M. Limback, Eds., June 21–24, 1993, Baltimore, MD, ASTM International, West Conshohocken, PA, 2009, pp. 285–302.

Reprinted from JAI, Vol. 7, No. 7
doi:10.1520/JAI103005
Available online at www.astm.org/JAI

V. N. Shishov[1]

The Evolution of Microstructure and Deformation Stability in Zr–Nb–(Sn,Fe) Alloys Under Neutron Irradiation

ABSTRACT: A review is given on the effect of neutron irradiation on the microstructure and properties of Zr–Nb and Zr–Nb–Fe (Sn,O) alloys. The in-reactor performance of Zr alloys is dependent on their composition and microstructure, and even small changes in the composition and processing lead to substantial changes in properties as a result of evolution of precipitates and matrix composition. The development of a new generation of alloys of Zr–Nb–Fe (Sn,O) system (that show higher resistance to the irradiation-induced growth, creep, and corrosion) required an examination of their microstructure during the manufacturing process and evolution after neutron irradiation. The basic irradiation phenomena involve irradiation-induced damages (formation of the **a**- and **c**-component dislocations) and redistribution of alloying elements. The influence produced by precipitates containing Zr, Nb, and particularly Fe on the properties under irradiation is demonstrated. Relationships between composition, microstructure, and irradiation-induced growth of the Zr–Nb–Fe–Sn are described. An increased content of iron (over limit of the solubility) in Zr–Nb alloys leads to lower irradiation growth and creep and to strengthening of the matrix as a result of Fe leaving Laves phase (HCP) particles with their transformation into β-Nb (bcc). β-Nb precipitates become depleted in niobium (or enriched in zirconium), and finely dispersed irradiation-induced secondary particles enriched in niobium are formed. The basic microstructures that illustrate neutron damage structures, precipitates instability, evolution, and irradiation growth are shown and discussed.

Manuscript received February 3, 2010; accepted for publication June 22, 2010; published online July 2010.

[1]A. A. Bochvar Research Institute of Inorganic Materials (VNIINM), Moscow 123060, Russia, e-mail: shishovv@bochvar.ru

Cite as: Shishov, V. N., "The Evolution of Microstructure and Deformation Stability in Zr–Nb–(Sn,Fe) Alloys Under Neutron Irradiation," *J. ASTM Intl.*, Vol. 7, No. 7. doi:10.1520/JAI103005.

Copyright © 2011 by ASTM International, 100 Barr Harbor Drive, PO Box C700, West Conshohocken, PA 19428-2959.

KEYWORDS: irradiation, Zr–Nb–Fe–Sn alloys, microstructure, phase, precipitates, dislocations, electron microscopy, growth, examination

Introduction

Zr alloys alloyed with Nb (Zr-1Nb and Zr-2.5Nb) or with Sn, Fe, Cr, and Ni (Zry-2, -4) have been widely used in water cooled nuclear reactor cores for 50 years and have demonstrated the unique combination of tensile and corrosion properties under irradiation. The choice of the alloy composition in many respects was determined experimentally. The Russian alloys for use as fuel claddings considering fuel assembly (FA) designs and reactor water chemistry were initially developed on the Zr–Nb base (recrystallized E110) [1–4], while the foreign ones were based on the Zr–Sn–Fe-(Cr,Ni) system (Zircaloy-2, -4). For the recent 20–30 years, due to higher loads and safety requirements of reactors, alloys containing Nb, Sn, and Fe have been developed and mastered.

The first of these alloys was designed in the USSR. The Zr-1Nb-1.2Sn-0.35Fe (% wt) alloy had some advantages, e.g., strength, resistance to nodular corrosion, irradiation creep, and irradiation-induced growth (IIG) [5–8]. This alloy was first reported in 1971 in Geneva [5]. 20 years ago, Professor A. Nikulina described it in her Kroll report. The alloy was named E635. With insignificant changes in its composition, it is used for core items in VVER reactors. Later on, proceeding from its behavior in practice as well as and in connection with the exhausting of Zircaloys' potentialities, the Zr–Nb–Fe–Sn systems—ZIRLO, NSF, NDA, MDA, HANA—were developed for the water chemistry of PWRs and BWRs. At that time A. Nikulina mentioned promising research into the structural changes of the E110, E125, and E635 alloys under irradiation and into the mechanisms and regularities of their irradiation resistance. Such research was initiated by her in the 1990s [4,7,9].

By the time I encountered Zr alloys (1984), I had already gained serious experience at Bochvar Institute of Inorganic Materials (VNIINM) in the area of materials science, irradiation-induced damages, and transmission electron microscopic (TEM) examinations of quite different metals and alloys. If in the case of the Zr–Nb system alloys much was understood and had already been done, the work on the Zr–Nb–Fe–Sn alloys had just started. The TEM investigations of their structure and phase composition had not been carried out at all. The technique of preparation and investigations did not present any difficulties, and in 1985, according to the assignment of the Zirconium Laboratory, the first results on the phase-structure state of cladding and channel tubes fabricated from the E110, E125, and E635 alloys were obtained and published in VNIINM reports.

Secondary phase precipitates (SPP) in the E635 alloy (Zr-1Nb-1.2Sn-0.35Fe) (% wt) were first identified using the electron diffraction method and X-ray energy dispersive spectrometry (EDS) microanalysis of SPPs extracted onto a carbon replica (Fig. 1). The elemental composition (34Zr-34Nb-32Fe (± 2, at. %)), the crystal lattice type (HCP), and its parameters ($a = 0.53$ nm and $c = 0.87$ nm) were quantitatively determined. Their typical morphology with

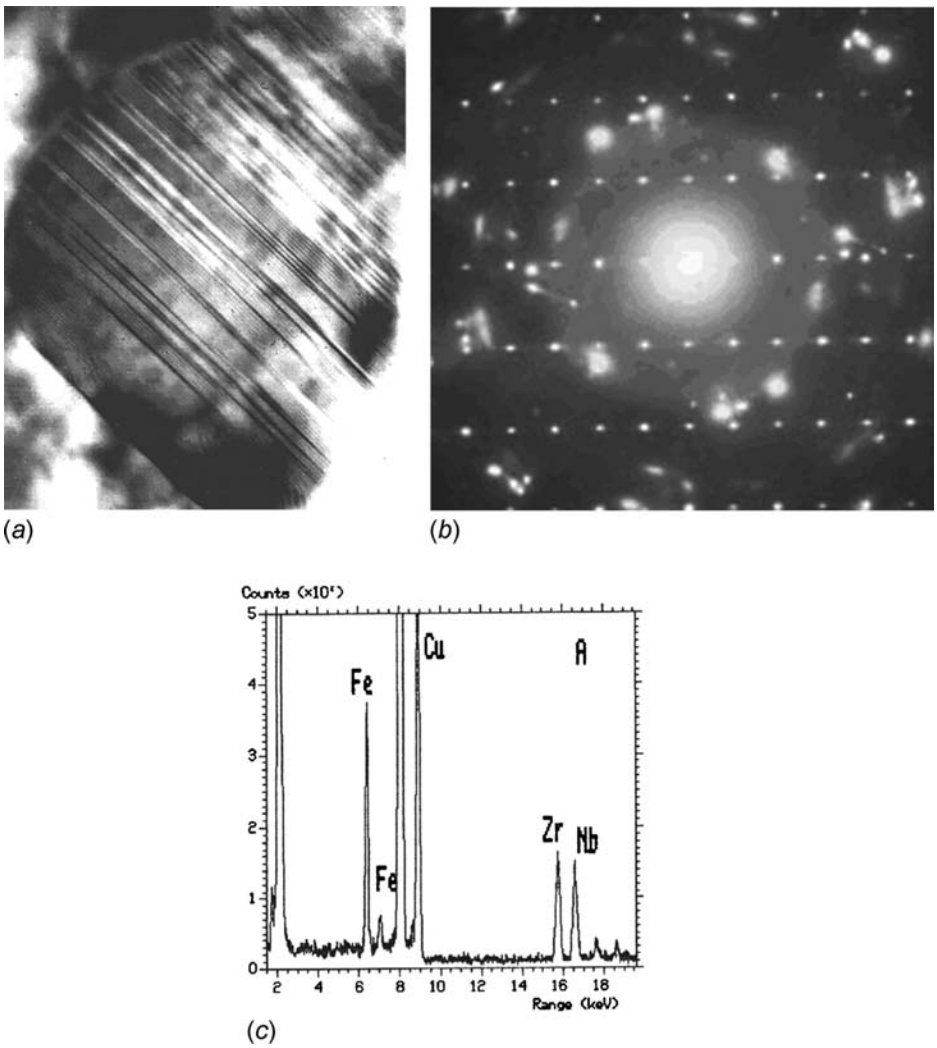


FIG. 1—*Identification of the Laves phase particle: (a) $Zr(Nb,Fe)_2$ by electron diffraction SAD; (b) HCP, parameters a=0.54 nm and c=0.87 nm, and EDS; (c) composition 35Zr-35Nb-30Fe (at. %).*

twins and stacking faults was studied. Proceeding from the published data on Zircaloys with the $Zr_2(Ni,Fe)$ and $Zr(Cr,Fe)_2$ phases, it may be assumed that the composition of the phase in the E635 alloy had to be of the type AB_2 or $A_2B-(Zr,Nb)_2Fe$ or $Zr(Nb,Fe)_2$, where A is Zr or $(Zr+Nb)$ and B is Fe or $(Fe+Nb)$. Since Zr and Nb have close atomic radii and compose solid solutions, many researchers assume that the correct writing is $(Zr,Nb)_2Fe$. However, the elemental composition unambiguously confirmed that it was the Laves phase

$Zr(Nb, Fe)_2$. At first, the results were published in VNIINM reports and later released in worldwide publications [9,10].

Then, there was a study of the formation of the microstructure in the process of fabrication of cladding and channel tubes from the alloys E110, E125, and E635 to optimize the conditions of their thermal and mechanical treatments and others. During the years that followed, experts from VIAM (Institute of Aviation Materials), KhPhTI (Kharkov Physical and Technical Institute), Institute of Reactor Materials (IRM), Research Institute of Atomic Reactors (RIAR), and Institute of Atomic Energy were attracted to the studies using also alloys irradiated in research (BOR-60, MIR, and SM) and commercial reactors (RBMK and VVER). As a result of joint efforts, late in the 1980s, the foundation to understanding the structure formation in the manufacturing of items from the Zr–Nb and Zr–Nb–Fe–Sn alloys was established. Some precipitates were identified; the first results on irradiation effected changes in the E110, E125, and E635 alloys were obtained [9–12].

At the same time, there appeared many questions related to the following:

- Full identification of SPPs in alloys having various compositions
- Changes in the phase composition upon variations in alloying element content and heat treatment conditions
- Evolution of the structure-phase state (SPPs and dislocation structure) and redistribution of alloying elements under irradiation
- Revealing mechanisms of **a**- and **c**-type dislocation loops formation
- Understanding the influence of the microstructure on properties of alloys—corrosion, IIG and creep, tensile properties, microhardness, etc.
- Quantification of structural characteristics of irradiated samples

Mechanisms and regularities of the processes taking place in the E110, E125, and E635 alloys under conditions of oxidation and neutron irradiation were not revealed. Interrelation between operating characteristics and the solid solution composition was not even discussed.

In 1993, I joined the Laboratory of Zirconium materials and fully concentrated on zirconium problems. Electron microscopy-related work was organized to study the structure-phase state of the Zr–Nb-(Fe–Sn) alloys during fabrication and under neutron irradiation. This was to establish the mechanisms and regularities of irradiation resistance and corrosion behavior, as well as the development of new advanced materials. At the IRM, research of the microstructure and properties of the E125 and E635 alloy channel tubes as long term operated in RBMK reactors was initiated and carried out with my direct participation (in the early 1990s) [9,13].

At the RIAR, joint work was aimed at determining irradiation growth, creep, tensile, and other properties of pilot and standard alloys irradiated in research and commercial reactors [14,15]. At the same time, the work was initiated to study the microstructure of irradiated Zr alloys using a modern analytical electron microscope and advanced quantitative techniques of ATEM examinations. The results appeared and were reported and broadly discussed at Russian and International Conferences on Zr [9,10,12,13,16–24]. The acquaintance, first with the papers and then personally, with leading foreign experts played a tremendous role in my research and understanding of zirconium

irradiated materials [25–45]. It became evident that the Zr–Nb-(Fe–Sn) alloys differ from Zircaloys in the behavior under neutron irradiation.

Out of Pile Characterization

Role of Iron in the Zr–Nb Alloys

The studies of the Zr alloys containing Fe and Nb has led to understanding of the most important role played by iron as the fastest diffusing and strengthening element determining the basic transformations in the Zr alloys and their properties [9,10,12,13,16,32,35,42]. First, an increased content of Fe (or its local non-uniformity) in the E635 alloy impaired its deformability and lead to cracking of billets and tubes during manufacturing. The phenomenon was studied, and the cause was revealed, viz., forming coarse SPP particles identified as $(Zr, Nb)_2Fe$, FCC (T-phase) [16,18–21]. Second, it was shown that a higher level of strengthening (increased ultimate tensile strength and elasticity) of the E635 channel tubes in comparison to the E125 alloy tubes was due not only to irradiation defects in the form of dislocation loops but also to the strain of the matrix lattice as a result of iron atoms leaving the Laves phase SPPs—the so-called solid solution strengthening [13,32,42]. It was for the first time that the change in the Laves phase composition under neutron irradiation was quantified—particles become depleted in Fe that enters the matrix and oversaturates it [9,10,13]. Third, the influence of the iron content on IIG, creep, corrosion behavior of the alloys was established [18–20,22–24]. Based on the understanding of the above phenomena, a new trend of developing materials for fuel claddings and other FA components, materials capable of combining the properties of the base alloys E110 and E635, appeared.

Structure Formation

The process of producing alloys and items and the content and distribution of alloying elements within a material significantly affect the dislocation structure and the phase composition of the items and their properties [4–8,46]. The regularities of the microstructure formation in manufacturing of a final item from an ingot were studied in detail. It was found out that the SPPs in the items are formed during deformation and anneals in the α–region; their composition is determined by the composition of the β-Zr phase after hot rolling in the $(\alpha + \beta)$-region and its decomposition. It was established that the composition and the structure-phase state at different stages of the technology process influenced the deformation ability of the alloys; the optimal composition of an alloy and heat treatment conditions were recommended.

The comprehension of the mechanisms forming the structures of items allows us to control them and get the needed structure with needed properties to be produced [16,18–23].

Depending on the processing conditions and the compositions of alloys, the type of SPPs in alloys of the Zr–Nb–Fe–Sn system is determined by solubility of the alloying elements Nb and Fe in β-Zr (high) and in α-Zr (limited) by their

total content in the alloy and by the ratio $R = (\mathrm{Fe}/\mathrm{Fe} + \mathrm{Nb}_{-0.3})$ determining a relative concentration of elements in precipitates. $\mathrm{Nb}_{-0.3}$ means the content of Nb in precipitates without Nb in the matrix (0.3 wt % is the solubility limit).

Microstructure of the Zr–Nb and Zr–Nb–Fe–Sn Alloys

In the initially recrystallized state, the E110 alloy (Zr-1Nb) contains β-Nb precipitates with a composition of 10 % Zr–90 % Nb (Fig. 2). Typical precipitates in the E635 alloy are the Laves phase $\mathrm{Zr(Nb, Fe)_2}$ (Fig. 2(*c*)) having HCP crystal lattice with parameters $a = 0.54$ nm and $c = 0.87$ nm and composition of 35Zr-35Nb-30Fe (at. %).

Changes in the alloy composition affect the composition of the Laves phase $\mathrm{Zr(Nb, Fe)_2}$ and also lead to the appearance of new phases. In the E635 alloy with lower (0.15 %) Fe, extra Nb (deficient iron) brings an additional phase, apart from $\mathrm{Zr(Nb, Fe)_2}-\beta-$Nb SPPs. Alloying of the Zr-1Nb alloy with iron in the quantity 0.03–0.15 % Fe also results in a structure with β-Nb and $\mathrm{Zr(Nb, Fe)_2}$ particles.

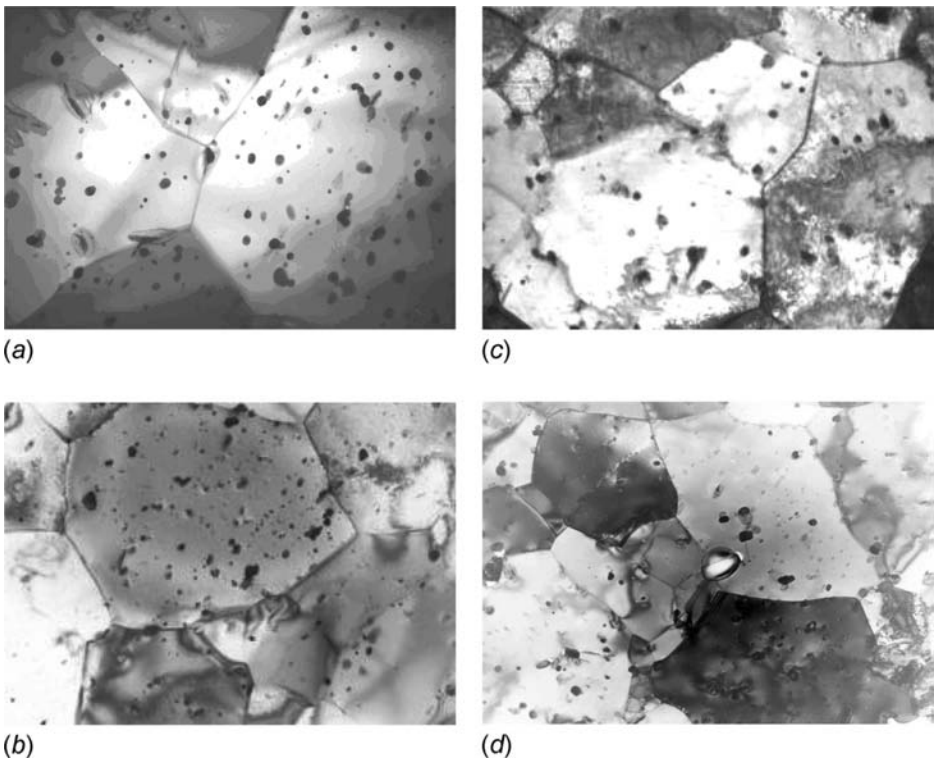


FIG. 2—*Microstructure of unirradiated cladding tubes from alloys:* (a) *Zr-1Nb, β-Nb particles, ×20 000;* (b) *E110M, Zr-1Nb-0.1Fe;* (c) *Zr-1Nb-0.3Fe-0.8Sn-Laves phase particles,* $Zr(Nb, Fe)_2$*; and* (d) *Zr-0.7Nb-0.6Fe-1.3Sn, Laves phase, and T-phase precipitates,* $(Zr, Nb)_2Fe$ *(×10 000).*

If iron in the alloy increases up to 0.45 % besides $Zr(Nb, Fe)_2$ particles, there are an additional phase depleted in $Nb-(Zr, Nb)_2Fe$ precipitates. Its characteristics are crystal lattice FCC, $a = 1.21$ nm, composition of 60Zr-10Nb-30Fe (at. %). Its typical size is 300–1000 nm, and the number density is much lower of that of Laves phase particles. As the quantity of Fe in the alloy increases, the established regularities of the phase state involve a consecutive transfer from phases having only Zr and Nb (BCC) to phases having Zr, less Nb, and more and more Fe in their composition (HCP and FCC). This fact is also confirmed in [47–50].

Composition of $Zr(Nb,Fe)_2$ Precipitates and Matrix

The analysis of composition of $Zr(Nb, Fe)_2$ precipitates showed that as the Fe content of the alloys decreases, the Fe content of the Laves phase also goes down, while the quantity of Nb is increased and vice versa, which proves their interchangeability in the lattice. Their total $(Nb + Fe)$ content is always up to 63–66 (at. %), while that of Zr is 33–37 (at. %) (Fig. 3).

When the alloy composition changes in wide range (0.20–0.45 %) Fe, the composition of the $Zr(Nb_{1-x}Fe_x)_2$ phase varies and $x = Fe/(Nb + Fe)$ (at. %) may be within the range of $0.3 \leq x \leq 0.6$. Thus, the range of the Laves phase existence (HCP) $Zr(Nb, Fe)_2$ is within $25\% < Fe < 36\% \bullet 41\% > Nb > 29\%$. If the ratio $Fe/(Fe + Nb)$ is below 0.3, it transforms into the BCC phase of the "β-Nb" type, which is also noticed under irradiation when as a result of iron leaving the Laves phase, the latter transforms to "β-Nb." An increase in the iron content of the alloy above 0.45 % wt. leads to formation of an extra phase depleted in $Nb-(Zr, Nb)_2Fe$. In this case, niobium atoms replace zirconium atoms. A specific character of the formation of different lattices is primarily due to high diffusion mobility of Fe atoms that tend to occupy respective positions while Nb atoms are built into the lattice later.

The work, which started in the USSR in the 1980s, to construct and study phase diagrams of Zr-base alloys [51] made a prominent contribution into the ideology of new Zr alloys development not only in Russia but also in the world [47–50]. A lot of studies on Nb and Fe contents in the Zr–Nb-(Fe) alloys influence on corrosion has been carried out [49,52–59]. Using the phase diagram of the Zr–Nb–Fe system [51] and the results of TEM examinations an improved Zr corner of the diagram was suggested for commercial, relatively short anneals at 580°C [18,19]. A large complex of material science studies was accomplished in this diagram in Refs [47–50]. It was proven that the Laves phase composition may vary depending on the alloy composition and heat treatment conditions.

The solubility of the alloying elements (Nb and Fe) in α-Zr that participate in the formation of SPPs is not high; according to the published data, it is less than 0.6 % Nb and 0.01 % Fe at 600°C [25]. In actual items subjected to not long-term heat treatment the equilibrium state is not achieved and those values change. Recently, received data of EDS and WDS X-ray microanalysis state that the content of Nb is equal $0.3 \pm 0.2\%$ and the content of Fe is $0.07 \pm 0.05\%$ in the matrix of the recrystallized alloy E635. The Nb content in the matrix of the E110 alloy is about $0.4 \pm 0.2\%$ [18].

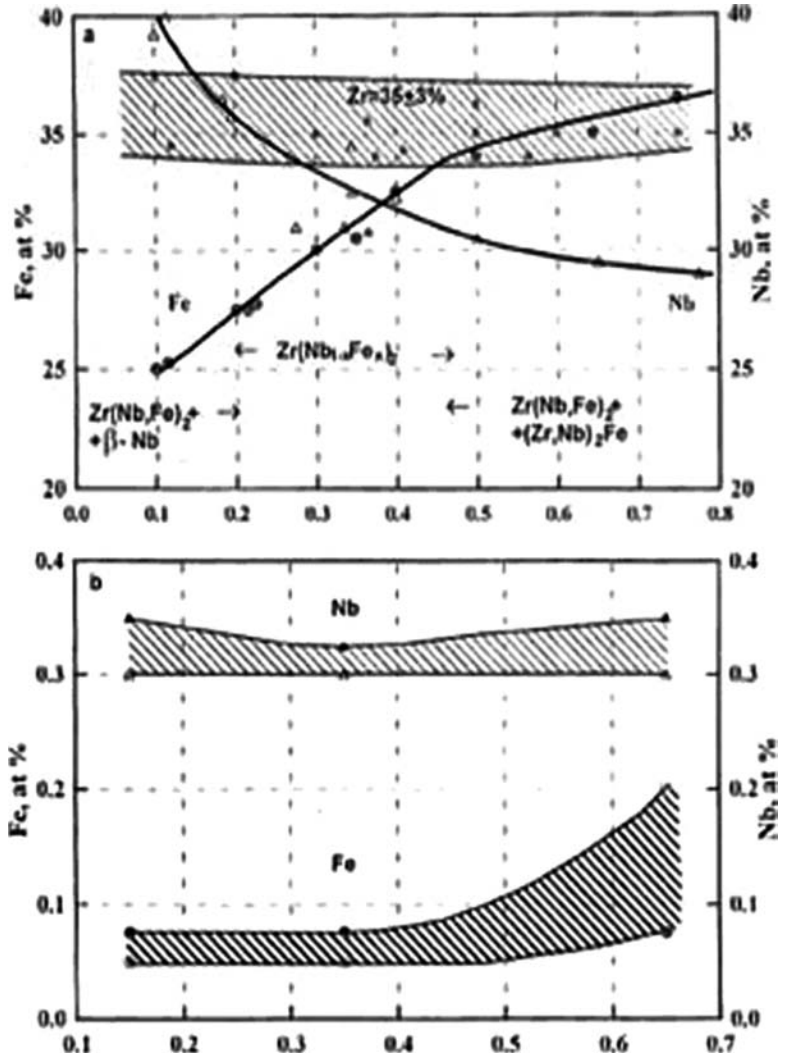


FIG. 3—*Dependence of the Laves phase* (a) *and matrix* (b) *composition on the iron content in the E635 type alloys [18].*

Structure-Phase State

The structure-phase states of the alloys have been studied in order to optimize the manufacturing process and clarify the interrelation between structure and shape changes [18–24]. The regularities of the phase transformations in the Zr–-Nb–Fe–Sn system alloys have been established. The dependence of phase dissolution and precipitation on the compositions of the alloys and temperature and the existence areas for all SPPs have been found [22,23]. As the anneal temperature rises above the $(\alpha/\alpha + \beta)$-transformation, the volume fraction of $Zr(Nb, Fe)_2$

and β-Nb particles decreases, and the precipitates of β-Zr • $(Zr, Nb)_2Fe$ are formed and grow (Fig. 4). The temperature of the β-Zr phase emergence, i.e., of the $\alpha \rightarrow \alpha + \beta$ transformation of iron-free Zr-1Nb and Zr-2.5Nb alloys, is 600°C.

In the presence of the $(Zr, Nb)_2Fe$ phase, the Nb content of the solid solution goes down to reach 0–0.2 %; therefore, in high Fe content alloys, the formation of β-Zr in the range of 640–680°C is delayed because of the existence and growth of the $(Zr, Nb)_2Fe$ phase. This occurs as a result of the dissolution of the original SPPs of the Laves phase and β-Nb as well and the diffusion of iron and niobium atoms; the dissolution process is completed at 700–750°C. The dissolution of the $(Zr, Nb)_2Fe$ phase particles proceeds later at 750–800°C. The dependence of the β-Zr volume fraction on the heating temperature demonstrates a sharp growth at 850–860°C. The anneal at 800°C followed by slow cooling does not fix the high temperature state; as a result of the diffusion, the $\beta - Zr + T \leftrightarrow \beta - Zr$ reaction has time to take place, and the β-Zr phase rich in Nb and Fe is formed.

Behavior under Irradiation

New Alloys of Zr–Nb–Fe-(Sn,O) System

Materials of VVER and RBMK claddings and other components of the FAs must ensure high resistance to shape changes (IIG and creep) and corrosion (also in Li water chemistry and steam quality up to 20 %) at burnups of 70–100 MW day/kg U. For VVER fuel claddings and spacer grid elements, the E110 alloy is used, and for FA components, the E635 alloy is used [4–8]. The E635 alloy, inferior to the E110 alloy in uniform corrosion, is resistant to nodular corrosion in boiling coolant containing oxygen, has high strength, and is stable to strain

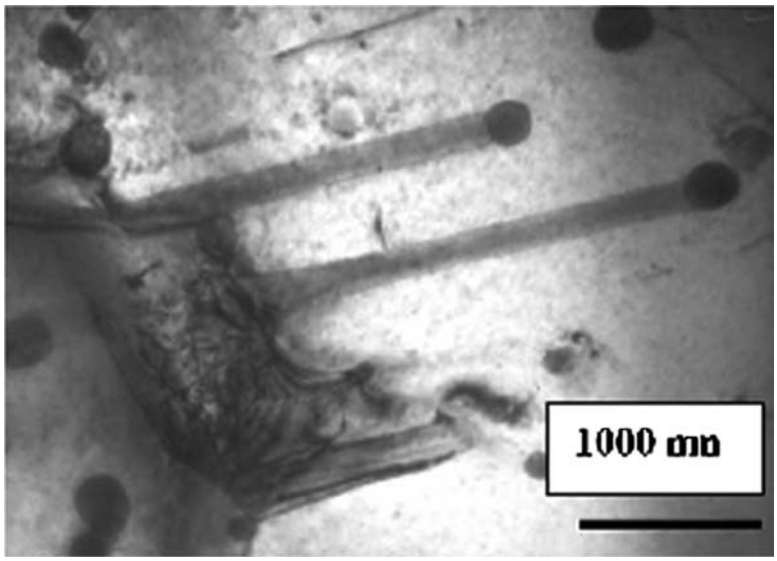


FIG. 4—*β-Zr and $(Zr, Nb)_2Fe$ phases formation via dissolving Laves phase particles.*

under stresses and irradiation. Considering these facts, when new alloys were designed, the main attention was paid to the alloys of Zr–Nb–Fe–Sn–O system, keeping the advantages of the base alloys. The modification of E110, for instance, involved its strengthening with oxygen and iron. The corrosion of E635 can be reduced via changing (decreasing) the content of tin and niobium. The program of such research required understanding the mechanisms of alloying and structure formation, which are applied to fabrication of items, microstructure evolution under irradiation in correlation with its properties.

Tubes were made from standard and modified alloys based on the E110 (0.05–0.24 %) Fe and E635 (0.5–2.5 %) Nb; (0.1–0.65 %) Fe; and (0.8–1.5 %) Sn. Their structural characteristics were determined before and after irradiation. To determine the IIG, creep, tensile properties, and microstructure, the specimens were irradiated in BOR-60 (the threshold energy here and further is $E > 0.1$ MeV). Fuel claddings, guide thimbles, and other components from the E110 and E635 alloys were tested after irradiation in VVER-1000 to the maximal burnup of 70 MW day/kg U.

Shape Changes

Under in-pile conditions, zirconium materials are subject to shape changes resulting from IIG strain and irradiation creep [25,44,45]. The IIG is usually defined as an elongation of tubes in the axial direction. It depends on the alloy composition, microstructure, texture, neutron fluence, and temperature [25,30,32,40,43]. The texture dependence on irradiation growth strain (ϵ) is determined by Kearns parameters f_L, i.e., $\varepsilon \sim (1 - 3f_L)$.

We have carried out systematic studies of the interrelation of the structure-phase state of irradiated zirconium alloys having different composition with IIG and irradiation creep as the basic constituents of shape changes in items [9,10,12,13,17–24]. As a result of the investigations, data of great importance were obtained that allow us to predict the in-pile behavior of the alloys and recommend the updated composition of the alloys.

Irradiation Growth

The dependences of IIG of the most frequently used Zr alloys have been analyzed and compared [19,22,23]. Because Zr materials were irradiated in various reactors having different energies of fast neutrons, we used the value of the damage dose expressed in displacements per atom (dpa). The comparison between the irradiation conditions in BOR-60, PWR, and VVER-1000 reactors implemented on the basis of the experimentally obtained data and the magnitude of the damage dose in dpa is presented in Fig. 5; it leads to the following ratio : 1 dpa = PWR $(0.5–0.8) \times 10^{25}$ n/m^2 $(E > 1$ MeV) = BOR 0.5×10^{25} n/m^2 $(E > 1$ MeV) = BOR 2×10^{25} n/m^2 $(E > 0.1$ MeV) = VVER 1.2×10^{25} n/m^2 $(E > 0.1$ MeV) = VVER $(0.7–0.8) \times 10^{25}$ n/m^2 $(E > 1$ MeV).

The IIG of the systems alloying with Nb (E110, E125, and M5); Sn, Fe, Cr, and Ni (Zry-2,-4), or by combined Nb, Fe, and Sn (E635, NSF, and ZIRLO) is quite different [43–45,60,61]. The alloys having various structure–phase states

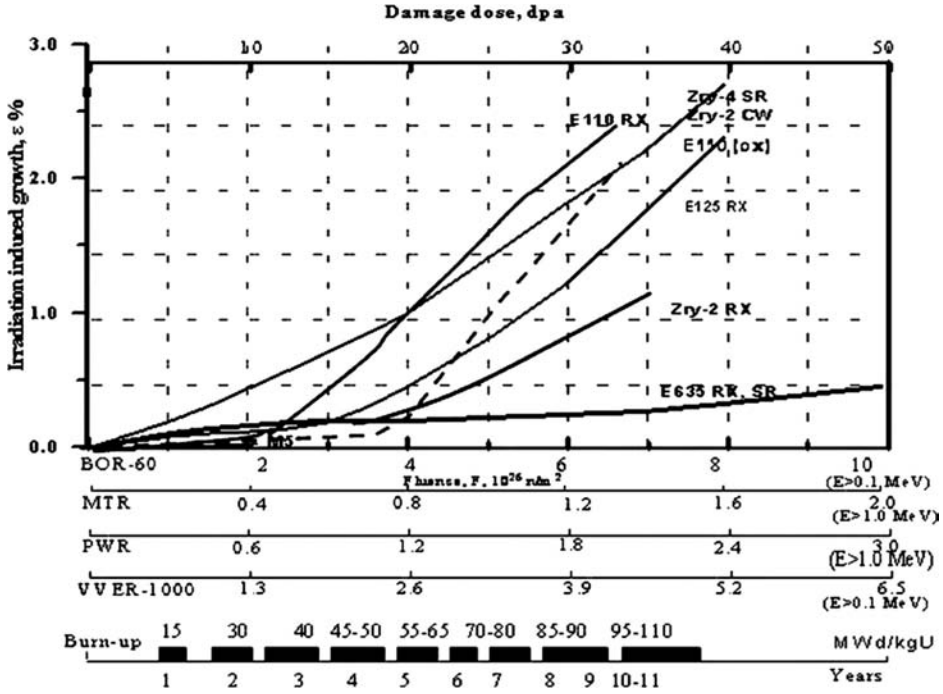


FIG. 5—*Irradiation growth of Zr alloys at 290–350°C as a function of neutron fluence and damage dose [19].*

also have different irradiation growths. The minimal one is found in alloys of Zr–Nb–Fe–Sn system. In different alloys, an accelerated growth begins at different doses after the saturation stage (i.e., the incubation period). Coldworked alloys feature an essentially complete absence of the incubation period [25,40,43–45].

Dependence of Irradiation-Induced Growth on the E635 Alloy Structure

The IIG of the E635 alloy in different structure state (51 % coldworked, annealed in α- or $(\alpha+\beta)$-area; quenched from $(\alpha+\beta)$-area; and β-quenched) is shown in Fig. 6. All annealed states demonstrate low irradiation growth at a high damage dose (20 dpa), which evidences a long incubation period that is determined by an α-matrix composition, the phase-state, and the original dislocation structure.

In the alloy quenched from the upper part of the $(\alpha+\beta)$-area at low doses, almost a linear growth is observed; then, a saturation stage sets off. The IIG of the β-quenched alloy is extremely low. Here, the role of the isotropic texture shows up and the relation $\epsilon \sim (1-3f_L)$ is proved.

The coldworked alloy grows according to the essentially linear law; however, the growth rate is low. A higher degree of coldworking leads to higher IIG [17–21]. The coldworked alloy has a cell dislocation structure with **a**- and **c**-type

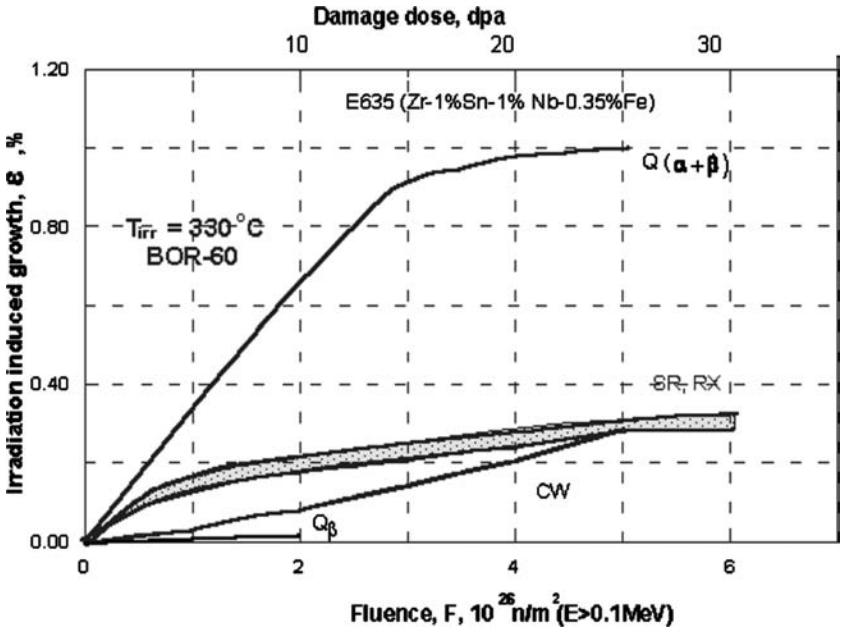


FIG. 6—*Influence of E635 alloy structure-phase state on irradiation growth under BOR-60 irradiation (E>0.1 MeV) at 330°C [19].*

dislocations of a higher density. The anneal of the cw alloy in the α-area gives rise to a partial recrystallization. After quenching from the upper part of the $(\alpha + \beta)$-area along with the α-Zr grains, α'-Zr grains form as a result of martensitic transformation. The α-Zr grains do not essentially contain Fe and Nb, while α'-Zr needles are oversaturated with Fe, Nb, and Sn. After β-quenching a completely martensitic structure α'-Zr is formed from the oversaturated phase [62–65]. α'-Zr contains up to 1 % Nb, 0.4 % Fe, and 1.2 % Sn.

Irradiation-Induced Growth Dependence on Alloying Composition

The most operative factor that affects the irradiation-induced growth of Zr–Nb–-Fe–Sn alloys is the content of iron (Figs. 7 and 8). The E635 type alloys containing 0.30–0.65 % Fe and up to 2 % Nb show similarly low IIG even at the dose of about 30 dpa. The influence exerted by variations in the Nb content of the alloy within 0.6–1.2 % and Fe in the range of 0.25–0.60 % on IIG is practically not noticeable. At the Fe content reduced to 0.15–0.10 % in the IIG versus fluence dependence, a breakdown appears and an accelerated growth starts (Fig. 7). The dose dependence of IIG of the Zr-1Nb type alloys with 0.01–0.25 % Fe shows the breakdown above which the strain rate sharply increases. As the iron content increases, the incubation period of those alloys prolongs and IIG is noticeably decreased (Fig. 7).

At different fluences, the dependence of the irradiation growth strain of specimens from Zr-1Nb type alloys with 0.01–0.25 % Fe on the iron content shows that even 0.03–0.05 % Fe substantially reduces IIG. The further

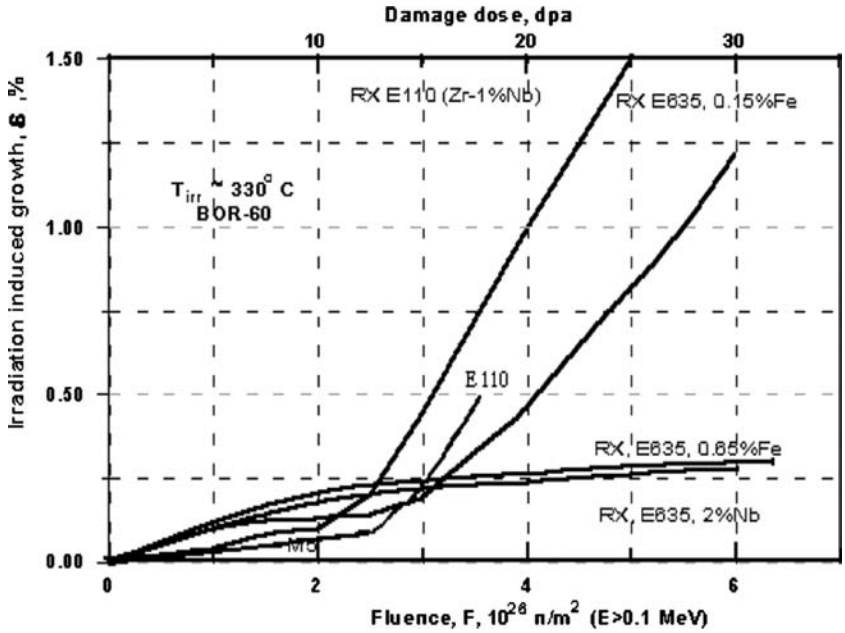


FIG. 7—*Irradiation-induced growth of E110 and E635 type alloys cladding tubes with different Fe, Nb, and Sn contents (wt %) under BOR-60 irradiation (E>0.1 MeV) at 330°C. RX E110 (Zr-1Nb), 100 ppm Fe; E110, 300 ppm Fe.*

increasing of Fe content does not considerably affect the IIG (Fig. 8). Thus, the relation of the irradiation growth to the iron content of the Zr-1Nb type alloys was revealed. It has been shown that a higher Fe content of the alloy lowers down IIG, but mainly at the expense of its increasing in solid solution. At the Fe content above the solubility limit, the effect becomes weaker.

Influence of Hydrogen on Irradiation-Induced Growth

The studies of the influence produced by the composition of Zr–Nb alloys with Fe and Sn revealed that the E635 alloy is substantially resistant to shape changes under oxidation and hydrogenation. Under irradiation in a Na cooled reactor (BOR-60), the content of hydrogen in coolant sometimes increases significantly, and the resultant hydrides lead to volume changes and influence the elongation of the samples. The decision was taken to cover all the sample surfaces in an oxide coat as it is done during the operation in reactors. With this aim in view, a series of experiments was carried out to introduce different quantities of hydrogen into specimens and to oxidize the surface. This kind of work also has a purely practical application because of hydrogen pick-up by zirconium alloys in reactors [38,62]. The hydrogen content of the E110 alloy increase to 200–500 ppm increases its IIG by a factor of 6–7 (at the doses of 10–15 dpa), in comparison to the original alloy with 5 ppm of hydrogen. At the same time, in the E635 alloy irradiation growth weakly depends on the content of hydrogen.

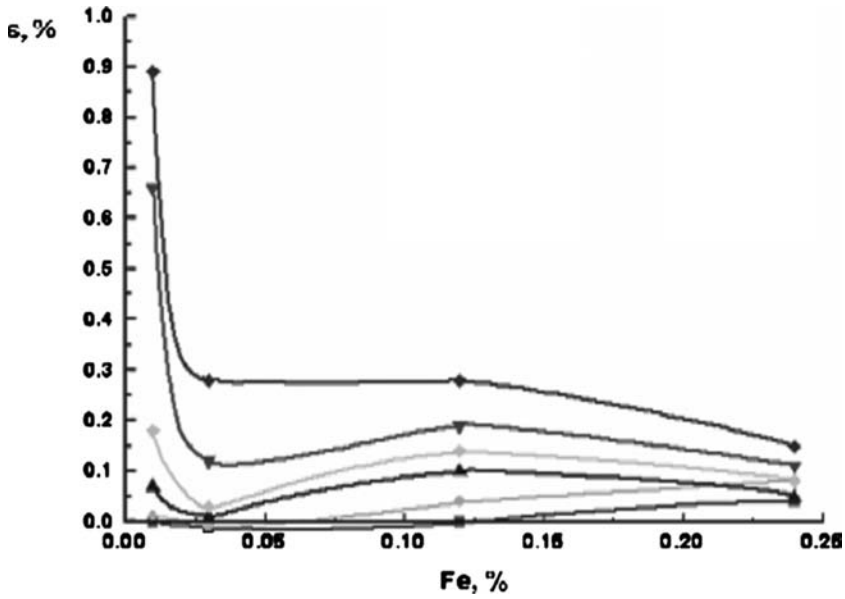


FIG. 8—*Irradiation-induced growth of Zr-1Nb cladding tubes versus Fe content (BOR-60 irradiation, E>0.1 MeV, and T=330°C), fluence:* ■, 0.7×10^{26} m^{-2}; ●, 1.8×10^{26} m^{-2}; ▲, 2.5×10^{26} m^{-2}; ◆, 3.8×10^{26} m^{-2}; ▼, 4.5×10^{26} m^{-2}; *and* ◇, 6.3×10^{26} m^{-2}.

Influence of Surface Oxide Coat on Irradiation-Induced Growthj

A thin oxide coat (1–5 μm) on the surface of the E110 tube specimens substantially decreases IIG. On the contrary, thicker coats of 10–15 μm enforce IIG of the alloys due to the hydrogen induction at oxidation. It has been established that a protective oxide coat (1–5 μm) creates tensile strains in the metal, and at the beginning, a negative growth may appear due to the stress relaxation. The existence of an oxide coat (1–15 μm) in the E635 alloy tubes does not influence its IIG, which might be due to its higher strength.

Influence of Irradiation Temperature on Irradiation-Induced Growth

The results of the measurements of IIG versus temperature of BOR-60 irradiation at the fluence $F = 4 \times 10^{26}$ m^{-2} have shown that lower growth is observed in the E110 type alloys (with no Sn) as the irradiation temperature rises from 315 to 345°C. The alloys of the E635 type do not show a noticeable decrease in IIG with a temperature rise.

Irradiation-Thermal Creep

The favorable effect of the iron alloying of Zr-1Nb also shows up in the irradiation-thermal creep resistance [5–8,22–24]. Additives of iron up to 0.1 % result in a significant reduction of strain (Fig. 9). As the iron content increases from 0.01 % to 0.12 %, the E110 alloy tubes irradiated to the fluence of

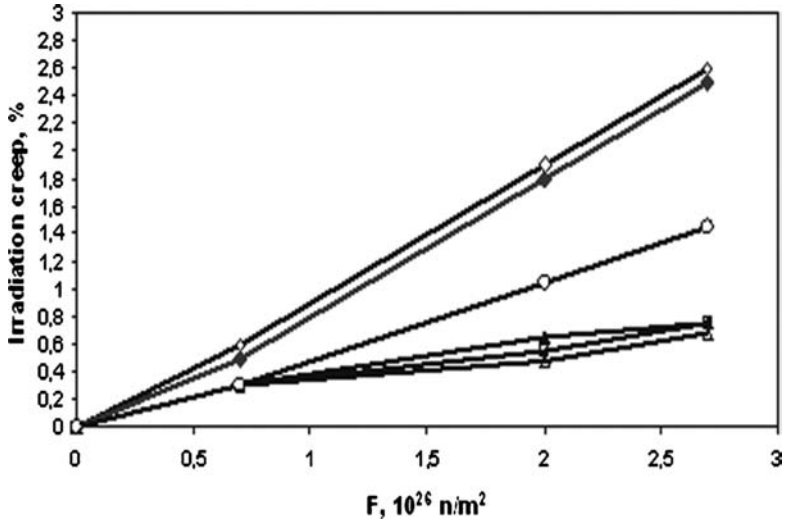


FIG. 9—*Neutron fluence dependence of irradiation creep strain of gas filled tubular samples from E110 and E635 type alloys irradiated at 325°C and tangential stress of 113 MPa:* ◇, *Zr-1Nb (100 ppm Fe);* ◆, *Zr-1Nb (150 ppm Fe);* ○, *E110M- Zr-1Nb (1000 ppm Fe);* △ , *Zr-0.8Sn-0.3Fe-1Nb;* ▲, *E635M -Zr-0.8Sn-0.3Fe-0.6Nb; and* □, *E635 (Zr-1.2Sn-0.3Fe-1.0Nb).*

1.3×10^{26} m^{-2} at 360–370°C were observed to decrease their creep strain by a factor of 2 (Fig. 10). The lowest level of strains is revealed in alloys of the E635 type. The creep strains of E635M (Zr-0.8Nb-0.3Fe-0.8Sn) and E635 (Zr-1Nb-0.3Fe-1.2Sn) tubes are essentially similar and are about 0.4 %.

Comparison between elongations and IIGs of E110 and E635 fuel claddings (diameter of 9.1×7.7 mm and wall thickness of 0.7 mm) irradiated in VVER-1000 and IIG samples irradiated in BOR-60 has shown that shape changes in the E110 items are to a larger extent controlled by their irradiation-thermal creep than those of the E635 ones. The acquired data allow us to predict shape changes in items produced from Zr alloys under nuclear reactor irradiation.

Tensile Properties

The yield strength of an alloy after irradiation depends on its Fe content and grows with its increase (Fig. 11). The substantial increase in $\sigma_{0,2}$ is observed as the Fe content grows and rises with its increases from 0.01 % to 0.12 %. Then the strength grows to a less extent, which corroborates our conviction that the cause of strengthening is the irradiation-induced solid solution supersaturation.

Structure and Phase States of Irradiated Zr Alloys

Under neutron irradiation, there occur the formation and evolution of defects such as dislocation loops of the **a**- and **c**-types that have Burgers vectors 1/

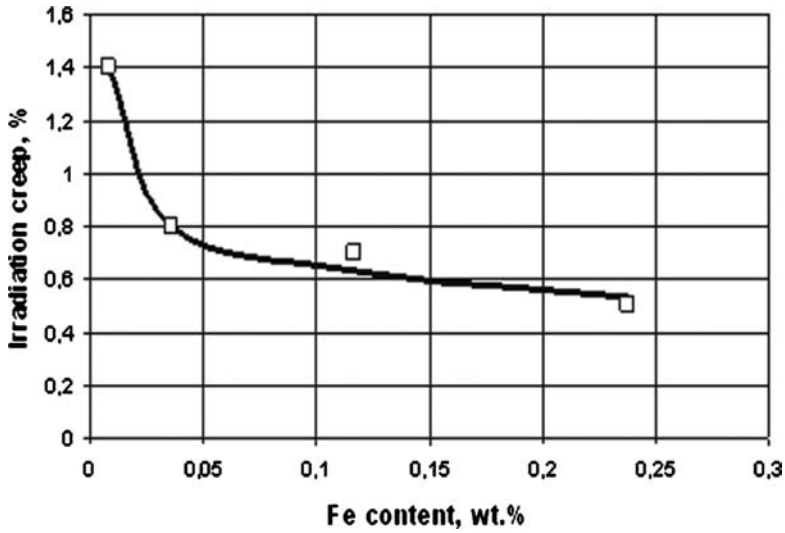


FIG. 10—*Influence of the iron content in the Zr-1Nb alloy on the irradiation creep strain (370°C, 113 MPa, and neutron fluence of* $1.3\times10^{26}\ m^{-2}$*).*

3[11.0] and 1/2[00.1], or 1/6[20.3]. The **c**-component dislocation loops lie in the basal or pyramid planes of the HCP lattice of the Zr matrix and, for the most part, have a vacancy character [25–32]. A substantial difference in the **c**-dislocation densities in different alloys irradiated to close fluencies has been revealed

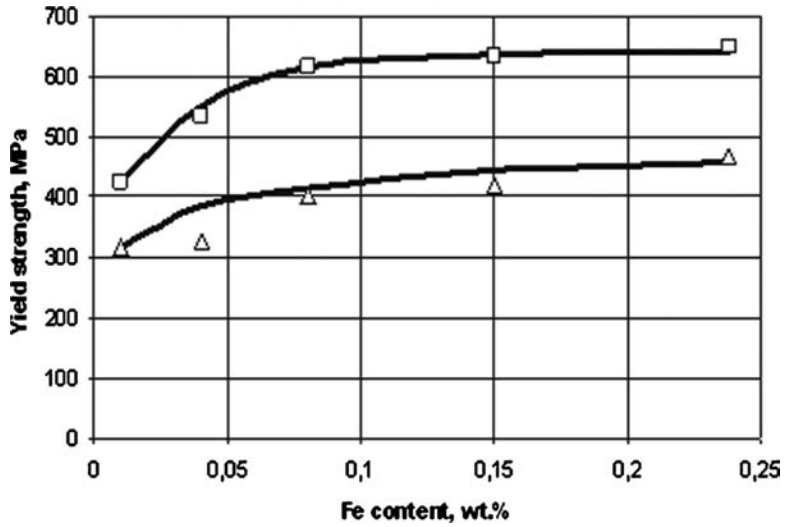


FIG. 11—*Influence of the iron content in the Zr-1Nb alloys on the yield strength at 20°C (□) and 350°C (△) after irradiation (BOR-60, 370°C, and neutron fluence* $1\times10^{26}\ m^{-2}$*).*

[40]. In the E635 alloys, **c**-dislocations nucleate and grow at high doses, and it correlates with the low level and a variation in the rate of IIG [9,10,12,13,17–23]. Regularities in structural changes of the alloys have been established. For the first time, a decrease in the Nb content of β-Nb particles under neutron irradiation was observed [9,10,13]. In Zr–Nb alloys irradiated to 20–30 dpa, the size of β-Nb particles increases a little, the number density lowers, and the Nb content of the particles decreases to 60–70 %; in this case the **c**-type dislocation density becomes noticeably higher (Fig. 12).

In the E110 and E635 alloys, niobium and iron redistribute between SPPs and the matrix. At low fluences, there are no changes in the Laves phase lattice, although its composition is already changed. When the specific composition is reached at the doses of about 10 dpa, the HCP phase transforms into a phase of the β–Nb type with the BCC lattice. The variations in the composition of the particles versus the fluence (or a damage dose) under irradiation are illustrated in Fig. 13. Small particles up to 150 nm are depleted in iron to a greater extent than the coarse ones. The periphery of precipitates is more depleted in iron than the central parts. The substructure looks polycrystalline (Fig. 14), which makes it noticeably different from SPPs in Zircaloys [25–32] and corroborates the important role played by the Nb and Fe combination in the resistance of phases under irradiation. The composition, the crystal lattice, and the type of the SPPs control their irradiation resistance. For instance, the HCP lattice is less irradiation resistant than the cubic one. Under the condition of the BOR-60 or VVER irradiation at 300–350°C, no amorphization of Laves phase precipitates $Zr(Nb, Fe)_2$ takes place.

Precipitates of a Nb—depleted coarser phase (T)—$(Zr, Nb)_2Fe$ having the FCC lattice, and the composition of 60Zr-10Nb–30Fe (at. %) seem not to experience any changes [9,13,18,19]. However, later on the periphery, the depletion with Zr and Fe and the formation of Nb-enriched particles were revealed (Fig. 15) [22,23].

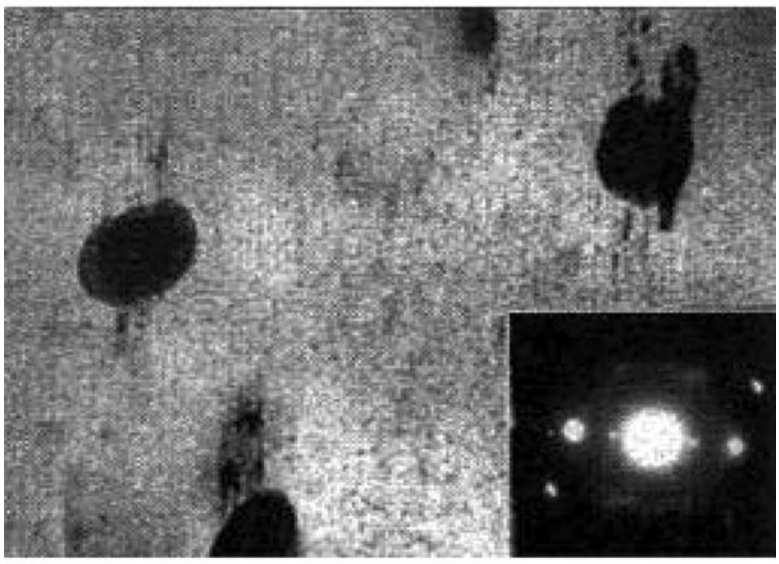
If before irradiation in the E635, the matrix contained no more than 0.4–0. 6% Nb and essentially no iron since all of it was available in Laves phase, after irradiation practically all iron goes into the matrix [18,22,23] and strengthens the alloy (Fig. 13). The α-Zr matrix becomes oversaturated with iron, which affects substantial changes in the corrosion and irradiation resistance of the alloy.

The precipitation of secondary irradiation-induced finely dispersed particles (IIP) was established. The particles assumingly have the BCC crystal lattice are enriched in Nb (and possibly in Fe). They are discovered in the E110 and to a less extent in the E635 (Fig. 16) [9,10,12,18–23]. Particles of this kind were more often revealed in Nb containing alloys [30,40]. Their identification is difficult because of their small size; they may look like and be interpreted as loops "in profile" [11].

We have determined that stresses in materials and alloying with iron leads to ordering of IIP. Their distribution along the basal planes (at 20°–30° deviation) is clearly related to the orientation-crystallographic correspondence of the BCC and HCP lattices (between the β- and α-phases) that was first established by Burgers [63].



(*a*)



(*b*)

FIG. 12—*Microstructure of cladding tubes from alloys irradiated to* $3.6\times10^{26}\ m^{-2}$*:* (a) *Zr-1Nb-β-Nb phase precipitates,* **c***-dislocations, secondary IIP particles;* (b) *Zr-0.8Nb-0.3Fe-1.2Sn-β-Nb type precipitates (former Laves phase),* **c***-dislocations,* **g**=*00.2.*

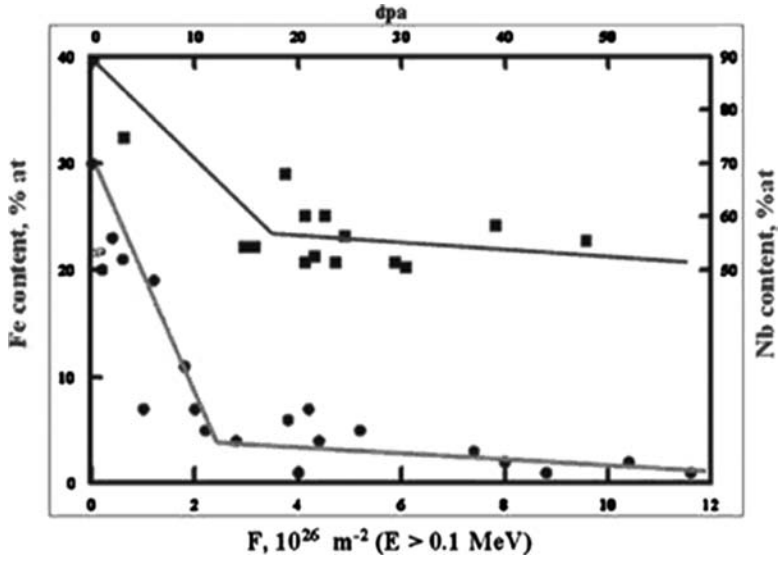


FIG. 13—*Content of iron (●) variation in Laves phase precipitates in E635 and niobium (■) in β-Nb in E110 under BOR-60, VVER, and RBMK neutron irradiation.*

Structure and Irradiation-Induced Growth

The analysis of the results of IIG and the microstructure has shown that the **c**-type dislocation density is increased (more than $1 \times 10^{14}\,m^{-2}$) in the alloys that are subject to a significant irradiation growth.

- Recrystallized Zr-1Nb alloy
- $(\alpha + \beta)$-quenched E635 alloy (in α-grains)
- In coldworked and annealed E635 alloys and its modifications having 0.65 % Fe and up to 2–3 % Nb irradiated to very high doses—more than 30 dpa

The IIG of alloys based on the E635 at high doses is noticeably lower than that of Zr–Nb or Zircaloys. The rate of the IIG of cw E635 is also substantially lower than that of all other cw alloys; this points to a specific role of the compositions. The investigation reveals a weak evolution of the **c**-component dislocations, primarily close to particles in the regions of the matrix enriched in iron.

Comparing the microstructure of the alloys (the density of **c**-dislocations) and IIG, we may conclude that the composition of the matrix plays the basic part. The alloy of the E635 composition has the longest incubation period before the onset of the growth acceleration that is practically independent on the structure state. It is the composition of the E635 alloy determining the original α-matrix solid solution composition ($Zr - 1.2\,\%\,Sn - 0.3\,\%\,Nb - < 0.02\,\%\,Fe$) and the composition of SPPs-$(Zr, Nb)_2Fe$ and the Laves phase that stimulates the low irradiation growth at high fluences. The role played by tin is not yet quite clear. The quantity of Nb and Fe, which is most favorable for many functional properties (irradiation growth, corrosion, and strengthening), is close to the solubility limit of the alloying elements in the matrix.

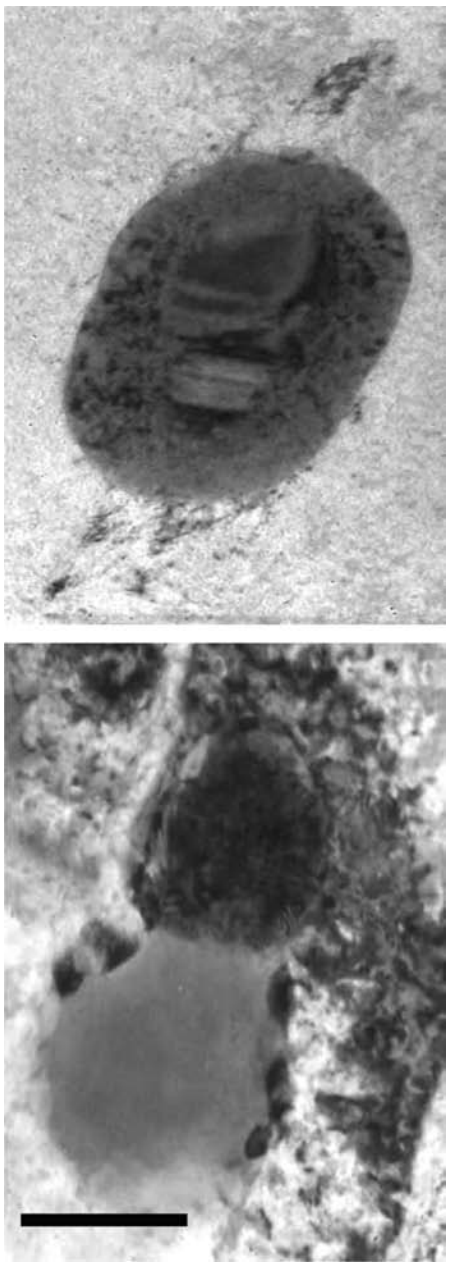


FIG. 14—*Laves phase precipitates* $Zr(Nb,Fe)_2$ *in E635 type alloy (Zr-0.8Nb-0.3Fe-1.2Sn) irradiated to the neutron fluence* $3.6\times10^{26}\,m^{-2}$*: Polycrystal precipitates at the periphery.*

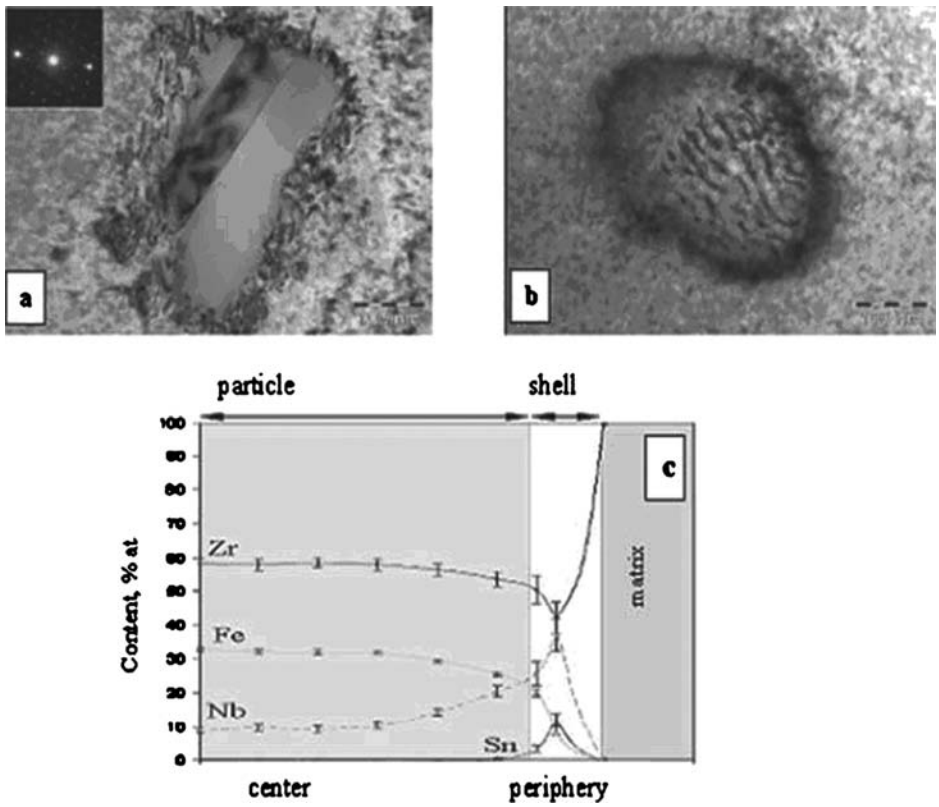
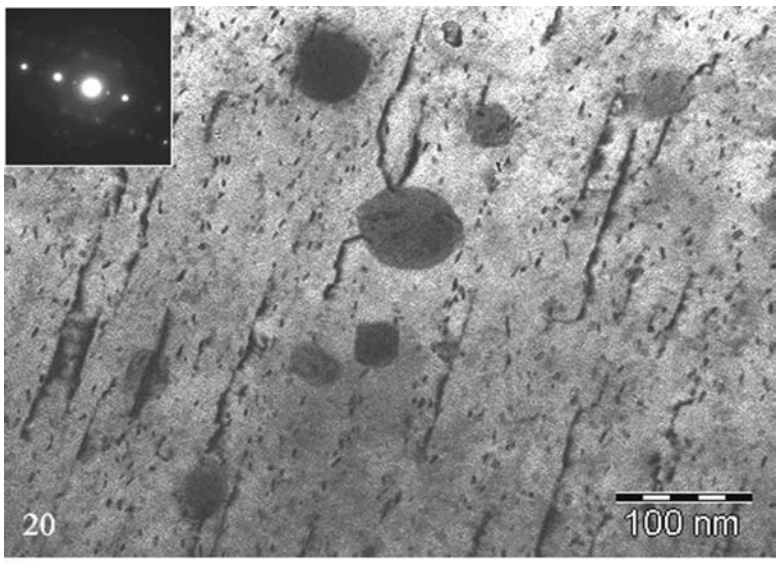


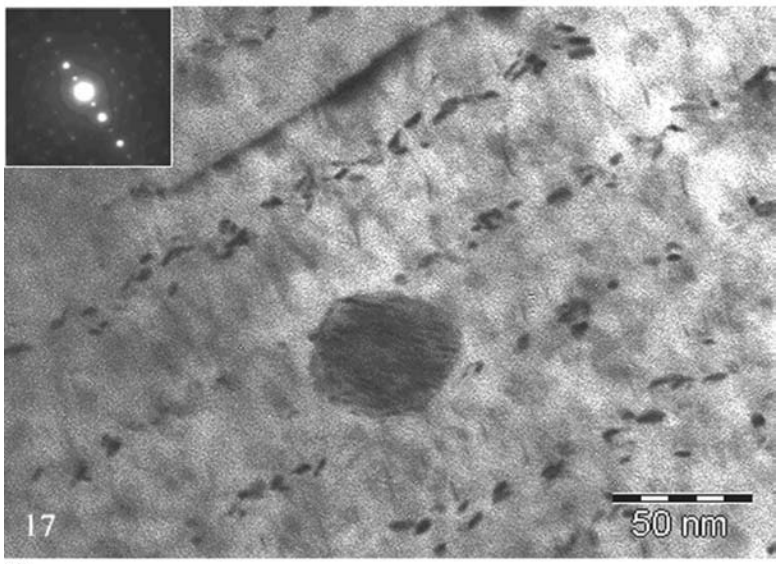
FIG. 15—*T-phase precipitates* $(Zr,Nb)_2Fe$ *in E635 type alloy (Zr-0.7Nb-0.3Fe-1.2Sn) irradiated to the neutron fluence* 3.6×10^{26} m^{-2}: (a) *plate precipitates at the periphery;* (b) *T-phase shell; and* (c) *element distribution within particle and on boundary with matrix.*

Currently, the common dependences of irradiation influence on the variations in the composition and crystal lattices of precipitates and the α-Zr matrix and on the relationship between a microstructure and properties have been established. Fundamental mechanisms of the irradiation-induced damageability, the influence of the structure-phase state and its evolution in the processes of irradiation on the properties of a material have not been fully ascertained so far; however, the proceeding processes are mechanistically understood. The further direction for future research involves studies of the process of forming irradiation-induced secondary precipitates in the alloys of the Zr–Nb-(Fe–Sn) system and their influence on the properties; the development of models; and the study of diffusion of Nb, Fe, and Sn under irradiation and the interrelation of the **a**- and **c**-component dislocations formation with the acceleration of an irradiation growth.

The influence of stress and iron alloying on the ordered distribution of **a**-type loops [22–24] under BOR-60 and VVER irradiation has been established. The **c**-dislocation formation and growth (Fig. 17) also depend on the alloy



(*a*)



(*b*)

FIG. 16—*(a) Microstructure of E110 alloy cladding tubes irradiated in VVER-1000 (burnup of 54 MW day/kg U): Finely IIP precipitates enriched in niobium, precipitates of β-Nb and* **c***-component dislocations,* **g***=00.2;* (b) *Microstructure of E110M alloy (Zr-1Nb-0.1Fe) irradiated in BOR-60 to the neutron fluence* $3.6\times10^{26}\ m^{-2}$*, ordered finely dispersed precipitates of β-Nb type (IIP).*

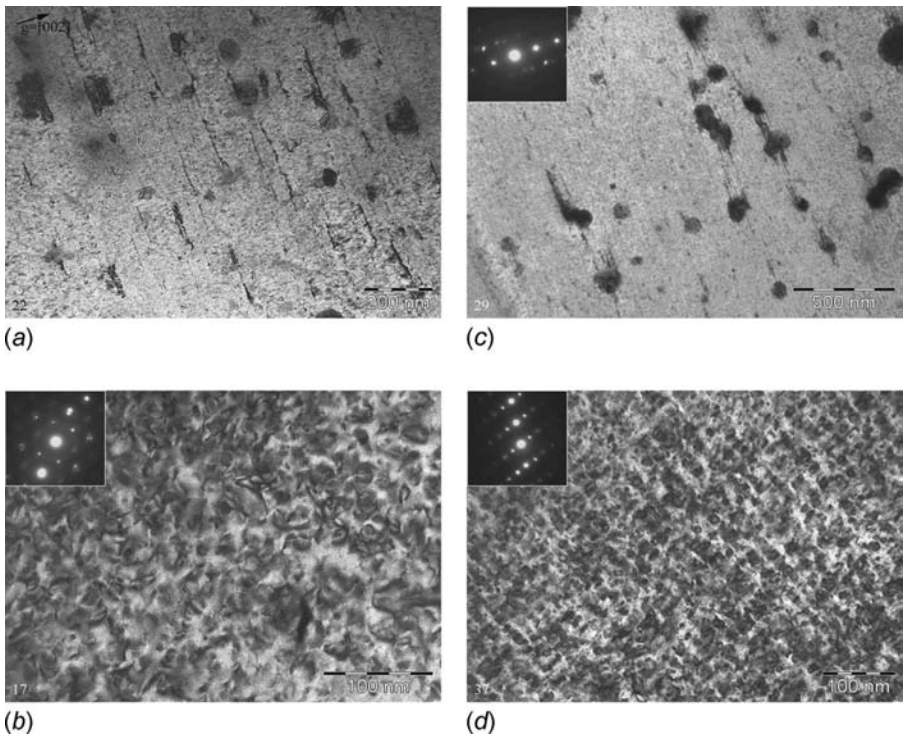


FIG. 17—*Microstructure of alloys irradiated in BOR-60 to the neutron fluence* 3.6×10^{26} m^{-2}*: Zr-1Nb (*a*) β-Nb precipitates,* **c***-dislocations,* **g***=00.2; (*b*) dislocation loops of a-type,* **g***=10.1; Zr-0.8Nb-0.3Fe-1.2Sn (c)* **c***-dislocations, β-Nb phase precipitates,* **g***=00.2; (*d*) ordered* **a***-type dislocation loops,* **g***=10.1.*

composition and irradiation conditions and correlate with irradiation growth strain. A higher iron (and tin) content in Zr–Nb alloys decreases the **c**-dislocation density and orders **a**-loops. As it is seen in Fig. 17, the ordering of **a**-loops and IIP particles and a decrease in the IIP and **c**-dislocation densities are interrelated and depend on stress and alloying first with iron and niobium and then with tin.

A higher iron content of the Zr–Nb alloy leads to a lower creep and strengthening of the matrix under irradiation. The ongoing processes in this case are the following:

- Laves phase precipitates are formed at the Fe content above the solubility limit
- Under neutron irradiation iron moves from particles to the matrix
- Matrix becomes supersaturated with iron, the lattice is distorted, stress fields retard the dislocations motion, the material is strengthened
- Fe-depleted Laves phase transforms from HCP to BCC of β-Nb type
- Under irradiation, initial β-Nb particles present in Zr–Nb alloys become depleted in Nb (or enriched in Zr)

- At the same time irradiation induces finely dispersed particles enriched with Nb and, perhaps, with iron, precipitate in the matrix
- Their distribution is controlled by crystallographically orientated correspondence of BCC and HCP lattices that are dependent on iron content and stresses of the alloy
- An increased iron content of Zr–Nb alloys and a tin addition promote a decrease of **c**-dislocation density by ordering **a**-loops, and ordering IIP with smaller sizes and lower concentration.

On the basis of a complex set of investigations and as a result of in-pile tests of advanced alloys, it has been established that the alloying of Zr-1Nb with iron leads to a higher resistance to irradiation and thermal creep, reduced irradiation growth, and increased strengths mostly because of raising the iron content of the solid solution. With the rise of the fluence, the advantages of the iron containing alloys will increase. The interrelation between the composition, microstructure, and properties of the alloys before and after neutron irradiation has been found. Proceeding from this fact, the following alloys have been developed: E110M (Zr-1%Nb-0.1 % Fe-0.13 % O) and E635M (containing Zr-0.8 % Nb-0.3 % Fe-0.8 % Sn).

Conclusion

The composition and the structure-phase state at different stages of the technology process influenced the deformation ability of the alloys; the optimal composition of an alloy and heat treatment conditions were advanced.

The interrelation between the structure-phase state of irradiated Zr–Nb and Zr–Nb–Fe–Sn system alloys and the shape changes of items (irradiation and thermal creep and irradiation-induced growth) were studied systematically. The most important data were acquired, which allowed us to predict the in-pile behavior of the alloys and recommend the advanced alloy compositions for high burnups and long-term exposures. The regularities in evolving of the microstructure and the microchemical composition of the Zr–Nb and Zr–Nb–-Fe–Sn system alloys under neutron irradiation were established.

The **c**-dislocation formation and growth depend on the alloy composition, irradiation conditions, and correlate with irradiation-induced growth. A higher iron (and tin) content in Zr–Nb alloys decreases the **c**-dislocation density and orders **a**-loops. An ordering of **a**-loops and IIP particles, and a decrease in the IIP and **c**-dislocation number densities are interrelated and depend on stress and alloying first with iron and niobium and then with tin. A higher iron content of the Zr–Nb alloy leads to a lower creep and strengthening of the matrix under irradiation.

β-Nb particles become Nb depleted or Zr enriched and dissolve partially, and an irradiation-induced precipitation of secondary finely dispersed particles takes place.

Under irradiation, the particles of the Laves phase (HCP) become depleted in iron and transformed into the phase of β-Nb (BCC) type. In this case, the matrix content of Fe increases, which results in substantial changes in corrosion and irradiation resistance.

Acknowledgments

It is great honor for the writer to receive the 2009 Kroll Medal personally, but first it is the recognition of achievements of Russian and Soviet radiation material science of zirconium. The writer would like to share the honor with the people he has been happy to work together in Russia for years and who have contributed a lot in his insight in Zr's and its alloys' behavior (A. Nikulina, Yu. Sokursky, P. Shebaldov, M. Peregud, V. Markelov, G. Kamyshev, M. Astrahantsev, V. Konkov, A. Tselischev, S. Averin, V. Panchenko, A. Kozlov, V. Shamardin, A. Novoselov, G. Kobylyanskiy, Z. Ostrovsky, and A. Obukhov). The list goes on. The writer appreciates the help and friendship he has received from international cooperation, joint projects, or discussions with colleagues: R. Adamson, M. Griffiths, D. Gilbon, C. Lemaignan, P. Rudling, V. Rebeyrolle, B. Cox, A. Motta, Y. S. Kim, and many others). The writer's special gratitude is to all the members of the laboratory in VNIINM whom the writer works with every day, as well as to the Institute and JSC TVEL authorities encouraging and assisting him in his research.

References

[1] Ambartsumyan, R. S., Kiselev, A. A., Grebennikov, R. V., Myshkin, V. A., Tsuprun, L. I., and Nikulina, A. V., "Mechanical Properties and Corrosion Resistance of Zirconium and its Alloys in Water, Steam and Gases at Elevated Temperature," *Proceedings of Second International Conference on the Peaceful Uses of Atomic Energy*, Vol. 6, Geneva, CH, 1958, United Nations, New York, p. 12, Conf. 15/P/2044.

[2] Amaev, A. D., Ambartsumyan, R. S., Kiselev, A. A., Konobeevskiy, S. T., Anisomova, I. A., Glukhov, A. M., Lebedev, L. M., Myshkin, V. A., Goncharov, V. V., Ivanov, E. G., Orlov, M. S., Pravdyuk, P. F., Ryazantsev, E. P., and Skvortsov, V. V., "Influence of Some Factors upon Hydriding and Variation Properties of Zirconium Alloy with 1 % Nb Used for Fuel Element Cladding in Water-Moderated Water-Cooled Power Reactors," *Proceedings of Third U.N. Int. Conf. on Peaceful Uses of Atomic Energy*, Geneva, CH, 1964, United Nations, New York, A/Conf. 28/P/342.

[3] Ageenkova, L. E., Nikulina, A. V., Shebaldov, P. V. and Peregud, M. M., "Structural and Phase Transformations in Zr–Nb Binary Alloys and Other Relation to Properties," *Proceedings of the International Conference on Irradiation Materials Science*, Vol. 6, Alushta, May 29, 1990, Kharkov, pp. 64–72.

[4] Shebaldov, P. V., Peregud, M. M., Nikulina, A. V., Bibilashvili, Yu. K., Lositski, A. F., Kuzmenko, N. V., Belov, V. I., and Novoselov, A. E., "E110 Alloy Cladding Tube Properties and Condition and Impurity Content," *12 International Symposium on Zr in the Nuclear Industry, ASTM STP1354*, Toronto, Canada, 1998, G. P. Sabol and G. D. Moan, eds., ASTM International, West Conshohocken, pp. 545-558.

[5] Amaev, A. D., Anisimova, I. A., Nikulina, A. V., Saenko, G. P., Sedova, A. V., and Fiveiskij, M. B., "Corrosion of Zr Alloys in Boiling Water Under Irradiation," *Proceedings of Fourth International Peaceful Uses of Atomic Energy*, Geneva, CH, 1971, United Nations, New York, A/Conf.49/P/428.

[6] Ageenkova, L. E., Zaviyalov, A. R., Nikulina, A. V., and Fiveisky, M. B., *Zr-2.5Nb and Zr-1Nb-0.1Sn-0.4Fe Alloy Creep and Its Dependence on Heat Treatment*, VNIINM, Moscow, 1977, Vol. 11, p. 22.

[7] Nikulina, A. V., Markelov, V. A., Peregud, M. M., Bibilashvili, Y. K., Kotrekhov, V. A., Lositsky, A. F., Kuzmenko, N. V., Shevnin, Y. P., Shamardin, V. K.,

Kobylyansky, G. P., and Novoselov, A. E., "Zirconium Alloy E635 as a Material for Fuel Rod Cladding and Other Components of VVER and RBMK Cores," *Zr in the Nuclear Industry: 11th International Symposium of ASTM STP 1295*, Garmisch-Partenkirchen, Germany, 1995, E. R. Bradley and G. P. Sabol, eds., ASTM International, West Conshohocken, pp. 785–804.

[8] Solonin, M. I., Bibilashvili, Yu. K., Nikulina, A. V., Shishov, V. N., Peregud, M. M., Novoselov, A. E.,"Zirconium Alloy for Fuel Assemblies of New Generation VVER," *International Topical Meeting "TopFuel'99," Proceedings of the SFEN/ENS Conference*, Avignon, France, Sept. 13–15, 1999, pp. 165–177.

[9] Shishov, V. N., Nikulina, A. V., Markelov, V. A., Peregud, M. M., Kozlov, A. V., Averin, A . V., Kolbenkov, S. F., and Novoselov, A. E., "Influence of Neutron Irradiation on Dislocation Structure and Phase Composition in Zr-Base Alloys," *11th International Symposium on Zr in the Nuclear Industry, ASTM STP 1295*, Garmisch-Partenkirchen, Germany, 1995, E. R. Bradley and G. P. Sabol, eds.ASTM International, West Conshohocken, PA, pp. 603–622.

[10] Nikulina, A. V., Shishov, V. N., Peregud, M. M., Tselishchev, A. V., Shamardin, V. K., and Kobylyansky, G. P., "Irradiation Induced Growth and Microstructure Evolution of Zr-1.2Sn-1Nb-0.4Fe Under Neutron Irradiation to High Doses," *18th Symposium on Effects of Radiation on Materials, ASTM STP 1325*, 1997, R. K. Nanstad, M. L. Hamilton, F. A. Garner, and A. S. Kumar, eds., ASTM International, West Conshohocken, PA, pp. 785–804.

[11] Gurovich, B. A., Astrahantsev, M. S., Platonov, P. A., and Yelesin, L. A., "Formation of Periodic Lattices of Radiation Defects in Zr-1% Nb Alloy During Irradiation by Fast Neutrons and Their Sensibility to Temperature and External Stresses," *Fiz. Met. Metalloved.*, Vol. 61, 1986, pp. 922–930.

[12] Nikulina, A. V., Markelov, V. A., Peregud, M. M., Voevodin, V. N., Panchenko, V. L., and Kobylyansky, G. P., "Irradiation-Induced Microstructural Changes in Zr-1 % Sn-1 % Nb-0,4 % Fe," *J. Nucl. Mater.*, Vol. 238, 1996, pp. 205–210.

[13] Averin, S. A., Panchenko, V. L., Kozlov, A. V., Shishov, V. N., Sinelnikov, L. P., Nikulina, A. V., "Evolution of Dislocation and Precipitate Structure in Zr Alloys Under Long-Term Irradiation," *12th International Symposium on Zirconium in the Nuclear Industry, ASTM STP 1354*, Toronto, 1998, G. P. Sabol and G. D. Moan, eds., ASTM International, West Conshohocken, PA, 2000, pp. 105–121.

[14] Nikulina A. V., Peregud M. M., Shamardin V. K., and Kobylyansky, G. P., "Metallurgical Factors Defining Materials Science," *Int. Conf. on Irradiation Materials Science*, May 1990, Alushta, Vol. 4, Kharkov, pp. 40–46.

[15] Zaimovsky, A. S., Nikulina, A. V., and Reshetnikov, N. G., *Zirconium Alloys in Nuclear Power*, Energoatomizdat, Moscow, 1994.

[16] Nikulin, S. A., Goncharov, V. I., Markelov, V. A., and Shishov, V. N., "Effects of Microstructure on Ductility and Fracture Resistance of Zr-1.3Sn-1Nb-0.4Fe Alloy," *Zirconium in the Nuclear Industry: 11th International Symposium, ASTM STP 1295*, Garmisch-Partenkirchen, Germany, 1995, E. R. Bradley and G. P. Sabol, Eds., ASTM International, West Conshohocken, PA, pp. 695–709.

[17] Kobylyansky, G. P., Shamardin, V. K., Ostrovsky, Z. E., Raetsky, V. M., Nikulina, A. V., Peregud, M. M., and Grigoryev, V. M., "Radiation Form Change of Zr Alloy Cladding and Channel Tubes at High Neutron Fluences," *Proceedings of the International Conference on Radiation Materials Science*, Vol. 4, Alushta, May 22–25, 1990, Kharkov, 1990, pp. 64–72.

[18] Shishov, V. N., Peregud, M. M., Nikulina, A. V., Shebaldov, P. V., Tselishchev, A. V., Novoselov, A. E., Kobylyansky, G. P., Ostrovsky, Z. E., and Shamardin, V. K., "Influence of Zirconium Alloy Chemical Composition on Microstructure Formation

and Irradiation Growth," *13th International Symposium on Zirconium in the Nuclear Industry, ASTM STP 1423*, Annecy, France, 2001, G. D. Moan and P. Rudling, eds., ASTM International, West Conshohocken, PA, pp. 758–779.

[19] Shishov, V. N., Peregud, M. M., Nikulina, A. V., Pimenov, Yu. V., Kobylyansky, G. P., Novoselov, E., Ostrovsky, Z. E., and Obukhov, A. V., "Influence of Structure–-Phase State of Nb Containing Zr Alloys on Irradiation Induced Growth," *14th International Symposium on Zirconium in the Nuclear Industry, ASTM STP 1467*, Stockholm, Sweden, 2004, P. Rudling and B. Kammenzind, eds., ASTM International, West Conshohocken, PA, pp. 666–685.

[20] Kobylyansky, G. P., Novoselov, A. E., Ostrovsky, Z. E., Shishov, V. N., Obukhov, A. V., Shishin, V. Yu., Nikulina, A. V., Peregud, D. W., Mahmood, S. T., White, D. W., Lin, Y.-P., and Dubecky, M. A., "Irradiation-Induced Growth and Microstructure of Recrystallized, Cold Worked and Quenched Zircaloy-2, NSF, and E635 Alloys," *15th ASTM International Symposium on Zirconium in Nuclear Industry, ASTM STP 1505*, Sunriver, OR, June 24–28, 2007, B. Kammenzind and M. Limback, Eds., ASTM International, West Conshohocken, PA, pp. 564–582.

[21] Nikulina, A. V., Kon'kov, V. F., Shishov, V. N., Shamardin, V. K., Novoselov, A. E., and Kobylyansky, G. P., "Zr-Nb Alloys for Use as Components of PWR Reactor Cores," *Proceedings of 5-th International Symposium on Contribution of Materials Investigation to the Resolution of Problems Encountered in Pressurized Water Reactors*, Fontevraud -5, 23-27 September 2002, Vol. 1, SFEN, Fontevraud, France pp. 505–515.

[22] Shishov, V. N., Peregud, M. M., Nikulina, A. V., Kon'kov, V. F., Novikov, V. V., Markelov, V. A., Khokhunova, T. N., Kobylyansky, G. P., Novoselov, A. E., Ostrovsky, Z. E., and Obukhov, A. V., "Structure-Phase State, Corrosion and Irradiation Properties of Zr–Nb–Fe–Sn System Alloys," *15th ASTM International Symposium on Zirconium in Nuclear Industry, ASTM STP 1505*, June 24–28, 2007, Sunriver, OR, ASTM International, West Conshohocken, PA, pp. 724–741.

[23] Shishov, V. N., Peregud, M. M., Nikulina, A. V., Kon'kov, V. F., Novikov, V. V., Markelov, V. A., Khokhunova, T. N., Kobylyansky, G. P., Novoselov, A. E., Ostrovsky, Z. E., and Obukhov, A. V., "Structure-Phase State, Corrosion and Irradiation Properties of Zr–Nb–Fe–Sn System Alloys," *J. ASTM Int.*, Vol. 5, No. 3, 2009, pp. 724–741.

[24] Shishov, V. N., Nikulina, A. V., Novikov, V. V., Markelov, V. A., and Peregud, M. M., "Microstructure and Deformation of Zirconium Alloy," *Nuclear Engineering and Technology*, 1st ed., Material Science and New Materials, Moscow, VNIINM, 2006, pp. 313–328.

[25] Lemaignan, C. and Motta, A. T., "Zirconium Alloys in Nuclear Applications," reprint from *Materials Science and Technology*, VCH Verlag GmbH, Weinheim, Germany, 1995.

[26] Griffiths, M., "Evolution of Microstructure in hcp Metals During Irradiation," *J. Nucl. Mater.*, Vol. 205, 1993, pp. 225.

[27] Griffiths, M., Gilbert, R. W. and Fidleris, V., "Accelerated Irradiation Growth of Zirconium Alloys," *Eighth International Symposium on Zr in the Nuclear Industry, ASTM STP 1023*, 1989, L. F. P. Van Swam and C. M. Eucken, eds., ASTM International, West Conshohocken, PA, p. 658.

[28] Griffiths, M., Holt, R. A., and Rogerson, A., "Microstructural Aspects of Accelerated Deformation of Zircaloy Nuclear Reactor Components During Service," *J. Nucl. Mater.*, Vol. 225, 1995, pp. 245.

[29] Holt, R. A., Causey, A. R., Christodoulou, N., Griffiths, M., Ho, E. T. C. and Woo, C. H., "Non-Linear Irradiation Growth of Cold Worked Zircaloy-2," *11th International Symposium on Zr in the Nuclear Industry, ASTM STP 1295*, Garmisch-

Partenkirchen, Germany, 1995, E. R. Bradley and G. P. Sabol, eds., ASTM International, West Conshohocken, PA, 1996, pp. 623–637.

[30] Gilbon, D., Soniak, A., Doriot, S., and Mardon, J.-P., "Irradiation Creep and Growth Behavior, and Microstructural Evolution of Advanced Zr-Base Alloys," *12th International Symposium on Zr in the Nuclear Industry, ASTM STP 1354*, Toronto, Canada, 1998, G. P. Sabol and G. D. Moan, eds., ASTM International, West Conshohocken, PA, 2000, pp. 51–73.

[31] Griffiths, M., Mecke, J. F., and Winegar, J. E., "Evolution of Microstructure in Zirconium Alloys During Irradiation," *11th International Symposium on Zr in the Nuclear Industry, ASTM STP 1295*, Garmisch-Partenkirchen, Germany, 1995, ASTM International, West Conshohocken, PA, 1996, pp. 580–602.

[32] Adamson, R. B., "Effect of Neutron Irradiation on Microstructure and Properties of Zircaloy," *12th International Symposium on Zr in the Nuclear Industry, ASTM STP 1354*, Toronto, Canada, 1998, ASTM International, West Conshohocken, PA, 2000, pp. 15–31.

[33] Seibold, A. and Garzarolli, F., "Influence of Composition and Condition on In-PWR Behavior of Zr–Sn-Nb–FeCrV Alloys," *Zirconium in the Nuclear Industry: 13th International Symposium, ASTM STP 1423*, Annecy, France, 2001, G. D. Moan and P. Rudling, eds., ASTM International, West Conshohocken, PA, pp. 743–757.

[34] Yueh, H. K., Kesterson, R. L., Comstock, R. J., Shah, H. H., Colburn, D. J., Dahlback, M., and Hallstadius, L., "Improved ZIRLO Cladding Performance Through Chemistry and Process Modifications," *14th International Symposium on Zirconium in the Nuclear Industry, ASTM STP 1467*, Stockholm, Sweden, 2004, P. Rudling and B. Kammenzind, eds., ASTM International, West Conshohocken, PA, pp. 330–346.

[35] King, A. D., Hood, G. M., and Holt, R. A., "Fe-Enhancement of Self-Diffusion in α-Zr," *J. Nucl. Mater.*, Vol. 185, 1991, pp. 174–181.

[36] Gilbon, D. and Simonot, C., "Effect of Irradiation on the Microstructure of Zircaloy-4," *Tenth International Symposium Zr in the Nuclear Industry, ASTM STP 1245*, Baltimore, MD, 21-24 June, 1993, A. M. Garde and E. R. Bradley, eds., ASTM International, West Conshohocken, PA, pp. 521–548.

[37] Mardon, J. P., Charquet, D., and Senevat, J., "Development of New Zr Alloys for PWR Fuel Rod Cladding," *Proc. ANS Int. Topical Meeting on LWR Fuel Performance*, West Palm Beach, FL, 1994, American Nuclear Society, LaGrange Park, IL, pp. 643–649.

[38] De Carlan, Y., Regnard, C., and Lemaignan, C., "Influence of Iron in the Nucleation of $\langle c \rangle$ -Component Dislocation Loops in Irradiated Zircaloy-4," *11th International Symposium on Zirconium in the Nuclear Industry, ASTM STP 1295*, Garmisch-Partenkirchen, Germany, 1995, E. R. Bradley and G. P. Sabol, Eds., ASTM International, West Conshohocken, PA, pp. 638–653.

[39] Griffiths, M., Winegar, J. E., Mecke, J. F., and Holt, R. A., "Determination of Dislocation Densities in Hexagonal Close-Packed Metals Using X-Ray Diffraction and Transmission Microscopy," *Adv. X-Ray Anal.*, Vol. 35, 1992, pp. 593–599.

[40] Griffiths, M., "A Review of Microstructure Evolution in Zirconium Alloy During Irradiation," *J. Nucl. Mater.*, Vol. 159, 1988, pp. 190.

[41] Motta, A. T., Faldowski, J. A., and Okamoto, P. R., "In Situ Studies of Phase Transformations in Zirconium Alloys and Compounds Under Irradiation," *Zirconium in the Nuclear Industry: Eleventh International Symposium, ASTM STP 1295*, Garmisch-Partenkirchen, Germany, 1995, E. R. Bradley and G. P. Sabol, Eds., ASTM International, West Conshohocken, PA, pp. 557–579.

[42] Kruger, R. M. and Adamson, R. B., "Precipitate Behaviour in Zirconium-Based Alloys in BWRs," *Proceedings of the Third International Conference on Evolution of*

Microstructure in Metals During Irradiation, Cleveland House, Muskoka, Ontario, Canada, Sept. 28–Oct. 2, 1992, R. A. Holt and R. G. Fleck, eds., AECL, pp. 242–250.

[43] Fidleris, V., Tucker, R. P., and Adamson, R. B., "An Overview of Microstructural and Experimental Factors That Affect the Irradiation Growth Behaviour of Zirconium Alloys," *Proc. Seventh Symp. on Zirconium in the Nuclear Industry, ASTM STP 939*, Strasburg, 1985, ASTM International, West Conshohocken, PA, 1987.

[44] Woo, C. H., "Theory of Irradiation Deformation in Non-Cubic Metals: Effects of Anisotropic Diffusion," *J. Nucl. Mater.*, Vol. 159, 1988, pp. 237–256.

[45] Holt, R. A., "Mechanisms of Irradiation Growth of Alpha-Zirconium Alloys," *J. Nucl. Mater.*, Vol. 159, 1988, pp. 310–338.

[46] Shishov, V. N., Markelov, V. A., Novikov, V. V., Nikulina, A. V., Kon'kov, V. F., Sablin, M. N., Peregud, M. M., Tselischev, A., Novoselov, A. E., Kobylyansky, G. P., Smirnov, V. P., and Markov, D. R., "Use and Improvement of E635 Alloy as Applied to Fuel Claddings and FA Structural Components of Water Cooled Reactors," *Proceedings of Sixth International Symposium on «Contribution of Materials Investigations to Improve the Safety and Performance of LWRs*, Fontevraud, France, Sept. 18–22, 2006, SFEN (AFSEN, AREVA, CEA, EDF), Fontevraud, France.

[47] Toffolon, C. and Brachet, J.-C., "Experimental Study and Preliminary Thermodynamic Calculations of the Pseudo-Ternary Zr–Nb–Fe-(O,Sn) System," *Zirconium in the Nuclear Industry: 13th International Symposium, ASTM STP 1423*, Annecy, France, 2001, G. D. Moan and P. Rudling, eds., ASTM International, West Conshohocken, PA, pp. 361–383.

[48] Toffolon-Masclet, C., Barberis, P., Brachet, J. C., Mardon, J. P., and Legran, L., "Study of Nb and Fe Precipitates In a-Phase Temperature Range (400 to 550C) in Zr–Nb-(Fe–Sn Alloys)," *Zirconium in the Nuclear Industry: 14th International Symposium, ASTM STP 1467*, Stockholm, Sweden, 2004, P. Rudling and B. Kammenzind, eds., ASTM International, West Conshohocken, PA, pp. 81–101.

[49] Barberis, P., Charquet, D., and Rebeyrolle, V., "Ternary Zr–Nb–Fe (O) System: Phase Diagram at 853K and Corrosion Behaviour in Domain Nb<0.8 %," *J. Nucl. Mater.*, Vol. 326, 2004, pp. 163–174.

[50] Toffolon-Masclet, C., Brachet, J.-C., Servant, C., Joubert, J. M., Barberis, P., Dupin, N. and Zeller, P., "Contribution of Thermodynamic Calculations to Metallurgical Studies of Multicomponent Zirconium Based," *15th ASTM International Symposium on Zirconium in Nuclear Industry, ASTM STP 1505*, Sunriver, OR, June 24–28, 2007, B. Kammenzind and M. Limback, eds., ASTM International, West Conshohocken, PA, 2009, pp. 754–775.

[51] Korotkova, N. V. and Alekseeva, Z. M., "Topology of the Phase Diagram Zr-Nb-Fe at the Temperature 500-800°C," *Izv. Akad. Nauk. SSSR, Met.*, Vol. 3, 1989, pp. 207–214.

[52] Jeong, Y. H., Kim, H. G., and Kim, D. J., "Influence of Nb Concentration in the α-Matrix on the Corrosion Behavior of Zr-xNb Binary alloys," *J. Nucl. Mater.*, Vol. 323, 2003, pp. 72–80.

[53] Tsuchiuchi, Y., Wacamatsu, R., Isobe, T., Watanabe, S., and Takabatake, H., "Manufacturing and Characterizations of J-Alloy, High Corrosion-Resistant Alloy for PWR Fuel Cladding Tube," *Top Fuel 2006, International Meeting on LWR Fuel Performance Nuclear Fuel: Addressing the Future*, Salamanca, Spain, 22-26 October, 2006, Transactions, European Nuclear Society, Salamanca, pp.635-640.

[54] Jeong, Y. H., Kim, H. G., and Kim, T. H., "Effect of β Phase, Precipitate and Nb-Concentration in Matrix on Corrosion and Oxide Characteristics of Zr-xNb Alloys," *J. Nucl. Mater.*, Vol. 317, 2003, pp. 1–12.

[55] Kim, H. G., Jeong, Y. H., and Kim, T. H., "Effect of Isothermal Annealing on the Corrosion Behavior of Zr-xNb Alloys," *J. Nucl. Mater.*, Vol. 326, 2004, pp. 125–131.

[56] Kim, H. G., Park, S. Y., Lee, M. H., Jeong, Y. H., and Kim, S. D., "Corrosion and Microstructural Characteristics of Zr–Nb Alloys with Different Nb Content," *J. Nucl. Mater.*, Vol. 373, 2008, pp. 429–432.

[57] Kim, H.-G., Park, J.-Y., and Jeong, Y.-H., "Phase Boundary of the Zr-Rich Region in Commercial Grade Zr–Nb Alloys," *J. Nucl. Mater.*, Vol. 347, 2005, pp. 140–150.

[58] Kim, H. G., Park, J.-Y., and Jeong, Y. H., "Ex-Rector Corrosion and Oxide Characteristics of Zr–Nb–Fe Alloys with the Nb/Fe Ratio," *J. Nucl. Mater.*, Vol. 345, 2005, pp. 1–10.

[59] Sabol, G. P., Comstock, R. J., Weiner, R. A., Laoroure, P., and Stanutz, R. N., "In Reactor Corrosion Performance of ZIRLO and Zircaloy-4," *Zirconium in the Nuclear Industry: Tenth International Symposium, ASTM STP 1245*, Baltimore, MD, 21-24 June, 1993, A. M. Garde and E. R. Bradley, Eds., ASTM International, West Conshohocken, PA, pp. 724–744.

[60] Bossis, P., Verhaeghe, B., Doriot, S., Gilbon, D., Chabretou, V., Dalmais, A., Mardon, J. P., Blat, M., and Miquet, A., "In PWR Comprehensive Study of High Burnup Corrosion and Growth Behavior of M5® and Recrystallized Low-Tin Zircaloy-4," *15th ASTM International Symposium on Zirconium in Nuclear Industry, ASTM STP 1505*, Sunriver, OR, June 24–28, 2007, ASTM International, West Conshohocken, PA, pp. 430–456.

[61] Bossis, P., Verhaeghe, B., Doriot, S., Gilbon, D., Chabretou, V., Dalmais, A., Mardon, J. P., Blat, M., and Miquet, A., "In PWR Comprehensive Study of High Burnup Corrosion and Growth Behavior of M5® and Recrystallized Low-Tin Zircaloy-4," *J. ASTM Int.*, Vol. 6, No. 2, 2009, pp. 430–456.

[62] Brachet, J.-C. and Portier, L., "Influence of Hydrogen Content on the α/β Phase Transformation Temperatures and on the Termal–Mechanical Behavior of Zry-4, M4 (Zr–Sn–Fe-V0, M5 (Zr–Nb-O) Alloys During the First Phase of LOCA Transient," *Zirconium in the Nuclear Industry: 13th International Symposium, ASTM STP 1423*, Annecy, France, 2001, G. D. Moan and P. Rudling, Eds., ASTM International, West Conshohocken, PA, pp. 673–701.

[63] Dobromyslov, A. V. and Taluts, N. I., *Structure of Zr and Alloys*, Russian Academy of Science, Ural Brench, Institute of Metall Physics, Ekaterinburgh, 1997.

[64] Massih, A. R., Anderson, T., Witt, P., and Dahlbäck, M., "Effect of Quenching Rate on the β to α Phase Transformation Structure in Zr Alloy," *J. Nucl. Mater.*, Vol. 322, 2003, pp. 138–151.

[65] Wenjin, Z., Yanzhang, L., Hongman, J., and Qian, P., "Effect of Heat Treatment and Nb and H Contents on the Phase Transformation of N18 and N36 Zirconium Alloys," *15th International Symposium on Zirconium in the Nuclear Industry, ASTM STP1505*, Sunriver Resort, OR, June 24–28, 2007, ASTM International, West Conshohocken, PA, 2008, Poster Session, paper 41.

Reprinted from JAI, Vol. 7, No. 8
doi:10.1520/JAI103057
Available online at www.astm.org/JAI

B. A. Cheadle[1]

The Development of Zr-2.5Nb Pressure Tubes for CANDU Reactors

ABSTRACT: The first reactor to use zirconium alloy tubes to contain hot pressurized water as a heat transport medium was the Hanford N reactor in 1962. For this reactor, three companies that had suitable extrusion and cold working equipment were given contracts to produce Zircaloy-2 tubes. All the companies were successful, and tubes from each company were installed in the reactor. When Canada decided to design and build a power reactor (nuclear power demonstration (NPD)), it elected to use the pressure tube concept and gave a contract to one of the companies (Chase Brass) to fabricate the Zircaloy-2 tubes. Douglas Point and Pickering Units 1 and 2 followed NPD, and all used similar Zircaloy-2 pressure tubes. A stronger tube was desired in order to thin the wall and improve the neutron economy. An alloy development program in the USSR had shown that the alloy Zr-2.5Nb looked very promising as a stronger alloy than Zircaloy-2, and both the USSR and Canada developed this alloy and subsequently used Zr-2.5Nb pressure tubes in their reactors. When both the Zircaloy-2 and Zr-2.5Nb pressure tubes were first installed in the reactors, several important properties and characteristics such as hydrogen ingress into the metal from corrosion in water, the enhancement of creep by neutron irradiation, shape change by neutron irradiation, reduction in fracture toughness by neutron irradiation, and delayed hydride cracking were not appreciated. These properties all led to problems during the service lives of the early tubes. Large research programs investigated these properties and showed that the α-grain size, shape, and crystallographic texture, the distribution of the β-phase, the dislocation type, and density as well as the micro-chemistry controlled the in-reactor properties of the tubes. This information enabled the design and operation of the reactors to be changed so that the tubes had satisfactory service lives. In addition, the

Manuscript received February 25, 2010; accepted for publication June 30, 2010; published online August 2010.
[1] Retired, Deep River, ON K0J 1P0, Canada.

Cite as: Cheadle, B. A., "The Development of Zr-2.5Nb Pressure Tubes for CANDU Reactors," *J. ASTM Intl.*, Vol. 7, No. 8. doi:10.1520/JAI103057.

Copyright © 2011 by ASTM International, 100 Barr Harbor Drive, PO Box C700, West Conshohocken, PA 19428-2959.

information was used to fabricate tubes that had much improved properties and service lives.

KEYWORDS: Zr-2.5Nb pressure tubes, CANDU reactors, fabrication

Introduction

The Kroll medal was awarded for my contributions to, and leadership of, the development and refinement of cold worked Zr-2.5 % Nb pressure tubes during the 1961–1997 period. It is a great honor to be recognized by the ASTM B10.02 and Kroll committees, and I thank them and my nominators for considering me worthy to join the previous winners of this prestigious award.

In 1961, when I started work at Atomic Energy of Canada Limited (AECL), many researchers in the United States, United Kingdom, Russia, Germany, and Sweden were all trying to identify the problems associated with the use of zirconium alloys as pressure retaining structural components in nuclear reactors. I will attempt to summarise how we developed CANadian DeUerium (CANDU) cold worked Zr-2.5Nb pressure tubes and gradually improved the fabrication process to produce tubes with much better properties and longer service lives.

How Did Canada Arrive at Using Cold Worked Zr-2.5Nb Pressure Tubes?

In 1954, Canada started to study the feasibility of nuclear power reactors that could compete economically with coal-fired stations [1]. The initial design for the nuclear power demonstration (NPD) reactor (1962–1985) was 20 MW and used natural uranium dioxide fuel, moderated, and cooled by heavy water. Two designs were considered, a steel pressure vessel and a design that used many small tubes to contain the fuel bundles and the pressurized heat transport system heavy water. In order for the tube design to be economic, a strong, corrosion resistant material that also had a low neutron capture cross section was required. Such tubes using the alloy Zircaloy-2 [2] were being developed for the Hanford N reactor. A study showed that power output had the largest effect on unit energy cost, and a reactor of at least 200 MW would be required to compete with coal-fired stations. Such a reactor would require a large pressure vessel that was beyond the fabrication experience at that time, and the capability to build such a vessel was not likely to be developed in Canada. Hence, the pressure tube design (Fig. 1) was selected using horizontal Zircaloy-2 tubes similar to the ones developed for the Hanford reactor.

Three manufacturers made the Zircaloy-2 pressure tubes for the Hanford N reactor. One of these, the Chase Brass and Copper Co. of Waterbury, Connecticut, was selected to make the tubes for NPD by a similar process to the one that they had used for the Hanford tubes. Preheated hollow billets were extruded into tubes that were cold drawn to both achieve the final dimensions and increase their strength, and finally stress relieved using an autoclaving process that produces a uniform black oxide on the surface (Fig. 2). Similar tubes were also made for the 200 MW Douglas Point reactor that followed NPD. In order to increase the power to 500 MW for the Pickering Units 1 and 2 reactors, the fuel

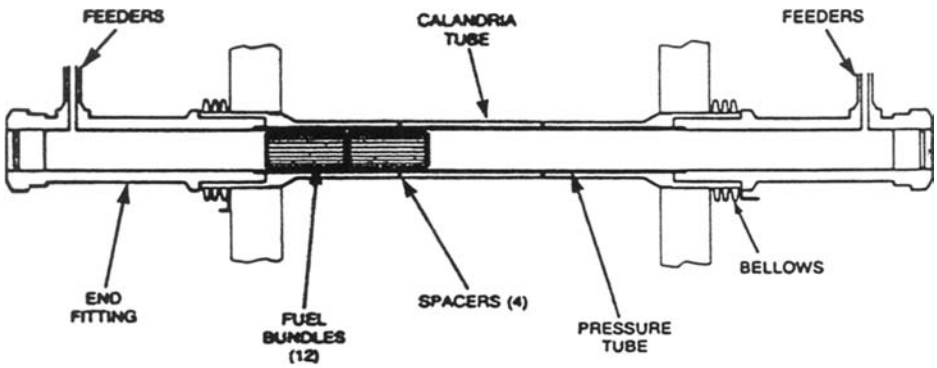


FIG. 1—*Schematic of a typical CANDU fuel channel.*

bundle diameter was increased and consequently also the diameter of the pressure tubes. The use of natural uranium dioxide fuel made neutron economy very important. Neutron economy could only be improved by reducing the amount of material in the core of the reactor, and the easiest item to reduce was the wall thickness of the pressure tubes. In order to do this, a stronger alloy was required, and the alloy Zr-2.5Nb developed by the USSR [3] for their pressure tubes was selected. This alloy is not only stronger than Zircaloy-2, but as for many steels, it can also be strengthened considerably by rapidly cooling from the β phase to form a martensitic microstructure, followed by aging to form small precipitates.

AECL initially directed its development towards this water quenched and aged condition, and tubes were fabricated by the Chase Brass and Copper Co. for the Gentilly 1 and Kanupp (still operating) reactors. The Fugen reactor in Japan also used similar Zr-2.5Nb pressure tubes, and the Russians developed their

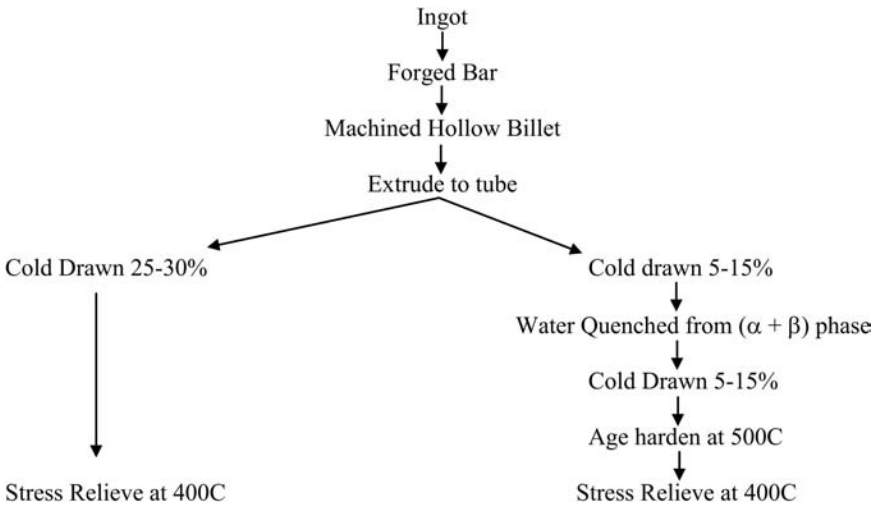


FIG. 2—*The fabrication steps for CANDU Zr-2.5Nb pressure tubes.*

own heat-treated variants. In the AECL process, extruded tubes were cold drawn, then heated into the α/β phase region and lowered into water, cold drawn to final size, and aged (Fig. 2). The tubes were quenched from the α/β phase rather than the β phase because heating in the β phase produced large β grains and when quenched this material could have poor ductility. Having some α grains present prevented large β grains forming, and there was little reduction in strength. However, there were concerns with not being able to prove that the required heat treatment temperature and cooling rate had been achieved for the whole of each tube. During the development, some tubes were also fabricated by a process of extrusion and cold drawing 25–30 %, similar to that used for the Zircaloy-2 tubes. These tubes were not as strong as the heat-treated tubes but were 40 % stronger than Zircaloy-2 tubes. Sections from both types of tube were installed in a loop in the National Reactor Universal test reactor, and the "cold worked" section had a lower diametral creep rate than the heat-treated section. Ontario Hydro chose cold worked Zr-2.5Nb pressure tubes for the Pickering Units 3 and 4 reactors, and they have been used for all subsequent CANDU reactors. The CANDU reactors and the pressure tubes that were initially installed are shown in Table 1.

We did attempt to develop a stronger, more creep resistant zirconium alloy than Zr-2.5Nb, and an alloy of Zr-3.5Sn-0.8Nb-0.8Mo that we called Excel showed a lot of promise but had some problems with hydrogen ingress. Since our utilities had gained much experience with Zr-2.5Nb and we had solved

TABLE 1—*CANDU reactors and the pressure tubes originally installed.*

Plant	Date of Startup	Pressure Tubes
NPD	1962	Zircaloy-2
Douglas Point	1967	Zircaloy-2
Gentily 1	1974	HT Zr-2.5Nb
Pickering A (1–2)	1971–1973	Zircaloy-2
Pickering A (3–4)	1971–1973	cw Zr-2.5Nb
Kanupp	1972	HT Zr-2.5Nb
Bruce A (1–4)	1977–1979	cw Zr-2.5Nb
Pickering B (5–8)	1983–1986	cw Zr-2.5Nb
Bruce B (5–8)	1985–1987	cw Zr-2.5Nb
Gentilly 2	1983	cw Zr-2.5Nb
Point Lepreau 1	1983	cw Zr-2.5Nb
Wolsong 1	1983	cw Zr-2.5Nb
Embalse	1984	cw Zr-2.5Nb
Darlington (1–4) 1	1990–1993	cw Zr-2.5Nb
Wolsong 2	1997	cw Zr-2.5Nb
Wolsong 3,4	1998–1999	cw Zr-2.5Nb
Cernavoda 1	1996	cw Zr-2.5Nb
Cernavoda 2,3,4,5	1996	cw Zr-2.5Nb
Qinshan 1,2	2005	cw Zr-2.5Nb

many of its problems, the development program on Excel was eventually stopped.

What Are CANDU Cold Worked Zr-2.5Nb Pressure Tubes?

At room temperature, zirconium is in the α phase, and the grains have a hexagonal crystal structure that results in them having anisotropic properties. Above 863°C, the α phase transforms to the β phase, which has a body-centered cubic crystal structure and isotropic properties. Niobium stabilises the β phase and has a very low solubility in the α phase so that the equilibrium microstructure of Zr-2.5Nb at room temperature is α grains that contain about 0.2 % Nb and β phase that contains 95 % Nb [4] (Fig. 3).

In the fabrication process [5,6] (Fig. 1), hollow billets are preheated to 815°C and extruded into tubes. Consequently, the microstructure of the billets when they are extruded consists of about 70 % small spherical α grains in a matrix of β grains [7] (Fig. 4). The extrusion deforms the α grains so that they are long and thin and also orients them so that the majority has their basal plane normals close to the circumferential direction of the tube (Fig. 5), which is very different to the crystallographic texture of fuel cladding where the basal plane normals are usually close to the radial direction. The extruded tubes are air-cooled and most of the β phase transforms to α phase by growth on the existing α grains and the remaining β phase becomes more enriched in Nb. Hence the microstructure of the extruded tubes consists of thin, flat, and elongated α

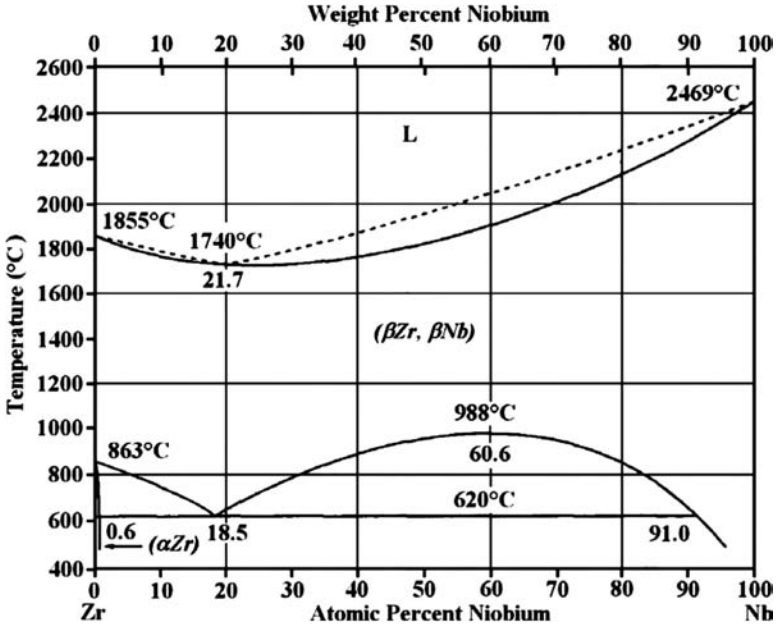


FIG. 3—*The zirconium niobium phase diagram (2).*

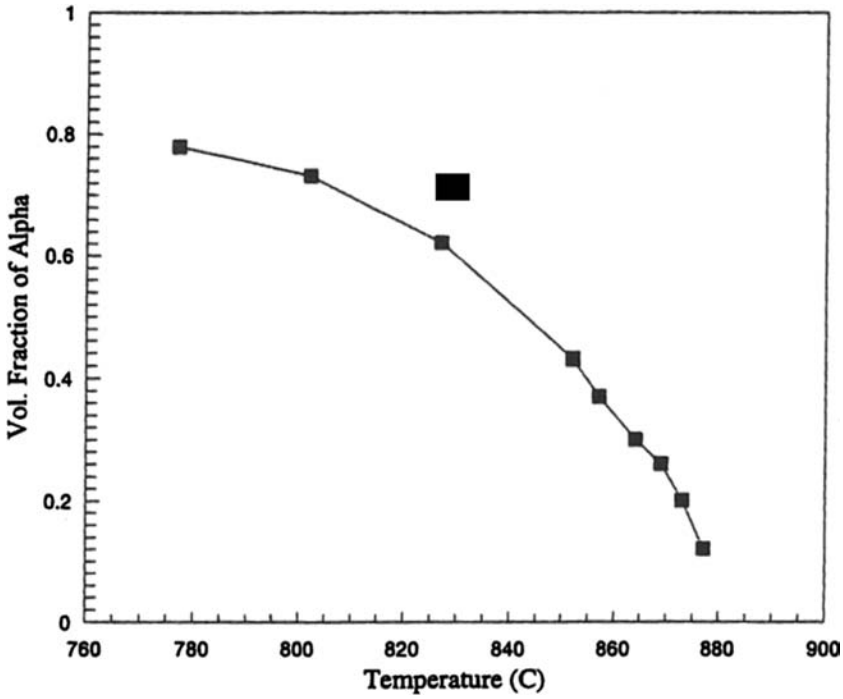


FIG. 4—*The calculated volume fraction of α phase in Zr-2.5Nb at different temperatures.*

grains that contain about 0.6 % Nb separated by a thin layer of β phase that has a composition of about Zr-20 wt % Nb (Fig. 6). The α grains contain more than the equilibrium amount of Nb, and if heated below 600°C, small β Nb precipitates will form. The metastable β phase will also transform to equilibrium α and β phase that contains 95 % Nb (Fig. 3).

We initially observed the Zr-20 wt % Nb β phase in the electron microscope using the replica technique, and I identified its composition from its lattice parameter using X-ray diffraction. I was only able to measure the crystallographic texture of our tubes when we acquired an X-ray diffractometer in the late 1960s, and I was able to construct inverse pole figures of pressure tubes, fuel cladding, and calandria tubes.

The preheated extrusion billets are much hotter than the extrusion chamber and cool during extrusion. Hence, the material that is first pushed between the die and the mandrel is hotter and has a smaller proportion of α phase in the microstructure than the cooler material at the back end of the billet (Fig. 4). This results in the back ends of the extrusions having a smaller α grain size and a slightly different crystallographic texture than the front ends.

Cold drawing 25–30 % further elongates the α grains and introduces dislocations that strengthen the tubes. The autoclaving process produces a uniform oxide on the tubes that is needed to prevent galling when the tubes are rolled into their

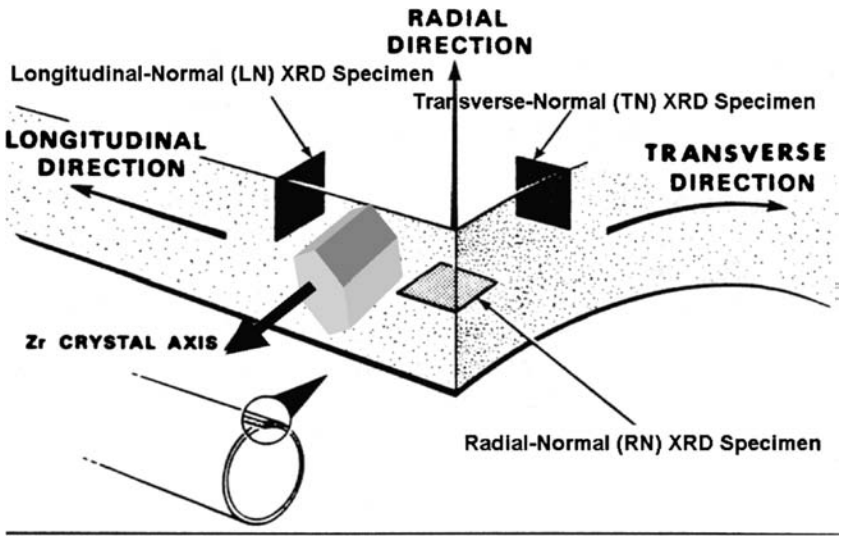


FIG. 5—*Illustration showing the crystallographic orientation of most of the α grains in cold worked Zr-2.5Nb pressure tubes.*

end fittings and also stress relieves the tubes, reducing the dislocation density. The strong crystallographic texture in the α grains results in the tubes having anisotropic properties with the circumferential tensile strength being higher than the axial strength. In addition, the differences in microstructure and crystallographic texture between the front and back ends result in the back ends being stronger than the front ends and also having a higher in-reactor diametral creep rate.

Although initially we thought that cold worked Zr-2.5Nb pressure tubes were relatively simple components, we eventually learned that they are quite complex, and their in-reactor behaviour is controlled by several interacting parameters. These parameters are as follows:

- Chemical composition, including the elements initially considered benign impurities
- The shape, size, and dislocation density of the α grains
- The crystallographic texture of the α grains
- The location and composition of the metastable β phase

At first, the challenge was to manufacture tubes that met the specifications of dimensions, mechanical properties, and freedom from defects. The effect that relatively small changes to each of the stages of the fabrication process could make on the properties of the tubes and their service lives was not appreciated.

The Parameters That Affect Service Life

In the CANDU fuel channel, the horizontal pressure tubes are joined to stainless steel end fittings by deformation joints or rolled joints that in turn are connected

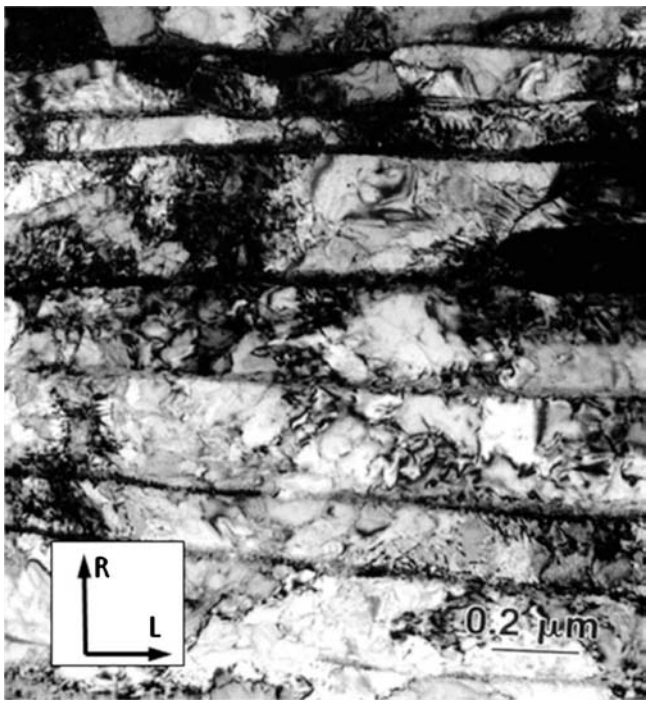


FIG. 6—*Thin film electron micrograph of a cold worked Zr-2.5Nb pressure tube showing the elongated α grains with a thin layer of β phase between them. R is radial direction, and L is longitudinal direction.*

to the reactor vessel end shields by bellows. The pressure tubes are separated from the cool heavy water (D_2O) moderator by a Zircaloy-2 calandria tube (Fig. 1). Since the pressure tubes contain the hot pressurized heavy water (D_2O) coolant, they are designed to the Boiler and Pressure Vessel Code that allows the tubes to be operated at 1/3 their axial ultimate tensile strength (UTS). The fuel bundle assembly sets the inside diameter, and the materials UTS at the operating temperature sets the minimum wall thickness. The corrosion behaviour during service requires a corrosion allowance to be added onto the calculated wall thickness. Since the tubes are initially only supported at each end, the weight of the fuel and heavy water produces a bow or sag that increases slowly with service due to creep. Eventually, the pressure tubes are supported by the colder calandria tube through spacers surrounding the pressure tube.

The service conditions of stress, temperature, and neutron flux impose a harsh operating environment, yet for a CANDU reactor to produce power most economically, the pressure tubes should have a service life of more than 25 years. Hence, the pressure tubes must not only maintain their strength and resistance to fracture but also their shape-diameter, length, and straightness (sag) for as long as possible. When zirconium alloy tubes were first used in reactors, it was known that neutron irradiation would increase their strength and reduce

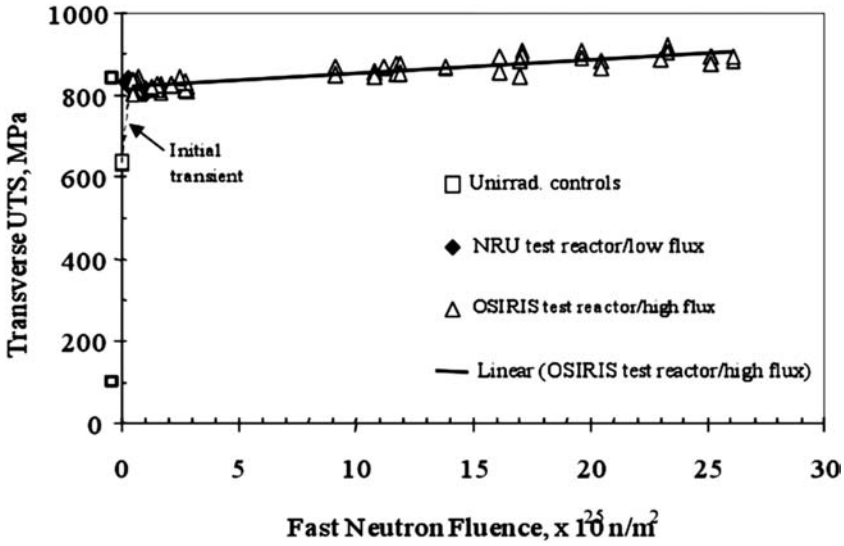


FIG. 7—*The effect of neutron irradiation on the UTS of Zr-2.5Nb pressure tube material at 240°C.*

their ductility and resistance to rupture, affect their corrosion resistance, and probably reduce their creep resistance. A consequence of the corrosion reaction is the pickup of hydrogen[2] into the zirconium, and it was known that precipitated zirconium hydrides could reduce fracture resistance. It was not known what the extent of these changes in properties would be and how they would affect the service lives of the tubes. In addition, the phenomenon of delayed hydride cracking (DHC) [8] in zirconium alloys was also not known.

Mechanical Properties

In general, the higher the strength, the lower the ductility. Neutron irradiation increases the strength and consequently reduces the ductility of cold worked Zr-2.5Nb pressure tube material [9] (Fig. 7). These changes initially occur quite rapidly with fluence, but further irradiation produces little further change. The increase in strength reduces the possibility of the heat transport system pressurized heavy water rupturing sound tubes. However, the concern has always been for a tube to contain a flaw that is sufficiently severe that it would propagate rapidly under the operating stress. The length of such a flaw is termed the critical crack length (CCL). After NPD and Douglas Point, all CANDU reactors had the annulus between the pressure tube and the calandria tube sealed (Fig. 1) and filled with a flowing inert gas that was monitored for humidity. It was assumed that if a flaw grew, it would grow through the relatively thin wall, the

[2]I will use the term hydrogen to include the deuterium picked up from corrosion in the reactor.

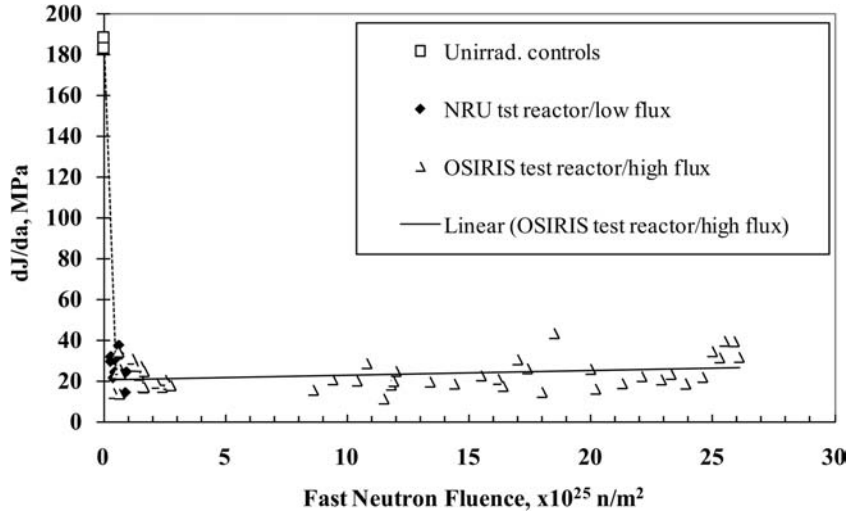


FIG. 8—*The effect of neutron irradiation on the fracture toughness of Zr-2.5Nb pressure tube material at 240°C.*

coolant would leak into the annulus and be detected by the humidity of the inert gas, and the reactor would be shut down before the flaw grew to the CCL.

Irradiation initially rapidly reduces the fracture toughness and CCL, but further reduction with fluence is small [9] (Fig. 8). When sufficient data on the effect of fluence on CCL had been gathered, it became apparent that the reduction in the fracture toughness of some tubes was considerably less than that in other nominally similar tubes (Fig. 9). It was eventually discovered that the tubes that had the smaller reductions in fracture toughness with fluence had a much lower chlorine concentration than the other tubes [10] (Fig. 10). Chlorine is a residual from the Kroll process, and it turned out that the tubes that had the low chlorine concentration had been made from ingots that had been made from 100 % recycled material. This resulted in the material being vacuum melted four times rather than the normal twice, which resulted in the volatile chlorine being removed. The chlorine, in combination with carbon, formed planes of weakness shown by fissures on the fracture surface. This information not only enabled other tubes that would be expected to have a low reduction in fracture toughness during service to be identified, but also all future ingots made from Kroll process material were melted four times and had high fracture toughness. The electrolytic process for refining zirconium does not use chlorine to separate the Hafnium and does not have this problem.

Corrosion, Hydriding, and Delayed Hydride Cracking

Corrosion of zirconium alloys in heavy water raises two problems: Metal loss from the formation of zirconium oxide and the ingress of hydrogen into the metal. The corrosion rate of the Zr-2.5Nb pressure tubes in-reactor is acceptably

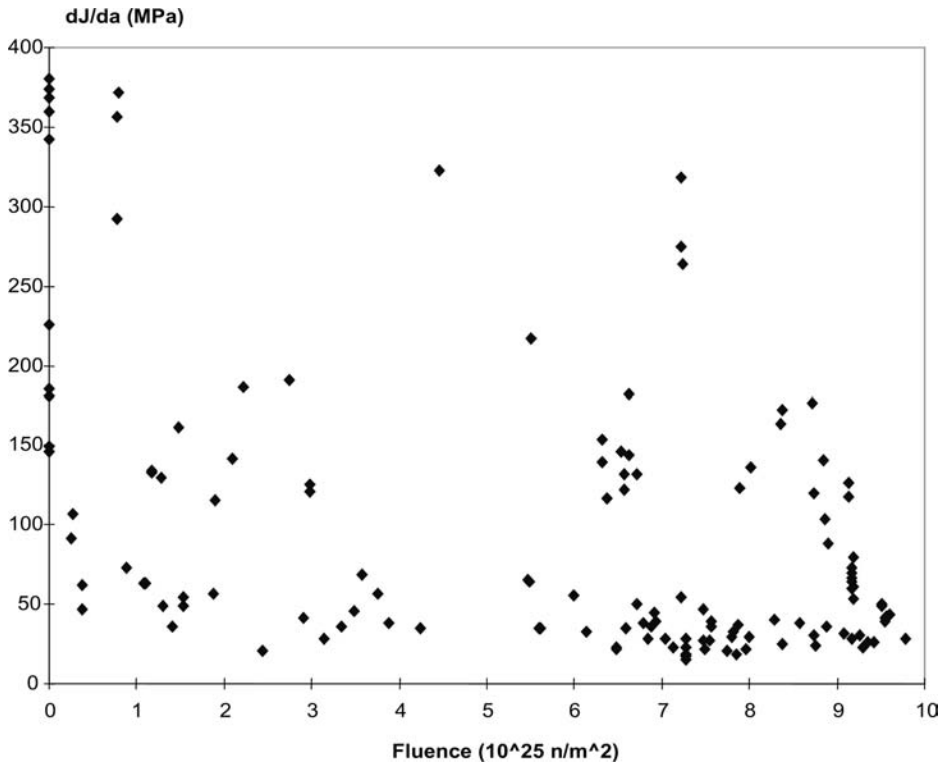


FIG. 9—*The fracture toughness of cold worked Zr-2.5Nb pressure tubes at 240–300°C after service in a CANDU reactor.*

low [11] (Fig. 11) and is accommodated by a small addition to the wall thickness.

At room temperature, hydrogen is insoluble in zirconium and is precipitated as zirconium hydride. However, solubility increases with temperature, and at the operating temperature range of CANDU pressure tubes (250°C coolant inlet end and 300°C coolant outlet end), about 30 and 60 ppm of hydrogen, respectively, are required before hydrides would be present during reactor operation. New pressure tubes contain a small amount of hydrogen that is picked up during the fabrication process, so initially hydrides are only present when the reactors are shut down and are at room temperature. However, with the ingress of hydrogen from corrosion, eventually hydrides will be present during reactor operation. When tubes were first removed from power reactors after several years of service, it was found that the pickup of the hydrogen into the metal as a percentage of that released during oxidation was very much lower for Zr-2.5Nb pressure tubes than for Zircaloy-2 [12] (Fig. 12).

The CCL of pressure tubes could be reduced by the presence of zirconium hydride platelets if they were orientated perpendicular to the major circumferential stress—radial hydrides. Fortunately, the fabrication process used for

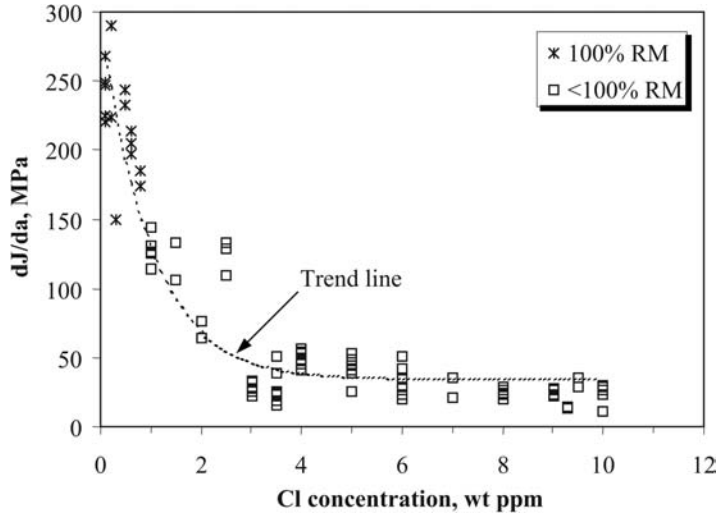


FIG. 10—*The effect of chlorine on the fracture toughness of irradiated Zr-2.5Nb pressure tube material at 240°C.*

CANDU pressure tubes results in the hydrides forming in the least deleterious orientation—circumferential hydrides.

A time dependent cracking phenomenon due to the presence of precipitated hydrides was first observed in titanium alloys and was called sustained load cracking [8]. We were investigating the phenomena in zirconium alloys when

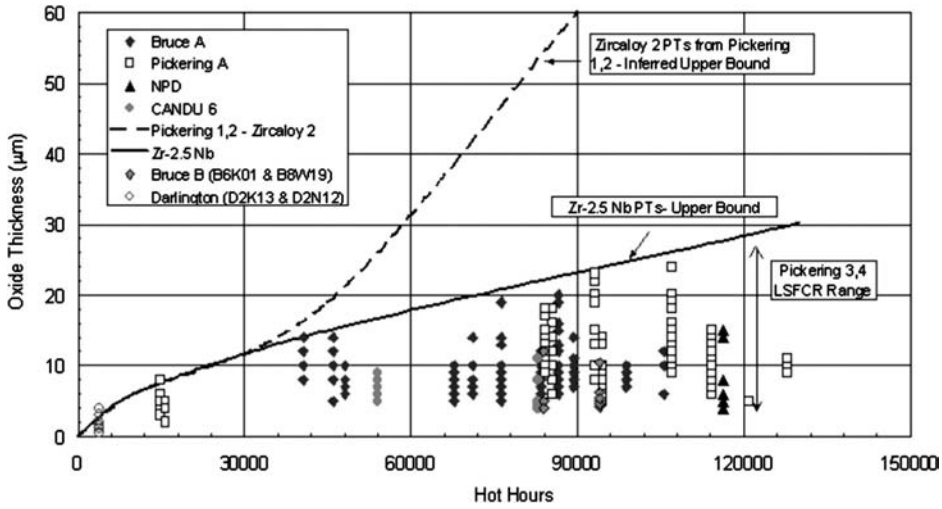


FIG. 11—*The oxide thickness on the inside surface of Zircaloy-2 and Zr-2.5Nb pressure tubes removed from CANDU reactors.*

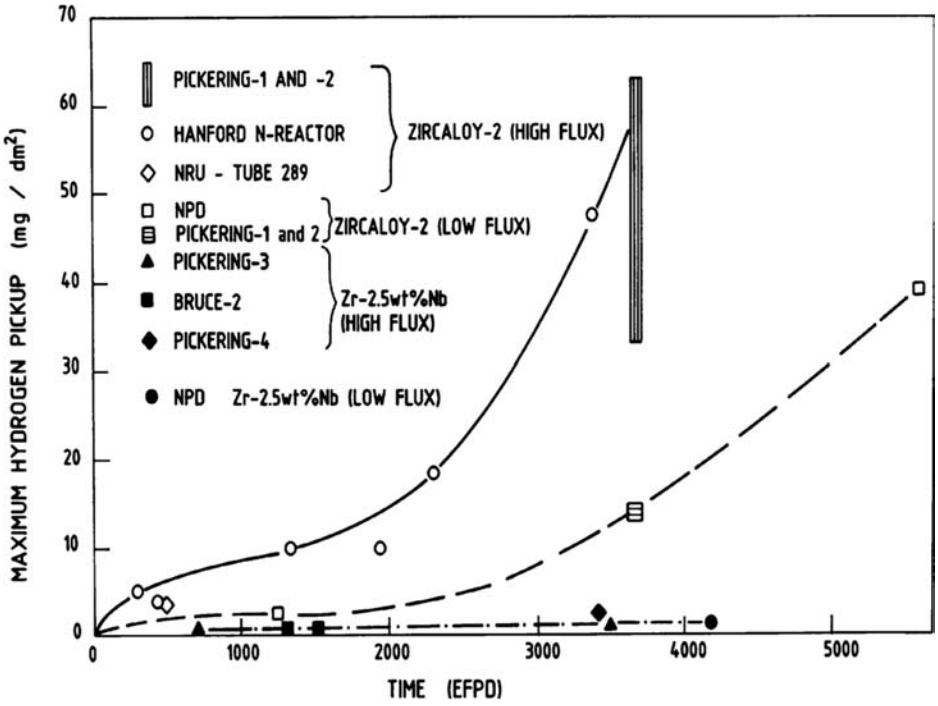


FIG. 12—*The hydrogen concentration of Zircaloy-2 and cold worked Zr-2.5Nb pressure tubes after service in reactors.*

cracks developed in Zr-2.5Nb pressure tubes installed in Pickering Units 3 and 4. The cracking mechanism was identified as being due to the cracking of hydrides and was termed DHC [8]. In this mechanism, if there is a sufficiently large stress gradient as typically present at the tip of a notch, hydrogen diffuses up the gradient and hydride precipitates at the tip of the notch (Fig. 13). Then, if the stress is sufficiently large, the hydride fractures and a crack is formed. Repetition of this process can grow a crack through the wall of a tube. Hence, the important parameters are the presence of surface notches or defects, the presence of hydrides (hydrogen plus deuterium concentration above terminal solid solubility), and the applied stress.

The cracking in the Pickering Units 3 and 4 reactors was at the rolled joints and was due to the rolling technique introducing very high residual stresses into the ends of the pressure tubes. These very high stresses acted on the hydrides present when the reactors were shut down at room temperature and initiated DHC. Eventually, the cracks penetrated the wall, and the leaks were detected by moisture in the annulus gas system [13]. Some DHC cracks also formed in some Zr-2.5Nb pressure tube in the Bruce reactors. These cracks initiated at small defects that had been introduced during the fabrication process and not detected by inspection.

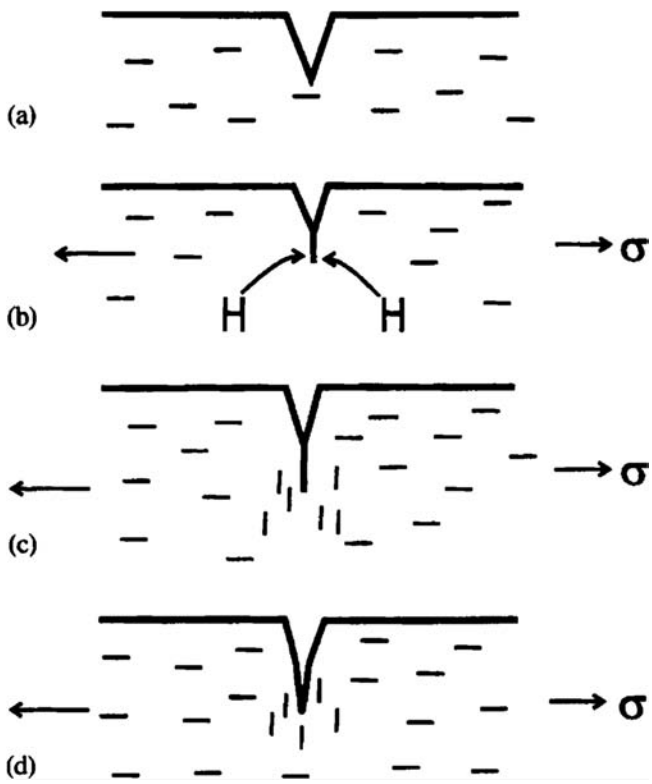


FIG. 13—*Schematic illustrating the mechanism of DHC.*

Another instance of DHC was in the Zircaloy-2 pressure tubes in Pickering Unit 2 where many tubes were able to sag into contact with their calandria tubes. This induced a thermal gradient through their walls, which caused the relatively high hydrogen concentration compared to Zr-2.5Nb tubes, to migrate down the thermal gradient to the colder region. Once the hydrogen concentration had reached a threshold concentration, it precipitated as a dense concentration that we described as a blister. Some of these blisters cracked from a combination of expansion and operating stresses and in one tube the cracks propagated by DHC to a critical length leading to unstable fracture [14].

Considerable effort has been made to understand and define the parameters of stress, notch size and shape, microstructure, crystallographic texture, temperature cycling, and irradiation that result in DHC.

The solutions to these problems were (1) an improved rolled joint design and rolling procedure plus stress relieving if necessary, (2) ensuring that the spacers were in their design location to minimise sag and moving them back into position if necessary, (3) changes to the ingot melting procedure to avoid shrinkage cavities plus improved inspection procedures, (4) stopping sand blasting during processing that could embed grains of sand into the surface, and (5) improving the surface finish to eliminate small surface defects.

In order to delay the service time when the hydrogen concentration reaches terminal solid solubility (initial concentration plus ingress from corrosion) and hydrides would be present at reactor operating temperatures, changes were made to several stages of the fabrication process to reduce the pickup of hydrogen [15]. These changes enabled the maximum hydrogen concentration of new pressure tubes to be reduced from 25 to 5 ppm.

Deformation during Service

Ideally, the pressure tube should retain its initial dimension and shape during service. An increase in the diameter of the tubes allows more heavy water coolant to flow over the top of the fuel bundles rather than through them, and some fuel elements receive less cooling than others (Fig. 14). Our initial concern was the increase in the rate of diametral creep due to irradiation, and when all the other problems have been solved, this is the property that probably controls the service life of cold worked Zr-2.5Nb pressure tubes. Diametral creep is quite sensitive to small changes in grain size, dislocation density, and crystallographic texture [16], and the small differences between the front and back ends of tubes produced by the extrusion process result in quite a different in-reactor creep rate. This is illustrated by the different behaviour when a tube is installed with its front end at the inlet end of a fuel channel compared to when the back end is installed at the inlet end [17] (Fig. 15.

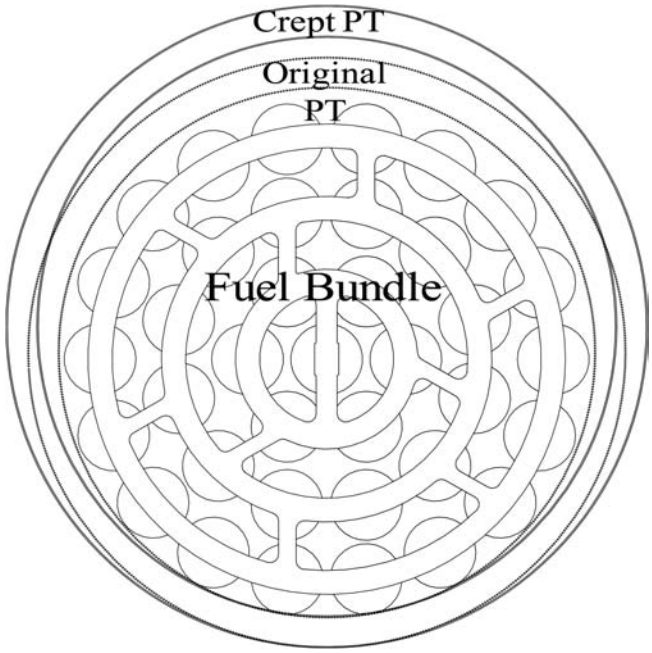


FIG. 14—*Schematic diagram showing the effect of diametral creep on the gap between a fuel bundle and the inside diameter of a pressure tube.*

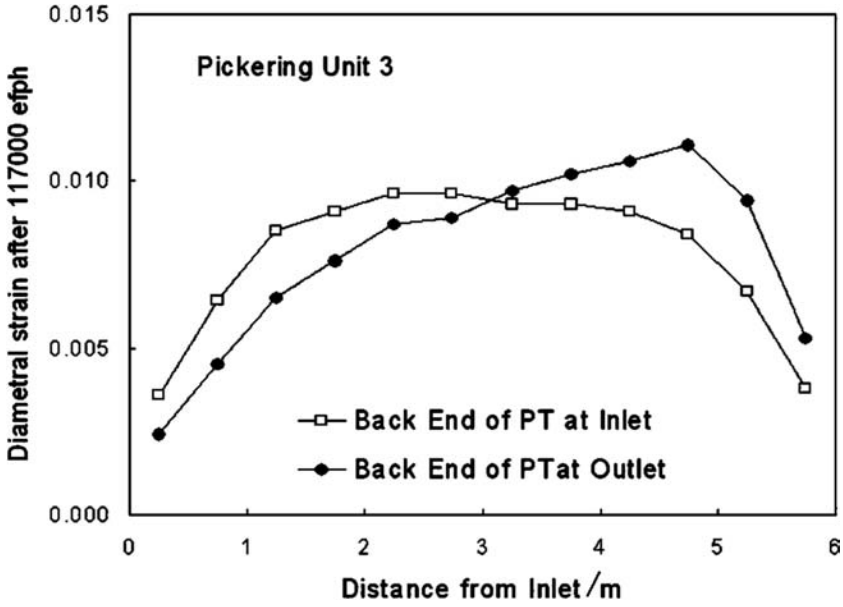


FIG. 15—*The diametral strain along the length of Zr-2.5Nb pressure tubes installed in Pickering Unit 3.*

In the early reactors, the travel on the bearings between the end fittings and the calandria vessel (Fig. 1) was sufficient for the predicted elongation due to thermal expansion and creep. However, it was soon realised that the tubes were elongating faster than expected due to the phenomena of irradiation growth, where irradiation changes the shape without any applied stress, adding to the elongation due to creep. The crystallographic texture of the tubes, with the majority of the α grains having their basal plane normals oriented close to the circumferential direction of the tube, results in the tubes elongating due to irradiation growth [18]. Increasing the length of the bearings in the end fittings solved the problem. Heat-treated Zr-2.5Nb pressure tubes have a much more random crystallographic texture and hence do not have the problem of elongation due to growth. The Kanupp reactor has heat-treated Zr-2.5Nb pressure tubes and consequently has not had a problem with pressure tube elongation and bearing travel.

The third concern in change in shape is the sag. The pressure tube is supported by the calandria tube through the garter spring spacers (Fig. 1). Since the calandria tube operates at 80°C, the temperature of the heavy water moderator, it provides most of the sag resistance for the channel. However, the pressure tube sags between the garter spring spacers due to creep and can touch the calandria tube if the length between spacers is too large.

Extensive studies showed that the in-reactor creep and growth rates of Zr-2.5Nb pressure tubes are a function of the stress, fluence, crystallographic texture, shape of the α grains, dislocation density, and the type of the dislocations.

Models have been developed so that the changes in diameter, length, and sag of the tubes during service can be predicted [19].

Development of the Fabrication Process

Since the first cold worked Zr-2.5Nb pressure tubes were made for Pickering Units 3 and 4, there has been continual process development in order to make tubes that would be less susceptible to the problems that had occurred and would have longer service lives. This was a team effort involving many people.

Several programs provided information that lead to improvements in the pressure tubes.

(1) Programs to develop solutions to the problems that occurred during operation provided an understanding of the effect of microstructure and chemical composition on in-reactor behaviour.
(2) Programs to monitor the changes in diameter, length, and sag and the deuterium concentration of pressure tubes during service.
(3) Programs to examine and test pressure tubes removed from reactors after several years' service.
(4) Programs involving fabrication of small batches of tubes to evaluate the effects of changes in the fabrication process on the properties. Some changes were designed to reduce the variability in the properties of nominally identical tubes. Other changes were designed to produce different microstructures or crystallographic textures and hence produce different properties. Some of the changes evaluated were as follows:

Billet	Hot piercing to produce a more uniform macrostructure; rejected due to increased defects Water quenching from the β phase to produce a more uniform macrostructure and microstructure [6]
Extrusion	The effect of preheat temperatures and soak times on the microstructure and crystallographic texture
Cold working	Pilgering as an alterative to cold drawing The effect of different amounts of cold work on properties
Heat treatments	Water quenching and aging Vacuum stress relieving instead of autoclaving

Combining the information from the first three programs was complicated by the pressure tubes not all being the same due to the continual development process and also their service conditions of stress, temperature, and fluence being different due not only to their location in a reactor but also the differences between individual reactors. However, we developed considerable understanding of how the chemistry, microstructure, and crystallographic texture controlled the in-service behaviour of the pressure tubes. The relationship between the composition and microstructure of CANDU cold worked Zr-2.5Nb pressure tubes, and their properties are shown in Table 2. There are many gaps where a

TABLE 2—*The effects of microstructural parameters and chemical composition on the properties of cold worked Zr-2.5Nb pressure tubes.*

	Parameter				
Property	Composition	α Grain Size and Shape	β Phase	Dislocation Density	Crystallographic Texture, fa, fr, ft
Biaxial strength–internalpressurization		Reduce		Increase	Increase fr or ft
Axial strength–uniaxial tensile	Increase O	Reduce		Increase	Increase fa
Fracture toughness	Reduce H, Cl, C, and P contents			Reduce	
Corrosion and *D*ingress	Optimize the Feand C	Reduce grainthickness	Transform thebeta phase ligaments		
Diametral strain		Increase grainthick-ness, makemore equiaxed			Reduce fr
Axial elongation				Possibly reduce	Increase fa
DHC	Reduce H, O	Possibly reduce	Possibly disperse	Reduce	Increase fr

parameter has either little or no affect on the property, or we do not yet know if there is an effect. In addition, there are many conflicts, particularly in the case of grain size/shape and crystallographic texture where improving one property may make another property worse. The many changes that have been made to the fabrication process for cold worked Zr-2.5Nb pressure tubes are summarised in Table 3.

The information has also been used to develop complex models that use the chemical composition, microstructure, and crystallographic texture of the individual tubes to predict the deformation behaviour and deuterium ingress during service [19,20].

The most recent large numbers of tubes fabricated were for Quinshan Units 1 and 2 and for the refurbishment of Point Lepreau. These tubes are considerably superior to the tubes first installed in Pickering Units 3 and 4, have much better properties, and will have much longer service lives.

TABLE 3—*Changes made to the fabrication of Zr-2.5Nb pressure tubes.*

Ingot	Sponge selected to reduce the variability in the oxygen concentration
	Improved vacuum pumps for the melting furnaces to lower the hydrogen concentration
	Changes made to the melting procedure to eliminate piping defects; improved inspection procedures
	Ingots from Kroll material melted four times to reduce the chlorine concentration
	Selection of sponge to minimise phosphorous and carbon concentrations
	Ingot diameter limited to improve the uniformity in microstructure
Forging	Rotary forging introduced to improve yield and uniformity of microstructure
Billet	β quenching of the hollow billet introduced to produce a more uniform microstructure and also less background noise in inspection
Extrusion	Preheating furnace changed from gas to electric to reduce the pickup of hydrogen
	Billet preheat time and temperature better controlled to produce a more uniform microstructure
	Extrusion presses used that have better control of speed and load to decrease the differences between tubes
Surface finishing	Stopped sand blasting the inside surface to eliminate the embedding of sand particles; inside surface honing introduced to improve surface finish; and pickling of the outside surface introduced to remove defects and improve surface finish
Autoclaving	Time reduced from 72 to 24 h
Inspection	Eddy current inspection added to the ultrasonic inspection and then high frequency ultrasonic introduced to improve the detection of defects.

Acknowledgments

The writer thanks Kit Coleman, Malcolm Griffiths, Ed Price, Ian Muir, and Vince Urbanic for their considerable help in preparing this paper. The successful development of Zr-2.5Nb pressure tubes has taken a lot of effort by many people, and the writer thanks all of his many colleagues for their considerable contributions, particularly his most frequent coauthors Kit Coleman, Chuck Ells, Ed Price, Sid Aldridge, Alan Causey, Vince Urbanicm and Ted Ibrahim. The writer also thanks Jim Baker from the Chase Brassand Copper Co. with whom he collaborated on many small orders of development pressure tubes. The writer was extremely fortunate in being able to work in a very stimulating environment and collaborated with many excellent people at the Chalk River Laboratories. This is illustrated by that one of his first supervisors, Chuck Ells, and several of his colleagues, Brian Cox, Bill Fidleris, Kit Coleman, Rick Holt, and Malcolm Griffiths, have been awarded Kroll medals.

References

[1] Rae, H. K., "Candu and Its Evolution," *Canada Enters the Nuclear Age*, McGill-Queen's University Press, Montreal, Canada, 1997, Chap. 9, pp. 191–215; ; Ells, C. E., "Fuel Channels," *Canada Enters the Nuclear Age*, McGill-Queen's University Press, Montreal, Canada, 1997, Chap. 12, pp. 233–254.

[2] Rickover, H. G., "The Decision to use Zirconium in Nuclear Reactors," *Zirconium Production and Technology: The Kroll Medal Papers 1975–2010*, ASTM International, West Conshohocken, PA, 2010.

[3] Ambartsumyan, R. S., Kiselev, A. A., Grebennikov, R. V., Myshkin, V. A., Tsuprun, L. J., and Nikulina, A. F., "Mechanical Properties and Corrosion Resistance of Zirconium and Its Alloys in Water, Steam and Gases at High Temperature," *Proceedings, Second International Conference on the Peaceful Uses of Atomic Energy*, United Nations, Geneva, 1958, Vol. 5, pp. 12–33.

[4] Abriata, J. P. and Bolcich, J. C., "The Nb–Zr System," *Bull. Alloy Phase Diagrams*, Vol. 3, No. 1, 1982, pp. 34–44.

[5] Cheadle, B. A., Aldridge, S. A., and Ells, C. E., "The Development of Texture and Structure In Zr-2.5Nb Extruded Tubes," *Can. Metall. Q.*, Vol. 11, 1972, pp. 121–127.

[6] Cheadle, B. A., *Fabrication of Zirconium Alloys into Components for Nuclear reactors, ASTM STP 633*, A. L. Low and G. W. Parry, Eds., ASTM International, West Conshohocken, PA, 1977, pp. 457–485.

[7] Chouby, R., Aldridge, S. A., Theaker, J. R., Cann, C. D., and Coleman, C. E., *Effects of Extrusion-Billet Preheating on the Microstructure and Properties of Zr-2.5Nb Pressure Tube Materials, ASTM STP 1295*, E. R. Bradleyand and G. P. Sabol, Eds., ASTM International, West Conshohocken, PA, 1996, pp. 657–675.

[8] Coleman, C. E., "Cracking of Hydride-Forming Metals and Alloys," *Comprehensive Structural Integrity*, I. Milne, R. O. Ritchie, and B. Karihaloo, Eds., Elsevier, Oxford, 2003, Vol. 6, Chap. 6.03, pp. 103–161.

[9] Pan, Z. L., St Lawrence, S., Davies, P. H., Griffiths, M., and Sagat, S., "Effect of Irradiation on the Fracture Properties of Zr-2.5Nb Pressure Tubes at End of Design Life," *J. ASTM Int.*, Vol. 2, 2005, Paper No. JAI12456, doi: 10.1520/JAI12456.

[10] Aitchison, I. and Davies, P. H., "Role of Microsegregation in Fracture of Cold-Worked Zr-2.5 Nb Pressure Tubes," *J. Nucl. Mater.*, Vol. 203, 1993, pp. 206–220.

[11] Leger, M., "The Technology of CANDU Fuel Channels," *Corrosion and Hydrogen Ingress, AECL Report*, 108US-31100-LS-001 Rev. 0, Atomic Energy of Canada Limited, Ontario, Canada, 2003, Chap. 9.

[12] Urbanic, V. F., Cox, B., and Field, G. J., "Long-Term Corrosion and Deuterium Uptake in CANDU-PHW Pressure Tubes," *Zirconium in the Nuclear Industry: Seventh International Symposium, ASTM STP 939*, R. B. Adamson and L. F. P. VanSwam, Eds., ASTM International, West Conshohocken, PA, 1987, pp. 189–20.

[13] Perryman, E. C. W., "Pickering Pressure Tube Cracking Experience," *Nucl. Energy*, Vol. 17, 1978, pp. 95–105.

[14] Field, G. J., Dunn, J. T., and Cheadle, B. A., "Analysis of the Pressure Tube Failure at Pickering NGS 'A' Unit 2 Nuclear Systems Department," *Can. Metall. Q.*, Vol. 24, 1985, pp. 181–188.

[15] Theaker, J. R., Chouby, R., Moan, G. D., Aldridge, S. A., Davis, L., Graham, R. A., and Colemen, C. E., *Fabrication of Zr-2.5Nb Pressure Tubes to Minimise the Harmful Effects of Trace Elements, ASTM STP 1245 A*, M. Garde and E. R. Bradley, Eds., ASTM International, West Conshohocken, PA, 1994, pp. 221–242.

[16] Griffiths, M., Davis, W. G., Causey, A. R., Moan, G. D., Holt, R. A., and Aldridge, S. A., "Variability of In-Reactor Diametral Deformation for Zr-2.5Nb Pressure Tubing," *Zirconium in the Nuclear Industry: 13th International Symposium, ASTM STP 1423*, G. D. Moan and P. Rudling, Eds., ASTM International, West Conshohocken, PA, 2002, pp. 796–810.

[17] Causey, A. R., Fidleris, V., MacEwan, S. R., and Schulte, C. W., *Influence of Radiation on Material Properties: 13th International Symposium, ASTM STP 956*, F. A. Garner, C. H. Henager, and N. Igata, Eds., ASTM International, West Conshohocken, PA, 1987, pp. 54–68.

[18] Bickel, G. A., and Griffiths, M., "Manufacturing Variability, Microstructure and Deformatiom of Zr-2.5Nb Pressure Tubes," *Zirconium in the Nuclear Industry: 15th International Symposium, ASTM STP 1505*, B. Kammenzind and M. Limback, Eds., ASTM International, West Conshohocken, PA, 2009, pp. 529–540.

[19] Christodoulou, N., Causey, A. R., Holt, R. A., Tomé, C. N., Badie, N., Klassen, R. J., Sauvé, R., and Woo, C. H., "Modeling In-Reactor Deformation of Zr-2.5Nb Pressure Tubes in CANDU Power Reactors," *Zirconium in the Nuclear Industry: Eleventh International Symposium, ASTM STP 1295*, E. R. Bradley and G. P. Sabol, Eds., ASTM International, West Conshohocken, PA, 1996, pp. 518–537.

[20] Bahurmuz, A. A., Muir, I. J., and Urbanic, V. F., "Predicting Oxidation and Deuterium Ingress for Zr-2.5Nb CANDU Pressure Tubes," *J. ASTM Int.*, Vol. 2, No. 5, 2005, Paper No. JAI12342, doi: 10.1520/JAI12342.

SCHEMEL AWARD PAPER

Reprinted from JAI, Vol. 7, No. 7
doi:10.1520/JAI102952
Available online at www.astm.org/JAI

Young-Jin Kim,[1] *Raul Rebak,*[1] *Yang-Pi Lin,*[2] *Daniel Lutz,*[2] *Douglas C. Crawford,*[2] *Aylin Kucuk,*[3] *and Bo Cheng*[3]

Photoelectrochemical Investigation of Radiation-Enhanced Shadow Corrosion Phenomenon

ABSTRACT: The photoelectrochemical investigation was performed by measuring the photoelectrochemical behavior of various alloys such as Zircaloy 2, 304 stainless steel (SS) and Alloy X-750 in 0.01*M* Na_2SO_4 at 25C or in high purity water at 300C under intense ultraviolet (UV) illumination. UV was selected because its photon energy (~5 eV) is similar to the energy gap of the electron-hole pairs in zirconium oxide. The data show that the photoexcitation of ZrO_2 caused the corrosion potential to shift in the anodic direction and produced anodic photocurrents under the oxidizing water chemistry condition when Zircaloy 2 electrode was galvanically coupled with dissimilar electrodes, such as Alloy X-750, 304 SS, or Pt, causing accelerated corrosion of Zircaloy. It is thus postulated that the photoelectrochemical enhancement of surface reaction kinetics at the ZrO_2 surface may be responsible for the radiation-enhanced corrosion on Zircaloy (i.e., shadow corrosion). In addition, it is revealed that no significant change in galvanic current between Zircaloy 2 and other dissimilar electrodes was measured in high temperature water containing only hydrogen that resulted in similar ECPs. These data thus clearly provide an explanation for why the radiation-enhanced corrosion of Zircaloy only occurs in BWRs but not PWRs. Based on galvanic corrosion, impedance, and transmission electron microscopy analysis, it is proposed that the defect structure of equiaxed grain layers may be responsible for the photoelectrochemical response of ZrO_2 in high temperature water. The

Manuscript received January 8, 2010; accepted for publication June 22, 2010; published online July 2010.
[1] GE Global Research Center, Schenectady 12309, NY.
[2] Global Nuclear Fuel—America, Wilmington, NC.
[3] Electric Power Research Institute, Palo Alto, CA.

Cite as: Kim, Y.-J., Rebak, R., Lin, Y.-P., Lutz, D., Crawford, D. C., Kucuk, A. and Cheng, B., "Photoelectrochemical Investigation of Radiation-Enhanced Shadow Corrosion Phenomenon," *J. ASTM Intl.*, Vol. 7, No. 7. doi:10.1520/JAI102952.

Copyright © 2011 by ASTM International, 100 Barr Harbor Drive, PO Box C700, West Conshohocken, PA 19428-2959.

mechanism of shadow corrosion is still highly debated but it appears to be similar to a process of galvanic corrosion in connection with sufficiently conducting Zr oxide structure. The galvanic corrosion data suggests that a Zr coating on the fuel assembly spacer (Alloy X-750 or 304 SS) may mitigate the shadow corrosion in BWRs.

KEYWORDS: Zr alloys, photoelectrochemistry, shadow corrosion, ECP, galvanic corrosion, impedance

Introduction

Zirconium alloys have been used most extensively as fuel assembly materials for water-cooled reactors [1,2]. Considerable research has been done to ensure that zirconium alloys are corrosion resistant in high temperature water and steam. Zirconium reacts with high temperature water and steam to form ZrO_2 and hydrogen [1,3,4]

$$Zr + 2H_2O \rightarrow ZrO_2 + 2H_2 \tag{1}$$

The nature of the mobile species could have influenced the efficiency of oxide formation. There is strong evidence that O^{-2} ions have a transport number close to 1.0 in even valent value metal oxide system such as Zr/ZrO_2 [5], but the existence of hydrides in the metal oxide or in the oxide after oxidation in steam raises several questions about H transport in some form. Oxide formation requires concurrent transport of oxygen from the oxide/water interface to the metal/oxide interface and of electrons from the metal to the oxide/water interface from an overall reaction of reaction 1.

Oxide films formed on metals and alloys has been characterized for many years because the chemical and physical properties of oxide films can alter the mechanism and kinetics of the corrosion processes [6]. The oxide films formed on metals and alloys exhibit semiconductive properties and photoelectrochemical method can be used to characterize the electrical property and consequently their susceptibility to general or localized corrosion [7–9]. The photoelectrochemical behavior of oxide films is largely influenced by their electronic properties.

When light of a suitable energy, hv, is absorbed by the oxide film, electrons can be excited from occupied electric states into unoccupied ones

$$hv \rightarrow e^- + h^+ \tag{2}$$

And, photoelectrochemically it would oxidize the water to produce oxygen

$$2H_2O + 4h^+ \rightarrow O_2 + 4H^+ \tag{3}$$

This reaction consequently alters the corrosion potential of semiconducting oxide surfaces.

One of the typical phenomena related to semiconductivity is the photoeffect. The concentration of carriers near the surface is increased by illumination. Illumination can create holes and electrons in the oxide if the incident photon's energy is large enough. The created holes and electrons flow in opposite directions because of the electric field in the oxide. This mechanism is generally used to explain the photocurrents generated from semiconductors immersed in solutions and also for anodic photocurrents on metals.

Depending on the properties of the oxide film with respect to its conduction type, different energetic conditions can be distinguished for an *n*-type or *p*-type semiconducting or an insulating film [9]. Under the conditions of a depletion layer at the film/solution interface in a semiconducting film, the electron/hole pair is separated in the electric field of the space charge layer. In a *p*-type semiconducting film, the electron migrates to the surface from where it can react with an unoccupied state in the electrolyte, which is represented by an oxidized chemical species. The hole flows to the backside contact, and the resulting current is cathodic. In an *n*-type oxide, illumination produces an anodic current because holes migrate to the oxide surface, reacting with occupied state and electrons move back.

Zirconium oxide (ZrO_2) may be formed in three different crystal structures—monoclinic, tetragonal, and cubic—and their structures are stable at different temperatures [3,10,11]. In general, ZrO_2 has a low electronic conduction and a high ionic (oxygen anion) conduction and the band gap for ZrO_2 is typically 5 eV [9]. When light is illuminated onto ZrO_2 that has formed over a metallic substrate such as a Zircaloy, electrons are excited from the valence band to the conduction band, and they migrate to the metal layer and produce a current called photocurrent. Since the generation of a photocurrent depends on the presence of an electric field in the oxide, there will usually be a photopotential where the electric field goes to zero and the photocurrent disappears. In a crystalline semiconductor, this zero photocurrent/potential is the so-called "flat-band potential." This photo-dissolution is attributed to oxidation of lattice oxide ions of ZrO_2 at the surface by photo-holes. The oxidation of semiconductors by holes in the valence band is well described [7]. After the surface recombination rate has reached its steady state, photo-holes oxidize the ZrO_2 lattices leading to dissolution of the oxide film and a concomitant reduction of the density of surface states. This results in a subsequent increase in the corrosion rate.

In nuclear reactor, various radiation sources are present in the core from low energy of UV light to hard γ-rays. Photons can be produced in the water surrounding nuclear fuel via the Cherenkov effect and excites the electrons of ZrO_2 affecting the electrochemical response [12]. The dominant source of Cherenkov-ray radiation is the electrons produced by the Compton scattering of γ-rays that are generated in-core, from structural materials or N-16. High energy radiation (i.e., γ-ray) affects mainly the material property but not the electrochemical behavior of the material (i.e., corrosion potential or galvanic current).

In operating BWRs, accelerated growth of ZrO_2 has been observed on a Zr alloy when it is in close proximity to a dissimilar material (e.g., Alloy X-750 and stainless steel (SS)). This anomalous oxide growth is called "shadow corrosion" since the pattern of the enhanced corrosion resembles the shape of the adjacent metallic components [13–17]. Several hypotheses have been put forth to explain

this phenomenon, including (1) galvanic corrosion driven by the corrosion potential difference between dissimilar alloys (e.g., Zircaloy 2 and Alloy X-750), (2) differences in the local radiolysis of water from altered radiation spectrum, and (3) "beta shine" (higher flux of energetic electrons).

Metallographic examination of shadow corrosion reveals a uniformly enhanced corrosion of the Zr alloys [18], as shown in Fig. 1. The enhancement is believed to result from an alteration in the electronic conduction or ionic (oxygen) diffusion in ZrO_2. Previous studies indicate that the ZrO_2 oxide film may possess semiconducting properties, where pairs of electrons and holes within the space charge layer may form and produce a change in electrode potential in the semiconductor. The electronic conductivity of ZrO_2 may be affected by the illumination of photons at certain energy levels.

Lysell et al. argued that the most likely cause of shadow corrosion is the theory of galvanic corrosion [14,15] and also stated that the reason shadow corrosion is not reproducible in autoclave (out-of-pile) tests is because of the photoconductivity effect caused by reactor produced radiation on the Zr alloy component. It is also interesting to note that a crevice geometry formed between Zircaloy and the different metal component (Alloy X-750) contributed to the shadow corrosion [17]. Recently, Adamson summarized the variables influencing shadow corrosion, mainly from field observations [19]. First, Adamson confirmed that shadow corrosion occurs only under radiation in a reactor and was never reproduced in autoclave laboratories. He also listed possible mechanisms by which radiation assist the shadow corrosion process, (1) increase the conductivity of the oxide film on the Zr alloy, (2) increase the conductivity of the water by ionizing it, and (3) accelerates the reaction of the reduction of molecular oxygen to form hydroxyl anions.

One of the factors from the reactors that are difficult to simulate in the laboratory is the effect of irradiation on the electrical properties of oxide film. Cox stated that the effect of irradiation may be simulated using a UV arc lamp if the

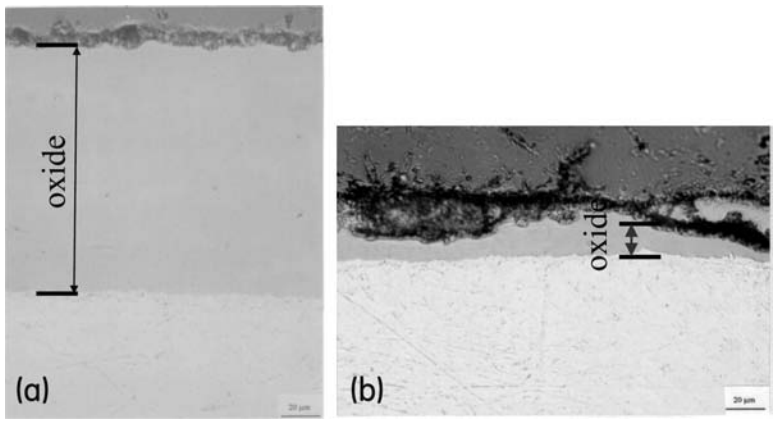


FIG. 1—*Oxide thickness (*a*) within and (*b*) away from a control blade handle shadow [18].*

photon energy is higher than the band gap of the oxide, the oxide is thin enough for the light to penetrate, and the light source is not far from the target [20].

Furthermore, the conductivity of the oxide is expected to be dependent in part on the composition of the Zr-based alloy. In most Zr-based alloy for nuclear applications, the alloy additions are generally in excess of the solubilities in the alloy and second phase particles (SPP) are generally formed; examples being $Zr_2(Ni, Fe)$ and $Zr(Cr, Fe)_2$ in Zircaloy-2 and $Zr(Cr, Fe)_2$ in Zircaloy-4.

The purpose of this paper is to investigate the photoelectrochemical corrosion characteristics of Zr and other alloys under UV irradiation by measuring the corrosion potential, impedance, and galvanic corrosion behavior, and the possible mechanism is proposed for a better understanding of shadow corrosion phenomena in BWRs.

Experimental Procedures

304 SS, Alloy X-750, and Zr alloys (Zircaloy 2, Zircaloy 4, GNF-Ziron, and GNF-NSF) in sheet form were used. Specimens of $1.25 \times 1.25 \times 0.12\,cm^3$ were cut from them and then polished using a wet 600-grit emery paper. Test specimens of 304 SS and Alloy X-750 were used in the as-received condition, while test specimens of Zr alloys (except intermetallic alloys) were further annealed for 1 min in 1050°C in Ar, immediately quenched in water, and etched in a $5\,\%\,HF + 45\,\%\,HNO_3 + 50\,\%\,H_2O$ solution for 30 s. All test specimens were then rinsed ultrasonically with high purity water. Specimens for electrochemical measurement were spot welded to a polytetrafluorethylene (PTFE) insulated 304 SS or Zircaloy wire, which were mounted in a Conax fitting. A nominal chemical composition of Zr alloys is listed in Table 1.

Three different intermetallic alloys ($Zr + Fe + Ni$, $Zr + Fe + Cr$, and $Zr + Fe + Ni + Si$) were melted and manufactured at GE Global Research Center by using an electric arc under argon gas. The alloy compositions were analyzed by X-ray fluorescence and listed in Table 1. The test electrodes of these intermetallic alloys are in the shape of irregular cast piece, and the electrical contact was made using a PTFE insulated Zircaloy 2 wire. No surface pretreatment was done before testing in a given condition.

Water in the loop was purified through a demineralizer, an organic removal column, and a sub-micron filter before passing into a 1 gal (3.78 L) glass

TABLE 1—*Nominal chemical composition of Zr alloys (in wt %).*

Test Alloys	Sn	Fe	Cr	Ni	Nb	Si	Zr
Zircaloy 2	1.3	0.18	0.1	0.07			Balance
Zircaloy 4	1.3	0.2	0.1				Balance
GNF-Ziron	1.3	0.25	0.1	0.07			Balance
GNF-NSF	1.0	0.35			1.0		Balance
$Zr + Fe + Ni$		14.0		9.8			Balance
$Zr + Fe + Cr$		28.1	26.1				Balance
$Zr + Fe + Ni + Si$		13.0		8.7		1.2	Balance

conditioning column. The water was equilibrated with appropriate mixtures of Ar, O_2, and H_2 to establish the desired water chemistry. SWAN FAM Oxytrace Oxygen and Orbisphere Models 26322 hydrogen monitors were used for measuring the dissolved oxygen and hydrogen, respectively, in the inlet and outlet streams. A platinum flag electrode was used to monitor the effective redox potential of the water. Electrochemical measurements in high temperature water were conducted in a 1 gal (3.78 L) SS autoclave by controlling the water chemistry conditions at a water flow rate of 100 cm^3/min.

Electrochemical measurements were conducted using a Gamry Reference 600 Potentiostat/Galvanostat/ZRA to evaluate the electrochemical response of oxide layers in 0.01*M* Na_2SO_4 solution at 25°C or in pure water at 300°C. Electrochemical impedance response was measured over the range of 1 mHz–100 kHz by superimposing a 10 mV alternating voltage with a sine wave pattern. The saturated calomel electrode and a Pt foil electrode were used as a reference electrode and a counter electrode, respectively, at 25°C. In high temperature water, electrochemical measurements were performed using a zirconia high temperature *p*H sensor with a copper/cuprous oxide internal junction as a reference electrode, with an Agilent Model 34970A electrometer. The measured values were converted to the standard hydrogen electrode scale on the basis of the calculated potential for the zirconia sensor in neutral water.

Photoelectrochemical response of oxidized surface was evaluated by introducing the UV light to the specimen through optical fiber glass. An Expo Omni-Cure Series 2000 was used as a UV light source. A schematic view of autoclave system for electrochemical measurement under UV illumination is shown in Fig. 2. The test specimen was irradiated through the sapphire window. A thin diamond disk made by chemical vapor deposition was placed on the top of

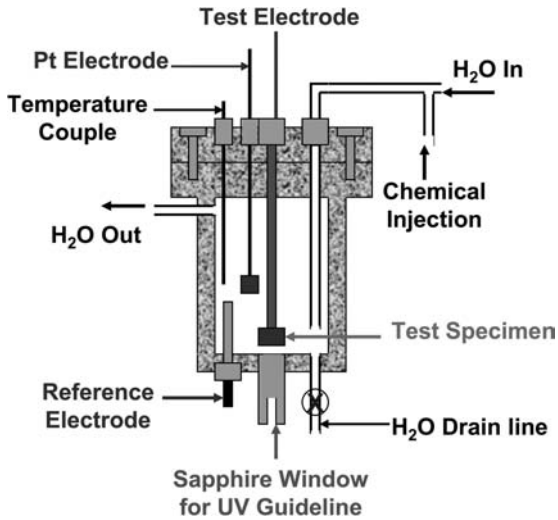


FIG. 2—*Schematic view of autoclave system for electrochemical test in high temperature water.*

sapphire window to protect it from dissolution in high temperature water and did not affect the UV intensity.

Experimental Results

Electrochemical Corrosion Potential Behavior

For a given water chemistry, the electrochemical corrosion potential (ECP) or corrosion potential is dependent on the oxide surface nature, such as oxide thickness, composition, conductivity, structure, etc. Also, a change in electrocatalytic nature of the surface associated with the chemical compositions of oxide layers can play a significant role in the ECP behavior of materials.

Figure 3 shows the ECP behavior of 304 SS, Alloy X-750, Pt and Zircaloy 2 electrodes in 300°C water containing 150 ppb H_2 or 1.1 ppm O_2. Under a non-oxidizing condition containing 150 ppb H_2, ECPs of test electrodes showed the similar low ECP values, while under a highly oxidizing water chemistry condition, 1.1 ppm O_2, the ECP of Zircaloy 2 is lower than other electrodes due to the formation of insulating oxide, ZrO_2, that limited the O_2 reduction kinetics.

It is interesting to note that shadow corrosion is observed only in BWR plants but not in PWR plants or in plants with high hydrogen content. This suggests that shadow corrosion may be caused by a separation in the corrosion potential of the two types of materials in the reactor environment. As shown in Fig. 3, when hydrogen is present in the system that forces both materials to have a low or similar corrosion potential, there is no difference of potential

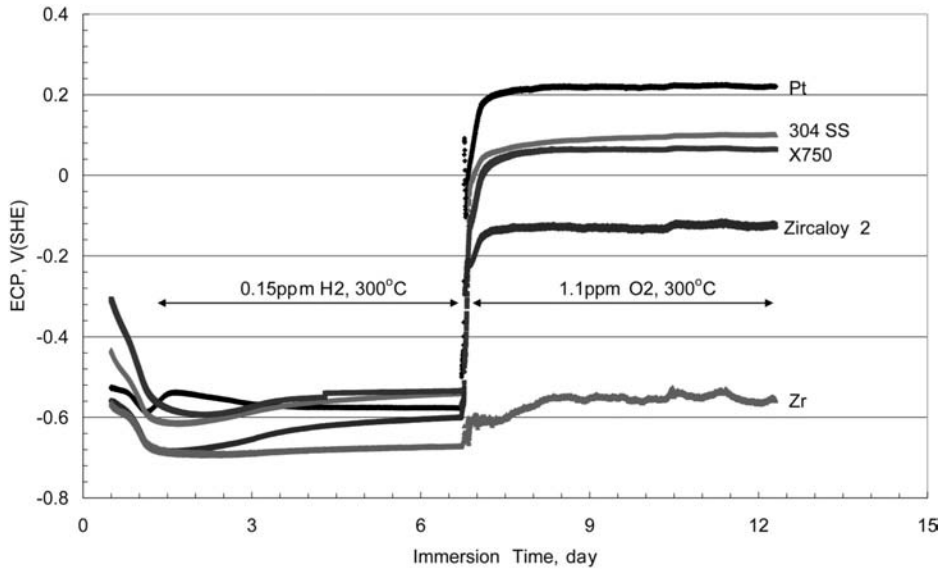


FIG. 3—*ECP of Zircaloy 2, 304 SS, Alloy X-750, Zr, and Pt electrodes in 300°C water containing 1.1 ppm O_2 or 0.15 ppm H_2.*

between both materials. The degree of galvanic corrosion between two dissimilar alloys will be addressed in a later section to understand the low susceptibility of shadow corrosion in PWRs. Based on experiences from BWR, CANDU, and PWR reactors, Cox suggested that a dissolved hydrogen content higher than 10 cm^3/kg may be necessary to eliminate the occurrence of shadow corrosion since the amount of hydrogen would guarantee that all the materials would be operating at the hydrogen reversible reaction potential [4].

Also, ECP of two GNF alloys (Ziron and NSF) was measured in high temperature water to compare the spontaneous oxidation kinetics for oxide formation. As shown in Fig. 4, GNF alloys reveal the similar ECP behavior compared to Zircaloy 2 or Zircaloy 4 in 300°C water containing 700 ppb O_2 and 800 ppb H_2O_2. Thus, the similar corrosion behavior is expected among test electrodes under the given test condition.

As described earlier, the presence of light source of a short wavelength (e.g., Cherenkov radiation) would alter the corrosion potentials of *n*-type semiconducting ZrO_2 formed on zirconium alloys or *p*-type semiconducting oxide formed on Alloy X-750. Figure 5 shows the effect of UV light on the ECP of Zircaloy 2, 304 SS, and Alloy X-750 in 0.01*M* Na_2SO_4 at 25°C. Test specimens have been pre-oxidized for 4 weeks in 300°C water containing 1.1 ppm O_2. As shown in Fig. 4, when the UV light was turned on, the corrosion potential of Zircaloy 2 immediately decreased and then increased when the UV illumination stopped. In contrast, the corrosion potential of Alloy X-750 increased when the UV light was turned on. It is known that the oxides become more conductive in the

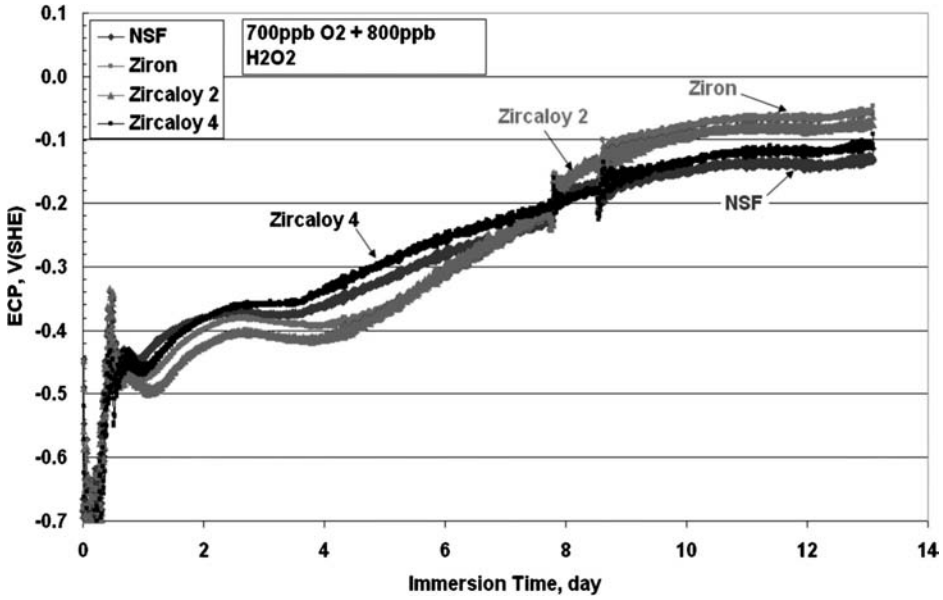


FIG. 4—*ECP of Zircaloy2, Zircaloy 4, Ziron, and NSF alloys in 300°C water containing 700 ppb O_2+800 ppb H_2O_2.*

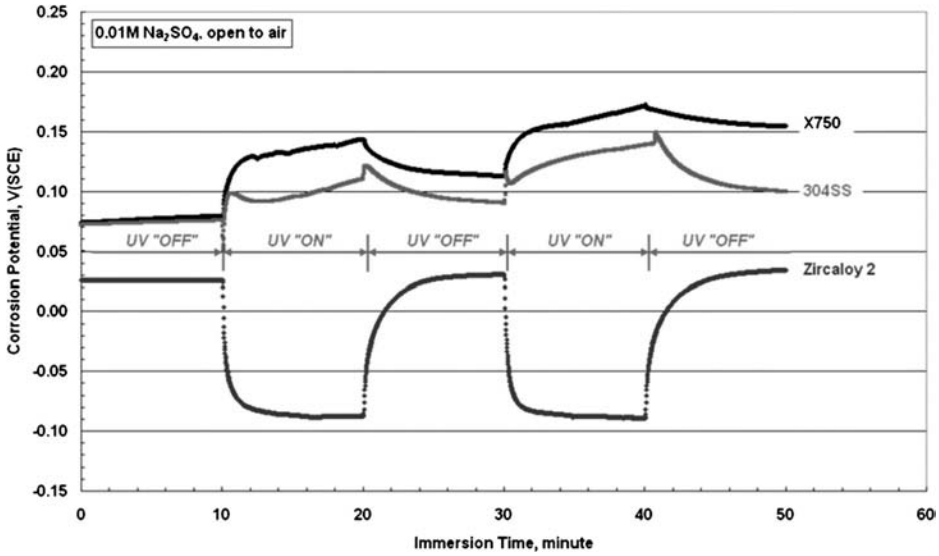


FIG. 5—*Effect of UV illumination on corrosion potential behavior of Zircaloy 2, 304 SS, and X750 electrodes in 0.01M Na_2SO_4 solution at 25°C. Test electrodes have been pre-immersed for 4 weeks in 300°C water containing 1.1 ppm O_2.*

radiation field since photons at UV and higher energies excite electrons from the valence band to the conduction band where they are free to move [9].

Therefore, it may be postulated that the difference of corrosion potential between Zircaloy 2 and Alloy X-750 becomes larger in the presence of UV light and consequently enhances the susceptibility of galvanic corrosion between Zircaloy 2 and X-750. The effect of UV irradiation on the ECP of Zirclaoy 2 and Alloy X-750 were also measured in 300°C water containing 1.1 ppm O_2. As shown in Fig. 6, UV irradiation increases the ECP of Alloy X-750 and decreases the ECP of Zircaloy 2, suggesting a larger ECP separation between Alloy X-750 and Zircaloy 2 under in-core water chemistry condition and consequently results in a higher susceptibility to galvanic corrosion.

It is well documented that the nodular corrosion behavior of Zircaloy is dependent on the distribution of the precipitates or SPP in the microstructure, e.g., $Zr_2(Ni, Fe)$ and $Zr(Cr, Fe)_2$ [21,22]. A uniform distribution of fine particles produces optimum resistance, while agglomerated coarse particles produce poor corrosion resistance in BWR. The role of the particles in the mechanism of the corrosion reaction has been well studied. The result of anodic polarization of the zirconium matrix by the highly cathodic precipitates has been postulated.

As shown in Fig. 7, when the UV light was turned on, the corrosion potential of the intermetallic alloys shifted to the positive direction, behaving as a *p*-type semiconductor. The chemical composition of intermetallic alloys is given in Table 1. It should be mentioned that the corrosion potential of each intermetallic alloy shown in Fig. 6 may not represent the absolute one of each alloy due to the irregular shape and unknown oxidation status of test specimens. This result

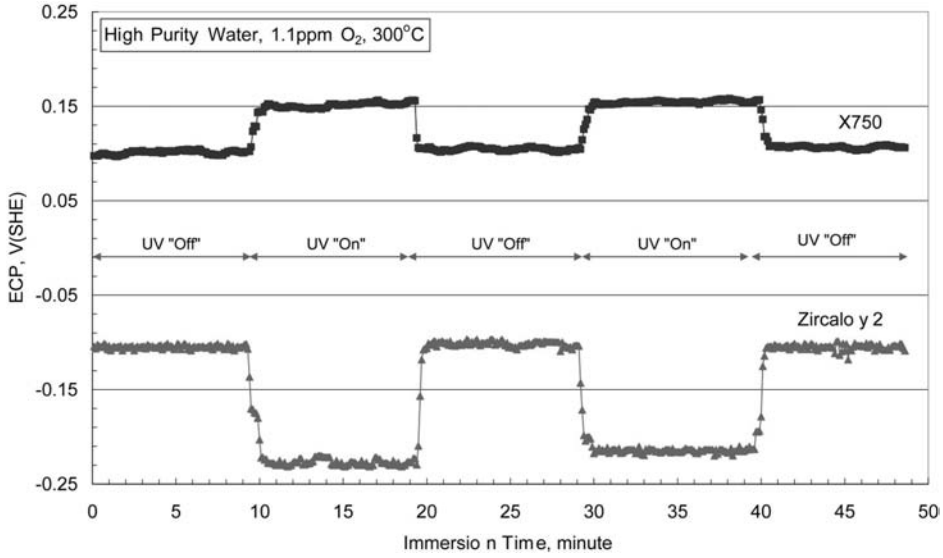


FIG. 6—*ECP of X750 and Zircaloy 2 electrodes in 300°C water containing 1.1 ppm O_2 with and without UV illumination.*

suggests that the intermetallic particles existing in Zircaloys at different size act as a cathode and eventually higher corrosion may occur at the interface of Zr matrix surrounding the SPP precipitates due to the galvanic coupling. The degree of corrosion potential difference for each SPP is expected to depend on

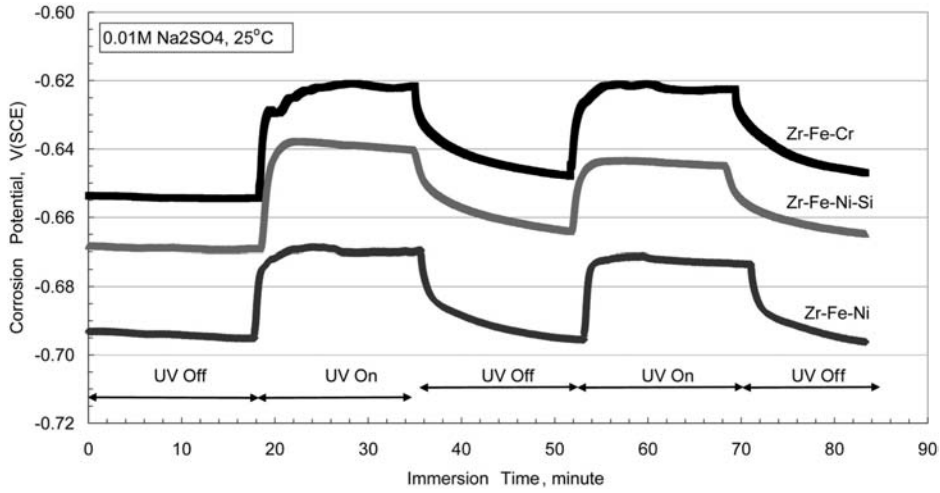


FIG. 7—*Corrosion potential behavior of different intermetallic alloys in 0.01M Na_2SO_4 solution at 25°C with and without UV illumination.*

the SPP size and distribution in the matrix. It has been reported that the Zr intermetallics affect the corrosion behavior of Zr alloys by acting as noble sites and enhance the galvanic corrosion [21,23].

Electrochemical Impedance Response

The use of electrochemical impedance spectroscopy (EIS) in evaluating the degradation of metals and their interaction with an aqueous environment has provided useful information that could not be obtained with traditional direct current electrochemical techniques in low-conductive media or through nonconducting or poorly conducting films where the high Ohmic contribution from solution or film resistance obscures the Faradaic response of the metal surface. One alternate feature is the non-destructive nature suitable for corrosion monitoring.

EIS has been also used to understand the electrochemical kinetics of Zr alloys and characterize their oxide films, such as oxide growth, diffusion process, and corrosion rate [24–30]. It was reported that the post-transition oxide film revealed much higher electric conductivity than the pre-transition oxide film [30]. The low electric conductivity for the pre-transition oxide film was explained by change in space charge layer as the oxide films grow.

Figures 8 and 9 show the typical Nyquist plot of electrochemical impedance behavior of oxidized Zirclaoy 2 and Alloy X-750 electrodes, respectively, measured in 0.01*M* Na_2SO_4 at 25°C. Before the ECP measurement, specimens have been pre-oxidized for 4 weeks in 300°C water containing 1.1 ppm O_2 without UV. It is clearly seen that the presence of UV light decreased the oxide impedance formed on Zircaloy 2, indicating the possible modification of electric

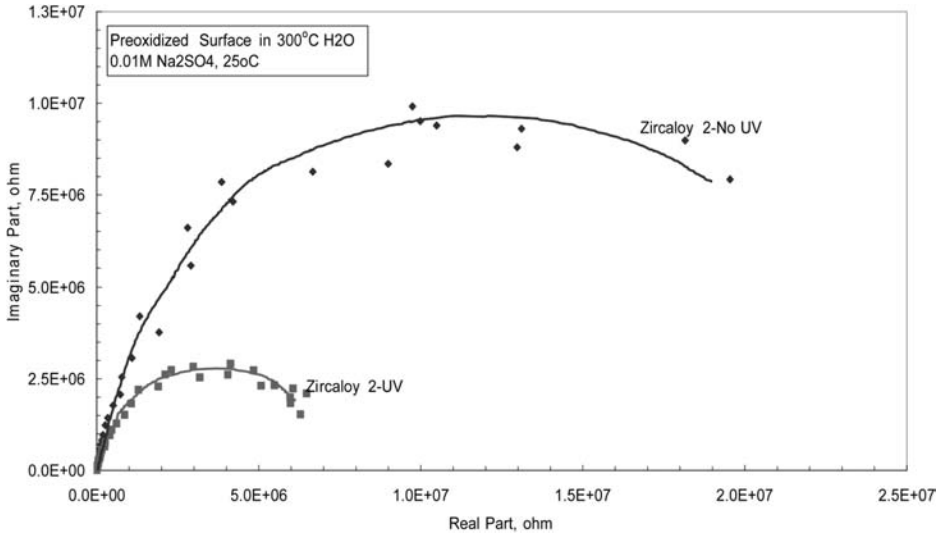


FIG. 8—*Nyquist plot for Zircaloy 2 electrode in 0.01M Na_2SO_4 solution at 25°C with and without UV illumination.*

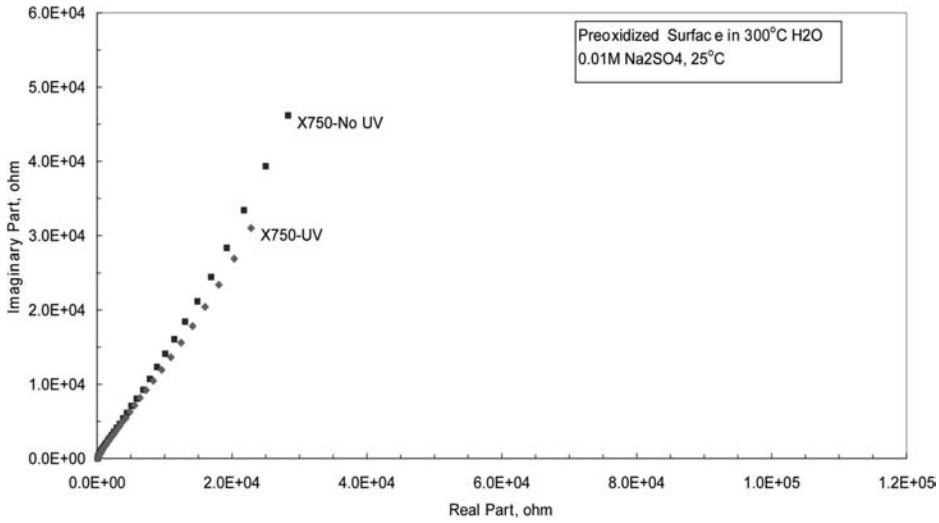


FIG. 9—*Nyquist plot for Alloy X750 electrode in 0.01M Na_2SO_4 solution at 25°C with and without UV illumination.*

conductivity of ZrO_2. Furthermore, the oxide impedance formed on X-750 is much lower than one formed on Zr alloys.

The oxide resistance or conductivity formed on Zircaloy 2 after a long term exposure (3 weeks or 4 months) to 300°C water containing 1.1 ppm O_2 was investigated by measuring the impedance in 300°C water. Test specimens were immersed for a given time with or without UV illumination. As shown in Fig. 10, the impedance spectra contain two semicircle regions and were confirmed by the Bode and phase angle plot (Fig. 11).

Impedance spectra can be interpreted into two oxide layers with different electric properties. It is clearly seen that the oxide impedance for Zr oxide formed after immersion for 4 months in high temperature water is much higher than the one formed after immersion for 3 weeks, suggesting a thicker and/or dense oxide.

The impedance spectra for Zircaloy 2 exposed for 4 months with and without UV light show the typical two time constants, representing two different kinetic processes. From the phase angle plot in Fig. 11, the low impedance at high frequencies can be attributed to the outer oxide layer that is exposed to high temperature water, while the high impedance at low frequencies is related to the inner oxide layer. Such a different impedance response at different frequencies has been attributed to variation of defects in the oxide film, such as electrons, vacancies, electron holes, etc. [24,25,30]. The outer oxide layer near the solution/oxide interface is known to be more porous and UV irradiation may alter the oxide conductivity. By comparing the impedance behavior at high frequencies for zirconium oxide formed for 4 months with or without UV irradiation under the given test condition, UV irradiation affects only the outer

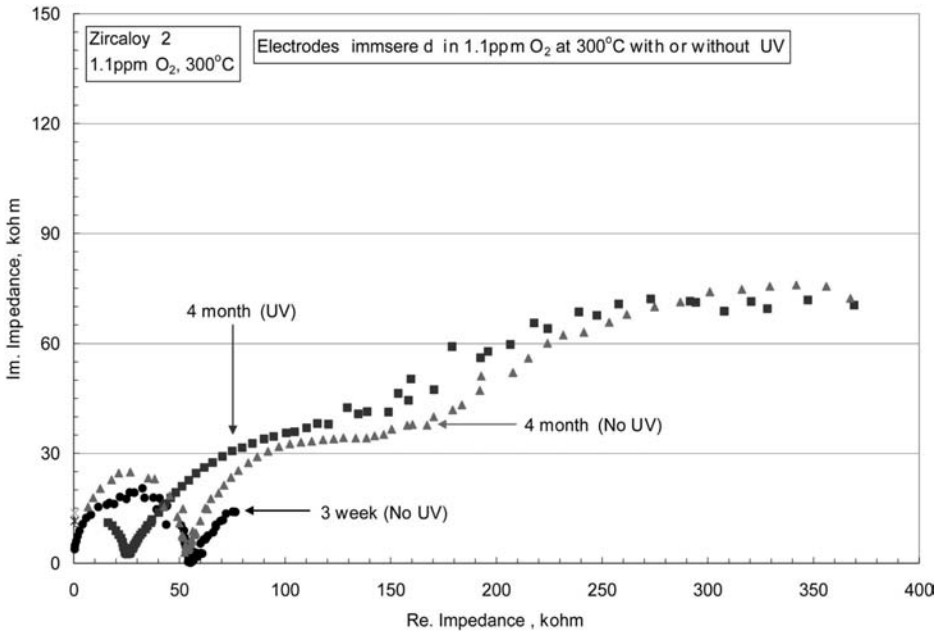


FIG. 10—*Electrochemical impedance spectra (Nyquist plot) of Zircaloy 2 coupled with Alloy X-750 electrode in 300°C water containing 1.1 ppm O_2 after exposure for 3 weeks or 4 months with or without UV illumination.*

oxide layer (Fig. 10), but there is no significant effect on the impedance of inner oxide layer controlling the diffusion kinetics of oxygen ion.

Galvanic Corrosion Behavior

Galvanic corrosion may occur when two different metals in contact (or connected by an electrical conductor) are exposed to a conductive solution. A difference in electrical potential exists between different metals and serves as the driving force to pass current through the metals. This current flow results in increased corrosion of one of the metals in the couple. The larger the potential difference between two metals, the greater the possibility of galvanic corrosion. Note that galvanic corrosion only causes increased deterioration of one of two metals. Galvanic corrosion can often be recognized by the increased amount of corrosion close to the junction of two metals.

Photoelectrochemical tests of Zr alloys at ambient temperature using monochromatic xenon light have been reported [23,31,32]. They observed a photocurrent response upon UV illumination and also observed the effect of oxide surface and applied potential on the amount of photocurrent. However, photoelectrochemical characteristics of Zr oxides have not been evaluated in high temperature and high purity water.

Figure 12 shows the galvanic current response of Zircaloy 2 coupled with Pt, Alloy X-750, Zircaloy 2, or pure Zr electrode in 0.01*M* Na_2SO_4 at 25°C. All

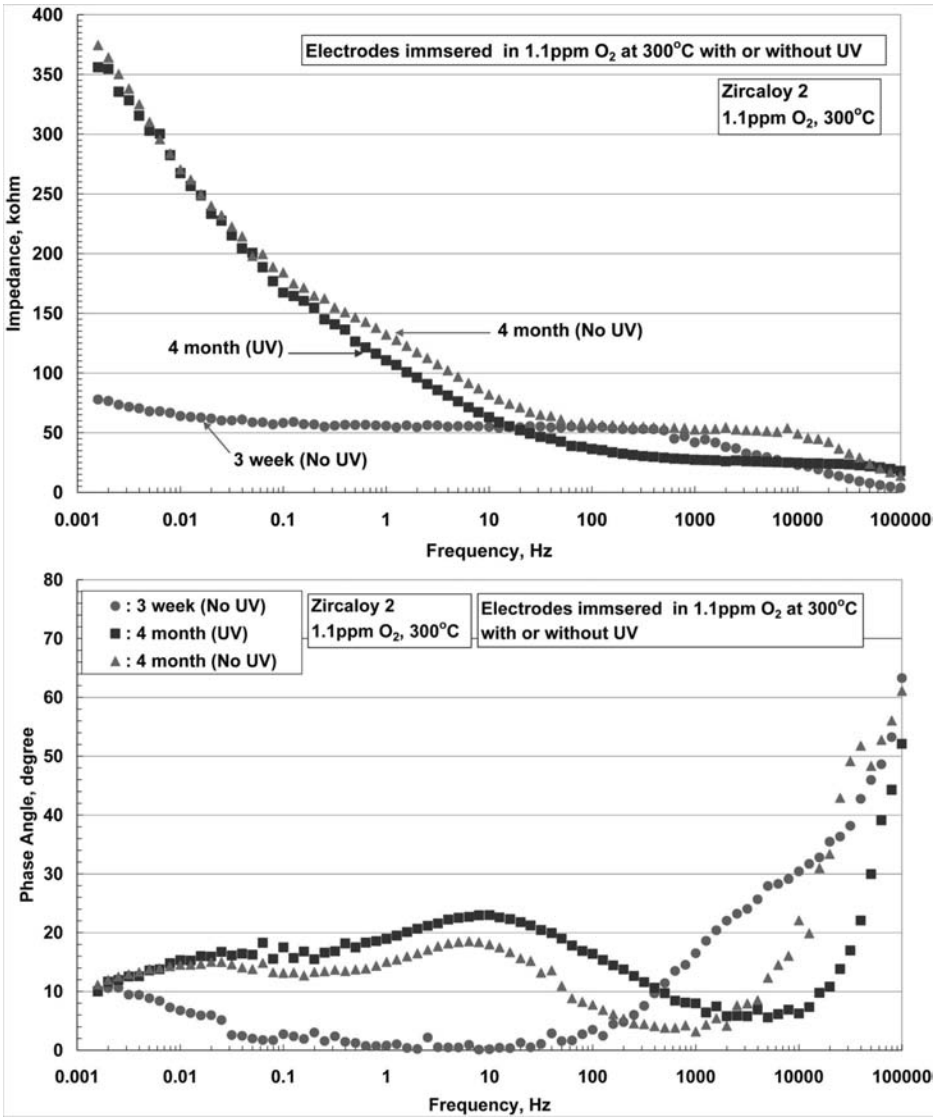


FIG. 11—*Impedance spectra (Bode and phase angle plots) of Zircaloy 2 coupled with Alloy X-750 in 300°C water containing 1.1 ppm O_2 after exposure for 3 weeks or 4 months with or without UV illumination. Impedance was measured in 300°C water containing 1.1 ppm O_2 without UV illumination.*

specimens were fully pre-oxidized in 300°C water as described previously. An anodic electrode is Zircaloy 2, and a cathodic electrode is Pt, Alloy X-750, pure Zr, or another Zircaloy 2 electrode. When the coupled specimens were illuminated by the UV light, the galvanic current immediately increased or decreased.

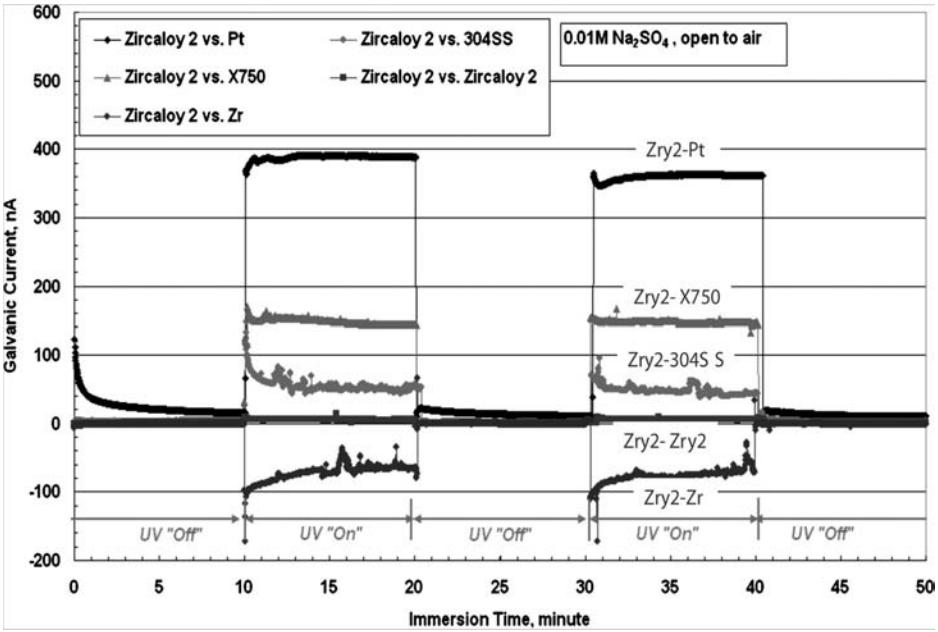


FIG. 12—*Galvanic current response of Zircaloy-X750, Pt, or Zircaloy 2 coupling in 0.01M Na_2SO_4 at 25°C with and without UV illumination.*

The most saturated galvanic current was measured on Zircaloy 2 coupled with Pt. No galvanic current was measured on Zircloy 2 coupled with another Zircaloy 2. The positive galvanic current indicates the galvanic current flow from Zircaloy 2 to Pt or Alloy X-750 electrode, indicating the anodic corrosion of Zircaloy 2.

It is interesting to note that, as shown in Fig. 12, the negative current flow was measured when Zircaloy 2 coupled with pure Zr was illuminated with the UV light. This negative current can be explained by the current flow from pure Zr to Zircaloy 2 due to the lower corrosion potential of pure Zr than Zircaloy 2. The presence of small amounts of alloying elements, Sn, Fe, Cr, and Ni, increases the electric conductivity through the oxide layer and hence increases the corrosion potential of Zircaloy 2.

A galvanic current of coupled electrodes was also measured in 300°C water containing 1.1 ppm O_2 and is shown in Figs. 13 and 14. This galvanic current behavior is very similar to one measured at ambient temperature. Based on the galvanic current behavior of Zircaloy 2 coupled with pure Zr, it is interesting to note that certain areas in fuel cladding surface where alloying elements are depleted by improper annealing treatment may be susceptible to higher galvanic corrosion. In order for reducing the accelerated corrosion along the fuel cladding, it is thus important to produce the cladding surface having the uniform distribution of SPPs. In general, the data in Fig. 14 suggest that the surface treatment, such as Zr coating, on fuel assembly spaces may reduce or mitigate the shadow corrosion on fuel cladding surface.

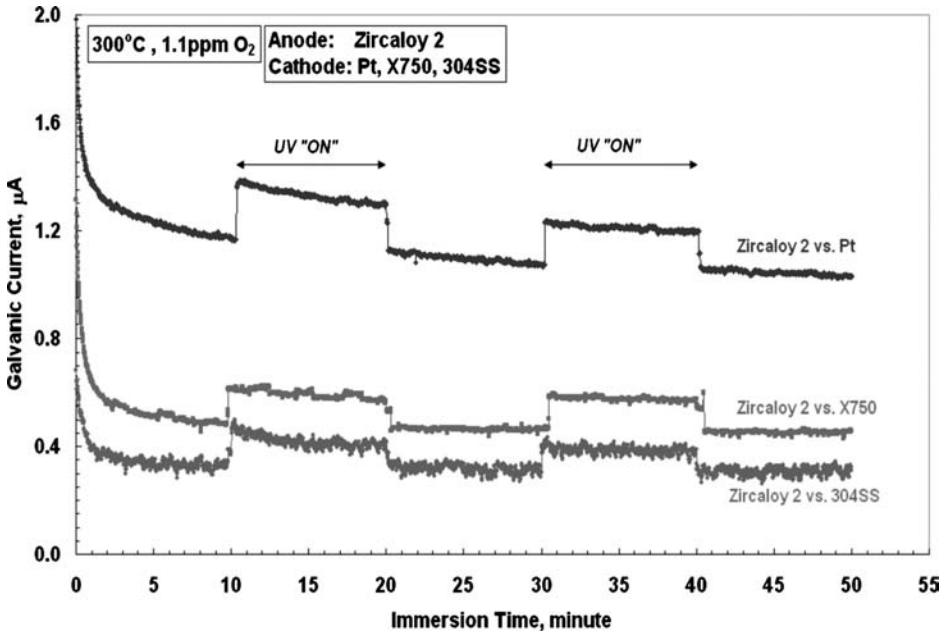


FIG. 13—*Galvanic current of Zircaloy 2 coupled with Alloy X-750, 304 SS, or Pt electrode in 300°C water containing 1.1 ppm O_2 with and without UV illumination.*

The measurement of galvanic current on two different GNF Zr alloys (Ziron and NSF) coupled with Alloy X-750 was also performed in high temperature water, shown in Fig. 15. Test specimens have been pre-oxidized under the same water chemistry condition before measuring the galvanic current. It is clearly seen that both GNF-Ziron and GNF-NSF alloys showed low increases in galvanic current when both alloys were exposed to UV light, compared to one on Zircaloy 2. These data suggest that both Ziron and NSF alloys may be less sensitive to photoelectrochemical response. But, more analysis (e.g., oxide structure, thickness, etc.) are needed to understand the difference of photoelectrochemical response in high temperature water.

The GNF-Ziron and Zircaloy 2 results in Fig. 15 are consistent with observations on cladding at a BWR plant. Figure 16 shows examples of Zircaloy 2 and Ziron cladding at spacer locations, where the cladding contacted with an Alloy X-750 spring. The examples are from the same axial elevation of rods in symmetric positions of fuel assembly spacers after one 18-month cycle of operation. In Fig. 16, it is clearly evident that Zircaloy 2 cladding shows more white nodules indicative of more shadow corrosion, while Ziron cladding showed fewer nodules.

Effect of Water Chemistry

Currently, many BWRs worldwide are operating with NobleChem™ or Online NobleChem™ (OLNC)). Both NobleChem™ and OLNC provide key benefits such

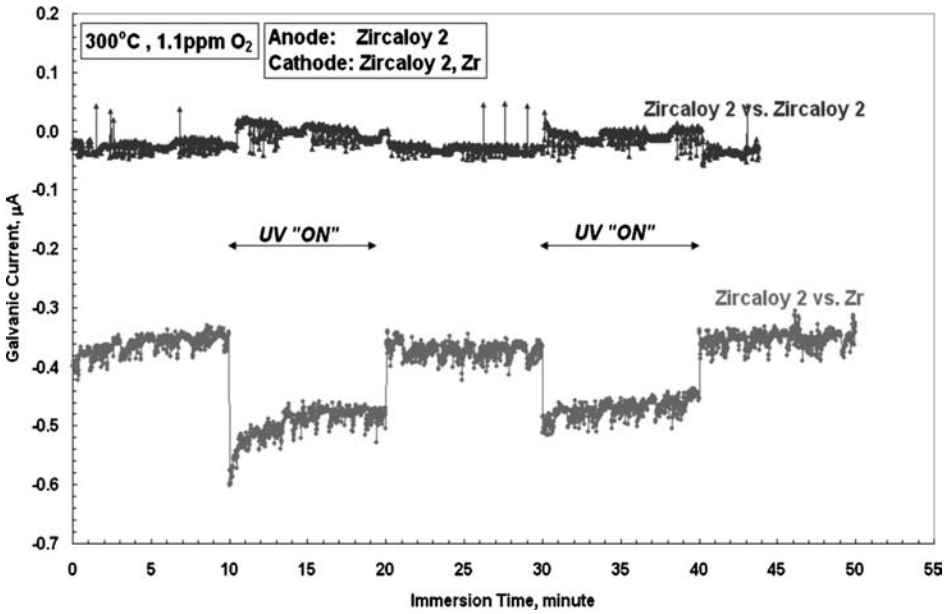


FIG. 14—*Galvanic current of Zircaloy 2 coupled with Zircaloy 2 or pure Zr electrode in 300°C water containing 1.1 ppm O_2 with and without UV illumination.*

as rapid ECP reduction and intergranular stress corrosion crack mitigation of BWR internals in the presence of low levels of hydrogen. The NobleChem™ process may affect the concentrations of hydrogen and oxygen in-core. Thus it is important to understand the ECP behavior of Zircaloy 2 and other alloys under various water chemistry conditions.

Figure 17 shows the ECP behavior of Zircaloy 2, 304 SS, Alloy X-750, and Pt electrodes as a function of immersion under various water chemistry conditions. It is clearly seen that the ECP difference between Zircaloy 2 and other alloys becomes smaller in the presence of hydrogen. When no oxygen is available, no significant ECP differences among alloys is observed. It is thus postulated that the presence of injected hydrogen may decrease the susceptibility of galvanic corrosion and eventually the shadow corrosion phenomena. This approach was evaluated by measuring the galvanic current under various water chemistry conditions and shown in Fig. 18.

As shown in Fig. 18, the presence of hydrogen decreases the galvanic current of Zircaloy 2 coupled with Alloy X-750. The highest galvanic current was measured when no hydrogen is present. It is also to note that the absence of oxygen (i.e., 40 ppb or 150 ppb H_2), the galvanic current was hardly measured either with or without UV illumination, mainly due to no significant ECP differences under the hydrogen water chemistry. These data suggest that the susceptibility of shadow corrosion phenomena may be reduced with addition of hydrogen that is attributed to decrease in ECP difference between two alloys.

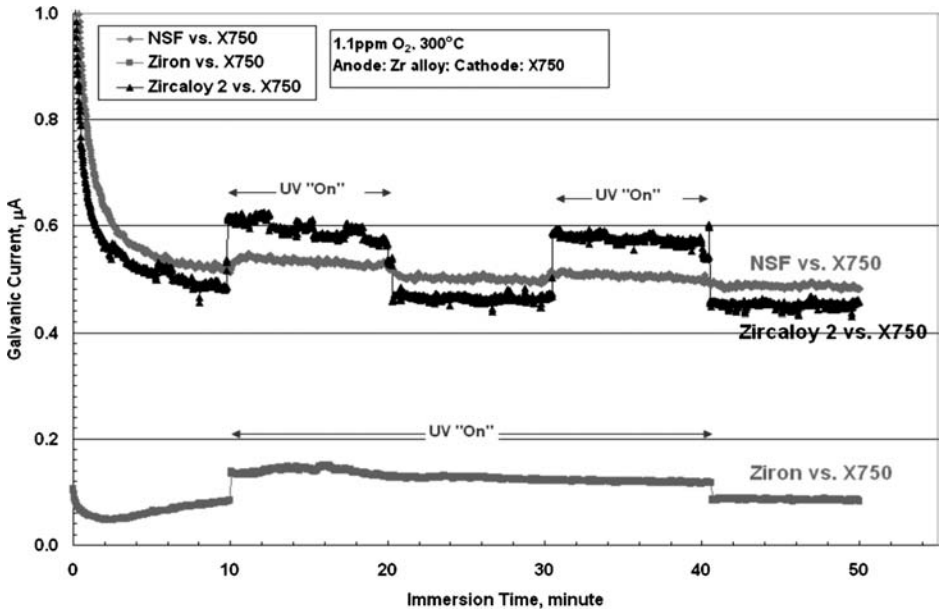


FIG. 15—*Galvanic current of Zircaloy 2, NSF, or Ziron coupled with Alloy X-750 in 300°C water containing 1.1 ppm O_2 with and without UV illumination.*

Effect of Electrode Gap on Galvanic Corrosion

Several investigators have reported that the distance between components is critical to form the shadow corrosion [13,19,33]. They also observed that the resultant oxide thickness depends on material surfaces and gap between two materials. It is reported that a crevice geometry formed between Zircaloy and the different metal components (Alloy X-750) may cause the shadow corrosion [17].

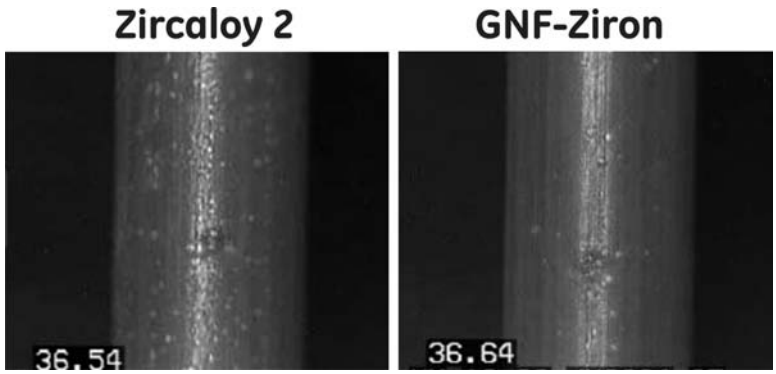


FIG. 16—*Surface morphology of GNF-Ziron and Zircaloy 2 cladding after 1 cycle at a BWR plant.*

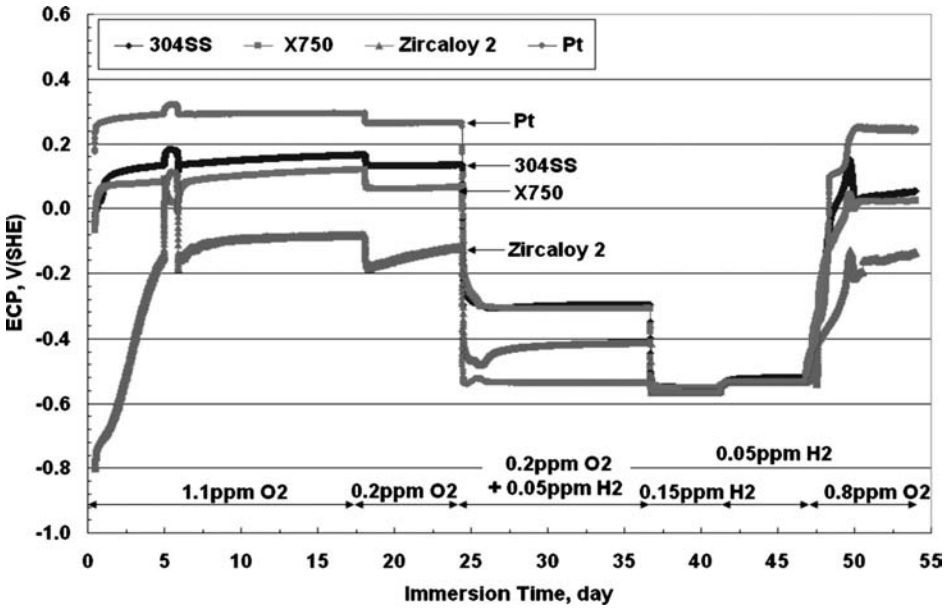


FIG. 17—*ECP of Zircaloy 2, 304SS, Alloy X-750, and Pt electrodes in 300°C water containing various concentrations of hydrogen and oxygen.*

Figure 19 shows the effect of electrode gap between Zircaloy 2 and Alloy X-750 on the galvanic current measured in 300°C water containing 300 ppb O_2. It is shown that the galvanic current strongly depends on the separation distance between Zircaloy 2 and Alloy X-750; increasing the galvanic current when two electrodes are closer.

The results in Fig. 19 indicates the galvanic nature of enhanced corrosion between Zircaloy 2 and a dissimilar alloy, however a typical galvanic corrosion mechanism cannot completely explain shadow corrosion phenomenon. Adamson described a case from the field in which shadow corrosion was "cast" over a Zr alloy channel from a SS handle of a control blade even though the handle could be more than 5 mm away from the channel [19]. This observation suggests that a formation of a special environment (i.e., concentration of impurities or radiolytic species and such) could be another important factor for shadow corrosion to occur. In addition, Adamson pointed out that in the classical type of galvanic corrosion, the cathode has to be of similar area or larger than the anode that is affecting but in the case of shadow corrosion the cathode (e.g. SS handle) is of much smaller area than the anode (Zr alloy channel).

Discussion

Metallic materials form oxide films on their surfaces when they are in contact with oxidizing environments. Once a metal oxide is formed, the electrochemical

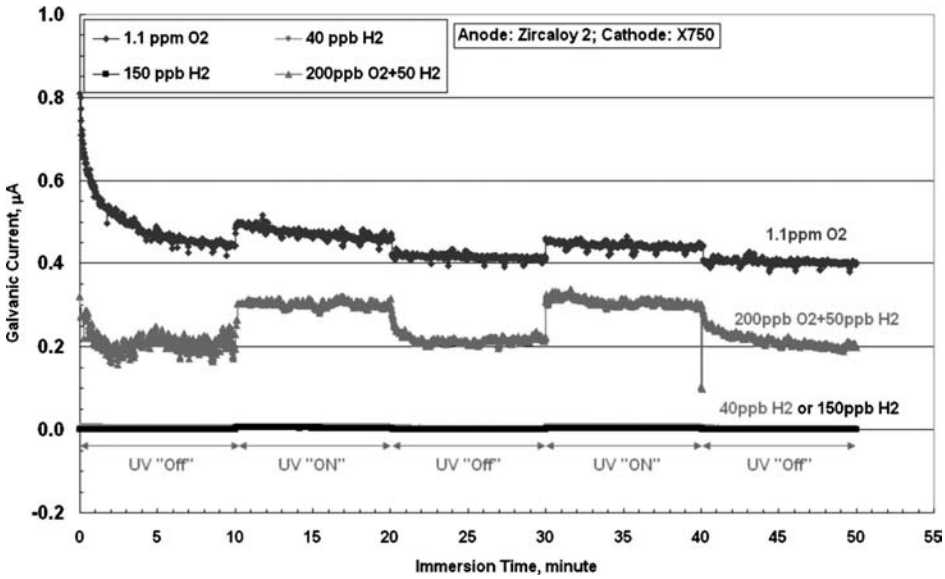


FIG. 18—*Effect of water chemistry on galvanic current of Zircaloy 2 coupled with Alloy X-750 with and without UV illumination.*

kinetic and response is then affected by the oxide property. Gerisher described the role of photo irradiation on the corrosion behavior of metals and alloys [34]. It has been reported that the photo irradiation improved the corrosion resistance of the passive film by modifying the oxide chemistry [35–37] and also hindered the chloride ions from penetrating into the films [36]. Based on the impedance response of zirconium oxide formed in high temperature water (see Figs. 10 and 11), the electrical resistance is significantly affected by a UV illumination on zirconium oxide formed on Zircaloy 2. It is thus important to understand the mechanistic relation between oxide films and impedance response on Zircaloy 2.

The oxide formed on Zircaloy-2 specimen for 3 months in 300°C water containing 1.1 ppm O_2 was analyzed by scanning electron microscopy (SEM), focus-ion beam–transmission electron microscopy (TEM), as shown in Fig. 20. The oxide film formed on Zr alloys is well known to consist of columnar grain layers at the oxide/matrix interface and thin equiaxed grain layers at the outermost surface. The outer oxide layer is known to be porous and an inner to be dense [31,32]. Based on the impedance result measured after immersion for 4 months, the UV light does not affect the total oxide impedance and hence the oxide structure.

In addition, in the semiconductor in contact with aqueous solution, changes in electrode potential occur primarily within the space charge layer [34,38]. The electron-hole distribution in this space charge layer determines the potential difference between the surface and the matrix. It is thus

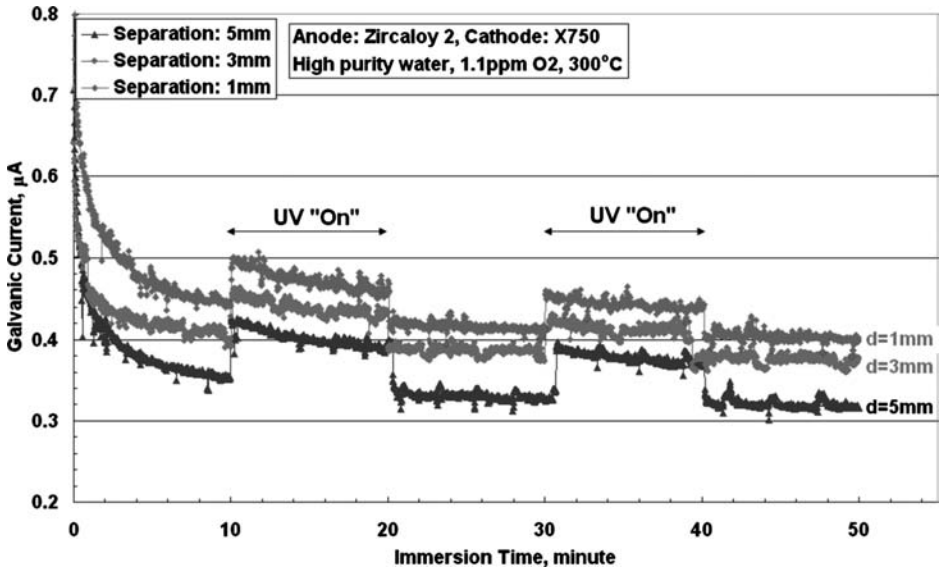


FIG. 19—*Effect of separation gap between Zircaloy 2 and Alloy X-750 on galvanic current in 300°C water containing 1.1 ppm O_2.*

postulated that UV illumination produces a space charge layer near the equiaxed grain layer at the Zr oxide/solution interface that may affect the photoelectrochemical response of ZrO_2. It has been also reported that two types of zirconium oxide structure exist in the forms of monoclinic and tetragonal phases in Zr oxide. In general, a higher fraction of tetragonal oxide has been reported at areas near the metal/oxide interface and the outer oxide layer contains a less fraction of tetragonal oxide [39–41]. Although tetragonal ZrO_2 is not a stable phase at low temperatures ($\sim 300^{\circ}C$), high compressive stresses, small grain sizes, and impurities such as Fe might stabilize tetragonal ZrO_2.

During high temperature oxidation, the tetragonal oxide is known to be transformed to monoclinic, which is associated with development of pores, cracks and defects in ZrO_2, mainly in the equiaxed grain layers. As shown in Fig. 10, UV irradiation decreases the impedance of oxide layer and consequently accelerates the corrosion oxide growth. It can be then postulated that under UV irradiation and oxidizing conditions, the development of a space charge layer within the porous outer oxide layer with a high fraction of monoclinic oxide in equiaxed grain layers may play an important role to control the electrochemical kinetics and photoelectrochemical response in high temperature water. In the presence of significant corrosion potential difference between Zircaloy and a dissimilar alloy, this modification in the electrical characteristic of the oxide then leads to enhanced corrosion of Zircaloy, i.e., shadow corrosion.

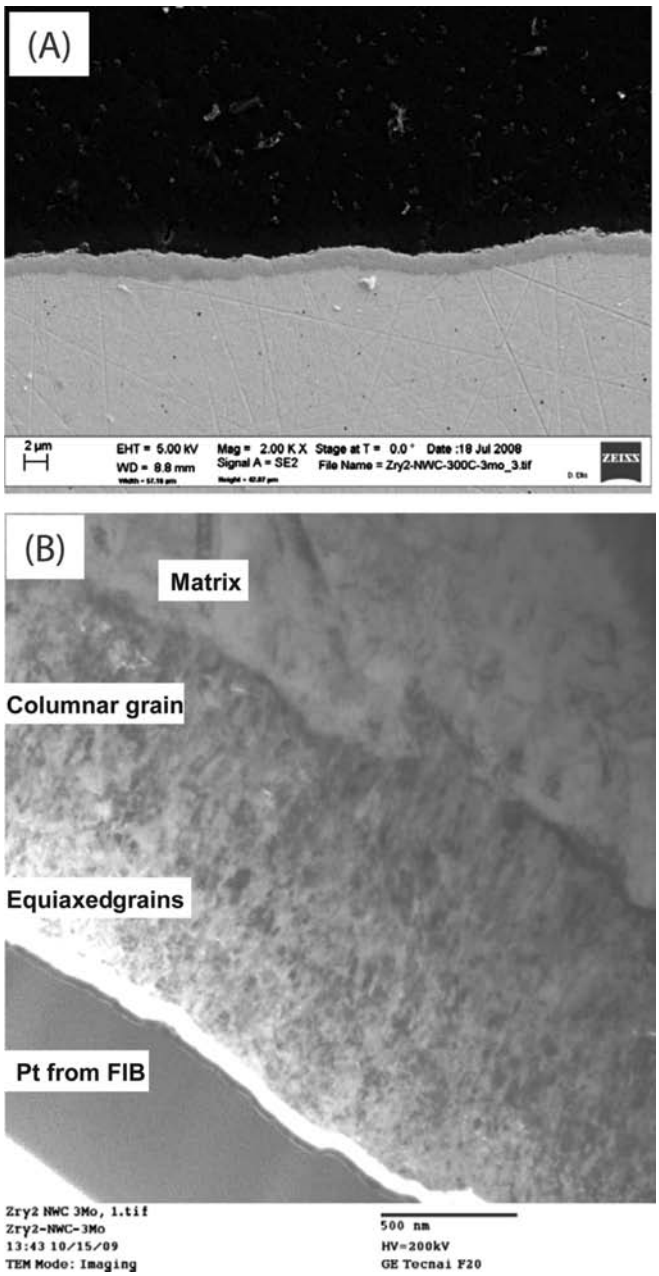


FIG. 20—*Cross-sectional views ((*a*): SEM; (*b*): TEM) of oxide formed on Zircaloy 2 after immersion for 3 months in 300°C water containing 1.1 ppm* O_2.

Conclusion

The photoelectrochemical behavior of oxides formed on Zircaloy 2 and other alloys was investigated by measuring the corrosion potential, galvanic current, and impedance with and without UV illumination. Under the oxidizing water chemistry condition, UV illumination shifted the corrosion potential of Zircaloy 2 to the negative direction, while the corrosion potential of Alloy X-750 or 304 SS to the positive direction. It was also revealed that the UV illumination increased the galvanic current of Zircaloy 2 coupled with dissimilar alloys, e.g., Alloy X-750, 304 SS, or Pt, and decreased the oxide impedance of zirconium oxide. This result indicates the possible susceptibility of galvanic corrosion, when these alloys are in contact. In addition, it is revealed that no significant change in galvanic current of Zircaloy 2 coupled with dissimilar alloys was measured in high temperature water containing only hydrogen that resulted in similar ECPs. These data thus clearly provide an explanation for why photoelectrochemical-enhanced corrosion of Zircaloy only occurs in BWRs, but not PWRs.

UV irradiation may enhance the generation of an electron-hole pair in particular within the equiaxed layer and thus shadow corrosion may be a consequence of the unique photoelectrochemical response of the oxides that develop over the dissimilar alloys (e.g., Zircaloy 2 and Alloy X-750). Based on galvanic corrosion, EIS, and TEM analysis, it is proposed that the defect structure of the equiaxed gain layer may be responsible for the photoelectrochemical response of ZrO_2 in high temperature water. The mechanism of shadow corrosion is still highly debated, but it appears to be similar to a process of galvanic corrosion in connection with the appropriate electrical conductivity of ZrO_2. The data in galvanic corrosion measurement suggest that a Zr coating on fuel assembly spacers (Alloy X-750 or 304 SS) may mitigate the shadow corrosion in BWRs.

Acknowledgments

This work was funded by EPRI (EPRI Contract No. EP-P26485/C12727) and GNF. The writers express their appreciation to Tim Jurewicz for experimental assistance and Lauraine Denault, Anthony Barbuto, and Michael Larsen for oxide analysis at GE Global Research Center.

References

[1] Cox, B., Garzarolli, F., Adamson, R., Rudling, P., and Strasser, A., *Fuel Material Technology Report*, Vol. 1, Advanced Nuclear Technology International (ANT), Skultuna, Sweden, October 2006.

[2] ASTM B350, 2007, "Standard Specification for Zirconium and Zirconium Alloy Ingots for Nuclear Application," *Annual Book of ASTM Standards*, ASTM International, West Conshohocken, PA.

[3] Cox, B., "Zirconium Alloy Corrosion," *Uhlig's Corrosion Handbook*, John Wiley and Sons, New York, 2000, p. 905.

[4] Cox, B., "Some Thoughts on the Mechanisms of In-Reactor Corrosion of Zirconium Alloys," *J. Nucl. Mater.*, Vol. 336, 2005, pp. 331–368.

[5] Dignam, M. J., "Mechanisms of Ionic Transport through Oxide Films," *Oxide and Oxide Films*, Vol. 1, J. W. Diggle, Ed., M. Dekker, New York, 1972, Chap. 2.
[6] Kim, Y. J., "Effect of Noble Metal Addition on Electrochemical Polarization Behavior of Hydrogen Oxidation and Oxygen Reduction on Type 304 Stainless Steel in High-Temperature Water," *Corrosion*, Vol. 55, No. 5, 1999, pp. 456–461.
[7] Madou, M. J., Frese, K. W., Jr., and Morrison, S. R., "Photo-electrochemical Corrosion of Semiconductors for Solar Cells," *Proceedings of the Society of Photo-Optical Instrumentation Engineers, Vol. 248, Role of Electro-Opt in Photovoltaic Energy Convers*, July 31–Aug, 1, 1980, San Diego, CA, pp. 88–95.
[8] Canfield, D. G. and Morrison, S. R., "Effect of Surface Films on Photo-Electrochemical Solar Cell Performance," *Appl. Surf. Sci.*, Vol. 10, No. 4, 1982, pp. 493–505.
[9] Morrison, S. R., *Electrochemistry at Semiconductor and Oxidized Metal Electrodes*, Plenum Press, New York, 1984.
[10] C. Lemaignan, "Corrosion or Zirconium Alloy Components in Light Water Reactors," *Corrosion: Environments and Industries*, ASM Metals Handbook, Vol. 13C, ASM International, Metals Park, OH, 2006, p. 415.
[11] Cox, B., "Oxidation of Zirconium and Its Alloys," *Advances in Corrosion Science and Technology*, Vol. 5, M. G. Fontana and R. W. Staehle, Eds., Plenum Press, New York, 1976, p. 173.
[12] Peter, A. M., "Prediction of Cherenkov Radiation Intensity Incident on BWR Fuel Cladding at Full Power," *Report No.* 2007GRC088, GE Global Research Center, Schenectady, NY, January 2007.
[13] Chen, S. F. and Adamson, R. B., "Observation of Shadow Phenomenon on Zr Alloys," *Proc. ANS 1994 International Topical Meeting in Light Water Reactor Fuel Performance*, West Palm Beach, FL, April 17–21, 1994.
[14] Lysell, G., Nystrand, A.-C., and Ullberg, M., "Shadow Corrosion Mechanism of Zircaloy," *J. ASTM Int.*, Vol. 2, No. 6, 2005, pp. .
[15] Lysell, G., Nystrand, A.-C., and Ullberg, M., "Shadow Corrosion Mechanism of Zircaloy," *Proceedings of the 14th International Symposium on Zirconium in the Nuclear Industry, ASTM STP 1467*, Stockholm, Sweden, June 13–17, 2004, P. Rudling and B. Kammenzind, Eds., ASTM International, West Conshohocken, PA, 2005, pp. 445–461.
[16] Ramasubramanian, N., "Shadow Corrosion," *J. Nucl. Mater.*, Vol. 328, 2004, pp. 249–252.
[17] Garzarolli, F., Hoffmann, P. B., and Seibold, A., "Shadow Corrosion or Crevice Corrosion?," *J. Nucl. Mater.*, Vol. 289, 2001, pp. 338–341.
[18] Adamson, R., Lutz, D., and Davies, J., "Hot Cell Observations of Shadow Corrosion Phenomeua," *Proceedings Factagung der KTG-Fachgruppe, Brennelemente und Kernbautelle*, Feb. 29–Mar. 1, 2000, Forschungszentrum, Karsruhe, 2000.
[19] Adamson, R., "Shadow Corrosion," *Corrosion Mechanisms in Zirconium Alloys*, ANT International, Skultuna, Sweden, 2007, pp. 4–12.
[20] Cox, B., "Discussion Section of Role of Iron for Hydrogen Absorption Mechanism in Zirconium Alloys," *Proceedings of the 14th International Symposium "Zirconium in the Nuclear Industry," ASTM STP 1467*, Stockholm, Sweden, June 13–17, 2004, P. Rudling and B. Kammenzind, Eds., ASTM International, West Conshohocken, PA, 2005, p. 384.
[21] Weidinger, H. G., Ruhmann, H., Cheliotis, G., Maguire, M., and Yau, T. L., "Corrosion and Electrochemical Properties of Zirconium Intermetallics," *Zirconium in the Nuclear Industry, ASTM STP 1132*, C. M. Eucken and A. M. Garde, Eds., ASTM International, West Conshohocken, PA, 1991, p. 499.

[22] Cheng, B., Kruger, R. M., and Adamson, R. B., "Corrosion Behavior of Irradiated Zircaloy," *Proc. Tenth Int. Sym. in the Nuclear Industry, ASTM STP 1245*, 1994, ASTM International, West Conshohocken, PA, pp. 400–418.

[23] Inagaki, M., Kanno, M., and Maki, H., "Effect of Alloying Elements in Zircaloy on Photo-Electrochemcial Characteristics of Zirconium Oxide Films," *Zirconium in the Nuclear Industry, ASTM STP 1132*, C. M. Eucken and A. M. Garde, Eds., ASTM International, West Conshohocken, PA, 1991.p. 437.

[24] Bojinov, M., Hanson-Lyyra, L., Kinnunen, P., Saario, Y. T., and Sirkid, P., "In-Situ Studies of the Oxide Film Properties on BWR Fuel Cladding Materials," *J. ASTM Int.*, Vol. 2, No. 4, 2004, pp. 367–382.

[25] Bojinov, M., Hanson-Lyyra, L., Kinnunen, P., Saario, Y. T., and Sirkid, P., "In-Situ Studies of the Oxide Film Properties on BWR Fuel Cladding Materials," *Proceedings of the 14th International Symposium on Zirconium in the Nuclear Industry, ASTM STP 1467*, Stockholm, Sweden, June 13–17, 2004, P. Rudling and B. Kammenzind, Eds., ASTM International, West Conshohocken, PA, 2005, p. 367–382.

[26] Forsberg, S., Ahlberg, E., and Limback, M., "Studies of Corrosion of Cladding Materials in Simulated BWR Environment Using Impedance Measurements," *J. ASTM Int.*, Vol. 4, No. 9, 2005, pp. 303–325.

[27] Forsberg, S., Ahlberg, E., and Limback, M., "Studies of Corrosion of Cladding Materials in Simulated BWR Environment Using Impedance Measurements," *Proceedings of the 15th International Symposium on Zirconium in the Nuclear Industry, ASTM STP 1505*, Sunriver, OR, June 24–28, 2007, B. Kammenzind and M. Limback, Eds., ASTM International, West Conshohocken, PA, 2005, pp. 303–325.

[28] Rishel, D. M., Eklund, K. L., and Kammenzind, B. F., "In Situ EIS Measurements of Irradiated Zircaloy-4 Post-Transition Corrosion Kinetics Behavior," *J. ASTM Int.*, Vol. 4, No. 9, 2005, pp. 326–358.

[29] Rishel, D. M., Eklund, K. L., and Kammenzind, B. F., "In Situ EIS Measurements of Irradiated Zircaloy-4 Post-Transition Corrosion Kinetics Behavior," *Proceedings of the 15th International Symposium on Zirconium in the Nuclear Industry, ASTM STP 1505*, Sunriver, OR, June 24–28, 2007, B. Kammenzind and M. Limback, Eds., ASTM International, West Conshohocken, PA, 2005, pp. 326–358.

[30] Nakikawa, S., Etoh, Y., Shimada, S., Kubo, T., Ito, K., and Harada, H., "Correlation Between Characteristics of Oxide Films Formed on Zr Alloys in BWRs and Corrosion Performance," *Proceedings of the 12th International Symposium on Zirconium in the Nuclear Industry, ASTM STP 1354*, Toronto, Canada, June 16–18, 1998, G. Sabol and G. Moan Limback, Eds. ASTM International, West Conshohocken, PA, 2000, pp. 815–835.

[31] Kakiuchi, K., Itagaki, N., Furuya, T., Miyazaki, A., Ishii, Y., Suzuki, S., Terai, T., and Yamawaki, M., "Role of Iron for Hydrogen Absorption Mechanism in Zirconium Alloys," *J. ASTM Int.*, Vol. 1, No. 10, 2004, pp. 349–366.

[32] Kakiuchi, K., Itagaki, N., Furuya, T., Miyazaki, A., Ishii, Y., Suzuki, S., Terai, T., and Yamawaki, M., "Role of Iron for Hydrogen Absorption Mechanism in Zirconium Alloys," *Proceedings of the 14th International Symposium on Zirconium in the Nuclear Industry, ASTM STP 1467*, Stockholm, Sweden, June 13–17, 2004, P. Rudling and B. Kammenzind, Eds., ASTM International, West Conshohocken, PA, 2005, pp. 349–366.

[33] Lysell, G., Charlotte Nystrand, A., and Ullberg, M., *ENS TOPFUEL 2001*, Stockholm, Sweden, May 27–29, 2001.

[34] Gerischer, H., "Electrochemical Behavior of Semiconductors under Illumination," *J. Electrochem. Soc.*, Vol. 113, No. 11, 1966, pp. 1174–1182.

[35] Breslin, C. B., Macdonald, D. D., Silora, E., and Sikora, J., "Influence of *uv* Light on the Passive Behaviour of SS316—Effect of Prior Illumination," *Electrochim. Acta*, Vol. 42, 1997, pp. 127–136.
[36] Schmuki, P. and Bohni, H., "Illumination Effects on the Stability of the Passive Film on Iron," *Electrochim. Acta*, Vol. 40, 1995, pp. 775–783.
[37] Macdonald, D. D., Sikora, E., Balmas, M. W., and Alkire, R. C., "The Photo-Inhibition of Localized Corrosion on Stainless Steel in Neutral Chloride Solution," *Corros. Science*, Vol. 38, 1996, pp. 97–103.
[38] *The Surface Chemistry of Metals and Semiconductors*, H. C. Gatos, Ed., John Wiley & Sons, New York, 1959.
[39] Woo, O. T., Lin, Y. P., and Khatmian, D., "Oxide Microstructure and Deuterium Ingress in Zr-2.5Nb CANDU Pressure Tubes," *Mater. High Temp.*, Vol. 20, No. 4, 2003, pp. 593–600.
[40] Yilmazbayhan, A., Breval, E., Motta, A., and Comstock, R., "Transmission Electron Microscopy Examination of Oxide Layers formed on Zr Alloys," *J. Nucl. Mater.*, Vol. 349, 2006, pp. 265–281.
[41] Une, K., Ishimoto, S., Sakamoto, K., Etoh, Y., Aomi, M., and Ito, K., "The Characterization of Oxide Layer of Zr-Based Alloys Focusing on Hydrogen Absorption Behavior," *Proceedings of Top Fuel 2009*, Paris, France, Sept. 6–10, 2009, Paper 2049.

DISCUSSION

Question 1, R. Adamson, Zircology Plus, USA:—Have you looked at the potential difference between Zircaloy and welded Zircaloy ? In the past, we have seen shadow corrosion effects when those two materials were coupled.

Author's Response:—The ECP of welded Zircaloy was not measured in this study. The authors agree with your observation since the heat affected zone by welding treatment may create areas with the depletion of SPPs and thus a low ECP. If the SPP depleted areas is coupled to the non-welded cladding surface, it is thus susceptible to shadow corrosion due to the ECP difference between two different surfaces.

Question 2, Antoine Ambard, EDF, France:—1) Does the intensity of the UV rays has an effect on the corrosion potential or the galvanic current in high temperature water? It should increase the production of electron-holes. 2) Do you have an idea of the intensity of UV in a typical core (BWR and PWR) and how does it compare to the one you used in your experiments? 3) Is there any lowering of the UV with the length they travelled into water? 4) With UV flux heterogeneity in core, we can even expect a galvanic coupling between various parts of a single fuel rod. 5) It is really a nice work!

Author's Response:—1) The effect of UV on ECP and galvanic current were measured in high temperature water and presented in this paper.

2) The predicted Cerenkov radiation intensity incident on fuel cladding in BWR has been calculated and values depend on wavelength range (A.M. Peter, GE-GRC Report, 2007GRC088). The calculated intensity is in rages of UV used for this experiment.

3) The UV intensity expects to be much lower in water than in air, but was not able to measure it in water.

4) I agree with you point. Areas with no or less SPPs expect to be more active than areas with more SPPs and is susceptible to high corrosion rate or shadow corrosion.

5) Thank you.

Question 3, Ken Yueh, EPRI, USA:—The increased potential and current observed in the experiment can be explained by photoelectric effects and conductivity changes in the presence of UV light. How does the increase in measured potential increase corrosion as in shadow corrosion? One way the corrosion can be increased is through increased electrical conductivity of the oxide, but that would only be true if the rate controlling step is electron conduction. Have you evaluated which is controlling and if improved electrical conductivity has an effect?

Author's Response:—As the galvanic corrosion considers as the primary mechanism of shadow corrosion, the increase in potential difference between Zircaloy cladding surface and X-750 spacer enhances the susceptibility of shadow corrosion by increasing the galvanic current. The increase in electric conductivity of ZrO_2 oxide also contributes to higher shadow corrosion and the effect of UV irradiation on the ZrO_2 impedance in high temperature water is presented in this paper. There are also many factors that affect the shadow corrosion in plant water chemistry, such as surface chemistry, radicals, impurities, etc.

BASIC METALLURGY

Reprinted from JAI, Vol. 7, No. 8
doi:10.1520/JAI103003
Available online at www.astm.org/JAI

J. K. Chakravartty,[1] *R. Kapoor,*[2] *A. Sarkar,*[2] *and S. Banerjee*[3]

Dynamic Recrystallization in Zirconium Alloys

ABSTRACT: In this investigation, the characteristics of dynamic recrystallization (DRX) in five Zr-alloys, namely, commercial pure zirconium (CP-Zr), Zircaloy-2 (Zr–Sn), Zr-2.5Nb (Zr–Nb), Zr-2.5Nb-0.5Cu (Zr–Nb-Cu), and Zr-1Nb-1Sn-0.1Fe (Zr–Nb–Sn–Fe), have been examined. For this purpose, processing maps were constructed using strain rate sensitivity (m) data as a function of temperature and strain rate. This has been done using compression tests carried out at constant true strain rate. The processing maps revealed the bounds of DRX domain as iso-contour of m in strain rate–temperature plane. Optical microscopy and transmission electron microscopy (TEM) were used to analyze the evolution of the microstructure and to ascertain the nature of dislocation mechanisms in deformed and quenched samples from the DRX domain. For all the alloys studied, TEM revealed complete modification of β-transformed microstructure to an equiaxed morphology containing dislocation substructure within. The variation of grain size with strain rate and temperature, high ductility, and a linear variation of log(grain size) with log(Z) (where Z is the Zener–Hollomon parameter) are some important characteristic features associated with DRX domains of Zr-alloys. While Nb exhibited strong influence on lowering the strain rate for the occurrence of DRX of CP-Zr, Sn addition (Zr–Sn) did not alter DRX characteristics. TEM observations neither revealed the nature of nucleation event nor identified the dislocation mechanism involved in the DRX process. In order to ascertain the rate controlling dislocation mechanism, the flow stress data were analyzed using a model of thermally activated flow. On the basis of

Manuscript received January 29, 2010; accepted for publication July 5, 2010; published online August 2010.

[1] Mechanical Metallurgy Section, Materials Group, Bhabha Atomic Research Centre, Mumbai 400085, India. (Corresponding author), e-mail: jayanta@barc.gov.in
[2] Mechanical Metallurgy Section, Materials Group, Bhabha Atomic Research Centre, Mumbai 400085, India.
[3] Department of Atomic Energy, Mumbai 400001, India.

Cite as: Chakravartty, J. K., Kapoor, R., Sarkar, A. and Banerjee, S., "Dynamic Recrystallization in Zirconium Alloys," *J. ASTM Intl.*, Vol. 7, No. 8. doi:10.1520/JAI103003.

Copyright © 2011 by ASTM International, 100 Barr Harbor Drive, PO Box C700, West Conshohocken, PA 19428-2959.

the magnitudes of activation energy and apparent activation area, the cross-slip of screw dislocation has been identified as the rate controlling mechanism involved in the DRX process. The activation energy has been found to increase by alloying elements, which is expected to lower stacking fault energy (SFE) and increase separation between the partials. Further analysis of the data using Friedel's model revealed that the activation energy for the cross-slip process can be decomposed into two parts—one related to the process of forming a constriction in the dissociated dislocations and the other needed for recombining the dissociated dislocations. While the former component (related to SFE) is dominant in Nb containing Zr-alloys, both the components are involved in controlling the deformation behavior of CP-Zr and Zr–Sn alloys. The effects of alloying elements on DRX characteristics and on the evolution of dislocation structure have been rationalized on the basis of cross-slip as the rate controlling dislocation mechanism in a qualitative manner. The importance of dynamic recovery in DRX process has been emphasized in view of this.

Introduction

Bulk metalworking of zirconium alloys for nuclear structural applications comprises a series of steps, each of which has important roles to play in determining the microstructure and properties of the finished product. These alloys are fabricated by processing routes that primarily involve melting, hot working, and secondary operations comprising cold working and annealing steps. Amongst these steps, hot working in the form of forging, extrusion, or rolling is very important, as, in addition to breaking the cast structure and shaping the ingot, this step is responsible for providing a chemically homogeneous product with a suitable microstructure and texture for subsequent processing. There are different types of restoration mechanisms that play role during hot working. Of the three important dynamic restoration mechanisms of hot deformation, namely, dynamic recovery (DRV), dynamic recrystallization (DRX), and superplasticity, the DRX is the most preferred mechanism as it enhances hot ductility, reconstitutes the initial microstructure, and refines the grain structure by movement of high angle boundaries resulting in improved mechanical properties of the product. In order to identify the deformation conditions that promote DRX, the hot deformation behavior of Zr and Zr-alloys has been extensively studied by the authors over a range of strain rate and temperature, which covers the conventional industrial working processes [1–7]. It has been established that Zr and Zr-alloys exhibit a variety of hot deformation mechanisms such as DRV, DRX, superplasticity, and flow instability depending on the temperature and strain rate. This has been accomplished by constructing processing maps, which are essentially a plot of efficiency parameter $(\eta = 2m/m + 1)$, where, $m =$ strain rate sensitivity $= \partial \ln \sigma / \partial \ln \sigma \ / \partial$ on a temperature–strain rate frame. These maps revealed that these mechanisms operate over a range of permitted strain rates and temperatures, are associated with different values of strain rate

sensitivities, and exhibit different products/deformed microstructures. It has also been recognized that the optimum hot working conditions were associated with the process of DRX which was also the dominant hot deformation mechanism in each of the alloys studied. Further, the strain rate and temperature conditions that favor DRX in these alloys have been observed to be dependent on the type of alloying additions (α or β stabilizer).

Although the earlier work carried out by the authors clearly established the relation between macroscopic deformation parameters and microsructural development, no attempt was made to identify which of the many dislocation mechanisms dominate in a given alloy during DRX. In this study a detailed comparison will be made between macroscopic and microscopic aspects of DRX of Zr-alloys based on our earlier work 1–7. Further, the principles of thermally activated deformation (TAD) will be employed with the objectives of identifying the microscopic deformation mechanisms and its relation to observed microstructural development during DRX and understanding the effect of alloying elements on DRX characteristics.

For this purpose, the database generated earlier for characterizing the hot deformation behavior of various zirconium alloys over a wide temperature and strain rate range has been utilized [1–7]. Studied here are five different alloys of zirconium: Commercial pure (CP) zirconium (containing oxygen, α stabilizer), Zircaloy-2 (primarily containing Sn, α-stabilizer), Zr-2.5Nb (primarily containing Nb, β stabilizer), Zr-2.5 Nb-0.5Cu (Nb and Cu, β stabilizers), and a quaternary alloy Zr-1Sn-1Nb-0.1Fe (containing both α and β stabilizers).

Experimental

Table 1 lists out the chemical composition of these alloys, hereafter identified as CP-Zr, Zr–Sn, Zr–Nb, Zr–Nb-Cu, and Zr–Nb–Sn–Fe. The starting microstructure for the materials used was transformed β, which was obtained by rapid quenching from the β phase field of the respective alloys. The starting microstructures are therefore essentially transformed β microstructure (consisting of martensitic α' platelets). Axisymmetric compression tests were performed at constant true strain rates to a true strain of 0.7. The tests were carried out over the temperature range of 650–1000°C and strain rate range of 10^{-3}–$100\,s^{-1}$. The experimental details are given elsewhere [2,7], and Table 1 gives the temperature range used for each alloy. The raw load-displacement data were processed to

TABLE 1—*Chemical composition (in wt %) of Zr and its alloys studied in this work. Test temperature ranges are also listed.*

Alloy	Sn	Nb	Fe	Cr	Ni	O	Cu	Zr	Test Temperature (°C)
CP-Zr	0.005	···	0.02	0.02	···	0.12	···	Bal.	650–850
Zr–Sn	1.55	···	0.12	0.1	0.05	0.12	···	Bal.	650–850
Zr–Nb	···	2.5	0.06	···	···	0.11	···	Bal.	650–950
Zr–Nb–Cu	···	2.5	···	···	···	0.11	0.5	Bal.	650–1050
Zr–Nb–Sn–Fe	1	1	0.1	···	···	0.11	···	Bal.	650–1050

generate true stress–true strain data and subsequently to compute m as a function of strain rate and temperature. In most of the aforementioned references, the stresses at prescribed strain rates, temperatures, and strains are well tabulated [1–5]. Optical microscopy (OM) and transmission electron microscopy (TEM) were used to observe the starting microstructure and the high temperature deformed and quenched microstructure. Although it has been mentioned earlier that Zr-alloys exhibited a variety of deformation mechanisms during hot deformation, for the purpose of the present study, we are interested with the domain of DRX and therefore will focus only on this domain. In view of this, the description of the deformed microstructure and stress-strain behavior will be restricted to experimental conditions commensurate with the domains of DRX in each of the processing maps.

Results

Flow Behavior

A detailed description of flow behavior of the alloys studied is given in earlier investigations [1–5]. Typical flow curves recorded in the DRX domain for CP-Zr and Zr–Sn in the α phase field and for Zr–Nb, Zr–Nb-Cu, and Zr–Nb–Sn–Fe in the $(\alpha + \beta)$ phase field are given in Fig. 1. After an initial period of strain

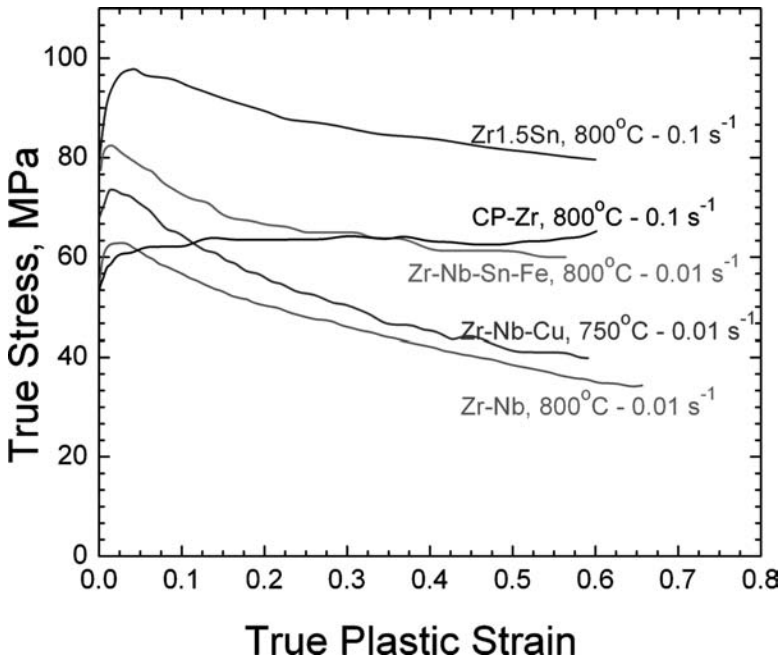


FIG. 1—*True stress versus true plastic strain curves for different Zr-alloys within the DRX domain. Deformation conditions have been indicated on the flow curves.*

hardening, the flow curve of CP-Zr exhibits steady state flow behavior, and for Zr–Sn, the flow stress initially goes through a maximum, followed by mild flow softening and steady state behavior sets in only after some strain. A pronounced flow softening is noted during the deformation of the Zr–Nb alloy, and steady state flow behavior is exhibited only at strains greater than 0.3. The extent of flow softening has been found to be dependent on strain rate and temperature. Similar flow behavior has been observed in Zr–Nb-Cu and Zr–Nb–Sn–Fe alloys in the $(\alpha + \beta)$ phase field. The steady state stress levels for all the Zr-alloys studied have been found to change significantly with strain and temperature within the domain of DRX, indicating that the flow behavior is thermally activated. It is generally thought that while a steady state flow behavior after brief initial hardening (as in CP-Zr) is associated with the process of DRV, the flow softening after a peak in stress-strain curve is indicative of DRX [8,9]. Titanium alloys with β transformed microstructure have been reported to exhibit flow softening when deformed in the $\alpha-\beta$ two phase field [10]. It may be noted here that the restoration mechanisms involved in the aforementioned cases cannot be arrived at on the basis of the shape of stress-strain curves alone unless confirmed by other modeling methods or detailed microstructural investigations. This will be addressed in the present work in the sections to follow.

Processing Maps

In earlier investigations, processing maps were constructed using variation of η with strain rate $\dot{\varepsilon}$ and temperature (T) following the dynamic materials model [11,12]. However, it was found that the variations of efficiency parameter and that of m were identical with $\dot{\varepsilon}$ and T [13]. Further, as a macroscopic deformation parameter, "m" is simpler to evaluate, useful for correlating with microstructure produced, and has wider applicability. In this investigation, we therefore propose to present processing maps as contour maps of m. In order to identify the bounds of each of the domain of DRX, processing maps showing iso-contours of strain rate sensitivity in temperature–strain rate frame are shown in Fig. 2, which depicts some representative processing maps of CP-Zr, Zr–Sn, Zr–Nb, and Zr–Sn-Nb-Fe alloys. It may be noted that the processing maps are for a nominal strain of 0.4 or higher, at which steady state stress-strain behavior was recorded for all the alloys studied. For Zr-alloys with α stabilizers (CP-Zr and Zr–Sn), the processing maps show deformation characteristics within the α phase field and reveal that the maps are similar (in terms of variation of m), indicating that α stabilizers do not influence the characteristics of the prevailing restoration process, which is DRX. In contrast to this, β stabilizer like Nb (as in Zr–Nb, Zr–Nb-Cu, and Zr–Nb–Sn–Fe) alters the deformation characteristics significantly by shifting the DRX domain to lower strain rates. Table 2 summarizes the important characteristics, namely, the bounds of the DRX domain, associated optimum hot working parameters and observed ductility with each of the Zr-alloys studied.

Deformed Microstructure

The samples deformed and quenched rapidly from the DRX domain of different Zr-alloys have been used to investigate microstructural development by

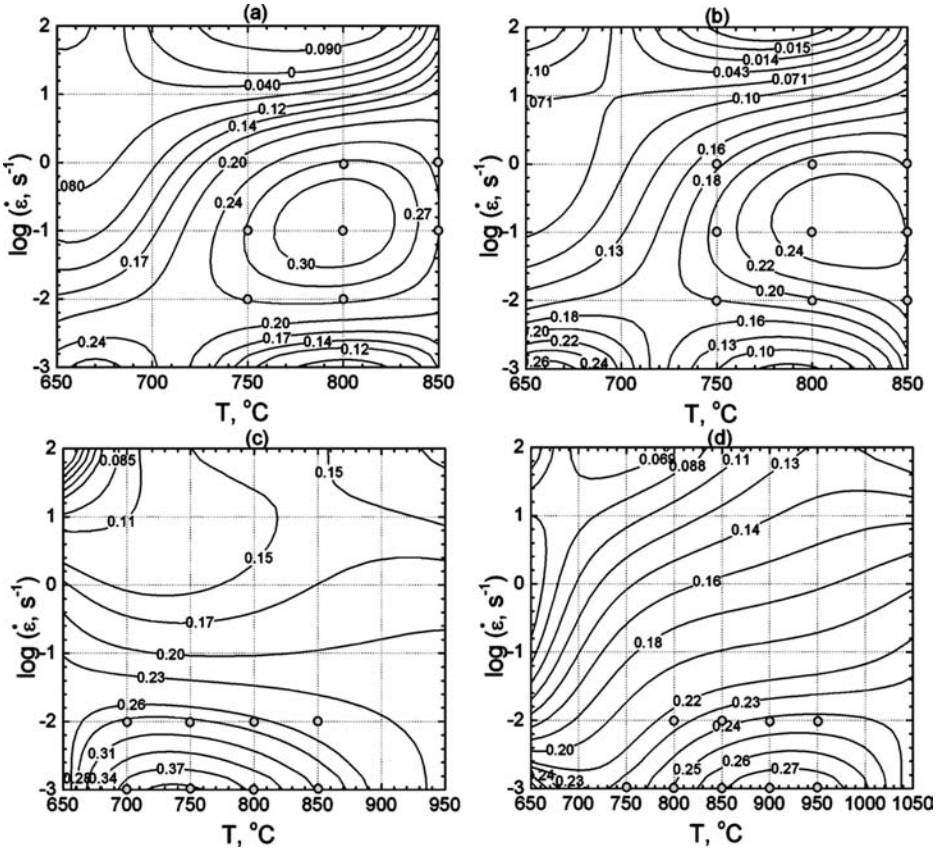


FIG. 2—*Strain rate sensitivity contour maps at a strain of 0.4 for all Zr-alloys studied (a) CP-Zr (b) Zr–Sn (c) Zr–Nb and (d) Zr–Nb–Sn–Fe. Circles marked on the plots indicate the* $\dot{\varepsilon}$ *and T conditions from where data points have been used for further analysis.*

employing both OM and TEM. As regards the evolution of microstructure, the deformation of CP-Zr and Zr–Sn within the DRX domain at 800°C and 0.1 s^{-1} (in the α phase field) to a true strain of 0.7 results in the formation of nearly equiaxed α grains by modifying the starting β transformed microstructure. OM (Fig. 3(*a*)3(*c*)) reveals the progressive development of the recrystallized structure with increasing strain until it has entirely replaced the original β transformed structure. Figure 3(*b*) reveals the nucleation of new DRX grains at the deformed and strained high angle interfaces of α' platelets (for a true strain of 0.3). The microstructure of Fig. 3(*c*) shows features of DRX α grains originating from the primary platelet interfaces, which are corrugated. A large proportion of high angle boundaries has been seen in the deformed structure. With increasing deformation beyond the steady state, there is no further noticeable change in the α grain morphology. The variations of DRX α-grain size with temperature and strain rate are shown in Fig. 4. It is seen that grain size varies with

TABLE 2—*Comparison of the hot deformation characteristics for various Zr-alloys: Optimum hot working parameters, deformation mechanisms, and deformed microstructure.*

Alloy	Bounds of DRX Domain (Optimum Hot Deformation Condition)		Ductility (%)	Deformation Mechanism	Deformed Microstructure
	T (°C)	$\dot{\varepsilon}$ (s^{-1})			
CP-Zr	730–850 (800)	10^{-1}–10^{0} (10^{-1})	≈ 180	DRX of α	Equiaxed α grains with serrated boundaries, dislocation substructure within the equiaxed grains
Zr–Sn	730–850 (800)	10^{-1}–10^{0} (10^{-1})	≈ 110	DRX of α	Similar as α-Zr
Zr–Nb	680–900 (750)	10^{-3}–5×10^{-2} (10^{-3})	≈ 120	DRX leading to spheroidization of α phase	Nearly equiaxed α-grains separated by β phase film; dislocation network within α-grains forming sub-boundaries
Zr–Nb–Cu	680–850 (750)	10^{-3}–5×10^{-2} (10^{-3})	≈ 120	DRX leading to spheroidization of α phase	Nearly equiaxed α-grains separated by β phase film; dislocation network within α-grains forming sub-boundaries
Zr–Nb–Sn–Fe	750–950 (900)	10^{-3}–5×10^{-2} (10^{-3})	≈ 200	DRX of α phase	Equiaxed α grains with β phase at the triple junctions of grains, dislocation substructure within α-grains

CHAKRAVARTTY ET AL., doi:10.1520/JAI103003 127

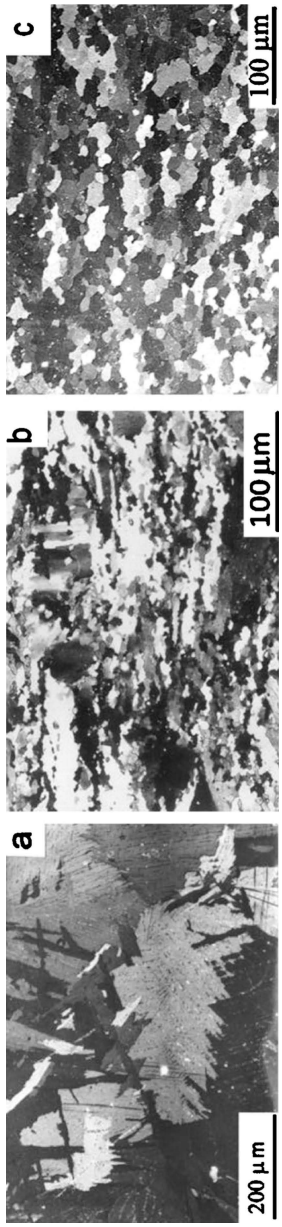


FIG. 3—*Optical micrographs of Zr–Sn: (a) Undeformed starting microstructure; (b) deformed 800°C, 0.1 s^{-1} to a true strain of 0.3; and (c) deformed 800°C, 0.1 s^{-1} to a true strain of 0.7. The compression axis is vertical.*

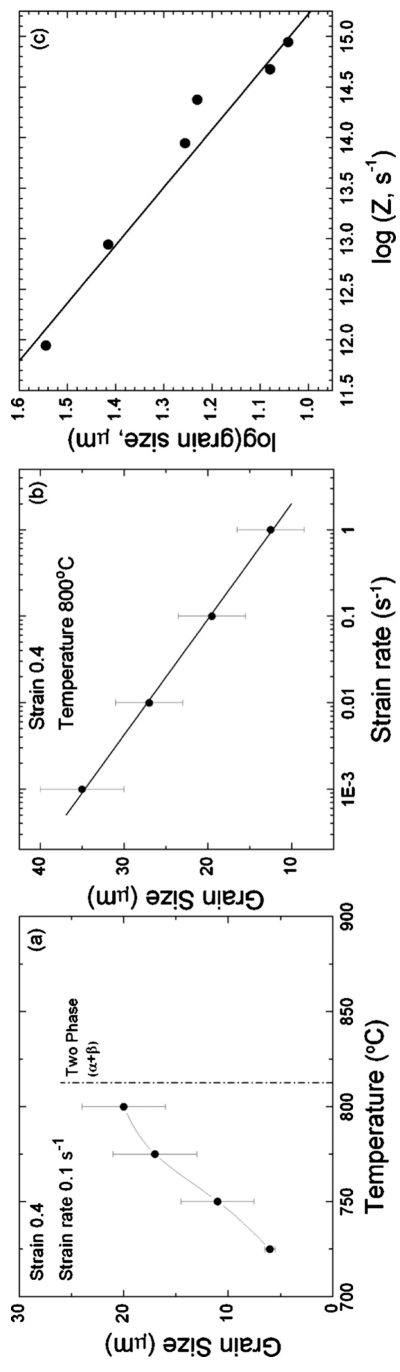


FIG. 4—*Variations in grain size with (a) temperature (b) strain rate, and (c) Zener–Hollomon parameter, Z corresponding to the DRX regime (temperature: 750–850°C; strain rate: 0.01–1 s* $^{-1}$*) for Zr–Sn.*

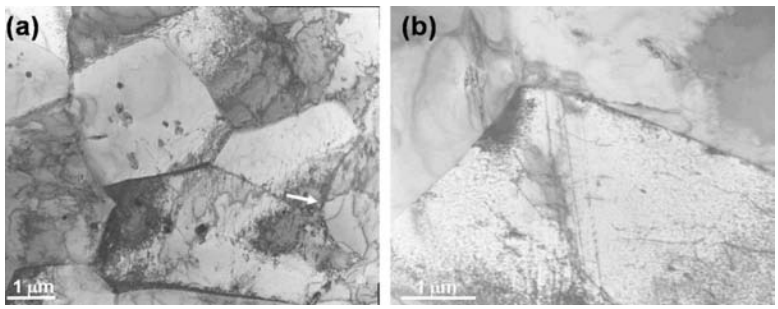


FIG. 5—*Transmission electron micrographs of samples deformed to a strain of 0.7 within DRX domain: (a) Zr–Sn deformed at 800°C and 0.01 s^{-1}; (b) CP-Zr deformed at 800°C and 0.01 s^{-1}.*

temperature in a sigmoidal fashion and that DRX grain size decreases with increasing strain rate. The combined effect of strain rate and temperature on grain size is depicted in Fig. 4(*c*), which shows a linear relationship between log(grain size) versus log(*Z*), where *Z* the Zener–Hollomon parameter $\left(Z \cdot \varepsilon{\cdot}\varepsilon \exp(Q/RT)\right)$. These variations are characteristic features of DRX [6,14,15]. The fact that Zr–Sn material undergoes DRX is further confirmed by TEM observation, which reveals that each of the equiaxed α-grains observed at OM level was further divided into subgrains containing dislocation substructures or cells within (Fig. 5(*a*)). Also, features resembling "bulging" were seen (indicated by an arrow) where a part of a boundary appeared to bulge into an area containing high dislocation density. This observation is in agreement with the proposed theory of nucleation of recrystallization by Bailey and Hirsh [16]. In an early work, Raybould and Sheppard reported the formation of similar substructures within equiaxed grains of hot extruded Al alloy [17]. Figure 5(*b*) reveals features of subgrains and dislocation structure within the equiaxed α-grains obtained by deforming CP-Zr within the DRX domain. CP-Zr exhibited DRX characteristics that were essentially similar to that in Zr–Sn 1. A comparison of the deformed microstructures of CP-Zr and Zr–Sn revealed that the latter possessed a finer subgrain structure and a higher dislocation density.

Hot deformation within two phase $(\alpha + \beta)$ field for Zr–Nb and Zr–Nb-Cu resulted in the complete modification of starting β-transformed structure to an elongated and a nearly equiaxed α-morphology with β phase either as the thin film separating two adjacent α-grains or at the triple junctions of α-grains (Fig. 6(*a*)6(*c*)) depending on the temperature and strain rate. For a given temperature of deformation, increasing the strain rate reduces the width (size) of the α-phase. This morphology appears to result from shearing of α plates and their subsequent spheroidization [10,18]. The spheroidization process has been viewed as a type of DRX since it consists of two competitive processes, namely, rate of nucleation and rate of migration [18]. The evolution of β transformed structure to globular morphology was found to be dependent on strain [4]. A

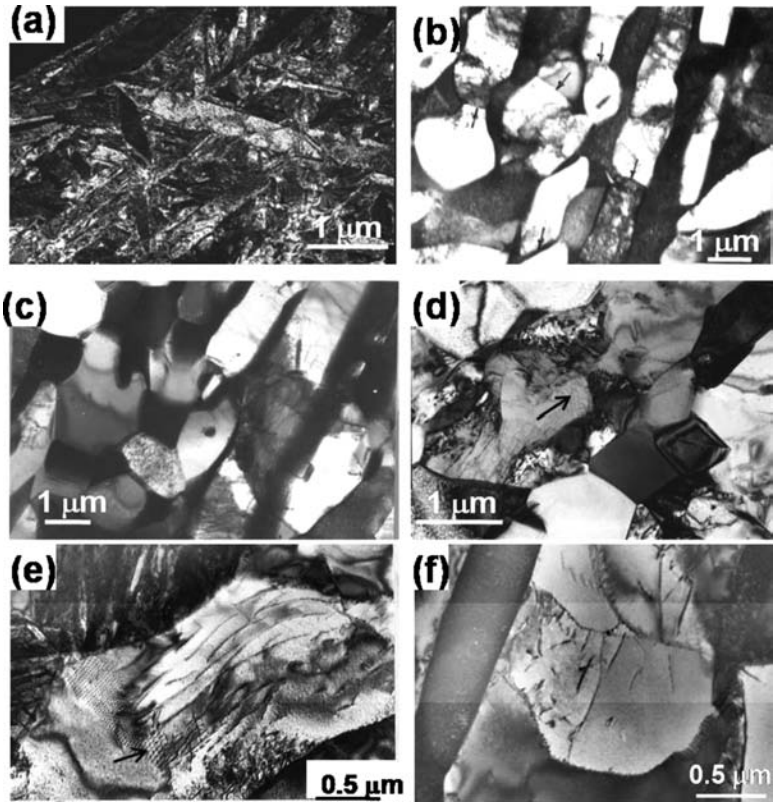


FIG. 6—*Transmission electron micrographs of Zr–Nb: (a) Undeformed starting microstructure; (b) deformed to a strain of 0.3 at 800°C, 0.001 s^{-1}; (c) deformed to a strain of 0.7 at 800°C, 0.001 s^{-1}; and (d) deformed to a strain of 0.7 at 850°C, 0.001 s^{-1}.*

majority of the equiaxed α grains is further divided into subgrains separated by twist boundaries (Fig. 6(*d*), indicated by an arrow). Also observed features of cell boundaries composed of dislocation tangles apparently transforming to regular dislocation networks by rearrangement of dislocations. A majority of these cell boundaries was composed of hexagonal dislocation network [4,5]. These micrographs depict typical features of deformed microstructure in two phase $(\alpha + \beta)$ field of Nb containing Zr-alloys and are qualitatively different from that observed in CP-Zr and Zr–Sn alloys. Besides modification of microstructure, other important features associated with DRX in these alloys are relatively high strain rate sensitivity and associated large ductility (Table 2). Similar deformation features have also been reported during hot deformation in the $(\alpha + \beta)$ phase of titanium alloys [19]. Zr–Nb–Sn–Fe alloy can be considered as a near α-alloy in which β volume fraction is much lower than Zr–Nb and Zr–Nb-Cu alloys. Important observations during DRX in this alloy are high strain rate

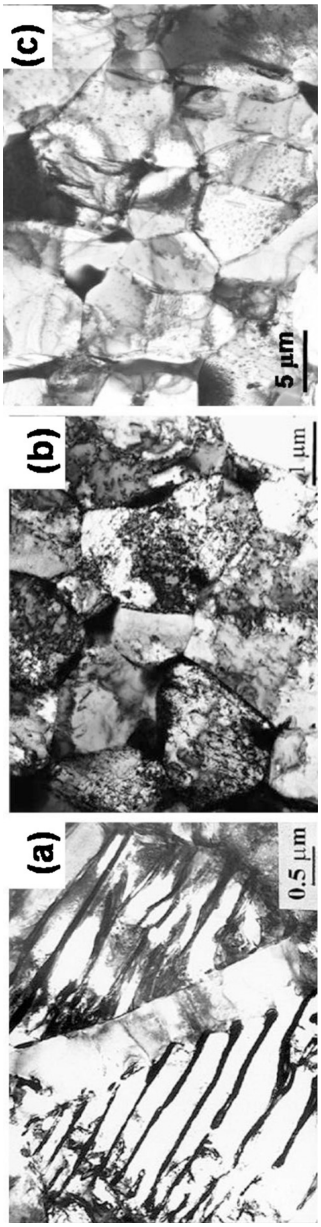


FIG. 7—*Transmission electron micrographs of Zr–Nb–Sn–Fe: (a) Undeformed starting microstructure; (b) deformed to a strain of 0.7 at 750°C, 0.001 s^{-1}; and (c) deformed to a strain of 0.7 at 800°C, 0.001 s^{-1}.*

sensitivity, evolution of the initial transformed β microstructure (consisting of α' platelets) to an equiaxed α morphology, and presence of substructure within equiaxed α grains and enhancement of hot ductility [20]. The DRX is further supported by the linear plot of log(grain size) versus log(Z) [20]. Some representative microstructures are given in Fig. 7 to illustrate the evolution of microstructure during DRX in Zr–Sn–Nb–Fe alloy. It is seen that the DRX results in the complete modification of the starting plate type β transformed material to fine equiaxed α-grains (Fig. 7(a)7(c)). The majority of the grain boundaries is of high angle type, and grains are found to contain tangled dislocation substructures within them, and this is to be expected during DRX as grains are nucleated and the dislocation structures develop within them on concurrent deformation. It has been suggested by Evangelista et al. that the presence of equiaxed grains containing substructure is a strong evidence of DRX [21].

Discussion

In the preceding sections, the occurrence of DRX in Zr-alloys studied has been established on the basis of developed microstructure, strain sensitivity, and ductility measurement. The effects of macroscopic deformation parameters (such as $\cdot\varepsilon$ and T) and the nature of alloying elements on the evolution of DRX microstructure have been described. It has also been noted that the DRX process resulted in a complete modification of transformed β (or plate type α' morphology) into an equiaxed to a nearly equiaxed α grains containing subgrains/dislocation network during deformation in α, $\alpha + \beta$ phase field of Zr-alloys. The subgrains within such grains have exhibited both low as well as high misorientations, and they appear qualitatively similar to those associated with DRV. It may be pertinent to note that the DRX process is considered essentially to be a nucleation and growth process [22–24]. While the nucleation step involves formation of a suitable high angle boundary or interface either by thermal recovery process (climb of edge dislocation) or by cross-slip of screw dislocations, the growth process is primarily associated with migration of the high angle interface. Therefore, it is likely that the kinetics of DRX process will be governed by one of the several mechanisms (associated nucleation and growth processes) involved and that DRX microstructure will reveal features of these processes. However, a thorough TEM examination of deformed samples neither revealed the nature of the DRX nucleation event nor identified the underlying dislocation mechanism responsible unambiguously. Before discussing further on the possible rate controlling mechanism involved in the DRX process, a short review of current understanding on the details of the restoration mechanisms of Zr-alloys will be in place.

The dynamic restoration mechanisms during creep and deformation at low rates in Zr and Zr-alloys at elevated temperatures have been examined in some details in the past [25–28]. Such information, however, is sparse or very limited for deformation behavior relevant to industrial processing conditions where higher rates of deformations are involved. Hayes et al. [27] compiled Zr creep data over a broad range of stresses (0.1–115 MPa) and temperatures

(300–850°C) and concluded that Zr obeys power law creep with DRV by dislocation climb as restoration mechanism in the five-power law regime. Jonas and co-workers [29,30] in an early study reported DRV of the α phase to be the restoration mechanism in Zr and Zr–Sn alloys on the basis that the estimated apparent activation energy. However, different rate controlling dislocation mechanisms, namely, climb of edge dislocation 30, cross-slip of screw dislocation [31], and thermally activated unpinning of dislocations from attractive junctions [32], have also been suggested to be responsible for DRV in Zr-alloys. Even during five-power law creep where dislocation climb control DRV is operative as the restoration mechanism for Zr-alloys, the activation energy for creep has been reported to be greater than that for self diffusion [28]. The observed discrepancies suggest that other competitive restoration mechanisms such as DRX and grain growth may be involved under the conditions of deformation. In a recent work, Perez-Prado et al. [28] studied in detail the development of microstructure, bulk texture, and microtexture in α-Zr and suggested DRV through dislocation climb to be the responsible restoration mechanism when α-Zr is deformed in the temperature range of 400–800°C at a strain rate of $5 \times 10^{-4}\,s^{-1}$. They also reported occurrence of high angle boundaries at larger strains, which appeared to result from geometric DRX, an alternative restoration mechanism widely reported during hot deformation of Al and Al alloys [33,34]. Under similar rate of deformation and at 700°C, Kassner and coworkers reported discontinuous DRX [35]. Ostberg and Attermo 36 found DRX to be involved in modifying the original Widmanstatten α plates to new equiaxed α grains during hot press forging of Zircaloy-2 carried out at 800°C and at an estimated strain rate of $0.4\,s^{-1}$. Garde et al. [37] studied hot tensile deformation behavior of Zircaloy-2 in the two phase $(\alpha + \beta)$ field at various strain rates. The microstructure evolved during deformation at temperatures around 850°C and at strain rates lower than $10^{-3}\,s^{-1}$ was characterized as equiaxed α grains separated by β phase. The phenomenon of grain boundary sliding has been attributed to be involved in the development of equiaxed α grains. When the deformation rates were increased ($\approx 0.1\,s^{-1}$) at the same deformation temperature, the starting microstructure was altered into elongated α grains separated by a thin film of β phase. These results clearly reveal the effect of strain rate and temperature on the restoration mechanisms. A similar elongated morphology of α grains separated by β phase has been reported by Ostberg and Attermo 36 during forging at 900°C and $0.4\,s^{-1}$, and on the basis of detailed metallographic analysis, they concluded the occurrence of DRX in the two phase $(\alpha + \beta)$ field. The development of the microstructure during hot extrusion of β-transformed Zr-2.5Nb have been studied by Cheadle et al. [38] and Perovic et al. [39], and they have noted the importance of temperature and deformation rate in influencing the microstructural evolution. In a recent study on the influence of deformation condition on texture evolution, Logé et al. [26] reported breaking up of the Widmanstatten structure (during plane strain compression) into a collection of equiaxed grains because of the combined effect of recovery and recrystallization in Zircaloy-2 when deformation was carried out at 800°C and at rates of $0.1–1\,s^{-1}$. These deformation conditions match well with the DRX conditions for the Zircaloy-2 of this work.

TABLE 3—*Kinetic parameters in the domain range of optimum hot working.*

Alloy	A	n	Q_{def} (KJ/mol)	Q_{SD} (KJ/mol)	Reference
CP-Zr	4.2×10^{16}	3.8	168	92.5	42
Zr–Sn	4.3×10^{21}	4.1	268	134.5	42
Zr–Nb	7.1×10^{15}	3.1	197	132	43
Zr–Nb–Cu	2.9×10^{14}	2.8	180	...	
Zr–Nb–Sn–Fe	1.2×10^{22}	3.3	325	...	

Clearly, the nature of dynamic restoration processes in Zr-alloys and their dependence on deformation conditions (strain rate and temperature) and composition are not satisfactorily elucidated. As regards the rate controlling mechanisms involved in DRX, there is very limited information available particularly at deformation rates relevant to industrial processing.

In the following, we make an attempt to identify the rate controlling dislocation mechanisms involved in DRX by employing both kinetic analysis and the theory of TAD.

Kinetic Analysis

In order to ascertain the mechanisms responsible for microstructural development during DRX, usually a power law equation relating stress, temperature, and strain rate of the form given below is used 14

$$\dot{\varepsilon} = C\left(\frac{\dot{\varepsilon}}{\mu}\right)^{n} \exp\left(\frac{-Q_{def}}{RT}\right) \tag{1}$$

where:

Q_{def} = activation energy of deformation,
n = stress exponent,
C = constant, and
μ = shear modulus taken [40,41] as

$$\mu = 35.5 - 0.0198(T - 273) \text{ for } \alpha \tag{2a}$$

$$\mu = 36.3 - 0.0223(T - 273) \text{ for } \alpha + \beta \tag{2b}$$

The constants n, Q_{def}, and C are evaluated using non-linear fitting of the data. These parameters for all the alloys are given in Table 3. It is generally thought that n and Q_{def} are characteristics of a given rate controlling mechanism. It is seen from the table that for all the alloys, n is in the range of 2.8–4.1 and Q_{def} is higher in Sn containing alloys compared to CP-Zr and Zr–Nb and Zr–Nb-Cu alloys. In addition to these, the Q_{def} values for Zr-alloys are larger than respective activation energies for self diffusion (Q_{SD}) [42,43]. These results suggest that a dislocation based transgranular mechanism is involved with the DRX process

in Zr-alloys of this study. However, this analysis does not lead to the identification of the exact dislocation mechanism responsible for the DRX process.

It is pertinent to mention here that since several mechanisms (slip of dislocation, dislocation interaction, formation of cell walls and subgrain boundaries, formation of high angle boundaries and their migration, etc.) are operating concurrently during DRX, it is difficult to identify the real rate controlling process. It is known that grain boundary migration (GBM), as involved in growth mechanism during DRX, depends primarily on diffusivity and that activation energy for GBM is equal to that for Q_{SD} [44–46]. Since $Q_{def} > Q_{SD}$ for all the Zr-alloys studied, it appears unlikely that DRX is GBM controlled. Further, it has been seen earlier that the rate of GBM is at least equal to or greater than the rate of formation of a large angle boundary/interface (the nucleation step) for Zr-alloys [1,2,4]. This stems from the fact that diffusivity is not altered significantly on alloying in Zr-alloys at least in the temperature range where DRX occurs. In contrast to this, the rate of nucleation has been found to change significantly with alloying [1,2,4]. In view of these, nucleation process might be considered as the likely rate controlling step. In the next section, we use the concept of TAD to identify the rate controlling dislocation mechanism involved in nucleation of DRX. TAD analysis has been successfully used to characterize DRX in titanium alloys [47].

Thermally Activated Deformation

The approach employed here is based on the concept that a single thermally activated dislocation mechanism may be rate controlling over a given temperature and strain rate range. In that case, the $\dot{\epsilon}$ and T can be related through a rate equation of the type [48–50]

$$\dot{\epsilon} = \dot{\epsilon}_o \exp(-\Delta G/RT) \tag{3}$$

where:

pre-exponential factor, $\dot{\epsilon}_o = \alpha b \rho_m \lambda \nu$,
α = scaling constant,
b = Burgers vector,
ρ_m = mobile dislocation density,
λ = spacing between obstacles,
ν = vibration frequency of the dislocation segment, and
ΔG is related to activation free energy and is dependent on both T and σ.

Equations of this form have previously been used successfully to identify rate controlling dislocation mechanism during hot deformation of Ti-alloys [47,51] and Zr-alloys [30,32]. It has been shown by Kocks [50] and Ono [52] that ΔG can be expressed as a non-linear function of shear modulus corrected stress ($\sigma' = \sigma/\mu$) given by

$$\Delta G = \Delta G_o \left[1 - \left(\frac{\sigma' - \sigma_i'}{\sigma_o'} \right)^{0.5} \right]^{1.5} \tag{4}$$

Here, ΔG_o represents the free energy required to overcome the barrier at 0 K, $\sigma_o^{'}$ $(= \sigma_o/\mu_o)$ represents the strength of the barrier at 0 K, and $\sigma_i^{'}$ represents the shear modulus corrected internal stress. The process of thermal activation usually assumes that the internal stress is of long-range nature and does not take part in the process of thermal activation. In the case of hot deformation, it is likely that the internal stresses will be very small, and thus $\sigma_i^{'}$ can be neglected. Combining Eqs 3 and 4

$$\ln \dot{\epsilon} = \ln \dot{\epsilon}_o - \frac{\Delta G_o}{RT}\left[1 - \left(\frac{\sigma^{'}}{\sigma_o^{'}}\right)^{0.5}\right]^{1.5} \tag{5}$$

Although Eq 5 is based on dislocations moving on a single slip system, when applied to polycrystals, with more than one phases following assumptions are made: (i) In the averaged sense, this form of the equation still holds; (ii) out of the many deformation processes occurring, the one which is rate controlling will be manifested in terms of the ΔG obtained; and (iii) in a two phase mixture, the phase that controls the deformation will have a large degree of representation through this equation. This equation can be thought of as a phenomenological constitutive equation with the fitted parameters having some physical significance. Hence, a comparison of these parameters for the different alloys may lead to a clearer understanding of the deformation mechanism and the effect of alloying on the DRX process. In addition to these, another important activation parameter, namely, the activation area (A), is also required to identify the dislocation mechanism. The experimental activation area A quantifies the average area on atomic scale swept out by mobile dislocations thermally activating from one barrier to the other. From the thermodynamic point of view, $A = V/b$, where V is the activation volume and is defined as $V = -\partial G/\partial \tau$. From Eq 4 and using $\sigma = M\tau$, where τ is shear stress and $M = 3$ is the Taylor factor, A can be expressed as

$$A = \frac{3M\Delta G_0}{4\sigma_0 b}\left(1 - \left\{\frac{\sigma^{'}}{\sigma_0^{'}}\right\}^{0.5}\right)^{0.5}\left(\frac{\sigma^{'}}{\sigma_0^{'}}\right)^{-0.5} \tag{6}$$

It may be noted here that the activation areas reported are apparent rather than true activation areas. The rate controlling mechanism is identified by comparing the experimentally determined stress dependence of activation area with those predicted by specific theories 49,50. σ, $\dot{\epsilon}$, and T associated with the DRX domain of a given map have been used to fit to Eq 6 to obtain the three variables, ΔG_o, $\sigma_o^{'}$, and A. The expressions of Eqs 2a and 2b giving variation of modulus μ (in GPa) with temperature have been used to normalize the stress values. The fitting was carried out by first keeping $\dot{\epsilon}_o$ fixed and using non-linear regression to obtain the optimum ΔG_o, $\sigma_o^{'}$ with the least square error (LSE) fit. $\dot{\epsilon}_o$ was then incrementally changed and the non-linear regression repeated till the lowest LSE fit was obtained. This enabled evaluation of various constants of Eq 5 for each alloy. It can be seen from Eq 5 that a plot of $(\sigma^{'}/\sigma_o^{'})^{0.5}$ versus

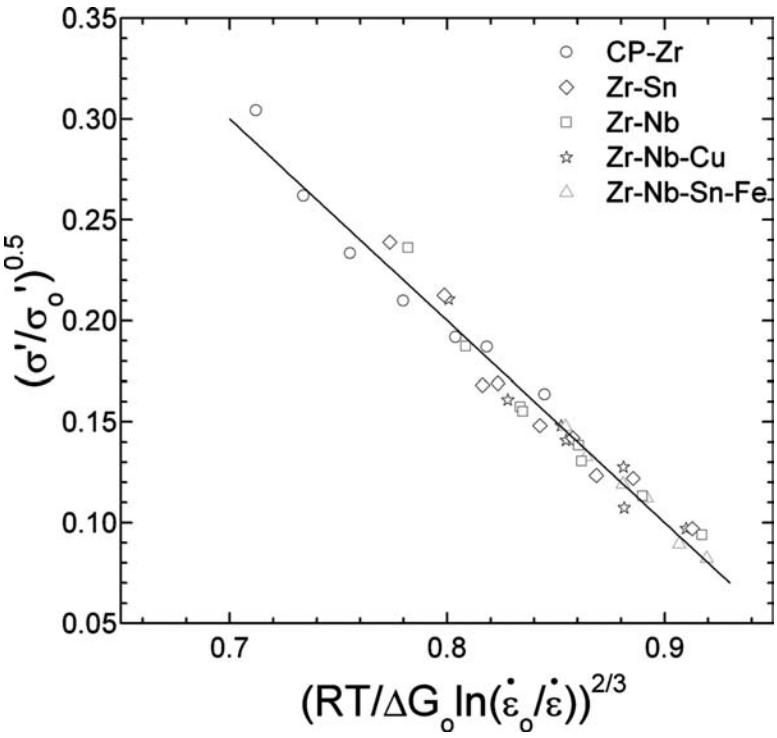


FIG. 8—*Plot of normalized stress as function of temperature compensated strain rate for all the Zr-alloys studied here in the α and α+β phase fields. It is seen that using the appropriate constants* $\dot{\epsilon}_o$, ΔG_o, *and* σ_o' *(different for each alloy as per Table 4), Eq 5 is fit well.*

$\left(RT/\Delta G_o \ln(\dot{\epsilon}_o/\dot{\epsilon})\right)^{2/3}$ should yield a straight line. The data plotted using the fitted parameters fall in a line, implying a very good fit, as shown in Fig. 8. The activation energy (ΔG) and A are calculated from the expressions given above and are plotted as a function of flow stress in Fig. 9. For comparison, the parameters ΔG_o and A for each of the alloys are given in Table 4. It is seen that there is significant variation in the values of ΔG_o for the alloys studied. All activation areas reported in this study are given in a normalized form by dividing by the square of the Burgers vector (b^2). For all the alloys studied, the A in the DRX domain lies in the range of $20b^2$–$60b^2$. The activation areas have relatively strong stress dependence and found to be independent of strain. Since oxygen content in Zr-alloys studied is nearly same, the observed changes in ΔG_o, σ_o', $\dot{\epsilon}_o$, and A are not therefore due to oxygen.

Regarding the rate controlling mechanism for the DRX process, the following possibilities may be considered: (i) Diffusional process such as climb of edge dislocations or non-conservative motion of jogged screw dislocation, (ii) thermal breaking of attractive junctions, and (iii) cross-slip. On the basis of the results of thermal activation analysis, the rate controlling mechanism of DRX

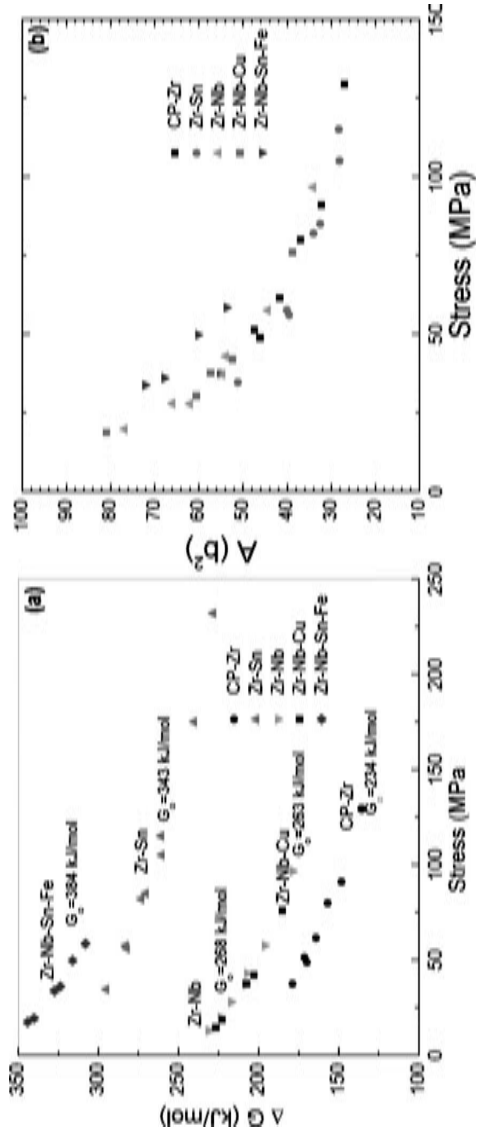


FIG. 9—*(a) Variation of ΔG with flow stress for various Zr-alloys in DRX domain. (b) Variation of activation area with flow stress for the various Zr-alloys.*

TABLE 4—*List of constants* $\dot{\epsilon}_o$, $\sigma_o^{'}$, *A, and* ΔG_o *obtained through fitting Eq 5 for various alloys. Corresponding estimated values of* ΔG_c *and* ΔG_r *are also shown.*

Alloy	$\dot{\epsilon}_o$ (s^{-1})	$\sigma_o^{'}$	A (b^2)	ΔG_o (kJ/mol)	ΔG_c (kJ/mol)	ΔG_r (kJ/mol)
CP-Zr	6.9×10^6	0.071	35–45	234	~ 200	~ 35
Zr–Sn	8.8×10^{11}	0.197	35–45	343	~ 300	~ 40
Zr–Nb	8.8×10^7	0.083	45–60	268	~ 260	~ 10
Zr–Nb–Cu	1.3×10^8	0.082	45–60	263	~ 255	~ 10
Zr–Nb–Sn–Fe	5.1×10^{12}	0.140	50–60	384	~ 370	~ 12

process in Zr-alloys of this study can be suggested as thermally activated cross-slip. This stems from the fact that the activation area obtained is in the range of $10b^2$–$100b^2$ and that it is coupled with an activation energy of deformation that is greater than that for self diffusion (Tables 3). The mechanisms such as climb ($A \sim b^2$) as well as thermal breaking away of attractive junctions (from $A \sim 10^2$ to $10^3 b^2$) can be ruled out as likely rate controlling dislocation mechanism involved in DRX [49,50]. Similar conclusions have been drawn during DRX (involving the process of spheroidization) of titanium alloys [47]. Further, if cross-slip is the rate controlling mechanism, the relation $(1/\sigma \cdot T) \propto -1/T$ should to also be obeyed [32,53]. The results depicted in Fig. 10 show that

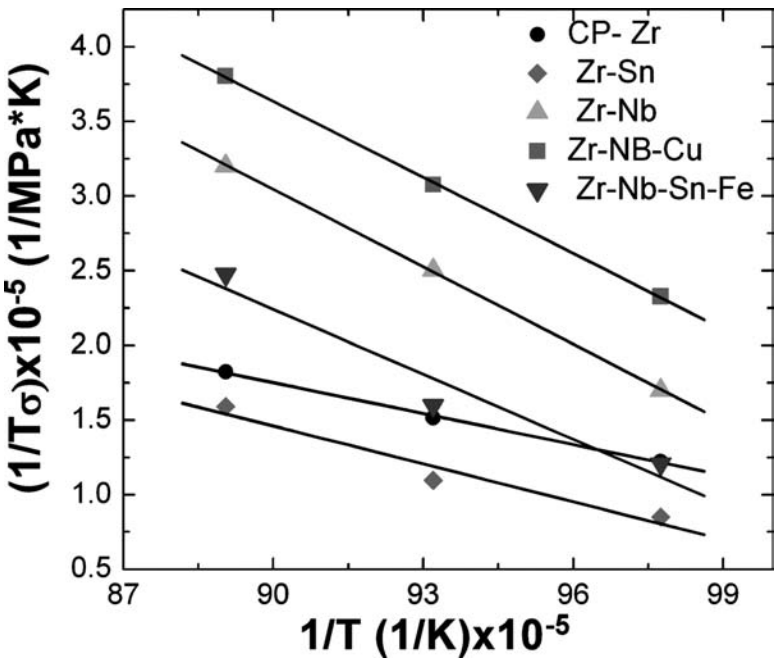


FIG. 10—*Effect of temperature on flow stress* (σ) *for various Zr-alloys in the DRX domain to examine the mechanism of cross-slip.*

$1/\sigma \cdot T$ decrease linearly with $1/T$ over the temperature range of respective DRX domains of Zr-alloys. Thus, it may be stated that the DRX process in Zr-alloys appears to be controlled by the cross-slip of screw dislocations. Also, it is seen that Nb (a β stabilizer) containing alloys exhibit identical slope that is different from the slope exhibited by CP-Zr and Zr–Sn alloys (containing primarily α stabilizing elements). This difference is likely to have some influence on the details of DRX characteristics.

It is known that Zr deforms normally by prism slip over a wide temperature range from ambient to α/β transformation temperature [31]. When dislocations on a prism plane assume screw orientation, they can dissociate into a pair of partials on basal plane separated by a stacking fault. For continued slip under applied stress, these partials recombine and screw components cross-slip on to the primary prismatic plane.

The activation energy ΔG_0 can therefore be decomposed essentially in to two parts such that $\Delta G_0 = \Delta G_c + \Delta G_r$, where ΔG_c is the energy to form constriction on the dissociated dislocation and ΔG_r is the energy involved in the recombination process of the partials [54–56]. While ΔG_c is controlled essentially by stacking fault energy (SFE) or separation of between the partials, ΔG_r is dependent on the difference between core energies of glissile and sessile structures of dislocation involved, line tension, and applied shear stress 31,54. Friedel worked out the following relationship [54–56]:

$$\Delta G_0 = \Delta G_c + \Delta G_r = \Delta G_c + \frac{2^{5/2} R^{3/2} \Gamma^{1/2}}{3\tau b} \tag{7}$$

where:

R = energy to recombine a unit length of the two partials,
τ = applied shear stress on the prism plane,
b = Burgers vector, and
Γ = line tension.

It is expected that the flow characteristics of an alloy will be governed by the relative contributions of these two factors under the given conditions of deformation. It is possible to approximate the ΔG_r from the knowledge of activation area and noting the relationship $A = 2^{5/2} R^{3/2} \Gamma^{1/2} / 3\tau^2 b^2$ [54].

Table 4 compares the relative contribution of each term within the DRX domain of Zr-alloys. It is seen that for CP-Zr and Zr–Sn, the contribution of ΔG_r is $\sim 15\,\%$, whereas for Nb containing materials (Zr–Nb, Zr–Nb-Cu, and Zr–Nb–-Sn–Fe), it is less than 5 %. This observation suggests that SFE or separation between the partials controls the deformation behavior of Nb containing alloys and that for CP-Zr and Zr–Sn alloys, both the factors are contributing to the process of cross-slip. This difference may be responsible for the observed variation in slopes of the plots in Fig. 10. It is also noted from Table 4 that the SFE is decreased on alloying by both Sn (α-stabilizer) and Nb (β-stabilizer) as ΔG_c component is enhanced compared to CP-Zr. This observation is consistent with the fact SFE is lowered on alloying [57]. The addition of Sn in α-Zr has been reported to lower the SFE and increase the separation of partials [58]. As regards

the effect of Nb on SFE of Zr, reliable data are not available in literature to confirm. Since both Sn and Nb decrease SFE, the maximum ΔG_0 is associated with the Zr–Sn–Nb–Fe alloy followed by Zr–Sn and remaining Nb containing alloys.

It remains now to investigate the effects of alloying additions on the strain rate for the occurrence of DRX domain. A generally accepted fact is that the process of DRX may be considered in terms of rate of nucleation and rate of growth of new strain free grains 22–24. For a successful formation of a DRX nuclei, a suitable interface that can migrate must be created in the deformed volume. This will require the development of a critical dislocation density, which is dependent on $\dot{\epsilon}$, T, and efficiency of prevailing recovery process (i.e., on the probability of recovery of dislocations). For a given temperature, the rate of interface formation can be related to probability of recovery process by a simple relation of the form [23]

$$R_F = \frac{\dot{\epsilon}}{bl}.P_R \tag{8}$$

where:

R_F = rate of interface formation,
P_R = probability of recovery of dislocation, and
l = dislocation link length.

While P_R is dependent on ΔG_0, which controls the recovery process, l is decided by the mean free path of dislocations, subgrain size, etc. [23]. The observed similar DRX characteristics ($\dot{\epsilon}$ and T conditions) of CP-Zr and Zr–Sn can be explained on the basis of the ratio (P_R/l). For a given R_F, since ΔG_0 is enhanced compared to CP-Zr on Sn addition, P_R is lowered. A corresponding decrease in l may also result from an increase in width of the dislocation core (consequence of lowering SFE), solid solution strengthening, and the presence of fine second phase particles to keep the ratio (R_F/l) constant. The values of $\sigma_o^{'}$ and $\dot{\epsilon}_o$ in Table 4 suggest a strong influence of Sn on l. In contrast to the effect of Sn, Nb addition is seen to lower the $\dot{\epsilon}$ for DRX. Zr–Nb and Zr–Nb-Cu alloys have ΔG_0 values, which are nearly similar to that for CP-Zr, and this result in comparable P_R values. In view of large size difference between Nb and Zr atoms (about 9 %) and a higher modulus of Nb, a strong interaction with glide dislocations is expected [59]. This will have a strong effect in lowering l. This is also corroborated by the fact that Nb containing alloys have higher $\dot{\epsilon}_o$ values compared to CP-Zr. Arguing in the similar lines, the reduction in l will be further enhanced in Zr–Nb–Sn–Fe alloy. A considerable reduction in $\dot{\epsilon}$ for DRX is therefore observed in Nb containing alloys. The TEM micrographs of deformed samples of Zr-alloys (Figs. 5–7) revealed different types of dislocation activities within the equiaxed DRX grains and found to contain a relatively high density of dislocations. From a comparison of deformed microstructures, it appears that Zr–Sn and Nb containing alloys have a finer substructure and a higher dislocation density compared to CP-Zr. These clearly indicate a significantly lower link length, l, in Zr–Sn and Nb-containing alloys (lowest being in Zr–Sn–Nb–Fe followed by Zr–Sn and remaining Nb containing alloys). This observation is readily understood if it is accepted that the magnitude of ΔG_0 governs the

process of recovery. When ΔG_0 is low, the recovery process is quick and efficient to lower the dislocation density such that a critical nucleus of large size is formed. In materials that recover less efficiently (higher ΔG_0), the dislocation density generated by deformation is larger, and the critical nuclei size is smaller. Thus a higher dislocation density and smaller subgrain size are the consequence of higher ΔG_0 values in Nb and Sn containing Zr-alloys compared to CP-Zr.

The explanation given on the observed effect of solutes on DRX characteristic is not exact and an over simplification of a complex phenomena and therefore to some extent speculative. In the absence of quality data on the effect of solutes on SFE and an appropriate model incorporating the effect of SFE and microstructural parameters on macroscopic deformation conditions, the explanation given for the observed DRX characteristics is tentative, and further studies are required in the subject. It is also emphasized on the basis of observations made that recovery has significant effect on the DRX process of Zr-alloys and therefore due consideration must be given for the role of DRV during modeling the DRX behavior.

Summary and Conclusion

The characteristics of DRX have been examined in Zr-alloys (containing both α and β stabilizing elements) using compression tests over a wide range of experimental conditions. The DRX observed for Zr-alloys in this study involves nucleation and growth processes as in well known discontinuous DRX. The factors influencing DRX have been identified. The following conclusions are drawn on the basis of analyses of stress-strain curve and microstructural evolution and using a model for thermally activated flow.

(1) A complete modification of β-transformed microstructure to an equiaxed morphology containing dislocation substructure within, variation of grain size with strain rate and temperature, and a linear variation of log(grain size) with log(Z) are some important characteristic feature of DRX in Zr-alloys studied.

(2) Nb has strong influence in altering the deformation conditions ($\dot{\epsilon}$ and T) for DRX of CP-Zr. The domain of DRX in Nb containing alloys shifts to lower strain rates compared to that for CP-Zr. Sn addition to CP-Zr does not alter the DRX conditions.

(3) The DRX process in these alloys appears to be controlled by the process of nucleation, which involves the formation of a high angle interface/boundary. The rate of interface formation is governed by DRV, with cross-slip of screw dislocations as the underlying dislocation mechanism. This has been established on the basis of magnitudes of activation area ($\approx 20b^2$–$60b^2$) and activation energy ($\geq$ activation energy for self diffusion in Zr) and confirmed by the fulfillment of the relation $(1/\sigma \cdot T) \propto (-1/T)$.

(4) The activation energies have been found to increase with alloying elements of either type—highest value is associated with Zr–Nb–Sn–Fe

followed by Zr–Sn and Nb containing alloys. The effect of solutes on activation energy appears to control the evolution of the microstructure and the dislocation structure. A higher value of ΔG_0 results in a finer subgrain size and a higher dislocation density.

(5) In Nb containing alloys, the contribution of recombination energy to the total activation energy (ΔG_0) appears to be negligible compared to the constriction energy, suggesting possible dominance of SFE in the DRX process. This may be responsible for the observed differences in DRX characteristics of Nb containing alloys as compared to CP-Zr and Zr–Sn alloys.

Acknowledgments

The writers wish to thank Mr. S. Neogy, Dr. R. Tewari and Dr. G. K. Dey of Materials Science Division, Bhabha Atomic Research Centre for their help in the TEM investigations.

References

[1] Chakravartty, J. K., Prasad, Y. V. R. K., and Asundi, M. K., "Processing Map for Hot Working of α-Zirconium," *Metall. Mater. Trans. A*, Vol. 22A, 1991, pp. 829–836.

[2] Chakravartty, J. K., Banerjee, S., Prasad, Y. V. R. K., and Asundi, M. K., "Hot Working Characteristics of Zircaloy-2 in the Temperature Range of 650–950°C," *J. Nucl. Mater.*, Vol. 187, 1992, pp. 260–271.

[3] Chakravartty, J. K., Prasad, Y. V. R. K., and Asundi, M. K., *Zirconium in the Nuclear Industry (Ninth Volume), ASTM STP 1132*, ASTM International, West Conshohocken, PA, 1991, p. 48.

[4] Chakravartty, J. K., Banerjee, S., and Prasad, Y. V. R. K., "Dynamic Recrystallization during Hot Working," *Mater. Sci. Technol.*, Vol. 12, 1996, pp. 705–716.

[5] Chakravartty, J. K., Dey, G. K., Banerjee, S., and Prasad, Y. V. R. K., "Characterization of Hot Deformation Behaviour of Zr-2.5 Nb-0.5 Cu Using Processing Maps," *J. Nucl. Mater.*, Vol. 218, 1995, pp. 247–255.

[6] Chakravartty, J. K., Kapoor, R., and Banerjee, S., "Characterization of Hot Deformation Behaviour of Zircaloy: a comparison between kinetic analysis and processing maps," *Z. Metallkd.*, Vol. 96, 2005, pp. 645–652.

[7] Chakravartty, J. K., 1992, "Optimization of Hot Workability and Control of Microstructure in Zirconium Alloys," °Ph.D. thesis, Indian Institute of Science, Bangalore.

[8] Luton, M. J. and Sellars, C. M., "Dynamic recrystallization in nickel and nickel-iron alloys during high temperature deformation," *Acta Metall.*, Vol. 17, 1969, pp. 1033–1043.

[9] Zahiri, H. S., Davies, C. H. J., and Hodgson, P. D., "A mechanical approach to quantify dynamic recrystallization in polycrystalline metals," *Scripta Materialia*, Vol. 52, 2005, pp. 299–304.

[10] Seshacharyulu, T., Medeiros, S. C., Frazier, W. G., and Prasad, Y. V. R. K., "Microstructural mechanisms during hot working of commercial grade Ti-6Al-4V with lamellar starting structure," *Mater. Sci. Eng., A*, Vol. 325, 2002, pp. 112–125.

[11] Prasad, Y. V. R. K., "Recent Advances in the Science of Mechanical Processing," *Indian J. Technol.*, Vol. 28, 1990, pp. 435–451.

[12] Prasad, Y. V. R. K. and Seshacharyulu, T., "Modelling of hot deformation for microstructural control," *Int. Mater. Rev.*, Vol. 43, 1998, pp. 243–258.
[13] Kapoor, R. and Chakravartty, J. K., "Characterization of hot deformation behavior of Zr-2.5Nb in β phase," *J. Nucl. Mater.*, Vol. 306, 2002, pp. 126–133.
[14] Jonas, J. J., Sellars, G. M., and McTegart, W. J., "Strength and structure under hot working conditions," *Metall. Rev.*, Vol. 14, 1969, pp. 1–24.
[15] Balasubrahmanyam, V. V. and Prasad, Y. V. R. K., "Deformation behavior of β titanium alloy Ti-10V-4.5Fe-1.5AL in hot upset forging," *J. Mater. Eng.*, Vol. A336, 2002, pp. 150–158.
[16] Bailey, J. E. and Hirsh, P. B., "The recrystallization process in some polycrystalline metals," *Proc. R. Soc. London*, Vol. A267, 1962, pp. 11–30.
[17] Raybould, D. and Sheppard, T., "Plastic Flow in Thermally Activated Mechanical-Working Process," *J. Inst. Met.*, Vol. 101, 1973, pp. 45–52.
[18] Seshacharyulu, T., Medeiros, S. C., Frazier, W. G., and Prasad, Y. V. R. K., "Hot working of commercial Ti-6Al-4V with an equiaxed α-β microstructure: materials modeling consideration," *Mater. Sci. Eng., A*, Vol. 284, 2000, pp. 184–194.
[19] Chen, C. C. and Coyne, J. E., "Deformation characteristics of Ti-6Al-4V alloy under isothermal forging conditions," *Metall. Trans. A*, Vol. 7A, 1976, pp. 1931–1941.
[20] Chakravartty, J. K., Kapoor, R., Banerjee, S., and Prasad, Y. V. R. K., "Characterization of hot deformation behavior of Zr-1NB-1Sn alloy," *J. Nucl. Mater.*, Vol. 362, 2007, pp. 75–86.
[21] Evangelista, E., McQueen, H. J., and Bonetti, E., "Deformation of Multiphase and Particle Containing Materials," *Fourth RISO International Symposium*, Denmark, 1983, Riso National Laboratory, Roskilde, Denmark, p. 243.
[22] Derby, B. and Ashby, M. F., "On Dynamic Recrystallization," *Scr. Metall.*, Vol. 21, 1987, pp. 879–884.
[23] Prasad, Y. V. R. K. and Ravichandran, N., "Effect of Stacking fault energy on the dynamic recrystallization during hot working FCC metals: A study using processing maps," *Bulletin of Materials*, Vol. 14, 1991, pp. 1241–1248.
[24] Doherty, R. D., Hughes, D. A., Humphreys, F. J., Jonas, J. J., Juul Jensen, D., Kassner, M. E., King, W. E., McNelley, T. R., McQueen, H. J., and Rollett, A. D., "Current Issues in Recrystallization: a review," *Mater. Sci. Eng., A*, Vol. 238, 1997, pp. 219–274.
[25] Fidleris, V. and Williams, C. D., "Influence of neutron irradiation on the creep of Zircaloy-2 at 300°C," *Electrochem. Technol.*, Vol. 4, 1966, pp. 258–267.
[26] Logé, R. E., Signorelli, J. W., Chastel, Y. B., Perrin, M. Y., and Lebenshon, R. A., "Sensitivity of α-Zy4 high-temperature deformation textures to the β-quenced precipitate structure and to recrystallization: application to hot extrusion," *Acta Mater.*, Vol. 48, 2000, pp. 3917–3930.
[27] Hayes, T. A., Kassner, M. E., and Rosen, R. S., "Steady state creep of α-Zirconium at temperatures up to 850°C," *Metall. Mater. Trans. A*, Vol. 33, 2002, p. 337.
[28] Perez-Prado, M. T., Barrabes, S. R., Kassner, M. E., and Evangelista, E., "Dynamic restoration mechanisms in α-zirconium at elevated temperatures," *Acta Mater.*, Vol. 53, 2005, pp. 581–591.
[29] Abson, D. J. and Jonas, J. J., "Substructure strengthening in zirconium and zirconium-tin alloys," *J. Nucl. Mater.*, Vol. 42, 1972, pp. 73–85.
[30] Luton, M. J. and Jonas, J. J., "Solute strengthening at high temperatures in zirconium-tin alloys," *Can. Metall. Q.*, Vol. 11, 1972, pp. 79–85.
[31] Akhtar, A., "Basal slip in zirconium," *Acta Metall.*, Vol. 21, 1973, pp. 1–11.
[32] Mehrotra, B. N. and Tangri, K., "High temperature (60–800°C) thermally activated deformation behavior of α-ZIRCALOY-4–oxygen alloys," *Acta Metall.*, Vol. 28, 1980, pp. 1385–1394.

[33] Henshall, G. A., Kassner, M. E., and McQueen, H. J., "Dynamic restoration mechanisms in Al-5.8 At. Pct Mg deformed to large strains in the solute drag regime," *Metall. Mater. Trans. A*, Vol. 23, 1992, pp. 881–889.
[34] Blum, W., Zhu, Q., Merkel, R., and McQueen, H. J., "Geometric dynamic recrystallization in hot torsion of Al-Mg-0.6Mn(AA5083)," *Mater. Sci. Eng., A*, Vol. 205, 1996, pp. 23–30.
[35] Daraio, C., Wang, M., and Kassner, M. E., Oregon State University, Corvallis, OR, June 2001 (unpublished).
[36] Ostberg, G. and Attermo, R., "Structure transformation in zircaloy-2 during hot working processes," *J. Nucl. Mater.*, Vol. 5, 1962, pp. 120–127.
[37] Garde, A. M., Chung, H. M., and Kassner, T. F., "Micrograin superplasticity in Zircaloy at 850°C," *Acta Metall.*, Vol. 26, 1978, pp. 153–166.
[38] Cheadle, B. A., Aldrige, S. A., and Ells, C. E., "Development of Texture and Structure in Zr-2.5 wt% Nb Extruded Tubes," *Can. Metall. Q.*, Vol. 11, 1972, pp. 121–127.
[39] Ho, E. T. C. and Perovic, V., "Deformation of Multiphase and Particle Containing Materials," *Fourth RISO International Symposium*, Denmark, 1983, Riso National Laboratory, Roskilde, Denmark, p. 301.
[40] Northwood, D.O., London, I. M., and Bahen, L. E., "Elastic Constants of Zirconium Alloys," *J. Nucl. Mater.*, Vol. 55, 1975, pp. 299–310.
[41] Rosinger, H. E. and Northwood, D. O., "The Elastic Properties of Zirconium Alloy Fuel Cladding and Pressure Tubing Materials," *J. Nucl. Mater.*, Vol. 79, 1979, pp. 170–179.
[42] Douglass, D. L., *Atomic Energy Review (Suppl.)*, IAEA, Vienna, Austria, 1971, pp. 136–310.
[43] Brandes, E. A., Ed., *Smithells Metals Reference book*, 6th ed., Butterworths, London, 1983, Chap. 11 and 13, p. 374.
[44] Senkov, O. N., Jonas, J. J., and Froes, F. H., "Steady Flow Controlled by the Velocity of Grain Boundary Migration," *Mater. Sci. Eng., A*, Vol. A235, 1998, pp. 49–53.
[45] Gottstein, G. and Shvindlerman, L. S., *Grain Boundary Migration in Metals*, CRC Press, Florida, 1999, p. 231.
[46] Smith, D. A., Rae, C. M., and Grovenor, C. R. M., *Grain Boundary Structure and Kinetics*, R. W. Balluti, Ed., Am. Soc. Mater., Metals Park, OH, 1988, p. 347.
[47] Seshacharyulu, T., Medeiros, S. C., Morgan, J. T., Malas, J. C., Frazier, W. G., and Prasad, Y. V. R. K., "Hot Deformation Mechanisms in ELI Grade Ti-6Al-4V," *Scr. Mater.*, Vol. 41, 1999, p. 283–288.
[48] Conrad, H., "Thermally Activated Deformation of Metals," *J. Met.*, Vol. 16, 1964, pp. 582–588.
[49] Evans, A. G. and Rawlings, R. D., "Thermally Activated Deformation of Crystalline Materials," *Phys. Status Solidi*, Vol. 34, 1969, p. 9–31.
[50] Kocks, U. F., Argon, A. S., and Ashby, M. F., Thermodynamics and Kinetics of Slip, Pergamon Press, Oxford, 1975.
[51] Senkov, O. N. and Jonas, J. J., "Effect of strain rate and temperature on the flow stress of β-phase Ti-hydrogen alloys," *Metall. Mater. Trans. A*, Vol. 27, 1996, p. 1303–1312.
[52] Ono, K., "Temperature Dependence of Dispersed Barrier Hardening," *J. Appl. Phys.*, Vol. 39, 1968, pp. 1803–1806.
[53] Flynn, P. W., Mote, J. D., and Dorn, J. E., "On the thermally activated mechanism of slip in magnesium single crystals," *Trans. ASME*, Vol. 221, 1961, pp. 1148–1154.
[54] Caillard, D. and Martin, J. L., *Thermally Activated Mechanisms in Crystal Plasticity*, Pergamon, Amsterdam, 2003.
[55] Friedel, J., *Dislocation*, Pergamon Press, New York, 1964, p. 379.

[56] Friedel, J., *Internal Stress and Fatigue in Metals*, Elsevier, Amsterdam, 1959, p. 238.
[57] Ueki, M., Horie, S., and Nakamura, T., "Factors affecting dynamic recrystallization of metals and alloys," *Mater. Sci. Technol.*, Vol. 3, 1987, pp. 329–337.
[58] Sastry, D. H., Luton, M. J., and Jonas, J. J., "Stacking fault energy and its effect on high temperature plastic flow in Zr-Sn alloys," *Philos. Mag.*, Vol. 30, 1974, pp. 115–127.
[59] Pahutova, M., Kuchanova, K., and Cadek, J., "Some Basic Creep characteristics of Zr-Sn-Mo and Zr-Sn-Mo-Nb Alloys: Part I Steady State Creep," *Mater. Sci. Eng.*, Vol. 27, 1977, p. 239–248.

DISCUSSION

Question 1, M. Griffith, AECL:—1) Can you summarize what effect the rate of deformation has on the average grain size for the alloys studied? 2) How do you correct for the effect of heating as a function of work rate to establish the temperature?

Author's Response:—1) In general, within the domain of DRX, the grain size increases with decreasing rate of deformation. Fig. 4 shows variation of average grain size with strain rate (rate of deformation) for Zr-Sn. This trend has also been seen with α grain size during DRX of Zr-Nb, Zr-Nb-Cu and Zr-Nb-Sn-Fe[20] alloys in two phase ($\alpha+\beta$).

2) The adiabatic temperature rise during compression testing was measured with a thermo-couple embedded in the specimen. The flow stress was corrected for the adiabatic temperature rise using linear interpolation of log (σ) vs (1/T). This correction was found to be significant at lower temperatures and at higher rates.

Question 2, Anand Garde, Westinghouse Electric Company, USA:—Can you comment on the impact of introduction of point defects due to irradiation damage on the shift of different regions of the deformation maps?

Author's Response:—In this investigation processing maps have been generated over the temperature range 650–1000°C. At these temperatures we feel that the defects produced due to irradiation will anneal out and therefore will not influence any domain in the processing maps.

Question 3, P. Barberis, CEZUS, France:—Is there an effect of the initial microstructure (beta-quenched : parallel plate/basket weave or recrystallized) on the DRX?

Author's Response:—We have studied Zr-2.5 Nb in different microstructural states. We found that the details of the DRX characteristics are not altered. The strain rate at peak DRX conditions was unchanged, but a small shift in temperature was noted [4]. We have studied also Zircaloy-2 in two initial microstructural states (beta-quenched [1] and α-annealed [unpublished]) and found that DRX conditions are not altered.

Question 4, Zhongwen Yao, Queens University:—Is the change on activation energy significant when changing alloying elements?

Author's Response:—The estimates of activation energy of deformation by kinetic analysis as well as by thermally activated deformation analysis show that there is a significant effect of alloying elements (Tables 3 & 4).

Question 5, BRACHET Jean-Christophe, CEA, France:—It seems to me that oxygen and probably some other impurities like Fe etc have an influence on static recrystallization. What about its influence on DRX? What are the oxygen concentrations in your alloys?

Author's Response:—It is known that oxygen is α stabilizer and therefore volume fraction of α as well as α to β transformation temperature will be influenced. This may shift the DRX domain. Further, in the temperature range of DRX of this study, oxygen atoms are not expected to act as barrier to dislocation glide. Thus the dislocation mechanism involved in DRX process of different Zr alloys of this study will not be influenced by oxygen. In this investigation oxygen content was in the range of 1100-1200 ppm for different Zr-alloys studied and the variation of thermally activated parameters are not due to oxygen. However, to assess the effect of oxygen on the DRX characteristics, similar studies with different oxygen content should be carried out. As regards the effect of Fe on the DRX, since Fe

is β stabilizer and has very limited solubility in α-phase, Fe may not have any influence on α-DRX characteristics.

Question 6, Young S. Kim, KAERI:—Please comment on why Zr-Nb-Sn-Fe alloy showed the highest activation energy when compared to the other alloys?

Author's Response:—It can be seen from Table 4 that the SFE is decreased on alloying by both Sn (α-stabilizer) and Nb (β-stabilizer) as ΔG_c component is enhanced compared to CP-Zr. Since both Sn and Nb decrease SFE, the maximum ΔG_0 is associated with Zr-Sn-Nb-Fe alloy followed by Zr-Sn and remaining Nb containing alloys. Please see discussion section for details.

Question 7, Young S. Kim, KAERI:—1) Please comment on why Zr-Nb-Sn-Fe alloy showed the highest activation energy when compared to the other alloys? 2) The author comments that stacking fault energy changed with the addition of Nb, Fe, Sn. Please comment on how much the stacking fault energy of zirconium matrix changed with each element? 3) According to your microstructure showing dislocations, it seems to me that cell type dislocations were formed. Could you comment on why cell type dislocations were formed?

Author's Response:—1) It can be seen from Table 4 that the SFE is decreased on alloying by both Sn (α-stabilizer) and Nb (β-stabilizer) as ΔG_c component is enhanced compared to CP-Zr. Since both Sn and Nb decrease SFE, the maximum ΔG_0 is associated with Zr-Sn-Nb-Fe alloy followed by Zr-Sn and remaining Nb containing alloys. Please see discussion section for details.

2) We have not estimated the stacking fault energy (SFE) values of the alloys studied. As regards the effect of alloying additions on SFE of CP-Zr, reliable data are not available in literature to confirm the effect of alloying. However, the values of ΔG_0 for different alloys indicate that SFE is reduced on alloying of either type.

3) Cross slip of screw dislocation have been identified as the rate controlling dislocation mechanism for DRX. It is known that Zr deforms normally by prism slip over a wide temperature range from ambient to α/β transformation temperature. When dislocations on a prism plane assume screw orientation, they can dissociate into a pair of partials on basal plane separated by a stacking fault. For continued slip under applied stress these partials recombine and screw components cross-slip on to the primary prismatic plane leading to formation of hexagonal networks/dislocation tangles. With further deformation these networks/ dislocation tangles develop into cells and then finally into subgrains. In fact these features are precursor to subgrains. Similar dislocation cell structure has been observed during hot extrusion of Al-alloy[17].

Question 8, Baifeng Luan, Chong Qing University, P. R. China:— 1) What is the effect of the second phase particles on the DRX in different zirconium alloys? 2) Does the second phase particle influence the Q value and how to remove it.

Author's Response:—1) In general the second phase particles which are stable at DRX temperatures are expected to promote the DRX process as nucleation process will be favored because of enhanced dislocation generation and interaction. In this study the DRX of α-phase has been established in single phase as well as two phase (α+β) phase field. α-phase in the alloys studied are not expected to contain significant volume fraction of second phase particles to influence the DRX characteristics.

2) Yes, in general the material containing second phase particles has higher Q value compared to that for single phase material. The changes in activation energy values seen in these alloys are due to alloying elements rather than the second phase particles. We can not comment on how to remove influence of second phase particles on activation energy.

Reprinted from JAI, Vol. 7, No. 7
doi:10.1520/JAI103011
Available online at www.astm.org/JAI

Maria Ivermark,[1] *Joseph Robson,*[2] *and Michael Preuss*[2]

Measurement and Modeling of Second Phase Precipitation Kinetics in Zirconium Niobium Alloys

ABSTRACT: Commercial zirconium alloys contain second phase particles (SPPs) that are precipitated during processing. These particles not only influence mechanical properties but more crucially also have a profound influence on the corrosion performance. To understand how to control evolution and size distribution of SPPs, it is necessary to know how alloy composition and process variables influence the precipitation kinetics. In this work, a detailed study has been performed of the precipitation kinetics in binary Zr-1 wt % Nb, Zr-2.6 wt % Nb, and ternary variants with added iron and tin. A numerical model has also been developed to predict the precipitation kinetics of β-Nb in niobium containing zirconium alloys. Precipitation has been tracked by synchrotron X-ray diffraction measurement of lattice parameter change in the zirconium matrix as solute is removed into SPPs. The X-ray data has been complemented by thermoelectric power measurements. The combination of these two approaches is shown to be effective in quantifying the overall precipitation kinetics of SPPs. The results confirm previous observations that without prior deformation, precipitation kinetics is very sluggish in the binary Zr–Nb system. Deformation accelerates precipitation, and this effect is much stronger for the 1 wt % Nb alloy than for 2.6 wt % Nb, because the supersaturation is least. Ternary additions also have a profound effect on the overall precipitation kinetics. Iron accelerates the rate of niobium loss from solution, whereas tin additions appear to increase the incubation time for the onset of precipitation of niobium.

Manuscript received January 31, 2010; accepted for publication May 21, 2010; published online July 2010.
[1] Westinghouse Electric Sweden AB, Västerås 721 63, Sweden.
[2] School of Materials, University of Manchester, Grosvenor St., Manchester M1 7HS, United Kingdom.

Cite as: Ivermark, M., Robson, J. and Preuss, M., "Measurement and Modeling of Second Phase Precipitation Kinetics in Zirconium Niobium Alloys," *J. ASTM Intl.*, Vol. 7, No. 7. doi:10.1520/JAI103011.

Copyright © 2011 by ASTM International, 100 Barr Harbor Drive, PO Box C700, West Conshohocken, PA 19428-2959.

KEYWORDS: zirconium alloys, precipitation kinetics, synchrotron X-ray, modeling

Introduction

Niobium is an important alloying element in several commercial zirconium alloys, and understanding the kinetics of its precipitation from or dissolution into the matrix is critical in predicting alloy performance. The possible equilibrium precipitate phases may be identified with reference to the Zr–Nb binary phase diagram [1] (Fig. 1). In Zr-alloys for nuclear applications, the alloying elements are normally completely dissolved into the β-phase matrix while only having a very limited solubility in α−Zr. During heat treating and particularly during ageing or stress relief heat treatment, second phase particles (SPPs) are formed when the solubility limit is exceeded [2]. The formation of precipitates involves several stages: Nucleation of the new phase from clusters of atoms, growth of these clusters by diffusion of atoms, and coarsening of the particles [3]. The diffusion rate depends upon several factors, such as diffusion path and temperature, and is several order of magnitudes faster for small interstitial-type elements (Cr, Fe, and O) compared to the self diffusion of Zr and substitutional-type elements (Nb and Sn) in α−Zr [4,5]. A number of common Zr-alloys including compositions, SPPs, solubility limits, and magnitude of diffusion rates of

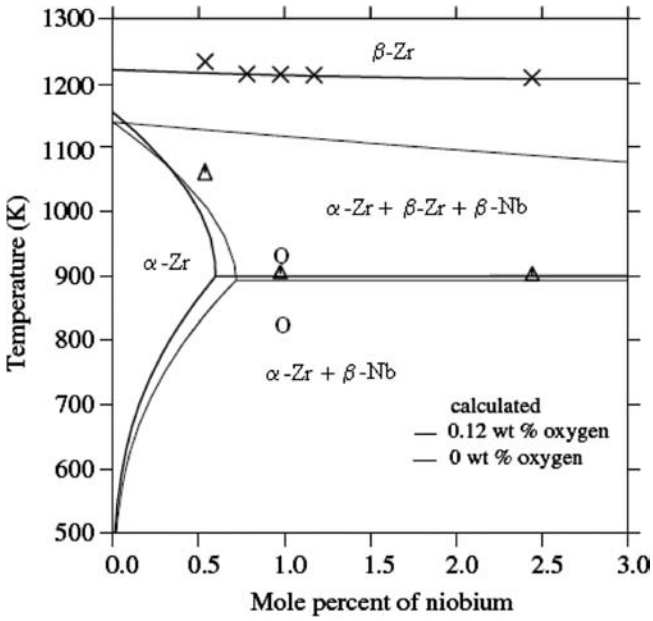


FIG. 1—*The Zr-rich corner of the calculated Zr–Nb phase diagram adapted from Ref [1] including the Zr-1 wt % Nb binary alloy measured by SXRD and heat treated at the two temperatures indicated by black circles. One heat treatment was performed in the α-Zr phase domain (823 K) and the other in the (α+β)-Zr phase domain (923 K).*

TABLE 1—*Commercial zirconium alloys used in nuclear reactors [37], their composition, family of SPPs, and solubility limits.*

Alloy	Nb (%)	Sn (%)	Fe (%)	Cr (%)	Ni (%)	O (ppm)	SPPs
ZIRLO	1.02–1.04	0.96–0.98	0.094–0.105	0.0079–0.0083	···	900–1200	$Zr(Nb,Fe)_2$ [36]
Zry-2	···	1.3–1.6	0.07–0.20	0.05–0.16	0.03–0.08	1000–1400	$Zr(Fe,Cr)_2$, $Zr_2(Fe,Ni)$ [38]
Zry-4	···	1.2–1.7	0.18–0.24	0.07–0.013	···	1000–1400	$Zr(Fe,Cr)_2$ [39]
M5	0.80–1.20	···	0.015–0.06	···	···	900–1800	$Zr(Nb,Fe)_2$, β–Nb [36]
Solubility limit (α–Zr) [a]	< 0.6		$<\sim 0.1$	$<\sim 0.2$	< 0.1		
Magnitude of diffusion, D (m^2/s) [b]	10×10^{-21}–10×10^{-25} [c]	10×10^{-21}–10×10^{-25} [c]	1×10^{-10}	1×10^{-15}	1×10^{-10}	1×10^{-17}	

[a] At room temperatures [14].
[b] Temperature range of 550–650°C [4].
[c] Substitutional-type diffuser range [4].

TABLE 2—*Chemical composition ranges of the Zr–Nb alloys studied.*

Sample	Composition (wt %)	Study
Zr–Nb binaries	0.1–2.6Nb	Ex situ
Zr–Nb binaries	1.0Nb, 2.6Nb	In situ
Zr–Nb ternary	1.0Nb-0.2Fe	In situ
Zr–Nb ternary	1.0Nb-0.8Sn	In situ

elements are summarized in Table 1. From an in-reactor performance point of view, it is important to recognise that some types of SPPs start dissolving during irradiation, affecting the performance of the material [6]. Of particular importance are Nb-containing zirconium alloys since SPPs in such alloys are significantly more stable during irradiation compared to Fe-containing particles, which dissolve during reactor operation [7]. So far, most corrosion research on zirconium alloys has focused on the oxide layer [8,9] and precipitation chemistry [10,11] as some of the dissolved precipitates are thought to be involved in oxide formation [12]. The average matrix chemistry, comprising the remnant alloying elements not bound up in the SPPs, is also likely to be important in the corrosion process [13]. To understand how the mean matrix chemistry evolves during processing and heat treatment of zirconium alloys is thus a key part of understanding the corrosion process. The low solubility of alloying elements in commonly used zirconium alloys makes the direct measurement of matrix chemistry very challenging [14]. This paper describes a new method for determining changes in matrix chemistry during SPP formation, thus providing complementary information to direct studies of SPPs themselves.

The first part of this paper summarizes the characterization of the matrix of zirconium alloys. Here, the difference in matrix composition is related to the *a*-lattice parameter variation using X-ray diffraction (XRD) complemented by thermoelectric power (TEP) measurements. Second, a detailed study of the precipitation kinetics in binary Zr−1 wt % Nb, Zr−2.6 wt % Nb alloys, and ternary variants with added tin and iron is described. These alloys were investigated in situ during heat treatment in the α−Zr + β−Nb phase and ($\alpha + \beta$) Zr-phase domains. Finally, the results of the present study, together with data from the literature, have been used to test a model for precipitation kinetics in zirconium alloys [15].

Experimental Procedures

Materials and Sample Preparation

In the present study, binary and ternary zirconium alloys were produced over a range of compositions to include those found in commercial zirconium alloys (see Table 2). The starting material consisted of zirconium chips from a low oxygen and low impurity ingot (Western Zirconium, United States), with Nb added in the range of 0.1–2.6 wt %. The binary and ternary niobium containing Zr-alloys were melted using an arc furnace technique [16] and remelted four

TABLE 3—*Sample preparation procedures.*

	Process	Temperature (°C)	Time (min)	Rate (°C/s)	Total Thickness Reduction (%)	Comment
1	Cross roll	540	···	···	50	
2	Anneal	600	60	···	···	
3	Cross roll	540	···	···	75	
4	β-heat treatment	1000	10	···	···	
5	Water quench	1000–25	···	1500[a]	···	
6	Rolling	25	···	···	82–87	Only SXRD samples

[a] Temperature monitored by two thermocouples mounted in the center and bottom end of a pure Zr sample using the same quenching method and setup as the investigated samples.

times under argon atmosphere for homogeneity and to avoid contamination from air impurities. The buttons were then cross rolled to a total rolling strain of 75 % over ten passes at 540°C, heat treated as thin matchsticks above the β-phase transformation temperature for 10 min in a vertical furnace, and followed by water quenching in an attempt to keep all alloying elements in solution (see Table 3). All heat treatments were performed under argon atmosphere in order to minimize oxidation of the sample surfaces. These matchstick samples were subsequently cut into suitable dimensions to undertake TEP, XRD, and synchrotron XRD (SXRD) measurements, respectively. Some SXRD samples were pre-rolled prior to in situ heat treatment to investigate the effect of deformation on the precipitation kinetics. This final rolling gave a total rolling strain of 87 %, which was performed after β-quenching at room temperature. The sample preparation procedures are more thoroughly described in Ref [17].

Ex-situ X-Ray Diffraction

With alloying elements present in the Zr structure, the lattice parameter will be affected as these elements occupy different sites within the cell. The compositional change due to variations in solute concentration will thus cause changes in the lattice parameter. These changes can be detected as phase peak shifts in an XRD diffraction spectrum. Several other factors, such as instrumentation contributions and sample quality, can also cause peak shifts, but measures can be taken to substantially limit those effects. A reliable Si powder standard calibrated each measurement run, and with long counting times over full diffraction pattern scans errors such as specimen displacement and zero shift were corrected. The lattice spacing, d_{hkl}, was measured using XRD, and the a-lattice parameter was determined for the studied alloys. The machine parameters are given in Table 4. Further processing of the data, including profile fitting and lattice parameter refinement, was conducted in order to minimize the peak shift attributed to sample conditions.

At small concentrations of substitutional alloying elements, it is usually found that there is a linear relationship between impurity concentration and the lattice parameter. This is stated in Vegard's law [18] given in Eq 1

TABLE 4—*Machine and analysis parameters used for the XRD lattice data.*

Philips PW37 10 Diffractometer	
Source	Cu−K_α radiation ($\lambda_{\alpha 1} = 1.540\,56$ Å ; $\lambda_{\alpha 2} = 1.544\,39$ Å)
Generator voltage	50 kV
Tube current	40 mA
Detector	Sealed xenon-filled proportional detector
Monochromator	Graphite diffracted beam monochromator
Filter	None
Receiving slit	0.200 mm
Specimen geometry	$15 \times 15\,mm^2$
Scan range	30°–120°
Step size	$0.02\,2\theta/^\circ$
Scan time per step	20 s
Data acquisition rate	19.5 h
Analysis	21 α−Zr peaks identified from reflections 100–213
Reference pattern	α−Zr a-lattice parameter = 3.242 Å [40]
Data handling	X'Pert Pro (Rietveld routine)

$$a_{\text{alloy}} = x \times a_{ae} + (1 - x) \times a_{\text{Zr}} \tag{1}$$

where:

a_{alloy} = lattice parameter in nm,

x = atomic fraction of the alloying element,

a_{ae} = lattice parameter of the alloying element (assuming the same crystal structure), and

a_{Zr} = lattice parameter of the base matrix.

Since pure Nb does not have the same crystal structure as α−Zr, it is necessary to use the atomic size [18] to calculate the Nb parameter used in Eq 1.

Thermoelectric Power

The change in Nb concentration in the binary Zr–Nb alloys was also analyzed by TEP measurements. One alloy (Zr−1.0 wt % Nb) was solutionized in the β-phase region as previously described, quenched, and heat treated for times ranging from 2 to 72 h at 450, 550, and 650°C, with TEP measured after each treatment. TEP appears as an electric potential difference when two metals in tight contact form a thermocouple with two junctions held under a temperature difference [19,20]. This power can generally be described by the Nordheim–-Gorter rule [21], which relates the measured TEP of the alloy (relative to reference metal) to the specific resistivity (α) of the alloying element, concentration, the specific TEP of the alloying element, and impurities and the resistivity of the alloy (ρ). The theory of TEP in transition metals and the application of TEP to

TABLE 5—*Machine [41] and analysis [40] parameters used for the in situ ESRF data.*

ID 31, European Synchrotron Radiation Facility, Grenoble, France	
Source	Synchrotron, 40 keV ($\lambda = 0.300\,112\,14$ Å)
Detector	Bank of eight (crystal monochromator) with a 2° separation; reproducible to tenth of a millidegree; instrument contribution 0.003° to FWHM
Specimen geometry	0.7 mm diameter, 2 mm length
Standard	Si powder
Data acquisition rate	70 s
Analysis	Ten peaks identified from reflections 100–004
Temperature	550 and 650°C for 2 h
Data averaging	84 runs (120 min)
Data handling	Topas (Rietveld refinement)

highly dilute alloys, such as the concentrations of the studied Zr–Nb alloys, are further discussed in Refs [22 and 23] and Refs [21 and 24], respectively.

In practice, two blocks are made from a reference metal and maintained at temperature T and $T + \Delta T$, respectively. The flat specimen is clamped on these blocks to provide a good thermal and electrical contact. Here, the relative TEP of the specimen, ΔS, at the mean temperature $(T + \Delta T)/2$ is given by Eq 2

$$\Delta S = \Delta V/\Delta T \ (\mu\text{V/K}) \tag{2}$$

where:

ΔV = low voltage between the reference blocks.

The measured TEP, which is the relative TEP of the specimen with respect to the reference metal, can then be plotted as a function of concentration of solid solution in the matrix. In Zr–Nb alloys, TEP becomes more negative with increasing solute concentration of Nb as further discussed in Ref 25.

The TEP was measured using a TechMetal Promotion instrument [20] (INSA, France). The temperature of the two copper blocks was held at 15±0.2 and 25±0.2°C, respectively, and the TEP of the specimen relative to a reference metal (Cu) was measured.

Synchrotron X-Ray Diffraction

The measurement of the change in lattice parameter related to the dissolution of precipitates into the matrix was conducted in situ at the high energy powder diffraction beam line ID31 (ESRF, France). The machine and analysis parameters are summarized in Table 5. During the experiment, the encapsulated cylindrical samples were rotated in order to improve the diffraction response. Measurements were carried out in transmission due to the high energy used during the experiment. Each detector was preceded by a Si 111 analyzer crystal to give very accurate peak positions, thus providing lattice parameter values

with errors less than a few tenths of mÅ. A calibration standard (Si powder) was also used before and after each experimental run. The heat treatment temperatures used for in situ studies were chosen to be both below and above the $\alpha \rightarrow \alpha + \beta$ transition in Nb-containing zirconium alloys, which is known to be around 600°C [1,25]. Thus the SXRD specimens were heated at 550 and 650°C for 2 h, respectively, in order to allow for precipitation. Table 2 summarizes the alloys used for in situ studies. Both the Zr−1 wt % Nb and Zr−2.6 wt % Nb alloy, rolled and undeformed, were studied at 650°C. The Zr−1 wt % Nb alloy, rolled and undeformed, was studied at 550°C, whereas only the rolled Zr−2.6 wt % Nb was studied at 550°C.

Each diffraction pattern was processed using Rietveld refinement in order to account for the effect of internal microstresses on the lattice spacings [26]. This refinement is a mathematical method to compare a measured diffraction pattern with a predicted spectrum of a certain crystal structure. The analysis of a whole diffraction pattern can thus be used to reduce microstress effects from individual grain families on the lattice parameter values as further described in Refs 27 and 28.

Modeling Precipitation Kinetics

The measurements of lattice parameter change during precipitation provide valuable data to test a recently developed model for precipitation kinetics in zirconium alloys. The advantages of such a model, once validated, is that it can be used to make predictions for compositions and thermal histories not studied experimentally.

The model developed in this work has been presented elsewhere [15], and only the key points will be summarized here. For full details of the model, see Ref 15.

- The model is based on the Kampmann and Wagner numerical (KWN) framework [29]. In this method, the evolution of precipitates is considered by tracking the full precipitate size distribution over a series of small time-steps.
- The precipitate size distribution is divided into a discreet number of size classes. In each time-step, new particles (formed by classical nucleation) are added to the distribution, and existing particles are exchanged between size classes under the influence of classical diffusion controlled growth.
- The mean matrix composition is calculated at each time-step from the precipitate composition and volume fraction and used to provide the matrix composition for the next time-step (the mean-field approximation).
- Regimes of nucleation, growth, and coarsening evolve naturally in the KWN model as the matrix composition changes.

The KWN method has been successfully used to predict precipitation kinetics in many alloy systems [29,30]. Like all phase transformation models, it relies on accurate thermodynamic and kinetic data (e.g., diffusion data). In the

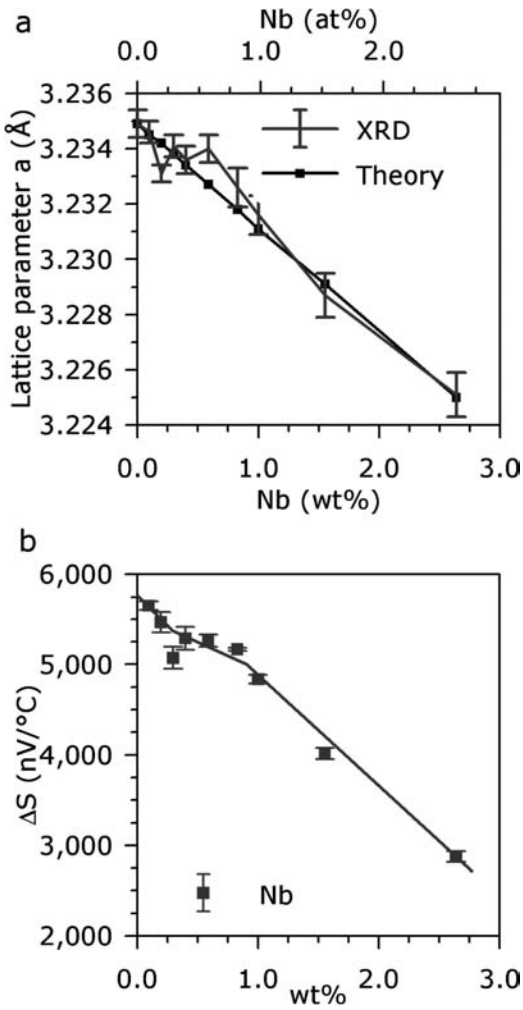


FIG. 2—*Comparison between measured and calculated a-lattice parameter shows a very good agreement for Zr–Nb binary alloys (a), where all Nb was successfully retained in solution after β-quenching. Each lattice parameter value is determined from 21 α-Zr peaks with measurement error bars as indicated. TEP measurements of Zr–Nb binary alloy show a decreasing TEP with increasing concentration of solid solution in the matrix (b). Average value of eight measurements per sample.*

case of modeling zirconium alloys, this data is not always available, particularly for ternary and higher order systems. In the present study, the model was applied only to predict precipitation kinetics in the Zr–Nb binary system, an example where the necessary thermodynamic and diffusion coefficient data are available. The equilibrium phase compositions were taken from Ref 1, which includes the effect of oxygen. Diffusion data was obtained from Ref 31.

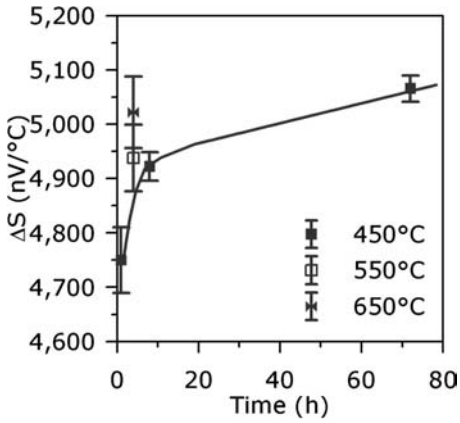


FIG. 3—*TEP measurement (average of eight values per sample) of Zr-1 wt % Nb heat treated at three different temperatures. More Nb precipitated with increased time and temperature, which decreased the amount of Nb in solid solution and thus increased TEP. Since TEP still showed an increasing trend after 72 h at 450°C, the equilibrium value of Nb solubility is indicated to not have been reached at this point. Longer heat treatments were, however, not performed to prove this.*

The other key parameter in the KWN model, which is generally unknown, is the interfacial energy of the precipitates. The interfacial energy is critical in determining the energy barrier for nucleation and the interfacial compositions (as a result of the Gibbs Thompson effect [32]), which in turn have a strong effect on nucleation, growth, and coarsening rates. Generally, the effective

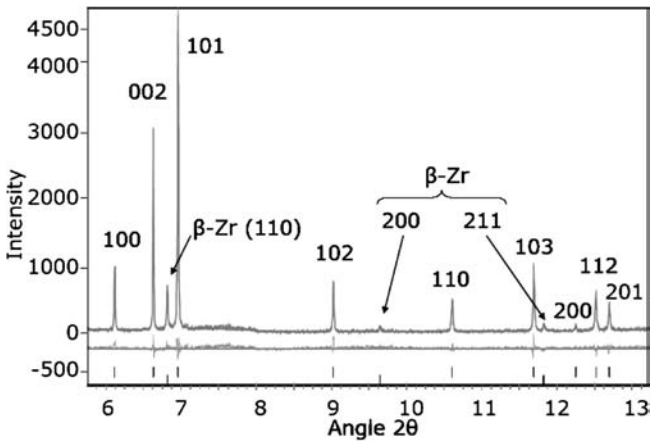


FIG. 4—*A Rietveld fitted in situ synchrotron diffraction pattern of Zr-2.6 wt % Nb at 650°C after 1600 s (~27 min). The first nine α-Zr peaks are indexed with additional β-Zr peaks around 6.8°, 9.6°, and 11.8°. The bottom gray line is the difference curve between experimental and calculated patterns with peak positions shown as vertical lines.*

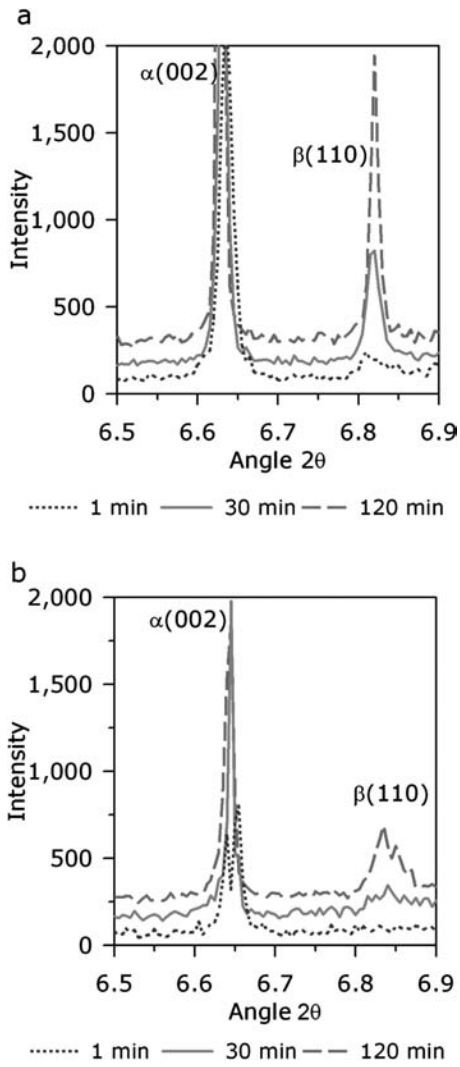


FIG. 5—*The development of β-Zr peak at 650°C for (*a*) β-quenched and rolled compared to (*b*) β-quenched Zr-2.6 wt % Nb. The intensity of β-Zr increased more dramatically and rapidly in the rolled sample compared to the only β-quenched sample.*

interfacial energy has to be obtained by tuning the model to fit experimental data, with the constraints that the interfacial energy should be physically reasonable for the interface type (e.g., coherent, incoherent).

There are additional complications when applying the KWN model to predict precipitation kinetics in the Zr–Nb binary system. For precipitation at 550°C, the equilibrium precipitate phase is $\beta-$Nb (~ 95 at. % Nb). For precipitation at 650°C, the equilibrium precipitate phase is $\beta-$Zr (~ 12 at. %). These phases have different interfacial energies and also have different morphologies.

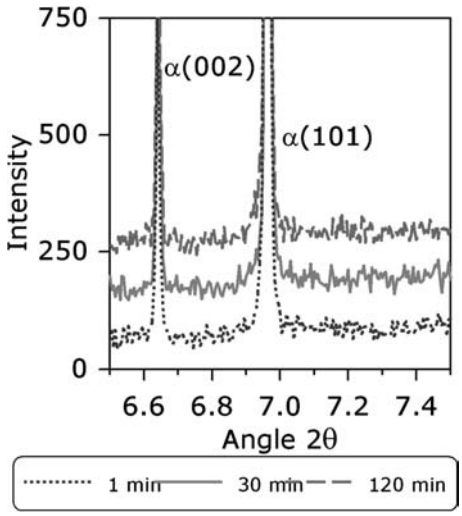


FIG. 6—*Lack of β-Nb peak; if present, the reflection of 110 is around 7.4° at 550°C for the β-quenched and rolled Zr-2.6 wt % Nb. Only α-Zr reflections 002 and 101 are present.*

Furthermore, precipitation is rarely observed to be homogeneous but occurs heterogeneously at certain sites (e.g., lath boundaries). In the present model, only the differences in interfacial energy and phase composition are considered.

Finally, to compare model predictions with experimental results, it is necessary to convert the model output into a suitable parameter. Experimentally, the precipitate volume fraction was inferred indirectly from the change in matrix chemistry as determined by measuring the lattice parameter change. The model

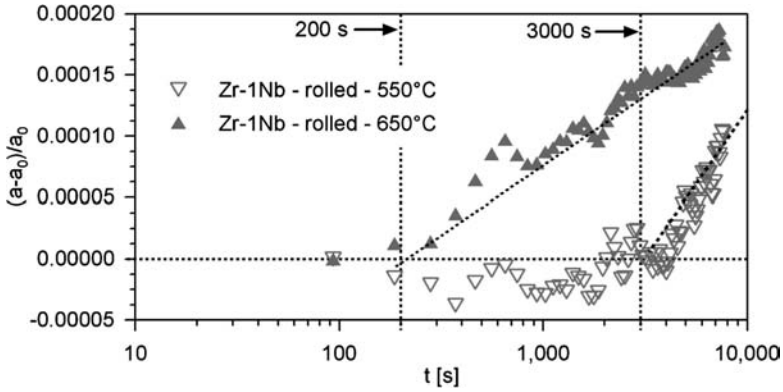


FIG. 7—*The kinetics compared for Zr-1 wt % Nb at two different temperatures. The samples were β-quenched and rolled before the heat treatment. The lattice parameters* $a_0(550^\circ C)=3.241$ Å, $a_0(650^\circ C)=3.242$ Å, $a(550^\circ C)=3.243$ Å, *and* $a(650^\circ C)=3.244$ Å *were estimated using the model. There is an almost immediate change at 650°C, whereas the change at 550°C becomes apparent after ~3000 s (1 h).*

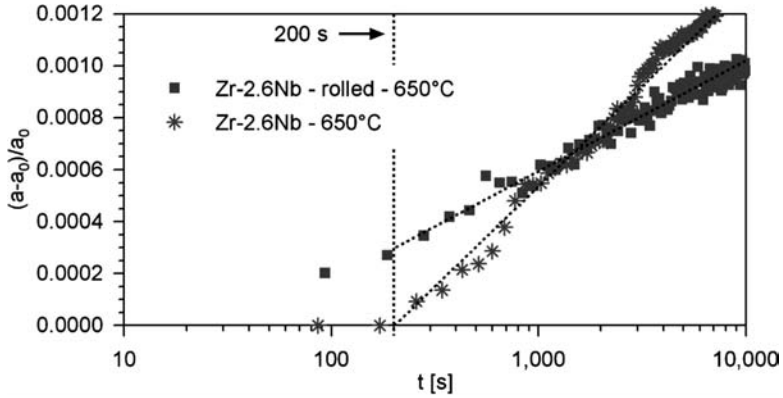


FIG. 8—*The evolution of lattice parameter for β-quenched and rolled Zr-2.6 wt % Nb and as-quenched Zr-2.6 wt % Nb binary alloys at 650°C, respectively. There was an initial difference in diffusion kinetics between quenched and rolled material. The initial* a_0 *and a(equilibrium) were estimated to be 3.232 and 3.244 Å, respectively.*

gives the matrix chemistry as one of its outputs. This was converted into a change in lattice parameter by application of Vegard's law.

Experimental Results

Ex Situ Binary Zr–Nb

The lattice parameters derived from XRD and the measured TEP are shown for solutionized and β-quenched Zr–Nb alloys with different niobium concentrations

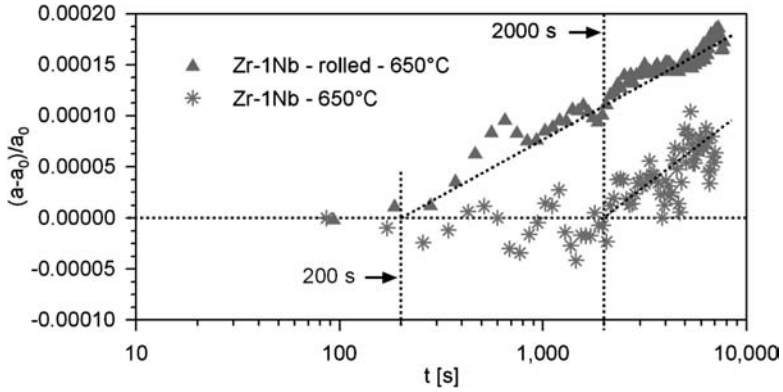


FIG. 9—*The evolution of lattice parameters for β-quenched and rolled Zr-1.0 wt % Nb and as-quenched Zr-1.0 wt % Nb binary alloys at 650°C, respectively. There was a small difference in kinetics between quenched and rolled materials. The precipitation starts after about 200 s for the rolled specimen but not until about 2000 s for the as-quenched material.*

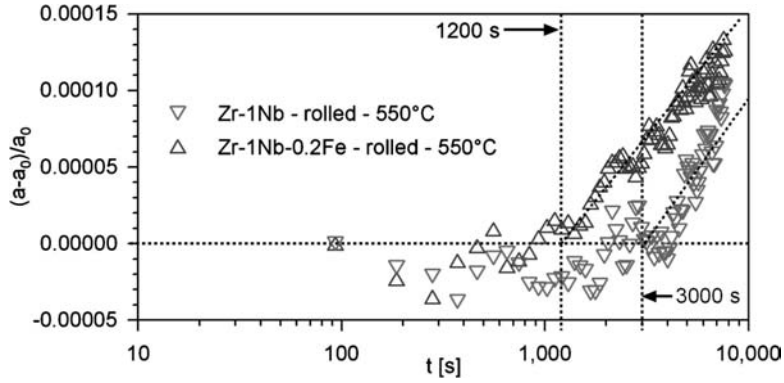


FIG. 10—*Comparison of alloys heat treated for 2 h at 550°C. The accelerated affect due to Fe addition is apparent at this temperature.*

in Fig. 2(*a*), 2(*b*), respectively. This allows both techniques to be compared and confirms the level of retained solute in binary Zr–Nb alloys. Also plotted in Fig. 2(*a*) is the expected change in lattice parameter from Vegard's law, assuming all of the niobium is retained in the solution during the quench. As expected, an increase in niobium content in the matrix leads to a reductionin the *a*-lattice parameter. The measured TEP is also reduced with increasing matrix niobium. The measured change in TEP for the Zr−1.0 wt % Nb alloy as a function of post-quench heat treatment time is shown in Fig. 3. Precipitation during heat treatment leads to a reduction of niobium in the matrix and hence an increase in TEP.

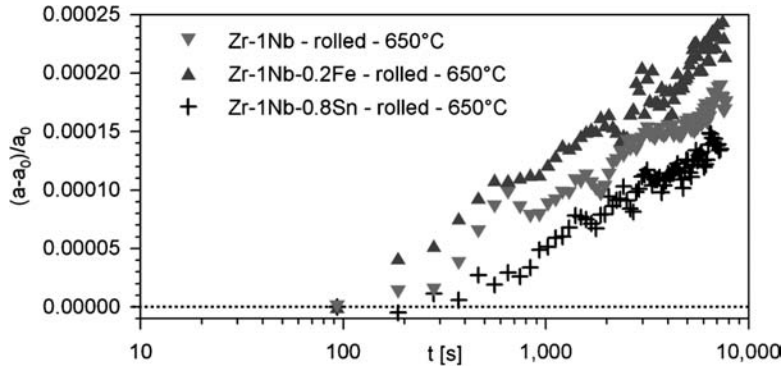


FIG. 11—*The evolution of lattice parameters for Zr-1.0 wt % Nb, Zr-1.0 wt %, Nb-0.2 wt % Fe, and Zr-1.0 wt % Nb-0.8 wt % Sn alloys at 650°C, respectively. Again, Fe seems to have an accelerated affect on the precipitate kinetics. Sn, on the other hand, appears to prolong the incubation time. However, Sn does not seem to affect the precipitation kinetics as both Zr-1 wt % Nb and the Zr-1.0 wt % Nb-0.8 wt % Sn alloys show a similar slope after the initial incubation time. The precipitation kinetics are faster compared to 550°C, which is expected due to faster diffusion rates.*

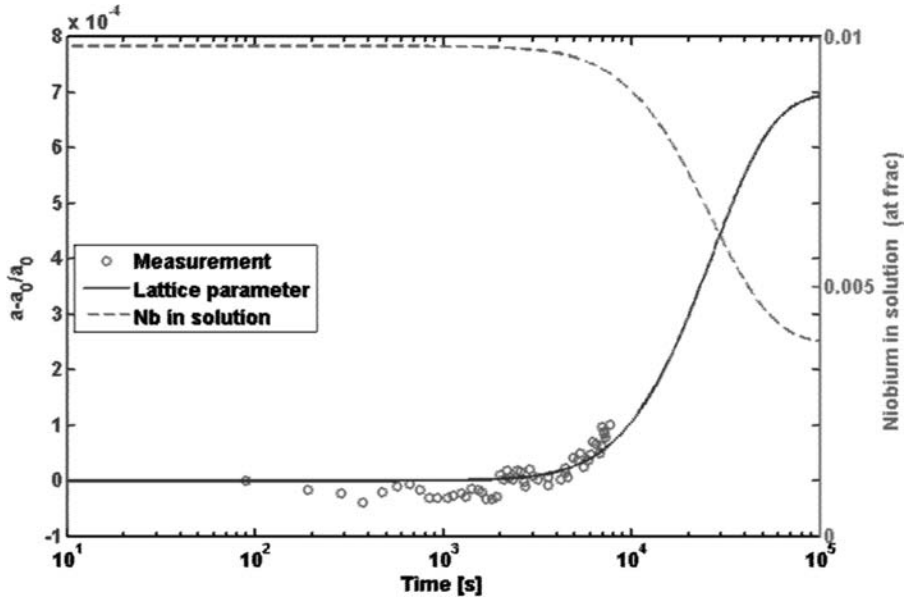


FIG. 12—*Predicted change in matrix niobium concentration and associated variation in lattice parameter for the Zr-1 wt % Nb alloy rolled and heat treated at 550°C. The experimental data for the lattice parameter variation are also shown. No precipitation or change in lattice parameter was observed or predicted in the unrolled specimen at 550°C.*

In Situ Binary Zr–Nb

An example of an indexed SXRD pattern is shown in Fig. 4, corresponding to the Zr−2.6 wt % Nb alloy after 1600 s (∼ 27 min) at 650°C. Each pattern was fitted with parameters taking possible phases, peak shape, preferred orientation, etc. into account. From the diffraction peaks, the *a*-lattice parameter was calculated, and its evolution depending on temperature was investigated. During annealing, the diffraction peaks shifted towards lower angles, i.e., the lattice parameter increased during annealing at constant temperature. According to Vegard's law, this indicates the expected depletion of niobium in the matrix.

Figure 5 shows the development of β−Zr peaks over time at 650°C for Zr−2.6 wt % Nb for (a) quenched and rolled sample and (b) "as-quenched" sample. The intensity of the β−Zr peak at 650°C increased over time as a result of an increased fraction of β−Zr in the alloy in both the unrolled and rolled materials. For the rolled material, the β−Zr peak was visually identified almost instantaneously with a rapid increase in intensity, whereas the as-quenched β−Zr peak appeared much later in the experiment with a slowly increasing intensity. Broader peaks are observed in the β-quenched and rolled samples compared to the undeformed structure, and this is consistent with the expectation that there are more dislocations and stresses introduced into the structure by the rolling process.

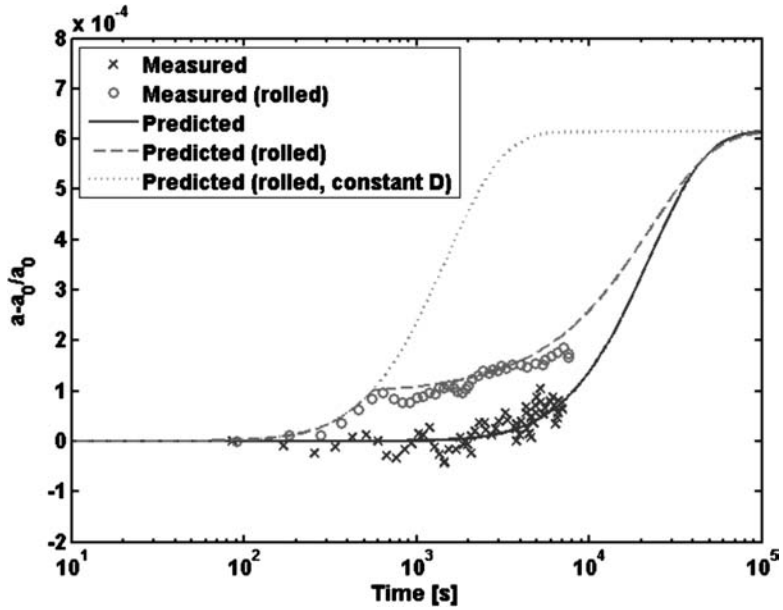


FIG. 13—*Predicted and measured lattice parameters change at 650°C in the unrolled and rolled Zr-1 wt % Nb alloys. A change in kinetics is observed in the rolled alloy at ~700 s and is accounted for in the model by reducing the effective diffusion coefficient (D) during heat treatment. If the diffusion coefficient is kept constant, the amount of precipitation and hence the lattice parameter change at times >700 s are overestimated.*

For specimens heat treated in situ at 550°C (rolled Zr−2.6 wt % Nb, Fig. 6), the expected precipitate phase is β−Nb. However, no peaks from this phase were detected at any time during the in situ study in either the rolled or undeformed material. However, sufficient precipitation did occur in the rolled specimen to produce a lattice parameter change in the matrix, which can be used to infer the volume fraction change, as discussed next. Figure 7 shows the relative change in *a*-lattice parameter over time for rolled Zr−1 wt % Nb heat treated at 550 and 650°C, respectively. There was a significant difference in lattice parameter evolution depending on temperature. In particular, it can be seen that the incubation time before the onset of a detectable change in the lattice parameter is much longer in the sample heat treated at 550°C. In the rolled specimen heat treated at 650°C, there is evidence for a significant change in the precipitation rate after about 600 s with distinct reduction in the rate of change of the lattice parameter around this time. Using the model, the a_0-values and expected values for infinite time *a* at temperature (i.e., at equilibrium) were also estimated for the binary alloys.

The difference in kinetics due to deformation for Zr−2.6 wt % Nb alloy at 650°C is illustrated in Fig. 8 and for the Zr−1 wt % Nb alloy in Fig. 9. The difference in incubation time for a detectable change in lattice parameter in the rolled Zr−2.6 wt % Nb compared to the non-rolled equivalent is approximately 200 s.

This is much less than the change in incubation time in the Zr−1 wt % Nb alloy, which is reduced from ~ 2000 s in the undeformed material to 200 s in the rolled alloy (1800 s difference). The same comparison cannot be made for the Zr−1 wt % Nb alloy at 550°C because no change in lattice parameter was detected for the unrolled specimen even at the longest heat treatment time (2 h). At this temperature, the incubation time for the onset of precipitation is therefore greater than the duration of the experiment (i.e., > 7200 s). The rolled Zr−1 wt % Nb alloy exhibited an incubation time of approximately 3000 s (Fig. 7).

In Situ Ternary Zr–Nb–Fe and Zr–Nb–Sn

The precipitation kinetics of several other Nb-containing zirconium alloys was also investigated at 550 and 650°C, respectively. Rolled Zr−1 wt %Nb−0.2 wt % Fe was compared to Zr−1 wt % Nb at 550°C (Fig. 10) and at 650°C (Fig. 11). At 650°C, rolled Zr−1 wt % Nb−0.8 wt % Sn was also studied. Adding Fe to the alloy reduced the incubation time before a lattice parameter change was detected compared to the Zr−1 wt % Nb binary alloy. On the other hand, adding Sn to the alloy appears to prolong the incubation time. After the incubation time for each alloy was exceeded, the rate of change of the lattice parameter is similar in all cases (the lines are approximately parallel). As in the binary rolled material, there is evidence for a reduction in the rate of lattice parameter change (slope) after 600 s for the binary and Zr−1 wt %Nb−0.2 wt % Fe alloy and after 1500 s for the Zr−1 wt % Nb−0.8 wt % Sn alloy.

Modeling Predictions and Comparison with Experiment

A comparison of the model against the available literature data for precipitation in binary Zr–Nb alloys is presented in detail elsewhere [15], and in this work only the application of the model to the new experimental data will be considered.

Figure 12 shows a comparison of model predictions and measurements for the Zr−1 wt % Nb alloy at 550°C after rolling. The model was also applied to the unrolled material, but consistent with the experimental observations, there was no predicted change in lattice parameter over a reasonable time-scale. Indeed, for the unrolled material, it was predicted that it would take over 114 years to reach equilibrium. The interfacial energy used for the unrolled specimen was $0.25\,J \cdot m^{-2}$. This value has been shown previously to give good predictions of literature data in other alloys [15].

To represent the effect of a reduced energy barrier to nucleation in the rolled material, the effective interfacial energy was adjusted to provide the best fit between the measured and predicted times for the onset of measurable precipitation. To achieve this fit, it was necessary to reduce the effective interfacial energy to $0.18\,J \cdot m^{-2}$. Using this value, a reasonable agreement can be obtained between the model and the limited data available, which cover only the early stages of precipitation. The model confirms that when the experiment terminated, the niobium concentration in the matrix was still far from equilibrium. The model predicts that it would take 26 h at 550°C to reach the equilibrium

volume fraction in this alloy, after the pre-rolling treatment used in this work. At 650°C, the precipitating phase is expected to be β−Zr. The predicted and measured precipitation kinetics is shown in Fig. 13. At this temperature, the precipitation in the non-rolled specimen is greatly accelerated over that at 550°C. Enhanced diffusion rates at the higher temperature will contribute to this acceleration, but this effect alone was insufficient to give predictions that agreed reasonably with experiment. The best fit to the experimental data in the unrolled case at 650°C was obtained using a value for the effective interfacial energy of $0.032\,J \cdot m^{-2}$.

The effect of rolling on the kinetics at 650°C is less strong than at 550°C. Fitting the model to the rolled data at 650°C was achieved by further reducing the effective interfacial energy to $0.029\,J \cdot m^{-2}$. It can be seen that using this value, the predictions match the measurements well in the earliest stages of precipitation but deviate after ~ 700 s. At this point, there is a marked change in gradient of the experimental data. Although the cause of this is unclear, it is possible that the defects leading to enhancement of the early stage kinetics are eliminated by annealing. It was found that this effect was best simulated in an approximate way by reducing the effective diffusion coefficient during the heat treatment. Physically, this effect would result from elimination of defects that enhance diffusion due to the recovery and recrystallization. To reproduce the change in gradient seen in the experimental data, it was necessary to reduce the effective diffusion coefficient by a factor of 18 once the time exceeded 540 s.

Discussion

The analysis of as-quenched Zr–Nb binary alloys by XRD and TEP (Fig. 2) showed a linearly decreasing trend with increasing amounts of solutes without reaching a horizontal plateau. The maximum level of a supersaturated Zr–Nb matrix has previously been reported to be $\sim 1.5\%$ Nb in a Zr-2.5 % Nb β-quenched alloy [33]. However, the results indicate that all added niobium is retained in solution after β-quenching even in alloys with 2.6 wt % Nb at the quench rate used here (~ 1500°C/s). Consistent with the conclusion that all the niobium was retained in the solution during the quench was the lack of a detectable β reflection in any of the as-quenched samples. Figure 2(*a*) shows that Vegard's law provides a good fit to the lattice parameter change across the composition range studied. This confirms the validity of using the measured lattice parameter change as a direct indication of the niobium in solution.

The TEP data supports the XRD data and also did not show a plateau that would indicate that the maximum solubility of Nb in the matrix had been reached. An increased niobium concentration in the matrix leads to a decreasing TEP, consistent with a previous study [25].

The TEP results for different precipitation heat treatments (Fig. 3) confirm the sluggish precipitation kinetics of β−Nb, as has been noted previously [9,15,34]. At 450°C, an increase in TEP associated with matrix depletion due to precipitation is easily measured; however these results also confirm that even after 72 h, a considerable supersaturation of niobium remains in solution.

The diffraction pattern shown in Fig. 5 after heat treatment for 1600 s at 650°C in the Zr−2.6 wt % Nb alloy shows clearly the β−Zr peaks associated with the precipitation of this phase. It is noteworthy that for heat treatment at 550°C, where the precipitate phase is β−Nb, no precipitate peaks were observed (Fig. 6) even when the lattice parameter measurements indicated that precipitation had occurred. This is likely to be due to the smaller volume fraction of β−Nb precipitates compared to β−Zr, which are below the limit directly detectable. However, as demonstrated, even when the β−Nb peaks cannot be found, the precipitation kinetics can be deduced from the change in matrix solute level derived from the lattice parameter change measured for the α−Zr matrix.

Previous studies [9,15,33] have investigated the difference in β-phase kinetics depending on heat treatment temperature. The time to reach β-phase equilibrium differs greatly, with "only" 10 h at 640°C compared to several hundred hours below the $(\alpha + \beta)$ transformation temperature [9,34]. These observations are consistent with the present results. In particular, both the present results and previous work suggest that even after 2 h at 650°C (the longest time used in the in situ study), the precipitate fraction is still well below the equilibrium value. At 550°C, no precipitation was detectable in the unrolled material, and even in the rolled specimen, a long incubation time ($\sim$ 3000 s) was measured (Fig. 7). This time is consistent with previous results from a cold work study of Zr−1 wt % Nb [34], which also showed detectable precipitation after 1 h at 550°C for the same alloy content.

Figures 8 and 9 show clearly the accelerating effect of pre-rolling on the precipitation kinetics. This acceleration is greatest in the more dilute alloy (Zr−1 wt % Nb). This observation implies that in addition to providing rapid diffusion pathways, the defects introduced by rolling also reduce the energy barrier to nucleation. This effect is most potent in the more dilute alloy, where the nucleation energy barrier will be greatest. This conclusion is also consistent with the modelling work, where it has been shown that a large reduction in nucleation energy barrier must be enforced in the model to correctly predict the precipitation kinetics in the rolled material.

An additional complicating effect during precipitation in the rolled material at 650°C is that recrystallization is expected to occur under these conditions. Recrystallization would be expected to lead to elimination of the defects accelerating precipitation and could even lead to a slowing of the kinetics if fast diffusion pathways were annealed out. This may explain why there is a cross over in Fig. 8 with the amount of precipitation in the unrolled material apparently overtaking that in the rolled material after $\sim$ 2000 s. However, this point needs further investigation to clarify. Evidence for the influence of recrystallization is also observed in the change of gradient noted for the data from rolled material (both binary and ternary alloys; Figs. 9 and 11). It is plausible that this change in gradient (which corresponds to a reduction in the precipitation rate) is due to recrystallization removing defects that accelerate precipitate nucleation and growth. The model predictions (Fig. 13) show that if the effect of recrystallization is not accounted for, no change in gradient would be expected and the predicted time taken to reach equilibrium would be much less than that measured. If, however, the model is modified by assuming that the diffusion rate is

reduced during heat treatment due to annealing, then the fit to the data is much improved.

The interpretation of the ternary data is complicated by the addition of an extra element. The addition of iron was observed to lead to a decrease in the time for the first observable change in lattice parameter. The lattice parameter change observed was, as in the case of the binary Zr–Nb alloys, a reduction and is dominated by the removal of niobium from solution into β−Zr (at 650°C, the temperature studied here). Although the iron content is low, there is a possibility of precipitation of $Zr(Nb, Fe)_2$, into which a small amount of the available niobium will partition. The addition of iron also reduces the total solubility limit of niobium in the matrix. The earlier apparent onset of precipitation in this alloy may be due to formation of the $Zr(Nb, Fe)_2$ phase. Nevertheless, regardless of how it precipitates, the present results indicate that iron has an accelerating effect in removing niobium from solution during heat treatment. The addition of tin leads to the opposite effect—a retardation in the removal of niobium from the matrix. At the levels of addition used here, tin is expected to be retained in solution. The origin of the retardation is not clear, but it may be related to the observation that tin slows down other thermally activated processes such as recrystallization in Zr–Nb alloys [35,36]. If this is the case, then it is likely that tin is acting by reducing the diffusion rate of niobium rather than an influence on the driving force for precipitation. Further studies are required to clarify these observations.

Conclusions

(1) Consistent with previous studies, the diffusion of Nb in Zr was found to be extremely sluggish. Nb was fully retained supersaturated in the solution after β-quenching in the range of alloys examined here (up to 2.6 wt % Nb) and precipitated very slowly at both 550 and 650°C, not having reached equilibrium even after 2 h.

(2) Deformation has an initial accelerating effect on precipitation in Zr–Nb alloys, mainly as an effect on the incubation time until precipitation occurs. The deformation effect was particularly profound for the slightly supersaturated Zr−1 wt % Nb alloy, with the time for a detectable change in matrix lattice parameter due to precipitation reduced by a factor of 10.

(3) The change in lattice parameter with time in deformed alloys heat treated at 650°C showed a distinct change in gradient early on during precipitation. Beyond this time, the precipitate rate was similar to or even less than in the undeformed material. It is proposed that this is due to recrystallization, which removes the defects responsible for enhancing the precipitation kinetics.

(4) A model has been applied to predict the precipitation kinetics of β−Zr and β−Nb in the binary Zr–Nb alloys. Correct prediction of the onset time for precipitation is only obtained if the effective interfacial energy for the β−Zr is taken as being $0.032\,J \cdot m^{-2}$, which is much lower than the value used for the β−Nb phase ($0.25\,J \cdot m^{-2}$).

(5) The model can be used to capture the effect of rolling on the precipitation kinetics but only by reducing the effective interfacial energy (energy barrier). At 650°C, a good fit to the data can only be achieved by allowing the diffusion rate to reduce during heat treatment, simulating removal of defects that act as fast diffusion pathways during high temperature heating.
(6) Addition of small quantities of Fe (0.2 wt %) to binary Zr–Nb alloys was observed to lead to accelerated precipitation, with a reduction in incubation time before the first detectable change in matrix lattice parameter. Addition of Sn (0.8 wt %) was observed to delay the initial precipitation of niobium from the matrix.

Acknowledgments

The writers would like to thank the EPSRC, BNFL, and Westinghouse Electric Sweden AB for funding of the project and Western Zirconium, United States, for provision of material and access to their melting facility. The authors acknowledge the European Synchrotron Radiation Facility for provision of synchrotron radiation facilities, and the authors would like to thank Dr. Alexander Evans for assistance in using beamline ID31. Dr. Xavier Kleber at Institut National des Sciences Appliquées (INSA) in Lyon, France is also greatly acknowledged for the support during the TEP measurements. Finally, Dr. Lars Hallstadius and Mats Dahlbäck, Westinghouse Electric, Sweden, are acknowledged for their expertise and support during the study.

References

[1] Pérez Jerlerud, R. and Massih, A. R., "Thermodynamic Evaluation of the Nb–O–Zr System," *J. Nucl. Mater.*, Vol. 360(3), 2007, pp. 242–254.
[2] Franklin, D. G. and Lang, P. M., "Zirconium-Alloy Corrosion: A Review Based on an International Atomic Energy Agency (IAEA) Meeting," *Zirconium in the Nuclear Industry: Ninth International Symposium, ASTM STP 1132*, Philadelphia, PA, 1990, ASTM International, West Conshohocken, PA, pp. 3–32.
[3] Robson, J. D., "Modelling the Overlap of Nucleation, Growth and Coarsening During Precipitation," *Acta Mater.*, Vol. 52, 2004, pp. 4669–4676.
[4] Hood, G. M., "Point Defect Diffusion in α-Zr," *J. Nucl. Mater.*, Vol. 159, 1988, pp. 149–175.
[5] Tendler, R., and Abriata, J. P., "Atomic Size and Fast Diffusion of Metallic Impurities in Zirconium," *J. Nucl. Mater.*, Vol. 150(3), 1987, pp. 251–258.
[6] Cox, B., "Some Thoughts on the Mechanisms of In-Reactor Corrosion of Zirconium Alloys," *J. Nucl. Mater.*, Vol. 336, 2005, pp. 331–368.
[7] Perovic, V., Perovic, A., Weatherly, G. C., and Purdy, G. R., "The Distribution of Nb and Fe in a Zr-2.5 wt% Nb Alloy, Before and After Irradiation," *J. Nucl. Mater.*, Vol. 224(1), 1995, pp. 93–102.
[8] Jeong, Y. H., Kim, H.-G., and Park, J.-Y., "Effect of the Nb/Fe Ratio on the Corrosion and Oxide Characteristics of Zr-*x*Nb-*y*Fe Alloys," *2004 International Meeting on LWR Fuel Performance*, Orlando, FL, 2004, American Nuclear Society, p. 1066.

[9] Jeong, Y. H., Kim, H. G., and Kim, T. H., "Effect of [Beta] Phase, Precipitate and Nb-Concentration in Matrix on Corrosion and Oxide Characteristics of Zr-*x*Nb Alloys," *J. Nucl. Mater.*, Vol. 317(1), 2003, pp. 1–12.

[10] Barberis, P., Ahlberg, E., Simic, N., Charquet, D., Lemaignan, C., Wikmark, G., Dahlbäck, M., Limbäck, M., Tägtström, P., and Lehtinen, B., "Role of the Second-Phase Particles in Zirconium Binary Alloys," *Zirconium in the Nuclear Industry: 13th International Symposium, ASTM STP 1423*, Annecy, France, 2002, ASTM International, West Conshohocken, PA, pp. 33–58.

[11] Rudling, P., Wikmark, G., Lehtinen, B., and Pettersson, H., "Impact of Second Phase Particles on BWR Zr-2 Corrosion and Hydriding Performance," *Zirconium in the Nuclear Industry: 12th International Symposium, ASTM STP 1354*, Toronto, Canada, 1998, ASTM International, West Conshohocken, PA, pp. 678–706.

[12] Baek, L. H. and Jeong, Y. H., "Depletion of Fe and Cr Within Precipitates During Zircaloy-4 Oxidation," *J. Mater. Mater.*, Vol. 304, 2002, pp. 107–116.

[13] Rudling, P. and Wikmark, G., "A Unified Model of Zircaloy BWR Corrosion and Hydriding Mechanisms," *J. Nucl. Mater.*, Vol. 265(1–2), 1999, pp. 44–59.

[14] Jeong, Y. H., Lee, K. O., and Kim, H. G., "Correlation Between Microstructure and Corrosion Behavior of Zr–Nb Binary Alloy," *J. Nucl. Mater.*, Vol. 302(1), 2002, pp. 9–19.

[15] Robson, J. D., "Modelling Precipitation in Zirconium Niobium Alloys," *J. Nucl. Mater.*, Vol. 377(3), 2008, pp. 415–422.

[16] Miller, G. L., *Zirconium*, 2nd ed., Metallurgy of the Rarer Metals Vol. 2, H. M. Finniston, Ed., Butterworths Scientific Publications, London, 1957, p. 548.

[17] Ivermark, M., 2009, "Characterisation of the Matrix Chemistry in Zirconium Alloys," °Ph.D. thesis, School of Materials, University of Manchester, United Kingdom, Bib Id 3032341.

[18] Denton, A. R. and Ashcroft, N. W., "Vegard's Law," *Phys. Rev. A*, Vol. 43(6), 1991, pp. 3161–3164.

[19] Merle, P. and Borrelly, R., "On the Possibility of Studying Recovery and Recrystallization Phenomena by Thermoelectric Power Measurements. Case of Zirconium Alloys," *Scr. Metall.* Vol. 20, 1986, pp. 1089–1094.

[20] TechMetal Promotion, *Thermoelectric Power Measurements*, INSA, Lyon, France, 2005.

[21] Houzé, M., Kleber, X., Fouquet, F., and Delnondedieu, M., "Study of Molybdenum Precipitation in Steels Using Thermoelectric Power Measurement," *Scr. Mater.*, Vol. 51(12), 2004, pp. 1171–1176.

[22] Potter, H. H., "Electrical Resistance and Thermoelectric Power of the Transition Metals," *Proc. Phys. Soc.*, Vol. 53, 1941, pp. 695–705.

[23] Bruno, E., Ginatempo, B., Guiliano, E. S., Ruban, A. V., and Vekilov, Yu. Kh., "Fermi Surfaces and Electronic Topological Transitions in Metallic Solid Solutions," *Phys. Rep.*, Vol. 249(6), 1994, pp. 353–419.

[24] Borrelly, R., Merle, P., and Adami, L., "Study of the Solubility of Iron in Zirconium by Thermoelectric Power Measurements," *Journal of Material Materials*, Vol. 170(2), 1990, pp. 147–156.

[25] Kim, S. J., Hong, H. S., and Oh, Y. M., "Study of the Thermoelectric Power Evolution of Zr-Based Alloys with Nb Additions," *J. Nucl. Mater.*, Vol. 306(2–3), 2002, pp. 194–201.

[26] Ortiz, M. and Pochettino, A. A., "Intergranular Thermal Stresses in Zirconium-Effects on X-Rays Macrostress Measurements," *J. Nucl. Mater.*, Vol. 229, 1996, pp. 65–72.

[27] Snyder, R. L., Characterization of Materials—X-Ray Diffraction," *Materials Science and Technology: A Comprehensive Treatment*, Vol. 2A, Part I, R. W. Cahn, P. Haasen, and E. J. Kramer, Eds., VCH Verlagsgesellchaft GmbH, Weinheim, Germany, 1992, p. 724.
[28] Rietveld, H. M., "A Profile Refinement Method for Nuclear and Magnetic Structures," *J. Appl. Crystallogr.*, Vol. 2, 1969, pp. 65–71.
[29] Kampmann, R. and Wagner, R., *Materials Science and Technology*, VCH, Weinheim, 1991, Vol. 5.
[30] Kamp, N., Sullivan, A., Tomasi, R., and Robson, J. D., "Modelling of Heterogeneous Precipitate Distribution Evolution During Friction Stir Welding Process," *Acta Mater.*, Vol. 54(8), 2006, pp. 2003–2014.
[31] Dyment, F. and Libanati, C. M., "Self-Diffusion of Ti, Zr, and Hf in Their hcp Phases, and Diffusion of Nb95 in hcp Zr," *J. Mater. Sci.*, Vol. 3(4), 1968, pp. 349–359.
[32] Christian, J. W., *Theory of Phase Transformations in Metals and Alloys Part 1*, Pergamon Press, Oxford, 1975.
[33] Toffolon, C., Brachet, J. C., Guilbert, T., Hamon, D., Urvoy, S., Servant, C., Charquet, D., Legras, L., and Mardon, J. P., "Viellissement Thermique des Alliages de Zirconium-Niobium en Phase Alpha (570 C)," *J. Phys. IV*, Vol. 11, 2001, pp. 99–108.
[34] Toffolon-Masclet, C., Barberis P., Brachet J., Mardon J., Legras L., , "Study of Nb and Fe Precipitation in α-Phase Temperature Range (400 to 550C) in Zr–Nb–(Fe–-Sn) Alloys," *Zirconium in the Nuclear Industry: 14th International Symposium, ASTM STP 1467*, Stockholm, Sweden, 2004, ASTM International, West Conshohocken, PA, pp. 81–101.
[35] Barberis, P., Charquet, D., and Rebeyrolle, V., "Ternary Zr–Nb–Fe(O) System: Phase Diagram at 853 K and Corrosion Behaviour in the Domain Nb⟨0.8%," *J. Nucl. Mater.*, Vol. 326(2–3), 2004, pp. 163–174.
[36] Kaufmann, A. R. and Magel, T. T., "Physical Metallurgy of Zirconium and Its Alloys," *The Metallurgy of Zirconium*, B. Lustman and F. Kerze, Eds., McGraw-Hill Book Company, Inc., New York, 1955, p. 776.
[37] ASTM B811–02, "Standard Specification for Wrought Zirconium Alloy Seamless Tubes for Nuclear Reactor Fuel Cladding," *Annual Book of ASTM Standards*, ASTM International, West Conshohocken, PA, 2007.
[38] Shimada, S., Etoh, Y., and Tomida, K., "BWR Zircaloy Cladding Corrosion Behavior—Effect of Microstructure," *J. Nucl. Mater.*, Vol. 248, 1997, pp. 275–280.
[39] Gros, J. P. and Wadier, J. F., "Precipitate Growth Kinetics in Zircaloy-4," *J. Nucl. Mater.*, Vol. 172(1), 1990, pp. 85–96.
[40] Ahlzén, P.-J., Andersson, Y., Rundqvist, S., and Tellgren, R., "A Neutron Diffraction Study of Zr3PD3-*x* ," *J. Less-Common Met.*, Vol. 161(2), 1990, pp. 269–278.
[41] Fitch, A. N., "The High Resolution Powder Diffraction Beam Line at ESRF," *J. Res. Natl. Inst. Stand. Technol.*, Vol. 109(1), 2004, pp. 133–142.

DISCUSSION

Question 1, Jean-Christophe Brachet, CEA, France:—1) TEP measurements should be influenced by the overall crystallographic texture evolution (during the ageing). Did you check that point (to be able to deconvolute such effects vs. the effect of Nb in solid-solution)? 2) It seems from your model that the pre-deformation (the rolling) influences the nucleation process (decreasing the interfacial energy). What about a possible influence on the "effective diffusion" of Nb (of the dislocations density) – via a diffusion-pipe "mechanism"?

Author's Response:—1) TEP measurements were only measured on the β-quenched material with highly randomized texture. The texture effect is thus minimal and TEP measurement is mainly an effect of Nb in solid solution. The TEP as an effect of annealing was not measured on the same sample and is therefore only used as an indicator that level of solid solution is decreasing during annealing.

2) It is likely that pipe-diffusion along defects has an accelerating effect on the nucleation and growth kinetics of precipitates. However, since the nucleation rate is more strongly influenced by interfacial energy (governing the energy barrier for nucleation), it is the availability of additional sites with a reduced nucleation energy barrier that is considered the dominant effect of rolling on the nucleation kinetics. However, it is accepted that a more accurate treatment of the problem should also include the effect of pipe-diffusion along dislocations.

Question 2, Mirco Grosse, Karlsruhe Institute of Technology, Germany:—Why have you applied wide angle scattering? Small angle scattering would be much more powerful to study these precipitation processes.

Author's Response:—This set-up was initially used to only track the lattice parameter evolution over a full diffraction pattern, not to particularly trace the precipitation evolution. The wide-angle scattering was used in the particular beam line (ESRF ID31, which is mainly used for stress measurements). Small angle scattering would have been preferred if the precipitation evolution had been the main objective of the study.

Question 3, Johannes Bertsch, Paul Scherrer Institut, Switzerland:—1) Could you please comment the 'homogeneity of the results', because what has been shown is an intergral snapshot? 2) Are there additional investigation techniques foreseen to obtain more detailed information, like micro-XRD or TEM?

Author's Response:—1) It is true that only a few specimens have been investigated in this study and could be seen as a 'snapshot'. Two or three ex-situ specimens per alloy composition and a minimum of one in-situ specimen per temperature were measured. The study was an initial attempt to monitor SPP kinetics through lattice parameter changes and could thus be expanded into repeated measurements and alloy combinations.

2) TEM has also been used in order to investigate type of SPP but is not included in this paper. Further studies using TEM would be needed to obtain more detailed information such as phase and chemistry of SPPs.

Question 4, Bo Cheng, EPRI, USA:—You indicated that the solubility of Nb in your samples was ~0.6%. Did you find an effect of Sn and Fe addition on the solubility of Nb in Zirconium?

Author's Response:—The solubility was not investigated. However, both TEP and XRD data indicated that the Nb solubility in binary Zr alloys may be higher than previously reported in literature

as no solubility plateau was reached in the manufactured alloys and no SPPs were identified in the quenched Zr-Nb alloys. The solubility of Nb mentioned was data found in open literature.

Question 5, J. K. Chakravartty, Bhabha Atomic Research Centre, India:—It is known that solubility of iron in α-Zr is negligible – what is the role of iron in accelerating the precipitation kinetics?

Author's Response:—Only speculations can be made because the iron-containing particles in the model alloys differ depending on system. Further investigations would be needed where the role of Fe is investigated.

Question 6, Arthur Motta, Penn State University, USA:—1) In an indirect measurement such as yours, how were you able to separate the effect of solid solution on lattice parameter that you study from the effect of other possible changes in microstructure that could occur during holding at high temp (650°C)? (Maybe consider repeating the experiment with cold-worked pure Zr) 2) The precipitates formed in ZrNbFe could be different from ZrNb. Is the Fe effect simply one of different precipitate nucleating? 3) If the Fe is not in solid solution as you say (and according to Fe solubility which is very low) how can it affect the lattice parameter? 4) Did you consider taking the experiment all the way to full precipitation to see if the lattice parameter continues to change?

Author's Response:—1) SXRD-measurements were performed on specimens from the same alloy origin that were either only beta-quenched or both beta-quenched and deformed. Cold-worked pure Zr was, however, not included in the measurement. This is definitely an aspect to consider in any future studies. The present study only measured beta-quenched pure Zr for calibration of the method with respect to lattice parameter change at temperature cycling from room temperature to high temperature and back.

2) That is a possibility and would be needed to studied further.

3) One speculation could be that Fe sits at grain boundaries thus affecting the diffusion path and facilitates diffusion of other alloying elements such as Nb to nucleate faster and initiate precipitation. The lattice parameter is then affected by Nb being removed from the Zr-matrix.

4) This was not done as the time to reach equilibrium was several hundreds of hours which would be impossible to study in-situ. The experiment could possibly be extended by long term annealing ex-situ followed by the same analysis. This however was outside the present scope of this study.

Question 7, Dr. Shishov, VNIINM Bochvar, Russia:—1) What is the Nb content in the alloys after annealings? 2) Have you provided a corrosion testing?

Author's Response:—1) The Nb content in the matrix was never quantitively analyzed in any other way than indirectly by comparing ex-situ measurements of the lattice parameter before and after heat treatment. The Nb content had then decreased by approximately 0.45wt% in the Zr-2.5Nb 650°C specimen.

2) Corrosion testing was not part of the scope of the study. This will be the subject of future work.

Question 8, David Dye, Imperial College, UK:—1) How did the α-Zr peak widths evolve in the rolled & undeformed materials and how did this compare to the β-Nb intensity/volume fraction?

2) If I understand you correctly, you suggest that in the worked material the decrease in rate of change of β-Nb volume fraction after the initial precipitation burst is due to the annealing away of, e.g. dissolutions. Does the peak width support this suggestion?

Author's Response:—1) α-Zr peak widths were broader in both rolled and undeformed material in the beginning of the heating experiment compared to two-hour α-Zr peaks. In the rolled material, the change in peak width during the experiment was much more marked than in the undeformed material. The correlation with β-Nb volume fraction is discussed in answer to (ii) below.

2) The sharp decrease in α-Zr peak width after the initial stage for the rolled material occurred at a time consistent with the measured change in precipitation kinetics. As suggested in the question, this would appear to support the hypothesis that the change in kinetics can be attributed to the annealing away of defects introduced during rolling.

Question 9, Mark Daymond, Queen's University, Canada:—Did you look for, or see, any evidence of ω-phase present for the case where β-Nb is thermodynamically stable.

Author's Response:—No, we did not see any evidence of ω-phase with SXRD or TEM. However, it is possible some ω-phase was present with a low volume fraction but undetected.

Question 10, Malcolm Griffiths, AECL, Canada:—How did you factor out the effects of residual stresses when monitoring the lattice parameter and associating this with the Nb content?

Author's Response:—Each set of measurement data was fitted using Rietveld refinement in which residual stresses were accounted for.

Reprinted from JAI, Vol. 7, No. 9
doi:10.1520/JAI103014
Available online at www.astm.org/JAI

Javier Romero,[1,3] *Michael Preuss,*[1] *João Quinta da Fonseca,*[1] *Robert J. Comstock,*[2] *Mats Dahlbäck,*[3] *and Lars Hallstadius*[3]

Texture Evolution of Zircaloy-2 During Beta-Quenching: Effect of Process Variables

ABSTRACT: The nuclear industry is interested in developing thermomechanical processes to produce random crystallographic orientation (texture) from cold-rolled Zircaloy-2 sheets used to manufacture boiling water reactor (BWR) channels. Randomized textures are beneficial because they minimize anisotropic irradiation-assisted growth, which in turn reduces bowing and uncontrolled deformation of BWR channels during service. The texture evolution of cold-rolled Zircaloy-2 sheets during the allotropic $\alpha \rightarrow \beta \rightarrow \alpha$ phase transformation was characterized by using synchrotron X-ray diffraction in situ and electron backscatter diffraction. The initial strong rolling texture is weakened only if the $\alpha \rightarrow \beta \rightarrow \alpha$ phase transformation is complete. Plastic deformation and grain growth in the β-phase lead to changes in the β texture and modify the inherited α texture. The global texture evolution is not sensitive to levels of stress that do not cause β plastic deformation. These findings demonstrate that accurate temperature control of the β-quenching process is of utmost importance in order to minimize undesirable irradiation growth of BWR channels during service, and that plastic deformation in the β phase can be employed to modify the inherited α texture. BWR channels with β-quenched textures will exhibit minimum irradiation growth caused by texture.

KEYWORDS: Zircaloy-2, texture, beta-quenching, synchrotron X-ray diffraction, variant selection

Manuscript received January 31, 2010; accepted for publication August 23, 2010; published online September 2010.

[1] School of Materials, The Univ. of Manchester, Manchester, M1 7HS, UK.
[2] Westinghouse Electric Company, Science and Technology Dept., Churchill, PA 15235.
[3] Westinghouse Electric Sweden, Västeräs, SE 72163, Sweden.

Cite as: Romero, J., Preuss, M., Quinta da Fonseca, J.ão, Comstock, R. J., Dahlbäck, M. and Hallstadius, L., "Texture Evolution of Zircaloy-2 During Beta-Quenching: Effect of Process Variables," *J. ASTM Intl.*, Vol. 7, No. 9. doi:10.1520/JAI103014.

Copyright © 2011 by ASTM International, 100 Barr Harbor Drive, PO Box C700, West Conshohocken, PA 19428-2959.

TABLE 1—*Nominal chemical composition of Zircaloy-2 (wt %).*

Sn	Fe	Cr	Ni	O
1.35	0.17	0.10	0.07	0.12

Introduction

During the production of boiling water reactor (BWR) channel sheets, a strong preferential crystallographic orientation (texture) is developed. This strong texture plays an important role on the performance of these components during service due to the strong anisotropy of properties observed in zirconium crystals. One very relevant example is anisotropic irradiation-assisted growth: Zirconium crystals grow in the direction parallel to the $\langle a \rangle$ axis and contract in the direction parallel to the $\langle c \rangle$ axis when subjected to irradiation [1,2]. A nonpreferential or randomized texture is highly desirable in order to minimize elongation, bowing, and uncontrolled deformation of BWR channels during service.

For this reason, the nuclear industry is interested in developing thermomechanical processes to produce random textures in flat products. This can potentially be achieved by taking advantage of the allotropic solid-state phase transformation undergone by zirconium at high temperature: From the hexagonal close-packed alpha (α) phase to the body-centred-cubic beta (β) phase. One of these processes is called β-quenching, which consists of heating the material above the transformation temperature (β-transus), followed by rapid cooling. Although this process has exhibited success in weakening the rolling texture [3], there is no consensus about the fundamental mechanisms responsible for this and in general for texture development during thermomechanical processing. This lack of knowledge is partially explained by the difficulty of obtaining direct experimental measurements of texture at high temperature.

This work aims to gain understanding on the mechanisms involved on texture evolution and development during $\alpha \rightarrow \beta$ and $\beta \rightarrow \alpha$ phase transformations of cold-rolled Zircaloy-2 sheets, as well as the effect of the process variables. For this purpose, in situ synchrotron X-ray diffraction (SXRD) experiments allowed for the first time, the study of texture evolution of both α and β phases during rapid thermomechanical cycling and at high temperature. The in situ SXRD experiments were complemented with subsequent electron backscatter diffraction (EBSD) studies on selected samples. This paper reviews sections of this work already published [4,5], and presents some additional results.

Experimental

The material employed in this study consisted of sheets of Zircaloy-2 received in as cold-rolled condition. The nominal chemical composition of the material is shown in Table 1. The thickness of the sheets was 0.9 mm, achieved after several steps of hot/cold-rolling, including intermediate annealing operations. The final thickness reduction was 55 %. Matchstick sized samples were cut from the sheets along the rolling direction using a precision diamond saw. The samples were 40 mm in length and $\sim$ 1 mm in width.

In Situ Synchrotron X-Ray Diffraction

The SXRD experiments were carried out in the beamline ID15B at the European Synchrotron Radiation Facility (ESRF) in Grenoble, France, using the setup shown schematically in Fig. 1. The transverse direction (TD) of the samples was parallel to the beam, while the normal direction (ND) and rolling direction (RD) were perpendicular to it. The beamline was used in transmission geometry, with a monochromatic beam with 0.2×0.2 mm size. A high-resolution two-dimensional (2D) X-rays detector was used to acquire diffraction patterns continuously (every 1.7 s) and in situ, while the samples were thermomechanically cycled on an electro thermal mechanical tester (ETMT). In this way, diffraction images could be recorded while the samples were subjected to thermal changes and mechanical load. The ETMT is a versatile stress rig that allows controlled resistive heating in miniature test pieces. The resistive nature of the heating system in the ETMT creates a parabolic temperature distribution along the sample, with the highest temperature halfway between the grips. Sample cooling is achieved by heat dissipation and conduction through water-cooled grips, when the electrical current through the sample is decreased. An inert atmosphere with argon at low pressure and constant flow was maintained throughout the tests in order to minimize the presence of oxygen surrounding the sample. Additional details of the experimental setup can be found elsewhere [4,5].

The thermomechanical cycles applied to the samples were designed to mimic the industrial β-quenching process, with variations in processing conditions, in order to study the effect of maximum temperature and stress. Table 2 shows the experimental matrix. Samples T1 and T2 were tested with no applied load and under load control, meaning that free thermal expansion and contraction was allowed without significant increase in the load applied to the sample. Samples S1 and S3 were tested applying load during the whole heat treatment, also under load control, while sample S2 was tested under displacement control

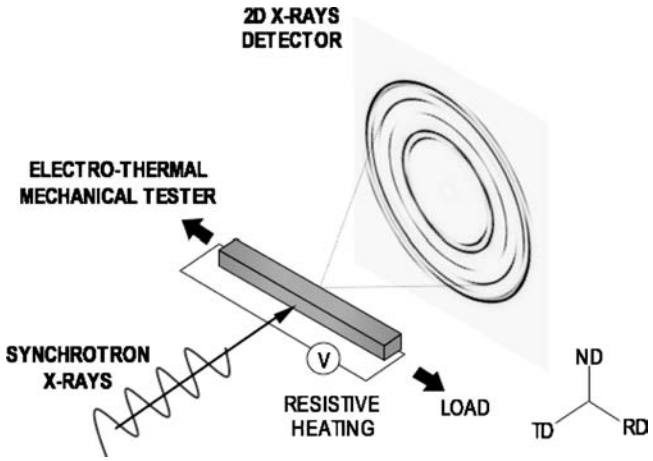


FIG. 1—*Illustration of the setup employed for in situ SXRD experiments.*

TABLE 2—*Experimental matrix for in situ SXRD experiment.*

Sample	Max. Temp. (°C)	Heating ($°C \cdot s^{-1}$)	Dwell (s)	Cooling ($°C \cdot s^{-1}$)	Load (N)
T1	950	10	3	50	0
T2	1000	10	10	10	0
S1	940	10	3	50	7
S2	950	10	0	50	(a)
S3	950	12	0	12	20 (b)

Note: (a)—constrained; (b)—large plastic deformation (failed).

and zero displacement during the thermal cycle. This means that in sample S2, there was stress in the sample, induced by thermal expansion/contraction and by the phase transformation. Sample S3 was tested by applying an approximate engineering stress of 20 MPa, suffering a significant amount of plastic strain leading to failure.

Due to the temperature distribution present during the tests in the ETMT, different peak temperatures were reached at different positions along the samples. Although the exact peak temperature was measured only at one point by means of a thermocouple spot-welded to the sample, it is possible to qualitatively correlate different peak temperatures with changes in texture, thanks to the temperature gradient. For this purpose, the collimated synchrotron X-ray beam was used to record diffraction patterns every 0.5 mm along the length of the samples (RD) at the end of the tests.

The 2D diffraction patterns acquired during the thermal cycle and the posterior scans were post-processed to extract texture information. For this purpose, the diffraction rings were converted into sets of diffraction spectra using FIT2D [6], and subsequently each set was analyzed using the Rietveld method as implemented in the software MAUD [7]. The texture is incorporated in the Rietveld refinement by using the E-WIMV [8] algorithm. Extended descriptions of these procedures can be found in Refs [9 and 10], and specific details for this experiment in Refs [4 and 5]. Recalculated pole figures are eventually obtained from the orientation distribution functions calculated from each diffraction pattern. Thanks to improved fitting procedures and the considerable amount of diffraction rings acquired, the SXRD results show a significant agreement with measurements made by well-established techniques such as laboratory X-ray diffraction using a goniometer. The quality of the results is discussed in detail in Ref 4.

Electron Backscatter Diffraction

Following the SXRD experiment, texture measurements using EBSD were carried out on selected samples. Different scanning electron microscopes (SEMs) were employed to collect data: Zeiss SUPRA 40, CamScan 2040S, Philips Sirion, and Philips XL30. All these SEMs were equipped with Oxford Instruments HKL

EBSD acquisition systems. The Channel 5 software suite [11] was used to post-process and analyze the results.

At room temperature after the thermal cycles, there is no presence of β phase. However, during post-processing of EBSD α data, it was possible to have an idea of the prior β grain size and shape before cooling by using a misorientation approach. In addition, the crystallographic orientation of the prior β grains could be obtained by applying the reconstruction algorithm developed by Davies et al. [12] to the α EBSD maps acquired.

Results

The series of pole figures in Fig. 2 illustrates the evolution of the texture of both α and β phases during a complete $\alpha \rightarrow \beta \rightarrow \alpha$ transformation. Orthotropic sample symmetry was detected in all the results; thus only one quadrant of each pole figure is shown. No sample symmetry was applied to produce SXRD pole figures, while orthotropic sample symmetry was applied to process EBSD results. The most important features of the starting texture, shown in Fig. 2(*a*), are the basal (0002) poles closely surrounding ND, and one $(11^{-}20)$ maximum at 30° from RD. These features are typical of cold-rolled zirconium sheets [3,13]. This strong rolling texture remains constant from room temperature to ~ 620°C. At this temperature, the texture begins to change towards that shown in Fig. 2(*b*), where a (0002) maximum concentrates at 30° from ND in the ND-TD plane, and the $(11^{-}20)$ maximum is parallel to RD. These changes are caused by recrystallization and grain growth [14,15]. The recrystallization texture stabilizes at ~ 730°C and remains unchanged until the onset of the phase transformation at ~ 810°C. The $\alpha \rightarrow \beta$ phase transformation finishes at ~ 940°C. Figure 2(*c*) shows the pole figures corresponding to an intermediate step of the phase transformation at 845°C, where the volume fraction of α and β is similar. At 935°C, the transformation is almost complete, illustrated by the pole figures in Fig. 2(*d*). At this point, the Rietveld analysis estimates the volume fraction of α-phase remaining in $\sim 2\%$.

Apart from small deviations in intensity, the α texture does not change significantly during the $\alpha \rightarrow \beta$ phase transformation. Opposite to observations from other authors in titanium and zirconium using neutron diffraction [15,16], the α texture appears to strengthen slightly, indicating that if any, there is preferential transformation of grains that are not aligned with the main texture components formed during recrystallization. On the other hand, the intensity of the maxima observed in the β pole figures clearly strengthens as the transformation develops in Fig. 2(*c*), 2(*d*), suggesting some kind of preferential growth after a relatively random nucleation. The β texture observed at the end of the $\alpha \rightarrow \beta$ transformation is not particularly strong. The most relevant feature is a (111) maximum parallel to RD. The (110) pole figure exhibits two maxima surrounding ND, one tilted ~ 60° towards RD and one tilted ~ 30° towards TD, the latter resembling the maximum of the (0002) α pole figure of the recrystallization texture before the transformation.

The $\alpha \rightarrow \beta$ phase transformation is certainly complete at 945°C when only β information is detected in the diffraction data and the start of a significant

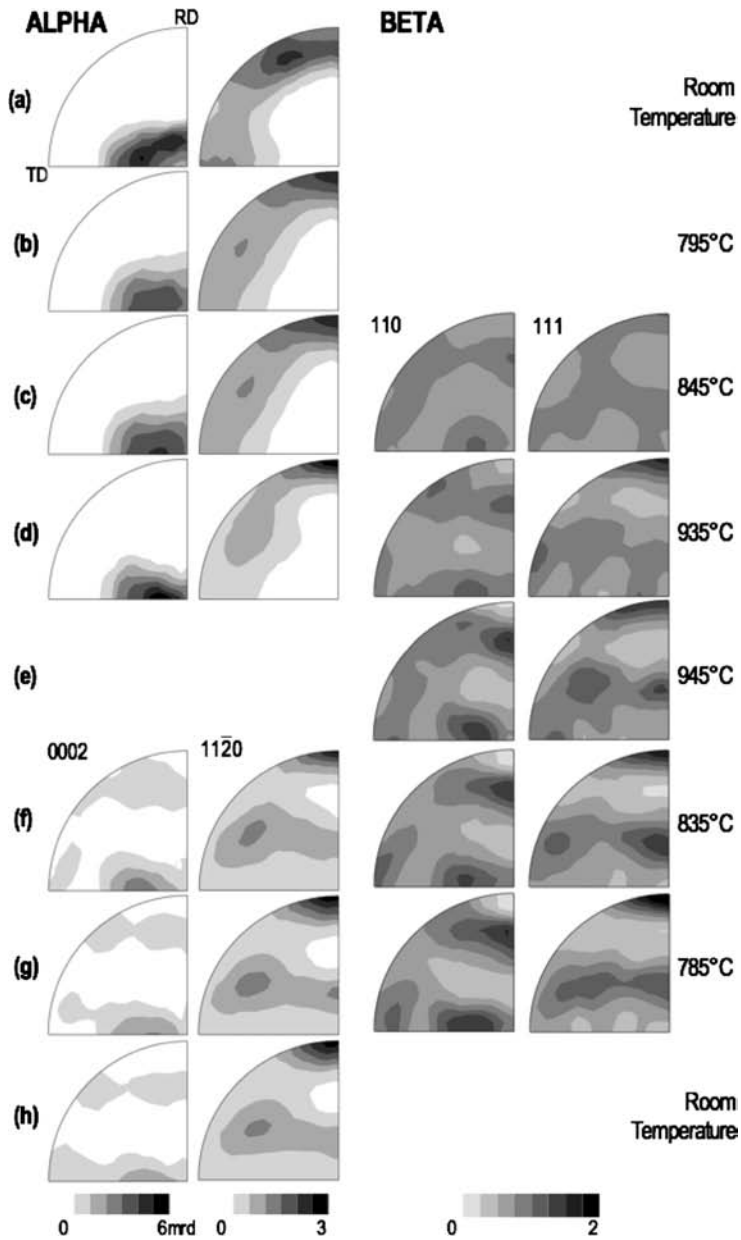


FIG. 2—*Pole figures obtained from in situ SXRD data during a complete α→β→α transformation: (a) Cold-rolled; (b) recrystallized before the start of the α→β phase transformation; (c) 46 % α and 54 % β; (d) at the end of the α→β phase transformation ~98 % β; (e) 100 % β before grain growth; (f) 15 % α and 85 % β; (g) 85 % α and 15 % β; and (*h*) after β-quenching.*

microstructural change is evidenced, probably the first stages of β grain growth. Scattered intensities along the diffraction rings at 945 and 950°C evidence extremely rapid grain growth once the β-transus has been exceeded. Although it was possible to extract texture information from diffraction images at 950°C, it is difficult to determine if the observed slightly sharper pole intensities obey to a genuine texture strengthening, or are caused by insufficient number of sampled grains. The relatively small volume of material that is irradiated in a SXRD experiment is a major disadvantage when evaluating global textures in the presence of grain growth, meaning that it was not possible to measure in situ the β texture beyond 945°C by using this technique. In this particular case, the irradiated volume was $\sim 0.2 \times 0.2 \times 1\,\text{mm}^3$, while the β grain size ranged between 70 and 150 μm.

In most of the tests carried out, the transformation upon cooling occurred very quickly. However, it is clear that even the initial fractions of α-phase produce pole figures with all the features seen on the final texture. The succession of α pole figures in Fig. 2(*f*)2(*h*) does not show significant changes from the initial α volume fraction ($\sim 15\,\%$) to the final texture at room temperature when the $\beta \rightarrow \alpha$ transformation is complete. The final texture is significantly weaker than the initial rolling texture, exhibiting evidence of new texture components developed during the phase transformation. The main features of the final texture are still the $(11^{-}20)$ maxima parallel to RD and the (0002) maxima at 30° from ND towards TD, but with significantly decreased intensities. This texture weakening is only possible if the peak temperature completely exceeds the transformation temperature. As it has been extensively reported in Ref [5], the post-treatment texture distribution along the samples shows that the inherited texture is very sensitive to the maximum temperature when it nears the β-transus. Sections of the sample reaching temperatures below 940°C exhibit exactly the same texture as before the transformation, i.e., the recrystallization texture, even though the microstructure undergoes a dramatic change. Figure 3 [5], illustrates how the texture index [17] and the Kearns factor [18] change suddenly along a sample heat treated in theETMT, more specifically sample T1. The evidence suggests that incomplete transformations or transformations with peak temperature very close to the β-transus result in perfect texture memory.

Effect of Stress and Plastic Deformation

Figure 4(*a*)4(*c*) compares the pole figures of the inherited α phase of the sample tested without applied stress (T1), with the samples tested under moderate stress (S1) and under constraint (S2). These pole figures are very similar, exhibiting only subtle differences in morphology and intensity. These results were confirmed by using EBSD. The high temperature β pole figures of these three samples at the end of the $\alpha \rightarrow \beta$ phase transformation, shown in Fig. 5(*a*)5(*c*), are practically identical. This evidence suggests that the effect of the level of stress undergone by these samples does not influence the development of the β texture during heating, and that the level of stress applied does not affect significantly the inherited global α texture.

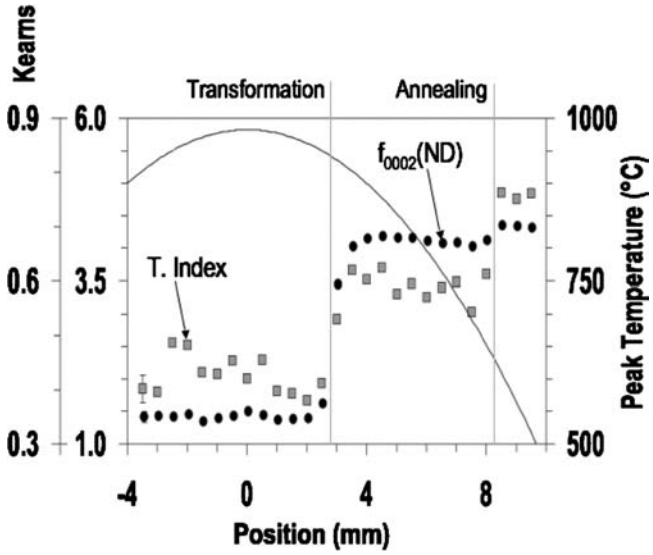


FIG. 3—*Kearns factor* f_{0002}^{ND} *and texture index along a sample heat treated in an ETMT (sample T1) [5]. The effect of the maximum temperature near the rmβ-transus (transformation) is significant.*

Sample S3 exhibited a similar behaviour during heating, as it can be seen in the β pole figures in Fig. 5(*d*). Although there is a hint of a previously unseen (100) pole maximum parallel to RD, the dominant components of the β texture at the end of the phase transformation are very similar compared to the other samples. Once the $\alpha \rightarrow \beta$ phase transformation was complete, an extreme plastic deformation led to the failure of sample S3. This sample underwent moderate β grain growth, and the crystal defects created during the plastic deformation contributed to produce an image with smooth diffraction rings, being reliable enough to extract the texture just before the failure, which is illustrated by the β pole figures in Fig. 5(*e*). These β pole figures are completely different to those seen in the other samples: Instead of the (111) maximum that dominates other results, there is a very strong (110) maximum parallel to the loading direction (RD). These pole figures display an almost perfect fibre texture, typical of body-centred-cubic materials under uniaxial tension [19], which was possible to produce, thanks to the softness and ductility of the β phase.

EBSD measurements carried out near the fracture of sample S3 resulted in pole figures with an extremely strong basal (0002) pole accumulation parallel to the loading direction (RD), shown in Fig. 4(*d*). It is evident that the inherited α texture is strongly influenced by the β texture before cooling, which in turn can be significantly modified by plastic deformation. This suggests that different levels of plastic deformation in the β phase produce different inherited α textures, which was subsequently confirmed by an additional EBSD map acquired in sample S3. This additional map was taken away

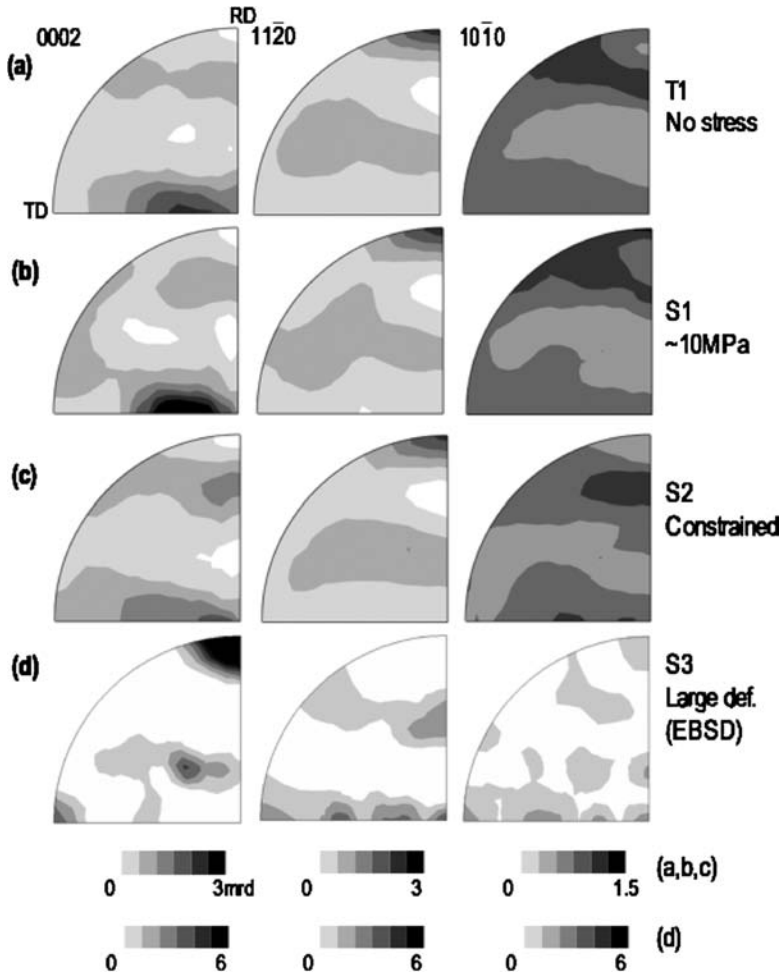


FIG. 4—*Inherited α pole figures of samples β-quenched under different schemes of stress/strain. The effect of stress is very small in (a)–(c), while large plastic deformation (d) causes a dramatic change in the inherited texture.*

($\sim$ 4 mm) from the fracture, where the necking of the sample started, i.e., the plastic deformation was moderated ($\sim$ 0.25 strain). Despite the relatively small size of the map (according to the β reconstruction it covered $\sim$ 150 β grains), the resultant texture is very close to random. The pole figures obtained from this map do not show discernible texture features and the resultant intensities are very low. Figure 6 shows the EBSD maps and pole figures obtained from sample S3, Fig. 6(*b*), 6(*c*), compared to those obtained from sample T1, Fig. 6(*a*). The colouring of the maps corresponds to an inverse pole figure, which is displayed in the legend. The dominant red/violet

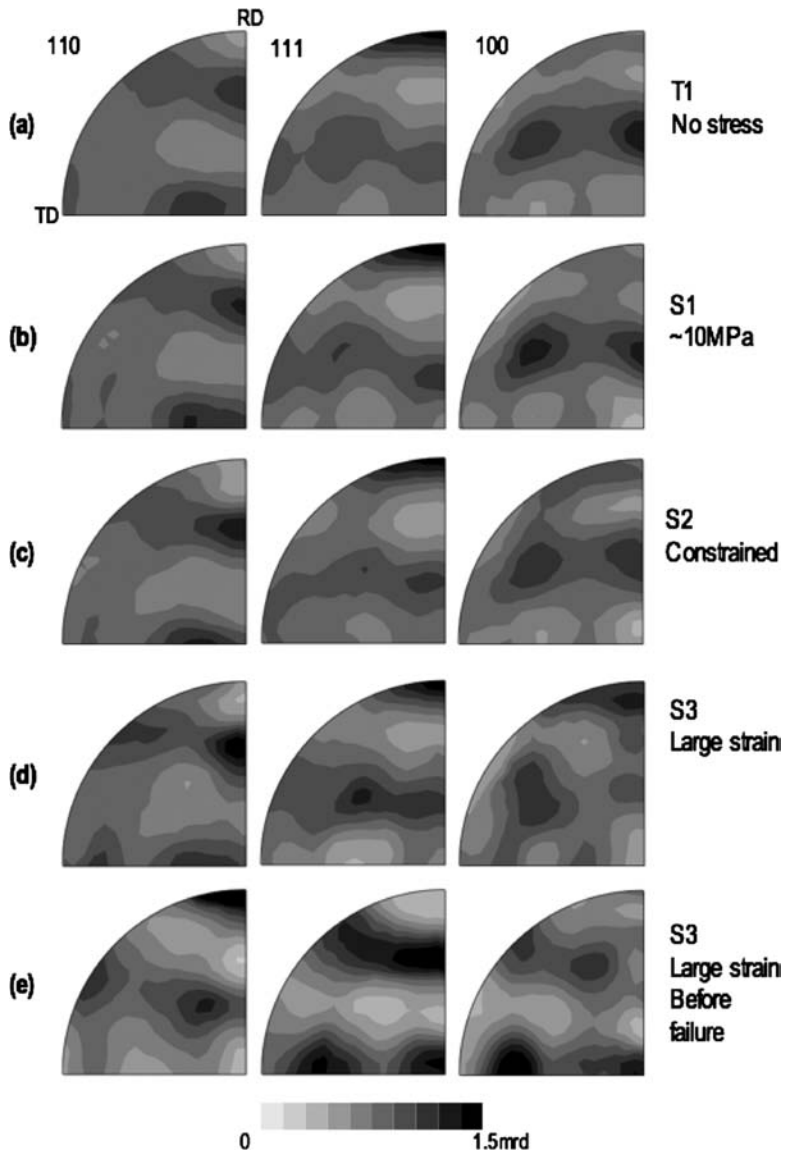


FIG. 5—*High temperature β pole figures of samples β quenched under different schemes of strain/stress. These pole figures were obtained at the end of the α→β phase transformation, i.e., at 940–950°C for each case, using SXRD.*

colour in Fig. 6(*b*) illustrates the strong alignment of (0002) poles with RD. At the same time the mixed colour in Fig. 6(*a*), 6(*c*) evidences the weakness of the texture, which is much more significant in the map of Fig. 6(*c*), as illustrated by the corresponding pole figures.

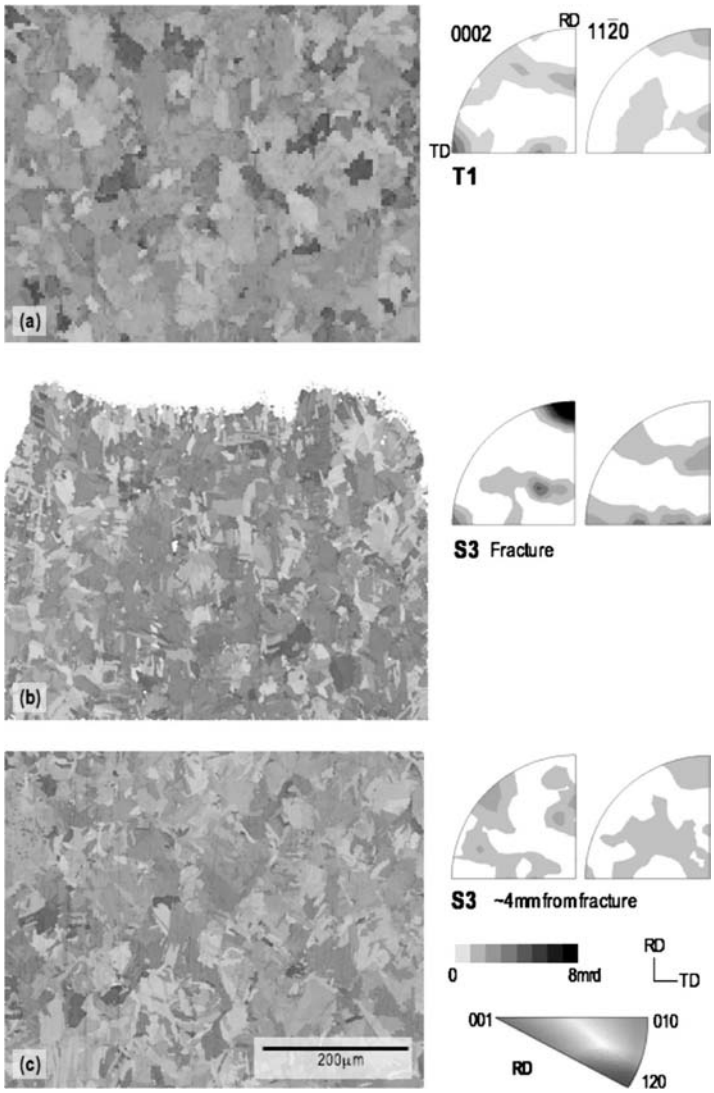


FIG. 6—*EBSD maps and pole figures obtained from two samples: (a) T1, β-quenched without applied stress, and [(b) and (c)] S3, sample that failed during β-quenching due to extreme plastic deformation.*

Discussion

The orientation relationship between the α and β phases [20] establishes that the (0002) planes of the α phase are parallel to the (110) planes of the β phase, and at the same time one of the $\langle 11\bar{2}0 \rangle$ directions of the α phase is parallel to one of the $\langle 111 \rangle$ directions of the β phase. According to this orientation relationship and the symmetry of the α and β phases, each α orientation can produce six

different β orientations, often called "variants." For the reverse transformation, a parent β orientation can produce 12 distinct α orientation variants [21,22]. The theoretical scenario of total absence of orientation variant selection would result in a practically random texture.

Figure 7(*a*) shows the theoretical β pole figures that are obtained by transforming the experimental recrystallization texture, Fig. 7(*c*), without variant selection. These calculated pole figures were obtained by using the software TEXTAN-III [23]. They are very similar to those in Fig. 7(*b*), obtained in situ using SXRD at the final stages of the $\alpha \rightarrow \beta$ phase transformation. This suggests that during heating there is very little, if any, selection of variants. Given that β textures measured in samples under moderate tensile stress and under constraint were very similar to a stress-free β texture, it can be inferred that those levels of stress do not influence significantly the selection of variants during heating.

On the other hand, if no variant selection is assumed during cooling, there is a more significant difference between calculated and experimental textures. Figure 8(*c*) shows the pole figures that are obtained by transforming the

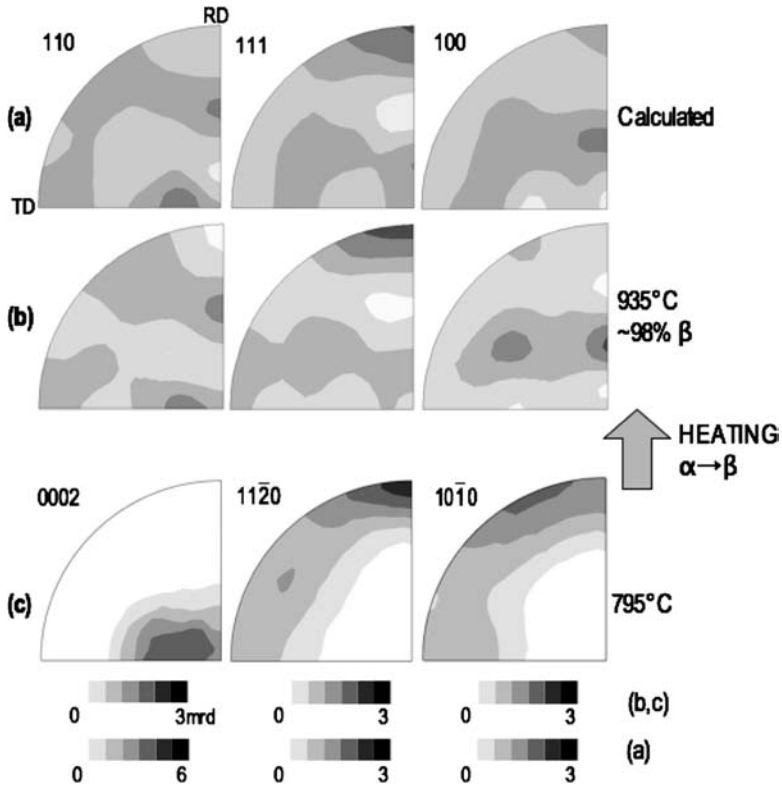


FIG. 7—*Pole figures illustrating the absence of variant selection during the $\alpha \rightarrow \beta$ phase transformation.*

experimental β texture at 945°C (a), i.e., assuming that the sample cools down immediately from that point. These pole figures are different to those obtained experimentally, shown in Fig. 8(*b*), exhibiting considerable differences in pole intensity. This suggests that there is indeed selection of variants after the $\alpha \rightarrow \beta$ transformation is complete, i.e., during β grain growth or during cooling, or both. The inherited α texture is purely dependant on the β texture present just before starting the $\beta \rightarrow \alpha$ transformation on cooling. Whatever mechanisms modifying the β texture (e.g., plastic deformation or preferential grain growth), will thereby modify the inherited α texture.

As mentioned before, the evolution of texture after the end of the $\alpha \rightarrow \beta$ phase transformation could not be measured reliably using SXRD due to the limited volume of material sampled and the grain growth observed. However, the reconstruction of the β phase from α EBSD maps allows estimating the texture at the start of the $\beta \rightarrow \alpha$ transformation. Figure 9 compares β pole figures obtained in situ at the end of the $\alpha \rightarrow \beta$ transformation, Fig. 9(*a*), 9(*b*), with those obtained by reconstructing an EBSD map in sample T2, Fig. 9(*c*), which maximum temperature was 1000°C. An apparent strengthening of the β texture

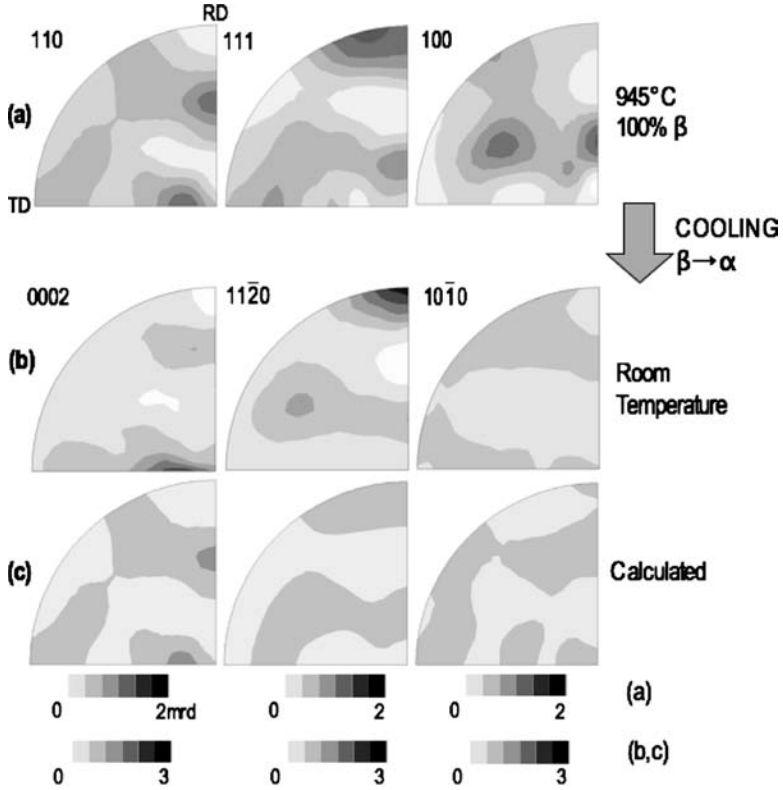


FIG. 8—*Pole figures illustrating the presence of variant selection during the β→α phase transformation.*

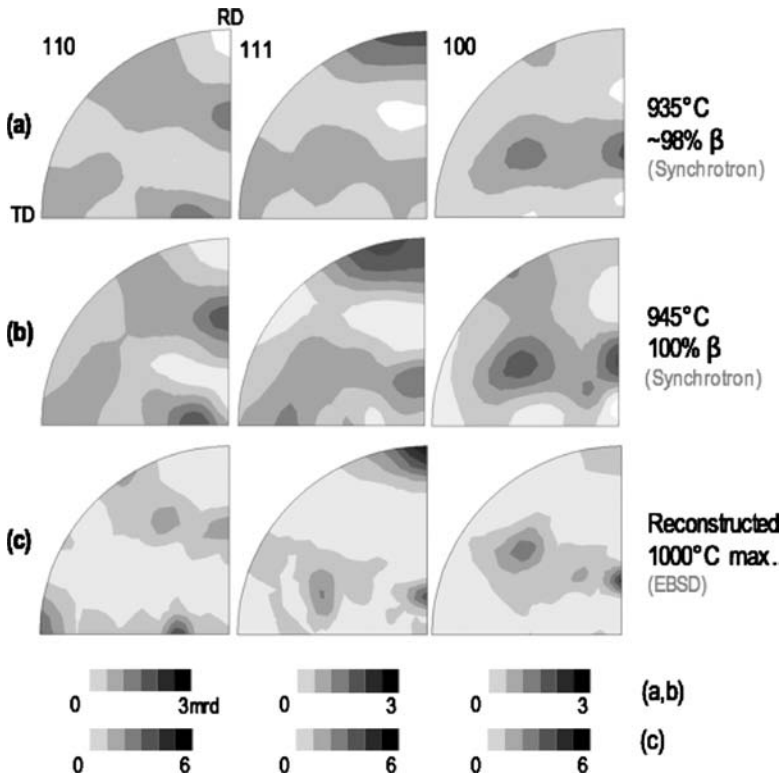


FIG. 9—*Pole figures illustrating the effect of the maximum temperature above the β-transus.*

with temperature is observed, which results in a slightly stronger inherited α texture. Figure 10 compares the pole figures obtained from α EBSD maps in samples T1 and T2 to illustrate the effect of the maximum temperature on the inherited texture. The EBSD results in Figs. 10(*c*) evidence another important fact: Basal (0002) pole maxima parallel to TD are underestimated in SXRD texture measurements for the particular geometry employed in the experiment. This is due to the absence of diffracted X-rays when the hexagonal crystals are aligned in that direction. This must be taken into account when drawing conclusions from SXRD data.

The strengthening of the global β texture may be caused by preferential growth. Further studies on samples heat treated at higher temperatures, which are not reported here, have provided supporting evidence for this hypothesis. Those β orientations that follow a strict orientation relationship with the main initial α texture components apparently grow at expense of those that nucleated more randomly, with a less strict orientation relationship with the initial α components.

In addition to the established fact that the behaviour of the texture in the β phase strongly influences the inherited α texture, the nucleation of α phase upon

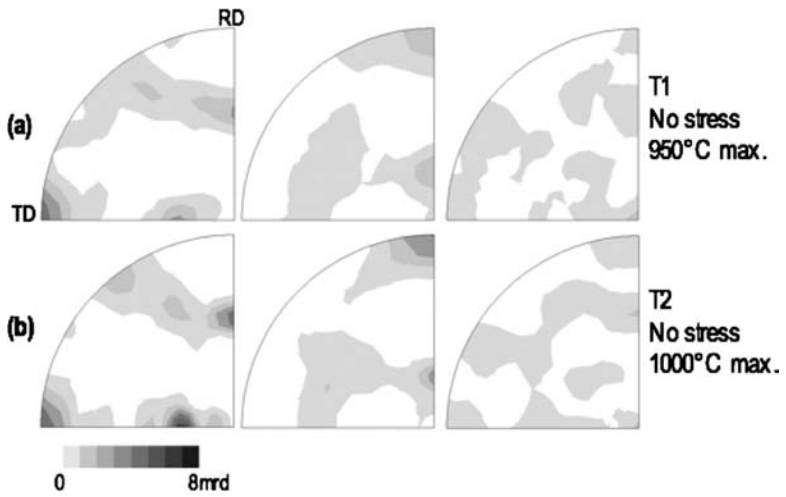


FIG. 10—*EBSD pole figures illustrating the effect of the maximum temperature above the β-transus on the inherited α texture.*

cooling may be influenced by other factors leading to variant selection. One common hypothesis is the preferential nucleation of certain α orientation variants in special β/β grain boundaries [24–27]. The probability of selection of variants at these special β/β grain boundaries decreases with β grain growth [5]. This explains the strong variant selection leading to perfect texture memory in samples β-quenched with maximum temperatures nearing the β-transus: The presence of untransformed α, apart from acting as biasing nuclei, inhibits β grain growth, thereby stimulating the selection of variants. When a strong β texture is developed, for example by plastic deformation in the β field, the grain boundary variant selection mechanism discussed here would be stimulated, due to the low misorientation at many β/β grain boundaries. This would explain not only the very strong inherited α textures obtained when strong plastic strain was applied to one of the in situ tested samples, but also apparent strengthening of the inherited α texture with increased peak temperature.

Conclusions

The initial strong rolling texture observed in cold-rolled Zircaloy-2 sheets is weakened by a complete β-quenching heat treatment. New texture components are observed, but there is evidence of variant selection.

There is no evidence of variant selection during the $\alpha \rightarrow \beta$ phase transformation, even in the presence of moderate stress. Any mechanism leading to variant selection during β-quenching of cold-rolled Zircaloy-2 acts during β grain growth or during the $\beta \rightarrow \alpha$ transformation on cooling, or both.

β-quenching treatments with peak temperatures close to the β-transus (940°C) are associated with perfect texture memory. It is unlikely that this texture memory is caused simply by nucleation of inherited α variants near to

untransformed α clusters, so an additional phenomenon should exist, probably selection of variants at special β/β grain boundaries.

Plastic deformation and grain growth in the β-phase lead to changes in the β texture, thereby modifying the inherited α texture. The global texture evolution is not sensitive to levels of stress that do not cause plastic deformation in the β-phase.

Considering the application of this work to an industrial β-quenching process, it has been demonstrated that the peak temperature plays a critical role in determining the presence or not of texture memory. In order to weaken the strong texture obtained after cold rolling, it is essential to exceed the β-transus. On the other hand, excessive peak temperature may result in undesirable β grain growth and strong inherited α texture components. This is also detrimental for the desired anisotropy of the material. The range of temperature recommended for β-quenching of channel sheet material is narrow, between 950 and 1050°C. Plastic deformation in the β phase remains as an alternative to weaken the inherited α texture even further. Plastic deformations in the range of 20 to 30 % along the RD produce practically random α texture. BWR channels with the textures obtained after β-quenching will exhibit minimum irradiation growth caused by texture.

Acknowledgments

The assistance of the scientists of the beamline ID15 in the ESRF is gratefully acknowledged. The writers would also like to thank Professor Pete Bate from the School of Materials in The University of Manchester for useful discussions.

References

[1] Fidleris, V., "The Irradiation Creep and Growth Phenomena," *J. Nucl. Mater.*, Vol. 159, 1988, pp. 22–42.

[2] Carpenter, G. J., Zee, R. H., and Rogerson, A., "Irradiation Growth of Zirconium Single Crystals: A Review," *J. Nucl. Mater.*, Vol. 159, 1988, pp. 86–100.

[3] Dahlbäck, M., Limbäck, M., Hallstadius, L., Barberis, P., Bunel, G., Simonot, C., Andersson, T., Askeljung, P., Flygare, J., Lehtinen, B., and Massih, A. R., "The Effect of Beta-Quenching in Final Dimension on the Irradiation Growth of Tubes and Channels," *J. ASTM Int.*, Vol. 2(6), 2005, pp. 276–304.

[4] Romero, J., Preuss, M., and Quinta da Fonseca, J., "Capturing the Texture Changes in a Zirconium Alloy During the Allotropic Phase Transformation," *Scr. Mater.*, Vol. 61, 2009, pp. 399–402.

[5] Romero, J., Preuss, M., and Quinta da Fonseca, J., "Texture Memory and Variant Selection During Phase Transformation of a Zirconium Alloy," *Acta Mater.*, Vol. 57(18), 2009, pp. 5501–5511.

[6] Hammersley, A. P., *FIT2D V9.129 Reference Manual V3.1*. (1998). European Synchrotron Radiation Facility (ESRF), Grenoble.

[7] Lutterotti, L., Matthies, S., Wenk, H.-R., Schultz, A. S., and Richardson, J. W., "Combined Texture and Structure Analysis of Deformed Limestone from Time-of Flight Neutron Diffraction Spectra," *J. Appl. Phys.*, Vol. 81, 1997, pp. 594–600.

[8] Matthies, S., Pehl, J., Wenk, H.-R., Lutterotti, L., and Vogel, S. C., "Quantitative Texture Analysis with the HIPPO Neutron TOF Diffractometer," *J. Appl. Crystallogr.*, Vol. 38, 2005, pp. 462–475.

[9] Ischia, G., Wenk, H.-R., Lutterotti, L., and Berberich, F., "Quantitative Rietveld Texture Analysis of Zirconium from Single Synchrotron Diffraction Images," *J. Appl. Crystallogr.*, Vol. 38, 2005, pp. 377–380.

[10] Lonardelli, I., Wenk, H.-R., Lutterotti, L., and Goodwin, M., "Texture Analysis from Synchrotron Diffraction Images with the Rietveld Method: Dinosaur Tendon and Salmon Scale," *J. Synchrotron Radiat.*, Vol. 12, 2005, pp. 354–360.

[11] *HKL Channel 5*, Oxford Instruments, Abingdon, UK, 2006.

[12] Davies, P. S., Wynne, B. P., and Rainforth, W. M., "Investigating Microstructural Evolution in the Near-α Alloy Timetal R834 Using Electron Backscatter Diffraction (EBSD)," *Ti-2007 Science and Technology*, M. Niinomi, S. Akiyama, M. Hagiwara, M. Ikeda, and K. Maruyama, Eds., The Japan Institute of Metals, Sendai, 2007, pp. 945–948..

[13] Ciurchea, D., Pop, A. V., Gheorghiu, C., Furtun, I., Todic, M., Dinu, A., and Roth, M., "Texture, Morphology and Deformation Mechanisms in β-Transformed Zircaloy-4," *J. Nucl. Mater.*, Vol. 231, 1996, pp. 83–91.

[14] Tenckhoff, E., *Deformation Mechanisms, Texture and Anisotropy in Zirconium and Zircaloy*, ASTM International, West Conshohocken, PA, 1988.

[15] Lonardelli, I., Gey, N., Wenk, H.-R., Humbert, M., Vogel, S. C., and Lutterotti, L., "In Situ Observation of Texture Evolution During $\alpha \rightarrow \beta$ and $\beta \rightarrow \alpha$ Phase Transformations in Titanium Alloys Investigated by Neutron Diffraction," *Acta Mater.*, Vol. 55(17), 2007, pp. 5718–5727.

[16] Wenk, H. R., Lonardelli, I., and Williams, D., "Texture Changes in the *hcp→bcc→hcp* Transformation of Zirconium Studied In-Situ by Neutron Diffraction," *Acta Mater.*, Vol. 52(7), 2004, pp. 1899–1907.

[17] Bunge, H. J., *Texture Analysis in Materials Science*, Butterworths, London, 1982.

[18] Kearns, J. J., "On the Relationship Among 'f' Texture Factors for the Principal Planes of Zirconium, Hafnium and Titanium Alloys," *J. Nucl. Mater.*, Vol. 299, 2001, pp. 171–174.

[19] Rollett, A. D. and Wright, A. D., "Typical Textures in Metals," *Texture and Anisotropy*, U. F. Kocks, C. N. Tome, and H. R. Wenk, Eds., Cambridge University Press, Cambridge, 1998, pp. 179–238.

[20] Burgers, W. G., "On the Process of Transition of the Cubic-Body-Centered Modification into the Hexagonal-Close-Packed Modification of Zirconium," *Physica (Amsterdam)*, Vol. 1(7-12), 1934, pp. 561–586.

[21] Humbert, M., Moustahfid, H., Wagner, F., and Philippe, M. J., "Evaluation of the High Temperature Texture of the Beta Phase of a TA6V Sample from the Individual Orientations of Grains of the Low Temperature Alpha Phase," *Scr. Metall. Mater.*, Vol. 30, 1994, pp. 377–382.

[22] Humbert, M., "Determination of the Orientation of a Parent Beta Grain from the Orientations of the Inherited Alpha Plates in the Phase Transformation from Body-Centred Cubic to Hexagonal Close Packed," *J. Appl. Crystallogr.*, Vol. 28, 1995, pp. 571–576.

[23] Bate, P., *TEXTAN III—A Program for the Analysis of Crystallographic Texture Using Harmonic Series Expansion*, (1990). School of Materials, The University of Manchester, Manchester, UK,.

[24] Gey, N. and Humbert, M., "Specific Analysis of EBSD Data to Study the Texture Inheritance Due to the Beta-Alpha Phase Transformation," *J. Mater. Sci.*, Vol. 38(6), 2003, pp. 1289–1294.

[25] Stanford, N. and Bate, P., "Crystallographic Variant Selection in Ti-6Al-4V," *Acta Mater.*, Vol. 52, 2004, pp. 5215–5224.

[26] Bhattacharyya, D., Viswanathan, G. B., and Fraser, H. L., "Crystallographic and Morphological Relationships Between β Phase and the Widmanstätten and Allotriomorphic α Phase at Special β Grain Boundaries in an α/β Titanium Alloy," *Acta Mater.*, Vol. 55, 2007, pp. 6765–6778.

[27] Humbert, M., Germain, L., Gey, N., Bocher, P., and Jahazi, M., "Study of the Variant Selection in Sharp Textured Regions of Bimodal IMI 834 Billet," *Mater. Sci. Eng., A*, Vol. 430, 2006, pp. 157–164.

DISCUSSION

Question 1, Suresh Yagrik, EPRI:—Was the temperature variation within your synchrotron sample (~300°C) by design or by limitation? With applied deformation, did it tend to complicate your interpretation of observations/results?

Author's Response:—The ETMT uses resistive heating, which creates the temperature distribution along the samples. The highest temperature is reached approximate halfway between water-cooled grips. With large deformation it is complicated to control the location of the maximum temperature. However, by examining the samples post-mortem it was possible to estimate the temperature distribution, due to the characteristic changes in the microstructure and the texture.

Question 2, Jean-Christophe Brachet, CEA:—1) Heating rate effect upon $\alpha \rightarrow \beta$ on the final inherited structure? 2) We have performed some indirect measurements on the texture evolution after achieving different fractions of β phase formed upon heating, and it seems from these measurements that the weakening of the initial texture was more or less proportional to the fraction of β formed. It seems contradictory to your results. Any explanation?

Author's Response:—1) We did run experiments with different heating rate ($2°Cs^{-1}$ and $10°Cs^{-1}$), but we could not find significant differences in inherited texture or microstructure.

2) Perhaps the most important observation in this work is the perfect texture memory occurring when the β-transus is not well exceeded. This was observed consistently in situ and also ex situ by heat treating samples at different maximum temperatures approaching the β-transus. This phenomenon has been also observed previously (see next question). The texture of cold-rolled Zircaloy-2 sheets is not weakened unless the material completely transforms to β-phase. We also believe that some β grain growth is required in order to avoid texture memory.

Question 3, Ron Adamson, Zircology Plus:—A number of years ago GE conducted studies similar to yours on Zircaloy-4, except individual specimens and standard X-Ray diffraction techniques were used. Our results are quite similar to yours in that only minor texture changes were observed until the $\alpha + \beta$ to β transus was approached. We found that re-heating the as-quenched structure (for instance to relieve internal stresses) could cause a change from the ideal $f = 0.33$ texture. Have you any data on this phenomenon?

Author's Response:—We did β-quench some samples multiple times in situ, and the results indicated that the α texture strengthens as the samples are re-quenched. By texture strengthening we mean that the same texture components observed after β-quenching the first time (including some new components respect to the recrystallization texture) are sharper. One important texture component that produces basal poles parallel to TD increases the Kearns factor in that direction.

Reprinted from JAI, Vol. 8, No. 1
doi:10.1520/JAI103066
Available online at www.astm.org/JAI

P. Mosbrucker,[1] *M. R. Daymond,*[1] *and R. A. Holt*[1]

In Situ Studies of Variant Selection During the α−β−α Phase Transformation in Zr-2.5Nb

ABSTRACT: In situ phase transformation experiments have been carried out using neutron and synchrotron X-ray diffraction to monitor the texture evolution and establish the criteria for variant selection during the $\alpha \rightarrow \beta \rightarrow \alpha$ phase transformation in Zr-2.5Nb. There is clear evidence of a strong variant selection occurring during the $\alpha \rightarrow \beta$ transformation and a weaker variant selection during the $\beta \rightarrow \alpha$ transformation. Further, comparing hot-worked specimens with those that have received additional cold-work revealed that cold-work introduced microstructural characteristics that inhibited the full development of the transformed texture seen in the hot-worked samples. A study of the effect of external biasing stresses during transformation was conducted. An external biasing stress was applied along the hoop axis during different components of the $\alpha \rightarrow \beta \rightarrow \alpha$ transformation. An external stress during heating does not appear to significantly influence variant selection, at least for the stress magnitudes tested here, while an external stress during cooling did have some influence on the resultant texture.

KEYWORDS: zirconium, phase transformation, internal stresses, neutron diffraction, X-ray diffraction, texture

Introduction

Several properties of alloys with a hexagonal crystal structure, such as zirconium and titanium, are dependent on the crystallographic texture. This arises from the significant anisotropy of properties at the crystallographic level, such as elasticity, thermal expansion, and plasticity [1]. There is thus a significant interest in understanding the mechanisms of texture development through

Manuscript received March 7, 2010; accepted for publication October 1, 2010; published online November 2010.
[1] Dept. of Mechanical and Materials Engineering, Queen's Univ., Kingston, ON, Canada, K7L 3N6.

Cite as: Mosbrucker, P., Daymond, M. R. and Holt, R. A., "In Situ Studies of Variant Selection During the α−β−α Phase Transformation in Zr-2.5Nb," *J. ASTM Intl.*, Vol. 8, No. 1. doi:10.1520/JAI103066.

Copyright © 2011 by ASTM International, 100 Barr Harbor Drive, PO Box C700, West Conshohocken, PA 19428-2959.

various thermo-mechanical processing steps, with the long term goal of optimizing the texture of final products.

In its pure form, zirconium exhibits an α hcp phase, which is stable at low temperatures, and a β bcc phase stable at elevated temperatures. Alloying elements affect the relative stability and produce a two phase $(\alpha + \beta)$ regime at intermediate temperatures. Some alloys are processed in the two phase regime, and most undergo heat treatments into the fully β-phase regime at some stage to homogenize the microchemistry. Hence, the way that texture is "inherited" during phase transformations is of considerable interest.

Zirconium-2.5 wt% Niobium is an alloy used in RBMK and second and third generation CANDU® pressurized heavy water nuclear reactors due to good mechanical strength, corrosion resistance, and creep resistance, combined with excellent neutronic properties [2]. The Zr-2.5Nb pressure tubes in CANDU reactors act as the primary containment vessel of high temperature D_2O inside the core; their behavior is strongly dependent on the texture of the tubes [2]. The Zr–Nb binary phase diagram in the vicinity of the α/β transus is a monotectoid with the monotectoid reaction at about 600°C and 20 wt% Nb. Thus, for the Zr–Nb binary system with more than ~ 0.6 wt% but less than 20 wt% Nb present, on cooling from the high temperature β_{Zr} phase there is a precipitation of α_{Zr} at the phase transformation temperature (~ 860°C for 2.5 % Nb) [3]. At temperatures close to 600°C, eutectoid decomposition occurs under equilibrium conditions and the remaining β_{Zr} transforms to α_{Zr} (~ 0.5 wt% Nb) and bcc β_{Nb} (~ 95 wt% Nb). However, this reaction is very slow and thus at room temperature the material typically consists of α_{Zr} and metastable β_{Zr}, with the Nb mostly in the β_{Zr} phase. The Nb content in the α_{Zr} is < 1 wt%, while in the β_{Zr} it is ~ 20 wt%.

The chemical composition of Zr-2.5Nb in commercial use is 2.5–2.8 wt% Nb, 950–1500 ppm O, < 1300 ppm Fe, and balance Zr [4]. The O and Fe are mainly concentrated in the α- and β-phases, respectively, and act as stabilizers [5]. The observed transformation temperature for 100 % β_{Zr} is raised by the presence of oxygen to $\sim$ 900–925°C [6]. For commercial Zr-2.5Nb alloys, the result is a room temperature material with roughly 90 % α-phase and 10 % β-phase; the microstructures obtained are highly analogous to those found for Ti-6Al-4V.

The transformation between the α-phase and the β-phase of both zirconium and titanium occurs, according to the Burgers relationship, with parallel planes in the two phases $\{110\}_\beta // \{0002\}_\alpha$, while parallel directions $\langle 111\rangle_\beta // \langle 11\bar{2}0\rangle_\alpha$ [7] are also maintained. The relationship between, $\{110\}_\beta$ and $\{0002\}_\alpha$ corresponds to closest packed planes, while the relationship between $\langle 111\rangle_\beta$ and $\langle 11\bar{2}0\rangle_\alpha$ corresponds to nearest neighbour directions [8]. The relationship has been observed for single crystals [9] and to be correct within measurement accuracy for polycrystals, e.g., Ref [10]. During heating, the transformation $\alpha \rightarrow \beta$ allows for six equivalent orientation variants; during cooling $(\beta \rightarrow \alpha)$, there are 12 equivalent orientation variants. The crystallographic relationship for the transformation is shown schematically in Fig. 1 (adapted from Ref [11]). During this transformation, there is also a significant transformation strain. For the transformation from $\beta \rightarrow \alpha$ under unconstrained conditions, this amounts to an ~ 10% contraction along a $\langle 100\rangle_\beta$ direction, and an ~ 2% contraction and

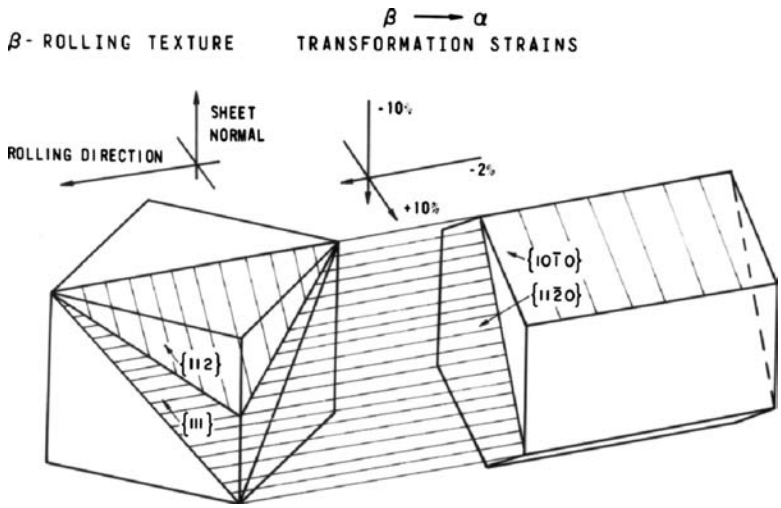


FIG. 1—*Schematic showing crystallographic relationship between α- and β-phases through the Burgers relationship, as well as the strain changes associated with the β to α transformation. The strains associated with the α to β transformation will simply be the reverse of the ones shown.*

$\sim 10\%$ expansion, respectively, along two perpendicular $\langle 110 \rangle_\beta$ directions (Fig. 1).

A number of authors have noted a "texture memory" effect; that is, when the material is transformed from the α-phase to the β-phase and back to the α-phase again, the original α-phase orientations are maintained either perfectly, or to some extent. For example, Cheadle and Ells [12] found that the α texture of such β-treated Zr-2.5Nb had cubic symmetry after a single cycle into the β-phase field, but that subsequent cycles had little further effect. Jourdan et al. [9] reported a memory effect in single crystals, while preservation of rolling textures through the phase transformation have been reported to various extents in polycrystalline zirconium (and titanium) [10,13]. A memory effect indicates that variant selection must be occurring, since if no variant selection occurred the texture would be expected to be significantly randomized by the phase transformation. However, reported results are not consistent, for example, in two very similar alloys of zirconium (Zircaloy-4 and Zircaloy-2) under admittedly different heating and cooling conditions; Romero et al. [14] reported no variant selection on heating, but significant selection on cooling, leading to randomization of the room temperature α-phase texture; Wenk et al. [10] reported near perfect texture memory; while Gey et al. [15] reported a strengthening of the room temperature α-phase texture. Furthermore, two of the three α texture components produced in Zr-2.5Nb by mechanical processing in the $(\alpha + \beta)$ phase field cannot be accounted for by any known deformation mechanisms of the α-phase per se, and appear to be related to variant selection during the transformation from α to β during or after processing [6,11,16].

Since the β-phase cannot be "quenched" to room temperature and the measurement of texture at 900°C+ is experimentally challenging, the majority of studies of such effects has focused on measurements of the α-phase. Interpreting changes in texture only at ambient conditions requires coupled assumptions to be made about the selection occurring during heating as well as during cooling. Studies of the high temperature phase using scanning electron microscope techniques [17] are somewhat ambiguous due to the presence of a free surface, which undoubtedly affects any variant selection that is influenced by the stress state. However, recently, diffraction using penetrating radiation (neutrons or synchrotron X-rays) has been demonstrated as a powerful technique for the measurement of bulk textures under non-ambient conditions, e.g., Refs [10 and 14]. In this paper, we report experimental measurements of texture through the $\alpha-\beta-\alpha$ phase transformation, carried out on a Zr-2.5Nb alloy, as well as preliminary findings of similar heating cycles under a biasing stress.

Material and Experimental Method

A Zr-2.5Nb alloy was studied throughout all experiments, sourced from a CANDU reactor pressure tube. The conventional CANDU manufacturing procedure for pressure tubes is [18] vacuum arc melt → press forge → rotary forge → machine billet → β-quench (optional) → (A) extrude at $\sim$ 815°C with an extrusion ratio $=\sim$ 10 : 1 → (B) cold draw 25–30 % (2 passes) → autoclave in steam at 400°C and 24 h. Material for the experiments conducted was taken from tubes with the optional β-quench after either steps (A) "hot-extruded" or (B) "cold-worked."

The typical microstructure of a pressure tube after cold-work includes primary α-grains with a plate-like shape and an aspect ratio of roughly 20:5:1 with a thickness of $\sim$ 0.34–0.45 μm [18,19]. The primary α is surrounded by an almost continuous network of prior β-grains (i.e., grains that were β-phase during the two phase extrusion processing at 815°C), which have subsequently transformed on cooling during and after extrusion. Occasionally, some of this β-phase transforms into a fine interpenetrating structure of secondary α with remnant β-phase. This β-phase exists as more or less continuous thin sheets between the secondary α grains. The small size of the β-grains makes determination of texture-orientation relationships between neighbouring grains challenging even at room temperature and requires a transmission electron microscope [16].

Texture Measurements by Neutron Diffraction

Samples of $\sim$ 1 cm^3 were cut from material obtained from both the hot-worked and cold-worked stages of a Zr-2.5Nb pressure tube, and were measured via neutron diffraction on the high-pressure preferred orientation (HIPPO) diffractometer [20] at the Los Alamos Neutron Science Centre (LANSCE) pulsed neutron source. The beam was collimated to a 10 mm diameter; the samples were positioned $\sim$ 9 m from the moderator. Sample heating was performed with a resistive furnace with vanadium heating elements and shields [21]. HIPPO's

unique large detector coverage allows for the measurement of a complete orientation distribution function (ODF) with only rotation about the vertical axis; the validity of these measurements was confirmed through comparison with conventional goniometer measurements of the initial texture under ambient conditions.

Samples were rotated about the vertical axis to four orientations: 0°, 45°, 67.5°, and 90°; data acquisition periods of about 20 min were sufficient to produce texture measurements of both the α and β phases. Data collected at the 150°, 90°, and 40° detector banks was binned into 98 histograms; these were refined simultaneously using a spherical harmonics approximation in general stucture analysis system (GSAS) [22] in order to produce an ODF. The results obtained were in good agreement with those achieved using the materials analysis using diffraction (MAUD) and an E-WIMV approach [23]. Pole figures were calculated using the computed ODF and plotted with Beartex [24].

Samples were heated to 625°C (at this temperature, the relative fractions of the α-phase and β-phase are the same as at room temperature) and the texture measured; samples were then heated to a maximum temperature at a rate of ~ 20°C/min, the texture was measured, and then the sample was cooled back down to 625°C at the same rate. This cycle was repeated. The studies outlined on this paper will focus primarily on those experiments where the maximum temperature was 975°C, i.e., fully within the β-phase regime. Some of these results are also reported in [25].

Texture Measurements by Synchrotron X-Ray Diffraction

X-ray texture measurements were performed at the I-ID beamline at the Advanced Photon Source (APS) at Argonne National Laboratories [26]. The beam was tuned to 87 keV with a beam size of $300 \times 300\,\mu m^2$ and a sample-to-detector distance of 1330 mm. Diffraction patterns were collected on a GE two-dimensional detector with a resolution of 2048×2048 pixels (where one pixel is $200\,\mu$m). Each "pattern" was measured as a summation of ten 0.2 s exposures in order to avoid detector saturation, while still obtaining good statistics for low intensity peaks.

Samples were prepared from hot-worked material in both cylindrical and cylindrical dogbone (for compression and tension tests, respectively), with a resulting gauge diameter of 3 mm and a gauge aspect ratio of $\sim 3:1$.

A series of loading-at-temperature experiments were performed using a hydraulic loading apparatus and an infrared "clamshell" line heater. To prevent oxidization, a small holding chamber made of quartz tubing was continuously flushed with argon gas in order to displace the lower-density oxygen. Samples were heated from room temperature to 250, 625, and 815°C (the extrusion temperature of CANDU pressure tubes) and then 975°C (full β-phase) at a heating rate of ~ 100°C/min; diffraction patterns at 0°, 8°, 16°, 24°, and 32° about the loading axis were measured, resulting in a hold of ~ 30 s at each temperature. Samples were then cooled and measured at each temperature above in turn. Using this heating schedule, samples were loaded either in tension (axial and hoop orientations) or in compression (axial, hoop, and radial orientations) in

three ways: (1) Stress on both heat up and cool down, (2) stress on heat up only, and (3) stress on cool down only. This discussion will focus on those results obtained under a constant force of 50 N (equivalent to a stress of 1.8 MPa) along the hoop direction.

The resulting spectra were divided (or "caked") into 36 10° sections (e.g., Ref [27]), each of which was averaged to produce a diffraction spectrum. The 36 spectra at all five rotation angles at a given temperature were refined simultaneously in MAUD using the Rietveld method, with texture incorporated via the E-WIMV algorithm [23]. Pole figures were plotted with Beartex [24]. Some comparisons between the use of neutron and synchrotron diffraction for measurement of texture can be found in [28].

Results

Neutron Diffraction

Measurements at 625°C —Measurements of texture made at 625°C are, as expected, equivalent to those measured at room temperature. Figure 2(*a*) shows the starting α-phase texture for a hot-extruded sample; note the strong hoop texture component of the (0002) normal. Figures 2(*b*), 2(*c*) show the texture of the sample after one and two cycles into the full β-phase (975°C), respectively. There is a significant change in texture through the first cycle with, for example, the strongest (0002) texture component moving from the hoop direction to the axial. In this case, there is only weak memory of the previous texture, and indeed a very strong variant selection is observed. After the second thermal cycle, some cubic symmetry is seen in the α-phase texture, although many features of the texture are preserved through the transformation. A third cycle (data not shown here due to space constraints) preserves the basic cubic symmetry, and thus a strong "memory" effect is seen.

Figure 3 displays the β-phase textures corresponding to the Fig. 2 α-phase textures. The initial texture is relatively weak. The initial β-phase texture (Fig. 3(*a*)) is *not* in a Burgers relation with the initial α-phase texture (Fig. 2(*a*)). Instead, the β-phase texture has either been generated during hot extrusion or may be a "remnant" left after all the β in the Burgers relation has been consumed. However, after one thermal cycle (Fig. 3(*b*)), the textures of the low temperature α- and β-phases are connected by the Burgers relation. There are then some shifting and strengthening of the major components on subsequent cycling, with a strong cubic symmetry apparent, with the cube rotated 45° relative to the sample coordinate system.

Measurements at 975°C —The β-phase texture found on initial heating to high temperature (975°C) is shown in Fig. 4. The high temperature β-phase texture is very different from that of the low temperature β-phase. This confirms that the high temperature β-phase is not formed by large scale growth of the existing β-phase grains, but instead occurs due to the transformation of (or nucleation from) the α-phase via the Burgers relationship. After the first cycle,

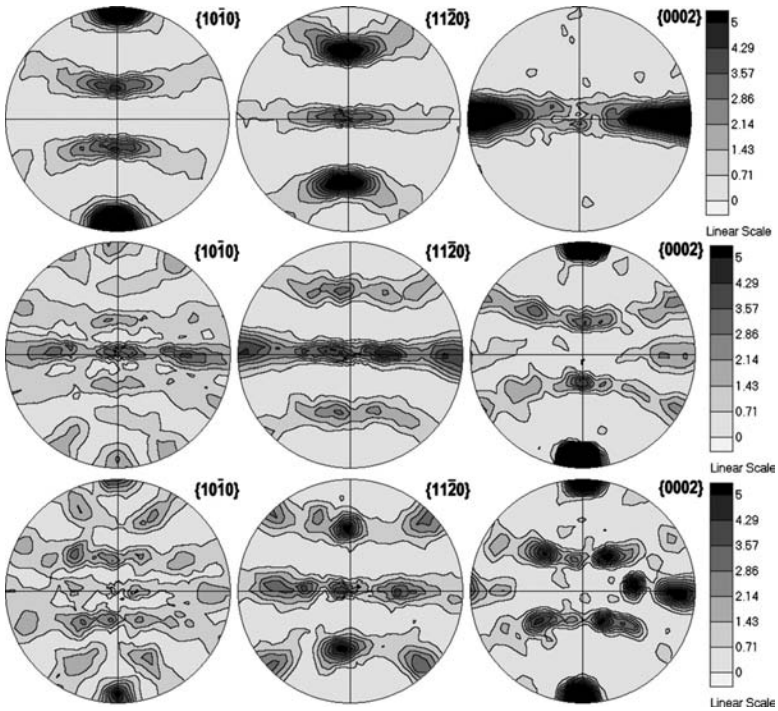


FIG. 2—*Low temperature (625°C) α-phase texture for the* 10$\bar{1}$0, 11$\bar{2}$0, *and (0002) pole figures for hot worked material:* (a) *Initial [max 16.4 mrd];* (b) *after 1 thermal cycle [max 28.8 mrd];* (c) *after 2 thermal cycles [max 12.1 mrd]. Axial vertical, radial in centre, hoop horizontal.*

the β-phase textures at 625°C and 975°C (Figs. 4(*b*)) become quite similar; cubic symmetry similarly is developed. The final low temperature α textures in the pole figures related via the Burgers criterion strongly resemble this high temperature β texture.

Influence of Prior Cold-Work—Figures 5–7 show a subset of equivalent data to that discussed above which was obtained for the cold-worked sample (taken after cold drawing, step B above). We would expect a higher dislocation density and internal stress to have been generated during this cold-work process. The initial texture of this material (Figs. 6(*a*)) shows many qualitative similarities to the hot-extruded tube (Figs. 3(*a*)), but is generally broader and less strong. Similarly, the high temperature texture for the cold-worked material shows several similarities to that of the hot-extruded material in Fig. 4. In comparison to the hot-worked, sample we notice that the drastic texture reorientation seen in the hot-worked sample ((0002) poles moving from hoop to axial) is repeated (Fig. 5(*a*), 5(*b*)); however, not all of the texture reorients in the cold-worked material,

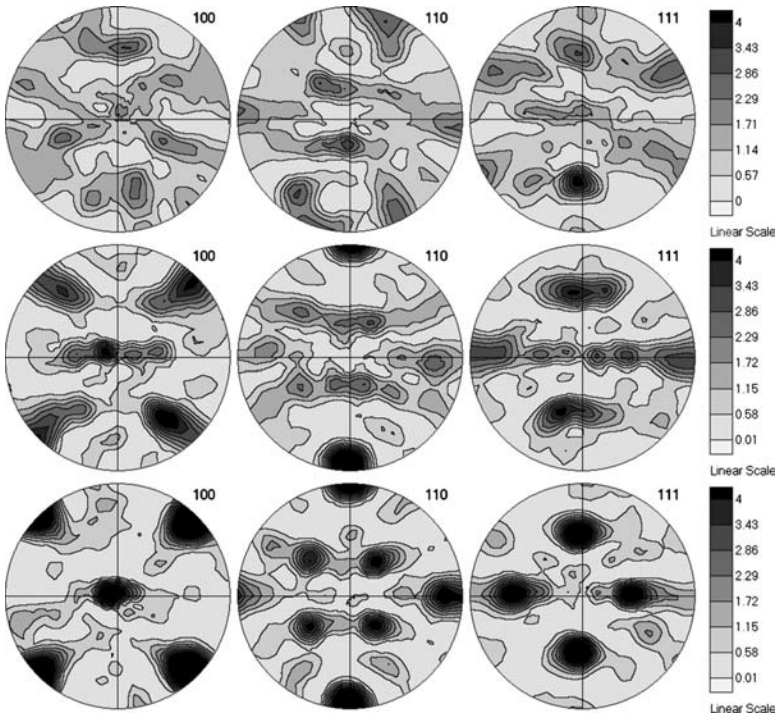


FIG. 3—*Low temperature (625°C) β-phase texture for the 100, 110, and 111 pole figures for hot worked material:* (a) *Initial [max 4.3 mrd];* (b) *after 1 thermal cycle [max 6.9 mrd];* (c) *after 2 thermal cycles [max 8.4 mrd]. Axial vertical, radial in centre, hoop horizontal.*

with significant intensity remaining in roughly the original orientation. This observation is reinforced by the calculated (0002) Kearns factors, shown in Table 1. In comparing Figs. 6 and 7, we see again that the *β*-phase high temperature texture is not inherited by large scale grain growth from the low

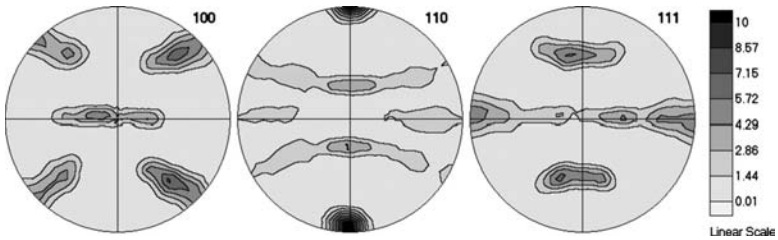


FIG. 4—*High temperature (975°C) β-phase texture for the 100, 110, and 111 pole figures for hot worked material on the first heating [max 12.5 mrd]. Axial vertical, radial in centre, hoop horizontal.*

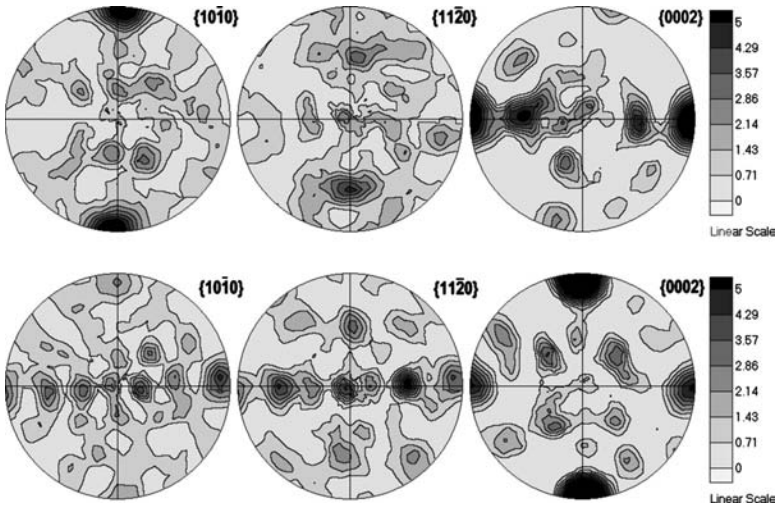


FIG. 5—*Low temperature (625°C) α-phase texture for the* 10$\bar{1}$0, 11$\bar{2}$0*, and (0002) pole figures for cold-worked material: (*a*) Initial [max 8.7 mrd]; (*b*) after 1 thermal cycle [max 14.1 mrd]. Axial vertical, radial in centre, hoop horizontal.*

temperature *β*-phase texture but must instead derive from the transformation of α-phase grains.

Synchrotron X-Ray Diffraction

Unstressed Thermal Cycling—One sample was subjected to the same thermal cycling schedule as described in the neutron diffraction experiments above to confirm agreement with the synchrotron diffraction measurements of texture; Figs. 8 and 9 show the low temperature (625°C) α-phase and high temperature (975°C) *β*-phase textures for the first cycle (further cycles not reproduced here due to space constraints). The resulting textures are in good agreement with those obtained via neutron diffraction (compare with Figs. 4(*a*), 4(*b*)).

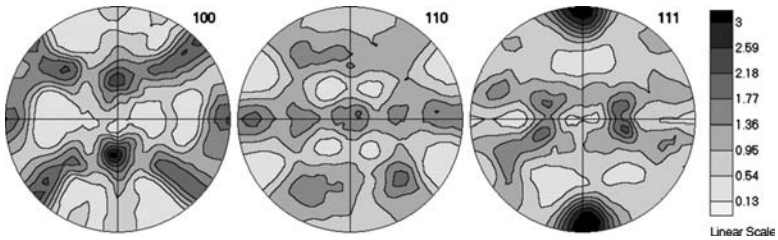


FIG. 6—*Initial low temperature (625°C) β-phase texture for the 100, 110, and 111 pole figures for cold-worked material [max 3.5 mrd]. Axial vertical, radial in centre, hoop horizontal.*

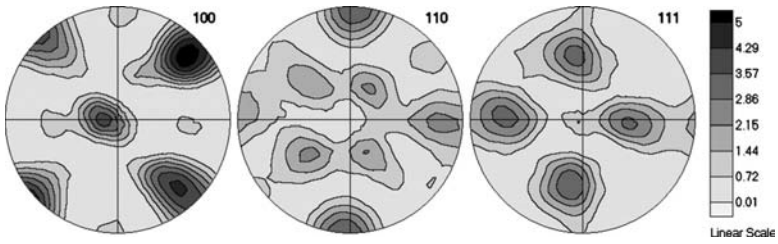


FIG. 7—*High temperature (975°C) β-phase texture for the 100, 110, and 111 pole figures for cold-worked material on the first heating. [max 5.6 mrd]. Axial vertical, radial in centre, hoop horizontal.*

Influence of Biasing Stress—Measurements at Low Temperature—We report here the low temperature (625°C) α-phase textures before and after the application of (a) 50 N constant stress both on heating and cooling, (b) 50 N stress on heating only, and (c) 50 N stress on cooling only for tension (Fig. 10) and compression (Fig. 11) applied along the hoop direction. First, we note that there is only a small texture variability for the initial samples (i); any variability is due to texture variation within the tube coupled with the relatively small grain sampling inherent to the synchrotron diffraction technique. In both Figs. 10 and 11, it can be seen that there is no significant qualitative difference in the textures for cases (a) and (b), i.e., if a stress is applied on heating, there appears to be only a small effect of subsequently applying a stress upon cooling. In fact, these textures appear to be quite similar to those obtained after a thermal cycle *without* stress (Fig. 9). However, one slight variation was observed; in Fig. 11(*c*) (ii), the compressive stress on cool down appears to inhibit the full reorientation of the texture to the strong axial (0002) texture that is seen elsewhere.

Influence of Biasing Stress—Measurements at High Temperature—Images (iv) of Figs. 11(*c*) show measurements of the {110} β-phase textures made at

TABLE 1—*Calculated (0002) Kearns factors for hot and cold-worked tube throughout two thermal cycles to the β-phase.*

Stage	F_T	F_A	F_R	F_T/F_A
Cold-worked				
Initial	0.4811	0.1677	0.3511	2.8688
1st heating	0.3093	0.4519	0.2388	0.6844
2nd heating	0.3282	0.4078	0.2639	0.8048
Hot-worked				
Initial	0.5952	0.0619	0.3429	9.6155
1st heating	0.2206	0.5815	0.1979	0.3794
2nd heating	0.3487	0.3436	0.3077	1.0148

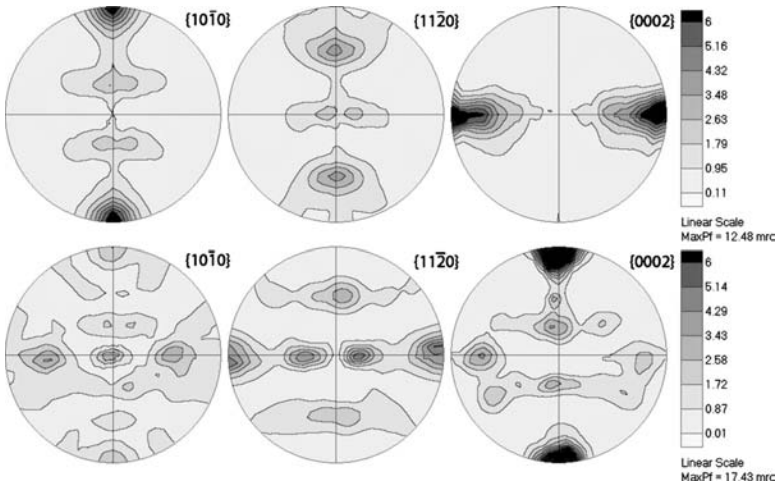


FIG. 8—*Low temperature (625°C) α-phase textures of hot-worked material measured via XRD with no stress bias:* (a) *Initial texture;* (b) *after one thermal cycle.*

975°C. Figures 11(*a*), representative of the texture with tensile and compressive stresses applied on heat up, respectively, do not differ qualitatively from those with no stress on heat up (Fig. 9), i.e., there are no new variants formed as a result of this applied stress. The statistics of the high temperature *β*-phase texture are, however, poorer than the low temperature. This is probably due to grain growth of the *β*-phase leading to relatively poor statistical sampling of grains.

Discussion

It is clear that during the $\alpha-\beta-\alpha$ phase transformation in Zr-2.5Nb, the Burgers relationship is followed, but not all variants are selected equally; there is variant selection on both heating, as evidenced by the strong $(110)_{\beta}$ axial component,

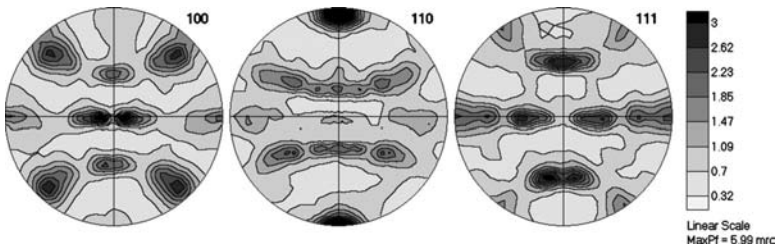


FIG. 9—*High temperature (975°C) β-phase textures of hot-worked material measured via XRD with no stress bias.*

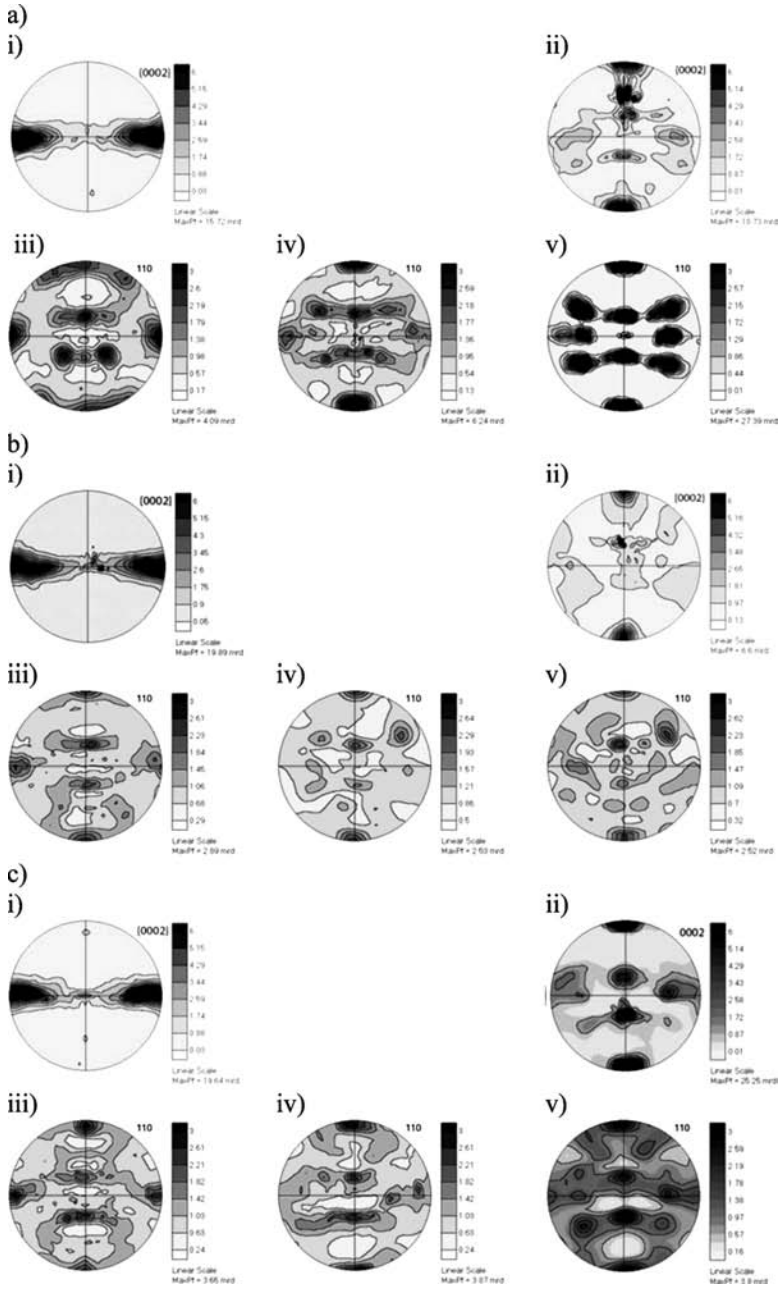


FIG. 10—*Texture for a tensile stress applied along the hoop direction: (i) Initial α texture (625°C); (ii) α texture after one thermal cycle (625°C); (iii) initial β texture (625°C); (iv) high temperature β texture (975°C); (v) final β texture after one thermal cycle (625°C) for:* (a) *Stress on heat up and cool down;* (b) *stress on heat up only; and* (c) *stress on cool down only.*

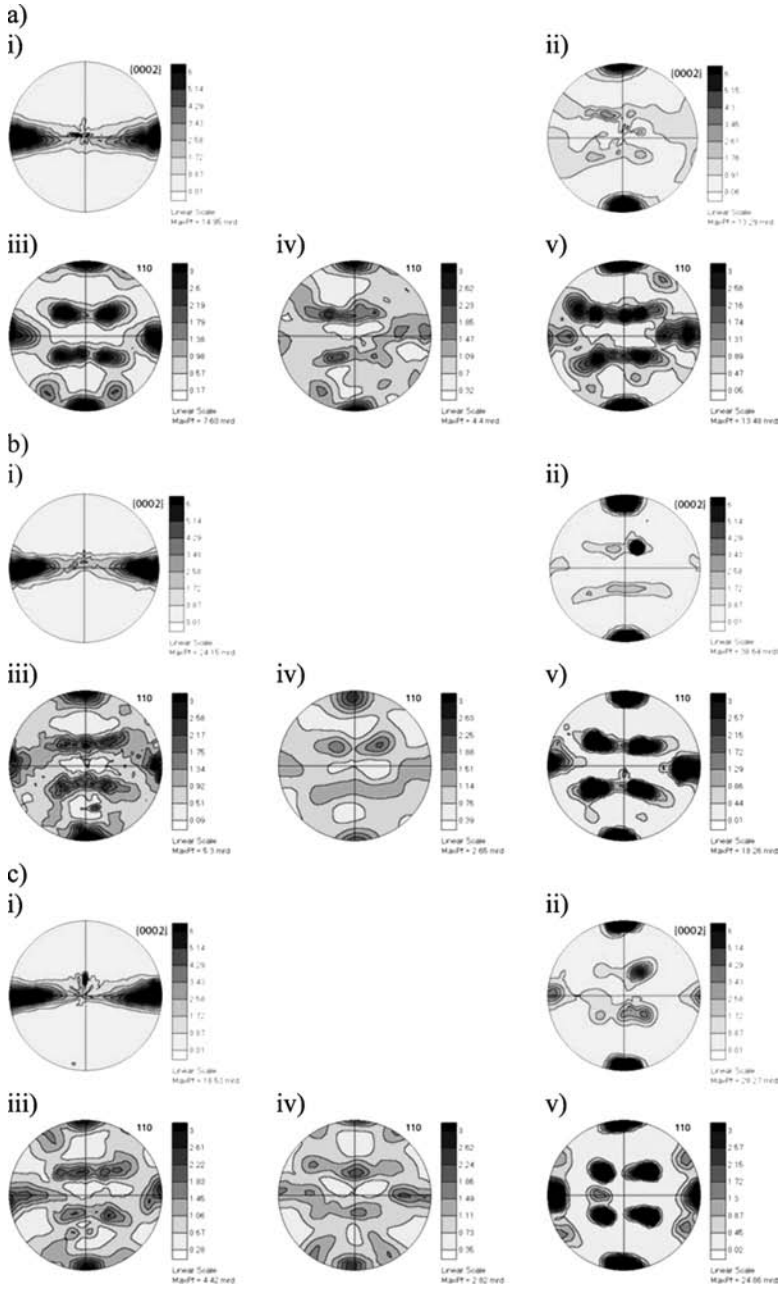


FIG. 11—*Texture for a compressive stress applied along the hoop direction: (i) Initial α texture (625°C); (ii) α texture after one thermal cycle (625°C); (iii) initial β texture (625°C), (iv) high temperature β texture (975°C); (v) final β texture after one thermal cycle for:* (a) *Stress on heat up and cool down;* (b) *stress on heat up only; and* (c) *stress on cool down only.*

Fig. 5, and cooling, evidenced by the very strong axial $(0002)_\alpha$ component, Fig. 3(*b*). There is also a memory effect as evidenced by the stability of the cubic symmetry of the textures on subsequent cycling. Both these effects have been inferred by previous workers from room temperature textures.

A notable characteristic of the Zr-2.5Nb alloy in [12] was that, unlike, e.g., Zircaloy-2, the α-phase did not appear to undergo recrystallization by the nucleation and growth of new crystals (which would be evidenced by a 30° rotation about the *c*-axis during heating). We see the same behaviour here: Fig. 2(*a*) shows the typical strong $(10\bar{1}0)_\alpha$ axial fibre from hot extrusion, despite the fact that the material has now been heated to 625°C. Based on other measurements, not reported due to space constraints, this $(10\bar{1}0)_\alpha$ fiber is, in fact, retained up to at least 875°C. It appears that the migration of high angle boundaries is inhibited in Zr-2.5Nb by the presence of the continuous *β*-network in the original microstructure. This lack of recrystallization is clearly reflected in the *β*-phase texture formed on initial heating (Fig. 4), where the $(110)_\beta$ maps to $(10\bar{1}0)_\alpha$ as well as $(0002)_\alpha$ through the Burgers relationship.

Though the data is not reported here, experiments carried out that did not go entirely into the *β*-phase regime (e.g., had a maximum temperature of 875°C) did not display the large texture changes observed upon thermal cycling (e.g., from Fig. 2(*a*) to Fig. 2(*b*)). A strong memory effect was instead observed. It is likely that this contributed to, for example, the strong memory effect seen by Wenk et al. [10]; (see diffraction pattern Fig. 1 from [10]) where the maximum temperature was not sufficient to fully enter the *β*-phase regime. Similar results are reported by Romero et al. [14].

Experiments conducted on the cold-worked material, as noted, produced a broader, less-strong texture that did not fully reorient to the strong axial (0002) texture seen in the hot-worked material. This is reinforced by the Kearns factors shown in Table 1. When comparing the high temperature *β*-phase {110} textures for the hot-worked and cold-worked material (Figs. 4 and 7, respectively), it can be seen that this "incomplete" reorientation in the cold-worked material is evident in the high temperature {110} texture. Whatever difference in transformation exists is likely occurring during heating. As the only difference between the hot- and cold-worked material is the additional 25–30 % cold draw and a 24 h autoclave in steam at 400°C, we would anticipate that microstructural or texture differences during this stage would be the driving factor for this difference in evolution. Comparing the initial α textures (Figs. 5(*a*)), there is little difference in the starting textures. However, in the cold-worked material, we would anticipate a much stronger dislocation density, and a higher internal stress state, than that of the hot-worked material. It is possible that this internal stress is inhibiting the reorientation of the (0002) poles to the axial direction.

Hutchinson et al. [29,30] reviewed a number of mechanisms for variant selection during cool down, with the particular aim to explain texture memory: (1) Stresses generated by the phase transformation strain during heat up biasing the subsequent transformation; (2) remnant thin films of the low temperature phase at the boundaries of the high temperature phase act as nuclei during cool down; and (3) grain boundaries are formed in the high temperature phase

with optimal characteristics for nucleation of certain orientations of the low temperature phase. Given the short hold times at high temperature, diffusional relaxation makes mechanism (1) extremely unlikely. Our observation of texture memory associated with incomplete transformation to the β-phase, along with that of Wenk et al. [10] and Romero et al. [14], lead to the conclusion that in cases where a remnant α-phase is present at high temperature, it acts to control the low temperature texture. Effectively, this represents the second mechanism reviewed by Hutchinson.

As noted, the high temperature β-phase is not formed by wholescale growth of the existing low temperature β-phase, but must instead occur either due to nucleation from the α-phase, or by preferential growth of selected existing β-orientations. The former is perhaps unlikely, unless nucleation occurs right at the $\alpha-\beta$ grain boundaries, because the Nb content of the α-phase is so low ($< 1\%$); hence there is minimal driving force for nucleation within the grain. Preferential growth of selected β-orientations is similar to the interpretations of how a high temperature β-phase texture is produced in Ti-6Al-4V [21,31]. In the cases of [21 and 31], the low temperature β-phase texture could not be measured due to poor statistics, and a growth mechanism was assumed by considering the low temperature α-phase texture and potential Burgers relationships. It should be noted of course that the balance between the growth of existing textures and the nucleation of new grains from the α-phase will be highly dependent on thermal ramp rates, but even at the relatively slow heating rates used in the neutron diffraction experiments, it is clear that wholescale growth of the majority of existing β-phase grains is not occurring.

The third mechanism reviewed by Hutchinson et al. is that of Stanford and Bate [32], who suggested a mechanism for texture memory and variant selection during cooling of Ti-6Al-4V that is based on the crystallography relationships across β-phase grain boundaries. If these boundaries are unchanged during a heating/cooling cycle, we can expect strong texture memory effects, while if they move (due to, e.g., grain growth), we can expect changes in the observed texture through a thermal cycle. It follows that any texture memory effect will be highly dependent on how the initial texture has been produced. Our starting material had α/β phase textures associated with hot extrusion in the two phase regime. Thermal cycling into the β-phase regime (with no stress applied) led to drastic changes in the texture on cooling. However, the α/β phase textures produced by cooling without applied load are, excepting grain growth, reproduced on a second thermal cycle, hence demonstrating a "texture memory."

In previous work, we have investigated the formation of texture on heat up and cool down with the use of an elasto-plastic self-consistent model. The model is based on the thermal anisotropy of the α-phase of zirconium, and the stresses generated by it during heating; these stresses could generate an internal bias for the selection of variants. For further details of the model, see [25]. We see that, on heat up, the addition of a selection criterion based on thermal stresses greatly improves the results of the model, and that there is very strong selection occurring. The model provides an excellent qualitative prediction of the textures obtained at high temperature, although the intensity is under predicted. On

cool down, even without variant selection initiated, we see roughly the correct texture, but with a dramatically different predicted intensity than seen experimentally. On cool down, there must therefore be some selection in order to produce the observed texture, but the selection process is not as significant as that which exists upon heating. This is likely because during cool down, thermal stresses must play a less significant role due to the thermally isotropic nature of the β-phase.

It is clear that some form of variant selection is associated with the extrusion process used in manufacturing pressure tubes from Zr-2.5Nb [6,11,16,33]. This process is normally carried out at 815°C, at which temperature the proportions of α and β are $\sim 60:40$. Prior to extrusion, the primary α and β both have rather random textures associated with the forging process. The α-phase has a Widmanstätten-like morphology resulting from β to α transformation after forging. The extruded texture comprises a predominantly transverse basal plane normal component with a strong $(10\bar{1}0)_\alpha$ axial fiber (Fig. 2(*a*)), which persists through the cold drawing stage (Fig. 5(*a*)). This component does not correspond to any known deformation system in the α-phase, and the crystals in this orientation are effectively dislocation free [16]. Also, the *c*-axes of the crystals associated with this texture are parallel to the long axes of the grains in the radial/transverse plane [16,33]. One possible explanation for this component is preferred growth of primary α grains in this orientation as a result of the stress/strain imposed by the extrusion process, combined with the strains associated with the Burgers relationship transformation. Further, crystals that are formed by transformation into the Widmanstätten-like morphology on cooling after extrusion exhibit a very strong selection of the variant with *c* in the axial direction of the tube [6,16]; the same preferred variant seen in Fig. 2(*b*). These observations suggest that mechanical processing influences variant selection and that stress, or constraint, may contribute to the variants observed. The preliminary results obtained from thermal cycling experiments under an external biasing stress are a step towards understanding this phenomenon.

A novel result reported here is the result of thermal cycling to the β-phase under the influence of hoop tensile and compressive stresses. In the case of both the hoop tensile and compressive stresses, upon heat up and cool down, the high temperature β-phase textures are qualitatively the same (see part (iv) of Figs. 11(*a*)11(*c*), respectively); further, there is little difference between the final (0002) textures where stress is applied throughout the full thermal cycle (Figs. 11(*a*)), where it is only applied on heat up (Figs. 11(*b*)), and where it is only applied on cool down (Figs. 11(*c*)). This would suggest that the application of stress on heat up does not discourage the selection of the variant that would otherwise occur in the absence of stress. It does not appear to have any other effect on selection, at least for stresses applied in this direction of the sample, where initially a very strong (0002) intensity is found. It is possible that the stresses applied were not large enough to provide a sufficient bias.

However, with a stress bias solely on cool down, in compression, we see that a larger proportion of the initial hoop (0002) texture is retained (Fig. 11(*c*)).

This texture feature is similar to that observed in the cold-worked sample (Fig. 5(*b*)), though there is not enough evidence to suggest that the two effects may be linked. Further, it is not clear why similar final α textures are not seen between all samples with stress applied in the hoop direction. One hypothesis for this imbalance of effect is that there may be an increased ability to affect texture on cool down. This could be related to the strength of the 'natural' variant selection at play. In the models discussed above, it was found that selection was very strong on heat up, but much weaker on cool down. It is possible that this difference in the relative strength of internal stress driven variant selection paves the way for the different impact of external stress on variant selection during heating and cooling.

Conclusions

We have carried out in situ measurements of the texture changes occurring during the $\alpha-\beta$ phase transformation both with and without stress in Zr-2.5Nb. We have observed the following.

- The texture of the β-phase is inherited from the α-phase on the initial heating. $\alpha \rightarrow \beta$ variant selection occurs, driven by the interaction between thermal stresses produced in the α-phase and the phase transformation strain. High levels of in situ stress biasing via internal stresses produced by cold-work do influence this selection process, but not to a great extent.
- There is a preferred $\beta \rightarrow \alpha$ variant selection during un-stressed cooling. Compared to random variant development, this selection does not significantly influence the location of the texture maxima (which was observed during heating) but does affect the magnitude of the maxima observed.
- There are dramatic changes to the α-phase texture during the first heating–cooling cycle. The β-phase texture on subsequent (second and third) heatings can still be described as being driven by thermal stresses.
- The cubic symmetry of the high temperature β-phase is inherited by the low temperature α-phase during the second cooling, i.e., changes in the high temperature β-phase texture are clearly reflected in the α-phase texture upon cooling.
- A near perfect memory effect is seen if the maximum temperature does not result in 100 % transformation into the β-phase.
- Stress biasing along the hoop axis during the heating cycle does not appear to significantly influence variant selection, at least for the stress magnitudes tested here. Stress biasing along the hoop axis during the cooling cycle has a slight influence on variant selection. For the hot worked sample this led to retention of the original (0002) component, resulting in an α-phase texture after one thermal cycle that was qualitatively similar to that seen for the cold-worked sample during un-stressed thermal cycling.

Acknowledgments

The writers would like to thank Sven Vogel and Helmut Reiche of HIPPO at LANSCE and Jon Almer of APS for their considerable help during experiments, as well as Song Cai for his work on some of the modeling and preliminary experiments. This work was sponsored by NSERC, COG, OPG, and Nu-Tech Precision metals under the Industrial Research Chair program in Nuclear Materials at Queen's University. The writers thank S. A. Aldridge of Nu-Tech Precision Metals, Inc., and J. M. Theaker of Atomic Energy of Canada, Ltd., for providing the experimental materials.

References

[1] Kocks, U. F., Tomé, C. N., and Wenk, H.-R., *Texture and Anisotropy*, CUP, Cambridge, 1998.
[2] Holt, R. A., "In-Reactor Deformation of Cold-Worked Zr–2.5Nb Pressure Tubes," *J. Nucl. Mater.*, Vol. 372(2–3), 2008, pp. 182–214.
[3] Liundin, C. E. and Cox, R. H., *USAEC Report GEAP-4089*, Vol. 1, 1962, p. 9.
[4] ASTM B353-07, 2010, "Standard Specification for Wrought Zirconium and Zirconium Alloy Seamless and Welded Tubes for Nuclear Service (Except Nuclear Fuel Cladding)," *Annual Book of ASTM Standards*, Vol. 2.04, ASTM International, West Conshohocken, PA, pp. 1–18.
[5] Perovic, V., Perovic, A., Weatherly, G. C., Brown, L. M., Purdy, G. R., Fleck, R. G., and Holt, R. A., "Microstructural and Microchemical Studies of Zr-2.5Nb Pressure Tube Alloy," *J. Nucl. Mater.*, Vol. 205, 1993, pp. 251–257.
[6] Li, Y., Rogge, R., and Holt, R. A., "Development of Local Microstructure and Crystallographic Texture in Extruded Zr–2.5Nb Tubes," *Mater. Sci. Eng., A*, Vol. 437(1), 2006, pp. 10–20.
[7] Burgers, W. G., "On the Process of Transition of the Cubic-Body-Centered Modification into the Hexagonal-Close-Packed Modification of Zirconium," *Physica A*, Vol. 1, 1934, pp. 561–586.
[8] van Ginneken, A. J. J. and Burgers, W. G., "The Habit Plane of the Zirconium Transformation," *Acta Crystallogr.*, Vol. 5(4), 1952, pp. 548–549.
[9] Jourdan, C., Gastaldi, J., Marzo, P., and Grange, G., "In Situ Statistical Study of the Nucleation, the Variant Selection and the Orientation Memory Effect During the $\alpha \Leftrightarrow \beta$ Titanium Martensitic Transformation," *J. Mater. Sci.*, Vol. 26(16), 1991, pp. 4355–4360.
[10] Wenk, H.-R., Lonardelli, I., and Williams, D., "Texture Changes in the hcp→bcc→hcp Transformation of Zirconium Studied In Situ by Neutron Diffraction," *Acta Mater.*, Vol. 52, 2004, pp. 1899–1907.
[11] Holt, R. A. and Aldridge, S. A., "Effect of Extrusion Variables on Crystallographic Texture of Zr-2.5 wt% Nb," *J. Nucl. Mater.*, Vol. 135, 1985, pp. 246–259.
[12] Cheadle, B. A. and Ells, C. E., "Effect of Heat Treatment on the Texture of Fabricated Zr-Rich Alloys," *Electrochem. Technol.*, Vol. 4, No. 7–8, 1966, pp. 329–336.
[13] Glavicic, M. G., Goetz, R. L., Barker, D. R., Shen, G., Furrer, D., Woodfield, A., and Semiatin, S. L., "Modeling of Texture Evolution during Hot Forging of Alpha/Beta Titanium Alloys," *Metall. Mater. Trans. A*, Vol. 39A(4), 2008, pp. 887–896.

[14] Romero, J., Preuss, M., and da Fonseca, J. Q., "Texture Memory and Variant Selection During Phase Transformation of a Zirconium Alloy," *Acta Mater.*, Vol. 57, 2009, pp. 5501–5511.
[15] Gey, N., Gautier, E., Humbert, M., Cerqueira, A., Bechade, J. L., and Archambault, P., "Study of the α/β Phase Transformation of Zy-4 in Presence of Applied Stresses at Heating: Analysis of the Inherited Microstructures and Textures," *J. Nucl. Mater.*, Vol. 302, 2002, pp. 175–184.
[16] Holt, R. A. and Zhao, P., "Micro-Texture of Extruded Zr–2.5Nb Tubes," *J. Nucl. Mater.*, Vol. 335, 2004, pp. 520–528.
[17] Seward, G. G. E., Prior, D. J., Wheeler, J., Celotto, S., Halliday, D. J. M., Paden, R. S., and Tye, M. R., "High-Temperature Electron Backscatter Diffraction and Scanning Electron Microscopy Imaging Techniques: In Situ Investigations of Dynamic Processes," *Scanning*, Vol. 24(5), 2002, pp. 232–240.
[18] Cheadle, B. A., *Proc. Third International Symposium on Zirconium in the Nuclear Industry, ASTM-STP-633*, Annency, France, 1977, ASTM International, West Conshohocken, PA, p. 457.
[19] Griffiths, M., Davies, W. G., Moan, G. D., Holt, R. A., Causey, A. R., and Aldridge, S., *Proc. 13th International Symposium on Zirconium in the Nuclear Industry, ASTM-STP-1423*, Quebec City, Canada, 2002, ASTM International, West Conshohocken, PA, pp. 796–810.
[20] Matthies, S., Pehl, J., Wenk, H. R., Lutterotti, L., and Vogel, S. C., "Quantitative Texture Analysis with the HIPPO Neutron TOF Diffractometer," *J. Appl. Crystallogr.*, Vol. 38(3), 2005, pp. 462–475.
[21] Lonardelli, I., Gey, N., Wenk, H.-R., Humbert, M., Vogel, S. C., and Lutterotti, L., "In Situ Observation of Texture Evolution During $\alpha \rightarrow \beta$ and $\beta \rightarrow \alpha$ Phase Transformations in Titanium Alloys Investigated by Neutron Diffraction," *Acta Mater.*, Vol. 55(17), 2007, pp. 5718–5727.
[22] Larson, A. C. and Von Dreele, R. B., "General Structure Analysis Program," *Report LAUR86-748*, Los Alamos National Laboratory, Los Alamos, NM, 1994.
[23] Lutterotti, L., Matthies, S., Wenk, H.-R., Schultz, A. S., and Richardson, J. W., "Combined Texture and Structure Analysis of Deformed Limestone from Time-of-Flight Neutron Diffraction Spectra," *J. Appl. Phys.*, Vol. 81(2), 1997, pp. 594–600.
[24] Wenk, H. R., Matthies, S., Donovan, J. J., and Chateigner, D. J., , "BEARTEX: A Windows-Based Program System for Quantitative Texture Analysis," J. Appl. Crystallogr., Vol. 31, No. 2, 1998, pp. 262–269.
[25] Daymond, M. R., Holt, R. A., Cai, S., Mosbrucker, P., and Vogel, S. C., "Texture Inheritance and Variant Selection Through an hcp–bcc–hcp Phase Transformation," *Acta Mater.*, Vol. 58(11), 2010, pp. 4053–4066.
[26] Haeffner, D. R., Almer, J. D., and Lienert, U., "The Use of High Energy X-Rays from the Advanced Photon Source to Study Stresses in Materials," *Mater. Sci. Eng., A*, Vol. 399, 2005, pp. 120–127.
[27] Daymond, M. R., Young, M. L., Almer, J. D., and Dunand, D. C., "Strain and Texture Evolution During Mechanical Loading of a Crack Tip in Martensitic Shape-Memory NiTi," *Acta Mater.*, Vol. 55, 2007, pp. 3929–3942.
[28] Wenk, H.-R., "Neutron Diffraction Texture Analysis," *Rev. Mineral. Geochem.*, Vol. 63, 2006, pp. 399–426.
[29] Hutchinson, B., Ryde, L., and Bate, P., "Transformation Textures in Steels," *Mater. Sci. Forum*, Vols. 495–497, 2005, pp. 1141–1150.
[30] Hutchinson, J. W., "Elastic-Plastic Behaviour of Polycrystalline Metals and Composites," *Proc. R. Soc. London*, Vol. 319, 1970, pp. 247–272.

[31] Bhattacharyya, D., Viswanathan, G. B., Vogel, S. C., Williams, D. J., Venkatesh, V., and Fraser, H. L., "A Study of the Mechanism of α to β Phase Transformation by Tracking Texture Evolution with Temperature in Ti–6Al–4V Using Neutron Diffraction," *Scr. Mater.*, Vol. 54(2), 2006, pp. 231–236.
[32] Stanford, N. and Bate, P. S., "Crystallographic Variant Selection in Ti–6Al–4V," *Acta Mater.*, Vol. 52, 2004, pp. 5215–5224.
[33] Griffiths, M., Holt, R. A., Li, J., and Saimoto, S., "Micro-Texture Analysis of Zr-2.5Nb Pressure Tubes," *Microstruct. Sci.*, Vol. 26, 1999, pp. 293–302.

DISCUSSION

Question 1, Javier Romero, Westinghouse, Sweden:—Could the reported variant selection during heating be occurring due to beta grain growth?

Author's Response:—It depends when exactly the beta grain growth you are referring to is occurring. If you mean during heat up in the two phase regime then, as we describe in the paper, we do indeed consider that the variant selection occurs due to preferential growth of selected existing beta-orientations. This is likely, compared to direct nucleation from the alpha phase, because of the very different Nb contents in the two phases, and the relatively short times available for Nb diffusion; hence there is minimal driving force for nucleation within the alpha grain. However the selected beta-orientation which is preferred to grow is determined by the local alpha environment. Modeling work (see Daymond, M.R. *et al*., Acta Mater., 2010, **58**(11), p. 4053-4066) has shown that this new variant appears to be selected due to the effects of thermal anisotropy prior to reaching the full beta regime.

If on the other hand you mean beta grain growth in the full-beta phase regime, then the answer is no. We have observed the texture evolution of our material in the full-beta phase, and found that this resulted in the development and strengthening of cubic symmetry in the texture, not the creation of the new variant itself. Measurements made in the beta phase during a hold on the order of 30 seconds have not differed, in terms of the variant selection being addressed, from those made with holds over an hour in length. Other tests on ramp rate variation, with extended holds in the alpha+beta regime have also not affected the qualitative texture changes, although the strength of the texture does change slightly.

Question 2, P. Barberis:—There is variant selection driven by elastic stress but no texture evolution on applying a stress during cooling. Is there a contradiction between these two statements?

Author's Response:—Perhaps there is some contradiction, but we should clarify. We are saying that internal stress generation on the length scales of grains, caused by thermal expansion anisotropy, can drive selection strongly. Internal stresses due to dislocation networks also have an effect. On the other hand, an external applied stress does not have much effect at all; we believe that alternate methods of relaxation (effectively creep) are relaxing the stress state experienced by the grain so that the external stress, at least at the magnitudes investigated here, does not have much effect.

FABRICATION AND MECHANICAL PROPERTIES

Reprinted from JAI, Vol. 7, No. 8
doi:10.1520/JAI102992
Available online at www.astm.org/JAI

A. Jardy,[1] *F. Leclerc,*[2] *M. Revil-Baudard,*[1,2] *P. Guerin,*[2]
H. Combeau,[1] *and V. Rebeyrolle*[2]

Segregation in Vacuum Arc Remelted Zirconium Alloy Ingots

ABSTRACT: Vacuum arc remelting of zirconium alloy ingots is a key step in the manufacturing process of fuel assembly components in nuclear reactors. The control of the analytical homogeneity is indeed fundamental to ensure the quality and the in-reactor performance of the final products. For this reason, together with other industrial companies, AREVA NP/CEZUS has undertaken for more than 20 years a partnership with the Nancy School of Mines, which has developed a specific code named SOLidification during Arc Remelting (SOLAR). The mathematical model is based on the solution of the coupled transient heat, momentum, and solute transport equations, under laminar or turbulent flow conditions, during the remelting and cooling of a cylindrical ingot. An important part of the overall work is the careful validation of numerical simulations. For this purpose, specific sets of thermophysical data have been determined for various zirconium alloys. The model results show good agreement with the observation of 6 tons ingots remelted under industrial conditions. The specific case of a single melt M5™[3] ingot was recently studied. The corresponding results are presented and discussed. The chemistry analysis has been enriched with structure examinations, aiming at improving the knowledge of solidification mechanisms in zirconium alloys. The use of SOLAR code to evaluate the ingot chemistry contributes to constantly improving the melting process applied to zirconium alloys in AREVA NP/CEZUS.

KEYWORDS: vacuum arc remelting, simulation, segregation, M5™

Manuscript received January 25, 2010; accepted for publication June 23, 2010; published online August 2010.
[1] Dépt. SI2M, Institut Jean Lamour—UMR 7198, Ecole des Mines, Parc de Saurupt, F-54042 Nancy Cedex, France.
[2] CEZUS Research Centre, AREVA, AREVA NP, Av. Paul Girod, F-73403 Ugine, France.

Cite as: Jardy, A., Leclerc, F., Revil-Baudard, M., Guerin, P., Combeau, H. and Rebeyrolle, V., "Segregation in Vacuum Arc Remelted Zirconium Alloy Ingots," *J. ASTM Intl.*, Vol. 7, No. 8. doi:10.1520/JAI102992.
[3] M5 is a trademark of AREVA NP.

Copyright © 2011 by ASTM International, 100 Barr Harbor Drive, PO Box C700, West Conshohocken, PA 19428-2959.

Introduction

High metallurgical quality ingots of zirconium alloys are necessary for nuclear applications. Zirconium alloy melting is the last step in the manufacturing process during which zirconium alloys are at the liquid state. Therefore, it determines the final products chemistry. A single melting is not sufficient, and remelting provides better chemical properties; this is the reason why the vacuum arc remelting (VAR) process is applied to zirconium alloys.

The principle of the VAR process, as illustrated in Fig. 1, consists of melting a consumable metallic electrode of the required grade under a high vacuum in order to obtain a sound ingot of good structural quality. During remelting, an electric arc is maintained between the tip of the electrode (which acts as the cathode) and the top of the secondary ingot in order to ensure melting of the electrode. Liquid metal falls through the arc plasma and progressively builds up the ingot, which solidifies in contact with a water cooled copper

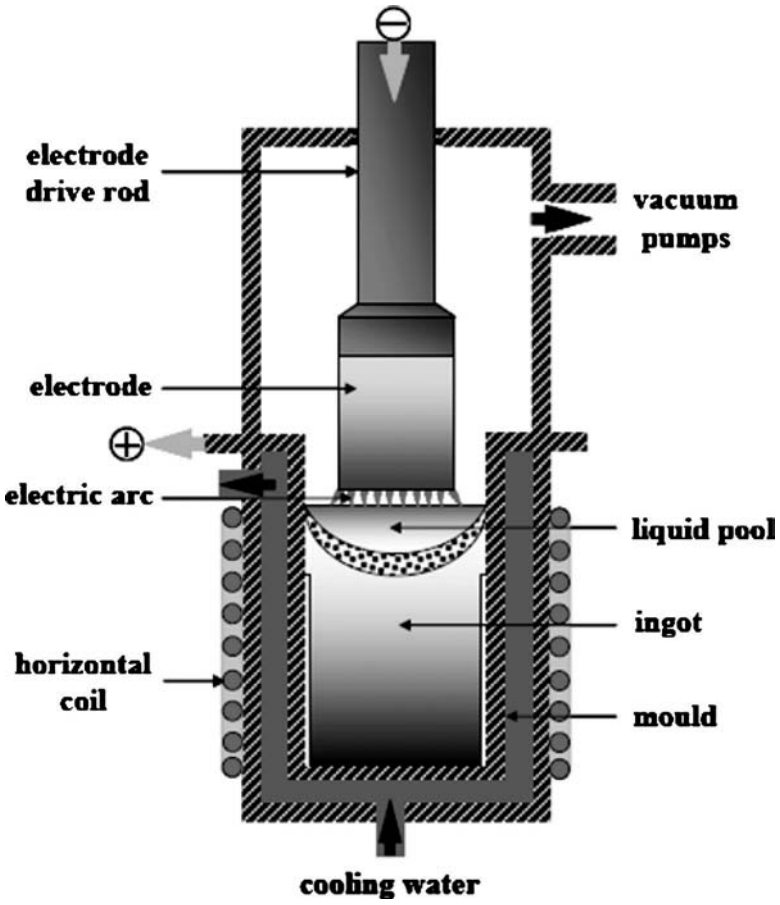


FIG. 1—*Schematic representation of the VAR process.*

crucible. During remelting, the ingot is composed of a liquid metal pool (melt pool), a mushy zone, and a solid part. An electromagnetic stirring can be applied thanks to external electric coils in order to improve the ingot chemical homogeneity.

The main challenge is to master the VAR process in order to ensure the soundness of the material and to control the analytical homogeneity of the final products so that they meet the required high quality level under operating conditions in reactor.

For this reason, AREVA NP/CEZUS has undertaken for more than 20 years a partnership with the Nancy School of Mines and other industrial companies. The School of Mines has developed a numerical model, named Solidification During Arc Remelting (SOLAR), which is aimed at simulating the ingot growth during the VAR process. This model is used by AREVA NP/CEZUS in order to acquire a deep understanding of the physical phenomena playing a key role in zirconium ingot melting, more particularly of the impact of melting parameters. It also allows to develop new melting sequences and to support the optimization of new products.

Description of the Numerical Model

Heat and mass transfer in the VAR ingot are directly related to the recirculating flow of liquid metal in the pool, partly caused by buoyancy forces generated because of the temperature difference between the heated free surface of the pool and the cooled crucible. Nevertheless, the metal flow is also partly driven by self-induced electromagnetic forces, magnetic stirring, and turbulence generation. Consequences on the pool shape and solidification process can be very significant.

Therefore, the first version of a comprehensive numerical model of the VAR process, named SOLAR, was developed 15 years ago at Nancy School of Mines and applied first to the simulation of zirconium and titanium remelting [1,2].

Since then, the model has been constantly improved. More recently, it was adapted for nickel-base superalloys and special steels [3,4]. In all cases, the purpose of the model is the numerical simulation of the whole VAR processing route, with the ultimate aim of process optimization. Based on the numerical solution of a set of partial differential equations, which represent the real physical phenomena, along with their required boundary conditions, SOLAR makes it possible to describe electromagnetism, fluid flow, heat transfer, phase change, and mass transfer during the growth and solidification of the VAR ingot and thus directly relates the melting parameters to the melt pool profile, hydrodynamic behavior of the liquid metal, local solidification conditions, and chemical segregation in the ingot.

An important feature of the model is its ability to simulate an actual processing route having 2 or 3 successive melts, as it is often the case for processing zirconium alloys, using the heterogeneous ingot obtained from the preceding melt as an electrode. This implies the possibility of "numerically assembling" several first melt ingots in order to build the second melt electrode.

As far as we know, no other modeling tool has ever been applied to the simulation of Zr ingot remelting. However, several numerical codes have been developed during the last 15 years to optimize the remelting of steels, superalloys, or titanium alloys. Among them, we will just briefly discuss two of them, considered as the most promising alternatives to the use of SOLAR.

The Basic Axisymmetric Remelting simulation code [5] has been developed by Specialty Metal Processing Corporation, grouping between others SANDIA National Laboratories, ALLVAC, and Carpenter Technology. As compared to our model, flow turbulence is not explicitly modelled but taken into account by multiplying the molecular viscosity by a constant coefficient.

A solidification micromodel based on cellular automata has been set up at Imperial College London in order to determine the distribution of nuclei, the size of the grains and their orientation during solidification of the ingot [6]. Recently, this model was included [7] in a macroscopic computation of the VAR process implemented within the PHYSICA software developed at the University of Greenwich and able to deal with full three-dimensional (3D) calculations.

Because of space limitations, it is not possible to give details of the constitutive equations used in SOLAR mathematical model nor of their boundary conditions. All of these can be found in works from Hans and Quatravaux [1–3], along with a full discussion of the model assumptions.

To summarize, the transient two-dimensional model takes into account the coupled transfers of heat, solutes and momentum, under turbulent flow conditions, during the remelting of a cylindrical ingot. The major physical phenomena that are simulated are listed below.

- Heat transfer: Heat transfer within the ingot by convection and conduction, heat supplied by the electric arc, heat content of the liquid droplets, dissipation of the latent heat of solidification, heat extraction at the ingot base and edge by contact with the mold or radiation in the shrinkage gap.
- Solute transfer: Transport of solute elements in the melt pool and mushy zone, input of matter and evaporation at the top of the ingot, solute redistribution at the solid-liquid interface.
- Momentum transfer: Natural convection due to temperature and solute concentration gradients, 3D forced convection related to electromagnetic stirring, turbulent flow conditions, and interaction between the solid and liquid phases within the mushy zone.

The following sections describe some important features of the model.

Heat Transfer and Solidification

The temperature distribution is governed by a classical energy conservation equation, solved through an explicit enthalpic formulation to compute accurately the solidification phenomenon. This requires the knowledge of the solidification path—i.e., the evolution of the liquid fraction with the temperature and solute concentrations—for a given alloy.

The heat loss to the mold at the baseplate and on the lateral surface is expressed by a Fourier condition. The corresponding heat transfer coefficient

takes into account the metal/mould interfacial resistance and radiation in the gap caused by the ingot shrinkage. The temperature distribution in the Cu mold is precisely calculated with a finite volume approach (see below), which simulates radial and axial conduction in a transient way, while the computation of heat transfer between the mold and cooling water accounts for the water flow and, if necessary, the nucleated boiling mechanism [8].

Liquid Flow and Liquid/Solid Interaction

The determination of metal flow in the melt pool and mushy zone is based on solving the vectorial Navier–Stokes equation using the continuum mixture theory proposed by Bennon and Incropera [9]. The principal assumptions of this part of the model are the following:

- The two-phase liquid-solid system is considered to be a continuum
- The mushy zone is assimilated to a porous solid characterized by its permeability
- The solidification is columnar and the solid is fixed

The momentum transfer equation can then be written as

$$\rho\frac{\partial\vec{\mathrm{V}}}{\partial t}+\rho\vec{\mathrm{V}}.(\vec{\nabla}\vec{\mathrm{V}})=\vec{\nabla}.\left((\mu+\mu_t)\vec{\nabla}\vec{\mathrm{V}}\right)-\vec{\nabla}P+\rho\vec{\mathrm{g}}+\vec{\mathrm{F}}_{\mathrm{el}}-\frac{\mu}{K}\vec{\mathrm{V}}$$

Although the model assumes axisymmetry (i.e., θ-independence), it is important to state that the three components (r,θ,z) of the velocity field are explicitly calculated.

In this equation, μ is the dynamic viscosity, μ_t the turbulent viscosity (see below), P is the pressure, K is the permeability of the mushy zone, $\vec{\mathrm{F}}_{\mathrm{el}}$ is the electromagnetic forces, $\vec{\mathrm{g}}$ is the gravity, ρ is the density, and $\vec{\mathrm{V}}$ is the velocity.

The model uses Boussinesq's hypothesis, taking density variations into account only in the gravity term, thus enabling the representation of natural convection due to temperature and solute concentration gradients.

To a first approximation, the permeability is estimated from a Kozeny–Carman relation

$$K=K_0\frac{g_{\mathrm{l}}^3}{(1-g_{\mathrm{l}})^2}$$

where:

K_0 = constant related to the characteristic dimensions of the solidification microstructure (mean interdendritic spacings) and

g_{l} = volumic liquid fraction.

In the fully liquid region ($g_{\mathrm{l}}=1$), the permeability is infinite, and flow is governed by the classical Navier–Stokes equation for turbulent conditions. Within the mushy zone, the permeability and the velocity decrease, and the source terms in the equation become preponderant. The equation then tends towards Darcy's law. When the liquid fraction becomes negligible, the permeability tends to zero, and the velocities also.

Electromagnetic Stirring

Apart from the movement in the (r, z) plane induced by temperature and solute driven convection, the hydrodynamic behavior of the melt pool and the mushy zone also involves a three-dimensional flow pattern caused by the electromagnetic forces. These arise due to the interaction between the melting current $\vec{J}$ and both the self-induced magnetic field $\vec{B}_{ind}$ and the magnetic field created by the external induction coils $\vec{B}_{ems}$. The model calculates these volume forces from the relation

$$\vec{F}_{el} = \vec{J} \times (\vec{B}_{ind} + \vec{B}_{ems})$$

The external stirring field has a significant effect on heat and solute transfer in the melt pool and mushy zone, particularly due to the periodic centrifugal force associated with the overall angular momentum. In the present state of the model, the effect of electromagnetic stirring on melt pool free surface dynamics is not represented, since a numerical study has concluded to a relatively small deviation from a flat horizontal surface.

Turbulence

SOLAR accounts for the turbulent nature of the metal flow by using the concept of turbulent viscosity. The latter is calculated with the aid of the standard Reynolds-averaged Navier–Stokes) $k-\varepsilon$ model originally developed by Launder and Spalding [10], adapted to describe the effect on the turbulence parameters of the liquid-solid interaction in the mushy zone. In order to remain coherent with the expression of the Navier–Stokes equations, this effect is translated mathematically by introducing additional source terms in the transport equations for k and ε. The same equations are thus used for both the melt pool and the mushy zone, the decrease in permeability during solidification being reflected by a rapid reduction in the turbulence of interdendritic flow.

Segregation

Segregation at the microscopic level takes place in the mushy zone where both liquid and solid phases exist. In the solute transfer equation, the solute liquid concentration is the main variable. It can be related to alloy concentration thanks to the knowledge of both the solidification path and the value of the partition ratio—i.e., the ratio between the concentrations in the liquid and solid phases at a given temperature. For multicomponent zirconium alloys, such as those employed in practice, such parameters are generally not known and must be deduced from simplifying assumptions.

As an example, the solidification path was long assumed to vary linearly between the solidus and liquidus temperatures, and it has recently been upgraded according to thermodynamics calculations based on the Lever rule assumption.

Computational Technique

The nine partial differential equations solved by the model are discretized using a finite volume method [11], with a fully implicit time scheme. The electromagnetic quantities (current density and Lorenz forces) are calculated at every significant change in the melting current, whereas fluid flow and heat transfer equations are solved in a coupled way at each time step.

It is well known in the computational fluid dynamics research field that mesh size and refinement near the walls and free surfaces are liable to have a strong influence on the numerical results. In particular, some refinement near the free surface is often required to obtain accurate results with a reasonable computing time. The model allows the user to design a mesh with such a refinement.

The computational time required for a full remelting simulation depends on the operating parameters. When SOLAR is run on the 3 GHz processors of Cezus Research Center, this time is typically around 3 h CPU for a final melt based on 6000 mesh cells and a 0.15 s time step.

Results Generated and Input Data

At any time during the melting and cooling stages, the model computes the melting current density in the ingot, electromagnetic force field, 3D (r, θ, z) velocity field in the melt pool and mushy zone, intensity of flow turbulence, temperature, and liquid fraction maps in the whole ingot, composition map for any given solute, and solidification conditions (thermal gradient at the solidification front, instantaneous cooling rate, and local solidification time).

It should be stated that the quality and validity of SOLAR results, as for any numerical model, are related to the precision and accuracy of the input data, which belong to one of the following three general categories:

- The operating process parameters
- The thermophysical properties of the remelted alloy
- The model parameters

Apart from the geometry of the cylindrical electrode and ingot, the most important operating process parameters, which must be recorded during actual remeltings, are the melt sequence—melting current, voltage and melt rate as a function of time—and stirring data, i.e., the axial magnetic field created by the coils and the reversal time when stirring is alternated.

In the case of Zr alloys, the thermophysical properties, such as the liquidus and solidus temperatures, emissivity, or kinematic viscosity, are generally only poorly known since specific experiments are very difficult to achieve because of the high temperature and reactivity with many elements.

The third category of input data is composed of a number of sub-models, which partly represent the way in which the physics is introduced in the code, for example, heat transfer coefficients, models for the coupled transfers in a porous medium (the mushy zone), statistical representation of turbulence. Among them, the boundary condition at the top of the ingot has been found to be one of the most critical and one of the least understood. The model uses profiles of current and power as prescribed electrical and thermal boundary conditions at the

ingot top. These profiles can only be estimated with specific arc models and detailed experimental observation, as discussed in the next section of this paper.

Behavior of the Electric Arc in Vacuum Arc Remelting

Knowledge of the electric arc in the VAR process is based on experimental studies performed at Sandia National Laboratories [12] in the 1980s on remelting of nickel- and iron-based alloy electrodes. We have performed similar experiments (including high-speed video observations of the arc and a spectroscopic study of the interlectrode plasma) on zirconium alloy electrodes [13]. One of the main conclusions from these observations is that the behavior of the electric arc in the VAR process is similar to the diffuse mode of a vacuum arc created between cold solid electrodes for the same range of current densities. The arc consists of several dispersed clusters of cathode spots moving over the whole surface of the cathode. Each cluster of spots is the source of a plasma jet expanding under vacuum in the electrode gap. An example of the observation of individual cathode spots composing clusters is presented on Fig. 2.

In order to precisely determine the distribution of thermal energy and electric current transferred to the surface of the melt pool (i.e., the influence of arc behavior on ingot growth and solidification), it is first necessary to describe as completely as possible the column of plasma generated by a single cluster of cathode spots [14]. Results from this "cluster model" indicate that, in all cases, the total energy flux density transmitted by a single cluster to the anode decreases rapidly with distance from the symmetry axis of the cluster, as shown in Fig. 3.

Second, a statistical model of the displacement of the clusters on the cathode surface has been developed [15], which describes the average movement from a random initial location of the clusters. It has been deduced from detailed observation in an industrial VAR furnace [13] of the main behavior of the cathode spot clusters in terms of trajectory, velocity, and lifetime.

Combining this model with the cluster model enables one to calculate readily the distribution of electric current and power at the surface of the ingot top. Not surprisingly, because of the difference in time scales (a cluster lifetime is

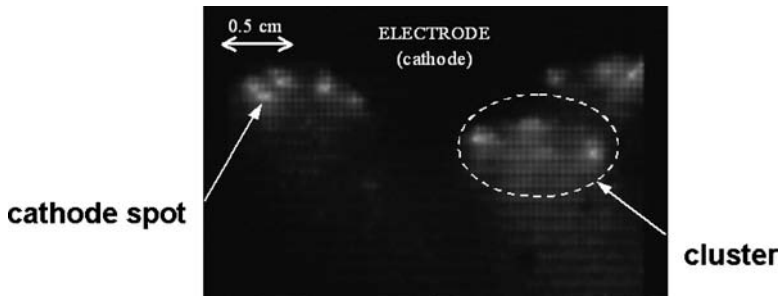


FIG. 2—*Video image of clusters of cathode spots taken during a VAR melt (exposure time of 300 μs).*

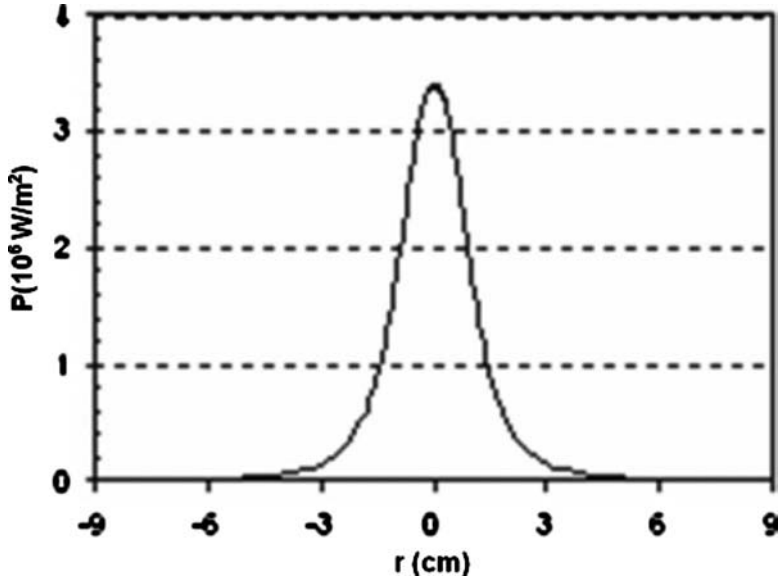


FIG. 3—*Distribution at the anode surface of the energy flux density supplied by the plasma jet emitted by a single cluster during the remelting of a zirconium electrode.*

typically 10–15 ms), the time-averaged result is axisymmetric so that this overall approach provides appropriate boundary conditions for the SOLAR code.

Application of the Model to Zircaloy-4 Remelting

Validation of the Model for Zircaloy-4

The numerical simulations have been extensively validated by comparing the model results for Zircaloy-4 alloys with the experimental examinations of various ingots remelted in pilot devices or full-scale furnaces. This section deals with a part of this validation work, which constitutes a necessary step prior to any predictive use for process optimization.

Melt pool Profile—A small (120 kg) Zircaloy-4 ingot was melted at the CEZUS Research Centre. During this melt, the operating parameters (current, voltage, and melt rate) were kept constant. A square wave alternating stirring cycle was used throughout. In order to clearly visualize the melt pool profile at different stages of remelting, the electrode was marked at five locations by the addition of iron.

Figure 4 shows the computed evolution of the melt pool depth versus the melting time. Because of the small scale and high melt rate, steady state was never reached during the melt.

The predicted melt pool profiles (taken within the mushy zone for liquid fraction $g_l = 0.5$) can be compared with the experimental observation of the

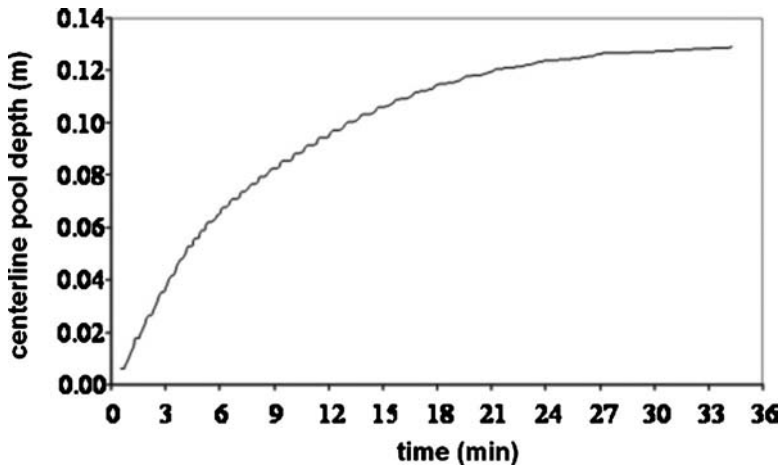


FIG. 4—*Small-scale Zircaloy-4 ingot. Variation of the computed melt pool depth with time.*

macrograph of the ingot on a longitudinal section. Such a comparison is made in Fig. 5 and shows quite a good agreement.

Chemical Segregation—In order to evaluate the ability of the model to represent the segregation pattern observed in industrial ingots, SOLAR has been used to simulate the triple VAR processing of Zircaloy-4. In the processing route, two ingots from the first melt are joined and welded to constitute the second electrode resulting in a rather complicated final segregation map. A simple result is the evolution of the radially averaged chemical content as a function of the height in the ingot. Figure 6 thus represents the iron segregation as predicted by the model.

The particular shape of the curve is induced by the combination of partition during solidification and the welding of the two first melt ingots. Dots on Fig. 6 mark the average chemical analyses of samples taken from 22 ingots processed using the same route. Once again, the very good overall agreement allows a confident use of the model for optimizing the process.

Details of the Computed Results for Zircaloy-4 Melting

In the validation process, the calculations were based on a common set of thermophysical properties for all the zirconium alloys corresponding to pure zirconium at the solid state (Table 1).

Subsequently, in order to simulate zirconium alloys remelting as accurately as possible, specific sets of thermophysical properties have been defined for various zirconium alloys using THERMOCALC™[4] [16] (TCC R version/Zirco base Zirc08), a software devoted to thermodynamic calculations for multi

[4]THERMOCALC is a trademark of Thermo-Calc Software.

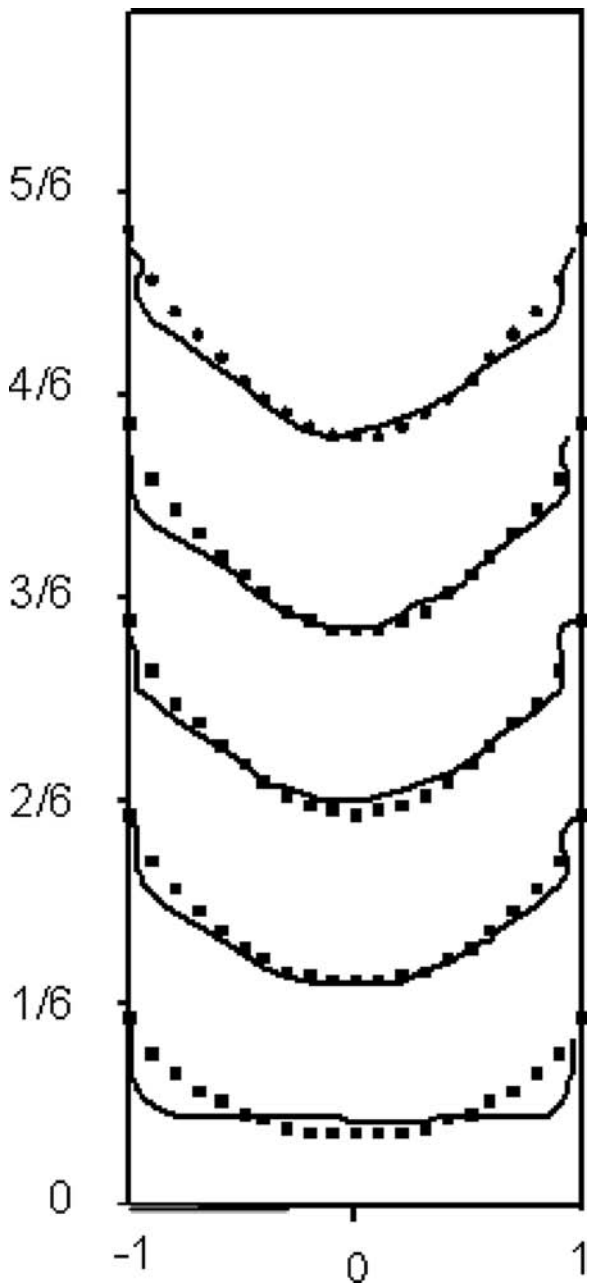


FIG. 5—*Small-scale Zircaloy-4 ingot (all dimensions are normalized). Comparison between calculated (dots) and measured (continuous lines) melt pool profiles.*

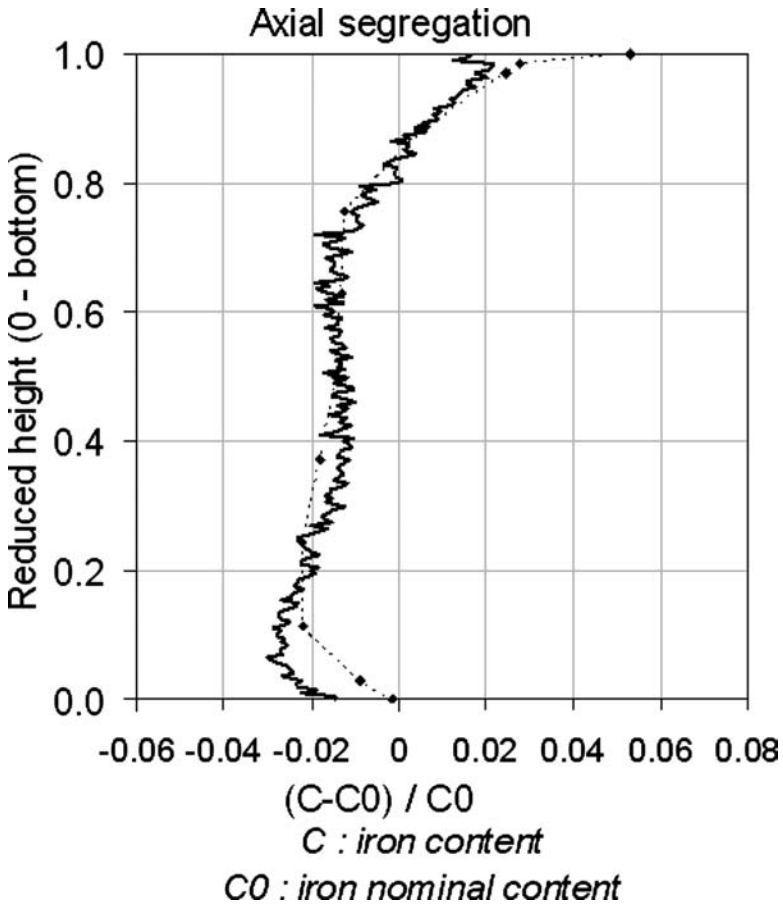


FIG. 6—*Full-scale (6 tons) Zircaloy-4 ingot. Axial iron distribution. Comparison between the calculated (continuous line) and measured (dots and dotted line) iron content.*

components alloys. The main thermophysical properties are summarized in Table 2 for Zircaloy-4.

The impact on the ingot chemistry of the change in the thermophysical properties used as SOLAR input data has been studied for the triple VAR processing of Zircaloy-4. In Fig. 7, the segregation of iron solute, which is predicted

TABLE 1—*Main thermophysical properties of zirconium alloys previously used in SOLAR.*

Solidification temperature interval (T_{liquidus}–T_{solidus} in K)	10
Specific heat at the liquid state (C_p in $\text{J} \cdot \text{kg}^{-1} \cdot \text{K}^{-1}$)	400
Latent heat of solidification (L in $\text{J} \cdot \text{kg}^{-1}$)	230×10^3

TABLE 2—*Main thermophysical properties of Zircaloy-4 alloy now used in SOLAR.*

Solidification temperature interval (T_{liquidus}–T_{solidus} in K)	75
Specific heat at the liquid state (C_p in $J \cdot kg^{-1} \cdot K^{-1}$)	460
Latent heat of solidification (L in $J \cdot kg^{-1}$)	240×10^3

by SOLAR in the final ingot, is displayed for both cases: The use of the upgraded set of data increases the computed segregation in Zircaloy-4 alloy. This is confirmed by the comparison in terms of overall macrosegregation indexes calculated by SOLAR, i.e., dispersion with regard to the nominal content: 0.9 %

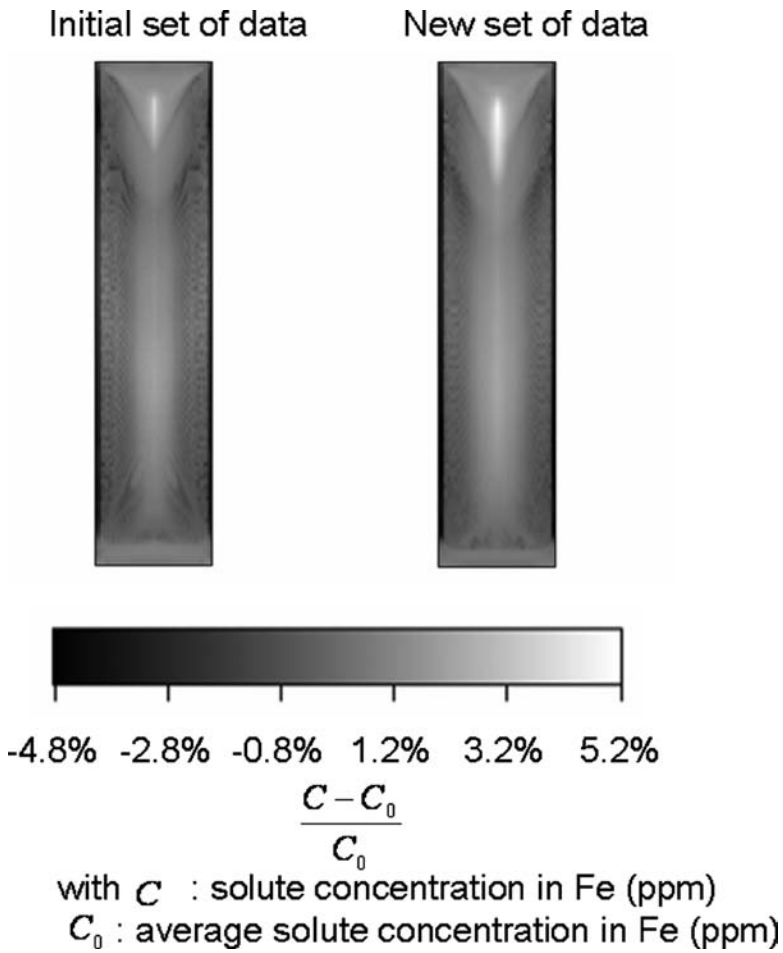


FIG. 7—*Impact of the thermophysical properties used as SOLAR input data on the predicted segregation in Zircaloy-4 ingots.*

previously against 1.03 % with new data. This is mainly due to the increase in the solidification temperature interval.

In addition to analytical segregation, the evolutions of the melt pool hydrodynamic and thermal behavior predicted by SOLAR (with adjusted thermophysical data) have been followed for the final melt of the triple VAR processing of Zircaloy-4 in Figs. 8 and 9.

Indeed, the shape and volume of the melt pool, and thus the width of the mushy zone, are strongly depending on the movements of the liquid metal. This directly impacts the segregation in the ingot.

According to Fig. 8, steady-state conditions are reached at roughly 50 % of the total melting time. During that final melt of Zircaloy-4 ingots, an alternated (period T) electromagnetic stirring was applied. In Fig. 9, the behavior of the melt pool is studied at eight distinct moments selected throughout one stirring period in the steady-state regime: A cyclic motion of the fluid in the pool occurs, which is directly linked to the three applied forces to the liquid metal.

These forces are the following:

(i) The thermal convection
(ii) The electromagnetic force resulting from the interaction between the melting current and the self-induced magnetic field
(iii) The centrifugal force resulting from the angular motion caused by the interaction between the melting current and the external stirring field. The angular motion and the resulting centrifugal force evolve cyclically according to the stirring changes. This induces a periodic (r, z) movement characterized by pulsations close to the surface of the liquid pool: The liquid metal flows successively towards the mould and towards the pool centre.

The liquid metal motion directly impacts solute distribution in the ingot and SOLAR allows evaluating the impact of changes in the melting parameters on the final ingot chemistry.

Specifically, the use of SOLAR to investigate the influence of the alternated stirring sequence (coil current and reversal time) has been detailed in several papers dealing mostly with steel or titanium remelting [17,18].

Application of the Model to M5™ Remelting

This section is dedicated to the specific study of segregation in M5™ ingots. An experiment has been carried out in an industrial VAR furnace at CEZUS plant in Ugine in order to validate the most recent version of the numerical model for M5™ ingots calculations.

Description of the Full-Scale Experiment

The validation has been performed in terms of analytical segregation, melt pool shape, and final shrinkage location in the ingot.

Melting of a Single Homogeneous Electrode—In order to ensure that the simulation input parameters are very close to the experimental conditions, one

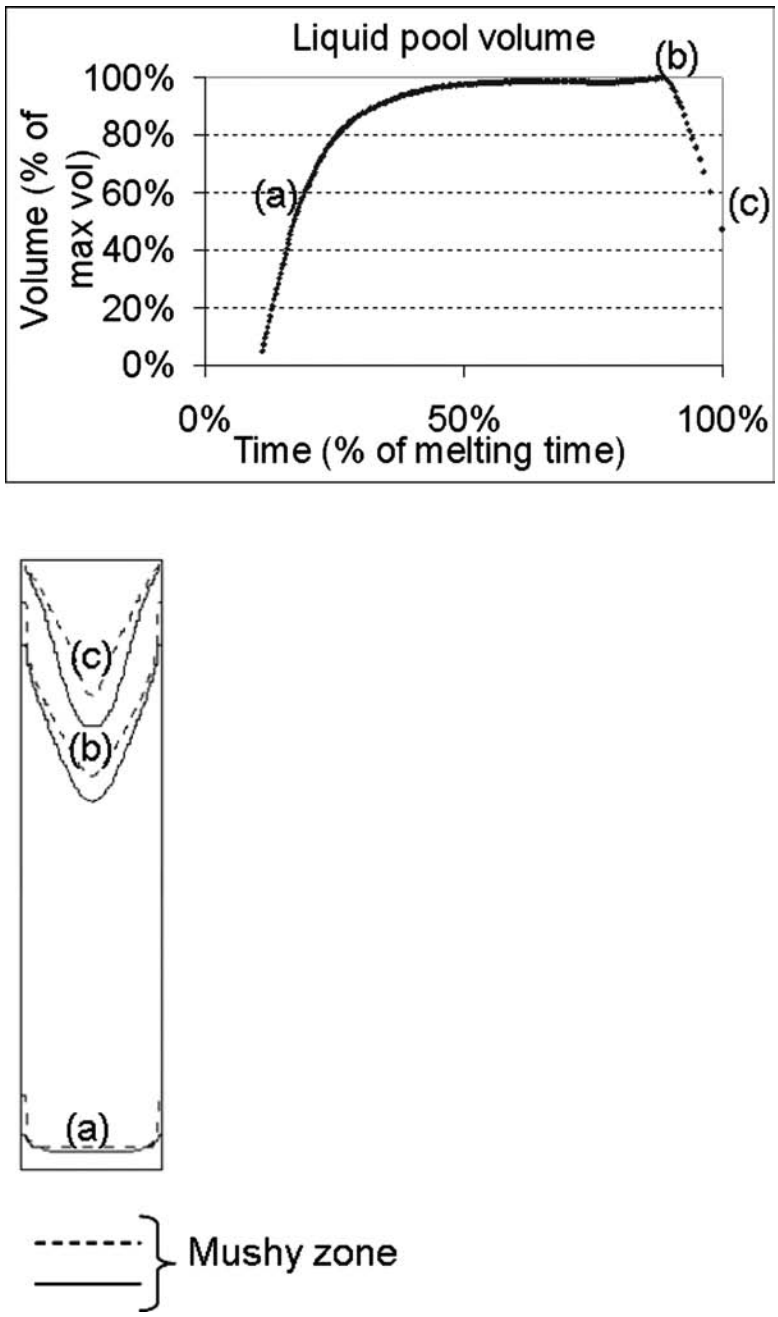


FIG. 8—*Evolution of the melt pool volume during the final melt of Zircaloy-4 alloy.*

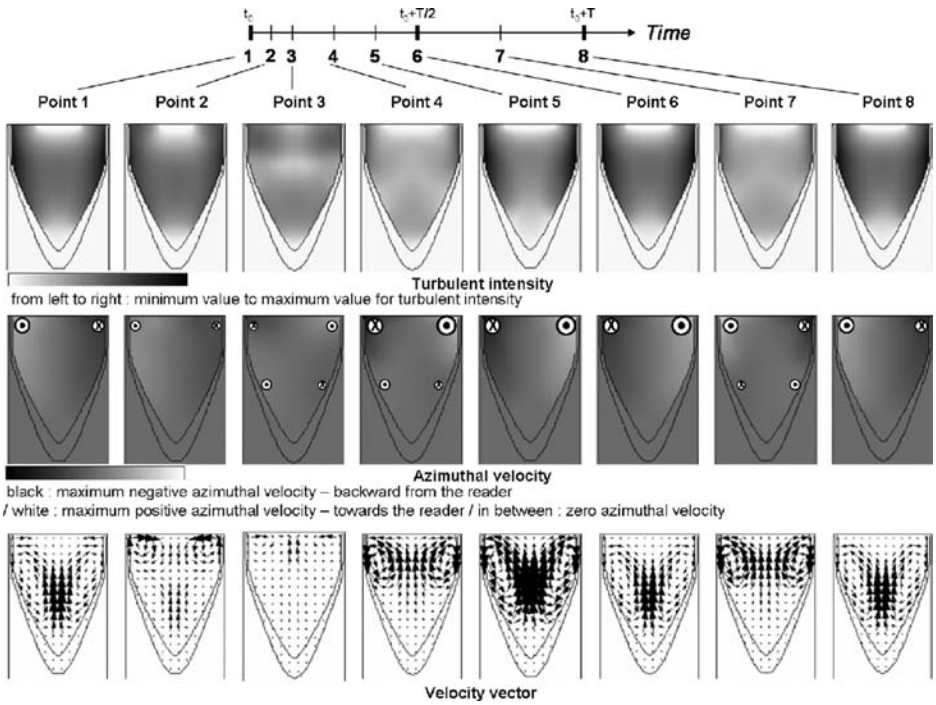


FIG. 9—*Evolution of the hydrodynamic and thermal behavior of the melt pool during a stirring cycle.*

single melt has been performed from a homogeneous electrode. For this purpose, the electrode was manufactured only from recycled materials originating from the same grade. The melting parameters were inspired from the usual practice during standard industrial melts of M5™ ingots, but specific conditions were defined: In particular, two melting velocities were successively applied. Besides, a fixed and strong stirring was temporarily used in order to try to mark several melt pools in the ingot. The corresponding melting parameters are displayed in Fig. 10.

In the next two sections, characterizations of the resulting ingot are detailed in terms of macrostructures and chemical content.

Macrostructures Description—The grains mentioned in this section refer to what is usually called "prior-β" grains, i.e., the cubic solid phase that is formed from the liquid phase during solidification. In zirconium alloys, a detailed macrographic observation of the primary β structure is difficult because of the allotropic β(cubic) $\rightarrow$ α(hexagonal) solid state transformation. Indeed, such a transformation might affect the primary β structure.

First, the longitudinal ingot macrostructure has been observed (Fig. 11(*a*)): Most of the ingot seems to be composed of randomly oriented grains of a few centimeters, which could be compared with equiaxed grains. However, at the

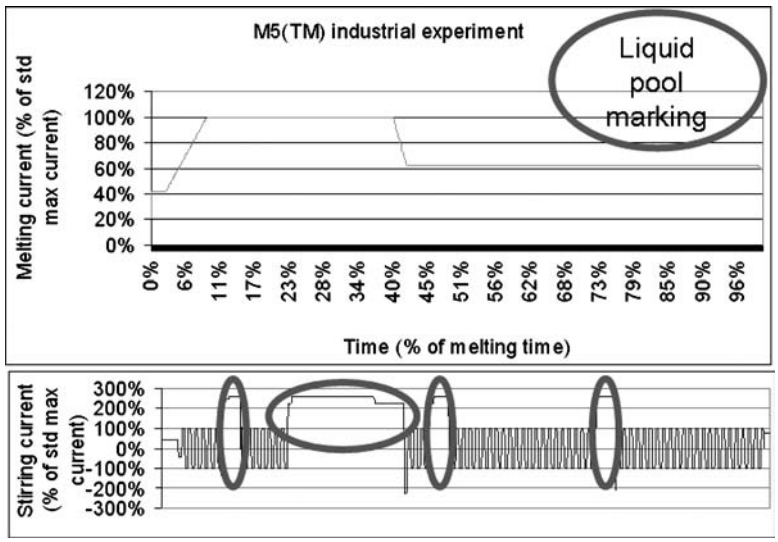


FIG. 10—*Melting conditions of the full-scale M5™ remelting experiment.*

bottom and periphery of the ingot, grains seem to be slightly larger and more specifically oriented: They might be assimilated to columnar grains. On the top longitudinal cross section, columnar grains are clearly visible. They arise from solidification from the top of the last melt pool, right after shutting off the arc. The final shrinkage is also visible on this picture.

Apart from the last pool, only two visible changes in the longitudinal macrostructure can be related to melt pool shapes, among the four attempts aimed at marking the pool (Fig. 10): They might respectively stand for the end of the second marking, which lasted longer than the other ones, and the start of the third marking.

The macrostructure has also been observed on three radial cross sections (Fig. 11(*b*)).

- Near the periphery, columnar grains are visible: They seem to be oriented following an azimuthal movement probably caused by the applied external electromagnetic stirring. The closer to the top of the ingot, the larger this columnar peripheral area.
- The inner macrostructure seems more equiaxed. However, the top and bottom cross sections both belong to zones that are mainly characterized by columnar grains parallel to the vertical thermal flux induced by solidification respectively from the top of the last melt pool and from the bottom of the ingot. Therefore, the seemingly equiaxed zone observed on both cross sections is actually made of transverse sections of perpendicular columnar grains. The closer to the bottom of the ingot, the smaller the grains.

Comparison between Measured and Predicted Niobium Contents—Chemical analyses were carried out along various radii at different heights in the ingot:

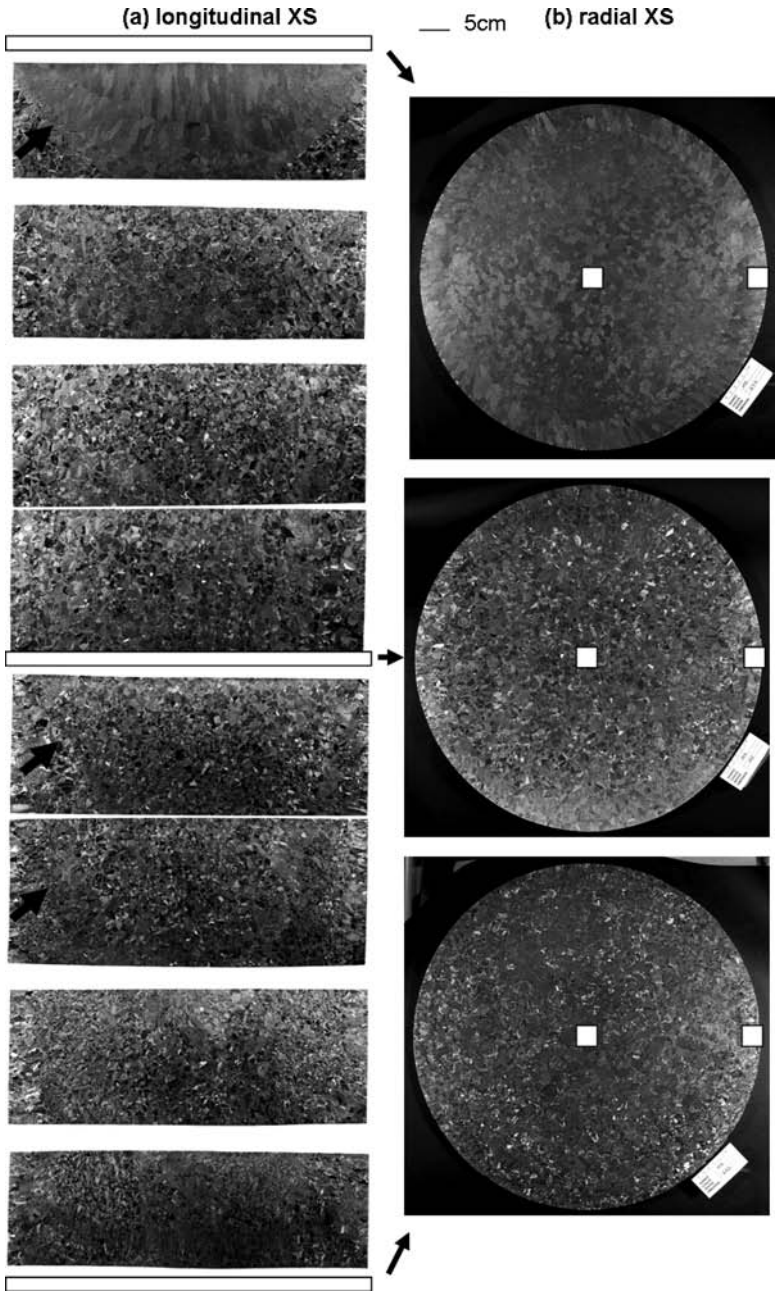


FIG. 11—*Macrographs on the M5™ ingot.*

$h = h_m$; $\frac{3}{4}h_m$; $\frac{1}{2}h_m$; and $\frac{1}{4}h_m$ (where h_m is the total ingot height). For every slice, the measured niobium content was plotted (Fig. 12) as a function of the radial location (from the centre ($r/r_m = 0$) to the edge ($r/r_m = 1$)). A horizontal line marks the homogeneous electrode concentration. SOLAR predictions at the ingot extreme periphery must be carefully handled since they can result from numerical instabilities.

We can observe that the niobium segregation is more pronounced in the lower half of the ingot than in the upper half. This is the consequence of the variation in the operating conditions. During the first part of the remelting, the high current and strong unidirectional magnetic stirring (Fig. 10, second marking) strengthen the flow in the melt pool and the mushy zone. Therefore, the segregation of Nb is increased. On the contrary, the low current and weak alternated stirring generate a limited radial segregation in the second part of the ingot. The Nb concentration predicted by SOLAR shows a reasonable agreement with the measured contents along each radius.

Figure 13 compares the SOLAR prediction with the measurements in terms of the evolution of radially averaged axial macrosegregation along the height in the ingot. According to the measurements, we notice that, at the bottom of the ingot, the average segregation is negative and becomes positive in the central and upper part, decreasing with the height. Finally, the important positive segregation at the top of the ingot corresponds to the enrichment of the final melt pool. The simulation results follow the same trend. SOLAR is found to predict with a satisfactory accuracy the chemical segregation pattern of a M5™ ingot processed under variable, hence unusual, operating conditions.

It can also be noticed that despite the predominance of equiaxed grains in the ingot as mentioned in the Macrostructures Description section, the model assuming the solid phase as fixed is in relatively good agreement with the macrosegregation measurements. The motion of equiaxed grains—which contain less solute—generally induces a negative segregation in the center of the ingot [19]. However, the intensity of this effect depends on the grains morphology: It is maximum in the case of globular grains. For dendritic grains, the volume of the solid phase is small with regard to the volume of the grain envelope. Then the severity of the macrosegregation, which is due to the packing of the grains, is less intense than for globular grains. Moreover, it has been showed [20] that an accumulation of dendritic equiaxed grain in the center of the product can reduce the intensity of the liquid flow and consequently reduce the macrosegregation level. Thus it can be deduced that the morphology of the grains is mainly dendritic in this experiment.

Simulation of the Nb Segregation in M5™ Industrial Ingots

In parallel to the M5™ full-scale experiment detailed here, comparisons between SOLAR predictions and industrial 6 tons M5™ ingots have also been performed in terms of Nb segregation after three melts.

In Fig. 14, the longitudinal segregation results are based on the measurements in 130 ingots.

Contrary to the experimental single melt ingot presented here, the Nb content in 6-ton industrial ingots remains very homogeneous, the longitudinal

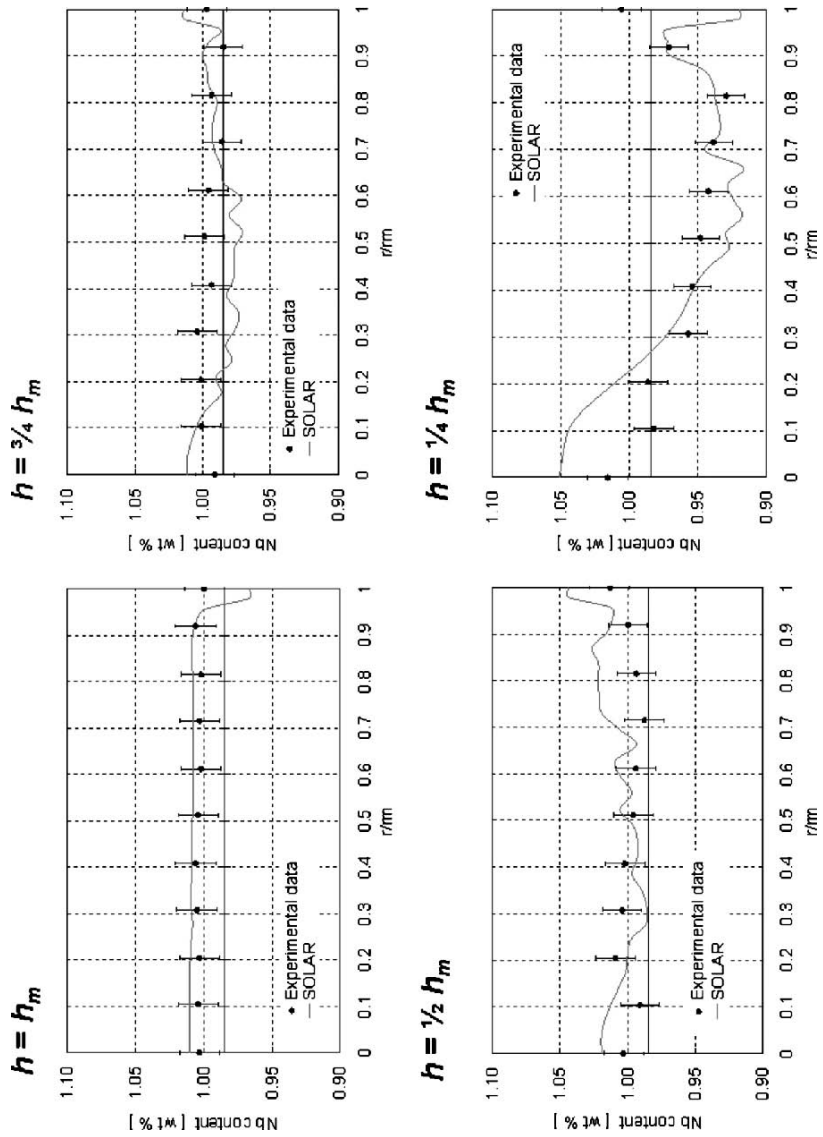


FIG. 12—*Segregation of Nb along several radii of the M5™ ingot-experimental data and model results.*

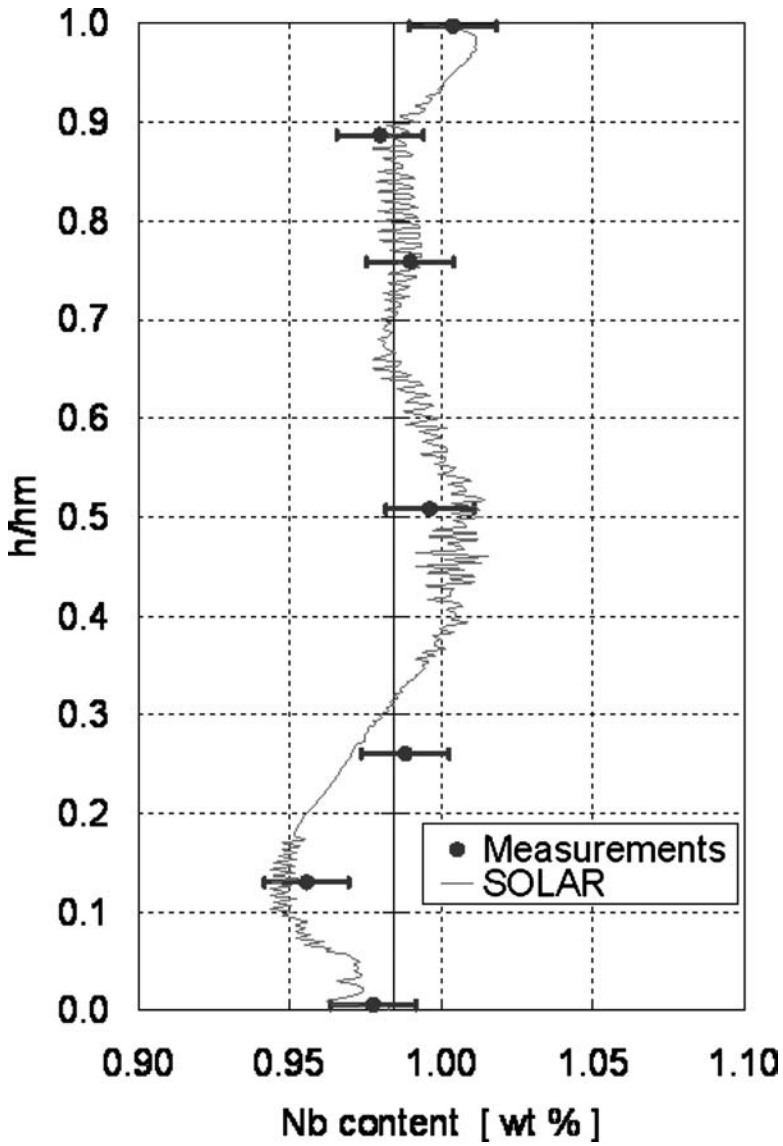


FIG. 13—*Average segregation of niobium along the height of the M5™ ingot-experimental data and model results.*

variation of the average measured content being of the order of 0.01 %. The simulated and measured Nb contents are in rather good agreement: In the middle of the ingot, the predicted Nb content belongs to the uncertainty interval, and in the other longitudinal parts of the ingot, the agreement between simulated results and average measurements is very good.

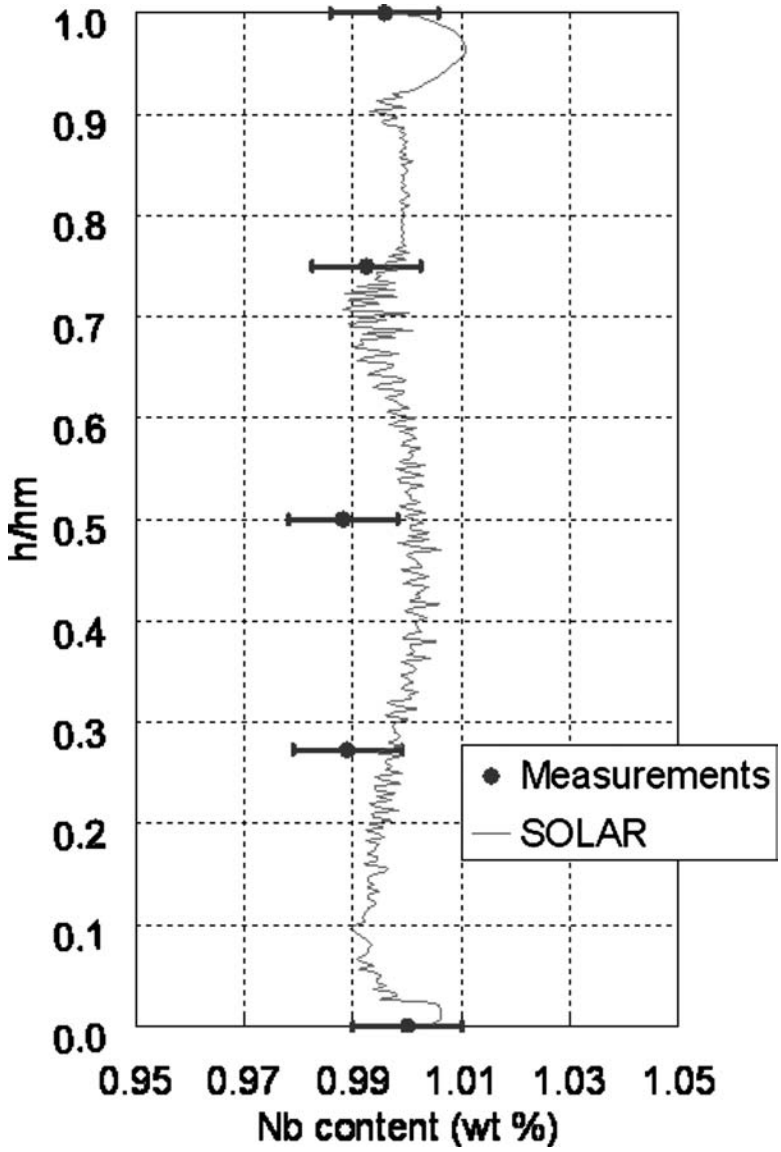


FIG. 14—*Full-scale M5™ ingot. Axial niobium distribution. Comparison between the calculated (continuous line) and measured (dots; the uncertainty is equal to the standard deviation calculated from 130 ingots) niobium content.*

Conclusion

The numerical model used for predicting the chemical segregation in VAR ingots made of zirconium alloys is validated according to industrial measurements. First of all, it is used by AREVA NP/CEZUS to improve the understanding of the influence of the process parameters on the final product chemistry. It also supports the development of new melting conditions and enables reducing the number of expensive industrial experiments.

Besides, this model is constantly improved by the Nancy School of Mines in terms of physics that are taken into account in the simulation. Works are performed in particular in order to improve segregation predictions. Also, a continuous effort is paid on the reduction of computational time without any loss of accuracy.

Acknowledgments

The writers wish to thank all the people at CEZUS Ugine plant who helped with the M5™ experiment reported in this paper. The present study also relies largely on the work achieved by several graduate students at Nancy School of Mines during the course of their Ph.D. theses, as well as on the valuable assistance from all the SOLAR Club partners in the development of the codes and validation trials. Furthermore, as a part of the Optimizing Processes based on Electrode Remelting with Arc or Slag (OPERAS) Project, this work was partly supported by the French National Research Agency (Grant No. ANR-08-MAPR-0006-04).

References

[1] Jardy, A., Hans, S., and Ablitzer, D., *Proc. Int. Symp. on Liquid Metal Processing and Casting*, Santa Fe, NM, 1994, A. Mitchell and J. Fernihough, Eds., AVS, New York, pp. 143–154.

[2] Jardy, A., Hans, S., and Ablitzer, D., *Proc. Seventh Int. Conf. on Modeling of Casting, Welding and Advanced Solidification Processes*, London, United Kingdom, 1995, M. Cross and J. Campbell, Eds., TMS-AIME, Warrendale, PA, pp. 205–212.

[3] Quatravaux, T., Ryberon, S., Hans, S., Jardy, A., Lusson, B., Richy, P. E., and Ablitzer, D., "Transient VAR Ingot Growth Modelling: Application to Specialty Steels," *J. Mater. Sci.*, Vol. 39(24), 2004, pp. 7183–191.

[4] Jardy, A. and Ablitzer, D., "Mathematical Modelling of Superalloy Remelting Operations," *Mater. Sci. Technol.*, Vol. 25(2), 2009, pp. 163–169.

[5] Bertram, L. A., Brooks, J. A., Evans, D. G., Patel, A. D., Van Den Avyle, J. A., and Wegman, D. D., *Proc. Int. Symp. on Liquid Metal Processing and Casting*, Santa Fe, NM, 1999, A. Mitchell, L. Ridgeway, and M. Baldwin, Eds., AVS, New York, pp. 156–167.

[6] Lee, P. D., Lothian, R., Hobbs, L. J., and McLean, M., *Proc. Int. Symp. on Superalloys*, Champion, PA, 1996, R. D. Kissinger, D. J. Deye, D. L. Anton, and A. D. Cetel, Eds., TMS-AIME, Warrendale, PA, pp. 435–442.

[7] Yuan, L., Lee, P. D., Djambazov, G., and Pericleous, K., "Numerical Simulation of the Effect of Fluid Flow on Solute Distribution and Dendritic Morphology," *Int. J. Cast Metals Research*, Vol. 22, 2009, pp. 204–207.

[8] Chapelle, P., Ward, R. M., Jardy, A., Weber, V., Bellot, J. P., and Minvielle, M., "Lateral Boundary Conditions for Heat Transfer and Electrical Current Flow

During Vacuum Arc Remelting of a Zirconium Alloy," *Metall. Mater. Trans. B*, Vol. 40, 2009, pp. 254–262.

[9] Bennon, W. P. and Incropera, F. P., "A Continuum Model for Momentum, Heat, and Species Transport in Binary Solid-Liquid Phase Change Systems – I. Model Formation," *Int. J. Heat Mass Transfer*, Vol. 32, 1987, pp. 1719–1731.

[10] Launder, B. E. and Spalding, D. B., "The Numerical Computation of Turbulent Flows," *Comput. Methods Appl. Mech. Eng.*, Vol. 3, 1974, pp. 269–289.

[11] Patankar, S. V., *Numerical Heat Transfer and Fluid Flow*, McGraw-Hill Company, New York, 1980.

[12] Williamson, R. L. and Zanner, F. J., "Voltage Signatures in VAR," *Proc. 1991 Vacuum Metallurgy Conf. on the Melting and Processing of Specialty Materials*, 1991, N. Bhat, E. W. Bloore, and D. R. Malley, Eds., ISS, Warrendale, PA, pp. 87–91.

[13] Chapelle, P., Bellot, J. P., Jardy, A., Czerwiec, T., Robbe, X., Champin, B., and Ablitzer, D., "An Experimental Study of the Electric Arc during Vacuum Arc Remelting," *J. High Temp. Mater. Processes*, Vol. 4, 2000, pp. 493–506.

[14] Chapelle, P., Bellot, J. P., Duval, H., Jardy, A., and Ablitzer, D., "Modelling of Plasma Generation and Expansion in a Vacuum Arc: Application to the Vacuum Arc Remelting Process," *J. Phys. D: Appl. Phys.*, Vol. 35, 2002, pp. 137–150.

[15] Chapelle, P., El Mir, H., Bellot, J. P., Jardy, A., Ablitzer, D., and Lasalmonie, D., "Modelling of the Arc Plasma Behaviour in the VAR Process," *J. Mater. Sci.*, Vol. 39, 2004, pp. 7145–7152.

[16] Sundman, B., Kansson, B., and Anderson, J.-O., "The Thermo-Calc Databank System," *CALPHAD: Comput. Coupling Phase Diagrams Thermochem.*, Vol. 9, 1985, pp. 153–190.

[17] Jardy, A., Quatravaux, T., and Ablitzer, D., *Proc. Symp. on CFD Modeling and Simulation of Engineering Processes*, Charlotte, NC, 2004, L. Nastac and B. Q. Li, Eds., TMS, Warrendale, PA, pp. 265–277.

[18] Wilson, A. F., Jardy, A., and Fox, S. P., *Proc. 11th World Conference on Titanium*, Kyoto, Japan, 2007, M. Ninomi, S. Akiyama, M. Ikeda, M. Hagiwara, and K. Maruyama, Eds., JIM, Sendai, Japan, pp. 869–872.

[19] Beckermann, C., "Modelling of Macrosegregation: Applications and Future Needs," *Int. Mater. Rev.*, Vol. 47, 2002, pp. 243–261.

[20] Combeau, H., Založnik, M., Hans, S., and Richy, P. E., "Prediction of Macrosegregation in Steel Ingots: Influence of the Motion and the Morphology of Equiaxed Grains," *Metall. Mater. Trans. B*, Vol. 40, 2009, pp. 289–304.

DISCUSSION

Question 1, Javier Romero, Westinghouse Electric Sweden AB:—What is the mesh size of the FEM model? Is it homogeneous? Does the meshing affect the results significantly?

Author's Response:—In the model, that is based on Finite Volume Method - not Finite Element -, the mesh can either be homogeneous or refined near the wall and free surface. The mesh size can have an influence on the numerical results, in particular near the free surface. The computing time is typically around 3h for a final melt, based on 6000 mesh cells and a 0.15 s time step.

Question 2, Vladimir Markelov, Bochvar Inst.-VNIINM:—Is it possible using your method to measure the impurities segregation: for example S, Fe and others in the M5™ ingots?

Author's Response:—Any solute segregation can be predicted by the model, even for a solute with a very low nominal content. This is the case for Fe, S and others in M5™. The accuracy of the prediction depends on the knowledge of the value of the solute partition ratio in Zirconium alloys.

Question 3, Brett Herb, ATI Wah Chang:—How was the chemistry measured for the data showing longitudinal variation in alloy elements? Specifically, was the chemistry from the ingot sidewall, radially across the cross-section of intermediate product, or at final size?

Author's Response:—In the example of the specific full-scale experiment on M5™ which was presented during the symposium, chemical analyses were carried out along various radii at different heights in the single-melt ingot. The niobium axial segregation was deduced from radially averaged values at these different heights.

On industrial M5™ ingots, measurements have been taken after the final melt, at different heights along one single axis close to mid-radius.

Reprinted from JAI, Vol. 8, No. 2
doi:10.1520/JAI103026
Available online at www.astm.org/JAI

A. Gaillac,[1] *C. Lemaignan,*[2] *and P. Barberis*[1]

Damage Build-Up in Zirconium Alloys During Mechanical Processing: Application to Cold Pilgering

ABSTRACT: Cold pilgering of zirconium alloys containing high content of alloying elements may be a critical issue regarding surface defects or serious cracks. A better knowledge of damaging mechanisms during pilgering is a way for optimizing the cold forming routes of cladding tubes. Behavior of Zircaloy-4, M5^{TM} (M5^{TM} is a trademark of AREVA NP) and Zr-Nb-Sn-Fe alloys under damaging conditions were investigated for this purpose. Cold pilgering is a cyclic deformation process. Depending on its position inside the grooves of the rolls, material is strained alternately in compressive and tensile modes. Thus, materials were first tested under low cycle fatigue (LCF) deformation routes. LCF tests showed that the differences observed in the number of cycles to failure between alloys are mainly a function of the differences in fracture toughness. Fractography of the fatigue and toughness tests samples also showed that the final propagation of the crack is always ductile, meaning that toughness is the function of the ductile tearing damage mechanisms at the crack tip. Therefore, tensile tests of notched axisymmetric samples were used to study the ductile damage build-up mechanisms, by varying the stress triaxiality. A detailed analysis of the fractured samples was used to quantify a ductile damage accumulation parameter, function of the deformation and the stress triaxiality. Size and repartition of second phase particles, grain to grain misorientations, grain size, and texture were identified as the main metallurgical parameters having an effect in the ductile damage by nucleation, growth, and coalescence of voids. These experimental results,

Manuscript received February 3, 2010; accepted for publication November 18, 2010; published online January 2011.
[1] AREVA/CEZUS Research Center, Avenue Paul Girod, F-73403 UGINE Cedex, France.
[2] CEA/DEN DEC-Dir, CEA Grenoble, 85X, F38041 Grenoble Cedex and INPG SIMAP, BP 75–F38402 St Martin d'Hères, Cedex, France.

Cite as: Gaillac, A., Lemaignan, C. and Barberis, P., "Damage Build-Up in Zirconium Alloys During Mechanical Processing: Application to Cold Pilgering," *J. ASTM Intl.*, Vol. 8, No. 2. doi:10.1520/JAI103026.

Copyright © 2011 by ASTM International, 100 Barr Harbor Drive, PO Box C700, West Conshohocken, PA 19428-2959.

combined with the material mechanical history, provided by nu-merical modeling of the cold pilgering process, are now used to improve the forming routes of cladding tubes, both by a mechanical way (cold pilgering stress state) and a metallurgical one (microstructure of alloys used for tubes rolling).

KEYWORDS: zirconium alloys, low cycle fatigue, cold pilgering, ductile damage, toughness

Introduction

During cold pilgering of zirconium alloys tubes, cracks may occur at the outside surface, leading to discarded tubes and important costs (see Refs 2 and 3 for a description of the cold pilgering process). For alloys with high content of alloying elements, and when longer cracks occur, especially those that run into the inner chamfer at the ends of the tube, mill and tools could run a risk in the case of a brutal propagation of the crack and opening of the tube (Fig. 1). Thus, a better knowledge of damaging mechanisms during pilgering is necessary to optimize the cold forming routes of cladding tubes, both by a mechanical way (cold pilgering stress state) and a metallurgical one (microstructure of alloys used for tubes rolling).

Experimental measurements [1], analytical models [2], and more recent finite element ones [2,3] showed that cold pilgering is a cyclic deformation process. Depending on its position inside the grooves of the rolls, the material is strained, up to 5 % at each stroke of the rolls, alternately in compressive and tensile modes.

In this low cycle fatigue (LCF) deformation route, bibliography about zirconium alloys is not very extensive. It mainly concerns mechanical behavior, and hardening or softening, depending on the strain amplitude applied to the specimen [4–6]. Lin showed that fatigue lifetime of Zircaloy-4 as a function of plastic strain amplitude follows a Manson-Coffin law and that a recrystallized material exhibits a higher lifetime than the stress relieved one [7]. LCF lifetime is also a function of the texture [6], it is higher when *c* axis are mainly in a perpendicular orientation from the fatigue stress direction. Second phase particles, such as hydrides, can reduce the fatigue life [8] of zirconium alloys. For a beta-treated zirconium alloy, Crépin showed the role played by the partial irreversibility of twinning on the fatigue cracks nucleation [9]. Fatigue cracks propagation is ductile and intra-granular for zirconium alloys [10]. Toughness of Zr alloys, which is quite high, is generally measured using the *J* integral (ASTM E1820 [11]). It amounts 200–300 kJ/m^2 at room temperature, but it is reduced as the second phase particles and hydrides concentration increase [10,12]. More generally, LCF lifetime of zirconium alloys is a function of the ductile damage mechanisms which occur at the crack tip.

Bibliography about damage of zirconium alloys mainly concerns in-reactor damage. Stress corrosion cracking, irradiation damage, hydrides weakening [12], and creep damage [13] were widely studied. Concerning ductile damage

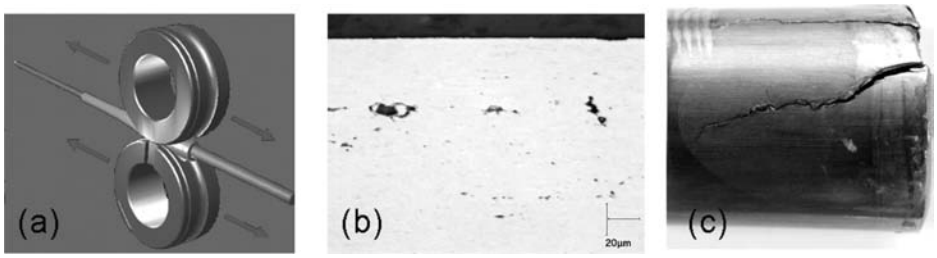


FIG. 1—*(a) The cold pilgering process; (b) voids under the outer surface of a Q alloy tube after cold pilgering; and (c) cracks on a Q alloy tube after cold pilgering.*

ofunirradiated and unhydrided zirconium alloys, references are less numerous. Whatever the temperature, fracture of zirconium alloys is always ductile and characterized by dimples on the fracture surface and a damage mechanism by nucleation, growth, and coalescence of voids.

From a macroscopic point of view, ductility of zirconium alloys, usually defined as the reduction of area of a tensile test specimen, is a function of the texture [14], the nature, size and repartition of the second phase particles [15,16], and the grain size [14].

To go further in the understanding of the ductile damage and the role played by microstructure of zirconium alloys, a detailed analysis of nucleation, growth, and coalescence of voids is needed. Voids nucleate at the strain localization zones, which can be the grain boundaries [14], the intersection of slip bands [17] or the second phase particles [18]. Growth of voids is intra-granular, and is a function of the crystallographic orientation of the grains next to the cavity [14] and the grain size [18]. Growth rate is a function of the strain rate and the stress triaxiality (hydrostatic stress divided by equivalent Von Mises stress). For a given stress triaxiality, the diameter of a void is a linear function of the strain [14], in agreement with the Rice and Tracey model [19]. Tubular cavities are frequently observed in zirconium alloys [14,18,20]. The axis of these tubular voids is directed towards the *c* axis of the grain where the void grew. Crépin showed that the hexagonal section of voids is due to the activation of the three prismatic slip systems [18]. Coalescence of voids is the last step in the ductile damage mechanism, leading to the fracture of the specimen. It occurs when the critical size of cavities, which is a function of cavities density and repartition, is reached. For zirconium alloys, coalescence of voids can occur for a low volume fraction of voids (2–3 %) [14,21]. Cracks developed on strain bands, along prismatic slip systems, are able to connect two cavities relatively far away from each other [14].

The aim of the present work is to identify the key metallurgical parameters responsible for the cracks and fractures observed after cold pilgering of some zirconium alloy tubes. For this purpose, various alloys and metallurgical states were studied using LCF, toughness, and tensile tests.

TABLE 1—*Composition of studied alloys (mass %).*

	Fe	Cr	Nb	Sn	O
Z4	0.2	0.1	···	1.3	0.13
M5™	···	···	1	···	0.14
Q	0.35	···	1	0.25	0.14

Materials

Tested materials were commercial ones: Zircaloy-4 and M5™,[3] and an experimental quaternary Zr–Nb–Sn–Fe alloy named Q. The composition of these alloys is given in Table 1.

Considering that defects and cracks mainly occur during the first cold pilgering pass, specimens taken from hot extruded tubes were studied first. The microstructure of these Zircaloy-4, M5, and Q extruded tubes were observed with a polarized light microscope after grinding up to a 1200 SiC paper and anodic oxidation. Microstructure after hot extrusion is always fibered in the extrusion direction. But some differences can be observed between the three alloys: Zircaloy-4 tube contains elongated grains, and small recrystallized ones (Fig. 2). M5 and Q ones only contain elongated grains.

Second phase particles in Zircaloy-4 (Fig. 3) are mainly $Zr(Fe,Cr)_2$ ones, they have a mean diameter around 170 nm, and a 0.5 % volume fraction (estimated in Ref [22]). They precipitate during the quench at the lath boundaries. After hot extrusion, they are aligned in the extrusion direction, as a consequence of laths deformation in the die. For the Q alloy, the observed second phases particles are βZr, $Zr(Nb,Fe)_2$ and some larger (up to 1 μm) $(Zr,Nb)_4Fe_2$. The total volume fraction of precipitates is around 2 % [23]. They are also aligned in the axial direction of the tube and have a mean diameter around 130 nm. The same distribution of precipitates, aligned in the extrusion direction, is found in the M5 alloy.

Four incomplete poles figures were measured, and then the orientation distribution function computed, and the complete pole figures reconstructed. The *c* axis is perpendicular to the extrusion direction. Their orientation from radial direction varies from 60° to 90° at mid-thickness of the tubes, as a function of the alloy (Fig. 4).

In order to study the effect of the grain size and the second phase particle distribution, specimens were also taken from Zircaloy-4 and M5 recrystallized bars, with an equiaxial grain size of approximately 5 μm and a homogeneous repartition of precipitates. Texture is also characterized by *c* axis perpendicular from the axial direction, and 60° rotated from the radial direction. Type and size of precipitates in Zircaloy-4 bars are similar to the extruded tubes ones. In M5 materials, precipitates are mainly metallic (βZr and βNb), with a few intermetallic $Zr(Nb,Fe)_2$.

[3] M5™ is a trademark of AREVA NP.

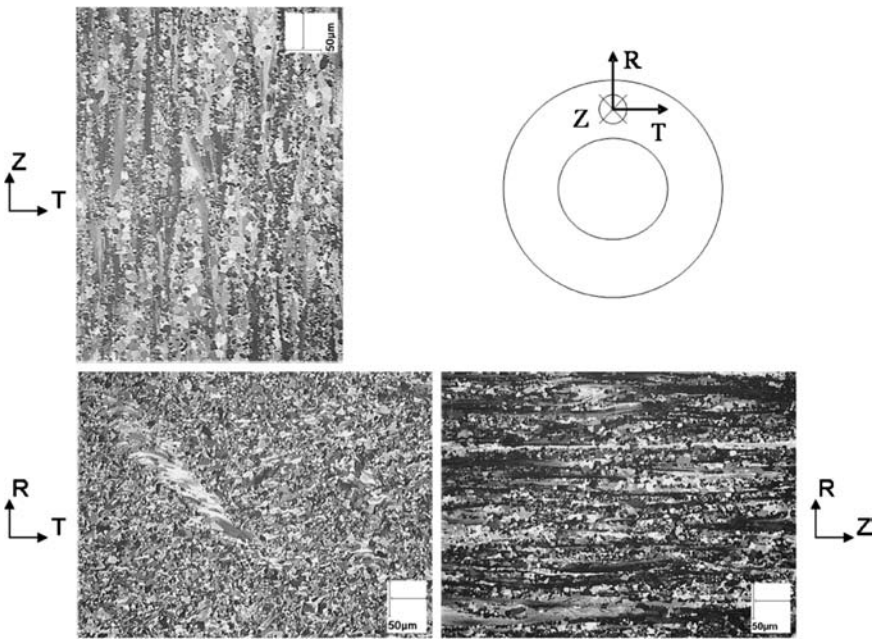


FIG. 2—*Microstructure of a Z4 hot extruded tube at mid-thickness.*

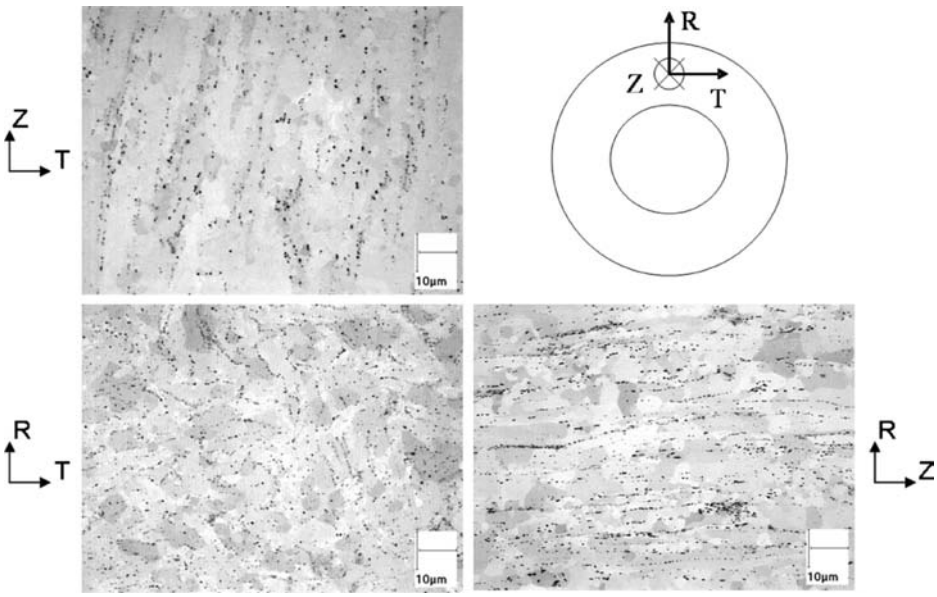


FIG. 3—*Second phase particles distribution in a Z4 hot extruded tube at mid-thickness.*

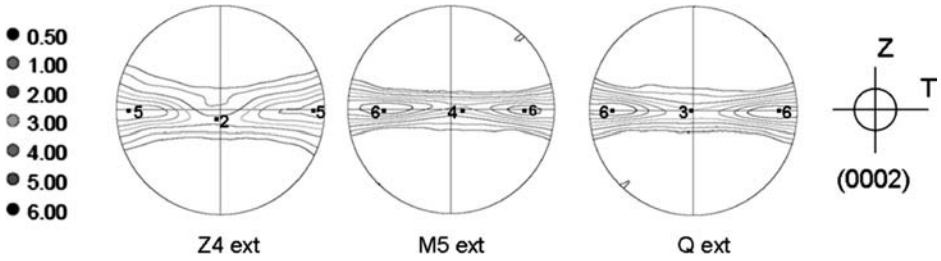


FIG. 4—*Texture of hot extruded tubes at mid-thickness.*

Tested materials are summarized in the Table 2.

Experimental Procedures

LCF Tests

Specimens were taken in the axial direction from extruded tubes, at the middle of the thickness, and from recrystallized bars. They were designed following the ASTM E606 [24] standard, with a diameter of 8 mm. LCF tests were conducted on a servo-hydraulic MTS machine. Symmetric tension-compression cyclic loading was employed under axial plastic strain control, monitored by a diametral extensometer considering anisotropy of material flow previously measured by tensile tests. A 5 Hz frequency triangular waveform was applied, with plastic strain amplitudes ($\Delta\epsilon_p/2$ on the Fig. 7) from 0.5 to 3 %, according to strain amplitudes undergone during cold pilgering.

TABLE 2—*Tensile test specimens list.*

Specimen Name	Tensile Direction	Metallurgical State	Alloy
Z4 ext	Z	Hot extruded tube	Zircaloy-4
Z4 ext_N2			
Z4 ext_N05			
Z4 ext_T	T		
Z4 rx	Z	Recrystallized bar	
M5 ext	Z	Hot extruded tube	M5™
M5 ext_N2			
M5 ext_N05			
M5 ext_T	T		
M5 rx	Z	Recrystallized bar	
Q ext	Z	Hot extruded tube	Q
Q ext_N2			
Q ext_N05			

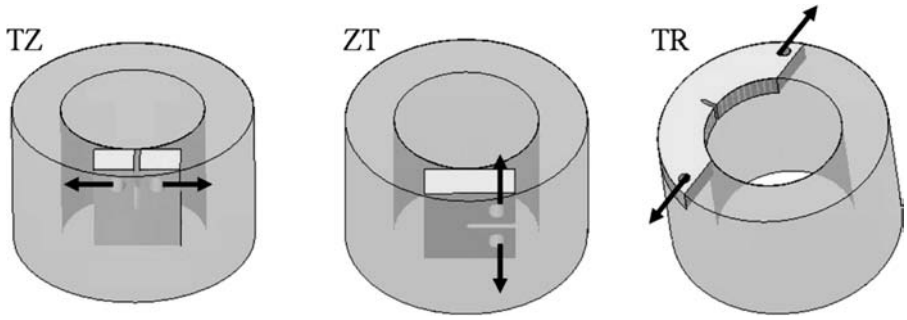


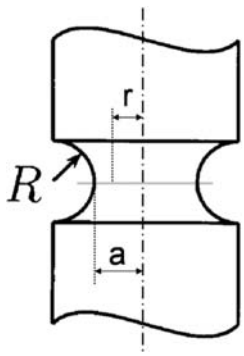
FIG. 5—*Orientation and name of toughness test specimens taken from extruded tubes.*

Fracture Toughness Tests

Fracture toughness tests were conducted following the ASTM E1820 standard. Specimens were cut in three directions (Fig. 5). They are named with two letters: The first one is the normal direction of the crack propagation plane; the second one is the crack propagation direction. V-shape notches were used to make the pre-cracking easier. The size of the specimens was limited by the thickness of the extruded tubes, which is 16 mm. The thickness is 12 mm for the TZ and ZT specimens, and 8 mm for the TR ones. After pre-cracking, specimen was put in tension, at a rate of 0.2 kN/s for the TZ and ZT specimens and at 0.07 kN/s for the TR ones.

Tensile Tests

Tensile tests of notched axisymmetric samples were used to study the ductile damage build-up mechanisms, by varying the stress triaxiality, which was assessed, as a first approach, by the analytical model initially proposed by Bridgman [25] (Fig. 6). These tests were conducted at a $5.10^{-4}\,s^{-1}$ constant strain rate.



$$\frac{\sigma_H}{\sigma_{eq}} = \frac{1}{3} + \ln\left(\frac{a^2 + 2aR - r^2}{2aR}\right)$$

Specimen suffix	Specimen geometry	a (mm)	R (mm)	Maximum stress triaxiality (r=0)
-	smooth	3	∞	0.33
_N2	notched	3	2	0.89
_N05	notched	3	0,5	1.71

FIG. 6—*Stress triaxiality of tensile test specimens.*

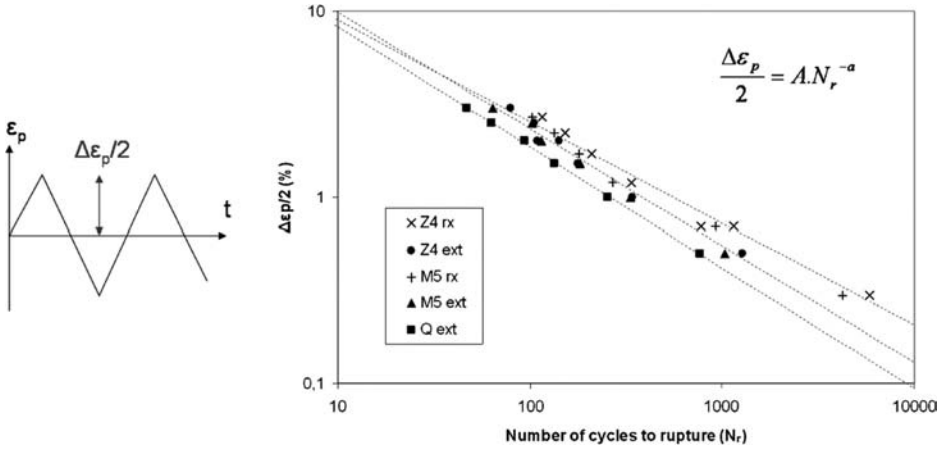


FIG. 7—*LCF life of tested specimens.*

Axisymmetric specimens (6 mm diameter, see Fig. 6) were taken in the axial direction from extruded tubes ("Z"), at the middle of the thickness, and from recrystallized bars (Z4 and M5). Some flat specimens (1×2 mm section in the strain zone) were also taken in the circumferential direction from extruded tubes Z4 and M5 ("T"). Tested samples are summarized in the following table.

Results

LCF

Analytical models [2], and more recent finite element ones [3] showed that cold pilgering is a cyclic deformation process. Thus, materials were first tested under LCF deformation routes.

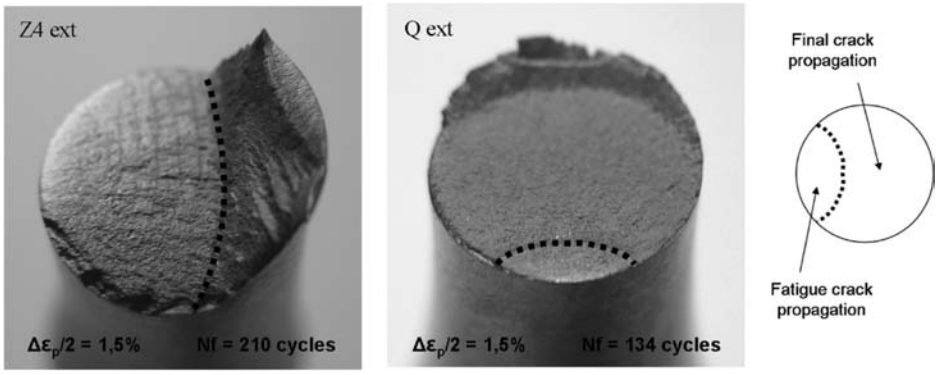


FIG. 8—*Fracture surface of fatigue test specimens.*

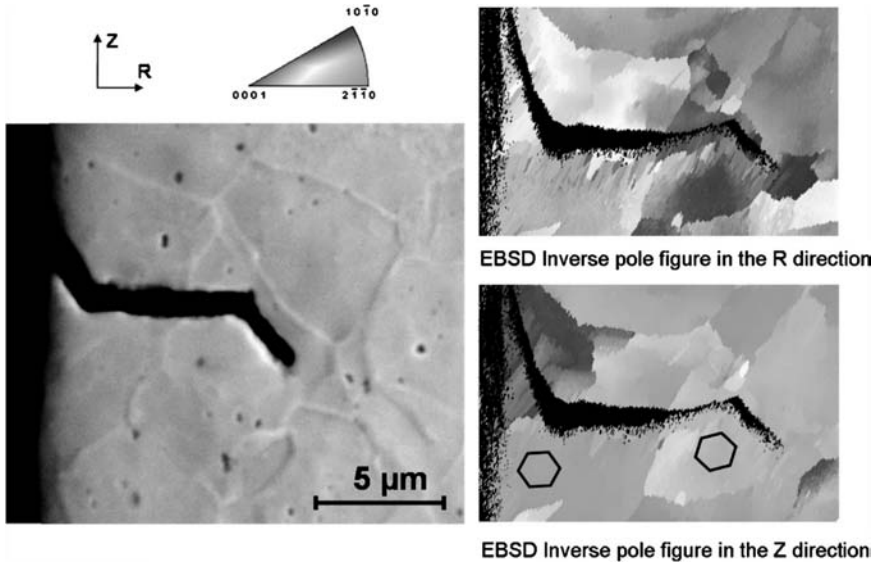


FIG. 9—*EBSD maps on Z4 fatigue tests samples showing the intergranular nucleation and propagation of the crack, along the prismatic slip systems.*

Stress amplitude as a function of strain amplitude and number of cycles was consistent with literature data [4–6], but was not interpreted further. Fatigue life of tested alloys fitted well with the Manson Coffin law (Fig. 7).

Z4 and M5 specimens from extruded tubes exhibit the same fatigue life. Recrystallized Z4 and M5 have a higher fatigue life than extruded ones, especially for low strain amplitudes, which is consistent with Lin observations [7]. Q alloy specimens from extruded tubes have a 30 % lower fatigue life than Z4 and M5 ones, whatever the applied strain amplitude. In order to explain the early fracture of Q alloy, fracture surfaces were examined (Fig. 8).

The transition from the fatigue to the final propagation of the main crack is clearly visible. At this point, the crack length, which is a function of the toughness of the alloy, is clearly lower for the Q alloy. EBSD observation of cracks showed that cracks nucleation and propagation is intra-granular, along the prismatic slip systems, and does not seem to follow precipitate alignments (Fig. 9).

Thus, assuming that crack propagation rate is not a function of the alloys and second phase particles, the lower fatigue life of Q alloy must be explained by a lower toughness that reduces the fatigue life by early fracture. To check this assumption, fracture toughness tests were carried out.

Fracture Toughness

Force versus displacement at the force application point, adjusted using the stiffness of the machine, was plotted (Fig. 10). According to ASTM E1820 standard, even for these relatively large specimens, these tests do not allow to

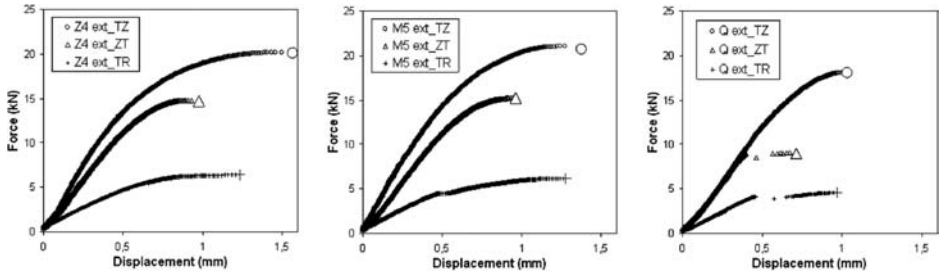


FIG. 10—*Force versus displacement curves of toughness tests.*

calculate the K_{IC} because of the large plastic strain at the crack tip (and thus the inflexion of the curve).

Therefore, the J integral was used to characterize the toughness of the specimens (ASTM E1820). Crack propagation, calculated using the stiffness loss of the specimen, was found negligible (around 0.1 mm). Thus, J integral was calculated at the time of the specimen fracture, and was named J_{IC} (Fig. 11). It was only possible for the TZ and ZT specimens, which are consistent with the ASTM E1820 standard.

J_{IC} integral of Z4 and M5 specimens is equal. Lower J_{IC} of Q alloy in the two directions confirms its low toughness in comparison to Z4 and M5, and explains its lower fatigue life during LCF tests and higher sensitivity to cold pilgering defects. For the three alloys, J_{IC} is three times less for the ZT specimen, that is, for crack propagation in the circumferential direction of the extruded tubes.

Fractography of the fatigue and toughness tests samples showed that the final propagation of the crack is always ductile, meaning that toughness is a function of the ductile tearing damage mechanisms at the crack tip.

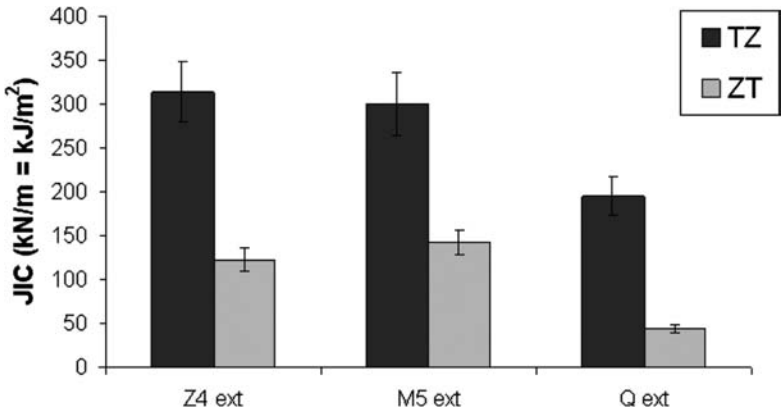


FIG. 11—J_{IC} *of specimens taken from hot extruded tubes.*

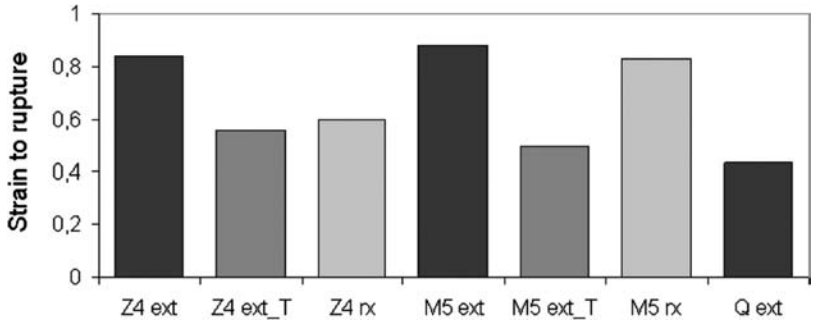


FIG. 12—*Strain to rupture of tested alloys after tensile tests.*

Ductile Damage

In order to understand the large differences in fracture toughness between alloys and crack propagation direction, ductile damage mechanisms have been studied, as a function of stress triaxiality, which is very high at the crack tip.

Tensile tests results will be presented from a macroscopic to a microscopic point of view, from ductility and stress triaxiality effect to a detailed analysis of nucleation, growth, and coalescence of voids.

Strain to Rupture—The first result of tensile tests concerning damage is the strain to rupture. It can be calculated after the test from the area of the fracture surface, even for the axisymmetric specimens and the flat ones. Figure 12 summarizes the results for specimens without notches, that is, noticing a large notch radius after necking, for stress triaxiality equal to 1/3.

Ductility of Z4 and M5 is almost equal for specimens machined out of extruded tubes. A difference between these two alloys appears for recrystallized specimen. It will be discussed later. In the transverse direction of the tubes, ductility is lower than in the axial direction. This result seemingly in contradiction to the toughness results (Fig. 11) will be explained later. Finally, ductility of Q alloy samples is lower than Z4 and M5 ones; a result consistent with toughness and fatigue results.

Strain to Rupture as a Function of Stress Triaxiality—Stress triaxiality is a well known mechanical parameter having an important role in the growth rate of voids (as a function of plastic strain), and thus in the ductility. In order to quantify this, tensile tests were carried out on smooth samples and notched ones (Fig. 6) taken from extruded tubes, in the axial direction. As we can see in Fig. 13, ductility is lower for high stress triaxiality. Q alloy has a much lower ductility, but loss of ductility due to stress triaxiality is similar for Z4, M5, and Q alloy.

Fracture Surfaces—Fracture surfaces exhibits dimples, characteristic of the ductile damage mechanism. They are quite equiaxial for the smooth specimens

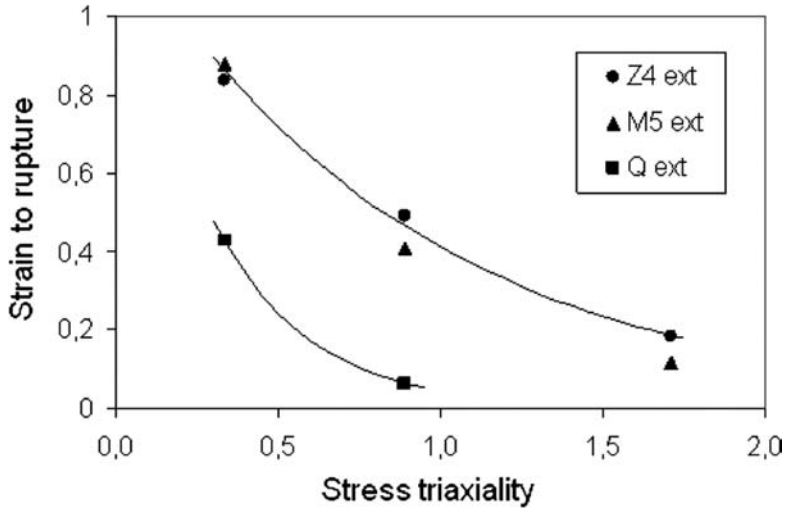


FIG. 13—*Strain to rupture as a function of stress triaxiality.*

with a low stress triaxiality. For high stress triaxiality, that is, for notched specimens, tubular dimples with hexagonal section are visible (Fig. 14). This is consistent with the void growth mechanism proposed by Crépin [18]. This growth mechanism, based on the activation of the three prismatic slip planes, seems to be active only at high stress triaxiality. This could be explained by the lower strains reached at high stress triaxiality, which only allows the activation of prismatic slip systems. At lower stress triaxiality, strain is higher and others slip systems can be active, leading to more spherical voids.

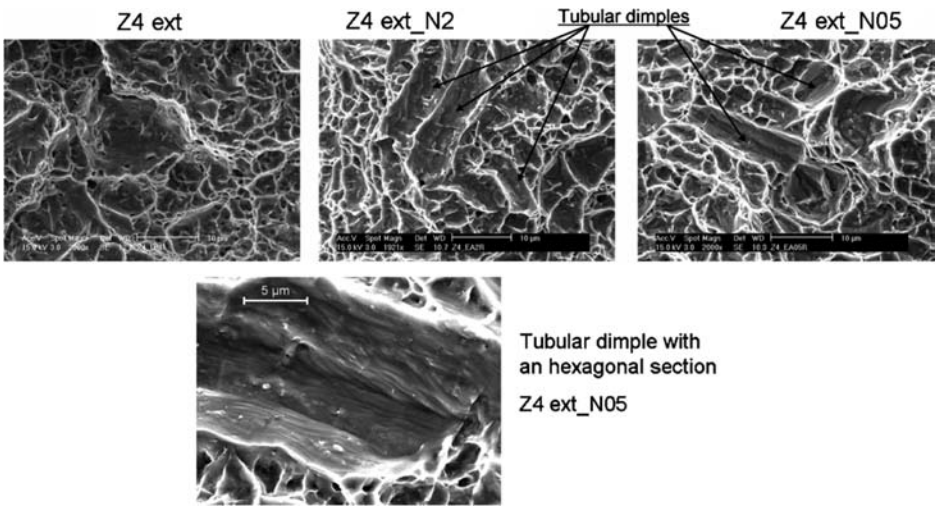


FIG. 14—*Voids at the fracture surface of Z4 tensile test specimens.*

Porosity Evolution—In order to examine and quantify porosity, broken specimens were cut along their axis, in the axial direction. They were polished using SiC paper, diamond, and a colloidal silica suspension. Polished specimens were observed in a scanning electron microscope (SEM), using the backscattered electrons detector for a good contrast, essential for the quantification of porosity with an automated image analysis.

The density and diameter of voids decrease as the distance from fracture surface increases, faster for notched specimens for which the strain is localized at the bottom of the notch. For smooth specimens, voids are only visible in the neck, meaning that voids nucleate after the necking. Many alignments of voids in the axial direction are visible for the specimens taken from extruded tubes, whereas voids are randomly distributed for the recrystallized specimens (Fig. 15).

Quantification of voids volume fraction was conducted using an automated image analysis of SEM pictures. Size of each image was $247 \times 168\,\mu$m. The

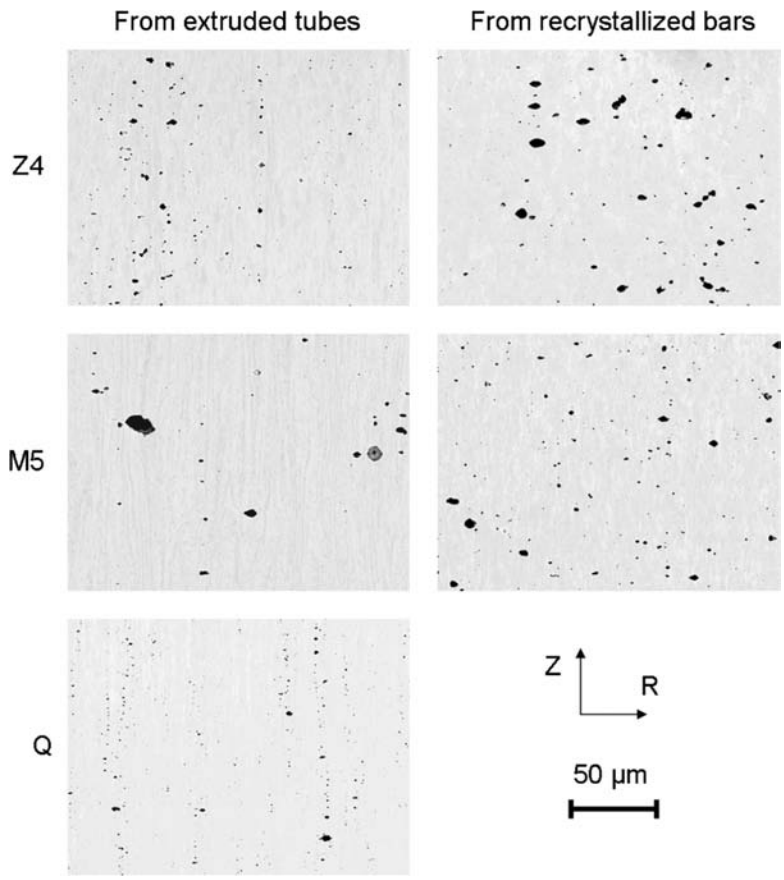


FIG. 15—*Voids under the surface of smooth tensile tests specimens.*

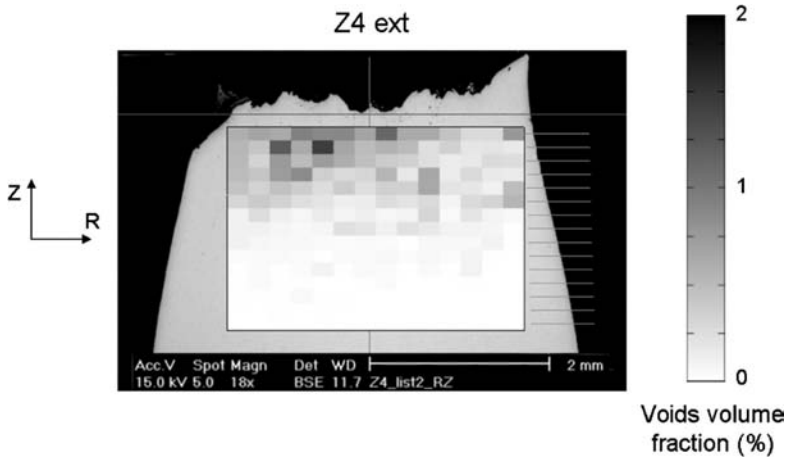


FIG. 16—*Mapping of the voids volume fraction in a Z4 broken tensile test specimen.*

number of images was up to 400 per specimen. Each line of images corresponds to a mean equivalent plastic strain, calculated from the diameter at the same axial position, taking into account anisotropy of material flow previously measured by tensile tests (Fig. 16). Thus, for each specimen, mean porosity volume fraction of each line can be plotted as a function of local equivalent plastic strain (Fig. 17). This analysis was not possible for the more severely notched specimens (_N05), for which voids were only localized at a few micrometers from the fracture surface, as well as the plastic strain.

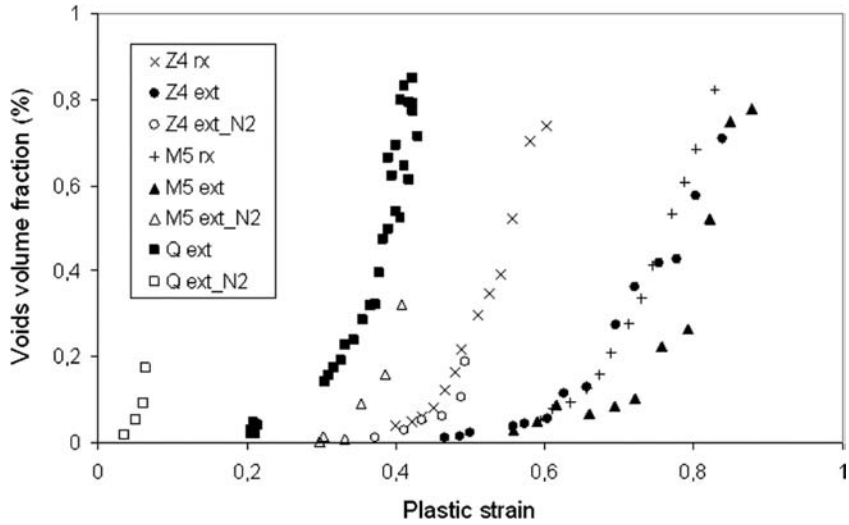


FIG. 17—*Voids volume fraction increase during tensile tests.*

These experimental results give a large amount of information on damage kinetics, as a function of alloy, metallurgical state, and stress triaxiality:

- *Nucleation of voids:* Voids nucleate at a 50 % plastic strain for Z4 and M5 smooth specimens from extruded tubes. The same result is noticed for the M5 recrystallized sample, whereas voids are visible from a 35 % plastic strain for the Z4 one. Q alloy is more sensitive to voids nucleation, which is visible from 20 % for smooth specimens. Voids nucleate sooner for high stress triaxiality levels. In comparison with Z4, voids nucleation in M5 seems to be more sensitive to stress triaxiality.
- *Porosity evolution:* Increase in void volume fraction has two contributions: New voids nucleation and void growth. Porosity increase rate is equal for all smooth tested specimens, and higher for high stress triaxiality levels.
- *Critical porosity and coalescence of voids:* Mean critical porosity is around 1.5 % for all smooth tested specimens and much lower (around 0.3 %) for high stress triaxiality levels. Thus, coalescence mechanisms do not seem to be a function of the composition of the alloys and the metallurgical state. On the other hand, it seems to be strongly dependent on the stress triaxiality.

In order to explain these results, a detailed analysis of nucleation, growth, and coalescence of voids, as a function of alloy and metallurgical state was carried out.

Nucleation of Voids—Voids nucleation kinetics can be plotted as a function of the equivalent plastic strain, using the number of voids detected on the SEM images (Fig. 18).

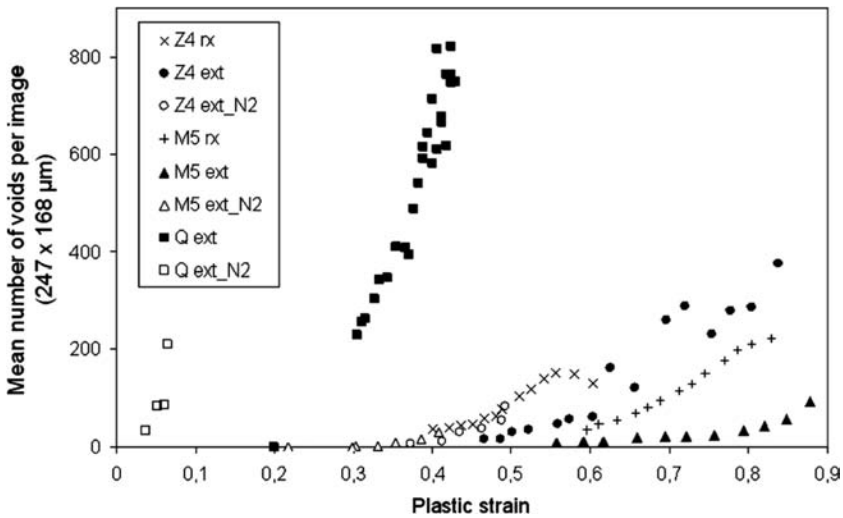


FIG. 18—*Voids nucleation kinetics.*

Contrary to the porosity kinetics previously showed (Fig. 17), the void nucleation kinetics of Z4 and M5 smooth specimens from extruded tubes are very different from each other. Voids are much more numerous for Z4. M5 recrystallized specimen exhibits more voids than the extruded one. For Z4, recrystallization does not have an effect on the void nucleation kinetics; number of voids in the recrystallized state is only limited by their coalescence. Number of voids in Q alloy is much higher than in Z4 and M5 at the same metallurgical state (extruded tubes). Stress triaxiality does not have an effect on the number of voids, which is only limited by their coalescence for the notched specimens.

In order to explain these differences between alloys and metallurgical states, voids must be observed in their metallurgical background. For this, samples were electro-polished and analyzed using EBSD and EDX (energy dispersive X-ray analysis) maps.

For Z4 and Q alloys, a majority of voids seems to nucleate on second phase precipitates, visible on the EDX maps (Fig. 19).

EBSD maps also showed that the length of precipitates alignments visible on the extruded tubes is higher than the length of grains and equal to the length of voids alignments. So, the brittle second phase precipitates are the main sites for ductile damage nucleation in Z4 and Q alloys.

In the case of M5, ductile βNb and βZr precipitates were not observed to be the cause for voids formation. EBSD maps showed that voids nucleate at the grain boundaries of highly disoriented grains (Fig. 20). Furthermore, length of grains is equal to length of voids alignments. So, grain to grain misorientations are the cause of M5 ductile damage.

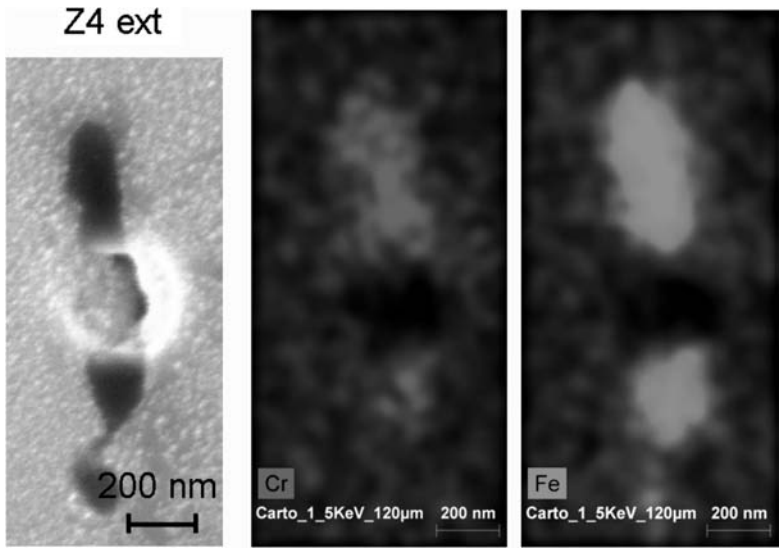


FIG. 19—*Void nucleated on a second phase particle in a Z4 tensile test specimen (secondary electrons, Cr, and Fe images).*

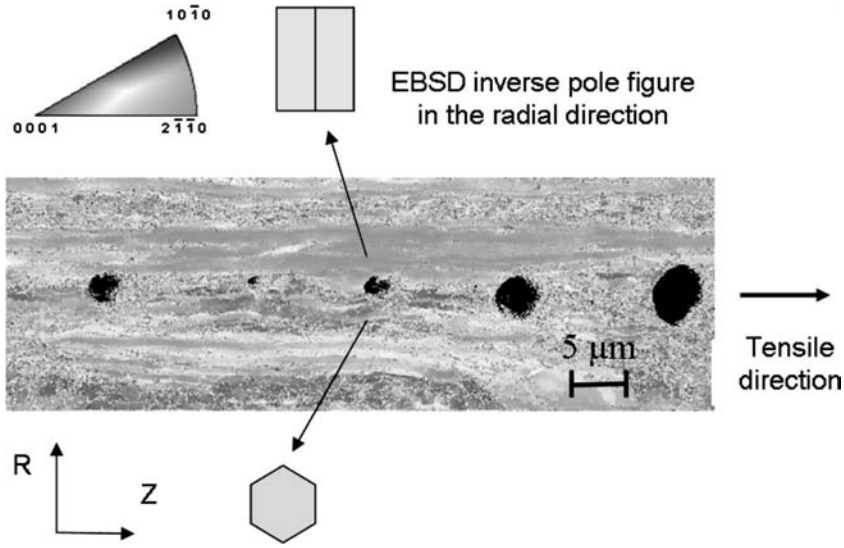


FIG. 20—*EBSD map of voids nucleated in M5, on grain boundaries of highly disoriented grains.*

These two mechanisms of voids nucleation give an explanation of voids nucleation kinetics previously mentioned (Fig. 18). Voids number in the recrystallized Z4 sample and the Z4 from extruded tubes appears to be controlled by the same mechanism because precipitates number is similar for these two samples. On the other hand, recrystallized M5 sample contains finer grains and more grain boundaries than the hot extruded one, and so, more voids after the tensile test. Finally, in comparison with Z4, voids in Q alloy, which contains a higher volume fraction of precipitates and some bigger precipitates, nucleates at lower plastic strain and are more numerous.

Voids Growth—Some elongated voids were observed using EBSD maps. They are elongated in the *c*-axis direction of the grain where they grew. Nevertheless, it was only observed for small voids. Size and shape of large ones seems to be a function of grain size, which means that voids growth is stopped or slowed down by grain boundaries.

Voids growth kinetics can also be plotted as a function of the equivalent plastic strain, using the equivalent diameter of voids (in the cut plane) detected on the SEM images (Fig. 21).

For the samples from extruded tubes, voids growth rate is higher for Z4 than for M5. It can be explained by the larger grains of the M5 extruded tubes. For the Z4 alloy, recrystallized samples exhibit a higher void growth rate, due to larger grains than in the extruded ones. The opposite is observed for the M5 alloy, which exhibits finer grains in the recrystallized state. Voids growth rate in the Q alloy is similar to that observed for Z4

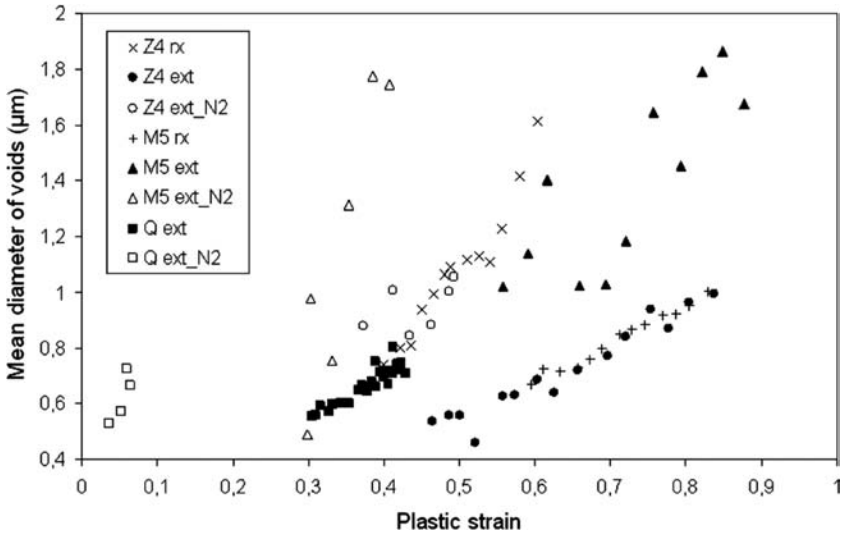


FIG. 21—*Voids growth kinetics.*

alloy. Size of voids in Q alloy is limited by their coalescence, which occurs sooner because of their high number. Finally, a higher voids growth rate is observed for high stress triaxiality, which is consistent with previous studies.

Coalescence of Voids—Coalescence occurs when the distance between voids, perpendicular to the tensile direction, is low enough regarding to diameter of voids. It can be showed plotting the mean distance between voids, perpendicularly to the tensile direction, as a function of mean voids diameter (Figs. 22 and 23). Coalescence criteria can be written as

$$l_{\text{mean}} = K \cdot d_{\text{mean}}$$

l_{mean} : Mean distance between voids, perpendicularly to the tensile direction

d_{mean} : Mean voids diameter

Coalescence criteria and the K parameter are the same for all alloys and metallurgical states. K is only a function of stress triaxiality: The higher the triaxiality, the higher the K value and the sooner the coalescence. For tensile samples taken from extruded tubes in the circumferential direction, the lower ductility previously observed (Fig. 12) can thus be explained by the alignments of voids, which result in a lower mean distance between voids in the perpendicular direction to the tensile direction.

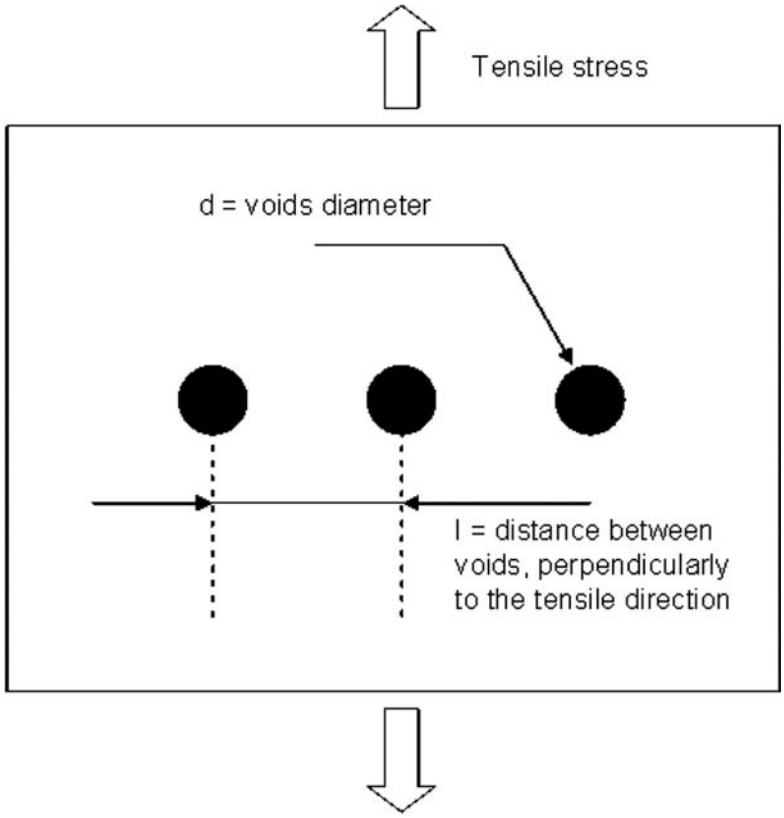


FIG. 22—*Schematic view of the variables used in the Fig. 23.*

Discussion

According to the tensile tests detailed analysis, the main metallurgical and mechanical parameters having a role in the ductile damage mechanism by nucleation, growth, and coalescence of voids can be summarized in the following diagram (Fig. 24).

These results can now be used for a better understanding of fatigue and toughness tests results. LCF tests showed that Q alloy specimens from extruded tubes have a lower fatigue life and toughness than Z4 and M5 ones. This can be explained by the larger $(Zr, Nb)_4Fe_2$ precipitates in the Q alloy, which make the nucleation of voids easier and by the higher number of precipitates, responsible for an early coalescence of voids at the crack tip. For Zr–Nb–Sn–Fe alloys with an iron content lower than 0.3 %, such large particles are not formed and ductility is higher.

For all the specimens taken from extruded tubes, a lower toughness was also observed for crack propagation in the circumferential direction. At the crack tip of the toughness specimens, and in the notched tensile test specimens, the low strain to rupture, due to high stress triaxiality is responsible for an

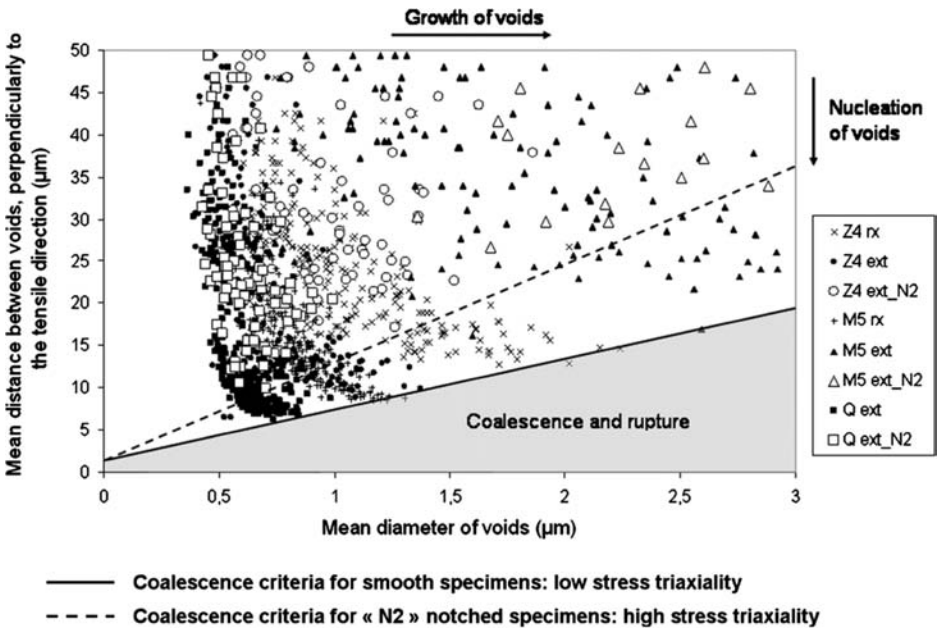


FIG. 23—*Coalescence criteria as a function of stress triaxiality.*

anisotropic growth of voids, which are elongated in the direction of the grain c axis where the void grew (Fig. 25). When the axis of these elongated voids are in the direction of the crack propagation, their coalescence and the crack propagation are easier. That is why the toughness of ZT specimens is lower.

In the case of lower stress triaxiality, strain can be higher and others slip systems than the prismatic ones are active, leading to spherical voids and not elongated ones. So, texture orientation is no more important in this case. Thus, the loss of ductility observed for the tensile tests in the circumferential direction is explained by the alignments of voids nucleation sites in the axial direction, which are responsible for an early coalescence of voids, perpendicular to the tensile direction.

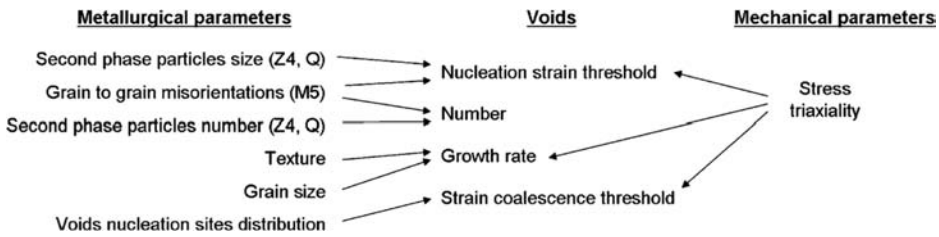


FIG. 24—*Metallurgical and mechanical parameters having a role in the ductile damage mechanisms.*

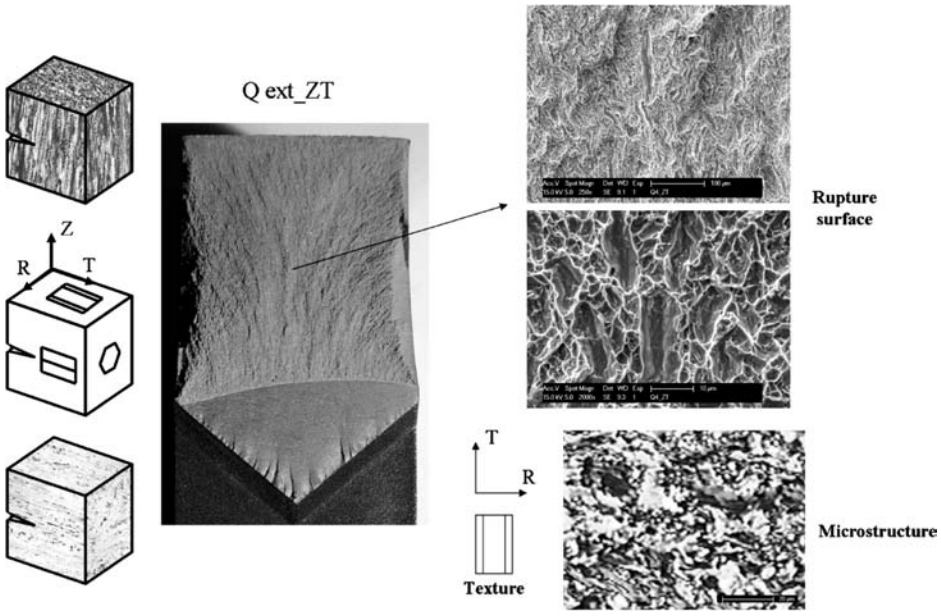


FIG. 25—*Fracture surface of the Q ext_ZT toughness test specimen.*

Summary and Conclusions

Cold pilgering of zirconium alloys containing high content of alloying elements may be a critical issue regarding surface defects or serious cracks. A better knowledge of damaging mechanisms during pilgering is a way for optimizing the productivity of the cold forming routes of cladding tubes. Behavior of Zircaloy-4, M5^{TM} and Zr–Nb–Sn–Fe alloy with 0.35 % of iron under damaging conditions were investigated for this purpose.

Cold pilgering is a cyclic deformation process. Depending on its position inside the grooves of the rolls, material is strained alternately in compressive and tensile modes. Thus, materials were first tested under LCF deformation routes. LCF tests on Q alloy specimens showed a lower fatigue life than for Z4 and M5 ones, which are equivalent. This is explained by the lower fracture toughness of the Q alloy. Toughness anisotropy is also revealed by additional tests conducted on samples with different orientations in the tube. Fractography of the fatigue and toughness tests samples also showed that the final propagation of the crack is always ductile, meaning that toughness is function of the ductile tearing damage mechanisms at the crack tip.

Therefore, tensile tests of notched axisymmetric samples were used to study the ductile damage build-up mechanisms, by varying the stress triaxiality. The link between the metallurgical state of the samples and the damage mechanisms by nucleation, growth, and coalescence of voids was analyzed using a detailed analysis of broken samples:

- For the Z4 and Q alloy, the type and size of second phase particles are responsible for the nucleation strain threshold of voids. The very low

number of intermetallic particles in M5^{TM} implies that voids nucleate later and at grain boundaries for the M5 alloy, due to the grain to grain misorientations.

- Voids growth rate is mainly a function of the grain size, the texture, and the stress triaxiality. In the case of high stress triaxiality, voids growth can be anisotropic, with elongated voids in the direction of the grain *c* axis where they grew.
- Finally, voids coalescence strain threshold is a function of the stress triaxiality, the number of voids and repartition of voids regarding tensile direction.

The lower fatigue life, toughness, and ductility of the Q alloy can be explained by the large $(Zr, Nb)_4Fe_2$ precipitates due to the high iron content, which make the nucleation of voids easier and by the higher number of precipitates, responsible for an early coalescence of voids. For ZrNbSnFe alloys containing 1 % Nb, the iron content should be limited to values lower than 0.30 %.

These experimental results, combined with the material mechanical history provided by numerical modeling of the cold pilgering process, are now used to improve the productivity of forming routes of cladding tubes, both by a mechanical way (cold pilgering stress state) and a metallurgical one (microstructure of alloys used for tubes rolling).

References

[1] Yoshida, H., Matsui, T., Otani, T., and Mandai, K., "Experimental Investigation of the Cold Pilgering of Copper Tubes," *CIRP Ann.*, Vol. 24, 1975, pp. 191–196.

[2] Aubin, J.-L., Montmitonnet, P., and Mulot, S. "Zirconium Alloy Cold Pilgering Process Control by Modeling," *ASTM STP1354*, ASTM International, West Conshohocken, PA, 2000, pp. 460–481.

[3] Lodej, B., Niang, K., Montmitonnet, P., and Aubin, J. L., "Accelerated 3D FEM Computation of the Mechanical History of the Metal Deformation in Cold Pilgering of Tubes," *J. Mater. Process. Technol.*, Vol. 177(1–3), 2006, pp. 188–191.

[4] Armas, A. F., Herenu, S., Bolmaro, R., and Alvarez-Armas, I., "Cyclic Softening Mechanisms of Zircaloy-4," *J. Nucl. Mater.*, Vol. 326(2–3), 2004, pp. 195–200.

[5] Bolmaro, R. E., Signorelli, J. W., Brokmeier, H.-G., Armas, A. F. Herenu, S., and Alvarez-Armas, I., "Cyclic Softening Mechanisms of Zyr-4 at Room Temperature: The Unlikely Influence of Texture Variations," *Scr. Mater.*, Vol. 51(6), 2004, pp. 617–621.

[6] Choi, H. I., Lee, D. H., and Kwun, S. I., "Fatigue Deformation Mechanism of the Annealed Zircaloy-4 with Texture," *Scr. Mater.*, Vol. 38(4), 1998, pp. 565–571.

[7] Lin, X. and Haicheng, G., "Low Cycle Fatigue Properties and Microscopic Deformation Structure of Zircaloy-4 in Recrystallized and Stress-Relieved Conditions," *J. Nucl. Mater.*, Vol. 265(1–2), 1999, pp. 213–217.

[8] Tan, J., Ying, S., Li, C., and Sun, C., "Effect of Zirconium Hydrides on Cyclic Deformation Behavior of Zr-Sn-Nb Alloy," *Scr. Mater.*, Vol. 55(6), 2006, pp. 513–516.

[9] Crépin, J., Bretheau, T., Caldemaison, D., and Ferrer, F., "Low Cycle Fatigue Behavior of [Beta] Treated Zirconium: Partial Irreversibility of Twinning and Consequences for Damage," *Acta Mater.*, Vol. 48(2), 2000, pp. 505–516.

[10] Bertolino, G., Meyer, G., and Perez Ipina, J., "In Situ Crack Growth Observation and Fracture Toughness Measurement of Hydrogen Charged Zircaloy-4," *J. Nucl. Mater.*, Vol. 322(1), 2003, pp. 57–65.

[11] ASTM E1820, 2003, "Standard Test Method for Measurement of Fracture Toughness," *Annual Book of ASTM Standards*, Vol. 03.01, ASTM International, West Conshohocken, PA.
[12] Grange, M., Besson, J., and Andrieu, E., "An Anisotropic Gurson Type Model to Represent the Ductile Rupture of Hydrided Zircaloy-4 Sheets," *Int. J. Fract.*, Vol. 105(3), 2000, pp. 273–293.
[13] Hayes, T. A., Rosen, R. S., and Kassner, M. E., "Creep Fracture of Zirconium Alloys," *J. Nucl. Mater.*, Vol. 353(1–2), 2006, pp. 109–118.
[14] Care, S. and Zaoui, A., "Cavitation at Triple Nodes in Alpha-Zirconium Polycrystals," *Acta Mater.*, Vol. 44(4), 1996, pp. 1323–1336.
[15] Nikulin, S. A., Shtremel, M. A., and Markelov, V. A., "Influence of Secondary Phase Particles on Zr-Alloy Plastic Flow Stability and Fracture," *J. Phys. IV*, Vol. 6, 1996, pp. 133–143.
[16] Nikulin, S. A. and Rojnov, A. B., "Effects of Microstructure on Zr-Alloy Ductility and Fracture Resistance," *Proceedings of the First Joint International Conference on Recrystallization and Grain Growth*, RWTH Aachen, Germany, Aug. 27–31, 2001, pp. 1371–1376.
[17] Elbachiri, K., Doumalin, P., Crépin, J., Bornert, M., Barberis, P., Rebeyrolle, V., and Bretheau, T. "Characterization of Local Strain Distribution in Zircaloy-4 and M5™ Alloys," *Zr in the Nuclear Industry: 15th Int. Symp., STP 1505*, Sunriver, OR, June 24–28, 2007, ASTM International, West Conshohocken, PA.
[18] Crépin, J., Bretheau, T., and Caldemaison, D., "Cavity Growth and Rupture of [Beta]-Treated Zirconium: A Crystallographic Model," *Acta Mater.*, Vol. 44(12), 1996, pp. 4927–4935.
[19] Rice, J. R. and Tracey, D. M., "On the Ductile Enlargement of Voids in Triaxial Stress Fields," *J. Mech. Phys. Solids*, Vol. 17, 1969, pp. 201–217.
[20] Watson, D., Warren, M. R., and Beevers, C. J., "Some Observations of Ductile Void Growth and Crack Propagation in Alpha Zirconium," *Can. Metall. Q.*, Vol. 11(1), 1972, pp. 53–61.
[21] Forscher, F., "Strain-Induced Porosity and Hydrogen Embrittlement in Zirconium," *J. Met.*, Vol. 8, 1956, pp. 536–543.
[22] Barberis, P., Ahlberg, E., Simic, N., Charquet, D., Dahlback, M., Limback, M., Tagstrom, P., Lemaignan, C., Wikmark, G., and Lehtinen, B., "Role of the Second-Phase Particles in Zirconium Binary Alloys," *ASTM STP 1423*, 2002, pp. 33–58.
[23] Chabretou, V., Hoffmann, P. B., Trapp-Pritsching, S., Garner, G., Barberis, P., Rebeyrolle, V., Vermoyal, J. J., "Ultra Low Tin Quaternary Alloy In-Pile Performance: Impact of Tin Content on Corrosion and Mechanical Resistance," *16th International Symposium on Zirconium Alloys in the Nuclear Industry*, Chengdu, China, May 2010, ASTM International, West Conshohocken, PA (to be published).
[24] ASTM E606, 2003, "Standard Practice for Strain-Controlled Fatigue Testing," *Annual Book of ASTM Standards*, Vol. 03.01, ASTM International, West Conshohocken, PA.
[25] Bridgman, P. W., *Studies in Large Plastic Flow and Fracture, with Special Emphasis on the Effects of Hydrostatic Pressure*, Harvard University Press, Cambridge, MA, 1964.

DISCUSSION

Question 1, Johannes Bertsch, Paul Scherrer Institut:—Is it intended to analyze the behavior also at higher temperatures?

Author's Response:—Pilgering of the Zr alloys tubes is a cold forming process. So the aim of this work was to study the damage behavior only at room temperature. For other applications, the same type of tests could be performed at higher temperatures.

Question 2, Vladimir Markelov, Bochvar Institut:—What is the optimum content of Fe and Sn for the Q type of alloys (Zr-Nb-Sn-Fe) for PWR fuel rods cladding application in your opinion?

Author's Response:—From a manufacturing point of view, we showed that a higher size and number of intermetallic precipitates reduces the ductility. So, alloys with high content of Fe (about 0.35% or higher) are more difficult to manufacture, leading to important cold pilgering costs.

Question 3, D. Banchik, Atomic Energy Commission of Argentina:—How do you distinguish between these types of defect from defects produced by lubrication failure?

Author's Response:—Lubrification failure can be responsible for cracks on the surface of the cold pilgered tubes. But from a local point of view, damage mechanisms are the same: high strains under the surface, nucleation of voids and coalescence to form a crack.

Question 4, Yao Zhongwen, Queen's University:—I can see those voids distributed along grain boundaries, do they play a more significant role on the mechanical failure?

Author's Response:—For M5™ alloy, ductile precipitates cannot be responsible for void nucleation. In this case, voids nucleate at the grain boundaries. For Zy-4 and Q alloy, voids nucleate mainly and earlier on the intermetallic precipitates, particularly if they are at grain boundaries, because of the strain localization. Therefore void nucleation occurs slightly later for M5™ than for Zy-4 and Q alloys. From this point of view, voids nucleated at grain boundaries without intermetallic precipitates play a less significant role on the mechanical failure.

Question 5, Ken Yueh, EPRI:—Were metallographic cross-sections prepared immediately after pilgering? If so how can you explain why pores (voids) shown are perfectly spherical? There should be some elongation of the pores formed at the end of the pilger deformation.

Author's Response:—The voids presented in figure 1 were observed just after pilgering. With the tensile tests, we showed that voids remains spherical for high strains. Thus, it is not surprising not to see elongated voids after pilgering.

Question 6, Suresh K. Yagnik, EPRI:—Further to results presented, did you also examine the process variables and mechanisms which minimize the discarded final cladding tubes and increase production yield?

Author's Response:—Damage data obtained with this work are now included in our numerical simulation of the cold pilgering. It allows us to quantify the effect of the pilgering parameters, such as feed rate, tools geometry, lubricant efficiency, … on the tube damage and was checked by experimental tests.

Question 7, Bo Cheng, EPRI:—Stringers of SPP were correlated to rapid oxide growth and spallation of many Zircaloy-4 channels in BWRs in the 1970s. It was found to result from hot working

from 800°C (high alpha or low alpha + beta phase field). Process modifications have been in place to avoid such occurrence. Would you place explanation which process step in Zr production would lead to formation of SPP stringers, and what criteria in SPP sizes you would recommend to avoid the problem?

Author's Response:—From a manufacturing point of view, small and well distributed precipitates increase the ductility and reduce the manufacturing costs. So, the cooling rate during the quench (acting on the size of the precipitates and the needle size) and the recristallization mechanisms during hot extrusion (distribution of the precipitates, grains shape and size) can have an effect on the ductility during cold pilgering.

Question 8, Jean-Christophe Brachet, CEA:— How do you deconvolve the respective contributions of SPP and of the (high angle) grain boundaries on the voids nucleation? One could suspect that part of the SPP are precipitated/located on the grain boundaries?

Author's Response:—For Zy-4 and Q alloy, when intermetallic precipitates are located at grain boundaries, particularly when grain to grain disorientation is high, nucleation of voids is easier. We did not examine clearly the amount of precipitates which are at grain boundaries, and the consequences on voids nucleation, in this study. This kind of quantification was made by Carre [13] on Zr-702.

Question 9, Dr. Shishov, Bochvar institute:— How SPPs $(Zr, Nb)_4Fe_2$ influence the voids formation in the Q alloy?

Author's Response:—Since the $(Zr, Nb)_4Fe_2$ precipitates in the Q alloy are the biggest, they are responsible of the nucleation of the first voids when strain is increasing. These precipitates explain the lower ductility, and the difficulty to manufacture this alloy.

Reprinted from JAI, Vol. 8, No. 1
doi:10.1520/JAI103015
Available online at www.astm.org/JAI

Mathieu Priser,[1,2] *Martin Rautenberg,*[1,3] *Jean-Marc Cloué,*[1] *Philippe Pilvin,*[2] *Xavier Feaugas,*[4] *and Dominique Poquillon*[3]

Multiscale Analysis of Viscoplastic Behavior of Recrystallized Zircaloy-4 at 400°C

ABSTRACT: Zirconium alloys are used in the nuclear industry as cladding tubes to prevent the fissile material from leaking into the coolant as the first safety wall of nuclear fuel. More and more requirements on fuel performance lead to stronger mechanical solicitations and integrity of cladding tubes has to be guaranteed. In this framework, the polycrystalline models, which are based on plasticity mechanisms, have interesting advantages compared to phenomenological ones. Some previous studies have shown that a polycrystalline approach could be very useful to describe the mechanical behavior of zirconium alloys. This modelling strategy has been successfully applied to fresh material and also, more recently, to irradiated material. The micromechanical approach has been developed in the light of transmission electron microscopy (TEM) observations. These experiments have been achieved to identify the main deformation mechanisms, which occur in several grains of relaxed and crept Zircaloy-4 samples. The main purpose of this paper is to describe an improved micromechanical model able to reproduce both the anisotropic creep behavior and the elasto-plastic behavior of unirradiated recrystallized Zircaloy-4 at 400°C. Finally, the quantitative analyses, which have been carried out with TEM correspond well with the results provided by the micromechanical approach.

KEYWORDS: Zircaloy-4, creep, relaxation, TEM, micromechanical approach

Manuscript received February 1, 2010; accepted for publication September 29, 2010; published online December 2010.

[1] AREVA, AREVA NP, 10 rue Juliette Récamier, F-69456 Lyon, France.
[2] LIMATB, Univ. Bretagne-Sud, rue de Saint-Maudé, F-56321 Lorient, France.
[3] CIRIMAT, CNRS/UPS/INPT, 4 allée Emile Monso, F-31030 Toulouse, France.
[4] LEMMA, Univ. de La Rochelle, ave. Michel Crépeau, F-17042 La Rochelle, France.

Cite as: Priser, M., Rautenberg, M., Cloué, J.-M., Pilvin, P., Feaugas, X. and Poquillon, D., "Multiscale Analysis of Viscoplastic Behavior of Recrystallized Zircaloy-4 at 400°C," *J. ASTM Intl.*, Vol. 8, No. 1. doi:10.1520/JAI103015.

Copyright © 2011 by ASTM International, 100 Barr Harbor Drive, PO Box C700, West Conshohocken, PA 19428-2959.

TABLE 1—*Chemical composition of the alloy.*

wt %, ASTM Standard	Sn	Fe	Cr	O	Zr
Zircaloy-4	1.30	0.21	0.10	0.125	Bal.

Introduction

Zirconium alloys are used in nuclear cores as cladding tubes in order to prevent the fissile material from leaking into the coolant as the first safety wall of nuclear fuel. It also has to ensure a good heat transfer between the fissile material and the coolant. More and more requirements on fuel performance lead to stronger mechanical solicitations, and the integrity of cladding tubes has to be guaranteed. Most of its lifetime, the cladding tube is mechanically loaded in a creep regime ($\sim 10^8\,s^1$), but during power transients (in particular during the pellet cladding interaction), the strain rates can reach much higher values (up to $10^2\,s^1$). For that reason, the thermo-mechanical loading histories of Zircaloy products are of prime interest and should be implemented into internal variable models. In this framework, the polycrystalline model, which is physically based on deformation mechanisms at grain scale, can be very useful. By comparing the results provided by the micromechanical approach and experimental measurements at microscopic transmission electron microscopy (TEM) and macroscopic (creep and relaxation tests) scale, we can build a sturdy model that provides interesting information both at microscopic and macroscopic scales.

Material

The investigated zirconium alloy in this paper is a recrystallized Zircaloy-4. Its chemical composition is given in Table 1. The specimens used in the present work are 130 mm long segments of guide-tubes for creep tests and 110 mm for relaxation tests. In this work, we want to characterize the viscoplastic behavior of a material (Zircaloy-4). Whether this alloy is used as a cladding tube or a guide-tube, it will have roughly the same mechanical behavior. Indeed, the thickness difference between the cladding tubes and guide-tubes implies a slight difference between the textures of both products resulting in a slightly different mechanical behavior. These tubes have an outer diameter of 12.45 mm and an inner diameter of 11.45 mm. They were formed by a cold pilgering rolling process. They were then subjected to a recrystallisation heat treatment, resulting in a fully recrystallized microstructure with an average grain size of about 5 μm. This cold-working forming process induces an anisotropic crystallographic texture in the polycrystalline alloy that can be seen on pole figures (Fig. 1). The *c*-axis of crystalline structure are mainly orientated around radial direction ("glasses texture") resulting in a mechanical anisotropy of zirconium products. All mechanical tests that have been observed under TEM were performed in the rolling direction (RD). The database is composed with creep tests along the rolling and transverse directions, as well as with biased creep tests that exhibit a very particular behavior. Moreover, relaxation tests along RDs were also included.

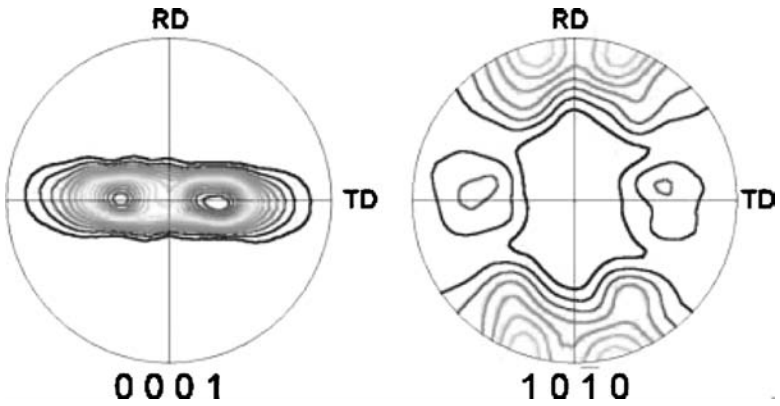


FIG. 1—*{0001} and {10–10} pole figures for a recrystallized zirconium alloy (EBSD analysis).*

For commercial use, the nominal temperature of the cladding tubes is smaller than the transus temperature α/β so that zirconium alloys are used as Zr−α, which is a hexagonal-close-packed (hcp) compound. Combining intrinsic anisotropy of low symmetrical lattice (such as hcp lattice) with the pronounced texture of the alloy leads to an anisotropic mechanical behavior. Anisotropy will be discussed here only for creep tests since relaxation tests were performed only along one RD.

Experimental Devices

Two kinds of tests were performed at 400°C: Creep tests and relaxation tests in order to discuss the different thermal processes, which occur during metal strengthening.

Creep Advanced Testing

Creep advanced testing (CAT) is a display that allows for multiaxial loadings: An axial load up to 5 kN and an internal pressure up to 200 bars 1. The axial and hoop strains are measured by using laser extensometers located in front of the small quartz windows of the radiative furnace, as detailed in Fig. 2. The hoop strains are deduced from the changes of the outer diameter of the tube. The axial deformations can be computed from the measurement of the distance between two strips. The strips are spot-welded on both ends of the gauge, which is 20 mm long. The total length of a sample is 130 mm. The samples are gripped with a combination of stainless steel plugs and a Swagelock® coupling device (see Fig. 3). A Zircaloy-4 core is introduced inside the tube to enhance a homogenous thermal gradient (+/2 K on the gauge). This gradient is regulated by three pairs of lamps, on the upper, lower, or middle zone of the furnace. Each pair of lamps is monitored independently by a temperature regulator and three thermocouples fixed on the upper, lower, or middle zone of the gauge by spot-

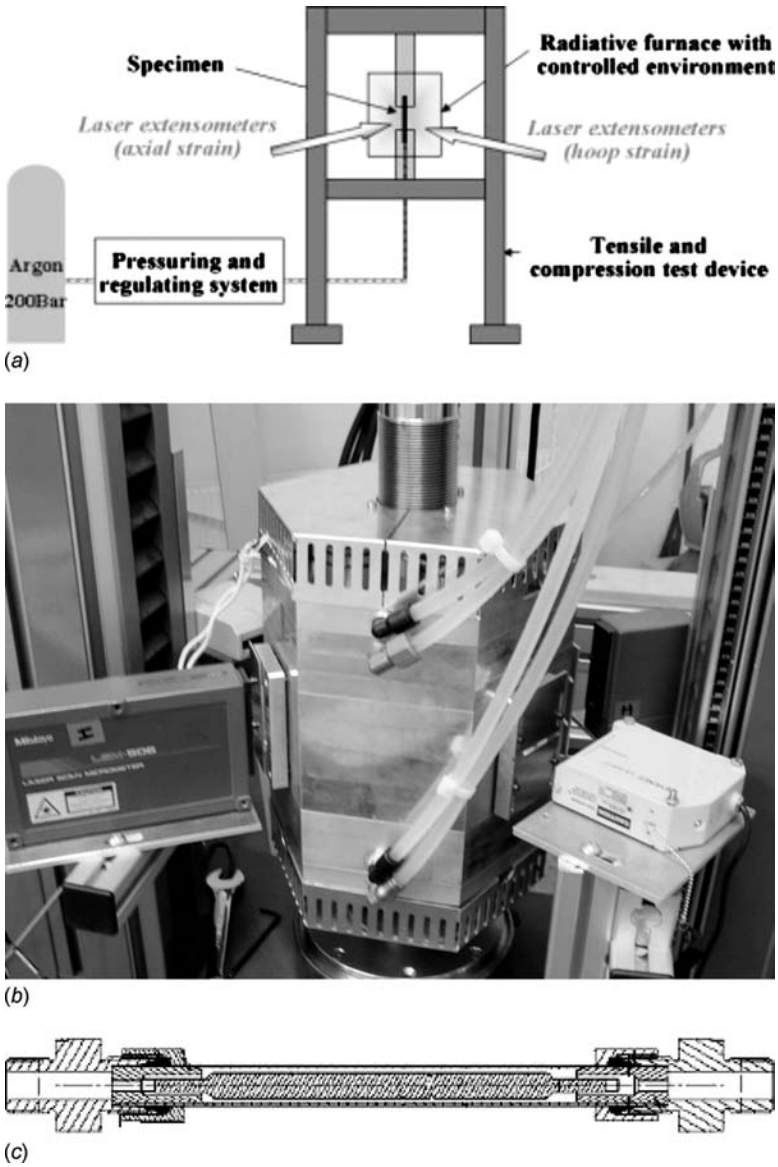


FIG. 2—*CAT: (a) Schema of the display; (b) picture of the laser extensometers and the furnace surrounding a sample gripped to the tensile electromechanical device; and (c) sample and clamping set.*

welding. All the creep tests are carried out by using the experimental procedure described by Grosjean 1,2. Then, the sample is gripped to the tensile electromechanical device, and a preload of 50 N force (i.e., a stress of $\sim$ 3 MPa) is applied along the tensile direction to avoid buckling. It induces an elastic loading of the

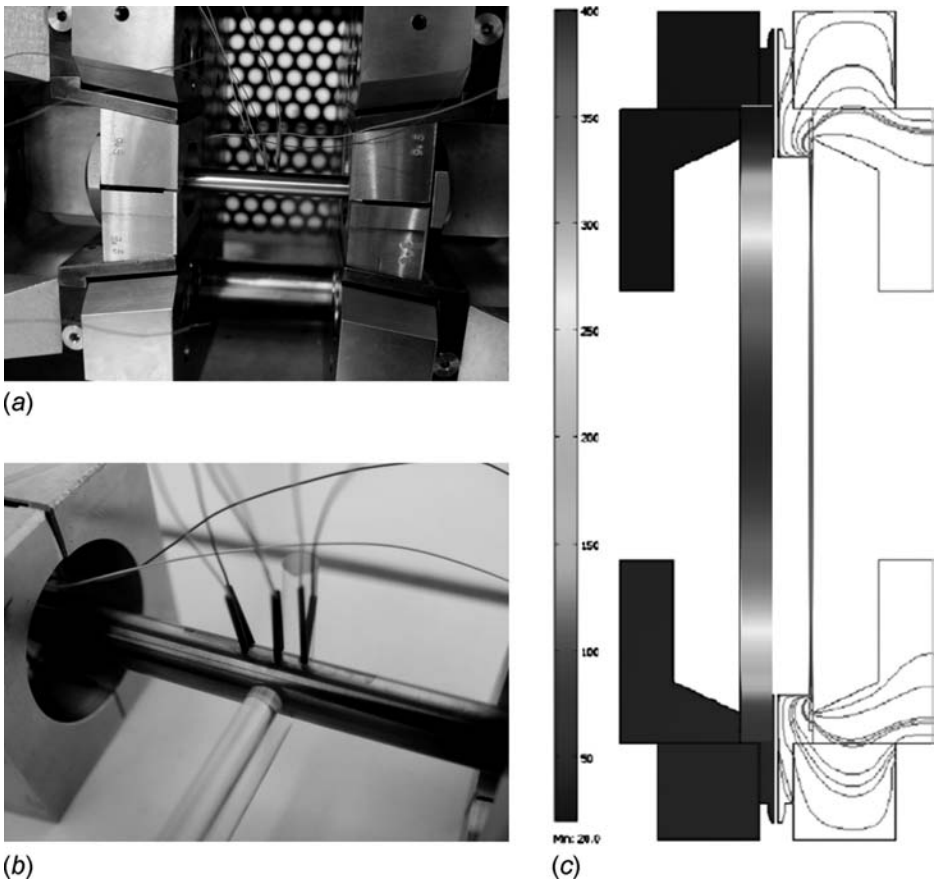


FIG. 3—*(a) Gleeble® system. (b) Hoop extensometer and welded thermocouples. (c) Simulation of thermo electrical coupled problem with COMSOL® (temperature field and heat current line).*

sample. The furnace is then moved around the sample and a heating is imposed from room temperature to 400°C at 50°C · min^{1}. The 50 N force is kept constant until a stable thermal gradient is obtained. The tests are realized under argon or under air if no internal pressure is needed. After a thermal gradient below 0.5 K is reached along the gauge, the mechanical loading is applied. The imposed force, and then the possible internal pressure target are reached at a strain rate of 10^{5} s^{1}, and maintained until a stabilized secondary creep is obtained. The tests are then stopped before reaching the tertiary creep. The thermal loading is decreased down to the room temperature under a controlled force of 50 N (3 MPa). It ensures that TEM post-mortem observations will not be biased by mechanisms due to a resistance to thermal expansion. During the test, the data from the extensometers and the load cell are collected with a frequency of 1 (creep step) or 10 Hz (transient step).

Relaxation Advanced Testing (Gleeble®)

Gleeble® is a thermo-mechanical device that was used to perform relaxation tests. In these tests, only hoop displacements are measured with a mechanical LVDT extensometer which is placed at the center of the sample. The temperature is measured with four thermocouples, three around the central area of the sample to estimate the local temperature gradient and one at the extremity of the sample to evaluate the whole temperature gradient on the sample. Contrary to the creep tests carried out on CAT display, the temperature is not regulated with a radiative furnace, but with an alternative electrical current. Both edges of the sample are cooled down with a water circulation resulting in fixed boundary conditions for temperature fields (room temperature for extremity of tensile heads). Due to Joule's effect, a 40 A electrical current produces a heating of the sample of about 400°C in the central area. The intensity of the electrical current is then regulated all along the test to keep the target temperature on the central thermocouple constant. The sample is heated at 10°C/s and instructions are then maintained for 5 min to homogenize the thermal gradient in the sample. Then, mechanical loading is applied with a 100 kN servo-hydraulic system. During the relaxation test, the axial displacement is imposed and kept constant for 2 min for each relaxation except for the last one which is twice as long. The mechanical tests are achieved under a secondary vacuum to avoid environmental effects.

Transmission Electron Microscopy Method

Thin foils were cut parallel to the free surface. The zones chosen for TEM observations are those where the deformation measurements were made, on the outer surfaces of the two tubes. Thin foils were first mechanically ground to a thickness of 150 μm and were then electrolytically polished with a Struers TenuPol®. Electrolytic polishing was done at a tension of 15 V in a 10 % perchloric acid–20 % 2-butoxyethanol–70 % methanol solution, at a temperature of 30°C. In order to relate the crystallographic orientations to the loading conditions, a notch corresponding to the axial direction of the cladding were placed on each thin foil and orientated parallel to the tilt axis of the sample holder. After all the polishing steps, the zone of the thin foil suitable for TEM observations was calculated to be 90 nm thick. The observations were carried out at a temperature of 20°C on a Jeol 2010 transmission electron microscope, working at 200 kV (tilt of $+/25^{\circ}$). For each sample investigated, 50 grains at least were randomly selected and observed under several diffraction conditions, to enable an accurate identification of their crystallographic orientations. The pole figures obtained for each sample are presented in Fig. 1. For each grain observed, a stereographic projection was built by using the software CaRine® 3.

An image analysis of the TEM pictures was carried out to determine the dislocation densities and the activated slip systems, regarding the stereographic projections of each grain. A slip system is declared to be activated inside a grain when three or more distinct dislocation lines of this system are observed. Therefore, a grain containing less than three dislocation lines for each of its potential slip systems is declared to carry no plastic deformation. A few hydrides were

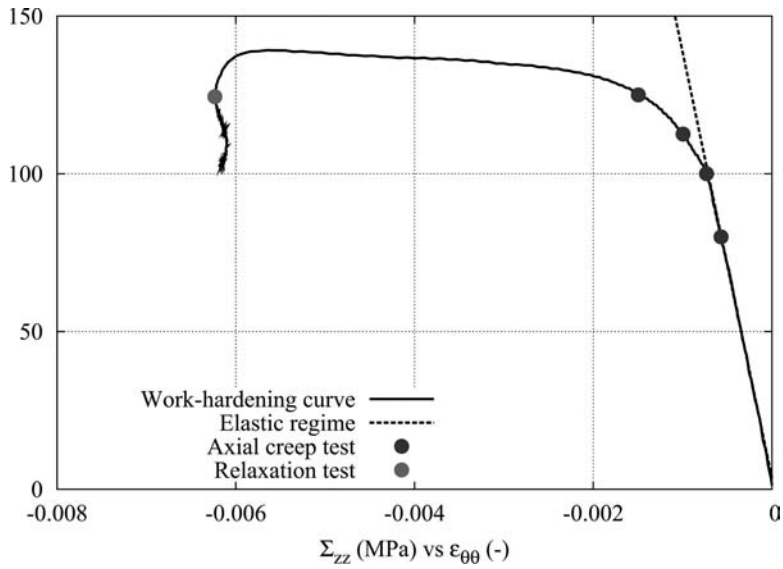


FIG. 4—*Applied stresses at the beginning of the creep tests on a stress-strain curve obtained at* $d\epsilon_{zz}/dt = 10^3\ s^1$ *and 400°C.*

present in grains due to the electrolytic polishing process, but they were easily distinguishable from dislocations and other precipitates.

Experimental Results

Mechanical Data

All the tests were realized at a temperature of 400°C. Figure 4 shows the different stress levels applied for the four axial creep tests on a stress/strain curve. These stresses are related to the mechanical conditions that were applied before the relaxation tests. Thus, we can notice that samples undergo much more plastic deformation before relaxation tests than during creep loadings. Nevertheless, the applied stresses at the end of both kinds of tests are similar. Furthermore, creep tests for specimens 2 and 3 were stopped at a hoop plastic strain level similar to the relaxation strain that was obtained from the relaxation test of specimen 13 (Tables 2 and 3). It enabled *post-mortem* TEM observations of samples. which differ by the strain rate only. TEM observations of a crept specimen were finally chosen to be carried out on specimen 2 as it reached a longer and more stable steady state than specimen 3 (Fig. 5). Moreover, relaxed sample 13 was the most suitable, among the relaxed specimens (Fig. 6), for TEM observations as it underwent only one relaxation.

The creep tests were observed to have steady state strain rates between 4.2×10^9 and $1.2 \times 10^7\ s^1$ (Table 2), with an applied stress varying between 80 and 125 MPa. Besides, relaxation tests (Table 3) exhibit hoop strain below

TABLE 2—*Creep tests results.*

Specimen Number	Duration of Test (h)	Axial Creep Strain (%)	Hoop Creep Strain (%)	Applied Stresses ($\sigma_{\theta\theta}\sigma_{zz}$) (MPa)	Steady State Axial Strain Rate (s^1)	Observed by TEM
1	119	0.23	0.31	0–80	4.2×10^9	No
2	60	0.92	0.54	0–100	2.5×10^8	Yes
3	20	0.64	0.46	0–112.5	4.5×10^8	No
4	27	2.22	1.42	0–125	1.2×10^7	No
5	42	0.45	0.05	100–100	3.9×10^8	No
6	41	1.09	0.06	110–110	4.8×10^8	No
7	62	0.08	0.11	80–0	8.8×10^{10}	No
8	60	0.04	0.24	100–0	1.8×10^9	No
9	40	0.01	0.35	130–0	9.8×10^9	No
10	30	0.18	0.84	150–0	1.5×10^8	No

TABLE 3—*Relaxation test results. For specimens 11 and 12, peak stresses and strain rates are given for the last relaxation.*

Specimen Number	Number of Relaxations	Plastic Hoop Strain (%)	Peak Stress (MPa)	Peak Strain Rate (s^1)	Observed by TEM
11	5	2.17	183	9.2×10^3	No
12	5	2.24	182	5.6×10^3	No
13	1	0.40	138	4.2×10^3	Yes

$9.2 \times 10^3\ s^1$ and higher than $1.0 \times 10^7\ s^1$ because the detection limit of the relaxation testing device did not allow the study of lower strain rates.

Activation Volume Analysis

The mechanical tests can be interpreted in terms of apparent activation volumes. These quantities can be seen as macroscopic signatures of microscopic viscoplastic mechanisms 4,5. A microscopic activation volume corresponding to a particular deformation mechanism is related to the area (multiplied by the Burgers vector to have a volume) swept by a dislocation before the activation of the considered mechanism, i.e., its contribution to grain deformation. For investigated temperature (400°C) and stress ranges ($\Sigma_{zz} < 200$ MPa), viscoplasticity is driven by dislocations glide on slip systems of hcp lattice 4,6. Apparent activation volumes can easily be linked to microscopic activation volumes through the Taylor factor for hcp alloys ($V_{app} = M_T V_\mu$). However, the Taylor factor highly depends on texture and is anisotropic for hcp and textured alloys. Nevertheless, apparent activation volumes which have been measured in our mechanical tests can be related to the main mechanisms of viscoplasticity in Zr alloys, namely the glide of dislocations. As viscous glide of dislocations depends on the depth of Peierls valleys and on short range obstacles, apparent volumes will differ from one mechanism to another and will depend on the chemical composition of the alloy (precipitates, solid solution,…). The apparent activation volume is defined as the macroscopic sensibility of viscoplastic flow to stress. In our particular case, if we consider the cylindrical coordinate system of tubular products, the apparent activation volume can be estimated with the following expressions:

$$V_{app} = k_B T \frac{\partial \ln|\dot{\epsilon}^{vp}_{\theta\theta}|}{\partial \Sigma_{zz}} \text{ or } V_{app} = k_B T \frac{\partial \ln|\dot{\epsilon}^{vp}_{zz}|}{\partial \Sigma_{zz}} \quad (1)$$

where:

Σ_{zz} = axial stress,
$\dot{\epsilon}^{vp}_{\theta\theta}$ = viscoplastic hoop strain rate,
$\dot{\epsilon}^{vp}_{zz}$ = viscoplastic axial strain rate,
T = temperature, and
k_B = Boltzmann′s constant.

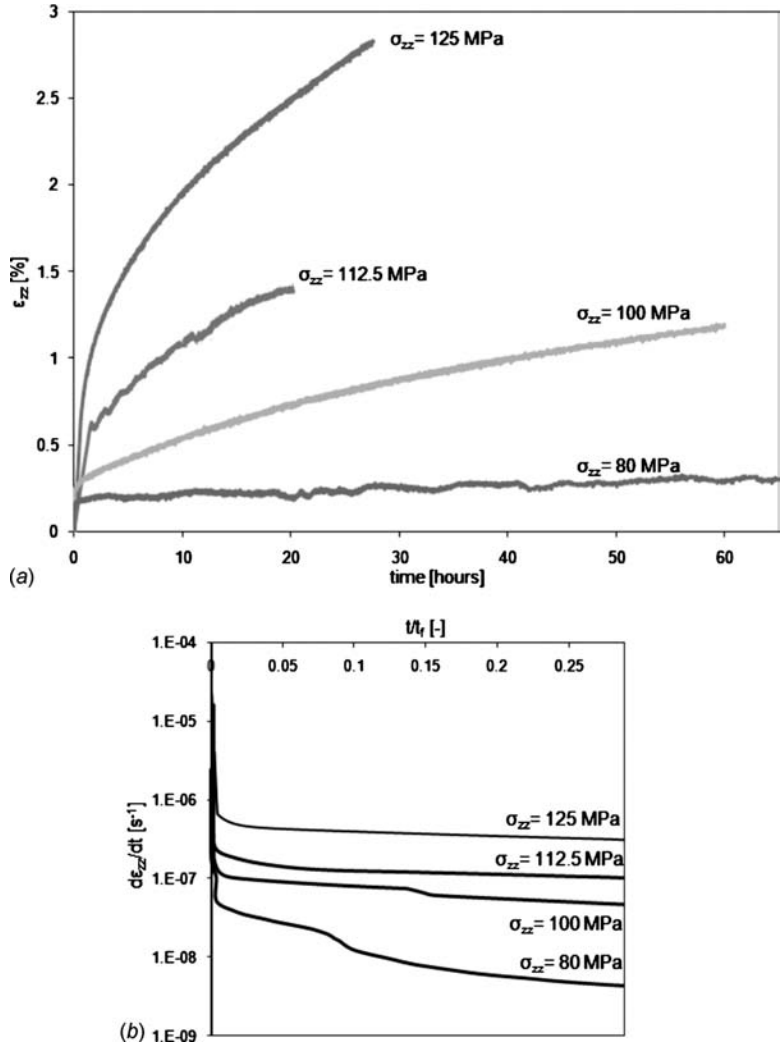


FIG. 5—*(a) Axial strain versus time for four different axial creep tests at 400°C. (b) Axial strain rate versus normalized time, t_f being the test duration.*

For creep tests, only the stationary strain rates have been taken into account to estimate the apparent activation volumes. Finally, the apparent activation volumes are obtained with a linear fit on experimental data (Fig. 7) in the graph $\ln|\dot{\epsilon}^{\mathrm{vp}}_{\theta\theta}|/\Sigma_{zz}$ and $\ln|\dot{\epsilon}^{\mathrm{vp}}_{zz}|/\Sigma_{zz}$. For the relaxation tests, the axial strain rate was estimated by using anisotropy ratio r estimated on stationary creep curves $r = \dot{\epsilon}^{II}_{zz}/\dot{\epsilon}^{II}_{\theta\theta} = 1.8$ 2. It seems that the estimation does not depend on the measured component of strain and we find $V_{\mathrm{app}} = 20b^3$ for the strain rates ($< 10^7\ \mathrm{s}^1$) obtained during the creep tests and $V_{\mathrm{app}} = 75b^3$ for the higher strain rates

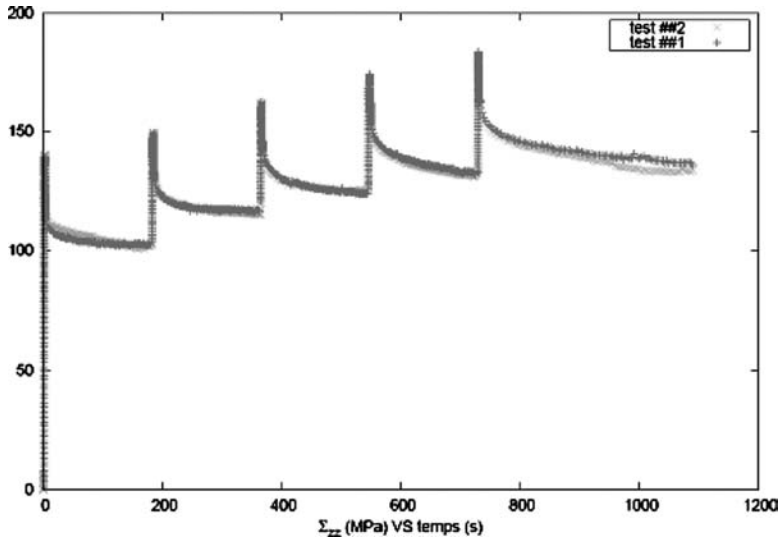


FIG. 6—*Relaxation behavior of Zy4-RX at 400°C.*

($> 10^7\,s^1$) obtained during the stress relaxations. This demonstrates that the thermally activated mechanisms might be significantly different in this range of high strain rates (between 10^5 and $10^6\,s^1$) and the maximum applied stresses ($\sigma_{zz} < 200$ MPa). The TEM analysis presented in the next part focuses on the

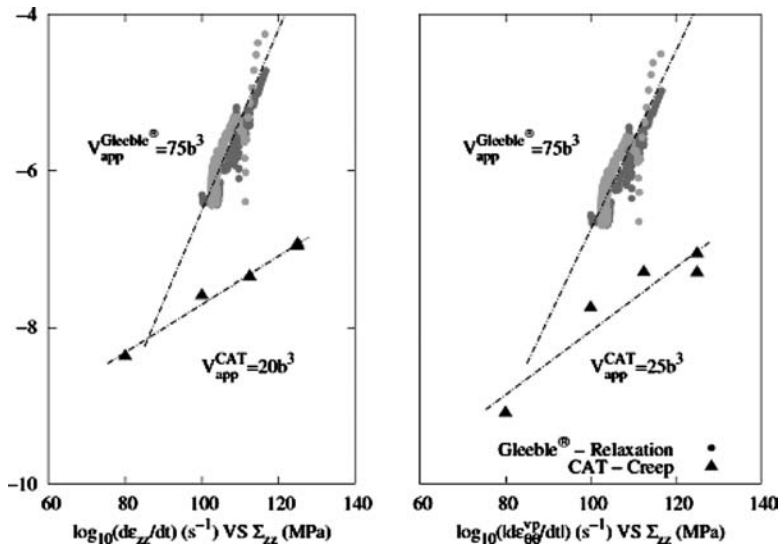


FIG. 7—*Estimations of apparent activation volumes in relaxed and crept samples toward axial (a) and hoop strain rates (b).*

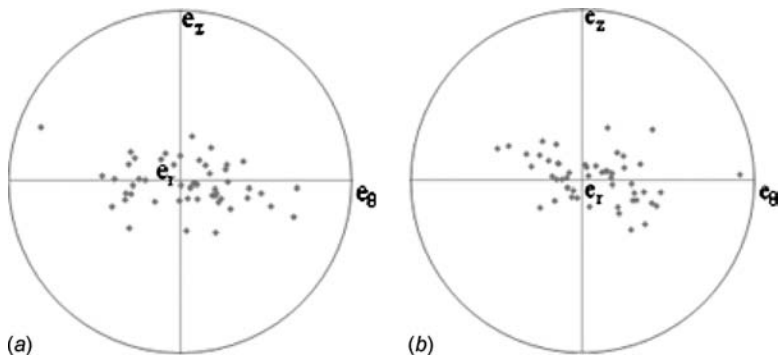


FIG. 8—*{0002} poles figures of observed grains from TEM observations of (a) the relaxed sample and (b) the crept sample.*

variation of thermally activated mechanisms between the two kinds of mechanical loadings.

Transmission Electron Microscopy Analysis

Although the activation volumes are significantly different, the microstructures of the crept and relaxed specimen are, at a first order, quite similar. As low strain levels were applied, we can assume that the specimens underwent no grain disorientations. We can see in Fig. 8 that the crystallographic orientations of the 50 grains selected for both specimens are comparable.

For plastically deformed grains, the dislocations are distributed rather homogeneously. Only the dislocations with $\langle a \rangle$ components have been observed. A predominance of prismatic glide has been noticed in both specimens. Nevertheless, it is important to notice that the number co-existing the prismatic slip systems within a grain vary significantly between both tests (relaxation and creep). Thus, the occurrence of grains containing only one or two active prismatic slip systems (Figs. 9 and 10) is larger for the relaxed sample. Consequently, the simultaneous activation of three prismatic slip systems (Fig. 11) is often observed in the grains of the crept sample. To allow for a better understanding, the dislocation lines presented in Figs. 9–11 have a marked screw character (dislocation segments are approximately parallel to the Burgers vector) because they are relatively straight. But the edge dislocations (dislocation segments orthogonal to the Burgers vector), as well as the curved dislocations, have also been observed, and should not be neglected.

A cross-slip (CS) has been observed for both kinds of mechanical loadings (Fig. 12). Here, the CS consists in the passing of a dislocation line from a prismatic plane to a first order pyramidal plane. From this statement, the dislocation line can move either in an upper prismatic plane ("double CS") or in its original prismatic plane ("simple CS"). In this case, a dislocation loop can expand and be left on the first order pyramidal plane, which can enhance various mechanisms, such as recovery. The CS is distributed homogeneously,

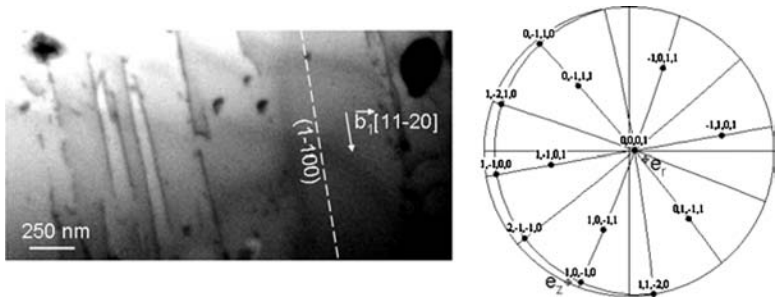


FIG. 9—*Prismatic slip system observed in the relaxed specimen* ($\mathbf{g} = [11–20]$) *and stereographic projection of the grain corresponding to the orientation for the picture.* $\mathbf{b}_1[11–20]$ *is the Burgers vector of the slip system, and the dashed line is the trace of (1–100), the plane of the slip system.*

regardless of the number of activated slip systems within a grain. We can estimate, from the observations, that a prismatic slip system has globally 40 % chances to activate the CS mechanisms (Fig. 14). The CS is enhanced by various factors such as the crystallographic orientation and the proximity of point defects (precipitates, dislocation lines, etc.). For example, in the case of a double CS, as described in Fig. 12, the crossing of the dislocation line from the prismatic plane P to the pyramidal plane π_1 is enhanced by the proximity of a precipitate (intermetallic phase). Its return in the prismatic plane is caused by the interaction with another dislocation line.

Another matter of importance is the ratio of grains without the plastic deformation for each specimen. This ratio is greater for the crept specimen (20 %) than for the relaxed specimen (10 %). It denotes clearly a strain rate effect (higher intergranular incompatibility during creep), as both specimen underwent the same strain level. However, an accurate link between the crystallographic orientations and the absence of plastic deformation would need investigations on a higher number of grains (Fig. 13).

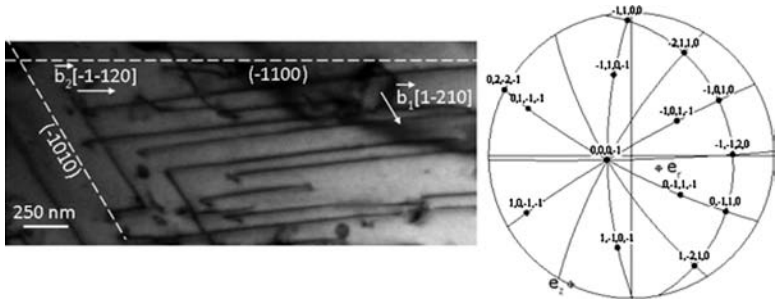


FIG. 10—*Combination of two prismatic slip systems observed in the relaxed specimen* ($\mathbf{g} = [02–21]$) *and stereographic projection of the grain corresponding to the orientation for the picture.*

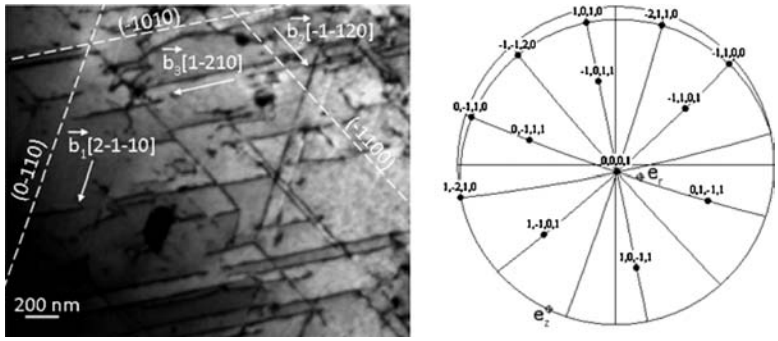


FIG. 11—*Combination of three prismatic slip systems observed in the relaxed specimen* (***g***=[*1–210*]) *and stereographic projection of the grain corresponding to the orientation for the picture.*

The statistical occurrence of slip systems in the two samples observed by TEM is presented in Fig. 14. These results are based on the observation, by conventional electron diffraction and imaging techniques, of 50 grains for each thin foil investigated.

The dislocation densities have also been investigated (Figs. 15 and 16). Even if the 50 grains observed in each sample have comparable average dislocation densities ($\langle\rho\rangle_{\text{relaxation}} = 1.95 \times 10^{14}\,\text{m}^2$; $\langle\rho\rangle_{\text{creep}} = 2.33 \times 10^{14}\,\text{m}^2$), a population of highly deformed grains has been observed in the sample deformed by creep (Fig. 16). This explains the difference between the standard deviations associated to the two distributions $\left(\sigma^2_{\text{relaxation}} = 1.04 \times (10^{14}\,\text{m}^2)^2;\right.$

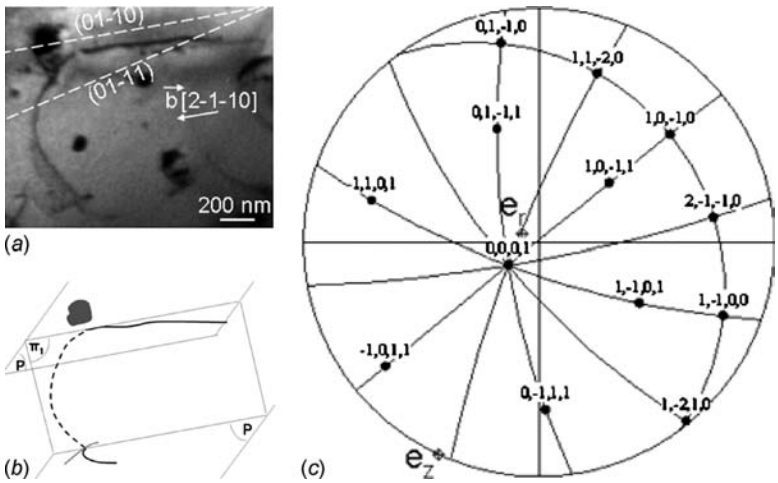


FIG. 12—*(a) Double CS mechanism observed in the relaxed specimen* (***g***=[*1–210*]). *(b) Schematic representation of the mechanism. (c) Stereographic projection of the grain corresponding to the orientation for the picture.*

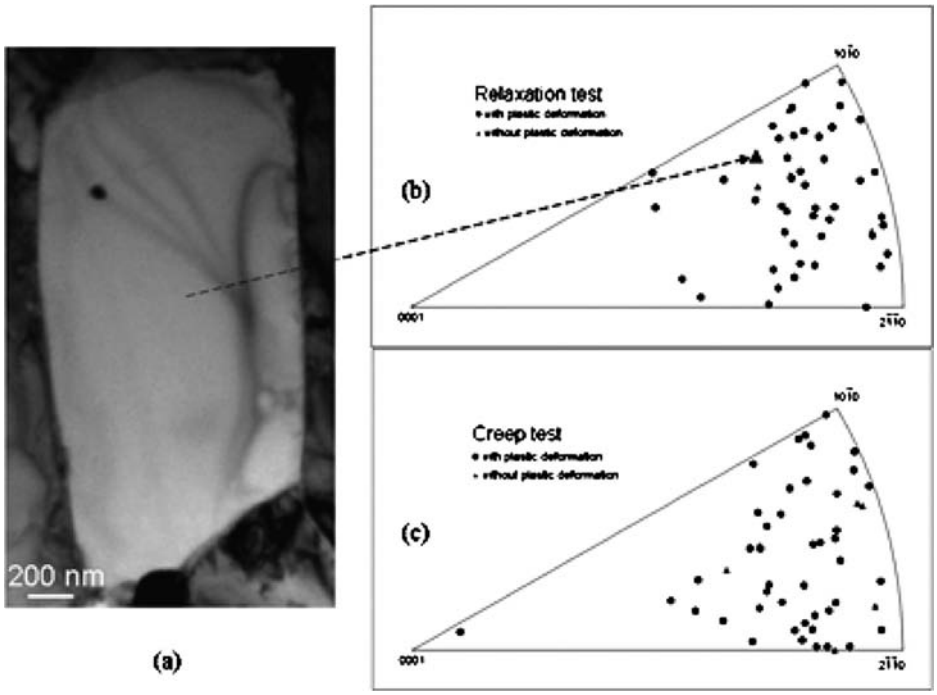


FIG. 13—*(a) Grain without plastic deformation, observed in the relaxed specimen* ($\mathbf{g}$=[*11–20*]). *(b) Inversed pole figure of the axial direction for the sample deformed by relaxation. The grain presented in (a) is marked with a bigger spot. (c) Inversed pole figure of the axial direction for the sample deformed by creep.*

$\sigma^2_{\text{creep}} = 1.81 \times (10^{14}\,\text{m}^2)^2\Big)$. The distributions of dislocation densities and the existence of the two categories of deformation appear in the plotting of the grain fraction f_G versus $\rho/\langle\rho\rangle$ (Fig. 16). For creep condition, the dipoles of screw dislocation are long, linear, numerous, and very narrow ($5\,\text{nm} < L_d < 100\,\text{nm}$). A weaker mobility of the screw dislocation can be associated to this phenomenon for creep.

The crept sample is also singular by its ability to activate substructures (Fig. 17). The interesting aspect of substructure is that the dislocations interact to form a locked configuration. Although the deformation is carried here by the three prismatic slip systems of the grains, several dislocation lines can exhibit $\langle a\rangle$ Burgers vectors lying in the basal plane. In such cases, we can assume that those dislocations result from a junction inside the basal plane of two dislocation lines belonging to two different slip systems. Those basal dislocations have a very low mobility and they consequently induce a global hardening of the considered grain. Their connections with prismatic dislocation can also be seen as strong pinning points. The dislocation substructures—at a more or less advanced step—have been observed in 18 % of plastically deformed grains inside the crept sample (5 % for the relaxed sample). The fact that substructures

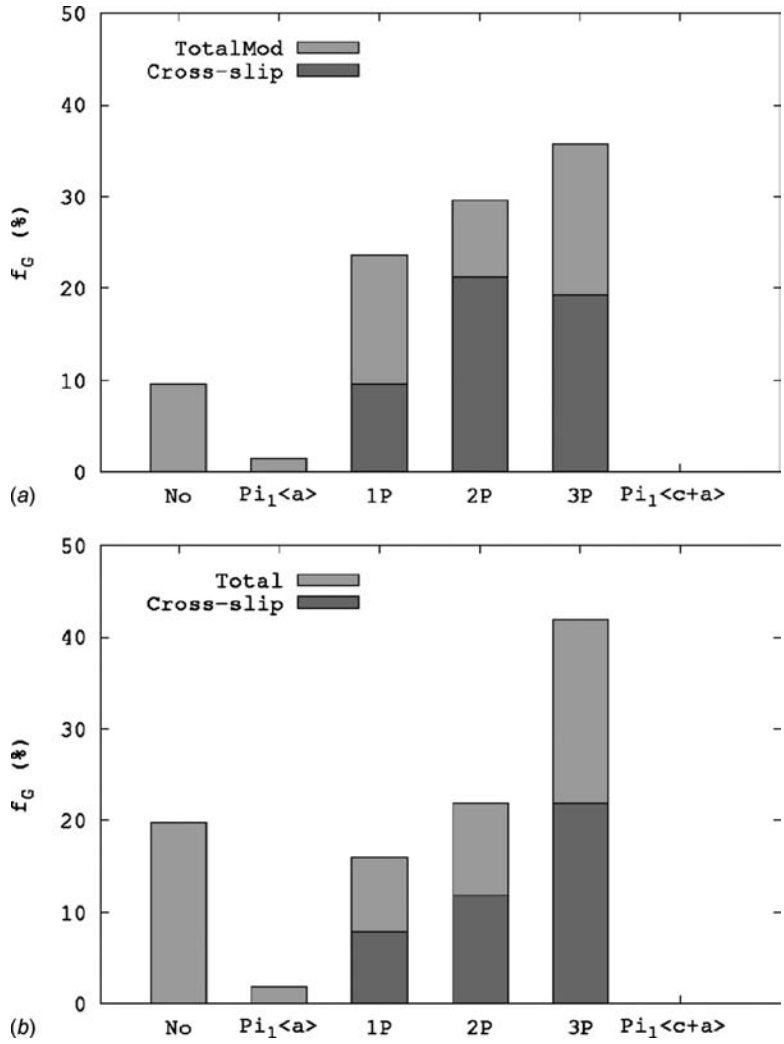


FIG. 14—*Occurrence of the slip system in relaxed sample (a) and crept sample (b).*

were not observed at the same frequency for each specimen shows that two different levels of internal stresses are present. As can be seen in the example given in Fig. 17, the stability of this mechanism implies that the basal plane hosts dislocation lines from one, two, or three primary slip systems. Therefore, substructures have been observed only in grains with sufficiently good crystallographic conditions, i.e., ($\mathbf{e_r}$; $\mathbf{c} > 45°$).

No evidence of dislocation climb has been observed in either specimens, as all the dislocation lines investigated belong to slip planes. Indeed, the dislocation climb can be identified when a dislocation line does not belong to a slip

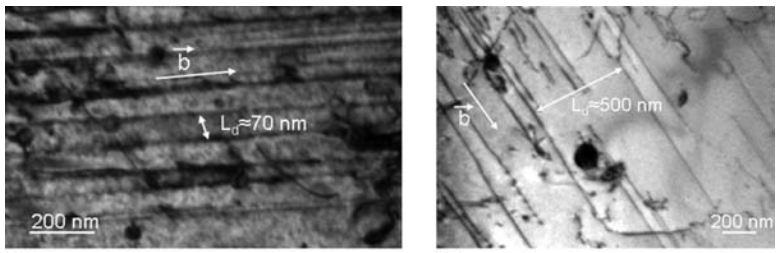


FIG. 15—*Observation of dipoles of screw dislocations: (a) In the crept sample* (**g**=[*01–11*]) *and (b) in relaxed sample* (**g**=[*11–20*]).

plane (i.e., prismatic, basal, or pyramidal plane), which shows that diffusion is occurring instead of glide. From this assessment, it can be supposed that the dislocation exhaustion is enhanced by glide mechanisms only, such as CS or annihilation at the grain boundary.

To synthesize, we can estimate that two main thermally activated processes seem to occur, namely friction stress and CS.

Polycrystalline Approach of Viscoplastic Behavior

The multiscale modelling describes the plastic flow of the polycrystal from the single crystal plasticity mechanism. Unfortunately, the mechanical behavior of the polycrystal cannot be obtained directly from an average of each single

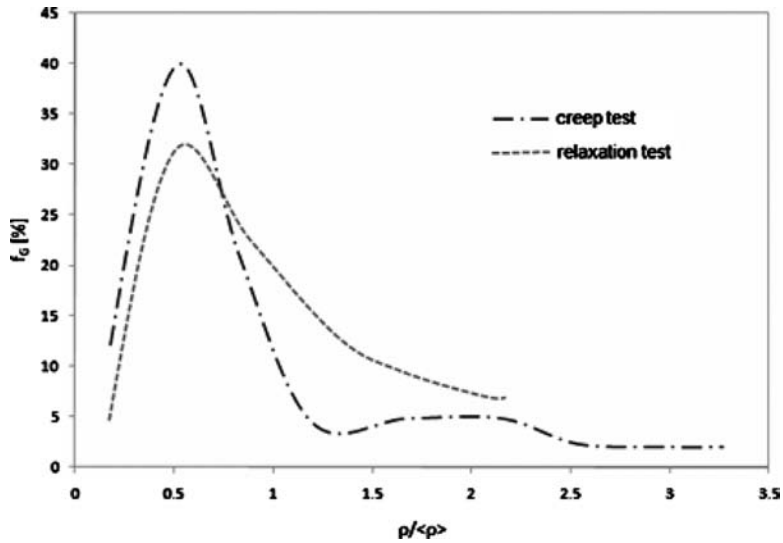


FIG. 16—*Distribution of dislocation densities computed after the TEM observation of 50 grains for the two kinds of mechanical loading.*

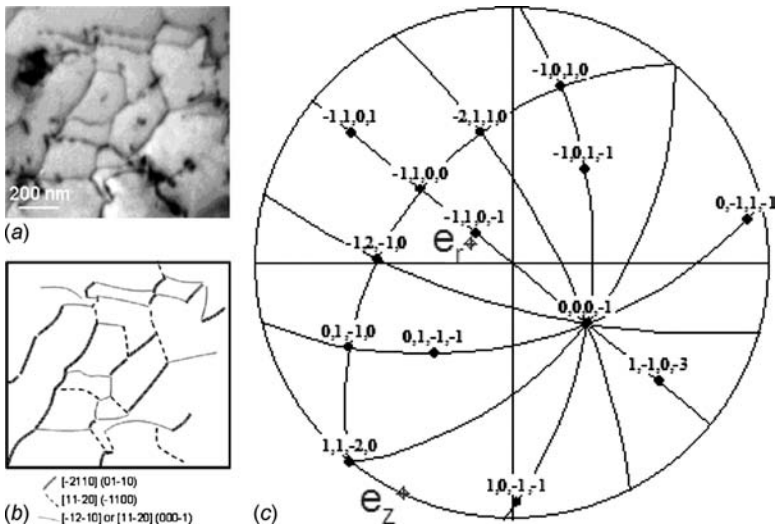


FIG. 17—*(a) Dislocation substructures observed in the specimen deformed by creep (**g**=[11–20]). (b) Schematic representation of the mechanism. (c) Stereographic projection of the grain corresponding to the orientation for the picture.*

crystal behavior because of intercrystalline interactions. The interactions between the crystallites in the polycrystal are taken into account with a self-consistent approach. The literature is well documented on that subject, but the topic is still under debate. To ensure the self-consistency of the heuristic transition scale rule used in the model, the finite element computations have been carried out on polycrystalline aggregates 7 but are not presented in this paper.

Single Crystal Behavior

The resolved shear stress on slip system (s), $\tau_g^{(s)}$, can be evaluated by projecting the stress in phase (g), $\underline{\underline{\sigma}}_g$, on the slip system (s) (n_s, l_s) with the following relations:

$$\tau_g^{(s)} = \underline{\underline{\sigma}}_g : \underline{\underline{\mu}}_g^{(s)} \text{ with } \underline{\underline{\mu}}_g^{(s)} = \frac{1}{2}(l_s \otimes n_s + n_s \otimes l_s) \tag{2}$$

In Eq 2, $\underline{\underline{\mu}}_g^{(s)}$ is the orientation tensor of slip system (s) of phase (g). The plastic hardening that occurs during the deformation is evaluated with an Orowan's law, and the effective stress driving viscoplasticity $\tau_{vp}^{(s)}$ can be written as

$$\tau_{\text{vp}}^{(s)} = |\tau_g^{(s)}|\tau_\mu^{(s)} \text{ with the Orowan's law } \tau_\mu^{(s)} = \tau_0 + \alpha\mu b\sqrt{\sum_{r\in S}\rho_r} \tag{3}$$

In these expressions, $\tau_\mu^{(s)}$ is the athermal stress on the slip system (s), τ_0 is the critical resolved shear stress (CRSS), α is a constant and depends on the

strength of obstacles created during the deformation (strength of junction between dislocations and "forest" dislocations), μ is the elastic shear modulus, b is the norm of the Burgers vector, S, is the set of slip systems and ρ_s is the dislocations density on the slip system (s). Assuming Schmid's law, when $\tau_{vp}^{(s)} > 0$, the slip system (s) flows and the corresponding shear rate $\dot{\gamma}_s$ can be evaluated by using the thermal activated process theory

$$\dot{\gamma}_s = \dot{\gamma}_0(T)\sinh\left(\frac{\max\left(0, \tau_{vp}^{(s)}\right)V_s}{k_B T}\right)\mathrm{sgn}\left(\tau_{vp}^{(s)}\right) \tag{4}$$

In Eq 4, the dot denotes the time derivative of the expression, $\dot{\gamma}_0$ is a constant (which depends on temperature), V_s is the activation volume, and k_B is the Boltzmann constant. The viscoplastic strain rate of phase (g) is finally obtained from a sum of the shear rates over the set of slip systems

$$\underline{\underline{\dot{\epsilon}}}_g^{vp} = \sum_{s\in S} \dot{\gamma}_s \underline{\underline{\mu}}_g^{(s)} \tag{5}$$

Finally, the dislocations density evolution on slip systems (s) is classically given by a balance between the production and dynamic annihilation. As CS seems to be a key mechanism of viscoplasticity of zirconium alloys, it has been taken into account in the model

$$\dot{\rho}_s = \frac{|\dot{\gamma}_s|}{b}\left\{\frac{1}{\lambda} 2 y_s P_{CS} \rho_s\right\} \text{ if } s \in P \tag{6}$$

$$\dot{\rho}_s = \frac{|\dot{\gamma}_s|}{b}\left\{\frac{1}{\lambda} + K_{CS} P_{CS} \rho_P 2 y_s \rho_s\right\} \text{ if } s \in \pi_1\langle a\rangle \tag{7}$$

where:

$$P_{CS} = \beta_o \exp\left(\frac{(\max_{s\in P} |\tau_{\pi_1\langle a\rangle}|\tau^{\mu}_{\pi_1\langle a\rangle})V_{CS}}{k_B T}\right) \tag{8}$$

λ = mean free path of dislocations,

y_s = critical annihilation length between two opposite sign dislocations, and

V_{CS} = activation volume of the CS process.

As the CS mechanism enhances the annihilation of the dislocations, it has been introduced in the annihilation term of Eq 6 through a probability term P_{CS}. The exponential term 8 in Eq 8 is related to the Boltzmann probability of the CS event from $P\langle a\rangle$ plane to $\pi_1\langle a\rangle$ taking into account the viscous component of the stress in $\pi_1\langle a\rangle$ plane. The CS can also contribute to pyramidal hardening and can act as a production term on the pyramidal plane.

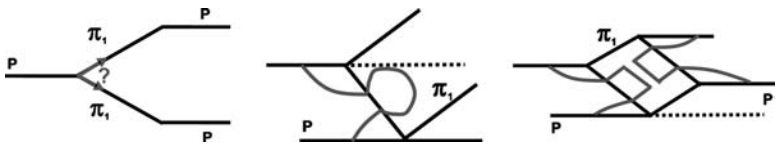


FIG. 18—*Schematic description of CS mechanism: Probability of the event and production and annihilation of dislocations on pyramidal plane.*

Cross-Slip Mechanism

When a dislocation glides on a prismatic plane, if this dislocation meets an obstacle such as a precipitate, for example, instead of going round this obstacle, which is energetically very costly, the dislocation can CS in a pyramidal plan. The effect of CS is mainly a softening effect, as prismatic glide of dislocation is the main deformation mechanism. With this CS mechanism, two opposite sign dislocations can interact with each other resulting in annihilation.

This mechanism depends on temperature (through its activation volume) and geometrical configuration (through the shear stress on the easiest CS plane) so that it will have an effect in viscoplastic anisotropy of Zy-4.

Transition Scale Rule

The polycrystalline behavior is deduced from single crystal behavior, described in the previous section, with a transition scale law. The transition scale scheme is based on the description of a homogeneous equivalent medium (HEM). All the phases *g* are considered to be embedded in an elasto-viscoplastic HEMn, the behavior of which is unknown. The sum of the behaviors of each phase over the set of phase orientation gives us the behavior of the HEM, which has the same properties as the infinite medium. Figure 19 shows a schematic representation of the self-consistent approach.

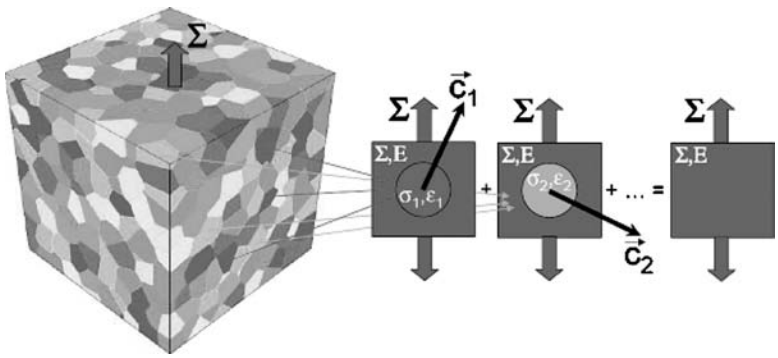


FIG. 19—*Principle of self-consistent scheme used for the multiscale approach.*

Pilvin proposed an heuristic law (beta rule) that is written

$$\underline{\underline{\sigma}}_g = \underline{\underline{\Sigma}} + 2\mu(1\beta_E)(\underline{\underline{B}} - \underline{\underline{\beta}}_g) \text{ with } \underline{\underline{B}} = \sum_{g \in G} f_g \underline{\underline{\beta}}_g \tag{9}$$

This localisation law allows one to compute the average stress in the phase g from the macroscopic stress Σ. The second term of Eq 9 is related to strain incompatibilities between the crystallographic phase g and the HEM. We can notice that the statistical description of the crystallite orientation or the texture (orientation distribution function) is explicitly taken into account into the model through the set G, which is the set of crystalline orientation associated with their volume fraction f_g. The evolution of β_g is then computed from the following relation:

$$\dot{\underline{\underline{\beta}}}_g = \dot{\underline{\underline{\epsilon}}} g^{\text{vp}} D(\underline{\underline{\beta}}_g - \delta \underline{\underline{\epsilon}}_g^{\text{vp}}) \dot{p}_g \text{ with } \dot{p}_g = \sqrt{\frac{2}{3} \dot{\underline{\underline{\epsilon}}}_g^{\text{vp}} : \dot{\underline{\underline{\epsilon}}}_g^{\text{vp}}} \tag{10}$$

where:

D and δ = tuning parameters that can be deduced from finite element computations.

Some authors 9 have also proposed introducing an additional term of viscoplastic accommodation in this transition scale rule to better describe the viscoplastic phenomena, such as the creep or relaxation. This additional term can be related, according to these authors, to a dynamic recovery of intergranular strengthening

$$\underline{\underline{\sigma}}_g = \underline{\underline{\Sigma}} + 2\underline{\mu}(1\underline{\underline{\beta_E}})(\underline{\underline{B}} - \beta_g) R \|\beta_g\|^m \beta_g \tag{11}$$

where:

m = intergranular accommodation exponent,

R = constant related to the intensity of the phenomenon, and

$\| \|$ = isotropic von Mises norm.

Finally, the macroscopic strain and stress tensors can be computed with an average over set G

$$\underline{\underline{E}} = \frac{1}{\Omega} \int_\Omega \epsilon d\Omega \approx \sum_{g \in G} f_g \underline{\underline{\epsilon}}_g \text{ and } \Sigma = \frac{1}{\Omega} \int_\Omega \underline{\underline{\sigma}} d\Omega \approx \sum_{g \in G} f_g \underline{\underline{\sigma}}_g \tag{12}$$

Results

Because of the TEM observations, only the prismatic glide of dislocations has been considered in the polycrystalline approach and the prismatic CRSS has been fitted to 25 MPa. As the CS mechanism seems to be a key mechanism of the viscoplasticity of Zy-4, it has also been taken into account into the model.

The polycrystalline model was identified by using SiDoLo software 10 based on the minimization of a cost function. In the identification process, the weight

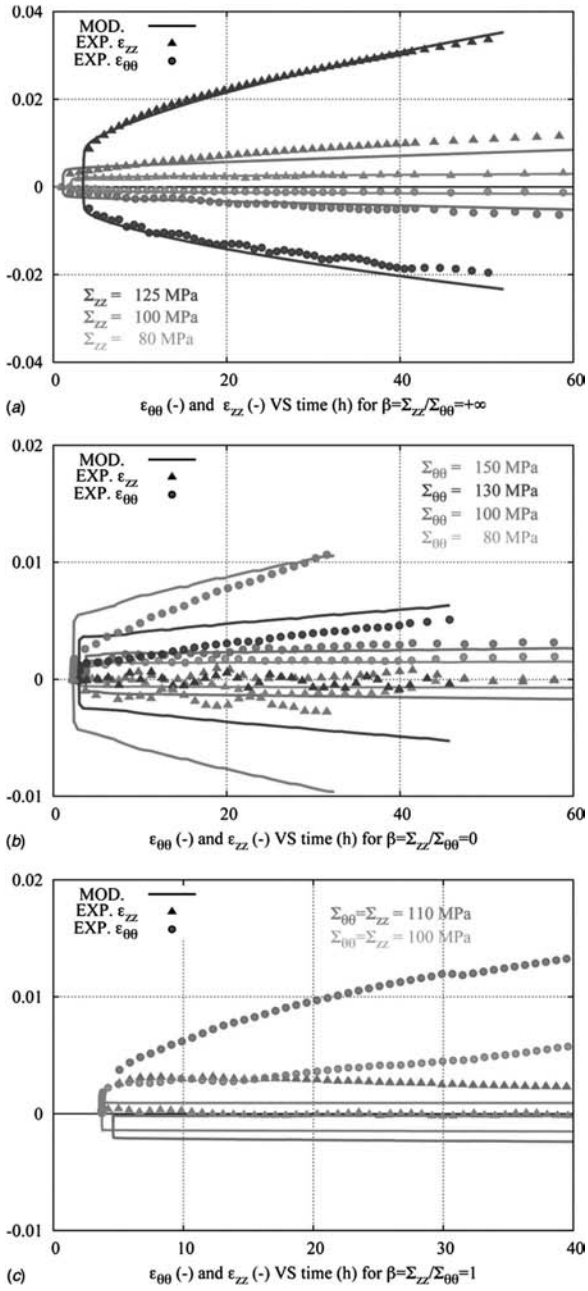


FIG. 20—*Creep behavior of Zy-4 at 400°C for several level of stress and for: (a) β=+∞; (b) β=0; and (c) β=1. Model/experiment comparison.*

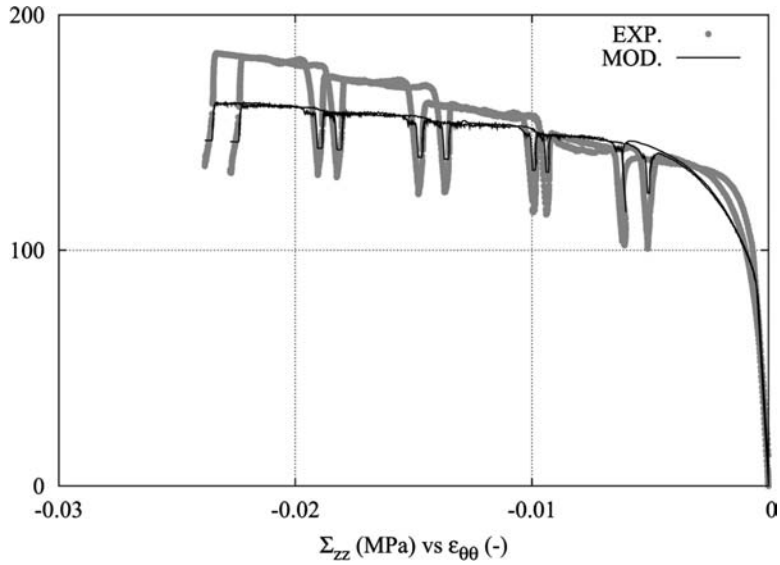


FIG. 21—*Relaxation behavior of Zy-4 at 400°C. Model/experiment comparison.*

of each test is linked to the mechanical response of the material. For the creep tests, the axial and hoop strain are taken into account, whereas for relaxation tests, only the axial stress is used to compute the cost function.

We can now compare the results provided by the polycrystalline approach to the experimental results. For the creep tests, the axial strain and hoop strain are plotted versus time, whereas for the relaxation tests, the axial stress is plotted versus hoop strain. We can notice that for uniaxial creep loadings, the simulation results are in very good agreement with the experimental results and that the plastic flow sensibility to macroscopic stress is well described by the model (see Fig. 20(*a*)). For the uniaxial relaxation tests, the stress level is also well estimated by the modelm (Fig. 21) but for "high" plastic deformation ($\epsilon^p_{\theta\theta} > 1$–$2\,\%$), the rotation of the grains is expected 1 and, therefore, texture evolution should be taken into account to have a better description of the experimental data. For purely hoop creep test ($\beta = \Sigma_{zz}/\Sigma_{\theta\theta} = 0$), the simulated hoop creep rates correspond well with experimental measurements, but not for axial creep stain rates. For that loading path, the axial creep stain rates are overestimated by the model (Fig. 20).

However, for biaxial creep loadings ($\beta = 1$)), the steady state creep rate is largely underestimated by the model (see Fig. 20(*c*)). Experimentally, a significant creep stain rate along the hoop direction is measured, but the model does not reproduce it. During the identification process, it has been pointed out from an heuristic approach that dynamic the recovery of intergranular hardening played an important role on viscoplasticty of Zr alloys. A significant increase of dynamic recovery in the model compared with uniaxial loadings could explain the stationary creep rates along the biaxial path. However, this phenomenon

TABLE 4—*Synthesis of TEM investigations.*

Sample	Grains Without Plastic Deformation (%)	Deformed Grains Activating $3P\langle a\rangle$ (%)	Deformed Grains with Substructure (%)	Size of Dipoles (nm)	Average Dislocation Density (10^{14} m^2)	Standard Deviation of Dislocation Density $\left((10^{+14}\ \mathrm{m}^2)^2\right)$	$P\langle a\rangle$ Activating CS (%)
Relaxed	10	40	5	100–800	1.95	1.03	40
Crept	20	53	16	5–800	2.33	1.81	40

has not been related to a particular mechanism and the implementation of this recovery term in the transition scale rule should be justified by using finite element computations on polycrystalline aggregates 7.

Discussion

Contribution of Experimental Investigations to Multiscale Modelling

Table 4 summarizes the principal results of TEM investigations that might be taken into account. The first remark that can be made considering these results is that, at 400°C, the intergranular compatibility is weaker in creep. Indeed, comparing with the relaxed specimen, the number of grains exhibiting no plastic deformation is higher, while the dislocation densities among plastically deformed grains are globally higher. The observation of the standard deviation of the dislocation densities or the ratio of plastically deformed grains containing three active prismatic slip systems leads to the same conclusion. Nevertheless, the fact that TEM investigations are based on post-mortem observations could lightly influence this data, as minor recovery processes can occur after the mechanical tests during the cooling of the samples. Besides, the absence of significant glide at grain boundaries in the case of the axial creep of Zircaloy-4 at 400°C 11 shows that the intergranular incompatibility can be compensated by the dislocation production. Thus, it could be possible that the production of substructures and narrow dipoles could induce the difference between the two apparent activation volumes that were previously presented. Furthermore, the apparent activation volume for creep $(20b^3)$ is in agreement with apparent activation volumes calculated for the relaxation tests performed at 400°C in the same range of stress and strain rate ($20b^3 < V_{app} < 30b^3$ for $\sigma_{zz} < 130$ MPa and $10^9\,s^1 < d\epsilon_{zz}/dt < 10^7\,s^1$, after Rupa 12).

For the creep tests, the local hardening of isolated grains can be linked to the ability of the dislocations to form substructures or a saturation of the grain with narrow dipoles. The latter phenomenon can be enhanced by the presence of oxygen. Oxygen can limit the motion of screw dislocations 6, i.e., expansion of the dipoles, which remain very narrow. This mechanism is rate sensitive 13,14 and occurs less easily at high strain rates. This can explain why a category of grains containing high dislocation densities and narrow dipoles has not been observed on the relaxed specimen, while it concerns 15 % of the plastically deformed grains of the crept specimen. Concerning dislocation substructures, they could be linked to heterogeneous internal stresses caused by the possible weaker intergranular compatibility within the crept specimen.

Viscoplastic/Plastic Behavior Transition

If the above mechanisms could partly explain the rate sensitivity of the apparent activation volume, they are not the main rate controlling mechanism. Several authors agree to consider that, between 300 and 400°C, the deformation is controlled by the glide of the dislocations 6,15,16. Thus, Moon et al. 16 developed a jogged-screw model applied between 250 and 600°C to β-quenched Zircaloy-4.

This model implies that the dislocation velocity is controlled by the dragging of jogs, or dipoles generated by double CS. The role of CS was also pointed out by Ferrer 15, who observed it at 400°C on crept samples of recrystallized zirconium alloys despites the absence of precipitates. Consequently, the presence of CS was supposed to be due to a change in the dislocation core. Thus, at 400°C, the temperature could easily enable a recombination of the core in the pyramidal plane, under the effects of thermal agitation.

The incoherent transition between the high strain rates activation volume and the low strain rates activation volume may be due to the strain rate dependent thermally activated mechanisms. These mechanisms may brutally vary at a strain rate between 10^6 and $10^7\,s^1$. This is precisely what can occur in the dynamic strain ageing situations. The dislocation mobility is kept low by the presence of oxygen interstitial atoms until the mechanical loading is high enough to allow an escape of dislocation lines, whose mobility increases drastically. A situation of dislocation locking by oxygen can be compared to what has been observed by TEM in several grains of the crept sample (Fig. 15).

However, the analysis based on apparent activation volumes has to be considered with circumspection. The apparent activation volumes that were calculated are only a macroscopic view of the "real" activation volumes. As was seen with TEM investigations, the intergranular incompatibilities were not similar for creep and for relaxation, the possibility to use a viscous Taylor factor should be questioned. Furthermore, the values of the Taylor factor given in several studies vary significantly. This factor can be between 4 14,17 and 2 18. Thus, a study of the sensitivity of the model to the values of the activation volumes could bring interesting results.

Conclusions

Polycrystalline modeling of the viscoplastic behavior of recrystallized zirconium alloys has been fully described in this paper. The development of this model has been largely based on TEM observations. For that reason, only the prismatic glide of dislocations and the CS mechanism from prismatic plane to pyramidal plane have been implemented into the model. Based on these plasticity mechanisms, it seems that the stress sensitivity of the viscoplastic flow is well described by the model for a uniaxial loading path in a large range of strain rates. It enables a modelling of creep behaviors as well as relaxation behaviors. However, for biaxial creep loading, the model does not reproduce stationary creep rate and that could be related to the effect of crystallographic anisotropy on the transition scale rule.

The limit of TEM investigations presented in this study mainly consists in their restriction to axial loadings. We can suppose that the same investigations applied to samples deformed by multiaxial creep loadings would lead to different results of the TEM analysis that could help the model to be more accurate in non-axial directions. Moreover, important observed mechanisms, such as dynamic strain ageing or dislocation substructures, have not been implemented in the model yet. The study of such mechanisms could lead to a better

understanding of internal stress distribution in the polycrystal, which can be an explanation of the mechanical anisotropy of recrystallized Zircaloy-4.

Acknowledgments

The writers would like to acknowledge C. Grosjean and J. Costa for their contribution to the mechanical testing and K. Niang for providing the guide-tubes.

References

[1] Grosjean, C., Poquillon, D., Salabura, J. C., and Cloué, J. M., "Cladding Tube Testing in Creep Conditions Under Multiaxial Loadings: A New Device and Some Experimental Results," *Proceedings of the 19th International Conference on Structural Mechanics in Reactor Technology*, Toronto, 2007, A Gupta, Ed., International Association for Structural Mechanics in Reactor Technology, e.v. (IASMiRT), Berlin, Germany.

[2] Grosjean, C. et al., "Experimental Creep Behavior Determination of Cladding Tube Materials Under Multi-Axial Loadings," *Mater. Sci. Eng., A*, 2009, pp. 332–336.

[3] *CaRine®*, (1989–2005), Boudias, C., Monceau, D., and Divergent, S. A., Compiègne, France.

[4] Caillard, D. and Martin, J. L., *Thermally Activated Mechanisms in Crystal Plasticity*, Pergamon Materials Series, Elsevier, Oxford, 2003, Vol. 8.

[5] François, D., Pineau, A., Zaoui, A., *Comportement Mécanique des Matériaux [Mechanical Behavior of Materials]*, Hermès Editions, Paris, 1995, Vol. 1.

[6] Geyer, P., 1999, "Comportement Élasto-Viscoplastique de Tubes en Zircaloy-4: Approche Expérimentale et Modélisation Micromécanique [Elasto-Viscoplastic Behavior of Zircaloy-4 Tubes: Experimental Approach and Micromechanical Modelling]," Ph.D. thesis, ENSMP, Evry, France, December.

[7] Priser, M., Pilvin, P., Parenteau, T., Cloué, J. M., Poquillon, D., and Feaugas, X. "Micro-Mechanical Approach of Anisotropic Creep Behavior of Zirconium Alloys," *Proc. of Int. Symp. on Plasticity and its Current Applications*, St Kitts and Nevis, 2010, NEAT Press, Maryland.

[8] Groh, S., Marin, E. B., Horstemeyer, M. F., and Zbib, H. M., "Multiscale Modeling of the Plasticity in an Aluminum Single Crystal," *Int. J. Plast.*, Vol. 25(8), 2009, pp. 1456–1473.

[9] Onimus, F. and Béchade, J. L., "A polycrystalline Modeling of the Mechanical Behavior of Neutron Irradiated Zirconium Alloys," *J. Nucl. Mater.*, Vol. 384(2), 2009, pp. 163–174.

[10] Pilvin, P., (2003), *SiDoLo*, SiDoLo Version 2.4495 Notice d'utilisation [User Manual], Laboratoire, Génie Mécanique et Matériaux, Univ. Bretagne-Sud, Lorient, France.

[11] Masson, R., 1998, "Estimations non Linéaires du Comportement Global de Matériaux Hétérogènes en Formulation Affine [Non-Linear Estimations of the Global Behavior of Heterogeneous Materilas in an Affine Formulation]," Ph.D. thesis, Ecole Polytechnique, Palaiseau, France.

[12] Rupa, N., 2000, "Effet de L'hydrogène et des Hydrures sur le Comportement Viscoplastique du Zircaloy-4 Recristallisé [Effect of Hydrogen and Hydrides on the Viscoplastic Behavior of Recrystallized Zircaloy-4]," Ph.D. thesis, UTC, Compiègne, France.

[13] Graff, S., 2006, "Viscoplastic Behavior of Zirconium Alloys in the Temperature Range 20°C–400°C: Characterization and Modelling of Strain Ageing Phenomena," Ph.D. thesis, ENSMP, ENSMP, Evry, France.
[14] Derep, J. L., Ibrahim, S., Rouby, R., and Fantozzi, G., "Deformation Behavior of Zircaloy-4 Between 77 and 900 K," *Acta Metall.*, Vol. 28, 1980, pp. 607–619.
[15] Ferrer, F., 1999, "Etude des Mecanismes de Deformation du Zirconium entre 25°C et 400°C. Influence d'une Faible Teneur en Soufre [Study of the Deformation Mechanisms of Zirconium Between 25°C and 400°C: Effects of a Low Sulfer Content]," Ph.D. thesis, Ecole Polytechnique, Palaiseau, France.
[16] Moon, J. H., Cantonwine, P. E., Anderson, K. R., Karthikeyan, S., and Mills, M. J., "Characterization and Modeling of Creep Mechanisms in Zircaloy-4," *J. Nucl. Mater.*, Vol. 353, 2006, pp. 177–189.
[17] Luton, M. J. and Jonas, J. J., *Proceedings Second International Conference on the Strength of Metals and Alloys*, Asilomar, CA, 1970, American Society for Metals, Cleveland, OH, Vol. 3, p. 1100–5.
[18] Trojanová, Z., Dlouhy, A., and Lukac, P., "Plastic Deformation of Zr–Sn Polycrystals at Intermediate Temperatures," *J. Mater. Sci.*, Vol. 30, No. 11, 1995, p. 2930-5.

DISCUSSION

Question 1, Malcolm Griffiths, AECL, Canada:—What is the empirically fitted stress dependence of the strain rate both experimentally and during modelling? i.e. What would be the dependence assuming a power law application?

Author's Response:—Considering a Norton type power law, it has been shown experimentally that the exponent was a function of the loading direction for multiaxial creep conditions. For recrystallized Zy-4 at 400°C, Norton exponent is evolving between 4 and 8 depending on the biaxiality of the loading and have a mean value of 6.

The stress sensitivity in the polycrystal modeling is more complex because phenomena are described on grain scale. The plastic flow is quantified with a hyperbolic sine law resulting from the thermally activated process theory. As the micro mechanical approach well described the macroscopic behavior in uniaxial loading conditions, the equivalent stress dependence will be the same as experimentally deduced, i.e. about 7.6. However, for other loading directions, the exponent will be different as macroscopic responses differ.

Question 2, Young Suk Kim, KAERI, Korea:—1) TEM observations showed planar type dislocations. Thus based on your results cross-slip should be suppressed rather than activated. Please comment why planar type dislocations were observed in your testing conditions. 2) Under which direction have you applied the uniaxial stress to the specimen where the planar type dislocations were observed under TEM?

Author's Response:—1) Dislocations microstructures, of both crept and relaxed samples, are mainly constituted with very long and narrow dipoles emitted from grain boundaries so that prismatic glide of screw dislocations is the main mechanism of viscoplasticity of Zy-4 at 400°C. The main part of these dislocations are screw dislocations which lie onto prismatic planes. When a dislocation meet an obstacle such as a precipitate or another dislocation for instance, it is energetically easier for the dislocation to change its slip plane rather than going round the obstacle. TEM observations are very local information so that the observation of planar type dislocations is not opposed to a cross slip mechanism. As we can see on Fig12 of the full length paper, cross slip event has been frequently observed in thin foils. We can explain the observation of planar type dislocations because of the high internal friction of HCP compounds (i.e. the depth of Peierls' valley)

2) Uniaxial stresses were applied along z-axis of cladding tubes. TEM observations have been carried out only on that particular loading directions but other previous studies have already shown that the prismatic glide of dislocations remains the driving mechanism of viscoplasticity. Thus, we expect that dislocations microstructures would also be constituted of planar type dislocations even for multiaxial loading directions.

Reprinted from JAI, Vol. 8, No. 2
doi:10.1520/JAI103238
Available online at www.astm.org/JAI

W. Li,[1] *R. A. Holt,*[2] *and S. Tracy*[3]

Polycrystalline Modeling of the Effect of Texture and Dislocation Microstructure on Anisotropic Thermal Creep of Pressurized Zr-2.5Nb Tubes

ABSTRACT: We have investigated the thermal creep of cold-worked Zr-2.5Nb tubes for a range of textures and stress states. The creep tests were performed on internally pressurized thin-wall standard (ratio of axial and transverse stress $R \approx 0.5$) and end-loaded (ratio of axial and transverse stress, $0.25 < R < 0.75$) capsules 10 mm in diameter $\times$ 40 mm long $\times$ 0.5 mm wall-thickness at a stress of 300 MPa at 350C where dislocation creep is the dominant operating mechanism. The tests showed an obvious correlation of anisotropic creep with the texture under different stress states. A self-consistent visco-plastic polycrystalline model based solely upon crystallographic texture showed a poor correlation with experimental results for radial basal textures, similar to that found previously for in-reactor creep. Hence texture alone is not sufficient to accurately predict the creep anisotropy. A modified self-consistent model is introduced to take into account different pre-existing anisotropic dislocation distributions (from cold-work) in different crystal orientations. Much better agreement with the experimental creep anisotropy was found, indicating that individual dislocation distributions in grains with different orientations are important in controlling the creep anisotropy. The predicted effect on creep anisotropy of introducing dislocation structures by a radically different strain path is very large.

KEYWORDS: Zr-2.5Nb, crystallographic texture, creep anisotropy, polycrystalline model

Manuscript received July 14, 2010; accepted for publication December 17, 2010; published online January 2011.

[1] College of the North Atlantic, 105 Main St., Burin Bay Arm, Newfoundland and Labrador, Canada, A0E 1G0.
[2] Queen's Univ. at Kingston, Ontario, Canada, K7L 3N6.
[3] Kinectrics Inc., 800 Kipling Ave., Toronto, Ontario, Canada, M8Z 6C4.

Cite as: Li, W., Holt, R. A. and Tracy, S., "Polycrystalline Modeling of the Effect of Texture and Dislocation Microstructure on Anisotropic Thermal Creep of Pressurized Zr-2.5Nb Tubes," *J. ASTM Intl.*, Vol. 8, No. 2. doi:10.1520/JAI103238.

Copyright © 2011 by ASTM International, 100 Barr Harbor Drive, PO Box C700, West Conshohocken, PA 19428-2959.

Introduction

Pressure tubes in CANDU® (CANada Deuterium Uranium) reactors are currently made from cold-worked Zr-2.5Nb. They are manufactured by hot extrusion followed by cold-drawing and are used in a cold-worked and stress-relieved condition. At the operating temperature (250–310°C), Zr-2.5Nb consists predominantly of hexagonal close packed (hcp) $\alpha-$Zr (containing about 0.6 wt% Nb) with $< 10\,\%$ body center cubic (bcc) $\beta-$Zr (containing about 50 wt% Nb), in which is embedded a small amount of Nb-depleted hcp ω phase [1]. The α-phase has strong crystallographic texture with basal plane (0002) normals concentrated in the transverse direction of the tubes [2].

During service, Zr-2.5Nb pressure tubes are irradiated by fast neutrons ($2–4 \times 10^{17}\,\mathrm{n \cdot m^{-2}\,s^{-1}}$, $E > 1\,\mathrm{MeV}$) [3] and operate under a biaxial stress, with a transverse stress of $\sim 130\,\mathrm{MPa}$ and an axial stress approximately one-half of the transverse stress [4]. The pressure tubes change in shape as a result of operating temperature, stress, and fast neutron irradiation and the deformation is anisotropic because of strong crystallographic texture. These anisotropic dimensional changes occur by three processes: irradiation growth, shape change due to fast neutron irradiation at a constant volume with no external stress, and irradiation and thermal creep, which cause a shape change at a constant volume under an applied stress with and without irradiation [5]. Thermal creep contributes a small proportion ($\sim 10\,\%$) compared with irradiation creep ($\sim 70\,\%$) of the total deformation [6–8], but it may contribute significantly to the anisotropic deformation of pressure tubes, especially at relatively high temperatures or stresses, for example, under accident conditions. It also contributes significantly to the deformation at the outlet end of a fuel channel where fast neutron flux is relatively low, but temperature and bending moment are high [3].

Although thermal creep may relax the stress concentration in the vicinity of a crack tip and mitigate the possibility of failure by the process of delayed hydride cracking [3,9], the anisotropic creep in pressure tubes potentially limits their service life. Increases in diameter result in loss of cooling effectiveness, and may require de-rating of the reactor, increases in length may exceed the allowances in the end hardware, and sag may result in contact of the hot pressure tube and cold calandria tube leading to the possibility of failure [10]. The anisotropic dimensional changes (i.e., elongation in the axial direction, diametral expansion, and wall-thickness reduction) also increase in the transverse stress which accelerates the deformation of pressure tubes. Therefore, there is a strong incentive to understand anisotropic creep and its relationship to crystallographic texture.

In previous attempts to model in-reactor deformation, Zr-2.5Nb tubes were only available with a few different crystallographic textures in which basal plane normals are concentrated in the transverse or radial direction [11]. This significantly restricts the understanding of the relationship between crystallographic texture and anisotropic creep. Holt et al. [3,5,12] considered dislocation glide as the strain-producing mechanism of irradiation creep of Zr alloy although there is no consensus regarding the mechanisms of irradiation creep [3,5,12,13]. The polycrystalline models that predict the effect of texture on the

anisotropy have been unable to rationalize the extreme behaviors of predominantly radial and predominantly transverse textures with realistic assumptions about the contributions of the different slip systems to the anisotropy of creep [14]. Moreover, crystallographic texture and stress state have not been investigated simultaneously under creep conditions for this alloy, i.e., biaxial creep tests carried out with different ratios of axial to transverse stresses on tubes with different textures. Such experiments can provide a valuable source of data with which to develop and modify models for creep anisotropy, and to optimize the crystallographic texture of Zr-2.5Nb tubes for creep resistance. In this paper, thermal creep of pressurized Zr-2.5Nb tubes with various textures at different ratios of axial: transverse stress (σ_A/σ_T) are reported in a stress and temperature regime (300 MPa transverse, 350°C) where dislocation creep is thought to be dominant and glide is thought to be the strain-producing mechanism [15]. The observed creep anisotropy as represented by the ratio of steady-state creep rate in the axial direction to that in the transverse direction is used to assess an existing self-consistent model SELFPOLY7 and a modified version SELFPOLY7-Q developed to improve the understanding of the factors affecting creep anisotropy.

Materials

Zr-2.5Nb micro pressure tubes (MPTs) and fuel sheathing (FS) tubes were used as experimental materials. The MPTs were manufactured by a process developed at Nu-Tech Precision Metal Inc. to provide a similar microstructure and texture to standard CANDU pressure tubes [14]. However, in order to obtain a range of different textures, the MPTs were extruded by varied combinations of temperatures and extrusion ratio (Table 1). The FS tubes used in the current project were manufactured for experimental fuel in the Atomic Energy of Canada Limited's WR1 reactor. The MPTs have textures varying between predominantly transverse and equally distributed in the radial-transverse plane, while the FS tubes provide a predominantly radial texture [14]. Two of the MPTs, 81F and 82F, have a strong axial texture component (F indicates that the tube specimens were made from the front-end of the tube—the end that emerged first from the extrusion press, and B indicates that the specimen was made from the

TABLE 1—*MPTs extrusion temperatures and ratios.*

	Extrusion		
Tubes Number	Temperature (°C)	Ratio	Billet Preparation
MPT63	815	10:1	β-quenched
MPT66	815	10:1	Slow-cooled
MPT72,73,74	650	10:1	Slow-cooled
MPT62	650	4:1	β-quenched
MPT65,76,77,79	650	4:1	Slow-cooled
MPT81,82	975	10:1	Slow-cooled

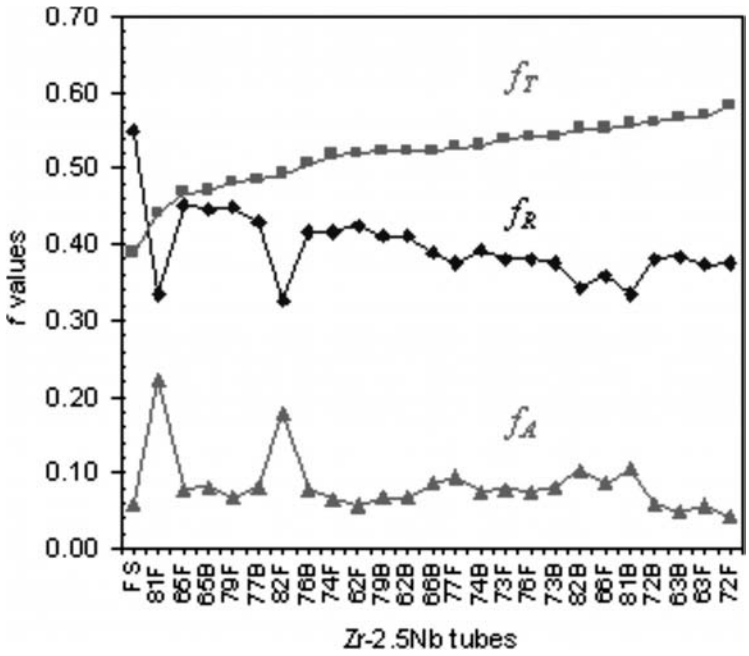


FIG. 1—*Variation of resolved factors of basal plane normals (Kearn's factors), f, in three directions (subscripts A=axial, T=transverse, and R=radial) for Zr-2.5Nb tubes [Figure was published in Ref [15]].*

back end). The resolved fractions of basal plane normals (or Kearn's factors) [16] in the three principal directions of each tube are shown in Fig. 1.

Tubes MPT63F, 65F, 66F, 72F, 73F, 74F, 76F, 77F, and 79F have highly elongated α-grains and thin film of β-phase at the boundaries as is the case of CANDU pressure tubes. However, billet preparation and extrusion conditions affect grain size of the tubes. For example, tube MPT63F (extruded after a β-quenched billet) has a finer grain size with a thickness of $\sim 0.2\,\mu$m in the α phase; while the tubes extruded after a slow-cooled billet have a larger grain thickness, e.g., tubes MPT66F, 72F, 73F, and 74F (extrusion ratio = 10 : 1) have a grain thickness in the α phase varying from 0.4–0.8 μm, and tubes MPT65F, 76F, 77F, and 79F (extrusion ratio = 4 : 1) have a thickness varying from 0.7–1.5 μm. The second type of α-grain structure (tubes MPT62F, 81B, and 82B) is equiaxed in radial-transverse section with the β-phase distributed at grain boundaries and corners with a grain diameter of 0.2–0.5 μm. The third type of microstructure, tubes MPT81F and 82F, comprises Widmanstätten α-plate with continuous $\beta-$Zr surrounding the plates, and a thickness of less than 0.5 μm. These microstructures are consistent with previous studies of the development of microstructure during extrusion of Zr-2.5Nb [17–20]. The FS microstructures consist of flattened α-phase with discontinuously distributed β-phase. Complete details of manufacture, texture and microstructure of the tubes are given in Refs [15 and 21].

Procedures

Tubes with a wall-thickness of ~ 0.46 mm and an outer diameter of ~ 10 mm (similar to the dimensions of FS tubes) were machined from the MPTs. Standard and end-loaded creep capsules (Fig. 2) were manufactured by cutting a 40 mm length from machined tubes, electron beam welding an end cap at each end and stress relieving for 24 h at 400°C. The standard capsule (Fig. 2(*a*)) was used to represent the stress state of a standard pressure tube in CANDU reactors, i.e., a constant stress ratio (~ 0.5) of the axial to transverse stresses. The end-loaded capsule (Fig. 2(*b*)) has two circumferential grooves at each end, which allow a sample holder to clamp over the ends and apply either a tensile or compressive load. The two smaller circumferential grooves in the end-loaded capsule give exact edges for precise measurements of the length (Fig. 2(*b*)). The creep capsules were internally pressurized with helium at room temperature and sealed by laser welding through a quartz window. The pressure at room

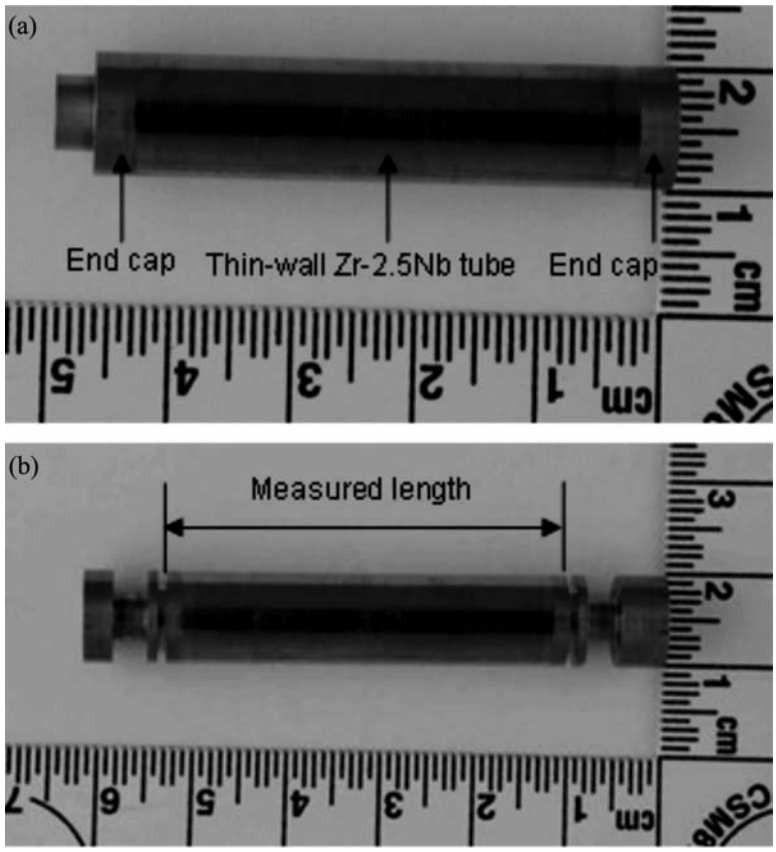


FIG. 2—*(a) Standard; (b) end-loaded creep capsules. The initial gauge length is 40 mm, the outer diameter is 10 mm, and the wall-thickness is 0.46 mm.*

temperature are calculated according to the ideal gas law, i.e., $P_1/T_1 = P/T$, where P_1 is the pressure at room temperature T_1, and P is the pressure at test temperature T. Average through-wall transverse and axial stresses at test temperature were calculated according to $\sigma_T = Pd/2t$ and $\sigma_A = 4L_A/(D^2 - d^2)\pi + Pd^2/(D^2 - d^2)$, where P is the internal pressure at test temperature, D and d are the outside and inside diameters, t is the wall-thickness, L_A is the external load in the axial direction, and T and A designate transverse and axial directions, respectively. When external axial stress L_A is zero, the stress ratio is 0.48. When an external axial compressive or tensile load L_A is added, a range of stress ratios is obtained. The specimen dimensions at room temperature (22°C) are used to calculate the stresses because the effect of thermal expansion at testing temperature (300–400°C) on dimension changes is negligible ($\sim 0.2\,\%$) and has little effect on the calculated stress.

The creep tests were carried out in Lindberg tube furnaces. The standard creep capsules were placed in a stainless steel holder with argon to flow to reduce oxidation. For end-loaded creep capsules, an end-loading creep rig was used to add an external load in the axial direction, which transferred a compressive force into either a compressive or tensile load on the specimen via two different sample holder designs. The creep rig set-up details are illustrated in Ref [21].

After each heating period, the capsules were cooled in the furnace for the first 30 min and then cooled in air to room temperature. Diameter and length were measured at room temperature by a laser dimensioning system [15,21]. The creep strains reported are relative to the dimensions of the pressurized capsule, prior to the first heating cycle. Length measurements were made every 5° and averaged. The diameter was measured every 5° at five axial locations and averaged. To assure an accurate measurement, a reference capsule was measured before and after each experimental specimen measurement. The accuracy of creep strains in both directions for an experimental capsule is approximately ± 0.02 %. In most cases the creep tests were terminated at about 1 % creep strain in the transverse direction to avoid the possibility of the specimens rupturing during handling. Steady-state was assumed to be reached when the curves of transverse creep strain versus time became approximately linear after a sharp decrease of strain rate during the primary creep stage. Steady-state creep rate was taken as the value of the slope by plotting a linear trend line from the last four data points in a given creep curve (usually about 0.5 % strain).

Results and Analysis

Standard Creep Tests

Figures 3 and 4 show creep strains versus time in the transverse and axial directions for all the tubes under a nominal transverse stress of 300 MPa at 350°C, respectively. For the denomination of the creep capsules, "F" indicates that the capsules were made from the front-end of the tube and "B" indicates that the specimen was made from the back end. The billet preparation is denoted as "S" or "Q" indicating that the billet of the tube was prepared by slow cooling or β-quenching. In the transverse direction, Fig. 3, capsule FS23 crept fastest and

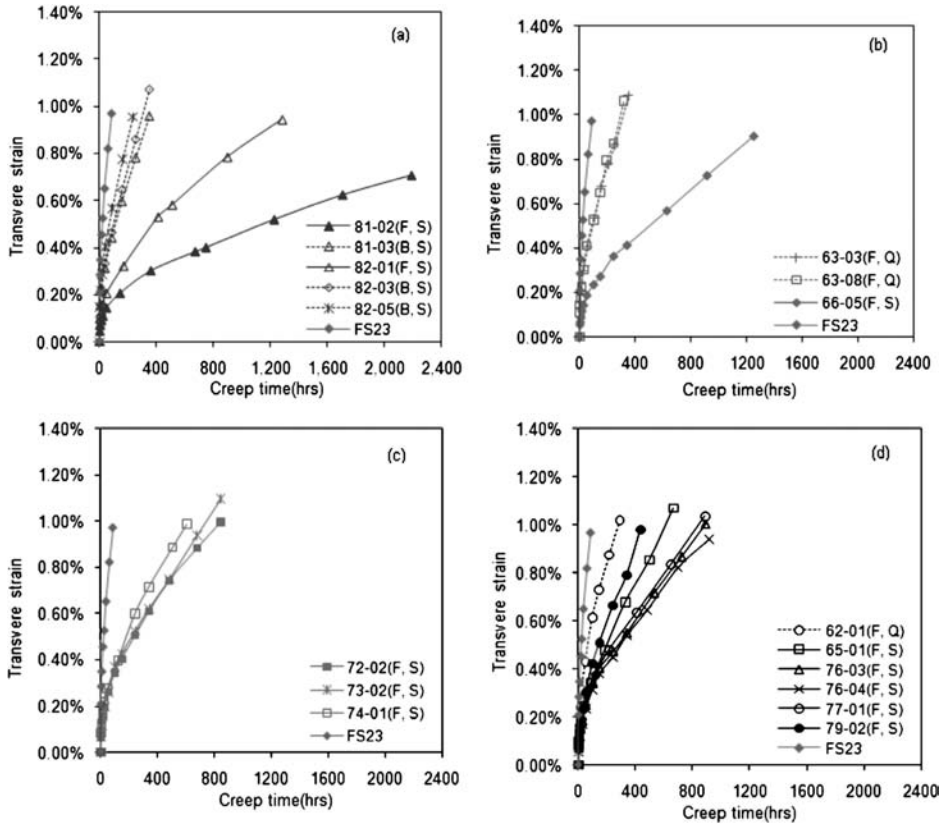


FIG. 3—*Creep strains versus creep time for internally pressurized FS and MPT capsules with different textures under a nominal transverse stress of 300 MPa at 350°C in the transverse direction. (a) Capsule FS23 and the MPT capsules made from tubes extruded with a ratio of 10:1 at the extrusion temperature of 975°C; (b) capsule FS23 and the MPT capsules made from tubes extruded with a ratio of 10:1 at the extrusion temperature of 815°C; (c) capsule FS23 and the MPT capsules made from tubes with the extrusion ratio of 10:1 at 650°C; (d) capsule FS23 and the MPT capsules made from tubes with the extrusion ratio of 4:1 at 650°C. Note that F or B, and S or Q denotes that the capsule was made from the front or back end, and the billet of the tube was prepared by slow cooling or β-quenching, respectively [Data in Figs. 3 and 4 were published in Ref [15]].*

took less than 100 h to reach 1 % transverse strain. At the other extreme, capsules MPT82-01(F,S) and 66-05(F,S) took more than 1200 h to reach ~ 1 % transverse strain and capsule MPT81-02(F, S) took over 2200 h to reach ~ 0.7 % (Fig. 3(*a*), 3(*b*)). Of the tubes made with an extrusion ratio of 10:1 at 650°C in Fig. 3(*c*), capsules MPT72-02(F,S) and 73-02(F,S) had a similar creep behavior, reaching 1 % transverse strain after ~ 800 h; capsule MPT74-01(F,S) showed a faster creep behavior in the transverse direction which may correspond to the smaller f_T (0.518) value compared with those of capsules MPT72F ($f_T = 0.582$)

and MPT73F ($f_T = 0.538$) in Fig. 1. Of the tubes made with an extrusion ratio of 4:1 at 650°C in Fig. 3(*d*), capsules MPT76-03(F,S), 76-04(F,S), and 77-01(F,S) exhibited a similar creep behavior; capsules MPT79-02(F,S) and 65-01(F,S) crept faster possibly because they have a smaller component of basal plane normals in the transverse direction (f_T) (Fig. 1). Specimens from tubes extruded from β-quenched billets, e.g., capsules MPT63-03(F,Q), 63-08(F,Q), and 62-01(F,Q), exhibited faster creep behaviours. Moreover, the specimens from the back ends, capsules MPT81-03(B,S), MPT82-03(B,S), and MPT82-05(B,S) crept much faster than the front-end specimens (Fig. 3(*a*)). These different creep behaviors between the front and back end capsules in tubes MPT81 and 82 may be related to the texture and microstructure variations along the axial direction of the tubes (Fig. 1).

In the axial direction (Fig. 4) specimen FS23 exhibited negative axial strains and a negative steady-state creep rate, which correlated with its fast creep behavior in the transverse direction. Capsule MPT81-02(F,S) (Fig. 4(*a*)) showed the slowest creep behavior in the axial direction, possibly because of a relatively strong axial component of basal plane normals in the front-end of the tube (Fig. 1). Capsules MPT65-01(F,S), 76-03(F,S), 76-04(F,S), 77-01(F,S), 79-02(F,S), and 82-01(F,S) also exhibited relatively low axial creep rates (Fig. 4(*a*), 4(*d*)). Capsule MPT66-05(F,S) exhibited near average behavior (Fig. 4(*b*)). In Fig. 4(*c*), capsules MPT72-02(F,S), 73-02(F,S), and 74-01(F,S) had the similar axial creep behavior. As with the transverse creep behavior, capsules MPT81-03(B,S), 82-03(B,S), 82-05(B,S), 62-01(F,Q), 63-03(F,Q), and 63-08(F,Q) all showed the fastest creep in the axial direction.

It can be seen that the capsules from the tubes extruded in the same nominal conditions exhibited slightly different creep behaviors. This variation may be attributed to the texture variation of the tubes in the same group; see the discrepancies in the values of the resolved fractions of basal plane normals in Fig. 1. The discrepancies in creep behavior may also be due to the texture gradient through the wall and along the axial direction of the tubes. Because the creep capsules were manufactured from a reduced section, the measured texture, representing a through-wall average, may not exactly represent the texture of the tested capsules. Li et al. [18] observed through-wall variations in MPTs after extrusion, although these were not statistically significant, except at the front-end of those extruded after preheating in the β-phase.

Capsule MPT66-05(F,S) (same extrusion condition as the pressure tubes in CANDU reactors) exhibited a good transverse creep resistance, but it showed relatively fast creep behaviour in the axial direction. Capsule MPT81-02(F,S) exhibited the slowest creep behavior in both the axial and transverse directions among all the tested capsules, indicating the best creep resistance in the tested tubes.

Creep Tests Under Different Stress States

End-loading tests were performed under a nominal transverse stress of 300 MPa at 350°C, and the axial stresses were varied by applying an external compressive or tensile load in the axial direction. A group of end-loaded FS capsules

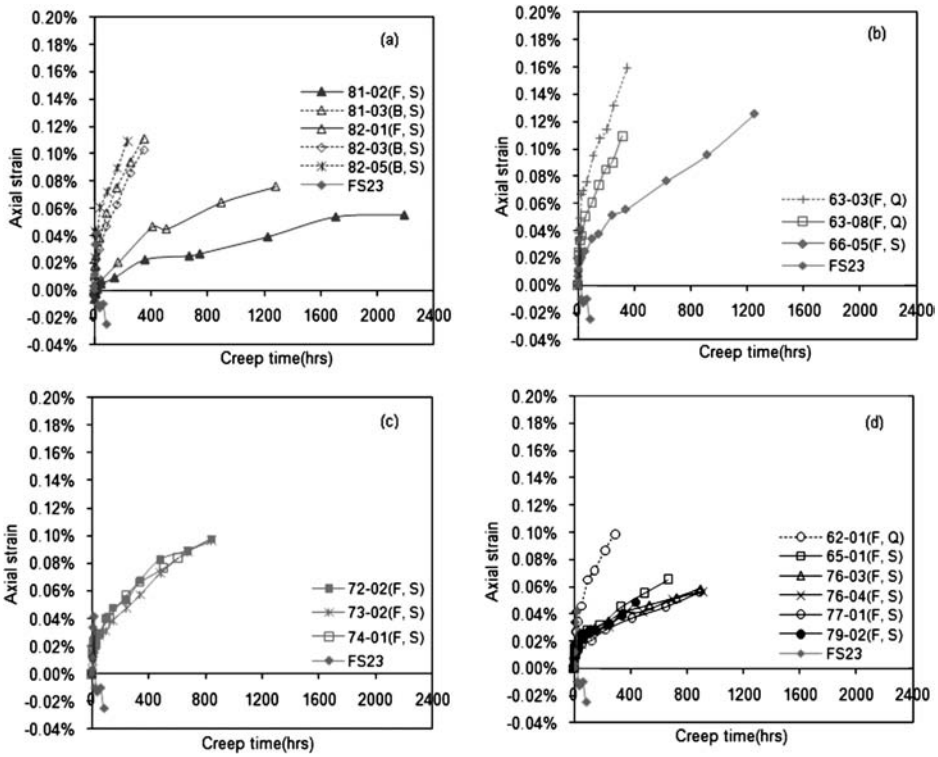


FIG. 4—*Creep strains versus creep time for internally pressurized FS and MPT capsules with different textures under a nominal transverse stress of 300 MPa at 350°C in the axial direction. (a) Capsule FS23 and the MPT capsules made from tubes extruded with a ratio of 10:1 at the extrusion temperature of 975°C; (b) capsule FS23 and the MPT capsules made from tubes extruded with a ratio of 10:1 at the extrusion temperature of 815°C; (c) capsule FS23 and the MPT capsules made from tubes with the extrusion ratio of 10:1 at 650°C; (d) capsule FS23 and the MPT capsules made from tubes with the extrusion ratio of 4:1 at 650°C. Note that F or B, and S or Q denotes that the capsule was made from the front or back end, and the billet of the tube was prepared by slow cooling or β-quenching, respectively [Data in Figs. 3 and 4 were published in Ref [15]].*

were tested at a stress ratios (σ_A/σ_T) ranging 0.26–0.70. Figure 5 shows the curves of creep strain versus time in both the transverse and axial directions. The transverse strains showed an increasing trend with decreasing stress ratio (Fig. 5(*a*)). An obvious dependence of creep strains on stress ratios appeared in the axial direction (Fig. 5(*b*)). The axial strains increased with an increasing external tensile stress in capsules FS18 ($\sigma_A/\sigma_T = 0.594$) and FS19 ($\sigma_A/\sigma_T = 0.690$) while the axial strains of FS20 ($\sigma_A/\sigma_T = 0.356$) and F17 ($\sigma_A/\sigma_T = 0.261$) are negative from the start and decrease with decreasing stress ratio. The transverse steady-state creep rate decreased with increasing stress ratio; the axial creep rate increased from negative (compressive and zero external

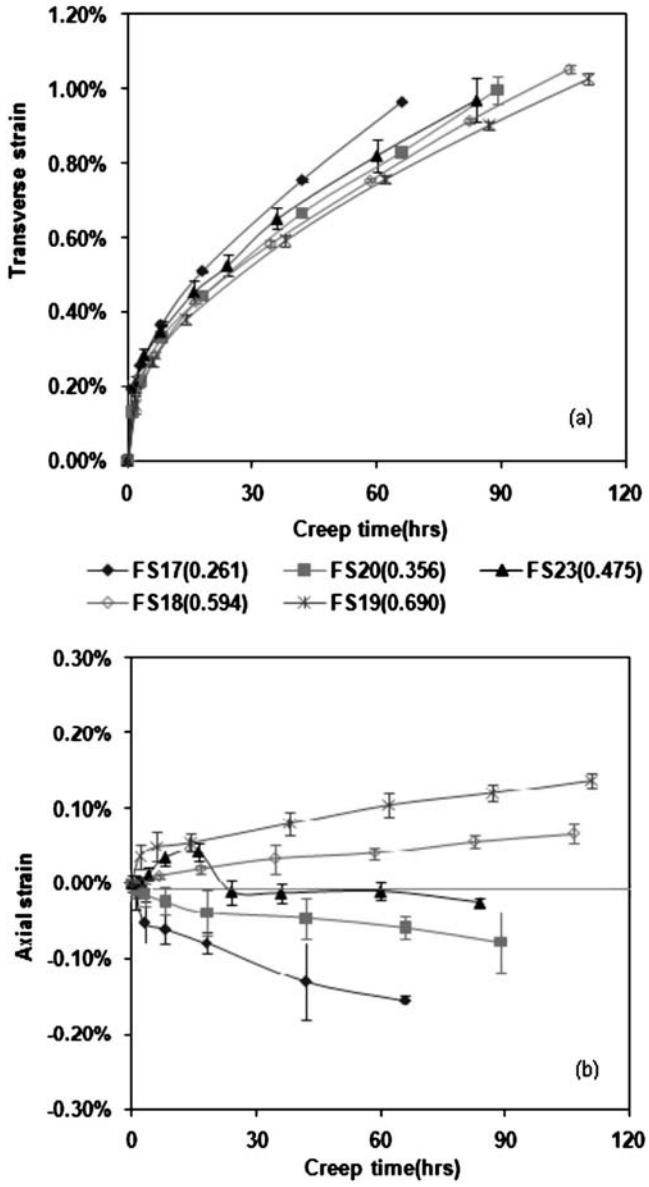


FIG. 5—*Creep strains versus time at a range of stress ratios* (σ_A/σ_T) *for internally pressurized FS capsules tested under a nominal transverse stress of 300 MPa at 350°C: (a) In the transverse direction; (b) in the axial direction.*

axial load) to positive (additional tensile axial loads) with increasing axial stress. The creep rate ratios ($\dot{\epsilon}_A/\dot{\epsilon}_T$) exhibited an apparent increasing trend with increasing stress ratio.

A limited number of end-loading tests on MPT capsules were carried out under an external compressive load of −900 N (a stress ratio of $\sigma_A/\sigma_T \approx 0.26$) and an external tensile load of +900 N (a stress ratio of $\sigma_A/\sigma_T \approx 0.70$) in the axial direction under a nominal transverse stress of 300 MPa at 350°C. Table 2 gives

TABLE 2—*Steady-state creep rates and ratios at different stress ratios in internally pressurized MPT capsules tested under a nominal transverse stress of 300 MPa at 350°C.*

Sample Number (MPT)	External Load (N)	Stress Ratio (A/T)	Steady-State Creep Rate ($\times 10^{-6}$ h^{-1})		Steady-State Creep Rate Ratio ($A:T$) ($\times 10^{-2}$)
			Axial	Transverse	
63-07(F, Q)	−900	0.266	−0.83±0.20	22.07±1.70	−3.75±0.95
63-03(F, Q)	0	0.477	2.80±0.24	21.30±0.74	13.15±1.21
63-05(F, Q)	900	0.692	7.77±0.90	21.72±1.62	35.77±4.93
66-07(F, S)	−900	0.262	−0.13±0.02	4.67±0.25	−2.79±0.40
66-05(F, S)	0	0.476	0.76±0.04	5.34±0.16	14.21±0.78
66-06(F, S)	900	0.687	1.93±0.11	4.40±0.26	43.78±3.57
76-02(F, S)	−900	0.264	−0.82±0.06	7.93±0.53	−10.38±1.01
76-03(F, S)	0	0.484	0.32±0.01	8.22±0.12	3.85±0.19
76-01(F, S)	900	0.700	2.81±0.20	7.44±0.47	37.81±3.57
72-01(F, S)	−900	0.265	−0.44±0.13	8.24±0.29	−5.34±1.60
72-02(F, S)	0	0.485	0.56±0.10	7.58±0.36	7.39±1.33
73-01(F, S)	−900	0.261	−0.66±0.07	6.38±0.27	−10.31±1.21
73-02(F, S)	0	0.484	0.78±0.09	9.46±0.12	8.23±0.97
74-01(F, S)	0	0.481	0.72±0.05	10.60±0.26	6.74±0.47
74-02(F, S)	−900	0.264	−0.41±0.06	9.85±0.71	−4.20±0.72
77-01(F, S)	0	0.478	0.41±0.02	8.28±0.06	4.89±0.20
77-02(F, S)	−900	0.266	−0.56±0.11	7.58±0.32	−7.36±1.43
79-01(F, S)	−900	0.264	−1.31±0.08	12.76±0.99	−10.27±0.99
79-02(F, S)	0	0.480	0.71±0.09	16.03±0.87	4.45±0.59
65-01(F, S)	0	0.479	0.68±0.05	12.08±0.45	5.64±0.47
65-02(F, S)	−900	0.264	−6.17±0.06	60.54±4.12	−10.19±0.70
81-01(F, S)	900	0.701	3.17±0.37	9.65±0.16	32.85±3.83
81-02(F, S)	0	0.480	0.21±0.04	2.13±0.12	9.78±2.12
81-03(B, S)	0	0.478	2.05±0.12	19.57±0.46	10.45±0.65
81-04(B, S)	−900	0.264	−1.58±0.15	16.75±0.77	−9.43±0.98
82-01(F, S)	0	0.477	0.37±0.04	4.81±0.20	7.63±0.97
82-02(F, S)	900	0.699	2.51±0.16	4.79±0.20	52.38±4.01
82-03(B, S)	0	0.478	2.15±0.10	22.89±0.44	9.38±0.48
82-04(B, S)	−900	0.265	−3.34±0.05	26.34±1.91	−12.89±0.95
82-05(B, S)	0	0.482	2.52±0.06	28.45±1.09	8.85±0.40

the stress ratios (σ_A/σ_T), steady-state creep rates and ratios ($\dot{\epsilon}_A/\dot{\epsilon}_T$). Generally, increasing axial stresses significantly increased the steady-state creep rates in the axial direction, while the transverse steady-state creep rates remained approximately the same or slightly decreased with increasing stress ratios (σ_A/σ_T). This is because that the MPTs have relatively large components of basal plane normals in the transverse direction, indicating better transverse creep resistance compared with the FS tubes. However, there are some exceptions, e.g., capsule MPT81-01(F, S) under an external axial load of +900 N ($\sigma_A/\sigma_T = 0.701$) crept almost five times faster in the transverse direction than the standard capsule, MPT81-02(F, S) ($\sigma_A/\sigma_T = 0.480$). The transverse steady-state creep of capsule MPT65-02(F, S) ($\sigma_A/\sigma_T = 0.264$) is five times larger than that of the standard capsule, MPT65-01(F, S) ($\sigma_A/\sigma_T = 0.479$). These results are inconsistent with expectations and with the results from all other capsules. Not much microstructure or texture variation is expected in these two tubes, so the explanation is not clear.

Discussions

Effect of Texture and Microstructure on Creep Anisotropy

The ratio of steady-state creep rate in the axial direction to that in the transverse directions ($\dot{\epsilon}_A/\dot{\epsilon}_T$) is a measure for the creep anisotropy of internally pressurized Zr alloys tubes in which the basal plane normals are predominantly distributed in the radial-transverse plane [8,11,14]. Figure 6(*a*) illustrates the variation of ($\dot{\epsilon}_A/\dot{\epsilon}_T$) versus texture parameter ($f_T - f_R$) for the standard FS and MPT capsules tested under a transverse stress of 300 MPa at 350°C. It can be seen that with increasing ($f_T - f_R$), the values of ($\dot{\epsilon}_A/\dot{\epsilon}_T$) increased. In general, the capsules from tubes MPT63F and 66F with an extrusion ratio of 10:1 at 815°C showed the highest values of ($\dot{\epsilon}_A/\dot{\epsilon}_T$), followed by those from tubes MPT81F&B and 82F&B (extruded at 975°C with a ratio of 10:1), tubes MPT72F, 73F, and 74F (extruded at 650°C with a ratio of 10:1), and tubes MPT76F, 77F, 79F, 62F, and 65F (extruded at 650°C with a ratio of 4:1) in a decreasing order. The FS tube exhibited a negative ($\dot{\epsilon}_A/\dot{\epsilon}_T$) value corresponding to $f_R > f_T$, indicating the poorest creep resistance in the transverse direction in the tested tubes. For each group of tubes with the same nominal extrusion condition (marked as the same color and symbol), their steady-state creep rate ratios ($\dot{\epsilon}_A/\dot{\epsilon}_T$) fell into a similar range.

Grain size (fine or coarse) is not a factor to significantly affect the creep anisotropy of the tested tubes, e.g., the values of steady-state creep rate ratios for capsules MPT63-03(F, Q) (a fine grain size) and MPT66-05(F, S) (a coarse grain size) are similar, although a finer grain size may have led to faster creep. Moreover, the grain structure differences within the tubes with the same nominal extrusion conditions seem not to influence the creep anisotropy of the tubes tested. For example, the values of ($\dot{\epsilon}_A/\dot{\epsilon}_T$) for the front and back ends capsules of tubes MPT81 and 82, are in a similar range and all closely distributed to the linear trend line in Fig. 6(*a*), which represents the trend of the effect of texture. Capsule MPT62-01(F, Q) (equiaxed grain shape in radial-transverse section) showed the highest value of steady-state creep rate ratios in the group with an

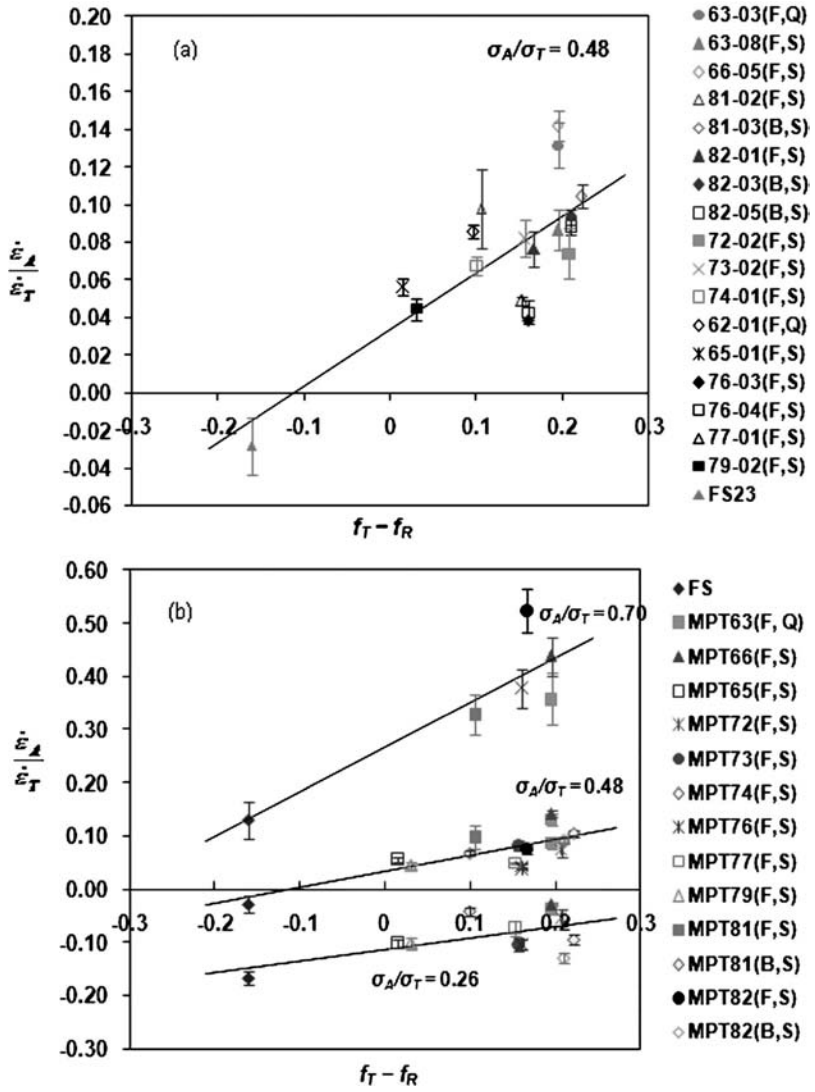


FIG. 6—*Variation of steady-state creep rate ratios* ($\dot{\epsilon}_A/\dot{\epsilon}_T$) *versus texture parameters* ($f_T - f_R$) *for internally pressurized FS and MPT capsules under a transverse stress of 300 MPa at 350°C: (a) At a constant stress ratio of ~0.48* (σ_A/σ_T); *(b) at varied stress ratios* ($\sigma_A/\sigma_T \approx 0.26$, *0.48, and 0.70). Note that F or B and S or Q indicated the specimen was made from the front or back end of the tube, and the tube billet preparation were slow-cooled or quenched.*

extrusion ratio of 4:1 at 650°C, but its value of the steady-state creep rate ratio is located at a similar distance above the trend line with capsule MPT65-01(F, S) (elongated grain shape) in spite of different grain structures. Furthermore, the distribution of β-phase also appears to have no significant effect on the creep

anisotropy, e.g., tubes MPT62F, 81B, and 82B have the β-phase broken up into discrete particles as opposed to the more continuous distribution of the other tubes, but their $(\dot{\epsilon}_A/\dot{\epsilon}_T)$ values are all in a similar range among the tubes with the same extrusion conditions.

The end-loaded capsules with both external compressive and tensile axial loads exhibited a similar texture dependence of creep anisotropy to the case of the standard capsules (Fig. 6(*b*)). The steady-state creep rate ratios $(\dot{\epsilon}_A/\dot{\epsilon}_T)$ exhibited an approximately linear increase with increasing $(f_T - f_R)$ for each stress state, as indicated by the linear trend lines in Fig. 6(*b*).

In brief, the only microstructural factor of *those examined* which strongly correlates with creep anisotropy is crystallographic texture although there may be small effects of grain structure, size, and β-phase distribution in the cold-worked Zr-2.5Nb tubes and these seem to be within the experimental error. The anisotropic hcp structure of α grains and strong texture of the materials are clearly key factors in determining the creep anisotropy.

Creep Anisotropy Modeling by the Existing Model— SELFPOLY7

"Self-consistent" methods allow for individual grains to deform differently and account for the interactions between grains and matrix to meet both equilibrium and compatibility conditions [22]. In early work, Adams [23] and Woo [24,25] developed the polycrystalline self-consistent formulation to analytically predict the steady-state linear irradiation creep in Zirconium alloys by assuming that the matrix was isotropic. In 1993, this self-consistent model was improved to be a numerical scheme, called SELFPOLY, which accounted for the texture and plate-like grain shapes of pressure tubes to simulate steady-state irradiation creep and growth [26]. Turner et al. [27] developed SELFPOLY N, which included the thermal creep case by adopting Hutchinson's [22] slip models for power-law steady-state creep behavior of polycrystalline aggregation. Version SELFPOLY7 is used in this paper.

In the thermal creep case, SELFPOLY7 assumes that the single crystal deformation strain rate is calculated by [27]

$$\dot{\epsilon}^c_{ij} = \sum_s \dot{\gamma}^s_0 \left(\frac{m^s : \sigma}{\tau^s} \right)^n m^s_{ij} \tag{1}$$

where:

s = slip system,
m^s = Schmid tensor corresponding to the slip system s,
σ = stress acting on the crystal,
τ^s = critical resolved shear stress (CRSS) for slip system s,
$\dot{\gamma}^s_0$ = reference shear strain rate, and
n = stress exponent.

The reference shear strain rate $\dot{\gamma}^s_0$ and the stress exponent n are assumed to be the same for all operating slip systems. The ratios of CRSS rather than absolute values are usually used and $\dot{\gamma}^s_0$ can be adjusted to obtain an absolute value in agreement with experimental measurements. SELFPOLY7 does not take into

account the effect of β-phase ($\sim 10\,\%$) in Zr-2.5Nb, and assumes that each grain has the same CRSS ratios for the applied slip systems of α–Zr and that for a given metallurgical condition these are also the same for materials with different crystallographic textures.

In the calculations, the textures of the materials were represented by the orientation distributions derived from the measured pole figure using Bunge's notation. An average grain shape ratio (axial: transverse: radial directions) was needed to be input in the calculation, based on electron microscope observations. Three slip systems: prismatic slip $\{10\bar{1}0\}\langle 11\bar{2}0\rangle$, basal slip $\{0001\}\langle 11\bar{2}0\rangle$, and pyramidal slip $\{10\bar{1}1\}\langle 11\bar{2}3\rangle$, were assumed to produce the creep strains. The stress exponent n was set as 6.4 based upon the value determined experimentally [15]. Note that the reference shear strain rate $\dot{\gamma}_0^s$ was not adjusted because its value did not affect the creep anisotropy, i.e., the steady-state strain rate ratio ($\dot{\epsilon}_A/\dot{\epsilon}_T$). The CRSS ratios for these three slip systems needed to be specified to achieve good matches with the experimental data. To determine one set of CRSS ratios that reasonably fits all the experimental data, a range of ratio values were tried from 1:100:100 to 1:1:1 (i.e., prismatic: basal: pyramidal slip). It was found that a constant CRSS within the trial ranges cannot reasonably fit all the experimental data from the tubes with the varied distributions of basal plane normals in the transverse-radial plane. Here, the ratios of 1:3:100 were chosen because it provided the best matches with the data. At the same time, the ratios of 1:2.60:13 obtained by Akhtar [28] from single crystal Zr under compression at $> 600^{\circ}$C and 1:1.25:2.83 derived by Cai et al. [29] from Zr-2.5Nb tension and compression at room temperature were also used to predict the creep anisotropy of the tubes. The grain shape ratios were set as 5:1:0.2 in the axial, transverse, and radial directions for most of the MPT capsules, except for tubes MPT62F, MPT81F&B, and MPT82F&B with a grain shape ratio of 2:0.2:0.2 based on the observed microstructure. For the FS capsule, a grain shape ratio of 6.3:1.36:0.8 was estimated based on the observation of Causey et al. [6]. Table 3 gives the list of parameters in SELFPOLY7. Figure 7 depicts the comparison between experimental and predicted ratio ($\dot{\epsilon}_A/\dot{\epsilon}_T$) versus texture parameter ($f_T - f_R$) for the tested standard FS and MPT capsules under a transverse stress of 300 MPa at 350°C.

At the CRSS ratios of 1:3:100, Fig. 7(*a*), a general increasing trend of steady-state creep rate ratios ($\dot{\epsilon}_A/\dot{\epsilon}_T$) with increased values of texture parameters

TABLE 3—*Parameters in SELFPOLY7 model.*

CRSS Ratio (Prismatic: Basal: Pyramidal Slips)	Stress Exponent	Grain Shape (Ratios in the Axial, Transverse, and Radial Directions)
1:3:100	$n = 6.4$	A grain shape ratio of 5:1:0.2 of tubes MPT63F, 65F, 66F, 72F, 73F, 74F, 76F and 79F; a grain shape ratio of 2:0.2:0.2 of tubes MPT62F, 81F, 81B, 82F and 82B; a grain shape ratio of 6.3:1.36:0.8 of FS tubes.
1:2.6:13	$n = 6.4$	
1:1.25:2.83	$n = 6.4$	

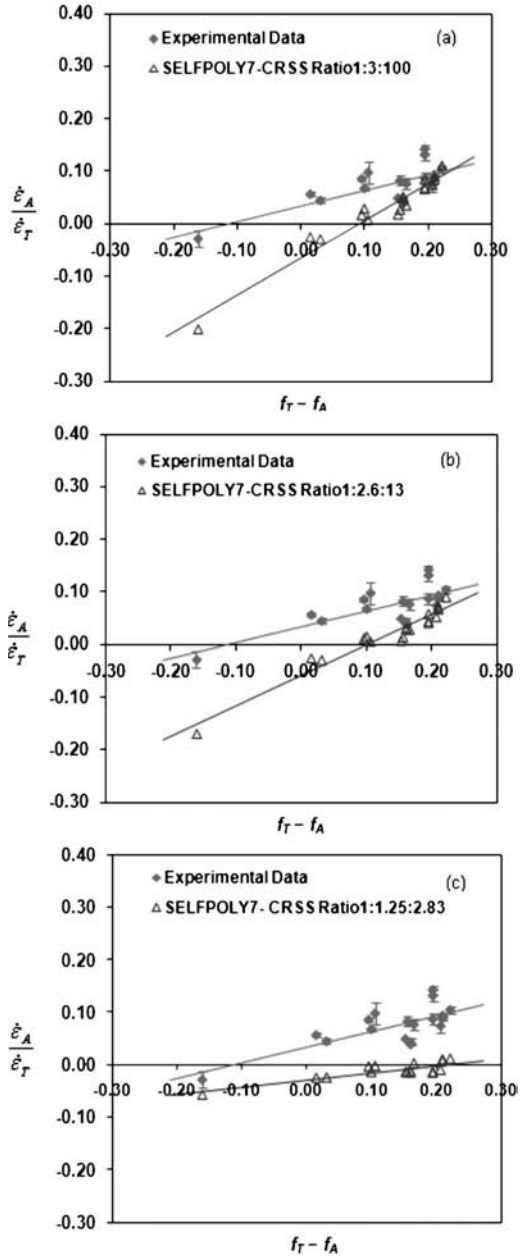


FIG. 7—*Experimental steady-state creep rates ratios* $(\dot{\epsilon}_A/\dot{\epsilon}_T)$ *and predictions by the SELFPOLY7 versus texture parameters* $(f_T - f_R)$ *for internally pressurized FS and MPT capsules tested under a transverse stress of 300 MPa at 350°C at a stress ratio* (σ_A/σ_T) *of ~0.48. SELFPOLY7 at the CRSS ratio of (a) 1:3:100; (b) 1:2.6:13; and (c) 1:1.25:2.83. The stress exponent n=6.4.*

$(f_T - f_R)$ was predicted, but the discrepancies between the predictions and experimental results increased as the values of $(f_T - f_R)$ decreased. There are some good quantitative agreements with the experimental results for capsules MPT72-02(F, S), 76-03(F, S), 76-04(F, S), 81-03(B, S), 82-03(B, S), and 82-05(B, S). However, for capsules MPT65-01(F, S) and 79-02(F, S), the model predicted a negative axial creep rate while the experimental result showed a positive value. Although the predicted ratios for capsules MPT62-01(F, Q) and 81-02(F, S) are positive, they are much smaller than the experimental values. Moreover, the model predicted a negative ratio for FS23, but it overestimated the experimental value by a factor of seven. The predictions using Akhtar's CRSS ratios from high temperature ($> 600°C$) (Fig. 7(*b*)) exhibited similar results to those by 1:3:100. The ratios of 1:1.25:2.83, while giving better agreement with the FS predicted much lower values of $(\dot{\epsilon}_A/\dot{\epsilon}_T)$ (Fig. 7(*c*)) compared with the rest of the experimental data.

Simulation of Non-Uniform Dislocation Distributions

One of the reasons for the poor agreement may be the assumption, in SELFPOLY7, that the single crystal creep response within a given material is identical regardless of its orientation. In real materials, different pre-existing dislocation distributions may exist in grains with different orientations, which results in non-identical anisotropic deformation of each grain. In this case, creep anisotropy is not dependent solely upon crystallographic texture but may also depend upon microstructural differences among differently oriented grains. It was reported that cold-worked pressure tubes contain $\langle a \rangle$ and $\langle c + a \rangle$ component dislocations with a density of $\sim 3\text{–}4 \times 10^{14}\,\mathrm{m}^{-2}$, and the densities and types of the dislocations in individual grains are largely determined by grain orientations [30]. It also had been found that the creep strains in-reactor creep are strongly related to the cold-working prior to creep, which was considered to be associated with the density and distribution of dislocations [6]. Moreover, the strains due to creep deformation are very small (e.g., $\leq 1\,\%$) compared with those from cold work ($> 25\,\%$), so the pre-existing dislocation structure or distribution is likely to have a strong influence on creep behavior of cold-worked Zr-2.5Nb tubes.

Because it is virtually impossible to use TEM or other experimental techniques to provide this quantitative information considering the extremely fine grain structures of the materials under study, an elasto-plastic self-consistent model (EPSC3) [31] was employed to simulate the pre-existing dislocation distributions prior to creep. The model has been successfully applied to interpret room temperature deformation mechanisms for both Zircaloy-2 and Zr-2.5Nb [29,32]. Here, the model is used to track the total shear strains γ^s for a slip system s in individual orientations, which are related to dislocation densities developed during cold work [33]. The calculations were carried out using the single crystal plasticity parameters derived by Cai et al. [29] on the slip systems: prismatic slip $\{10\bar{1}0\}\langle 11\bar{2}0\rangle$, basal slip $\{0001\}\langle 11\bar{2}0\rangle$, and pyramidal slip $\{10\bar{1}1\}\langle 11\bar{2}3\rangle$, which provided the best fit for tension and compression tests on Zr-2.5Nb at room temperature.

Typical cold working strains and modeling process on MPT and FS tubes were presented in Refs [21 and 33]. The important factor is the ratio of

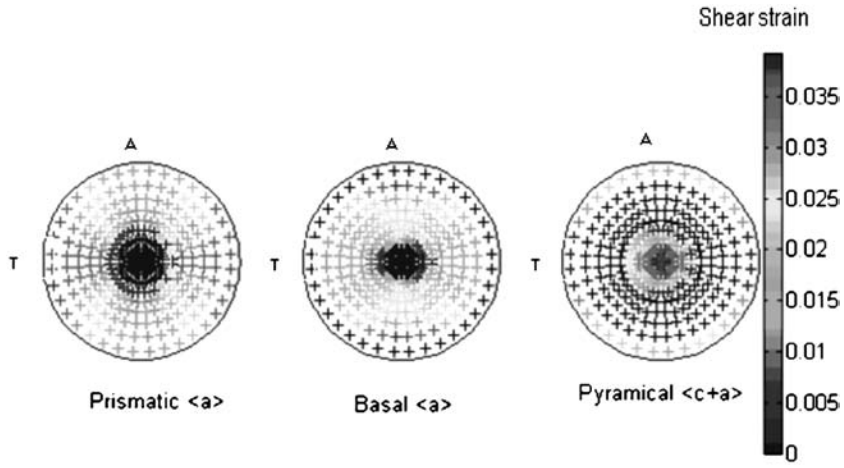


FIG. 8—*Simulated distributions of shear strains for each slip mode corresponding to the c-axes orientation of grains for MPT at 3.2 % total strain. The center is the radial direction, the left and right is the transverse direction, and the top and bottom is the axial direction.*

wall-thickness strain to diameter strain, typically > 2. Non-uniform distributions of dislocations were derived, e.g., Fig. 8 illustrates the shear strain distributions of tube MPT66 in the slip modes of prismatic, basal, and pyramidal corresponding to the *c*-axis orientation of grains. It is shown that the grains with the *c*-axis oriented in the transverse direction have high prismatic $\langle a \rangle$ shear strains, but very little pyramidal $\langle c + a \rangle$ and basal $\langle a \rangle$ shear strain. Most of high pyramidal $\langle c + a \rangle$ shear strains are contained in the grains with the *c*-axis oriented near the radial direction and a small proportion in the axial direction. Basal $\langle a \rangle$ shear strains are contained in an annulus around the radial direction but concentrated in the grains with *c*-axis aligned near the axial-radial plane.

In the calculation, the measured textures from the cold-worked Zr-2.5Nb tubes were used because there is no better option. Note that version EPSC3 does not account for lattice rotation or texture evolution, and lattice rotation may occur and result in local stress relaxation and eventually changes stress states in individual grains. Although a visco-plastic self-consistent model [34] can be used to calculate the evolution of texture from the extrusion stage, the simulations do not give good enough agreement with the measured textures of the tubes to perform subsequent calculations. Hence, the EPSC model was chosen here. In spite of these difficulties, the predicted dislocation distribution is expected to be a plausible representation of the actual situation. For example, in the grains with the *c*-axis in the radial direction, the wall-thickness reduction forces the deformation along the *c*-axis by pyramidal $\langle c + a \rangle$ slip, resulting in a high density of dislocations with *c*-component Burgers vectors. Grains with the *c*-axis in the transverse direction can be easily deformed by prismatic $\langle a \rangle$ slip during wall-thickness reduction and axial extension. This results in the

formation of a high density of *a*-type dislocations. Griffiths et al. [35] observed high densities of $\langle c+a \rangle$ type dislocations on a transverse tensile specimen from a Zr-2.5Nb plate in which the *c*-axis were oriented in the transverse direction. There were few *c*-component dislocations found in the specimen after a tensile deformation is applied along the longitudinal direction, while high densities of *a*-type dislocations were observed. These experimental observations are consistent with our simulation.

In the modification, it is assumed the created shear strain γ^s in cold work is related to the mobile dislocation density subsequently available for creep, and the dislocation densities of each slip mode *s* are assumed to be linearly proportional to the total shear strains calculated from the EPSC3. It is also assumed that the pre-existing dislocations are the only sources to contribute to creep shear strains in individual grains, i.e., at the steady-state, creep deformation would occur predominantly by the slip of existing dislocations rather than by creation of new dislocations. This is reasonable because the strains introduced during cold work ($> 25\,\%$) are much larger than the strains introduced during creep ($\leq 1\,\%$).

To take into account the anisotropic and non-uniform of dislocations on creep shear strain rate, the shear strain rate contributed by slip system *s* in a single crystal was modified to

$$\dot{\epsilon}^s = \rho_m^s b^s \bar{\upsilon} \cong \dot{\gamma}_0^s \left(\frac{m^s : \sigma}{\tau^s} \right)^n m_{ij}^s = \rho_m^s b^s \bar{\upsilon}_0^{s'} \left(\frac{m^s : \sigma}{\tau^s} \right)^n m_{ij}^s \tag{2}$$

which is based on the formula in the SELFPOLY7, Eq 1, and the Weertman's model [36–38], $\dot{\epsilon} = \rho_m b \bar{\upsilon}$, where ρ_m is the mobile dislocation density, b is the magnitude of Burgers vector, and $\bar{\upsilon}$ is the mean velocity of mobile dislocations. In Eq 2, it is assumed that the terms b and ρ_m are included in $\dot{\gamma}_0^s$ and we define a new term $\bar{\upsilon}_0^{s'}$, referring to the reference average velocity of mobile dislocation for each slip system. Note that the magnitude of the Burgers vector of pyramidal $\langle c+a \rangle$ slip is larger than those of prismatic and basal $\langle a \rangle$ slip by a factor of 1.88, i.e., $|b_{1/3\langle 11\bar{2}3 \rangle}| = 1.88 |b_{1/3\langle 11\bar{2}0 \rangle}|$ based on the c/a ratio of 1.593 for $\alpha-$Zr [5]. The modified model is referred to SELFPOLY7-Q.

In the SELFPOLY7-Q modeling, the high temperature ratios of 1:2.6:13 ($> 600^\circ$C) [28] and room temperature ratios of 1:1.25:2.83 [29] were first tried to predict the creep anisotropy of the tubes (Fig. 9(*a*), 9(*b*)). Note that 50 % sharing of prismatic $\langle a \rangle$ and basal $\langle a \rangle$ slip was applied to allow for cross slip between basal and prismatic planes [21,33].

Compared with the predictions by the SELFPOLY7 in Fig. 7, the predictions with both CRSS ratios are significantly improved (Fig. 9(*a*), 9(*b*)). However, the prediction with CRSS ratios of 1:2.6:13 largely underestimates the values of $(\dot{\epsilon}_A/\dot{\epsilon}_T)$ because of too much contribution of prismatic slip to the transverse strains. Conversely, high contributions of pyramidal or basal slip in the ratios of 1:1.25:2.83 resulted in higher predicted $(\dot{\epsilon}_A/\dot{\epsilon}_T)$ values compared with the experimental data. An intermediate value of 1:1.4:4.1 was chosen which provided good matches with the experimental results as shown in Fig. 9(*c*). It can be seen

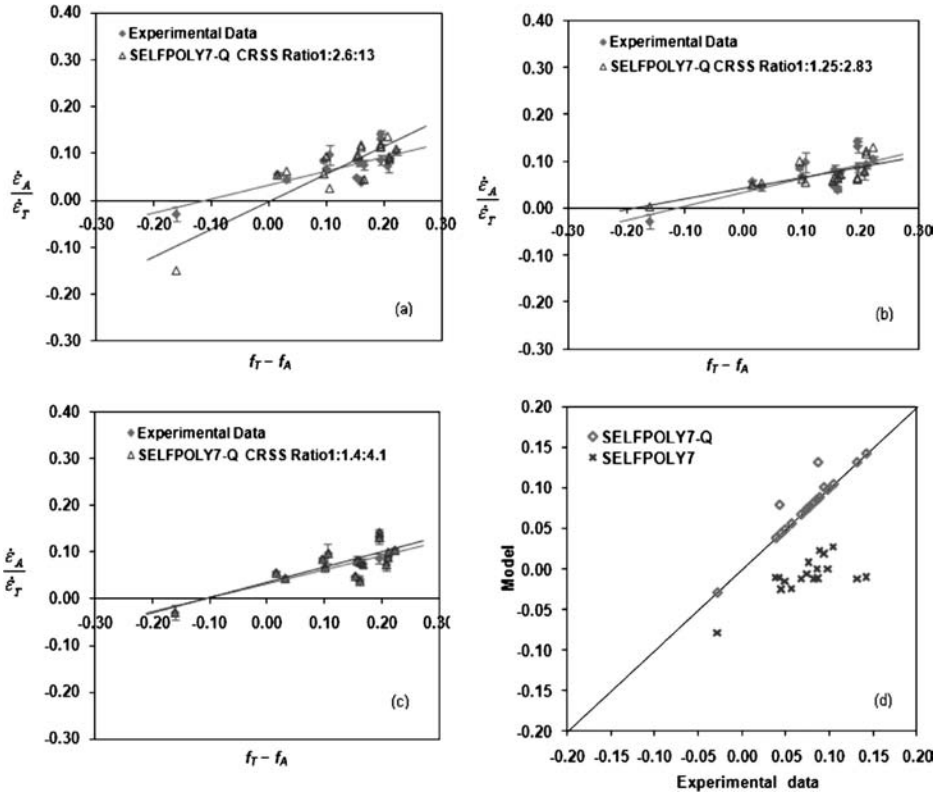


FIG. 9—*Experimental creep anisotropy* $(\dot{\epsilon}_A/\dot{\epsilon}_T)$ *of internally pressurized standard creep capsules under a transverse stress of 300 MPa at 350°C compared with predictions by SELFPOLY7-Q at the CRSS ratios of (a) 1:2.6:13; (b) 1:1.25:2.83; (c) 1:1.4:4.1; and (d) comparison of predicted values of* $(\dot{\epsilon}_A/\dot{\epsilon}_T)$ *by the SELFPOLY7 and SELFPOLY7-Q versus experimental data. Note that the error bars were omitted to demonstrate the figure (d) clearly.*

that the predicted $(\dot{\epsilon}_A/\dot{\epsilon}_T)$ almost perfectly matched the experimental values of the FS capsule and provided better matches with most of MPT creep anisotropy data. Improvements were also achieved for the samples in which the *c*-axis in the radial-transverse plane have relatively strong bias to the radial direction of the tubes, i.e., $f_T - f_R < 0.15$, such as capsules MPT65-01(F, S) and 79-02(F, S). For this type of texture, the easy prismatic slip predicted by the SELFPOLY7 significantly increased the transverse strain contributions from the grains with the *c*-axis in the radial direction, resulting in a negative creep rate in the axial direction; while the SELFPOLY7-Q greatly reduced the contribution of prismatic slip in these grains and they were deformed primarily by pyramidal $\langle c + a \rangle$ slip which is more isotropic, giving little axial strain. As a result, the SELFPOLY7-Q predictions significantly narrowed the overall distribution against the experimental data (Fig. 9(*d*)) compared with SELFPOLY7.

Figure 10(*a*) illustrates the comparison of experimental and predicted results by SELFPOLY7-Q for the end-loaded MPT and FS capsules with an external axial tensile (+900 N) or compressive (−900 N) load under a nominal transverse stress of 300 MPa at 350°C. Figure 10(*b*) shows the comparison between the experimental data and the predicted ratios ($\dot{\epsilon}_A/\dot{\epsilon}_T$) by both models. It was shown that the SELFPOLY7 predictions underestimated the values of steady-state creep rate ratios ($\dot{\epsilon}_A/\dot{\epsilon}_T$) in most of the capsules at different stress ratios, which indicated that too much contribution of prismatic slip to the grains with the *c*-axis oriented in the radial direction. The predictions by the SELFPOLY7-Q exhibited much better agreement with the experimental data (Fig. 10(*b*)). Again, the poor simulation obtained by SELFPOLY7, which effectively assumes an isotropic dislocation distribution, indicated that texture alone is not the only determining factor of creep anisotropy. However, it is noticed that the deviation between the experimental data and SELFPOLY7-Q predictions still exceed the experimental error in spite of the better agreement. Further improvements to dislocation distribution simulations may be made using more advanced polycrystalline models [39–44]. Furthermore, the current model only takes into account the initial dislocation density derived from cold work as an initial mobile dislocation density and assumes that the dislocation density does not change during creep for simplification. In a real case, the mobile dislocation density may change and increasing density increases the creep rate, which can also lead to hardening effect. Therefore, more advanced and powerful creep models that can take into account more potential factors to affect creep anisotropy, simulate the whole process of creep, i.e., not just limited on the steady-state stage, and also provide dislocation evolution information during creep, are required to accurately predict and better interpret the creep anisotropy of cold-worked Zr-2.5Nb tubes.

An important consequence of these findings is that, with a fixed crystallographic texture, creep anisotropy could vary significantly if dislocations are introduced by different strain paths. One example of this that could be important is the plastic relaxation of stresses at a notch tip under plane-strain constraint. For pressure tube in CANDU reactors, the flaws of interest are partial wall, planar flaws in the radial-axial plane. Plastic relaxation at such flaws occurs under plane-strain in the radial-transverse plane. The dislocation structures introduced by such plastic relaxation would be expected to be quite different from those introduced by the cold working process, during which the wall and diameter are reduced in a ratio of about 6.6:1, and axial extension occurs. The shear strain distribution introduced for a typical CANDU pressure tube texture (strong transverse distribution of the *c*-axes) in the latter case resembles that shown in Fig. 8. The shear strain distribution for radial-transverse plane is shown in Fig. 11. The difference is remarkable, crystals with their *c*-axis radial exhibit high shears by prismatic $\langle a \rangle$ slip, as opposed to pyramidal $\langle c + a \rangle$ shear, while crystals with their *c*-axis transverse exhibit high levels of pyramidal $\langle c + a \rangle$ shear, as opposed to prismatic $\langle a \rangle$ shear. Table 4 shows the relative creep strains calculated for biaxial loading ($\sigma_A/\sigma_T = 0.48$) using SELFPOLY7-Q, making the same assumptions used in predicting the creep anisotropy of the capsules. Note that the creep anisotropy induced by plane-strain deformation in the

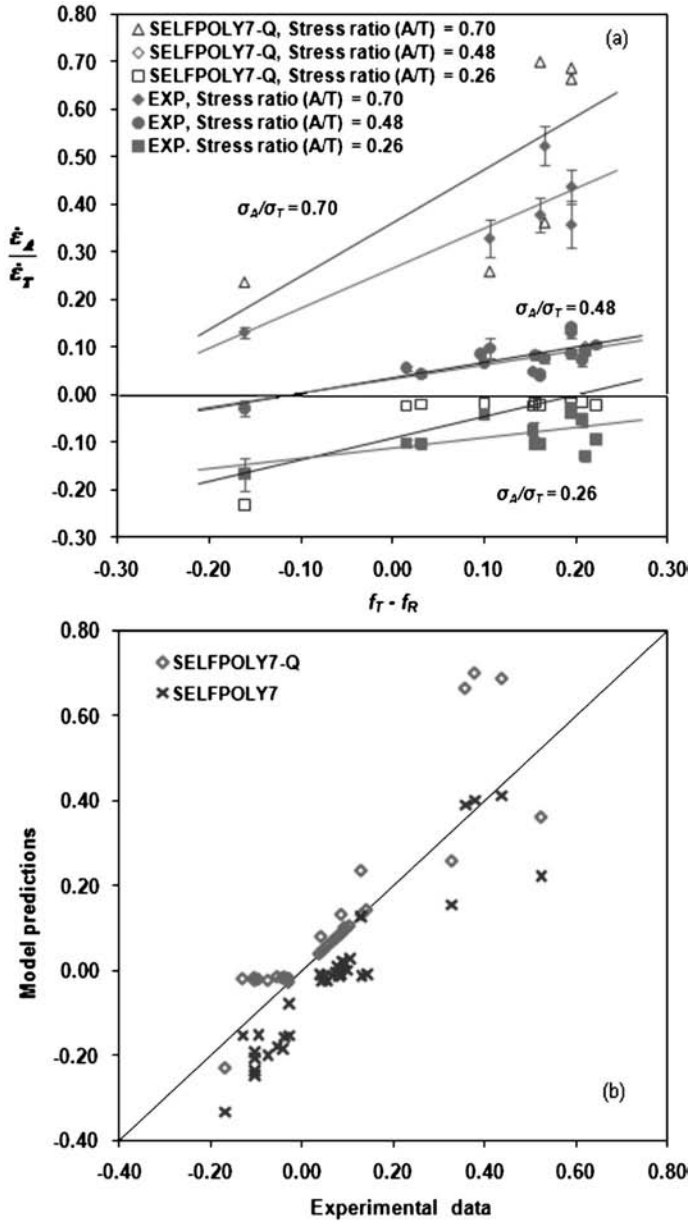


FIG. 10—*Experimental and predicted steady-state creep rate ratios* $(\dot{\epsilon}_A/\dot{\epsilon}_T)$ *for internally pressurized FS and MPT capsules at different stress ratios* (σ_A/σ_T) *under a transverse stress of 300 MPa at 350°C. (a) Comparison of the experimental and predicted values of* $(\dot{\epsilon}_A/\dot{\epsilon}_T)$ *by the SELFPOLY7-Q versus texture parameters* $(f_T - f_R)$*; (b) comparisons of the predicted values of* $(\dot{\epsilon}_A/\dot{\epsilon}_T)$ *by the SELFPOLY7 and SELFPOLY7-Q versus experimental data. Note that the error bars were omitted to demonstrate the figure (b) clearly.*

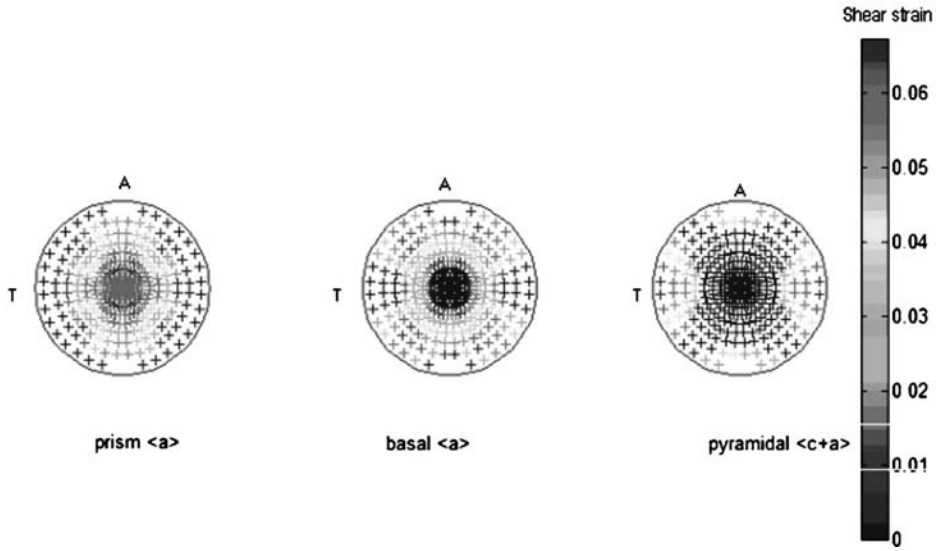


FIG. 11—*Simulated distributions of shear strains for each slip mode corresponding to the c-axes orientation of grains for a standard pressure tube subjected to 3.2 % plane-strain in the radial-transverse plane. The center is the radial direction, the left and right is the transverse direction and the top and bottom is the axial direction.*

radial-transverse plane is very different from that from cold work, despite the fact that the texture is identical. The transverse strain is much higher for the plane-strain case, and the axial strain is negative instead of positive—creep anisotropy that would normally be associated with a radial distribution of *c*-axes, if texture alone were controlling creep anisotropy.

Conclusions

Cold-worked Zr-2.5Nb pressure tubes exhibited a variety of crystallographic textures and microstructures after different manufacturing procedures, providing valuable materials to investigate the factors affecting the creep anisotropy of this material.

TABLE 4—*Relative steady-state creep strain rates for biaxially loaded tubes with dislocation structures introduced by cold-drawing (with a wall reduction 6.6 times of the diameter reduction) and by plane-strain in the radial-transverse plane.*

Mode of Deformation	Axial Strain Rate	Transverse Strain Rate	Wall-Thickness Strain Rate	Ratio Axial/Transverse
Cold-drawing	0.12	1.00	−1.12	0.12
Plane-strain	−0.22	3.3	2.08	−0.07

Crystallographic texture strongly correlates with the anisotropic creep behavior and creep anisotropy of Zr-2.5Nb tubes in the regime where dislocation creep is the dominant mechanism. Steady-state creep rate ratios between the axial and transverse directions exhibit an approximately linear increasing trend as the resolved faction of basal plane normals $(f_T - f_R)$ increases.

The existing self-consistent polycrystalline model SELFPOLY7, which is based solely upon crystallographic texture and a tacit assumption of uniform dislocation distributions, cannot capture the creep anisotropy for all the cold-worked Zr-2.5Nb tubes, especially for the tubes with stronger radial textures. The poor predictions implied that texture alone is not sufficient to accurately predict the creep anisotropy of cold-worked Zr-2.5Nb tubes.

Non-uniform dislocation distributions of individual grains with different orientations were derived from the elasto-plastic self-consistent model ESPC3 by using the single crystal plasticity parameters previously determined for Zr-2.5Nb. A modified version, SELFPOLY7-Q, which takes into account the pre-existing dislocation structures created during cold work, provided much better agreements with the experimental data from the tubes with different crystallographic textures and different stress states.

The non-uniform distributions of dislocations for grains with different orientations greatly reduces the contribution of prismatic $\langle a \rangle$ slip in the grains with the c-axis in the radial direction and they deform primarily by pyramidal $\langle c + a \rangle$ slip.

A consequence of these conclusions is that the introduction of dislocations by a completely different strain path can radically change the creep anisotropy of a material with a given crystallographic texture.

Acknowledgments

The writers would like to thank Dr. R. Rogge and Dr. M. Gharghouri (NRU at CRL) for helping with texture measurements; F. Butcher (CRL) for helping on the pressurization of creep capsules; Dr. Y. Zhang for his help with the Z-Mike laser sensor system programming; and Dr. I. Yahubsov and Dr. A. Khan for helping with the TEM microstructural observations. This research project is sponsored by NSERC, COG, OPG, and Nu-Tech Precision Metals Inc. under the Industrial Research Chair Program in Nuclear Materials at Queen's University in Canada.

References

[1] Aldridge, S. A. and Cheadle, B. A., "Age Hardening of Zr-2.5 wt % Nb Slowly Cooled from the (α+β) Phase Field," *J. Nucl. Mater.*, Vol. 42, 1972, pp. 32–42.

[2] Cheadle, B. A., "Fabrication of Zirconium Alloys into Components for Nuclear Reactors," *Proc. 3rd Int. Conf. on Zirconium in the Nuclear Industry, ASTM STP 633*, A L. Lowe, Jr. and G. W. Parry, Eds., ASTM International, West Conshohocken, PA, 1977, pp. 457–485.

[3] Holt, R. A., "In-Reactor Deformation of Cold-Worked Zr–2.5Nb Pressure Tubes," *J. Nucl. Mater.*, Vol. 372, 2008, pp. 182–214.

[4] Ross-Ross, P. A. and Hunt, C. E. L., "The In-Reactor Creep of Cold-Worked Zircaloy-2 and Zirconium-2.5 wt % Niobium Pressure Tubes," *J. Nucl. Mater.*, Vol. 26, 1968, pp. 2–17.
[5] Franklin, D. G., Lucas, G. E., and Bement, A. L., *ASTM STP 815*, ASTM International, West Conshohocken, PA, 1983.
[6] Causey, A. R., Holt, R. A., and MacEwen, S. R., "In-Reactor Creep of Zr-2.5Nb," *Proc. 6th Int. Conf. on Zirconium in the Nuclear Industry, ASTM STP 824*, ASTM International, West Conshohocken, PA, 1984, pp. 269–288.
[7] Fleck, R. G., Elder, J. E., Causey, A. R., and Holt, R. A., "Variability of Irradiation Growth in Zr-2.5Nb Pressure Tubes," *Proc. 9th Int. Conf. on Zirconium in the Nuclear Industry, ASTM STP 1245*, ASTM International, West Conshohocken, PA, 1994, pp. 168–182.
[8] Causey, A. R., Holt, R. A., Christodoulou, N., and Ho, E. T. C., "Irradiation-Enhanced Deformation of Zr-2.5Nb Tubes at High Neutron Fluences," *Proc. 12th Int. Conf on Zirconium in the Nuclear Industry, ASTM STP 1354*, ASTM International, West Conshohocken, PA, 2000, pp. 74–85.
[9] Sagat, S., Newman, G. W., and Scarth, D. A., "Crack Initiation by Delayed Hydride Cracking at Sharp Notches in Zr-2.5Nb Alloys," *Proc. Int. Conf for Hydrogen Effects on Material Behaviour and Corrosion Deformation Interactions*, Moran, WY, Sept. 22–26, 2002, pp. 289–299.
[10] Field, G. J., Dunn, J. T., and Cheadle, B. A., "Analysis of Pressure Tube Failure at Pickering NGS 'A' Unit 2," *Can. Metall. Q.*, Vol. 24, 1985, pp. 181–188.
[11] Christodoulou, N., Causey, A. R., Woo, C. H., Tomé, C. N., Klassen, R. J., and Holt, R. A., "Modelling the Effect of Texture and Dislocation Structure on Irradiation Creep of Zirconium Alloys," *Effects of Radiation on Materials: 16th International Symposium, ASTM STP 1175*, ASTM International, West Conshohocken, PA, 1994, pp. 1111–1128.
[12] MacEwen, S. R. and Fidleris, V., "Verification of a Model for In-Reactor Creep Transients in Zirconium," *Philos. Mag.*, Vol. 31, 1975, pp. 1149–1157.
[13] Matthews, J. R. and Finnis, M. W., "Irradiation Creep Models—an Overview," *J. Nucl. Mater.*, Vol. 159, 1988, pp. 257–285.
[14] Causey, A. R., Edler, J. E., Holt, R. A., and Fleck, R. G., "On the Anisotrophy of In-Reactor Creep of Zr-2.5Nb," *Proc. 9th Int. Conf., Zirconium in the Nuclear Industry, ASTM STP 1245*, ASTM International, West Conshohocken, PA, 1994, pp. 202–220.
[15] Li, W. and Holt, R. A., "Anisotropic Thermal Creep of Internally Pressurized Zr-2.5Nb Tubes," *J. Nucl. Mater.*, Vol. 401, 2010, pp. 25–37.
[16] Holt, R. A. and Ibrahim, E. F., "Factors Affecting the Anisotropy of Irradiation Creep and Growth of Zirconium Alloys," *Acta Metall.*, Vol. 27, 1979, pp. 1319–1328.
[17] Holt, R. A. and Aldridge, S. A., "Effect of Extrusion Variables on Crystallographic Texture of Zr-2.5 wt% Nb," *J. Nucl. Mater.*, Vol. 135, 1985, pp. 246–259.
[18] Li, Y., Rogge, R., and Holt, R. A., "Development of Local Microstructure and Crystallographic Texture in Extruded Zr-2.5Nb Tubes," *Mater. Sci. Eng., A*, Vol. 437, 2006, pp. 10–20.
[19] Holt, R. A. and Zhao, P., "Micro-Texture of Extruded Zr-2.5Nb Tubes," *J. Nucl. Mater.*, Vol. 335, 2004, pp. 520–528.
[20] Zhao, P. and Holt, R. A., "Microstructural Evolution and Micro-Texture in Zr-2.5Nb Tubes," *Mater. Sci. Forum*, Vols. 475–479, 2005, pp. 1421–1424.
[21] Li, W., 2009, "Effect of Texture on the Anisotropic Thermal Creep of Pressurized Zr-2.5Nb Tubes," °Ph.D. Thesis, Queen's University, Kingston, Ontario, Canada.
[22] Hutchinson, J. W., "Bounds and Self-Consistent Estimates for Creep of Polycrystalline Materials," *Proct. R. Soc. London, Ser. A*, Vol. 348, 1976, pp. 101–127.

[23] Adams, B. L., "Internal Stress Buildup in SIPA Creep," *J. Nucl. Mater.*, Vol. 115, 1983, pp. 49–55.
[24] Woo, C. H., "Polycrystalline Effects on Irradiation Creep and Growth in Textured Zirconium," *J. Nucl. Mater.*, Vol. 131, 1985, pp. 105–117.
[25] Woo, C. H., "Effect of Intergranular Interaction in the Anistropy of Irradiations Creep and Growth in Zirconium," *Proc. Int. Conf., Materials for Nuclear Reactor Core Applications*, Vol. 1, British Nuclear Energy Society, London, England, 1987, pp. 65–71.
[26] Tomé, C. N., So, C. B., and Woo, C. H., "Self-Consistent Calculation of Steady-State Creep and Growth in Textured Zirconium," *Philos. Mag. A*, Vol. 67, 1993, pp. 917–930.
[27] Turner, P. A., Tomé, C. N., Christodoulou, N., and Woo, C. H., "A Self-Consistent Model for Polycrystals Undergoing Simultaneous Irradiation and Thermal Creep," *Philos. Mag. A*, Vol. 79, 1999, pp. 2505–2524.
[28] Akhtar, A., "Compression of Zirconium Single Crystals Parallel to the c-Axis," *J. Nucl. Mater.*, Vol. 47, 1973, pp. 79–86.
[29] Cai, S., Daymond, M. R., and Holt, R. A., "Modeling the Room Temperature Deformation of a Two-Phase Zirconium Alloy," *Acta Mater.*, Vol. 57, 2009, pp. 407–419.
[30] Griffiths, M., Holt, R. A., Li, J., and Saimoto, S., "Microtexture Analysis of Zr-2.5Nb Pressure Tubing," *Microstructure Sci. ASM International*, Vol. 26, 1998, pp. 293–301.
[31] Turner, P. A., Christodoulou, N., and Tomé, C. N., "Modeling the Mechanical Response of Rolled Zircaloy-2," *Int. J. Plast.*, Vol. 11, 1995, pp. 251–265.
[32] Xu, F., Holt, R. A., and Daymond, M. R., "Modeling Lattice Strain Evolution During Uniaxial Deformation of Textured Zircaloy-2," *Acta Mater.*, Vol. 56, 2008, pp. 3672–3687.
[33] Li, W., Holt, R. A., Daymond, M., and Xu, F., "Influence of Prior Dislocation Structure on Creep Anisotropy of Cold-Worked Zr-2.5Nb tubes," *J. Nucl. Mater.*, submitted, 2010.
[34] Lebensohn, R. A. and Tomé, C. N., "A Self-Consistent Anisotropic Approach for the Simulation of Plastic Deformation and Texture Development of Polycrystals: Application to Zirconium Alloys," *Acta Metall. Mater.*, Vol. 41, 1993, pp. 2611–2624.
[35] Griffiths, M., Sage, D., Holt, R. A., and Tomé, C. N., "Determination of Dislocation Densities in HCP Metals from X-Ray Diffraction Line-Broadening Analysis," *Metall. Mater. Trans. A*, Vol. 33, 2002, pp. 859–865.
[36] Weertman, J., "Theory of Steady-State Creep Based on Dislocation Climb," *J. Appl. Phys.*, Vol. 26, 1955, pp. 1213–1217.
[37] Weertman, J., "Steady-State Creep Through Dislocation Climb," *J. Appl. Phys.*, Vol. 28, 1957, pp. 362–364.
[38] Weertman, J., "Dislocation Climb Theory of Steady-State Creep," *Trans. Am. Soc. Met.*, Vol. 61, 1968, pp. 681–694.
[39] Clausen, B., Brown, D. W., Tomé, C. N., Balogh, L., and Vogel, S. C., "Challenges in Materials Science and Possibilities in 3D and 4D Characterization Technique," *Proc. 31st Annual Ris Symposium on Materials Science*, Ris, Denmark, Sept. 6–10, 2010.
[40] Zaoui, A. and Masson, R., "Micromechanics-Based Modeling of Plastic Polycrystals: an Affine Formulation," *Mater. Sci. Eng., A*, Vol. 285, 2000, pp. 418–424.
[41] Brenner, R., Béchade, J. L., Castelnau, O., and Bacroix, B., "Thermal Creep of Zr–Nb1%–O Alloys: Experimental Analysis and Micromechanical Modelling," *J. Nucl. Mater.*, Vol. 305, 2002, pp. 175–186.

[42] Brenner, R., Masson, R., Castelnau, O., and Zaoui, A., "A 'Quasi-Elastic' Affine Formulation for the Homogenised Behaviour of Nonlinear Viscoelastic Polycrystals and Composites," *Eur. J. Mech. A/Solids*, Vol. 21, 2002, pp. 943–960.

[43] Lebensohn, R. A., Liu, Y., and Ponte Castaneda, P., "On the Accuracy of the Self-Consistent Approximation for Polycrystals: Comparison with Full-Field Numerical Simulations," *Acta Mater.*, Vol. 52, 2004, pp. 5347–5361.

[44] Gilormini, P., Nebozhyn, M. V., and Ponte Castaneda, P., "Accurate Estimates for the Creep Behavior of Hexagonal Polycrystals," *Acta Mater.*, Vol. 49, 2001, pp. 329–337.

DISCUSSION

Question 1, F. Onimus, CEA:—The chosen applied stress shown in this study is 300 MPa. With this high applied stress, all the slip system can be activated. What would be the effect of a lower applied stress and how the model is able to reproduce the behaviour for a lower applied stress?

Author's Response:—The current model calculates the steady state of the creep. The assumed active slip systems are set as the input parameters before running the model. It is assumed that there are no changes on them during steady-state creep deformation at a certain values of applied stress. At the lower stress, it is possible that different assumed slip systems are set to be activated in order to fit and interpret the creep behaviour.

Question 2, Michael Preuss, University of Manchester:—Could you please explain from where you obtained the CRSS data and if they were really attained for test temperature?

Author's Response:—The CRSS ratios were obtained on the basis of the best match with the experimental data. Before setting the selected CRSS ratios for the slip systems, two reference ratios from the previous studies (1:1.25:2.83 from S. Cai and 1:2.6:13 from A. Akhtar in prismatic, basal and pyramidal slips) were applied and the calculated results with them were analysed and compared with the experimental data. The final selected CRSS ratios of 1:1.4:4.1 (which were reasonably consistent with the reference data) were obtained on the basis of the best match with the experimental data.

Question 3, Ron Adamson, Zircology PWS:—How did you obtain the "dislocation density during fabrication" which you used to modify the SELFPOLY7 model?

Author's Response:—The dislocation density during fabrication was obtained by a self consistent polycrystalline model simulation. Firstly, the shear strains for the grains with different orientations were calculated from EPSC model by modelling the cold work process. Secondly, it is assumed the created shear strain in cold work is related to the mobile dislocation density subsequently available for creep, and the dislocation densities of each slip mode are proportional to the total shear strains calculated from the EPSC3. Thirdly, a corresponding relationship was established between the individual orientation and its calculated dislocation structure, which worked as input file for the modified SELFPOLY7 model.

Question 4, Antoine AMBARD, EDF:—1) How do you introduce the shear strain into SELFPOLY? Do you just add the calculated strain coming from EPSC to the creep strain from SELFPOLY or does it (the shear strain) modify internal parameter into your model? (Note that this question is the same with the question 2) Do you take β-phase into account? And is there any difference regarding β-phase distribution in your various alloys?

Author's Response:—1) The shear strains for the grains with different orientations were calculated from EPSC model by modelling the cold work process. It is assumed the simulated shear strain in cold work is related to the mobile dislocation density subsequently available for creep, and the dislocation densities of each slip mode are proportional to the total shear strains calculated from the EPSC3. A corresponding relationship was established between the individual orientation and its calculated dislocation structure. At the last, the results were applied as input for each orientation (or the grains with different orientations) in the modified SELFPOLY7 to take into account of the effect of dislocation structure on the creep.

2) The β-phase is not taken into account in the current calculation. There are some differences regarding to the β-phase distribution in the studied alloys. The first type of distribution is that the

thin film of β-phase is at the boundaries of the elongated α-phase, as is the case of CANDU pressure tubes. The second one is that the β-phase distributed at grain boundaries and corners of the equiaxed α grains. The third is that continuous β-Zr surrounds the Widmanstätten α-plate plates. The FS tubes have the discontinuously distributed β-phase surrounding the flattened α-phase. Complete details of microstructure of the tubes can be found from J. Nucl. Mater. 401 (2010) 25-37 by W. Li and R. A. Holt. To take into account of the β-phase may be another factor to improve the creep anisotropy modelling.

Reprinted from JAI, Vol. 8, No. 2
doi:10.1520/JAI103521
Available online at www.astm.org/JAI

G. A. Bickel,[1] *M. Griffiths,*[1] *A. Douchant,*[1] *S. Douglas,*[1]
O. T. Woo,[1] *and A. Buyers*[1]

Improved Zr-2.5Nb Pressure Tubes for Reduced Diametral Strain in Advanced CANDU Reactors

ABSTRACT: In an Advanced CANDU Reactor (ACR) (ACR is a registered trademark of Atomic Energy of Canada Limited), pressure tubes of cold-worked Zr-2.5Nb materials will be used in the reactor core to contain the fuel bundles and the light water coolant. They will be subjected to higher temperature, pressure, and flux than those in a CANDU (CANDU is a registered trademark of Atomic Energy of Canada Limited) reactor, and accordingly require a thicker wall (6.5 mm for ACR versus 4.2 mm for CANDU). In order to ensure that these tubes will perform acceptably over their 30-year design life in such an environment, a study to model and forecast the performance of these thicker pressure tubes has been undertaken. One of the main requirements for the pressure tube is to have low diametral creep. Based on previous experience with CANDU reactor pressure tube performance and manufacture, an assessment of the grain structure and texture of the ACR pressure tubes indicates that the in-reactor creep deformation will be improved. Analysis of the distribution of texture parameters from a trial batch of 26 tubes shows that the variability is reduced relative to tubes fabricated in the past. This reduction in variability together with a shift to a coarser grain structure will result in a reduction in diametral creep design limits and thus a longer economic life for the fuel channels of the advanced CANDU reactor.

KEYWORDS: zirconium, crystallographic texture, grain thickness, irradiation creep, deformation

Manuscript received October 22, 2010; accepted for publication January 5, 2011; published online January 2011.

[1] Atomic Energy of Canada Ltd., Chalk River, Ontario, Canada.

Cite as: Bickel, G. A., Griffiths, M., Douchant, A., Douglas, S., Woo, O. T. and Buyers, A., "Improved Zr-2.5Nb Pressure Tubes for Reduced Diametral Strain in Advanced CANDU Reactors," *J. ASTM Intl.*, Vol. 8, No. 2. doi:10.1520/JAI103521.

Copyright © 2011 by ASTM International, 100 Barr Harbor Drive, PO Box C700, West Conshohocken, PA 19428-2959.

Introduction

The pressure tubes designed for use in the advanced CANDU reactor are made from Zr-2.5Nb. The tubes are fabricated by a two-stage forging process to convert cast ingots into logs that are then hollowed to produce billets suitable for extrusion. The billets are extruded in the $\alpha + \beta$ phase and cold worked to produce tubes that are approximately 117 mm outer diameter and 104 mm inner diameter. These tubes are stress relieved prior to installation in a CANDU reactor. During service these pressure tubes operate with coolant temperatures between about 275 and 321°C, and at coolant pressures of about 12 MPa corresponding to hoop stresses in the tubes of about 100 MPa. The maximum flux of fast neutrons in the pressure tubes from the fuel is about $3.8 \times 10^{17}\ \mathrm{n \cdot m^{-2} \cdot s^{-1}}$. The performance of the pressure tubes during operation is a function of the fabrication history of the tubes and the operating conditions, both of which vary.

The manufacturing sequence is summarized as follows:

(1) Separating hafnium and other impurities from zirconium with a solvent extraction process;
(2) Producing impure zirconium tetrachloride by heating zirconium oxide in the presence of coke and chlorine;
(3) Reducing the zirconium tetrachloride to pure zirconium by vapor reaction with magnesium under inert gas, heating the resulting mixture of pure zirconium and magnesium chloride in vacuum to evaporate magnesium chloride, and then obtaining zirconium sponge;
(4) Crushing and inspecting the sponge, compacting it with appropriate additions of alloying elements, and welding together the compacts and recycled material;
(5) Quadruple vacuum arc melting the welded consumable-electrode to consolidate, refine, and homogenize the zirconium alloy into a final ingot;
(6) Cutting the ingot into three sections that are individually preheated into the β phase and then press forged;
(7) Rotary forging into logs after reheating in the $\alpha + \beta$ phase field;
(8) Cutting the logs into billets;
(9) Hot piercing or machining to generate a centre hole in each billet;
(10) Solution annealing in the β phase and quenching of the hollow billets, followed by final machining to produce billets ready for hot extrusion;
(11) Copper-cladding the billets with a thin steel layer between the copper and the zirconium to prevent zirconium-copper alloying;
(12) Extruding the hollow billets in the $\alpha + \beta$ phase;
(13) Cold drawing, also described as cold work, to reduce the wall thickness to specification;
(14) Honing inside surface and grinding outside surface;
(15) Pickling and cleaning; and
(16) Autoclaving to stress relieve the tube and provide a protective oxide layer on the surface.

These steps are generic to modern manufacturing practice and largely differ from the historical pressure tube manufacturing by evolutionary improvements

to process control. The only process steps that have significantly changed are the number of melts to produce ingots and β-quenching. Some very early tubes were made from double melted ingots and not β-quenched, later billets from double melted ingots were quenched as solids, and the modern tubes are made from quadruple melted ingots with a β-quench at the hollow billet stage. The quadruple melting reduces the levels of volatile impurities and the β-quenching provided a reduction in the tube-to-tube variability. Although the ACR tubes are thicker than standard CANDU tubes, the extrusion ratio, extrusion speed, and extrusion temperature are nominally the same for both.

For a given set of operating conditions there is considerable variability in deformation behavior of pressure tubes that can be related to variations in the as-fabricated microstructure [1–4]. Texture and grain thickness can affect both the anisotropy and magnitude of deformation strain. In general, pressure tubes that have a higher radial basal texture parameter or Kearns factor, f_R [5], and have grains that are thinner in the radial direction tend to exhibit higher diametral strain and lower elongation rates compared with the average [2–4]. These same microstructural variables affect the deformation behavior along a given tube because of a gradual change in grain structure and crystallographic texture from one end of the tube to the other. The primary cause of the difference in microstructure along a given tube is the temperature change during the extrusion process. This end-to-end variation itself varies from tube-to-tube, due to variations in extrusion conditions from one extrusion run to the next, and also due to variations in ingot chemistry and billet processing.

The diametral expansion and elongation rates of pressure tubes in CANDU reactors due to irradiation deformation are important properties that limit the useful life of the reactor and the maximum power level for reactor operation. Diametral expansion, in particular, is the main life-limiting factor for the ACR reactor. The deformation rates are a direct function of the microstructure (for example, crystallographic texture and grain size) and operating conditions (stress, temperature, and neutron flux), but are also indirectly dependent on the operating conditions because of the modifying effects of the irradiation on the microstructure [6–10]. Therefore, the in-reactor deformation behavior of pressure tubes is controlled both by the as-fabricated microstructure and the microstructure that evolves during irradiation. Over many years, data concerning the in-reactor deformation behavior has been accumulating from thousands of pressure tubes operating in CANDU reactors. Many of these tubes were commissioned before 1980 and have now either been decommissioned or are near end-of-life; these are called historical CANDU pressure tubes in this paper. Accordingly, a significant share of the data comes from these historical CANDU pressure tubes. More recently, large numbers of tubes have been manufactured for replacements and refurbishment of these same reactors; these are called recent CANDU pressure tubes in this paper. The data concerning deformation behavior of these younger tubes is much less extensive than from the historical CANDU pressure tubes.

Previous work has shown by statistical analysis how manufacturing variables and microstructure are related to the in-reactor deformation behavior of pressure tubes with a focus on diametral creep [1] in one case and elongation in

another [2,3]. This current work utilizes the information and understanding gleaned from these earlier studies to show how pressure tubes produced for the Advanced CANDU Reactor (ACR) design will have improved diametral creep characteristics compared with conventional pressure tubes. The key difference between the CANDU pressure tube design and ACR pressure tube design is the wall thickness; 4.2 mm for CANDU tubes and 6.5 mm for ACR tubes. The larger wall thickness is intended to reduce the stresses in the tubes and therefore lower the creep rates that would be too high at the ACR operating temperatures. However, additional gains are also realized because of improvements in the microstructure. The primary focus of this paper is to show how the design targets for diametral strain are being achieved based on the ACR pressure tube microstructure.

Results

The microstructure of CANDU reactor pressure tubes consists of elongated, platelet-like grains of hexagonal-close-packed (hcp) α–Zr, partially surrounded by a thin network of filaments of body-centred-cubic β–Zr. These β–Zr filaments are metastable and initially contain about 20 % Nb. The stress-relief treatment results in partial decomposition of the β–Zr filaments with the formation of hcp ω-phase particles that are low in Nb, surrounded by an Nb-enriched β–Zr matrix [6]. Transmission electron micrographs of typical microstructures for CANDU and advanced CANDU reactor pressure tubes looking along the tube are shown in Fig. 1. The microstructures are very similar in appearance and have to be characterized by detailed measurements of many thousands of grains from multiple pressure tubes.

The microstructural parameters used to characterize the pressure tube material are minimum grain thickness, measured using transmission or scanning electron microscopy, and Kearns' texture parameters, measured by X-ray diffraction (XRD), for each of the three principle directions of the pressure tube, Fig. 2. The hcp α–Zr grains are oriented with their unique **c**-axes aligned in the radial-transverse plane but mostly tilted towards the transverse direction as illustrated in Fig. 2. For this reason the largest texture parameter is always obtained for the transverse direction.

The minimum dimension grain thickness measurements are currently considered to be the most reliable quantitative measure for describing differences in grain morphology [1]. This measurement method has been completed from transmission electron microscope (TEM) carbon replica images of back[2] offcut[3] material from 23 historical CANDU pressure tubes and compiled in Table 1. The distance of the minimum grain dimension is measured manually at approximately 1 μm intervals for each recognizable grain (to account for the fact that

[2]The tube front-end exits the extrusion press first and the back-end exits the extrusion press last.
[3]An offcut is the excess material trimmed from both tube ends to meet dimensionality requirements.

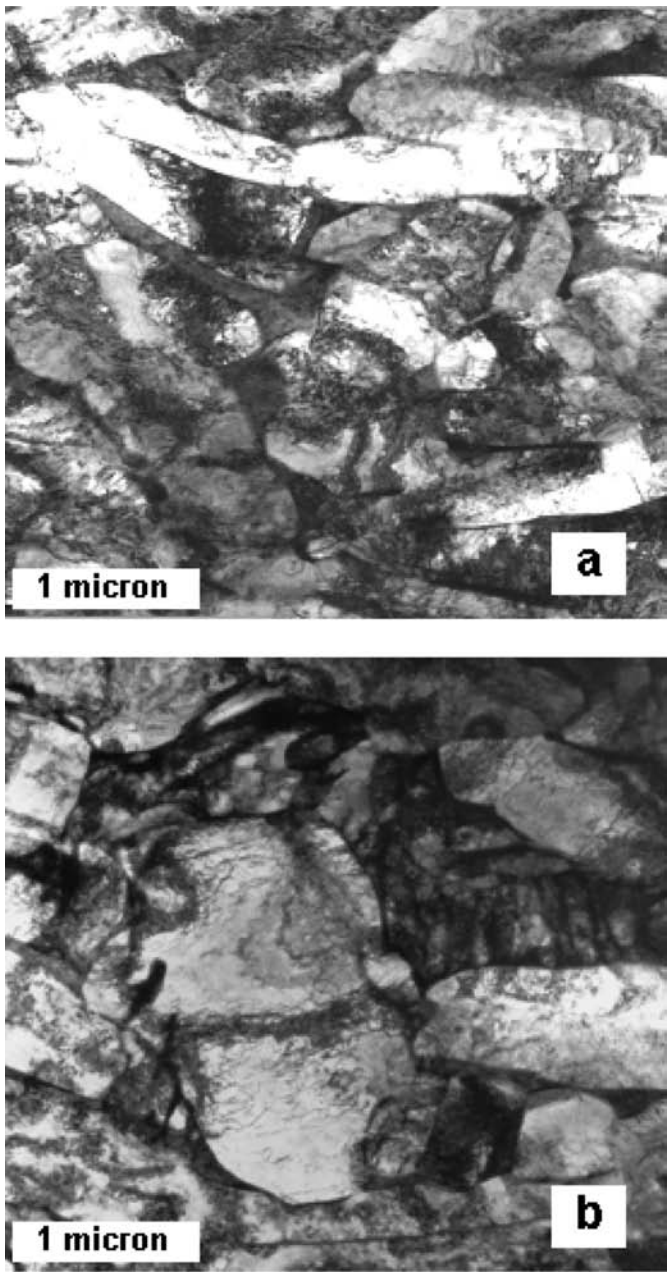


FIG. 1—*Typical TEM micrographs illustrating microstructure for: (a) ACR pressure tubing; (b) CANDU pressure tubing. The specimens are taken from the front-ends of the finished extruded tubes looking down the longitudinal axis.*

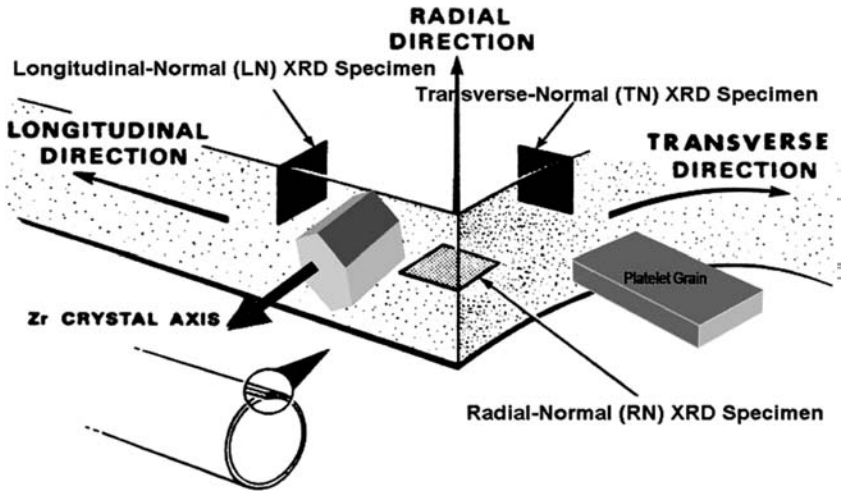


FIG. 2—*Schematic illustration of principal directions, orientation of XRD samples, main crystallographic orientations, and typical grain morphology for a Zr-2.5Nb pressure tube.*

there is a large variation in grain widths) and the distribution of these minimum grain thickness values is averaged to determine the mean value of the minimum grain thickness. More recent measurements from scanning electron microscope (SEM) images are also compiled along with the earlier TEM measurements in Table 1. These later SEM measurements should in principle be commensurate with the TEM carbon replicas but there is potential for bias between these sets of measurements. Texture analysis was performed by XRD on these same pressure tubes and the Kearns radial texture parameters (f_R) [5] are also listed in Table 1.

Multivariate Relationships

Texture and grain size are considered to be the key microstructural variables that explain diametral strain in CANDU pressure tubes. Although dislocation density might also be a factor to consider, previous work [1] has shown that it is not a significant variable for the pressure tubes manufactured according to the scheme outlined in the introduction. Other variables could be considered such as elemental impurity levels but these are regarded as indirectly explanatory variables, i.e., such variables may affect the grain structure and perhaps play a role in the development of texture during extrusion but the deformation is ultimately explained by the resultant texture and grain size. Texture and grain size also tend to be correlated as a result of the extrusion process [2–4]. Comparing the front and back-ends of the tube reveals the most prominent correlation; front-ends show larger grain thickness and lower radial texture than back-ends (Figs. 3 and 4).

It is therefore important to look at the effects of texture and grain thickness simultaneously. Figure 5 shows a three-dimensional (3D) plot of the diametral

TABLE 1—*Radial grain thickness, radial texture, and diametral strain residual inputs corresponding with the back-ends of historical CANDU Zr-2.5Nb pressure tubes.*

Tube Serial Number	Back Radial Texture f_R	Back Arithmetic Mean (Microns)		Measured/Predicted Diametral Strain Residual[c]
		TEM[a]	SEM[b]	
012	0.355	0.332		0.841
062	0.375	0.342		0.848
088	0.321	0.362		0.961
098	0.337	0.324		1.144
169	0.309	0.387		0.640
258	0.352	0.461		0.829
308	0.349	0.423		0.768
350	0.355	0.396		0.758
054	0.365	0.426		0.972
063	0.305	0.331		0.781
104	0.306	0.333		0.971
184	0.363	0.35		0.843
218	0.421	0.247		1.312
283	0.373	0.321		1.253
287	0.315	0.311		1.021
382	0.378	0.312		0.968
136	0.317	0.386		0.813
156	0.339	0.268		1.172
160	0.368	0.355		0.986
196	0.356	0.345		1.123
201	0.368	0.315		1.213
316	0.338	0.362		0.679
340	0.347	0.324		0.948
001[d]	0.383		0.291	0.853
014[d]	0.350		0.352	0.703
027[d]	0.362		0.329	0.758
024[d]	0.405		0.180	1.544
028[d]	0.403		0.184	1.469

[a]Mean value of minimum grain thickness distribution on carbon replicas by TEM.
[b]Mean value of minimum grain thickness distribution from images by SEM.
[c]Calculated using model of Ref 11.
[d]Tubes from manufacturing routes where the extrusion ratio and cold work process was modified 13.

strain dependence on grain thickness and radial texture. As a result of the manufacturing process, texture and grain thickness tend to be correlated: In this population sample the data cluster along the plane diagonally bisecting the f_R and grain thickness axes. Figure 5 shows only the back-end grain thickness and

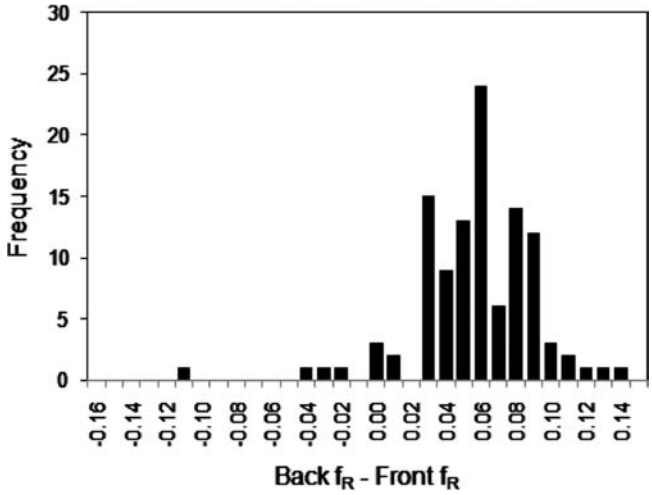


FIG. 3—*Distribution of differences between back-end and front-end radial texture parameter on individual historical CANDU pressure tubes. The tube back-end generally has a higher radial texture than the front-end.*

texture measurements taken from Table 1. Radial texture, f_R (in contrast to the transverse or longitudinal texture parameters) is chosen as the figure-of-merit for texture because it tends to give the cleanest correlations with deformation. The z-axis in Fig. 5 is the diametral strain residual after regressing out the effect of operating conditions for a given nominal (not average) pressure tube using a

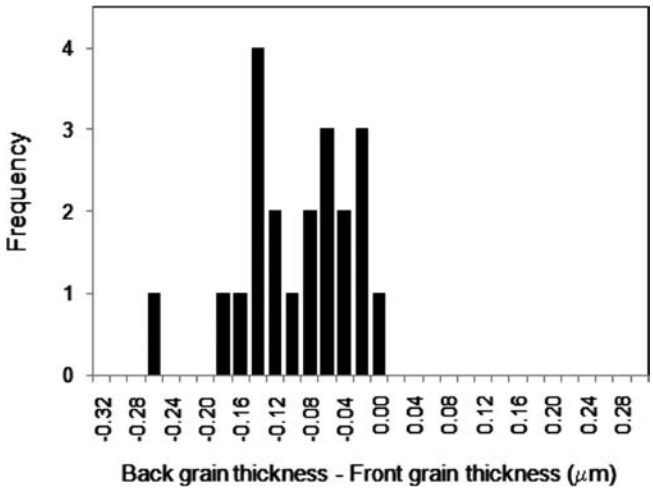


FIG. 4—*Distribution of differences between back-end and front-end mean grain thickness on individual historical CANDU pressure. The tube front-end always has a larger mean grain thickness than the back-end.*

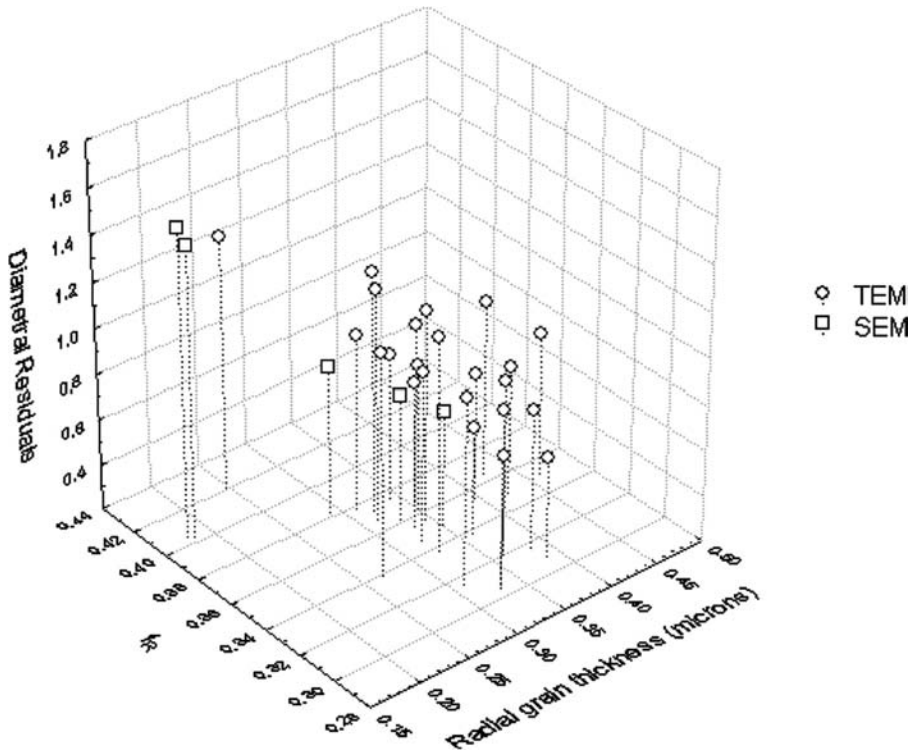


FIG. 5—*Diametral residuals (measured/predicted at the operating conditions appropriate for the ACR maximum strain location) as a function of the Kearn's radial texture parameter and the mean radial grain thickness (both from the back-end offcut). Drop lines terminating on the f_R-grain thickness plane are included to help visualize the 3D perspective.*

model that has been described previously [11]. These residuals are tabulated in Table 1 together with the texture and grain size variables.

The residuals plotted in Fig. 5 should reflect the dependence of diametral strain on texture and grain thickness that is not already captured in the deformation model. However, if the model does not perfectly capture the operating conditions, such a residual analysis could falsely attribute model biases to a material property effect. Caution must be exercised when drawing conclusions from such an analysis. However, use of one other unpublished empirical model showed very similar grain thickness and texture dependence, thus supporting the premise that the residuals describe the remaining material variability including grain thickness and texture. Fitting the residuals in Fig. 5 may provide the prediction and the uncertainty for the residual diametral strain dependence on texture and grain thickness. From this fit, the model bias can be determined for a given texture and grain thickness, and a better estimate of the predicted diametral strain can thereby be made. Figure 6 shows the fitted surface to the

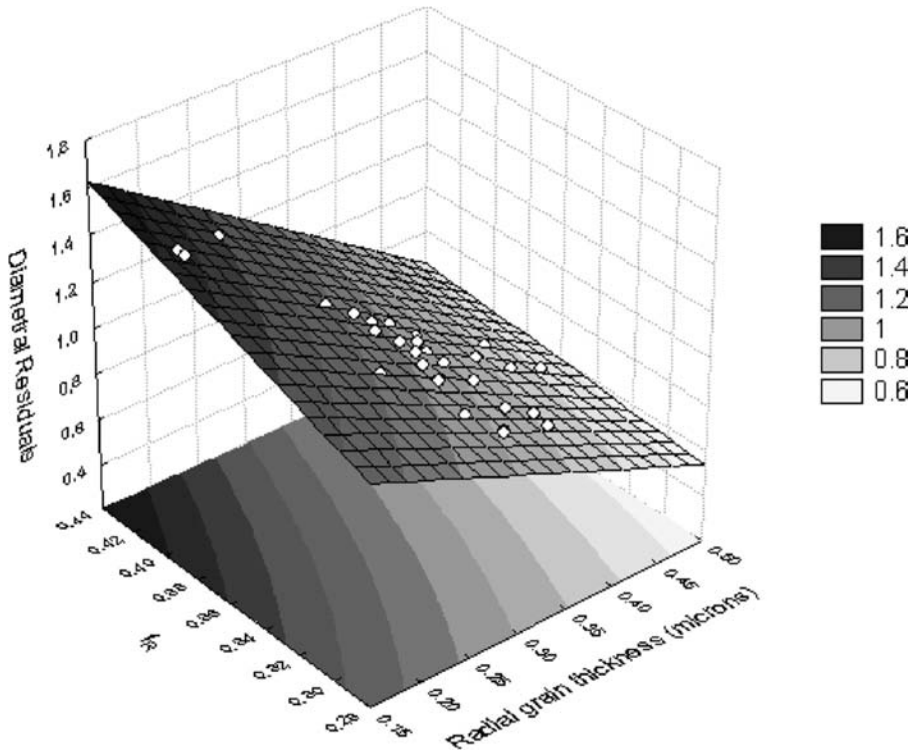


FIG. 6—*Diametral residuals (measured/predicted) fitted surface as a function of Kearn's radial texture parameter and the mean radial grain thickness. White dots locate the predicted value of the diametral residuals for the observed texture and grain thickness. Fitting results tabulated in Table 2.*

data from Fig. 5. This surface accurately captures the trends within the measurement residuals but should not be used for extrapolation too far outside the range of measurements. The fitted model and the fitting statistics for radial texture, grain thickness, and diametral strain of these historical CANDU tubes are compiled in Table 2.

Back-End Diametral Strain of ACR Pressure Tubes

For this study, a model intended to apply to pressure tubes under typical CANDU operating conditions [11] is used to predict the diametral strain that would be experienced if the texture and grain thickness were changed to that expected for actual ACR pressure tubes in the higher temperature ACR design. The ACR diametral strain maximum occurs close to the inlet[4] and has operating

[4]The inlet refers to the fuel channel end where the coolant enters the pressure tube. The outlet refers to the end of the fuel channel where the heated coolant exits the pressure tube.

TABLE 2—*Fitting statistics and results for historical CANDU pressure tubes.*

N (number of observations)				28
Degrees of freedom				25
$\mathbf{R^2}$ (adjusted multiple-correlation coefficient)				0.57035
$\mathbf{s^2}$ (squared standard deviation of the regression)				0.02245
Model: Diametral residual $= a_0 + a_1 \cdot f_R + a_2 \cdot f_R \cdot$ mean grain thickness				
Parameter	Value	sd	τ	$p(\tau)$
a_0	0.3414	0.40522	0.842	0.41
a_1	3.8685	0.97845	3.954	0.00056
a_2	−6.3149	1.42868	4.420	0.00017

Note: sd = standard deviation; τ = studentτs t-value for the parameter being different from zero; and $p(\tau)$ = probability that τ could be at least this large by chance.

conditions that overlap the historical CANDU tubes at their outlet location; the CANDU model can be applied with validity to ACR conditions at the location of the strain maximum. Furthermore, the back-end of the pressure tube is located at the inlet in the ACR design and the back-ends of the historical CANDU pressure tubes used in this study are at the outlet. This study is therefore limited to the back-end of the pressure tube under very similar operating conditions (the ACR tube strain maximum location referenced to the CANDU tube outlet). The historical CANDU tubes have a mean radial texture, f_R, of 0.353±0.025 at the back-end. For the ACR tubes, the radial texture has a similar mean but with much less variance as observed: $f_R = 0.356 \pm 0.009$ at the back-end (Table 4). A comparison of these f_R distributions are shown in Fig. 7.

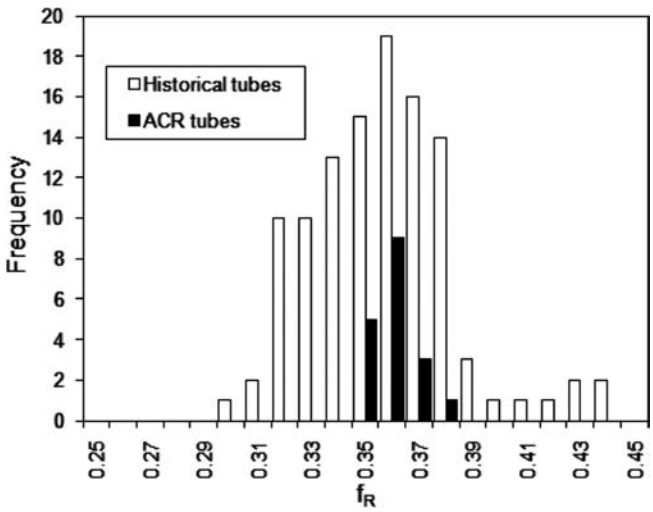


FIG. 7—*Distribution of the back radial texture parameter for the historical CANDU tubes and recent ACR tubes.*

TABLE 3—*Arithmetic mean radial grain thickness for back-end of ACR pressure tubes.*

Tube	Mid-Wall Grain Thickness (Microns)	Ingot
ACR-1	0.443	A
ACR-12	0.414	B
ACR-13	0.402	B
ACR-14	0.495	B
ACR-15	0.409	B
Average	0.433	
sd	0.038	

The radial grain thickness for the back-ends of the ACR tubes (Table 3) were, in general, coarser than the radial grain thickness of the CANDU reactor pressure tubes (Table 1). The mean value of the five grain thickness determinations of ACR qualification tubes is 0.433 μm (Table 3) compared to the mean value from 23 CANDU tubes (TEM determinations in Table 1) which is 0.348 μm. From this, it is straightforward to substitute these independent variables into the model equation of Table 2 giving a diametral strain residual of 0.931 ± 0.029 for the CANDU fleet tubes compared with 0.745 ± 0.060 for the ACR pressure tube.

Using 436 CANDU tubes for comparison between measured diametral strain and the calculated strain using the model outlined in Ref [11, the code over-predicts diametral strain at the ACR maximum strain location by 0.002 72 after 27 years of full power. This over-prediction is about 8 % of the calculated strain. Since not all tubes have both grain thickness and texture measured, only a small subset (Table 1) of these tubes with diametral gaugings could be used to develop the dependence of diametral strain on texture and grain thickness (section "Multivariate Relationships"). Nevertheless, with this smaller data set, the model over-predicts the diametral strain by about 7 %, a value quite close to the larger data set. The small data set (in Table 1) is thus deemed representative of the larger.

The residual of 0.931 (7 %) at conditions representing the ACR maximum strain location numerically corresponds to an over-prediction of 0.002 38 strain after 27 years. Shifting the prediction for the ACR strain maximum location to account for the ACR grain thickness and texture lowers the residual to 0.745 (25 %) and increases the diametral strain over-prediction to 0.0085 strain after 27 years. Hence the new ACR tubes are anticipated to creep slower for this new texture and grain thickness combination and the prediction using the model described in Ref [11 is expected to be biased by 25 % (instead of just 7 % for the average of the CANDU pressure tube data set). This means that there is an additional 18 % lower diametral strain predicted for ACR tubes relative to the average CANDU pressure tube. The underlying variability for the CANDU reactor tubes is $\pm 0.005\,15$ after 27 years. This should be combined in quadrature with the uncertainty of the bias from the residual fit evaluated at the ACR grain thickness and texture:

TABLE 4—*Radial texture parameters used for assessing material variability.*

Historical CANDU			Recent CANDU			ACR		
Tube Number	Front f_R	Back f_R	Tube Number	Front f_R	Back f_R	Tube Number	Front f_R	Back f_R
002	0.298	0.380	001	0.343	0.366		Ingot A	
023	0.282	0.340	012	0.309	0.354	ACR-1	0.296	0.363
061	0.285	0.312	014	0.328	0.356	ACR-2	0.307	0.344
151	0.276	0.358	016	0.332	0.367	ACR-3	0.288	0.342
166	0.322	0.373	020	0.325	0.385	ACR-4	0.308	0.357
221	0.308	0.353	029	0.320	0.356	ACR-5	0.306	0.356
236	0.315	0.370	031	0.307	0.365	ACR-6	0.321	0.376
258	0.333	0.378	032	0.330	0.361	ACR-7	0.296	0.354
283	0.298	0.373	034	0.311	0.352	ACR-8	0.308	0.359
346	0.331	0.368	037	0.336	Not measured	ACR-9	0.310	0.359
008	0.301	0.361	038	0.311	0.361		Ingot B	
042	0.344	0.312	041	0.318	0.373	ACR-12	0.331	0.361
048	0.311	0.348	045	0.330	0.356	ACR-14	0.332	0.351
055	0.294	0.345	051	0.336	0.374	ACR-16	0.329	0.351
079	0.293	0.349	053	0.322	0.373	ACR-17	0.320	0.344
094	0.322	0.364	060	0.307	0.366	ACR-18	0.348	0.350
127	0.296	0.316	065	0.323	0.382	ACR-19	0.330	0.350
155	0.264	0.322	075	0.311	0.375	ACR-20	0.335	0.358
196	0.300	0.356	080	0.340	0.380	ACR-21	0.344	0.358
233	0.311	0.371	097	0.319	0.363	ACR-22	0.346	0.367
			099	0.327	0.359			
			118	0.316	0.354			
			141	0.312	0.367			

TABLE 4—*Continued*

Historical CANDU			Recent CANDU			ACR		

TABLE 4—*Continued*

Tube Number	Front f_R	Back f_R	Tube Number	Front f_R	Back f_R	Tube Number	Front f_R	Back f_R
			161	0.309	0.354			
			181	0.322	0.347			
			205	0.326	0.365			
			222	0.323	0.361			
			240	0.315	0.347			
			297	0.288	0.307			
			300	0.331	0.359			
			303	0.346	0.355			
			306	0.317	0.322			
			342	0.336	0.368			
			354	Not measured	0.348			
			355	0.312	0.363			

$$\sqrt{\left(0.060 \cdot \frac{0.002\,72}{0.08}\right)^2 + (0.005\,15)^2}$$

which leads to a bias and uncertainty of $-0.0085 \pm 0.005\,54$ (one sigma) for the ACR maximum strain location assuming the same degree of material variability for ACR tubes as CANDU tubes.

Material/Microstructural Variability of ACR Pressure Tubes

It is expected that improvements in the manufacturing specifications and better process control for the ACR tubes should reduce the variability in deformation behavior and therefore the engineering design limits. As the properties of pressure tubes depends on their microstructures the likely changes in diametral strain variability can be assessed by studying the texture variability of modern tubes, which is significantly lower than the historical tubes on which the above analysis was based.

It is assumed here that texture variability can be a surrogate for all microstructure variability. Indeed, for elongation, f_R accounts for the majority of the observed elongation variability [2,3]. Both f_R and elongation variability have been reduced significantly for modern era pressure tubes [2,3,12]. The same improvement in variability is expected to hold for diametral strain. The bias and uncertainty estimate for ACR pressure tubes in section "Back-End Diametral Strain of ACR Pressure Tubes" utilized a fit to historical pressure tubes. If the ACR pressure tubes are expected to exhibit less variability, then the uncertainty estimate from section "Back-End Diametral Strain of ACR Pressure Tubes" should be adjusted. In this study, the radial texture distribution for the population of historical CANDU pressure tubes is compared with the radial texture distribution of the ACR qualification tubes and other recent tubes (Table 4). Accordingly, the appropriate uncertainty estimate can be updated.

The f_R distributions for the historical CANDU tubes are plotted in Fig. 8(*a*) for both the front and the back-ends. The front $f_R = 0.312 \pm 0.026$ and the back $f_R = 0.353 \pm 0.025$. The f_R distribution for one of the most recent production orders tabulated in Table 4 and shown in Fig. 8(*b*) indicates considerably less population variance. For these recent CANDU tubes the front $f_R = 0.322 \pm 0.012$ and the back $f_R = 0.360 \pm 0.015$. That is a reduction in texture variability of $> 50\,\%$ at the front-end and 40 % at the back-end.

A limited set of textures is available for ACR tubes (Table 4). The f_R distribution for tubes from these two ingots combined is shown in Fig. 8(*c*). The front f_R mean is 0.320 with a population standard deviation of ± 0.018 and the back $f_R = 0.356$ with a population standard deviation of ± 0.009. It is only two ingots so it will be subject to sampling error problems and that may explain the increase in spread on the front end compared to the recent CANDU tubes which are averaged over a lot more than just two ingots (for the same reason the population standard deviation of ± 0.009 on the back-end might not be realistic and could increase with more data). The ACR pressure tubes show an f_R variability that is consistent with the recent CANDU tubes. Accordingly, the f_R distribution for the more numerous recent CANDU tubes (Fig. 8(*b*)) are used for updating

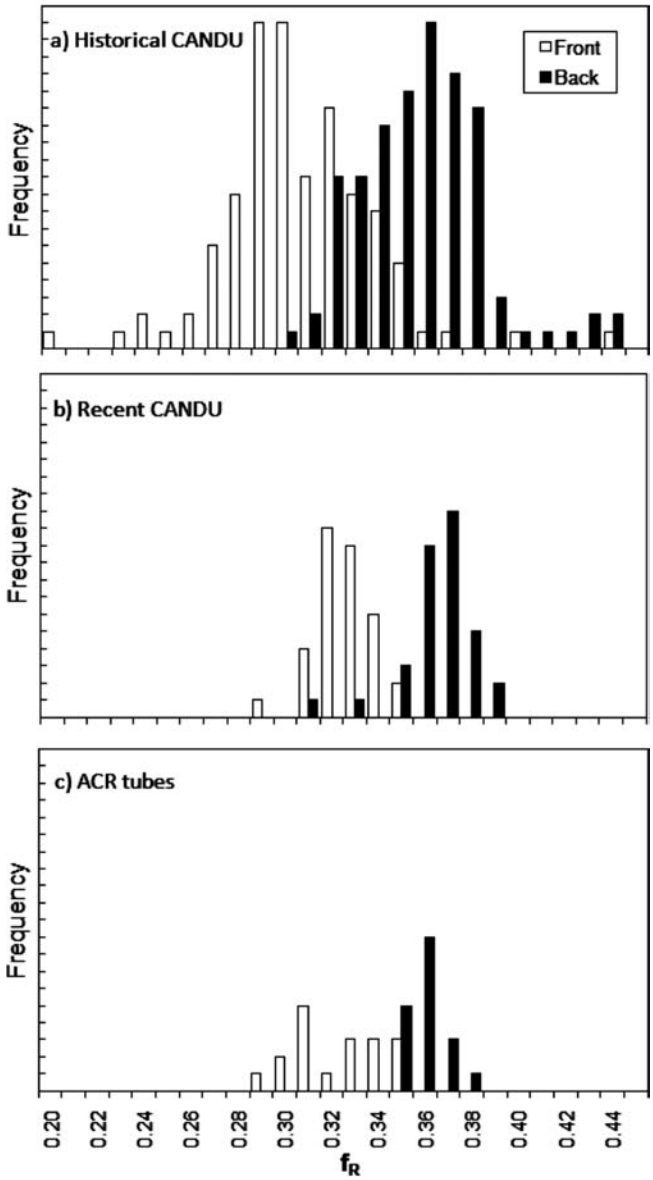


FIG. 8—*Radial texture parameter distribution for the front and back of (a) historical CANDU tubes; (b) recent CANDU tubes; and (c) ACR tubes.*

the uncertainty in the next paragraph. In as much as the reduction in texture variability represents the improvement in deformation variability, the back-end of the ACR tubes should exhibit a 40 % reduction in variability as compared to the historical tubes used to establish the uncertainty in section "Back-End Diametral Strain of ACR Pressure Tubes."

In section "Back-End Diametral Strain of ACR Pressure Tubes" the CANDU model bias resulting from a change in grain thickness for ACR pressure tubes was calculated, and the bias and uncertainty was derived for the maximum strain location. With the additional effect from the reduction in texture variability the estimated uncertainty must be combined in quadrature with the uncertainty from the residual fit evaluated at the ACR grain thickness and texture, leading to an updated uncertainty of

$$\sqrt{\left(0.060 \cdot \frac{0.002\,72}{0.08}\right)^2 + \left(\frac{0.015}{0.025} \cdot 0.005\,15\right)^2} \rightarrow \pm 0.003\,71 \text{ (one sigma)}$$

for the ACR maximum strain location.

Figure 9 shows the bias attributed to the coarser grain size of the ACR pressure tube and the effect of reducing uncertainty on the predicted diametral strain of an ACR pressure tube relative to the model derived for CANDU pressure tubes. Figure 9 shows that a significant improvement in diametral strain and variability is anticipated for ACR tubes when compared to the strain observed for historical CANDU pressure tubes.

Discussion

Over the past 25 years there have been a number of different initiatives and improvements in Zr-2.5Nb pressure tube manufacturing that have been reported [12–14]. Improvements related to fracture, delayed-hydride-cracking, corrosion, and deuterium pick-up were largely achieved through control of alloying elements and impurities [14]. Tailoring the microstructure through manufacturing to control the mechanical properties [12] and deformation

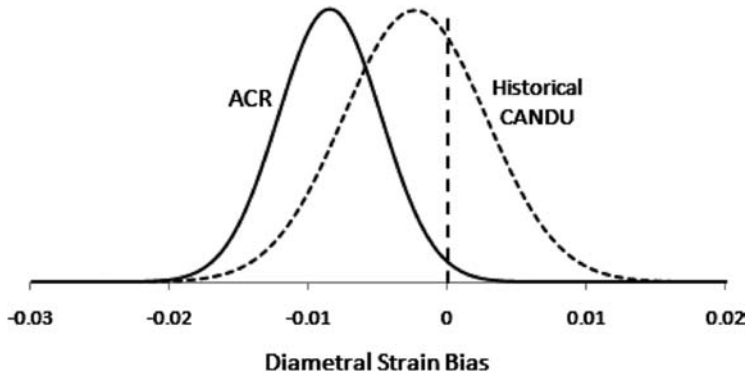


FIG. 9—*Probability density function of the updated bias expected for the ACR pressure tube prediction at end-of-life compared to historical pressure tubes. The variability (width) of the ACR tubes is lower than the variability of the historical CANDU tubes. A negative bias means that the tubes will strain less than the model prediction (vertical line).*

behavior [13] has also been addressed. However, there is often a trade-off between improving one property or component of deformation with another property or component of deformation. For example, creating tubes to reduce elongation [13] has resulted in higher diametral creep [4]. Adopting a quadruple melting practice to reduce volatile impurities such as chlorine to improve fracture toughness [15] also affects the texture [2,3], and this could influence other properties including deformation behavior.

More recent work showed that the two main microstructural variables that correlated with diametral strain for in-service CANDU reactor pressure tubes were grain thickness and texture. It was shown that in order to avoid high diametral strain one would aim to fabricate pressure tubes with grain thickness $> 0.3\,\mu$m and with the lowest possible radial basal texture parameters [1]. Corresponding but opposite correlations with texture have been observed for elongation [2–4]. Grain structure, in particular, appears to have significant effects on diametral strain at the pressure tube back-end (the end leaving the extrusion press last) and this is because of the non-linear effect of grain size (greater dependence of diametral creep at small grain thickness) [1].

The grain size of ACR pressure tubing is generally coarser than CANDU pressure tubes. One possible explanation for this is due to the slower cooling rate after extrusion for the thicker tube (6.5 mm wall thickness for ACR compared with 4.2 mm for a CANDU pressure tube); this may limit nucleation of new alpha-phase grains and therefore promote grain growth/coarsening of existing alpha-phase grains [16]. Alternatively, for similar reasons, the larger billets may favor having a coarser grain structure and a coarser grain structure in the billet results in a coarser grain structure in the final pressure tube [17]. From the point of view of improving diametral creep, therefore, a shift to thicker pressure tubes is likely to result in coarser grain structures without any significant effect on texture.

Conclusions

ACR pressure tubes are predicted to exhibit approximately 18 % less diametral strain at ACR operating conditions near the maximum strain location compared to an average CANDU pressure tube. This benefit is gained from a coarser grain size in the finished tube which is likely the result of billet processing and slower cooling rates in the as-extruded tube. Uncertainty limits due to microstructural variability have been reduced by 40 % for ACR pressure tubes (and current production pressure tubes) due to improved process control in modern manufacturing. Both the change in microstructure and the reduced variability have made a significant improvement in the predicted diametral strain for the ACR reactor.

Acknowledgments

The writers would like to thank Xuejun Wei, Simon Kim, Kit Coleman, and Jim Theaker for various contributions to the development of this paper.

References

[1] Griffiths, M., Davies, W. G., Causey, A. R., Moan, G. D., Holt, R. A., and Aldridge, S. A., "Variability of In-Reactor Diametral Deformation for Zr-2.5Nb Pressure Tubing," *Zirconium in the Nuclear Industry: 13th International Symposium, ASTM STP 1423*, G. D. Moan and P. Rudling, Eds., Annecy, France, June 2001, ASTM International, West Conshohocken, PA, 2002, pp. 796–810.

[2] Bickel, G. A. and Griffiths, M., "Manufacturing Variability, Microstructure and Deformation of Zr-2.5Nb Pressure Tubes," *J. ASTM Int.*, Vol. 4, No. 10, 2007, Paper ID JAI101126.10.1520/JAI103521.

[3] Bickel, G. A. and Griffiths, M., "Manufacturing Variability, Microstructure and Deformation of Zr-2.5Nb Pressure Tubes," *Zirconium in the Nuclear Industry: 15th International Symposium, ASTM STP 1505*, B. Kammenzind and M. Limback, Eds., Sunriver, OR, June 2007, ASTM International, West Conshohocken, PA, 2009, pp. 529–540.

[4] Bickel, G. A. and Griffiths, M., "Manufacturing Variability and Deformation for Zr-2.5Nb Pressure Tubes," *J. Nucl. Mater.*, Vol. 383, 2008, pp. 9–13.

[5] Kearns, J. J., "Thermal Expansion and Preferred Orientation in Zircaloy," Report No. WAPD-TM-472, Bettis Atomic Power Laboratory, Pittsburgh, PA, November 1965.

[6] Griffiths, M., Mecke, J. F., and Winegar, J. E., "Evolution of Microstructure in Zirconium Alloys During Irradiation," *Zirconium in the Nuclear Industry: 11th International Symposium, ASTM STP 1295*, E. R. Bradley and G. P. Sabol, Eds., Garmisch-Partenkirchen, Germany, Sept. 1995, ASTM International, West Conshohocken, PA, 1996, pp. 580–602.

[7] Griffiths, M., Wang, N., Buyers, A., and Donohue, S. A., "Effect of Irradiation Damage on the Deformation Properties of Zr-2.5Nb Pressure Tubes," *J. ASTM Int.*, Vol. **5**, No. 1, 2008, Paper ID: JAI101133.

[8] Griffiths, M., Wang, N., Buyers, A., and Donohue, S. A., "Effect of Irradiation Damage on the Deformation Properties of Zr-2.5Nb Pressure Tubes," *Zirconium in the Nuclear Industry: 15th International Symposium, ASTM STP 1505*, B. Kammenzind and M. Limback, Eds., Sunriver, OR, June 2007, ASTM International, West Conshohocken, PA, 2009, pp. 541–549.

[9] Griffiths, M., Christodoulou, N., and Donohue, S. A., "Damage Dependence of Irradiation Deformation of Zr-2.5Nb Pressure Tubes," *J. ASTM Int.*, Vol. **2**, No. 7, 2005, Paper ID: JAI12432.

[10] Griffiths, M., Christodoulou, N., and Donohue, S. A., "Damage Dependence of Irradiation Deformation of Zr-2.5Nb Pressure Tubes," *Zirconium in the Nuclear Industry: 14th International Symposium, ASTM STP 1467*, P. Rudling and B. Kammenzind, Eds., Stockholm, Sweden, June 2004, ASTM International, West Conshohocken, PA, 2005, pp. 686–708.

[11] Christodoulou, N., Causey, A. R., Holt, R. A., Tomé, C. N., Badie, N., Klassen, R. J., Sauvé, R., and Woo, C. H., "Modeling In-Reactor Deformation of Zr-2.5Nb Pressure Tubes in CANDU Power Reactors," *Zirconium in the Nuclear Industry: 11th International Symposium, ASTM STP 1295*, E. R. Bradley and G. P. Sabol, Eds., Garmisch-Partenkirchen, Germany, Sept. 1995, ASTM International, West Conshohocken, PA, 1996, pp. 518–537.

[12] Choubey, R., Aldridge, S. A., Theaker, J. R., Cann, C. D., and Coleman, C. E., "Effects of Extrusion-Billet Preheating on the Microstructure and Properties of Zr-2.5Nb Pressure Tube Materials," *Zirconium in the Nuclear Industry: 11th International Symposium, ASTM STP 1295*, E. R. Bradley and G. P. Sabol, Eds., Garmisch-

Partenkirchen, Germany, Sept. 1995, ASTM International, West Conshohocken, PA, 1996, pp. 657–675.

[13] Fleck, R. G., Price, E. G., and Cheadle, B. A., "Pressure Tube Development for CANDU Reactors," *Zirconium in the Nuclear Industry: Sixth International Symposium, ASTM STP 824*, D. G. Franklin and R. B. Adamson, Eds., Vancouver, British Columbia, June 28–July 1, 1982, ASTM International, West Conshohocken, PA, 1984, pp. 88–105.

[14] Coleman, C. E., Cheadle, B. A., Cann, C. D., and Theaker, J. R., "Development of Pressure Tubes with Service Life of Greater Than 30 Years," *Zirconium in the Nuclear Industry: 11th International Symposium, ASTM STP 1295*, E. R. Bradley and G. P. Sabol, Eds., Garmisch-Partenkirchen, Germany, Sept. 1995, ASTM International, West Conshohocken, PA, 1996, pp. 884–898.

[15] Theaker, J. R., Choubey, R., Moan, G. D., Aldridge, S. A., Davis, L., Graham, R. A., and Coleman, C. E., "Fabrication of Zr-2.5Nb Pressure Tubes to Minimize the Harmful Effects of Trace Elements," *Zirconium in the Nuclear Industry: Tenth International Symposium, ASTM STP 1245*, A. M. Garde and E. R. Bradley, Eds., Baltimore MD., June 21–24, 1993, ASTM International, West Conshohocken, PA, 1994, pp. 221–242.

[16] Cheadle, B. A., Aldridge, S. A., and Ells, C. E., "Development of Texture and Structure in Zr-2.5 wt% Nb Extruded Tubes," *Can. Metall. Q.*, Vol. **11**(1), 1972, pp. 121–127.

[17] Cheadle, B. A., "Fabrication of Zirconium Alloys into Components for Nuclear Reactors," *Zirconium in the Nuclear Industry: 3rd International Symposium, ASTM STP 633*, A. L. Lowe and G. W. Parry, Eds., Quebec City, Canada, Aug. 1976, ASTM International, West Conshohocken, PA, 1977, pp. 457–485.

DISCUSSION

Question 1, Ron Adamson, Zircology Plus:—Could you comment on the effect of the higher temperatures (up to 325°C) of ACR on creep and growth relative to the standard CANDU (up to 305°C)?

Author's Response:—Tests on creep capsules irradiated in OSIRIS up to 340°C (unpublished) show an increase in diametral strain rate with increasing temperature for a given stress but, surprisingly, the axial strain is insensitive to temperature. The irradiation growth (zero stress case) for these same creep capsules is practically zero in both the axial and transverse directions at ACR temperatures in contrast to lower temperatures.

Question 2, Wenjing Li, Queens University and College of the North Atlantic:—What creep mechanism was assumed for diametral creep modelling?

Author's Response:—The model was based on a semi-empirical equation described in: Christodoulou, N., Causey, A.R., Holt, R.A., Tomé, C.N., Badie, N., Klassen, R.J., Sauvé, R., and Woo, C.H., "Modeling In-Reactor Deformation of Zr-2.5Nb Pressure Tubes in CANDU Power Reactors," *Zirconium in the Nuclear Industry: Eleventh International Symposium*, ASTM STP 1295, E.R. Bradley and G.P. Sabol, Eds., ASTM, West Conshohocken, PA, 1996, pp. 518-537. Other than the empirically derived temperature, stress and flux dependence in this model the material dependent creep term is dependent on the product of two parameters - $C_4(x)$ and $K_4(x)$, where x is the distance along the tube. The diametral creep parameter ($K_4(x)$) is a function of axial location and was derived from an empirical fit to diametral creep data (in the reference above the fit was to axial stress-relaxation data giving a very different $K_4(x)$ parameter). Although the parameter $C_4(x)$ is based on dislocation slip the fitted $K_4(x)$ term was derived after $C_4(x)$ had been applied and this therefore makes $C_4(x)$ redundant everywhere except at the 3 metre location. $K_4(x)$ is dependent on the grain structure and the dominant mechanism is therefore believed to be mass-transport by diffusional flow.

Question 3, Vladimr Markelov, Bochvar Inst. (VNIINM):—What is the main limitation factor for the lifetime of the ACR pressure tubes (creep, fracture toughness or DHC)?

Author's Response:—Diametral creep is the main life-limiting property of CANDU pressure tubes.

Question 4, Young Suk Kim, KAERI:—Please comment on why the back to front positions of ACR tubes change when compared to the positions of the traditional pressure tubes in the reactor.

Author's Response:—Until recently, CANDU reactors had pressure tubes installed with the back-end at the outlet. The back-end has finer grain structure and larger radial texture than the front-end. Past evidence suggested that the back-end microstructure would promote higher diametral strain than the front-end so the CANDU design was changed to place the back-end at the colder inlet. The benefit of this new practice is confirmed with the work presented here and the ACR design specifies back-ends at the inlet.

Question 5, J. K. Chakravartty, Bhabha Atomic Research Centre, India:—It is known that the scale of the microstructure & texture are decided by the extrusion temperature and rate. Extrusion parameters for ACR are similar to those of conventional CANDU practice. What are the reasons then for improved performance of ACR pressure tubes?

Author's Response:—ACR and CANDU tubes are extruded under very similar conditions. However, the ACR tube is thicker and that likely affects the cooling rate of the extruded hollow.

Question 6, Joe Rashid, ANATECH:—In order to understand the comparison; how would the comparison look if you were to subject the ACR tubes to CANDU conditions and the CANDU tube to ACR conditions? This would make the comparison independent of reactor operating conditions.

Author's Response:—Various experiments are underway that allow a comparison of ACR-like pressure tube material with CANDU-like pressure tube material under the same irradiation environment.

Question 7, Jun Cui, Kinetrics:—Can the author please comment on what is the potential difference with regards to DHC and fracture toughness between ACR tubes and traditional/historical CANDU tubes? Was any study done on this and what is the observation?

Author's Response:—The fracture and delayed-hydride-cracking properties of ACR tubes are very similar to the best of the CANDU pressure tubes.

Question 8, N. Saibaba, Nuclear Fuel Complex, India:—Is the improvement in diametral creep due to increase in the thickness or also due to microstructure & texture control? Can we get thicker grains radially by starting with billets of bigger grains at extrusion? What is the relation between the creep and radial thickness of the grains? Can we attain better diametral creep with further increase in radial grain thickness? Effect of aspect ratio in addition to radial grain thickness may be explained.

Author's Response:—At this time it is assumed that the tube thickness variable leads to the change in microstructure. The grain thickness is our only indication of microstructural change and the texture does not differ from standard thickness tubes. Controlling the billet grain structure is also expected to affect the radial grain thickness of the extruded pressure tube. A moderate increase in grain thickness is expected to decrease the diametral strain but we have little data and experience with grain thickness very much bigger than that seen in these ACR tubes. We have only focussed on the radial grain thickness as one tractable figure-of-merit to describe the change in microstructure. Aspect ratio will be an important factor as well.

Reprinted from JAI, Vol. 8, No. 6
doi:10.1520/JAI103213
Available online at www.astm.org/JAI

N. Saibaba,[1] *S. K. Jha,*[1] *S. Tonpe,*[1] *Kumar Vaibhaw,*[1]
V. Deshmukh,[1] *S. V. Ramana Rao,*[1] *K. V. Mani Krishna,*[2]
S. Neogy,[2] *D. Srivastava,*[2] *G. K. Dey,*[2] *R. V. Kulkarni,*[3]
B. B. Rath,[3] *E. Ramadasan,*[3] *and S. A. Anantharaman*[3]

Microstructural Studies of Heat Treated Zr-2.5Nb Alloy for Pressure Tube Applications

ABSTRACT: Zr-2.5Nb alloy is used as pressure tube material in pressurized heavy water reactors (PHWR). Generally, these pressure tubes are used in the cold drawn condition. Heat treated Zr-2.5Nb alloy pressure tubes are used in reaktor bolshoy moshchnosti kanalniy and FUGEN type of reactors. In recent times, there has been a greater interest toward increasing the life of pressure tubes in advanced reactors. In the present work, fabrication parameters were optimized to manufacture heat treated Zr-2.5Nb alloy tube. A quenching dilatometer study was performed to establish the continuous cooling transus temperature for the alloy used in this study. Heat treatment under controlled condition in a dilatometer was performed to study microstructure at different soaking temperatures and cooling rates. In the dilatometer, during gas quenching, quenching rates were varied from 0.06 to 100C/s to assess the effect of cooling rate on resulting microstructures. Soaking temperature

Manuscript received June 17, 2010; accepted for publication April 15, 2011; published online July 2011.
[1] Nuclear Fuel complex, Hyderabad, India, 500062. (Corresponding author), e-mail: nsai@nfc.gov.in
[2] Materials Science Division, Bhabha Atomic Research Centre, Mumbai, India, 400085.
[3] Post Irradiation and Examination Division, Bhabha Atomic Research Centre, Mumbai, India, 400085.
16th International Symposium on Zirconium in the Nuclear Industry on 9–13 May 2010 in Chendu, China.

Cite as: Saibaba, N., Jha, S. K., Tonpe, S., Vaibhaw, K., Deshmukh, V., Ramana Rao, S. V., Mani Krishna, K. V., Neogy, S., Srivastava, D., Dey, G. K., Kulkarni, R. V., Rath, B. B., Ramadasan, E. and Anantharaman, S. A., "Microstructural Studies of Heat Treated Zr-2.5Nb Alloy for Pressure Tube Applications," *J. ASTM Intl.*, Vol. 8, No. 6. doi:10.1520/JAI103213.

Copyright © 2011 by ASTM International, 100 Barr Harbor Drive, PO Box C700, West Conshohocken, PA 19428-2959.

and cooling rates were varied to obtain martensitic microstructure with appropriate volume fractions of primary α. On the basis of the results obtained during controlled heat treatments performed in the quenching dilatometer, 883C was selected as the soaking temperature and water as the quenching medium for the $\alpha + \beta$ quenching operation for large dimension tubes. The $\alpha + \beta$ quenched microstructures, consisting of fine martensite phase along with 20%–25% primary α volume fraction, were used for further cold deformation and subsequent aging below the recrystallization temperature. Aging at 540C produced fully recovered and tempered structure consisting of β_{Nb} of equilibrium composition. Mechanical properties of the finished heat treated pressure tube (aged at 515C/24 h) produced with the present route were similar to the cold work pressure tube. Tube produced with 540C/24 h aging exhibited substantially higher yield strength value at reactor operating temperature (300C). The bulk texture at different stages of fabrication was evaluated. The volume fraction of the primary α phase significantly controls the final texture.

KEYWORDS: Zr-2.5wt%Nb, heat treated pressure tube, transus temperature, PHWR, quenching, ageing

Introduction

Zirconium and its alloys are extensively used as structural materials in nuclear reactors, because of their unique combination of good corrosion resistance in water, good mechanical properties, and low capture cross section for thermal neutrons [1–5]. Zr-2.5Nb alloy is presently being used as a pressure tube material due to its higher strength, and creep and fracture resistance. Zr-2.5Nb alloy is a two phase material that is amenable to different heat treatments leading to a wide range of equilibrium and nonequilibrium phase transformations [6–11]. The final microstructure depends on the nature of these transformations, which depend on composition, soaking temperature, and cooling rate. Generally, Zr-2.5Nb alloy is used in the cold worked condition in CANDU type pressurized heavy water reactors. However, in reaktor bolshoy moshchnosti kanalniy (RBMK) and FUGEN type reactors, Zr-2.5Nb alloy pressure tube is used in a heat treated condition [12]. The satisfactory performance (and the life) of the pressure tubes depend mainly on its dimensional stability in the reactor [12–17]. The dimensional changes in the axial and diametral directions are due to the net effect of thermal creep, irradiation creep, and irradiation growth [13–20]. Both irradiation creep and growth are strong functions of several metallurgical parameters which include the shape, the size, and the size distribution of the grains, the distribution of various phases, the interfacial structure, and the crystallographic texture [13–16]. The major factors controlling the creep rates in pressure tubes include grain size, texture, and oxygen content.

There has been continuous efforts toward improving the resistance to irradiation induced creep and growth through the modification of the microstructure of the pressure tube material to achieve longer life of the pressure tube in next generation reactors [12]. Many researchers have studied changes in

microstructure and their effect on the properties by altering the conventional route of pressure tube fabrication.

The fabrication of pressure tubes involves thermomechanical treatments, and the final microstructure developed as a result of these fabrication steps determines their long-term and short-term properties. It is important to understand the influence of each of these fabrication steps on microstructure and crystallographic texture in order to optimize pressure tube fabrication. This requires an in-depth understanding of the mechanisms of microstructural evolution during these processing steps. In the Indian nuclear reactor program, an attempt is being made to develop heat treated (quenched and aged) pressure tubes with improved properties in comparison to the conventional fabrication route adopted for the cold worked (pilgered) route, practiced in Nuclear Fuel complex, Hyderabad. The aim is to develop a heat treatment route that produces mechanical properties at operating temperatures that are better than those of current pressure tubes, (which are in the cold-worked and stress-relieved condition) and that will have enhanced microstructural stability during the high temperature irradiation.

The objective of the present study is to optimize the fabrication processing parameters with special reference to quenching and aging treatments. In this study the microstructural evolution at different stages of fabrication as a function of fabrication parameters has been characterized. The mechanical properties and texture of relevant samples have been evaluated.

Experimental

Zr-2.5Nb alloy ingots of 350 mm diameter were produced in a consumable vacuum arc melting furnace. The quadruple melting was carried out to reduce the impurity elements (mainly interstitials such as hydrogen, chlorine, and phosphorus). The chemical composition of the alloy is given in Table 1. In order to break up the cast structure, these ingots were further extruded to billets of 230 mm diameter size. Hollow machined billets were subsequently water quenched to achieve compositional and microstructural homogeneity. The quenched billets were soaked at 800°C for 1 h followed by extrusion with an extrusion ratio of 9.4:1. The hot extruded blank of Zr-2.5Nb alloy was further subjected to cold deformation of 41% by pilgering. This pilgered tube formed the starting material in the present study for various heat treatments in $\alpha + \beta$ phase field as detailed in the Fig. 1. The heat treatment conditions were determined after establishing the

TABLE 1—*Chemical composition of material used for the trials.*

Element	Wt. %/ppm
Niobium	2.68
Oxygen	1137
Nitrogen	28
Iron	650
Tin	25

$\beta/\beta+\alpha$ continuous cooling transus temperature for this composition. In the present study, a quenching dilatometer (DIL 805) has been used for this purpose. The temperature measurement in the dilatometer was calibrated using the Curie temperature of pure nickel. S–type thermocouples welded to samples were used for the temperature measurement with ± 0.1°C accuracy. Samples were initially soaked at 400°C for 30 min in the dilatometer to relieve the residual stresses. On the basis of the quenching dilatometer studies, various heat treatment conditions (soaking temperature and cooling rate) were selected. In general, soaking times were chosen to achieve the equilibrium conditions, which in the present case will be greater than several hundred hours [21]. The aim of the present study was to elucidate the microstructural evolution under practical conditions of pressure tube manufacturing in which soaking times are typically of the order of several minutes. Hence the soaking time was kept 30 min for all the quenching studies performed in this work. Samples subjected to various quenching treatments were further cold worked 23% by pilgering. These samples were finally given ageing treatments at two different temperatures (540 and 515°C) for 24 h. These samples were then autoclaved at 290°C for 120 h.

Samples from each of the above processing steps were subjected to detailed characterization using optical, scanning electron microscopy (SEM) and transmission electron microscopy (TEM). Mechanical properties of the selected samples were evaluated using a tensile testing machine. Samples were cut in both longitudinal and transverse directions for examination of microstructures.

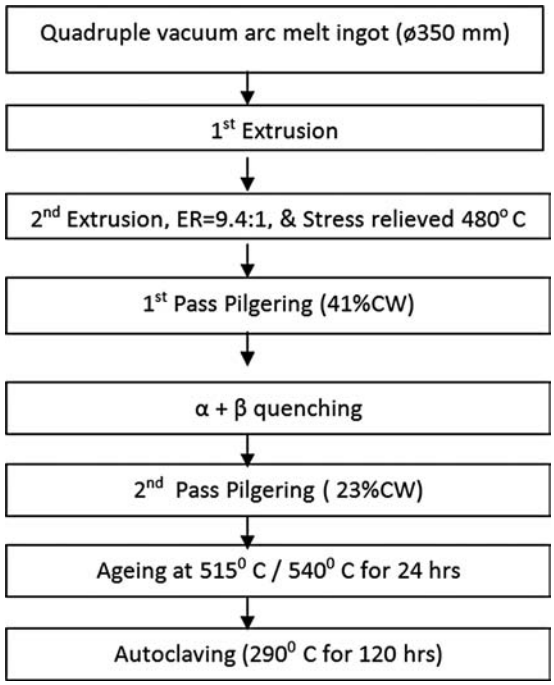


FIG. 1—*Fabrication flow sheet for heat treated pressure tube.*

Samples for optical microscopy were chemically etched in a 5% HF + 45% HNO_3 solution and those for SEM in a 8% HF + 45% HNO_3 solution. Disc samples 3 mm diameter for the TEM examination were punched from mechanically thinned specimens. Twin jet thinning was employed to make electron transparent specimens using a potential of 20 V and an electrolyte of 20% perchloric acid and 80% methanol, maintained at −45°C. The TEM examination was carried out in a JEOL 2000FX microscope. The chemical analysis of the α and β phases were carried out by energy dispersive spectroscopy (EDS) in a Philips-430T microscope. The volume fractions of the two phases, as well as the thicknesses and the aspect ratios of these two phases, were estimated using digital image processing. Samples for crystallographic texture evaluation were cut in the three principal directions (axial, radial, and circumferential) from the pressure tube. Several of these strips were mounted together to provide sufficient surface area for x-ray diffraction. The samples representing the three principal directions were polished mechanically as well as chemically for the x-ray diffraction experiments.

Results and Discussion

Determination of $\beta \rightarrow \alpha + \beta_{Zr}$ Continuous Cooling Transus Temperature

In order to determine the heat treatment temperature to achieve the desirable phases with appropriate composition and volume fraction, it is important to

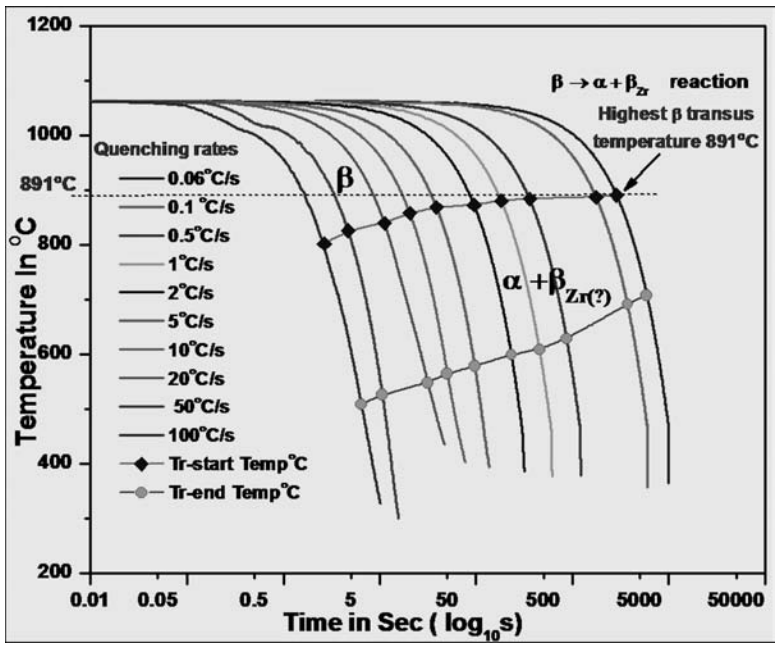


FIG. 2—*Cooling curves obtained from quenching dilatometer superimposed with the transus temperatures.*

know the accurate phase transition temperatures. The $\beta \rightarrow \alpha + \beta_{Zr}$ continuous cooling transus temperature is known to depend on the oxygen content in addition to the niobium concentration in the alloy [22,23]. In the present study, $\beta \rightarrow \alpha + \beta_{Zr}$ the continuous cooling transus temperature was determined using quenching dilatometer. The samples were cooled from the beta phase field at different cooling rates. The variation in the slope of the change in length (Δl) versus temperature curve indicates the phase transition event (temperature). The first and second inflection points of the cooling curves (Δl versus temperature) correspond to $\beta \rightarrow \alpha + \beta_{Zr}$ and $\beta_{Zr} \rightarrow \alpha + \beta_{Nb}$ transition temperatures. Figure 2 shows a cooling curve obtained from the quenching dilatometer superimposed on the transus temperatures for Zr-2.5% Nb pressure tube material used in the present investigation. From this study, β, ($\alpha + \beta_{Zr}$) and ($\alpha + \beta_{Nb}$) phase fields have been demarcated as shown in Fig. 2. It can be observed that the ($\alpha + \beta_{Zr}$) regime starts at 891°C for the sample cooled at the slowest cooling rate. Thus, the highest $\beta \rightarrow \alpha + \beta_{Zr}$ continuous cooling transus temperature,

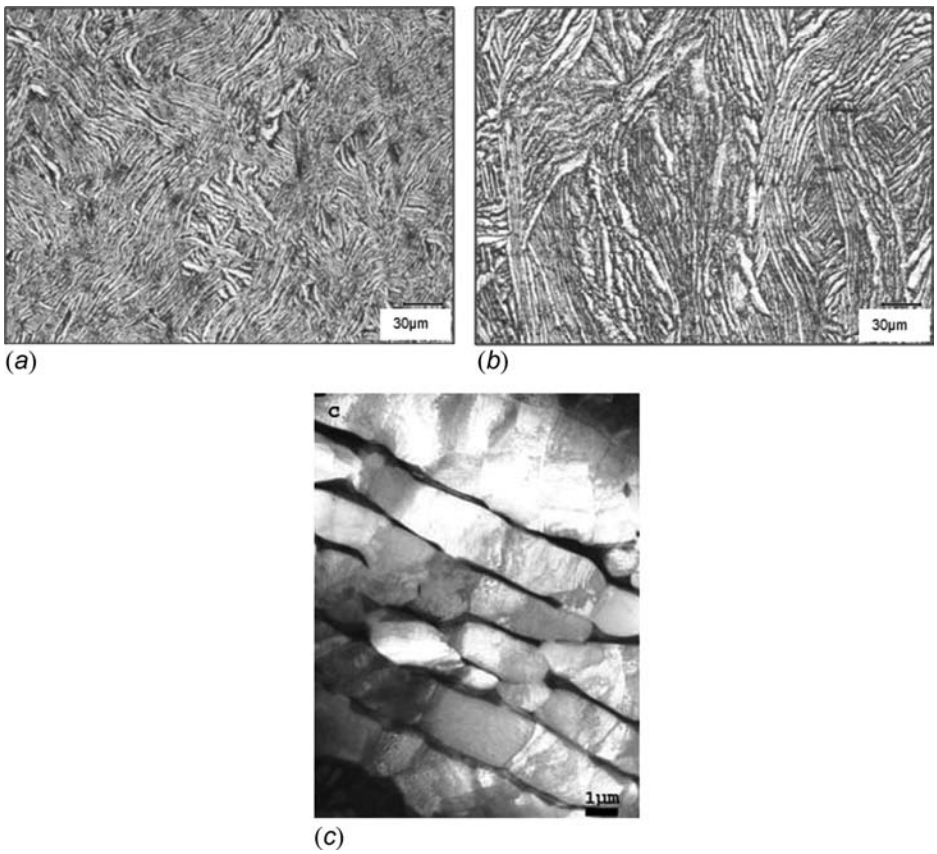


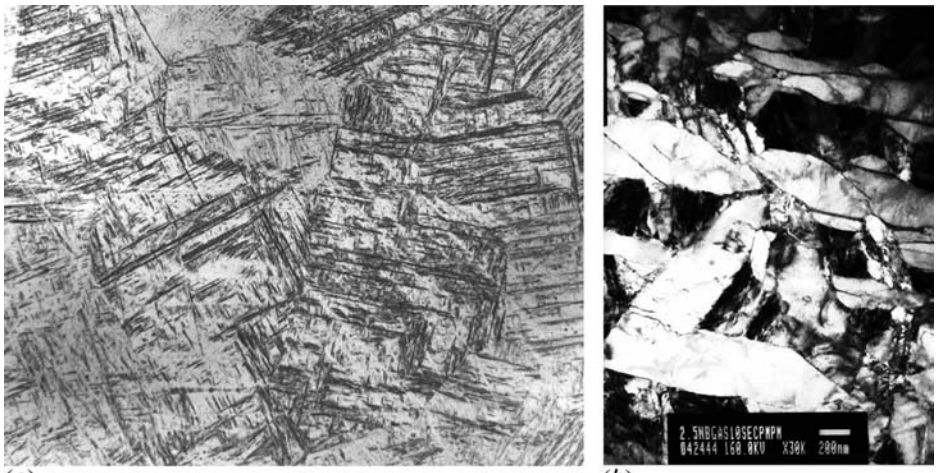
FIG. 3—*Micrographs after first extrusion (a) optical-longitudinal, (b) optical-transverse, and (c) TEM-longitudinal.*

891°C, for this alloy has been taken as the transition temperature. Therefore, the heat treatment temperature was selected above and below this temperature for quenching from β and $\alpha + \beta$ phase field, respectively.

Microstructural Evolution

Microstructure after First Extrusions—The extrusion process was performed at 800°C with an extrusion ratio of 4:1 to break up the cast structure of the ingot and to achieve homogeneity in structure and composition. 350 mm diameter ingot was reduced to 230 mm diameter size billet. The resulting microstructure is shown in Fig. 3. Optical micrographs obtained from the longitudinal and transverse sections of the extruded billets exhibited packets of lamellar α grains randomly oriented in all directions similar to those observed in the Widmanstatten structure. The average width of the alpha grains was 2–3 μm and average length of a grain along axial-circumferential section was 200–300 and 100–150 μm in sections defined by the radial and the circumferential directions. Beta phase was present at the α/α interfaces. The TEM micrographs obtained at higher magnification showed the β phase distribution more clearly. The microstructure also suggested dynamic recrystallization of the α grains. The refined and uniform microstructures suggested that the cast structure was completely removed during the hot extrusion process.

β Quenched Microstructure—Zr-2.5Nb alloy billets were heated at 1000°C and quenched in water to obtain fine α grains and homogeneity in composition, microstructure, and texture. Optical micrographs showed fine needle-like structure within the prior beta grains (Fig. 4). Bright field TEM micrographs showed martensitic microstructure consisting of coarse lath martensites (Fig. 4). The laths were oriented in certain crystallographic directions as observed in earlier



(*a*) (*b*)

FIG. 4—*Microstructures after beta quenching (a) optical and (b) TEM.*

studies [5–8]. The microstructure obtained confirmed that beta quenching achieved the objectives (fine grains and homogeneity) of this fabrication step.

Microstructure after Second Hot Extrusion—Zr-2.5Nb was extruded at 800°C, with an extrusion ratio of 9.4:1, in this fabrication step. The secondary electron micrograph images obtained from the longitudinal and transverse sections in the SEM shown in Fig. 5. During the extrusion process, the α grains become elongated in the axial direction of the tube and were reduced in thickness in the radial direction. The longitudinal section exhibited α phase with a lamellar morphology aligned along with the extrusion direction. The transverse section exhibited α lamellae, whose average length, width, and thickness were in

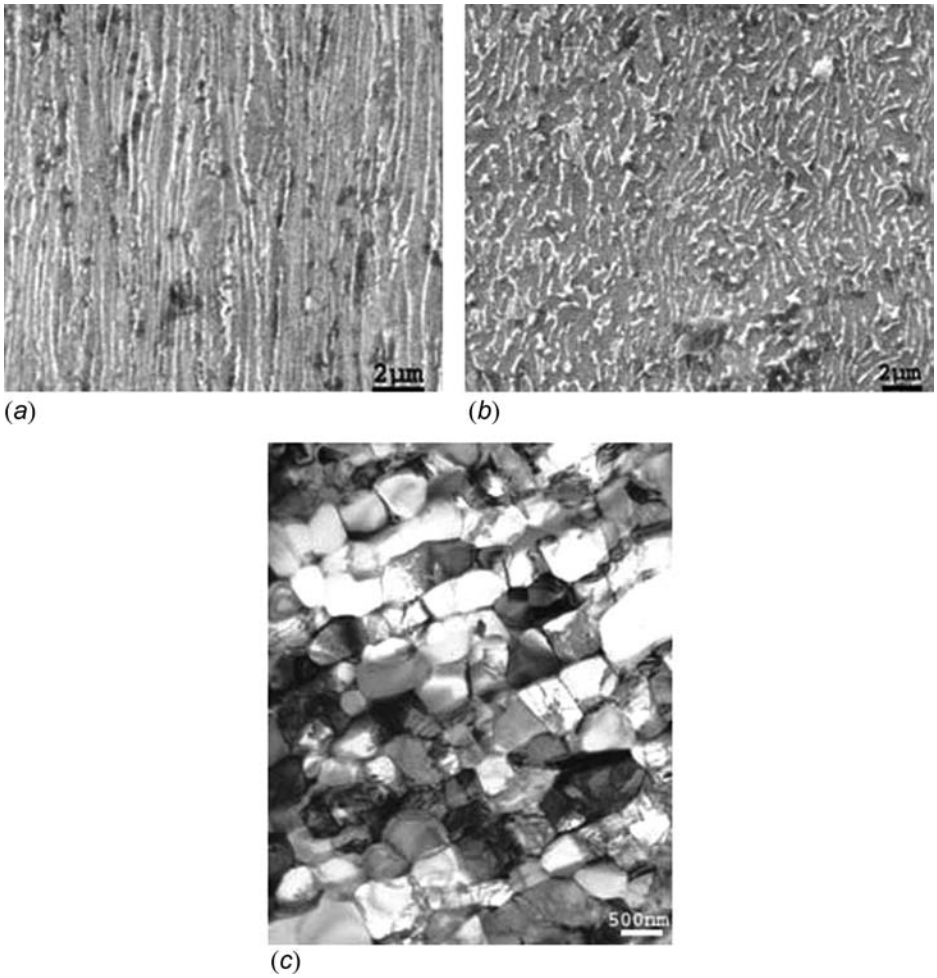


FIG. 5—*Microstructures after second extrusion (a) SEM-longitudinal, (b) SEM-transverse, and (c) TEM-longitudinal.*

the range of 15–20, 1–2.5, and 0.3–0.5 μm, respectively. Beta phase was present as thin wafers between two α lamellae and had an average thickness of 0.02–0.05 μm. The TEM micrographs of the longitudinal section revealed further finer details of microstructure (Fig. 5). The α lamellae were found to consist of dynamically recrystallized α grains stacked in the extrusion direction.

Microstructure after First Cold Deformation—The aim of this cold deformation process was to reduce the wall thickness and the OD (outer diameter) of the tubes. Pilgering was used to impart 41% of cold work. SEM micrographs of the two cross sections of the tube are shown in Fig. 6. Due to the large deformation, the microstructure could not be revealed clearly in the TEM. However, the lamellar structure of the phase was retained. The TEM micrograph also revealed the presence of high dislocation density after this operation.

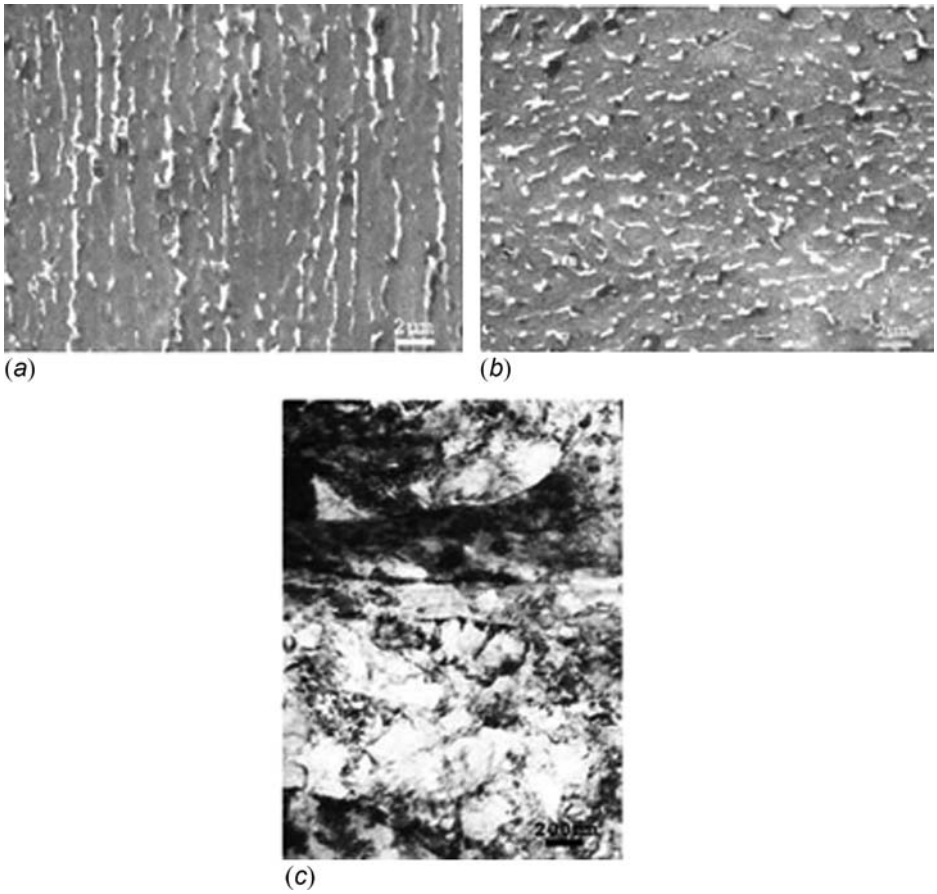


FIG. 6—*Microstructures after first pilgering(a) SEM-longitudinal, (b) SEM-transverse, and (c) TEM-longitudinal.*

$\alpha + \beta$ *Quenched Microstructure*—One of the aims of the present study was to investigate the influence of quenching rate in determining the nature of the transformation (diffusional and/or displacive) and resulting morphology of the products. Quenching treatments were carried out in a controlled fashion, using a quenching dilatometer, to study the evolution of microstructures as a function of different cooling rates. It may be noted that transformation from the β phase

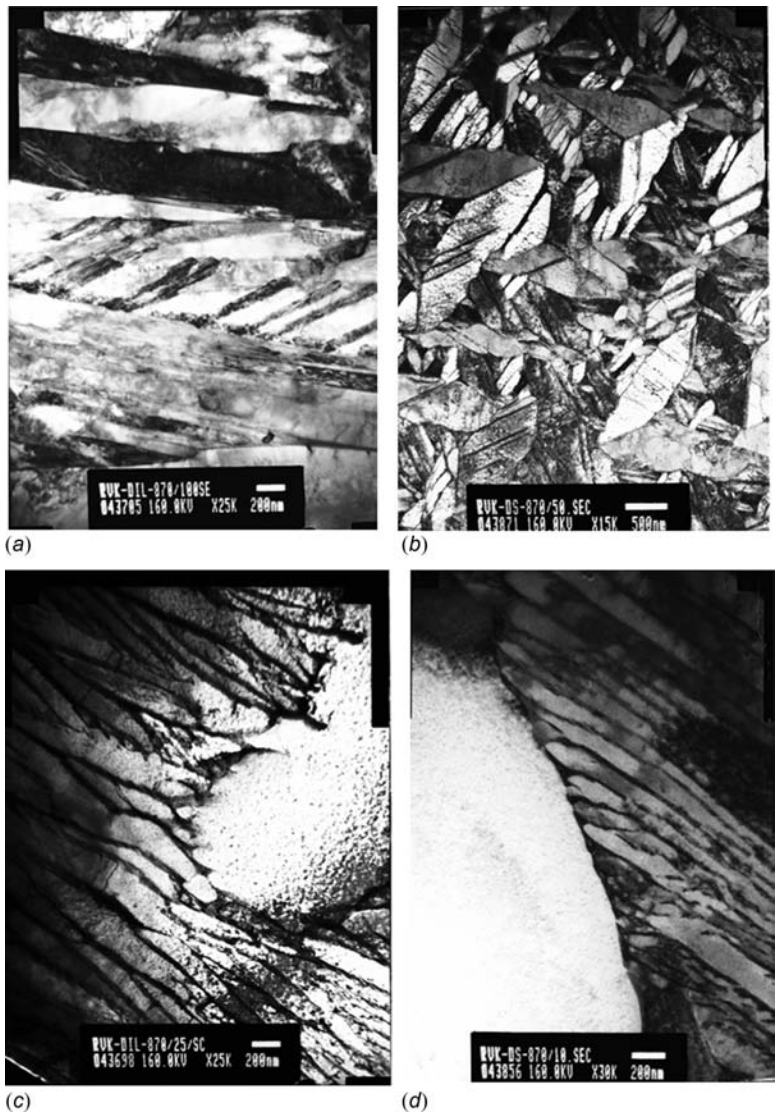


FIG. 7—*Microstructures after* ($\alpha + \beta$) *gas quench from 883°C (soaked for 30 min) and quenched with cooling rates (a) 100°C/s, (b) 50°C/s, (c) 25°C/s, and (d) 10°C/s.*

field at different cooling rates has been reported in literature by many workers [5–7,23,24]. However, systematic studies of the transformation from the $\alpha + \beta$ phase field as a function of cooling rate have not been reported extensively in the open literature. In addition to cooling rate, the effect of soaking temperature in the $\alpha + \beta$ phase field has been also examined in the present study.

Bright field TEM micrographs of samples cooled from 883°C at different cooling rates in argon are shown in Fig. 7. All the samples showed primary α and transformed β phases. Samples cooled at the rate of 100 and 50°C/s showed predominantly martensitic transformation. At a higher cooling rate of 100°C/s, internally twinned martensite plates were observed, whereas internally slipped martensite and a minor fraction of primary α phase were the major features observed in samples subjected to relatively lower cooling rates of 50°C/s. The martensite plates were seen to have formed in self accommodating morphologies (see Fig. 7), thus reducing the transformation strain energies.

At slower cooling rates, the transformed β product was observed to be Widmanstatten $\alpha + \beta$. The β phase was present between the Widmanstatten lamellae. With a decrease in the cooling rate the width of the Widmanstatten plates became larger and their morphology progressively changed from being sharp straight lamellae to more irregular shaped lamellae. The morphological features are summarized in Table 2.

Figure 8 shows various microstructures obtained from gas quenching at 870°C. As expected, the volume fraction of primary α phase increased with the lowering of soak temperature (water quenching: 44, 34, and 15% for soaking temperatures 860, 885, and 910°C, respectively gas quenching: 58, 40, and 24% for soaking temperatures 860, 885, and 910°C, respectively). This effect was more pronounced in samples cooled with lower cooling rates. Comparison of Figs. 7 and 8 reveals that the probability of martensitic transformation is higher with lowering of soaking temperature for a given cooling rate. This increased probability may be attributed to a higher Nb content in the β phase at the lower soaking temperatures which increases the driving force for the martensitic transformation. Martensite could be obtained even at a 25°C/s cooling rate. This is also true for observation of a higher incidence of internally twinned

TABLE 2—*Microstructure details as a function of cooling rate (when cooled from 883°C).*

Cooling Rate (°C/s)	Phase	Microstructural Features
100	α + Internally twinned martensite	(sample quenched at 100°C/s) Grain size prior β ~10-15 μm Grain size α ~1-3 μm Primary α percentage ~3% Martensite plates 0.5-3 μm
50	α + Internally slipped martensite	
25	α + Widmnstatten	(sample quenched at 0.06°C/s) Grain size prior β ~10 μm Grain size α ~1-3 μm Primary α percentage = 5%–8% Widmanstatten plates dimensions: length = 10–20 μm width ~1-2 μm
10	α + Widmanstatten	
0.5	α + Widmanstatten	

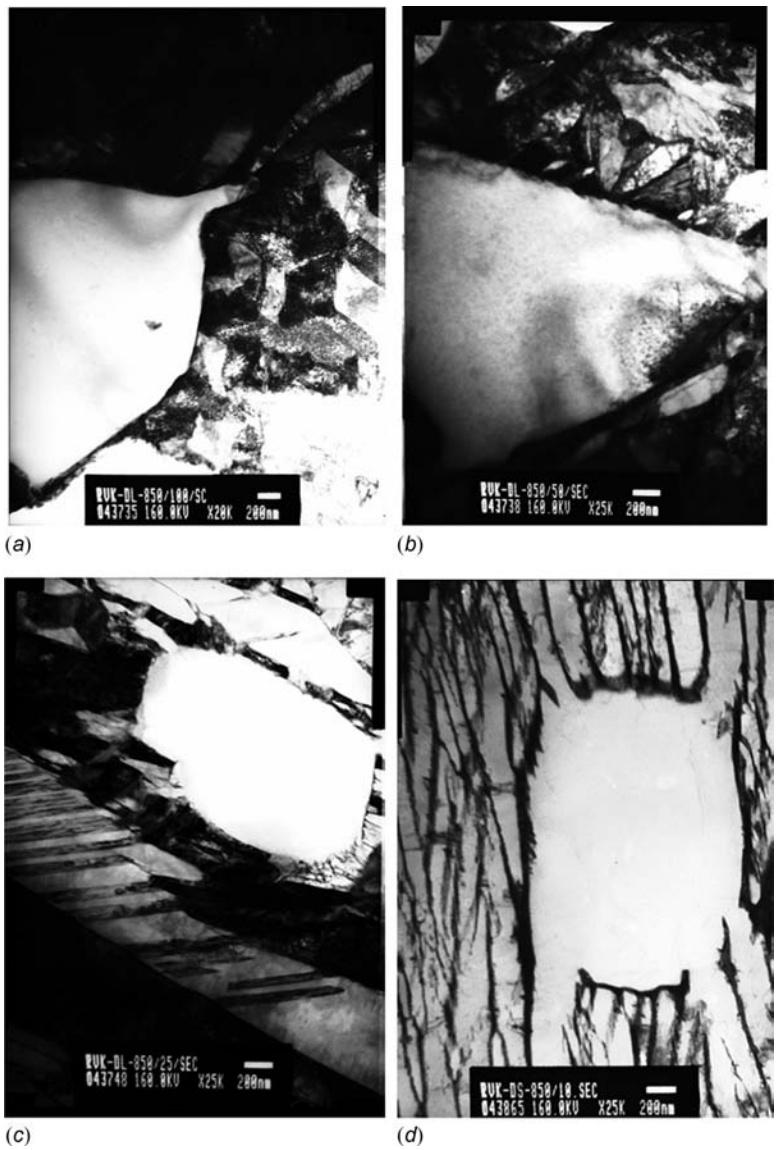


FIG. 8—*Microstructures after (α + β) gas quench from 870°C (soaked for 30 min) and quenched with cooling rates (a) 100°C/s (b) 50°C/s (c) 25°C/s and (d) 10°C/s.*

martensite. Since martensite was forming at a lower temperature the matrix became stronger and hence promoted the formation of internally twinned martensite. The Widmanstatten α plates became finer with lower soaking temperatures and all the other observations were similar to those observed at 883°C. The summary of microstructural observations is given in Table 3. On the basis of these observations it may be concluded that in order to obtain primary α and

TABLE 3—*Microstructure details as a function of cooling rate (when cooled from 870°C).*

Cooling Rate (°C/s)	Phase	α Vol. Frac (%)
100	α + internally twinned martensite	15-20
50	α + internally slipped martensite	15-20
25	α + Slipped martensite	15-20
10	α + Widmanstatten	15-25

a martensitic microstructure after $\alpha + \beta$ quenching, a minimum cooling rate is required that is a function of soaking temperature.

It was shown in earlier reports [11–14] that the properties of fabricated tubes (crystallographic texture, mechanical properties, etc.,) arestrong functions of the amount of primary α phase present in the microstructure (after the quenching treatment), which in turn is dependent on the soaking temperature in the $\alpha + \beta$ phase field [25]. In the present study, the amount of primary or retained α phase has been determined through SEM in the gas quenched and water quenched samples, after soaking at different temperatures; the details are given in Table 2.

On the basis of the results obtained during controlled heat treatment performed in the quenching dilatometer, 883°C was selected as the soaking temperature and the water was selected as the quenching medium for $\alpha + \beta$ quenching operation for large dimension tubes (100 mm OD × 4.5 mm WT × 500 mm length). Quenching was performed after heating in a horizontal furnace. The SEM and TEM micrographs of the quenched sample are shown in Fig. 9. From SEM micrographs the primary α volume fraction was found in the range of 20%–25%. The primary alpha volume fraction was expected to be around 5% under the controlled quenching conditions as per the dilatometer study.

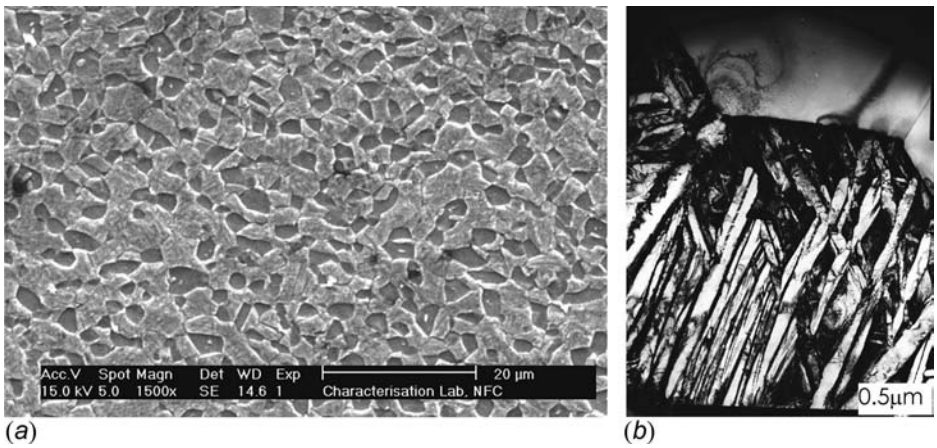


FIG. 9—*Microstructures after (α + β) quench of first pass pilgered tubes (a) SEM micrograph and (b) TEM micrograph.*

However, the observed higher values can be attributed to the larger volume of material compared to the sample size in the dilatometer and also to the longer transfer time from the furnace to the quenching medium that gave a lower quenching temperature. The TEM micrographs obtained at higher magnification revealed the transformed β microstructure. It could be seen that all of the β phase had transformed to the lath martensite. The $\alpha + \beta$ quenched microstructure consisting of fine martensite phase along with 20%–25% primary α volume fraction were used for further processing as described in the fabrication flow chart (Fig. 1).

Microstructure after Second Stage Deformation—The $\alpha + \beta$ quenched samples were cold deformed 23% (by pilgering). The objective of this cold deformation process was to achieve the final dimensions of the tube. Additionally during this fabrication stage a complex network of dislocations was introduced in both the primary α and the martensitic phases in $\alpha + \beta$ quenched sample. The TEM micrograph revealed the presence of such microstructures (Fig. 10).

Microstructural Evolution During Aging—One of the consequences of the two thermomechanical treatments (quenching and deformation) is the creation of a large number of nucleation sites for fine precipitation of β_{Nb} phase. The interfaces of the fine martensitic microstructure provided a large volume fraction of nucleation sites. Cold deformation of the martensitic microstructure



FIG. 10—*TEM longitudinal micrograph after second pass pilgering.*

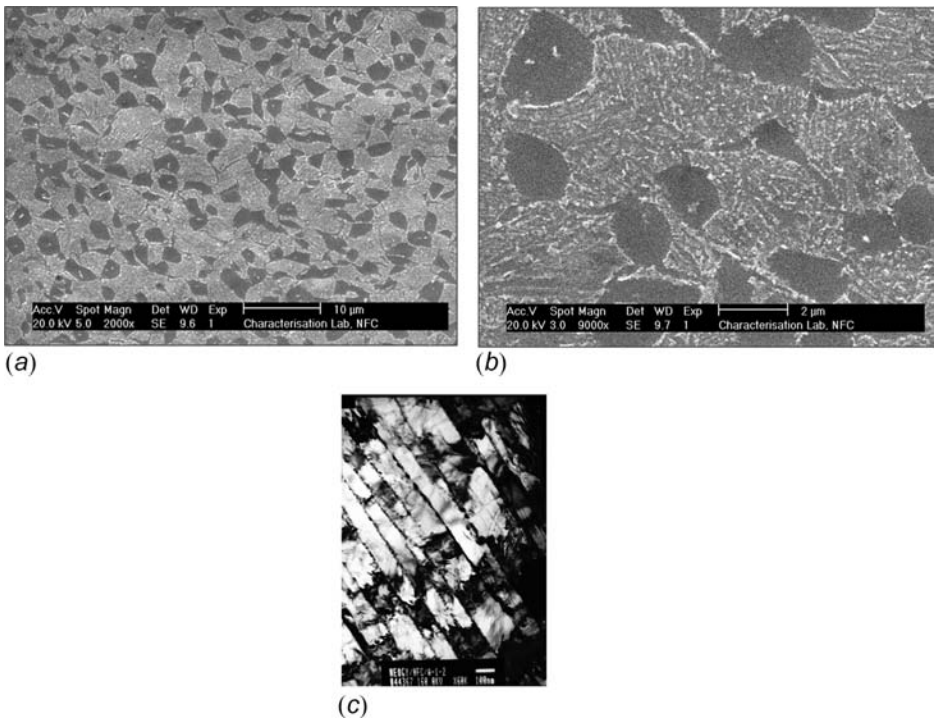


FIG. 11—*Micrographs after water quench from 883°C (soaked for 30 min) and aged at 515°C (24 h) (a) SEM-longitudinal, (b) SEM-transverse, and (c) TEM-longitudinal.*

resulted in a considerable increase in the dislocation density and in the dislocation substructure [26]. These resulted in dislocation enhanced diffusion by the pipe diffusion mechanism and led to precipitation of β_{Nb} from the supersaturated martensitic phase during the subsequent aging process. Therefore, an ageing treatment was given below the monotectoid temperature (610°C) to obtain fine β precipitates having composition close to equilibrium along with retained primary α. Two different ageing temperatures (540 and 515°C) below the recrystallization temperature were used in the present study after the second pilgering operation (see Fig. 1). The microstructures are presented in Figs. 11 and 12. Some of the salient observations from these microstructures are:

(a) No recrystallization of the microstructure at 515 or at 540°C.
(b) Fully recovered structure at 540°C for 24 h where as only partial recovery (60%–70%) at 515°C for 24 h.
(c) Complete tempering of martensite at 540°C, with partial tempering of the same at 515°C.
(d) In the case of sample aged at 515°C for 24 h, small β precipitates (with sizes less than 15 nm) were observed only at the α/α lath interfaces.
(e) No appreciable precipitation of β particles within primary α at both aging temperatures of 540 and 515°C.

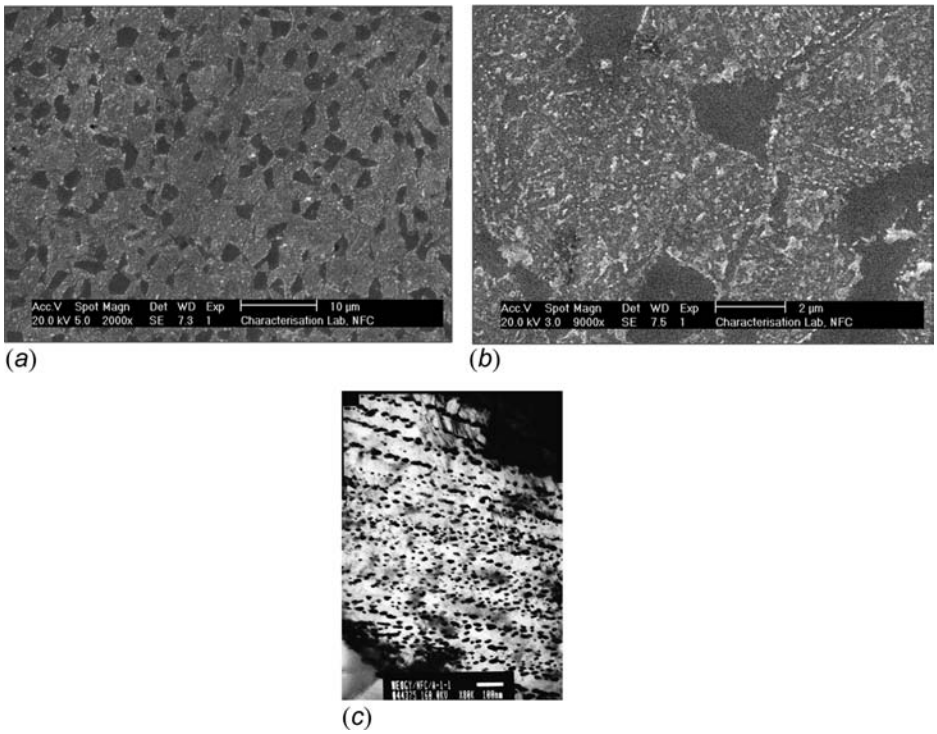


FIG. 12—*Micrographs after water quench from 883°C (soaked for 30 min) and aged at 540°C (24 h) (a) SEM-longitudinal, (b) SEM-transverse, and (c) TEM-longitudinal.*

Compositional analysis of the β phase was carried out by EDS in TEM. The average composition in samples aged at 515°C was showing 40–50 wt. % Nb whereas, for samples aged at 540°C it was 75%–80%Nb. This study shows that a temperature of 540°C is required to attain the equilibrium concentration of Nb (85%) in β precipitates during aging for a period of 24 h. In other words, aging treatment at 515°C for 24 h may lead to a higher probability of compositional and associated microstructural changes under reactor operating conditions.

Finally, the autoclaving treatment, carried out at 290°C for 120 h, did not modify the microstructure to any noticeable extent (Fig. 13).

Mechanical Properties

Table 4 shows the mechanical properties of the final tubes that were processed by water quenching followed by cold work and ageing (Fig. 1).The mechanical properties were evaluated for the two ageing conditions. Comparing these properties with that of the cold worked pressure tube (Table 4), it can be seen that mechanical properties in all the three cases are nearly in the same range. The only exception is the higher yield strength (YS) value at 300°C in the case of tube aged at 540°C for 24 h.



FIG. 13—*TEM micrographs after autoclaving (290°C/120 h).*

For the sample aged at 515°C the ultimate tensile strength (UTS) value is noticeably higher than that for the sample aged at 540°C. This observation may be explained in following manner. The aged microstructure in both cases would have well dispersed dislocation structures (though the dislocation density might

TABLE 4—*Mechanical properties of full scale heat treated pressure tube spool pieces (90.25 mm OD × 3.8 mm WT).*

		UTS (MPa)		YS(MPa)		EL(%)	
Tube condition/ mech Properties		RT (20°C)	HT (300°C)	RT (20°C)	HT (300°C)	RT (20°C)	HT (300°C)
HT	Ageing						
883°C/30 m	540°C/24 h	749	494	581	468	10	18
883°C/30 m	515°C/24 h	770	497	560	377	13	18.5
CWSR pressure tubes (typical value)		735	502	553	383	16	23.8

be larger in case of partially recovered 515°C aged sample) so that they are expected to have nearly similar YS at room temperature. However, the fine distribution of small β particles act as effective dislocation obstacles in the 515°C aged sample, thus leading to a higher work hardening rate in comparison to the 540°C sample and giving rise to a higher UTS value.

At a higher temperature (300°C), thermally assisted movement of dislocations overcoming obstacles (β particles) would determine the mechanical properties. The resistance to the movement would be weaker when the size of the particles is small. Thus, sample aged at 515°C, having smaller β particles, would show a lower YS. In the case of sample aged at 540°C due to larger particle size and higher particle density, initial dislocation motion is rather difficult and the observed YS higher. However, during plastic deformation, dislocation multiplication would become the dominant factor in samples aged at 515°C. This increase in dislocation density would result in more strain hardening and lead to a UTS value similar to that of samples aged at 540°C.

Thus, the aim of the present study (to produce fine grained microstructures containing fine precipitates of equilibrium β_{Nb} phase with similar mechanical properties) could be achieved.

Textural Evolution

Table 5 lists the crystallographic textural evolution as characterized by Kearns orientation parameter (f), which represents the fraction of basal poles of hexagonal-closed-packed alpha phase oriented in a given direction. The texture after the second extrusion had basal poles oriented predominantly in the transverse direction as reported in the earlier studies [3,5]. In the present study, the effect of quenching rate on the texture evolution has been examined. The tubes were soaked at 883°C, and quenched using argon gas or water. Water quenching was performed in horizontal as well as vertical type of furnaces. In the case of the horizontal furnace, the sample transfer time was longer and effective cooling

TABLE 5—*Texture coefficients in three principle directions of the tube.*

Condition	f_R	f_T	f_L
After second extrusion	0.29	0.61	0.10
As ($\alpha+\beta$) water quenched (883°C/30 Mins) (effective higher cooling rate-vertical furnace)	0.30	0.33	0.37
As ($\alpha+\beta$) water quenched (883°C/30 Mins) (effective lower cooling rate-horizontal furnace)	0.38	0.49	0.13
As ($\alpha+\beta$) Argon quenched (883°C/30 Mins)	0.43	0.47	0.10
As aged 540°C/24 h, (after WQ)	0.36	0.50	0.14
As aged 515°C/24 h, (after WQ)	0.37	0.51	0.12
Cold worked pressure tube	0.28–0.32	0.60–0.65	0.07–0.012

rate was lower than the vertical furnace. The texture results for all the three differently quenched samples are given in Table 5.

The main observations from that in Table 5 on texture evolution during quenching can be summarized as (a) the resultant texture from water quenching in horizontal furnace and gas quenching were similar and only slightly different from pre-quenching texture (hot extrusion texture + cold worked).[4] (b) Quenching using the vertical furnace with effectively higher cooling rate resulted in nearly random texture.

These observations can be rationalized in the following way. In case of water quenching in the horizontal furnace (with relatively lower cooling rates and lower quenching temperatures) and gas quenching, the volume fraction of the primary alpha was relatively higher (25%–30%) and hence only minor modifications in texture were observed. However, samples subjected to water quenching using a vertical furnace showed a primary alpha volume fraction of only 10%. When such a microstructure with a high amount of beta is quenched, the contribution of transformation texture to the final texture will be high (as seen in the nearly random distribution of the basal poles). These results highlight the importance of the volume fraction of the primary alpha phase at the quenching temperature on the quenching texture. However, further deformation and aging treatments of the water quenched samples (in the horizontal furnace) did not change the texture substantially. The tubes aged in two different conditions (540 and 515°C) exhibited nearly similar texture parameters. This similarity suggests that deformation and aging treatments did not modify texture significantly.

Conclusions

A modified heat treatment fabrication route for the production of pressure tubes was explored. The effect of the process parameters on the microstructure was studied. Some of the important conclusions reached in the present study are summarized below:

- The first extrusion process produced a uniform structure and the as-cast structure was broken up. The second extrusion produced a fine $(\alpha + \beta)$ lamellar structure.
- During $\alpha + \beta$ quenching the soaking temperature determined the volume fraction of the primary α. The required cooling rate to obtain martensitic microstructure increased with higher soaking temperatures.
- Ageing at 540°C resulted in the formation of fine β_{Nb} precipitates of equilibrium composition, whereas the β_{Nb} phase composition did not attain the equilibrium composition after ageing at 515°C.
- Mechanical properties of the finished heat treated pressure tube (aged at 515°C/24 h) produced with the present route were similar to the cold work pressure tube. Tube produced with 540°C/24 h aging exhibited substantially higher YS value at reactor operating temperature (300°C).
- The bulk textures at different stages of fabrication were evaluated. The effect of the quenching rate and the retained primary α volume fraction

was studied. The effect of the latter was found to be more dominant. Further cold working and ageing resulted in insignificant modification of texture of the pressure tube.

References

[1] Cheadle, B. A., Coleman, C. E., and Licht, H., "CANDU-PHW Pressure Tubes: Their Manufacture, Inspection, and Properties," *Nucl. Technol.*, Vol. 57, 1982, pp. 413–25.

[2] *ASTM STP 824*, Fleck, R. G., Price, E. G., Cheadle, B. A., Franklin, D. G., and Adamson, R. B., Eds., ASTM, Philadelphia, PA, 1984, pp. 88–105.

[3] Cheadle, B. A., "Zirconium in the Nuclear Industry," *ASTM STP 633*, 1977, p. 457.

[4] *ASTM STP 633*, Lowe, A. L. Jr., and Parry, G. W., Eds., Philadelphia, PA, 1977, pp. 457–485.

[5] Srivastava, D., Dey, G. K., and Banerjee, S., "Evolution of Microstructure During Fabrication of Zr–2.5 Wt pct Nb Alloy Pressure Tubes," *Metall. Mater. Trans. A*, Vol. 26, 1995, 2707.

[6] Srivastava, D., 1997, Ph.D. thesis, I.I.Sc. Bangalore, India.

[7] Banerjee, S. and Mukhopadhyay, P., *Phase Transformations: Examples from Titanium and Zirconium Alloys*, Pergamon Press, Tarrytown, NY, 2007.

[8] Tewari, R., Srivastava, D., Dey, G. K., Chakravarty, J. K., and Banerjee, S., "Microstructural Evolution in Zirconium Based Alloys," *J. Nucl. Mater.*, Vol. 383, 2008, pp. 153–171.

[9] Perovic, V., Weatherly, G. C., and Simpson, C. J., "Hydride Precipitation in α/β Zirconium Alloys," *Acta Metall.*, Vol. 31, 1983, pp. 1381–1391.

[10] Luo, C. P. and Weatherly, G. C., "The Precipitation Behavior of a Zr–2.5 wt pct Nb Alloy," *Metall. Trans. A*, Vol. 19, 1988, pp 1153–1162.

[11] Griffiths, M., Winegar, J. E., and Buyers, A. J., "Manufacturing Variability and Deformation for Zr-2.5Nb Pressure Tubes," *Nucl. Mater.*, Vol. 383, No. 1–2, 2008, pp. 28–33.

[12] Coleman, C., Griffiths, M., Grigoriev, V., Kiseliov, V., Rodchenkov, B., and Markelov, V., *ASTM STP 1505*, Sunriver, OR, 2009, pp. 699–723.

[13] Holt, R. A., "In-reactor Deformation of Cold-Worked Zr–2.5Nb Pressure Tubes," *J. Nucl. Mater.*, Vol. 372, No. 2–3, 2008, pp. 182–214.

[14] Griffiths, M., Wang, N., Buyers, A., and Donohue, S. A., *ASTM STP 1505*, Sunriver, OR, 2009, pp. 541–549.

[15] Rodgers, D. K., Coleman, C. E., Griffiths, M., Bickel, G. A., Theaker, J. R., Muir, I., Bahurmuz, A. A., Lawrence, S. St., and Resta Levi, M., "In-reactor Performance of Pressure Tubes in CANDU Reactors," *J. Nucl. Mater.*, Vol. 383, No. 1–2, pp. 22–27.

[16] Himbeault, D. D., Chow, C. K., and Puls, M. P., "Deformation Behavior of Irradiated Zr–2.5 Nb Pressure Tube Material," *Metall. Mater. Trans. A*, Vol. 25, 1994, pp. 135–142.

[17] Griffiths, M., Christodoulou, N., and Donohue, S. A.," Damage Dependence of Irradiation Deformation of Zr–2.5Nb Pressure Tubes," *J. ASTM Int.*, Vol. 2, 2005, pp. 161–181.

[18] Coleman, C. E., Causey, A. R. and Fidleris, V., "In-Reactor Creep of Zirconium–2.5 wt. % Niobium at 570 K," *J. Nucl. Mater.*, Vol. 60, 1976, pp. 185–194.

[19] Koike, M. and Asada, T., "Irradiation Creep and Growth of Pressure Tubes in HWR Fugen," *J. Nucl. Mater.*, Vol. 159, 1988, pp. 62–74.

[20] Goncharov, V. V., Platonov, P. A., Ivanov, A. N., and Frolov, I. A., "Investigation of In-Reactor Creep and Irradiation Growth of Zirconium–2.5 wt. % Niobium Channel Tubes," *J. Nucl. Mater.*, Vol. 90, 1980, pp. 224–231.

[21] I. T. Bethune, and C. D. Williams, "The $\alpha/(\alpha+\beta)$ Boundary in the zr-nb System," *J. Nucl. Mater.*, Vol. 29, 1969, pp. 129–132.

[22] Hunt, C. E. L. and Niessen, P., "The Effect of Oxygen on the Equilibrium $\beta/\alpha+\beta$ Transformation Temperature of Zirconium-Niobium Alloys," *J. Nucl. Mater.*, Vol. 35, 1970, pp. 134–136.

[23] Hunt, C. E. L. and Niessen, P., "The Continuous Cooling Transformation Behaviour of Zirconium-Niobium-Oxygen Alloys," *J. Nucl. Mater.*, Vol. 38, 1971, pp. 17–25.

[24] Higgins, G. T. and Banks, F. E., "The Basic Features of the Isothermal Pro-Monotectoid Transformation in Zr-2.5 Weight Percent Niobium Alloy," *J. Electrochemical Technol.*, Vol. 4, 1966, pp. 341–346.

[25] V. Fidleris, "The Creep Strength of Quenched and Aged Zr–2.5 wt. % Nb Alloy," *J. Nucl. Mater.*, Vol. 54, 1974, pp. 199–211.

[26] Kapoor, K., Padmaprabu, C., Saroja, S., Paul, T., Rao, S. V. R., Sanyal, T., Rao, M. N., Saibaba, N., and Kashyap, B. P., "On Secondary β-Nb Phase Precipitation within Primary α-Zr Phase in Zr-Nb Alloys During Tensile Deformation," *J. ASTM Int.*, Vol. 2, No. 5, 2005, pp. 102–128.

[27] Cheadle, B. A., Ells, C. E., and Evans, W., "The development of texture in zirconium alloy tubes," *J. Nucl. Mater.*, Vol. 23, 1967, pp, 199–208.

[28] Kiran Kumar, M., Samajdar, I., Venkatramani, N., Dey, G. K., Tewari, R., Srivastava, D., and Banerjee, S., "Explaining Absence of Texture Development in Cold Rolled Two-Phase Zr-2.5 wt% Nb Alloy," *Acta Mater.*, Vol. 51, 2003, pp. 625–640.

DISCUSSION

Question 1, Michel Preuss, University of Manchester, UK:—You mentioned that creep is critical but you only showed flow stress data. Could you please explain that?

Author's Response:—In order to increase the life of pressure tube it is important to keep the creep rate of the material (both axial as well as diametral) as low as possible The aim of the present study was to develop and optimize the fabrication flow sheet to produce pressure tube by heat treatment route. In this work the tubes were successfully fabricated with desirable, microstructure, texture and mechanical properties. The creep properties of these tubes are being evaluated.

Question 2, V. Markelov, Bochvan Inst, VNIIM:—1) How can you explain the lower YS after 515C ageing treatment compared to after 540C ageing temperature? 2) Please comment why the heat treated tubes showed a lower elongation than that of the cold worked tube if so what is the advantage of heat treated PT's than the cold worked tubes.

Author's Response:—1) In this study, it was observed that ageing at 515C did not result in precipitation of beta particles of equilibrium composition and also their size was much smaller. At room temperature, the YS values of samples aged at 515C and aged at 540C were not very much different. Whereas YS at 300C showed much lower value in the case of 515C aged samples. This aspect is explained in the text of the manuscript as: "At higher temperature (300°C), thermally assisted movement of dislocations overcoming obstacles (Beta particles) would determine the mechanical properties. The resistance to the movement would be weaker when the size of the particle is small. Thus, sample aged at 515°C having smaller beta particles would show lower YS. In the case of sample aged at 540°C due to larger particle size and higher particle density, initial dislocation motion is rather difficult thus accounting for the observed higher YS. However, for the similar reasons with the progress of the deformation, dislocation multiplication would become the dominant factor in sample aged at 515°C.

2) The main aim of this study was to fabricate heat treated pressure tube which would eventually show superior creep resistance. Higher YS values at 300C in the case of sample aged at 515 is expected to show better creep properties. The observation of lower elongation value in the heat treated samples may be due to the presence of very fine microstructure with fine beta precipitate being present.

HYDRIDING – HYDROGEN EFFECT

Reprinted from JAI, Vol. 7, No. 7
doi:1520/JAI102979
Available online at www.astm.org/JAI

H. M. Nordin,[1] *A. J. Elliot,*[2] *and S. G. Bergin*[3]

High Temperature Aqueous Corrosion and Deuterium Uptake of Coupons Prepared from the Front and Back Ends of Zr-2.5Nb Pressure Tubes

ABSTRACT: Pressure tubes for CANada Deuterium Uranium (CANDU) reactors are extruded from billets of Zr-2.5Nb, at a temperature of ~815C, and then cold drawn to give a final length of ~6 m. The manufacturing process often results in a variation of properties along the length of a tube including grain structure, texture, dislocation density, and phase distribution. This variation affects the mechanical and deformation properties as well as the aqueous oxidation and deuterium uptake behavior along the installed pressure tube. The orientation of the installed pressure tube in the reactor, with its axial variation of properties, is an important factor in the effective optimization of its service life. This work reports on the differences in aqueous oxidation and deuterium uptake between the extruded front- and back-end sections of a number of pressure tubes. The corrosion tests were conducted in heavy water in static autoclaves at Chalk River Laboratories and in a heavy water re-circulating loop in the Halden Boiling Water Reactor. The test conditions, such as water chemistry and temperature, were similar to those in the primary heat transport system of a CANDU reactor. The results indicate that under some exposure conditions, the deuterium uptake may beup to 40 % lower for back-end coupons compared to front-end coupons. Several microstructural factors including texture, grain

Manuscript received January 13, 2010; accepted for publication June 22, 2010; published online July 2010.

[1] Materials and Mechanics Branch, Chalk River Laboratories, Atomic Energy of Canada, Limited, Chalk River, ON K0J 1J0, Canada, e-mail: nordinh@aecl.ca
[2] Reactor Chemistry and Corrosion Branch, Chalk River Laboratories, Atomic Energy of Canada, Limited, Chalk River, ON K0J 1J0, Canada.
[3] Materials and Mechanics Branch, Chalk River Laboratories, Atomic Energy of Canada, Limited, Chalk River, ON K0J 1J0, Canada, e-mail: bergins@aecl.ca

Cite as: Nordin, H. M., Elliot, A. J. and Bergin, S. G., "High Temperature Aqueous Corrosion and Deuterium Uptake of Coupons Prepared from the Front and Back Ends of Zr-2.5Nb Pressure Tubes," *J. ASTM Intl.*, Vol. 7, No. 7. doi:1520/JAI102979.

Copyright © 2011 by ASTM International, 100 Barr Harbor Drive, PO Box C700, West Conshohocken, PA 19428-2959.

size, and concentrations of alloying elements may cause the observed differences in deuterium uptake. The results will be discussed within the current mechanistic understandings of Zr-2.5Nb corrosion and deuterium ingress.

KEYWORDS: pressure tube, Zr-2.5Nb, deuterium ingress, microstructure, texture

Introduction

A CANada Deuterium Uranium (CANDU) power reactor is a pressurized heavy water reactor that uses natural uranium in the fuel and heavy water as both the coolant and the moderator. Pressure tubes manufactured from Zr-2.5Nb contain the fuel bundles and coolant within the reactor. Each reactor contains 380–480 pressure tubes, arranged horizontally within the reactor (Fig. 1). Heavy water coolant passes through the tubes at a pressure of 10–11 MPa, temperatures between 250 and 312°C, and a fast neutron flux of up to $\sim 4 \times 10^{13}$ n/cm^2/s. These pressure tubes form the primary pressure boundary in the core. In this environment, the inside surface of the Zr-2.5Nb pressure tubes develops an oxide film and absorbs a fraction of the deuterium released during the corrosion process. If sufficient quantities of deuterium are absorbed into the metal, there is the potential for the precipitation of deuterides, which can adversely affect the properties of the tube thereby limiting its operational lifetime.

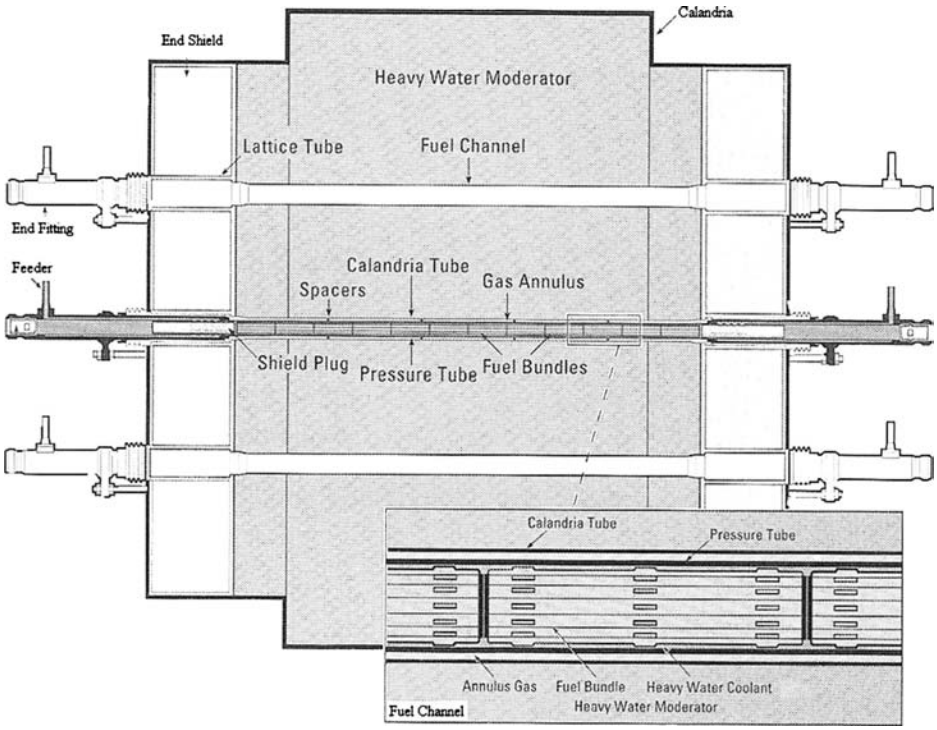


FIG. 1—*Schematic diagram of a CANDU reactor core showing the horizontal pressure tubes.*

Pressure tubes are fabricated by a forging process to convert cast ingots into two logs that are 280 cm long by 21 cm in diameter. The logs are machined to produce hollow billets, which are extruded at 815°C and cold worked 27 % to produce tubes that are 6 m long with an outside diameter of 11.2 cm. The extruded tubes are stress relieved at 400°C for 24 h. The resulting microstructure consists of elongated grains of hcp $\alpha-$Zr, partially surrounded by a thin network of filaments of bcc $\beta-$Zr.

The extrusion process is known to result in an axial variation of microstructure and texture along the pressure tube [1,2]. This axial variation in parameters is primarily due to the difference in the starting and final extrusion temperatures. The extrusion temperature at the front-end of the pressure tube is determined by the soak temperature (815°C) and the time it takes to reach the extrusion press. The extrusion temperature at the back-end is related to the amount of cooling that has occurred during the extrusion process and the adiabatic heating caused by deformation that occurs during extrusion.

Deformation and mechanical properties of pressure tubes are related to microstructure, texture, and composition [1,2]. These factors may also affect oxidation and deuterium pickup. The objective of this paper is to examine the difference in deuterium pickup rate from coupons fabricated from the extruded front end (end out of the extrusion press first, referred to as front-end coupons) and back end (end out of the extrusion press last, referred to as back-end coupons) of the pressure tube. The role of microstructure, texture, and concentration of alloying elements on the difference in deuterium pickup rate between front- and back-end coupons will be examined. The results will be discussed within the current mechanistic understandings of Zr-2.5Nb corrosion and deuterium ingress.

Experimental Details

Materials and Coupon Fabrication

Corrosion coupons were prepared from the extruded front and back ends of the 17 different Zr-2.5Nb pressure tubes listed in Table 1. A summary of the test conditions each tube was exposed to is also provided in Table 1. These pressure tubes are typical of those that are installed in current reactors. There are variations in the fabrication history (e.g., some were β-quenched) and amount of cold work each extruded tube received. Other parameters for the tubes such as minor alloy element concentration, grain size, and texture are listed in Table 2.

For the tests conducted in static autoclaves, the majority of coupons was fabricated from the pressure tube to be 15 mm wide × 30 mm long and retained the full wall thickness of the tube (~ 4 or 6 mm). These coupons were all abraded using 320 grit SiC paper, degreased in an ultrasonic bath containing methanol for 3 min, and air dried. Coupons from Tube A used in the static autoclave tests were fabricated by machining the tube to 10 mm wide × 30 mm long × 1 mm thick. These coupons were not abraded.

For the tests conducted in the re-circulating loop, the coupons were machined from the mid-wall of the pressure tube and retained the original curvature of the tube (30 mm axial × 10 mm transverse × 1 mm radial). The

TABLE 1—*Tube properties and conditions under which coupons were tested.*

Tube	Beta-Quench	Melt	Cold Work (%)	Surface Finish	Test Temperature (°C)	Test Type	Maximum Exposure Time (Days)
Tube A	Yes (hollow billet)	Quad	12	Machined	300, 335	Static autoclave	1200, 1500
Tube B	Yes (hollow billet)	Quad	12	Abraded; machined and prefilmed	300, 335; 335	Static autoclave; Halden in- and out-of-flux	600, 1800; 575, 535
Tube C	Yes (hollow billet)	Quad	12	Abraded	300, 335	Static autoclave	600, 1800
Tube D	Yes (hollow billet)	Quad	27	Abraded; machined and prefilmed	300, 335; 335	Static autoclave; Halden in- and out-of-flux	600, 1800; 575, 535
Tube E	Yes (hollow billet)	Quad	27	Abraded	300, 335	Static autoclave	600, 1800
Tube F	Yes (hollow billet)	Quad	27	Abraded	300, 335	Static autoclave	600, 600
Tube G	No	Double	27	Abraded	300	Static autoclave	450
Tube H	No	Double	27	Abraded	300	Static autoclave	450
Tube I	No	Double	27	Abraded	300	Static autoclave	450
Tube J	No	Double	27	Abraded	300	Static autoclave	450
Tube K	No	Double	27	Abraded	300	Static autoclave	450
Tube L	No	Double	27	Abraded	300	Static autoclave	450
Tube M	No	Double	27	Abraded	300	Static autoclave	450
Tube N	Yes (forged log)	Double	27	Abraded	300	Static autoclave	450
Tube O	Yes (forged log)	Double	27	Abraded	300	Static autoclave	450
Tube P	Yes (hollow billet)	Quad	12	Machined and prefilmed	335	Halden in- and out-of-flux	575, 535
Tube Q	Yes (hollow billet)	Quad	27	Machined and prefilmed	335	Halden in- and out-of-flux	575, 535

TABLE 2—*Texture, grain thickness, and Fe and C concentrations for the tubes used in this work.*

	Percent Nb in Beta Phase (wt %)		Texture						Minimum Grain Thickness (μm)		Chemistry (μg/g±10 %)			
			Front			Back			Front	Back	Front		Back	
Tube	Front	Back	f_R	f_T	f_L	f_R	f_T	f_L	Arithmetic Mean	Arithmetic Mean	Fe	C	Fe	C
Tube A	...	...	0.329	0.618	0.052	0.357	0.605	0.038	0.379±0.206	0.339±0.143	1140	83	1110	80
Tube B	49	50	0.321	0.621	0.058	0.358	0.595	0.047	0.419±0.171	0.397±0.175	1110	95	1130	93
Tube C	50	54	0.327	0.617	0.056	0.36	0.592	0.048	0.433±0.217	0.301±0.161	1120	95	1110	85
Tube D	54	60	0.352	0.594	0.054	0.385	0.568	0.047	0.468±0.194	0.310±0.121	1130	95	1130	90
Tube E	54	60	0.325	0.617	0.057	0.355	0.594	0.051	0.406±0.174	0.326±0.160	1110	90	1130	85
Tube F	60	62	0.343	0.601	0.056	0.384	0.566	0.05	0.539±0.226	0.375±0.164	440	67	440	75
Tube G	52	51	0.322	0.598	0.08	0.391	0.554	0.055	0.612±0.289	0.422±0.186	835	180	920	170
Tube H	53	54	0.298	0.6	0.102	0.34	0.593	0.067	0.549±0.321	0.406±0.201	930	187	990	180
Tube I	51	53	0.293	0.583	0.122	0.34	0.592	0.067	0.600±0.241	0.444±0.194	680	137	720	142
Tube J	48	49	0.268	0.638	0.087	0.342	0.583	0.071	0.528±0.231	0.452±0.190	580	150	610	160
Tube K	51	49	0.301	0.625	0.067	0.332	0.593	0.068	0.563±0.255	0.449±0.204	540	172	540	138
Tube L	42	49	0.284	0.583	0.125	0.344	0.581	0.071	0.645±0.283	0.438±0.204	500	195	510	158
Tube M	44	51	0.291	0.595	0.109	0.347	0.578	0.069	0.580±0.237	0.364±0.142	670	145	640	163
Tube N	42	53	0.29	0.619	0.085	0.347	0.58	0.067	0.580±0.219	0.397±0.176	430	138	460	94
Tube O	45	52	0.285	0.616	0.095	0.345	0.587	0.064	0.557±0.265	0.399±0.202	450	104	450	125
Tube P	48	50	0.327	0.62	0.054	0.354	0.598	0.048	0.410±0.153	0.329±0.124	1200	85	1110	80
Tube Q	54	58	0.319	0.617	0.063	0.373	0.579	0.049	0.550±0.183	0.318±0.115	1100	90	1100	62

coupons were degreased and prefilmed at 400°C for 24 h in 0.7 MPa light water steam, produced an adherent surface oxide of about 0.7–1.8 μm thick.

Static Autoclave Tests

Coupons were exposed in $\sim$ 1200 mL of heavy water in Hastelloy autoclaves, which operated at 300 or 335°C. The autoclaves were purged with Ar gas for $\sim$ 1 h and then evacuated on heat up until a temperature of 40°C was reached. Lithium oxide was added to the autoclave solutions to raise the apparent $p\mathrm{H_a}$ to 10.5, which was measured with a pH meter calibrated for light water.

The autoclaves were operated for 150 day exposure intervals for a total test time of 450 days or 600 days at 300°C (except Tube A, which had a total test time of 1200 days exposure) and $\sim$ 1800 days at 335°C (except for Tube A with 1500 days exposure and Tube F with 600 days exposure).

Halden Boiling Water Reactor

The coupons were exposed in a re-circulating heavy water loop installed in the Halden Reactor, Norway. The loop was designed to perform aqueous corrosion tests within the temperature range of 250–335°C under chemistry conditions similar to those in the primary heat transport system of a CANDU reactor. The chemical purity of the coolant was maintained by a side-stream purification circuit, which used a strong acid–strong base mixed bed ion-exchange resin. The $p\mathrm{H_a}$ of the coolant was controlled by the concentration of LiOD in the loop. An acid-form mixed bed column was available for removing lithium ions. For the majority of the tests, the $p\mathrm{H_a}$ was controlled within the range of 10.2–10.6. The dissolved deuterium concentration in the coolant was controlled within the 5–10 mL/kg range by adding heavy water to the loop that had either a higher or a lower concentration of dissolved deuterium. This range of deuterium concentration ensured that the radiolytic production of oxygen was suppressed.

The out-of-flux component of the test was conducted using an autoclave at a temperature of 335°C that was located in the reactor hall, well away from the core. Coupons tested in-flux were mounted in in-flux assemblies (IFAs) that were located within the reactor core. Within the IFA, coupons were inserted into an independently heated test channel maintained at 335°C through which the heavy water coolant passed. The fast neutron flux was $3–5 \times 10^{13}$ n/cm^2/s, typical of the flux found along a fuel channel in a CANDU reactor. The neutron flux profile for the coupons exposed in-core was set by booster fuel rods positioned outside of the test channel within the IFA.

The corrosion coupons, which were mounted on holders in groups of up to four were stacked with 1 mm thick washers separating them on the mounting posts. To compensate for thermal expansion, the coupons were held in place by a spring-loaded mounting clip. All components in contact with or nearby the coupons were fabricated from either Zircaloy −2 or −4 in order to minimize galvanic effects. The coolant flow over the samples in the IFAs was near 1.0 m/s, whereas the flow in the out-of-core autoclaves was near 0.2 m/s.

Coupon Analysis

At the end of each exposure interval, the coupons were removed from the loop at Halden (~ 180 days) or the static autoclaves (150 days) and were dried and then re-weighed. In selected coupons, a small piece (~ 0.1–0.4 g) of each was sectioned using a saw, and the hydrogen and deuterium concentrations in the small pieces were measured using hot vacuum extraction mass spectrometry (HVEMS) [3].

Results

Static Autoclave Tests

In general, oxygen and deuterium pickup was a linear function of exposure time for each pressure tube. Figure 2 shows the oxygen and deuterium pickup results for Tube D. The linear oxygen and deuterium pickup kinetics are representative of the results for all tubes. Figure 2(*b*) also indicates the difference in deuterium pickup between the front- and back-end specimens.

Figure 3 shows the front-end pickup rate versus the back-end pickup rate for oxygen and deuterium pickup rates at 300 and 335°C. At 300°C, the oxygen pickup rate for the front- and back-end specimens is the same for the majority of the tubes. Three tubes (A, K, and N) show that the oxygen pickup rate at the front end is higher than for the back end. With the exception of Tube A, which was tested for 1200 days, all specimens were tested for a relatively short period of time (450 or 600 days). With longer exposure time, the difference in oxygen pickup rate between the front- and back-end specimens may become more apparent. At 335°C, the oxygen pickup rate for the front-end specimens is greater than for the back-end specimens. The deuterium pickup rate is greater for the front-end specimens in the majority of the tubes tested at 300°C and for all of the tubes tested at 335°C. The test at 300°C is based on a short exposure time and with very few coupons from the same tube. It is possible that with greater exposure time, a noticeable difference in pickup rate between the front- and back-end specimens may have been observed.

Tables 3 and 4 show the percent difference in pickup rate at 300 and 335°C, respectively. As expected, the pickup rates are higher at 335°C than at 300°C. The results indicate that on average, the deuterium pickup rate is about 25 % lower for back-end coupons. However, the deuterium pickup rate may be up to 40 % lower for back-end coupons compared to front-end coupons.

Tubes A–F have lower oxygen and deuterium pickup rates than Tubes G–O regardless of the front- and back-end differences in deuterium pickup rate (Table 3). There were several differences in the fabrication processes used to make the tubes (Table 1. Tubes A–F were all quad melted and beta-quench, while tubes G–O were all double melted and the majority of the tubes were not beta-quenched. As well, Table 2 indicates that Tubes A–F had a lower C concentration and a higher Fe concentration than Tubes G–O.

Halden Tests

Figure 4 shows the oxygen and deuterium pickup for Tube D both in-flux and out-of-flux. The linear behavior of the pickup was typical of that seen

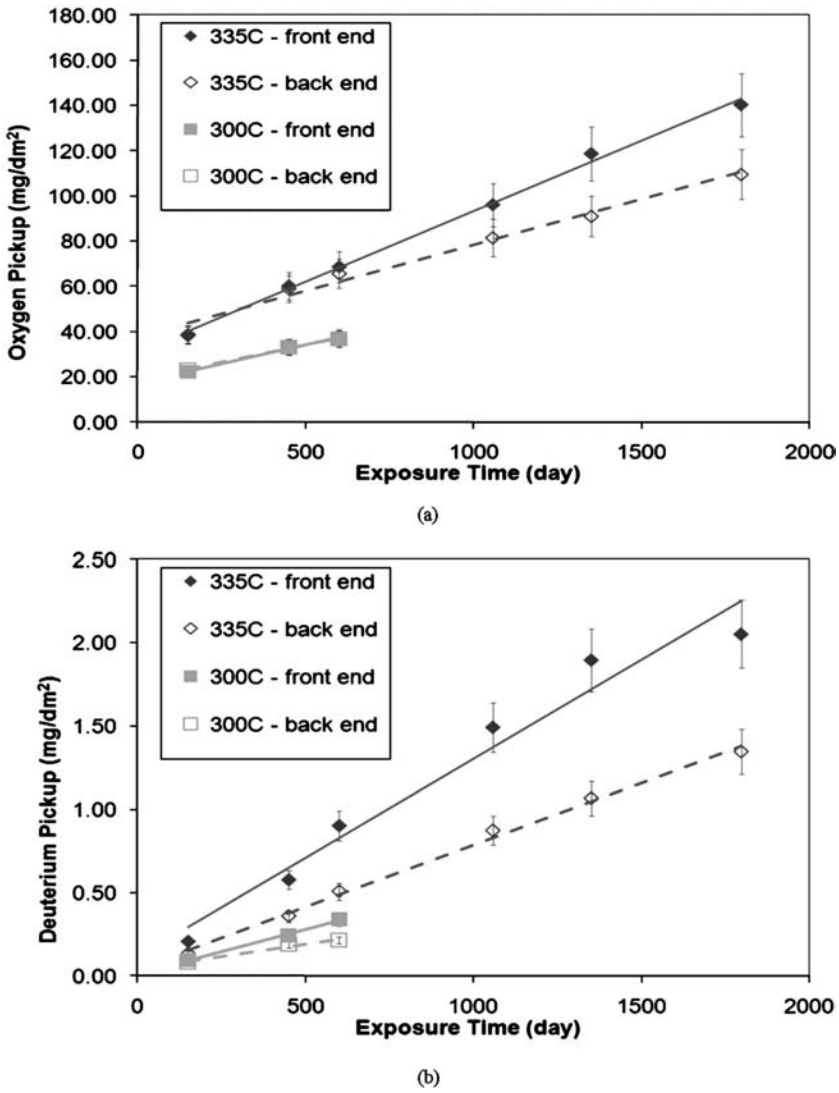


FIG. 2—*(a) Oxygen and (b) deuterium pickups for Tube D. The linear behavior of the oxygen and deuterium pickups at 300 and 335°C is representative of the behavior of all tubes tested.*

in all tubes. Tables 5 and 6 give the oxygen and deuterium pickup rates for out-of-flux and in-flux results, respectively. Oxygen pickup rates for the coupons tested in-flux are notably lower than for the coupons tested out-of-flux. The deuterium pickup rates were similar for both groups of specimens.

Figure 5 shows the front-end pickup rate versus the back-end pickup rate for oxygen and deuterium pickup rates at 335°C in- and out-of-flux. The oxygen

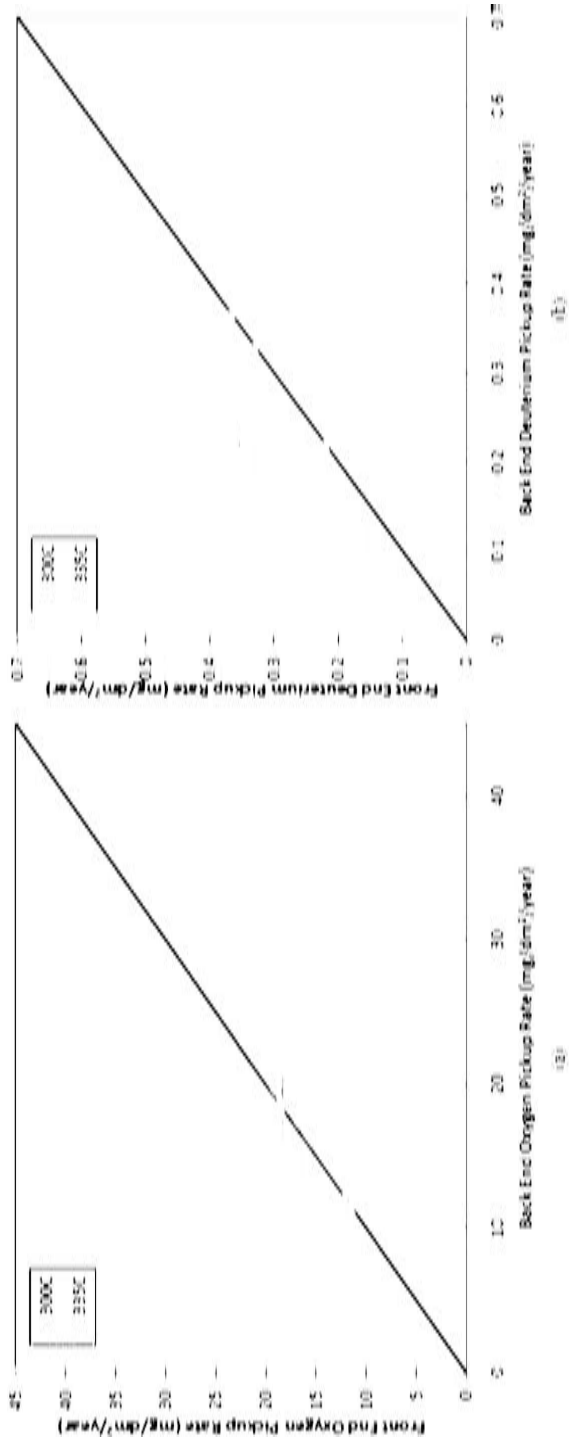


FIG. 3—*Comparison of front- and back-end pickup rates for (a) oxygen pickup rate and (b) deuterium pickup rate.*

TABLE 3—*Comparison of oxygen and deuterium pickup rates at 300°C.*

Tube	Front-End Oxygen Pickup Rate (mg/dm^2/year)	Back-End Oxygen Pickup Rate (mg/dm^2/year)	Percent Difference in Oxygen Pickup Rate (%)	Front-End Deuterium Pickup Rate (mg/dm^2/year)	Back-End Deuterium Pickup Rate (mg/dm^2/year)	Percent Difference in Deuterium Pickup Rate (%)
Tube A	15.6	12.6	19	0.19	0.15	22
Tube B	12.2	12.1	1	0.22	0.15	33
Tube C	13.3	12.2	8	0.22	0.22	0
Tube D	11.8	11.2	5	0.18	0.11	40
Tube E	11.8	11.4	3	0.18	0.15	20
Tube F	15.4	14.4	6	0.15	0.11	25
Tube G	19.4	18.6	4	0.33	0.29	11
Tube H	18.8	18.5	1	0.33	0.33	0
Tube I	18.4	18.3	0	0.33	0.26	22
Tube J	18.9	19.5	−3	0.37	0.37	0
Tube K	17.5	13.0	26	0.37	0.26	30
Tube L	18.3	18.4	0	0.47	0.33	31
Tube M	18.6	17.6	5	0.40	0.37	9
Tube N	17.5	14.5	17	0.33	0.22	33
Tube O	16.6	17.5	−5	0.33	0.18	44

TABLE 4—*Comparison of oxygen and deuterium pickup rates at 335°C.*

Tube	Front-End Oxygen Pickup Rate (mg/dm^2/year)	Back-End Oxygen Pickup Rate (mg/dm^2/year)	Percent Difference in Oxygen Pickup Rate (%)	Front-End Deuterium Pickup Rate (mg/dm^2/year)	Back-End Deuterium Pickup Rate (mg/dm^2/year)	Percent Difference in Deuterium Pickup Rate (%)
Tube A	24.0	16.5	31	0.37	0.22	40
Tube B	31.7	27.8	12	0.62	0.51	18
Tube C	31.3	25.1	20	0.58	0.47	19
Tube D	22.7	14.9	34	0.44	0.26	42
Tube E	25.7	17.8	31	0.47	0.33	31
Tube F	38.6	30.5	21	0.55	0.40	27

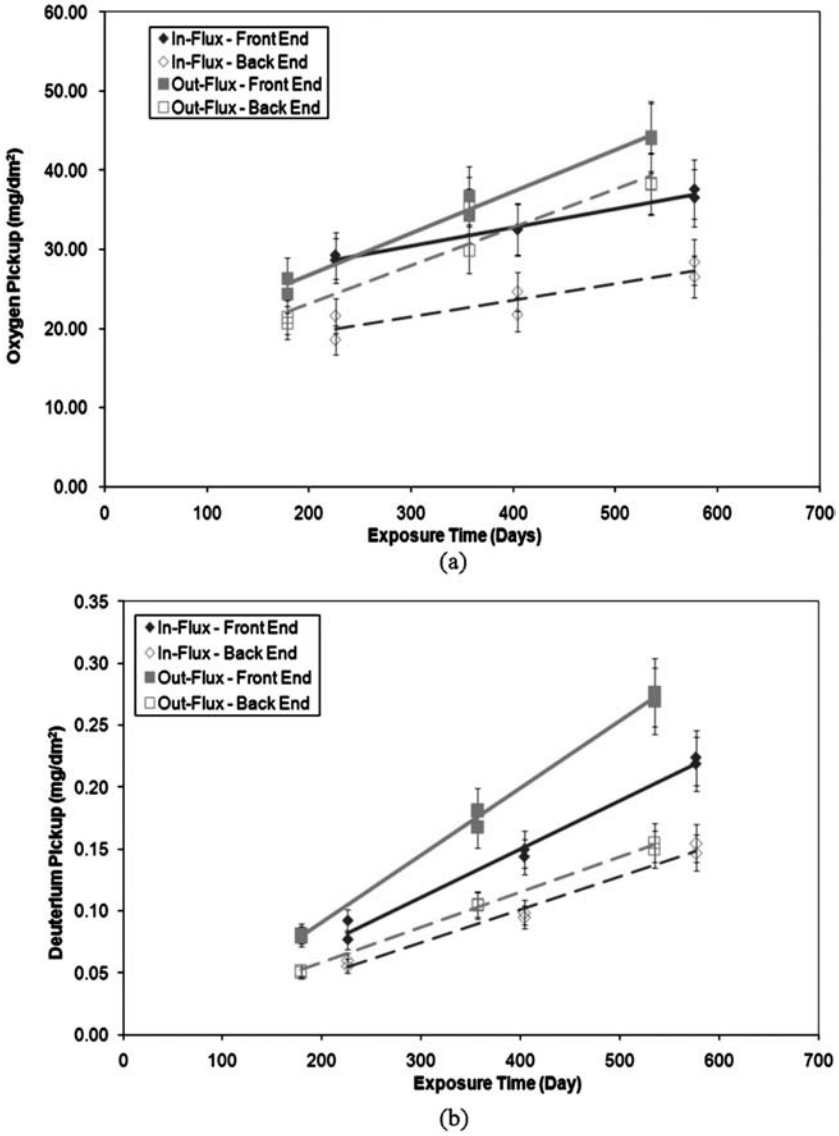


FIG. 4—*(a) Oxygen and (b) deuterium pickups for Tube D. The linear behavior of the oxygen and deuterium pickups at 335°C in- and out-of-flux is representative of the behavior of all tubes tested.*

pickup rate for the front- and back-end specimens is the same for all of the coupons tested out-of-flux. In-flux, for two tubes the oxygen pickup rate is lower for back-end coupons than for front-end coupons. Deuterium pickup rates are lower for back-end coupons than front-end coupons both in- and out-of-flux.

TABLE 5—*Comparison of oxygen and deuterium pickup rates for coupons tested out-of-flux at 335°C.*

Tube	Front-End Oxygen Pickup Rate ($mg/dm^2/year$)	Back-End Oxygen Pickup Rate ($mg/dm^2/year$)	Percent Difference in Oxygen Pickup Rate (%)	Front-End Deuterium Pickup Rate ($mg/dm^2/year$)	Back-End Deuterium Pickup Rate ($mg/dm^2/year$)	Percent Difference in Deuterium Pickup Rate (%)
Tube B	18.7	19.5	−4	0.18	0.11	40
Tube D	19.3	18.9	9	0.18	0.11	40
Tube P	18.7	17.6	−1	0.22	0.15	33
Tube Q	20.5	19.3	6	0.22	0.11	50

TABLE 6—*Comparison of oxygen and deuterium pickup rates for coupons tested in-flux at 335°C.*

Tube	Front-End Oxygen Pickup Rate ($mg/dm^2/year$)	Back-End Oxygen Pickup Rate ($mg/dm^2/year$)	Percent Difference in Oxygen Pickup Rate (%)	Front-End Deuterium Pickup Rate ($mg/dm^2/year$)	Back-End Deuterium Pickup Rate ($mg/dm^2/year$)	Percent Difference in Deuterium Pickup Rate (%)
Tube B	10.41	9.97	4	0.15	0.11	25
Tube D	12.46	9.24	26	0.15	0.11	25
Tube P	8.44	7.67	9	0.15	0.11	25
Tube Q	11.32	7.31	35	0.15	0.11	25

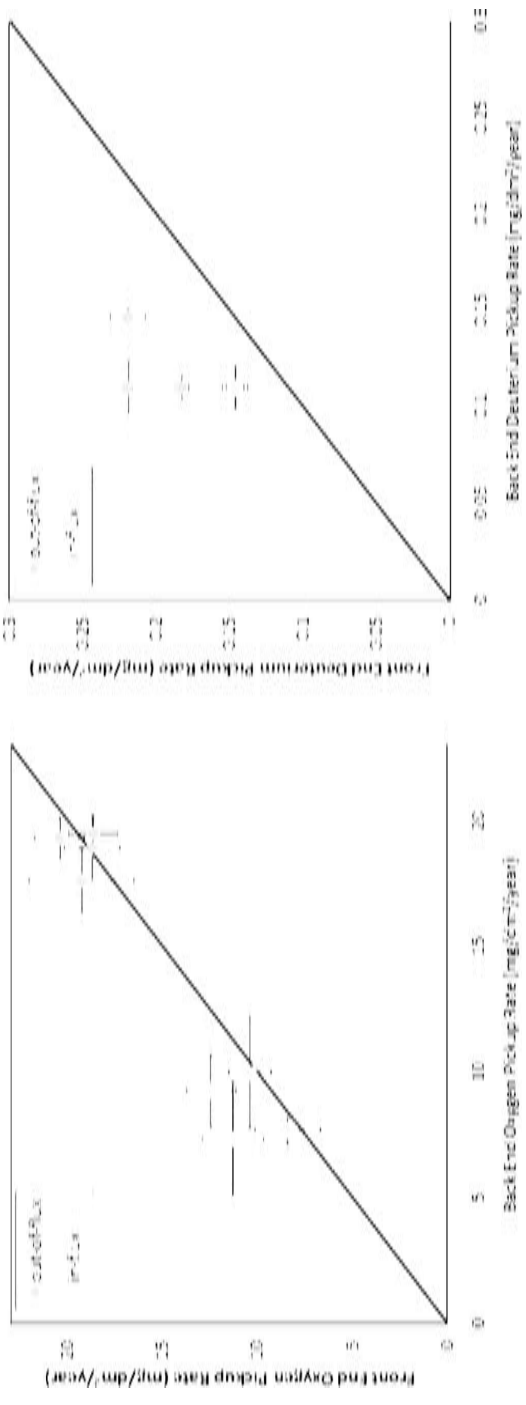


FIG. 5—*Comparison of front- and back-end pickup rates for specimens tested at Halden for (a) oxygen pickup rate and (b) deuterium pickup rate.*

Statistical Analysis

The data indicate that there is a difference in deuterium pickup rates between the front- and back-end coupons tested. The question remains whether the difference in deuterium pickup rates between front- and back-end coupons is statistically significant or not. A paired *t*-test was conducted on deuterium pickup values and several other factors such as minimum grain thickness, texture, and Fe and C concentrations that were considered as a possible cause for the difference in deuterium pickup rate between the front- and back-end coupons.

A paired *t*-test determines if there is a statistically significant difference between two observations (deuterium pickup rate from the front and back ends) made on one set of individual objects (tube) at a specified level of significance. The following hypotheses were tested using the paired *t*-test at a level of significance of 0.05 (i.e., 95 % confidence level):

$$\text{null hypothesis} : \mu_D = 0$$

$$\text{alternative hypothesis} : \mu_D \neq 0$$

where:

μ_D=mean difference between the values of front- and back-end pairs.

The results of the paired *t*-test are presented in Table 7. The first two columns of the table give the mean value of the parameter for the front- and back-end specimens, respectively. Columns 3 and 4 indicate whether the null hypothesis was accepted (i.e., the two means are the same) or rejected (i.e., the two means are different). The last column provides the *P* value indicating the probability of rejecting the null hypothesis given that it is true. If the *P* value is smaller than the level of significance (0.05), then the null hypothesis can be rejected indicating that the mean value of the parameter at the front end is different than the mean value of the parameter at the back end.

The conducted paired *t*-tests show that at the 95 % confidence level, there is a statistically significant change in deuterium pickup rate from front to back end at 300 and 335°C in static autoclaves and for the out-of-flux tests conducted at Halden. It is likely that the 25 % difference observed in deuterium pickup rates between front- and back-end coupons tested in-flux is also significant. However, the paired *t*-test could not be applied to these data as there is no variance in the difference between front- and back-end coupons.

Table 8 and Fig. 6 show the factors that are correlated with deuterium pickup rate at 300°C for the front- and back-end coupons. It was postulated that the other parameters that show a statistically significant difference from front to back end, based on the paired *t*-test, may be a cause of the difference in deuterium pickup between the front- and back-end coupons. There does not seem to be a single factor that causes the difference, but quite possibly it is caused by variations of several factors or synergistic effects between factors. In fact, some of the variables are correlated, for example, Fe concentration with some of the texture parameters. Correlations were only examined for the 300°C static autoclave data as there were only six tubes tested at 335°C and 15 tested at 300°C.

TABLE 7—*Results from the paired t-test to determine the factors that show a statistically significant difference between front- and back-end coupons.*

Parameter	μ_f (Mean Front-End Coupons)	μ_b (Mean Back-End Coupons)	Same ($\mu_f - \mu_b = 0$)	Different ($\mu_f - \mu_b \neq 0$)	*P* Value
Deuterium pickup rate at 300°C (static autoclave) (mg/dm^2/year)	0.29	0.23		√	0.0003
Oxygen pickup rate at 300°C (static autoclave) (mg/dm^2/year)	16.27	15.32		√	0.0261
Deuterium pickup rate at 335°C (static autoclave) (mg/dm^2/year)	0.51	0.37		√	6×10^{-5}
Oxygen pickup rate at 335°C (static autoclave) (mg/dm^2/year)	28.99	22.10		√	0.0001
Deuterium pickup rate at 335°C (Halden out-flux) (mg/dm^2/year)	0.20	0.12		√	0.0029
Oxygen pickup rate at 335°C (Halden out-flux) (mg/dm^2/year)	19.29	18.81	√		0.4688
Deuterium pickup rate at 335°C (Halden in-flux) (mg/dm^2/year)	0.15	0.11	. . . [a]	. . . [a]	. . . [a]
Oxygen pickup rate at 335°C (Halden in-flux) (mg/dm^2/year)	10.66	8.55	√		0.0979
[Fe] (ppm wt)	778	793	√		0.0839
[C] (ppm wt)	129	123	√		0.2182
Percent Nb in the beta phase	50	53		√	0.0021
f_R	0.31	0.36		√	1×10^{-9}
f_T	0.61	0.58		√	7×10^{-6}
f_L	0.08	0.06		√	0.0002
Minimum grain thickness (μm)	0.52	0.39		√	6×10^{-8}

[a] Not able to complete the paired *t*-test as the tubes have the same deuterium pickup values for the front- and back-ends. In using the paired *t*-test, it is assumed that the difference between the pairs is randomly distributed and there is a variance between the pairs. With the values all being the same (Table 6), the difference between the front- and back-end pairs are not randomly distributed and there is no variance; therefore, the paired *t*-test does not apply.

TABLE 8—*Correlation table showing the parameters correlated with deuterium pickup.*

	Correlation Factor	
Parameter	Front	Back
Oxygen pickup rate	0.79	0.79
[Fe]	−0.59	−0.33
[C]	0.87	0.90
Percent Nb in the beta phase	−0.74	−0.71
f_R	−0.85	−0.49
f_T	0.21	−0.08
f_L	0.85	0.78
Minimum grain thickness	0.79	0.58

Discussion

Oxygen and Deuterium Pickup Model

Figure 7 shows schematically the corrosion and deuterium ingress processes in zirconium [4–10]. During the corrosion process in an aqueous solution, the inside surface of the Zr-2.5Nb pressure tube is covered with a layer of zirconium oxide.

In its simplest form the corrosion reaction between Zr and heavy water can be expressed as follows:

$$Zr + 2D_2O \rightarrow ZrO_2 + 2D_2 \tag{1}$$

Corrosion is an electrochemical process made up of two components: Anodic and cathodic reactions. At the metal-oxide interface, the oxidation reaction occurs

$$Zr + 2O^{2-} \rightarrow ZrO_2 + 4e^- + 2 \text{ vacancies} \tag{2}$$

The electrons and vacancies produced by the above reaction migrate to the oxide-solution interface to maintain charge neutrality. The vacancies interact with oxygen ions, and the electrons are consumed through the cathodic reactions

$$2 \text{ vacancies} + 4e^- + 2D_2O \rightarrow 2O^{2-} + 4D \tag{3}$$

and/or

$$D^+ + e^- \rightarrow D \tag{4}$$

the deuterium atoms generated can combine to form D_2

$$D + D \rightarrow D_2 \tag{5}$$

or they can migrate through the oxide layer via oxide crystallite grain boundaries into the underlying metal. If the solubility limit of deuterium in the metal is exceeded, zirconium hydrides form

$$Zr + xD \rightarrow ZrD_x \tag{6}$$

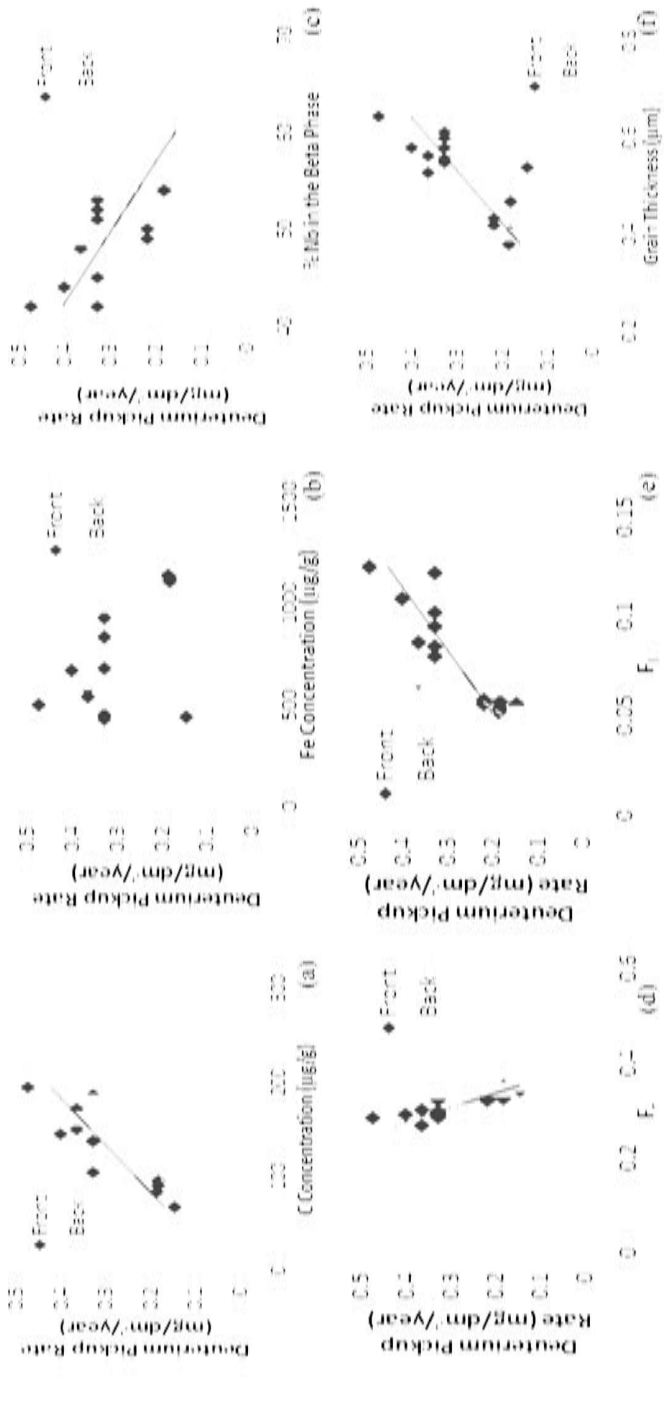


FIG. 6—*Plots showing relationship between deuterium pickup rate and* (a) *carbon concentration* (b) *Fe concentration,* (c) *percent Nb in the beta phase,* (d) *texture parameter* F_r, (e) *texture parameter* F_t, *and* (f) *minimum grain thickness.*

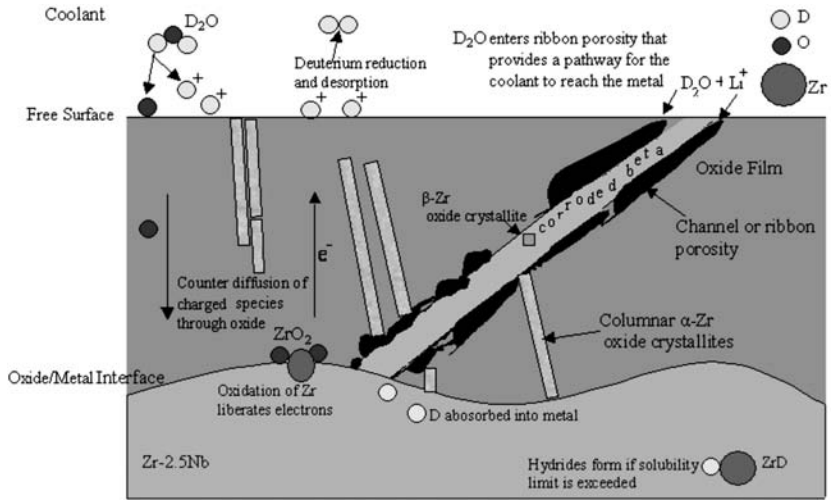


FIG. 7—*A simplified schematic diagram illustrating the general oxygen and deuterium ingress processes in Zr-2.5Nb [4].*

In the early stages of oxidation, the oxide layer is thin and protective. It is formed by epitaxial growth of zirconia crystallites on the zirconium metal [5]. Initially, the oxide structure is largely tetragonal, stabilized by the high compressive stress and possibly other factors like interfacial energy, chemical doping, and very fine grain structure. During oxide growth, the stresses in the oxide resulting from the volume expansion induce preferential oxide orientation that

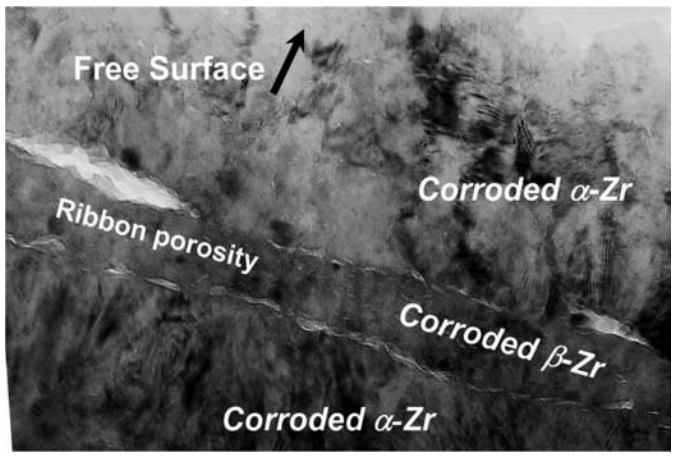


FIG. 8—*A transmission electron microscope image of the oxide film formed on Zr-2.5Nb pressure tube material [4]. Channel or ribbon porosity is formed on either side of the corroded β−*Zr *phase along prior α/β boundaries. The formation of channel porosity is used as the basis of the deuterium ingress model.*

reduces the stresses resulting in columnar oxide grains oriented in the growth direction. As the oxide continues to grow, the compressive stresses are reduced and the oxide eventually transforms from the tetragonal phase to monoclinic [6]. This transformation is accompanied by the development of fine pores [7,8].

Transmission electron microscopy images of the oxide film formed on Zr-2.5Nb pressure tube material shows long channels of porosity formed on either side of the corroded β−Zr phase (Fig. 8). This porosity needs to be incorporated into the model for deuterium ingress. The central idea behind the model for deuterium ingress (Fig. 7) is the development of interconnected channel or ribbon porosity forming along prior α/β boundaries that may extend from the free surface to the oxide/metal interface [9–11]. The microstructure of Zr-2.5Nb pressure tubes consists of hexagonal α−Zr grains surrounded by ligaments of bcc β−Zr phase. The oxidized β−Zr has a different microstructure than the oxidized α−Zr [9,12,13]. This results in the columnar oxide crystallites terminating at the α−Zr/β−Zr boundary. The oxide between the fine pores associated with the oxide crystallites that terminate at the α−Zr/β−Zr boundary is susceptible to dissolution by the high temperature and high *p*H aqueous solution. This creates meandering channel porosity that originates at the free surface and extends into the oxide film. The number of channels that form and the direction they take within the film depend on the continuity and distribution of the network of α−Zr/β−Zr boundaries in the pressure tube.

Effect of Fabrication Processes on Oxygen and Deuterium Pickup

The results presented in Table 3 indicate that the oxygen and deuterium pickup rates can be grouped into two categories: The first for Tubes A–F and the second for Tubes G–O. There were several differences in the fabrication processes used to make the tubes including the number of times the ingot material was melted, whether or not beta-quenching was used, and differences in the Fe and C concentrations.

Previous studies have shown that beta-quenched tubes have a lower corrosion rate than non-beta-quenched tubes [14]. Beta-quenching results in a uniform microstructure with a relatively fine distribution of β−Zr phase [14]. The majority of the

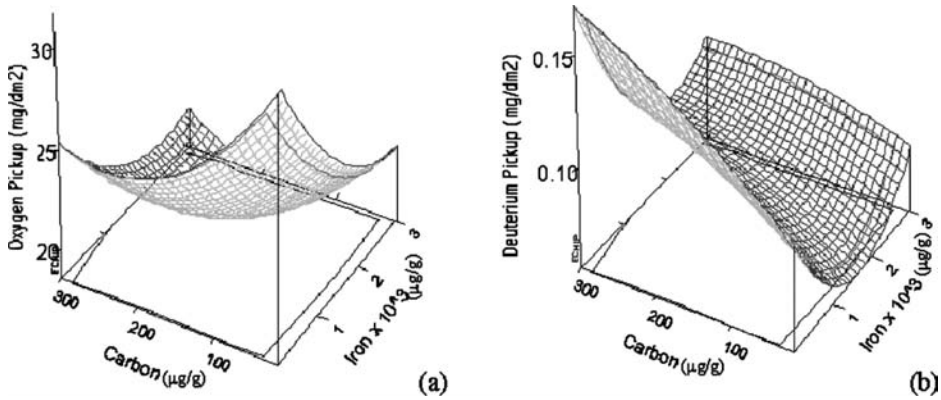


FIG. 9—*The effect of Fe and C on oxygen and deuterium pickup in micro-pressure tubes tested at 300°C for 150 days [11].*

tubes in the group G–O is non-beta-quenched, while those in the group A–F are beta-quenched. The beta-quenched tubes have a lower deuterium pickup rate as expected.

Quad melting of the ingots was found to reduce initial hydrogen, chlorine, and phosphorous concentrations and to improve the fracture toughness properties of the tubes [15]. Measurements made on double melted and quad melted tubes removed from a reactor do not shown a difference in deuterium pickup [15].

The other notable difference is the majority of the tubes in group A–F have a lower C concentration and higher Fe concentration than the tubes in group G–O. The effect of impurities on oxidation and deuterium ingress in Zr-2.5Nb alloys has been studied both in- and out-of-flux [16–18]. A designed experiment conducted to establish the effect of alloying element concentration on deuterium pickup indicated that Fe and C are the main alloying elements that influence corrosion and deuterium pickup. Figure 9 illustrates the effect these alloying elements have on corrosion and deuterium ingress in Zr-2.5Nb-Fe/C/Si/Cr micro-pressure tubes. The results observed in this work are consistent with the effect seen in the microtubes.

Although fabrication processes may affect the deuterium pickup rate, there is still a difference in deuterium pickup rate between the front and back ends of the pressure tube.

Effect of Various Parameters on Oxygen and Deuterium Pickup

Although a detailed understanding of the corrosion and deuterium ingress process for Zr–2.5Nb pressure tubes has yet to be developed, the above discussion provides a broad framework for current understanding of the process. In addition to the framework provided above, an understanding of how chemistry (impurity elements), microstructure, and texture affect oxygen and deuterium pickup is needed to interpret the results of this experiment.

Impurities—In the current tests, carbon is positively correlated with deuterium pickup rate for the front and back ends. This is consistent with the effect of carbon seen in the microtubes [16–18]. For Fe, there is a weak negative correlation with deuterium pickup rate for the front end, which is also consistent with the effect seen in Fig. 9 as the range of Fe concentrations studied would be to the left of the minimum seen in Fig. 9. A correlation does not exist between Fe and deuterium pickup rate for the back-end coupons. It is possible that the effect of Fe in the back-end coupons is masked by other parameters such as the much smaller grain sizes seen in the back-end coupons.

The difference in C and Fe concentrations between the front- and back-end coupons was not statistically significant. Although both Fe and C play a role in oxygen and deuterium pickup, they are not the main factors responsible for the difference in deuterium pickup rate between front- and back-end coupons. However, the impurity elements may also affect other parameters such as the microstructure. For instance, Fe is distributed throughout the β-phase and concentrated at α/β interfaces, giving rise to smaller α-grains and a larger volume of $\beta-$Zr [19]. The effect of grain size on oxidation and deuterium pickup will be discussed later in the paper.

Content of Nb in the Beta Phase—The percent Nb in the beta phase is negatively correlated with deuterium pickup rate for both the front- and back-end

coupons. More percent Nb indicates that there is more beta-phase transformation, and this would create less continuity between the α/β grain boundaries. With less continuity in α/β grain boundaries, there should be less ribbon porosity forming, creating fewer interconnected pathways from the oxide/D_2O interface to the oxide/metal interface and lower deuterium pickup.

The percent Nb in the beta phase is derived from a lattice parameter measurement assuming that the Nb content is the only controlling factor. It is possible that variations in the percent Nb from the front to back end of the tubes is related to temperature variations in the autoclaves used for the 24 h stress relief at 400°C. If the percent Nb is a true measure of the beta phase decomposition, then this may indicate that the tubes are installed in the autoclave in the same orientation with the front end placed where the temperature in the autoclave is slightly cooler so that less beta phase decomposition occurs.

In addition to the Nb content, the lattice parameter that is measured by X-ray diffraction may be affected by other variations in the concentration of elements and by differences in the residual stresses of the tubes. The back ends tend to be harder than the front ends, so there may be higher residual stresses in the back end even after autoclaving. The higher residual stresses would likely be seen as higher compression in the radial direction for the back end, resulting in the lattice parameter measurement being smaller and the percent Nb in the beta phase interpreted as being higher.

Although the true interpretation of the percent Nb in the beta phase value is not known, the data for this relatively small set of tubes indicate that there is a statistically significant difference between this value for front and back end coupons and that this value is correlated with deuterium pickup rate.

Texture Parameters—Texture of pressure tubes is established during the extrusion process. The α-grains tend to have basal poles distributed within 30° of the transverse direction in the radial-transverse plane. Texture varies along the length of the tube. Self-diffusion and diffusion of impurities in $\alpha-$Zr are anisotropic with diffusion parallel to the **c**-axis being faster than diffusion parallel to the **a**-axis [20]. Diffusion is slowest in the basal plane; therefore, tubes with a higher number of basal planes oriented in the radial direction should have lower oxygen and deuterium pickup. A comparison of the pickup values for Tube D (high f_R parameter) and Tube J (low f_R parameter) shows this effect.

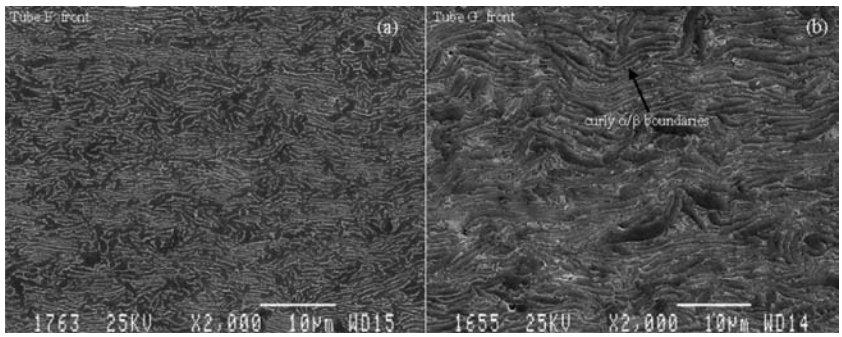


FIG. 10—*Representative SEM images showing the microstructure of each tube.*

TABLE 9—*Description of the microstructure seen in SEM images from the front- and back-end coupons.*

Tube	Grain Structure Description Front	Grain Structure DescriptionBack
Tube F	Relatively uniform small α-grains; uniform α/β boundaries	Relatively uniform small α-grains; uniform α/β boundaries
Tube G	Large α-grains; some coarse α-grains; curly α/β boundaries	Mixture of small platelet like α-grains with a few coarse α-grains; small areas of curly α/β boundaries but mostly uniform α/β boundaries
Tube H	Coarse α-grains; large amount of Widmanstätten structure; mostly uniform α/β boundaries	Mixture of coarse and fine α-grains; small areas of Widmanstätten structure; mostly uniform α/β boundaries
Tube I	Relatively uniform large α-grains; mostly uniform α/β boundaries	Mixture of coarse and fine α-grainsmostly uniform α/β boundaries
Tube J	Large α-grains; small amounts of Widmanstätten structure; regions of curly α/β boundaries	Small α-grains; small amounts of Widmanstätten structure; uniform α/β boundaries
Tube K	Large α grains; curly α/β boundaries; coarse β−Zr phase	Mixture of large and small α-grains; curly α/β boundaries
Tube L	Large α-grains; moderate amount of Widmanstätten structure; uniform α/β boundaries; coarse β−Zr phase	Fine α-grains; mostly uniform α/β boundaries, some curly regions
Tube M	Large α-grains; coarse β−Zr	Bands of fine α-grains separated by large α-grains; bands of thin β-filaments separated by regions of coarser curlier structure
Tube N	Relatively uniform large α-grains; coarse β−Zr	Mixture of large and fine α-grains; mostly uniform α/β boundaries with some curly regions
Tube O	Coarse α-grains; large amount of Widmanstätten structure; curly α/β boundaries	Mixture of coarse and fine α-grains; curly α/β boundaries

The texture parameter f_R is negatively correlated with deuterium pickup rate for the front-end coupons. The back end has higher f_R parameters than the front, so it may be expected that the back ends would have lower deuterium pickup for this reason, but the correlation between f_R and deuterium pickup for the back-end coupons is very weak. The f_L texture parameter is positively correlated with deuterium pickup rate for both the front- and back-end coupons. The f_L texture parameter tends to be lower for back-end coupons.

Deuterium ingress is dependent on the orientation and distribution of β−Zr ligaments, which affect the formation of channel porosity. The texture can be associated with the distribution of β−Zr. Curly microstructures (Fig. 10) suggest a rotation of the **c**-axis of the crystal, which causes the β−Zr filaments to be oriented perpendicular to the free surface [21].

Texture parameters were shown to have a statistically significant difference for the front- to back-end coupons, so these parameters likely have a role in causing the difference in deuterium pickup rate observed between front- and back-end coupons.

Grain Microstructure—Table 9 describes the microstructure seen in the coupons. The tube-to-tube microstructural variability observed is related to the differences in the manufacturing process (extrusion temperature, billet soak time, billet grain size, and cooling temperature). Microstructural analysis indicates that the uniformity of the α-phase and β-phase significantly affects corrosion and deuterium pickup [21–23].

Qualitatively, the differences in minimum grain thickness between the front and back ends can also be considered as differences in the α/β grain boundary continuity. As seen in Table 2, the front-end coupons have a larger grain thickness than the back-end coupons (likely due to the higher extrusion temperature at the front end). The continuity of the α/β boundaries is greater at the front end, leading to higher deuterium pickup rates. The back end also has more β-phase decomposition, representing a disruption of the α/β grain boundary continuity and therefore lower deuterium pickup.

Although a detailed understanding of the corrosion and deuterium ingress process for Zr-2.5Nb pressure tubes has yet to be developed, the above discussion provides the broad framework of a general understanding of the process by which the results of tests can be interpreted. The effect of several factors on oxygen and deuterium pickup has also been discussed in terms of how the effect can be related to the model of deuterium ingress. The exact cause of deuterium pickup rates being lower for back-end coupons than for front-end coupons is unknown, but it is likely related to the manufacturing process and synergistic relationships between texture, microstructure, and microchemistry.

Conclusion

Static autoclave tests at 300 and 335°C along with tests conducted both in and out-of-flux at 335°C at the OECD Halden Research Reactor have indicated that there is a statistically significant difference in deuterium pickup rate between coupons prepared from the front end of the pressure tube and those prepared from the back end. On average, the difference in deuterium pickup rate is 25 %,

with the back-end coupons being lower than the front-end coupons. However, the difference in deuterium pickup rate may be as high as 40 %.

Statistically significant differences between front- and back-end coupons were also observed for the percent Nb in the β-phase, the texture parameters, and the minimum grain thickness. These factors along with the Fe and C concentrations are correlated with the deuterium pickup rate. It is unlikely that the observed difference in deuterium pickup rates between front- and back-end coupons is due to one single factor. The cause is likely linked to the variability in several factors that results during the manufacturing process and the synergistic interactions between these factors.

The deuterium ingress model presented is based on the development of interconnected channel or ribbon porosity that may extend from the free surface to nearly the oxide/metal interface [4–10]. The possible effect of texture, grain size, and percent Nb in the β-phase and Fe and C on the continuity of alpha/beta boundaries and how this may affect the development of channel porosity have been discussed. Although a detailed understanding of the corrosion and deuterium ingress process for Zr-2.5Nb pressure tubes has yet to be developed, the deuterium ingress model provides a broad framework of a general understanding of the process.

Acknowledgments

The writers would like to thank A. Buyers, A. Gin, and A. Shaddick for their technical assistance; the staff at the Halden reactor for the excellent operation of the loop; the staff in the hot cells and HVEMS facility at AECL-CRL; O. T. Woo for assistance with completing the grain size measurements; and V. Urbanic, R. Ploc, G. McRae, M. Griffiths, and G. Bickel for insightful discussions about interpretation and physical meaning of the results.

References

[1] Bickel, G. A. and Griffiths, M., "Manufacturing Variability, Microstructure and Deformation of Zr-2.5Nb Pressure Tubes," *Zirconium in the Nuclear Industry: 15th International Symposium, ASTM STP 1505*, B. Kammenzind and M. Limbäck, Eds., ASTM International, West Conshohocken, PA, 2009, pp. 529–538.

[2] Griffiths, M., Wang, N., Buyers, A., and Donohue, S. A., "Effect of Irradiation Damage on the Deformation Properties of Zr-2.5Nb Pressure Tubes," *Zirconium in the Nuclear Industry: 15th International Symposium, ASTM STP 1505*, Sunriver, OR, 2009, B. Kammenzind and M. Limbäck, Eds., ASTM International, West Conshohocken, PA, pp. 541–549.

[3] Bickel, G. A., Green, L. W., James, M. W. D., Lamarche, T. G., Leeson, P. K., and Michel, H., "The Determination of Hydrogen and Deuterium in Zr-2.5Nb Material by Hot Vacuum Extraction Mass Spectrometry," *J. Nucl. Mater.*, Vol. 306, 2002, pp. 21–29.

[4] Urbanic, V. F. and Ploc, R. A., private communication, 2006.

[5] Ploc, R. A., "Electron Diffraction Studies of ZrO2 on α-Zr (1120)," *J. Nucl. Mater.* Vol. 113, 1983, pp. 75–80.

[6] Godlewski, J., Gros, J. P., Lambertin, M., Wadier, J. F., and Weidinger, H., "Raman Spectroscopy Study of the Tetragonal-to-Monoclinic Transition in Zirconium Oxide Scales and Determination of Overall Oxygen Diffusion by Nuclear Microanalysis of O^{18}," *Zirconium in the Nuclear Industry: Ninth International Symposium, ASTM STP 1132*, C. M. Euchen and A. M. Garde, Kobe, Japan, 1991, Eds., ASTM International, West Conshohocken, PA, pp. 416–436.

[7] Cox, B., "Effects of Irradiation on the Oxidation of Zirconium Alloys in High Temperature Aqueous Environments," *J. Nucl. Mater.*, Vol. 28, 1968, pp. 1–47.
[8] Cox, B., "Processes Occurring During the Breakdown of Oxide Films on Zirconium Alloys," *J. Nucl. Mater.*, Vol. 29, 1969, pp. 50–66.
[9] Ploc, R. A. and McRae, G. A., "Deuterium Absorption in CANDU Zr-2.5Nb Pressure Tubes," *Proceedings of the 14th International Corrosion Conference* (CDROM), Cape Town, South Africa, Sept. 26–Oct. 1, 1999.
[10] Ploc, R. A. and Newcomb, S. B., "Porosity in Zr-2.5-Nb Corrosion Films," *Micorscopy of Oxidation-3*, S. B. Newcomb and J. A. Little, Eds., Institute of Materials, London, 1997, pp. 475–487.
[11] Ploc, R. A., "Mechanism of Deuterium Pickup in Zr-2.5Nb Alloy," *Microscopy of Oxidation 4*, G. Tatlock and S. B. Newcomb, Eds., Institute of Materials, London, 1999.
[12] Lin, Y. P. and Woo, O. T., "Oxidation of β-Zr and Related Phases in Zr-Nb Alloys: An Electron Microscopy Investigation," *J. Nucl. Mater.*, Vol. 277, 2000, pp. 11–27.
[13] Lin, Y. P., "Nature of Oxidised β-Phases in Zr-2.5Nb Alloy," *Micorscopy of Oxidation-3*, S. B. Newcomb and J. A. Little, Eds., Institute of Materials, London, 1997, pp. 462–474.
[14] Warr, B. D., Perovic, V., Lin, Y. P., and Wallace, A. C., "Role of Microchemistry and Microstructure on Variability in Corrosion and Deuterium Uptake of Zr-2.5Nb Pressure Tube Material," *Zirconium in the Nuclear Industry: 13th International Symposium, ASTM STP 1423*, Annecy, France, 2002, G. D. Moan and P. Rudling, Eds., ASTM International, West Conshohocken, PA, pp. 313–338.
[15] Theaker, J. R., Choubey, R., Moan, G. D., Aldridge, S. A., Davis, L., Graham, R. A., and Coleman, C. E., "Fabrication of Zr-2.5Nb Pressure Tubes to Minimize the Harmful Effects of Trace Elements," *Zirconium in the Nuclear Industry: Tenth International Symposium, ASTM STP 1245*, Baltimore, MD, 1994, A. M. Garde and E. R. Bradley, Eds., ASTM International, West Conshohocken, PA, pp. 221–242.
[16] Ploc, R. A., "The Effect of Minor Alloying Elements on Oxidation and Hydrogen Pickup in Zr-2.5Nb, "*Zirconium in the Nuclear Industry: Thirteenth International Symposium, ASTM STP 1423*, Annecy, France, 2002, G. D. Moan and P. Rudling, Eds., ASTM International, West Conshohocken, PA, pp. 297–312.
[17] Ploc, R. A., "The Influence of Impurities in Zr-2.5Nb and Their Effect on Deuterium Pickup at 573 K in D_2O," *J. Phys. IV*, Vol. 03, 1993, pp. C9-763–C9-770.
[18] Ploc, R. A., "Residual Carbon Impurities in Zr-2.5Nb and Their Effect on Deuterium Pickup," *J. Nucl. Mater.*, Vol. 279, 2000, pp. 344–350.
[19] Griffiths, M., Private Communication, 2002.
[20] Pemsler, J. P., "Diffusion of Oxygen in Zirconium and Its Relation to Oxidation and Corrosion," *J. Electrochem. Soc.*, Vol. 105, No. 6, 1958, pp. 315–322.
[21] Warr, B. D., Perovic, V., and Lin, Y. P., "Role of Microchemistry and Microstructure on Variability in Corrosion and Deuterium Uptake of Zr-2.5Nb Pressure Tube Material," *Zirconium in the Nuclear Industry: 13th International Symposium, ASTM STP 1423*, G. D. Moan and P. Rudling, Eds., ASTM International, West Conshohocken, PA, 2002, pp. 313–336.
[22] Urbanic, V. F. and Gilbert, R. W., "Effect of Microstructure on the Corrosion of Zr-2.5Nb Alloy," Presented at the *IAEA Technical Committee Meeting on Fundamental Aspects of Corrosion of Zirconium-Base Alloys for Water Reactor Environments*, Portland, OR, Sept. 11–15, 1989, IAEA.
[23] Urbanic, V. F. and Griffiths, M., "Microstructural Aspects of Corrosion and Hydrogen Ingress in Zr-2.5Nb," *Zirconium in the Nuclear Industry: 12th International Symposium, ASTM STP 1354*, Toronto, Ontario, Canada, 2000, G. P. Sabol and G. D. Moan, Eds., ASTM International, West Conshohocken, PA, pp. 641–657.

DISCUSSION

Question 1, P. Bossis, CEA, France:—What was the difference in corrosion kinetics and hydrogen pick-up fraction between in-flux and out-of-flux samples?

Author's Response:—Table 5 and Table 6 in the paper provide the oxygen and deuterium pickup rates for the coupons tested out-of-flux and in-flux respectively. The oxygen pickup rate out-of-flux was higher than the in-flux rate. The deuterium pickup rates were similar both in and out-of-flux. After more than 500 days exposure, the percent theoretical uptake tended to be lower for back end coupons than for front-ends. For the front end specimens, the percent theoretical uptake was higher out-of-flux than in-flux. The back end specimens showed lower percent theoretical uptake out-of-flux than in-flux.

Question 2, V. Markelov, VNIINM, Russia:—1) What is the typical carbon content in the pressure tube material: 100 or 200 ppm? 2) Please comment on a change of the Nb content in the β-Zr for the back end and the front end specimens after in-flux and out-of-flux corrosion tests.

Author's Response:—1) For tubes fabricated prior to ~2002, the average carbon content in the pressure tubes is 125 ppm. For tubes fabricated more recently the specification for carbon was modified such that the maximum carbon content is 125 ppm.

2) The %Nb in the beta phase data presented in this paper were measured prior to completing any corrosion tests. As the %Nb was not measured after these tests, no data exist to confirm how the %Nb concentrations changed after testing. It is thought that, for the out-of-flux tests the %Nb values should increase due to thermal decomposition of the beta phase. For the in-flux tests, beta phase decomposition was likely suppressed due to irradiation.

Question 3, A. Motta, Penn State University, USA:—1) Was the hydrogen pickup rate difference due to higher corrosion or higher pickup fraction? 2) Is there higher corrosion rate of the β-grains compared to the α-grains? 3) Have you considered performing a quantification of the α-β grain boundary microstructure in terms of its overall orientation to support your hypothesis of H pickup mechanism?

Author's Response:—1) Table 3–Table 6 in the paper shows the oxygen pickup rates. Table 7 shows there was a statistically significant difference in oxygen pickup rate between front and back end specimens tested in static autoclaves but the difference in oxygen pickup rate was not statistically significant for specimens tested both in- and out-of-flux at Halden.

2) Reference [22] and [23] indicate that corrosion of β-Zr is faster than α-Zr. With the experiments described in this paper, the authors are not able to determine the individual corrosion rates of the α-Zr and β-Zr phases.

3) No quantification has been attempted. Consideration will be given toward incorporating this type of assessment into future studies on deuterium pickup mechanisms.

Question 4, P. Rudling, ANT International, Sweden:—You showed a weak dependence between deuterium pickup and Fe content in the Zr-2.5Nb material. A few years ago Dr. Ploc showed a dramatic reduction in deuterium pickup and corrosion rate with increased Fe content in the Zr-2.5Nb material. Are your results in contradiction to the results by Dr. Ploc?

Author's Response:—Dr. Ploc's results (reference [16] in the paper) were based on a statistically designed experiment conducted on thirty-one Zr-2.5Nb-Fe/C/Si/Cr micro pressure tubes which were

fabricated under very controlled conditions. The ranges of concentrations tested were: 30–300 μg/g C, 50–3000 μg/g Fe, 50–1000 μg/g Cr and 10 –500 μg/g Si. In Dr. Ploc's test, oxygen and deuterium pickup were described by a quadratic dependence on Fe and C concentrations.

In the experiment described in this paper the fabrication conditions of the tubes were not as controlled as in Dr. Ploc's experiment and there are many variables between the tubes that were not well controlled as the focus for this work was on front to back end differences. For the most part the variations between the tubes are not that important as comparisons are made between the front and back of the same tube. The relationships examined assume a linear relationship between Fe and deuterium pickup and does not consider the effect of other variables such as C. The general trend that as Fe increases deuterium pickup decreases is visible for the front end specimens but is harder to see for the back end specimens. It is possible that other variables are affecting the deuterium pickup rate and these are masking the effect of Fe. For example: Tube F has the lowest Fe (~440 μg/g), lowest C (~70 μg/g) and highest %Nb in the beta phase of all of the tubes studies. This tube also shows one of the lower deuterium pickup rates at 300°C. Dr. Ploc's work showed a quadratic effect of Fe and C. Therefore, it is not surprising that only weak linear relationships were seen between Fe and deuterium pickup as the effect should be a quadratic relationship with Fe and C. Only a narrow range (compared to Dr. Ploc's study) of impurity element concentrations were present in the tubes used in this study and the data are not sufficient to create a similar relationship as seen in Dr. Ploc's work.

Reprinted from JAI, Vol. 8, No. 5
doi:10.1520/JAI102950
Available online at www.astm.org/JAI

K. Une,[1] *K. Sakamoto,*[2] *M. Aomi,*[3] *J. Matsunaga,*[4] *Y. Etoh,*[5] *I. Takagi,*[6] *S. Miyamura,*[7] *T. Kobayashi,*[8] *and K. Ito*[9]

Hydrogen Absorption Mechanism of Zirconium Alloys Based on Characterization of Oxide Layer

ABSTRACT: In order to get a better understanding of the mechanism governing hydrogen absorption behavior in Zr-based alloys, various characterization techniques were applied to the oxide layers of three alloys: Zry-2, GNF-Ziron (Zry-2-based alloy with ~0.26 wt % Fe), and VB (Zr-based alloy containing ~0.5 wt % Sn, ~0.5 wt % Fe, and ~1 wt % Cr). Out-of-pile corrosion tests were carried out in 400 °C steam and 290 °C LiOH water. For both tests, the hydrogen absorption decreased with higher iron content in the alloys, in the order of

Manuscript received January 7, 2010; accepted for publication April 8, 2011; published online May 2011.

[1] Nippon Nuclear Fuel Development, Co., Ltd., 2163 Narita-cho, Oarai-machi, Ibaraki-ken 311-1313, Japan, e-mail: une@nfd.co.jp
[2] Nippon Nuclear Fuel Development, Co., Ltd., 2163 Narita-cho, Oarai-machi, Ibaraki-ken 311-1313, Japan, e-mail: kan.sakamoto@nfd.co.jp
[3] Nippon Nuclear Fuel Development, Co., Ltd., 2163 Narita-cho, Oarai-machi, Ibaraki-ken 311-1313, Japan, e-mail: masaki.aomi@gnf.com
[4] Nippon Nuclear Fuel Development, Co., Ltd., 2163 Narita-cho, Oarai-machi, Ibaraki-ken 311-1313, Japan, e-mail: matsunaga@nfd.co.jp
[5] Nippon Nuclear Fuel Development, Co., Ltd., 2163 Narita-cho, Oarai-machi, Ibaraki-ken 311-1313, Japan, e-mail: etoh@nfd.co.jp
[6] Dept. of Nuclear Engineering, Kyoto Univ., Yoshida, Sakyo-ku, Kyoto 606-8501, Japan, e-mail: takagi@nucleng.kyoto-u.ac.jp
[7] Dept. of Nuclear Engineering, Kyoto Univ., Yoshida, Sakyo-ku, Kyoto 606-8501, Japan, e-mail: satoshi1.miyamura@toshiba.co.jp
[8] Dept. of Nuclear Engineering, Kyoto Univ., Yoshida, Sakyo-ku, Kyoto 606-8501, Japan, e-mail: qq4c8asd@jewel.ocn.ne.jp
[9] Global Nuclear Fuel Japan Co., Ltd., 3-1 Uchikawa 2-chome, Yokosuka-shi, Kanagawa-ken 239-0836, Japan, e-mail: kunio.ito@gnf.com

Cite as: Une, K., Sakamoto, K., Aomi, M., Matsunaga, J., Etoh, Y., Takagi, I., Miyamura, S., Kobayashi, T. and Ito, K., "Hydrogen Absorption Mechanism of Zirconium Alloys Based on Characterization of Oxide Layer," *J. ASTM Intl.*, Vol. 8, No. 5. doi:10.1520/JAI102950.

Copyright © 2011 by ASTM International, 100 Barr Harbor Drive, PO Box C700, West Conshohocken, PA 19428-2959.

Zry-2>GNF-Ziron>VB, despite different kinetics of a parabolic law in the former test and a linear law in the latter test. The acceleration of hydrogen absorption in the LiOH water was ascribed to the formation of degraded or open grain boundaries up to locations very near the metal/oxide interface. The pre-transition steam oxides of 1.4–1.7 μm had a double layer structure composed of the outside non-protective oxide of monoclinic ZrO_2 with faster diffusivity and the inside barrier layer of predominantly tetragonal ZrO_2 with slower diffusivity. The thickness of the barrier layer of about 0.8–0.9 μm was not changed for the different alloys. The diffusion coefficient of deuterium in the VB oxide was approximately half of that in the GNF-Ziron oxide. This factor for the diffusivity was consistent with their hydrogen pickup performance. The higher compressive stress in the barrier layer was directly linked to the higher hydrogen pickup resistance of the alloys. Preferential dissolution of alloy elements from the second-phase particles (SPPs) into the oxide matrix was evinced for iron, and was very limited for chromium and nickel. These two elements had a tendency to exist as precipitates in the oxide layers, chromium mainly as oxide, and nickel mainly as metal. The superior hydrogen absorption performance of VB containing higher iron content and the SPPs with larger size and number density was attributable to the dissolved iron effect and higher compressive stress state generated from the delayed oxidation of the SPPs in the barrier layer.

KEYWORDS: zirconium alloys, alloy elements, hydrogen absorption, corrosion, oxide layer, characterization, microstructure, diffusion, mechanism

Introduction

The current Japanese boiling water reactor (BWR) fuel claddings have good corrosion resistance and hydrogen absorption properties during service. However, accelerated hydrogen absorption in the claddings has been reported as significant at high burnups after five irradiation cycles [1]. This phenomenon is one of the most important issues limiting high burnup fuel performance from the viewpoint of cladding integrity. Indeed, outside-in type cracking of high burnup BWR fuels has been observed at power ramp tests [2]. We have been researching advanced cladding materials with higher corrosion resistance and lower hydrogen absorption properties. A promising next generation material is GNF-Ziron with higher iron contents (e.g., 0.25 wt %), which are beyond the content specification of Zry-2 [3–6]. The superior corrosion and hydrogen pickup properties of GNF-Ziron at high exposures have been demonstrated through a cooperative project with Japanese utilities [3–6]. The hydrogen pickup fraction of GNF-Ziron was about half that of Zry-2 after six irradiation cycles.

To pursue further extension of fuel burnup and to achieve more robust fuels, advanced cladding materials have to be developed, based on a better understanding of the mechanism governing hydrogen absorption behavior both for in-pile and out-of-pile conditions. An important point is to find effective out-of-pile test techniques for screening their hydrogen absorption performance. In our previous papers [7,8], the hydrogen pickup properties of different alloys

obtained under three different out-of-pile corrosion conditions of 400°C steam, 475°C supercritical water, and 290°C LiOH aqueous solution, were compared with their in-pile data. Among these conditions, the 290°C LiOH water test, which considerably accelerated the corrosion and hydrogen pickup rates, well screened the hydrogen pickup behavior of the alloys. From detailed examinations, especially focusing on their oxide layers [8], this phenomenon was ascribed to the enhanced dissolution of iron from iron-containing particles in both the LiOH water and in-pile conditions. However, there are still some discrepancies and unknown phenomena for the hydrogen pickup property. In addition, the comprehensive mechanism has not been clarified.

It is understood that the oxide layer formed on Zr alloys has a protective nature against corrosion and hydrogen pickup. This protectiveness of the oxide varies with time, and significantly depends on corrosion conditions of the environment and temperature. For this barrier concept [9–11] controlling corrosion and hydrogen pickup, various models have been proposed, the presence of substoichiometric Zr oxide or sub-oxide layers [12–14], tetragonal ZrO_2 phase [10,14,15], and compressive stress in the region close to the metal/oxide interface. The fact that the protective nature of the oxide varies largely with the chemistry of the alloy materials and also the process variables at a given environment indicates that the character of the oxide layer is certainly changed by these two factors. In other words, in order to understand the role of alloy elements on barrier performance, the presence and chemical state of the alloy elements in the oxide have to be examined first, and the oxide microstructure, crystal structure, and barrier performance have to be correlated with alloy element behavior.

In this subsequent study building on our previous papers [7,8], we applied additional examination techniques for the characterization of the oxide layer in three different zirconium-based alloys: Zry-2, GNF-Ziron, and VB, which had been corroded in high temperature steam and LiOH-containing water. For the microstructure examinations of the oxide, scanning electron microscopy (SEM), transmission electron microscopy (TEM), and scanning transmission electron microscopy (STEM) techniques were applied. The crystal structure and stress state in the oxide layer were examined by Raman spectroscopy. The presence and chemical state of alloy elements in the oxide layer were examined by electron probe microanalysis (EPMA) and secondary ion mass spectroscopy (SIMS) mapping. Combining these analytical results with our on-going X-ray absorption fine structure (XAFS) experiments using synchrotron radiation [16], we are continuing to clarify the alloy element behavior of Fe, Cr, Ni, and Sn. Finally, we examined the diffusion behavior of the hydrogen isotope deuterium in the oxide layer by using a nuclear reaction method, and the relationship between the barrier performance and the role of alloy elements was discussed.

Experimental

Materials and Corrosion Tests

Strips (thickness: 0.5–0.6 mm) of three different Zr-based alloys were used. Table 1 summarizes the chemical composition of the alloys: Zry-2, GNF-Ziron,

TABLE 1—*Chemical composition of Zr-based alloys.*

	Composition (wt %)			
Alloys	Sn	Fe	Cr	Ni
Zry-2	1.36	0.18	0.11	0.07
GNF-Ziron	1.46	0.26	0.10	0.05
VB	0.5	0.5	1.0	...

and VB. GNF-Ziron contains a higher iron content than Zry-2. VB is the alloy with the highest contents of iron and chromium, and it does not contain any nickel. All alloys were finally annealed under recrystallization annealing conditions with different annealing temperatures and times. There was a small difference in the second-phase particle (SPP) size distribution between Zry-2 and GNF-Ziron, while larger size and higher number density of the SPPs were observed for VB.

The out-of-pile tests were carried out in two different corrosion environments of high temperature steam at 400°C and 1*M* LiOH-containing water at 290°C. After measuring weight gain, the hydrogen contents of the specimens were analyzed by the hot vacuum extraction method. Oxide layer thickness was calculated from the relationship of 14.6 mg/dm^2 weight for 1 μm of oxide.

Characterization of Oxide Layer

After obtaining the weight gain and hydrogen absorption data of the corroded samples, the oxide layers were subjected to detailed examinations. Cross-sectional bulk specimens for SEM observations, and EPMA and SIMS analyses were prepared by using a cross-sectional polisher of the JEOL SM-09010 with an Ar ion beam of 4 kV. Cross-sectional oxide specimens for TEM and STEM examinations were done by a focused ion beam method with the Hitachi FB-2100, using a Ga^+ ion beam of 40 kV.

Backscattered electron (BSE) images by SEM of the Hitachi SU-70 were obtained at an acceleration voltage of 2 kV. TEM and STEM micrographs and electron diffraction patterns were obtained with the Hitachi HF-2000 and HF-2200F.

Elemental analyses in metal and oxide regions by EPMA using the Shimadzu 8007 were conducted at conditions of 20 kV and 50 nA. Under these conditions, the region excited by the 1 μm electron beam used is broadened to about 1.5–2 μm. Therefore, characteristic X-ray intensities of Zr, Fe, Cr, and Sn measured by EPMA are regarded as averaged values in the excited region containing many SPPs. The X-ray intensity of each alloy element was normalized by the intensity of Zr at the same analyzing location.

SIMS mapping analyses in metal and oxide regions were performed using the Cameca NanoSIMS 50. The primary beam of Cs^+ of 8 kV and 27 nA, focused to about 50 nm diameter, was used to sputter negative secondary ions from the sample surface. Secondary ions were mapped on five detectors simultaneously.

The ion species analyzed were ^{16}O, ^{58}Ni, $^{52}Cr^{16}O$, $^{56}Fe^{16}O$, and $^{120}Sn^{16}O$. An image resolution of 256×256 pixels with a count time of 30 ms per pixel was obtained.

The Raman spectra of the oxide layer were measured by the Horiba Lab-RAM HR-800 with the perfect confocal condition. Radiation excitation was the 523 nm line of a yttrium aluminum garnet laser. The oxide samples were prepared on a tapered cross-section, which geometrically enlarged the thickness of the exposed oxide by a factor of about 10. Laser output power was 50 mW, corresponding to a power at the sample surface of 10 mW. The tetragonal fraction of the oxide layer was quantitatively derived from the Raman peaks of monoclinic- and tetragonal-ZrO_2 [17].

The diffusion property of the hydrogen isotope deuterium in the oxide layer was examined by the nuclear reaction analysis (NRA) method. Two types of experiments were adopted. The first was to measure the deuterium concentration in the oxide layer at room temperature after being corroded in a D_2O steam ($400^\circ C \times 15$ days) or LiOD-containing D_2O water ($290^\circ C \times 1.7$ days). The second was to measure the in situ deuterium concentration in the oxide layer at 300°C under exposure to deuterium plasma. The oxide samples corroded in H_2O steam ($400^\circ C \times 10$ days) and LiOH-containing water ($290^\circ C \times 1$ day) were subjected to the in situ experiments, and were heated in a chamber by a heater. A probing beam of 1.7 MeV $^3He^+$ ions from the 4 MV Van de Graaff accelerator of Kyoto University irradiated the oxide surface at 45° and protons produced by the reaction $D(^3He, p)^4He$ were detected by a solid-state detector. The energy spectrum of the protons was converted into a depth profile of deuterium by the energy analyzing method. Due to a finite resolution of the total detecting system ($\sim 0.15\,\mu m$), deuterium seems to be present in negative depth. Details of the present NRA experiments were described elsewhere [18,19].

Results

Hydrogen Absorption Kinetics

Table 2 summarizes the corrosion and hydrogen pickup data of the three alloys of Zry-2, GNF-Ziron, and VB. The hydrogen pickup data are normalized as the specimen thickness of 0.6 mm because of the different specimen thicknesses. The corrosion kinetic curves obtained in 400°C steam and 290°C LiOH water were previously reported [8]. Figure 1(*a*), 1(*b*) shows the hydrogen absorption kinetics of the three alloys in the two different corrosion conditions. In the 400°C steam test, VB has a superior hydrogen pickup property. Comparing Zry-2 and GNF-Ziron shows that the hydrogen absorption of the latter is a little lower. The hydrogen absorption rate of the three alloys follows nearly a parabolic rate law before the transition below 100 ppm hydrogen, while the oxidation rate reported previously follows a cubic rate law [8]. Both kinetic laws suggest so-called diffusion-controlled phenomena. The transition timing of hydrogen pickup coincides with that of oxidation. In the LiOH water environment, the hydrogen absorption rate is much higher and is according to the linear rate law, compared to the 400°C steam. Although there is no significant

TABLE 2—*Summary of corrosion and hydrogen pickup data.*

		Zry-2			GNF-Ziron			VB		
Corrosionqa Atmosphere	Time (Day)	Weight Gain (mg/dm^2)	Hydrogen (ppm)	Hydrogen Pickup Fraction (%)	Weight Gain (mg/dm^2)	Hydrogen (ppm)	Hydrogen Pickup Fraction (%)	Weight Gain (mg/dm^2)	Hydrogen (ppm)	Hydrogen Pickup Fraction (%)
Steam at 400°C	10	23	53	35.9	25	43	27.3	20	19	15.4
	20	31	74	37.4	30	72	37.9	26	26	15.9
	42	40	98	38.4	39	82	33.1	...	...	...
	70	61	176	45.3	60	139	36.4	40	41	16.0
	105	66	208	49.6	70	165	37.8	45	64	22.2
LiOH water at 290°C	1	20	116	91.3	21	28	20.8	16	16	15.8
	2	...	...	...	48	110	35.9	32	19	9.5
	3	41	238	91.1	48	92	30.0	59	49	13.0
	6	80	430	84.5	96	188	30.7	99	104	16.6
	9	134	723	84.9	146	325	35.0	...	...	...
	12	204	1055	81.3	229	396	27.3	...	...	...
	13	...	...	...	...	...	...	244	254	16.9

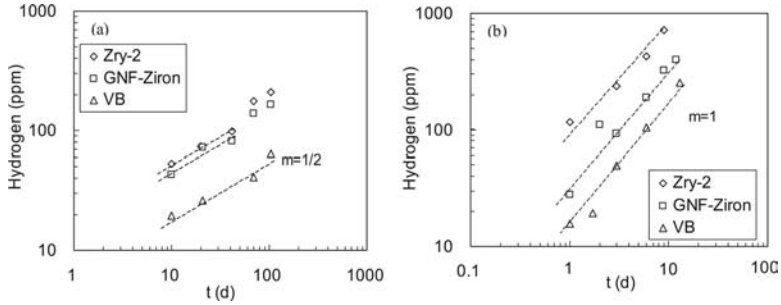


FIG. 1—*Hydrogen absorption kinetics in (a) 400°C steam and (b) 290°C LiOH-containing water. "m" in the figures denotes the slopes of the plots.*

difference in the previously reported LiOH oxidation rates [8], a clear difference in the hydrogen absorption property is seen among the three alloys. The resultant hydrogen pickup fractions are shown in Fig. 2(*a*), 2(*b*) for the 400°C steam test and the 290°C LiOH water test, respectively. An important point is that this order of hydrogen pickup property, especially observed in the LiOH water tests, appears to be consistent with the in-pile hydrogen absorption behavior after four or six irradiation cycles, as described previously [7]. Relative pickup fraction values of the irradiated specimens reported in Ref [7] are 1.0 for Zry-2, 0.5 for GNF-Ziron, and 0.4 for VB.

Microstructure Examinations

Figure 3(*a*)3(*c*) shows BSE images for the pre-transition oxide layers (about 1.5 μm) and Fig. 3(*d*)3(*f*) for the post-transition oxide layers (about 3.5–4 μm), which were corroded in 400°C steam. A few microcracks are seen even for the pre-transition thin steam oxide layers. It may be noteworthy that some tiny microcracks appear in the metal/oxide interface region of GNF-Ziron and VB. On the contrary, many microcracks appear in the post-transition steam oxide layers. The microcrack frequency for VB appears to be lower than for the other

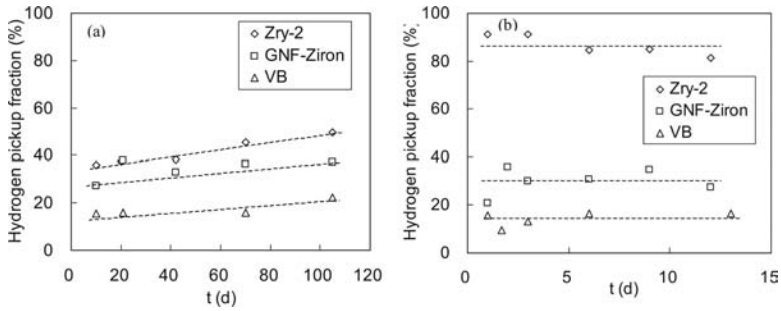


FIG. 2—*Hydrogen pickup fraction in (a) 400°C steam and (b) 290°C LiOH-containing water.*

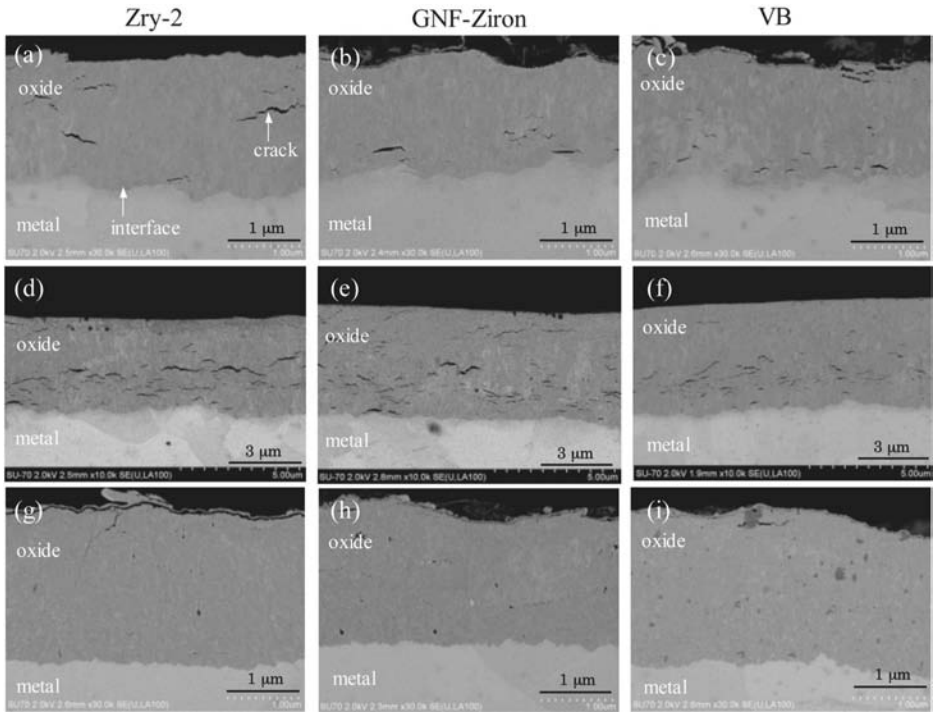


FIG. 3—*BSE images of [(a)–(c)] pre-transition oxide specimens, [(d)–(f)] post-transition oxide specimens corroded in 400°C steam, and [(g)–(i)] 290°C LiOH water corroded specimens. (a), (d), and (g): Zry-2; (b), (e), and (h): GNF-Ziron; (c), (f), and (i): VB.*

two alloys, and an even lower frequency of microcracks in the outside region to about 2 μm depth is common. This indicates that the occurrence of microcracks significantly increases when the oxide thickness exceeds 2 μm. This oxide thickness for the frequent occurrence of microcracks suggests some correlation between the occurrence of microcracks and the transition phenomenon for the steam forming oxide layers. A careful examination of the slight contrast changes of the steam oxide layers indicates growth of columnar grains. The BSE images of the 290°C LiOH water corroded specimens with oxide layers of about 2 μm are given in Fig. 3(*g*)3(*i*). An obvious difference is seen between the oxides in the different environments. Namely, microcracks in the LiOH water grown oxide layers are rarely seen, despite accelerated oxidation and hydrogen pickup rates. Even in thicker LiOH oxides of about 10 μm, the appearance is not much changed.

Figure 4(*a*), 4(*b*) shows TEM images for the pre-transition steam oxides (thickness: 1.4 μm) of Zry-2 and VB, taken from the metal/oxide region. In the interface region of the VB oxide, many SPPs of Zr–Fe–Cr and isolated microcracks attached to the SSPs are observed. On the other hand, the number of SPPs is limited in the interface region of Zry-2. In both oxides, no long and interlinked microcracks are observed. For the Zry-2 oxide, an interface layer of

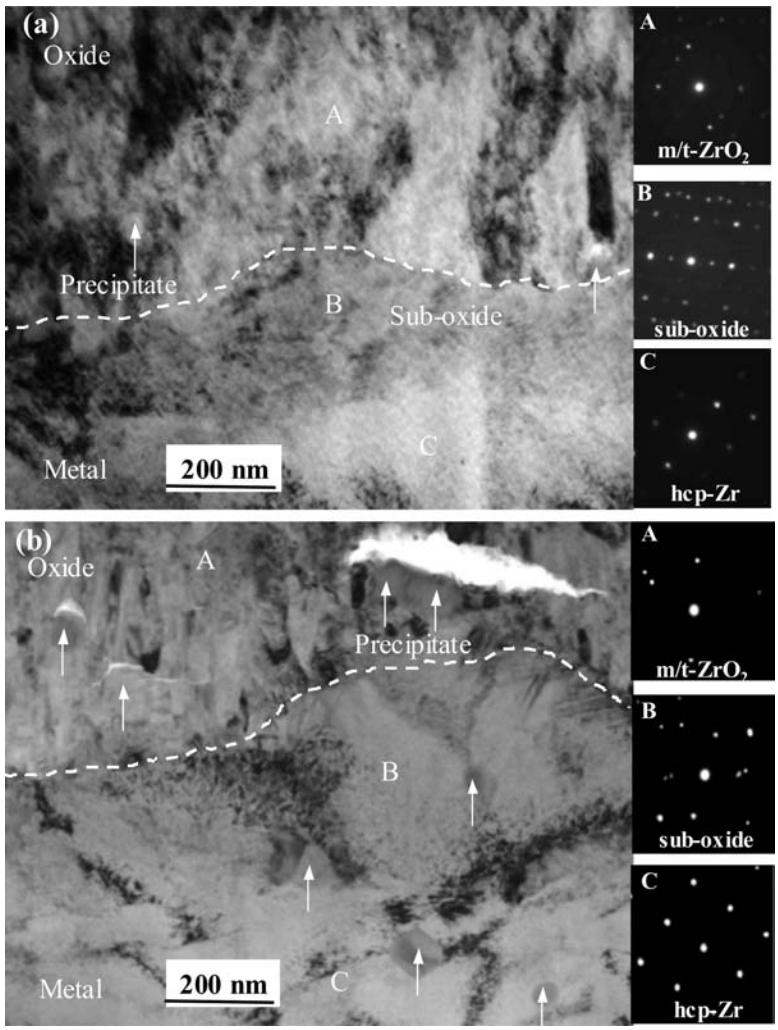


FIG. 4—*TEM images in the metal/oxide interface region of (a) Zry-2 and (b) VB corroded in 400°C steam for 10 days. The oxide thickness is 1.4 μm for both Zry-2 and VB. Three electron diffraction patterns in the TEM images were obtained from oxide, interface sub-oxide, and metal regions.*

about 200 nm with a slightly different contrast between the metal and ZrO_2 oxide regions is recognized, while the interface layer for the VB oxide is not so clear in this TEM image. Each selected area diffraction pattern in Fig. 4(*a*), 4(*b*) indicates a tetragonal plus monoclinic ZrO_2 in the oxide and a hexagonal Zr in the metal, in addition to an unidentified phase in the interface layer.

In the STEM images of Fig. 5(*a*), 5(*d*) for the pre-transition steam oxides, the interface layers are clearly observed for both Zry-2 and VB alloys due to the

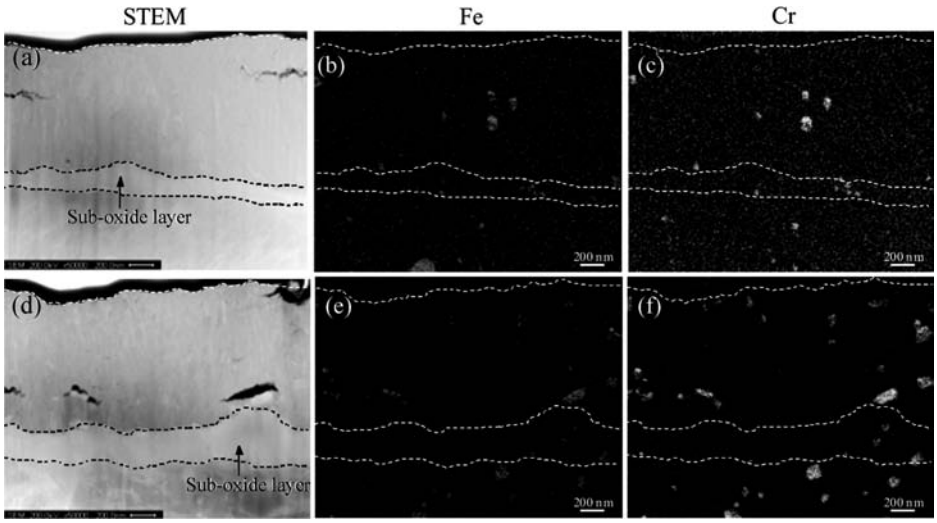


FIG. 5—*STEM images and elemental mappings of Fe and Cr of [(a)–(c)] Zry-2 and [(d)–(f)] VB corroded in 400°C steam for 10 days. The oxide thickness is 1.4 μm for both Zry-2 and VB.*

effect of mass difference (Z contrast). The thicknesses of the respective Zry-2 and VB specimen interface layers are about 200 and 300 nm. This interface layer is probably associated with sub-oxide [12,13,20]. In the metal/oxide interface region, oxygen potential is expected to be very low, when the protectiveness of the oxide layer is maintained. In this condition, it is reasonable that sub-oxides of Zr_3O or Zr_2O exist between the metal and oxide regions. The presence of the rhombohedral Zr_3O has been confirmed near the metal/oxide interface of Zr alloys from an analysis of X-ray diffraction patterns using microbeam synchrotron radiation [20]. In the elemental mapping images of iron and chromium obtained by energy dispersive spectroscopy for the pre-transition steam oxides, there exists a clear difference in the SPP distribution between the two alloys. The size and number density of SPPs containing iron and chromium of the VB specimen are much larger than those of the Zry-2 specimen, both in the metal and oxide regions. The fact that the SPPs exist as isolated precipitates in the pre-transition steam oxides is compatible with SIMS mapping results, which are described later.

Figure 6(*a*), 6(*b*) are the corresponding TEM images for the thin LiOH water oxides of Zry-2 and VB, taken from the metal/oxide interface region. The oxide thickness is 1.6 μm for Zry-2 and 1.1 μm for VB. For both oxides, there are extremely well-developed networks of degraded grain boundaries of 20–30 nm equiaxed grains. This degraded grain boundary structure is observed throughout the region from the surface to near the metal/oxide interface, except in the very narrow region of 50–100 nm adjacent to the metal/oxide interface. The present observation is consistent with the findings of other investigators

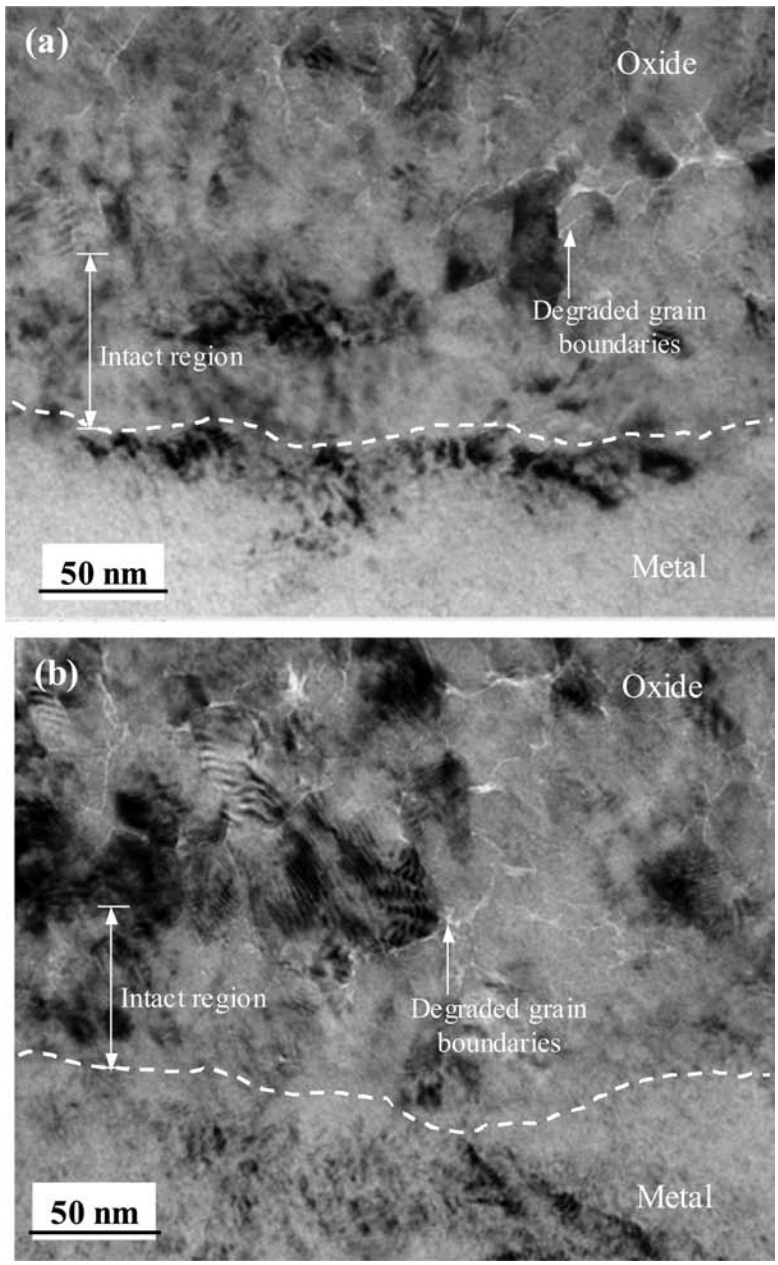


FIG. 6—*TEM images in the metal/oxide interface region of (a) Zry-2 and (b) VB corroded in 290°C LiOH water for 1 day. The oxide thickness is 1.6 and 1.1 μm for Zry-2 and VB, respectively.*

[10,21,22], who commented about an open grain boundary or loose area. The accelerated oxidation and hydrogen pickup rates are certainly connected with this degraded grain boundary structure. Through these fast paths, OH^- and Li^+ ions would intrude quickly to sites near the metal/oxide interface.

Raman Spectroscopy

It is known that monoclinic ZrO_2 transforms to tetragonal ZrO_2 at high compressive stresses, and that the t-ZrO_2 phase is frequently observed in the inner oxide close to the metal/oxide interface [8–10,15,23]. In this study, Raman spectroscopy was used to characterize the crystal structure of the ZrO_2 layer formed on the three alloys corroded in 290°C LiOH water and 400°C steam. Oxide thicknesses are all in the range of 1.1–1.6 μm, and tapered cross-sectional specimens were used. All the LiOH oxides showed only the monoclinic structure even at the locations very close to the metal/oxide interface. This result is completely compatible with previous Raman measurements of Zry-2 specimens [8]. The stabilization of m-ZrO_2 probably suggests a low compressive stress state in the LiOH oxides due to the formation of the degraded grain boundaries. Raman results for the pre-transition oxides corroded in 400°C steam for 10 days are shown in Fig. 7(*a*), 7(*b*). The former is the variation of the tetragonal ZrO_2 fraction from the metal/oxide interface evaluated from the ratio of the tetragonal and monoclinic Raman peaks [17]. In the evaluation, two monoclinic peaks of 178 and 189 cm^{-1} and one tetragonal peak of 278 cm^{-1} were used. The latter figure is the corresponding wavenumber variation of the monoclinic peak of around 189 cm^{-1}. These data are the average values of several line analyses. The wavenumber becomes higher with higher compressive stresses [15]. In Fig. 7(*c*), evaluated compressive stresses are plotted when applying the reported Gruneisen coefficient of 2.5 cm^{-1}/GPa [15] to the present data. In the stress evaluation, the wavenumber of a powder specimen of GNF-Ziron oxide layer (dotted line in Fig. 7(*b*)) is assumed to correspond to the zero stress state.

The tetragonal fraction at the metal/oxide interface ranges from 50 % to 90 %, depending on alloy variation, and it gradually decreases going toward the outer region for the three alloys, as shown in Fig. 7(*a*). The high tetragonal fraction region (more than 30 %) appears to be about 0.6 μm from the interface, which is in good agreement with the previous results for Zry-2 [8]. This stabilization of the tetragonal phase must originate from high compressive stress. The highest tetragonal fraction is apparent for the VB oxide, and no significant difference is seen between the Zry-2 and GNF-Ziron oxides. Also, in Fig. 7(*b*), 7(*c*), the highest wavenumber and compressive stress are detected throughout the oxide region of VB, and the level of the compressive stress at the interface ranges from 0.3 to 1.7 GPa. Then, a small difference exists between Zry-2 and GNF-Ziron in the inner oxide region. The compressive stress in the inner oxide region of about 0.6 μm becomes higher in the order of $\mathrm{Zry}-2 < \mathrm{GNF}-\mathrm{Ziron} < \mathrm{VB}$, which is consistent with the hydrogen pickup resistance of the three alloys.

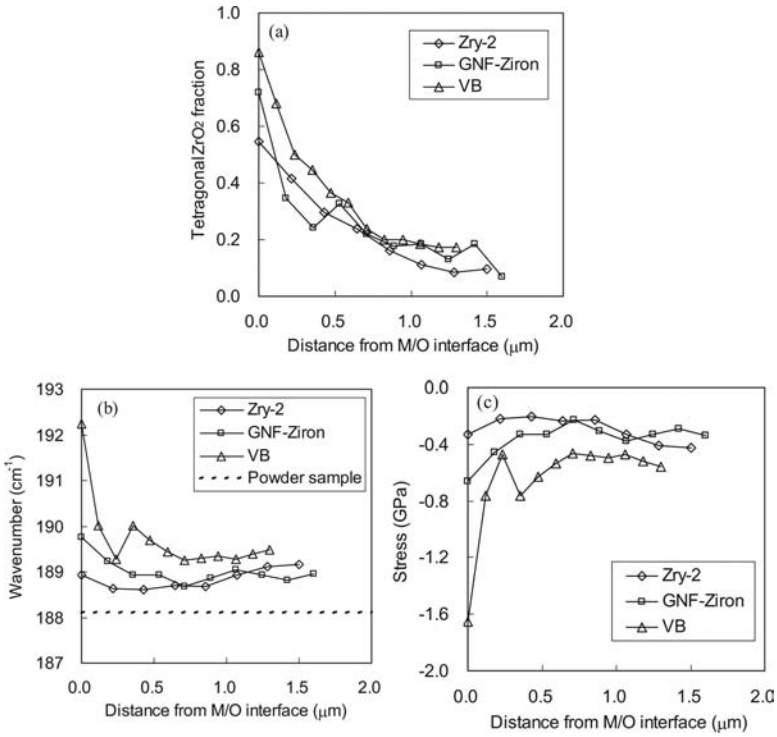


FIG. 7—*Raman spectroscopy results for pre-transition oxides of the three alloys corroded in 400°C steam for 10 days. (a): Depth distribution of tetragonal fraction of ZrO_2; (b): Depth distribution of wavenumber of monoclinic ZrO_2 peak; (c): Depth distribution of compressive stress.*

SIMS Mapping

SIMS mappings of alloy elements iron, chromium, nickel, and tin were made using the NanoSIMS system with a spatial resolution of 50 nm. In the present analyses, five secondary ions of ^{16}O, ^{58}Ni, $^{52}Cr^{16}O$, $^{56}Fe^{16}O$, and $^{120}Sn^{16}O$ were recorded simultaneously for 290°C LiOH water (oxide: 2.9 μm) and 400°C steam (2.7 μm) corroded Zry-2 specimens, and 400°C steam corroded VB specimens (3.3 μm). The SIMS mapping images of the secondary ions are given in Fig. 8 for the first specimen, Fig. 9 for the second specimen, and Fig. 10 for the third specimen. The 64 color levels corresponding to the ion intensities at each pixel are logarithmically spread in three orders from red to black. Roughly, the saturation level in each image corresponds to red, the 1/10 level corresponds to yellow-orange, and the 1/100 level to blue-green. The dotted lines in each image denote the interface of the metal/oxide and the oxide surface derived from their ^{16}O images. The oxygen cluster ions of $^{52}Cr^{16}O$, $^{56}Fe^{16}O$, and $^{120}Sn^{16}O$ were selected by reason of their chemical states in the oxide layers as estimated by our on-going XAFS examinations [16]. The metal ion of ^{58}Ni was also selected

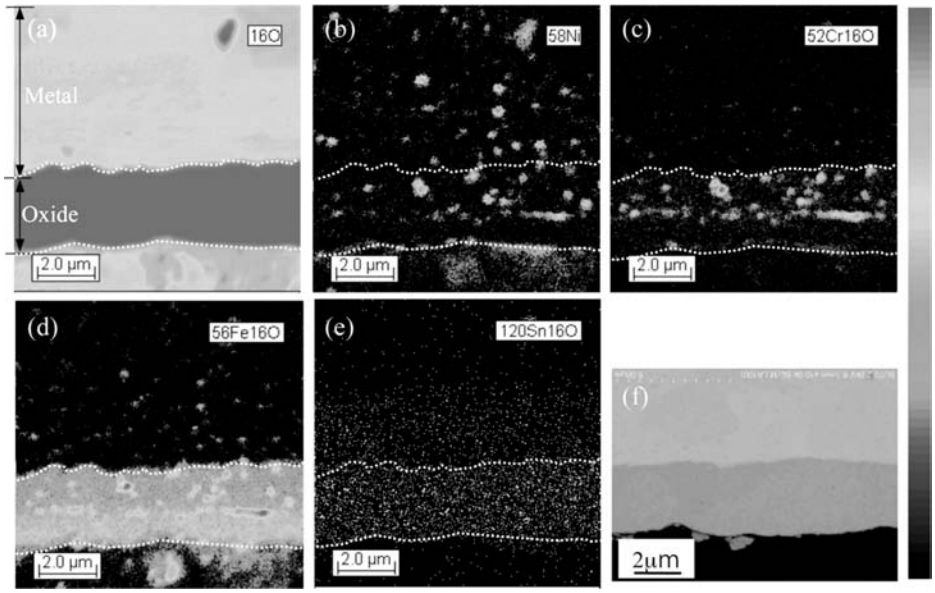


FIG. 8—*SIMS secondary ion images for Zry-2 corroded in 290°C LiOH water for 3 days. (a): ^{16}O; (b): ^{58}Ni; (c): $^{52}Cr^{16}O$; (d): $^{56}Fe^{16}O$; (e): $^{120}Sn^{16}O$; (f): BSE image. The location of the BSE image is different from the location of the SIMS analyses. The 64 color levels corresponding to the ion intensities at each pixel are logarithmically spread in three orders.*

from the estimated chemical state. The present NanoSIMS system cannot provide ion induced secondary electron images at the analyzing locations. Therefore, BSE images in the figures were obtained at locations different from the SIMS analyzing locations before subjecting them to the NanoSIMS analyses.

In the case of the LiOH water oxide of Zry-2 (Fig. 8), a noticeable difference is seen for the alloy element distributions between iron and the other two elements of chromium and nickel. These three elements are known to exist as inter-metallic particles of $Zr(Fe,Cr)_2$ and $Zr_2(Fe,Ni)$ in the metal region. In the oxide layer, iron has a stronger tendency to disperse uniformly or dissolve from the iron-containing SPPs. In contrast, chromium and nickel have a stronger tendency to exist as isolated precipitates. In the metal region, $^{52}Cr^{16}O$ ions are rarely detected, and ^{58}Ni ions are clearly detected at the same levels as those in the oxide layer. These facts suggest that chromium in the precipitates exists mainly as an isolated oxide phase in the oxide layer, and nickel in the precipitates exists mainly in the metallic state even in the oxide region. This estimation on the chemical states of alloy elements is in accordance with our recent XAFS data [16]. The data of $^{120}Sn^{16}O$ indicate a uniform distribution in the oxide. Moreover, there seems to exist almost no precipitate in the outermost oxide region of about 1 μm from the surface, which indicates the dissolution of the

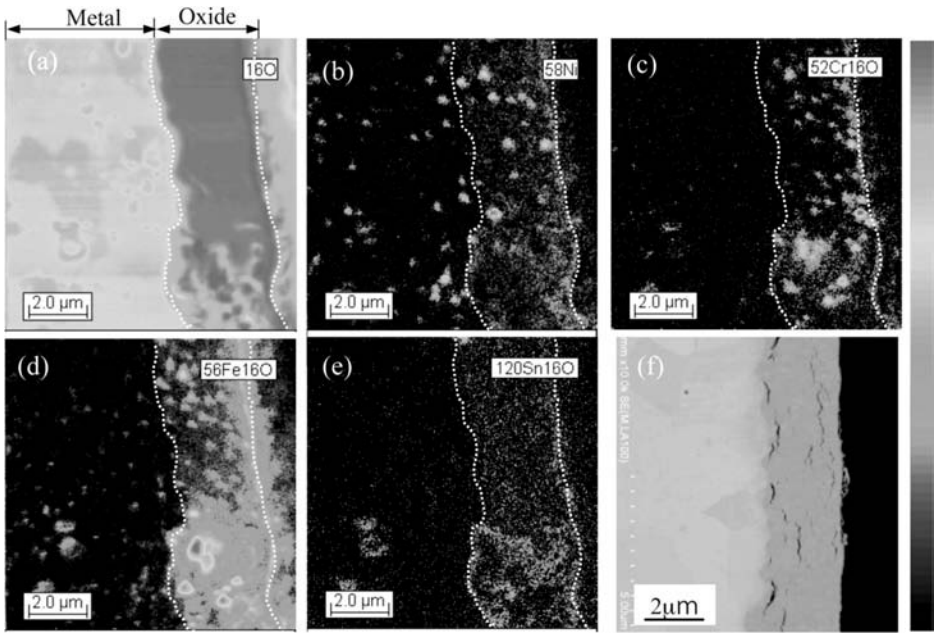


FIG. 9—*SIMS secondary ion images for Zry-2 corroded in 400°C steam for 43 days. (a): ^{16}O; (b): ^{58}Ni; (c): $^{52}Cr^{16}O$; (d): $^{56}Fe^{16}O$; (e): $^{120}Sn^{16}O$; (f): BSE image. The location of the BSE image is different from the location of the SIMS analyses. The 64 color levels corresponding to the ion intensities at each pixel are logarithmically spread in three orders.*

precipitates of Zr–Fe–Cr and Zr–Fe–Ni into the LiOH solution through the open grain boundaries.

In the case of the steam oxide of Zry-2 (Fig. 9), the distributions of chromium and nickel have almost the same tendency. An important point is that the level of homogenization of iron in the oxide layer appears to be lower than for the case of the LiOH oxide. This difference is attributable to the difference in the oxygen atmosphere in the oxide layer, as discussed later. The much higher oxygen potential in the LiOH water oxide must enhance the oxidation and dissolution of iron into the ZrO_2 matrix. In the region near the large iron particles and the surface, somewhat higher iron concentrations are detected. Figure 10 shows the SIMS mapping results of the steam corroded VB specimen. In this specimen, $^{120}Sn^{16}O$ ions were not counted. There are many more iron and chromium precipitates in the VB steam oxide layer compared to the corresponding Zry-2 specimen (Fig. 9). The chemical state of the Zr–Fe–Cr precipitates in the oxide layer is expected to be mainly in the oxidation state, since the secondary ions detected are $^{52}Cr^{16}O$ and $^{56}Fe^{16}O$. Also in this VB oxide, the dissolution of iron from the precipitates is more apparent than chromium, and it becomes more noticeable toward the oxide surface. In contrast, the numbers of the

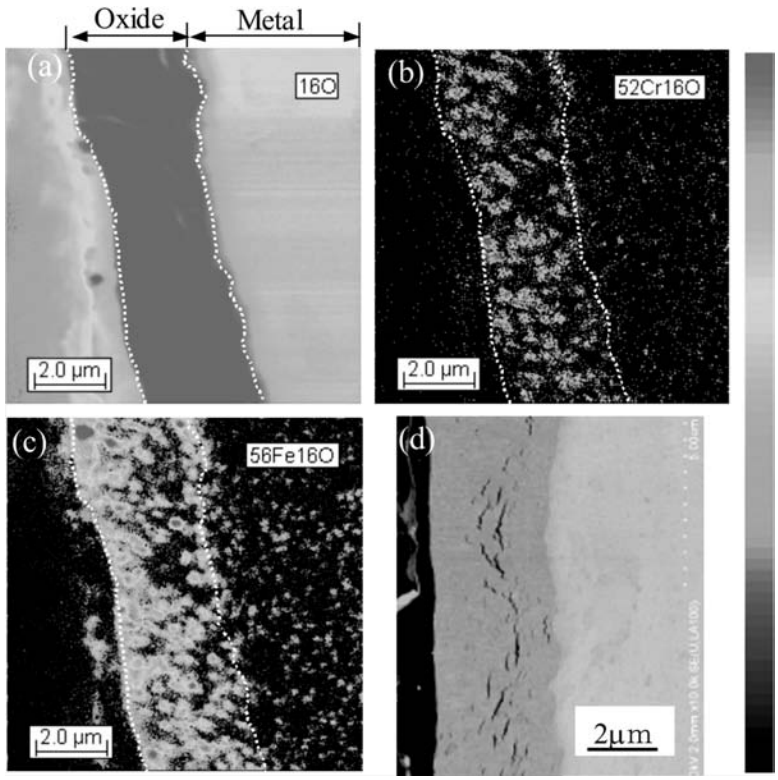


FIG. 10—*SIMS secondary ion images for VB corroded in 400°C steam for 105 days. (a): ^{16}O; (b): $^{52}Cr^{16}O$; (c): $^{56}Fe^{16}O$; (d): BSE image. The location of the BSE image is different from the location of the SIMS analyses. The 64 color levels corresponding to the ion intensities at each pixel are logarithmically spread in three orders.*

precipitates that were counted become fewer toward the oxide/metal interface. This suggests that the chemical state of the Zr–Fe–Cr precipitates changes along the oxide depth, and that it is in the metallic state near the interface region.

EPMA

EPMA examinations were performed to elucidate the change of the state of agglomeration for the alloy elements of iron, chromium, and tin in the oxide matrix. EPMA sensitivity is known to depend on chemical state and precipitate size, especially for larger precipitates of more than several tens of nanometers. Accordingly, when the alloy elements existing as particles or a segregated phase in the metal disperse or dissolve into the oxide matrix, their characteristic X-ray intensities normalized by zirconium intensity will increase in the oxide layer, compared to the intensities in the metal region.

The characteristic X-ray intensities of the alloy elements in the LiOH water and steam corroded specimens of the three alloys were measured both in the

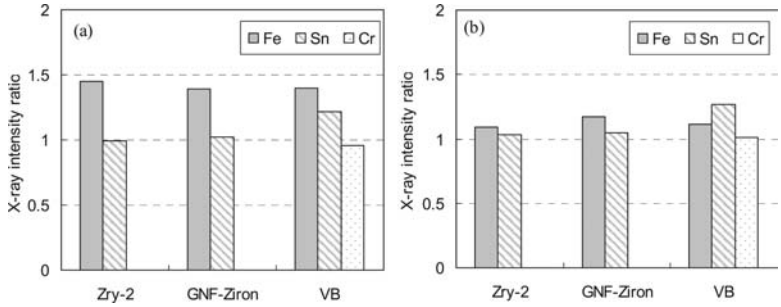


FIG. 11—*Characteristic X-ray intensity ratio of in-oxide to in-metal measured by EPMA for the three alloys corroded in (a) 290°C LiOH-containing water and (b) 400°C steam. The oxide thickness is in the range of 3–4.5 μm.*

metal and oxide regions, using conventional EPMA of 1 μm beam diameter. The oxide thickness of the specimens was in the range of 3–4.5 μm. Each elemental X-ray intensity was normalized by zirconium intensity measured at the same location, and converted to the relative intensity of each element. The relative intensity ratios of in-oxide to in-metal are listed for iron, chromium, and tin in Fig. 11(*a*), 11(*b*). The data on chromium for Zry-2 and GNF-Ziron are not presented because of lower X-ray counts for reliable analyses. The relative intensity ratios of iron in the LiOH water oxide of the three alloys are almost the same, about 1.4, while the ratios in the steam oxides are 1.1–1.2. This indicates that the preferential iron dissolution or dispersion of iron-containing particles is more enhanced in the LiOH water oxide than in the steam oxide. For the relative intensity ratio of chromium in VB, almost no dispersion or dissolution is recognized both in the LiOH water and steam oxides. Also regarding tin behavior in Zry-2 and GNF-Ziron, almost the same relative intensity ratios of unity are measured. An exception is seen for both types of VB oxides, for which the increases of the relative tin intensity would be associated with some homogenizing process of segregated tin in the VB metal. These EPMA results are qualitatively in good accordance with the present SIMS mapping results. Namely, iron tends to be preferentially dissolved in the oxides, especially in the LiOH water oxides, while chromium tends to exist as an isolated oxide phase in the oxide layer.

Diffusion Behavior

The diffusivity or mobility of hydrogen in the oxide layer primarily controls the hydrogen pickup rate of zirconium alloys. In the present study, NRA was applied to measure the distribution of deuterium. Figure 12(*a*), 12(*b*) shows the deuterium distributions in the LiOD water (290°C × 1.7 days) and D_2O steam corroded oxides (400°C × 15 days). Their oxide thickness is in the range of 1.5–2.8 μm for the former oxides and 1.5–1.7 μm for the latter oxides.

For the LiOD water corroded specimens of Fig. 12(*a*), almost flat deuterium distributions are detected in the entire oxide regions, and the level

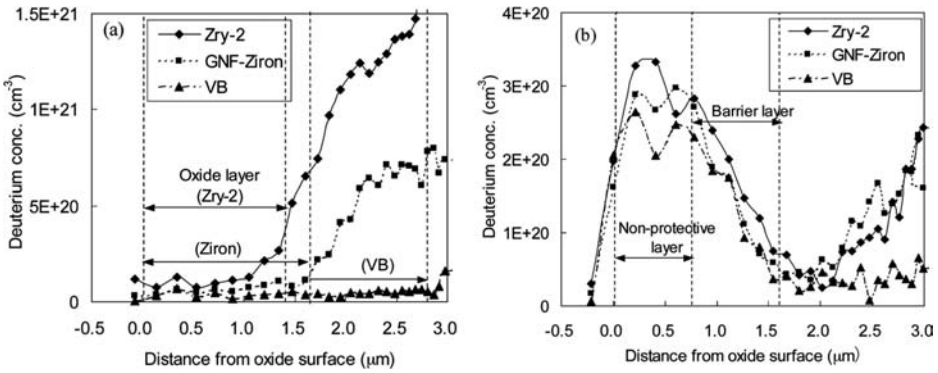


FIG. 12—*Depth profiles of deuterium concentration in oxides corroded in (a) 290°C LiOD-containing water for 40 h and (b) 400°C D_2O steam for 15 days.*

of the three oxides increases in the order of $\mathrm{VB}(0.3 \times 10^{20}\,\mathrm{cm}^{-3}) < \mathrm{GNF-Ziron}(0.6 \times 10^{20}\,\mathrm{cm}^{-3}) < \mathrm{Zry{-}2}(1 \times 10^{20}\,\mathrm{cm}^{-3})$. The number density of $2.8 \times 10^{20}\,\mathrm{cm}^{-3}$ corresponds to 1 at% of deuterium in ZrO_2. For the Zry-2 and GNF-Ziron specimens, deuterium accumulates in the metal region near the oxide/metal interface. This is probably because tensile stress, loaded in the metal region adjacent to the oxide layer, enhances hydride precipitation. Deuterium in the deep metal region would diffuse to the interface to form hydride during cooling. In fact, almost no significant increase near the oxide/metal interface was confirmed for a quenched Zry-2 specimen in an additional experiment; rather, they showed a roughly flat distribution.

Figure 12(*b*) shows the deuterium profiles of the three alloys corroded in the D_2O steam environment at 400°C for 15 days. There exists a double layer structure in the 1.5–1.7 μm oxide layers from the viewpoint of the diffusion characteristics of deuterium, which consists of mild or nearly flat profiles in the outside layer of about 0.8 μm and steep profiles that are almost linear in the inside oxide layer of the remaining $\sim$ 0.8–0.9 μm oxide layers. An almost linear profile means a steady state diffusion there after the corrosion period of 400°C $\times$ 15 days. In order to explain these deuterium profiles, the double layer oxide structure composed of the outside oxide with much faster diffusivity and the inside oxide with slower diffusivity has to be anticipated. Namely, the former and the latter layers are regarded as non-protective and protective barrier oxide layers. For the inside barrier layer, almost the same barrier oxide thickness and concentration gradient are seen, irrespective of alloy variations. However, comparing the hydrogen pickup fraction of the three alloys in the steam environment, the factor of the hydrogen pickup fraction of VB is about 0.4–0.5 of those for Zry-2 and GNF-Ziron. In order to understand the superiority of VB, the diffusion coefficient in the VB oxide must be about half the coefficients in the other two alloy oxides.

To examine the diffusion behavior of the hydrogen isotope of deuterium under non-steady state conditions, in situ diffusion experiments were carried out. The sample that had been corroded in H_2O steam at 400°C for 10 days was

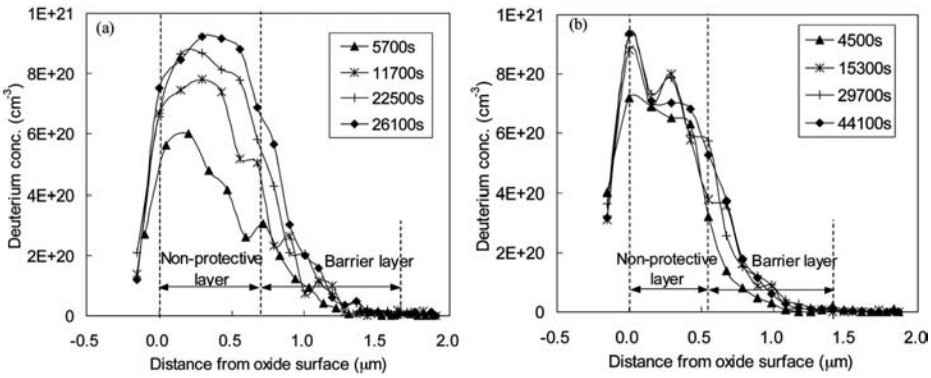


FIG. 13—*In situ diffusion profiles of deuterium at 300°C in deuterium plasma atmosphere for pre-transition oxides of (a) GNF-Ziron and (b) VB corroded in 400°C H_2O steam.*

set in a vacuum chamber and heated at 300°C. Then one side of the sample was exposed to deuterium plasma. As the energy of the deuterium particles in the plasma was very low, typically 1 eV, deuterium was softly charged to the oxide surface. Under the plasma exposure, the deuterium depth profile at the plasma-exposed surface was observed by the NRA at several times.

Figure 13(*a*) shows the deuterium profiles in the steam oxide specimen of GNF-Ziron with 1.7 μm oxide layer thickness. Up to an exposure time of about 10 000 s, the concentration near the oxide surface increases quickly and then approaches a constant value of the steady state. For the profiles beyond 11 700 s, the double layer structure is demonstrated by the nearly flat profile in the outside region of about 0.7–0.8 μm and the steep non-steady state profile in the inside region of about 0.9 μm. This double layer structure observed in the in situ experiments is very similar to the steady state results, as seen in Fig. 12(*b*). From the transient profiles measured in the inside barrier layer, the diffusion coefficient of deuterium was estimated. In the estimation, the numerical calculation code HYDIF, which can deal with diffusion problems of a one-dimensional multi-layer structure with different diffusivities by the difference method [24], was used. For $t = 26\,100$ s, the diffusion coefficient in the inside barrier layer is estimated to be 2.5×10^{-14} cm^2/s. Figure 13(*b*) is the corresponding deuterium profiles measured by the in situ diffusion experiments at 300°C for the VB oxide of 1.4 μm. Also in this sample, the double layer structure is clearly recognized, consisting of the non-protective 0.6 μm outside layer and the protective 0.8 μm inside layer. Examining the complicated profiles observed in the outside layer of 0.6 μm in detail indicates that two oxide layers may exist, not a single layer. The figures show that there is no significant difference in the profiles in the inside barrier layer between the GNF-Ziron and VB oxides. Nevertheless, the evaluated diffusion coefficients for the VB oxide are 1.3×10^{-14} cm^2/s at 29 700 s, and 8.9×10^{-15} cm^2/s at 44 100 s. These values are half of that for GNF-Ziron (2.5×10^{-14} cm^2/s at $t = 26\,100$ s). The lower

diffusivity in the VB oxide than in the GNF-Ziron oxide is important with respect to the lower hydrogen pickup property of the former.

In the past, hydrogen isotope (H, D, T) diffusion in the oxide layer formed on pure Zr and many zirconium alloys has been examined by various techniques such as NRA, thermal desorption method, and SIMS profiling. The oxide layers were prepared under various atmospheres of air and oxygen gas, steam, and water at high temperature. However, there is a wide variation in the diffusion coefficients of 3–4 orders of magnitude in the temperature range of interest. The present diffusion coefficients at 300°C for GNF-Ziron ($\sim 3 \times 10^{-14}$ cm^2/s) and VB ($\sim 1 \times 10^{-14}$ cm^2/s) are located in the middle of the literature data (1×10^{-15}–1×10^{-13} cm^2/s) reported by Khatamian [25–27] for various Zr–Nb alloys (Zr-1Nb, Zr-2.5Nb, Zr-15Nb, Zr-20Nb) and Zircaloy-2, and McIntyre et al. [28] and Elmoselhi et al. [29] for Zr-2.5Nb, but about 2–3 orders of magnitude higher than those by Khatamian [25] for pure Zr, Austin et al. [30] and Kunz et al. [31] for Zircaloy-2, and Warr et al. [32] for Zr-2.5Nb. Although the reason for this large difference is not rationalized, it may be caused by the differences of experimental procedure; alloy material, oxide film preparation method, hydrogen isotope injection method, and analytical method for deriving the diffusion coefficient. From the viewpoint of a microscopic diffusion mechanism, the heterogeneous microstructures in the oxide layer such as micropores, microcracks, second phases, and precipitates, may act as fast diffusion paths for hydrogen.

Discussion

Hydrogen Absorption Mechanism in LiOH Water Corroded Oxide

Many investigators [11,21,33] have reported that the corrosion rate is significantly accelerated by the addition of LiOH into a water environment. Moreover, the acceleration strongly depends on LiOH concentration. The LiOH concentration of 1*M* used in this study is high enough to accelerate the oxidation rate. In addition to the oxidation rate, in this study, the hydrogen absorption rate is also increased, strongly depending on the variation of alloys (Fig. 1(*b*)). The higher oxidation and hydrogen absorption rates are directly associated with their linear kinetics law describing the post-transition behavior, even from the early corrosion stage of 1 day at 290°C. At this stage, the oxide thickness is only 1–1.5 μm. For the case of the steam oxide, this thickness is in the pre-transition stage. Phenomenologically, the hydrogen absorption in the LiOH water environment, as well as the oxidation, is regarded as rate-controlled by surface reactions of the hydrogen and oxygen species, not by their diffusion in the oxide layer.

Some mechanisms have been suggested to account for the acceleration of the oxidation rate by LiOH addition. The key factors of the LiOH effects are: Increased numbers of anion vacancies [34], pore formation due to preferential cubic or tetragonal ZrO_2 dissolution [35], modified crystal growth of equiaxed grains [33], and disappearance of the barrier layer at the metal/oxide interface [20]. From the present BSE image examinations (Fig. 3), it is concluded that there is no direct relationship between the occurrence of microcracks and the

acceleration of oxidation and hydrogen absorption caused by LiOH addition. In fact, the LiOH oxides have a much lower frequency of microcracks. In contrast, microcracks in the steam corroded oxides were observed rather more frequently.

From the detailed TEM examination of the LiOH water oxides (Fig. 6), extended networks of degraded grain boundaries were formed from the surface to near the metal/oxide interface, leaving the very thin intact region of 50–100 nm thickness from the interface. In this region, intact ZrO_2 is continuously formed, and at the same time their grain boundaries are continuously attacked and degraded. From the linear kinetic law for the hydrogen pickup rate, the thickness of this intact layer is suggested to be a constant 50–100 nm for the present LiOH corrosion condition. In addition to the TEM observations, the presence of OH^- ions was confirmed by previous Fourier transform infrared examinations only for the LiOH water oxides, not for the steam oxides [8], which is consistent with the results in the literature [33]. SIMS analyses were conducted for the Li^+ ions [11,21,33], and they indicated that a high concentration of lithium penetrated to a region near the metal/oxide interface, and that the lithium in the oxides was easily leached by warm dilute nitric acid. In the previous glow discharge optical emission spectroscopy analyses [8], a high concentration of lithium with roughly flat profiles was also detected until near the interface. These microstructure observations and analyses indicate a direct attack of OH^- and Li^+ ions of high concentration up to the metal/oxide interface region through the degraded grain boundary networks. In order to know how and to what extent open channel structure develops, BET examinations for measuring the surface area of open channels should be made. Eventually, much higher oxidation and hydrogen absorption rates in the LiOH oxides would occur due to the intrusion of water containing OH^- ions along the open grain boundaries.

The most probable process for the formation of degraded or open grain boundaries is the preferential grain boundary dissolution of ZrO_2 in the LiOH-containing water, as suggested in the literature [35]. Figure 14 shows a thermodynamic assessment of the ZrO_2–LiOH–H_2O solution system at 290°C using the HSC Chemistry 5.1 code, which can calculate multi-component equilibrium compositions in heterogeneous systems [36]. Ion concentrations of OH^-, Li^+, and $HZrO_3^-$ increase with higher LiOH concentrations or higher *p*H conditions. In the solutions of more than 0.2*M* LiOH, undissolved LiOH becomes stable. Zirconate ions of $HZrO_3^-$ are formed by the reaction of $ZrO_2 + OH^- \rightarrow HZrO_3^-$; therefore, ZrO_2 can dissolve into higher LiOH solutions of, e.g., more than 0.1*M*. The deuterium concentrations in the bulk oxides of the three alloys after being corroded in the LiOD solution, which were analyzed by the NRA technique, vary with the alloy variation and range from 0.3×10^{20} (VB) to $1 \times 10^{20}\,cm^{-3}$ (Zry-2), as shown in Fig. 12(*a*). This order of the deuterium concentration for Zry−2 > GNF − Ziron > VB may correspond to the degree of degradation of grain boundaries in each sample. Assuming that the grain size of ZrO_2 is 30 nm and the radius of OH^- ions is 0.4 nm, the concentration of absorbed ions in the grain boundaries is $2.0 \times 10^{20}\,cm^{-3}$. This value has to be halved because of the co-existence of Li^+ ions. The estimated ion concentration of $1.0 \times 10^{20}\,cm^{-3}$ is roughly consistent with the NRA results.

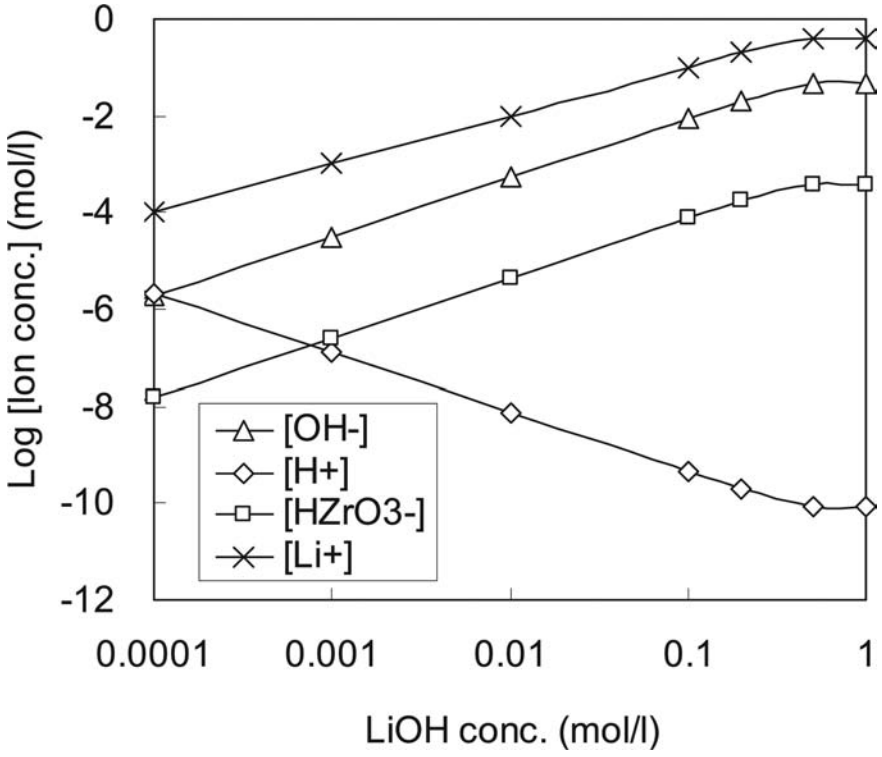


FIG. 14—*Thermodynamic assessment of ZrO_2–LiOH–H_2O aqueous system at 290°C by HSC Chemistry 5.1 code [25].*

The oxygen potentials in the LiOH solutions calculated by the HSC Chemistry 5.1 code increase with higher LiOH concentrations, and they are 4.4×10^{-6} atm for 1×10^{-4} *M* LiOH solution and 1.4×10^{-2} atm for 1*M* LiOH solution. Accordingly, microscopically porous LiOH oxides present up to near the metal/oxide interface are always exposed to a very high oxygen atmosphere. This oxidative atmosphere brings about more accelerated oxidation of Zr–Fe–Cr and Zr–Fe–Ni particles and preferential dissolution of iron into ZrO_2 matrix in the LiOH water environment. This high oxygen potential may be the reason why the sub-oxide layer was not observed in the LiOH water specimens.

At the front of the degraded grain boundaries, the dissociation of H_2O may arise according to the reactions of $H_2O + 2e- \rightarrow O^{2-} + H_2$ and $H_2O + V_{o}^{2+} \rightarrow O_o + 2H^+$ on the actual ZrO_2 surface containing oxygen vacancies, V_{o}^{2+}.\ The dissociated O^{2-} and H^+ ions diffuse toward Zr metal and react with it, as $Zr + 2O^{2-} \rightarrow ZrO_2 + 4e^-$ and $Zr + xH^+ \rightarrow ZrH_x + xh^+$. The linear kinetic law of oxidation and hydrogen absorption, as observed in the present LiOH corrosion tests, would be related to the dissociation reaction rates of H_2O at the front of the degraded grain boundaries. The SPPs containing nickel at the front region of the degraded grain boundaries may accelerate the dissociation

reaction of H_2O, because nickel exists mainly as metal precipitates as suggested by the SIMS mapping (Figs. 8 and 9) and the XAFS data [16]. In this sense, VB with no nickel is favorable for lower hydrogen absorption property.

Hydrogen Absorption Mechanism in Steam Corroded Oxide

The rate controlling process for hydrogen absorption in the steam oxides can be regarded as the diffusion of the hydrogen containing species in the protective oxide layer. In fact, the hydrogen absorption rate in the steam oxides follows the parabolic law during the pre-transition period, as shown in Fig. 1(*a*). The oxidation rate followed the cubic law for the same specimens [8]. The present results are consistent with a barrier layer concept of the oxide layer, which has been accepted for the corrosion kinetics [9–11]. When the oxide layer grows to a critical thickness, depending on corrosion conditions and alloy variations, the oxide layer becomes degraded from the viewpoint of diffusion property. This degradation of the oxide layer would be apparent from the occurrence of microcracks, formation of pores and open channels, and evolution of the oxide microstructure. These kinds of degradation in the oxide layer offer a fast diffusion path or diffusivity for oxygen and hydrogen, which might be linked with the transition of corrosion and hydrogen absorption rates. In the present steam environment, the barrier layer was identical for oxidation and hydrogen absorption processes. The oxidation rate is believed to be controlled by the diffusion of O^{2-} ions or electrons. Though there is no direct evidence, the hydrogen absorption rate could be rate-controlled by proton diffusion. By reviewing the diffusion coefficients of oxygen and hydrogen in ionic crystal ZrO_2, i.e., $D_O \geq D_H$, some interaction may occur between an interstitial hydrogen ion and an oxygen ion to form a OH complex when oxygen vacancies are introduced, as in the case of the degradation of stabilized ZrO_2 in humid atmosphere [37].

The previous Raman mapping for the steam corroded Zry-2 [8] indicated the stable tetragonal region of about 0.6–0.7 μm from the metal/oxide interface for the pre-transition steam oxide and a degradation of the stable tetragonal region for the post-transition oxide. Many microcracks observed after the transition would be caused by the phase transition of tetragonal to monoclinic ZrO_2 due to the lowering of compressive stress, because of a volume increase of 5 % during the transition. Moreover, the diffusion profiles of deuterium measured in the present NRA experiments for the pre-transition steam oxides of 1.4–1.7 μm distinctly demonstrate the presence of the barrier layer of about 0.8–0.9 μm for deuterium diffusion, as shown in Fig. 13. The thickness of this barrier layer agrees with the reported barrier layer thickness of 0.4–1 μm evaluated from impedance measurements [9]. There seems to be a coincidence of the inside barrier region obtained in the diffusion experiments and the higher compressive stress region obtained in the Raman experiments. Furthermore, from a comparison between Fig. 7(*a*), 7(*c*), the discrimination of the hydrogen absorption property of the present alloys could be well represented by the compressive stress rather than by the tetragonal fraction. An examination of the relationship between the tetragonal ZrO_2 fraction and corrosion rate of Zr alloys has suggested no direct relation between them [20]. Consequently, the lower hydrogen absorption property in VB, compared to Zry-2 and GNF-Ziron,

is due to higher compressive stress in the oxide. The reported high performance of Zr–Nb alloys regarding corrosion and hydrogen pickup [23] could be understood from the compressive stress concept.

Occasionally, the sub-oxide layer between hexagonal metal and ZrO_2 oxide has been suggested to be responsible for the barrier nature against corrosion [12–14], though the phase has not been clearly identified. Also, in the present TEM and STEM observations, the sub-oxide layer of about 0.2–0.3 μm thickness was found. However, the profiles of deuterium near the metal/oxide interface region obtained in the present diffusion experiments (Figs. 12 and 13) do not support the existence of another barrier layer there. If the sub-oxide has an oxygen-ordered structure of Zr metal, such as Zr_3O or Zr_2O, this phase can be rejected as the barrier layer against hydrogen diffusion.

Role of Alloy Elements on Hydrogen Absorption

As described in the previous paper [8], there was no significant variation in the oxidation rates among the three alloys of Zry-2, GNF-Ziron, and VB both in the 400°C steam and 290°C LiOH-containing water. In contrast, the hydrogen absorption rate depends largely on the alloys, especially in the LiOH water. For the present three alloys, not only the iron content, but also contents of tin, chromium, and nickel vary. In another previous paper [7], Zry-2-based alloys with various iron contents were examined in LiOH water, and the importance of iron content for the hydrogen pickup was demonstrated. An assessment by crystal chemistry predicts that iron and tin would be soluble in the ZrO_2 lattice. In the case of the coordination number (CN) of 7 for monoclinic ZrO_2, the ionic radius is 0.72 nm for Fe^{3+} and 0.75 nm for Sn^{+4} compared to 0.78 nm for Zr^{+4}. For chromium and nickel, the values at CN = 6 are reported as 0.62 nm for Cr^{+3} and 0.69 nm for Ni^{2+} [38]. Smaller differences of ionic radius between the foreign cations and the Zr^{4+} are favorable toward dissolution. Therefore, the element most likely to be affecting the hydrogen absorption seems to be iron among the three elements contained in the SPPs. Actually, the preferential dissolution of iron is significant as seen from the present SIMS mapping and EPMA analyses (Figs. 8–11), and is especially apparent in the LiOH oxides. From detailed TEM examinations of $Zr(Fe, Cr)_2$ precipitates in the oxide layer of Zry-4, iron dissolution into the ZrO_2 matrix has been confirmed, especially after the transition [39].

Figure 15 shows the relationship between the hydrogen pickup fraction of the three alloys and the relative dissolved iron contents in the LiOH and steam oxides, which was re-evaluated from the EPMA results of Fig. 11. For the steam oxides, the pickup fraction decreases gradually with the dissolved iron. For the LiOH oxides, quite high hydrogen absorption appears in Zry-2 in spite of a significant amount of dissolved iron. There is a drastic change in the dissolved iron effect between Zry-2 and GNF-Ziron where the amount of dissolved iron increases from Zry-2 to GNF-Ziron. Namely, in the LiOH oxides, there seems to be a critical concentration of dissolved iron to lower the hydrogen absorption. In Fig. 15, only the effect of iron is examined. Besides the iron effect, an incorporated effect of nickel may have to be taken into consideration, as reported in the literature [40], because nickel in VB alloy is eliminated.

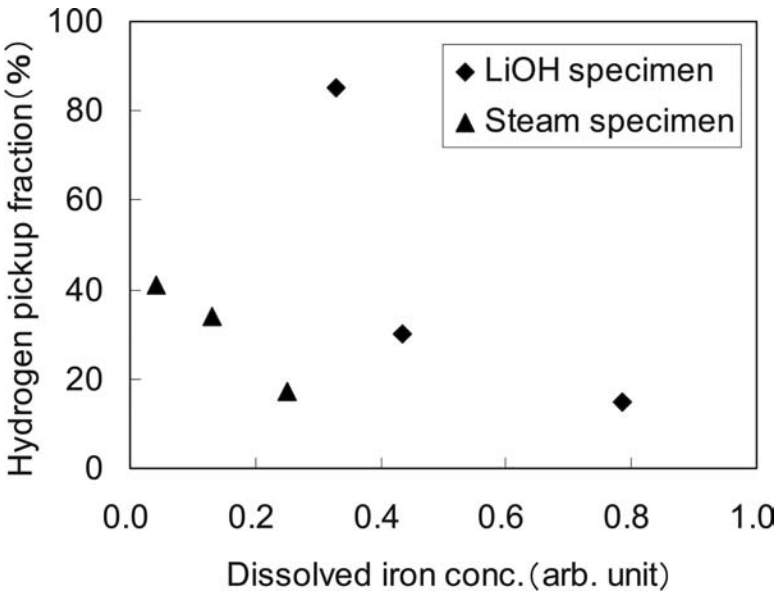


FIG. 15—*Relationship between hydrogen pickup fraction and relative dissolved iron concentration in oxides of the three alloys.*

The improvement of hydrogen absorption properties by increasing iron contents in Zr–Sn–Fe–Cr–(Ni) alloys has been demonstrated by out-of-pile tests in steam and water [6,7,40,41] and in-pile tests [3,5,6,42]. Two possible mechanisms can be considered: Decreased diffusivity and electrochemical potential. When Fe^{3+} of lower valence is dissolved substitutionally in the ZrO_2 lattice, anti-Frenkel defects of oxygen vacancies are created according to the reaction

$$Fe_2O_3 \rightarrow 2Fe_{Zr}^{-} + V_O^{2+} + 3O_o$$

$$[V_O^{2+}] = 1/2[Fe_{zr}^{-}]$$

$$n = K[Fe_{zr}^{-}]^{-1/2} po_2^{-1/4}$$

where:

$[V_O^{2+}]$ and n = concentrations of oxygen vacancies and electrons, which increase and decrease with the dissolved iron, respectively.

The mobility of interstitial protons would be suppressed by the formation of defect clusters containing oxygen vacancies and oxygen ions. In fact, the diffusion coefficient of deuterium in the VB oxide containing more dissolved iron is lowered to half of that in the GNF-Ziron oxide (see Fig. 13(*a*), 13(*b*)). Another explanation is

that the decreased number of electrons may lower the electrochemical potential gradient in the oxide for the driving force of proton diffusion [41].

Under the in-pile condition, most of the iron in the Zr–Fe–Cr and Zr–Fe–Ni particles has been confirmed to be forcibly dissolved in the metal by neutron radiation or radiation-induced dissolution [4,5]. In this situation, iron in the oxide must be dissolved. In this context, one of the key factors to screen the hydrogen absorption property of various alloys and to simulate the in-pile hydrogen pickup property by out-of-pile tests may be a preferential dissolution of iron in both environments.

Almost all the chromium in the Zr alloys exists as Zr–Fe–Cr particles in the metal, and the chromium exists as unoxidized and/or oxidized particles of, presumably, Cr_2O_3 in the oxide layer. Consequently, chromium in the oxide layer does not influence the lattice defect structure of ZrO_2, like the iron situation. In the inner protective oxide region, oxygen potentials are expected to be too low to oxidize the particles in a short period, and the particles oxidize slowly during a long period. The gradual oxidation of the particles must compress the surrounding oxide matrix continuously, since the molar volumes of Cr_2O_3 and Fe_2O_3 are larger than their metallic state by factors of 1.5 and 2.2, respectively. A much larger size and number density of the particles in the VB oxide would induce a higher compressive stress state continuously, compared to the cases of Zry-2 and GNF-Ziron. The higher compressive stress has some role with respect to the suppressed hydrogen pickup property of VB, in addition to the effect of VB being nickel-free.

Conclusions

The hydrogen absorption behavior in zirconium-based alloys is affected primarily by the characteristics of the oxide layer. In order to characterize the oxide layer, various examinations were made for three alloys, Zry-2, GNF-Ziron (Zry-2-based alloy with ~ 0.26 wt % of Fe), and VB (Zr-based alloy containing ~ 0.5 wt % of Sn, ~ 0.5 wt % of Fe, and ~ 1 wt % of Cr). Specimens were corroded in two different test environments of 400°C steam and 1*M* LiOH water at 290°C.

(1) The hydrogen absorption rate in the LiOH water corrosion tests was considerably higher compared to that in the steam corrosion tests; the former test specimens followed the linear law and the latter followed the parabolic law. The hydrogen pickup fraction in the LiOH water tests decreased in the order of $\text{Zry}-2 > \text{GNF} - \text{Ziron} > \text{VB}$, which was the same as the order of low to high iron contents in the alloys. Also in the steam tests, the same order of performance was found, and the superiority of VB with higher iron and chromium concentrations was remarkable.

(2) The much higher oxidation and hydrogen pickup rates in the LiOH water was ascribed to the formation of degraded or open grain boundaries on equiaxed grains up to locations near the metal/oxide interface, leaving a very thin intact region of 50–100 nm. From these microstructural observations and the confirmation of OH^- ions in the oxides, easy intrusion of water containing OH^- ions along the open grain boundaries was directly connected to the reaction-controlled linear law. The open

grain boundaries were possibly generated by the dissolution of ZrO_2 into high concentration LiOH solutions through the formation of $HZrO_3^-$ ions. The variation among the alloys of hydrogen pickup property in the LiOH water arose from the differences of the open grain boundary formation and the dissociation reaction of H_2O at the front of the degraded grain boundaries.

(3) The rate controlling process for hydrogen absorption in the pre-transition steam oxides was regarded as the diffusion of hydrogen ions in the inside barrier layer. The transition timing of hydrogen pickup and oxidation was identical. The transition was always accompanied by the frequent occurrence of microcracks. The pre-transition oxides of 1.4–1.7 μm had a double layer structure composed of the outside non-protective oxide of monoclinic ZrO_2 with faster diffusivity and the inside protective or barrier layer of predominantly tetragonal ZrO_2 with slower diffusivity. The thickness of the barrier layer was always about 0.8–0.9 μm, irrespective of the alloy variation. The diffusion coefficient of deuterium in the VB barrier oxide was roughly half of that in the GNF-Ziron oxide. This factor for the diffusivity was consistent with their hydrogen pickup performance. The higher compressive stress in the barrier layer was directly linked to the higher hydrogen pickup resistance of the alloys. It was found from the in situ diffusion profiles that the sub-oxide layer of about 0.2–0.3 μm observed between ZrO_2 oxide and hexagonal Zr metal did not have a protective nature for hydrogen diffusion.

(4) Distinguished preferential dissolution of iron into the oxide matrix from the SPPs was evidenced, and the dissolution of chromium and nickel was very limited. These two elements had a tendency to exist as precipitates, chromium mainly as oxide, and nickel mainly as metal. The accelerated dissolution of iron in the LiOH water oxide was caused by the higher oxidative atmosphere. The hydrogen pickup fraction decreased with higher dissolved iron in the oxides with different tendencies both in the LiOH water and steam oxides. The improvement of the hydrogen absorption property by increasing iron contents in the alloys was rationalized by the decreased diffusivity of hydrogen ions through the change of the lattice defect structure in ZrO_2, when trivalent Fe^{+3} ions were dissolved substitutionally in it. In addition to the iron dissolution effect, delayed oxidation of the SPPs in the barrier oxide layer would work to maintain a higher compressive stress state. This could explain the superior hydrogen absorption performance of VB containing the SPPs with larger size and number density, compared to the other two alloys.

References

[1] Hirano, Y., Mozumi, Y., Kamimura, K., and Tsukuda, Y., "Irradiation Characteristics of BWR High Burnup 9×9 Lead Use Assemblies," *Proc. of 2005 Water Reactor Fuel Performance Mtg.*, Kyoto, Japan, Oct. 2–5, 2005, Atomic Energy Society of Japan, Tokyo.

[2] Shimada, S., Etoh, Y., Hayashi, H., and Tsukuda, Y., "A Metallographic and Fractographic Study of Outside-In Cracking Caused by Power Ramp Tests," *J. Nucl. Mater.*, Vol. 327, 2004, pp. 97–113.

[3] Etoh, Y., Shimada, S., Adamson, R. B., Yasuda, T., Kogai, T., and Ishii, Y., "Irradiation Behavior of Zr Alloys for Ultra High Burnup Fuel," *Proc. of Int. Topical Mtg. on Light Water Reactor Fuel Performance*, Portland, OR, 1997, Americal Nuclear Society, IL, pp. 211–218.

[4] Ishimoto, S., Kubo, T., and Kubota, O., "Development of New Zirconium Alloys for High Burnup Fuel," *Proc. of ENS Topfuel 2003, Wurtzburg*, Germany, March 16–19, 2003, European Nuclear Society, Brussels.

[5] Takagawa, Y., Ishimoto, S., Etoh, Y., Kubo, T., Ogata, K., and Kubota, O., "The Correlation Between Microstructures and In-BWR Corrosion Behavior of Highly Irradiated Zr-Based Alloys," *14th Int. Symposium on Zirconium in the Nuclear Industry, ASTM STP 1467*, Stockholm, 2004, ASTM International, West Conshohocken, PA, pp. 386–403.

[6] Ishimoto, S., Etoh, Y., Matsumoto, T., Lutz, D., and Takagi, A., "Improved Zr Alloys for High Burnup BWR Fuel," *Proc. of ENS Topfuel*, Salamanca, Spain, Oct. 22–25, 2006, European Nuclear Society, Brussels.

[7] Aomi, M., Etoh, Y., Ishimoto, S., Une, K., and Ito, K., "The Hydrogen Pick-Up Behavior for Zirconium-Based Alloys in Various Out-of-Pile Corrosion Test Conditions," *Proc. Topfuel 2009, Paris*, France, Sept. 6–10, 2009, European Nuclear Society, Brussels.

[8] Une, K., Ishimoto, S., Sakamoto, K., Etoh, Y., Aomi, M., and Ito, K., "The Characterization of Oxide Layer of Zirconium-Based Alloys Focusing on Hydrogen Absorption Behavior," *Proc. Topfuel 2009, Paris*, France, Sept. 6–10, 2009, European Nuclear Society, Brussels.

[9] Garzarolli, F., Seidel, H., Tricot, R., and Gros, J. P., "Oxide Growth Mechanism on Zirconium Alloys," *Ninth Int. Symposium on Zirconium in the Nuclear Industry, ASTM STP 1132*, Kobe, 1991, ASTM International, West Conshohocken, PA, pp. 395–415.

[10] Beie, H. J., Mitwalsky, A., Garzarolli, F., Ruhmann, H., and Sell, H. J., "Examinations of the Corrosion Mechanism of Zirconium Alloys," *10th Int. Symposium on Zirconium in the Nuclear Industry, ASTM STP 1245*, Baltimore, 1994, ASTM International, West Conshohocken, PA, pp. 615–643.

[11] Pecheur, D., Godlewski, J., Peybernes, J., Fayette, L., Noe, M., Frichet, A., and Kerrec, O., "Contribution to the Understanding of the Effect of the Water Chemistry on the Oxidation Kinetics of Zircaloy-4 Cladding," *12th Int. Symposium on Zirconium in the Nuclear Industry, ASTM STP 1354*, Toronto, 2000, ASTM International, West Conshohocken, PA, pp. 793–811.

[12] Harada, M. and Wakamatsu, R., "The Effect of Hydrogen on the Transition Behavior of the Corrosion Rate of Zirconium Alloys," *15th Int. Symposium on Zirconium in the Nuclear Industry, ASTM STP 1505*, Sunriver, 2009, ASTM International, West Conshohocken, PA, pp. 384–402.

[13] Wadman, B., Lai, Z., Andren, H. O., Nystrom, A. L., Rudling, P., and Pettersson, H., "Microstructure of Oxide Layers Formed During Autoclave Testing of Zirconium Alloys," *10th International Symposium on Zirconium in the Nuclear Industry, ASTM STP 1245*, Baltimore, 1994, ASTM International, West Conshohocken, PA, pp. 579–598.

[14] Anada, H. and Takeda, K., "Microstructure of Oxides on Zircaloy-4, 1.0Nb Zry-4 and Zry-2 Formed in 10.3MPa Steam at 673K," *11th International Symposium on Zirconium in the Nuclear Industry, ASTM STP 1295*, Garmisch-Partenkirchen, 1996, ASTM International, West Conshohocken, PA, pp. 35–54.

[15] Godlewski, J., Bouvier, P., Lucazeau, G., and Fayette, L., "Stress Distribution Measured by Raman Spectroscopy in Zirconia Films Formed by Oxidation of Zr-Based Alloys," *12th Int. Symposium on Zirconium in the Nuclear Industry, ASTM STP 1354*, Toronto, 2000, ASTM International, West Conshohocken, PA, pp. 877–900.

[16] Sakamoto, K., Une, K., and Aomi, M., "Chemical State of Alloying Elements in Oxide Layer of Zr-Based Alloys," *Proc. of 2010 LWR Fuel Performance TopFuel/WRFPM*, Orland, FL, Sept. 26–29, 2010, American Nuclear Society, IL.

[17] Clarke, D. R. and Adar, F., "Measurement of the Crystallographically Transformed Zone Produced by Fracture in Ceramics Containing Tetragonal Zirconia," *J. Am. Ceram. Soc.*, Vol. 65, No. 6, 1982, pp. 284–288.

[18] Takagi, I., Yoshida, K., Shin, K., and Higashi, K., "A Combined Technique of Nuclear Reaction Analysis and Plasma-Driven Permeation for a Quantitative Study on Deuterium Trapping," *Nucl. Instrum. Methods Phys. Res. B*, Vol. 84, 1994, pp. 393–399.

[19] Takagi, I., Sugiura, R., Shirai, K., and Higashi, K., "Deuterium Retention and Diffusion in ETP-10 Graphite Exposed to RF Plasma at Room Temperature," *Fusion Sci. Technol*, Vol. 41, 2002, pp. 902–906.

[20] Motta, A. T., Yilmazbayhan, A., Comstock, R. J., Partezana, J., Sabol, G. P., Lai, B., and Cai, Z. "Microstructure and Growth Mechanism of Oxide Layers Formed on Zr Alloys Studied with Micro-Beam Synchrotron Radiation," *14th Int. Symposium on Zirconium in the Nuclear Industry, ASTM STP 1467*, Stockholm, 2004, ASTM International, West Conshohocken, PA, pp. 205–232.

[21] Pecheur, D., Godlewski, J., Billot, P., and Thomazet, J., "Microstructure of Oxide Films Formed During the Waterside Corrosion of the Zircaloy-4 Cladding in Lithiated Environment," *11th Int. Symposium on Zirconium in the Nuclear Industry, ASTM STP 1295*, Garmisch-Partenkirchen, 1996, ASTM International, West Conshohocken, PA, pp. 94–113.

[22] Zhou, B. X., Li, Q., Yao, Y., Liu, W. Q., and Chu, Y. L., "Effect of Water Chemistry and Composition on Microstructural Evolution of Oxide on Zr Alloys," *15th Int. Symposium on Zirconium in the Nuclear Industry, ASTM STP 1505*, Sunriver, 2009, ASTM International, West Conshohocken, PA, pp. 360–383.

[23] Petigny, N., Barberis, P., Lemaignan, C., Valot, Ch., and Lallemant, M., "In Situ XRD Analysis of the Oxide Layers Formed by Oxidation at 743 K on Zircaloy 4 and Zr-1NbO," *J. Nucl. Mater.*, Vol. 280, 2000, pp. 318–330.

[24] Takagi, I., Une, K., Miyamura, S., and Kobayashi, T., "Deuterium Diffusion in Steam-Corroded Oxide Layer of Zirconium Alloys," *J. Nucl. Mater* (submitted).

[25] Khatamian, D. and Manchester, F. D., "An Ion Beam Study of Hydrogen Diffusion in Oxides of Zr and Zr-Nb (2.5 wt%)," *J. Nucl. Mater.*, Vol. 166, 1989, pp. 300–306.

[26] Khatamian, D., "Diffusion of Hydrogen in the Oxides of Zr-1Nb, Zr-2.5Nb and Zr-20Nb Alloys," *Z. Phys. Chem.*, Vol. 181, 1993, pp. 435–440.

[27] Khatamian, D., "Hydrogen Diffusion in Oxides Formed on Surfaces of Zirconium Alloys," *J. Alloys Compd.*, Vols. 253–254, 1997, pp. 471–474.

[28] McIntyre, N. S., David, R. D., Weisener, C. G., Warr, B. D., and Elmoselhi, M. B., "SIMS Studies of Hydrogen Diffusion Through Oxides on Zr-Nb Alloys," *Surf. Interface Anal.*, Vol. 17, 1991, pp. 757–763.

[29] Elmoselhi, M. B., Warr, B. D., and McIntyre, S., "A Study of the Hydrogen Uptake Mechanism in Zirconium Alloys," *10th Int. Symposium on Zirconium in the Nuclear Industry, ASTM STP 1245*, Baltimore, 1994, ASTM International, West Conshohocken, PA, pp. 62–79.

[30] Austin, J. H., Elleman, T. S., and Verghese, K., "Tritium Diffusion in Zircaloy-2 in the Temperature Range −78 to 204°C," *J. Nucl. Mater.* Vol. 51, 1974, pp. 321–329.

[31] Kunz, W., Munzel, H., and Kunz, U., "Tritium Release from Zircaloy-2: Dependence on Temperature, Surface Conditions and Composition of Surrounding Medium," *J. Nucl. Mater.*, Vol. 136, 1985, pp. 6–15.

[32] Warr, B. D., Elmoselhi, M. B., Newcomb, S. B., McIntyre, N. S., Brennenstuhl, A. M., and Lichtenberger, P. C., "Oxide Characteristics and Their Relationship to Hydrogen Uptake in Zirconium Alloys," *Ninth Int. Symposium on Zirconium in the Nuclear Industry, ASTM STP 1132*, Kobe, 1991, ASTM International, West Conshohocken, PA, pp. 740–757.

[33] Ramasubramanian, N. and Balakrishnan, P., "Aqueous Chemistry of Lithium Hydroxide and Boric Acid and Corrosion of Zircaloy-4 and Zr-2.5Nb Alloys," *10th Int. Symposium on Zirconium in the Nuclear Industry, ASTM STP 1245*, Baltimore, 1994, ASTM International, West Conshohocken, PA, pp. 378–399.

[34] Hillner, E. and Chirigos, J.N., "The Effect of Lithium Hydroxide and Related Solutions on the Corrosion Rate of Zircaloy in 680 F Water," *Report No.* WAPD-TM307, Bettis Atomic Power Lab, PA, 1962.

[35] Cox, B. and Wu, C., "Dissolution of Zirconium Oxide Film in 300 °C LiOH," *J. Nucl. Mater.*, Vol. 199, 1993, pp. 272–284.

[36] Outokumpu Reseach Oy, Finland, http://www.outokumputechnology.com (Last accessed December 22, 2009).

[37] Yoshimura, M., Noma, T., Kawabata, K., and Somiya, S., "Role of H_2O on the Degradation Process of Y-TZP," *J. Mater. Sci. Lett.*, Vol. 6, 1987, pp. 465–467.

[38] Shannon, R. D., "Revised Effective Ionic Radii and Systematic Studies of Interatomic Distances in Halides and Chalcogenides," *Acta Crystallogr.*, Vol. A32, 1976, pp. 751–767.

[39] Pecheur, D., Lefebvre, F., Motta, A. T., and Lemaignan, C., "Precipitate Evolution in the Zircaloy-4 Oxide Layer," *J. Nucl. Mater.*, Vol. 189, 1992, pp. 318–332.

[40] Takeda, T., Harada, M., Ishii, Y., and Miyazaki, A., "Effect of Metallographic Factor on Hydrogen Pick-Up Properties of Zircaloy-2," *J. Nucl. Sci. Technol.*, Vol. 43, No. 9, 2006, pp. 984–990.

[41] Kakiuchi, K., Itagaki, N., Furuya, T., Miyazaki, A., Ishii, Y., Suzuki, S., Terai, T., and Yamawaki, M., "Role of Iron for Hydrogen Absorption Mechanism in Zirconium Alloys," *14th Int. Symposium on Zirconium in the Nuclear Industry, ASTM STP 1467*, Stockholm, 2004, ASTM International, West Conshohocken, PA, pp. 349–366.

[42] Kakiuchi, K., Ohira, K., Itagaki, N., Otsuka, Y., Ishii, Y., and Miyazaki, A., "Irradiated Behavior at High Burnup for HiFi Alloy," *J. Nucl. Sci. Technol.*, Vol. 43, No. 9, 2006, pp. 1031–1036.

DISCUSSION

Question 1, M. Preuss, Manchester University:—1) The stress differences in the oxide between the three alloys at the metal/oxide interface seem very large (–400 MPa versus –1600 MPa). Do you really think this is reasonable?

Author's Response:—1) Raman spectra measurements were carried out with good reproducibility by line scanning mode of more than 3 lines for each oxide specimen, and the obtained data were averaged. The evaluated compressive stresses of –1.6 to –0.4 GPa are reasonably consistent with literature data obtained by Raman spectroscopy and XRD. We believe that the stress level near the metal/oxide interface must be a promising index representing the barrier performance of oxide layer.

Question 2, D. Rugg, Rolls-Royce:—Is the number + site of degraded/open boundaries injured by the specimen preparation? This might be expected as a result of the large growth stresses relieved during sectioning.

Author's Response:—The degraded/open grain boundaries observed only in the LiOH-water oxide were not generated during the specimen preparation. We prepared the TEM specimens by a focused ion beam technique (FIB). By using this technique, these types of microstructure damage have never been introduced.

Question 3, S. Yagnik, EPRI:—1) Did you confirm, in TEM studies, the observation of grain boundary degradation with lower concentration of LiOH? 2) The details of HPU mechanism from out-of-pile corrosion tests have to be confirmed for in-pile HPU mechanism. The link you have stated is the ranking of HPU fractions for the three alloys between in-pile and out-of-pile tests. Do you have any comments about in-pile mechanism of HPU that may be similar or different than the mechanism explained here.

Author's Response:—1) We have confirmed the degraded grain boundaries by TEM, for 1M LiOH- and 0.1M LiOH-water oxides. The oxidation and hydrogen absorption rates drastically decreased with lower LiOH concentrations. This suggests that the degree of the degraded grain boundary structure tends to lower with decreasing LiOH concentration.

2) We have learned the HPU mechanism from the oxide layers corroded in out-of-pile condition. The chemical state and preferential dissolution of the alloys elements played an important role to the hydrogen diffusivity, through the change of lattice defect structure of ZrO_2 oxide and the compressive stress state generated by the delayed oxidation of the SPPs. In in-pile condition, radiation-induced dissolution or segregation of the alloy elements and the accumulation of radiation damage in the oxide matrix have to be incorporated with the above out-of-pile phenomena. The detailed characterization of the oxide layer of irradiated materials is needed to find out the predominant factors in the in-pile HPU mechanism.

Question 4, J. Bertsch, PSI:—At PSI we made same corrosion experiments on binary alloys, which also show the going into solution and diffusion of Fe. The Fe accumulates at spots on the oxide surface. a) Do you also see accumulation of Fe, e.g. at the surface? b) Do you think that the Fe distribution (if not completely homogeneous) may play a role?

Author's Response:—We have not analyzed the alloy element distribution on the oxide surface. The preferential dissolution of Fe from the SPPs into the oxide matrix was clearly detected on the cross sectional oxide layers by Nano-SIMS mapping and EPMA analysis. The dissolved Fe, especially in the region near the M/O interface, would play an important role to suppress hydrogen diffusion.

Question 5, P. Bossis, CEA:—1) Is there a difference in the morphology of ZrO_2 grains between 1 M LiOH water and steam samples, regarding columnar or equiaxed microstructure? 2) What is the detection limit of the FTIR technique for OH? What is the hydrogen content in the oxide formed in steam? So is it possible to state on the presence of OH groups in the oxide formed in steam?

Author's Response:—1) There was a distinct difference in grain structure between 1 M LiOH-water and steam oxides. In the former oxide, well-developed networks of degraded grain boundaries of 20–30 nm equiaxed grains were entirely observed, while in the latter oxide columnar grain structure was mainly recognized.

2) We have confirmed the deuterium concentration in the oxides corroded in LiOD-containing D_2O water (290°C × 40 h) and D_2O steam (400°C × 15 d) by using a nuclear reaction analysis. In the LiOD-water oxide, the deuterium concentration of $0.3 - 1.0 \times 10^{20}$ cm^{-3} was detected. Therefore, the detection limit of the FTIR system is considered to be lower than above values. The concentration in the D_2O steam oxide was $1 - 3 \times 10^{20}$ cm^{-3}. Consequently, deuterium present in the steam oxide can be judged to exist mainly as deuterium ions or atoms, not as OD ions, because OD bonds have never been detected for the steam oxides.

Question 6, Y.S. Kim, KAERI:—Please comment on why OH^- was not observed in the oxide during corrosion in pure water condition. You observed OH^- only under LiOH solutions. I think no observation of OH^- in water may be related to low concentration of OH^- in the oxide in water. Please comment on my comment.

Author's Response:—The hydrogen migration or diffusion mechanism in the oxide layer is closely related with the chemical state of hydrogen. We detected OH bonds only in the LiOH-water oxide, never in the steam oxide. We believe that OH^- ions exist on the degraded grain boundaries of the LiOH-water oxide and migrate along them, and that H^+ ions would be responsible for the diffusion species in the steam oxide.

Question 7, A. Motta, PSU, USA:—1) If your autoclave is made of stainless steel, do you believe that the Fe you observed dissolved in the oxide comes from Fe dissolved in solution? 2) Can you describe the method for stress measurement using Raman shift? Could the specimen geometry affect the state of stress? 3) Was the stage of the oxide relative to transition the same in the three alloys in which stress was measured?

Author's Response:—1) In our EPMA analyses, we have evaluated the contribution of Fe in the oxide that came from the environments of LiOH-containing water or steam by measuring the Fe concentration in a Zr-Nb alloy oxide with very low Fe content. Indeed, the level of Fe contamination in the LiOH-water oxide was much higher than that in the steam oxide. The EPMA data were corrected by this effect. Even after making the correction, the preferential Fe dissolution in the oxide layers from the SPPs was significant, especially in the LiOH-water oxides.

2) Raman spectra of the oxide layer were measured for bulk oxide specimens with tapered cross section which increased the thickness of exposed oxide by a factor of about 10. The planar or depth resolution of the present Raman system is about 1 mm. Therefore, except for free oxide surface, most of the measured Raman signals came from the stressed oxide matrix.

3) The oxide layer thickness of the three alloys used for the Raman examinations was 1.4–1.7 mm of the pre-transition condition.

Reprinted from JAI, Vol. 8, No. 3
doi:10.1520/JAI102960
Available online at www.astm.org/JAI

Toshio Kubo,[1] *Hiroaki Muta,*[2] *Shinsuke Yamanaka,*[2]
Masayoshi Uno,[3] *and Keizo Ogata*[4]

In Situ Scanning Electron Microscope Observation and Finite Element Method Analysis of Delayed Hydride Cracking Propagation in Zircaloy-2 Fuel Cladding Tubes

ABSTRACT: The objective of the present research is to build a modeling method for delayed hydride cracking (DHC) of zirconium alloys. DHC tests were carried out on Zircaloy-2 cladding tubes in the chamber of a scanning electron microscope to directly observe the crack propagation and measure the crack velocity in the radial direction. These in situ observations showed that a sharply tipped crack propagated at a relatively high rate, while the velocity decreased when the crack tip was blunted, supporting the occurrence of intermittent crack propagation that could be expected from the DHC mechanism. V-K_I curves or diagrams of crack velocity, V, versus stress intensity factor at a crack tip, K_I, were obtained as a function of 0.2 % offset yield stress, hydride orientation, and pre-crack depth. The steady state crack velocity and the threshold stress intensity factor for the onset of the crack propagation tended to increase or decrease, respectively, with an increase in the 0.2 % offset yield stress. Analyses of stress distribution and hydrogen diffusion around a crack tip were made using a finite element computer code. The analyses showed that a strong hydrostatic pressure field was generated

Manuscript received January 8, 2010; accepted for publication January 31, 2011; published online March 2011.

[1] Nippon Nuclear Fuel Development Co., Ltd., 2163 Narita-cho, Oarai-machi, Ibaraki 311-1313, Japan.
[2] Osaka Univ., 2-1 Yamadaoka, Suita, Osaka 565-0871, Japan.
[3] Fukui Univ., 3-9-1 Bunkyou, Fukui-shi, Fukui 910-8507, Japan.
[4] Japan Nuclear Energy Safety Organization, 3-17-1 Toranomon, Minato-ku, Tokyo 105-0001, Japan.

Cite as: Kubo, T., Muta, H., Yamanaka, S., Uno, M. and Ogata, K., "In Situ Scanning Electron Microscope Observation and Finite Element Method Analysis of Delayed Hydride Cracking Propagation in Zircaloy-2 Fuel Cladding Tubes," *J. ASTM Intl.*, Vol. 8, No. 3. doi:10.1520/JAI102960.

Copyright © 2011 by ASTM International, 100 Barr Harbor Drive, PO Box C700, West Conshohocken, PA 19428-2959.

concentrically around the crack tip and hydrogen diffused towards the crack tip according to the hydrostatic pressure gradient. The crack velocity was estimated from the calculated hydrogen flux rate assuming the critical hydrogen quantity for the crack propagation. There was good agreement between the experiments and the calculations regarding the crack velocity and its dependency on K_I. Calculations showed that the increase in the 0.2 % offset yield stress would accelerate the crack propagation by increasing the hydrostatic pressure at the crack tip.

KEYWORDS: BWR, fuel cladding tube, Zircaloy-2, PCI, delayed hydride cracking, hydrogen diffusion, hydride, in situ observation, FEM analyses

Introduction

The excellent pellet cladding interaction (PCI)-resistance of zirconium-lined Zircaloy-2 fuel cladding tubes for boiling water reactors (BWRs) has been widely demonstrated by many ramp tests up to about 50 GWd/tU [1]. Four segmented rods, however, failed in the ramp tests at about 60 GWd/tU [2,3]. Destructive post irradiation examinations (PIEs) showed that the rods failed with the outside-in cracking mode, where cracks are initiated outside the cladding tubes and propagated inwards [3–6]. Detailed metallographic and fractographic examinations revealed that the cracks initiated at radial hydrides near the outer surface and propagated inwards in the radial direction as step-by-step cracking of hydrides at a crack tip (delayed hydride cracking (DHC)) [3]. Though the failure power levels well exceeded the design maximum power, the outside-in type failure of fuel rods has been a potential concern for maintaining fuel integrity during a rapid power increase at high burnup. Extensive research programs have been carried out to clarify the mechanism of the outside-in type failure and quantify the conditions for the failure [7–9].

Though extensive studies have been made on the DHC of zirconium alloys [10–25], the presently available knowledge is still insufficient to provide a quantitative description of the DHC mechanism under the PCI condition during the power increase at high burnup. The DHC is affected by a number of factors, such as hydrogen diffusion, stress concentration, and hydride precipitation in the vicinity of a crack tip, which are all interrelated. Modeling of DHC requires not only experimental efforts to clarify these factors but an analytical approach to integrate them into the total mechanism.

The objective of the present research is to build a modeling method for the DHC of zirconium alloys. DHC tests were carried out in the chamber of a scanning electron microscope (SEM) to directly observe the crack propagation and measure the crack velocity in the radial direction of the cladding tubes. Analyses of stress distribution and hydrogen diffusion around a crack tip were made using a finite element computer code to calculate the hydrogen flux rate into the crack tip and estimate the crack velocity. The DHC mechanism was then considered based on the experimental and analytical results.

Experimental Procedures

Materials

Cold-worked zirconium-lined Zircaloy-2 tubes (diameter, 11.2 mm; wall thickness, 0.7 mm) were used. The chemical composition, texture characteristics, and 0.2 % offset yield stress of the tubes are given in Tables 1, respectively. The basal pole figure of the tubes is given in Fig. 1. The maximum basal plane intensity occurs at about $\pm 35^\circ$ from the radial towards the transverse direction of the plane, which is typical of Zircaloy-2 cladding tubes. Some were annealed at 723 or 783 K for 2 h for stress relieving. The 0.2 % offset yield stresses in Table 3 were obtained by tensile tests in the axial direction at 523 and 548 K. The 0.2 % offset yield stresses of the test materials were almost equivalent to those of irradiated Zircaloy-2 tubes (fluence $> 10^{25}\,1/\mathrm{m}^2$, $E > 1\,\mathrm{MeV}$) [26]. The strain hardening exponent of irradiated materials was very small compared with non-irradiated materials [26] because of the dislocation channeling effects. The tubes were charged with hydrogen by heating at 588 K for 24 h in an aqueous solution of 2 mol/L lithium hydroxide. The hydrogen concentrations in Zircaloy-2 matrix, which were measured by hot vacuum extraction after removing the zirconium-liner, were from about 90 to 130 ppm. Some of the hydrogen charged tubes were simultaneously subjected to thermal cycling and tensile circumferential stress to obtain radial hydrides. The thermal cycling was between 423 and 663 K and the circumferential stress of 160 MPa was applied by internal pressurization. The number of the thermal cycling was five, while the holding time at 663 K was 1 h for each cycle and 5 h in total. 5 h at 663 K would be sufficiently long for dissolution of almost all the hydrides. During the thermal cycling, hydrides dissolved at 663 K and re-precipitated in the radial direction due to the circumferential tensile stress when the temperature was being

TABLE 1—*Chemical composition of the test material.*

Sn wt %	Fe wt %	Cr wt %	Ni wt %	O ppm	C ppm	Si ppm	H ppm	N ppm
1.35	0.17	0.11	0.06	1200	140	92	< 3	21

TABLE 2—*Texture characteristics of the test material.*

Basal Pole Orientation	Kearn's Factor		
α [a]	f_a [b]	f_t [c]	f_r [d]
$\pm 35^\circ$	0.045	0.309	0.646

[a]The angle between the basal pole maxima of texture and the radial direction of cladding.
[b]Axial texture parameter.
[c]Tangential texture parameter.
[d]Radial texture parameter.

TABLE 3—*0.2 % offset yield stresses of the test materials.*

Temperature (K)	CW[a] (MPa)	723KSR[b] (MPa)	783KSR[c] (MPa)
523	610	540	320
548	600	520	310

[a]CW: Cold-worked.
[b]Stress relieved at 723 K.
[c]Stress relieved at 748 K.

lowered. Stress relieving effects at 663 K for 5 h would be very small. Figure 2 reproduces optical micrographs showing hydride distributions in transverse cross sections of the Zircaloy-2 tubes. Hydride density was higher in the zirconium-liner than the Zircaloy-2 matrix and hydrides were depleted in a region close to the zirconium-liner. Most hydrides in the Zircaloy-2 matrix oriented in a circumferential direction after the hydrogen charge (Fig. 2(*a*); hereafter, this material was denoted as circumferentially hydrided material), while essentially all hydrides were oriented in the radial direction after the thermal cycling (Fig. 2(*b*); hereafter, this material was denoted as radially hydrided material). The hydride distribution such as that shown in Fig. 2(*b*) has not been seen in fuel cladding tubes irradiated in BWRs even after power ramp tests. However, these specimens were also used in the present experiment for the basic study on effects of hydride orientation.

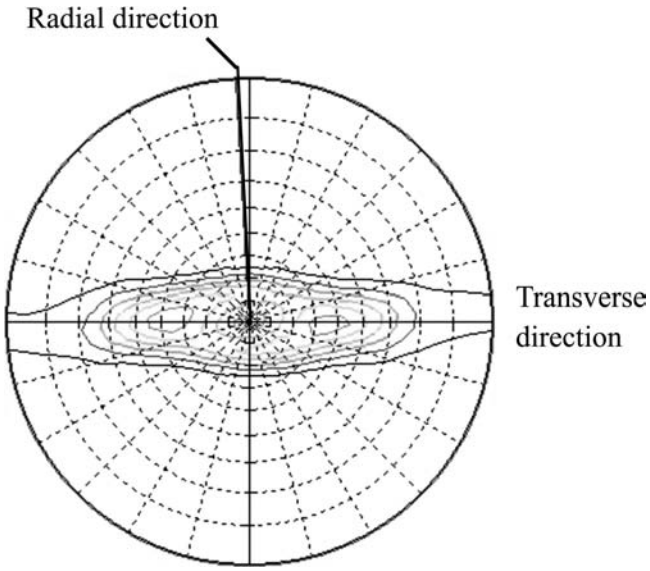


FIG. 1—*Basal plane pole figure of the test material. The maximum intensity occurs at about ±35° from the radial towards the transverse direction of the plane.*

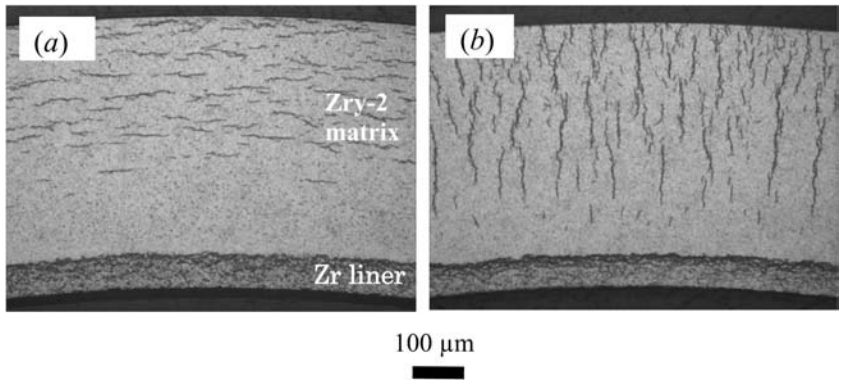


FIG. 2—*Optical micrographs showing hydride distributions in test materials after (*a*) the hydrogen charge and (*b*) the thermal cycling. Most hydrides in Zircaloy-2 matrix oriented in the circumferential direction after the hydrogen charge, while essentially all hydrides oriented in the radial direction after the thermal cycling.*

Test Specimens

Destructive PIEs showed that long and shallow axial cracks (the ratio of the depth to the crack length was smaller than about 0.2) were formed on the outer surfaces in the ramp tests [3]. Pre-cracks simulating the long and shallow axial cracks were formed on the outer surfaces of the tubes, as shown in Fig. 3 by cyclic loading together with a coating of methanol solution of iodine on the outer surfaces. The coating of the iodine solution on the outer surfaces enhanced the pre-cracking, so cracks were formed only on the outer surface. The depth of pre-cracks was controlled by varying the number of cycles of loading. Then, the Zircaloy-2 tubes were cut at the middles of the cracks and ring specimens of 3 mm height were taken. The transverse cross sections at the middles of the cracks were polished to get a flat and smooth surface so that cracks and hydrides could be observed under a SEM. Polishing was done with silicon carbide papers and a 0.04 μm silica suspension. Finally, specimens were cleansed by ultrasonic washing in acetone and then ethanol for 30 min. SEM micrographs of pre-cracks were taken before the tests and their depth was measured on the micrographs. The depth was from about 30 to 220 μm. The length of the pre-cracks was from about 1.5 to 2 mm and the ratio of the crack depth to the crack length was smaller than 0.2. The characteristics of the specimens are summarized in Table 4.

Test Apparatus for Delayed Hydride Cracking Tests in the Scanning Electron Microscope Chamber

A schematic of the test apparatus for the in situ observation of the DHC propagation is given in Fig. 4. The ring tensile test method was used since it is a straightforward technique using a compact and simply-shaped specimen. A ring specimen was put on a tensile device, which was placed in the chamber of a

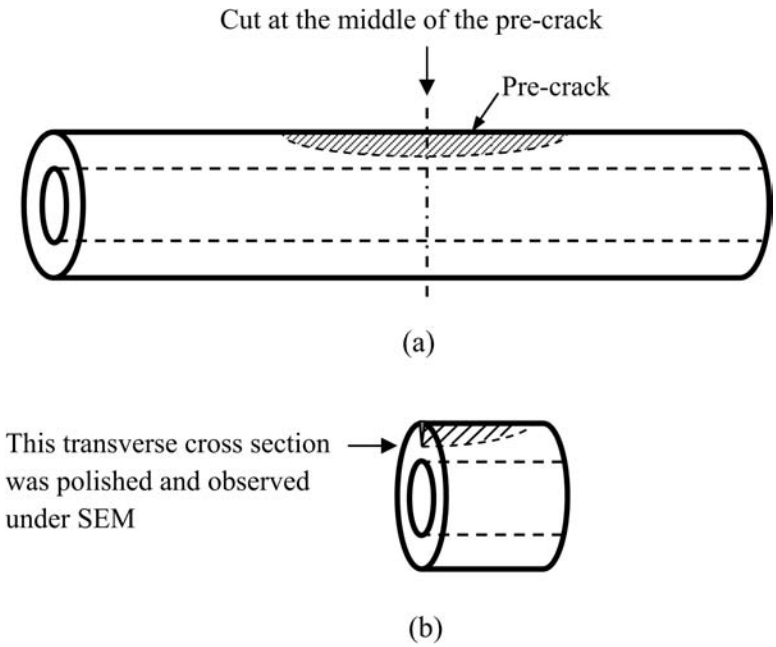


FIG. 3—*Schematics showing a process of taking a ring specimen from a Zircaloy-2 tube with a pre-crack on its outer surface. (*a*) Zircaloy-2 tube with a pre-crack on an outer surface and (*b*) ring specimen cut from the tube.*

TABLE 4—*Characteristics of the test specimens. C2 and R2 are from Ref 11.*

Sample Number	Hydrogen Concentration[a] (ppm)	Hydride Distribution	Heat Treatment	Depth of Pre-Crack (μm)	Test Temperature (K)	Ref.
C1	93	C[b]	CW[c]	56	523	P.S.[d]
C2	105	C	CW	142	523	11
C3	93	C	CW	30	548	P.S.
C4	105	C	SR[e] at 723 K	55	548	P.S.
C5	129	C	SR at 783 K	76	548	P.S.
R1	111	R[f]	CW	153	523	P.S.
R2	121	R	CW	216	523	11
R3	121	R	CW	89	548	P.S.
R4	121	R	CW	46	548	P.S.

[a]Hydrogen concentration in Zry-2 matrix.
[b]C: Circumferentially hydrided.
[c]CW: Cold-worked.
[d]Present study.
[e]SR: Stress relieved.
[f]R: Radially hydrided.

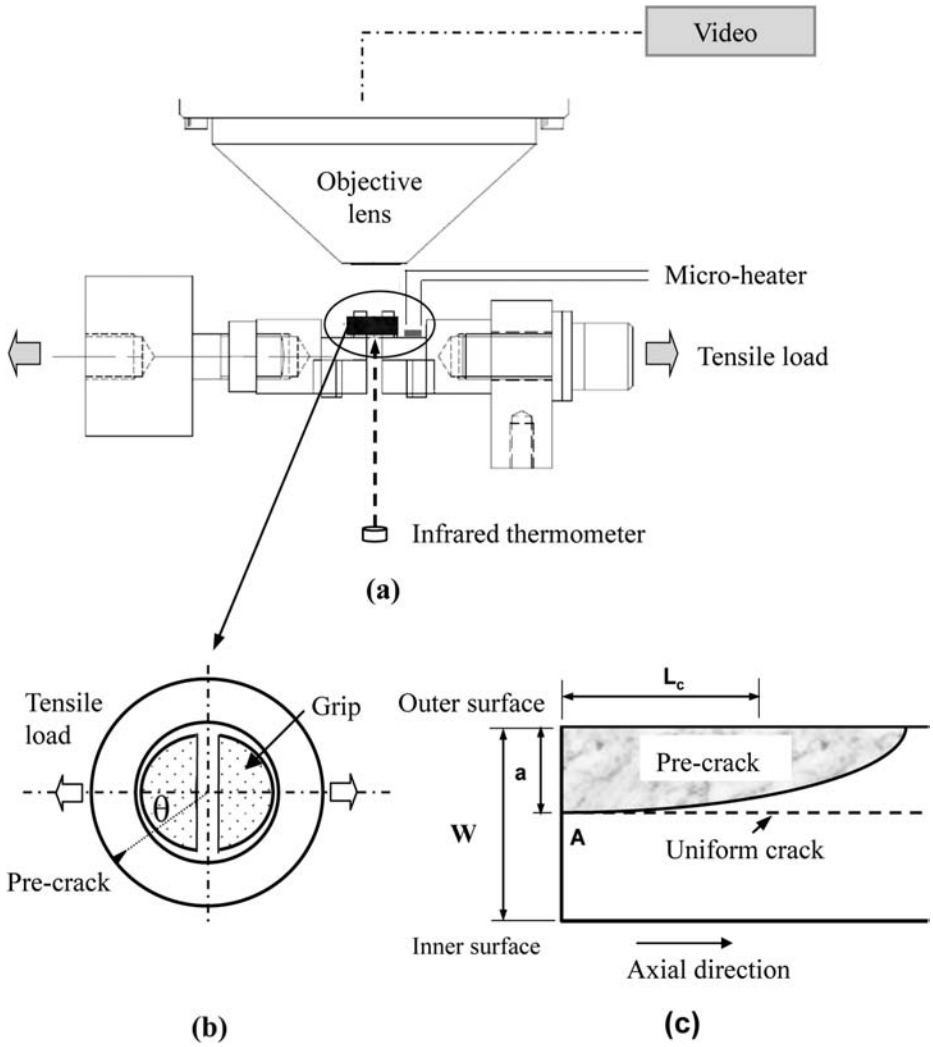


FIG. 4—*Schematics of the test apparatus and a test specimen for the in situ observation of the DHC propagation under a SEM.* (a) *Test apparatus;* (b) *configuration of a specimen; and* (c) *cross sectional view of the pre-crack.*

Hitachi S-3000N SEM equipped with a four-segment back scatter detector. A polished transverse cross section was placed face to face with the objective lens. The angle between a crack and a loading direction was about 40° (Fig. 4(*b*)). The specimen was heated by a microheater and stretched slowly at a constant displacement rate. The temperature was measured with an infrared thermometer. A comparison curve was obtained prior to the tests between measurements by the infrared thermometer and thermocouples. The load and displacement were measured by a 5 kN small-sized load cell and an inductive displacement

transducer, respectively. The crack propagation in the radial direction was continuously observed and recorded. The hydrides could be observed at 293 K utilizing a back scattered electron imaging (BSE) technique.

Test Conditions

Ring tensile tests at a slow constant displacement rate were carried out in the SEM chamber and the crack propagation in the radial direction was continuously observed and recorded. The test temperatures were 523 and 548 K while the cross head displacement rate was 2 μm/min. Specimens were heated at 598 K for 30 min to dissolve hydrides and this was followed by lowering their temperature slowly to the desired test temperatures before the ring tensile tests were started. For the radially hydrided material, the circumferential tensile stress of 120 MPa was applied when temperature was being lowered from 598 K to the desired test temperatures so that radial hydrides could re-precipitate. The circumferentially hydrided material was stress-free during the pre-heating and mainly circumferential hydrides would have re-precipitated.

Stress Intensity Factor, K_I

A thin wall tube such as a Zircaloy-2 fuel cladding tube does not necessarily meet the requirements of linear fracture mechanics. In the present study, however, the stress intensity factor at a crack tip, K_I, was determined as a tentative index in the following way.

A schematic of a pre-crack is given in Fig. 4(*c*). When the shape of the long and shallow pre-crack was approximated by a semi-ellipse, K_I at A in Fig. 4(*c*) was given as a function of crack depth, a, ratio of crack depth to crack length, L_c, and ratio of crack length to specimen thickness [27]. The difference between K_I of the pre-crack at A and K_I of a uniform crack was less than about 5 % when a/L_c was smaller than 0.2. Since a/L_c was smaller than 0.2 under the present experimental condition, K_I of a uniform crack was used in the present study for simplicity.

K_I of a uniform crack in a plate of finite thickness was given by the following formula from linear fracture mechanics [28].

$$K_I = \sigma\sqrt{\pi a}\, f(\xi) \tag{1}$$

$$f(\xi) = 1.12 - 0.23\xi + 10.55\xi^2 - 21.72\xi^3 + 30.39\xi^4 \tag{2}$$

$$\xi = a/W \tag{3}$$

where:

K_I = stress intensity factor at a crack tip (MPa $\cdot$ m$^{1/2}$),
σ = nominal circumferential stress (MPa),
a = crack depth (m), and
W = wall thickness (m).

The nominal circumferential stress was approximated by the following equation.

$$\sigma = \frac{P}{2WL} \times 10^{-6} + \sigma_b \tag{4}$$

where:

P = load (N),

L = height of the ring (m), and

σ_b = bending stress (MPa).

When the crosshead displacement was small and most of the specimen's inner surface was out of contact with the grip, the deformed specimen shape could be approximated by an ellipse. Then, the bending moment in the specimen was given by the following equation [29].

$$M = \frac{Pr_1(\sin\theta - 2/\pi)}{2} \tag{5}$$

where:

M = bending moment (Nm),

r_1 = mid-radius of specimen (m), and

θ = angle between a crack and the loading direction (degrees, see Fig. 4(*b*)).

The pre-crack was placed at $\theta = 40^\circ$ where the bending moment was the smallest, as shown by the Eq 5. Since the specimen surface came in contact with the grip shortly after the start of the tensile test, σ_b was corrected using Eqs 4 and 6.

$$\sigma_b = \left\{\frac{E(W-a)}{2}\right\}\left(\frac{1}{r_2} - \frac{1}{r_1'}\right) \tag{6}$$

$$r_1' = r_1 - \frac{a}{2} \tag{7}$$

where:

E = Youngs modulus (MPa) and

r_2 = radius of the grip (m).

Experimental Results and Discussions

Crack Propagation Behavior

Figure 5 gives results of the in situ observations at 523 K for the cold-worked circumferentially hydrided material (hereafter, test materials are always cold-worked ones unless otherwise specified). The crack depth was intermittently measured on SEM micrographs and plotted in Fig. 5(*a*) versus time. The nominal circumferential stress is also given in Fig. 5(*a*). The figure showed that stress

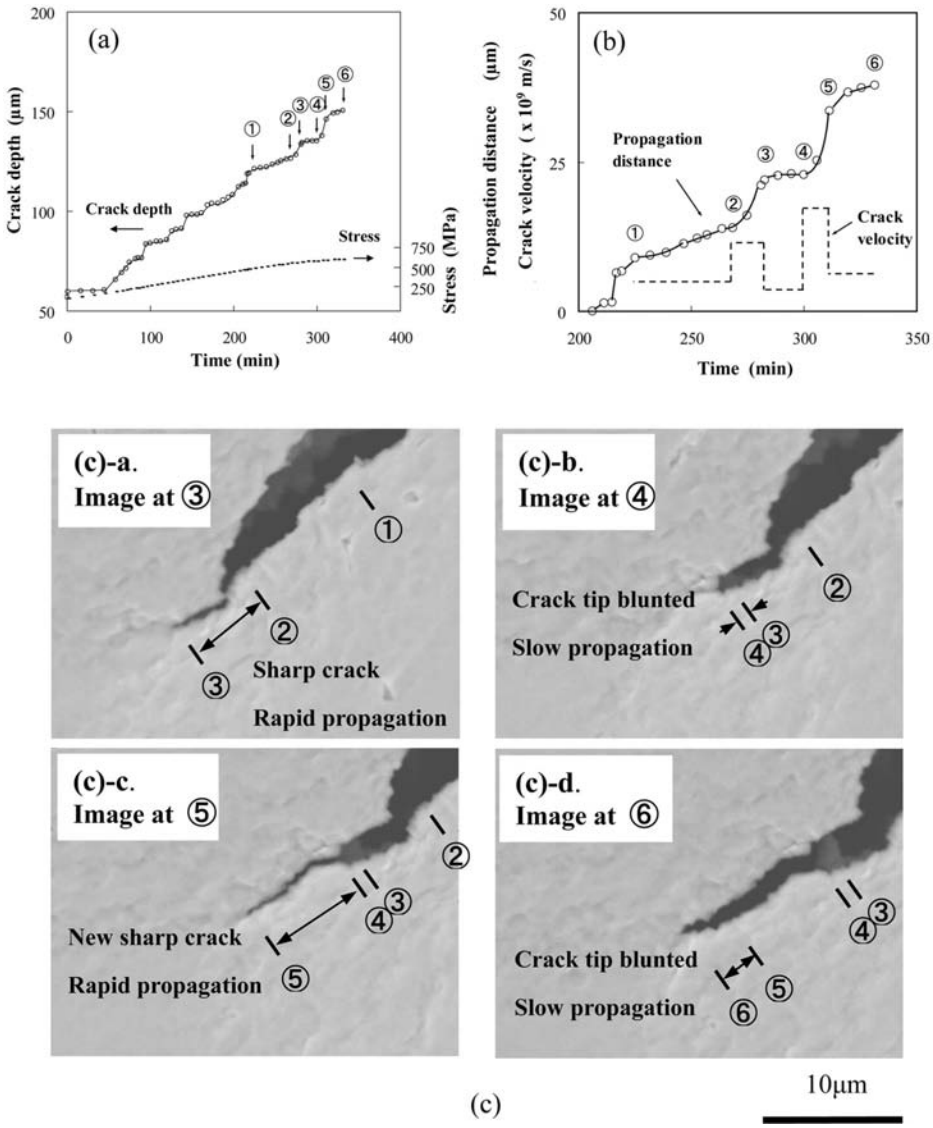


FIG. 5—*Results of the in situ observations at 523 K for the cold-worked circumferentially hydrided material. (a) Crack depth and stress versus time; (b) propagation distance and crack velocity versus time in intervals from ① to ⑥; and (c) SEM micrographs taken in intervals from ① to ⑥. The numbers in the micrographs correspond to those in Fig. 5(a), 5(b).*

was mostly within the elastic stage at least macroscopically. The crack propagated by the repetition of somewhat stepwise propagations followed by a slower propagation. The intermittent propagation of DHC has been expected theoretically [30] and was observed with acoustic emission and potential drop [31]. Taken together, however, the crack could be considered to have propagated almost steadily after the onset of the crack propagation. The intervals ① to ⑥ in Fig. 5(*a*) are enlarged and given in Fig. 5(*b*). The average crack velocity in each interval is also shown in Fig. 5(*b*). Examples of SEM images taken in the intervals ① to ⑥ are given in Fig. 5(*c*). Detailed observations of the crack propagation in the intervals ① to ⑥ showed that the crack propagated in an intermittent fashion depending on the sharpness of the crack tip. The crack propagated relatively slowly at a velocity of about 2×10^{-9} m/s in the interval ① to ②. A sharp crack appeared (Fig. 5(*c*)-a.) and propagated at a higher velocity of about 9×10^{-9} m/s in the interval ② to ③. The velocity decreased to about 0.9×10^{-9} m/s and the crack tip was blunted and rounded by the local plastic deformation in the interval ③ to ④ (Fig. 5(*c*)-b.). A new sharp crack initiated at the blunted crack tip (Fig. 5(*c*)-c.) and propagated at 15.6×10^{-9} m/s in the interval ④ to ⑤, which was again followed by the crack tip blunting in the interval ⑤ to ⑥ (Fig. 5(*c*)-d.). These observations showed that faster propagation periods with sharp crack tips and slower propagation periods with blunted crack tips appeared alternately. The propagation distance from ① to ⑥ was about 30 μm and the length of one propagation interval was about 10 μm (Fig. 5(*b*)). The latter value was used in the estimation of crack velocity from the hydrogen flux rate (see next section).

The results of the in situ observations at 548 K are given in Fig. 6. Crack depth, average crack velocity, and SEM images are arranged in the same manner as in Fig. 5. The crack propagated at a much higher rate at 548 K than at 523 K. Though the stepwise propagation similar to that observed at 523 K was also seen when the crack depth was relatively small, there was a tendency that the propagation became steadier or less intermittent as crack depth increased, which was consistent with the observation by Shek et al. [31]. After the crack had extended to about 380 μm, the crack velocity increased rapidly till the crack propagated through the wall and the specimen fractured. The velocity was almost constant in the intervals ① to ⑥, as shown in Fig. 6(*b*). Microscopic observations showed that the crack tip was mostly sharp though slight blunting was sometimes observed, as shown in the interval ④ to ⑤ (Fig. 6(*c*)-c.).

Effects of Material Strength, Hydride Orientation, and Depth of Pre-Crack

$V-K_I$ curves or diagrams of crack velocity, V, versus stress intensity factor, K_I, are given in Fig. 7 for the cold-worked material and the materials stress relieved at 723 and 783 K for 2 h (hereafter, the materials stress relieved at 723 and 783 K are denoted as 723KSR and 783KSR, respectively). Hydrides were circumferentially orientated in all these materials. The 0.2 % offset yield stresses of the cold-worked material, 723KSR, and 783KSR at 548 K are 600 MPa, 520 MPa, and 310 MPa, respectively, as shown in Table 3. 723KSR and 783KSR were not fully recrystallized, and fine grain structures elongated in the rolling direction

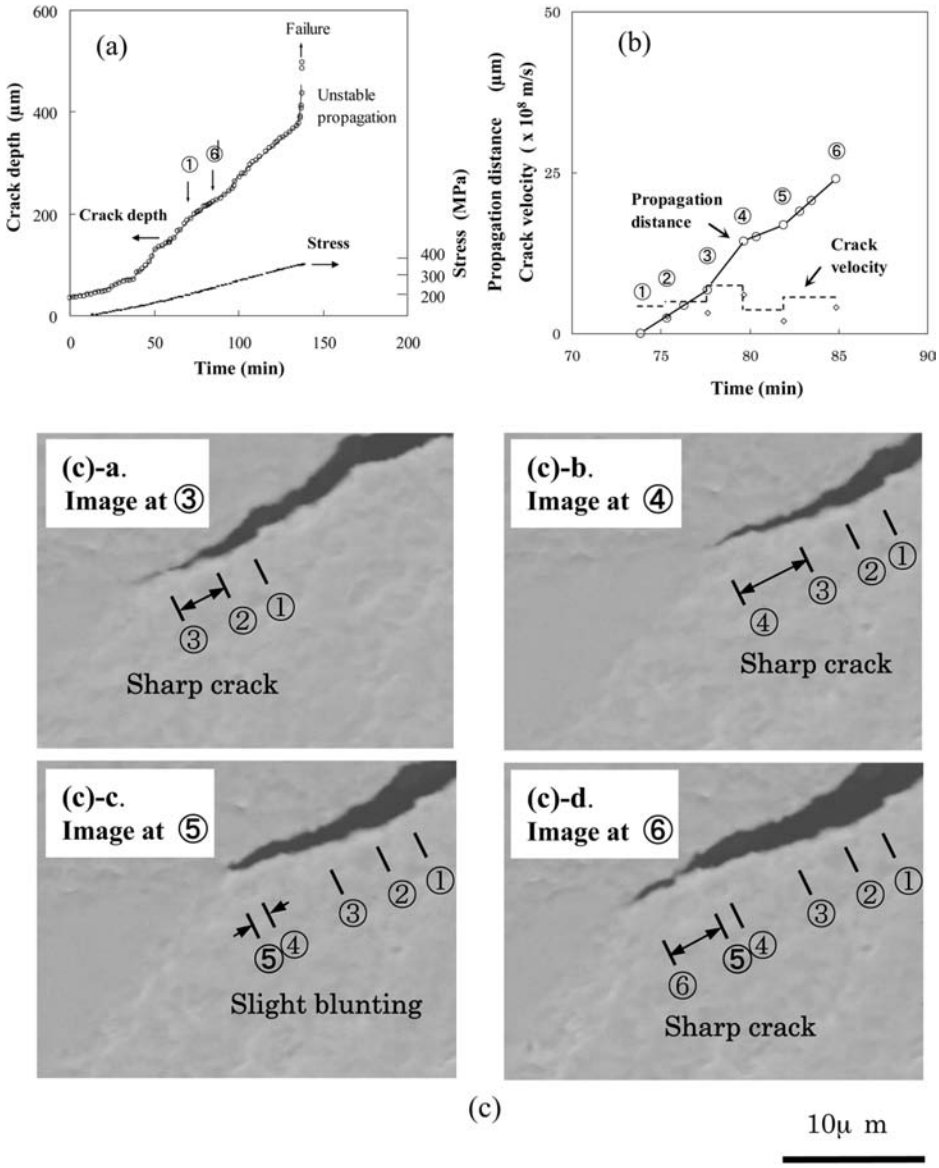


FIG. 6—*Results of the in situ observations at 548 K for the cold-worked circumferentially hydrided material. (*a*) Crack depth and stress versus time; (*b*) propagation distance and average crack velocity versus time in intervals from ① to ⑥; and (*c*) SEM micrographs taken in intervals from ① to ⑥. The numbers in the micrographs correspond to those in Fig. 6(*a*), 6(*b*).*

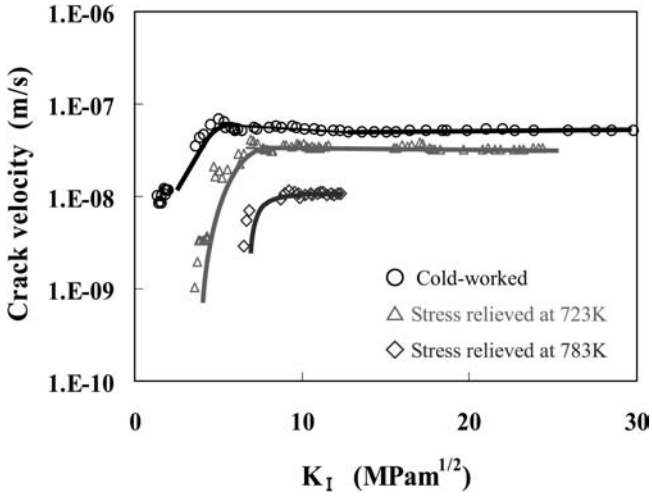


FIG. 7—*$V-K_I$ curves for the cold-worked material and materials stress relieved at 723 and 748 K. Test temperature was 548 K and all the materials were circumferentially hydrided.*

(axial direction) remained in these materials. In the case of the cold-worked material, the crack propagation started when K_I exceeded the threshold stress intensity factor, K_{IH}. The velocity increased rapidly with an increase in K_I immediately after the onset of the crack propagation. The velocity was almost steady or slightly dependent on K_I when K_I exceeded an another threshold stress intensity factor, $K_{I\text{th}}$. The same tendency was observed in the 723KSR and 783KSR. The steady state crack velocity, V_s, and the threshold stress intensity factors, K_{IH} and $K_{I\text{th}}$, tended to increase or decrease, respectively, with an increase in the 0.2 % offset yield stress, as shown in Table 5. The present K_{IH} data were somewhat smaller than literature data [18]. Since crack propagation was observed with the magnification of 3000 under a SEM, small crack movements of submicron in the very early stage of the start of the crack propagation could be observed in the present experiment. This might contribute to smaller K_{IH} in the present experiment compared with literature data.

The effects of material strength on the DHC velocity have been reported by several authors [18,22,32] and influences of not only the yield stress but microstructures such as hydride distribution and residual stresses have been discussed. Residual stresses have influences on hydride distribution [33] and may affect hydrogen diffusion in the matrix and hydride precipitation at a crack tip. In the present study, however, hydrogen diffusion analyses were done placing emphases mainly on the effects of the yield stress. Results are described in the next section.

$V-K_I$ curves are compared in Fig. 8 for the circumferentially and the radially hydrided materials. Little significant difference was seen in the $V-K_I$ curves between the two materials independent of test temperature and pre-crack depth. V_s and K_{IH} of these materials are plotted in Fig. 9 versus pre-crack depth.

TABLE 5—*Steady state velocity and threshold stress intensity factors of test materials. Test temperature was 548 K.*

Material	0.2 % Yield Stress at 548 K (MPa)	V_s [a] ($\times 10^{-8}$ m/s)	$K_{I\text{th}}$ [b] (MPa)	K_{IH} [c] (MPa)
CW[d]	600	5.2	4.6	1.4
723KSR[e]	520	3.4	6.5	3.6
783KSR[f]	310	1.1	8.7	6.5

[a]Steady state velocity.
[b]Threshold stress intensity factor for steady propagation.
[c]Threshold stress intensity factor for the start of the propagation.
[d]Cold-worked materials.
[e]Annealed at 723 K for stress relieving.
[f]Annealed at 783 K for stress relieving.

It was clearly seen that V_s was faster and K_{IH} was smaller at 548 K than at 523 K. However, little significant difference was seen in V_s and K_{IH} between the circumferentially and the radially hydrided materials. It was reported that in the case of short time tensile tests at 293 K, the radially hydrided material fractured in a brittle manner because of fracture of pre-existing radial hydrides, while the circumferentially hydrided material exhibited large plastic deformation [11]. It was also reported that the short time brittle fracture was not observed at temperatures higher than 473 K in either the radially hydrided or the circumferentially hydrided materials with pre-existing radial hydrides being intact [11]. These results indicated that the pre-existing radial hydrides were less brittle at high temperatures, which was consistent with literatures [34–37]. The ductility of the hydrides at high temperatures might be one of the important factors that could explain the small effects of the pre-existing radial hydrides on the short time brittle fracture at high temperatures. The present DHC test results showed that the effects of the pre-existing radial hydrides were also small on the DHC at temperatures higher than 523 K. The pre-existing radial hydrides did not seem to be a predominant path for the crack propagation of DHC. The reason was not fully understood at present. Radial hydrides that precipitated at a crack tip during DHC tests might be different from the pre-existing radial hydrides in thickness, microstructures, crystallographic orientation, chemical composition, and so on, which might be important factors to be considered.

A thin wall tube such as a Zircaloy-2 cladding tube does not necessarily meet the requirements of linear fracture mechanics. The crack propagation might not be accurately described with a parameter of fracture mechanics when pre-crack depth is, for example, as deep as 220 μm, which accounts for about one third of the thickness of the Zircaloy-2 matrix. In addition, hydride distribution is not uniform in the radial direction. V_s and K_{IH} were plotted in Fig. 9 versus pre-crack depth to examine the existence of influencing factors other than a parameter of linear fracture mechanics. Figure 9 showed that not only V_s but K_{IH} were almost independent of the pre-crack depth. This result would indicate that a parameter of linear fracture mechanics played a predominant role and K_I could be used as

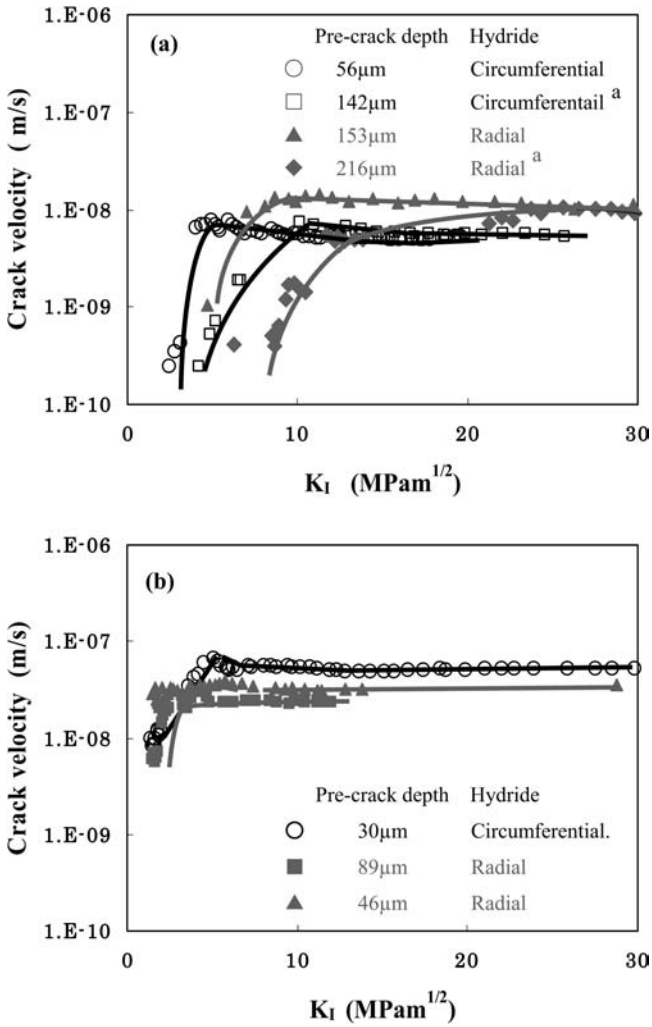


FIG. 8—*$V-K_I$ curves for the radially and the circumferentially hydrided materials tested at (*a*) 523 K and (*b*) 548 K, showing only a small difference in DHC properties between the two materials. Materials are cold-worked. Diagrams indicated with a in the figure are from Ref 11.*

a tentative index in the analyses of the crack propagation in Zircaloy-2 tubes under the present experimental conditions.

Back Scattered Electron Imaging and Scanning Electron Microscope Observations After Delayed Hydride Cracking Tests

The DHC test of the circumferentially hydrided material at 523 K was interrupted at ⑥ in Fig. 5 and detailed observations were made at 298 K by the use of

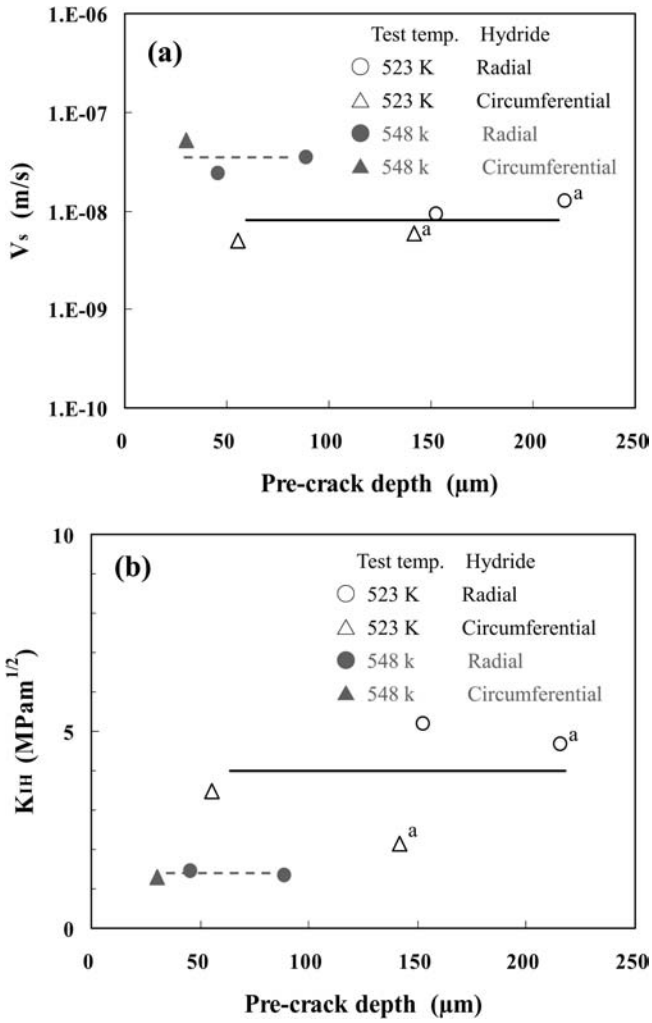


FIG. 9—*Dependencies of* (a) V_s *and* (b) K_{IH} *on pre-crack depth, showing only small effects of pre-crack depth on the DHC properties. Materials were cold-worked. Data indicated with a in the figure are from Ref 11.*

the BSE. Stress was unloaded prior to lowering temperature. The BSE images given in Fig. 10 showed that the crack propagated in the radial direction across the circumferential hydrides and a radial hydride precipitated at the crack tip. Since the material had only a few radial hydrides before the DHC test and temperature was lowered without circumferential tensile stress afterwards, the radial hydride at the crack tip would be formed most probably during the DHC test. Radial hydrides emanating from the crack tip were reported in literatures

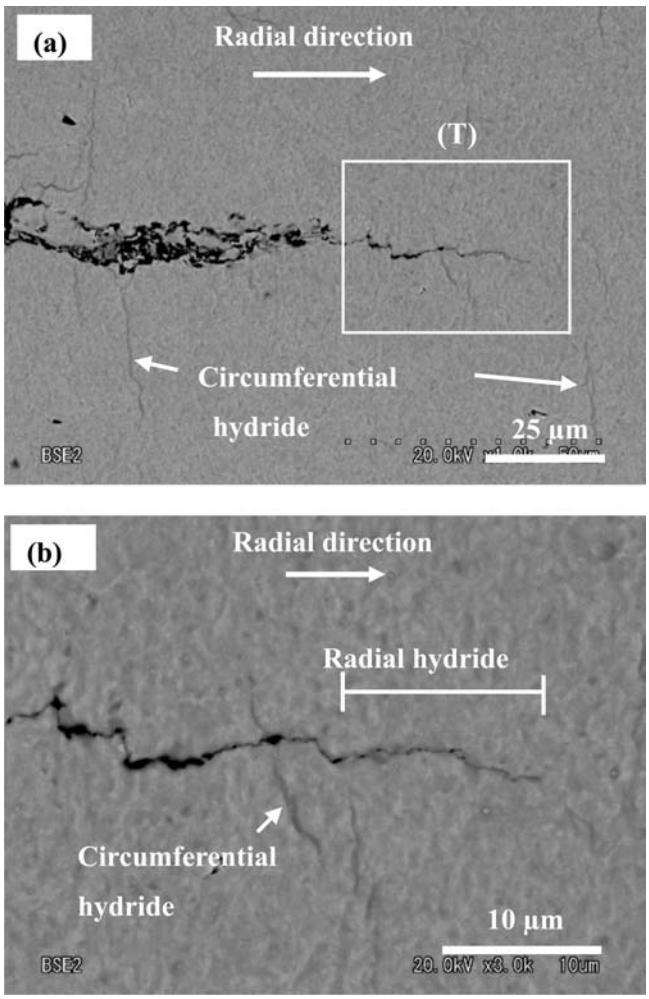


FIG. 10—*BSE images taken at 298 K after the DHC test at 523 K for the cold-worked circumferentially hydrided material. (*a*) Incipient crack propagating in the radial direction across the circumferential hydrides and (*b*) magnified image of (T), showing a partially fractured radial hydride at a crack tip.*

[10,31,38]. Several microcracks were formed in the radial hydrides in Fig. 10, suggesting that fracture of the hydride would be brought about by the coalescence of these microcracks. It was presumed from these observations that the intermittent propagation shown in Fig. 5 might possibly be attributable to the repetition of the formation and the fracture of the radial hydride at the crack tip. The precipitation and partial cracking of radial hydrides at a crack tip had also been observed in fuel cladding tubes that were subjected to ramp tests in a test reactor [3]. The thickness of the radial hydride was from about 0.1 to

0.2 μm, while its length was about 10 μm. These values were used in the estimation of crack velocity (see next section).

Figure 11 reproduces micrographs of the fracture surface after the DHC test. ② in Fig. 11 was the fracture surface produced during the DHC test. The fracture surface was mostly brittle and it would have been produced mainly by the fracture of hydride platelets. The general appearance of the fracture surface was independent of the test temperature, hydride orientation, or the material strength. Striations were not observed in the present Zircaloy-2 specimens. Though striations were often associated with DHC in Zr-2.5Nb pressure tube material [19], they have not been seen in Zircaloys [3,18,22]. Figure 11(*a*) showed that the shape of the crack after the DHC test could be approximated by a semi-ellipse. It was reported that crack velocity was smaller near surfaces than in the interior of the specimen due to a less constrained stress state near the surfaces [13,19]. The local surface effects should be taken into account when the crack velocity is determined from the crack depth on the specimen surface. However, it seemed to be small in the case of thin walled Zircaloy-2 tubes under the present experimental condition.

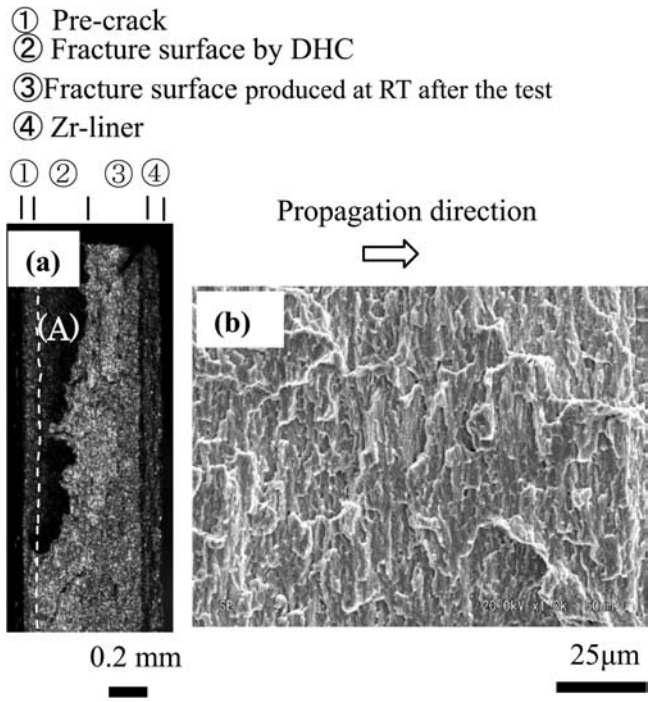


FIG. 11—*Fracture surface of the cold-worked radially hydrided material after DHC test at 523 K.* (a) *Low magnification optical micrograph of the fracture surface and* (b) *high magnification view of the area (A).*

Finite Element Method Analyses on Stress Concentration and Hydrogen Diffusion Around a Crack Tip

DHC is caused by the concentration of hydrogen towards the crack tip. The hydrogen flux depends on the gradients of hydrogen concentration, temperature, and hydrostatic pressure. Therefore, evaluation of stress distribution and hydrogen diffusion behavior is necessary to analyze the crack propagation. Previously, DHC of fuel cladding has been simulated by a FEM based on a hydride and solid solution composite model [39,40]. This combined model considers coupled processes of the hydrogen diffusion, energy flow, and hydride precipitation. The material in the model is assumed to be elastic. In this section, the present experimental results of DHC were simulated by a simpler model, which only considers hydrogen flux around the crack tip and does not consider the hydride precipitation. The crack propagation velocity was estimated from the calculated hydrogen flux to the crack tip.

Calculation Method

The commercial finite element code ABAQUS ver. 6.7 was employed for simulation. The hydrogen flux was determined from two-step calculations. As the first step, the hydrostatic pressure stress gradient around the crack tip, which is the driving force of hydrogen, was simulated. The geometry of the calculation model is shown in Fig. 12. A two-dimensional pre-cracked plate (0.7 mm thick) was used to simulate the experiment. Three models with different crack depths of 50, 100, and 200 μm were used. Applied tensile stress was changed from 10 to 500 MPa. The constant environmental temperature was set to 523 or 548 K. True stress–true strain input data were determined from experimental data for stress relieved and cold-worked Zircaloy-2 obtained at 548 K (see Table 3). Zircaloy-2 was assumed to be isotropic in the present analyses. The following equation was used.

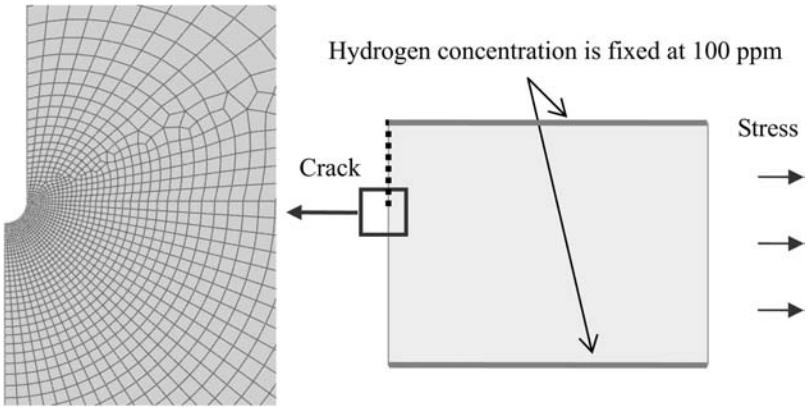


FIG. 12—*FEM simulation model geometry.*

$$\sigma = K\epsilon^n \left(\frac{\epsilon'}{10^{-3}}\right)^m \tag{8}$$

where:

σ = true effective stress,
ϵ = true effective plastic strain, and
ϵ' = rate of change of true effective plastic strain.

The strength coefficient, K, strain hardening exponent, n, and strain rate sensitivity, m, are material-dependent parameters. In this study, ϵ' and m were assumed to be 10^{-4} and 0.02 [41]. The parameters of K and n were determined from the 0.2 % offset yield stress and ultimate tensile stress of each specimen using the following relations [41].

$$\text{true yield strength} = \left[\frac{K}{E^n}\left(\frac{\epsilon'}{10^{-3}}\right)^m\right]^{1/(1-n)} \tag{9}$$

$$\text{true ultimate strength} = K\left(\frac{\epsilon'}{10^{-3}}\right)^m \left(\frac{n}{1+m}\right)^n \tag{10}$$

where:

E = Young's modulus.

The stress state near the specimen surface may be different from that in the interior. However, the surface effects were not taken into account in the analyses, since the surface effects were not large under the present experimental condition.

As the second step, hydrogen diffusion was simulated using the obtained hydrostatic pressure stress gradient and temperature data. The hydrogen diffusion was assumed to be driven by the gradient of chemical potential μ [42,43].

$$\mu = \mu_0 + RT\ln\varphi + p\text{-}V_H \tag{11}$$

$$J = -\frac{Dc}{RT}\cdot\frac{\partial\mu}{\partial x} \tag{12}$$

Then, the hydrogen flux J was written by

$$J = -sD\left(\frac{\partial\varphi}{\partial x} + \kappa_p\frac{\partial p}{\partial x}\right) \tag{13}$$

where:

s = hydrogen solubility,
D = diffusivity,
κ_s = thermal transport coefficient, and
κ_p = pressure stress factor.

φ is normalized hydrogen concentration and equal to c/s, c is hydrogen mass concentration. p is equivalent hydrostatic pressure stress, represented by $p = -\sum\sigma_{ii}/3$. A positive p value means compressive stress field is generated at the point and negative p means tensile stress field is generated. These two terms in Eq 13 represent the diffusion by gradients of hydrogen concentration and hydrostatic pressure stress. The κ_p could be written by

$$\kappa_p = \varphi \frac{V_H}{RT} \tag{14}$$

where:

R = gas constant and

V_H = partial molar volume of hydrogen in the solid solution.

The reported values of D [44], s [45], κ_s [45], and V_H [46] were used in this simulation. The hydrogen solid solubility is available above 770 K in the literature [45]; therefore, extrapolated data were used in the calculation.

Since the average hydrogen concentration in the present specimens was about 100 ppm, the initial hydrogen concentration was set to 100 ppm. Zirconium hydride must be precipitated at the concentration. However, in this calculation all the hydrogen can be assumed to dissolve in the matrix for simplification except in the vicinity of the crack tip. We focused on only the hydrogen flux around the crack tip. The hydrogen concentration on the surfaces was maintained at a constant value of 100 ppm, which worked as a hydrogen supply source. The minimum hydrostatic pressure stress point where the hydrogen concentration is maximized acts as a sink for hydrogen. It is assumed that the maximum hydrogen concentration in solution at the sink is 150 ppm and excess hydrogen flows into the sink to form hydrides. In the simplified calculation model, the hydrogen continues to flow from source to sink according to the concentration and stress gradients. We evaluate the steady state hydrogen flow rate caused by hydrostatic pressure gradient near the crack tip.

Calculation Results and Discussions

Figure 13(*a*) shows the hydrostatic pressure stress distribution around the crack tip at 523 K with an applied stress of 100 MPa. A strong tensile stress field was generated concentrically around the crack tip. The steady state hydrogen concentration distribution is shown in Fig. 13(*b*). According to the hydrostatic pressure stress gradient, hydrogen concentration increased near the crack tip. The steady state hydrogen distribution was achieved in about several tens of seconds at the present conditions.

Figure 14(*a*) shows hydrostatic pressure stress along the crack tip with different applied stresses. The hydrostatic pressure stress had a minimum peak around 0.1 to 2 μm from the crack tip, depending on the value of the applied stress. It was caused by plastic deformation. The concentrated stress generated the plastic strain, which relaxed the stress gradient near the crack tip. The minimum hydrostatic pressure stress increased with increasing applied stress until reaching 300 MPa. Above the applied stress of 300 MPa, there was little change

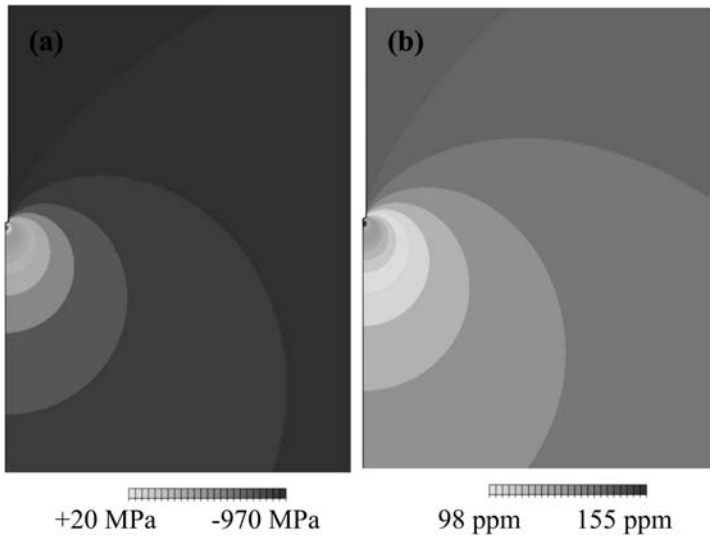


FIG. 13—*Distributions of (*a*) hydrostatic pressure and (*b*) hydrogen concentration for cold-worked specimen at 523 K. Applied stress, 100 MPa; crack depth, 100 μm.*

in the stress value and distribution. Under the conditions, increasing applied stress only widened the strain field and had little influence on the hydrostatic pressure stress gradient. The hydrogen flux is shown in Fig. 14(*b*). The hydrogen diffused towards the minimum hydrostatic pressure stress point. In this figure, the hydrogen flux from the crack tip to the minimum stress point is not plotted. Corresponding to the hydrostatic pressure stress gradient, the hydrogen flux had a maximum near the point and decreased with distance from the crack tip.

According to Figs. 5 and 10, the length of one crack propagation interval could be assumed to be about 10 μm. From the experimental result, the average hydrogen flux was estimated by integration of hydrogen flux for a 10 μm distance from the maximum point. Figure 15 shows the stress intensity factor K_I versus averaged hydrogen flux for crack depths of 50, 100, and 200 μm. K_I was estimated by Eq 1. The difference among the three crack depth models was negligible, so the hydrogen flux and K_I appeared to have a one-to-one relation. The hydrogen flux increased with K_I up to about 5 MPa · $m^{1/2}$, and became approximately constant. The behavior was similar to that of crack velocity, indicating that there is a linear relation between the hydrogen flux and the crack velocity. To make a correlation between the hydrogen flux and crack velocity, it is assumed that there is a critical hydride thickness for each crack growth. If the hydride thickness is determined, crack velocity V_{calc} can be estimated by $V_{calc} = \Delta L/\Delta t$, where ΔL is the length of one crack propagation interval and Δt is the required time to generate the critical hydride thickness. Now ΔL is experimentally estimated to 10 μm, as described above. The critical hydride thickness is assumed to 0.16 μm in the calculation. The value roughly corresponds to the hydride thickness observed after the crack propagation test, e.g., Figure 10. The

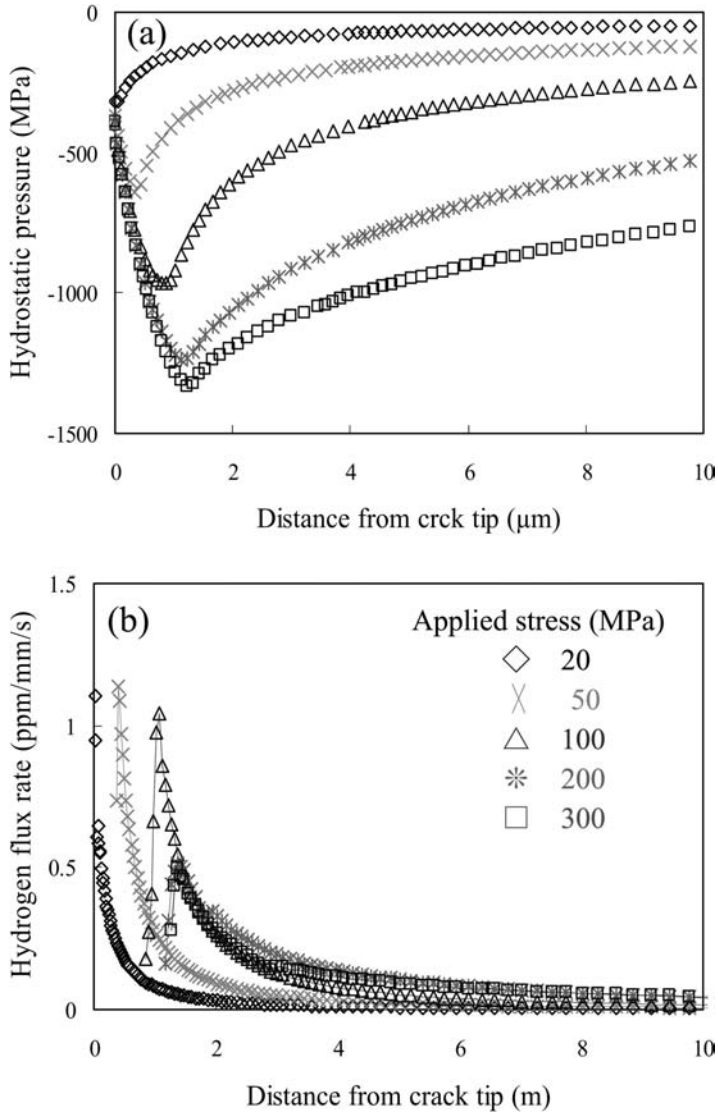


FIG. 14—(a) *Hydrostatic pressure and (*b*) hydrogen flux rate along the crack tip for cold-worked specimen at 523 K. Crack depth, 100 μm.*

required time is determined as the critical hydrogen quantity divided by the calculated hydrogen flux rate. The critical hydrogen quantity is calculated from the critical thickness and assumed hydride composition and density $\rho : H/Zr = 1.6(\delta - ZrH_{1.6})$, $\rho = 5.65\,g/cm^3$.

The relation between estimated V_{calc} and K_I is shown in Fig. 16 with the present experimental data. The estimated constant-V_{calc} value was about

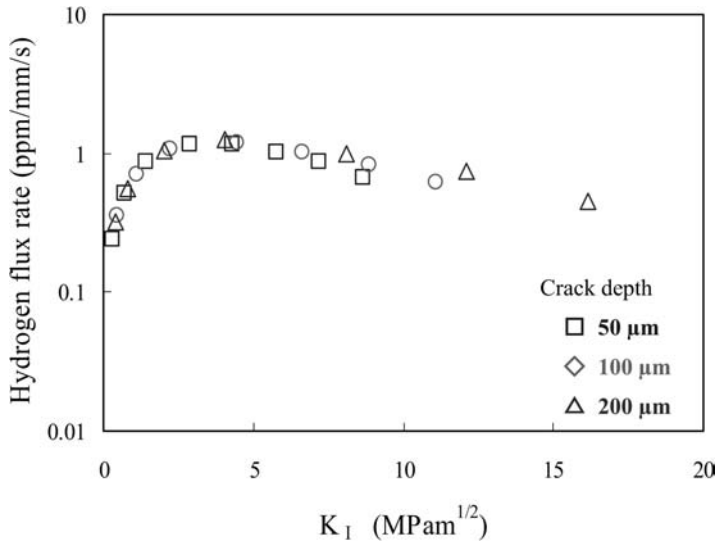


FIG. 15—*Relation between K_I and calculated hydrogen flux rate for cold-worked specimen at 523 K.*

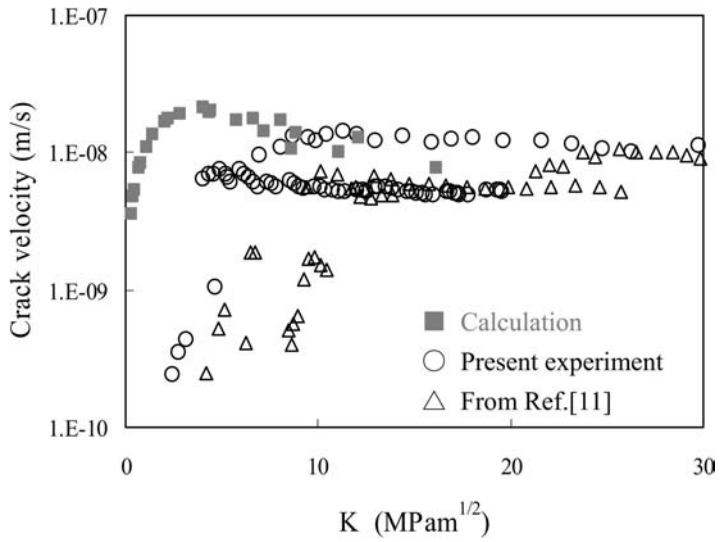


FIG. 16—*Crack velocity estimated by FEM calculation for cold-worked specimen at 523 K. Experimental results are also shown by open symbols. Data indicated with Δ are from Ref 11.*

10^{-9}–10^{-8} m/s and in good agreement with the experimental data as well as the K_I dependence.

The hydrogen flux rate significantly depends on the temperature and the material properties, especially on the $\sigma - \epsilon$ relation. Figure 17 shows the relation between estimated crack velocity and 0.2 % offset yield stress for three simulated specimens. The $\sigma - \epsilon$ inputs were determined from experimental data for the cold-worked and two stress relieved specimens. The crack velocity increased with 0.2 % offset yield stress, which qualitatively corresponded to the experimental results. Calculational results showed a somewhat smaller dependency on the 0.2 % offset yield stress than the experimental results. This result would possibly be attributable to factors other than the yield stress, such as anisotropy of Zircaloy-2 and microstructures. As is well-known for steel, high yield strength generates a strong and wide field of tensile stress, which consequently leads to high hydrogen flux rate. Figure 18 shows hydrostatic pressure stress along the crack tip for the three simulated specimens at 548 K. The minimum hydrostatic pressure stress value and the gradient were significantly different according to the input data. This result qualitatively corresponded to previous experimental test results for cladding [15,47] and theoretical work; for example, by Li et al. [48]. The effects of temperature on crack velocity were complex because the temperature affected both hydrogen diffusion behavior and $\sigma - \epsilon$ relations. The increase of temperature promoted the hydrogen diffusion and decreased the yield strength, which are conflicting effects for hydrogen flux. Generally, the percentage change of yield strength with temperature was smaller for strengthened specimens, e.g., cold-worked and irradiated materials. For these materials, the hydrogen flux rate was considered to increase more effectively with increasing temperature.

In this section, the crack velocity was estimated from hydrogen flux by FEM. With the plastic strain near the crack tip taken into account, the

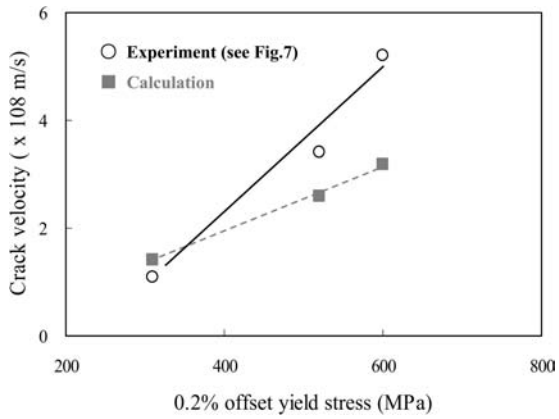


FIG. 17—*Crack velocity versus 0.2 % offset yield stress estimated by FEM calculation for cold-worked specimen at 548 K. Experimental results are also shown in open symbols. Crack depth was 100 μm.*

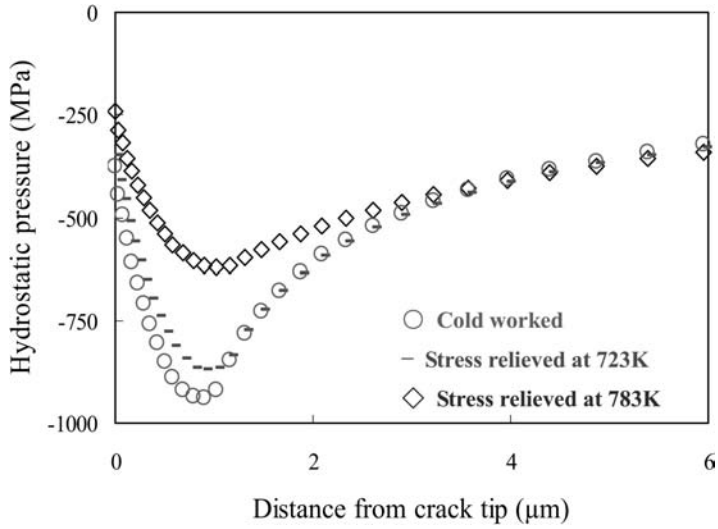


FIG. 18—*Hydrostatic pressure distributions along a crack tip. Crack depth, applied stress, and temperature are 100 μm, 100 MPa, and 548 K, respectively.*

experimentally obtained crack velocity and 0.2 % offset yield stress dependence were qualitatively simulated. This result indicated that the $\sigma - \epsilon$ relation of cladding material was one of the most important factors for the DHC.

As for a DHC model of zirconium alloys, the latest and detailed review was given by Puls [21], who showed that DHC occurs primarily due to stress-driven diffusion of hydrogen to the crack tip, i.e., the gradient in chemical potential induced by the tensile stress at the crack tip is the driving force for the hydrogen diffusion. McRae et al. [49] developed a DHC model called the diffusion first model on the same physical fundamentals as those of Puls [21] and showed that the model explained much of the phenomenology of DHC. The present DHC model is in principle the same as that of McRae et al. in that both solved a diffusion equation with appropriate boundary conditions assuming that the hydrogen diffusion was driven by the gradient of chemical potential (see Eqs 11 and 12). McRae et al. obtained analytical solutions by solving a steady state equation, $\nabla J = -\partial C/\partial t = 0$, while the present study conducted numerical calculations as a function of time using a FEM. The present calculations showed that J was almost constant after 10 s, clearly showing that the steady state was reached. This would be because hydrogen diffusion is very fast and hydrogen migration occurs only in the vicinity of the crack tip.

Conclusions

DHC tests were carried out in the chamber of a SEM to directly observe the crack propagation and measure the crack velocity in the radial direction of Zircaloy-2 cladding tubes. FEM analyses were also made to calculate the

hydrogen flux rate into the crack tip and estimate a crack velocity. Salient results are as follows.

(1) A sharply tipped crack propagated at a relatively high rate while the velocity decreased when the crack tip was blunted, supporting the occurrence of intermittent crack propagation, which could be expected from the DHC mechanism. BSE observations after the DHC tests showed that a radial hydride with several microcracks precipitated at a crack tip. It was presumed that the intermittent propagation might possibly be attributable to the repetition of the formation and the fracture of the radial hydride at the crack tip.

(2) The steady state crack velocity, V_s, and the threshold stress intensity factor for the onset of the crack propagation, K_{Ic}, tended to increase or decrease, respectively, with an increase in the 0.2 % offset yield stress.

(3) Little significant difference was observed in V_s or K_{Ic} between the circumferentially and the radially hydrided materials. The pre-existing radial hydrides did not seem to be a predominant path for the crack propagation of DHC.

(4) The FEM analyses showed that a strong hydrostatic pressure field was generated concentrically around the crack tip and hydrogen diffused towards the crack tip according to the hydrostatic pressure gradient. The crack velocity was estimated from the calculated hydrogen flux rate into the crack tip assuming the critical hydrogen quantity for the crack propagation. There was good agreement between the experiments and the calculations regarding the crack velocity and its dependency on K_I.

(5) Calculations showed that the increase in the 0.2 % offset yield stress would accelerate the crack propagation mainly by increasing the hydrostatic pressure at the crack tip.

Acknowledgments

This work is a cooperative study by Osaka University and Nippon Nuclear Fuel Development Co., Ltd. and funded by Japan Nuclear Energy Safety Organization. The writers are very grateful to all the members of these organizations for their contributions. Special thanks are due to the Messrs. Masato Ito and Yu Endo of Osaka University for their contributions to FEM analyses.

References

[1] Ohara, H., Irube, M., Futakuchi, M., Nomata, T., and Iwata, S., "Fuel Behavior During Power Ramp Tests," *Proceedings of the International Topical Meeting on Light Water Reactor Fuel Performance*, West Palm Beach, FL, April 17–21, 1994, ANS, La Grange Park, IL, pp. 674–686.

[2] Sakurai, H., Wakashima, Y., Ito, K., Sasaki, T., Nomata, T., Tsukuda, Y., Hayashi, H., and Kubota, O., "Irradiation Characteristics of High Burnup BWR Fuels," *Proceedings of the International Topical Meeting on Light Water Reactor Fuel Performance*, Park City, UT, April 10–13, 2000, ANS, La Grange Park, IL, pp. 515–525.

[3] Shimada, S., Etoh, Y., Hayashi, H., and Tsukuda, Y., "A Metallographic and Fractographic Study of Outside-In Cracking Caused by Power Ramp Tests," *J. Nucl. Mater.*, Vol. 327, 2004, pp. 97–113.

[4] Ogata, K., Aomi, M., Baba, T., and Kamimura, K., "Progress in the Research Programs to Elucidate Axial Cracking Fuel Failure at High Burnup," *Proceedings of the International Topical Meeting on Light Water Reactor Fuel Performance*, San Francisco, CA, Sept. 30–Oct. 3, 2007, ANS, La Grange Park, IL.

[5] Hayashi, H., Ogata, K., Baba, T., and Kamimura, K., "Research Program to Elucidate Outside-In Failure of High Burnup Fuel Cladding," *J. Nucl. Sci. Technol.*, Vol. 43, No. 9, 2006, pp. 1128–1135.

[6] Hayashi, H., Tsukuda, Y., Shimada, S., and Etoh, Y., "Outside-In Failure of High-Burnup BWR Segment Rods Caused by Power Ramp Tests," *Proceedings of the International Topical Meeting on Light Water Reactor Fuel Performance*, Wurtzburg, Germany, March 16–19, 2003, ANS, La Grange Park, IL.

[7] Ogata, K., Baba, T., Kamimura, K., Etoh, Y., and Ito, K., "Separate Effects of Factors Affecting Outside-In Cracking of High Burnup Fuel Cladding," *Proceedings of the International Topical Meeting on Light Water Reactor Fuel Performance*, Seoul, South Korea, Oct. 19–23, 2008, ANS, La Grange Park, IL.

[8] Ogata, K., Baba, T., Kamimura, K., Higuchi, T., Etoh, Y., and Ito, K., "Effects of Heat Flux on Hydrogen Diffusion Induced Crack Propagation in Zr-Lined Zircaloy-2 Cladding Tube," *Proceedings of the International Topical Meeting on Light Water Reactor Fuel Performance*, Paris, France, Sept. 6–10, 2009, ANS, La Grange Park, IL.

[9] Sakamoto, K., Nakatsuka, M., and Higuchi, T., "Simulation of Cracking During Outside-In Type Failure of High Burnup Fuel Cladding Tubes," *Proceedings of the International Topical Meeting on Light Water Reactor Fuel Performance*, Seoul, South Korea, Oct. 19–23, 2008, ANS, La Grange Park, IL.

[10] Kubo, T., Sakamoto, K., and Higuchi, T., "Development of a New Technique for the In-Situ Observation of the DHC Process Under an SEM to Measure the Crack Extension Rate in a Radial Direction of Zry-2 Tubes," *Proceedings of the International Topical Meeting on Light Water Reactor Fuel Performance*, Seoul, South Korea, Oct. 19–23, 2008, ANS, La Grange Park, IL.

[11] Kubo, T., Sakamoto, K., Higuchi, T., Yamanaka, S., and Ogata, K., "In-Situ SEM Observation of Delayed Hydride Cracking Propagation in the Radial Direction of Zircaloy-2 Fuel Cladding Tubes," *Proceedings of the International Topical Meeting on Light Water Reactor Fuel Performance*, Paris, France, Sept. 6–10, 2009, ANS, La Grange Park, IL.

[12] Sakamoto, K., Nakatsuka, M., Higuchi, T., and Ito, K., "Role of Radial Temperature Gradient in Outside-In Type Failure of High Burnup Fuel Cladding Tubes During Power Ramp Tests," *Proceedings of the International Topical Meeting on Light Water Reactor Fuel Performance*, Paris, France, Sept. 6–10, 2009, ANS, La Grange Park, IL.

[13] Coleman, C. E., Grigoriev, V., Inozemtsev, V., Markelov, V., Roth, M., Makarevucious, V., Kim, Y. S., Ali, K. L., Chakravartty, J. K., Mizrahi, R., and Lalgudi, R., "Delayed Hydride Cracking in Zircaloy Fuel Cladding–An IAEA Coordinated Research Program," *Nucl. Eng. Technol.*, Vol. 41, 2009, pp. 171–178.

[14] Kim, Y. S., "Delayed Hydride Cracking of Spent Fuel Rods in Dry Storage," *J. Nucl. Mater.*, Vol. 378, 2008, pp. 30–34.

[15] Kim, Y. S., "Stage I and II Behaviors of Delayed Hydride Cracking Velocity in Zirconium Alloys," *J. Alloys Compd.*, Vol. 453, 2008, pp. 210–214.

[16] Cirimello, P., Domizzi, G., and Haddad, R., "Influence of Metallurgical Variables on Delayed Hydride Cracking in Zr-Nb Pressure Tubes," *J. Nucl. Mater.*, Vol. 350, 2006, pp. 135–146.

[17] Kim, Y. S., Kim, S. K., and Cheong, Y. M., "Delayed Hydride Crack Velocity of Zirconium Alloys with the Direction of an Approach to Temperature," *J. Nucl. Sci. Technol.*, Vol. 43, No. 9, 2006, pp. 1120–1127.

[18] Grigoriev, V. and Jakobsson, R., "Delayed Hydrogen Cracking Velocity and J-Integral Measurements on Irradiated BWR Cladding," *Zirconium in the Nuclear Industry: 14th International Symposium, ASTM-STP-1467*, Stockholm, Sweden, June 13–17, 2004, P. Rudling and B. Kammerzind, Eds., ASTM International, West Conshohocken, PA, 2005, pp. 711–728.

[19] Coleman, C. E. and Inozemtsev, V., "Measurement of Rates of Delayed Hydride Cracking (DHC) in Zr-Nb Alloys–An IAEA Coordinated Research Project," *Zirconium in the Nuclear Industry: 15th International Symposium, ASTM-STP-1505*, Sunriver, OR, June 24–28, 2008, B. Kammerzind and M. Limback, Eds., ASTM International, West Conshohocken, PA, 2009, pp. 244–266.

[20] Schofield, J. S., Darby, E. C., and Gee, C. F., "Temperature and Hydrogen Concentration Limits for Delayed Hydride Cracking in Irradiated Zry-2," *Zirconium in the Nuclear Industry: 13th International Symposium, ASTM-STP-1423*, Annecy, France, June 10–14, 2001, G. D. Moan and P. Rudling, Eds., ASTM International, West Conshohocken, PA, 2002, pp. 339–357.

[21] Puls, M. P., "Review of the Thermodynamic Basis for Models of Delayed Hydride Cracking Rate in Zirconium Alloys," *J. Nucl. Mater.*, Vol. 393, 2009, pp. 350–367.

[22] Efsing, P. and Pettersson, K., "Delayed Hydride Cracking in Irradiated Zircaloy Cladding," *Zirconium in the Nuclear Industry: 12th International Symposium, ASTM-STP-1354*, Toronto, Canada, June 15–18, 1998, G. P. Sabol and G. D. Moan, Eds., ASTM International, West Conshohocken, PA, 2000, pp. 340–355.

[23] Sagat, S., Chow, C. K., Puls, M. P., and Colemen, C. E., "Delayed Hydride Cracking in Zr Alloys in a Temperature Gradient," *J. Nucl. Mater.*, Vol. 279, 2000, pp. 107–117.

[24] Kim, Y. S., Matvienko, Y. G., Cheong, Y. M., Kim, S. S., and Kwon, S. C., "A Model of the Threshold Stress Intensity Factor, K_{IH}, for Delayed Hydride Cracking of Zr-2.5Nb Alloy," *J. Nucl. Mater.*, Vol. 278, 2000, pp. 251–257.

[25] Sakamoto, K. and Nakatsuka, M., "Development of Experimental Technique for Simulation of Axial Cracking of High Burnup Fuel Cladding Tubes," *Proceedings of the International Topical Meeting on Light Water Reactor Fuel Performance*, Salamanca, Spain, Oct. 22–26, 2006, ANS, La Grange Park, IL, pp. 355–361.

[26] Yasuda, T., Nakatsuka, M., and Yamashita, K., "Deformation and Fracture Properties of Neutron Irradiated Recrysrallized Zircaloy-2 Cladding Under Uniaxial Tension," *Zirconium in the Nuclear Industry: Seventh International Symposium, ASTM-STP-939*, Strasbourg, France, June 24–27, 1985, R. B. Adamson and L. F. P. Van Swam, Eds., ASTM International, West Conshohocken, PA, 1987, pp. 734–747.

[27] Murakami, Y., Aoki, S., Miyata, H., Tohgo, K., Hasebe, N., Miyazaki, N., Toya, M., Itoh, Y., Terada, H., and Yuuki, R., *Stress Intensity Factors Handbook*, Vol. 1, Pergamon Press, Oxford, U.K., 1986, pp. 42–44.

[28] Murakami, Y., Aoki, S., Miyata, H., Tohgo, K., Hasebe, N., Miyazaki, N., Toya, M., Itoh, Y., Terada, H., and Yuuki, R., *Stress Intensity Factors Handbook*, Vol. 1, Pergamon Press, Oxford, U.K., 1986, pp. 9–10.

[29] Timoshenko, S., *Strength of Materials Part 1: Elementary Theory and Problems*, 3rd ed., D. Van Nostrand Company, Inc., New York, 1955, Chap. 12.

[30] Dutton, R., Nuttall, K., Puls, M. P., and Simpson, L. A., "Mechanisms of Hydrogen Induced Delayed Cracking in Hydride Forming Materials," *Metall. Mater. Trans. A*, Vol. 8A, 1977, pp. 1553–1562.
[31] Shek, G. K., Jovanovic, M. T., Seahra, H., Ma, Y. Ki, D., and Eadie, R. L., "Hydride Morphology and Striation Formation During Delayed Hydride Cracking in Zr-2.5%Nb," *J. Nucl. Mater.*, Vol. 231, 1996, pp. 221–230.
[32] Coleman, C. E., Griffith, M., Grigiriev, V., Kiseliov, V., Rodchenkov, B., and Markelev, V., "Mechanical Properties of Zr-2.5Nb Pressure Tubes Made from Electric Powder," *Zirconium in the Nuclear Industry: 15th International Symposium, ASTM-STP-1505*, Sunriver, OR, June 24–28, 2007, B. Kammerzind and M. Limback, Eds., ASTM International, West Conshohocken, PA, 2009, pp. 699–723.
[33] Nakatsuka, M. and Sakamoto, K., "A Numerical Simulation Model for Studying the Effects of Stress Levels, Multi-Axial Stress State and Texture on Hydride Reorientation in Zr Alloys," *Proceedings of the International Topical Meeting on Light Water Reactor Fuel Performance*, Seoul, South Korea, Oct. 19–23, 2008, ANS, La Grange Park, IL.
[34] Arsene, S., Bai, J. B., and Bompard, P., "Hydride Embrittlement and Irradiation Effects on the Hoop Mechanical Properties of Pressurized Water Reactor (PWR) and Boiling-Water Reactor (BWR) ZIRCALOY Cladding Tubes: Part I. Hydride Embrittlement in Stress-Relieved Annealed, and Recrystallized ZIRCALOYs at 20 C and 300 C," *Metall. Mater. Trans. A*, Vol. 34, 2003, pp. 553–566.
[35] Veleva, M., Arsene, S., Record, M.-C., Bechade, J. L., and Bai, J., "Hydride Embrittlement and Irradiation Effects on the Hoop Mechanical Properties of Pressurized Water Reactor (PWR) and Boiling-Water Reactor (BWR) ZIRCALOY Cladding Tubes: Part II. Morphology of Hydrides Investigated at Different Magnifications and Their Interaction with the Processes of Plastic Deformation," *Metall. Mater. Trans. A*, Vol. 34, 2003, pp. 567–578.
[36] Arsene, S., Bai, J. B., and Bompard, P., "Hydride Embrittlement and Irradiation Effects on the Hoop Mechanical Properties of Pressurized Water Reactor (PWR) and Boiling-Water Reactor (BWR) ZIRCALOY Cladding Tubes: Part III. Mechanical Behavior of Hydride in Stress-Relieved Annealed and Recrystallized ZIRCALOYs," *Metall. Mater. Trans. A*, Vol. 34, 2003, pp. 579–588.
[37] Kubo, T., Sakamoto, K., and Higuchi, T., manuscript in preparation.
[38] Northwood, D. O. and Kosashi, U., "Hydride and Delayed Hydride Cracking in Zirconium and its Alloys," *Int. Met. Rev.*, Vol. 28, 1983, pp. 92–121.
[39] Varias, A. G. and Massih, A. R., "Simulation of Hydrogen Embrittlement in Zirconium Alloys Under Stress and Temperature Gradients," *J. Nucl. Mater.*, Vol. 279, 2000, pp. 273–285.
[40] Feng, J. L., Varias, A. G., and Sui, Y. K., "Finite Element Analysis for Steady-Sate Hydride-Induced Fracture in Metals by Composite Model," *Int. J. Solids Struct.*, Vol. 43, 2006, pp. 2174–2192.
[41] *MATPRO Ver. 11, A Handbook of Material Properties for Use in the Analysis of Light Water Reactor Fuel Rod Behavior, NUREG/CR-0479, TREE-1280, Rev 2*. (1981). D. L. Hagrman, G. A. Reymann, and R. E. Mason, Eds., EG&G Idaho, Inc., Idaho Falls, ID.
[42] *ABAQUS Ver. 6.7 User Guide*. (2007). SIMULIA, Rising Sun Mills, RI.
[43] Sofronis, P. and McMeeking, R. M., "Numerical Analysis of Hydrogen Transport Near a Blunting Crack Tip," *J. Mech. Phys. Solids*, Vol. 37, 1989, pp. 317–350.
[44] Sawatzky, A., "Hydrogen in Zircaloy-2: Its Distribution and Heat of Transport," *J. Nucl. Mater.*, Vol. 2, 1960, pp. 321–328.

[45] Yamanaka, S., Miyake, M., and Katsura, M., "Study on the Hydrogen Solubility in Zirconium Alloys," *J. Nucl. Mater.*, Vol. 247, 1997, pp. 315–321.
[46] MacEwen, S. R., Coleman, C. E., Ells, C. E., and Faber, J., Jr., "Dilation of h.c.p. Zirconium by Interstitial Deuterium," *Acta Metall.*, Vol. 33, 1985, pp. 753–757.
[47] Singh, R. N., Roychowdhury, S., Sinha, V. P., Sinha, T. K., De, P. K., and Banerjee, S., "Delayed Hydride Cracking in Zr–2.5Nb Pressure Tube Material: Influence of Fabrication Routes," *Mater. Sci. Eng., A*, Vol. 374, 2004, pp. 342–350.
[48] Li, J. C., Oriani, R. A., and Darken, L. S., "The Thermodynamics of Stressed Solids," *Z. Phys. Chem., Neue Folge*, Vol. 49, 1966, pp. 271–279.
[49] McRae, G. A., Coleman, C. E., and Leitch, B. W., "The First Step for Delayed Hydride Cracking in Zirconium Alloys," *J. Nucl. Mater.*, Vol. 396, 2010, pp. 130–143.

DISCUSSION

Question 1, C. E. Coleman, AECL, Canada:—What were the values of K_H obtained in these experiments?

Author's Response:—The values of K_H were about 4 MPa at 523 K and 1.5 MPa at 548 K. It has been known that K_H is significantly variable depending on test method, specimen shape, dimension, material strength and so on. Since crack propagation was observed with the magnification of 3000 under a SEM in the present experiment, even very small crack extension of submicron in an early stage of the crack initiation could be observed. This would contribute to relatively small K_{IH} in the present experiment compared with literature data.

Question 2, A. Motta, Pennsylvania State University, USA:—Did you perform 2D or 3D calculation? If 2D, would you expect the hydrogen concentration at the crack tip to be different for the surface of the sample and the bulk, due to different states of the stress?

Author's Response:—We performed 2D calculation. The stress state and hydrogen concentration are expected to be different for the surface and bulk. At the surface area, plastic field around the crack tip is large under the plain stress sate, which would disperse the hydrogen and decrease the hydrogen concentration at the crack tip. It also affects the stress gradient. However, these effects rarely appeared in the present calculation because of the long crack length.

Effect of solute segregation on the surface is another factor to be considered. However, its effects on crack velocity would be small since segregation would be limited to a surface region of several nm in depth.

Surely the local surface effects should be taken into account when the crack velocity is determined from the crack depth on the specimen surface. However, present fractographic observation showed that the crack could be approximated by a semi-ellipse, showing that the effects was not large in the case of thin walled Zircaloy-2 tubes under the present experimental condition.

Question 3, Y. S. Kim, KAERI, Korea:—Please explain how hydrogen can diffuse to the crack tip due to the stress gradient. In a closed system such as zirconium + H system, hydrogen cannot move to the stressed region.

Author's Response:—In the present analysis, the hydrogen concentration on the surfaces was maintained at a constant value, which worked as a hydrogen supply source. This assumption would be appropriate since the surface is far away from a crack tip and the volume of the test material is very much larger than that of a region near a crack tip where hydrogen is accumulated. The minimum hydrostatic pressure stress point at a crack tip, where the hydrogen concentration is maximized, acts as a sink for hydrogen. The hydrogen continues to flow from a surrounding region to a crack tip according to the concentration and stress gradients.

Question 4, J. Desquines, IRSN, France:—Can you detail your modeling options: did you choose large strain modeling to achieve detailed description of the stress field at the crack tip? Can you comment on the expected influence of grain size compared to the maximum stress extension at the crack tip?

Author's Response:—Large deformation and strain occurred at the crack tip, therefore they should be considered. The calculation code ABAQUS used in the present study has a fully nonlinear formulation for almost all the elements by default. We used the appropriate element, large deformation option and arranged the time incrementation parameter. Creep is not considered in this calculation.

The present test material is a cold worked Zircaloy-2 tube and its grain size is smaller than 1μm, which is slightly smaller or almost equivalent to the maximum stress extension. The crack initiation would be dependent on crystallographic orientation of grains at a crack tip. Grain size of recrystallized Zircaloy-2 tube, for example, is usually about 3μm, which is larger than the maximum stress extension. The tube with larger grain size would be more strongly dependent on grain crystallographic orientation at a crack tip and expected to be more susceptible to DHC, if mechanical strength is identical.

Reprinted from JAI, Vol. 8, No. 2
doi:10.1520/JAI102948
Available online at www.astm.org/JAI

M. Y. Yao,[1] *J. H. Wang,*[1] *J. C. Peng,*[2] *B. X. Zhou,*[1] *and Q. Li*[2]

Study on the Role of Second Phase Particles in Hydrogen Uptake Behavior of Zirconium Alloys

ABSTRACT: In an effort to better understand the role of second phase particles (SPPs) in the hydrogen uptake of zirconium alloys, four alloys and four heat treatments for each alloy were chosen to prepare specimens with different SPPs size distributions and area fractions. The hydrogen uptake performance of these specimens was investigated after autoclave testing in 400C/10.3 MPa steam. Results show that the hydrogen uptake is not always in a strict corresponding relationship with the corrosion resistance among the specimens, but it is closely related to the size, area fraction, and compositions of the SPPs. In the case of Zry-2 and Zry-4, the hydrogen uptake fraction (HUF) increased with increasing size and area fraction of the SPPs. The dependence was more notable for the Zry-2 than the Zry-4. In the case of N36 and N18, the HUF had only a slight variation with the size and area fraction of the SPPs. No matter which heat treatment was employed, the corrosion resistance of the N18 specimens was superior to the N36 specimens, but the HUF of the former was larger than that of the latter. These results clearly demonstrate that the effect of the size and area fraction of SPPs on the hydrogen uptake depends on the SPP compositions. Pressure-composition-temperature and kinetics of absorbing and desorbing hydrogen tests were conducted on $Zr(Fe,Cr)_2$, $Zr_2(Fe,Ni)$, $Zr(Nb,Fe)_2$, and β-Nb alloys (which may be found as SPPs in the four zirconium alloys tested) as well as on pure zirconium. Results show that $Zr(Nb,Fe)_2$, $Zr_2(Fe,Ni)$, and $Zr(Fe,Cr)_2$ alloys have a stronger reversible ability for hydrogen absorption

Manuscript received January 6, 2010; accepted for publication January 18, 2011; published online February 2011.
[1] Institute of Materials, Shanghai Univ., Shanghai 200072, People's Republic of China (Corresponding author), e-mail: yaomeiyi@shu.edu.cn
[2] The Key Laboratory for Advanced Micro-Analysis, Shanghai Univ., Shanghai 200444, People's Republic of China.

Cite as: Yao, M. Y., Wang, J. H., Peng, J. C., Zhou, B. X. and Li, Q., "Study on the Role of Second Phase Particles in Hydrogen Uptake Behavior of Zirconium Alloys," *J. ASTM Intl.*, Vol. 8, No. 2. doi:10.1520/JAI102948.

Copyright © 2011 by ASTM International, 100 Barr Harbor Drive, PO Box C700, West Conshohocken, PA 19428-2959.

and desorption than β-Nb alloy and pure zirconium. Based on the testing results, a model correlating the hydrogen uptake performance to the reversible ability of the SPPs to absorb and desorb hydrogen is proposed. The model can successfully explain the results.

KEYWORDS: zirconium alloys, hydrogen uptake, corrosion resistance, heat treatments, second phase particles

Introduction

Zirconium alloys have been widely used as the cladding material for fuel rods in pressurized water reactors. They are exposed to water at high temperature and high pressure during service. The corrosion reaction with water to form the oxide has to be matched by the evolution of hydrogen. A fraction of the hydrogen produced from the corrosion is taken up by the alloy. Since the solid solubility of hydrogen in α-Zr is very low and reduces with decreasing temperature (e.g., it is less than 1 μg/g at ambient temperature and it is 200 μg/g at 400°C [1]), the remainder of the hydrogen is precipitated as zirconium hydride, causing hydrogen embrittlement of the alloy. An in situ transmission electron microscope (TEM) observation has confirmed that the zirconium hydride precipitates, grows, and cracks at the tip of cracks induced by tensile stresses, which is the essential process of hydrogen-induced delayed cracking (HIDC) [2,3]. Studies in the past 40 years have indicated that corrosion, hydrogen uptake, and the concomitant HIDC are mechanisms for the failure of zirconium alloys used as nuclear fuel cladding as well as other structural parts in light water and heavy water reactors [4–7]. With the requirement of extending fuel assembly burn-up, hydrogen ingress is receiving more attention.

The general understanding is that the higher the weight gain, the higher the hydrogen uptake for a given alloy, as the hydrogen produced as a result of the corrosion reaction has also increased. So, generally speaking, an improvement in the corrosion resistance by adjusting the heat treatment procedure or alloying composition can also reduce the amount of hydrogen uptake. For example, the hydrogen uptake of M5 [8] and ZIRLO [9] alloys are significantly lower than that of Zircaloy-4 (denoted as Zry-4). In a previous paper [10], however, it was found that a lower weight gain did not show a lower amount of hydrogen uptake in the molten zone of zirconium-alloy welding specimens. That is to say, the relative hydrogen uptake from specimen to specimen does not always correspond to the relative corrosion weight gain from specimen to specimen. It was obvious that the hydrogen uptake increased with the increase of Cr content in the molten zone. This illustrates that hydrogen uptake is also a function of alloy composition.

Recently, more and more investigators have realized that the second phase particles (SPPs) play an important role in the hydrogen uptake of zirconium alloys, but there is no general agreement on how the SPPs affect the hydrogen uptake. The first thought is that the SPPs affect the oxide layer characteristics (such as cracks, pores, and dense barrier layer thickness), thereby influencing the hydrogen uptake [11–16]. The second thought is that the unoxidized SPPs in

the oxide film can act as a preferred path for hydrogen transport through the oxide film [7,17–21]. The third thought is that the SPPs in the metallic state acts as trapping sites while the microcracks resulting from the transition of tetragonal-to-monoclinic ZrO_2 provide the fast transport route of hydrogen through the oxide [22,23].

In order to better understand the role of SPPs in the hydrogen uptake of zirconium alloys, four zirconium alloys and four heat treatments for each alloy were chosen to prepare specimens with different SPPs compositions, amounts, and sizes. In this paper, the hydrogen uptake behavior of these specimens corroded in 400°C/10.3 MPa steam is investigated and the involved mechanism is discussed.

Experimental Procedures

Materials

The four alloys used for the present investigation were Zry-4, Zircaloy-2 (Zry-2), N36, and N18. Their chemical compositions are listed in Table 1. The Zry-4 and Zry-2 are well known Zr-Sn alloys. The N18 alloy is an advanced Zr-Sn-Nb alloy with a low Nb content that was developed by China. Compared to the N18 alloy, the N36 alloy does not contain Cr but contains a higher Nb content. In fact, its composition is close to the ZIRLO alloy. From previous investigations, it is known that the SPPs are $Zr(Fe,Cr)_2$ in Zry-4 [19], $Zr_2(Fe,Ni)$ and $Zr(Fe,Cr)_2$ in Zry-2 [7,20,24], β-Nb and $Zr(Nb,Fe)_2$ in N36 [25–27], and $Zr(Fe,Cr)_2$ with Nb in N18 [26]. The as-received Zry-4 and Zry-2 plates at 0.6 mm thickness were fabricated by conventional procedures [28] and underwent a final recrystallization anneal at 600°C for 1 h. The as-received N36 and N18 plates at 1 mm thickness were also fabricated by conventional procedures for Zr-Sn-Nb alloys [29] and underwent a final recrystallization anneal at 580°C for 2 h.

Heat Treatments

Zry-4 and Zry-2 specimens—The heat treatment procedures for the Zry-4 and Zry-2 alloys are shown in Fig. 1(*a*). First, 25 × 20 mm specimens were cut from the as-received plates. Then the specimens were heated to 1020°C for 0.5 h, 800°C for 36 h, and 720°C for 10 h in a vacuum furnace followed by pushing the furnace away from the quartz tube and cooling by spraying water (denoted as AC). The specimens treated in the above three ways and the as-received

TABLE 1—*The composition of zirconium alloys (in mass fraction %).*

Alloy	Sn	Fe	Cr	Ni	Nb	O	C	Si	N	H
Zircaloy-4	1.5	0.2	0.1	/	/	0.11	0.010	< 0.004	0.007	0.003
Zircaloy-2	1.5	0.2	0.1	0.05	/	0.12	0.012	< 0.004	0.007	0.002
N36	1.0	0.3	0.1	/	0.35	0.10	0.010	< 0.004	0.006	0.003
N18	1.0	0.3	/	/	1.0	0.13	0.010	< 0.004	0.005	0.002

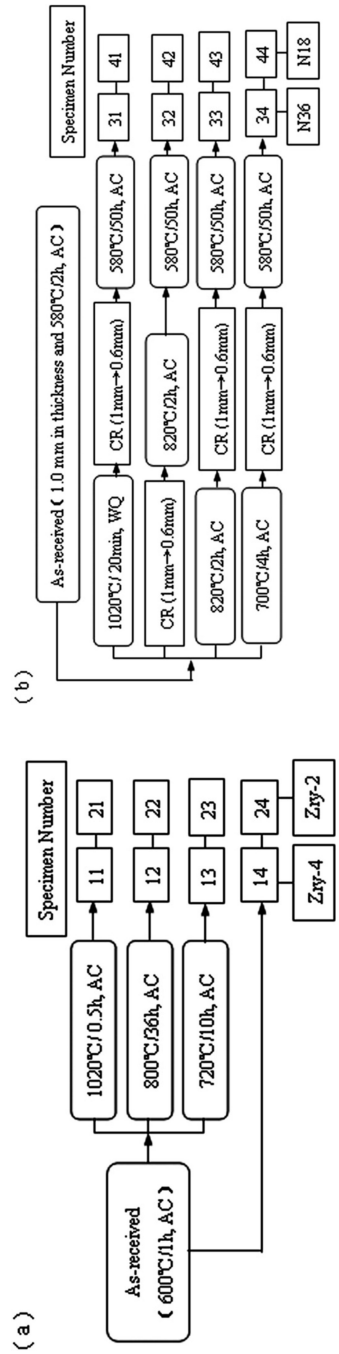


FIG. 1—*The heat treatment procedures and corresponding designation of (a) Zry-4 and Zry-2 and (b) N36 and N18 alloys.*

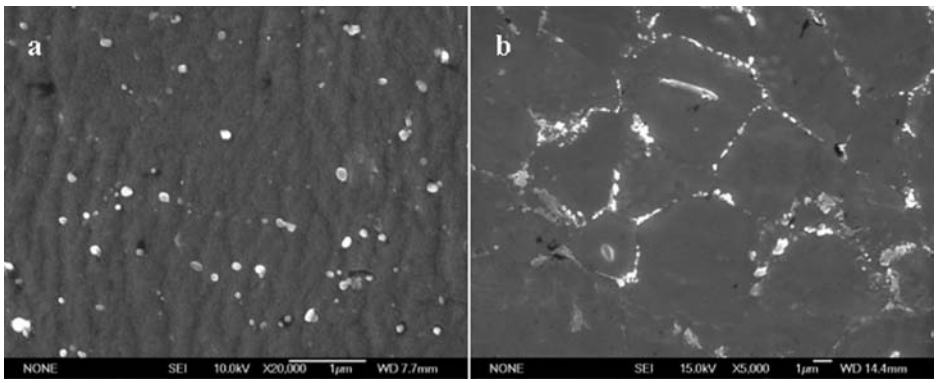


FIG. 2—*SEM micrographs of the SPPs in Specimens (a) 31 and (b) 32.*

specimens annealed at 600°C will be described hereafter as Specimens 11, 12, 13, and 14 for the Zry-4, and Specimens 21, 22, 23, and 24 for the Zry-2, respectively.

N36 and N18 Specimens—The heat treatment procedures for the N36 and N18 alloys are shown in Fig. 1(*b*). In the case of Specimen 31 for the N36 alloy and Specimen 41 for the N18 alloy, the heat treatment procedures are as follows: (1) Strips at 8 mm width were cut from the as-received plates. (2) The strips were sealed in evacuated quartz capsules at about 5×10^{-3} Pa and heated to 1020°C (β phase) for 20 min. (3) The capsules were then quenched into water and broken simultaneously (denoted as WQ). (4) The strips were cold rolled from 1 mm to 0.6 mm and were cut into specimens with 25 mm in length. (5) The specimens were heated to 580°C for 50 h to decompose the residual β-Zr from the former β-quenching. In the case of Specimens 33 and 34 for the N36 alloy and Specimens 43 and 44 for the N18 alloy, they were first heated to 820°C for 2 h and 700°C for 4 h, respectively; then they were prepared in the same way as the procedures (4) and (5) for Specimen 31. In the case of Specimens 32 and 42, they were first cold rolled from 1 mm to 0.6 mm; then they were heated to 820°C for 2 h; finally, they were prepared in the same way as procedure (5) for Specimen 31. Prior to each heat treatment, the specimens were cleaned and pickled in a solution of $10\,\%\,HF + 45\,\%\,HNO_3 + 45\,\%\,H_2O$ (in volume) for the Zry-4 and Zry-2, and in a solution of $10\,\%\,HF + 30\,\%\,HNO_3 + 30\,\%\,H_2SO_4 + 30\,\%\,H_2O$ (in volume) for the N36 and N18 alloys.

Microstructural Characterization

The SPPs distribution was examined using a JSM-6700F scanning electron microscope (SEM). The specimens for SEM examination were prepared by pickling in a solution of $30\,\%\,HF + 10\,\%\,HNO_3 + 60\,\%$ glycerol (in volume). The SPPs analysis was carried out at an acceleration voltage of 10 kV and at a magnification of between ×5000 and ×20000 depending on the specimen (Fig. 2). The size

distribution and the area fraction of the SPPs were measured using German SIS image analysis system (Version 5.0). More than eight fields and 400 particles per specimen were analyzed to determine the size distribution and area fraction.

In the case of the Zr-Sn-Nb alloys, it was found that the SPPs were more finely and uniformly distributed when the specimens were heat-treated by β-quenching, cold rolling, and annealing at 580°C, which is lower than the monotectic reaction temperature (610°C), as shown in Fig. 2(*a*); while the SPPs distribute mainly along the grain boundaries when the specimens were heat-treated in the $\alpha + \beta$ two-phase region before final annealing at 580°C, as shown in Fig. 2(*b*). It is well known that β-quenching puts more alloying elements into a supersaturated solid solution in the α matrix. Meanwhile, subsequent cold rolling and annealing make the alloying elements supersaturated in solid solution in the α matrix to precipitate as SPPs and the residual β-Zr to decompose into α-Zr and β-Nb. Therefore, the SPPs are more finely and uniformly distributed in the α-Zr when the specimens were heat-treated in such a way. When heat-treated in the $\alpha + \beta$ two-phase region, the residual β-Zr is mainly distributed along the grain boundaries, so after the subsequent annealing at 580°C, the SPPs resulting from the decomposition of the residual β-Zr are mainly distributed along the grain boundaries.

Corrosion Tests

The corrosion tests were performed in H_2O steam at 400°C/10.3 MPa in a static autoclave. The corrosion behavior was evaluated by weight gain as a function of exposure time. The reported weight gain is a mean value obtained from three specimens. Prior to the corrosion tests, the specimens were cleaned and pickled in the same solution as was used to prepare them for heat treatment, sequentially rinsed in cold tap water, boiling deionized water, and then blow-dried with warm air.

Hydrogen Analysis

The hydrogen content in all the corroded specimens after each exposure was analyzed by the hot vacuum extraction method with LECO Model RH-600 equipment. The reported hydrogen content is also a mean value obtained from three measurements for each corroded specimen and the standard deviation was less than 10 μg/g. For each measurement, a corroded specimen with a weight between $0.1 \sim 0.2$ g was used. All tested specimens were ultrasonically cleaned in acetone before measurement.

The hydrogen uptake fraction (HUF), which is defined as a ratio of the measured hydrogen content in the specimen to the theoretical value calculated from the corrosion reaction, was used to characterize the hydrogen performance.

Second Phase Particle Alloys Preparation and Hydrogen Absorption and Desorption Characteristic Tests

As mentioned in the introduction, the SPPs may play an important role in the hydrogen uptake of zirconium alloys. Hence, a separate study of the hydrogen

absorption and desorption characteristics of the SPP alloys is carried out to further understand the hydrogen uptake mechanism affected by the SPPs. Many studies have been performed on the hydrogen absorption and desorption characteristics of the $Zr(Fe,Cr)_2$ alloy as a hydrogen storage material [30–33], but they mainly have been concerned on its characteristics at near ambient temperature. So, it is necessary to investigate the hydrogen absorption and desorption characteristics of SPP alloys at high temperature.

According to the SPP compositions in the four alloys, five alloys, including two $Zr(Fe,Cr)_2$ alloys with Fe/Cr atomic ratios of 2 and 0.5 (denoted as $Zr(Fe,Cr)_2$ R2 and $Zr(Fe,Cr)_2$ R0.5, respectively), one $Zr_2(Fe,Ni)$ alloy with an Fe/Ni atomic ratio of 1, one $Zr(Nb,Fe)_2$ alloy with an Nb/Fe atomic ratio of 1, and one β-Nb alloy (10Zr-90Nb, mass fraction percent), were chosen for this study. Each SPP alloy was arc melted six times under argon in a nonconsumable arc melting furnace. X-ray diffraction analysis showed that the five SPP alloys were of the same structure as the SPPs in the four investigated zirconium alloys. The pressure-composition-temperature (P-C-T) and kinetic characteristics for the five SPP alloys and pure zirconium in a powder state ($38.5 \sim 55\,\mu$m in size) were measured at 4 MPa H_2 pressure, 360°C using a Suzuki-Shokan multi-channel Seivert-type P-C-T system. Before the P-C-T and kinetics tests, each sample was activated three times with a 1 h hydrogen absorbing cycle at 4 MPa H_2 pressure followed by a 1 h hydrogen desorbing cycle at 360°C.

Results

Microstructural Characteristics

Zry-4 Specimens—The results from the SEM analysis of the specimens are summarized in Table 2. In the case of the Zry-4, the mean diameter of the SPPs in Specimen 11 is very small, only 35 nm, whereas Specimen 12 has the largest mean diameter of the SPPs, 280 nm. Specimens 13 and 14 have similar mean SPPs diameters of 216 and 180 nm, respectively. The area fraction of the SPPs in Specimen 11 is also very small, only 0.1 %, whereas Specimens 12 and 13 have a larger and similar SPPs area fraction, 1.9 % and 2.0 %, respectively. Specimen 14 has a moderate SPPs area fraction, 1.2 %. The SPPs size distributions of the specimens are illustrated in Fig. 3(*a*). It is clear that Specimen 11, which was heat-treated at 1020°C/0.5 h, by far has the smallest SPPs size distribution with 85 % of the SPPs being less than 50 nm. Specimens 12, 13, and 14, which were heat-treated in the α-phase temperature range ($800 \sim 600$°C), all have a higher fraction of SPPs in sizes between 50 and 300 nm, $70 \sim 80$ %; the fraction of SPPs larger than 300 nm decreases with decreasing heat-treatment temperature.

Zry-2 Specimens—In the case of the Zry-2, the mean diameter of the SPPs in Specimen 21 is very small, only 61 nm, whereas Specimen 22 has the largest mean diameter of the SPPs, 494 nm, followed by Specimens 23 (323 nm) and 24

TABLE 2—*The mean size and area fraction of the SPPs in the four zirconium alloys with different heat treatments.*

Alloy	Number	SPPs mean size(nm)	SPPs area fraction(%)
Zry-4	11	35	0.1
	12	280	1.9
	13	216	2.0
	14	180	1.2
Zry-2	21	61	0.6
	22	494	1.9
	23	323	1.3
	24	136	0.7
N36	31	77	5.9
	33	320	5.9
	33	209	6.0
	34	197	5.4
N18	41	58	2.3
	42	350	1.6
	43	243	2
	44	242	2.9

(136 nm). The area fractions of the SPPs in Specimens 21 and 24 are smaller and similar, only 0.6 % and 0.7 %, respectively, while Specimen 22 has the largest SPPs area fraction, 1.9 %. Specimen 23 has a moderate SPPs area fraction, 1.3 %. The SPPs size distributions of the specimens are illustrated in Fig. 3(*b*). It is clear that Specimen 21, which was heat-treated at 1020°C/0.5 h, by far has the smallest SPPs size distribution with 50 % of the SPPs less than 50 nm. Specimens 22, 23, and 24, which were heat-treated in the α-phase temperature range (800 ~ 600°C), all have a higher fraction of SPPs in sizes between 50 and 300 nm, 53 ~ 74 %, and the fraction of SPPs larger than 300 nm decreases with decreasing heat-treatment temperature. The trend for Zry-2 specimens is to have larger SPPs than Zry-4 specimens.

N36 Specimens—In the case of the N36 alloy, the mean diameter of the SPPs in Specimen 31 is very small, only 77 nm, whereas Specimen 32 has the largest mean diameter of the SPPs, 320 nm. Specimens 33 and 34 have a moderate and similar mean diameter of the SPPs of 209 and 197 nm, respectively. The area fractions of the SPPs among the four specimens are close to each other, 5.4 ~ 6.0 %. The SPPs size distributions of the specimens are illustrated in Fig. 3(*c*). It is clear that Specimen 31, which was heat-treated by the "1020°C/20 min, WQ + CR + 580°C/50 h, AC" process, by far has the smallest SPPs size distribution with 80 % of the SPPs less than 100 nm in diameter. Specimens 32, 33, and 34 all have a higher fraction of the SPPs between 100 and 300 nm, 59 %, 67 %, and 50 %, respectively. The cold rolling before annealing at 580°C/50 h decreases the SPPs size.

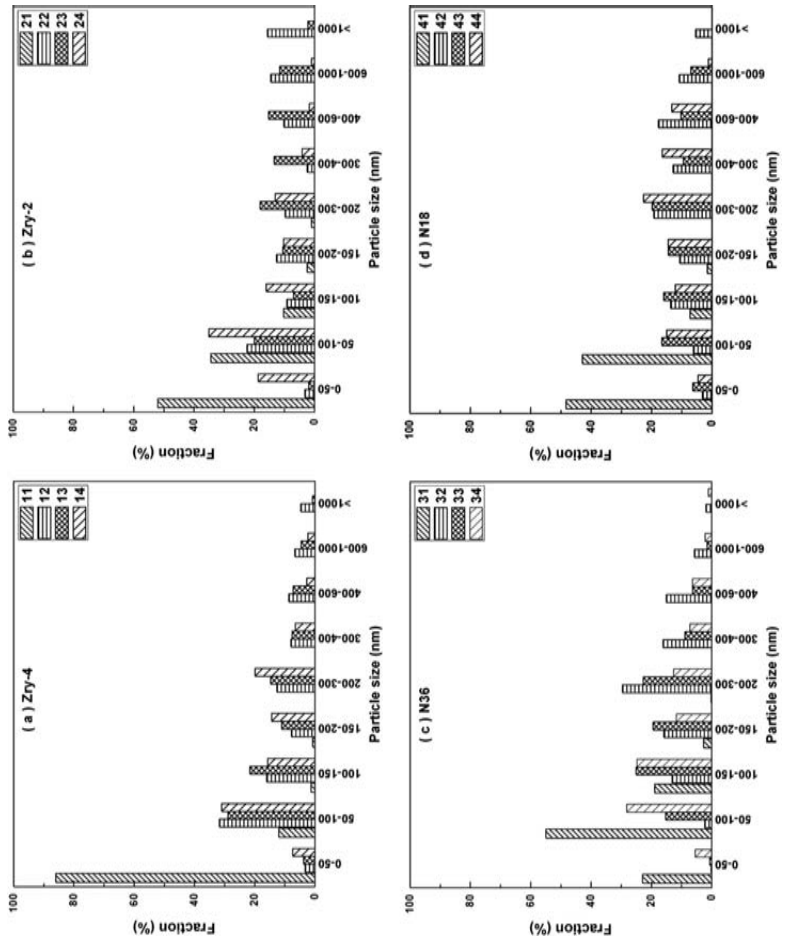


FIG. 3—*The SPPs size distribution for the specimens.*

N18 Specimens—In the case of the N18 alloy, the mean diameter of the SPPs in Specimen 41 is very small, only 58 nm, whereas Specimen 42 has the largest mean diameter of the SPPs, 350 nm. Specimens 43 and 44 have a moderate and similar mean diameter of the SPPs of 243 and 242 nm, respectively. The area fractions of the SPPs in the four specimens are $1.6 \sim 2.9\,\%$ and decrease in the sequence of Specimen $44 > 41 > 43 > 42$. The SPP size distributions of the specimens are illustrated in Fig. 3(*d*). It is clear that Specimen 41, which was heat-treated by the "1020°C/20 min, WQ + CR + 580°C/50 h, AC" process, by far has the smallest SPPs size distribution with 90 % of the SPPs less than 100 nm in diameter. Specimens 42, 43, and 44 all have a similar size distribution of SPPs with less than 400 nm diameter and the SPPs size fractions with less than 400 nm diameter decrease in the sequence of Specimen $44 > 43 > 42$.

Comparing the effect of heat treatments on the size distribution and area fraction of the SPPs in the four alloys (Table 2 and Fig. 3), it is clear that the heat treatment effect decreases in the sequence of Zry−2 > Zry−4 > N18 > N36 for the SPPs size distribution while it decreases in the sequence of Zry−4 > Zry−2 > N18 > N36 for the SPPs area fraction. Moreover, the SPPs area fraction is the largest for the N36 alloy due to a higher content of alloying elements, followed by the N18 alloy.

Corrosion and Hydrogen Uptake Behavior

Zry-4 Specimens—The hydrogen uptake content ΔW_H of the Zry-4 specimens is plotted against the weight gain ΔW_O in Fig. 4(*a*). In the early stage of corrosion, the HUF, i.e., $d\Delta W_H/d\Delta W_O$, is similar among the four types of Zry-4 specimens. As the corrosion proceeds, the $d\Delta W_H/d\Delta W_O$ shows differences among the four types of Zry-4 specimens and increases in the sequence of Specimens $11 < 14 < 13 < 12$. It is well known that at the same weight gain, the theoretical hydrogen content from corrosion is the same. So, if the hydrogen uptake of these specimens is the same, these curves should overlap. However, it is obvious that the hydrogen contents are different among the four specimens at the same weight gain. This illustrates that the heat treatments have a significant effect on the hydrogen uptake of the Zry-4 from corrosion.

Figure 4(*b*) shows the weight gain and hydrogen uptake content of the Zry-4 specimens corroded in 10.3 MPa steam at 400°C for 302 days. Specimen 11 exhibits the largest weight gain ($267\,\mathrm{mg/dm^2}$) but a lower hydrogen uptake content ($288\,\mu\mathrm{g/g}$). The weight gain of Specimen 12 ($238\,\mathrm{mg/dm^2}$) is only a little lower than that of Specimen 11; however, the hydrogen uptake content of the former ($543\,\mu\mathrm{g/g}$) is much higher than that of the latter. The weight gain of Specimen 13 ($147\,\mathrm{mg/dm^2}$) is about half of Specimen 11 but the hydrogen uptake content of the former ($273\,\mu\mathrm{g/g}$) is similar to the latter. In a word, the weight gain increases in the sequence of Specimens $14 < 13 < 12 < 11$ but the hydrogen uptake content increases in the sequence of Specimens $14 < 13 < 11 < 12$. This illustrates that the hydrogen uptake does not have a strict corresponding relationship with the corrosion resistance. That is to say, it is not always true that the higher the weight gain of the specimen, the higher the hydrogen content in the specimen for different heat-treated specimens.

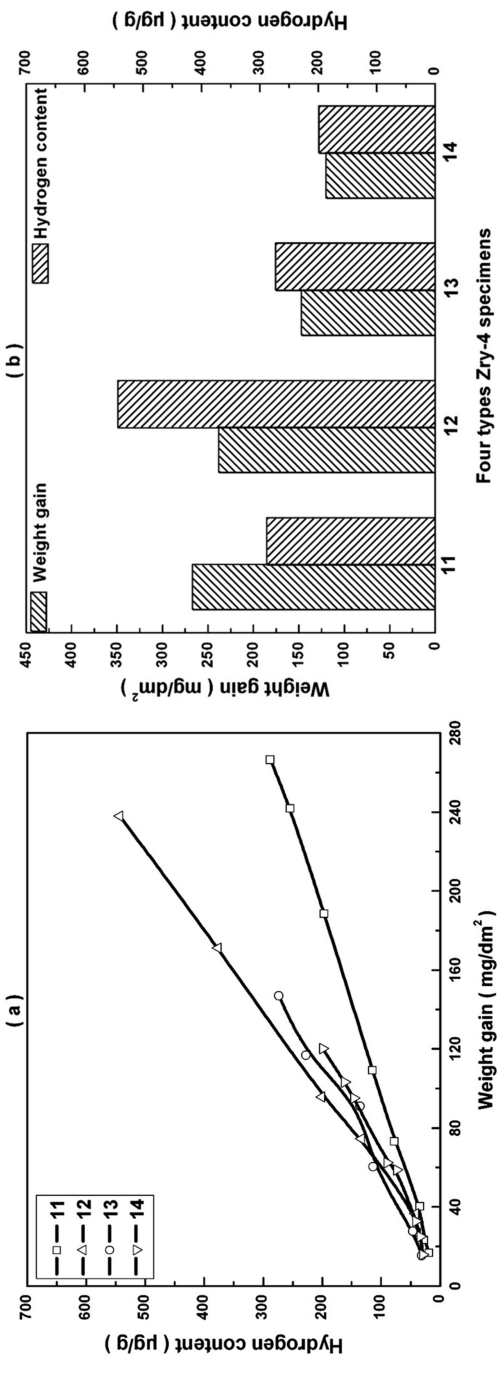


FIG. 4—*The corrosion and hydrogen uptake behavior of the Zry-4 specimens tested in 400°C/10.3 MPa steam: (a) The curve of the hydrogen uptake versus weight gain. (b) Corrosion weight gain and hydrogen uptake content of the specimens corroded for 302 days.*

Zry-2 Specimens—Figure 5 shows the corrosion and hydrogen uptake behavior of the Zry-2 specimens corroded in 10.3 MPa steam at 400°C. In the early stage of corrosion, the $d\Delta W_H/d\Delta W_O$ is similar among the four types of Zry-2 specimens. As the corrosion proceeds, the $d\Delta W_H/d\Delta W_O$ shows differences among the four types of Zry-2 specimens and increases in the sequence of Specimens $21 \approx 24 < 23 < 22$ (Fig. 5(*a*)). This difference illustrates that the heat treatments also have a significant effect on the hydrogen uptake of Zry-2 from corrosion.

From Fig. 5(*b*), it can be seen that Specimens 21 and 22 exhibit similar weight gains (226 and 231 mg/dm^2) but the former has a much lower hydrogen uptake content than the latter (272 and 630 μg/g, respectively). Specimens 23 and 24 also exhibit similar weight gain (162 and 164 mg/dm^2); however, the former has a higher hydrogen uptake content than the latter (333 and 216 μg/g). In a word, the weight gain changes in the sequence of $24 \approx 23 < 21 \approx 22$ but the hydrogen uptake content changes in the sequence of $24 < 21 < 23 < 22$. This further illustrates that the hydrogen uptake does not have a strict corresponding relationship to the corrosion resistance.

N36 Specimens—Figure 6 shows the corrosion and hydrogen uptake behavior of the N36 specimens corroded in 10.3 MPa steam at 400°C. It is clear that the heat treatments have little effect on the hydrogen uptake of the N36 specimens but the hydrogen uptake does not always have the same corresponding relationship to the weight gain. For example, Specimen 32 exhibits the largest weight gain; however, the hydrogen uptake content is not the largest.

N18 Specimens—Figure 7 shows the corrosion and hydrogen uptake behavior of the N18 specimens corroded in 10.3 MPa steam at 400°C. It is clear that the heat treatments also have little effect on the hydrogen uptake of the N18 specimens and again, the hydrogen uptake does not always have the same corresponding relationship to the corrosion resistance.

Relationship Between Hydrogen Uptake and Second Phase Particles

It is clear from Figs. 4–7 that the phenomenon of no strict corresponding relationship between hydrogen uptake and corrosion resistance generally exists among the different heat-treated specimens with the same composition as well as across the alloys with different compositions in this study. For example, the weight gain of the N36 specimens is much larger than that of the N18 specimens but the HUF of the former is lower than the latter (as shown in Figs. 6 and 7). This indicates that the hydrogen uptake behavior is indeed markedly influenced by the chemical composition and the heat treatments.

It is well known that the chemical composition of zirconium alloys will affect the composition of the SPPs that form and the heat treatments will affect the size and amount of the SPPs. Figure 8 shows the relationship between the HUF and the size and area fraction of the SPPs for the specimens tested in 10.3 MPa steam at 400°C for 302 days. In the case of the Zry-4 and Zry-2, the

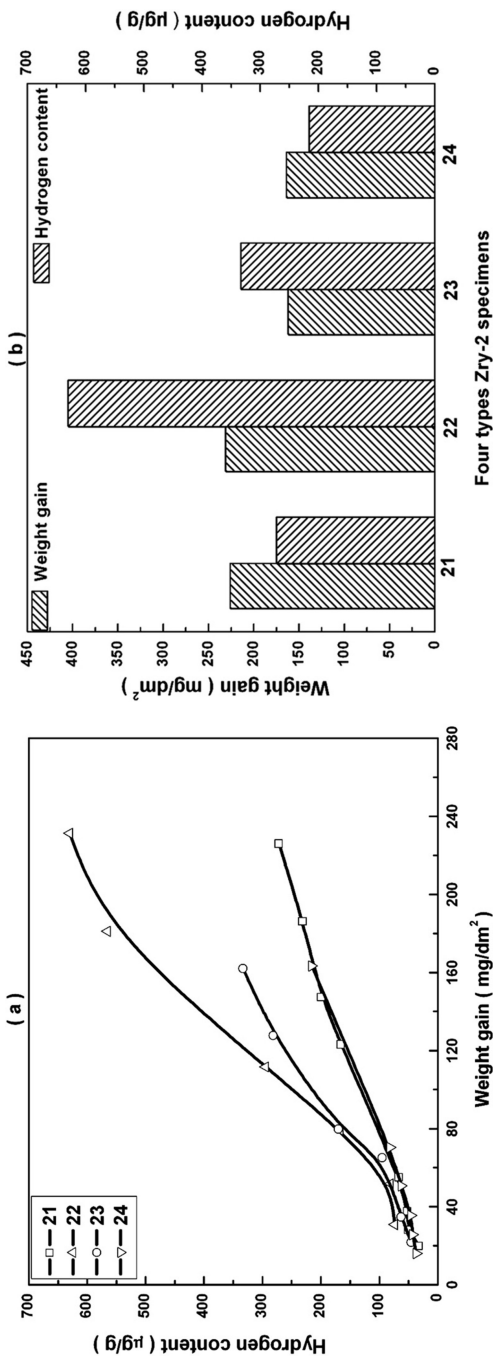


FIG. 5—*The corrosion and hydrogen uptake behavior of the Zry-2 specimens tested in 400°C/10.3 MPa steam: (a) The curve of the hydrogen uptake versus weight gain. (b) Corrosion weight gain and hydrogen uptake content of the specimens corroded for 302 days.*

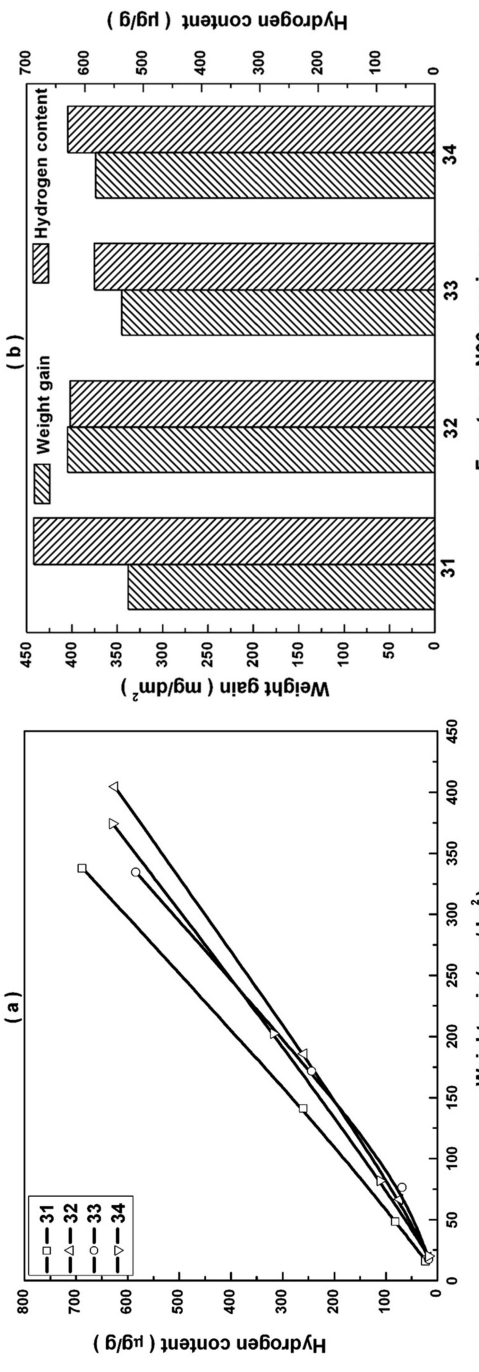


FIG. 6—*The corrosion and hydrogen uptake behavior of the N36 specimens tested in 400°C/10.3 MPa steam: (a) The curve of the hydrogen uptake versus weight gain. (b) Corrosion weight gain and hydrogen uptake content of the specimens corroded for 302 days.*

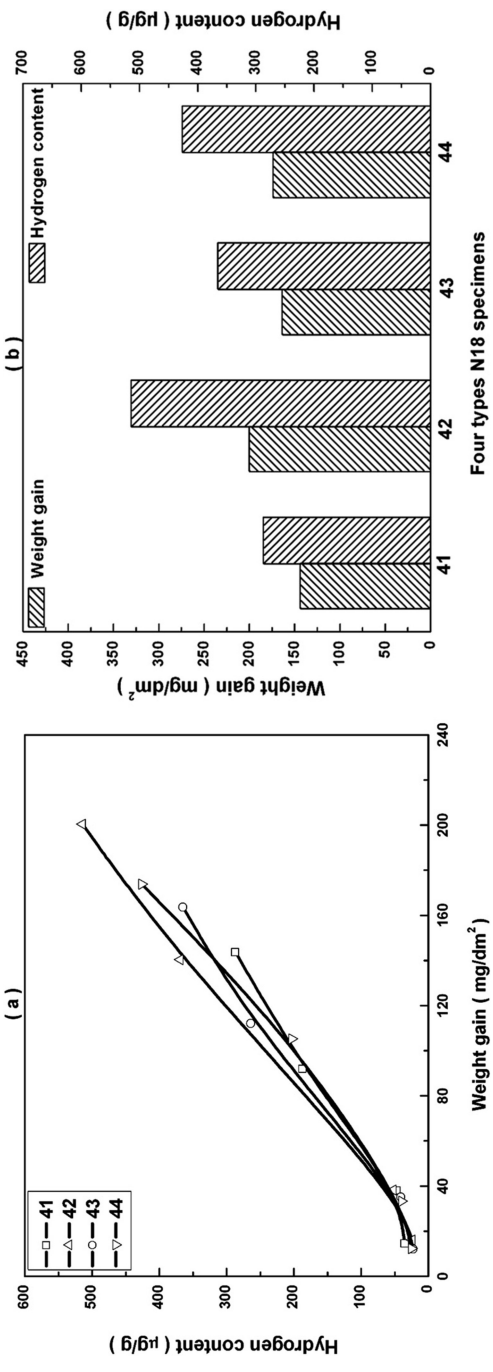


FIG. 7—*The corrosion and hydrogen uptake behavior of the N18 specimens tested in 400°C/10.3 MPa steam: (a) The curve of the hydrogen uptake versus weight gain. (b) Corrosion weight gain and hydrogen uptake content of the specimens corroded for 302 days.*

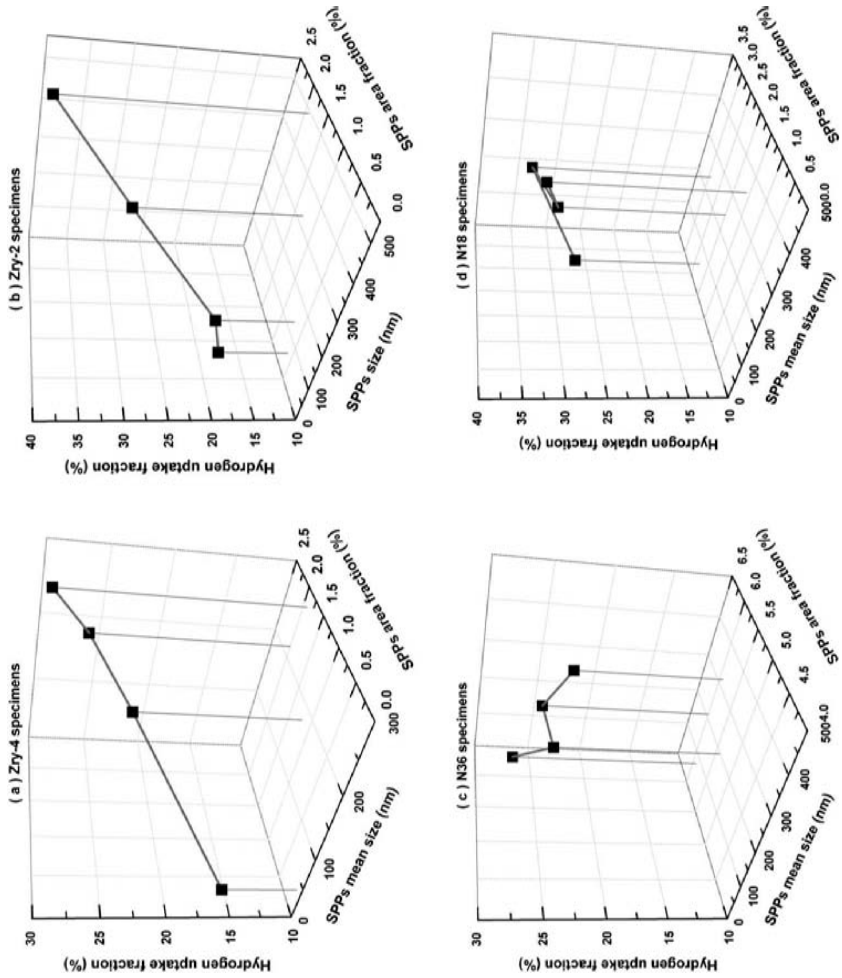


FIG. 8—*The relationship of the HUF and the size and area fraction of the SPPs for the specimens tested in 10.3 MPa steam at 400°C for 302 days.*

HUF increases with the increase in the size and area fraction of the SPPs (Fig. 8(*a*), 8(*b*)). In the case of the N36 or N18 alloys, it is not a simple relationship between the HUF and the size and area fraction of the SPPs. The size and area fraction of the SPPs show a less monotonic effect on the hydrogen uptake behavior. Moreover, it is obvious that the difference in hydrogen uptake among the four specimens for the four alloys decreases in the sequence of Zry−2 > Zry−4 > N18 > N36 (Fig. 8).

Hydrogen Absorption and Desorption Characteristic of the Second Phase Particles Alloys and Pure Zr

Figure 9 shows the hydrogen absorption and desorption characteristic curves of the five SPPs alloys and pure Zr tested in 4 MPa H_2 pressure at 360°C. The kinetics data of the absorbing and desorbing hydrogen are summarized in Table 3. From the activation curves (Fig. 9(*a*)), it can be seen that for the $Zr(Fe,Cr)_2$, $Zr(Nb,Fe)_2$, and β-Nb alloys, the amount of hydrogen absorption are similar among the three activation times for each alloy. This indicates that the alloys can absorb and desorb hydrogen freely and have been activated completely after three activation cycles in 4 MPa H_2 pressure at 360°C. For the $Zr_2(Fe,Ni)$ alloy and pure Zr, however, the amount of hydrogen absorption is greatly different between the first and the following two activation cycles. The amount of hydrogen absorption decreases from 3.1 to 1.5 H/M for $Zr_2(Fe,Ni)$ alloy and from 1.94 to 0.1 H/M for pure Zr. This illustrates that a fraction of the hydrogen is transformed into the irreversible hydride for the $Zr_2(Fe,Ni)$ alloy and most of the hydrogen is transformed into the irreversible hydrides for pure Zr. In the P-C-T curves (Fig. 9(*b*)), which were determined after three activation cycles, it is obvious that the contents of the reversible hydrogen absorption and desorption (H_{rev}, which is defined as the difference between the maximum content of hydrogen absorption and the hydrogen content on the P-C-T curve at 0.01 MPa H_2 pressure, as shown in Fig. 9(*b*)) decrease in the sequence of $Zr(Nb,Fe)_2 > Zr_2(Fe,Ni) > Zr(Fe,Cr)_2$ R0.5 > $Zr(Fe,Cr)_2$ R2 > β−Nb > Zr, and their H_{rev} values are 1.93, 1.19, 0.89, 0.42, 0.28, and 0.14 H/M, respectively (Table 3). The H_{rev} values of the $Zr(Fe,Cr)_2$ alloys increase with decreasing Fe/Cr ratio, which agrees with the results reported in the literature 30–34. Kinetic tests of hydrogen absorption and desorption (Table 3), which are measured after determining the P-C-T curves, show that $Zr(Nb,Fe)_2$, $Zr_2(Fe,Ni)$, and $Zr(Fe,Cr)_2$ alloys absorb and desorb hydrogen with a higher speed and larger content. That is to say, these materials have a strong reversible ability to absorb and desorb hydrogen, which decreased in the above sequence. However, β-Nb alloy and pure Zr can only absorb hydrogen easily but desorb hydrogen difficultly. That is to say, they have a weak reversible ability to absorb and desorb hydrogen. It should be pointed out that the hydrogen absorption and desorption kinetics of pure Zr does not represent its intrinsic characteristic due to its difficulty in hydrogen desorption but it illustrates that hydrogen is difficult to be further absorbed when a hydride layer is formed on the Zr matrix. Based on the above results, it can be concluded that the reversible ability for hydrogen absorption and desorption of $Zr(Nb,Fe)_2$, $Zr_2(Fe,Ni)$, and $Zr(Fe,Cr)_2$ alloys are

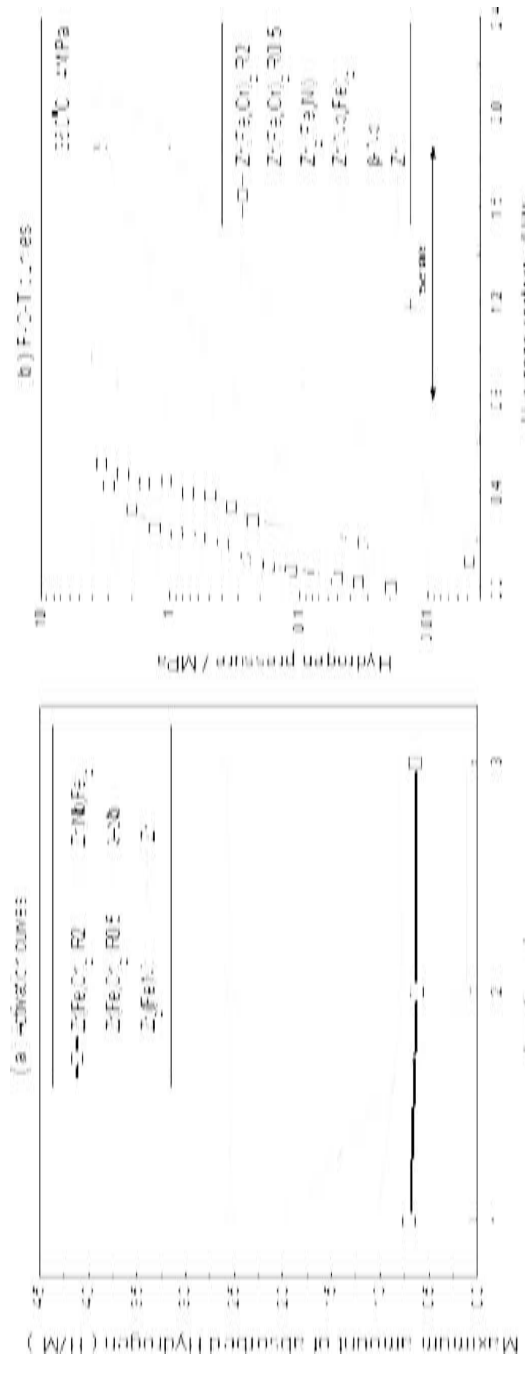


FIG. 9—*Hydrogen absorption and desorption characteristic curves of the SPPs alloys and pure Zr tested in hydrogen atmosphere at 360°C and 4 MPa.*

TABLE 3—*The H_{rev} and kinetics of absorbing and desorbing of the SPPs alloys and pure Zr tested in hydrogen atmosphere at 360°C and 4 MPa.*

	Kinetics [(H/M)/s]		
Materials Number	Absorbing Hydrogen	Desorbing Hydrogen	H_{rev} (H/M)
$Zr(Fe,Cr)_2$ R2	0.020	0.012	0.42
$Zr(Fe,Cr)_2$ R0.5	0.032	0.013	0.89
$Zr_2(Fe,Ni)$	0.083	0.051	1.19
$Zr(Nb,Fe)_2$	0.220	0.060	1.93
β-Nb	0.059	0.006	0.28
Zr	0.044	0.007	0.14

larger than that of β-Nb alloy and pure Zr. This indicates that hydrogen can be more easily and quickly captured and transported by these alloys.

Discussion

It is generally believed that hydrogen is generated at the oxide/environment interface through the discharge of a proton by an electron migrating through the oxide film. Thus, the oxide characteristics (e.g., pores, small cracks, and the dense barrier layer thickness) are key factors affecting the hydrogen uptake behavior. Based on such an assumption, some investigators believe that SPPs affect the hydrogen uptake behavior by affecting the oxide characteristics [11–16]. According to this thought, the hydrogen uptake of zirconium alloys from corrosion should have a direct corresponding relationship with the corrosion resistance. That is to say, the hydrogen content in the specimen with superior corrosion resistance should be less than that in the specimen with inferior corrosion resistance because on one hand, the specimen with superior corrosion resistance generates less hydrogen and on the other hand, the specimen with superior corrosion resistance possesses less pores and cracks in the oxide. Thus, it is more difficult for hydrogen to transport through the oxide. high resolution scanning electron microscope observation of the fracture surface of the oxide film on Zry-4 specimens corroded for 302 days also proves that the pores and cracks in the oxide films on Specimens 13 and 14 with superior corrosion resistance are indeed less than that of Specimens 11 and 12 with inferior corrosion resistance (Fig. 10). However, under the same exposure time of 302 days, the weight gain of Specimen 11 is 267 mg/dm^2 and its HUF is 16 % while the weight gain of Specimen 12 is a little less than that of Specimen 11, 238 mg/dm^2, but its HUF is 29.6 %, which is about twice as much as Specimen 11. That is to say, the hydrogen uptake is not always in a strict corresponding relationship with the corrosion resistance among the four Zry-4 specimens. This phenomenon of no strict corresponding relationship between hydrogen uptake and corrosion resistance generally exists in the different heat-treated specimens with the same composition as well as across the alloys with different compositions in this study (Figs. 4–7) and was also observed in many other

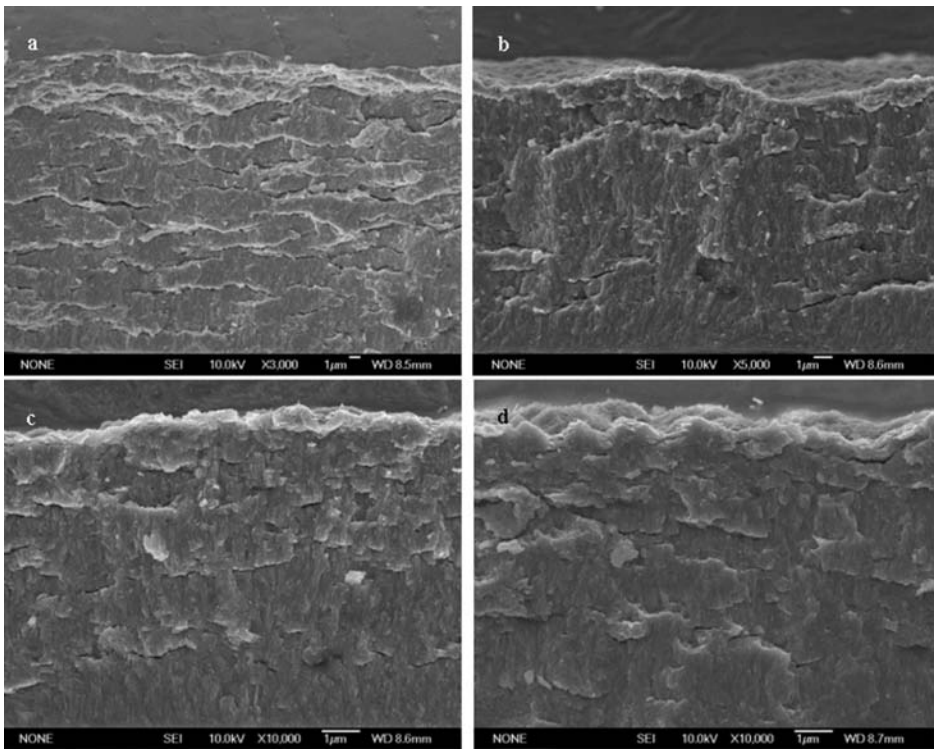


FIG. 10—*The fracture surface morphology of the oxide films formed on the Zry-4 specimens (a) 11, (b) 12, (c) 13, and (d) 14 in a steam at 400°C/10.3 MPa for 302 days.*

studies 10,19,20. Therefore, the thought that SPPs only affect the hydrogen uptake behavior by affecting the oxide characteristics cannot reasonably explain the results that the hydrogen uptake is not always in a strict corresponding relationship with the corrosion resistance.

Hatano et al. 19,20 studied the hydrogen uptake behavior of two types of Zry-4 and Zry-2 specimens containing fine and coarse SPPs in the pre-transition period of oxidation in steam and also found that the amount of hydrogen uptake of the specimen containing the fine SPPs was smaller than that of the specimen containing the coarse ones, which they explained with the model that the $Zr(Fe,Cr)_2$ SPPs remaining unoxidized in the oxide film act as the short-circuiting route in the hydrogen transport through the oxide film. Tägstrom et al. [7] also put forward a similar thought as Hatano's, but believed that the amount of the SPPs had a greater influence on the hydrogen uptake behavior than the size of the SPPs. Lelièvre et al. [18] studied the deuterium distribution in the oxide layers formed on Zry-4 and Zry-2 specimens in 400°C steam by nuclear analysis. The results showed that zirconium hydrides were very often detected under the metal/oxide interface in the vicinity of the SPPs in a 0.7 μm thick oxide, while this correlation was not observed in a 1.4 μm

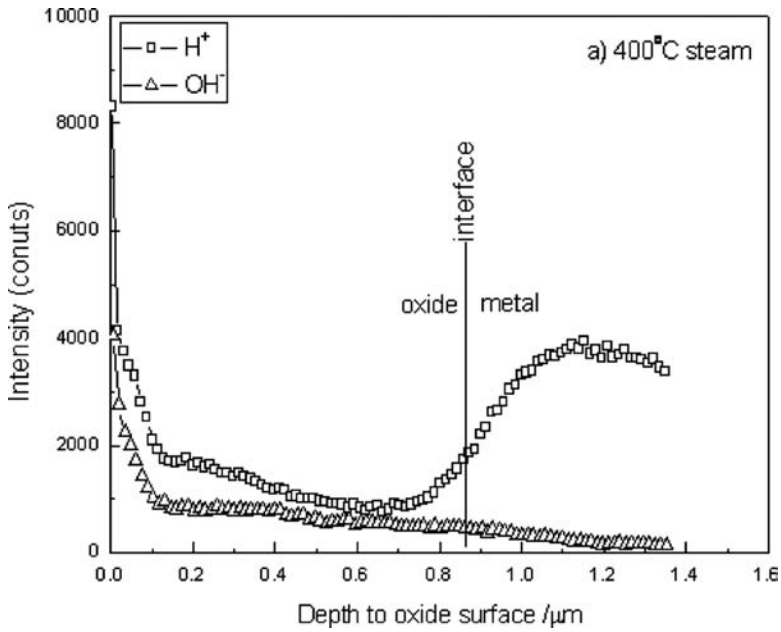


FIG. 11—*The profiles of H^+ and OH^- ions in the oxide layer formed on Specimen 14 in 10.3 MPa steam at 400°C (Its weight gain is 13.2* mg/dm^2*).*

thick oxide. This was interpreted as an indication of the role of SPPs as hydrogen diffusion short-circuits through the oxide layer, but only when these SPPs are metallic and still in contact with the metal, i.e., at the very early stage of oxidation. This thought can reasonably explain the effect of SPPs on the hydrogen uptake behavior of zirconium alloys at the early stage of oxidation but not for the case at the later stage of oxidation, because the SPPs in the oxide film will be oxidized with the process of oxidation. If still based on the assumption that the hydrogen is generated at the oxide/environment interface, the hydrogen transporting through the oxide film, i.e., the oxide characteristic, will again become the key factor affecting the hydrogen uptake behavior.

Is hydrogen generated at the metal/oxide interface when zirconium alloys react with water or H_2O steam? Based on the hydrogen defect theory in oxides [35–38], when metals or alloys are oxidized in atmospheres containing H_2O steam, the proton easily combines with the oxygen ion to form new ions, such as OH^-. The charge and size of OH^- are smaller than those of the oxygen ion. The activation energy for migration of OH^- through the oxide is lower than that of oxygen ion. So, it can be reasonably concluded that the diffusion of OH^- is faster than the oxygen ion. Secondary ion mass spectroscopy (SIMS) analysis was used to detect the H^+ and OH^- ion profiles in the oxide layer on Specimen 14, which was formed by oxidation in 10.3 MPa H_2O steam at 400°C to a weight gain of about 13 mg/dm^2. The results show that both H^+ and OH^- ions exist in the oxide layer (Fig. 11). Since the oxidizing reaction of zirconium alloys in

water or H_2O stream always takes place at the metal/oxide interface, it is possible that there are half-cell reactions of $2H_2O + 2e \rightarrow H_2 + 2OH^-$ (cathodic reaction) and $2OH^- + Zr \rightarrow ZrO_2 + H_2 + 2e$ (anodic reaction). Based on the hydrogen defect theory and the SIMS results, it can be hypothesized that besides hydrogen being generated at the oxide/environment interface, OH^- can also directly react with zirconium to produce hydrogen at the metal/oxide interface after transporting through the oxide layer. Moreover, a fraction of the hydrogen generated at the oxide/environment interface will also transport through the oxide to the metal/oxide interface. Thus, the microstructural characteristics at the metal/oxide interface, e.g., the size, amount, and composition of the SPPs, will likely become the key factors affecting the hydrogen uptake from corrosion.

From Fig. 8, it can be seen that the hydrogen uptake indeed does have a good corresponding relationship with the size or area fraction of the SPPs. In the case of the Zr-Sn alloys (Zry-2 or Zry-4), the HUF of the four specimens increased significantly with increases in the SPPs size and SPPs area fraction. The dependence was more notable for the Zry-2 alloy than for the Zry-4 alloy. In the case of the Zr-Sn-Nb alloys (N36 or N18), the HUF of the four specimens had only a slight variation with the size and area fraction of the SPPs. No matter which heat treatment was employed, the corrosion resistance of the N18 specimens was obviously superior to the N36 specimens but the HUF of the N18 specimens was larger than that of the N36 specimens. These results clearly demonstrate that the effect of the size and area fraction of the SPPs on the hydrogen uptake is different for the zirconium alloys with different types of SPPs.

P-C-T and kinetics tests on the SPP alloys in a hydrogen atmosphere have revealed that the $Zr(Nb,Fe)_2$, $Zr_2(Fe,Ni)$, and $Zr(Fe,Cr)_2$ alloys possess a stronger reversible ability for hydrogen absorption and desorption than pure Zr and β-Nb (Fig. 9). Moreover, the SPPs oxidation is slower than that of α-Zr [39–41]. An in situ investigation of the hydride decomposition and reprecipitation by TEM showed that when irradiated by the convergent electron beam in the TEM, the hydride in the Zry-4 decomposed; when ending the irradiation, fine hydrides reprecipitated around the $Zr(Fe,Cr)_2$ SPPs during cooling (Fig. 12) [42]. This illustrates that the hydrogen could be captured by $Zr(Fe,Cr)_2$ SPPs faster and in greater quantity than by the α-Zr matrix and then released to form hydrides around the SPPs during cooling. It provides a direct proof that the $Zr(Fe,Cr)_2$ SPPs possess a stronger reversible ability for hydrogen absorption and desorption than the α-Zr matrix.

Based on the above analysis, a model for the effect of SPPs on the hydrogen uptake is proposed as follows (as shown in Fig. 13): The water molecules in the corrosion medium get electrons diffusing from the metal/oxide interface to the outer surface of the oxide film and the reaction of $H_2O + e \rightarrow H + OH^-$ takes place; OH^- ions go through the oxide film to the metal/oxide interface and react with zirconium ($2OH^- + Zr \rightarrow ZrO_2 + 2H + 2e$) to generate hydrogen; moreover, a fraction of the hydrogen generated at the oxide/environment interface will also transport through the oxide to the metal/oxide interface. Thus, hydrogen migrating through to the metal/oxide interface will be a key step for hydrogen uptake. In this case, the SPPs' reversible ability for absorbing and desorbing

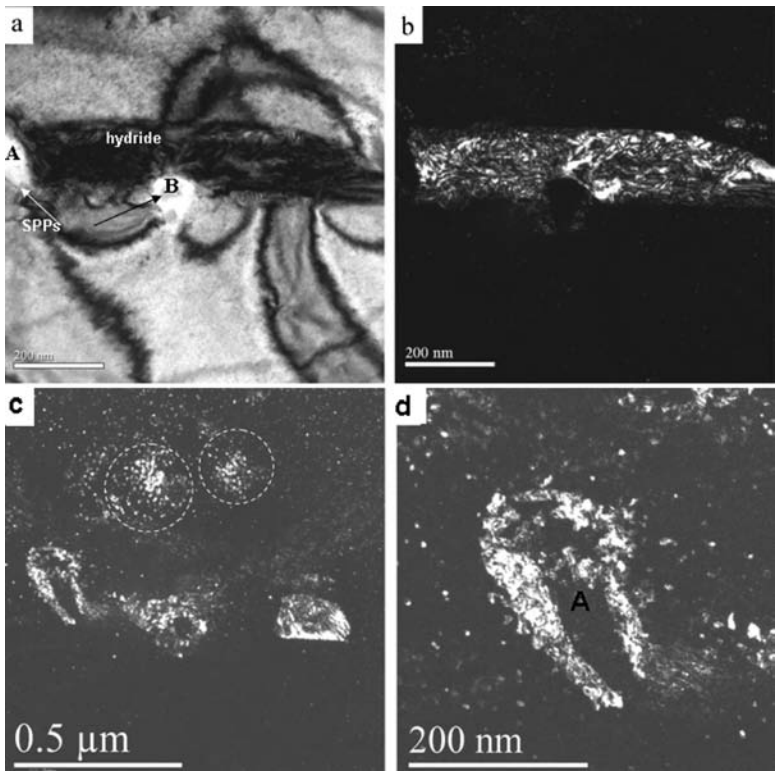


FIG. 12—*In situ investigation results of the hydride decomposition and reprecipitation in the Zry-4 by TEM: The bright filed image (a) and dark field image (b) of the hydride and SPPs around it before electron irradiation; the lower magnification image (c) and higher magnification image (d) of fine hydrides reprecipitated around the* $Zr(Fe,Cr)_2$ *SPPs during cooling after the original hydrided irradiated by the convergent electron beam.*

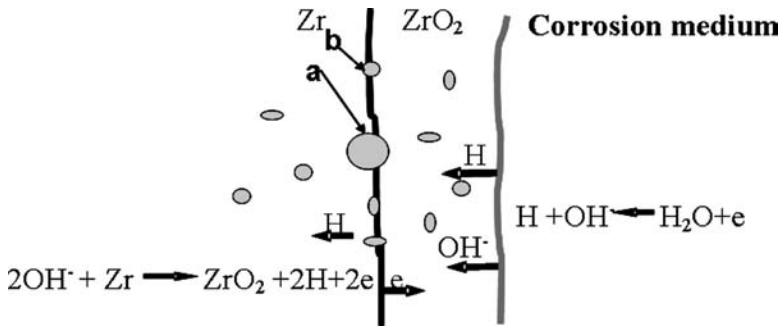


FIG. 13—*Schematic diagram of the hydrogen uptake model of zirconium alloys from corrosion.*

hydrogen will affect the hydrogen uptake performance. When the SPPs possess a stronger reversible ability to absorb and desorb hydrogen, much more hydrogen can be captured and the hydrogen can be transported faster into the matrix by them embedded at the metal/oxide interface. So, the hydrogen uptake is higher. In this case, the size and amount of the SPPs will have a great effect on the hydrogen uptake. When the SPPs possess a weaker reversible ability for absorbing and desorbing hydrogen, the role in transporting the hydrogen into the matrix is not obvious. So, the hydrogen uptake is lower. In this case, the size and amount of the SPPs have little effect on the hydrogen uptake.

The hydrogen uptake model can successfully explain the results in this study. The SPPs are $Zr(Fe,Cr)_2$ in Zry-4 [19], $Zr_2(Fe,Ni)$ and $Zr(Fe,Cr)_2$ in Zry-2 [7,20,24], β-Nb and $Zr(Nb,Fe)_2$ in N36 [25–27], and $Zr(Fe,Cr,Nb)_2$ in N18 [26]. The reversible ability for hydrogen absorption and desorption for the $Zr_2(Fe,Ni)$ alloy is stronger than for the $Zr(Fe,Cr)_2$ alloy, so the HUF of Zry-2 specimens is larger than that of Zry-4 specimens. The HUF difference among the four Zry-2 specimens is also larger than that among the four Zry-4 specimens. Specimens 12 and 22 containing the coarsest and higher area fraction SPPs possess the highest HUF; the SPPs in Specimens 11 and 21 containing the finest and lowest area fraction SPPs possess the lowest HUF. Because $Zr(Nb,Fe)_2$ and $Zr(Fe,Cr)_2$ alloys possess a stronger reversible ability for hydrogen absorption and desorption, N18 specimens with $Zr(Fe,Cr,Nb)_2$ SPPs show a higher HUF among the four alloys. Most of the SPPs in the N36 alloy are β-Nb, so the HUF of N36 specimens is relatively low.

Conclusions

Zry-4, Zry-2, N36, and N18 alloys and four different heat treatments for each alloy were chosen to prepare the specimens with different SPPs compositions, amounts, and sizes. The hydrogen uptake performance of these specimens was investigated after autoclave testing in 400°C/10.3 MPa steam. Meanwhile, P-C-T and kinetics of absorbing and desorbing hydrogen tests were carried out on $Zr(Fe,Cr)_2$, $Zr_2(Fe,Ni)$, $(Zr,Nb)_2Fe$, $Zr(Nb,Fe)_2$, and β-Nb alloys (which may be found as SPPs in the above four zirconium alloys) as well as pure Zr. The following conclusions have been obtained.

(1) The hydrogen uptake shows a significant difference and is not always in a strict corresponding relationship with the corrosion resistance among the specimens. It is closely related to the size, area fraction, and composition of the SPPs, and the effect of the size and area fraction of the SPPs on the hydrogen uptake depends on the SPP compositions.

(2) In the case of the Zr-Sn alloys (Zry-2 or Zry −4), the HUF of the four specimens increased significantly with an increase in size and area fraction of the SPPs. The dependence was more notable for the Zry-2 than for the Zry-4.

(3) In the case of the Zr-Sn-Nb alloys (N36 or N18), the HUF of the four specimens had only a slight variation with the SPPs size and SPPs area fraction. No matter which heat treatment was employed, the corrosion

resistance of the N18 specimens was obviously superior to the N36 specimens, but the HUF of the N18 specimens was larger than that of the N36 specimens.

(4) $Zr(Nb, Fe)_2$, $Zr_2(Fe, Ni)$, and $Zr(Fe, Cr)_2$ alloys possess a stronger reversible ability for hydrogen absorption and desorption than β-Nb alloy and pure Zr, and their reversible ability for hydrogen absorption and desorption decreases in the above sequence. The $Zr(Fe, Cr)_2$ alloys' reversible ability for hydrogen absorption and desorption increases with decreasing Fe/Cr ratio.

(5) A model for the effect of SPPs on the hydrogen uptake is proposed: Getting the hydrogen through to the metal/oxide interface is the key step for hydrogen uptake. Thus, the hydrogen uptake performance is closely related to the SPPs' reversible ability for absorbing and desorbing hydrogen. When the SPPs possess a stronger reversible ability for absorbing and desorbing hydrogen, the size and amount of the SPPs embedded at the metal/oxide interface will have a great effect on the hydrogen uptake. When the SPPs possess a weaker reversible ability for absorbing and desorbing hydrogen, the size and amount of the SPPs embedded at the metal/oxide interface have little effect on the hydrogen uptake.

Acknowledgments

The writers would like to express their thanks to Mr. Xinshu Huang and Shu'an Wang of the Key Laboratory for Nuclear Fuel and Materials, Nuclear Power Institute of China for help in the analysis of the hydrogen contents. The writers also wish to acknowledge Mr. Yuliang Chu and Weijun Yu of the Instrumental Analysis and Research Center of Shanghai University for help in the microstructural analysis. This study is partly supported by grants from the National High Technology Research and Development Program of China (863 Program) (Grant No. 2008AA031701) and the Shanghai Leading Academic Discipline Project (Grant No. S30107).

References

[1] Kearns, J. J., "Terminal Solubility and Partitioning of Hydrogen in the Alpha Phase of Zirconium, Zircaloy-2 and Zircaloy-4," *J. Nucl. Mater.*, Vol. 22, 1967, pp. 292–303.

[2] Cann, C. D. and Sexton, E. E., "An Electron Optical Study of Hydride Precipitation and Growth at Crack Tips in Zirconium," *Acta Metall.*, Vol. 28, 1980, pp. 1215–1221.

[3] Zhou, B. X., Zeng, S. K., and Wang, S. X., "In Situ Electron Microscopy Study on Precipitation of Zirconium Hydrides Induced by Strain and Stress in Zircaloy-2," *Acta Metall. Sin.*, Vol. 25, 1989, pp. A190–195.

[4] Perryman, E. C. W., "Pickering Pressure Tube Cracking Experience," *Nucl. Energy*, Vol. 17, 1978, pp. 95–105.

[5] Simpson, C. J. and Ells, C. E., "Delayed Hydrogen Embrittlement in Zr-2.5 wt % Nb," *J. Nucl. Mater.*, Vol. 52, 1974, pp. 289–295.

[6] Ploc, R. A., "The Effect of Minor Alloying Elements on Oxidation and Hydrogen Pickup in Zr-2.5Nb," *Zirconium in the Nuclear Industry: 13th International Symposium, ASTM-STP-1423*, Annecy, France, 2002, ASTM International, West Conshohocken, PA, pp. 297–310.

[7] Tägstrom, P., Limbäck, M., Dahlbäck, M., Andersson, T., and Pettersson, H., "Effects of Hydrogen Pickup and Second-Phase Particle Dissolution on the In-Reactor Corrosion Performance of BWR Claddings," *Zirconium in the Nuclear Industry: 13th International Symposium, ASTM-STP-1423*, Annecy, France, 2002, ASTM International, West Conshohocken, PA, pp. 96–118.

[8] Mardon, J. P., Charquet, D., and Senevat, J., "Influence of Composition and Fabrication Process on Out-of-Pile and In-Pile Properties of M5 Alloy," *Zirconium in the Nuclear Industry: 12th International Symposium, ASTM-STP-1354*, Toronto, Canada, 2000, ASTM International, West Conshohocken, PA, pp. 505–524.

[9] Sabol, G. P., Kilp, G. R., Balfour, M. G., and Roberts, E., "Development of a Cladding Alloy for Higher Burnup," *Zirconium in the Nuclear Industry: Eighth International Symposium, ASTM-STP-1023*, San Diego, CA, 1989, ASTM International, West Conshohocken, PA, pp. 227–244.

[10] Yao, M. Y., Zhou, B. X., Li, Q., Liu, W. Q., and Chu, Y. L., "The Effect of Alloying Modifications on Hydrogen Uptake of Zirconium-Alloy Welding Specimens During Corrosion Tests," *J. Nucl. Mater.*, Vol. 350, 2006, pp. 195–201.

[11] Cox, B., "A Mechanism for the Hydrogen Uptake Process in Zirconium Alloys," *J. Nucl. Mater.*, Vol. 264, 1999, pp. 283–294.

[12] Cox, B. and Wong, Y.-M., "A Hydrogen Uptake Micro-Mechanism for Zr Alloys," *J. Nucl. Mater.*, Vol. 270, 1999, pp. 134–146.

[13] Cox, B., "Hydrogen Uptake During Oxidation of Zirconium Alloys," *J. Alloys Compd.*, Vol. 256, 1997, pp. 244–246.

[14] Rudling, P. and Wikmark, G., "A Unified Model of Zircaloy BWR Corrosion and Hydriding Mechanisms," *J. Nucl. Mater.*, Vol. 265, 1999, pp. 44–59.

[15] Elmoselhi, M. B., "Hydrogen Uptake by Oxidized Zirconium Alloys," *J. Alloys Compd.*, Vol. 231, 1995, pp. 716–721.

[16] Khatamian, D., "Hydrogen Diffusion in Oxides Formed on Surfaces of Zirconium Alloys," *J. Alloys Compd.*, Vols. 253–254, 1997, pp. 471–474.

[17] Barberis, P., Ahlberg, E., Simic, E., Charquet, D., Lemaignan, C., Wikmark, G., Dahlbäck, M., Tägtström, P., and Lehtinen, B., "Role of the Second-Phase Particles in Zirconium Binary Alloys," *Zirconium in the Nuclear Industry: 13th International Symposium, ASTM-STP-1423*, Annecy, France, 2002, ASTM International, West Conshohocken, PA, pp. 33–55.

[18] Lelièvre, G., Tessier, C., Iltis, X., Berthier, B., and Lefebvre, F., "Impact of Intermetallic Precipitates on Hydrogen Distribution in the Oxide Layers Formed on Zirconium Alloys in a Steam Atmosphere: A ^{2}D (^{3}He,p)$\propto$ Nuclear Analysis Study in Microbeam Mode," *J. Alloys Compd.*, Vol. 268, 1998, pp. 308–317.

[19] Hatano, H., Hitaka, R., Sugisaki, M., and Hayashi, M., "Influence of Size Distribution of $Zr(Fe,Cr)_2$ Precipitates on Hydrogen Transport through Oxide Film of Zircaloy-4," *J. Nucl. Mater.*, Vol. 248, 1997, pp. 311–314.

[20] Hatano, Y., Isobe, K., Hitaka, R., and Sugisaki, K., "Role of Intermetallic Precipitates in Hydrogen Uptake of Zircaloy-2," *J. Nucl. Sci. Technol.*, Vol. 33, No. 12, 1996, pp. 944–949.

[21] Ramasubramanian, N., Billot, P., and Yagnik, S., "Hydrogen Evolution and Pickup During the Corrosion of Zirconium Alloys: A Critical Evolution of the Solid State and Porous Evolution Oxide Electrochemistry," *Zirconium in Nuclear Industry:*

13th International Symposium, ASTM-STP-1423, Annecy, France, 2002, ASTM International, West Conshohocken, PA, pp. 222–244.

[22] Lim, B. H., Hong, H. S., and Lee, K. S., "Measurement of Hydrogen Permeation and Absorption in Zirconium Oxide Scales," *J. Nucl. Mater.*, Vol. 312, 2003, pp. 134–140.

[23] Große, M., Lehmann, E., Steinbrück, M., Kühne, G., and Stuckert, J., "Influence of Oxide Layer Morphology on Hydrogen Concentration in Tin and Niobium Containing Zirconium Alloys After High Temperature Steam Oxidation," *J. Nucl. Mater.*, Vol. 385, 2009, pp. 339–345.

[24] Ruding, P., Lundblad-Vannesjö, K., Vesterlund, G., and Massih, A. R. "Influence of Second-Phase Particles of Zircaloy Corrosion in BWR Evironments," *Zirconium in the Nuclear Industry: Seventh International Symposium, ASTM-STP-939*, Strasbourg, France, 1987, ASTM International, West Conshohocken, PA, pp. 292–306.

[25] Comstock, R. J., Schoenberger, G., and Sable, G. P., "Influence of Processing Variables and Alloy Chemistry on the Corrosion Behavior of ZIRLO Nuclear Fuel Cladding," *Zirconium in the Nuclear Industry: 11th International Symposium, ASTM-STP-1295*, Garmisch-Partenkirchen, Germany, 1996, ASTM International, West Conshohocken, PA, pp. 710–725.

[26] Li, Z. K., Zhou, L., and Zhao, W. J., "Effect of Intermediate Annealing on Out-of Pile Corrosion Resistance of Zirconium-Based Alloy," *Rare Met. Mater. Eng.*, Vol. 30, No. 1, 2001, pp. 52–54.

[27] Toffolon-Masclet, C., Barberis, P., Brachet, J.-C., Mardon, J.-C., and Legras, L., "Study of Nb and Fe Precipitation in α-phase Temperature Range (400 to 500°C) in Zr-Nb-(Fe-Sn) Alloys," *Zirconium in the Nuclear Industry: 14th International Symposium, ASTM-STP-1467*, Stockholm, Sweden, June 13–17, 2004, ASTM International, West Conshohocken, PA, pp. 81–101.

[28] Eucken, C. M., Finden, P. T., Trapp-Pritsching, S., and Weidinger, H. G., "Influence of Chemical Composition on Uniform Corrosion of Zirconium-Base Alloys in Autoclave Tests," *Zirconium in the Nuclear Industry: Eighth International Symposium, ASTM-STP-1023*, San Diego, CA, 1989, ASTM International, West Conshohocken, PA, pp. 113–127.

[29] Sabol, G. P., Comstock, R. J., Weiner, R. A., Larouere, P., and Stanutz, R. N., "In-Reactor Corrosion Performance of ZIRLO™ and Zircaloy-4," *Zirconium in the Nuclear Industry: Tenth International Symposium, ASTM-STP-1245*, Baltimore, MD, 1994, ASTM International, West Conshohocken, PA, pp. 724–744.

[30] Shaltiel, D., Jacob, I., and Davidov, D. "Hydrogen Absorption and Desprption Properties of AB_2 Laves-Phase Pseudobinary Alloys," *J. Less-Common Met.*, Vol. 53, 1977, pp. 117–131.

[31] Qian, S. H., 1989, "Hysteresis and Sloping Plateau Pressures in $Zr(Fe_x,Cr_{1-x})_2$-H Systems," Ph.D. dissertation, Windsor University, Windsor, ON, Canada.

[32] Douglas, G. I., 1985, "Hydrogen Storage Characteristics of $Zr(Fe_x,Cr_{1-x})_2$," Ph.D. dissertation, Windsor University, Windsor, ON, Canada.

[33] Esayed, A., 1993, "Hysteresis in Metal-Hydrogen Systems," Ph.D. dissertation, Windsor University, Windsor, ON, Canada.

[34] Kakiuchi, K., Itagaki, N., Furuya, T., Miyazaki, A., Ishii, Y., Suzuki, S., Terai, T., and Yamawaki, M., "Role of Iron for Hydrogen Absorption Mechanism in Zirconium Alloys," *Zirconium in the Nuclear Industry: 14th International Symposium, ASTM-STP-1467*, Stockholm, Sweden, 2004, ASTM International, West Conshohocken, PA, pp. 349–365.

[35] Norby, T., Dyrlie, O., and Kofstad, P., "Ptotonic Conduction in Acceptor-Doped Cubic Rare-Earth Sesquioxides," *J. Am. Ceram. Soc.*, Vol. 75, No. 5, 1992, pp. 1176–1181.

[36] Norby, T. and Kofstad, P., "Electrical Conductivity of Y_2O_3 as a Function of Oxygen Parti Pressure in Wet and Dry Atmospheres," *J. Am. Ceram. Soc.*, Vol. 69, No. 11, 1986, pp. 784–789.

[37] Norby, T. and Kofstad, P., "Proton and Native-Ion Conductivites in Y_2O_3 at High Temperatures," *Solid State Ionics*, Vol. 20, 1986, pp. 169–184.

[38] Thomas, D. G. and Lander, J. J., "Hydrogen as Donor in Zinic Oxide," *J. Chem. Phys.*, Vol. 25, No. 6, 1956, pp. 1136–1142.

[39] Pêcheur, D., Lefebvre, F., Motta, A. T., Lemaignan, C., and Charquet, D., "Oxidation of Intermetallic Precipitates in Zircaloy-4: Impact of Irradiation," *Zirconium in the Nuclear Industry: Tenth International Symposium, ASTM-STP-1245*, Baltimore, MD, 1994, ASTM International, West Conshohocken, PA, pp. 687–705.

[40] Pêcheur, D., "Oxidation of β-Nb and $Zr(Fe,V)_2$ Precipitates in Oxide Films Formed on Advanced Zr-Based Alloys," *J. Nucl. Mater.*, Vol. 278, 2000, pp. 195–201.

[41] Weidinger, H. G., Ruhmann, H., Cheliotis, G., Maguire, M., and Yau, T.-L., "Corrosion-Electrochemical Properties of Zirconium Intermetallics," *Zirconium in the Nuclear Industry: Ninth International Symposium, ASTM-STP-1132*, Kobe, Japan, 1991, ASTM International, West Conshohocken, PA, pp. 499–534.

[42] Peng, J. C., 2009, "In-Situ Investigation of Oxide Formation and Hydride Precipitation in Zircaloy-4 by Transmission Electron Microscope," M.S. dissertation, Shanghai University, Shanghai, China, pp. 34–38.

DISCUSSION

Question 1, Arthor Motta, Penn State University:—1) I understand that your hydrogen adsorption/desorption are done in powders. Would these powders react with air? How would you be able to tell if they did? 2) Did the hydrogen pickup fraction change as a function of corrosion kinetics for each sample? (i.e. Was f_H content with corrosion time?)

Author's Response:—1) Yes, these powders would react with oxygen from air according to the fact that the Gibbs free energy (ΔG) of reaction between zirconium/oxygen is negative. It is difficult to identify the oxide layer because it is too thin. Perhaps it could be detected by atom probe tomography (APT).

2) Yes, the hydrogen uptake fraction changed as a function of corrosion time (as shown in Fig.1). This difference is possibly related to the characteristics of oxide layer, as well as the size and amount of SPPs. However, the mechanism about the difference hasn't been clarified so far.

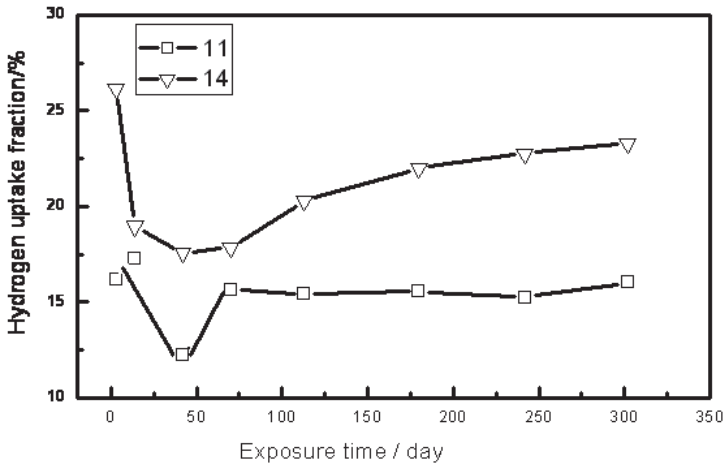


FIG. 1. The curve of the hydrogen uptake fraction vs exposure time for different Zircaloy-4 specimens corroded in 400°C/10.3 MPa steam. (The number of specimens is the same as that in the text.)

Question 2, Philippe Bossis, CEA:—What is the crystallographic character /composition of all the "massive precipitates" prepared? Was it checked?

Author's Response:—We denoted "massive precipitates" as SPP alloys in the text. All the SPP alloys were analyzed by XRD. $Zr(Fe,Cr)_2$ SPP alloys with Fe/Cr atomic ratio of 2 and 0.5 are hexagonal; $Zr_2(Fe,Ni)$ SPP alloy with Fe/Ni atomic ratio of 1 is tetragonal; $Zr(Nb,Fe)_2$ SPP alloy with Nb/Fe atomic ratio of 1 is hexagonal; β-Nb SPP alloy with 10 %Zr (mass fraction) is cubic.

Question 3, David Rugg:—Were the powders tested in the hydride/dehydride studies tested in the passive condition?

Author's Response:—No, the powders weren't tested in the passive condition. They were activated before testing the hydrogen adsorption/desorption characteristics.

Question 4, Zhongwen Yao, Queen's University:—What's the energy of electrons? How do you characterize the hydrides? Temperature?

Author's Response:—The accelerated voltage is 200 kV for the electron beam irradiating on the hydrides. The hydrides were characterized by selected area diffraction patterns. It's not possible to measure the temperature at the hydride irradiated by electron beam. But it could be estimated based on the fact that hydrides would be decomposed above 600°C

Reprinted from JAI, Vol. 8, No. 1
doi:10.1520/JAI103033
Available online at www.astm.org/JAI

Kimberly B. Colas,[1] *Arthur T. Motta,*[1] *Mark R. Daymond,*[2] *Matthew Kerr,*[2] *and Jonathan D. Almer*[3]

Hydride Platelet Reorientation in Zircaloy Studied with Synchrotron Radiation Diffraction

ABSTRACT: Hydrogen ingress into zirconium alloy fuel cladding in light water reactors can degrade cladding performance as a result of the formation of brittle hydrides. In service, hydrides normally precipitate in the circumferential direction and are homogeneously distributed through the cladding thickness in ideal cases. However, temperature and stress gradients in the cladding can promote hydrogen redistribution. This hydrogen redistribution is responsible for the formation of hydride rims, dissolution, and reorientation of hydride precipitates and for the formation of brittle hydrides at stress concentration locations, all of which can reduce cladding resistance to failure. Thus, it is crucial to understand the kinetics of hydride dissolution and precipitation under load and at temperature. Studies of hydrogen behavior in zirconium alloys are normally performed post facto, which causes them to suffer both from a scarcity of data points and from the confounding effects of studying hydrides at room temperature that might be dissolved at higher temperature. In the current study, we have used synchrotron radiation diffraction to study the kinetics of hydride precipitation and dissolution in situ (under load and at temperature). Samples of hydrided Zircaloy-4 were examined in transmission by using 80 keV synchrotron radiation while undergoing heating and cooling in a furnace. Temperatures ranged from 20 to 550C, and loads from 75 to

Manuscript received February 8, 2010; accepted for publication October 23, 2010; published online December 2010.
[1] Dept. of Mechanical and Nuclear Engineering, Penn State Univ., University Park, PA 16802.
[2] Dept. of Mechanical and Materials Engineering, Queen's Univ., Kingston, ON K7L 2N8,Canada.
[3] Advanced Photon Source, Argonne National Laboratory, Argonne, IL 60439.

Cite as: Colas, K. B., Motta, A. T., Daymond, M. R., Kerr, M. and Almer, J. D., "Hydride Platelet Reorientation in Zircaloy Studied with Synchrotron Radiation Diffraction," *J. ASTM Intl.*, Vol. 8, No. 1. doi:10.1520/JAI103033.

Copyright © 2011 by ASTM International, 100 Barr Harbor Drive, PO Box C700, West Conshohocken, PA 19428-2959.

100 MPa were applied. The hydrides dissolved and reprecipitated in a different orientation when sufficiently high loads were applied. Through careful study of the intensities and full-width half maxima of the diffraction peaks as a function of time, load, and temperature, it was possible to identify the characteristic diffraction patterns for the reoriented hydrides so that the kinetics of dissolution, reprecipitation, and orientation of the hydrides could be followed. The analysis of the diffraction patterns allowed a detailed understanding of the kinetics of hydride evolution under temperature and stress, as presented in this work.

KEYWORDS: zirconium hydrides, reorientation, synchrotron radiation diffraction, strain broadening

Introduction

Zirconium alloys used for reactor core structural components and fuel cladding can be embrittled by the presence of zirconium hydride precipitates, which form as a result of hydrogen ingress due to the phenomena associated with reactor corrosion and water radiolysis [1]. The hydrides observed in fuel cladding exposed to reactor environment are most often face-centered-cubic δ-hydrides ZrH_x (where $x \sim 1.6$) [2], although γ- and ε-hydrides are occasionally observed [3,4]. δ-hydrides are shown by electron microscopy to be platelet-shaped and to form with a near $(111)_\delta \parallel (0002)_\alpha$ orientation relationship with the α-zirconium matrix [5]. The larger hydride plates observed optically have been reported to be constituted of a stacking of several of these smaller platelets [6]. The orientation and morphology of these larger hydrides plates are primarily dependent on the zirconium matrix microstructure, thermal history, and stress state (both applied and residual). During drying and storage, high temperatures (of up to 400°C) can be attained, and part of the hydride population can dissolve and reprecipitate with a different orientation. In the absence of an applied stress field, hydride precipitation is dependent on the texture of the zirconium matrix and is governed by the orientation of the last compressive step in the thermo-mechanical treatment which normally results in planar or "circumferential" hydrides [7]. However, the presence of a sufficiently high applied tensile stress field (typically starting at around 80 MPa) during cooling causes the hydride platelets to precipitate preferentially perpendicular to the applied tensile stress direction. The level of applied stress required for hydride reorientation depends on the microstructure, prior processing, and hydrogen concentration as well as thermo-mechanical loading [8]. Because of this, concern has arisen that such hydride reorientation could occur during dry storage of spent fuel, especially in the case of high burn-up and corresponding high hydrogen concentrations, causing the fuel cladding to become more brittle. As a result, an understanding of hydride reorientation phenomena is of great technological importance.

Most analyses of changes in hydride microstructure have been performed post facto, at room temperature, and after applied stress has been removed. Typically, the hydride orientation is determined by using metallography before and after the heating/loading cycles [9–11]. It would be of great interest to

combine the post facto metallographic techniques with in situ measurements of hydride reorientation. Recent studies using high energy synchrotron X-ray diffraction have demonstrated that it is possible to observe zirconium hydride phases and to distinguish the crystallographic nature of the hydride phases present (δ from γ, for example) [12]. The strain measurements of zirconium hydrides embedded in a zirconium alloy matrix have also been conducted, both in the bulk and at notch tips [13,14]. Synchrotron measurements have proven to be reliable in measuring internal strains, comparing favorably to measurements made at neutron diffraction sources [15,16]. The advantage of a synchrotron source is that these measurements can be made with shorter exposure times and with higher resolution, owing to the high photon flux available. In addition, high energy beams allow the examination of thicker samples.

The in situ synchrotron diffraction experimental set-ups such as the one presented in this paper could be used to study many essential features of the behavior of hydrides under temperature and stress. In this study, high energy X-rays were used in transmission to obtain diffraction data while the sample was loaded at temperature. These techniques were used to observe hydride reorientation in the matrix of zirconium alloys during heating and cooling cycles under stress. Further experiments could be conducted involving full reorientation of the entire population of hydrides, multiple temperature cycles to study the possible memory effect on hydride precipitation, and/or materials with composition and textures differences. The work on the determination of the terminal solid solubility of hydrogen using this technique has also been performed and will be published elsewhere. The aim of this study is to follow the process of hydride reorientation in situ by using synchrotron X-ray diffraction.

Experimental Procedures

Material and Sample Preparation

Zircaloy-4 base alloy furnished by Western Zirconium was used in this study. The material was in the form of a 0.5 mm thick sheet in the recrystallized condition. An optical metallograph of the as-received material is shown in Fig. 1(*a*). The

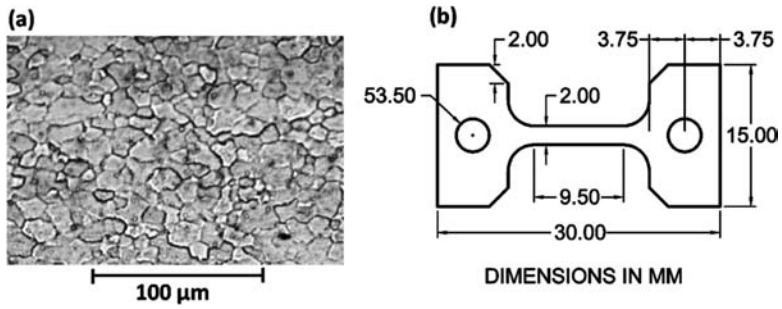


FIG. 1—(a) *Optical image of grain structure of the cross section of as-received material and (*b*) sample dimensions. The sample thickness is 0.5 mm.*

grains are equiaxed and their diameter is $\sim 10\ \mu$m. These samples were machined to a tensile "dog-bone" shape with a reduced width at the gage section to obtain stress concentration, as seen in Fig. 1(*b*). The tensile axis of the sample is aligned with the rolling direction. The sample dimensions are detailed in Fig. 1(*b*).

These samples were hydrogen-charged by high temperature gas diffusion, for which several steps were needed. First, the native oxide layer present on the surface of the samples was removed by dipping the samples for 1 min in a solution of 1 part hydrofluoric acid, 10 parts nitric acid, and 10 parts H_2O. Second, by using an electron-beam evaporator, a thin layer of nickel (200 Angstoms thick) was deposited into the sample surface to prevent the native oxide from reforming while still allowing hydriding [17]. The samples were then hydrogen-charged in a vacuum furnace using a mixture of 12 % hydrogen and 88 % argon, introduced at 450°C. Several temperature cycles were necessary to charge to the desired levels of hydrogen. The total time at 450°C was 3 h, so no significant recrystallization occurred [18]. The final hydrogen contents of the sample were measured by hot vacuum extraction performed by Luvak, Inc. The samples used in this study were charged to 525 ± 10 wt ppm of hydrogen.

After hydrogen-charging, metallography was performed to characterize the hydride morphology. The samples were mounted in a cross section in epoxy casts and mechanically polished to 1200 grit silicon carbide paper, followed by chemical etching using the same solution used for oxide layer removal. This solution preferentially etched the zirconium hydrides, which allowed their observation by using optical microscopy. One example of such an examination is shown in Fig. 2 for a sample with 525 wt ppm of hydrogen. It is seen that in the initial state, the hydride platelets (dark lines) are mostly perpendicular to the normal direction (ND), and thus they are in-plane, or circumferential hydrides. The hydride orientation was estimated using image analysis. Each individual particle was counted as a circumferential hydride, a mixed hydride, or a radial hydride. The circumferential hydrides were those whose normals were oriented between 0° and 40° from the ND (or radial direction for a cladding tube), the mixed hydrides were those whose normals were oriented between 40° and 65° from the ND, and the radial hydrides were those whose normals were oriented between 65° and 90° from the ND [19].

Temperature and Load

While being analyzed by synchrotron X-ray diffraction, the samples underwent heating and cooling cycles under load. The samples in this study were heated up to 550°C in order to dissolve all the hydrides in the matrix (the solubility of hydrogen in zirconium at 550°C is about 640 wt ppm [20]), then cooled back to room temperature under tensile load applied in the rolling direction (RD). An example of a typical temperature/load run is shown in Fig. 3. Each sample was cycled only once, and the time at maximum temperature (550°C) was at most 15 min, so no significant grain growth or recrystallization has occurred [18]. The testing temperature was controlled by using an optical furnace and the sample temperature was monitored by using K-type thermocouples, which were spot welded into the sample surface. The MTS® frame used for tensile

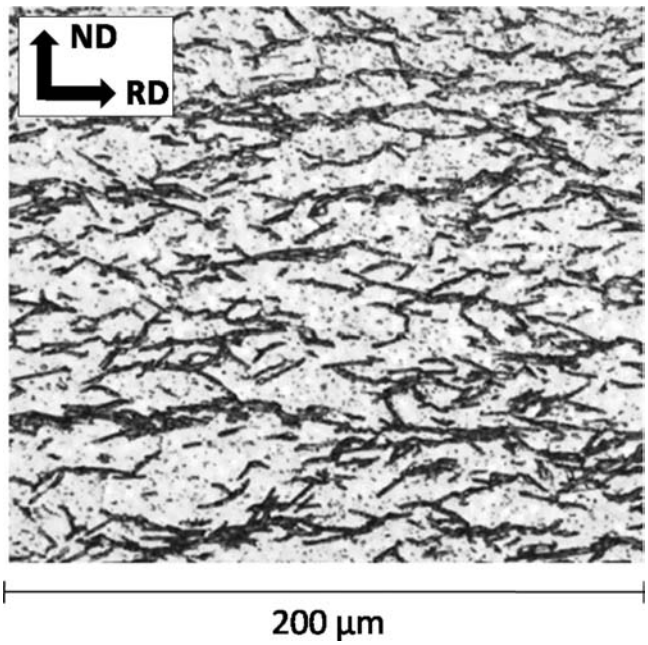


FIG. 2—*Optical metallograph of a Zircaloy-4 sample hydrided to 525 wt ppm. The sample orientation is represented by the black arrows.*

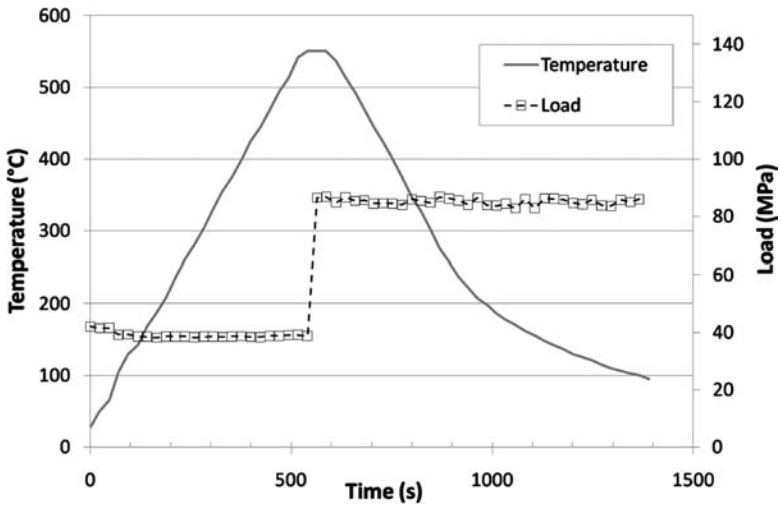


FIG. 3—*Typical in situ heat/load cycle.*

testing allowed the computer monitoring of the applied load and the displacement or the displacement rate of the crosshead. The applied (engineering) stress was determined by dividing the applied force by the initial gage cross section.

Synchrotron Data Acquisition

The X-ray diffraction examination of the samples was conducted at beamline 1-ID at the Advanced Photon Source at Argonne National Laboratory with the objective of observing the dissolution and precipitation kinetics of the zirconium hydrides. The experimental geometry is described in Fig. 4. The experiments were conducted in transmission geometry by using 80 keV X-rays ($\lambda = 0.015\,\text{nm}$) and a beam size of $0.3 \times 0.3\,\text{mm}^2$ [21]. This experimental set-up allows the observation of the hydride diffracted intensity as the sample is heated or cooled under load. A high-speed area detector (1 s time resolution) was used to collect diffraction patterns, allowing the full diffraction rings to be recorded. Because the data was obtained in transmission, the diffraction signal is averaged over the full sample thickness. The diffraction rings can be integrated over their full circumference or over selected angular ranges to obtain the diffracted intensity from planes oriented in particular directions of interest relative to the macroscopic sample directions. A typical diffraction pattern integrated over the full circumference for a sample with 525 wt ppm of hydrogen is presented in Fig. 5. For this study, it was chosen to integrate the diffraction rings around specific orientations close to the RD and transverse direction (TD) as illustrated in

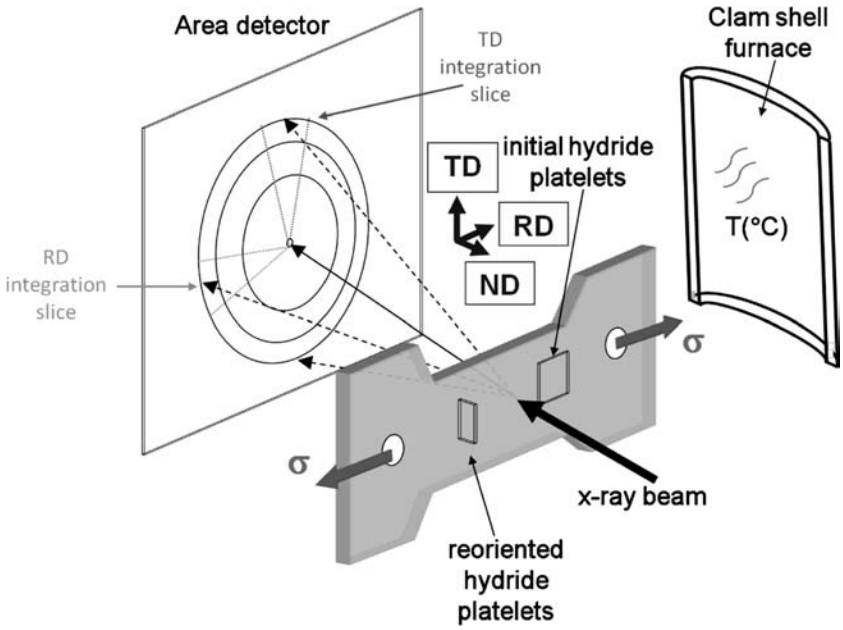


FIG. 4—*Experimental set-up of beamline 1-ID. The integration directions are indicated on the area detector.*

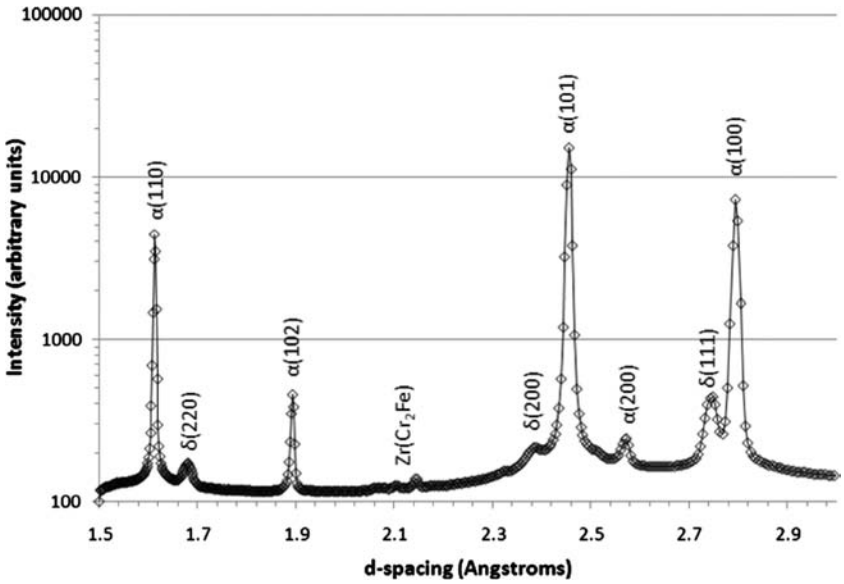


FIG. 5—*X-ray diffraction pattern of a Zircaloy-4 material sample with 525 wt ppm of hydrogen (logarithmic scale).*

Fig. 4. The diffraction signals from the "TD" come from crystallographic planes with normals parallel to the TD (within a $\pm 10^{\circ}$ angular range around the TD) and diffraction signals in the "RD" come from crystallographic planes, which have their normals parallel to the RD (in a $\pm 10^{\circ}$ angular range around the RD).

Synchrotron Data Analysis

The typical raw data obtained during this experiment was in the form of ten two-dimensional images successively obtained using the plate detector for each diffraction pattern recorded (this was necessary to avoid saturation of the detector for the high intensity Zr peaks while still obtaining good statistics for the weak hydride peaks). The ten images were summed and averaged to create the diffraction pattern. Using a computer routine, the full diffraction rings were integrated over four specific angular ranges of $\pm 10^{\circ}$ around 0°, 90°, 180°, and 270°. The data from the angular ranges obtained was then averaged (average of the sum of 0° and 180° ranges (RD) and average of the sum of 90° and 270° ranges (TD)) and reduced to a file suitable for analysis. The diffraction peaks obtained were then analyzed by using a single peak fitting routine available within the GSAS/Rawplot® program [22]. General structure analysis system (GSAS) is primarily a Rietveld refinement program that can fit all the different parameters that would affect peak height, shape and position. Rawplot is a subroutine that allows faster fitting of only the peak shape, position and intensity of the raw data. The peaks were fitted using a pseudo-Voigt function, which is a convolution of Gaussian and Lorentzian peak shapes. In the GSAS fitting

routine, the Lorentzian full-width at half maximum (FWHM) was kept constant, while the Gaussian FWHM was allowed to vary; the Lorentzian FWHM is normally associated with instrumental broadening (which was determined independently in this study by using a calibration powder to be 0.22×10^{-2} degrees in 2θ), whereas the Gaussian FWHM is normally associated with sample broadening, such as size or strain broadening [23]. The background was fitted over the entire diffraction range by using a third-degree polynomial function and subtracted from the data prior to fitting. This allowed iterative fitting of the diffraction peaks to obtain (i) the peak positions, (ii) the integrated intensity, and (iii) the Gaussian FWHM of the refined peaks. The instrumental broadening was determined by running a ceria standard powder used as a reference for broadening and subtracted in quadrature from each peak to isolate the sample contribution to line broadening. When measured under stress, the peak positions can be related to the elastic strain of the diffracting crystallites, while peak broadening can originate from various causes, including size broadening, inhomogeneous elastic strain, and from plastic strain broadening [23].

Results and Discussion

As explained in the previous section, the analysis of the diffraction data yields peak positions (and thus *d*-spacing), integrated intensities, and FWHM for each peak. As mentioned above, these values can be obtained by integration over the full diffraction ring or along portions of the ring oriented along particular directions. As a sample is heated and cooled under load, diffraction patterns are constantly recorded, enabling us to observe each of the parameters mentioned above as a function of time. The evolution of the above parameters with time allows us to follow the evolution of strain and stress of the phases present as a function of temperature and applied load. It should be noted, however, that the strain (and resulting stress) is calculated from the *d*-spacing shift and peak broadening and is not directly measured in our experiment.

X-Ray Diffraction Patterns

The diffraction pattern presented in Fig. 5 results from integration over the full diffraction ring of a sample containing 525 wt ppm of hydrogen. The α-zirconium and δ-hydride peaks were indexed using expected *d*-spacing values from the powder diffraction files indicated in Table 1 from Ref 2. Three δ-hydride peaks $(111)_\delta$, $(200)_\delta$, and $(220)_\delta$ and five α-zirconium peaks are observed. For the zirconium matrix, the intensity of the $(002)_\alpha$ peak is small compared to that of the $(100)_\alpha$ and $(101)_\alpha$ peaks (the prism planes and the pyramidal planes, respectively). This results from the basal texture created upon cold rolling, causing the basal poles to be preferentially aligned along the ND, and thus not in a strong diffraction condition in our transmission set-up. Table 1 shows a comparison of the peak positions determined from the experiment and those from the respective powder diffraction files. The α-zirconium peaks correspond well to the powder diffraction files, to the fourth significant digit, while the δ-hydride peaks agree to the third significant digit. The difference between the observed

TABLE 1—*Measured and expected peak positions for a Zircaloy-4 sample with 525 wt ppm of hydrogen (for two integration directions) for an X-ray energy of 80 keV. PDF stands for powder diffraction file, which serve as a reference for our phases 2.*

Phase	HKL	Integration Direction	Powder Diffraction Files Values (°)	Experimental 2θ (°)	Difference (%)
$\alpha-$Zr (PDF number: 5-0665)	100	TD	3.1461	3.1460	−0.0032
		RD	3.1461	3.1447	−0.0445
δ-hydride(PDF number: 34-0649)	111	TD	3.1894	3.2032	0.4327
		RD	3.1894	3.2030	0.4264
$\alpha-$Zr (PDF number: 5-0665)	002	TD	3.4213	3.4191	−0.0643
		RD	3.4213	3.4211	−0.0058
$\alpha-$Zr (PDF number: 5-0665)	101	TD	3.5800	3.5800	0.0000
		RD	3.5800	3.5774	−0.0726
δ-hydride(PDF number: 34-0649)	200	TD	3.6818	3.6877	0.1602
		RD	3.6818	3.6853	0.0951
$\alpha-$Zr (PDF number: 5-0665)	102	TD	4.6484	4.6460	−0.0516
		RD	4.6484	4.6446	−0.0817
δ-hydride(PDF number: 34-0649)	220	TD	5.2098	5.2352	0.4875
		RD	5.2098	5.2334	0.4530
$\alpha-$Zr (PDF number: 5-0665)	110	TD	5.4486	5.4513	0.0496
		RD	5.4486	5.4484	−0.0037

and theoretical peak position in the hydrides could indicate that the hydrides are elastically strained in the compressive direction due to the thermal expansion mismatch between the hydrides and the α-zirconium matrix or that the hydrides have a slightly different stoichiometry than that reported in the literature.

If it is assumed that such a *d*-spacing change is caused by elastic strain, it is possible to estimate the stresses. When integrating the diffraction data obtained for this sample along the two particular directions, TD and RD, we obtain information on planes that are oriented perpendicular to these directions. Figure 6 shows the diffraction patterns integrated over the TD and RD for the sample shown in Fig. 5 (525 wt ppm of hydrogen). Only the 2θ region encompassing the $(111)_\delta$ and the $(100)_\alpha$ peaks is shown. The expected peak positions from Ref 2 are represented by the solid vertical lines. While the zirconium matrix peak is close to the expected peak position, the δ-hydride peak is shifted towards a lower *d*-spacing, suggesting that the hydrides precipitate particles are under a compressive strain. This is true both for hydrides oriented in the TD and the RD. The strain can be calculated from this difference in *d*-spacing by the following formula:

$$\varepsilon = (d_{\text{measured}} - d_{\text{PDF}})/d_{\text{PDF}} \tag{1}$$

where:

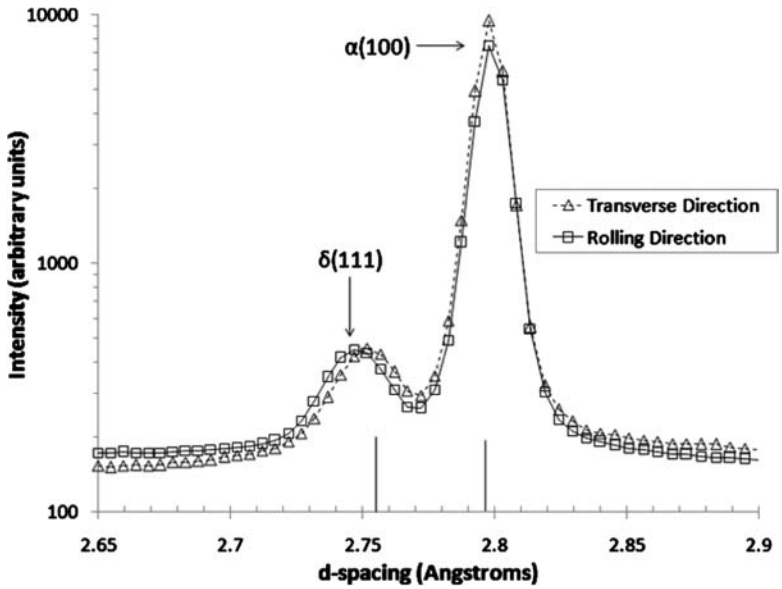


FIG. 6—*X-ray diffraction pattern of the two integration slices of a Zircaloy-4 sample with 525 wt. ppm of hydrogen (respective TD and RD angles of ±10°). The expected peak position for δ(111) and α(100) are represented by the solid vertical lines.*

ε = strain,
$d_{\text{measured}} = d$-spacing measured from X-ray diffraction, and
$d_{\text{PDF}} = d-$spacing reported in Ref 2.

For the TD we find $\varepsilon_{\text{TD}} = (2.752 - 2.76)/2.76 = -2.9 \times 10^{-3}$, and for the RD we find $\varepsilon_{\text{RD}} = (2.747 - 2.76)/2.76 = -4.7 \times 10^{-3}$. Using the values of ~ 100 GPa for the elastic constant of the δ-hydride [24] and ~ 0.322 for Poisson's ratio for the hydrides [25], the stresses were calculated in the two directions based on a tri-axial stress state. Using the plane strain assumption to account for the condition in the un-measured ND direction, we obtain $\sigma_{\text{TD}} = 740$ MPa in compression in the TD and $\sigma_{\text{RD}} = 870$ MPa in compression in the RD. For a plane stress condition, we find $\sigma_{\text{TD}} = 490$ MPa in compression in the TD and $\sigma_{\text{RD}} = 630$ MPa in compression in the RD. The actual stress state in the hydrides will be somewhere between the values obtained for the assumptions of plane stress and plane strain. Given the geometry of the hydrides platelets and the preferential orientation relationship between the hydrides and the matrix in the ND, we expect the hydrides to be closer to a plane strain condition than plane stress. Given the plane strain assumption, we obtain a maximum stress component of 870 MPa (in compression) that can be compared to the value of ~ 800 MPa obtained by Kerr *et al.* for hydride fracture under a tensile applied load 26. To compare the measured values with a yielding condition, we calculate the von Mises equivalent stress for a plane strain assumption (308 MPa) and for a plane stress assumption (570 MPa), both are somewhat below the hydride yield stress measured by Puls *et al.* of $\sim$ 500–800 MPa for hydride plasticity at room temperature using microhardness indentation [24].

A compressive stress state is expected for the hydrides since under stress-free conditions, since the hydride phase is less dense than the zirconium matrix from which it is formed (i.e., undergoes a volume expansion relative to the matrix). The fact that the hydride planes are slightly more stressed in the RD than in the TD could be due to the difference in the basal plane fraction in these two directions. If a direction contains a higher percentage basal poles aligned with it (within $\pm 10^{\circ}$), then the thermal expansion coefficient will be different in this direction compared to the other directions due to the anisotropic properties of zirconium 18, which could lead to small differences in the compression of the hydride planes as they precipitate upon cooling. In our sample, there is a higher fraction of basal poles parallel to the RD (typical recrystallized texture 18), thus leading to a larger thermal expansion coefficient and to higher compressive strains in the hydride in that direction.

The observation of the evolution of peak position and FWHM has been carried out systematically for samples that showed reoriented hydrides after thermal cycling under load and for samples that did not. Figures 7 and 8 compare the $(111)_{\delta}$ and $(220)_{\delta}$ hydride peaks for a sample that was heated and cooled under an applied tensile load of 75 MPa along the RD (no reorientation). In Fig. 7, it is observed that the $(111)_{\delta}$ peaks in the TD and the RD are initially of the same width and located approximately at the same peak position. After applying load in the RD, the $(111)_{\delta}$ peak in the RD appears to have shifted to a larger d-spacing, which is consistent with the fact that the planes in the RD are in tension. On the contrary, the planes in the TD have shifted towards a smaller d-

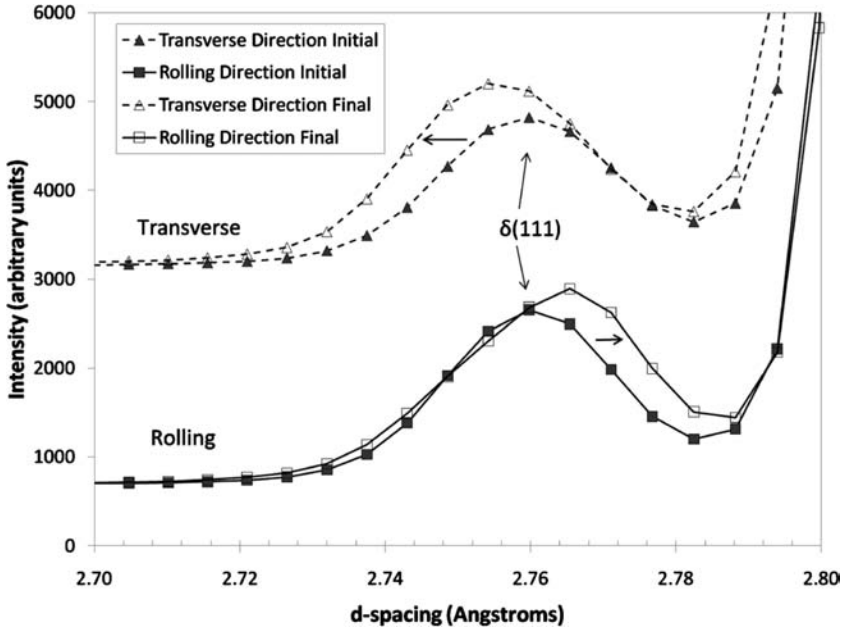


FIG. 7—*Diffraction patterns of a sample with 525 wt ppm of hydrogen at the initial state and after loading at 75 MPa (no reorientation). Close-up on the δ(111) hydride peak.*

spacing, implying that those planes are in compression. This is consistent with the fact that as a tensile load is applied in the RD, Poisson's ratio implies that the planes perpendicular to the RD (such as the TD planes) would be compressed. The same behavior is observed in the $(220)_\delta$ planes (Fig. 8). The RD planes shift to larger *d*-spacing (and thus they are in tension), while the TD planes shift towards a smaller *d*-spacing (and thus are in compression). It should also be noted that in their final state, we also observe a broadening of $(111)_\delta$ and $(220)_\delta$ RD peaks relative to the initial value but not of the peaks in the TD. This is most likely due to non-uniform strain broadening, as discussed below.

Figures 9 and 10 compare the diffraction patterns of two hydride peaks for a sample that was heated and cooled under an applied load of 85 MPa and that shows reoriented hydrides (as explained above, the reorientation has been characterized by image analysis, an image of the micrograph showing reorientation can be seen in Fig. 15). In Fig. 9, we can see that initially the $(111)_\delta$ peaks from the TD and the RD have the same width and approximately the same peak position (the slight shift could be due to residual stresses in the matrix that affected the hydrides as they precipitated). After the thermal cycle under load in which the hydrides were dissolved and reoriented, we observe that the RD peak has shifted to the tension side (larger *d*-spacing) and the TD peak has shifted to the compression side (smaller *d*-spacing), which is consistent with an applied

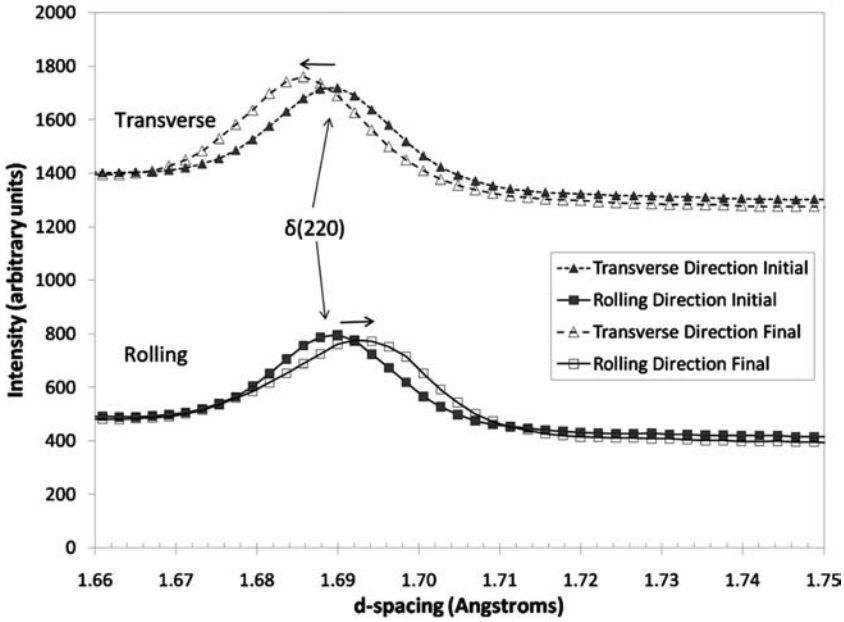


FIG. 8—*Diffraction patterns of a sample with 525 wt ppm of hydrogen at the initial state and after loading at 75 MPa (no reorientation). Close-up on the δ(220) hydride peak.*

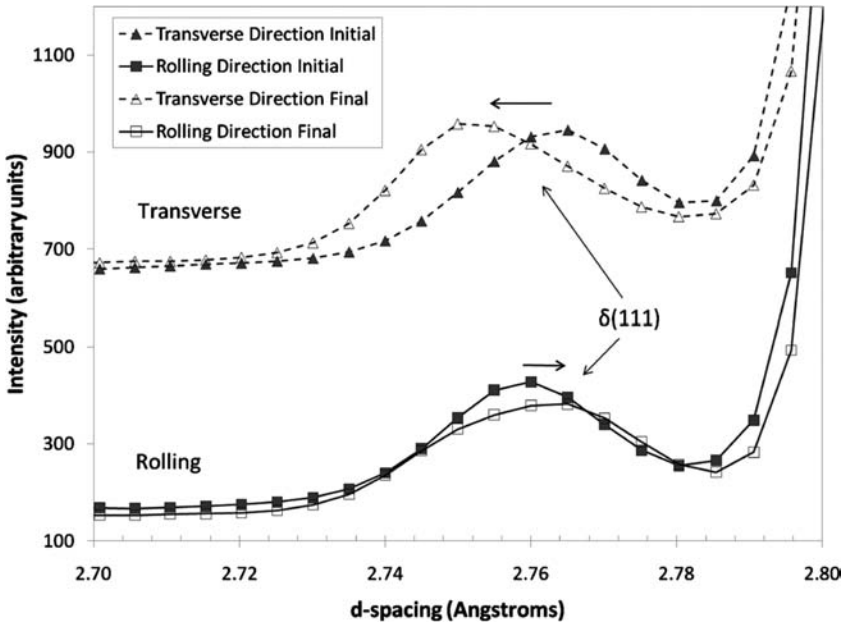


FIG. 9—*Diffraction patterns of a sample with 525 wt ppm of hydrogen at the initial state and after loading at 85 MPa (with reorientation). Close-up on the δ(111) hydride peak.*

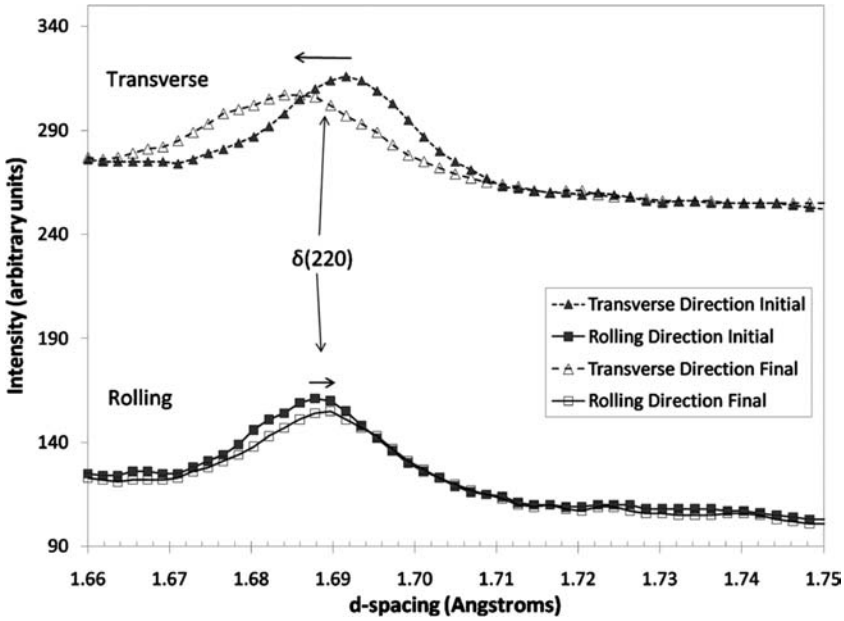


FIG. 10—*Diffraction patterns of a sample with 525 wt ppm of hydrogen at the initial state and after loading at 85 MPa (with reorientation). Close-up on the δ(220) hydride peak.*

tensile load in the RD. In addition, the RD peak is much broader after reorientation than before, whereas the TD peak width has not changed. In Fig. 10, the evolution of the $(220)_{\delta}$ peak is shown before and after reorientation. The same type of shift previously seen in Fig. 9 is observed, with the RD peak shifting to a

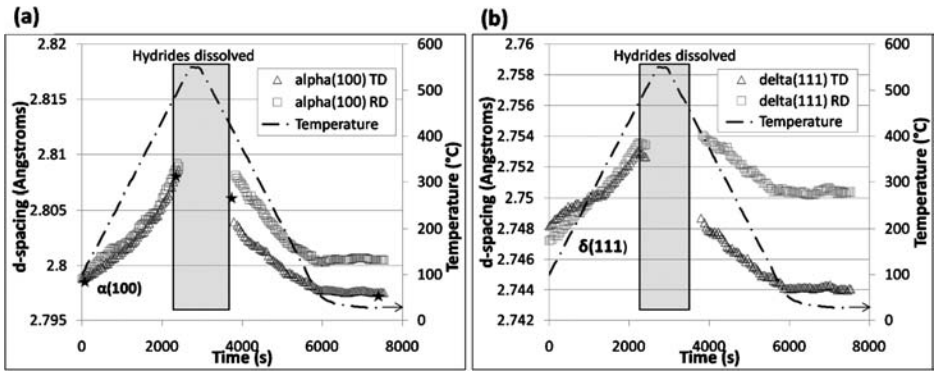


FIG. 11—*The d-spacing of* (a) *α(100) and* (b) *δ(111) peaks for a Zircaloy-4 sample with 520 wt ppm of hydrogen for hydrides precipitated under 75 MPa applied load in the RD without reorientation (the expected thermal expansion stars come from Ref 24).*

higher *d*-spacing and the TD peak shifting to a lower *d*-spacing. In this figure, however, the TD peak broadens significantly, whereas the RD peak has the same width before and after reorientation. The observed peak broadening is attributed to different strains in hydrides that are reoriented compared to strains in hydrides that are not reoriented, as discussed in more detail below.

Evolution of d-Spacing with Time and Temperature

Recording data while heating and loading enables us to observe the evolution of selected parameters with time and temperature. Figure 11(*a*), 11(*b*) shows the evolution of the *d*-spacing of the $(100)_\alpha$ peak and the $(111)_\delta$ peak for both integration directions for a sample heated and cooled under an applied load of 75 MPa. Factors influencing the lattice parameter include the temperature (thermal expansion), elastic stress/strain, and chemical composition. In the left-hand side of Fig. 11(*a*) and Fig. 11(*b*) (between 0 and 3000 s), the temperature steadily increases (at 0.2°C/s), which entails an increase of the *d*-spacing of the zirconium peaks by thermal expansion. Some expected points for the thermal expansion of the zirconium peaks [27] are plotted as stars for reference. Once at 550°C (around 3300 s), the tensile load is applied in the RD. When the load is applied, the RD peaks of both the zirconium and the hydride shift to a larger *d*-spacing, whereas the TD peaks of both phases shift to a smaller *d*-spacing. The shift away from the initial value of the hydride planes in the TD and the RD is $\sim 3.1 \times 10^{-3}$ Å. That of the zirconium planes in the TD and the RD is $\sim 1.5 \times 10^{-3}$ Å.

In Fig. 12, the same graphs shown in Fig. 11 are plotted for a sample that showed partial reorientation after being loaded at 85 MPa during cooling. The $(100)_\alpha$ and $(111)_\delta$ peaks behave similarly, as shown in Fig. 11: When the load is applied, the RD peaks shift to a larger *d*-spacing than initially, whereas the TD peaks shift to a smaller *d*-spacing than initially. The previous observations are confirmed by Fig. 13 where the same plots as in Figs. 11 and 12 are shown for a sample partially reoriented under 100 MPa load. In this case, we observe the same expected behavior for the zirconium peaks and for the hydride peaks. The last point of the graphs (after 1500 s) was recorded under zero applied load. We see that the hydride peaks are still shifted with respect to their initial peak position, indicating that this difference in strain is caused by permanent strain in the hydrides rather than by elastic stress from the applied load.

Intensity and Full-Width at Half Maximum Evolution with Time and Temperature

Observing the evolution of the integrated intensity and the FWHM for the $(111)_\delta$ hydride peaks with time and temperature can give additional information on the dissolution and precipitation of hydrides and on the broadening of the peaks. The evolution of the FWHM and the integrated intensity of the $(111)_\delta$ is presented in Fig. 14 for both TD and RD as a function of time for a sample heated and cooled under 75 MPa applied load. In this case, the hydride particles did not undergo reorientation. The temperature curve is shown as a dotted line, linked to the right-hand ordinate axis. The tensile load was applied in the RD

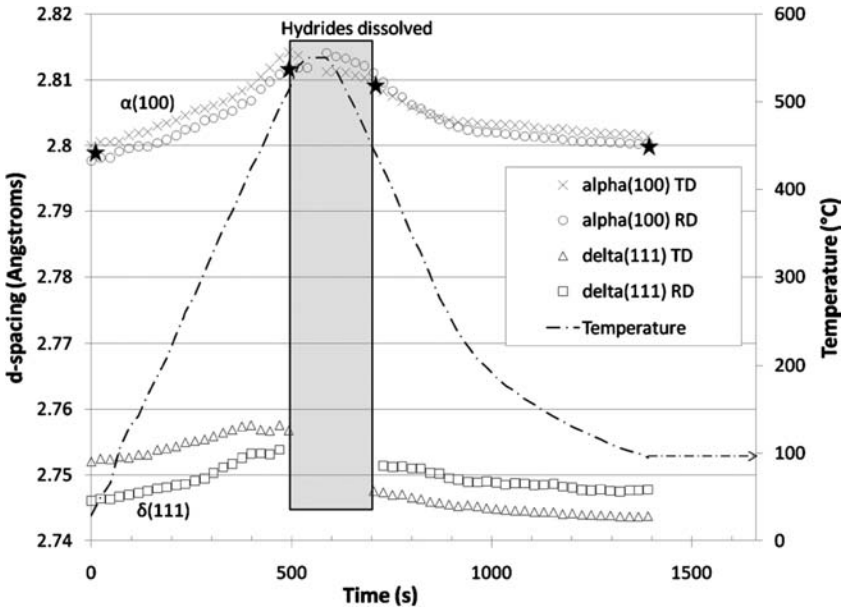


FIG. 12—*The d-spacing of α(100) and δ(111) peaks for a Zircaloy-4 sample with 525 wt ppm of hydrogen cooled under 85 MPa applied load in the RD (the stars indicate the expected thermal expansion stars come from Ref 24). This cycle resulted in hydride reorientation.*

once the sample temperature reached 550°C as shown in the bottom of the figure and most of the hydrides were dissolved. The load was kept constant thereafter. The metallographs of the cross section of the sample taken before and after the experiment are also shown in Fig. 14 (it should be noted that metallography was performed on the exact same sample before and after the X-ray diffraction experiment; after the first metallographic observation, the sample was repolished to remove any effect from etching). On both of these metallographs, the hydride platelets are perpendicular to the ND, confirming that no hydride reorientation has occurred. In this figure, we can follow the dissolution of the hydride particles as the hydride peak intensity curve decreases as the temperature reaches $\sim$ 550°C and returns to higher values upon cooling.

The examination of the changes in the $(111)_\delta$ peak FWHM can be related to strain or size broadening. Initially, the FWHM for both TD and RD are similar (as also shown in Fig. 7). When the hydrides start to dissolve, the $(111)_\delta$ hydride peak FWHM diminishes. This could be because since the hydrides are smaller, they are less strained in the zirconium matrix or because the most strained hydrides dissolve preferentially. The shape of the hydride particles dissolving could also be changing, leading to a lower strain on the hydride planes. When cooling under load, as the hydride particles reprecipitate, the FWHM increases. This is likely due to strains developed during the hydride growth process due to

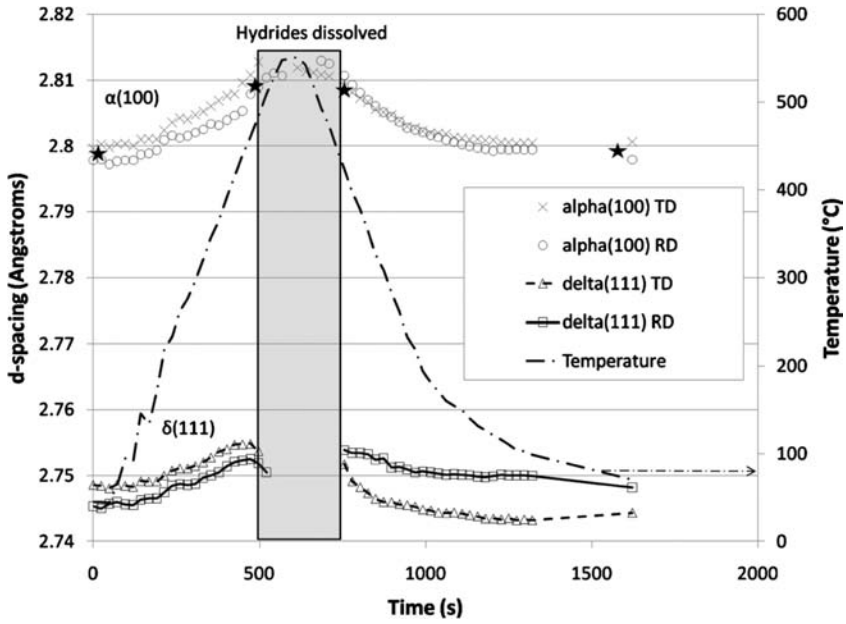


FIG. 13—*The d-spacing of α(100) and δ(111) peaks for a Zircaloy-4 sample with 525 wt ppm of hydrogen cooled under 100 MPa applied load in the RD (the expected thermal expansion stars come from Ref 24). This cycle resulted in hydride reorientation.*

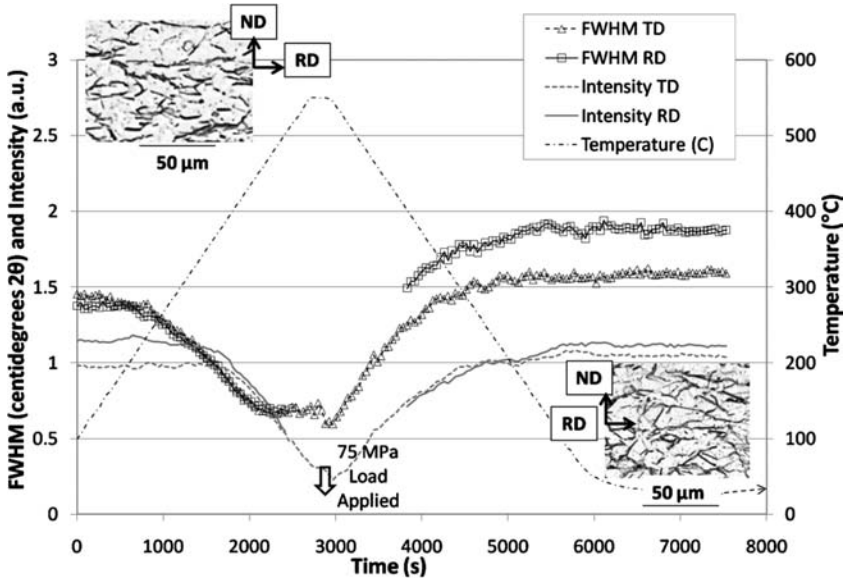


FIG. 14—*Time evolution of the FWHM (and intensity) of the δ(111) peaks of a Zircaloy-4 sample with 525 wt ppm of hydrogen heated and cooled under 75 MPa applied load in the RD (no reorientation of hydrides). The applied load and temperature are also shown.*

the thermal expansion mismatch between the hydrides and the matrix. As the temperature decreases, the hydrides contract faster than the matrix, thus implying a higher strain on the precipitates and a higher strain broadening (the thermal expansion coefficient of the hydrides is $\alpha_{\text{hydrides}} = 14.2 \times 10^{-6}/^{\circ}\text{C}$ and that of α-zirconium is $\alpha_{\text{Zr}} = 6 \times 10^{-6}/^{\circ}\text{C}$ [18]). Once the load is applied in the RD, the FWHM in both directions increases as strain develops in the hydride particles in both the TD and the RD. Since the hydrides are under a tensile load in the RD, a TD strain results from Poisson's ratio, and thus both integration directions exhibit broadening. This broadening is likely tensile in the RD and compressive in the TD, although this cannot be readily determined from the diffraction peak widths.

Similar curves were plotted for samples cooled under 85 and 100 MPa, respectively. in Figs. 15 and 16. The analysis of the hydride peak intensities before and after heat treatment, performed using GSAS, shows that the diffracted intensities of the hydride peaks for the reoriented samples do not change significantly. The study of the peak shape (specifically peak broadening), however, was able to provide a consistent "diffraction signature" associated with reoriented hydride particles. The metallographs taken before and after the 85 MPa experiment are represented in Fig. 15. Initially, the hydrides platelets are oriented in the circumferential direction with their normal parallel to ND. After

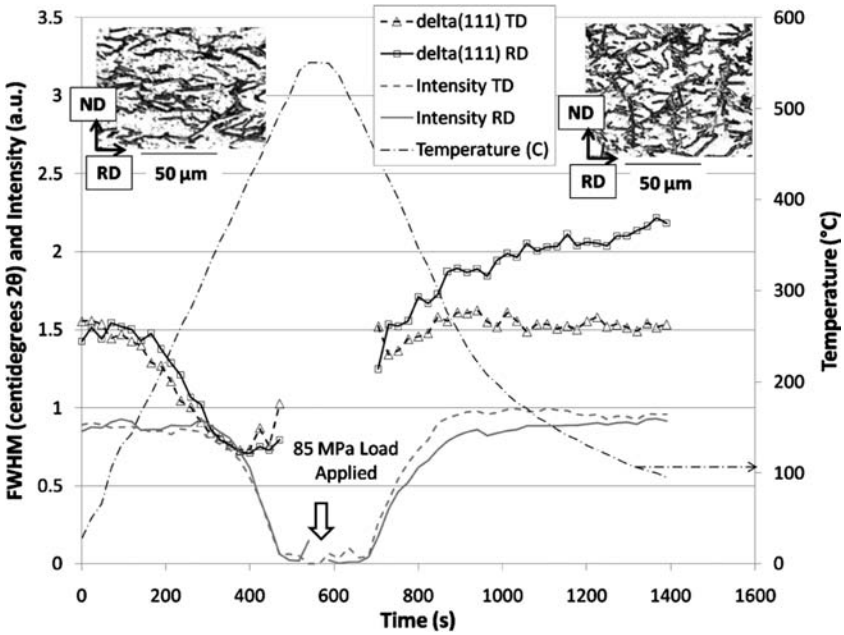


FIG. 15—*Time evolution of the FWHM (and intensity) of the δ(111) peaks of a Zircaloy-4 sample with 525 wt ppm of hydrogen heated and cooled under 85 MPa applied load in the RD (this resulted in hydride reorientation). The applied load and temperature are also shown.*

the experiment (metallograph on the right-hand side of Fig. 15), some hydrides have reoriented and are now perpendicular to the load axis (which is the RD). Figure 15 shows that the hydride $(111)_\delta$ peak FWHM for the TD bank returns to its initial value after reprecipitation. However, for the peaks in the RD, the FWHM after reprecipitation is larger than previously and continues to increase as the temperature decreases below 150°C. This behavior is also observed for the sample held at 100 MPa (Fig. 16). This particular behavior of the RD bank of the hydrides is only observed in samples where hydride reorientation occurs and can therefore be considered a "signature" of reoriented hydride samples. The difference in the reoriented hydrides is that the broadening of the $(111)_\delta$ peak is *larger* in the RD than in the TD and increases continuously at the temperature decreases. We should note that the diffraction signal of the RD bank after hydride reorientation comes both from $(111)_\delta$ planes whose normals are *aligned* with the stress and planes whose normals are *perpendicular* to the applied stress. In contrast, the signal for the TD bank comes only from $(111)_\delta$ planes whose normal are perpendicular to the stress. As explained below, the peak broadening of the hydride peaks is likely due to strain broadening for the cases studied here. Since size broadening is shown not to be a factor (see next section), a plausible explanation for the broadening difference between the RD and the TD is that more strain (either plastic or elastic) is accumulated in the direction normal to the hydride platelet as it precipitates and grows than in the

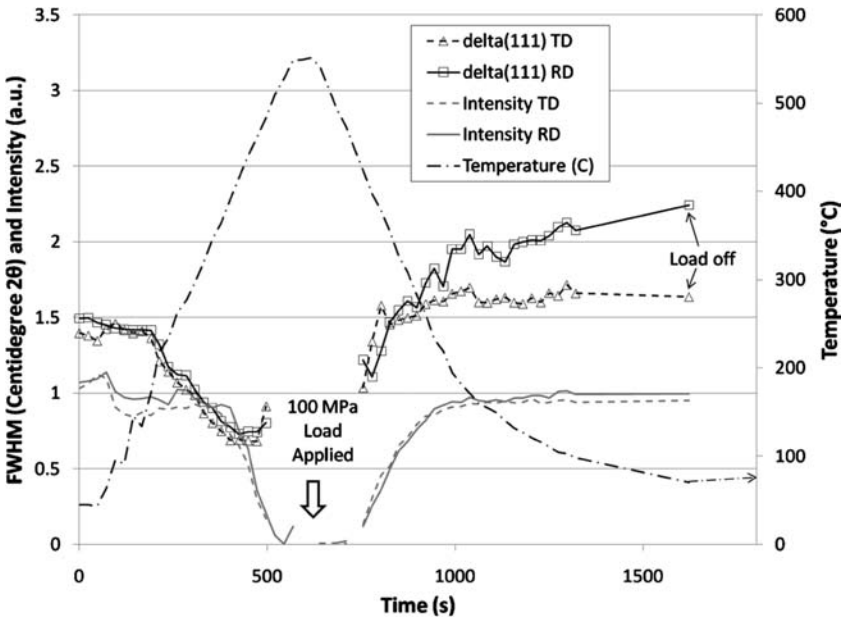


FIG. 16—*Time evolution of the FWHM (and intensity) of the δ(111) peaks of a Zircaloy-4 sample with 525 wt ppm of hydrogen heated and cooled under 100 MPa applied load in the RD (this resulted in hydride reorientation). The applied load and temperature are also shown.*

other direction. In fact, this is where the strain is most likely to accumulate during the plate-like precipitate growth 28. The examination of Fig. 16 shows that even after the stress was removed towards the end of the run, the observed broadening remained, which suggests that the strain causing the broadening is likely *plastic* strain, likely in the form of dislocations, although there will also be a contribution from residual elastic strain (stress) due to the size and shape misfit between the precipitates and matrix.

Williamson–Hall Plots

The broadening observed in the previous graphs can be caused by several factors. Strain broadening and size broadening both could cause the broadening observed during our experiment (once instrumental broadening has been taken out). In order to quantitatively differentiate between strain and size broadening and to better understand the general state of strain of the hydrides, an analysis was carried out using Williamson–Hall plots [23]. The following relations allow us to distinguish between the two types of broadening [23]:

$$\mathrm{FWHM}_{\mathrm{sample}} \propto \varepsilon \frac{\sin\theta}{\cos\theta} \ \text{strain broadening} \tag{2}$$

$$\mathrm{FWHM}_{\mathrm{sample}} \propto \frac{0.9\lambda}{t\cos\theta} \ \text{size broadening} \tag{3}$$

where:

$\mathrm{FWHM}_{\mathrm{Sample}}$ = measured FWHM minus the instrumental broadening (in radians 2θ),

θ = Bragg angle (in radians),

ε = lattice strain,

t = sample particle size (in nanometre), and

λ = X − ray beam wavelength (in nanometre).

A Williamson–Hall plot presents FWHM $\times \cos\theta$ (noted B) as a function of $\sin\theta$ for different peaks of the same phase. Strain broadening varies with the 2θ value of the peak under consideration, whereas size broadening is independent of angle when plotted in the Williamson–Hall plots. Therefore, the slope of the curves plotted is proportional to strain, and the y-intercept is proportional to the amount of size broadening [23]. A Williamson–Hall plot is presented in Fig. 17(*a*) for the same Zircaloy-4 sample as observed previously with 525 wt ppm of hydrogen for hydrides precipitated at slow cooling rate under no load and shown in Fig. 6. Only two, $(111)_\delta$ and $(220)_\delta$, out of the three hydride peaks are used in these graphs since the third hydride peak $(200)_\delta$ is too small and is highly convoluted with a very large α-zirconium peak and thus its shape cannot be fitted properly. By fitting the two points to a linear curve, we observe that the y-intercept is close to zero for both TD and RD. This implies that there is negligible size broadening of the hydride peaks. This is likely because the hydride particles we are detecting are too big to induce significant size broadening. The

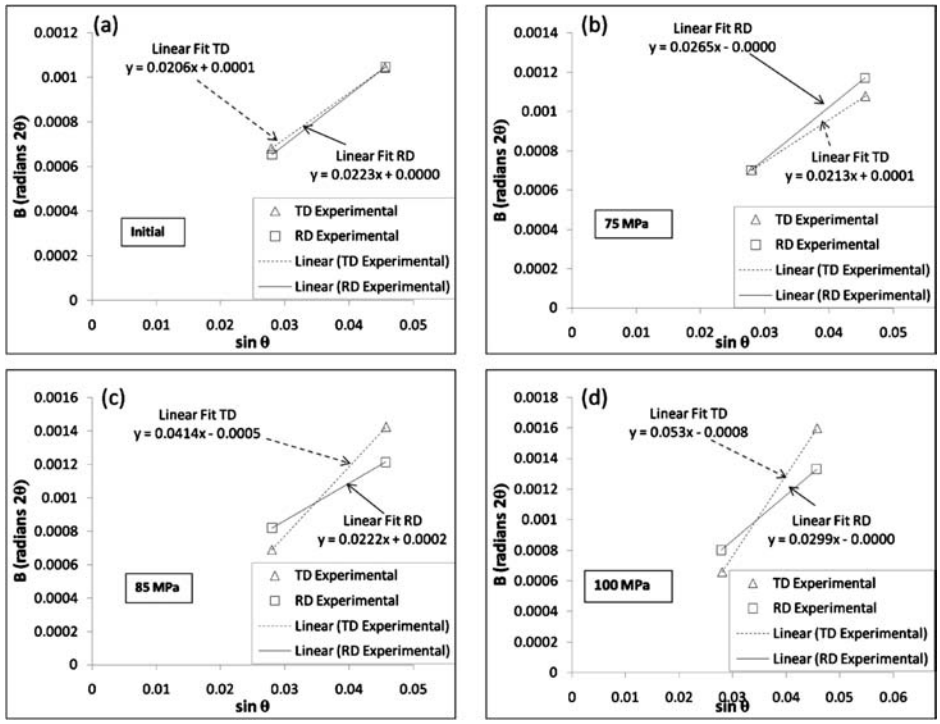


FIG. 17—*Williamson–Hall plot for the final state of a Zircaloy-4 with 525 wt ppm of hydrogen heated up 550°C and cooled:* (a) *Under no load;* (b) *under 75 MPa applied load in the RD (no reorientation);* (c) *under 85 MPa applied load in the RD (hydride reorientation); and* (d) *under 100 MPa applied load in the RD (hydride reorientation).*

slopes of the fitted line in Fig. 17(*a*) are similar for both TD and RD. This is consistent with the previous observation from the *d*-spacing calculation that both directions are strained to a similar amount, although the RD is slightly more strained than the TD (probably due to the presence of more basal planes of the zirconium matrix in the RD).

Figure 17(*b*) shows the Williamson–Hall plot for a diffraction pattern taken from a sample loaded at 75 MPa and taken at time $t = 7500$ s, which corresponds to the final data point in Fig. 14. Similarly to Fig. 17(*a*), no hydride size broadening is observed in this sample. The slopes of the curve have increased slightly, suggesting that more strain accumulates in the hydrides as they are pulled in tension. Also, the hydride peaks in the RD seem to be more strained than the ones in the TD with a very large broadening of the $(220)_\delta$ peak. This means that the $(220)_\delta$ peaks oriented perpendicular to the loading direction are more strained than the $(111)_\delta$ peaks oriented in the same direction. This is likely due to different strain accommodation in the hydride platelet (the $(111)_\delta$ direction comes out of the hydride platelet).

Figure 17(*c*), 17(*d*) shows Williamson–Hall plots for the 85 MPa and the 100 MPa reoriented samples, respectively. Again, no size broadening is observed. The analysis of the slopes from Fig. 17(*c*), 17(*d*) compared to those in Fig. 17(*a*) suggests that the strain is larger on the TD than the RD (higher slope). This is paradoxical, considering the larger strain broadening observed in the $(111)_\delta$ in Figs. 15 and 16. However, because hydride reorientation was not complete (half of the hydrides present at the end are in-plane hydrides), it is likely that much of the $(220)_\delta$ peak intensity in the RD comes from in-plane hydrides. The analysis mentioned above is only properly valid if the same hydride particle contributes to the intensity of both $(111)_\delta$ and $(220)_\delta$. To summarize, the data is consistent with greater strain observed in the direction normal to the hydride platelets.

In summary, the observed strain in the direction normal to the hydrides platelets is likely caused by a combination of the accommodation of size-mismatch (volume expansion during hydride precipitation) and differential thermal expansion of the hydrides and matrix. The data collected in this study shows an identifiable diffraction signature for hydride reorientation. The main feature of this signature is that the FWHM continues to increase in the RD with time as the temperature decreases, whereas the FWHM remains unchanged in the TD. The second observation is that the strain in the TD is much higher than that in the RD. The *d*-spacing behavior of reoriented hydrides is the same as the behavior for samples under tensile stress without reorientation. This implies that this reorientation signature is not due to differences in the *d*-spacings but to another phenomenon. A possible explanation is that the diffraction signal from the $(220)_\delta$ peaks comes mostly from circumferential hydrides, whereas the diffraction signal from the $(111)_\delta$ peaks comes mostly from reoriented hydrides.

Conclusions

Detailed X-ray diffraction measurements were performed on various hydrided zirconium alloys samples using synchrotron radiation. The objective of the study was to understand the state of strain of hydrides as they precipitate in a zirconium matrix under load and when reorienting. The secondary objective of this study was to determine if there is a diffraction signature associated with hydride reorientation. Both in situ and ex situ experiments were performed on samples of different orientations, under different levels of load, and the results were compared to metallographical examination. The hydride strain was measured by comparing both *d*-spacing variations and the hydride peak broadening. The conclusions are as follows.

(1) Hydrides particles precipitated under zero applied load are strained in compression in both directions (TD and RD), but the stresses remain in the elastic regime.

(2) The analysis of the dependence of the observed hydride peak broadening on $\sin\theta$ indicates that most of the hydride peak broadening is caused by strain rather than by size. This is true both in the as-prepared

hydrided samples and in those that underwent heat treatment and cooling under stress.

(3) When hydrides are heated and stressed in the RD during cool-down but do not reorient, the peak FWHM in the TD and in the RD changes in a constant manner (i.e., reaches a plateau) relatively to the initial value. The variations in the hydride plane *d*-spacing are consistent with the planes whose normals are parallel to the loading axis (RD) being under tension and those whose normals are perpendicular to the loading axis (TD) being under compression.

(4) A distinct diffraction signature associated with hydride reorientation has been identified for hydrided Zircaloy-4 samples, which are heated and cooled under stress applied in the RD. This signature is present only when the sample is cooled under an applied stress sufficient to reorient hydrides. The FWHM of the $(111)_\delta$ hydride peaks in the RD and TD is markedly different in samples with reoriented hydrides compared to those in which reorientation did not occur. In samples where reorientation occurred, the FWHM of the $(111)_\delta$ peaks in the TD returns to the initial value upon cooling, while that for the RD increases steadily as temperature is lowered and precipitation proceeds. In contrast, in the non-reoriented samples, the FWHM of the $(111)_\delta$ peaks *for both TD and RD* return to the original value.

Acknowledgments

This research was funded by the Materials World Network Grant No. DMR-0710616 from the National Science Foundation, with corresponding funding from NSERC for the Canadian partners. The writers are grateful for their support. The research for this publication was supported by the Pennsylvania State University Materials Research Institute Nano Fabrication Network and the National Science Foundation Cooperative under Agreement No. 0335765, National Nanotechnology Infrastructure Network, with Cornell University. The use of the Advanced Photon Source was supported by the U.S. Department of Energy, Office of Basic Energy Sciences under Contract No. DE-AC02-06CH11357.

References

[1] Coleman, C. E. and Hardie, D., "The Hydrogen Embrittlement of [Alpha]-Zirconium—A Review," *J. Less-Common Met.*, Vol. 11(3), 1966, pp. 168–185.

[2] International Center for Diffraction Data, The Powder Diffraction File, Newton Square, PA, 2006.

[3] Bradbrook, J. S., Lorimer, G. W., and Ridley, N., "The Precipitation of Zirconium Hydride in Zirconium and Zircaloy-2," *J. Nucl. Mater.*, Vol. 42(2), 1972, pp. 142–160.

[4] Beck, R. L., "Zirconium-Hydrogen Phase System," *Transactions of the ASME*, Vol. 55, 1962, pp. 542–555.

[5] Perovic, V., Weatherly, G. C., and Simpson, C. J., "Hydride Precipitation in [a]/[b] Zirconium Alloys," *Acta Metall.*, Vol. 31(9), 1983, pp. 1381–1391.

[6] Chung, H. M., Daum, R. S., Hiller, J. M., and Billone, M. C., "Characteristics of Hydride Precipitation in Spent-Fuel Cladding," *Zirconium in the Nuclear Industry: 13th International Symposium, ASTM STP 918*, 2002, ASTM International, West Conshohocken, PA, pp. 78–101.

[7] Ells, C. E., "Hydride Precipitates in Zirconium Alloys (A Review)," *J. Nucl. Mater.*, Vol. 28(2), 1968, pp. 129–151.

[8] Kearns, J. J. and Woods, C. R., "Effect of Texture, Grain Size, and Cold Work on the Precipitation of Oriented Hydrides in Zircaloy Tubing and Plate," *J. Nucl. Mater.*, Vol. 20(3), 1966, pp. 241–261.

[9] Singh, R. N., Kishore, R., Singh, S. S., Sinha, T. K., and Kashyap, B. P., "Stress-Reorientation of Hydrides and Hydride Embrittlement of Zr-2.5 wt% Nb Pressure Tube Alloy," *J. Nucl. Mater.*, Vol. 325(1), 2004, pp. 26–33.

[10] Hardie, D. and Shanahan, M. W., "Stress Reorientation of Hydrides in Zirconium-2.5 % Niobium," *J. Nucl. Mater.*, Vol. 55(1), 1975, pp. 1–13.

[11] Kammenzind, B. F., Berquist, B. M., Bajaj, R., Kreyns, P. H., and Franklin, D. G., "The Long-Range Migration of Hydrogen Through Zircaloy in Response to Tensile and Compressive Stress Gradients," *Zirconium in the Nuclear Industry: 12th International Symposium, ASTM STP 1354*, 2000, ASTM International, West Conshohocken, PA, pp. 196–233.

[12] Daum, R. S., Chu, Y. S., and Motta, A. T., "Identification and Quantification of Hydride Phases in Zircaloy-4 Cladding Using Synchrotron X-Ray Diffraction," *J. Nucl. Mater.*, Vol. 392(3), 2009, pp. 453–463.

[13] Kerr, M., Daymond, M. R., Holt, R. A., Almer, J. D., and Stafford, S., "Observation of Growth of a Precipitate at a Stress Concentration by Synchrotron X-Ray Diffraction," *Scr. Mater.*, Vol. 62(6), 2010, pp. 341–344.

[14] Kerr, M., Daymond, M. R., Holt, R. A., Almer, J. D., Stafford, S., and Colas, K. B., "Fracture of a Minority Phase at a Stress Concentration Observed with Synchrotron X-Ray Diffraction," *Scr. Mater.*, Vol. 61(10), 2009, pp. 939–942.

[15] Turski, M., Bouchard, P. J., Steuwer, A., and Withers, P. J., "Residual Stress Driven Creep Cracking in AISI Type 316 Stainless Steel," *Acta Mater.*, Vol. 56, 2008, pp. 3598–3612.

[16] Daymond, M. R., Young, M. L., Almer, J. D., and Dunand, D. C., "Strain and Texture Evolution During Mechanical Loading of a Crack Tip in Martensitic Shape-Memory NiTi," *Acta Mater.*, Vol. 55(3929), 2007, pp. 3929–3942.

[17] Pierron, O. N., Koss, D. A., Motta, A. T., and Chan, K. S., "The Influence of Hydride Blisters on the Fracture of Zircaloy-4," *J. Nucl. Mater.*, Vol. 322(1), 2003, pp. 21–35.

[18] Douglass, D. L., "The Metallurgy of Zirconium," *Atomic Energy Review*, Z. I. Turkov, Ed., International Atomic Energy Agency, Vienna, Austria, 1971.

[19] Raynaud, P. A. C., *Crack Growth Through the Thickness of Thin-Sheet Hydrided Zircaloy-4*, Ph.D. Thesis, The Pennsylvania State University, University Park, 2009.

[20] McMinn, A., Darby, E. C., and Schofield, J. S. "The Terminal Solid Solubility of Hydrogen in Zirconium Alloys," *Zirconium in the Nuclear Industry: 12th International Symposium, ASTM STP 1354*, 2000, ASTM International, West Conshohocken, PA, pp. 173–195.

[21] Haeffner, D. R., Almer, J. D., and Lienert, U., "The Use of High Energy X-Rays from the Advanced Photon Source to Study Stresses in Materials," *Mater. Sci. Eng., A*, Vol. 399(1–2), 2005, pp. 120–127.

[22] Larson, A. C. and Von Dreele, R. B., *General Structure Analysis System (GSAS)*, Los Alamos National Laboratory, Los Alamos, NM, Report LAUR 86-748, 2000.

[23] Snyder, R. L., Fiala, J., and Bunge, H., *Defect and Microstructure Analysis by Diffraction*, International Union of Crystallography Monographs on Crystallography, Oxford University Press, New York, NY, 1999.

[24] Puls, M. P., Shi, S.-Q., and Rabier, J., "Experimental Studies of Mechanical Properties of Solid Zirconium Hydrides," *J. Nucl. Mater.*, Vol. 336(1), 2005, pp. 73–80.
[25] Yamanaka, S., Yamada, K., Kurosaki, K., Uno, M., Takeda, K., Anada, H., Matsuda, T., and Kobayashi, S., "Characteristics of Zirconium Hydride and Deuteride," *J. Alloys Compd.*, Vol. 330–332, 2002, pp. 99–104.
[26] Kerr, M., Daymond, M. R., Holt, R. A., and Almer, J. D., "Strain Evolution of Zirconium Hydride Embedded in a Zircaloy-2 Matrix," *J. Nucl. Mater.*, Vol. 380(1–3), 2008, pp. 70–75.
[27] Yamanaka, S., Yoshioka, K., Uno, M., Katsura, M., Anada, H., Matsuda, T., and Kobayashi, S., "Thermal and Mechanical Properties of Zirconium Hydride," *J. Alloys Compd.*, Vol. 293–295, 1999, pp. 23–29.
[28] Massih, A. R. and Jernkvist, L. O., "Stress Orientation of Second-Phase in Alloys: Hydrides in Zirconium Alloys," *Comput. Mater. Sci.*, Vol. 46, 2009, pp. 1091–1097.

DISCUSSION

Question 1, Ted Darby, Rolls-Royce:—Did you observe any effect of stress on the hydride dissolution (Tssd) and precipitation (Tssp) temperatures? If so, how significant was the effect?

Author's Response:—We performed some preliminary experiments that indicate some effect of applied stress on the precipitation temperature, but little effect on the dissolution temperature. Further studies are needed to better quantify this effect.

Question 2, Bo Cheng, EPRI:—What is the solubility limit of hydrogen that the SXRD technique can detect?

Author's Response:—It has been found by some of our collaborators [Vizcaino] that samples containing 20 wt.ppm of hydrogen produce a measurable diffraction signal when examined with synchrotron radiation.

[Vizcaino] Vizcaino P., Banchik A.D., Abriata J.P., Journal of Material Science, Vol. 42, No. 16, pp. 6633-6637, 2007.

Question 3, David Dye, Imperial College, UK:—1) Aren't the packets of hydrides composed of platelets ~10 nm × 100 nm in size? So, I would expect to see some size broadening, which you don't appear to see. What is the implication, if any? 2) Strain broadening is conventionally due to the strain field around the defects such as dislocations. Do your results therefore suggest that some of the hydrides are plastically deforming?

Author's Response:—1) Given our temperature history, our smaller hydrides that stack up to compose the large hydrides are about 40 nm × 200 nm. The broadening for this size of particles would be of at the maximum 3.4×10^{-4} radians. The instrumental broadening has been measured by the use of a ceria powder standard to be approximately 3.8×10^{-5} radians (in 2θ). The typical full-width at half-maximum for our samples once the instrumental broadening has been taken out is 2.6×10^{-4} radians (in 2θ). This means that indeed some size broadening could be expected. The fact that it is not observed could imply either that the smaller hydrides are actually larger than this value or that this size of particle would not lead to a broadening significant enough to be detected by our technique.

2) Strain broadening can also arise from non-uniform states of strain in the particle (for example due to local grain neighborhood effects) or represent a distribution of strains in a population of particles. It is not necessarily linked to plastic deformation in the hydride itself although we have interpreted it as such, and other authors have suggested plasticity in hydrides e.g. [Arsene].

[Arsene] S. Arsene, J. Bai and P. Bompard, Met. Mat. Trans. A, v34A, pp. 579-588 (2003).

Question 4, Joe Rashid, Anatech:—1) Can this technique be adapted to hydride reorientation under variable stress? 2) Secondly, the stress level used is almost at the threshold value for reorientation. Do you plan to extend your work to higher stresses? 3) Thirdly, it would be interesting to use your technique to measure the solubility limits (dissolution and precipitation), and to determine whether they depend on stress.

Author's Response:—1) In principle this technique could certainly be used under variable stress. However, this would render the data analysis much more complex.

2) Yes, we plan to extend our work to stresses high enough to reorient 100% of hydrides. These stresses would likely be around 75–85% of the yield stress of the material.

3) This technique has indeed been used to obtain some preliminary measurements of the solubility limits and the effect of stress on those. These preliminary results are presented in a paper recently accepted in Acta Materialia entitled: In-situ study of hydride precipitation kinetics and re-orientation in Zircaloy using synchrotron radiation.

Question 5, Shioro Ishino, University of Tokyo (retired):—Have you studied the effect of repeated temperature cycles? Dislocation existing around hydrides may cause memory effect, which will become apparent in the repeated experiments. If the maximum temperature of the temperature cycle goes to around 600ºC or above, the memory effect will disappear.

Author's Response:—This is indeed a very interesting phenomenon that could be observed using the in-situ synchrotron technique. Some preliminary runs of repeated temperature cycles have been performed and it seems that the precipitation temperature is more affected than the dissolution temperature by repeating temperature cycles. Further studies are underway to study this effect in more detail.

Question 6, Mirco Grosse, Karlsruhe Institute of Technology, Germany:—Can you exclude a sub-stoichiometric hydride as the reason for the measured peak shift?

Author's Response:—A sub-stoichiometric hydride is an alternate explanation for the observed peak shift. However, from the literature on similar material and temperature history, the expected hydride in our sample is the delta phase ZrH_x with x ~ 1.66. It is also expected that the hydrides would be in elastic compression in the material so explaining the observed peak shift by a reasonable value of elastic strain in the hydride phase seems appropriate.

Question 7, Javier Romero, Westinghouse Electric Sweden AB:—Did you notice changes in crystallographic orientation (hydrides) during the tests or between reoriented and non-reoriented hydrides? This is, is the crystallographic orientation of the hydrides the same before and after reorientation?

Author's Response:—The individual hydride orientation and orientation relationship cannot be determined in a straight forward manner using our diffraction data. This comes from the fact that several planes with the same multiplicity participate in the hydride diffraction pattern and we are probing a large diffraction volume (transmission X-ray diffraction with 200×200 microns beam spot size). To answer this question, transmission electron microscopy would be the most appropriate tool.

Question 8, Suresh K. Yagnik, EPRI:— Have you observed hydride behavior during heat up as they tend to become ductile from the brittle behavior at room temperature? Is it possible to deduce or confirm this anticipated behavior from your diffraction data?

Author's Response:—To discern between 'ductile' and 'brittle' behavior at different temperatures we would have to compare the plastic strain in the hydrides at these two temperatures. Since fracture is not observed in our experiments, it would not be an easy task to perform the measurements proposed.

Question 9, Young Suk Kim:—Please comment on if the gamma hydride is observed in your experiment. If not, could you comment why?

Author's Response:—The gamma hydride was not observed in our experiment. Only delta hydrides, determined using the powder diffraction file number 00-034-0649 were identified. We did not expect gamma hydride in this experiment because our material is not submitted to favorable conditions for gamma formation such as quenching, long hold at temperature or high levels of hydrogen contents.

Reprinted from JAI, Vol. 8, No. 1
doi:10.1520/JAI102957
Available online at www.astm.org/JAI

S. Valance,[1] *J. Bertsch,*[2] *and A. M. Alam*[3]

Statistical Analysis of Hydride Reorientation Properties in Irradiated Zircaloy-2

ABSTRACT: The orientation of hydrides in fuel cladding determines the anisotropic fracture behavior of Zircaloy and the failure modes of cladding tubes. Approach coupling experiments using the cladding tube deformation test and finite element analysis have successfully led to the quantification of the stress influencing reorientation of hydrides in unirradiated samples. An improved version of this procedure was applied to six samples of irradiated Zircaloy-2 from two different rods with three classes of thermo-mechanical loading. It was found that at medium maximum temperature, when no more than half of the hydrides were dissolved, the mechanical loading showed no measurable effect. When most of the hydrides were dissolved, the orientation and location of the hydrides depended strongly on the mechanical loading: The hydrides spatial location followed the hoop tensile stress. When the number of loading cycles was raised, the fraction of radial hydrides increased even for very low hoop tensile stress. The inner side of the cladding showed a marked depletion of hydrides whatever the size of the hoop stress. Since our test setup involved a tri-axial stress state, the possible influence of the other components of the stress tensor was evaluated. Through the use of a classical nucleation law, it was shown that for our test setup, the hoop stress was the important mechanical quantity. Therefore, the inner side depletion of hydrides may be attributed to three other factors: Residual stress, a memory effect, and a pumping effect by the inner liner.

KEYWORDS: Zircaloy-2, hydrides, reorientation, irradiated, fuel cladding

Manuscript received January 8, 2010; accepted for publication September 29, 2010; published online December 2010.

[1] Dept. of Nuclear Energy and Safety, Laboratory for Nuclear Materials, Paul Scherrer Institut, CH-5232 Villigen PSI, Switzerland (Corresponding author), e-mail: Stephane.Valance@psi.ch
[2] Dept. of Nuclear Energy and Safety, Laboratory for Nuclear Materials, Paul Scherrer Institut, CH-5232 Villigen PSI, Switzerland.
[3] Alstom Power, 5401 Baden, Switzerland.

Cite as: Valance, S., Bertsch, J. and Alam, A. M., "Statistical Analysis of Hydride Reorientation Properties in Irradiated Zircaloy-2," *J. ASTM Intl.*, Vol. 8, No. 1. doi:10.1520/JAI102957.

Copyright © 2011 by ASTM International, 100 Barr Harbor Drive, PO Box C700, West Conshohocken, PA 19428-2959.

Introduction

The orientation of hydride platelets is a critical parameter determining the failure behavior and toughness of Zircaloy cladding tubes [1]. In a tube, when the normal to the hydride platelet is parallel to the radial direction, the hydrides are called "circumferential hydrides," whereas when the normal to the hydride platelets is parallel to the circumferential direction, the hydrides are called "radial hydrides." The latter hydrides promote embrittlement. Early work on this subject has provided guidelines for the fabrication of cladding tubes that favors the orientation of hydrides toward the circumferential direction [2,3].

These studies have been extended to determine the thermo-mechanical conditions of reorientation of hydrides from the circumferential to radial orientations. According to kinetic models, this reorientation is characterized by two threshold stresses oriented with respect to the orientation of hydrides platelets under a stress free state. The lower threshold stress is related to the minimal tensile stress perpendicular to the normal of the hydrides in their natural orientation leading to the first appearance of reoriented hydrides. The upper threshold stress corresponds to the minimal stress necessary to reorient all possible hydrides.

The commonly used procedure to determine the reorientation stress for a particular material is to machine a tapered uni-axial tension specimen [4–7]. With such a specimen, the tensile stress can be varied continuously in the range where reorientation takes place. The determination of a lower and an upper threshold stress is straightforward. In such a study, the specimens can be hydrogenated prior to the application of a reorientation thermo-mechanical loading using a maximum temperature sufficient to dissolve all the hydrides. The latter also minimizes any memory effect due to a possible preference of precipitation at a previously occupied site.

Whereas general agreement on test techniques for plate materials has been reached, standard testing for hydride reorientation in tubes is still being discussed. One approach is to prepare a flat sample from the tube [8]. This technique may not preserve the texture of the alloy and produces residual stresses that can affect the results of the reorientation test. The tube can be internally pressurized during the hydrogenation procedure [9]. The main advantage of this approach is the constant hoop stress within the test sample that facilitates the post-test analysis. A third technique, which does not require the development of a specific test device is to use a ring tensile test setup [10,11]. This experimental approach has to be complemented by a finite element analysis (FEA) to determine the stress field. Since handling irradiated materials is difficult, the last method has been chosen using the test setup depicted in Fig. 1. This method of testing enables us to compare results obtained from reorientation tests with fracture tests on cladding material [12].

Among the parameters that have been studied as possibly influencing hydride reorientation are the maximum temperature, the hydrogen concentration, the number of loading cycles, the orientation with respect to rolling direction, and the initial thermal treatment. A recent study on irradiated BWR cladding tubes [13] showed that for tubes with a burn-up of about 50 GWd/TU and for a dissolution temperature of around 300°C, the lower stress threshold for hydride reorientation was less than 70 MPa.

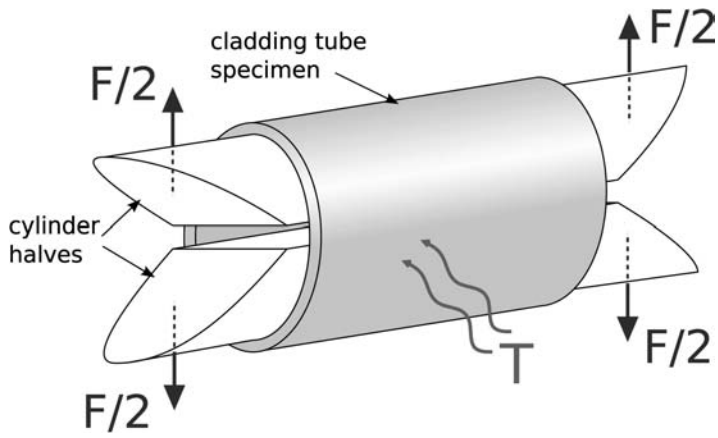


FIG. 1—*Thermo-mechanical loading of the cladding tube sample.*

The reorientation threshold is defined for tests using a peak temperature above the terminal solid solubility for dissolution: All of the hydrogen contained in the sample can form reoriented hydrides on cooling if the reorientation stress is large enough.

During multiple loadings, hydrides that have not been reoriented during the previous loading step, may dissolve, and can be reoriented during the current loading step [9]. For samples recovered from a nuclear power plant, the density of hydrides is higher on the external side than the central and inner regions of the cladding tube. Thus, temperature cycling may have an important effect on the reorientation behavior by redistributing the hydrogen within the tube cross-section.

In this document, we describe the characteristics of the cladding tube, the hydride reorientation tests, and the analysis procedure. The analysis provides spatial distributions of hydrides as well as a quantification of the geometric characteristics of the hydrides over the whole tube cross-section. The picture analysis is then coupled with an FEA of the test setup to determine the stress that each hydride encountered and thus give information on the local stress leading to reorientation. A model based on a precipitate nucleation law is used to determine the component of the stress tensor leading to reorientation; the effect of the tri-axial stress state is shown to have no influence on the reorientation of hydrides.

Test Description

Sample Characteristics

This study was done on six Zircaloy-2 (LK3/L) test samples (Table 1) removed from a Swiss BWR. The manufacture process included annealing with an accumulated annealing parameter of 6.31×10^{-15} h. The samples were taken from two rods that had undergone seven reactor cycles for a burn-up of around 66 GWd/TU. These samples have been thoroughly examined after irradiation and fully characterized [14].

TABLE 1—*Characteristics of the tested samples.*

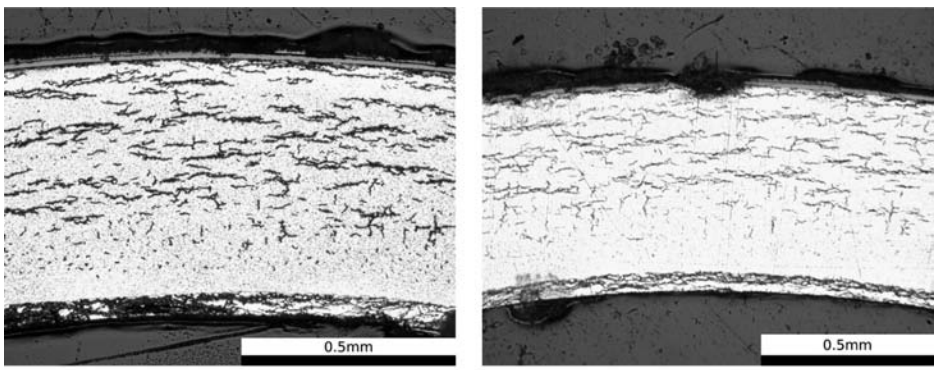
Segment[a]	*H* Total (ppm)	*H* Metal Concentration (ppm)	T_{max} (°C)	F_{hold}(N)	Loading Cycles	Burn-up (MWd/kgU)	Calc. Node
AEB067-E4-GC	251.	222.	394.	283.	1	66.0	14
AEB067-E4-HI	241.	215.	395.	283.	3	61.0	18
AEB067-E4-HD	297.	271.	334.	284.	1	63.6	16
AEB071-E4-FF	325.	296.	422.	285.	1	67.4	11
AEB071-E4-FK	355.	318.	422.	283.	3	66.8	13
AEB071-E4-IC	285.	258.	355.	283.	1	63.1	17

[a] Segment designation is as follows: Fuel assembly–rod–sample.

The hydrogen concentration was measured by hot gas extraction on samples extracted from the same rods. The measurements presented in Table 1 are the hydrogen concentrations in segments contiguous with the tested samples. The hydrogen concentration was expected to exhibit no significant variations between contiguous segments. The measurement technique enabled separation between hydrogen in the metal matrix and in the outer oxide layer. For this study, the hydrogen concentration in the metal matrix was of most interest. Figure 2 shows the chemically etched cross-section of the cladding tube when received from the power plant. In this state, the measured fraction of radial hydrides was around 10 % for rod AEB071-E4 and 9.2 % for rod AEB067-E4.

Loading and Testing Characteristics

To study hydride reorientation, the approach was as follows: A test sample, 12 mm long, was extracted from the defueled and cleaned fuel rod. Then, it was submitted to a thermo-mechanical loading to promote hydride reorientation (Fig. 3). The cooling rate was sufficiently slow to reach equilibrium [10]. After chemical etching, a micrographic analysis of the cross-section of the sample was done. The reorientation stress was determined using an FEA of the test setup.



(a) AEB067-E4 (b) AEB071-E4

FIG. 2—*Cross-section macrographs of the rods before reorientation tests.*

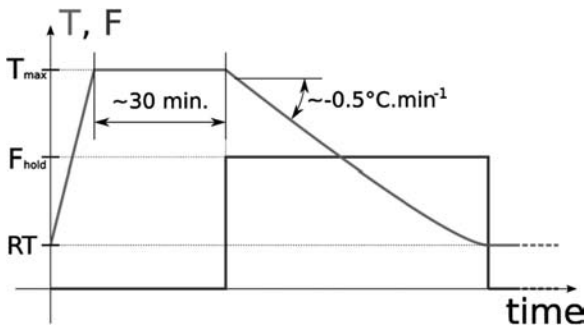


FIG. 3—*History of the thermo-mechanical loading during one cycle.*

Taking into account the structural and loading symmetries, only one eighth of the test setup was modeled. According to previous work [10] and since the contact surfaces were lubricated, the friction coefficient at the contact interface between the mandrel and the sample was set to zero. The material behavior was taken to be elasto-plastic for the mandrel and the cladding tube material. As checked with the computations, the size of the thermo-mechanical loading was not big enough to reach the yield strength of the cladding.

The main characteristics of the thermo-mechanical loading are summarized in Table 1. They can be divided in three categories as follows:

- High temperature (394 and 422°C), one loading cycle (AEB067-E4-GC, AEB071-E4-FF),
- Medium temperature (334 and 355°C), one loading cycle (AEB067-E4-HD, AEB071-E4-IC), and
- High temperature (395 and 422°C), three loading cycles (AEB067-E4-HI, AEB071-E4-FK).

These three types of loading permit coverage of a wide range of reorientation conditions for each rod.

Terminal Solubility Under Testing Conditions

Figure 4 depicts the dissolution terminal solid solubility of hydrogen in Zircaloy-2 for unirradiated [15–17] and for irradiated [18] materials. The irradiated samples used in the study to determine terminal solubility had undergone three reactor cycles in a commercial reactor. A slight increase of the terminal solubility limit for the irradiated material was observed. This variation is not of primary importance because, as depicted in Fig. 4, during testing, almost all the hydrides were dissolved for samples loaded at high temperature for one and three cycles. For samples loaded at medium temperature, i.e., AEB067-E4-HD and AEB071-E4-IC, about half the hydrides were not dissolved during the tests. For these samples, the reorientation procedure should not furnish much reorientation since, at most, half of the quantity of hydrides could undergo reorientation.

After the first dissolution-precipitation cycle, depending on the maximum temperature, the effect of irradiation on the terminal solubility may recover.

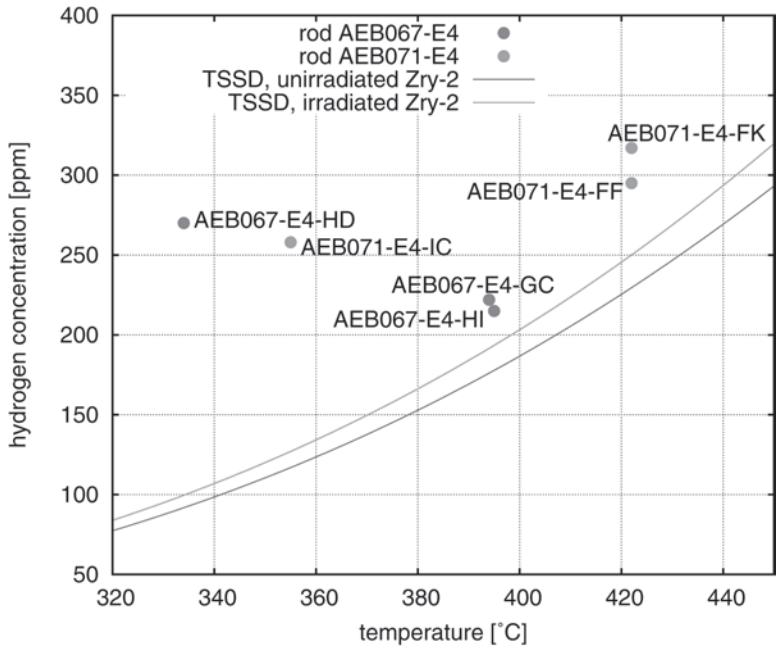


FIG. 4—*Temperature dependence of the dissolution terminal solid solubility (TSSD) of hydrogen for irradiated and unirradiated Zircaloy-2.*

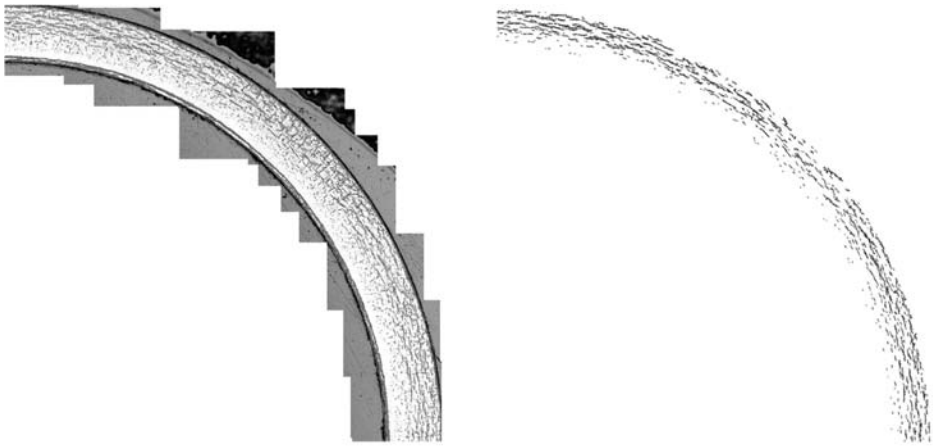
Thus, for the samples receiving three cycles, there may be more remaining hydrides at the second and third cycles than in the first cycle.

Hydrides Recognition and Distribution

Picture Segmentation Software

The determination of the stress leading to the reorientation of hydrides implies a reliable observation of the location, size, and orientation characteristics of each hydride revealed by the chemical etching process. To get information on the whole cross-section of the cladding tube, a software for automatic segmentation was developed using the C++ language. Hydrides were considered circumferential when they were oriented within $+/-45^{\circ}$ from the circumferential direction. Calculations have shown that most of the initial hydrides were oriented in a range of $+/-15^{\circ}$ with respect to the circumferential orientation. The minimal length considered for hydrides was 15 μm. The algorithm used in this software was as follows:

- Stitch together macrographs to obtain a picture of the whole tube cross-section
- Convert pictures in gray level using the picture red channel
- Convert gray level into black and white using a cluster threshold algorithm
- Identify circumferential hydrides (Fig. 5):



(a) AEB067-E4-GC (b) AEB067-E4-GC

FIG. 5—*Segmentation of circumferential hydrides:* (a) *Original picture and* (b) *precipitates identified as circumferential hydrides. Only the top right part of the rod is depicted.*

- Mark connected black pixels in the circumferential direction
- Make range selection on the marked pixels
- Determine size and orientation characteristics, and filter out particles that do not satisfy selection criteria
- Erase circumferential hydrides from the original picture
- Identify radial hydrides (Fig. 6):
- Mark connected black pixels in the radial direction
- Make range selection on the marked pixels
- Determine size and orientation characteristics, and filter out particles that do not satisfy selection criteria

This software enabled sampling information on the whole cross-section of the cladding tube. The collected data were hydride orientation, location, and size. Since the analysis was done on the whole cross-section, the orientation with respect to the cladding tube was defined in cylindrical coordinates based on the center of the cladding tube. The coordinates of the applied mechanical loading are depicted in Fig. 7. The treatment of the whole cladding tube permitted computation of the weighted distribution of the radial, d_r, and circumferential, d_θ, length of hydrides, as defined by

$$d_r(r) = \frac{1}{L}\frac{\partial}{\partial r}\sum_{i|r_i<r} l_i \text{ and } d_\theta(\theta) = \frac{1}{L}\frac{\partial}{\partial \theta}\sum_{i|\theta_i<\theta} l_i$$

where:

l_i denotes the length of the ith hydride located at position (r_i, θ_i).

The derivatives were calculated numerically; data were filtered in order to remove high frequency variations. To enable comparison, these distributions were normalized by the sum of hydrides length, L.

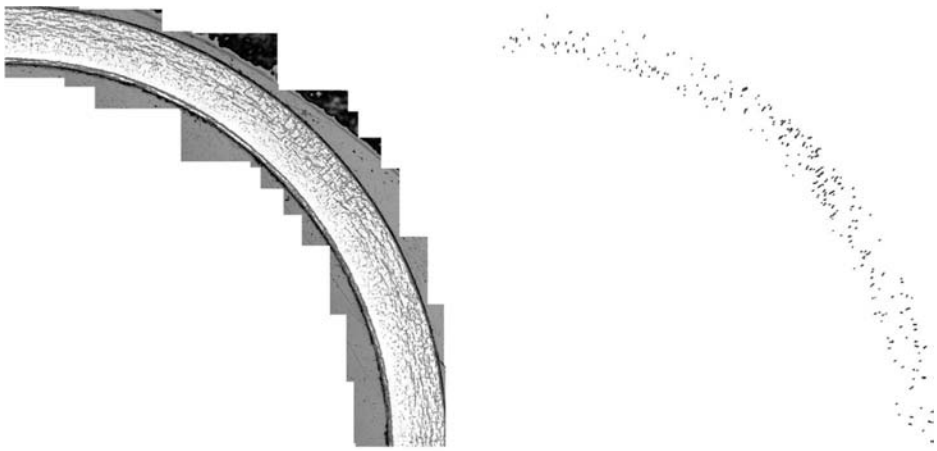


FIG. 6—*Segmentation of radial hydrides: (*a*) Original picture and (*b*) precipitates identified as radial hydrides. Only the top right part of the rod is depicted.*

Global Quantities

The etching conditions can vary from one sample to another (Fig. 8), thus modifying the apparent size of hydrides. To minimize this variation, only the lengths of the hydrides were measured because this dimension is not much affected by a variation of the etching conditions. Once the identification of the hydrides on the whole cross-section was done, the averaged quantities of each type of hydride were computed (Table 2 and Fig. 9).

During the segmentation and analysis process, the inner, heavily hydrided liner and outer oxidized layer were automatically removed, as they were not

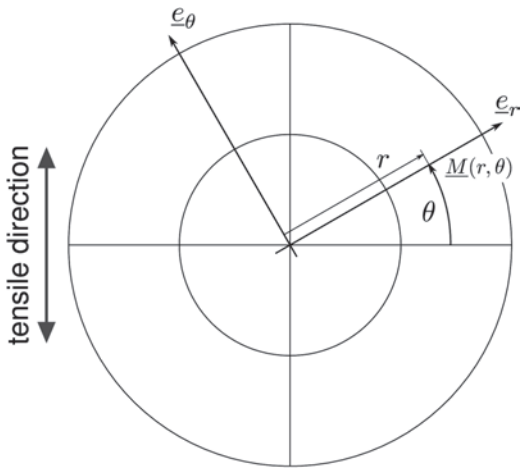


FIG. 7—*Definition of the cylindrical coordinates with respect to the tensile direction.*

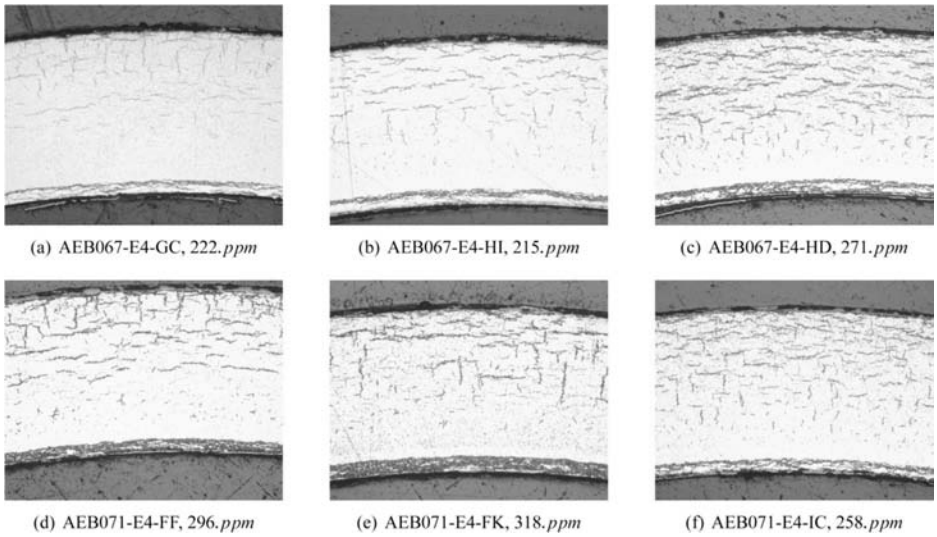


FIG. 8—*Effect of etching on the apparent size of the hydrides.*

relevant for our study. Consequently, the total length of hydrides and the total hydrogen concentration were not correlated.

For the high temperature loadings for one or three cycles, the fraction of reoriented hydrides and the most frequent hydride length were similar for each rod. More hydrides were reoriented when the number of cycles was increased: About 20 % with one cycle tests and about 30 % with tests using three cycles. This fraction was not affected by the initial difference in hydrogen concentration of the two rods, unlike in the tests using a medium temperature. The difference between these two testing regimes was the quantity of remaining hydrides at the maximum temperature. Thus, we infer that the quantity of remaining hydrides when the sample is mechanically loaded has an influence on the fraction of hydrides that are reoriented.

Location and Spatial Distribution

The locations of hydrides of various lengths are depicted in Fig. 10 for circumferential hydrides and in Fig. 11 for radial hydrides.

Radial hydrides were preferentially located in the outer third part of the tube when the maximum temperature was high. When the maximum temperature was medium, radial hydrides were almost homogeneously located with a slightly higher presence in the middle part of the tube wall. For the same hydrogen concentration, a higher density of radial hydrides led to a lower density of circumferential hydrides. This conclusion was particularly demonstrated with three loading cycles at the high maximum temperature. The external loading had less influence when the maximum temperature was low than when it was high. When the higher testing temperature was used, the biggest hydrides only formed at the load application points on the outer part of the cladding. When the medium temperature was used, the biggest hydrides were observed in the inner part of the cladding at 90° from the load application points.

TABLE 2—*Averaged quantities on the cladding tube cross-section.*

Loading							
High temp., one cycle		AEB067-E4-GC			AEB071-E4-FF		
High temp., three cycles			AEB067-E4-HI			AEB071-E4-FK	
Medium temp., one cycle				AEB067-E4-HD			AEB071-E4-IC
Hydrogen content (ppm)		222.	215.	271.	296.	318.	258.
Total length (mm)	Circumferential	44.	66.	152.	90.	67.	81.
Radial	11.	29.	28.	24.	27.	36.	
Sum	55.	95.	180.	114.	93.	127.	
Most frequent length	Circumferential	22.	21.	26.	24.	25.	23.
(μm)	Radial	18.	19.	18.	20.	20.	21.
Total quantity	Circumferential	1237	1493	2354	1414	1057	1886
	Radial	346	805	977	730	725	1106
Fraction of radial (%)	Total length	19.3	30.8	15.8	21.3	28.5	30.8
	Total quantity	21.9	35.0	29.3	34.0	40.7	37.0

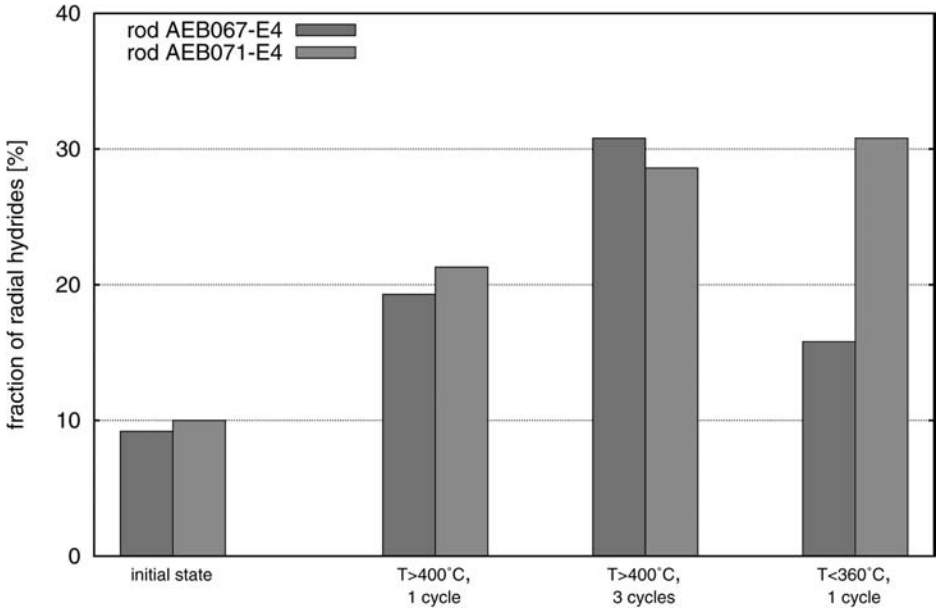


FIG. 9—*Fraction of radial hydrides before and after reorientation tests based on total length.*

Figures 12 and 13 depict the distribution of hydrides in the radial and the circumferential directions, respectively. For samples that had a high maximum temperature, there were two peaks (90° and 270°) in the number of radial hydrides at the load application points. These two peaks for the radial hydrides corresponded to two minima for the circumferential hydrides. This quantification confirmed the visual impression in Figs. 10 and 11. This localization of reoriented hydrides was not reflected by the overall measure of fraction of reoriented hydride. It is thus important when assessing the toughness of a tube with respect to radial hydrides to ensure that the loading has been homogeneous and not localized, as in the present study.

With the medium peak temperatures, the influence of the externally applied load was expected to be less important due to the lower quantity of dissolved hydrogen. This expectation was verified for sample AEB067-E4-HD where the reorientation fraction was around 16 %. This expectation was not fulfilled by sample AEB071-E4-IC, which was tested under similar conditions, but where the reorientation fraction was about 31 %. As indicated in Fig. 4, the amount of dissolved hydrogen was slightly greater in the latter than the former specimen, although it is unlikely that such a small difference in hydrogen in solution would lead to a difference of a factor of two in the reorientation fraction. This behavior could be explained by a high hydrogen concentration in the liner of this specimen. If true, the hydrogen concentration in the bulk of the cladding tube would be lower than estimated, providing favorable conditions for hydrides reorientation. Thus, it is difficult to draw a conclusion on the effect of the thermo-mechanical loading when much of the hydrogen is not in solution at

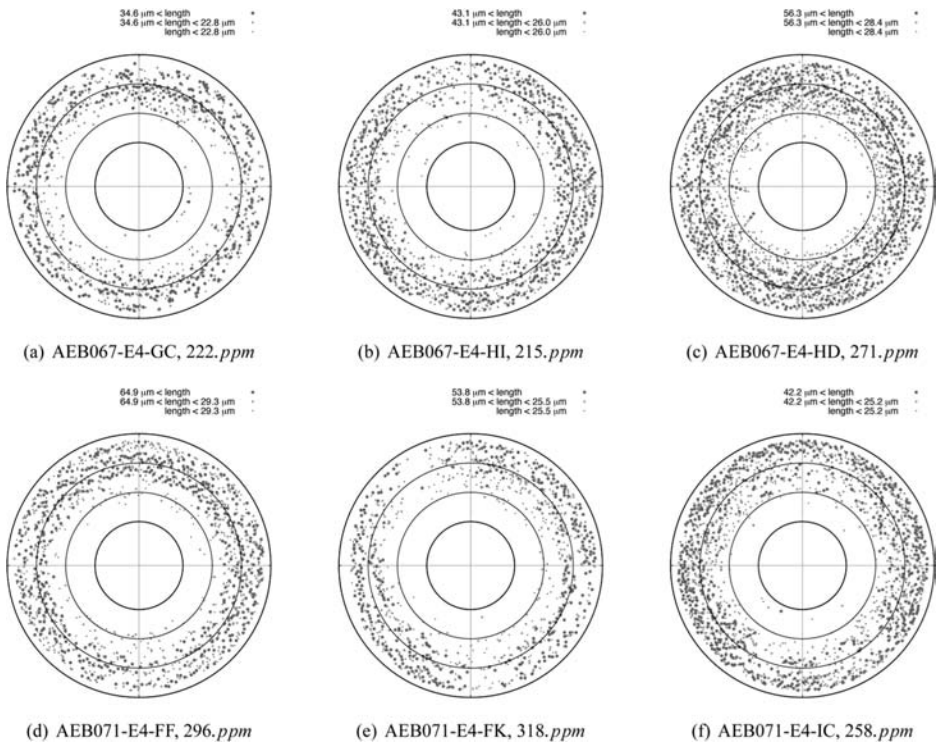


FIG. 10—*Location of circumferential hydrides. Length classes vary from specimen to specimen.*

the maximum temperature. The reproducibility between these two samples was poor despite the testing conditions being close, and no further analysis in terms of applied stress is presented.

Stress Distribution

Reorientation Behavior

We are interested in the loading conditions leading to the formation of radially oriented hydrides because of their importance when assessing the integrity of cladding tubes. The formation of radially oriented hydrides is expected to be driven by the tensile stress in the circumferential direction, i.e., hoop stress. Figure 14 depicts the hoop stress calculated by FEA for one cycle and three cycle loadings at high maximum temperatures.

Figure 15 displays the fraction of radial hydrides as a function of the hoop stress for the two temperature histories. For the single cycle loading at high maximum temperature, the fraction of reoriented hydrides exhibited a lower threshold just below 50 MPa for rod AEB067-E4. For rod AEB071-E4, the determination of the lower threshold for reorientation was not clear but was assessed to be around 50 MPa.

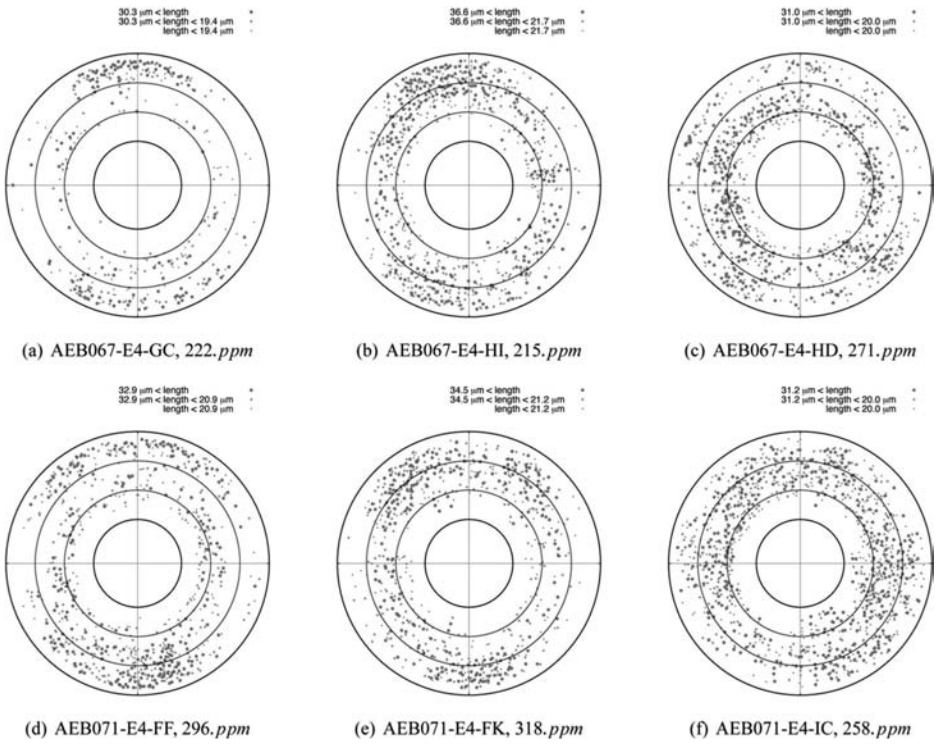


FIG. 11—*Location of radial hydrides. Length classes vary from specimen to specimen.*

With multiple loading, the reorientation curves for both specimens showed a plateau once the hoop stress was positive. In previous work using uni-axial loading on unirradiated material, multiple cycles increased the maximal fraction of reoriented hydrides without affecting the lower and upper reorientation thresholds [5]. The behavior observed here was a constant fraction of radial hydrides in any part submitted to a tensile hoop stress. When the spatial distribution of hydrides was compared with the areas where the lower threshold stress was exceeded (Fig. 16), it is seen that the inner side of the cladding tube exhibits atypical behavior; few hydrides precipitate, so even if the hoop tensile stress was large enough, there was no hydride reorientation. The concentration of hydrogen was low in this area.

A definitive conclusion on the effect of applied stress on hydride reorientation cannot be drawn without knowing the residual stress state in the sample. Although fuel performance codes provide the history dependence of the residual stress state of a rod, this stress estimate is for a complete rod and cannot be applied directly to an extracted and defueled segment. From a previous study [8], the residual hoop stress is expected to be compressive on the inner side and tensile on the outer side of the tube. Under such a residual stress state, the threshold applied stress determined above may be lower than one determined with no residual stress. When three cycles were imposed, the coincidence that

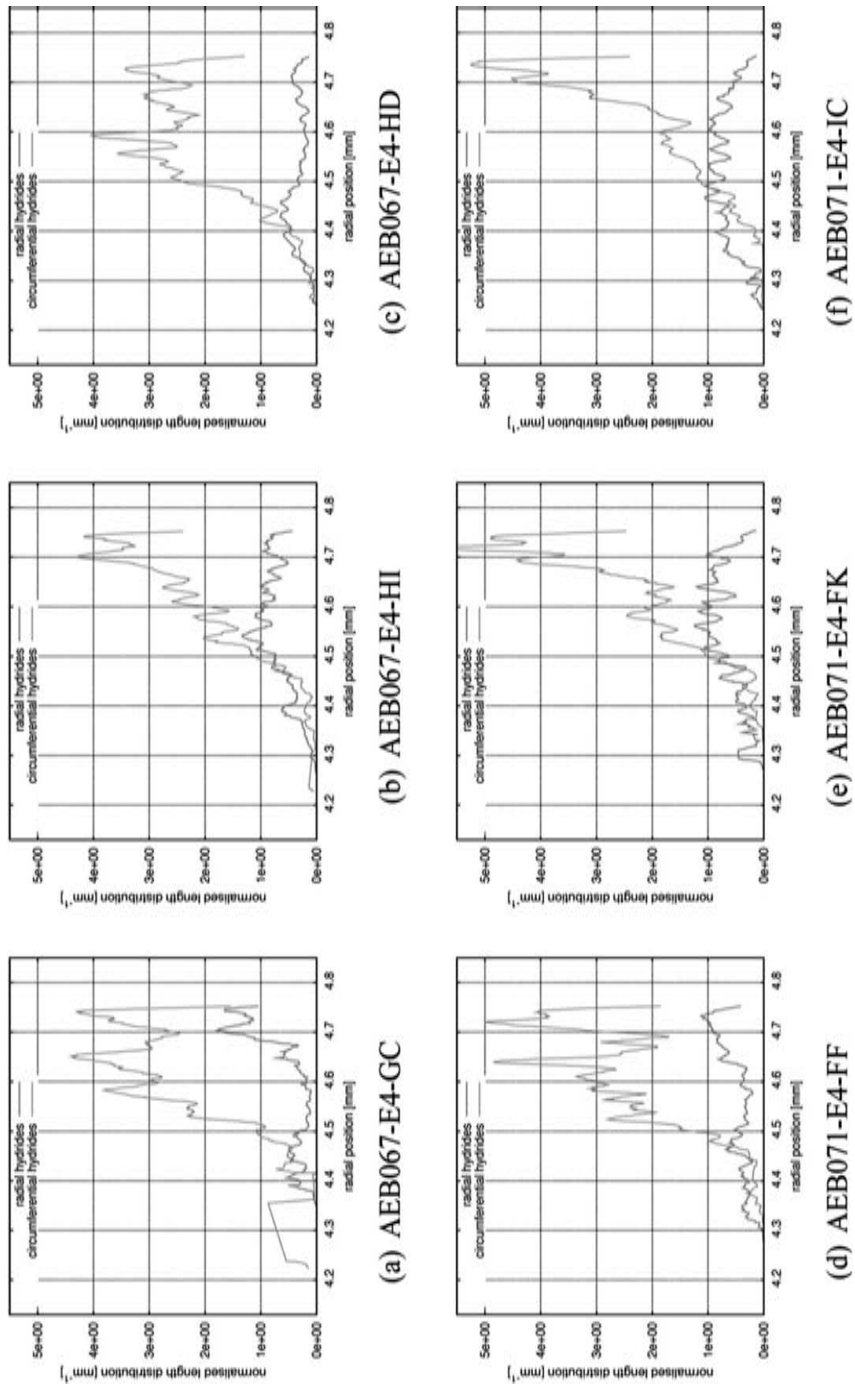


FIG. 12—*Distribution of hydrides, averaged in the circumferential direction.*

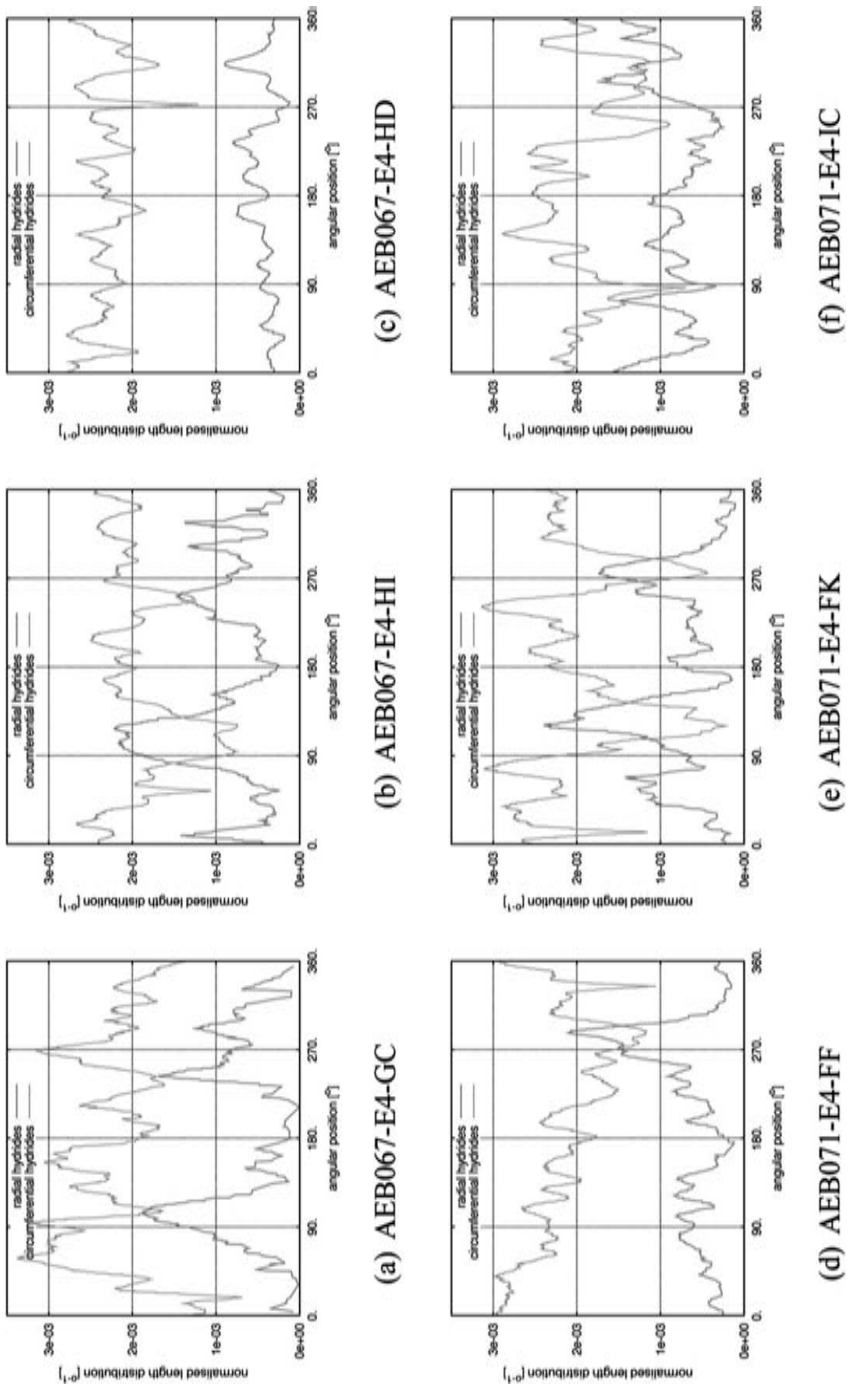
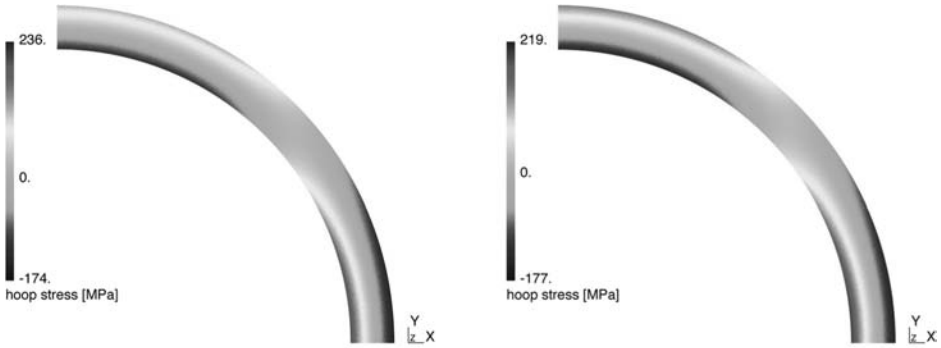


FIG. 13—*Distribution of hydrides, averaged in the radial direction.*



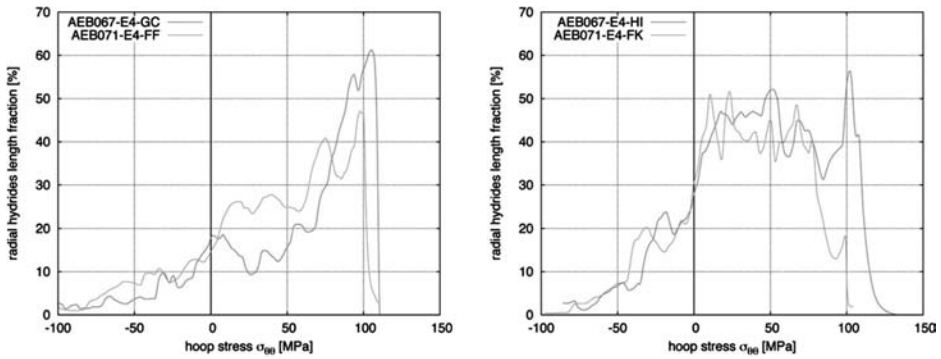
(a) AEB067-E4-GC (b) AEB067-E4-HI

FIG. 14—*Distribution of the hoop stress for* (a) *one cycle loading at the high maximum temperature and* (b) *three cycle loading at the high maximum temperature. Tensile direction is along the y-axis.*

the reorientation threshold corresponded to the switch between compressive and tensile residual hoop stress seems unlikely. Either the residual stress was very low compared with the applied stress, or the residual stress annealed out when the samples were heated.

The reorientation of hydrides was absent at high tensile stress on the inner side of the cladding because of the low concentration of hydrogen, i.e., few hydrides. Three possible mechanisms are responsible for this observation.

- The outer side of the tube is cooler than the inner side during reactor operation and wet storage. Hydrogen diffuses down the temperature gradient through the tube wall favoring hydrides precipitation in the outer region.
- Preferential precipitation of hydrides on previously occupied sites [6]—the "memory effect"—prevents precipitation at other sites even with a homogeneous temperature distribution.



(a) high temperature, one cycle (b) high temperature, three cycles

FIG. 15—*Fraction of radial hydrides as a function of the hoop stress.*

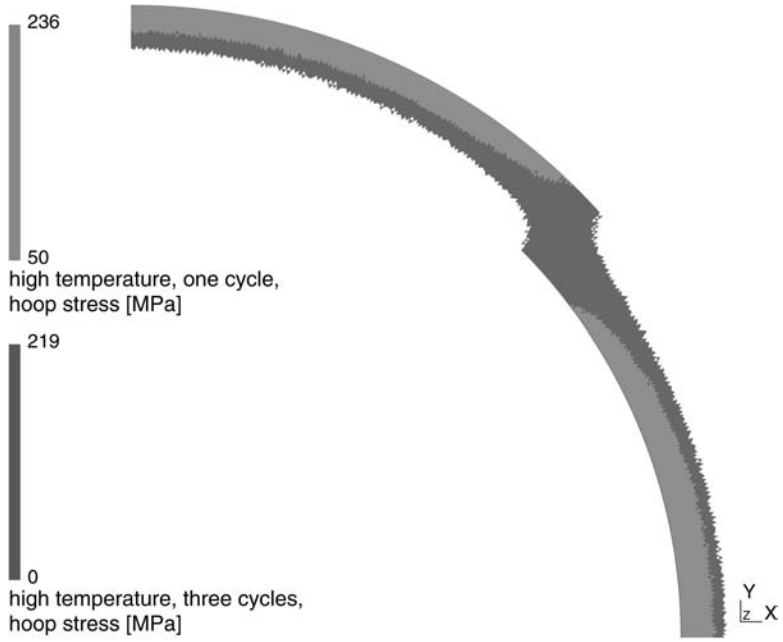


FIG. 16—*Areas where orientation should occur according to threshold stress and depending on the loading type.*

- The inner liner on the test material is a preferred site for hydride precipitation because it has a lower terminal solid solubility than the material of the remainder of the tube wall. Consequently, hydrogen is drained from adjacent areas—the "pumping effect"—leading to depletion in hydride precipitates in the inner regions.

Interaction Energy for Reorientation

The effect of stress tri-axiality on the formation of reoriented hydrides has not been assessed because most studies on hydride reorientation have been done in uni-axial tension. The reorientation of hydrides was observed with very low hoop stresses with multiple cycles loading. A tri-axial stress may play a role in this behavior by favoring reorientation where the hoop stress is not necessarily the largest component of the stress and other components may be involved. The current test setup induced a multi-axial stress state; the hoop and axial stresses dominated but varied continuously within the sample, whereas the radial and shear components of the stress tensor were so small that they could be ignored.

To assess the consequences of such a stress state, we have to determine the mechanical quantity that determines the reorientation. A widely used model for reorientation [7,19–22] assumes that the fraction of reoriented hydrides is driven by the nucleation rate in two preferential directions, the radial and circumferential directions. The quantity of importance is the difference between the interaction energies for radial and circumferential hydrides, $\Delta E_{\text{int}}^{R-C}$, defined by

$$\Delta E_{\text{int}}^{R-C} = \alpha E_{\text{int}}^{R} - \beta E_{\text{int}}^{C}$$

where:

α, β = two constants depending on the inter- and intra-granular nucleation volume and

$E_{\text{int}}^{R}, E_{\text{int}}^{C}$ = interaction energies for radial and circumferential hydride formation, respectively.

With this approach and data proposed by Ref [7, the energy driving the process is given by

$$\Delta E_{\text{int}}^{R-C} = \tfrac{1}{2} V_{\text{intra}}^{\prime 0} E_{\text{int}}^{C} + \left((1 - \xi^{0}) V_{\text{inter}}^{\prime 0} + \xi^{0} V_{\text{intra}}^{\prime 0} \right) E_{\text{int}}^{R}$$

where:

$V_{\text{intra}}^{\prime 0} = 4.3 \times 10^{-27}\ \text{m}^3$ and $V_{\text{inter}}^{\prime 0} = 15 \times 10^{-27}\ \text{m}^3$ = critical nucleus volumes for intra- and inter-granular hydrides, respectively, and

ξ^{0} = fraction of intra-granular radial hydrides, taken as 0.3.

The interaction energy for hydrides in the radial and circumferential directions is the doubly contracted tensor product between the transformation strain and the stress due to externally applied load. Their values are

$$E_{\text{int}}^{C} = 0.072\sigma_{rr} + 0.0456\sigma_{\theta\theta} + 0.0456\sigma_{zz},\ E_{\text{int}}^{R} = 0.0456\sigma_{rr} + 0.072\sigma_{\theta\theta} + 0.0456\sigma_{zz}$$

The dependence of the fraction of radial hydrides with respect to the interaction energy is depicted in Fig. 17. This dependence is similar to that of the hoop stress, Fig. 15, especially for the tests using three loading cycles, confirming that hydrides reorient as soon as the interaction energy is positive. The reorientation at low hoop stress for tests using multiple cycles cannot be attributed to the non-hoop components of the stress tensor.

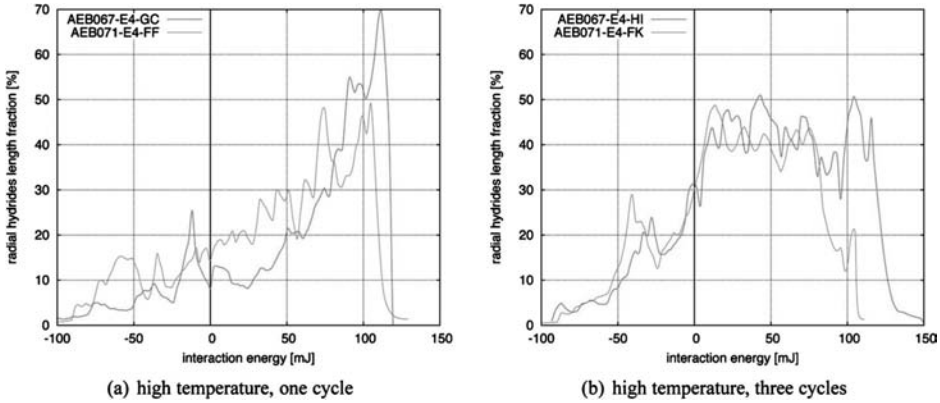


FIG. 17—*Fraction of radial hydrides as a function of the interaction energy.*

Conclusion

In this work, we have analyzed the thermo-mechanical conditions leading to the formation of radially oriented hydrides in irradiated Zircaloy-2 cladding tubes. Three different loading sequences were used on two different rods. The test setup provided multi-axial thermo-mechanical loading. Only two of our loading scenarios were amenable to analysis. In the tests using a medium maximum temperature, many hydrides were not dissolved, and only a small fraction of hydrides was susceptible to reorientation. In these tests, the external applied stress had no significant influence on the final distribution and presence of radially oriented hydrides.

For tests using a high maximum temperature, most of the hydrogen was in solid solution, and the mechanical loading had a strong influence on the hydride location and orientation in both rods. The overall fraction of reoriented hydrides was similar, independent of the initial hydrogen concentration, confirming that at the maximum test temperature, almost all hydrides were dissolved.

The effect of increasing the loading cycles was to increase the fraction of radially oriented hydrides. This result was expected from the literature review: Hydrides that have not been reoriented at one loading cycle may be reoriented with subsequent cycles. The cycling tended to homogenize the distribution of hydrides in the radial direction.

The hoop stress determined the threshold of reorientation. For one cycle at the high temperature, reorientation started at a hoop stress of about 50 MPa. This value was lower than the one determined in our previous study on unirradiated Zircaloy-2, which was in the range 65–74 MPa. This reduction was consistent with observations of reorientation of hydrides in irradiated Zircaloy-2 tubes [13]. When three cycles were used with a high maximum temperature, hydrides reoriented once the hoop stress was positive. This last result was not expected from previous studies on unirradiated test samples.

Acknowledgments

The writers are grateful to Swissnuclear, which sponsored the development of the test method, and Westinghouse Electric Sweden AB together with Kernkraftwerk Leibstadt AG for providing the tested irradiated claddings.

References

[1] Daum, R. S., Majumdar, S., and Billone, M. C., "Experimental and Analytical Investigation of the Mechanical Behavior of High-Burnup Zircaloy-4 Fuel Cladding," *J. ASTM Int.* Vol. 5(5), 2008.

[2] Marshall, R. P., "Influence of Fabrication History on Stress-Oriented Hydrides in Zircaloy Tubing," *J. Nucl. Mater.*, Vol. 24(1), 1967, pp. 34–48.

[3] Marshall, R. P., "Control of Hydride Orientation in Zircaloy by Fabrication Practice," *J. Nucl. Mater.*, Vol. 24(1), 1967, pp. 49–59.

[4] Singh, R. N., Lala Mikin, R., Dey, G. K., Sah, D. N., Batra, I. S., and Ståhle, P., "Influence of Temperature on Threshold Stress for Reorientation of Hydrides and Residual Stress Variation Across Thickness of Zr–2.5 Nb Alloy Pressure Tube," *J. Nucl. Mater.*, Vol. 359(3), 2006, pp. 208–219.

[5] Sakamoto, K., and Nakatsuka, M., "Stress Reorientation of Hydrides in Recrystallized Zircaloy-2 Sheet," *J. Nucl. Sci. Technol.*, Vol. 43(9), 2006, pp. 1136–1141.
[6] Bai, J. B., Prioul, C., and Francois, D., "Hydride Embrittlement in ZIRCALOY-4 Plate: Part I. Influence of Microstructure on the Hydride Embrittlement in ZIRCALOY-4 at 20 °C and 350 °C," *Metall. Mater. Trans. A*, Vol. 25(6), 1994, pp. 1185–1197.
[7] Bai, J. B., Ji, N., Gilbon, D., Prioul, C., and François, D., "Hydride Embrittlement in ZIRCALOY-4 Plate: Part II. Interaction Between the Tensile Stress and the Hydride Morphology," *Metall. Mater. Trans. A*, Vol. 25(6), 1994, pp. 1199–1208.
[8] Singh, R. N., Kishore, R., Singh, S. S., Sinha, T. K., and Kashyap, B. P., "Stress-Reorientation of Hydrides and Hydride Embrittlement of Zr–2.5 wt% Nb Pressure Tube Alloy," *J. Nucl. Mater.*, Vol. 325(1), 2004, pp. 26–33.
[9] Chu, H. C., Wu, S. K., Chien, K. F., and Kuo, R. C., "Effect of Radial Hydrides on the Axial and Hoop Mechanical Properties of Zircaloy-4 Cladding," *J. Nucl. Mater.*, Vol. 362(1), 2007, pp. 93–103.
[10] Alam, A. M. and Hellwig, C., "Cladding Tube Deformation Test for Stress Reorientation of Hydrides," *J. ASTM Int.*, Vol. 5(2), 2007.
[11] Hong, S. I. and Lee, K. W., "Stress-Induced Reorientation of Hydrides and Mechanical Properties of Zircaloy-4 Cladding Tubes," *J. Nucl. Mater.*, Vol. 340(2–3), 2005, pp. 203–208.
[12] Bertsch, J. and Hoffelner, W., "Crack Resistance Curves Determination of Tube Cladding Material," *J. Nucl. Mater.*, Vol. 352(1–3), 2006, pp. 116–125.
[13] Aomi, M., Baba, T., Miyashita, T., Kamimura, K., Yasuda, T., Shinohara, Y., and Takeda, T., "Evaluation of Hydride Reorientation Behavior and Mechanical Properties for High-Burnup Fuel-Cladding Tubes in Interim Dry Storage," *J. ASTM Int.*, Vol. 5(9), 2008.
[14] Ledergerber, G., Abolhassani, S., Limbäck, M., Lundmark, R. J., and Magnusson, K.-Å., "Characterization of High Burnup Fuel for Safety Related Fuel Testing," *J. Nucl. Sci. Technol.*, Vol. 43(9), 2006, pp. 1006–1014.
[15] McMinn, A., Darby, E. C., and Schofield, J. S., "The Terminal Solid Solubility of Hydrogen in Zirconium Alloys," *Zirconium in the Nuclear Industry: 12th International Symposium*, June 15–18, 2000, ASTM International, West Conshohocken, PA.
[16] Une, K. and Ishimoto, S., "Terminal Solid Solubility of Hydrogen in Unalloyed Zirconium by Differential Scanning Calorimetry," *J. Nucl. Sci. Technol.*, Vol. 41(9), 2004, pp. 949–952.
[17] Une, K., Ishimoto, S., Etoh, Y., Ito, K., Ogata, K., Baba, T., Kamimura, K., and Kobayashi, Y., "The Terminal Solid Solubility of Hydrogen in Irradiated Zircaloy-2 and Microscopic Modeling of Hydride Behavior," *J. Nucl. Mater.*, Vol. 389(1), 2009, pp. 127–136.
[18] Vizìcano, P., Banchik, A. D., and Abriata, J. P., "Solubility of Hydrogen in Zircaloy-4: Irradiation Induced Increase and Thermal Recovery," *J. Nucl. Mater.*, Vol. 304(2–3), 2002, pp. 96–106.
[19] Chu, H. C., Wu, S. K., and Kuo, R. C., "Hydride Reorientation in Zircaloy-4 Cladding," *J. Nucl. Mater.*, Vol. 373(1–3), 2008, pp. 319–327.
[20] Ells, C. E., "The Stress Orientation of Hydride in Zirconium Alloys," *J. Nucl. Mater.*, Vol. 35(3), 1970, pp. 306–315.
[21] Puls, M. P., "Effect of Stress on Hydride Reorientation in Zirconium Alloys," *Solute—Defect Interaction. Theory and Experiment*, Kingston, Ontari, Canada, 1985, pp. 426–433.
[22] Sauthoff, G., "Orienting of Precipitating Au Particles in an Fe-Mo-Au Alloy by External Elastic Stress. Pt. 1. Elastic Energy Considerations," *Z. Metallkd.*, Vol. 66(2), 1975, pp. 106–109.

DISCUSSION

Question 1, Joe Rachid, ANATECH:—The low threshold value for hydrides reorientation of 50.MPa is almost half of that reported for Zircaloy-4 material. Can this difference be attributed to the initial presence of hydrides in Zry-2 which could promote earlier–with respect to stress–reorientation?

Author's Response:—The low threshold value observed is on the low side of the expected range for irradiated Zircaloy. The obtained results do not enable to conclude on the influence of initially present hydrides in the cladding. However, regarding usual multiple cycles experiments, the hypothesis of an enhanced reorientation due to radial hydrides previously formed due to reactor operation, can be seriously considered.

Question 2, Suresh Yagnik, EPRI:—You observed no reorientation at inner liner region. It tends to act as a sink for hydrogen. Did the presence of liner complicate the interpretation of data and how did you quantify or factor that out?

Author's Response:—The liner itself has not been analyzed. The inner side effectively presents a lack of hydrogen on the inner side, but still exhibits reorientation. Since reorientation is measured as a fraction of total hydride quantity, this lack of hydrogen is not apparent in the final results. Thus no particular action has been taken to quantify this phenomenon.

Reprinted from JAI, Vol. 7, No. 5
doi:10.1520/JAI103008
Available online at www.astm.org/JAI

C. Coleman,[1] *V. Grigoriev,*[2] *V. Inozemtsev,*[3] *V. Markelov,*[4] *M. Roth,*[5] *V. Makarevicius,*[6] *Y. S. Kim,*[7] *Kanwar Liaqat Ali,*[8] *J. K. Chakravartty,*[9] *R. Mizrahi,*[10] *and R. Lalgudi*[11]

The Effect of Microstructure on Delayed Hydride Cracking Behavior of Zircaloy-4 Fuel Cladding—An International Atomic Energy Agency Coordinated Research Program

Manuscript received January 30, 2010; accepted for publication April 8, 2010; published online June 2010.

[1] Researcher Emeritus, Chalk River Laboratories (CRL), AECL, Chalk River, ON K0J 1J0, Canada, e-mail: colemanc@aecl.ca
[2] Senior Specialist, Studsvik Nuclear AB, SE-611 82 Nyköping, Sweden.
[3] Nuclear Fuel Specialist, International Atomic Energy Agency (IAEA), Wagramer Strasse 5, P.O. Box 100, Vienna 1400, Austria.
[4] Head of Department, The Joint Stock Company A. A. Bochvar High-Technology Research Institute of Inorganic Materials (JSC VNIINM), 5a Rogov St., Moscow 123098, Russia.
[5] Head, Materials Testing Group, Institute for Nuclear Research (INR), Romanian Authority for Nuclear Activities (RAAN), Campului St., No. 1, 115400 Mioveni, P.O. Box 78, Piteşti, Romania.
[6] Senior Researcher, Laboratory of Materials Research and Testing, Lithuanian Energy Institute (LEI), Breslaujos str. 3, LT-44403 Kaunas, Lithuania.
[7] Head, Zirconium Team, Korea Atomic Energy Research Institute (KAERI), Daejeon 305-353, Korea.
[8] Senior Researcher, Pakistan Institute of Nuclear Science and Technology (PINST), P.O. Nilore, Islamabad, Pakistan.
[9] Head, Mechanical Metallurgy Section, Materials Group, Bhabha Atomic Research Centre (BARC), Mumbai 400-085, India.
[10] Senior Researcher, Materials Dept., National Atomic Energy Commission (CNEA-CAC), Av. Gral. Paz 1499, B1650KNA San Martín, Pcia. de Buenos Aires, Argentina.
[11] General Manager, Materials Science and Technology Centre, Energy and Nuclear Research Institute (ENRI), Av. Prof. Lineu Prestes 2242, Cidade Universitària 05508-000, C.P. 11049, Sao Paulo, Brazil.

Cite as: Coleman, C., Grigoriev, V., Inozemtsev, V., Markelov, V., Roth, M., Makarevicius, V., Kim, Y. S., Liaqat Ali, K., Chakravartty, J. K., Mizrahi, R. and Lalgudi, R., "The Effect of Microstructure on Delayed Hydride Cracking Behavior of Zircaloy-4 Fuel Cladding—An International Atomic Energy Agency Coordinated Research Program," *J. ASTM Intl.*, Vol. 7, No. 5. doi:10.1520/JAI103008.

Copyright © 2011 by ASTM International, 100 Barr Harbor Drive, PO Box C700, West Conshohocken, PA 19428-2959.

ABSTRACT: The rate of delayed hydride cracking (DHC) has been measured in Zircaloy-4 fuel cladding in several metallurgical conditions using the pin-loading tension technique. In light water reactor (LWR) cladding in the cold-worked and cold-worked and stress-relieved conditions, the cracking rate followed Arrhenius behavior up to about 280 °C, but at higher temperatures the rate declined with no cracking above 300 °C. Non-LWR cladding appeared to behave in the same manner. In LWR cladding in the recrystallized condition, the cracking rate was highly variable because it depended on K_I within the test range up to 25 MPa$\sqrt{}$m, whereas in the other LWR claddings, cracking rate was independent of K_I, indicating that K_{IH} was below 11 MPa$\sqrt{}$m. The main role of microstructure was to control the material strength; the cracking rate increased as the strength increased. Although all the claddings had a radial texture, it did not protect the cladding from DHC. The DHC fracture surface consisted of flat broken hydrides, often in arcs, but no striations were observed, except in one specimen subjected to thermal cycles.

KEYWORDS: Zircaloy-4 fuel cladding, delayed hydride cracking (DHC), pin-loading tension (PLT), microstructure, temperature dependence, K_I dependence

Introduction

Like other hydride-forming metals, zirconium is susceptible to embrittlement by hydrogen when hydrides are formed [1]. The embrittlement takes two forms: Short-term loss of toughness and a stable time-dependent crack growth mechanism called delayed hydride cracking (DHC). During DHC, hydrides nucleate and grow slowly in the high stress region of a stress-raiser such as a crack tip. When they reach a critical condition, probably related to size, they fracture, the crack extends, and the process is repeated. The characteristics of the mechanism are the following.

- Time is often required between the imposition of stress and the start of cracking. This period is called the incubation time.
- Loading must exceed a threshold condition for cracking, often characterized as K_{IH}. The rate of any subsequent cracking, V, is almost independent of K_I.
- The temperature dependence of cracking is complicated and is described in the schematic diagram depicted in Fig. 1 [2]. The maximum value of V has an apparent Arrhenius behavior and follows

$$V = A \exp(-Q/RT) \tag{1}$$

where:

Q = activation energy for DHC in kJ/mol,
R = gas constant (8.314 kJ/mol K),
T = temperature in K, and
A = constant.

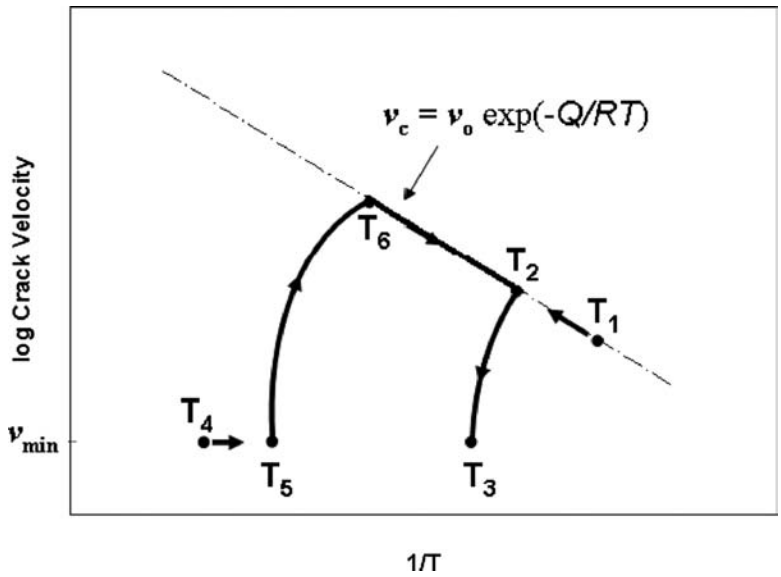


FIG. 1—*Temperature dependence of DHC in zirconium alloys, showing the importance of temperature history on cracking rate.*

If the temperature is attained by heating from T_1, initially V follows Eq 1, but as the temperature is increased, V starts to decline at T_2 and cracking eventually stops at T_3. On cooling from a high temperature, T_4, a temperature is reached where cracking will reinitiate, T_5, and reach a maximum value at T_6; at lower temperatures V follows Eq 1.

- The amount of hydrogen present in the material should be sufficient for hydrides to be precipitated at the crack tip.
- The material microstructure may affect V through its effect on the diffusivity of hydrogen, material strength, and mode of hydride precipitation, for example, through crystallographic texture.
- A sharp decline in DHC is observed at high test temperatures despite the temperature being attained by cooling and sufficient hydrogen being present to form hydrides. In Zr–2.5Nb the upper temperature limit, T_0, is about 310°C [3].

In components, time-dependent cracking was discovered during the storage at room temperature of Zr–2.5Nb fuel cladding before irradiation [4]. High residual stresses from welding were an important factor in these fractures. High residual stresses were also responsible for cracking in Zr–2.5Nb pressure tubes. The source of these stresses was either the process used to join the pressure tube to the ends of its fuel channel [5] or from tube straightening [6]. Several examples show that fuel cladding made from Zircaloy is also not immune from DHC. In some Zircaloy nuclear fuel cladding used in boiling-water reactors (BWR), hydride cracking was strongly implicated in long splits that allowed substantial leakage of fission products [7–9]. If the cladding wall is penetrated

during operation, for example, by fretting, water from the heat-transport system can enter the fuel cavity where, because of the lower pressure, steam is produced. Much hydrogen is generated because the steam oxidizes the fuel and the inside surface of the cladding, reducing the partial pressure of oxygen and leaving a gas rich in hydrogen. This process is called "oxygen starvation." At some distance from the primary defect, the gas stream becomes almost pure hydrogen, and with breakdown of the protective oxide layer, copious quantities of hydrogen may be absorbed by the cladding [10]. Sometimes, "sunbursts" of hydride formed on the inside surface. With fuel expansion during fuel rearrangement, the hydrided cladding was stressed, which led to crack initiation. The cracks grew through-wall, propagated axially, and could be over 1 m long. Brittle regions in "chevrons" characterized the fractures, with the crack being longer on the outside surface than the inside surface of the cladding [11]. The lower bounds of the crack velocities were in the range 2.5×10^{-7}–6.6×10^{-7} m/s based on assuming constant growth rates in the time between first detection of the defect and removal of the fuel. The mechanism of cracking appeared to be a form of DHC [8,12], perhaps exacerbated by a continuous additional supply of hydrogen from the steam inside the fuel element [13,14]. A DHC-type of mechanism has been identified as being responsible for radial cracking starting at the outside surface of BWR fuel cladding when power ramped after a high burn-up [15]. Tests on unirradiated cladding demonstrated that the velocity of DHC in the radial direction of the tube obeyed Eq 1, and V was about 10^{-7} m/s at 275°C [16,17]. Cracks in the axial direction, about 20 mm long and close to the endplugs of Canada Deuterium Uranium (CANDU) fuel, have been detected [18]. The burn-up was very low, 0.4 GWd/t, so the inventory of fission products would be too small to cause stress-corrosion cracking. Several partial radial cracks had also started from the inside surface. The hydrogen concentration was 42 ppm, which may have been picked up from residual moisture in the fuel. The source of the large hoop stress driving the crack was attributed to fuel expansion from the fuel operating well outside its design power, although the cause of this anomaly was not identified.

The two technologically important quantities for DHC are the conditions for crack initiation, K_{IH}, and the rate of crack propagation, V. The latter was the subject of the first part of this International Atomic Energy Agency (IAEA) coordinated research program (CRP) on Zr–2.5Nb pressure tube material [19]. As an extension of this CRP, the rate of DHC has been measured in Zircaloy-4 fuel cladding.

Several methods are available to test fuel cladding for DHC. The first such successful testing was obtained using a center-cracked half-tube loaded in tension [20]. To gain insight on the long splits, tubing containing a central axial crack was loaded by a wedge and mandrel—the SPLIT test [13]. The radial crack propagation from the outside surface has been studied by internally pressurizing tubes containing small axial cracks [16,17]. Axial crack propagation has been measured using the pin-loading tension (PLT) technique [21]. This last method was originally developed at Studsvik for fracture toughness evaluation of thin walled tubing [22,23] and was chosen for the CRP program because

TABLE 1—*Dimensions of test materials.*

	Materials				
Dimensions	LWR SandvikLot 86080	LWR SandvikLot 83786	CANDU ZircatecLot 226289	CANDU SandvikLot 81101	Atucha FAE Lot MA-61
Outside diameter, D (mm)	9.5	9.5	13.1	13.1	11.9
Wall thickness, t (mm)	0.57	0.60	0.39	0.39	0.55
D/t	16.7	15.8	33.6	33.6	21.6

- Its loading is similar to that in a compact toughness specimen used for Zr–2.5Nb;
- In a comparison of test methods for fracture toughness of Zircaloy-4 fuel cladding, the PLT technique provided the lowest values of $J_{0.2}$ and dJ/da, indicating that this technique provides good constraint and limits plasticity at the crack tip [24]; and
- The technique was thought to be amenable to technology transfer.

The IAEA set up this extension to the CRP with the objective of transferring "know-how" on laboratory practices to the member states who were unfamiliar with DHC testing of fuel cladding using the PLT method. The first objective of the program was to establish a uniform and consistent laboratory practice to determine the DHC velocity in the axial direction of fuel cladding so that a meaningful inter-laboratory comparison of the results could be made. A preliminary evaluation showed that the technology transfer was successful [25]. The data from this first trial are included here for completeness. Using six versions of Zircaloy-4 fuel cladding, the second objective was to examine the effects of microstructure on V.

Experimental Details

Test Materials

The material used for the first trial was standard light water reactor (LWR) Zircaloy-4 cladding from Sandvik Lot 86080 [25]. For comparison with this initial trial, samples from Sandvik Lot 83786 were obtained in the cold-worked (CW) condition. During fabrication the final pilgering imposed 80 % CW based on area reduction on a cylindrical mandrel. The dimensions of the tubing are given in Table 1, and the chemical composition is given in Table 2; this material had a slightly higher concentration of oxygen than Lot 86080. The material was tested in the CW condition. Sections of tubing were also heat-treated to simulate that used for pressurized water reactors—CW and stress relieved (CWSR) 480°C for 3.5 h—and for BWRs—recrystallized annealed (RXA) 565°C for 1.5 h. The initial CW microstructure consisted of elongated grains that were little changed by the stress-relieving treatment but completely recrystallized by the higher temperature anneal, with grains that were almost equiaxed having a

TABLE 2—*Chemical composition of test materials.*

	Materials				
Element	LWR Sandvik Lot 86080	LWR Sandvik Lot 83786	CANDU Zircatec Lot 226289	CANDU Sandvik Lot 81101	Atucha FAE Lot MA-61
Sn (wt %)	1.25	1.26	1.3	1.35	1.29
Fe (wt %)	0.22	0.23	0.22	0.22	0.23
Cr (wt %)	0.1	0.12	0.12	0.10	0.12
O (ppm)	1180	1272	1180	1260	1200
Si (ppm)	100	100	100	60	98
C (ppm)	120	120	140	120	132
N (ppm)	49	41	24	< 30	28
H (ppm)	7	7	8	13	4

TABLE 3—*Texture factors for basal planes in test materials.*

	Materials					
Texture Factors	LWR Sandvik Lot 86080 CWSR	LWR Sandvik Lot 83786 CW	LWR Sandvik Lot 83786 CWSR	LWR Sandvik Lot 83786 RXA	CANDU Zircatec Lot 226289	Atucha FAE Lot MA-61
F_R	0.65	0.65	0.64	0.60	0.65	0.56
F_T	0.30	0.29	0.31	0.34	0.30	0.29
F_L	0.05	0.06	0.05	0.06	0.05	0.15

mean diameter of about 3 μm. The basal plane normals were concentrated about 30° from the radial direction; the texture factors, F, in the three principal directions—radial, R; transverse, T; and axial, A—are summarized in Table 3. The basal plane normals rotated a small amount from the radial direction toward the transverse direction with heat-treatment. The ultimate tensile strength (UTS) was measured with ring tensile tests; it was reduced by heat-treatment and test temperature, Table 4.

Three other batches of cladding were tested. For the CANDU cladding supplied by Zircatec, the last stage of cold-working was about 90 %, and the final stress relieving was 500°C for 8 h. The composition of the Zircaloy-4, Table 2, and the (0002) distribution Table 3, were similar to those of the LWR cladding. The dimensions of the CANDU cladding differ from the LWR cladding having a larger diameter and thinner wall, Table 1. It also has lower strength, Table 4. The clearly defined grains were elongated in the axial direction but almost equiaxed on the transverse-radial section with a mean grain diameter of about 4 μm. For the CANDU cladding supplied by Sandvik, the composition of the Zircaloy-4 is given in Table 2. This CANDU cladding also differs from the LWR cladding

TABLE 4—*Tensile properties of test materials.*

Material	Test Temperature(°C)	UTS(MPa)
Sandvik, Lot 86080, CWSR	200	543
	250	502
	290	477
	320	459
Sandvik, Lot 83786, CW	200	588
	250	532
	290	498
	320	475
Sandvik, Lot 83786, CWSR, 480°C for 3.5 h	200	570
	250	510
	290	489
	320	466
Sandvik, Lot 83786, RXA, 565°C for 1.5 h	25	517
	250	270
	350	228
CANDU, Zircatec, Lot 226289, 500°C for 8 h	22	606
	100	509
	200	415
	300	370
	350	346
CANDU, Sandvik, Lot 81101	20	589
	250	424
Atucha, FAE, Lot MA-61	20	575
	200	406
	250	367
	300	346

having a larger diameter and thinner wall, Table 2, and lower strength, Table 4. The grain size was about 5.8 μm on the transverse-radial section but elongated in the longitudinal direction. For the Atucha cladding, the last stage of cold-working was 57 %, and the final stress relieving was 510°C for 8.5 h. The composition of the Zircaloy-4, Table 2, and the (0002) distribution, Table 3, again were similar to those of the LWR cladding. The Atucha cladding had a larger diameter but similar wall thickness as the LWR cladding, Table 1, and lower strength, Table 4. The clearly defined grains were elongated in the axial direction but almost equiaxed on the transverse-radial section, with a mean grain diameter of about 2 μm in the radial direction and 3 μm in the transverse direction.

Specimen and Fixture Preparation

After cleaning the cladding, a layer of hydride was deposited on the surfaces electrolytically using 0.1*M* H_2SO_4, a temperature of 65±5°C, and a current

density of 1 kA/m^2. Diffusing the hydrogen into the metal by annealing at 410°C for 24 h added a homogeneous hydrogen concentration of about 200 ppm. The resulting hydrides had their plate normal in the radial direction. The hydrogen concentration was confirmed by analysis using an inert gas fusion technique. For a few specimens the hydrogen was added gaseously at 400°C, with similar results.

The test specimen is shown Fig. 2. The 13 mm long specimen (c_A) contained diametrally opposite axial notches at both edges with those at one end being sharpened by fatigue at room temperature for a starting length of a_A; the notch at the other end provided an effective specimen length of b_A. The notch that was fatigued to a crack was 0.15 mm wide, while the rear notch was 0.5 mm wide. The fatigue pre-cracking was done at 1–5 Hz with starting maximum loads of 200–300 N cycled down to 50 N. The maximum load was gradually reduced to 90–100 N as the crack progressed. The final load was chosen to be lower than the starting load for the DHC test, typically 160 N, so the plastic zone at the crack tip from fatigue did not interfere with DHC. Between 8000 and 50 000 cycles were required to produce a suitable starting crack, about 1.5 mm in length. The crack length was measured either visually on the surface or using potential drop (PD).

The PLT fixture is shown schematically in Fig. 2. Most of the fixtures were made from Nimonic 90, but successful testing has been achieved using fixtures made from carbon steel. The fixture consisted of two halves, which, when placed together, form a cylindrical holder, A. The diameter of the holder allowed it to be inserted into the specimen while maintaining a small gap. The fixture halves were loaded in tension through pins at B and rotated about a pin C at the ends of the cylindrical holder providing similarity to the loading of a compact toughness specimen but on two cracks. Care was taken to line up the pre-cracked notches with the join of the two halves of the fixture.

Delayed Hydride Cracking Testing

To start a DHC test, the specimen was heated to and held at a temperature of 50–75°C above the test temperature for 1 h, then cooled with no undercooling to

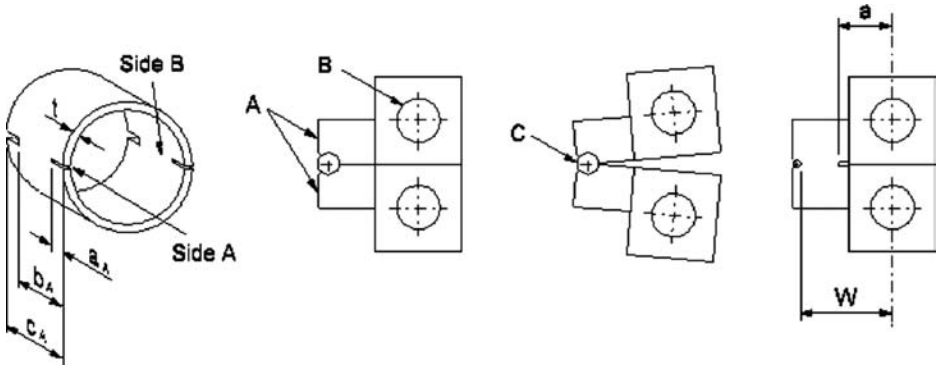


FIG. 2—*Schematic diagram of test specimen and PLT fixture.*

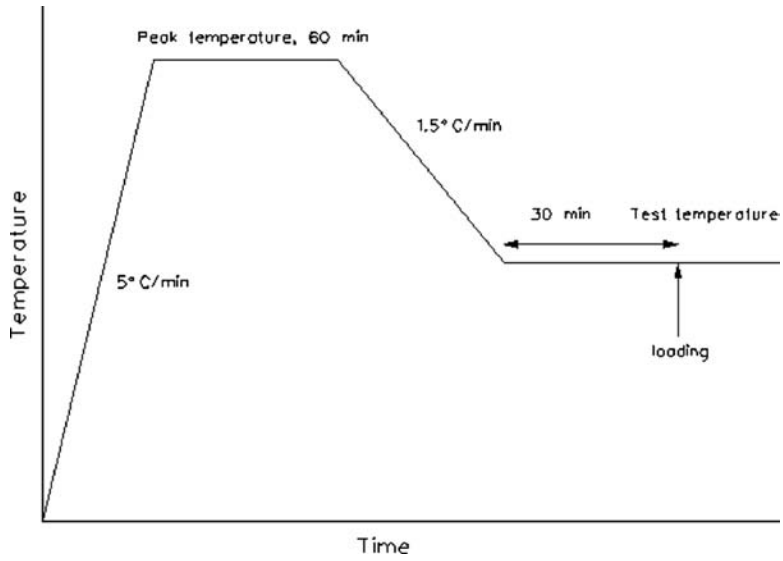


FIG. 3—*Schematic diagram of temperature cycle used for DHC tests.*

the test temperature. This temperature history encourages cracking and minimizes variation; this sequence represents T_4 to below T_6 in Fig. 1 rather than T_1 to T_3 in Fig. 1, where cracking can be difficult. After a short period at constant temperature, at least 30 min, the specimen was loaded to a K_I of about 15 MPa$\sqrt{}$m. The test history is depicted in Fig. 3. The value of K_I was calculated from Eq 2

$$K_I = [P/(2t\sqrt{W})]f(a/W) \tag{2}$$

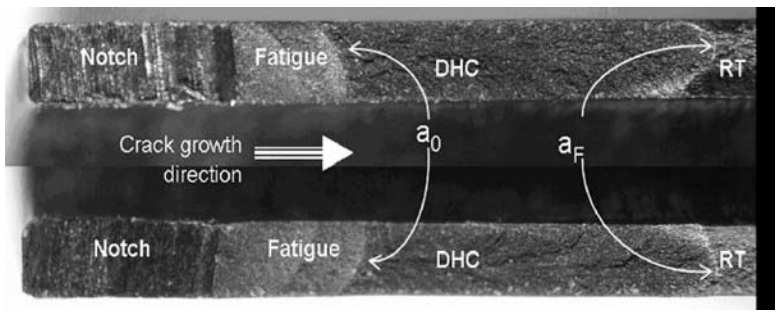


FIG. 4—*View of the fracture surfaces of CWSR Zircaloy-4 specimen (200 ppm of hydrogen). The top and bottom edges are the outside surfaces of the cladding. The initial* (a_0) *and the final* (a_F) *lengths of the DHC crack are indicated as well as the areas of notch, fatigue pre-cracking, DHC crack propagation, and room temperature fracture after the DHC test (RT). The cladding wall thickness is 0.57 mm.*

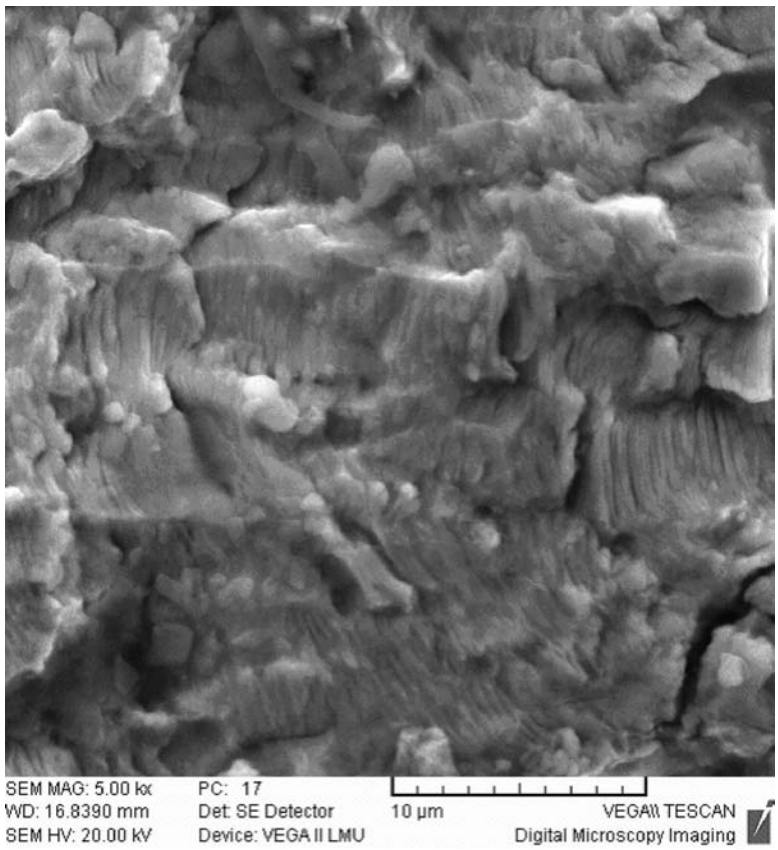


FIG. 5—*Fatigue striations formed at room temperature on specimen of CANDU Zircaloy-4 fuel cladding tested at 250°C.*

where:

P = load (N),

t = wall thickness of the cladding (m),

W = effective width of specimen (m), being the distance from the load line to the axis of rotation (see Fig. 2),

a = effective crack length (m), being the distance from load line to the crack tip (see Fig. 2), and

$f(a/W)$ = geometry correction factor.

The value of $f(a/W)$ was determined experimentally from compliance measurements, resulting in

$$f(a/W) = 92.203 - 468.73(a/W) + 787.15(a/W)^2 - 360.99(a/W)^3 \qquad (3)$$

for LWR cladding [26] and

$$f(a/W) = -0.4759 + 13.185(a/W) + 39.533(a/W)^2 - 23.65(a/W)^3 + 12.135(a/W)^4 - 2.9162(a/W)^5 \quad (4)$$

for CANDU cladding [27].

Cracking was detected either by PD or by displacement equivalent to crack opening. Once the cracks had extended 2–3 mm, the load was removed and the specimen was cooled to room temperature. The crack surfaces were lightly heat-tinted from oxidation, and the ends of the crack could usually be discerned on the fracture surface. An alternative was to briefly fatigue the specimen to mark the end of the DHC. Subsequently, the specimen was broken open, and the fracture surface was examined. A typical pair of fracture surfaces is shown in Fig. 4. In this example the delayed hydride crack is about 3 mm long. Crack growth by DHC, $a_F - a_0$ (Fig. 4), was estimated on each crack from the average of nine equally spaced measurements; the value for the specimen, a_S, was the average of the values of the two cracks. Often an incubation period, t_i, was required before DHC started; cracking time, t_T, was taken as (time under load—t_i). Crack velocity,

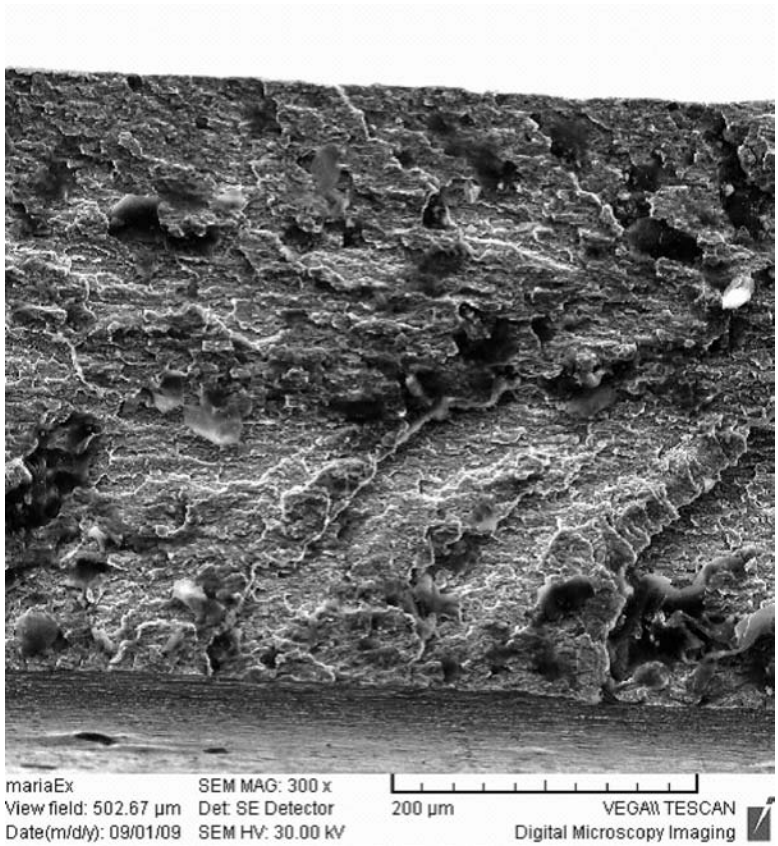


FIG. 6—*DHC in CANDU Zircaloy tested at 250°C. Cracking from right to left.*

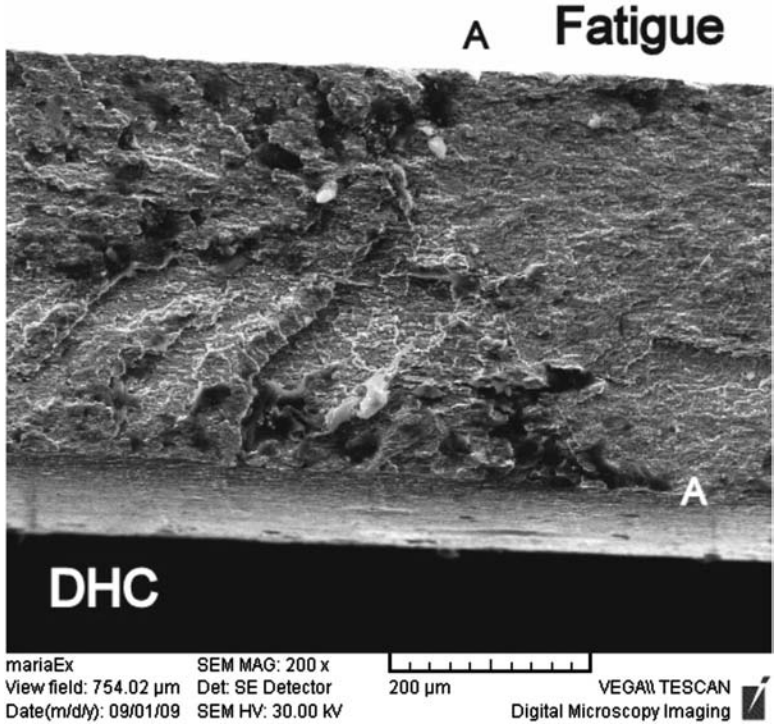


FIG. 7—*Interface between fatigue pre-crack and DHC in CANDU Zircaloy tested at 250°C. Cracking from right to left.*

V, in the axial direction of the cladding was a_S/t_T. Scanning electron microscopes were used to examine the fracture surfaces of some specimens to provide details of the fracture mechanism. Cracking was evaluated in the temperature range of 144–302°C.

All the testing and examinations were performed in the ten laboratories listed with the authors' names.

Results

Fracture Surfaces

The periods of the different fracture modes were not only distinguishable by oxidation, Fig. 4, but the microfractographic features were different. The pre-fatigue region contained typical striations formed at room temperature and subsequently oxidized during DHC testing, Fig. 5. DHC is shown in Fig. 6 as areas of flat fracture corresponding to cracked hydrides, interspersed by curved

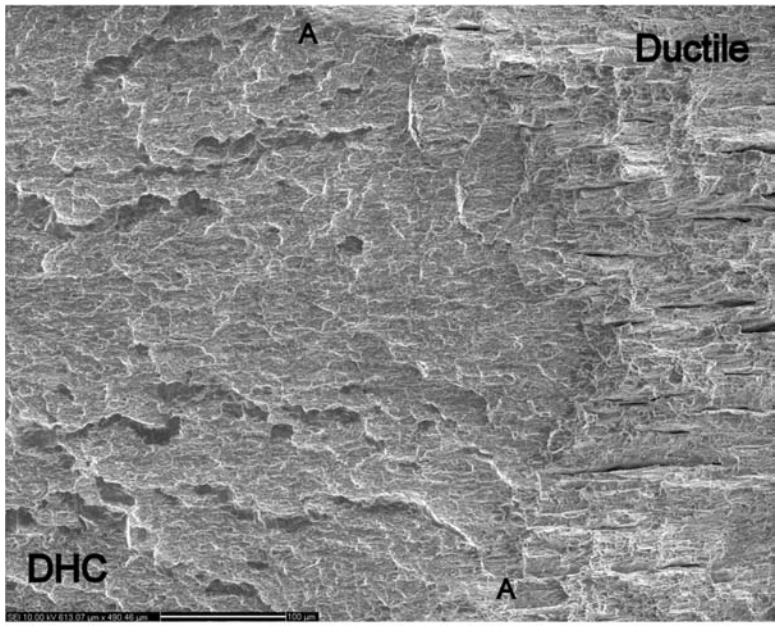


FIG. 8—*Interface between DHC at 144°C and ductile fracture at 25°C after DHC test. CWSR Zircaloy-4 fuel cladding. Cracking from left to right.*

features that correspond to changes in crack plane or direction. The interface between fatigue and DHC, Fig. 7, or DHC and ductile fracture, Fig. 8, were easily distinguished along *A–A*. The post-test stage of the fracture surface consisted of ductile fracture formed when the specimen was broken open at room

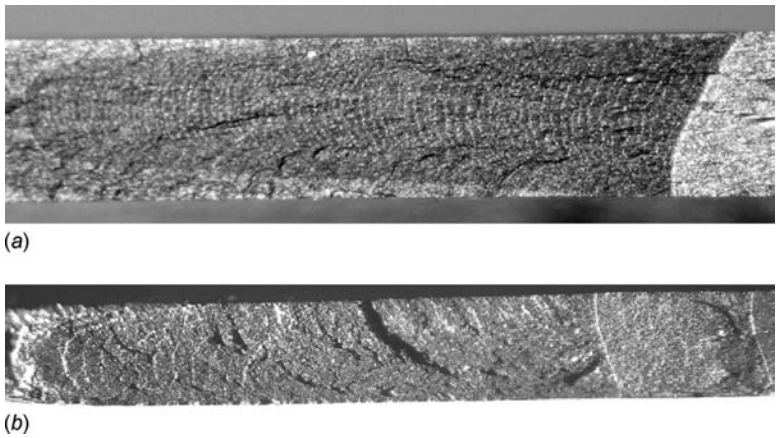


FIG. 9—*Striations observed on* (a) *CWSR Zr–2.5Nb cladding tested at 250°C and* (b) *on one specimen of CWSR Zircaloy-4 during DHC with thermal cycles.*

temperature; the large fissures between the areas of ductile dimples are probably fractured circumferential hydrides that are perpendicular to the fracture plane, Fig. 8. Fractographs of the materials in all metallurgical states showed the same features. To date, the DHC striations usually seen in Zr–2.5Nb, Fig. 9(*a*), have been observed only once, Fig. 9(*b*). This specimen was CWSR Zircaloy-4 cladding, and the striations were in the high K_I region, between about 25 and 40 MPa$\sqrt{m}$. This specimen had been subjected to 12 temperature cycles between 248 and 270°C. The cladding made from Zr–2.5Nb was in the CWSR condition and tested at 250°C; the striations were very similar to those observed on the DHC fracture surfaces of Zr–2.5Nb pressure tube materials [19].

Incubation Times

The time before continuous DHC started was very variable in all the materials. At test temperatures below 280°C, some specimens appeared to start cracking immediately on application of the load, whereas others required considerable time before cracking started. Factors contributing to the variability in the start of DHC are the sensitivity of the crack detection system and the variation in the preparation of the starter-crack by fatigue. In all materials except RXA, the incubation time had mean values between 3 % and 7 % of the test time; thus errors in their determination contributed only a small error to the value of crack velocity. Unlike with Zr–2.5Nb [19], no temperature dependence of the incubation time could be discerned.

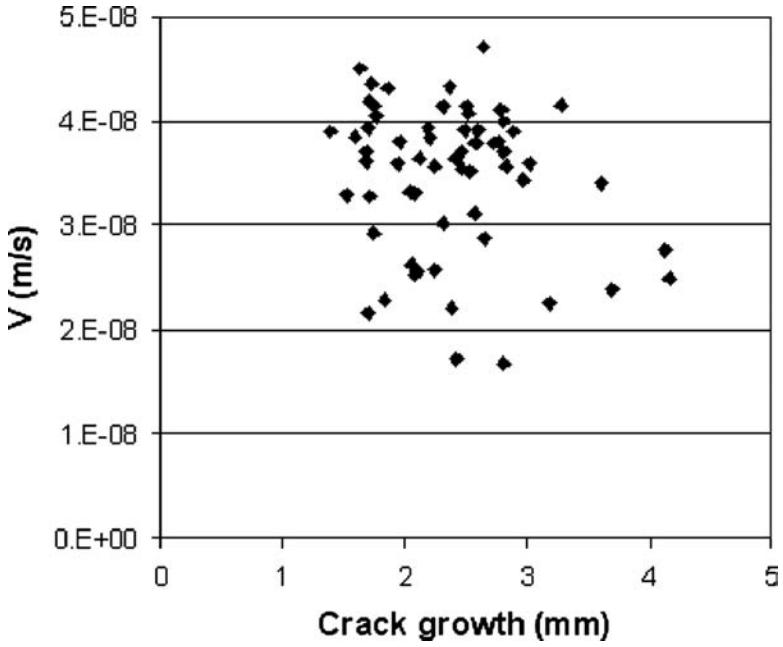


FIG. 10—*No dependence of V on crack length; CWSR material tested at 250°C. (Data from Ref 25 and this paper.)*

Crack Velocities

The initial value of K_I depends on the load and the crack length after fatigue. The load is well known, but the initial crack length has some variation because it is difficult to measure accurately before the DHC test. For these tests the target for the initial value of K_I was 15 MPa$\sqrt{}$m. In practice it varied between 11.0 and 25.0 MPa$\sqrt{}$m, but the mean value for all the tests was 16.4 MPa$\sqrt{}$m, close to the target, with a moderate dispersion of 3.0 MPa$\sqrt{}$m. Most laboratories obtained seemingly valid results with amounts of crack growth varying from 0.4 to 4.2 mm; the mean value for all the tests on LWR CW and CWSR materials was 2.0±0.86 mm. Consequently the final value of K_I had a wide range, up to 43 MPa$\sqrt{}$m. One expects that V should be independent of either initial or final K_I (so long as K_{IH} is exceeded) and therefore crack length, and the results confirm this expectation. For example, Fig. 10 shows the lack of dependence of the crack velocity on amount of crack growth in CWSR material at 250°C.

The temperature dependence of V for the CW and CWSR materials is depicted in Fig. 11. Below about 280°C the velocity followed Eq 1, with Q

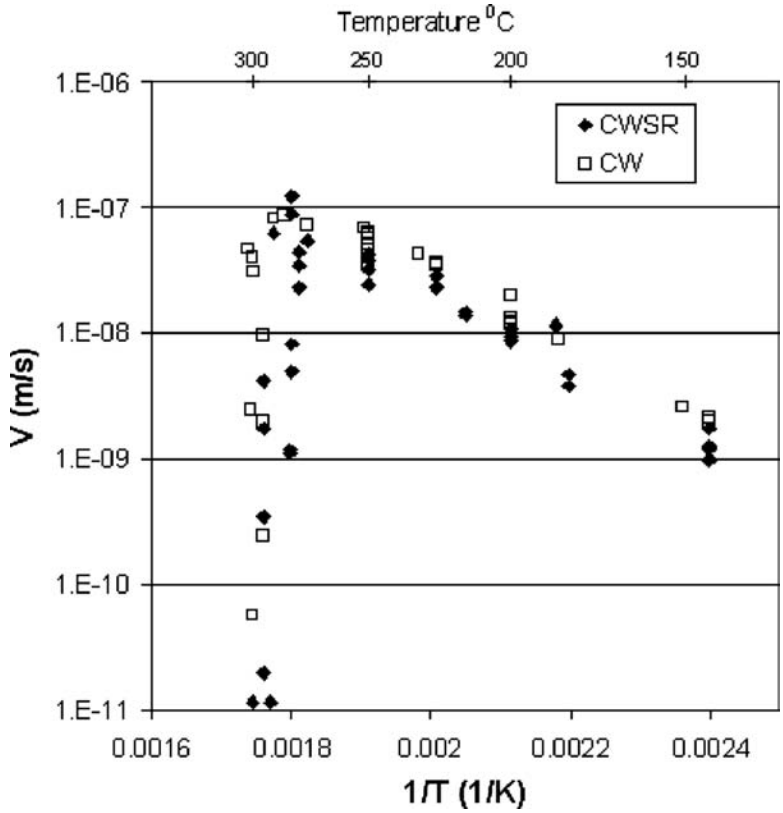


FIG. 11—*Temperature dependence of V in Zircaloy-4 fuel cladding in the CW and CWSR conditions.*

around 55 kJ/mol. Above 280°C, *V* was very scattered and declined until cracking was absent at 295°C. (In tests at high temperature where no cracking was observed, the plotted value was obtained by dividing an assumed crack propagation of 0.01 mm by the test time.) The behavior of the RXA material was quite different—often cracking was reluctant to start, and when it was observed, its rate was very scattered, Fig. 12, making evaluation of any temperature dependence unclear. (Using an upper bound line of the data may indicate similar temperature dependence to that of the other cladding, but such a treatment is difficult to justify with the current large variation.) The number of tests on the non-LWR materials was only sufficient to obtain general trends, Fig. 13. The CANDU Zircatec and Atucha materials had similar values of *V* and showed the now-expected drop at high test temperatures. The CANDU Sandvik cladding cracked faster than the other two materials; it only provided a hint of decline at the highest test temperature, 295°C, since *V* was similar to that at 250°C.

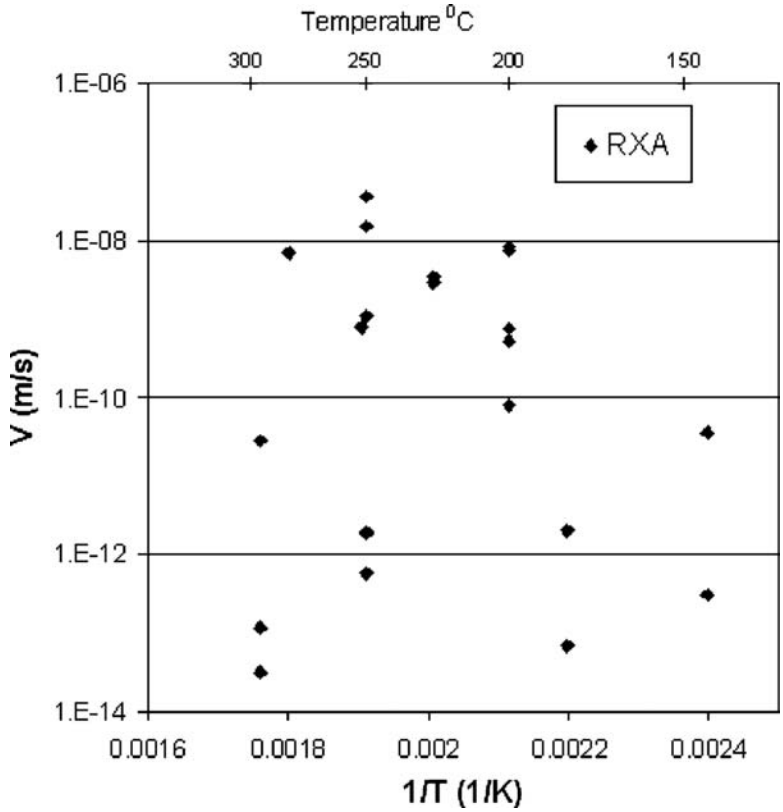


FIG. 12—*Temperature independence of V in Zircaloy-4 fuel cladding in the RXA condition.*

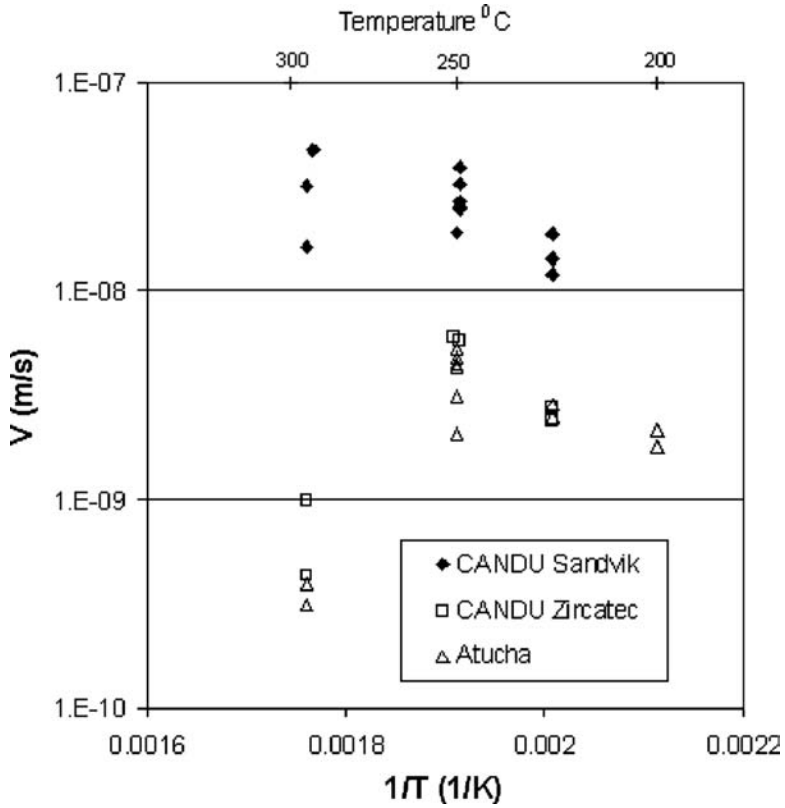


FIG. 13—*Temperature dependence of V in Zircaloy-4 fuel cladding representing CANDU, from Zircatec and Sandvik, and Atucha.*

Discussion

For both batches of LWR cladding in the CWSR condition, the values of V and their temperature dependence were in very good agreement, Fig. 14, showing that the testing technique was under control and reproducible. Compared with CWSR material, the CW material had similar temperature dependence, but slightly higher values of crack velocity (below 275°C the average value was about a factor of 1.5 higher) and maybe a slightly higher temperature for the start of the decline in V, 285 versus 275°C, Fig. 11.

In the usual picture of DHC, after K_{IH} is exceeded, the crack velocity is almost independent of K_I and crack length. The crack velocity at 250°C of CWSR material was insensitive to crack length, Fig. 10, and therefore K_I over a wide range of values. The implication is that K_{IH} for this material was lower than 11 MPa$\sqrt{}$m, the lowest value tested at which cracking was observed. The results on RXA material at 250°C indicate that the crack velocity was highly K_I-dependent in this condition, Fig. 15, suggesting that K_{IH} is large for this material, perhaps as high as 25 MPa$\sqrt{}$m. (In this figure K_I is taken as (initial

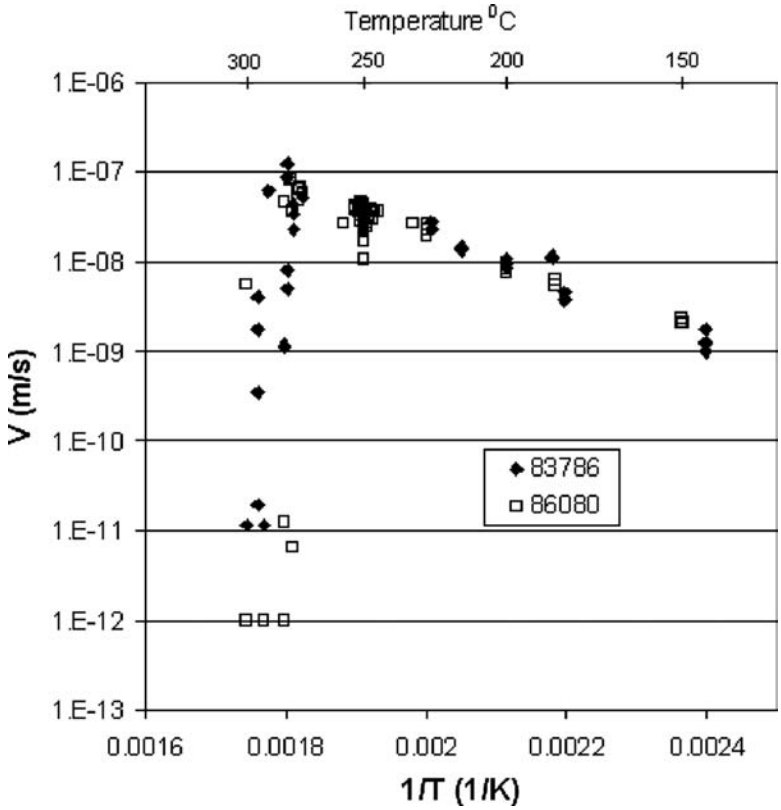


FIG. 14—*Comparison of DHC behavior of LWR Zircaloy-4 fuel cladding in the CWSR condition; data for Lot 86080 from Ref 25.*

value + final value)/2.) This high sensitivity to K_I also explains the large variation in values of V obtained in this material and frequent difficulty with initiating cracking.

The mean values of V for CW and CWSR materials from this study were higher than those from measurements on pressure tubes made from Zircaloy-2 [28,29], Fig. 16, but similar to the few measurements on Zircaloy-4 fuel cladding [16,20,21], suggesting similar temperature dependence, independent of test direction on the plane perpendicular to the hoop stress, Fig. 17. The variability in values can be attributed to

- Differences in the histories of temperature can contribute large variations in crack velocity through the behavior illustrated in Fig. 1,
- The small number of samples tested; the process of DHC is highly variable and even in well-controlled testing, the crack velocity in fuel cladding can vary by a factor of about three [25] (small numbers of specimens may lead to large variations in apparent temperature dependence), and

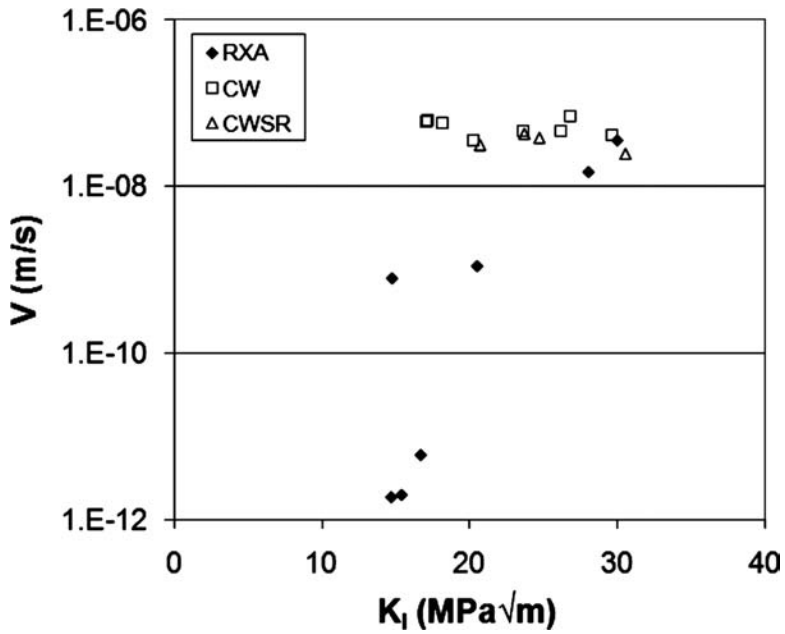


FIG. 15—K_I *dependence of V at 250°C for Zircaloy-4 fuel cladding in three metallurgical conditions.*

- Differences in microstructure, including texture, and strength.

In Zr–2.5Nb [30] and Zircaloy-2 pressure tubes [28], the crack velocity and K_{IH} are very sensitive to testing direction and cracking plane. This behavior is attributed to crystallographic texture. In pressure tubes in the CW condition, the basal plane normals are strongly oriented in the transverse direction. Cracking in the axial direction driven by a hoop stress is much faster and requires a much lower K_{IH} than cracking in the circumferential direction driven by an axial stress. The explanation is that hydrides reorient readily from the circumferential orientation to the radial direction with a hoop stress but not with an axial stress because the normal to the basal planes of the zirconium crystals, which are close to the habit planes of hydride, are parallel with the hoop direction and not the axial direction. A radial texture has been proposed to protect Zr–2.5Nb from DHC [31,32]. In all the fuel cladding tested in this study, the texture was highly radial, Table 3, yet DHC was observed at velocities slightly higher than in pressure tube materials with transverse textures. The threshold tensile stress to start reorienting hydrides in Zircaloy-4 fuel cladding is low—typical values are 120 MPa for CWSR cladding and 70 MPa for RXA cladding [33]—so difficulty in reorienting hydrides does not provide an impediment for DHC in cladding since the tensile stresses at the crack tip exceed the threshold stresses for hydride reorientation.

The value of DHC velocity is dominated by the diffusivity and the solubility limits of hydrogen in the zirconium alloy and to a lesser extent by the strength. Zircaloy-4 is essentially a single-phase alloy, with a distribution of intermetallic

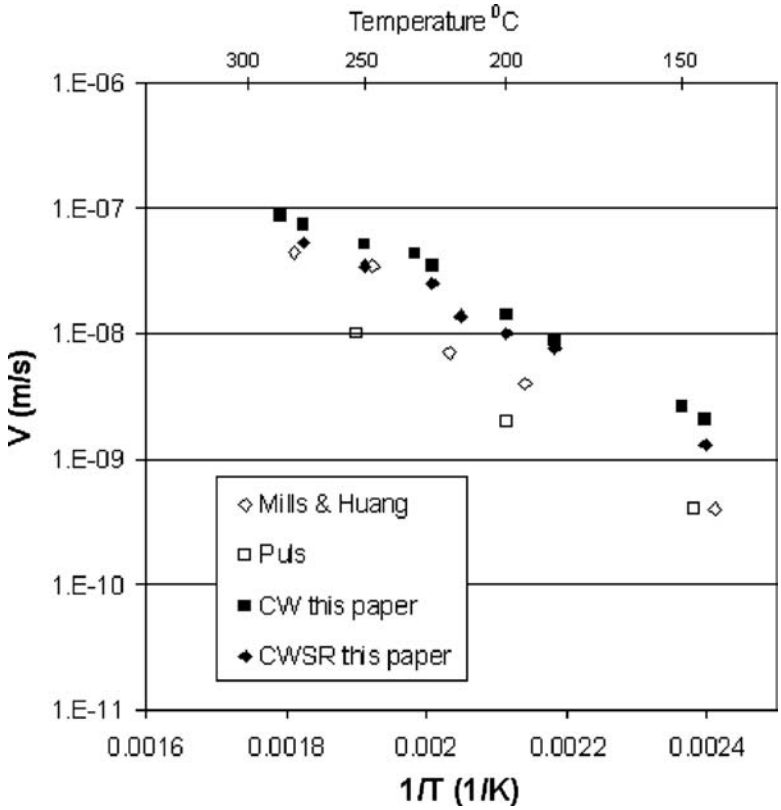


FIG. 16—*Comparison of temperature dependence of DHC in Zircaloy-2 pressure tubes 28,29 and Zircaloy-4 fuel cladding [this paper] up to 280°C.*

particles, and, with little error, the heat-treatments should not affect the diffusivity or solubility limits. Although yield strength would be the preferred over UTS as the strength variable for fracture analysis, only the latter values were available. Comparing V at a single temperature can be used to evaluate the effect of strength on V. A modest correlation ($R^2 = 0.84$) is found between UTS and the mean value of V at 250°C for the current batches of fuel cladding, except the RXA material, Fig. 18. The RXA material was excluded from the linear fit, but it was included in the figure for completeness and to emphasize how its behavior was different from that of the other tubing. The CANDU Sandvik cladding was stronger than the other two non-LWR claddings, and its higher value of V reflects this added strength. Values from Zircaloy-2 pressure tubes are in general agreement with those for fuel cladding, indicating that it is strength rather than texture that is causing the difference in values shown in Fig. 16.

In this study, the fracture surfaces attributed to DHC were clearly distinct from those made by fatigue or ductile rupture. As previously observed with Zircaloy [20,21,28], the fractographic features called striations were absent, with

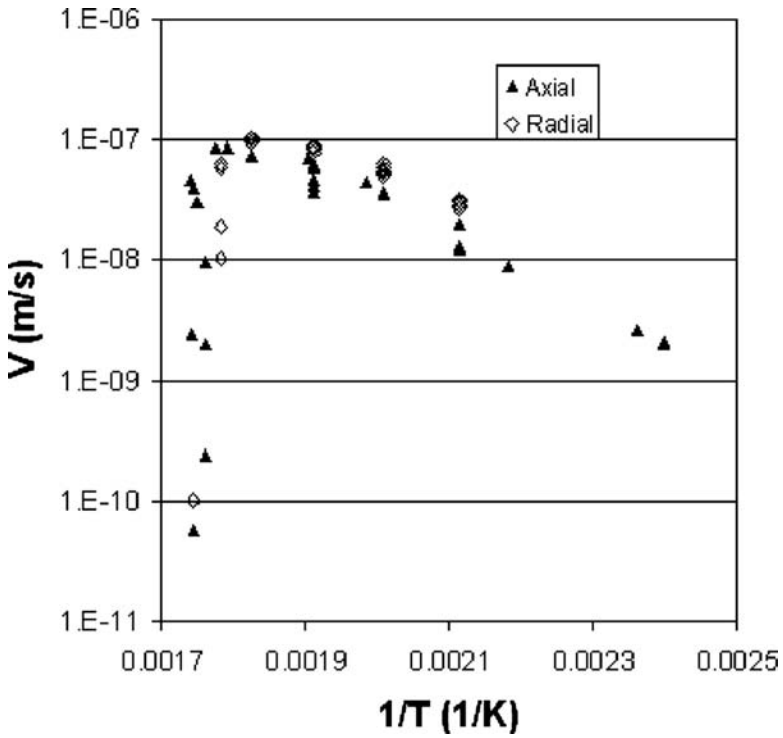


FIG. 17—*Comparison of temperature dependence of cracking in axial (this paper) and radial 16 directions in CW Zircaloy-4 fuel cladding.*

one exception, Fig. 9(*b*). These observations are in marked contrast to the fractography of Zr–2.5Nb where striations are easily and commonly observed, Fig. 9(*a*). Striations are bands across most of the width of a specimen, perpendicular to the crack growth direction, consisting of regions of ductile fracture bounding cleavage of hydride. They tend to remain almost a constant width and coplanar as the crack extends. In Zircaloy, the hydrides fracture on different planes along the crack front with ductile fracture between the brittle plates. The size of the brittle areas is variable, so bands of consistent width are not formed. This observation supports the idea that the microstructural features contributing to the difference in behavior of the two materials are probably the fine scale of the grains and the presence of a β-phase in Zr–2.5Nb. The single observation of striations in Zircaloy-4 may be linked to the thermal cycles imposed during the test where each striation corresponded to the stopping and restarting of cracking. The general lack of striations with DHC in Zircaloy in isothermal tests suggests that they are not a fundamental characteristic of DHC.

The decline of DHC at high temperatures has been observed in both Zr–2.5Nb [3,34,35] and Zircaloy [36]. This feature is apparent in each of the cladding materials tested, except for the RXA material where the scatter obscures any temperature dependence. As an example, Fig. 19 is a comparison

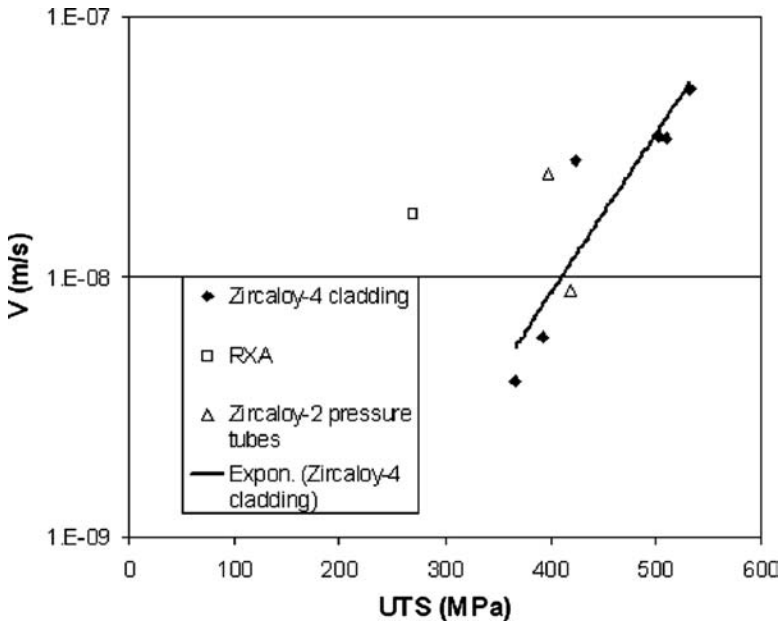


FIG. 18—*Effect of strength on mean DHC velocity in Zircaloy at 250°C.*

of the behavior of CW Zr–2.5Nb pressure tube material [34] and Zircaloy-4 fuel cladding in the CW and CWSR conditions. In Zr–2.5Nb the crack velocity starts to deviate from the Arrhenius correlation at about 310°C with no cracking detected at 350°C, while in the current Zircaloy-4 the initial deviation is between 275 and 285°C with no cracking at 300°C.

The rate of DHC can be suppressed when

- The hydrogen concentration is insufficient for hydrides to form at the crack tip (the current specimens contained 200 ppm hydrogen, which is sufficient for hydrides to be present at temperatures up to 360°C even on cooling to the test temperature; thus the observed reduced rate of cracking is not caused by lack of hydride),
- the temperature history prevents hydrides from forming at the crack tip (heating to the test temperatures may cause this situation even if hydrides are present in the metal matrix [37]; in the current tests the test temperature was always attained by cooling from at least 50°C above the test temperature with no undercooling, so this effect is not the cause of the reduced velocity), and
- K_{IH} is greater than the applied K_I. (In Zr–2.5Nb, K_{IH} has little temperature dependence at temperatures below 300°C, but at higher temperatures it increases rapidly [35]. Zircaloy-4 likely behaves in a similar manner, implying that K_{IH} increases to values greater than 16 MPa$\sqrt{m}$ above 280°C.) A corollary to this behavior is that V and the crack suppression temperature will appear to depend on K_I. Close to the critical

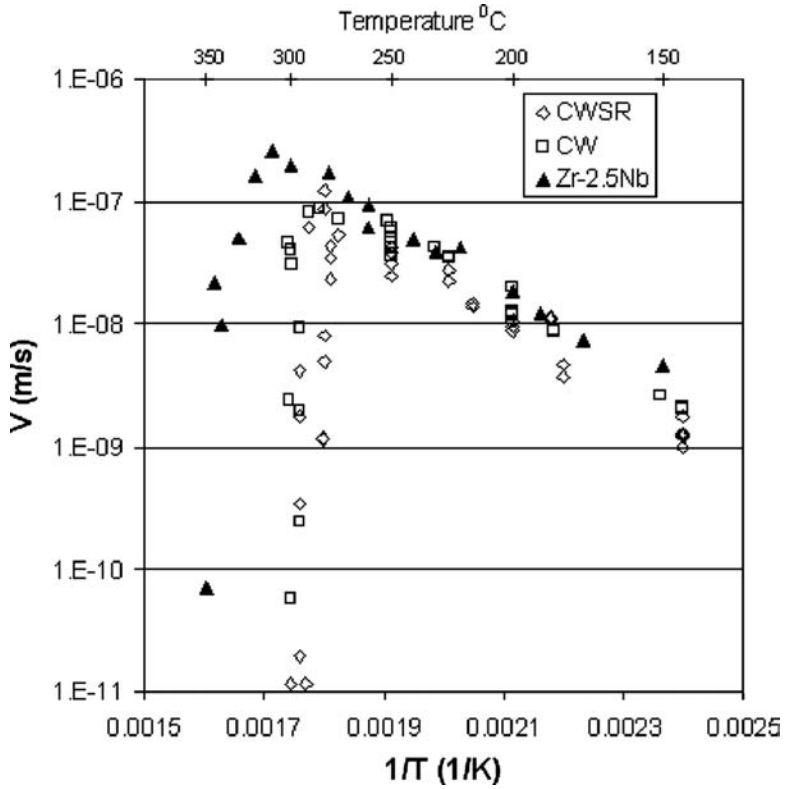


FIG. 19—*Comparison of decline in DHC at high test temperatures in CW Zr–2.5Nb 34 and CW and CWSR Zircaloy-4 fuel cladding [this paper].*

temperature, a small amount of evidence supports this conclusion. In Zr–2.5Nb the range of the suppression temperature increased from 280–313 to 328–359°C when K_I was increased from 13 to 17 MPa$\sqrt{m}$ [3]. In the current study, at 283°C in one specimen no cracking was detected after 9000 s at a K_I of 15 MPa$\sqrt{m}$, but once K_I was increased by about 7 %, the crack progressed but at a much reduced rate based on expectations from an extrapolation of Eq 1.

The maximum value of V in this study was 1.2×10^{-7} m/s at 282°C for CWSR material, which is two to six times lower than the rates estimated from splits in LWR cladding [14]. The current results are not suitable for direct application to the behavior of fuel cladding because the material is unirradiated. The added strength generated by irradiation has two consequences: The crack velocity is increased by a factor between three and ten [20,21], easily agreeing with the rates observed in-reactor, and the high temperature decline in velocity is postponed to higher temperatures [35]. Other differences between cladding on an operating fuel element and these laboratory experiments include temperature gradients, which can increase crack velocity and postpone the response of

V when the temperature is attained by heating [38,39]. During dry storage of spent fuel, the cladding may reach temperatures of around 400°C. The high temperature limit suggests that failure by DHC should not be possible for several years as the fuel cools toward the temperatures at which cracking may be observed.

Summary

The rate of DHC has been evaluated in Zircaloy-4 fuel cladding in several metallurgical conditions using the PLT technique. At temperatures below about 280°C, the cracking followed an Arrhenius behavior, but at higher temperatures the rate declined with no cracking above 300°C. The main role of microstructure is to control the material strength; the cracking rate increased as the strength increased. The radial texture did not protect the cladding from DHC. In all the cladding, except that in the recrystallized condition, cracking rate was independent of K_I, indicating that K_{IH} was below 11 MPa$\sqrt{m}$. In the recrystallized material the cracking rate was highly variable because it depended on K_I within the test range of up to 25 MPa$\sqrt{m}$. The DHC fracture surface consisted of flat broken hydrides, often in arcs, and, with one exception, no striations were observed.

Acknowledgments

The writers are grateful to the IAEA for financial support. The authors would also like to acknowledge the following technical assistance: A. Buyers, A. Lockley, and Zhang He (Atomic Energy of Canada Limited, CRL) characterized the materials; R. Jakobsson and B. Johansson (Studsvik) and P. Kotov (Bochvar Institute) provided mechanical testing; M. Mihalache (INR) performed fractography; and R. N. Singh and G. Sanyal (BARC) helped with the DHC testing. Zircatec donated CANDU cladding, and CONUAR-FAE donated Atucha cladding.

References

[1] Coleman, C. E., "Cracking of Hydride-Forming Metals and Alloys," *Comprehensive Structural Integrity*, Vol. 6, I. Milne, R. O. Ritchie, and B. Karihaloo, Eds., Elsevier, Kidlington, Oxford, UK, 2003, Chap. 6.03, pp. 103–161.

[2] Cheadle, B. A., Coleman, C. E., and Ambler, J. F. R., "Prevention of Delayed Hydride Cracking in Zirconium Alloys," *Zirconium in the Nuclear Industry—Seventh International Symposium, ASTM STP 939*, Strasbourg, France, June 24–27, 1985, R. B. Adamson and L. F. P. Van Swam, Eds., ASTM International, West Conshohocken, PA, 1987, pp. 224–240.

[3] Smith, R. R. and Eadie, R. L., "High Temperature Limit for Delayed Hydride Cracking," *Scr. Metall.*, Vol. 22, 1988, pp. 833–836.

[4] Simpson, C. J. and Ells, C. E., "Delayed Hydrogen Embrittlement in Zr–2.5 wt%Nb," *J. Nucl. Mater.*, Vol. 52, 1974, pp. 289–295.

[5] Perryman, E. C. W., "Pickering Pressure Tube Cracking Experience," *Nucl. Energy*, Vol. 17, 1978, pp. 95–105.

[6] Platonov, P. A., Ryazantseva, A. V., Saenko, G. P., Knizhnikov, Y. N., and Viktorov, V. F. "The Study of Cause of Cracking in Zirconium Alloy Channel Tubes," *Poster Paper at ASTM Zirconium in the Nuclear Industry—Eighth International Symposium*, San Diego, CA, June 19–23, 1988, ASTM, Philadelphia, PA, 1988, available as AECL Report RC-87.

[7] Jonsson, A., Hallstadius, L., Grapengiesser, B., and Lysell, G., "Failure of a Barrier Rod in Oskarshamn-3," *Fuel for the '90's, International Topical Meeting on LWR Fuel Performance*, Avignon, France, April 21–24, 1991, American Nuclear Society, La Grange Park, IL and European Nuclear Society, Brussels, Belgium, 1991, pp. 371–377.

[8] Schrire, D., Grapengiesser, B., Hallstadius, L., Lundholm, I., Lysell, G., Frenning, G., Ronnberg, G., and Jonsson, A., "Secondary Defect Behaviour in ABB BWR Fuel," *International Topical Meeting on Light Water Reactor Fuel Performance*, West Palm Beach, April 17–21, 1984, American Nuclear Society, La Grange Park, IL, 1994, pp. 398–409.

[9] Armijo, J. S., "Performance of Failed BWR Fuel," *International Topical Meeting on Light Water Reactor Fuel Performance*, San Diego, CA, June 19–23, 1988, American Nuclear Society, La Grange Park, IL, 1994, pp. 410–422.

[10] Clayton, J. C., "Internal Hydriding in Irradiated Defected Zircaloy Fuel Rods," *Zirconium in the Nuclear Industry—Eighth International Symposium, ASTM STP 1023*, L. F. P. Van Swam and C. M. Eucken, Eds., ASTM International, West Conshohocken, PA, 1989, pp. 266–288.

[11] Lysell, G. and Grigoriev, V., "Characteristics of Axial Splits in Failed BWR Fuel Rods," *Ninth International Symposium on Environmental Degradation of Materials in Nuclear Power Systems—Water Reactors*, Newport Beach, CA, August 1–5, 1999, The Minerals, Metals and Materials Society, Warrendale, PA, 1999, pp. 1169–1175.

[12] Efsing, P. and Pettersson, K., "Delayed Hydride Cracking in Irradiated Zircaloy Cladding," *Zirconium in the Nuclear Industry—12th International Symposium, ASTM STP 1354*, Toronto, Canada, June 15–18, 1998, G. P. Sabol and G. D. Moan, Eds., ASTM International, West Conshohocken, PA, 2000, pp. 340–355.

[13] Edsinger, K., Davies, J. H., and Adamson, R. B., "Degraded Fuel Cladding Fractography and Fracture Behavior," *Zirconium in the Nuclear Industry—12th International Symposium, ASTM STP 1354*, Toronto, Canada, June 15–18, 1998, G. P. Sabol and G. D. Moan, Eds., ASTM International, West Conshohocken, PA, 2000, pp. 316–339.

[14] Edsinger, K., "A Review of Fuel Degradation in BWRs," *Int. Topical Meeting on Light Water Reactor Fuel Performance*, Park City, April 10–13, 2000, American Nuclear Society, La Grange Park, IL, 2000, pp. 162–179.

[15] Shimada, S., Etoh, E., Hayashi, H., and Tukuta, Y., "A Metallographic and Fractographic Study of Outside-In Cracking Caused by Power Ramp Tests," *J. Nucl. Mater.*, Vol. 327, 2004, pp. 97–113.

[16] Sakamoto, K., Nakatsuka, M., and Higuchi, T., "Simulation of Cracking During Outside-In Type Failure of High Burn-Up Fuel Cladding Tubes," *Water Reactor Fuel Performance Meeting*, Seoul, Korea, October 19–23, 2008, Korean Nuclear Society, Seoul, Korea, 2008, Paper 8009.

[17] Ogata, K., Baba, T., Kamimura, K., Etoh, Y., and Ito, K., "Separate Effects of Factors Affecting Outside-In Cracking of High Burnup Fuel Cladding," *Water Reactor Fuel Performance Meeting*, Seoul, Korea, October 19–23, 2008, Korean Nuclear Society, Seoul, Korea, 2008, Paper 8130.

[18] Unnikrishnan, K., Mishra, P., Jathar, V. P., Kumar, S., Sahoo, K. C., and Anantharaman, S., "Observation of Delayed Hydride Cracking in PHWR Fuel Assembly,"

Tenth CNS International Conference on CANDU Fuel, Toronto, Canada, October 5–8, 2008, Canadian Nuclear Society, Toronto, ON, Canada, 2008.

[19] Coleman, C. E. and Inozemtsev, V. V., "Measurement of Rates of Delayed Hydride Cracking (DHC) in Zr–2.5Nb alloys—An IAEA Coordinated Research Project," *J. ASTM Int.*, Vol. 5, 2008, paper ID JAI101091.

[20] Efsing, P. and Pettersson, K., "The Influence of Temperature and Yield Strength on Delayed Hydride Cracking in Hydrided Zircaloy-2," *Zirconium in the Nuclear Industry—Eleventh International Symposium, ASTM STP 1295*, Garmisch-Partenkirchen, Germany, September 11–14, 1995, E. R. Bradley and G. P. Sabol, Eds., ASTM International, West Conshohocken, PA, 1996, pp. 394–404.

[21] Grigoriev, V. and Jakobsson, R., "Delayed Hydrogen Cracking Velocity and J-Integral Measurements on Irradiated BWR Cladding," *J. ASTM Int.*, Vol. 2, 2005, paper ID JAI12434.

[22] Grigoriev, V., Josefsson, B., Lind, A., and Rosborg, B., "A Pin-Loading Tension Test for Evaluation of Thin-Walled Tubular Materials," *Scr. Metall. Mater.*, Vol. 33, No. 1, 1995, pp. 109–114.

[23] Grigoriev, V., Josefsson, B., and Rosborg, B., "Fracture Toughness of Zircaloy Cladding Tubes," *Zirconium in the Nuclear Industry—Eleventh International Symposium, ASTM STP 1295*, Garmisch-Partenkirchen, Germany, September 11–14, 1995, E. R. Bradley and G. P. Sabol, Eds., ASTM International, West Conshohocken, PA, 1996, pp. 431–447.

[24] Yagnik, S. K., Ramasubramanian, N., Grigoriev, V., Sainte-Catherine, C., Bertsch, J., Adamson, R., Kuo, R.-C., Mahmood, S. T., Fukuda, T., Efsing, P., and Oberländer, B. C., "Round-Robin Testing of Fracture Toughness Characteristics of Thin-Walled Tubing," *J. ASTM Int.*, Vol. 5, 2008, paper ID JAI101140.

[25] Coleman, C., Grigoriev, V., Inozemtsev, V., Markelov, V., Roth, M., Makarevicius, V., Kim, Y. S., Kanwar, L. A., Chakravartty, J. K., Mizrahi, R., and Lalgudi, R., "Delayed Hydride Cracking in Zircaloy Fuel Cladding—An IAEA Coordinated Research Programme," *Nucl. Eng. Technol.: Int. J. Korean Nucl. Soc.*, Vol. 41, 2009, pp. 171–178.

[26] Grigoriev, V. and Jakobsson, R., "DHC Axial Crack Velocity Measurements in Zirconium Alloy Fuel Cladding," *STUDSVIK/N-05/281*, Studsvik Nuclear AB, 2005, ISBN 91-7010-377-1.

[27] Roth, M., Compliance measurements based on Ref [26, INR, June 23, 2009.

[28] Huang, F. H. and Mills, W. J., "Delayed Hydride Cracking Behavior for Zircaloy-2 Tubing," *Metall. Trans. A*, Vol. 22A, 1991, pp. 2049–2060.

[29] Puls, M. P., Simpson, L. A., and Dutton, R., "Hydride-induced crack growth in zirconium alloys," *AECL Report* AECL-7392, Atomic Energy of Canada Limited, Whiteshell Nuclear Research Establishment, Pinawa, Manitoba, Canada, 1982.

[30] Coleman, C. E., "Effect of Texture on Hydride Reorientation and Delayed Hydrogen Cracking in Cold-Worked Zr–2.5Nb," *Zirconium in the Nuclear Industry—Fifth International Conference, ASTM STP 754*, Boston. MA, August 4–7, 1980, D. G. Franklin, Ed., ASTM International, West Conshohocken, PA, 1982, pp. 393–411.

[31] Coleman, C. E., Cheadle, B. A., Cann, C. D., and Theaker, J. R., "Development of Pressure Tubes with Service Life Greater Than 30 Years," Garmisch-Partenkirchen, Germany, September 11–14, 1995, *Zirconium in the Nuclear Industry—Eleventh International Symposium, ASTM STP 1295*, E. R. Bradley and G. P. Sabol, Eds., ASTM International, West Conshohocken, PA, 1996, pp. 884–898.

[32] Kim, S. S. and Kim, Y. S., "K_{IH} in Radial Textured Zr–2.5%Nb Pressure Tube," *J. Nucl. Mater.*, Vol. 279, 2000, pp. 286–292.

[33] Aomi, M., Baba, T., Miyashita, T., Kamimura, K., Yasuda, T., Shinohara, Y., and Takeda, T., "Evaluation of Hydride Reorientation Behavior and Mechanical Properties for High-Burnup Fuel-Cladding Tubes in Interim Dry Storage," *J. ASTM Int.*, Vol. 5, 2008, paper ID JAI101262.

[34] Sagat, S. and Puls, M.P., "Temperature Limit for Delayed Hydride Cracking in Zr–2.5Nb Alloys," *17th Inter. Conf. Structural Mechanics in Reactor Technology*, Prague, Czech Republic, August 17–22 2003, International Association for Structural Mechanics in Reactor Technology, Berlin, Germany, 2003, Paper G06-4.

[35] Resta Levi, M. and Puls, M. P., "DHC Behaviour of Irradiated Zr–2.5Nb Pressure Tubes up to 365°C," *18th Inter. Conf. on Structural Mechanics in Reactor Technology*, Beijing, China, August 7–12 2005, International Association for Structural Mechanics in Reactor Technology, Berlin, Germany 2005, Paper G10-3.

[36] Mahmood, S. T., Farkas, D. M., Adamson, R. B., and Etoh, Y., "Post-Irradiation Characterization of Ultra-High-Fluence Zircaloy-2 Plate," *Zirconium in the Nuclear Industry: 12th International Symposium, ASTM STP 1354*, Toronto, Canada, June 15–18, 1998, G. P. Sabol and G. D. Moan, Eds., ASTM International, West Conshohocken, PA, 2000, pp. 139–169.

[37] Ambler, J. F. R., "Effect of Direction of Approach to Temperature on the Delayed Hydrogen Cracking Behavior of Cold-Worked Zr–2.5Nb," *Zirconium in the Nuclear Industry: Sixth International Symposium, ASTM STP 824*, Vancouver, Canada, June 28–July 1, 1982, D. G. Franklin and R. B. Adamson, Eds., ASTM International, West Conshohocken, PA, 1984, pp. 653–674.

[38] Sagat, S., Chow, C. K., Puls, M. P., and Coleman, C. E., "Delayed Hydride Cracking in Zirconium Alloys in a Temperature Gradient," *J. Nucl. Mater.*, Vol. 279, 2000, pp. 107–117.

[39] Sakamoto, K., Nakatsuka, M., Higuchi, T., and Ito, K., "Role of Radial Temperature Gradient in Outside-In Type Failure of High Burn-Up Fuel Cladding Tubes During Power Ramp Tests," *Proc. Top Fuel 2009*, Paris, France, September 6–10, 2009, French Nuclear Energy Society, Paris, 2009, Paper 2076.

DISCUSSION

Question 1, Javier Romero, Westinghouse Electric Sweden AB:—What would be an explanation of faster crack propagation in radial-textured LWR cladding, when compared to not so strong radial-textured materials?

Author's Response:—We would expect the opposite to what your question suggests. For example, DHC on the plane with its normal parallel with the hoop direction should be faster in material with a transverse texture than in material with a radial texture. Two effects cause this behaviour: susceptibility to form radial hydrides with a hoop stress and the hoop strength itself are both greater with a transverse texture than with a radial texture. Radial hydrides assist the passage of a crack. The rate of DHC depends on the rate of hydrogen diffusing into the region of the stressed crack tip [1]. Hydrogen diffusion to a crack tip results from a gradient in chemical potential, μ, the size of which depends on the prevailing hydrostatic stress, σ_H. At a crack tip, $\sigma_H = \theta.\sigma_y$, where σ_y is the yield stress and θ is a proportionality constant that depends on the geometrical constraint. With all other factors such as solubility limit and diffusivity of hydrogen being constant, as σ_y increases the rate of diffusion of hydrogen to the crack tip increases and therefore the rate of cracking increases.

Question 2, Zhongmen Yao, Queen's University, Canada:—Where did you get this information: Hydrides present up to 360°C?

Author's Response:—To propagate DHC the concentration of hydrogen at the crack tip must exceed the solubility limit for hydride precipitation, TSSP. In our specimens the hydrogen concentration was 200 ppm and the temperature for hydride precipitation for this hydrogen concentration is about 360 °C [2]. Lack of hydrides is not the explanation for the decline in cracking rate because it happens at about 280 °C where hydrides would still be present in the cladding.

Question 3, Bo Cheng, EPRI, USA:—There are people holding the belief that Zircaloy, particularly recrystallized ones, is not susceptible to DHC, and radial hydride formation under stress at temperature is required to propagate cracks. To address the question, did you perform metallographic examination to separate DHC and hydride-assisted cracking?

Author's Response:—We have not yet done metallography on a stopped crack. We would expect that the formation of radial hydrides at the crack tip would be part of the DHC process so the observation of radial hydrides at and close to the crack tip would not necessarily separate DHC from rapid hydride-assisted cracking. Crack extension, as detected by crack-opening or potential drop, was observed to increase slowly with time and the rates of this crack growth fit with expectations of the rates of DHC.

Question 4, Sun Chao, NPIC, China:—I found that it is very difficult to observe striations line on DHC fracture surfaces of Zr-4 alloy. How can explain it?

Author's Response:—Your observations are in agreement with ours. Striations are regions of hydride cracking separated by ductile fracture of the zirconium alloy. Their spacings are remarkably consistent across the full width of a specimen suggesting that the size of the hydride that cracks is constant. Striations are commonly observed in Zr-2.5Nb alloys. Compared with Zircaloy, the usual scale of the microstructure in Zr-2.5Nb is about ten times smaller, the grains tend to be more uniform in shape and orientation, and the absolute dispersion of the grain size is smaller. In Zr-2.5Nb the hydrides at the crack tip will be confined to a narrow band of grains and the steps between the planes of hydrides will be small and the fracture surface will appear uniform leading to striations. When the grain size is

increased the striations are wider [3] strongly suggesting that hydride precipitation at the crack tip is closely related to the underlying microstructure of the alloy. Thus it is not surprising that the product of cracking should be so different between alloys with different microstructures. In the relatively large grained Zircaloy, the hydrides will vary in size and direction between adjacent grains, and adjacent planes of cracked hydride will be well separated, thus breaking up the uniformity of the crack front and preventing the formation of striations.

Question 5, Jun Cui, Kinectrics, Canada:—Author speculates that low DHCV at high temp could be due to $K_I \rightarrow K_{IH}$ and used Resta Levi's K_{IH} data from Zr-Nb to support this. Any plans to measure K_{IH} on testing material to confirm this in the K_{IH} CRP in future?

Author's Response:—This paper concluded the current CRP. The proposal for a new CRP includes specific measurements of K_{IH}.

Question 6, Arthur Motta, Penn StateUniversity, USA:—You associate the drop-off in velocity of the crack at 300°C with K ~ KIH. Do you believe the reason for this is the change in strength of the matrix? Could it be related to changes in mechanical properties of hydrides embedded in the Zr matrix?

Author's Response:—The fracture toughness of zirconium hydride is very low and has little temperature dependence up to 300 °C [4]. The change in strength of the zirconium alloy matrix to the point where the tensile stress is insufficient to fracture hydrides at the crack tip is the most likely explanation for the drop-off in velocity.

Question 7, Johannes Bertsch, Paul Scherrer Institut:—1) How was it possible to measure the low crack growth (fastest 8.6 mm/day) rates with, for instance, crack opening, especially with curved crack fronts? 2) Do you see effects of the sample size, pressure tube versus cladding tube? [Could explain different lines on slide 24 *(FIG 16 in paper)*]. 3) How does irradiated material react?

Author's Response:—1) The instrumentation was used to detect when cracking started, providing the incubation time, and, from calibration, used to provide a rough guide to the extent of cracking. Because of the curved crack front, the amount of cracking was measured on the fracture surface itself, usually from nine equally spaced measurements across the width of the specimen. Each specimen had two cracks so the amount of cracking was an average of the two values. The crack velocity was taken as the extent of crack growth divide by the cracking time (i.e. total time – incubation time.)

2) An increase in specimen thickness is expected to increase the crack growth rate through an increase in the hydrostatic stress at the crack tip. If θ (see question 1) is increased from 1.4 (cladding; plane stress) to 2.4 (pressure tube, plane strain), the crack growth rate should increase by about 50% [1]. The results in FIG. 16 show the opposite behaviour illustrating that other factors, such as material strength and microstructure, dominate the thickness effect.

3) Neutron irradiation tends to increase the yield strength and therefore the hydrostatic stress at the crack tip. Consequently, the DHC growth rate in irradiated materials tends to be greater than in unirradiated materials – see answer to Question 1.

Question 8, Young Suk Kim:— 1) The striation spacing was observed in Zircaloy-4. Please explain why the striation spacing was difficult to observe in Zircaloy-4. If that is related to the presence of Nb, this argument cannot explain the observation of the striations in Zircaloy-4 even though the observation of the striations was only once. 2) According to your claim, if the applied K_{IH} increased to a higher value, then you expect no drop of DHC velocity?

Author's Response:—1) The single observation reported in this paper of features that looked like striations was correlated exactly with a crack that was stopped and restarted several times by temperature cycling. Similar bands were observed in the early cracks in Zr-2.5Nb pressure tubes; these cracks grew during reactor shutdowns and stopped when the reactor went back to power [5]. The discussion to Question 4 provides an answer to the lack of striations in Zircaloy. If striations are a phenomenon peculiar to alloys containing β-phase or a very refined structure, then they are not a characteristic feature of DHC but a characteristic of the alloy or microstructure.

2) The explanation is exactly the opposite to your question. In Zr-2.5Nb, below the drop-off temperature, the cracking rate follows Arrhenius behaviour and K_{IH} has little temperature dependence. From 300 to 340°C, K_{IH} increases by about two times, for example, from about 8 to 16 MPa$\sqrt{}$m. When the applied K_I is close to K_{IH} the crack growth rate declines and, if K_I is below K_{IH}, cracking is absent. Thus there is a temperature above which it is difficult to grow a crack by DHC. The explanation for the decline in cracking rate and a critical drop-off temperature in Zircaloy-4 is based on the analogy with Zr-2.5Nb.

Question 9, Joe Rashid, Anatech:—Crack extension under DHC is a function of the stress state at the crack tip and the hydride's morphology there, which is also function of the local stress conditions (triaxiality, plastic zone size, etc). In thick specimens, plain strain specimens, the crack tip stress state is three-dimensional and hydrides can be oriented normally to the stress direction. The situation is different in thin, plane stress specimens. K_{IH}, which is a function of the applied, uniaxial far field stress, would not be sufficient to describe what goes on in the various specimens, which differ in geometry, strength, etc. Perhaps, what is needed is another "unifying" parameter called "crack-tip stress triaxiality factor". Any future work on quantifying this "new" parameter would be most useful, and could explain current results.

Author's Response:—Although the use of K_I for fuel cladding is probably outside the strict application of linear elastic fracture mechanics formulation, it provides a useful guide. Since it is being used on specimens of the actual component, it can be used without the need to make interpretations for size and geometry. For models of crack growth rate based on the gradient in chemical potential derived from the hydrostatic stress [1], simply using θ of 1.4 and appropriate diffusivities and solubility limits [2], provides a good quantitative description of the current results on fuel cladding, FIG. 1. The measured value at the lowest temperature is higher than the predicted value possibly because γ-hydride rather than δ-hydride is cracking; γ-hydride and δ-hydride have different solubility limits.

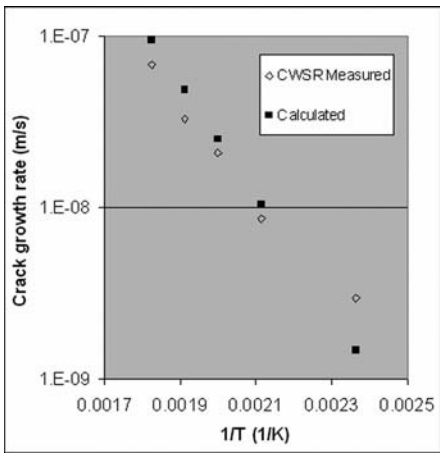


FIG. 1. Comparison of measured and calculated DHC growth rates in Zircaloy-4 in the cold-worked stress-relieved condition.

References

1. McRae, G. A., Coleman, C. E., Leitch, B. W., The first step for delayed hydride cracking in zirconium alloys, *J. Nucl. Mater.*, Vol. 396, 2010, pp. 130–143.
2. McMinn, A., Darby, E. C., Schofield, J. S., "The Terminal Solid Solubility of Hydrogen in Zirconium Alloys," *Zirconium in the Nuclear Industry-Twelfth International Symposium, ASTM STP 1354,* G. P. Sabol and G. D. Moan, Eds., ASTM International, West Conshohocken, PA, 2000, pp. 173–195.
3. Shek, G. K., Jovanovic, M. T., Seahra, H., Ma, Y., Li, D., and Eadie, R. L., "Hydrode, Morphology and Striation Formation during Delayed Hydride Cracking in Zr-2.5%Nb", *J. Nucl. Mater.,* Vol. 231, 1996, pp. 221–230.
4. Simpson, L. A., Cann, C. D., "Fracture Toughness of Zirconium Hydride and its Influence on the Crack Resistance of Zirconium Alloys", *J. Nucl. Mater.*, Vol. 87, 1979, pp. 303–316.
5. Causey, A. R., Urbanic, V. F., and Coleman, C. E., "In-reactor oxidation of crevices and cracks in cold-worked Zr-2.5 wt% Nb", *J. Nucl. Mater.,* Vol. 71, 1977, pp. 25–35.

Reprinted from JAI, Vol. 8, No. 4
doi:10.1520/JAI103251
Available online at www.astm.org/JAI

Mirco Grosse[1]

Neutron Radiography: A Powerful Tool for Fast, Quantitative and Non-Destructive Determination of Hydrogen Concentration and Distribution in Zirconium Alloys

ABSTRACT: The hydrogen concentration in zirconium alloys used in nuclear fuel cladding can be determined quantitatively, rapidly and non-destructively with a spatial resolution of 25 μm by neutron radiography. Because the total neutron cross section of hydrogen is more than one order of magnitude higher than that of zirconium, low concentrations of hydrogen can be measured. Calibration measurements have been performed and confirm the linear dependence of the total macroscopic neutron cross section on the hydrogen to zirconium atomic ratio as expected from theoretical analysis. The fast and non-destructive character of the method provides the possibility of in situ investigations. Examples of in situ investigations of the diffusion of hydrogen into Zircaloy-4 and of hydrogen uptake during steam oxidation are given. For the steam oxidation experiments a fast hydrogen uptake was found during the first 10 s. After this first step, the hydrogen concentration in the sample decreases slightly. If breakaway oxidation occurs, additional hydrogen absorption takes place. The hydrogen concentration can then increase by nearly one order of magnitude by this process. The influence of variations in the total gas flow and the steam flow on the hydrogen uptake was investigated, too.

KEYWORDS: neutron radiography, zirconium alloys, hydrogen uptake

Manuscript received July 12, 2010; accepted for publication March 23, 2011; published online May 2011.

[1]Institute for Applied Materials, Karlsruhe Institute of Technology, P.O. Box 3640, D-76021 Karlsruhe, Germany

Cite as: Grosse, M., "Neutron Radiography: A Powerful Tool for Fast, Quantitative and Non-Destructive Determination of Hydrogen Concentration and Distribution in Zirconium Alloys," *J. ASTM Intl.*, Vol. 8, No. 4. doi:10.1520/JAI103251.

Copyright © 2011 by ASTM International, 100 Barr Harbor Drive, PO Box C700, West Conshohocken, PA 19428-2959.

Introduction

Within the framework of the QUENCH program at the Karlsruhe Institute of Technology (the former Forschungszentrum Karlsruhe), loss of coolant accidents (LOCA) and severe accident scenarios (accidents beyond design basis) are studied experimentally in large-scale cladding tube simulator bundle tests [1–4]. After loss of coolant, the fuel rods become overheated. Reflooding of the reactor core induces a high production of water steam which oxidizes the hot fuel cladding in a strongly exothermic reaction. The chemical reaction can be described on a first order by

$$2H_2O + Zr \Longleftrightarrow ZrO_2 + 2x^*H_2 + 4(1 - x)H_{absorbed} \quad (1)$$

The produced hydrogen can be released as H_2 gas into the environment or can be absorbed by the remaining metallic zirconium. Detailed descriptions of these processes are given in Ref 5. The release of molecular hydrogen H_2 causes the risk of a hydrogen detonation in the environment. The absorbed hydrogen embrittles the metallic β–Zr phase with the consequence of reduced thermomechanical resistance. The absorbed hydrogen can be accumulated in the remaining metal. If the temperature escalates, a very fast oxidation occurs and the hydrogen is released at once, thus changing the time scale of hydrogen release into the environment.

The amount of absorbed hydrogen is usually determined quantitatively by hot vacuum extraction. This method is destructive and does not give any information about the local hydrogen distribution in the sample.

A quantitative analysis of neutron radiographs is used to determine the hydrogen concentration in cladding tube segments in a non-destructive, fully quantitative and fast manner (illumination time between 10 and 300 s per frame) with a spatial resolution between 25 and 100 μm. The non-destructive and fast character of neutron radiography (NR) provides the possibility of in situ investigations of the hydrogen uptake and release. Because the microscopic total hydrogen cross section σ_H for thermal or cold neutrons is about one order of magnitude higher than the cross section of zirconium σ_{Zr} or the mean cross section of Zr–Sn or Zr–Nb alloys, the method is a powerful tool for these investigations. Minimal concentrations of about 0.5 at.% ($\sim$ 50 wppm) for ex situ and 0.3 at.% ($\sim$ 30 wppm) for in situ measurements can be detected.

In this study, NR is introduced including its theoretical basis. Examples for the application of NR in ex situ investigations of samples withdrawn from large-scale QUENCH tests [1–4] and from laboratory-scale separate-effects tests and in in situ investigations of isothermal hydrogen uptake will be given. In particular, the in situ experiments provide new information about hydrogen uptake never obtained by other methods before.

Theoretical Background

The basic principle of NR is the following: A parallel neutron beam with large cross section and relative homogeneous intensity distribution transmits a

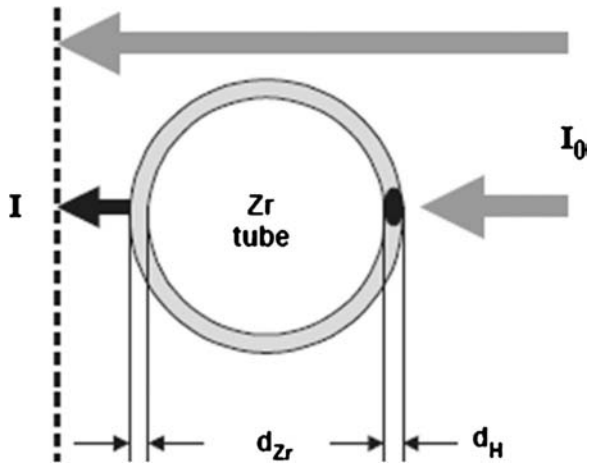


FIG. 1—*Schematic representation of NR of a Zr cladding tube.*

sample and will be detected with sufficient spatial resolution. Figure 1 shows a schematic representation of the method. Different intensities at positions behind the specimens arise from different path lengths through the material and different neutron attenuations of different sample materials.

Figure 2 reveals three Zry-4 cladding tube segments with a length of 20 mm and inner and outer diameters of 9.75 and 10.50 mm, respectively, annealed in flowing Ar/H_2 gas mixture at different temperatures and hydrogen partial pressures. The hydrogen concentrations (18810, 5290, and 2660 wppm, respectively) were determined by weight gain measurements. The horizontal intensity distribution is given together with the radiographs. The shape of the intensity distributions is typical for tube-shaped specimens with the longest path through the material of neutrons passing the specimen tangential close to the inner radius of the tube.

In order to determine the hydrogen concentration from the neutron radiographs the images have to be analysed quantitatively. The neutron transmission of a sample measured for each pixel can be described by

$$T(x,y) = \frac{I(x,y) - I_B(x,y)}{I_0(x,y) - I_B(x,y)} = \exp\Big(- \Sigma_{\text{total}}(x,y)s(x,y)\Big) \tag{2}$$

$T(x,y)$ is the neutron transmission detected at the spatial position (x,y), $I(x,y)$ the intensity behind the sample at this position, $I_B(x,y)$ the background intensity measured with a "black" Cd specimen being completely intransparent for neutrons, $I_0(x,y)$ is the intensity before the sample, $\Sigma_{\text{total}}(x,y)$ the total macroscopic neutron cross section of the sample and $s(x,y)$ the path length through the sample. The total macroscopic neutron cross section Σ_{total} is the sum over all isotopes i of the microscopic total neutron cross section σ_i multiplied by its number density N_i. In the system of steam oxidized cladding material, Σ_{total}

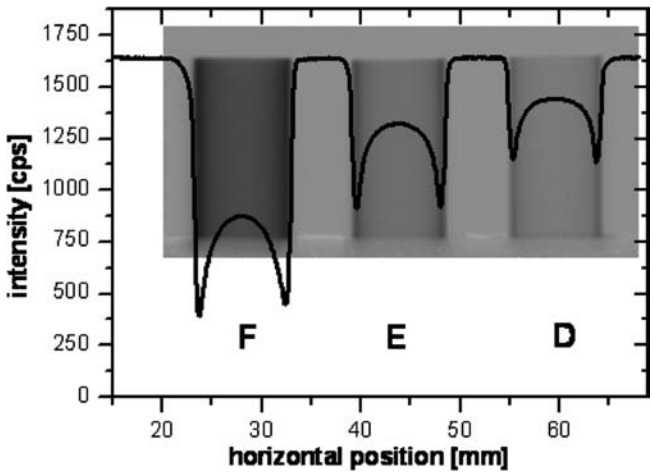


FIG. 2—*Example of neutron radiographs of Zry-4 cladding tube segments together with their horizontal intensity distribution at axial middle positions.*

depends only on the chemical composition of the alloy and the amount of consumed oxygen and absorbed hydrogen

$$\Sigma_{\text{total}} = \sum_i N_i \sigma_i = \underbrace{N_{\text{Zr}}\sigma_{\text{Zr}} + N_{\text{Nb}}\sigma_{\text{Nb}} + N_{\text{Sn}}\sigma_{\text{Sn}} + \cdots}_{\Sigma_{\text{cladding material as received}}} + N_{\text{H}}\sigma_{\text{H}} + N_{\text{O}}\sigma_{\text{O}} \tag{3}$$

From Eq 3 it can be concluded that the macroscopic neutron cross section of the sample linearly depends on the H/Zr atomic ratio. The same is valid for the O/Zr ratio. The calibration has to be performed for both, the effect of hydrogen and oxygen, separately. With additional knowledge from metallographic investigations or of the known oxidation kinetics the effect of oxygen can be estimated and subtracted to extract the effect of hydrogen.

It has to be mentioned that the total microscopic neutron cross section depends not only on the type of isotope but also on its chemical bonding. If the applied neutron spectrum and the chemical bonding state of all relevant elements in the sample are known, the correlation factor between the total macroscopic neutron cross section and the hydrogen concentration can be calculated. However, due to uncertainties in the neutron spectrum and of the bonding state of the elements (e.g., oxygen can be in the oxide layer but also absorbed in the α−Zr, hydrogen can be dissolved in the metallic matrix or be precipitated with different hydride microstructures) the method has to be calibrated experimentally.

Materials and Measurements

Up to now measurements were performed on Zry-4, Dx/D4 Duplex claddings, M5^{TM}, both produced by AREVA, the Russian VVER type cladding material

TABLE 1—*Concentration of the main alloying elements of the investigated materials (in wt %, Zr—balance).*

Alloy	Sn	Nb	Fe	Cr
D4	0.50	...	0.50	0.20
E110	...	0.97	...	...
M5™	...	1.00	0.035	...
Zirlo™	0.99	1.02	0.11	...
Zircaloy-4	1.50	...	0.21	0.10

E110 and Westinghouse ZIRLO™ alloy. The chemical compositions of the materials are given in Table 1. A large number of investigations were performed. However, the paper is focused to introduce the method. Therefore, only few examples of the investigations will be given. A detailed presentation of all results will be given elsewhere.

For the measurements, segments of a length of 20 mm were cut from commercial cladding tubes. The ex situ measurements were performed on specimens oxidized isothermally in steam in a horizontal tube furnace in flowing atmosphere using argon as an inert reference gas. The gas composition was controlled by "Bronkhorst" mass flow controllers, evaporator and mixer. The gas atmosphere was monitored by mass spectrometer analysis of the furnace off-gas.

The samples were shifted from an air-lock into the furnace at test temperature. After about 100 s for temperature equilibration the steam was switched on. After a predefined time the steam flow was switched off and the specimens remained in flowing argon atmosphere until they were removed into the air lock. The samples cooled down in the air-lock to room temperature in argon within about 300 s.

The hydrogen pre-loaded calibration specimens were produced by annealing of cladding tube segments in an Ar/H_2 atmosphere applying different temperatures and hydrogen partial pressures. The absorbed hydrogen was determined by measurement of the weight gain of the specimens. The specimens used for the calibration of the effect of oxide were produced by annealing in Ar/O_2 atmosphere at 1100°C for various times. The oxide layer thicknesses were determined by metallographic investigations after the calibration NR measurements.

The radiography measurements were performed at the ICON facility at the Swiss neutron source SINQ (Paul Scherrer Institute Villigen, Switzerland). Due to the limited field of view (28 mm × 28 mm for the highest spatial resolution microtomography setup), large specimens withdrawn from the large-scale QUENCH tests had to be measured sequentially. They were moved with a step size of 20 mm by a computer controlled, motorized positioning system after each measurement.

For the in situ measurements the in situ NR reaction oven (INRRO) facility was constructed. Materials with highest neutron transmission were used for the furnace tube, the electrical resistivity heater and the windows for the neutron beam located at the opposite sites of the furnace. A schematic representation of the INRRO-facility is given in Fig. 3.

In the case of in situ experiments, the calibration of the correlation between hydrogen concentration and total macroscopic neutron cross section is more

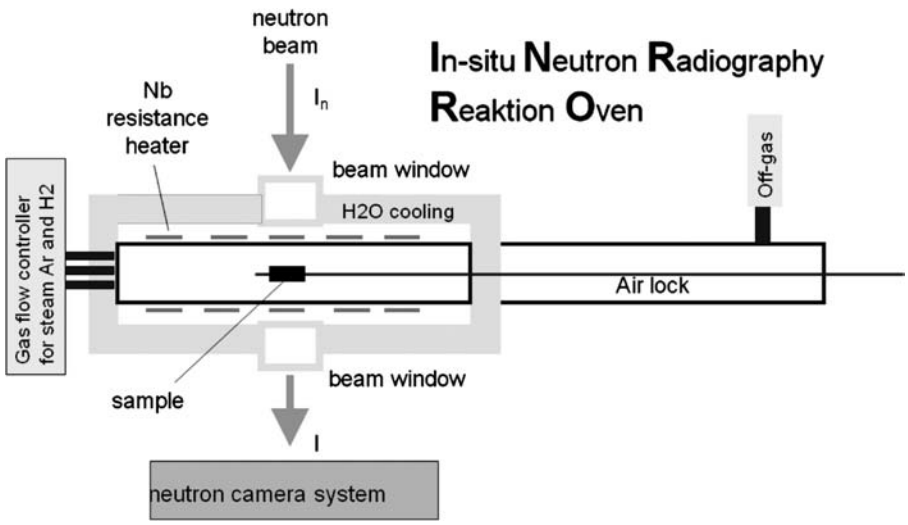


FIG. 3—*Scheme of the INRRO facility.*

difficult, because hydrogen is very volatile at temperatures of 900°C and above and specimens preloaded with hydrogen would release the hydrogen during short times. Therefore, equilibrium between the hydrogen partial pressure p_{H_2} in the Ar/H_2 furnace atmosphere and the hydrogen concentration in the zirconium alloy $C_H^{(m)}$ was established. This equilibrium is defined by Sieverts' law

$$C_H^{(m)} = K_S * \sqrt{p_{H_2}} \tag{4}$$

$$K_S = \exp\left(\frac{\Delta_S S}{R} - \frac{\Delta_S H}{R \cdot T}\right) \tag{5}$$

where:

K_S = Sieverts constant,
T = absolute temperature,
R = gas constant ($8.31\,\mathrm{J\,mol^{-1}\,K^{-1}}$),
$\Delta_s S$ and $\Delta_s H$ = free dissolution entropies and enthalpies, respectively.

The parameters of Sieverts' law were determined in Ref 6.

The NR in situ investigations were performed at the ICON and at the ANTARES facility at the Munich research reactor FRM-2 (TU Munich, Germany).

Results and Discussion

Calibration Measurements

In order to use NR to measure hydrogen concentrations in zirconium alloys the correlation between total macroscopic neutron cross section of the sample and

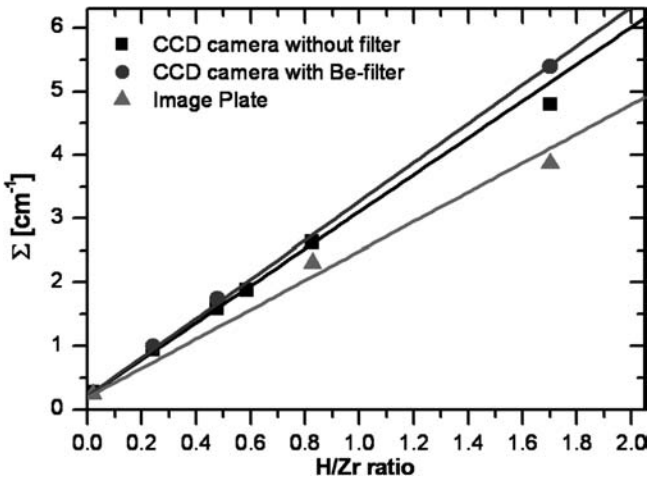


FIG. 4—*Linear correlation between total macroscopic neutron cross section and H/Zr atomic ratio for three experimental setups*

the hydrogen concentration has to be calibrated [7]. As Figs. 4 and 5 show, the experimental calibration performed with specimens of known hydrogen content and oxide layer thicknesses, respectively, confirms this linear dependence expected from Eq 3. The influence of the oxide layer is much lower than the effect of hydrogen. It can be corrected for steam oxidised specimens if the oxide layer thickness can be estimated.

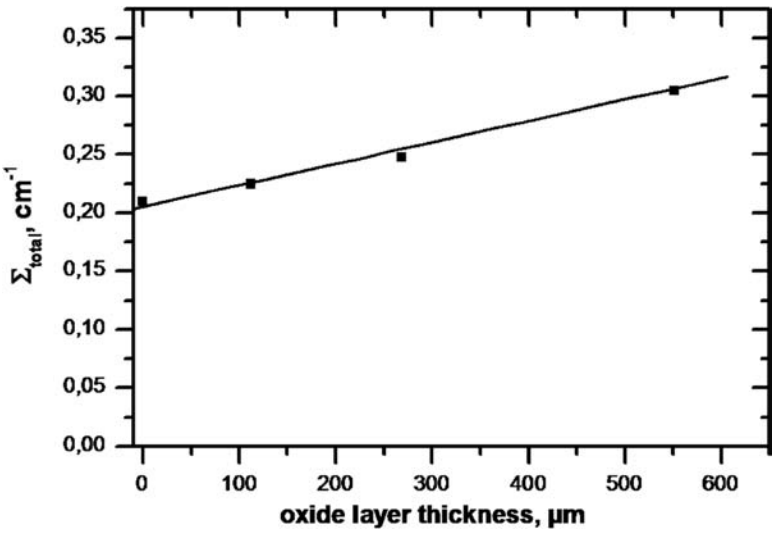


FIG. 5—*Linear correlation between total macroscopic neutron cross section and oxide layer thickness*

The parameters of this correlation were determined experimentally for all applied setups (neutron spectra, detection systems). From Eq 3 it can be derived that the slope of the curves given in Fig. 4 equals σ_H/N_{Zr}. The intersection with the Σ_{total} axis ($H/Zr = 0$) gives the total macroscopic cross section of the pure Zr alloy and the slope of the curve the effect of hydrogen uptake.

The calibration of the in situ experiments were performed using equilibrium conditions between hydrogen partial pressure in the INRRO gas atmosphere and the hydrogen concentration in the metal according to Eqs 4 and 5. The radiography images were compared to the image of the sample at temperature but without hydrogen containing atmosphere (pure Ar). Figure 6 shows the neutron transmitted intensity and the total macroscopic neutron cross section calculated from the transmission of a Zry-4 cladding tube segment annealed at 1000°C in Ar/H_2 atmosphere containing hydrogen partial pressures of 3.85, 7.41, and 13.80 kPa (50 ln/h Ar, 2, 4, and 8 ln/h H_2), respectively. The correlations between total neutron cross section and hydrogen concentration in the zirconium alloy calculated according to Eqs 4 and 5 are given in Fig. 7 for all temperatures investigated. A linear dependence of the total neutron cross section on the H/Zr atomic ratio was found, independently on the temperature.

It turned out that the total neutron cross section of hydrogen dissolved in β−Zr is not significantly dependent on temperature. The total microscopic neutron cross section is more than two times higher than the cross section of the zirconium hydrides occurring at room temperature as a comparison of the slopes of the correlation lines in Fig. 4 and 7 shows.

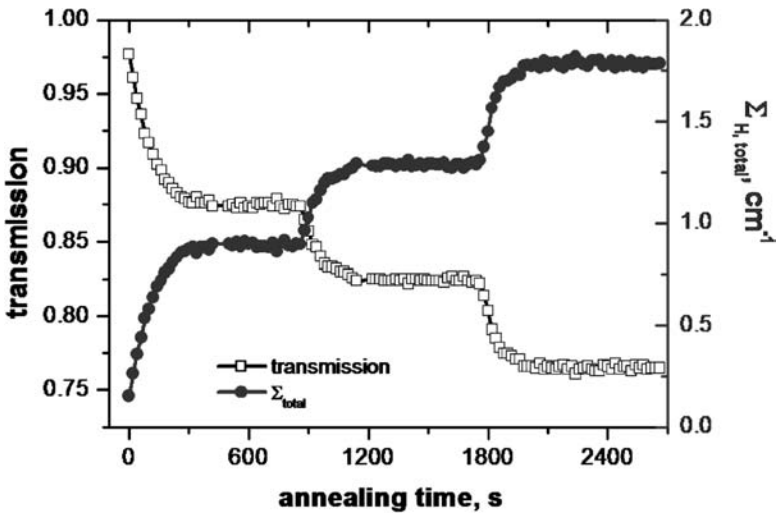


FIG. 6—*Dependence of the neutron transmission and of the total macroscopic neutron cross section of hydrogen dissolved in β-Zr on the annealing time and hydrogen partial pressure at 1000°C (the three steps correspond to hydrogen partial pressures of 3.85, 7.41 and 13.80 kPa, respectively).*

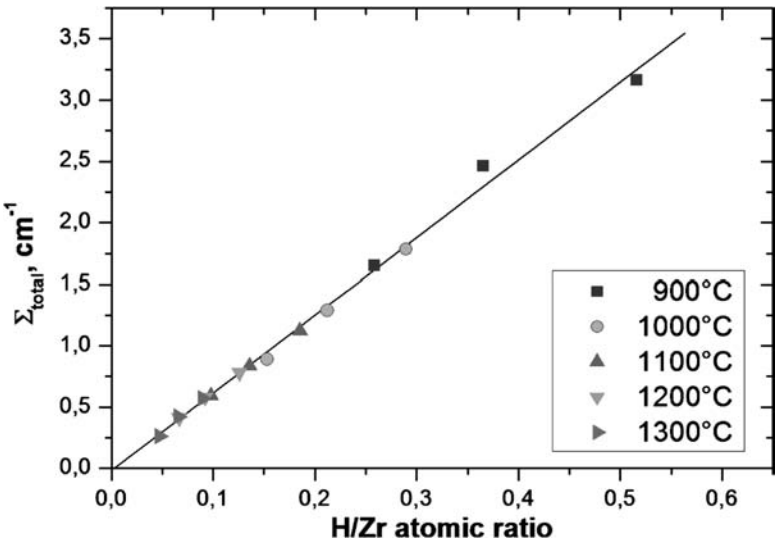


FIG. 7—*Dependence of the total macroscopic neutron cross section on the concentration of hydrogen dissolved in β-Zr at various temperatures.*

Examples of Ex Situ applications

The determination of hydrogen concentrations in corner rods and in a cladding tube of the QUENCH-15 bundle test [4] simulating a severe accident scenario with a ZIRLO^{TM} cladding are studied as an example of ex situ measurements. In order to perform post-test examinations of the QUENCH test bundles, corner rods and cladding tubes were withdrawn from the bundle. The samples undergo NR to determine their hydrogen concentration and distribution before the destructive metallographic investigations are performed. Figure 8 compares the hydrogen distribution in various specimens taken from the test bundle. Strong differences between the different alloys were found. The E110 corner rods have absorbed about one order of magnitude more hydrogen compared to the Zry-4 and ZIRLO^{TM} specimens. This is in agreement with the results of the QUENCH-12 (VVER bundle) [2] and the QUENCH-14 (M5^{TM}) [3] tests. The reason is the breakaway effect occurring over a wide temperature range in E110 and probably causing hydrogen enrichment in cracks formed in the oxide layer. The local hydrogen partial pressure increases with the consequence of additional hydrogen uptake according to Eq 4.

For the time dependence of the hydrogen uptake and release in specimens with compact oxide layers a mathematical model was developed [8]. After reaching a maximal concentration, hydrogen is released with time. This release can be understood taking into account the parabolic oxidation kinetics and the Sieverts' law. In specimens with breakaway oxidation the hydrogen concentration is about one order of magnitude higher than expected. A possible reason

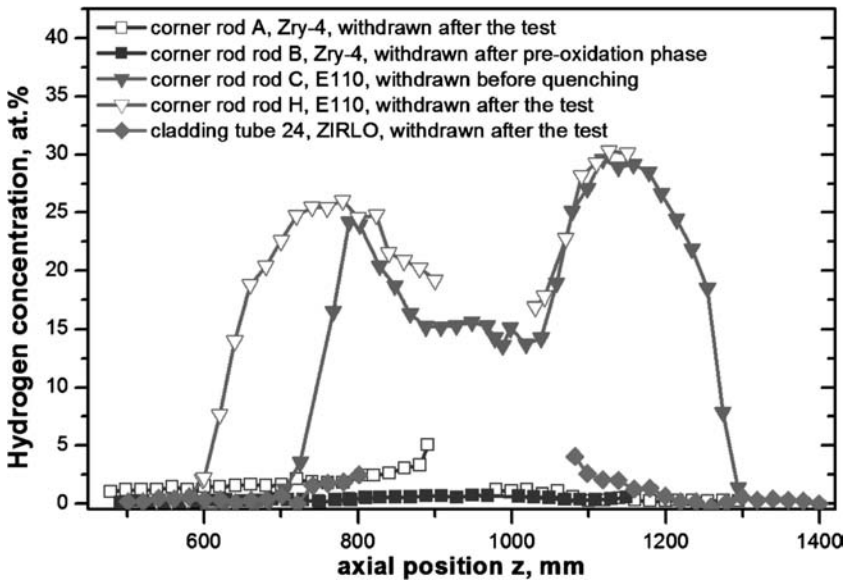


FIG. 8—*Axial hydrogen distribution in specimens prepared from the QUENCH-15 bundle test.*

for this effect can be hydrogen enrichment in the oxide crack structure. A detailed discussion is given in [9,10].

In the actual literature strong discrepancies in the published quantities of hydrogen absorbed in Zry-4 or M5™ are found for several temperatures (see Ref 11 and the references in it). Therefore, some parameters determining the quantity of absorbed hydrogen were analysed. The influence of the gas flow parameters on hydrogen uptake was studied in Ref 12. Presenting the details of the analysis and the model for the influence of experimental conditions exceeds the objective of this paper introducing NR as a method for hydrogen determination in zirconium alloys. However, some results will be given now. Basis of the analysis is that the hydrogen concentration in the remaining metallic zirconium depends on the hydrogen partial pressure in the surrounding gas atmosphere. The hydrogen partial pressure is determined by the total pressure and the hydrogen concentration in the atmosphere. The hydrogen concentration depends on the steam oxidation rate and the total gas flow in the case of steam saturation and on the steam flow under steam starvation conditions. Figure 9 gives the influence of the argon and steam flow rates on the hydrogen concentration in ZIRLO™. Generally it was found that the lower the total gas flow and the higher the hydrogen concentration in the gas phase, the stronger is the hydrogen uptake. The results of the calculations are shown in Fig. 9. Different total and steam gas flow rates were related to the measurements with 50 ln/h argon and 50 g/h steam. The comparison of the experimental data with the calculated one shows that the different gas flow rates explain the differences measured. Only for the measurements with 18 ln/h argon and 2 g/h steam the

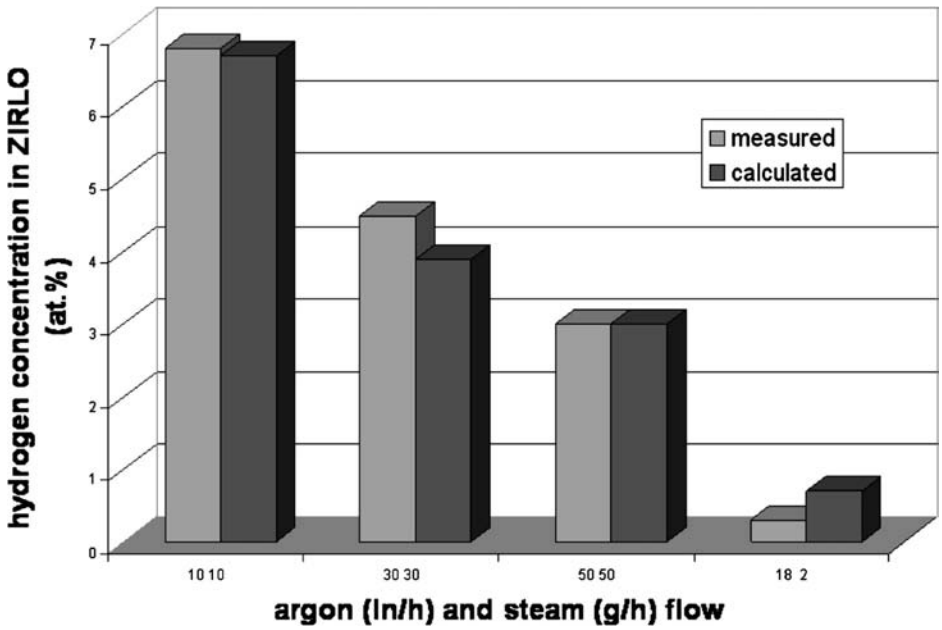


FIG. 9—*Dependence of hydrogen uptake on total gas and steam flow rates.*

model does not fit well. The measured concentration is more than two times smaller than expected from the model. The reason for this discrepancy is not yet clear. A possible explanation could be a lower chemical heat removal under steam starvation conditions and a higher surface temperature at the specimen. A detailed mathematical description of the model and a discussion of parameters influencing the hydrogen uptake are given in Ref 12. The analysis shows that the quantity of the hydrogen uptake is not a material property. It strongly depends on environmental conditions. Therefore, hydrogen concentrations are comparable only for identical experimental conditions. Different experimental conditions can explain the discrepancies in the published hydrogen concentrations [11].

Examples of In Situ Investigations

Three examples for in situ investigations will be given: The investigation of the hydrogen diffusion in the β phase of Zry-4 and the hydrogen uptake during steam oxidation of ZIRLO^{TM} at 1100°C and of Zry-4 at 1000°C.

Figure 10 gives a sequence of NR images taken during hydrogen diffusion from the gas phase into a Zry-4 solid cylinder. By oxidation of the cylinder side surface and one base surface the hydrogen uptake could only take place through the left base surface in significant manner. Due to a constantly applied gas flow of Ar/H_2; the hydrogen concentration at the sample surface keeps constant. On this basis the diffusion can be described by

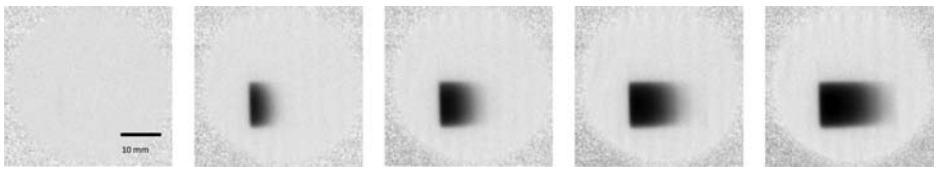


FIG. 10—*NR image sequence of the hydrogen diffusion into Zry-4 at 1173 K measured at ICON.*

$$c(x,t) = c_0\left(1 - erf\left(\frac{x}{2\sqrt{Dt}}\right)\right) \tag{6}$$

Figure 11 gives the fit of the experimental data with the model given in Eq 6. The diffusion coefficient of $D_H(T = 1373\,\mathrm{K}) = 3.39 \times 10^{-4}\,\mathrm{cm^2\,s^{-1}}$ determined by the fit agrees well with the values given in Ref 13 ($2.9 \times 10^{-4}\,\mathrm{cm^2\,s^{-1}}$) and Ref 14 ($2.5 \times 10^{-4}\,\mathrm{cm^2\,s^{-1}}$).

Another example of in situ NR experiments is investigations of the hydrogen uptake during steam oxidation. Figure 12 shows the time dependence of the hydrogen concentration in a ZIRLO^{TM} tube segment at 1100°C. It should be noted that the initial hydrogen uptake during steam oxidation is very fast (within 10 s). Most of the hydrogen was absorbed during the first neutron exposure time after switching on the steam flow. A rough comparison with the oxidation kinetics shows that in this time about 75 % of the hydrogen produced by the steam oxidation is absorbed.

If the breakaway effect occurs during steam oxidation additional hydrogen is absorbed. Figure 13 shows the dependence of the total hydrogen

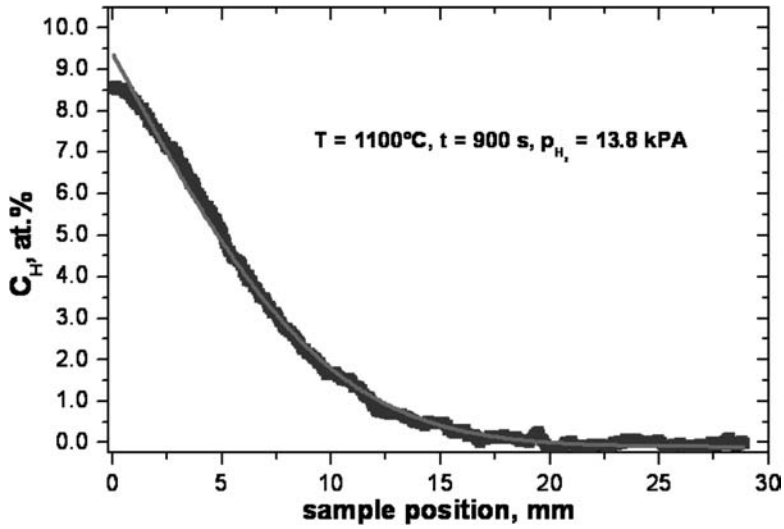


FIG. 11—*Hydrogen distribution after 900 s diffusion at 1100°C in Zry-4 cylinder.*

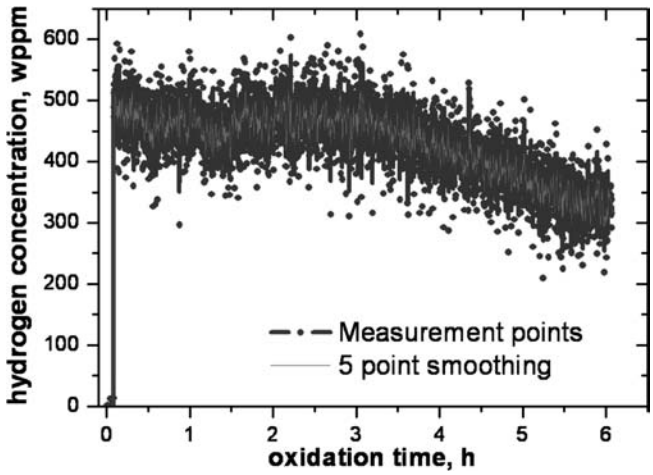


FIG. 12—*Kinetics of hydrogen uptake during steam oxidation of ZIRLO™ at 1100°C.*

concentration in the whole sample on the oxidation time. As mentioned before, the hydrogen enrichment in open cracks can be the reason for this additional uptake. In Zry-4 the hydrogen uptake starts at 1000°C with the fast absorption as reported for ZIRLO™ at 1100°C and a slight decrease of the hydrogen concentration after short time. After about 1800 s the breakaway effect occurs and the hydrogen concentration in the sample increases by a factor of 7 to 8.

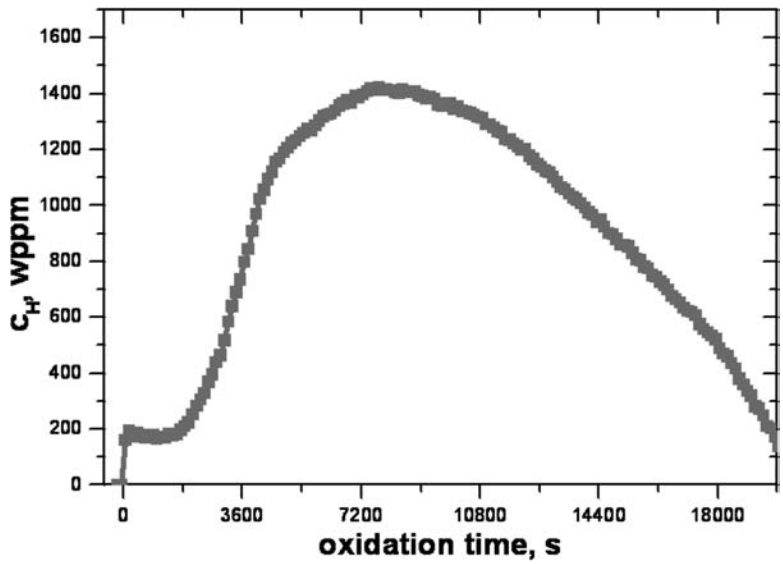


FIG. 13—*Kinetics of hydrogen uptake during steam oxidation of Zry-4 at 1000°C.*

After about 9000 s maximal hydrogen concentration is reached before it decreases again due to the consumption of the metallic phases. The solubility of hydrogen in the remaining oxide phase is close to zero.

Conclusions

The given results show that NR provides the possibility to investigate hydrogen in zirconium alloys. The following items can be summarized and concluded:

- A spatial resolution of 25 μm can be achieved.
- The method can be calibrated by measurements of specimens with known hydrogen concentration. A linear dependence of the total macroscopic neutron cross section and the H/Zr atomic ratio exists. The effect of oxygen on Σ_{total} can be corrected. On this basis a fully quantitative analysis of the hydrogen concentration in zirconium alloy is possible.
- The fast and non-destructive character of NR provides the possibility of in situ investigations with a time resolution of few seconds.

The method was applied for ex- and in situ studies of the hydrogen uptake during steam oxidation under LOCA and severe accident conditions. Here the following results were obtained:

- Strong differences between different cladding alloys were found. Crack formation in the oxide layer strongly influences the hydrogen uptake.
- The total gas flow rate and the steam flow rate have a strong effect on the hydrogen uptake.

Therefore, hydrogen concentrations in zirconium alloys can only be compared if the experimental conditions are comparable.

Acknowledgments

The neutron radiography experiments were performed at the ICON facility at the Swiss neutron source SINQ (Paul Scherrer Institute Villigen, Switzerland) and at the ANTARES facility at the Munich research reactor FRM-2 (Technical University Munich, Germany). The author thanks G. Frey, G. Kühne, E. Lehmann, P. Vontobel, and A. Kaestner from PSI and B. Schillinger and E. Calzada from TUM for their support in the neutron radiography experiments and the QUENCH team at KIT in particularly M. van den Berg (FONTYS Univ. Eindhoven (NL)), M. Steinbrück, J. Stuckert, J. Moch, L. Sepold, and U. Stegmaier for performing the large-scale QUENCH tests.

References

[1] Sepold, L., Große, M., Steinbrück, M., and Stuckert, J., "Severe Fuel Damage Experiments with Advanced Cladding Materials to be Performed in the QUENCH Facility (QUENCH-ACM)," *Proc. of the 16th Internat. Conf. on Nuclear Engineering (ICONE-16)* (CD-ROM), Orlando, FL, May 11–15, 2008, ASME, New York, Paper ICONE16-48074.

[2] Stuckert, J., Birchley, J., Große, M., Haste, T., Sepold, L., and Steinbrück, M., "Experimental and Post-Test Calculation Results of the Integral Reflood Test QUENCH–12 with a VVER-Type Bundle," *Ann. Nucl. Energy*, Vol. 36, 2009, pp. 183–192.

[3] Stuckert, J., Birchley, J., Große, M., Jaeckel, B., and Steinbrück, M., "Experimental and Calculation Results of the Integral Reflood Test QUENCH–14 with M5@ Cladding Tubes," *Ann. Nucl. Energy*, Vol. 37, 2010, pp. 1036–1047.

[4] Stuckert, J., Große, M., and Steinbrück, M., "Experimental Results of Reflood Bundle Test QUENCH-15 with ZIRLOTM Cladding Tubes," *Proc. 2010 International Congress on Advances in Nuclear Power Plants (ICAPP '10)*, San Diego, CA, June 13–17, 2010, La Grange Park, IL, Paper 10286.

[5] Wagner, C., "Die Löslichkeit von Wasserdampf in ZrO_2-Y_2O_3-Mischkristallen," *Ber. Bunsenges. Phys. Chem*, Vol. 72, 1968, pp. 778–781.

[6] Steinbrück, M., "Hydrogen Absorption by Zirconium Alloys at High Temperatures," *J. Nucl. Mater.*, Vol. 334, 2004, pp. 58–64.

[7] Grosse, M., Lehmann, E., Vontobel, P., and Steinbrueck, M., "Quantitative Determination of Absorbed Hydrogen in Oxidised Zircaloy by Means of Neutron Radiography," *Nucl. Instrum. Methods Phys. Res. A*, Vol. 566, 2006, pp. 739–745.

[8] Grosse, M., Steinbrueck, M., Lehmann, E., and Vontobel, P., "Kinetics of Hydrogen Absorption and Release in Zirconium Alloys During Steam Oxidation," *Oxid. Met.*, Vol. 70, 2008, pp. 149–162.

[9] Grosse, M., Kühne, G., Steinbrück, M., Lehmann, E., Vontobel, P., and Stuckert, J., "Quantification of Hydrogen Uptake of Steam-Oxidized Zirconium Alloys by Means of Neutron Radiography," *J. Phys.: Condens. Matter*, Vol. 20, 2008, pp. 104263.

[10] Große, M., Lehmann, E., Steinbrueck, M., Kühne, G., and Stuckert, J., *J. Nucl. Mater.*, Vol. 385, 2009, p. 339.

[11] Brachet, J. C. and Vandenberghe, V., "Comments to Papers of J. H. Kim et al. [1] and M. Große et al. [2] Recently Published in JNM "On the Hydrogen Uptake of Zircaloy-4 and M5^{TM} Alloys Subjected to STeam Oxidation in the 1100–1250 °C Temperature Range," *J. Nucl. Mater.*, Vol. 395, 2009, pp. 169–172.

[12] Grosse, M., Steinbrueck, M., and Stuckert, J., "Parameters Influencing the Secondary Hydrogenation of Zr-Sn and Zr-Nb Alloys During Steam Oxidation Under LOCA and Severe Accident Conditions," *Proc. 18th Intern. Conf. on Nucl. Engin. ICONE18* (CD-ROM), Xi'an, China, May 17–21, 2010, Paper ICONE18-29405.

[13] Simeno, M., *Nippon Kinzoku Gakkaishi*, Vol. 24, 1960, pp. 249–254.

[14] Gelezunas, V. L., Conn, P. G., and Price, R. H., "The Difference Coefficients for Hydrogen in β-Zirconium," *J. Electrochem. Soc.*, Vol. 110, 1963, pp. 799–805.

DISCUSSION

Question 1, Yong Hwan Jeong:—Your hydrogen concentration seems to be high. How do you calibrate the hydrogen concentration? How do you know if your hydrogen concentration is correct or not?

Author's Response:—The calibration was performed using cladding tube segments annealed in Ar/H2 atmosphere. The quality of the gas atmosphere was checked by mass spectrometer measurements of the off-gas composition. The amount of absorbed hydrogen was pre-defined according to Sieverts' law and determined by the measurement of the mass gain. Calibration measurements were performed during each beam time with a very good reproducibility, when the same experimental setup is used. The results of the hydrogen determination by means of neutrons were also compared with the result of hydrogen determination by hot extraction at the same specimens, giving good agreements between the two methods.

Question 2, Ken Yueh, EPRI:—1) How much metal Zr was consumed after 6 h of oxidation? Could the conversion of metal to oxide have release some of the absorbed hydrogen resulting in lower measured hydrogen concentration near the end of the test? 2) In your axial hydrogen diffusion test, is sufficient data captured to allow calculation of H diffusion coefficient? Did you also study other temperatures?

Author's Response:—1) I agree with this. The metallic phases in Zry-4 are nearly completely consumed after 6 h steam oxidation at 1000°C. The oxides can not absorb hydrogen in a significant amount. Therefore the hydrogen concentration in the sample is after 6 h steam oxidation at 1000°C close to zero.

2) The diffusion coefficients can be calculated from the data. Experiments at 850, 900, 1000, 1100 and 1200°C are performed. The results of these investigations will be published elsewhere.

Question 3, Arthur Motta, Penn State University:—1) What is the lower limit of detection of H in your technique? 2) What is the error?

Author's Response:—1) In standard experiments the detection limit of ex-situ investigations is less than 100 ppm, in in-situ measurements, where the radiography images can be referenced by the image of the as received state; it is less than 30 ppm.

2) The relative error of the hydrogen determination is about 10 %.

Question 4, Jean-Christophe Brachet, CEA, France:—How can you explain the progressive release of hydrogen from the sample during oxidation at high temperature, because we know that, from nuclear microprobe measurements (ERDA), nearly all the hydrogen is pushed into the internal remaining β layer and then, there are two external layers (ZrO_2, α(O)) which would prevent the release of the hydrogen?

Author's Response:—At first, at the temperatures investigated the whole sample is β Zr before starting oxidation. There are two processes resulting in a decrease of the hydrogen content in the sample:

1) The consumption of the β phase by the growth of ZrO_2 and α(O) layers (in our experiments from both sides of the tube wall). The solubility of hydrogen in ZrO_2 is close to zero and in α(O) much smaller than in β-Zr.

2) The system tries to establish the thermodynamic equilibrium. The equilibrium between hydrogen partial pressure in the gas phase and the hydrogen concentration in the β phase can be described by the Sieverts' law. Due to the parabolic oxidation kinetics the hydrogen partial pressure in the gas phase decreases (the hydrogen source term depends on time with the power -1/2). The consequence is that hydrogen has to flow from the sample into the gas phase to establish the thermodynamic equilibrium. You are right that the external ZrO_2 layers hint this flow. The hydrogen concentration in the α(O) phase is in equilibrium with the concentration in the β phase even if they differ strongly. On this basis α(O) can not really be a barrier for hydrogen. Cracks in the oxide can act as transport ways to pass this layer. However, our experimental results show that this hydrogen flow really exists.

CORROSION – OXIDE LAYER CHARACTERIZATION

Reprinted from JAI, Vol. 8, No. 6
doi:10.1520/JAI102956
Available online at www.astm.org/JAI

Pia Tejland,[1] *Mattias Thuvander,*[1] *Hans-Olof Andrén,*[1] *Sorina Ciurea,*[2] *Thomas Andersson,*[2] *Mats Dahlbäck,*[3] *and Lars Hallstadius*[3]

Detailed Analysis of the Microstructure of the Metal/Oxide Interface Region in Zircaloy-2 after Autoclave Corrosion Testing

ABSTRACT: Two varieties of Zircaloy-2, with different second phase particle (SPP) size distributions and different corrosion resistance, were oxidized in a steam autoclave. Transmission electron microscopy (TEM) of large thin-foil cross-sections of the oxide and the adjacent metal shows an undulating metal/oxide interface in both materials with a periodicity of slightly less than 1 μm and an amplitude of around 100 nm. The SPPs oxidize slower than the surrounding metal, and the absence of volume increase leads to void and crack formation as the SPPs become embedded in the oxide. On SPP oxidation, iron diffuses out of the particles into the surrounding oxide. A sub-oxide with an oxygen content of approximately 50 at. % and a layer thickness of about 200 nm was observed close to the metal/oxide interface. There is a 200 nm oxygen concentration gradient into the metal, from the level close to the sub-oxide of about 30 at. % down to a few atomic percent. All tin in the matrix is incorporated in the sub-oxide, and no segregation to the metal/oxide interface was found.

KEYWORDS: Zircaloy-2, sub-oxide, SPP, oxide crack, oxide void, atom probe, HAADF, TEM

Manuscript received January 28, 2010; accepted for publication April 22, 2011; published online July 2011.

[1] Department of Applied Physics, Chalmers University of Technology, SE-412 96 Göteborg, Sweden (Corresponding author), e-mail: pia.tejland@chalmers.se
[2] Sandvik Materials Technology, R&D, SE-811 81 Sandviken, Sweden.
[3] Westinghouse Electric Sweden, SE-721 63 Västerås, Sweden.

16th International Symposium on Zirconium in the Nuclear Industry on 9 – 13 May 2010 in Chengdu, China.

Cite as: Tejland, P., Thuvander, M., Andrén, H.-O., Ciurea, S., Andersson, T., Dahlbäck, M. and Hallstadius, L., "Detailed Analysis of the Microstructure of the Metal/Oxide Interface Region in Zircaloy-2
after Autoclave Corrosion Testing," *J. ASTM Intl.*, Vol. 8, No. 6. doi:10.1520/JAI102956.

Copyright © 2011 by ASTM International, 100 Barr Harbor Drive, PO Box C700, West Conshohocken, PA 19428-2959.

Nomenclature

ADF = Annular dark field
APT = Atom probe tomography
BWR = Boiling water reactor
EDX = Energy dispersive x-ray spectroscopy
FIB = Focused ion beam
HAADF = High-angle annular dark field
SEM = Scanning electron microscopy
SPP = Second phase particle
STEM = Scanning transmission electron microscopy
TEM = Transmission electron microscopy

Introduction

Zirconium alloys are used in the nuclear industry as fuel cladding tubes because of their low cross-section for thermal neutron capture, high mechanical strength, and good corrosion properties. However, the environment in the reactors is quite aggressive and causes the tubes to gradually oxidize. It would be helpful to understand the oxidation mechanisms better when developing alloys aimed at a longer in-reactor lifetime. The oxidation process of zirconium alloys has been vastly studied before and one conclusion that has been drawn is that the size of second phase particles (SPPs) has a major influence on the oxidation rate. [1–4]. However, it is not clear exactly how they influence the oxidation process. In this study the microstructure of the oxide and the metal/oxide interface of two Zircaloy-2 materials with different heat treatments and therefore different size distributions of SPPs has been investigated. The main focus of the study has been to compare the two materials in order to find out more in detail how they differ from each other and ultimately try to understand why the SPP size difference is of such great importance for the oxidation process. Also, some general investigations of the interface morphology, SPP oxidation and oxygen content have been performed in order to better understand the oxidation process of Zircaloy-2.

The main investigation method in this study has been transmission electron microscopy (TEM). For preparation of thin foils, the focused ion beam (FIB) in-situ lift-out technique was used. This technique renders large foils with homogeneous thickness, allowing for large areas to be observed, which gives a good overview of the microstructure of the oxide and the underlying metal [5]. The technique has previously been used for studying zirconium alloys [6,7], but never before Zircaloy-2. In addition, the metal/oxide interface region was analyzed with atom probe tomography (APT).

Materials

Tube samples of Zircaloy-2, a material widely used in boiling water reactors (BWR), have been investigated in this study. The chosen materials are commercial alloys that have been extensively used in nuclear reactors. Hence, long-term

in-pile data are available [8], as well as irradiated material for possible future studies.

Zircaloy-2 is a zirconium alloy containing additions of tin and oxygen for improving mechanical strength, and iron, chromium and nickel for improving the corrosion performance. While some of the added iron, chromium and nickel stays in solid solution in the matrix, [9–13], most of these elements form intermetallic second phase particles. These particles exist in two different families, one has the composition $Zr(Fe,Cr)_2$ and the other $Zr_2(Fe,Ni)$. The chemical compositions of the two alloys studied in this work are given in Table 1. They have similar chemistry, only the amount of tin and iron differ slightly.

Both materials received an 80% area reduction during manufacturing, followed by the same final anneal and therefore have the same grain size and dislocation density. The main difference between the materials is their final thermal treatment. The cumulative heat treatment of a material is often described by the normalized annealing parameter A, defined as

$$A = \sum t_i exp(-Q/RT_i)$$

where i corresponds to the ith heat treatment (after the last β-quench operation) of the material at the temperature T_i (K) during the time t_i (h), R is the gas constant and Q an activation energy (63 kcal/mol). This value of the activation energy is based on the corrosion during autoclave tests at 400°C and 10.3 MPa for 72 days [14], and it is therefore not directly connected to the SPP coarsening. During heat treatment coarsening of the SPPs takes place leading to a decreasing number density. As can be seen in Table 2, Material A has a lower value of log A, corresponding to less heat treatment and consequently smaller (mean size 20 nm) SPPs, while Material B has undergone more heat treatment (higher value of log A) and thus contains larger (mean size 76 nm) SPPs. SPP size distributions were obtained using TEM. Because of the higher iron content of Material B the expected volume fraction of SPPs in this material is somewhat larger than in Material A. In spite of this, the very large difference in SPP mean size between the materials means that the number density of SPPs in Material A must be considerably higher than in Material B. This reasoning is based on the equation linking number density and volume fraction

TABLE 1—*Chemical composition of the two studied Zircaloy-2 materials.*

Element	Material A	Material B
Sn (%)	1.46	1.32
Fe (%)	0.12	0.17
Cr (%)	0.10	0.10
Ni (%)	0.05	0.05
Si (ppm)	80	70
O (ppm)	1240	1300
N (ppm)	40	50

TABLE 2—*Heat treatment and average SPP size for the two studied Zircaloy-2 materials.*

Parameter	Material A	Material B
Heat treatment (log A)	−16.0	−13.9
SPP average size (nm)	20	76

$$N_V = \left(\frac{f_P}{d^3}\right)\left(\frac{6}{\pi}\right)$$

where N_v is the number density, f_P is the volume fraction of the particles, and d is the mean particle diameter. The role of volume fraction of SPPs has been investigated before, with the conclusion that the corrosion behavior of Zr binary alloys in autoclave depends primarily on the volume fraction of SPPs and second on their size and nature, and that the corrosion resistance is improved by a higher volume fraction and a larger SPP size. [15].

The materials were oxidized in steam autoclaves at temperatures of 400 and 415°C (where the higher temperature was used for achieving thick oxides within a reasonable time frame) and a pressure of 10.3 MPa from 3 to 150 days to achieve different oxide thicknesses, see Table 3. From this table it is apparent that Material B, with the larger SPPs, has the superior oxidation behavior. Besides the autoclaved materials with oxide thicknesses of roughly 1, 2, and 9 μm also un-oxidized material has been available for observation and analysis. In the table all available material is presented, with the materials studied in the present work highlighted in bold type.

Experimental Methods

The main instrument for investigations has been TEM with different types of detectors. Imaging has been performed using high angle annular dark field (HAADF) imaging, giving atomic number contrast. Energy dispersive X-ray spectroscopy (EDX) has been used for chemical analysis of the materials. The instrument used for these investigations was an FEI Tecnai G2 microscope with

TABLE 3—*Autoclave data (at a pressure of 10.3 MPa) and the resulting weight gains and corresponding oxide thicknesses. Materials in bold type are the ones mentioned in this paper, the others are to be used in coming studies.*

Alloy	Temp (°C)	Time (days)	Weight gain (mg/dm^2)	Oxide thickness (μm)
Material A	400	3	18.9	1.3
Material A	400	6	33.9	2.3
Material A	415	30	132.5	8.8
Material B	400	3	15	1
Material B	400	15	27.5	1.8
Material B	415	150	135	9

an EDAX EDX detector. In addition, bright field TEM imaging was performed using a Philips CM200 microscope.

Scanning electron microscopy (SEM) has also been used in this work for studying TEM thin films. The specimens have been analyzed using EDX and imaged with scanning TEM (STEM) using an annular dark field (ADF) detector. The instrument used for these investigations was a Leo Ultra 55 FEG SEM with an Oxford Instruments INCA EDX detector.

The TEM foils were prepared using the FIB-SEM in-situ lift-out technique, described in Fig. 1. A FIB-SEM is a combined focused ion beam and SEM instrument that allows milling and deposition of material using ions in combination with conventional imaging using electrons. In a first step a protective layer of Pt is deposited on top of the region of interest from which the TEM foil will be taken. Using gallium ion milling two trenches are then created leaving the Pt protected region in-between (Fig. 1:1). The lamella is lifted out using an Omniprobe micromanipulator attached by Pt deposition (Fig. 1:2–4). The lamella is attached to a copper holder again using Pt deposition (Fig. 1:5). The micromanipulator is cut loose and final thinning is performed using ion milling at successively decreasing currents and voltages. In order for the specimen not to bend, two parts are thinned to final thickness leaving a reinforcing bar in-between (Fig. 1:6). This means that in one specimen two thin areas are created that are available for TEM imaging and analysis. The instrument used for manufacturing TEM foils was an FEI Strata 235 Dual Beam system.

One of the alloys (Material B) was also studied with atom probe tomography (APT). This method requires specimens in the shape of sharp needles (tip radius <50 nm), and these were also prepared using the FIB-SEM, see Fig. 2. A

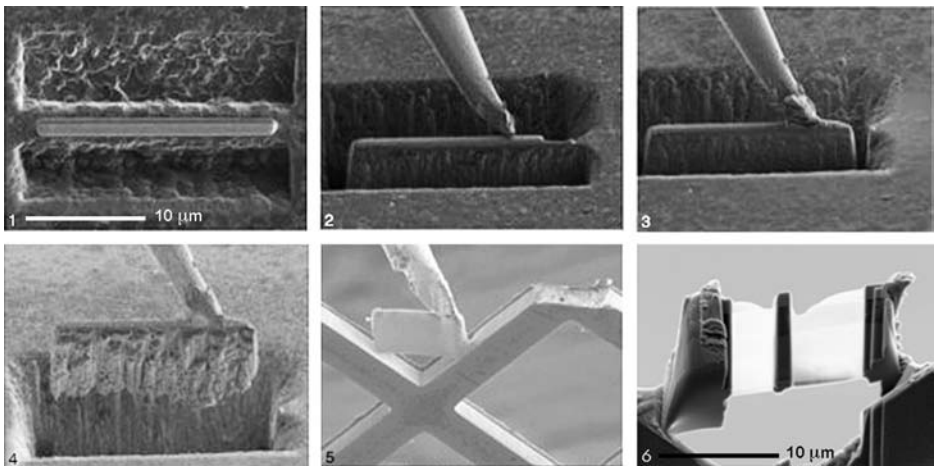


FIG. 1—*SEM images of an in-situ lift-out sequence. A protective Pt strip is deposited and a lamella is created by milling two trenches adjacent to the Pt strip (1). A micromanipulator needle is inserted and attached to the lamella using Pt deposition (2). The lamella is cut loose (3), lifted out (4) and attached to a copper grid (5). The micromanipulator needle is cut loose and final thinning takes place (6).*

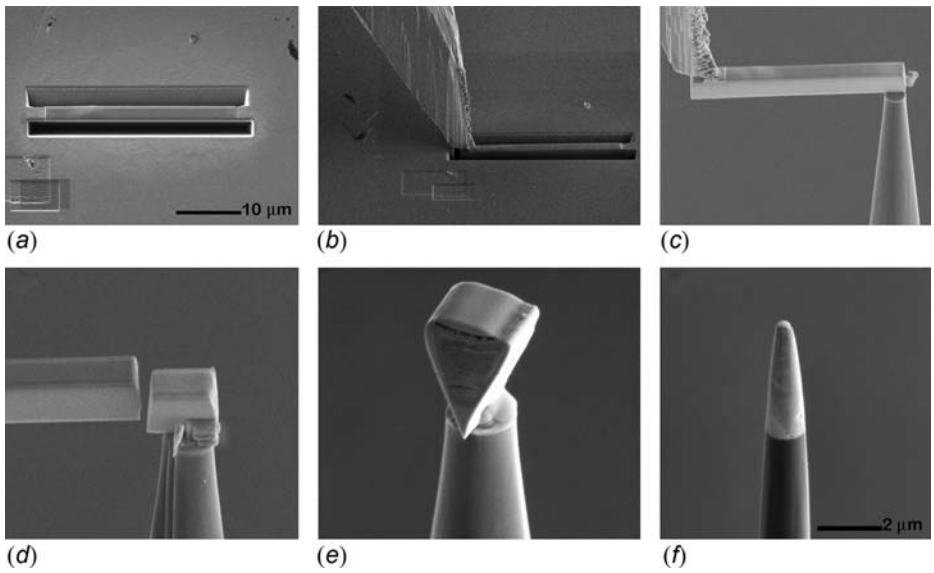


FIG. 2—*SEM images of the lift-out procedure for an APT needle. A protective Pt strip is deposited to protect the surface and a triangular prism is created by ion milling (a). The prism is attached to a micromanipulator needle using Pt deposition (b), lifted out and attached to a pre-sharpened silicon post (c). A slice is cut off from the prism (d-e) and then final sharpening using ion milling takes place. The final result is shown in (f).*

triangular prism, 30 μm long and 2 μm wide, was cut out along the oxide-metal interface, and 2 μm thick slices of the prism were fastened by Pt deposition to pre-sharpened silicon tips, 2 μm in diameter and 100 μm high, in a similar manner as described by Miller et al. [16]. The metal/oxide interface was oriented perpendicular to the specimen axis. By gallium ion milling using the method of Larson et al. [17], the specimen was then shaped into a sharp tip with the interface located within 100 nm from the tip.

APT analysis was performed with an Imago LEAP 3000X HR instrument in laser mode, using a specimen temperature of 70 K, laser pulse frequency of 200 kHz and laser pulse energy of 0.5 nJ. These conditions gave a ratio between the Zr^{2+} and Zr^{3+} peaks in the mass spectrum of approximately 20 (a commonly used measure of the evaporation field during APT analysis). APT data were evaluated with the IMAGO IVAS 3.4.1 software using background corrections. The outermost part of the specimen needle suffers from radiation damage from the gallium ion irradiation during preparation in the FIB-SEM. Therefore the first part of the APT analysis containing implanted gallium was discarded from the volume that was evaluated.

Results and Discussion

Most of the work was performed on both Material A and B with oxides of around 1 μm (i.e., pre-transition oxide), except for the study of the metal/oxide

interface morphology that was also performed on un-oxidized Material A, and the study of SPP oxidation that was also performed on the 9 μm thick oxide of Material B.

Interface Morphology

A first observation when looking at the metal/oxide interface is that it is not a straight line, the interface undulates in a periodic way, see Fig. 3. This waviness of the interface has been observed many times before, and it seems to exist on two levels. On the first level the undulations are on a large scale of typically 20 μm, [18,19,21,22], and on the second level this coarser structure is found to be made up of finer undulations of about 1 μm [18,20–22]. The wavy interface is most likely a two-dimensional representation of the three-dimensional "cauliflower" oxide structure reported by some researchers. [19,21,23]. In their images it is possible to distinguish both the coarser and the finer structure. However, many of the previous studies have been carried out with SEM, and no further mention is made of the finer scale. On the smaller TEM-scale, the electron-transparent areas of the specimens have in the past been too small to provide any overview of the interface. In this study the FIB-SEM in-situ lift-out method has been used to produce TEM foils, resulting in thin areas large enough to observe several micrometers of interface. This technique was also used by Bossis et al. [20], who examined the interface of oxidized Zircaloy-4 and revealed undulation on a finer scale. They also made an attempt to link the interface morphology to the presence of lateral cracks. However, the interface of Zircaloy-2 has never been thoroughly investigated, before this study. In an attempt to find the origin of the undulations, several aspects have been investigated.

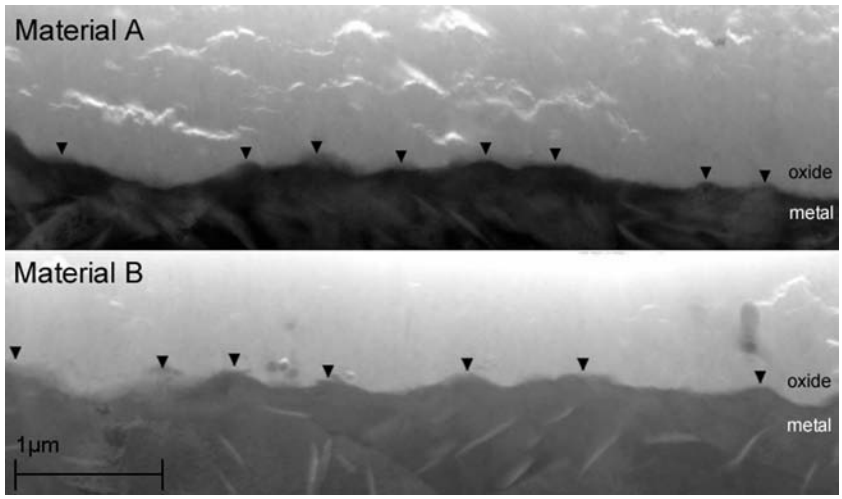


FIG. 3—*STEM ADF images of the undulating metal/oxide interface of Materials A and B with an oxide thickness of 1 μm. Arrows indicate wave crests.*

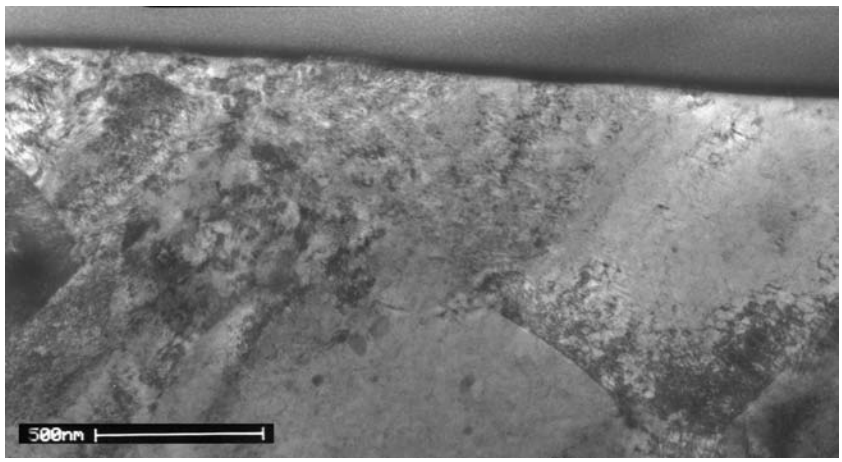


FIG. 4—*Bright-field TEM image of an un-oxidized sample of Material A showing that the original surface before oxidation is straight. The natural oxide is only 50 nm thick. Note the high dislocation density induced by the tube grinding process.*

First, the impact of the original surface was investigated, by studying un-oxidized material. The cross-section specimens were prepared perpendicular to the tube axis, i.e., parallel to the tangential grinding direction. This surface is flat on a micrometer scale (see Fig. 4) so the waves have not come from simply following the original surface geometry but have appeared and evolved during oxidation.

Second, the impact of surface treatment was investigated. A comparison was made between the inner and outer surface of the tubes. The inner surface is pickled, leading to a rougher topography on a large scale since different grains are etched to different depths, depending on crystallographic orientation. The metal/oxide interface of the specimen from the inner surface appears to be rougher than the interface of the specimen from the outer, ground surface (see Fig. 5), suggesting that a coarser initial topography may increase the waviness of the interface somewhat. This investigation was carried out on Material A, but since both materials have undergone the same surface treatment the results are valid for both alloys.

Third, the impact of the SPPs was investigated. Since the main difference between Material A and B is the SPP size distribution, this investigation was carried out by comparing the periodicity and the amplitude of the waves in the two materials, both with an oxide thickness of 1 μm, see Fig. 3. Along these interfaces, which are 5.6 μm long, eight wave crests were distinguished in Material A and seven in Material B, so they have a similar periodicity of slightly less than 1 μm. The amplitudes of the waves also appear to be similar in the two materials, around 100 nm.

In conclusion, the examination of the interface morphology did not give any clear answers to the origin of the wavy interface. However, some theories concerning the waviness of the interface can be ruled out:

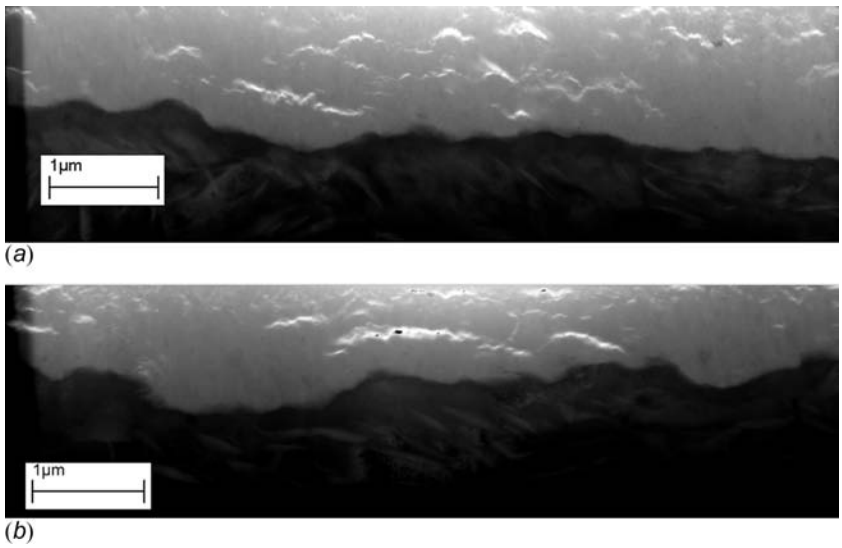


FIG. 5—*Comparison of metal/oxide interfaces of Material A with an oxide thickness of 1 μm, outer surface (a) and inner surface (b) of the tube. STEM ADF images.*

1. Since a very similar wavy interface was found in Zircaloy-2 (in the present study) and Zircaloy-4 [20], and can be seen in other kinds of zirconium alloys [18,19,21–23], the alloy chemistry does not seem to influence the waviness of the interface.
2. The undulations do not come from the initial surface topography, even though it seems that the surface treatment may play a small role.
3. An often-presented theory is that the wavy interface is connected to the SPPs [18,19,23]. This theory can now also be ruled out, since the two materials with very different SPP size distributions do not show any significant difference in the waviness.

Another explanation for the wavy appearance of the interface is that a flat interface would induce very high compressive stresses in the material. These stressed could be reduced by the creation of undulations [7,19,24]. To the present authors, this is the theory that now seems most likely.

SPP Oxidation

The following EDX investigations were performed on Material B, but the results are also valid for Material A, since the composition of the particles as well as the surrounding metal matrix is essentially the same in the two materials, only the SPP size distribution differs. The results are to be considered as semi-quantitative or qualitative since no corrections have been made to compensate for foil thickness effects.

Figure 6 displays the results of EDX analyses of the oxygen content in $Zr(Fe,Cr)_2$ SPPs, located in three different environments. Figure 6(*a*) shows a

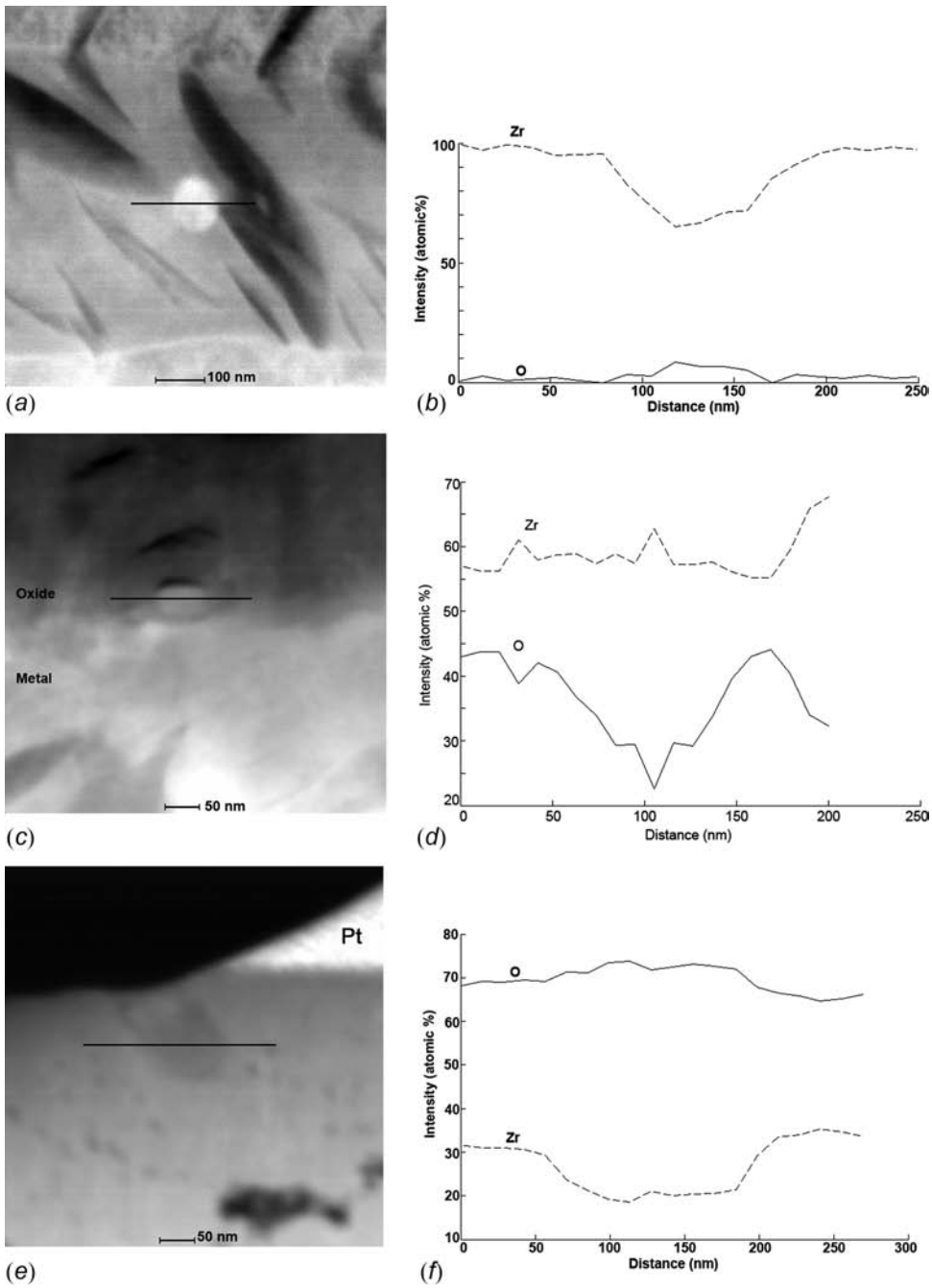


FIG. 6—*HAADF TEM images of SPPs and corresponding Zr and O TEM EDX line scans. SPP in the metal (a) and (b), in the oxide close to the interface (c) and (d) and 9 μm away from the interface (e) and (f) of Material B.*

particle in the metal matrix, and Fig. 6(*b*) the corresponding zirconium and oxygen EDX line scans. This SPP is naturally not oxidized, since the oxidation front has not yet reached it. Surprisingly, a small increase in oxygen content is seen in the particle, but this is most probably due to some kind of artifact. Figure 6(*c*) shows a particle embedded in the oxide but close to the metal/oxide interface, and Fig. 6(*d*) the corresponding zirconium and oxygen EDX line scans. The oxygen content decreases significantly in the particle compared to the surrounding oxide, indicating that it is not oxidized. The oxygen level of the oxide is not the expected 67 at. % of zirconia, indicating that this area consists of the sub-oxide reported on further down in this paper. Also, at the end of the line scan the oxygen level decreases again. Since the interface is very uneven, this decrease in oxygen content is probably due to the fact that the EDX line scan reaches a part of the interface that is not yet oxidized. Figure 6(*e*) shows a particle located in the oxide around 9 μm away from the interface and Fig. 6(*f*) the corresponding zirconium and oxygen EDX line scans. The oxygen content increases in the particle, indicating that this particle is oxidized. The oxygen content analyses of SPPs prove that they oxidize slower than the surrounding matrix. This has never before been shown for Zircaloy-2 with normal heat treatments, but the finding is in good agreement with previous studies performed on other alloys with varying SPP sizes [25–30]. The nickel containing SPPs were not studied, but based on the above mentioned results, in combination with literature findings, the conclusion can be drawn that the same behavior should be valid also for these particles.

The iron and chromium contents of the same three particles are shown in Fig. 7, in order to illustrate the Fe/Cr ratio and how it changes as the particles oxidize. Figure. 7(*a*) shows the iron and chromium EDX line scans of the metal-surrounded particle [seen in Fig. 6(*a*)]. The Fe/Cr ratio is approximately 1. Figure 7(*b*) shows the iron and chromium EDX line scans of the particle in the oxide close to the metal/oxide interface [seen in Fig. 6(*c*)]. The Fe/Cr ratio is still close to 1, but with a slightly smaller iron content. Figure 7(*c*) shows the iron and chromium EDX line scans of the oxidized particle 9 μm from the metal/oxide interface (seen in Fig. 6(*e*). This particle also shows a small nickel content, indicating that a Zr_2(Fe,Ni) particle is located on top of the Zr(Fe,Cr)$_2$ particle. This influences the iron content that is somewhat higher in the area of the small nickel-containing particle. Still, a rough estimate is that the Fe/Cr ratio is around $2/5 = 0.4$ in this oxidized Zr(Fe,Cr)$_2$ particle. The analyses of iron and chromium content of the SPPs show that as the particles are oxidized the iron level decreases, indicating that iron diffuses out of the particles upon oxidation. The same EDX investigation has been performed on nickel-containing particles and a preliminary result is that they show a similar behavior, but no clear data are available to present here. In a particle embedded in the metal the Fe/Ni ratio is higher than 1, and in a particle embedded in the oxide it is close to or slightly less than 1.

The phenomenon of iron diffusion upon SPP oxidation is well known and has been reported for several alloys, usually with customized heat treatments to create large SPPs [29,31]. The diffusion has also been studied as an effect of irradiation [28,29,32,33]. The present study now confirms that diffusion occurs

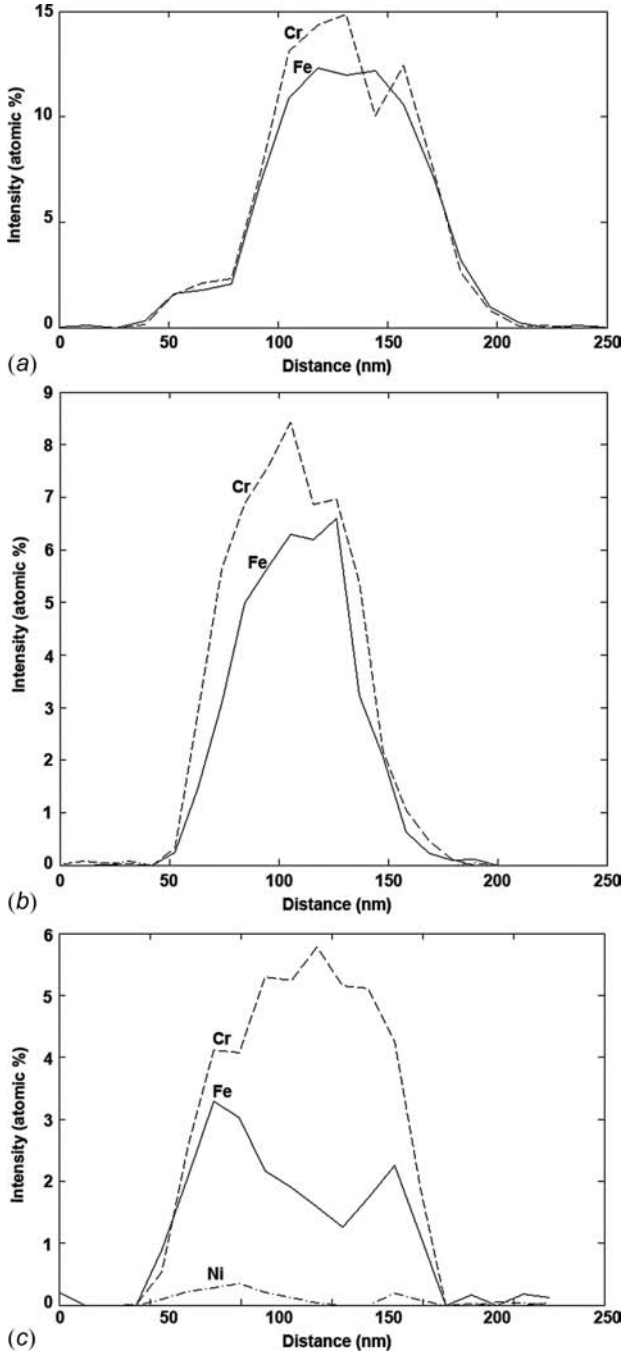


FIG. 7—*Fe, Cr (and in one case Ni) TEM EDX line scans of SPPs in the metal (a), in the oxide close to the interface (b) and 9 μm away from the interface (c) of Material B.*

also in Zircaloy-2 materials with normal heat treatments, oxidized in autoclave, i.e., without the influence of irradiation.

Voids and Cracks

There is a substantial amount of small (mostly less than 1 μm) lateral cracks found in the oxide (see Figs. 3 and 5). Many researchers have reported on larger cracks recurring periodically at the transitions between successive cube-root sections of the weight gain curve [25,27,34,35], but there also exists a lot of smaller cracks in-between these periods, in the pre-transition oxide [20]. The occurrence of these cracks could possibly be a result of specimen preparation but, even so, the cracks indicate where areas of weaker oxide, more susceptible to ion milling and stress relief, are found.

It is evident, when comparing the two materials of this study, that there are significantly more cracks in the oxide of Material A than in that of Material B, see Fig. 3. The same method for sample preparation has been used for both materials, so even if some cracks could come from sample preparation, the result still indicates a difference in oxide properties of the materials.

Voids have been observed adjacent to some SPPs, mainly those close to the metal/oxide interface, and always above the SPP, i.e., on the side facing away from the metal interface, see Fig. 8. In a study by Yilmazbayhan et al. [25] similar voids were observed. The explanation given in that study is that they are an artifact; cracks formed during specimen preparation as a result of accumulated stresses, which cause foil buckling.

Based on the knowledge that oxidation of zirconium leads to a substantial volume increase, with a Pilling–Bedworth ratio of 1.56, most of which is perpendicular to the metal/oxide interface, we suggest another likely scenario of what happens (see Fig. 9):

1. The oxidation front meets a particle.
2. Since the particle oxidizes slower than the surrounding matrix, the particle represents an absence of volume increase.
3. This absence of volume increase gives rise to tensile stresses in the oxide surrounding the particle. This stress can be relieved in two ways:
   (i) By forming a void in the oxide, primarily above the particle.
   (ii) By forming a crack further up in the oxide.

The geometry of the void seems to follow the particle geometry, as a spherical particle gives rise to a rounded void while a cuboidal particle gives rise to a void with a sharper edge, see Fig. 8. It can be noted that the voids above the spherical particles seem smaller relative to the void above the cuboidal particle. This might indicate that the metal, and subsequent oxide adheres harder to particles of spherical geometry. As can be seen in Fig. 6(*c*), above the spherical particle there is a crack a little bit higher up, suggesting that not all the tensile stress was relieved by the relatively small void created, while in the case of the cuboidal particle no such cracks are seen.

Further into the oxide—away from the metal interface—these kinds of apparent particle/void combinations are scarcer. This might be due to the fact that eventually the particles do oxidize and the voids are filled with material.

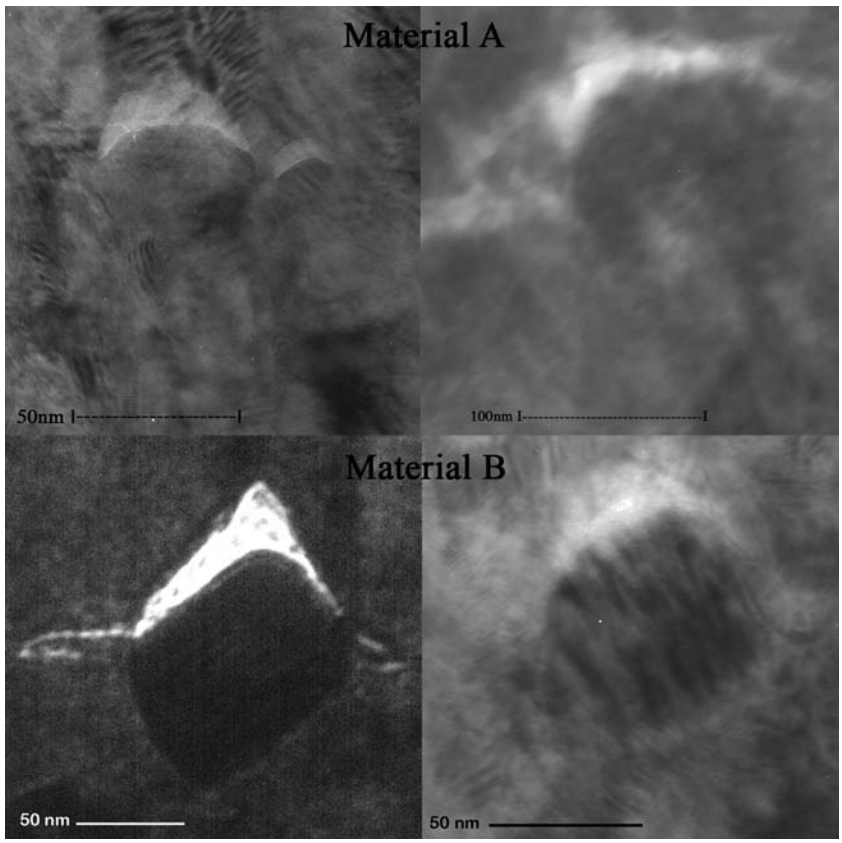


FIG. 8—*Bright-field TEM images of SPPs with voids just above them, on the side away from the metal/oxide interface, found in both materials (in 1 μm thick oxide).*

Another possibility is that as the oxidation progresses the voids lead to formation of cracks that grow and combine to larger continuous cracks making it harder to link a specific particle to a specific part of the crack.

In a later stage of the oxidation process, the cracks formed in the proposed way will probably grow and combine, creating larger cracks. These cracks will then eventually combine to form the large periodically recurring cracks associated with transition that can be seen in thicker oxide layers.

An assumption that the above-described scenario is one of the reasons for crack initiation and subsequent propagation is consistent with our observation that the material with the largest amount of particles, Material A, also has the largest number of cracks (Fig. 3). The particles in Material B are fewer but also larger. Since there are fewer cracks in this material it seems that the number density of particles is a more important parameter than the particle size when it comes to crack formation.

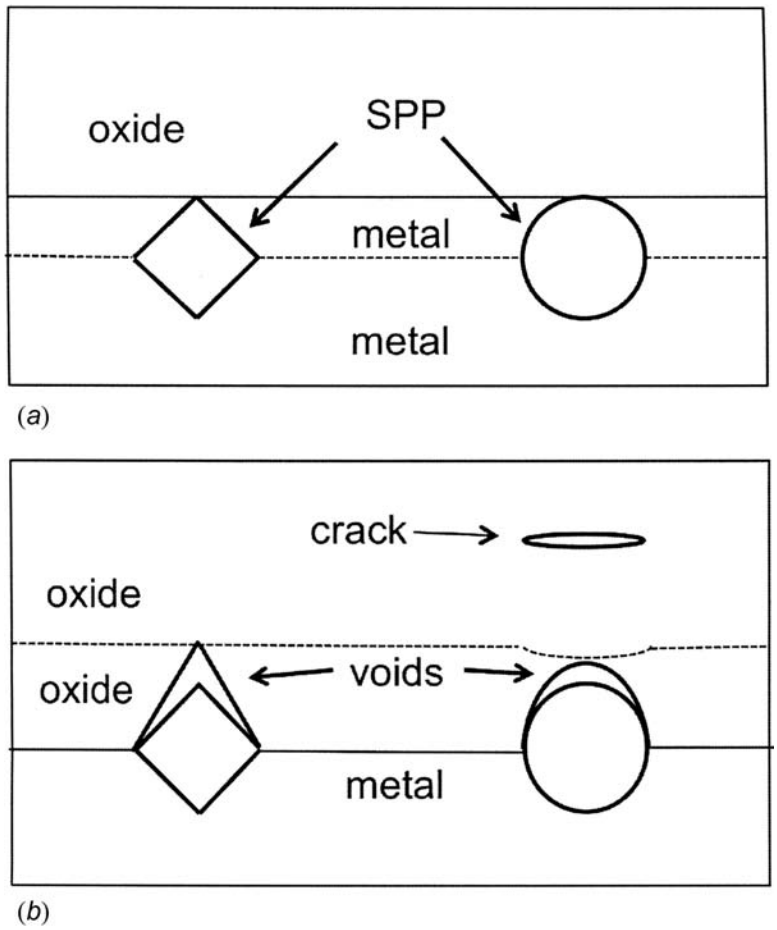


FIG. 9—*Schematic diagram of void and crack formation at SPPs. When the metal layer between the full and dashed line in (a) oxidizes, it expands perpendicular to the interface and forms the layer between the dashed and full line in (b). Since the SPPs are not oxidized, a void (left) is formed or, if the oxide first adheres to the SPP, a crack in the oxide and a smaller void form (right).*

Another possible source of crack formation is when particles in the oxide layer oxidize and thereby increase in volume. The relative importance of that potentially competing mechanism cannot be assessed from this work.

Oxygen Content

Several researchers have reported the presence of a sub-stoichiometric oxide layer adjacent to the metal/oxide interface [12,18,20,25,36–40].

The possible presence of a sub-oxide in Zircaloy-2 has been investigated by EDX line scans over the metal/oxide interface. Figure 10 shows that the oxygen

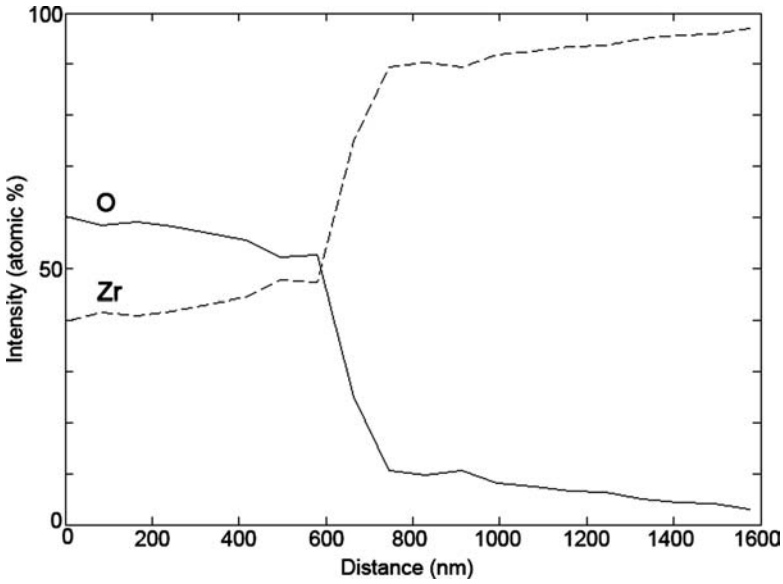


FIG. 10—*Zr and O TEM EDX line scan showing an indication of a 200 nm thick layer of sub-oxide at the metal/oxide interface of Material B with an oxide thickness of 1 μm.*

profile forms a plateau at a concentration close to 50 at. % of oxygen. This indicates that close to the interface there is a sub-oxide, with a composition corresponding to ZrO and a thickness of approximately 200 nm.

The oxygen content in the adjacent bulk oxide was measured to slightly less than the 67 at. % that would be expected for zirconia, ZrO_2. The difference is probably an artifact caused by x-rays generated by stray electrons hitting the zirconium metal matrix. This interpretation is supported by the fact that a small copper signal was also recorded, most likely originating from the supporting copper grid. Also, it is difficult to accurately correct for x-ray absorption of the low-energy O_K radiation. In the outermost part of the oxide an oxygen content very close to 67 at. % has indeed been confirmed using EDX.

Investigations concerning the oxygen ingress into the metal have also been performed using EDX line scans. EDX profiles have been made in both materials, in two different metal grains in each material and also within each grain one "wave crest" and one "trough" has been investigated. However, no significant difference between these measurements was found, the line scans all show a profile of about 200 nm where the oxygen content decreases from around 50 at. % down to a few atomic percent. One example of these profiles from Material B is shown in Fig. 11. As can be seen in Table 1, the amount of oxygen should be close to 1 at. % (1300 wt. ppm corresponds to 0.7 at. %). This discrepancy is most probably due to surface oxidation of the foil. It is worth noticing that there is a steep decrease from the 50 at. % of the sub-oxide down to the approximate oxygen solubility level in Zr metal, 29 at. %, after which a smooth diffusion gradient into the metal matrix follows.

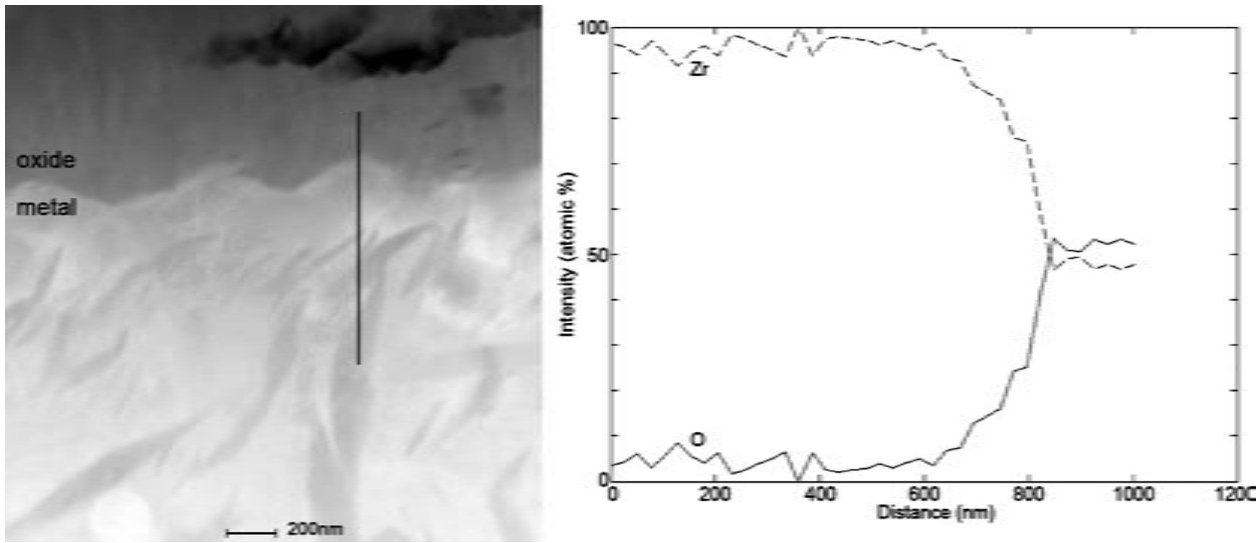


FIG. 11—*O and Zr TEM EDX line scan in Material B with an oxide thickness of 1 μm, showing that the oxygen content decreases over 200 nm from 50 at. % to a few at. %.*

An APT investigation was made of Material B with a 1 μm thick oxide layer. The specimen was prepared from the metal/oxide interface region, and a concentration profile through the oxide and into the metal is shown in Fig. 12. Again, the oxide close to the interface contains around 50 at. % of oxygen and is therefore understood to represent a sub-oxide, ZrO. At the metal/sub-oxide interface there is a sharp decrease in oxygen content, just a few nanometers wide, to around 30%. The width of the step is of the same size as the spatial resolution of the method used to construct the concentration profile (so-called proxigram), so the step is probably sharp on an atomic scale. After the step a smooth diffusion profile into the metal is found. As the APT investigation only runs 50 nm into the metal, the oxygen content is still above 10 at. % when the concentration profile ends.

Composition of the Sub-Stoichiometric Oxide Layer

The composition of the sub-oxide, as determined by APT analysis, is given in Table 4. In addition to zirconium and oxygen, tin was found and also small amounts of carbon and aluminum. As a comparison, the composition of the

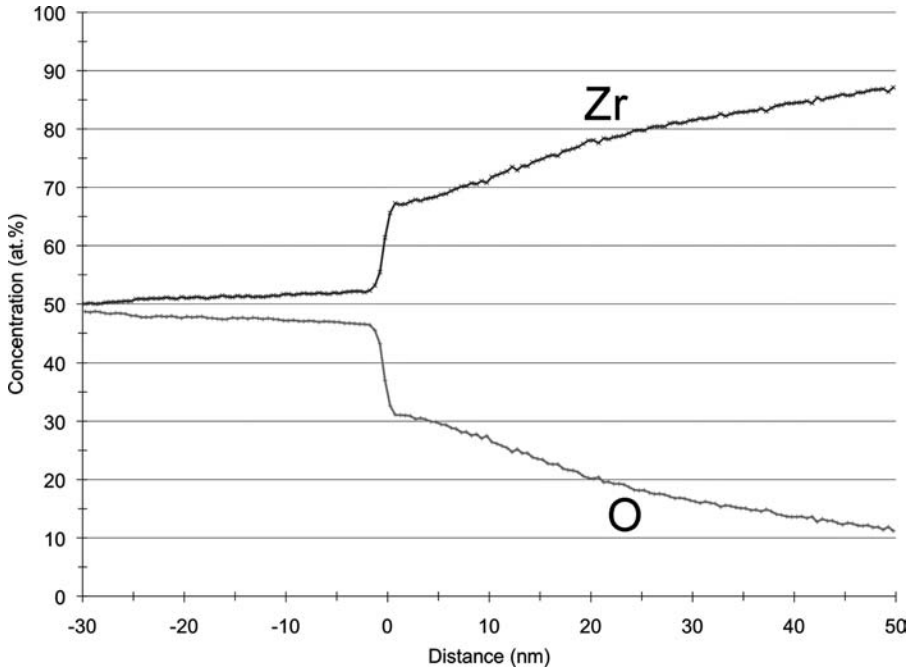


FIG. 12—*APT concentration profile through the metal/oxide interface in material B with an oxide thickness of 1 μm. Note the presence of a sub-oxide and the sharp step in oxygen (lower curve) content to the maximum solubility in the matrix, around 30 at. %. Proximity histogram with origin at the interface (iso-concentration surface with 40 at. % non-molecular Zr ions).*

TABLE 4—*APT analysis of Material B with an oxide thickness of 1 μm. Errors represent one standard deviation of the counting statistics. The hydrogen content might include some hydrogen gas from the vacuum chamber adsorbed onto the specimen surface, and is therefore an upper bound.*

	Total Content (at. %)		O Removed (at. %)	
Element	Sub-oxide	O diff. zone	Sub-oxide	O diff. zone
Zr	51.77±0.05	82.06±0.059	97.68±0.09	97.80±0.07
O	47.0±0.05	16.09±0.056	. . .	. . .
Sn	0.591±0.008	0.781±0.013	1.115±0.015	0.931±0.016
C	0.045±0.002	0.084±0.004	0.085±0.004	0.100±0.005
Al (ppm)	56±8	98±15	106±15	116±18
H (upper bond)	0.570±0.008	0.971±0.015	1.075±0.015	1.16±0.02
Number of atoms in analyzed volume	975 188	430 361	975 188	430 361

underlying metal matrix (i.e., the oxygen diffusion zone, where the oxygen content varies between 31 and 11 at. %) is also shown in Table 4. To facilitate the comparison, the oxygen has been removed from the data in the two columns on the left. The measured tin concentration agrees well with the chemical composition in Table 1 (1.32 wt. % corresponds to 1.01 at. %). Carbon and aluminum were not included in the chemical analysis in Table 1, but the contents are well within the limits of the ASTM specification of Zircaloy-2 [41]. Small amounts of silicon, iron, nickel and chromium were also found but were difficult to quantify because of overlaps in the spectrum. It is clear that the above-mentioned elements have approximately the same ratio to zirconium in the sub-oxide and the metal. Consequently all tin, carbon, and aluminum are incorporated in the oxide, which is consistent with the absence of any segregation to the metal/sub-oxide interface.

Although APT in principle detects all elements with the same efficiency, determination of the hydrogen content in the oxide and the metal can be difficult, since hydrogen (and water vapor) may adsorb on the specimen surface during analysis and may be removed during field evaporation pulses. It should be noted that hydrogen adsorption is a dynamic process that occurs during the course of an APT analysis, and cannot be avoided by removing adsorbed hydrogen before the analysis commences. Adsorbed hydrogen will then appear in spectra at the same position as any hydrogen dissolved in the material. Although analysis was made under good ultra-high vacuum conditions (pressure better than 10^{-10} torr) adsorption cannot be completely ruled out. The value for hydrogen concentration given in Table 4 is therefore an upper bound. Around 1 at. % (corresponding to approximately 110 wt. ppm) of hydrogen was found in the metal close to the interface, and around 0.6 at. % in the sub-oxide. Since hydrogen pick-up is an important degradation mechanism, the ability of APT to detect hydrogen with high spatial resolution may become important in future studies.

Conclusions

In order to learn more about the oxidation process of zirconium alloys, the microstructure of two variants of Zircaloy-2 with different SPP size (oxidized in steam autoclave) was studied by means of electron microscopy and microanalysis. Since the two materials have different oxidation behaviors, the focus was to find differences in microstructure between the materials, as these differences might help us understand what causes the difference in oxidation behavior. In the search for such microstructural differences, several investigations were performed. The investigations did not show any clear differences between the materials, but a number of general conclusions could be drawn:

1. The metal/oxide interface below the pre-transition oxide scale (1 μm oxide thickness) is undulating on a micrometer scale. Both materials studied show undulation with a periodicity of slightly less than 1 μm and an amplitude of around 100 nm. The geometry of this interface does not follow the geometry of the original surface, which is much flatter on the micrometer scale.
2. The SPPs oxidize slower than the metal and when they do, iron diffuses out of the particles into the surrounding oxide.
3. A sub-stoichiometric oxide layer with an oxygen content of approximately 50 at. % and a layer thickness of about 200 nm has been observed adjacent to the metal/oxide interface.
4. There is a 200 nm wide oxygen concentration gradient in the metal, from around 30 at. % at the metal/sub-oxide interface down to a few atomic percent.
5. All tin in the metal matrix is incorporated in the sub-oxide. No segregation to the metal/sub-oxide interface was found.

Although these findings are of importance for the general understanding of the oxidation process, none of them answer the question of what the difference is between the two materials. However, a theory concerning the formation of voids and cracks has also been presented in this study, and this theory is closely related to the difference between the materials. It explains how un-oxidized SPPs incorporated in the oxide are responsible for the formation of small voids and cracks. This implies that the number of SPPs matter more than the size, i.e., a material with more SPPs would also be expected to have more lateral cracks (and thus a poorer corrosion resistance). This finding correlates very well with the materials studied here, as the material with the highest number of SPPs exhibits the poorest corrosion resistance. Also, the most striking difference in the microstructure of the two materials is the number of lateral cracks, where the material with more SPPs has most cracks. Thus, it seems that we have found one clue to why the size distribution of SPPs is an important factor in the oxidation process of Zircaloy-2.

Acknowledgements

Sandvik Materials Technology is thanked for supplying the materials and performing the autoclave testing. Kristoffer Fagerlund is thanked for APT

specimen preparation and for running the APT instrument. This work was carried out with the financial support of Westinghouse Electric Sweden AB, Sandvik AB, Vattenfall Nuclear Fuel AB, OKG AB, and the Swedish Radiation Safety Authority.

References

[1] Rudling, P. and Wikmark, G., "A Unified Model of Zircaloy BWR Corrosion and Hydriding Mechanisms," *J. Nucl. Mater.*, Vol. 265, 1999, pp. 44–59.

[2] Garzarolli, F., Steinberg, E., and Weidinger, H. G., "Microstructure and Corrosion Studies for Optimized PWR and BWR Zircaloy Cladding," *Zirconium in the Nuclear Industry, Eighth International Symposium, ASTM STP 1023*, L. F. P. Van Swam and C. M. Eucken, Eds., ASTM International, West Conshohocken, PA, 1989, pp. 202–212.

[3] Eucken, C. M., Finden, P. T., Trapp-Pritsching, S., and Weidinger, H. G., "Influence of Chemical Composition on Uniform Corrosion of Zirconium-Base Alloys in Autoclave Tests," *Zirconium in the Nuclear Industry, Eighth International Symposium, ASTM STP 1023*, L. F. P. Van Swam and C. M. Eucken, Eds., ASTM International, West Conshohocken, PA, 1989, pp. 113–127.

[4] Garzarolli, F., Stehle, H., and Steinberg, E., "Behavior and Properties of Zircaloys in Power Reactors: A Short Review of Pertinent Aspects in LWR Fuel," *Zirconium in the Nuclear Industry: Eleventh International Symposium, ASTM STP 1295*, E. R. Bradley and G. P. Sabol, Eds., ASTM International, West Conshohocken, PA, 1996, pp. 12–32.

[5] Mayer, J., Giannuzzi, L., Kamino, T., and Michael, J., "TEM Sample Preparation and FIB-Induced Damage," *MRS Bull.*, Vol. 32, 2007, pp. 400–407.

[6] Ni, N., Lozano-Perez, S., Jenkins, M. L., English, C., Smith, G. D. W., Sykes, J. M., and Grovenor, C. R. M., "Porosity in Oxides on zirconium Fuel Cladding Alloys, and Its Importance in Controlling Oxidation Rates," *Scr. Mater.*, Vol. 62, 2010, pp. 564–567.

[7] Abolhassani, S., Restani, R., Rebac, T., Groeschel, F., Hoffelner, W., Bart, G., Goll, W., and Aeschbach, F., "TEM Examinations of the Metal-Oxide Interface of Zirconium Based Alloys Irradiated in a Pressurized Water Reactor," *J. ASTM Int.*, Vol. 2, No. 6, 2005.

[8] Tägtström, P., Limbäck, M., Dahlbäck, M., Andersson, T., and Pettersson, H., "Effects of Hydrogen Pickup and Second-Phase Particle Dissolution on the In-Reactor Corrosion Performance of BWR Claddings," *Zirconium in the Nuclear Industry: Thirteenth International Symposium, ASTM STP 1423*, G. D. Moan and P. Rudling, Eds., ASTM International, West Conshohocken, PA, 2002, pp. 96–118.

[9] Yilmazbayhan, A., Delaire, O., Motta, A. T., Birtcher, R. C., Maser, J. M., and Lai, B., "Determination of the Alloying Content in the Matrix of Zr Alloys Using Synchrotron Radiation Microprobe X-ray Fluorescence," *J. Nucl. Mater.*, Vol. 321, 2003, pp. 221–232.

[10] Wadman, B., Andrén, H.-O., Nyström, A.-L., Rudling, P., and Pettersson, H., "Microstructural Influence on Uniform Corrosion of Zircaloy Nuclear Fuel Claddings," *J. Nucl. Mater.*, Vol. 200, 1993, pp. 207–217.

[11] Thuvander, M. and Andrén, H.-O., "Methods of Quatitative Matrix Analysis of Zircaloy–2," *Ultramicroscopy*.

[12] Hutchinson, B., Lehtinen, B., Limbäck, M., and Dahlbäck, M., "A Study of the Structure and Chemistry in Zircaloy–2 and the Resulting Oxide After High Temperature Corrosion," *J. ASTM Int.*, Vol. 4, No. 10, 2009.

[13] Hudson, D., 2010, "Zirconium Oxidation on the Atomic Scale," Ph.D. thesis, Oxford, UK
[14] Andersson, T., Thorvaldsson, T., Wilson, A., and Wardle, A. M., "Influence of Thermal Processing and Microstructure on the Corrosion Behaviour of Zircaloy–4 Tubing," *Improvements in water reactor fuel technology and utilization*, IAEA, Vienna, Austria, 1987, pp. 435–449.
[15] Barberis, P., Ahlberg, E., Simic, N., Charquet, D., Lemaignan, C., Wikmark, G., Dahlbäck, M., Limbäck, M., Tägtström, P., and Lehtinen, B., "Role of the Second-Phase Particles in Zirconium Binary Alloys," *Zirconium in the Nuclear Industry: Thirteenth International Symposium, ASTM STP 1423*, G. D. Moan and P. Rudling, Eds., ASTM International, West Conshohocken, PA, 2002, pp. 33–58.
[16] Miller, M. K., Russell, K. F., and Thompson, G. B., "Strategies for Fabricating Atom Probe Specimens With a Dual Beam FIB," *Ultramicroscopy*, Vol. 102, 2005, pp. 287–298.
[17] Larson, D. J., Foord, D. T., Petford-Long, A. K., Liew, H., Blamire, M. G., Cerezo, A., and Smith, G. D. W., "Field-ion Specimen Preparation Using Focused Ion-beam Milling," *Ultramicroscopy*, Vol. 79, 1999, pp. 287–293.
[18] Wadman, B., 1993, "Mechanisms of Uniform Corrosion of Zirconium Alloys in Water and Steam", Ph.D. thesis, Department of Physics, Chalmers University of Technology, Göteborg.
[19] Hutchinson, B. and Lehtinen, B., "A Theory of the Resistance of Zircaloy to Uniform Corrosion," *J. Nucl. Mater*. Vol. 217, 1994, pp. 243–249.
[20] Bossis, P., Lelièvre, G., Barberis, P., Iltis, X., and Lefebvre, F., "Multi-Scale Characterization of the Metal-Oxide Interface of Zirconium Alloys," *Zirconium in the Nuclear Industry: Twelfth International Symposium, ASTM STP 1354*, G. P. Saboland and G. D. Moan, Eds., ASTM International, West Conshohocken, PA, 2000, pp. 918–945.
[21] Gebhardt, O., Hermann, A., Bart, G., Blank, H., Garzarolli, F., and Ray, L. F., "Investigation of In-Pile Grown Corrosion Films on Zirconium-Based Alloys," *Zirconium in the Nuclear Industry: Eleventh International Symposium, ASTM STP 1295*, E. R. Bradley and G. P. Sabol, Eds., ASTM International, West Conshohocken, PA, 1996, pp. 218–241.
[22] Blank, H., Bart, G., and Thiele, H., "Structural Analysis of Oxide Scales Grown on Zirconium Alloys in Autoclaves and in a PWR," *J. Nucl. Mater.*, Vol. 188, 1992, pp. 273–279.
[23] Wikmark, G., Rudling, P., Lehtinen, B., Hutchinson, B., Oscarsson, A., and Ahlberg, E., "The Importance of Oxide Morphology for the Oxidation Rate of Zirconium Alloys," *Zirconium in the Nuclear Industry: Eleventh International Symposium, ASTM STP 1295*, E. R. Bradley and G. P. Sabol, Eds., ASTM International, West Conshohocken, PA, 1996, pp. 55–73.
[24] Parise, M., Sicardy, O., and Cailletaud, G., "Modelling of the Mechanical Behavior of the Metal-Oxide System During Zr alloy Oxidation," *J. Nucl. Mater.*, Vol. 256, 1998, pp. 35–46.
[25] Yilmazbayhan, A., Breval, E., Motta, A. T., and Comstock, R. J., "Transmission Electron Microscopy Examination of Oxide Layers Formed on Zr alloys," *J. Nucl. Mater.*, Vol. 349, 2006, pp. 265–281.
[26] Pêcheur, D., Lefebvre, F., Motta, A. T., Lemaignan, C., Charquet, D., and Wadier, J. F., "Oxidation of Intermetallic Precipitates in Zircaloy–4: Impact of Irradiation," *Zirconium in the Nuclear Industry: Tenth International Symposium, STP 1245*, A. M. Garde and E. R. Bradley, Eds., ASTM International, West Conshohocken, PA, 1994, pp. 687–705.
[27] Park, J.-Y., Yoo, S., Choi, B.-K., and Jeong, Y., "Oxide Microstructure of Advanced Zr Alloys Corroded in 360 °C water loop," *J. Alloys Compd* Vol. 437, 2007, pp. 274–279.

[28] Iltis, X., Lefebvre, F., and Lemaignan, C., "Microstructural Study of Oxide Layers Formed on Zircaloy–4 in Autoclave and in Reactor. Part II: Impact of the Chemical Evolution of Intermetallic Precipitates on their Zirconia Environment," *J. Nucl. Mater.*, Vol. 224, 1995, pp. 121–130.

[29] Pêcheur, D., Lefebvre, F., Motta, A. T., Lemaignan, C., and Wadier, J. F., "Precipitate Evolution in the Zircaloy–4 Oxide Layer," *J. Nucl. Mater.*, Vol. 189, 1992, pp. 318–332.

[30] Hatano, Y. and Sugisaki, M., "Oxidation Behavior of Iron and Nickel in Zr_2(Fe,Ni) Precipitates in Zircaloy–2," *J. Nucl. Sci. Technol.*, Vol. 33, 1996, pp. 829–833.

[31] Hatano, Y. and Sugisaki, M., "Auger Electron Spectroscopy Study of Oxidation Behavior of Iron and Chromium in $Zr(Fe,Cr)_2$ Precipitate in Zircaloy–4," *J. Nucl. Sci. Technol.*, Vol. 34, 1997, pp. 264–268.

[32] Etoh, Y. and Shimada, S., "Neutron Irradiation Effects on Intermetallic Precipitates in Zircaloy as a Function of Fluence," *J. Nucl. Mater.*, Vol. 200, 1993, pp. 59–69.

[33] Griffiths, M., "A Review of Microstructure Evolution in Zirconium Alloys During Irradiation," *J. Nucl. Mater.*, Vol. 159, 1988, pp. 190–218.

[34] Yilmazbayhan, A., Motta, A. T., Comstock, R. J., Sabol, G. P., Lai, B., and Cai, Z., "Structure of Zirconium Alloy Oxides Formed in Pure Water Studied With Synchrotron Radiation and Optical Mmicroscopy: Relation to Corrosion Rate," *J. Nucl. Mater.*, Vol. 324, 2004, pp. 6–22.

[35] Bouineau, V., Ambard, A., Bénier, G., Pêcheur, D., Godlewski, J., Fayette, L., and Duverneix, T., "A New Model to Predict the Oxidation Kinetics of Zirconium Alloys in a Pressurized Water Reactor," *J. ASTM Int.*, Vol. 5, No. 5, 2006.

[36] Anada, H. and Takeda, K, "Microstructure of Oxides on Zircaloy–4, 1.0Nb Zircaloy–4, and Zircaloy–2 Formed in 10.3-MPa Steam at 673 K," *Zirconium in the Nuclear Industry: Eleventh International Symposium, ASTM STP 1295*, E. R. Bradley and G. P. Sabol, Eds., ASTM International, West Conshohocken, PA, 1996, pp. 35–54.

[37] Hudson, D., Ni, N., Lozano-Perez, S., Saxey, D., English, C., Smith, G. D. W., Sykes, J., and Grovenor, C., "The Atomic Scale Structure and Chemistry of the Zircaloy–4 Metal-Oxide Interface," *14th International Conference on Environmental Degradation of Materials in Nuclear Power Systems*, Virginia Beach, VA, August 23–27, 2009, American Nuclear Society, La Grange Park, IL.

[38] Nishino, Y., Krauss, A.R., Lin, Y.P. and Gruen, D.M., "Initial Oxidation of Zirconium and Zircaloy–2 with Oxygen and Water Vapor at Room Temperature," *J. Nucl. Mater.*, Vol. 228, 1996, pp. 346–353.

[39] Moseley, P. T. and Hudson, B., "Phases Involved in the Corrosion of Zircaloy by Hot Water 350-Degrees-C," *J. Nucl. Mater.*, Vol. 99, 1981, pp. 340–344.

[40] Iltis, X. and Michel, H., "Transmission Electron Microscopy Study of a Locally Ordered Zr-O Solid-Solution Obtained by an Oxidation Treatment of a Zircaloy–4 Alloy," *J. Alloys Compd.*, Vol. 177, 1991, pp. 71–82.

[41] ASTM Standard B 353.89, 1990, *Annual Book of ASTM Standards*, American Society of Testing and Materials, West Conshohocken, Philadelphia, PA.

DISCUSSION

Question 1, Arthur Motta, Penn State:—1) Did you observe the redistribution of Fe within the intermetallic precipitates that was observed by Pêcheur et al in 1992? 2) Was the oxide formed on the precipitates higher in tetragonal content than that formed in the matrix?

Author's Response:—1) The precipitates in these materials are so much smaller than those investigated by Pêcheur (approximately 70 nm compared to 300 nm), so it is hard to observe any redistribution within the precipitates. This was not done.

2) This was not investigated.

Question 2, Philippe Bossis, CEA:—How can the periodicity of cracks usually observed in oxide layers be related to the absence of periodicity of the precipitates' distribution, according to the proposed mechanism?

Author's Response:—The voids are very small, not large enough to cause continuous cracks. The formation of large cracks has more to do with the stresses within the material. Stress is built up as the oxide layer grows thicker and at a certain level of stress the larger cracks can propagate. This would lead to periodically recurring cracks even with a less periodic distribution of precipitates.

Question 3, Bo Cheng, EPRI:—The sub-oxide with 50% oxygen you found at the metal-oxide interface, and you also show undulated metal-oxide interface. In my earlier study, a distinct oxygen-rich diffusion layer was observed after long-term exposure at 400°C. So, there appears to have oxygen diffusion activity involved in the growth of the oxide in 400°C steam. Will you be able to map out the distribution of oxygen near the metal-oxide interface to further understanding the corrosion process?

Author's Response:—Some EDX line scans have been made perpendicular to the metal/oxide interface. Oxygen mapping is planned.

Question 4, Linjiang Chai, Chongquing Universtiy:—The values of accumulated annealing parameters of the two materials in your presentation are of order-difference with previous studies. Can you give out the value of Q/R you've selected and why?

Author's Response:—This information is found in the article, Q is 63000 cal/mol.

Question 5, Pierre Barberis, AREVA:—1) Diffusion profiles have been measured: do you compare them at a given oxide thickness or at a given corrosion time? 2) Does the fact that there is no difference between materials A and B mean that there is a difference in diffusion coefficient in the metal? In the barrier oxide layer thickness?

Author's Response:—1) At a given oxide thickness (mostly in this article 1 mm oxide scales have been observed). For material A this thickness was achieved in 3 days and for material B it took 9 days, this information can be found in the article.

2) The diffusion coefficient should be the same for both materials, this is not the rate-determining step of the oxidation process. The SPPs are too far apart in both materials to make any important contribution to the diffusion. The size distribution of SPPs is the only main difference between the two alloys, so they should have the same diffusion coeffient. Further investigations are needed to find out if there is any difference in barrier oxide layer thickness.

Question 6, Michael Preuss, University of Manchester, UK:— Do you know how far away in terms of days were your oxides from transition?

Author's Response:— Since we do not know exactly at what oxide thickness transition occurs it is hard to say how far away from transition we are.

Reprinted from JAI, Vol. 8, No. 1
doi:10.1520/JAI102951
Available online at www.astm.org/JAI

B. X. Zhou,[1] *J. C. Peng,*[2] *M. Y. Yao,*[1] *Q. Li,*[2] *S. Xia,*[1] *C. X. Du,*[1] *and G. Xu*[1]

Study of the Initial Stage and Anisotropic Growth of Oxide Layers Formed on Zircaloy-4

ABSTRACT: An in situ investigation of the epitaxial oxide layer formed on a thin specimen heated in a transmission electron microscope was carried out. Some dot-like grains about 10 nm in size were formed on the surface of a relatively thin area. The dot-like grains are monoclinic zirconium oxide and have an orientation relationship of (001)m//(0$\bar{1}$11)α-Zr, (001)m//(1$\bar{1}$01)α-Zr, with the α-Zr matrix. Some long strip-like grains, probably a new kind of zirconium suboxide, were formed on the surface of a relatively thick area. The strip-like grains have a bcc structure with a lattice parameter a=0.66 nm and have an orientation relationship of $(110)_{\mathrm{bcc}}//(10110)_{\alpha-\mathrm{Zr}}$, $[1\bar{1}10]_{\mathrm{bcc}}//[0001]_{\alpha-\mathrm{Zr}}$ with the α-Zr matrix. The relationship between the thickness of oxide layers and the grain orientations of the α-Zr matrix was studied with coarse-grained Zircaloy-4 specimens through autoclave corrosion tests at 500 and 400°C in superheated steam, and at 360°C in both lithiated and deionized water for long time exposure. The results show that the anisotropic growth of oxide layers on the grain surface with different orientations is considerable. However, the relationship between the thickness of oxide layers and the grain orientations of the α-Zr matrix varies with corrosion temperature and water chemistry. The largest variation of oxide thickness developed during corrosion tests at 500°C. The thickest oxide layers were formed on those grains whose surface orientations were distributed around the planes from (01$\bar{1}$0) to ($\bar{1}$2$\bar{1}$0). The thicker oxide layers on these grains were further developed into nodular corrosion. When the specimens were corroded at 360°C in lithiated water, the thickest oxide layers formed on those grains, whose surface

Manuscript received January 7, 2010; accepted for publication October 1, 2010; published online November 2010.
[1] Institute of Materials, Shanghai Univ., Shanghai 200072, People's Republic of China.
[2] The Key Laboratory for Advanced Micro-Analysis, Shanghai Univ., Shanghai 200444, People's Republic of China.

Cite as: Zhou, B. X., Peng, J. C., Yao, M. Y., Li, Q., Xia, S., Du, C. X. and Xu, G., "Study of the Initial Stage and Anisotropic Growth of Oxide Layers Formed on Zircaloy-4," *J. ASTM Intl.*, Vol. 8, No. 1. doi:10.1520/JAI102951.

Copyright © 2011 by ASTM International, 100 Barr Harbor Drive, PO Box C700, West Conshohocken, PA 19428-2959.

orientations tilted from 15 to 30° away from the (0001) plane. When the specimens were corroded at 400°C in superheated steam and at 360°C in deionized water, the difference between the thickness of oxide layers on different grain surfaces was less prominent.

KEYWORDS: Zircaloy-4, corrosion, epitaxial oxide layer, anisotropic oxidation, textures, coarse grain, transmission electron microscopy

Introduction

Zirconium alloys of a hexagonal close-packed crystal structure have a prominent anisotropic characteristic in comparison with metals of a cubic structure. The anisotropic characteristic is bound to be reflected in the corrosion behavior of zirconium alloys since strong textures are produced in sheet or tubular materials during the fabrication process. It is worthwhile to make further investigations of the anisotropic growth of the oxide layer because this is one of the essential issues for better understanding of the corrosion mechanism of zirconium alloys.

It is hard, if not impossible, to prepare single crystals of zirconium alloys, even specimens with large grains, because the mobility of the grain boundaries is obstructed by the formation of many second phase particles (SPPs) distributed in the α–Zr matrix and the decrease of the temperature of the α/β phase transformation after the addition of alloying elements. Most existing research on the relationship between the growth of an epitaxial oxide layer and the crystal orientation of a metal matrix was carried out with small single crystals or coarse grains of pure zirconium, and the testing time was relatively short in different conditions and at different temperatures, such as 1 h in oxygen at 415°C [1], 3 days in water (18.6 MPa) at 360°C [2], 40 min in steam (0.1 MPa) at 500°C [3], and 1 h in dry air at 350–400°C [4]. The thickness of epitaxial oxide layers was very small, only 25 nm to $\sim 1\ \mu$m. A summary of oxidation anisotropy data was given by Ploc [5] and Cox [6] and was described in more detail by Kim et al. [7]. The results were inconsistent with each other. The reasons for the inconsistency might be attributed to the fact that the corrosion tests were carried out in different conditions, at different temperatures, and for different exposure times. Kim et al. [7] discussed the oxidation characteristics at the initial stage, which are controlled by oxygen diffusion, and the preferred growth of oxide. At this stage, the growth of oxide is related to the crystallographic relationship between the oxide layer and the metal matrix. But at the later stage, the microstructure difference between oxide layers, including the microstructural evolution during the corrosion process, should be taken into account for further growth of the oxide as discussed in a previous paper [8], because the oxygen ions pass the barrier of the oxide layer and reach the oxide/metal interface to form zirconium oxide.

Kim et al. [7] investigated the oxidation characteristics of the basal (0001) plane and the prism $(11\bar{2}0)$ plane with small single crystals of pure zirconium. Oxidation tests were carried out in water (18.9 MPa) at 360°C for 200 h exposure. The results showed that the oxidation rate of the $(11\bar{2}0)$ prismatic plane was faster than that of the (0001) basal plane. When the oxide layer on the

prism $(11\bar{2}0)$ plane was spalling off at $\sim 20\,\mu$m after 60 h exposure, the oxide layer on the basal (0001) plane was only $\sim 2\,\mu$m. Zhou et al. [9] pointed out that the nodular corrosion resistance of Zircaloy-4 specimens was not only related to the temperature of heat treatments, but also the textures of the specimen. This illustrates that the anisotropic character of oxide growth is involved in the corrosion process. In order to clarify the inconsistent results obtained in the past, corrosion tests at different temperatures and in different water chemistry using Zircaloy-4 coarse-grained specimens are considered in the present work. In situ investigation of the epitaxial oxide layer formed on a thin specimen heated in a transmission electron microscope (TEM) was also performed. The goal of this work is to highlight the role of anisotropic growth and the microstructural evolution of the oxide layer in corrosion behavior at different temperatures and in different water chemistry for long-term exposure.

Experimental Procedures

The Preparation of Coarse-Grained Specimens

In order to investigate the relationship between the oxide layer thickness and the grain orientation of the metal matrix, the effect of grain boundaries on the growth of the oxide layer must be taken into account. In order to minimize this effect, specimens with coarse grains should be prepared.

Flat Zircaloy-4 samples with a composition of 1.44 % Sn, 0.24 % Fe, and 0.11 % Cr (in mass fraction), $20 \times 8\,\text{mm}^2$ in size, were cut from a 1 mm thick plate, vacuum sealed under 5×10^{-3} Pa in quartz capsules, annealed at 1020°C for 20 min, and then quenched into water while simultaneously breaking the quartz capsules. They were pickled in a mixed solution of $10\,\%\,\text{HF} + 45\,\%\,\text{HNO}_3 + 45\,\%\,\text{H}_2\text{O}$ (in volume) to remove the blue thin oxide on the surface caused by water quenching and then rinsed in cold tap water. The specimens were vacuum annealed again at 800°C for 10 h to grow the coarse grains. Since a microstructure with fine martensite and a high density of dislocations was produced by water quenching from the high temperature β phase region, coarse grains could be grown during annealing at 800°C in the high temperature alpha phase region. Annealing at 700°C in a vacuum for 100 h, after the growth of coarse grains at 800°C, was adopted to reduce the supersaturated solid solution of alloying elements in the $\alpha-$Zr matrix. Finally, specimens with coarse grains of 0.2–0.8 mm in diameter were obtained. Some SPPs in the $\alpha-$Zr matrix grew up to the range between 0.5 and $0.8\,\mu$m since specimens were annealed at 800°C for 10 h. But some SPPs in less than $0.1\,\mu$m can be also detected, which might be precipitated during annealing at 700°C.

Corrosion Tests and the Determination of the Relationship Between the Oxide Layer Thickness and the Grain Orientations of the Metal Matrix

The specimens divided into four groups were first pickled in a mixed solution of $10\,\%\,\text{HF} + 45\,\%\,\text{HNO}_3 + 45\,\%\,\text{H}_2\text{O}$, then rinsed in cold tap water, and finally rinsed in boiling deionized water. Corrosion tests were carried out in static

autoclaves at 500°C/10.3 MPa or 400°C/10.3 MPa superheated steam and at 360°C/18.6 MPa deionized water or lithiated water of 0.01*M* LiOH.

After the corrosion tests, the specimens were mounted into a Bi–Pb alloy to prepare specimen cross-sections. Then, the specimen sections were ground with sand paper, mechanically polished, and pickled in a mixed acid solution as mentioned above to remove the deformation layer on the section surface. Electron backscatter diffraction (EBSD) was employed for the determination of grain orientations of the metal matrix on the specimen sections using a HKL™ EBSD equipment attached to a CamScan Apollo-300 scanning electron microscope (SEM), and the thickness of the oxide layers was also measured from SEM micrographs at the magnification of 500–5000 times.

The Preparation of Transmission Electron Microscope Specimens for In Situ Investigation of the Epitaxial Oxide Layer

The double-jet electropolishing method was adopted to prepare thin specimens for TEM examination. Electropolishing was carried out at about −40°C with 50 V dc in an electrolyte of 10 % $HClO_3$ + 90 % ethanol (in volume). Thin specimens placed in a specimen heating holder were heated in the specimen chamber of a TEM (Hitachi H-800). After making a general examination, the specimens were cooled down and transferred to a JEM-2010F TEM for recording high resolution lattice images.

A DigitalMicrograph™ was used for processing the high resolution lattice images recorded by charge coupled device (CCD) camera. The fast Fourier transforms (FFTs), which are involved in DigitalMicrograph™, can reveal the periodic contents of images and also work on regions of interest with appropriate dimensions placed on an image. They are useful for image analysis and filtering to obtain information about the crystal structure and the defects in crystals.

The Preparation of the Specimen Surface for Scanning Electron Microscope Examination

A JSM-6700F SEM was employed for examining the grain morphology of the oxide layer on the specimen surface after corrosion tests. A thin layer of iridium coating on the specimens applied by sputtering is required for improving the quality of images.

Experimental Results and Discussion

Initial Stage of the Oxidation

Even in the high vacuum condition ($\sim 10^{-3}$ Pa) of the TEM, a thin oxide film formed with different interference colours that outline the original metal grain structure after the specimen was heated for 2 days at 200°C, as shown in Fig. 1. This indicates that the in situ investigation of epitaxial oxide layer growth on zirconium alloys by TEM is possible.

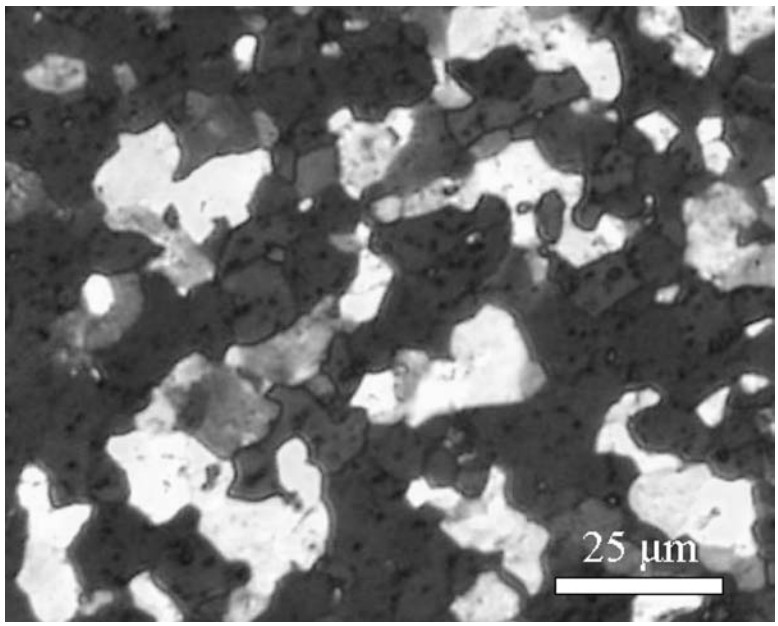


FIG. 1—*A thin oxide film formed with different interference colours to outline the original grain structure of a Zircaloy-4 specimen heated at 200°C in TEM for 2 days of exposure (optical miscroscopy).*

When a thin specimen was heated at 400°C for 2 h, different morphologies and different crystal structures of the epitaxial oxide layers were observed around the penetrated hole of the thin specimen at different distances from the edge of the hole, as shown in Fig. 2. At the relatively thin area around the hole, some dot-like grains about 10–20 nm in size were detected by a selected area diffraction (SAD) pattern and the bright/dark field images, as shown in Fig. 3. Figure 4(*a*) shows the high resolution lattice image for both the dot-like grains and the α−Zr matrix, and the FFT patterns indexed for both areas are also incorporated in this figure. Figure 4(*b*) shows the high resolution lattice image for the dot-like grains only. By analyzing the indexed FFT patterns and measuring the line spacing, it is indicated that the dot-like grains are monoclinic zirconium

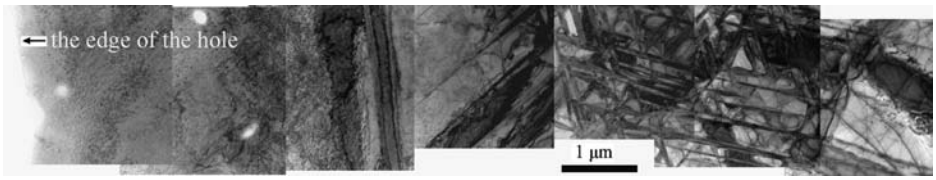


FIG. 2—*Different morphologies and different crystal structures of the epitaxial oxide layers formed around the hole of a thin specimen at different distances.*

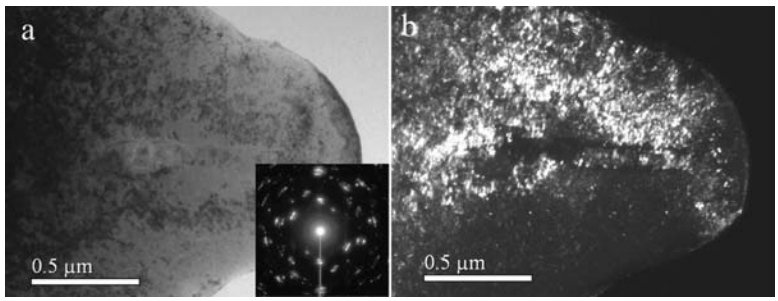


FIG. 3—(a) *The bright field image, (*b*) dark field image, and SAD pattern of the dot-like grains formed on the relatively thinner area near the hole of a thin specimen.*

oxide ($m-ZrO_2$), and have an orientation relationship of $(001)_m//(0111)_{\alpha-Zr}$, $(111)_m//(1101)_{\alpha-Zr}$ with the α−Zr matrix. This relationship is inconsistent with the data obtained through experiments or by theoretical prediction in the past, which were discussed by Ploc [5]. Perhaps this relationship is different on different α−Zr crystal planes on which the $m-ZrO_2$ grows.

As the lattice parameter of the α−Zr is known, the spacing of crystal planes for $m-ZrO_2$ in the thin layer oxide can be determined accurately by calibration of the values obtained from measuring the lattice spacing on the high resolution lattice image with the inverse FFT operation. The *d* values of (001), $(\bar{1}11)$ and (111) planes for $m-ZrO_2$ of the dot-like grains are 0.482, 0.273, and 0.240 nm, respectively, and the *d* values of these planes for the standard $m-ZrO_2$ (No. 37-1484) are 0.508 70, 0.316 47, and 0.284 06 nm. It is clear that the lattice parameter of $m-ZrO_2$ formed on the thin specimens at the initial stage is smaller than that of standard $m-ZrO_2$ owing to the constraint of the α−Zr matrix due to a high Pilling–Bedworth (PB) ratio of 1.56. The difference of the spacing for different crystal planes compared to the standard $m-ZrO_2$ is about 5–15 % smaller. There must be a high compressive stress produced during the formation of the oxide layer. When looking at the high resolution lattice image in

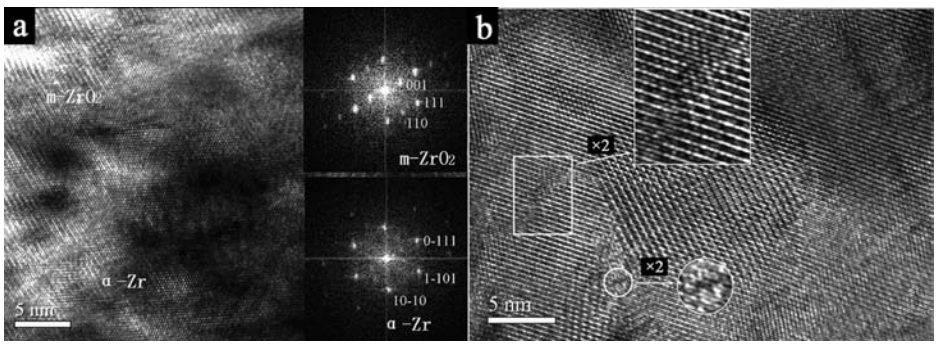


FIG. 4—*High resolution lattice images of the dot-like grains showing the orientation relationship with (*a*) α−Zr matrix and (*b*) some defects in the lattice.*

Fig. 4(*b*) carefully, the distortion of the lattice image by the existence of defects, including some dislocations, and the formation of a "cell structure" of about 10 nm with a little difference in orientation between each cell are revealed. Some parts of the image containing defects are further enlarged to see them in detail and are also incorporated in Fig. 4(*b*). This is the reason that the SAD pattern shown in Fig. 3(*a*) is like a diffraction pattern of a strong fiber texture. The nanocrystals of $m-ZrO_2$ in the thin oxide layer have detached from the restriction of the matrix and adjusted their orientation as a unit of about 10–20 nm to form Moiré patterns as shown in Fig. 5 after further growth of the oxide layer.

Many long strip-like grains grown at relatively thick areas on the thin specimen with a certain distance from the edge of the hole were observed. This distance in Fig. 2 is between 6 and 10 μm. These strip-like grains formed on the (0001) plane of the $\alpha-Zr$ matrix crossed each other to form a 60° angle as shown in Fig. 6 and preferentially grew up along the $\langle 11\bar{2}0\rangle_{\alpha-Zr}$ direction at a rate of ~ 100 nm/min. A SAD pattern including the $\alpha-Zr$ matrix and the long strip-like grains was indexed and is incorporated in Fig. 6. Through the analysis of the SAD pattern, a bcc structure with a lattice parameter $a = 0.66$ nm and the orientation relationship of $(110)_{bcc}//(10\bar{1}0)_{\alpha-Zr}$, $[110]_{bcc}//[0001]_{\alpha-Zr}$ with the $\alpha-Zr$ matrix was identified. This long strip-like phase is likely a new kind of zirconium suboxide that has not been documented yet. Oxygen was adsorbed on the surface of the specimen and diffused into the $\alpha-Zr$ matrix during specimen heating at 400°C in vacuum: consequently, the oxygen content of the matrix at the relatively thick area will be lower than at the relatively thin area. This might explain the fact that the oxide structure formed on the surface at different

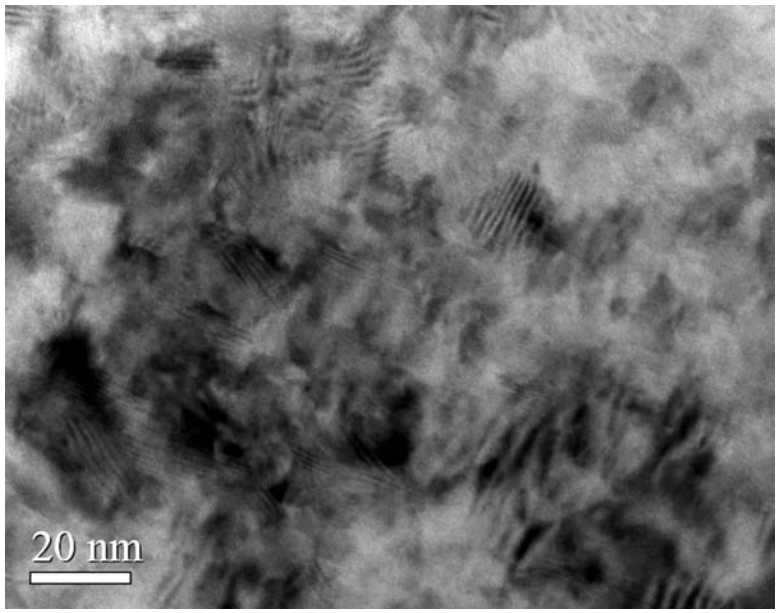


FIG. 5—*The Moiré patterns in the areas of the dot-like grains formed.*

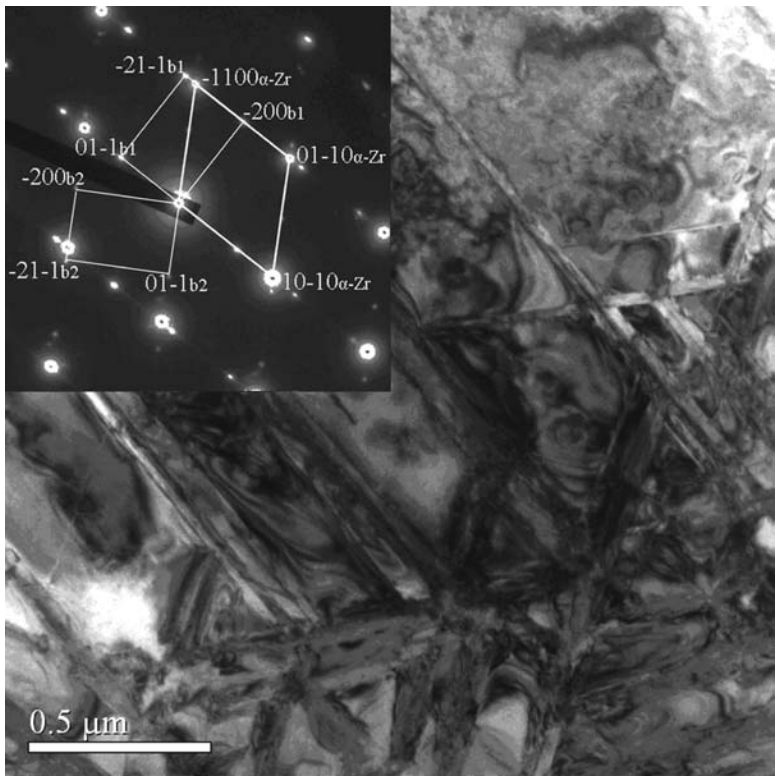


FIG. 6—*The morphology and SAD pattern of the long strip-like grains formed on the relatively thicker area at a certain distance from the edge of the hole.*

thickness areas around the hole is different. An attempt was made to investigate whether this kind of phase could transform to other structures after a long time exposure at 400°C. But this failed due to contamination after heating for a long time.

Corrosion Behavior of the Coarse-Grained Specimens During Autoclave Testing

The weight gains versus exposure time for the specimens corroded at 360°C in deionized water and in lithiated water and at 400 and 500°C in superheated steam are shown in Fig. 7(*a*)-7(*d*), respectively. An average value of weight gain was taken from four to six specimens. The variation in weight gains for parallel coarse-grained specimens was higher than the spread for fine-grained specimens. This means that the grain number on the surface of coarse-grained specimens is not sufficient to give reasonable statistical figures of weight gain. In other words, big specimens with large surface areas are needed, since the thickness of oxide layers on metal grains with different orientations is different.

There is no obvious transition phenomenon, particularly for the coarse-grained specimens corroded at 360°C in lithiated water. In general, the

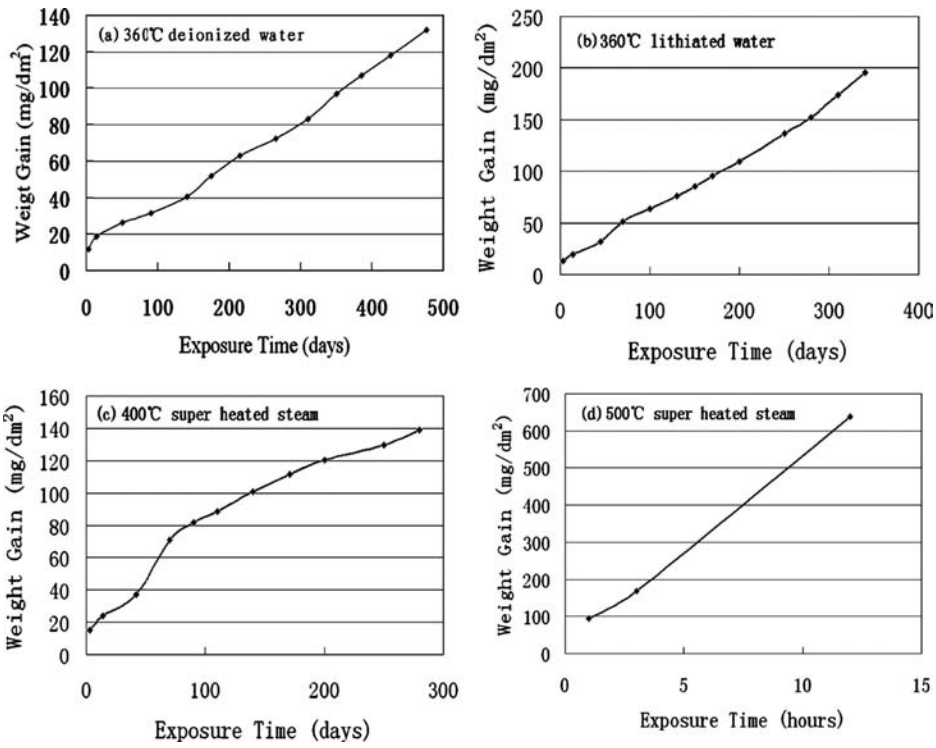


FIG. 7—*The weight gain versus exposure time of the specimens corroded at different temperatures and in different water chemistry:* (a) *360°C/18.6 MPa deionized water;* (b) *360°C/18.6 MPa lithiated water with 0.01M LiOH;* (c) *400°C/10.3 MPa superheated steam; and* (d) *500°C/10.3 MPa superheated steam.*

corrosion transition appears after 100 days exposure of Zircaloy-4 fine-grained specimens corroded at 360°C in lithiated water, and the corrosion rate is accelerated markedly after the transition. The difference of the transition phenomena between coarse-grained and fine-grained specimens is related to the anisotropic growth of the oxide layer and the textures of the specimens to be discussed in the latter part of this paper.

Surface Morphology of the Specimens After Corrosion Tests

The surface morphology of the specimens after corrosion tests is shown in Fig. 8. The undulation of the oxide layer on the specimen surface is obvious due to the variation of the oxide thickness on different grains, but it was developed to a different extent for specimens corroded at different temperatures and in different water chemistry. The most serious one was developed during the corrosion test performed at 500°C in superheated steam. The thicker oxide layers on those grains were developed in a lenticular shape when the exposure time lasted from 3 to 12 h as shown in Fig. 9. It shows that nodular corrosion took

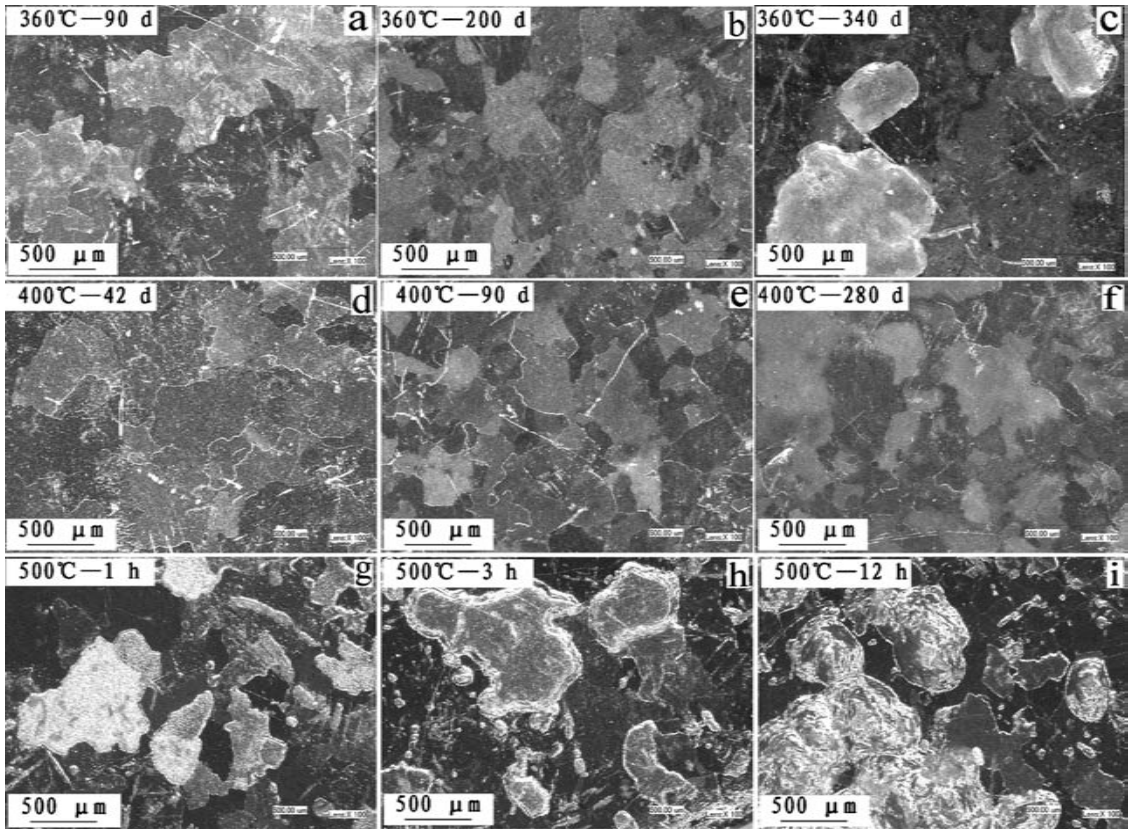


FIG. 8—*Optical micrographs of the surface morphology of the specimens corroded at different temperatures, in different water chemistry, and for different time exposures: [*(a)*–*(c)*] Corroded at 360°C in lithiated water; [*(d)*–*(f)*] corroded at 400°C in superheated steam; and [*(g)*–*(i)*] corroded at 500°C in superheated steam.*

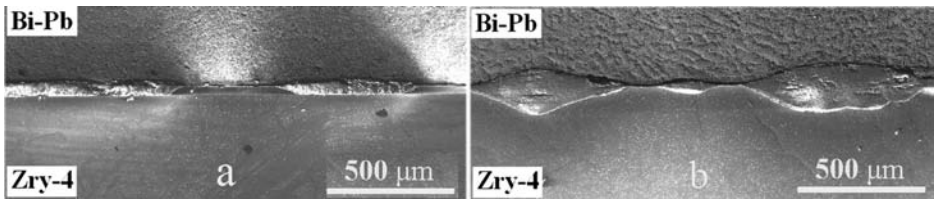


FIG. 9—*The morphology of the specimen sections corroded at 500°C in superheated steam for (*a*) 3 h exposure and (*b*) 12 h exposure showing the development of nodular corrosion (SEM).*

place. A lot of cracks on the surface of nodules look like a flower as shown in Fig. 10(*a*). When the corrosion tests were carried out at 360°C in lithiated water, thicker oxide layers on some grains were developed after 340 days exposure, but they were not in a lenticular shape when examined on the sections and not many cracks appeared on the surface of the thickest oxide layers as shown in Fig. 10(*b*). The difference of oxide layer thickness on the different grains for the specimens corroded at 400°C in superheated steam after 280 days exposure and at 360°C in deionized water after 476 days exposure was also detected, but it was not as serious as the specimens corroded at 500°C in superheated steam or at 360°C in lithiated water. Due to the similarity of the surface morphology of specimens corroded at 360°C in deionized water to those corroded at 400°C in superheated steam, only the surface morphologies of specimens corroded at 400°C in superheated steam are given in Fig. 8.

Grain Morphology of Oxide on the Specimen Surface

In order to get more information about the characteristics of anisotropic growth of oxides, the grain morphology of oxides on the surface of the specimens corroded at different temperatures in different water chemistry and for different exposure times was examined using a SEM. Particularly, the morphology

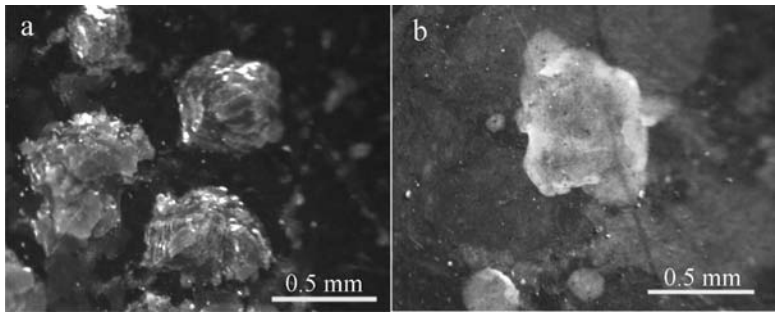


FIG. 10—*The surface morphology of (*a*) the nodules corroded at 500°C in superheated steam for 12 h exposure and (*b*) the thickest oxide layers corroded at 360°C in lithiated water for 340 days exposure.*

difference of oxide grains on the oxide layers with different thicknesses for a same specimen was compared. Cracks on the oxide surface, micro-cracks along grain boundaries, and pores on triple junctions of grain boundaries were revealed on the relatively thick oxide layers after long time exposure. The difference of oxide grain morphology on the oxide layers of different thicknesses is more obvious when the specimens were corroded at 500°C in superheated steam and at 360°C in lithiated water than at 400°C in superheated steam and at 360°C in deionized water. Some typical morphologies of oxide grains are shown in Fig. 11, and the corrosion conditions, weight gains, and the average thickness of oxide layers for these specimens used for the examination of the grain morphology of oxide are given in Table 1. The average thickness of an oxide layer is calculated according to its weight gain ($1\ \mu m = 15\ mg/dm^2$). The average thickness of oxide layers for these four specimens is comparable. The morphology of grains formed on the thicker oxide layer areas of the specimen corroded at 500°C after 1 h exposure is shown in Fig. 11(*a*). Some lumps protruded on the oxide surface to make it relatively rough, and grains less than 30 nm in diameter were revealed much more clearly by the pores and micro-cracks formed along grain boundaries. But a relatively smooth surface with the micro-cracks along the grain boundaries was revealed on thinner oxide layers as shown in Fig. 11(*b*). The morphology of grains formed on thicker or thinner oxide layers for the specimen corroded at 400°C after 90 days exposure is shown in Fig. 11(*c*), 11(*d*). Except for a little difference in grain size, pores and micro-cracks along grain boundaries were revealed in both cases. The different morphologies of grains formed on thicker or thinner oxide layers for the specimen corroded at 360°C in lithiated water after 90 days exposure are shown in Fig. 11(*e*), 11(*f*). It is interesting to note that grains with some orientation on the surface could grow up into a strange shape like whiskers, about 50 nm in diameter and up to several hundred nanometres in length. The mechanism of this phenomenon is not clear, but it must be related to the decrease in the free surface energy of zirconium oxide formed in lithiated water as compared to the discussion of the growth mechanism of metal whiskers of Sn in the middle of the last century [10]. The decrease of the free surface energy of zirconium oxide formed in lithiated water was discussed in a previous paper [8]. More whisker-like grains on the relatively thick oxide layers had grown up towards different directions from the surface in comparison with those on the thinner oxide layers. It seems that a certain crystal direction is parallel to the axis of whisker-like grains. This means that grain orientations of oxide in thicker oxide layers varied considerably compared with those in thinner oxide layers; therefore, this difference must be related to the orientations of the original metal grains. The microstructure and the orientation of oxide layers formed on the metal grains with different orientations must be different. In order to clarify this relationship, some more detailed investigations are needed. The same results were observed on the specimens corroded at 360°C in lithiated water for 200 days exposure, but the whisker-like grains were more on the thicker oxide layers than those for 90 days exposure. The different morphologies of grains formed on thicker or thinner oxide layers for the specimen corroded at 360°C in deionized water after 265 days exposure are shown in Fig. 11(*g*), 11(*h*). There were no whisker-like

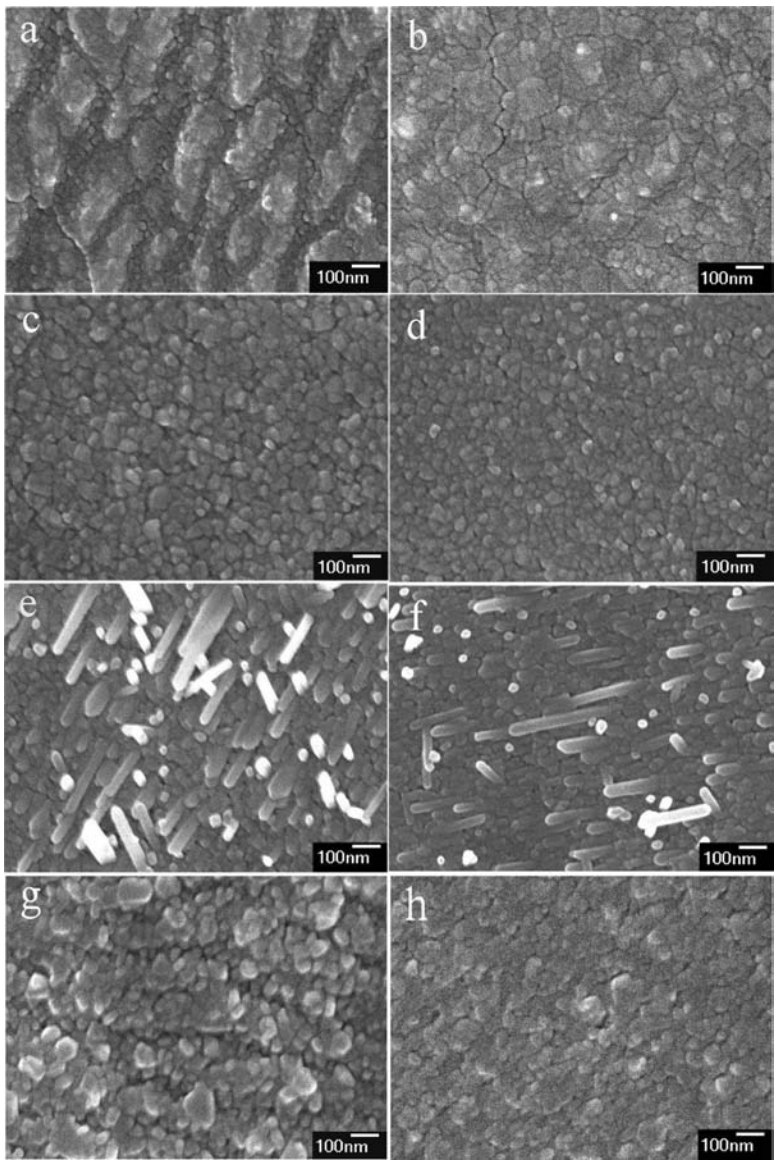


FIG. 11—*The morphology of oxide grains on the surface of the specimens corroded at [*(a) *and* (b)*] 500°C in steam for 1 h exposure, [*(c) *and* (d)*] 400°C in steam for 90 days exposure, [*(e) *and* (f)*] 360°C in lithiated water for 90 days exposure, and [*(g) *and* (h)*]* 360°C *in deionized water for 265 days exposure.* (a), (c), (e), *and* (g) *show the grain morphology on the thicker oxide layers, and* (b), (d), (f), *and* (h) *show the grain morphology on the thinner oxide layers.*

TABLE 1—*Specimens used for the examination of the grain morphology of oxide.*

	Exposure Time	Weight Gain (mg/dm^2)	Average Thickness of Oxide (μm)
500°C in superheated steam	1 h	94.5	6.3
400°C in superheated steam	90 days	81.6	5.4
360°C in lithiated water	90 days	61.5	4.1
360°C in deionized water	265 days	65.8	4.4

grains grown on the surface of oxide layers, but the pores and micro-cracks were obviously developed on thicker oxide layers than on thinner oxide layers.

The Relationship Between the Thickness of the Oxide Layer and the Surface Orientation of Metal Grains

Figure 12 shows the relationship between the oxide layer thickness and the surface orientation of metal grains obtained from the specimen corroded at 500°C in superheated steam for 3 h exposure. The weight gain of this specimen is 161 mg/dm^2 and the average thickness of the oxide layer is 10.7 μm. The poles of the surface orientation of 97 metal grains on which the oxide layer thickness was measured are plotted in an inverse pole figure as shown in Fig. 12(*a*). There is no texture in the specimen as the distribution of poles is random. The difference of oxide layer thickness is divided into three ranges: 3–6, 10–20, and 30–60 μm; then three lines of different thickness are used to link the poles having the same range of oxide layer thickness as shown in Fig. 12(*b*). The anisotropic growth of the oxide layer is prominent, and the thickness difference of the oxide layers on different grains of the $\alpha-$Zr matrix is more than 20 times. The oxide layers are the thickest on the surface orientation of metal grains distributed in the range from $(01\bar{1}0)$ to $(12\bar{1}0)$, and the maximum thickness reached 60 μm. A mean thickness of oxide layers from 10 to 20 μm is observed on the surface orientation of metal grains distributed in the range from 40 to

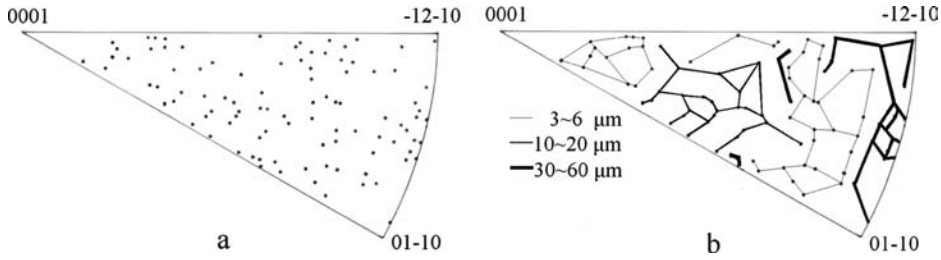


FIG. 12—(a) *Inverse pole figure showing the orientations of the metal grain surface on which the thickness of the oxide layer was measured. (*b*) The relationship between the oxide thickness and the grain surface orientations of the metal matrix for the specimens corroded at 500°C in superheated steam after 3 h exposure.*

60° away from (0001). On other surface orientations of metal grains, the thickness of oxide layers is only 3–6 μm.

Figure 13 shows the relationship between the oxide layer thickness and the surface orientation of metal grains obtained from the specimen corroded at 400°C in superheated steam for 280 days exposure. The weight gain of this specimen is 140 mg/dm^2 and the average thickness of the oxide layer is 9.3 μm. The poles of the surface orientation of 86 metal grains on which the oxide layer thickness was measured are plotted in an inverse pole figure as shown in Fig. 13(*a*). The oxide layer thickness is divided into two ranges: 5–8 and 9–12 μm; then two lines of different thickness are used to link the poles having the same range of oxide layer thickness as shown in Fig. 13(*b*). Two poles having an oxide layer thickness of 14–15 μm are incorporated in the range of 9–12 μm, and denoted with an underline in Fig. 13(*b*). In general, the thickness of oxide layers is somewhat different on different surface orientations of metal grains after the specimen is corroded at 400°C in superheated steam, but it is not as prominent as for the specimen corroded at 500°C in superheated steam. Some relatively thick oxide layers from 9 to 12 μm were observed on the surface orientation of metal grains distributed within 50° around the [0001] direction as shown in Fig. 13(*b*).

Figure 14 shows the relationship between the oxide layer thickness and the surface orientation of metal grains obtained from the specimen corroded at 360°C in lithiated water for 340 days exposure. The weight gain of this specimen is 210 mg/dm^2 and the average thickness of the oxide layer is 14 μm. The poles of the surface orientation of 92 metal grains on which the oxide layer thickness was measured are plotted in an inverse pole figure as shown in Fig. 14(*a*). The oxide layer thickness is divided into three ranges: 8–11, 12–20, and 25–65 μm; then three lines of different thickness are used to link the poles having the same range of oxide layer thickness as shown in Fig. 14(*b*). The thickest oxide layers were detected on the surface orientation of metal grains distributed in the range from 15 to 30° away from the (0001) plane, and the maximum thickness of the oxide layer reached 65 μm. The mean thickness of oxide layers, from 12 to 20 μm, was observed on the surface orientation of metal grains distributed

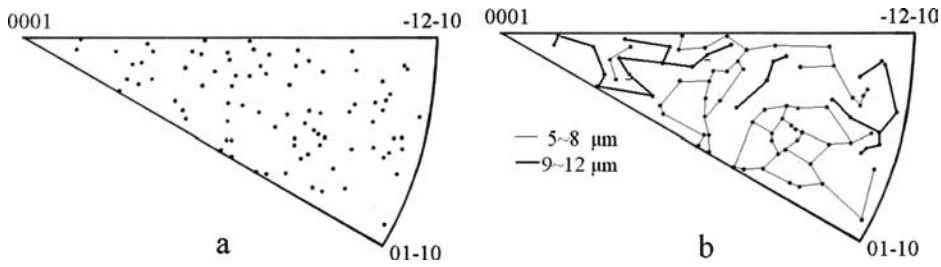


FIG. 13—(a) *Inverse pole figure showing the orientations of the metal grain surface on which the thickness of the oxide layer was measured.* (b) *The relationship between the oxide thickness and the grain surface orientations of the metal matrix for the specimens corroded at 400°C in superheated steam after 280 days exposure.*

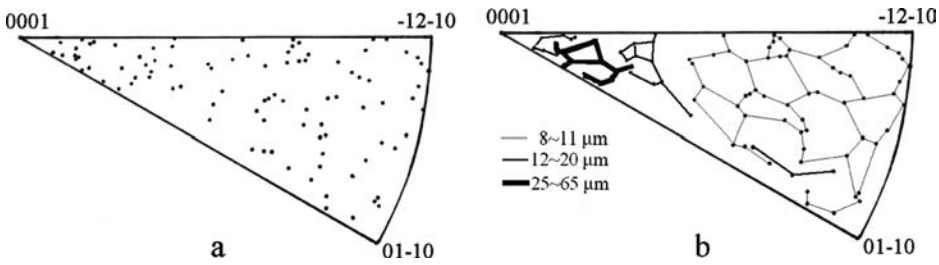


FIG. 14—(a) *Inverse pole figure showing the orientations of the metal grain surface on which the thickness of the oxide layer was measured.* (b) *The relationship between the oxide thickness and the grain orientations of the metal matrix for the specimens corroded at 360°C in lithiated water after 340 days exposure.*

about 15° around the area where the thickest oxide layer was detected. In other areas, the thickness of oxide layers was only 8–11 μm, except for three poles that had an oxide layer thickness of 15–20 μm.

Figure 15 shows the relationship between the oxide layer thickness and the surface orientation of metal grains obtained from the specimen corroded at 360°C in deionized water for 476 days exposure. The weight gain of this specimen is 134 mg/dm^2 and the average thickness of the oxide layer is 8.9 μm. The poles of the surface orientation of 119 metal grains on which the oxide layer thickness was measured are plotted in an inverse pole figure as shown in Fig. 15(*a*). The oxide layer thickness is divided into two ranges: 5.5–8.5 and 9–11 μm; then two lines of different thickness are used to link the poles having the same range of oxide layer thickness as shown in Fig. 15(*b*). Some relatively thick oxide layers, from 9 to 11 μm, were detected on the surface orientation of metal grains distributed within 45° around the [0001] direction. This relationship between the oxide layer thickness and the surface orientation of metal grains is different in comparison with that obtained from specimens corroded at 360°C in lithiated water, but it is similar to specimens corroded at 400°C in superheated steam.

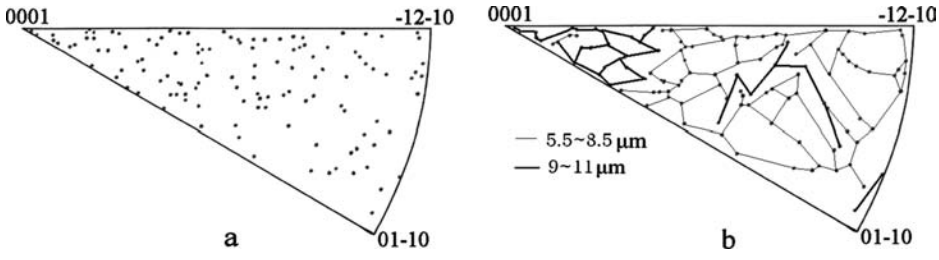


FIG. 15—(a) *Inverse pole figure showing the orientations of the metal grain surface on which the thickness of the oxide layer was measured.* (b) *The relationship between the oxide thickness and the grain orientations of the specimens corroded at 360°C in deionized water for 476 days exposure.*

The summary of weight gain, average thickness of the oxide layer, and the range of the oxide thickness distributed on different metal grains of four specimens used for analyzing the relationship between the oxide thickness and the grain orientation of the metal matrix is given in Table 2. The average thickness of the oxide layer for these four specimens is comparable, from 9 to 14 μm, but the range of the oxide thickness distributed on different metal grains is obviously different. The anisotropic growth of the oxide layer is more prominent for specimens corroded at 500°C in superheated steam and at 360°C in lithiated water than those corroded at 400°C in superheated steam and at 360°C in deionized water.

The Variation of the Relationship Between the Anisotropic Growth of the Oxide Layer and the Surface Orientation of Metal Grains

It is clear from Figs. 12–15 that the relationship between the anisotropic growth of the oxide layer and the surface orientation of metal grains varies with the corrosion temperature and water chemistry for long time exposure. This means that the thickness of oxide layers does not only depend on the surface orientation of metal grains. There must be another factor playing an important role in affecting the growth of the oxide layers at the later stage of the oxidation.

A new oxide layer is always formed on the oxide/metal interface. The microstructural evolution of the oxide certainly affects the diffusion of oxygen ions and anion vacancies, and, consequently, changes the conditions for continued oxide growth. Zhou et al. [8] investigated the effect of water chemistry and composition on the microstructural evolution of oxide on zirconium alloys, and pointed out that the defects consisting of vacancies and interstitials were produced during oxide growth due to the high compressive stress caused by a high PB ratio of 1.56. The characteristics of oxides with such a microstructure have an internal cause, and the temperature and the time are the external causes that induced the microstructural evolution through the diffusion, annihilation, and condensation of vacancies and interstitials under the action of stress, temperature, and time during the corrosion process. It was observed in the middle of the oxide layer that the vacancies absorbed by grain boundaries formed the pores to weaken the bonding strength between grains, and then the microcracks formed through the development of the pores. The corrosion temperatures, as well as the water chemistry, certainly affect the microstructural evolution and, consequently, the behavior of oxide growth. The results obtained by in situ investigation of epitaxial oxide layer growth using TEM also show that the defects were produced during oxide growth (Fig. 4).

Li^+ and OH^- incorporated in oxide films were adsorbed on the wall of pores or entered into vacancies [11–13] to reduce the free surface energy of zirconium oxide during exposure in lithiated water [8]. As a result, the diffusion of vacancies and the formation of pores were enhanced, including the acceleration of the microstructural evolution and the degradation of the corrosion resistance. In other words, the growth rate of oxide layers was accelerated. The relationship among the corrosion temperature and water chemistry, the surface orientation of metal grains, and the anisotropic growth of oxide layers is schematically shown in Fig. 16. The most important factor affecting the characteristic of oxide

TABLE 2—*Specimens used for analyzing the relationship between the oxide thickness and the grain orientations of the metal matrix.*

	Exposure Time	Weight Gain (mg/dm^2)	Average Thickness of Oxide (μm)	The Range of the Oxide Thickness Distributed on Different Metal Grains (μm)
500°C in superheated steam	3 h	161	10.7	3–60
400°C in superheated steam	280 days	140	9.3	5–12
360°C in lithiated water	260 days	210	14	8–65
360°C in deionized water	476 days	134	8.9	5.5–11

layer growth is the microstructural evolution of the oxide layers at the later stage of oxidation, which is put into a thicker frame in Fig. 16. In the early stage of the oxide layer growth, the diffusion of oxygen into the α−Zr matrix and the oxide crystal matched with the metal crystal orientation play an important role. Therefore, the epitaxial oxide layer grown on metal grains with different interference colours can outline the original grain structure of the α−Zr matrix (Fig. 1). But at a later stage of the oxidation, the oxide layer growth mostly depends on the microstructural evolution of the oxide layers. As a result, the variation of the relationship between the anisotropic growth of the oxide layer and the surface orientation of the metal grains with the corrosion temperature and water chemistry could be better understood. But the mechanism of this phenomenon is not clear so far. Further investigation is needed.

The Relationship Between the Corrosion Resistance and the Textures of the Specimens

The thickness of the oxide layers on the metal grains with different orientations is markedly different after the coarse-grained specimens were corroded for a long time exposure. The relationship between the anisotropic growth of the oxide layers and the surface orientation of the metal grains varies with the temperature and water chemistry of the corrosion tests. It is deduced that there must be a relationship between the corrosion resistance and the textures of the specimens, which could also vary with corrosion temperature and water chemistry.

A typical (0001) pole figure and inverse pole figures of normal direction (ND), rolling direction (RD), and transverse direction (TD) for a Zircaloy-4 sheet

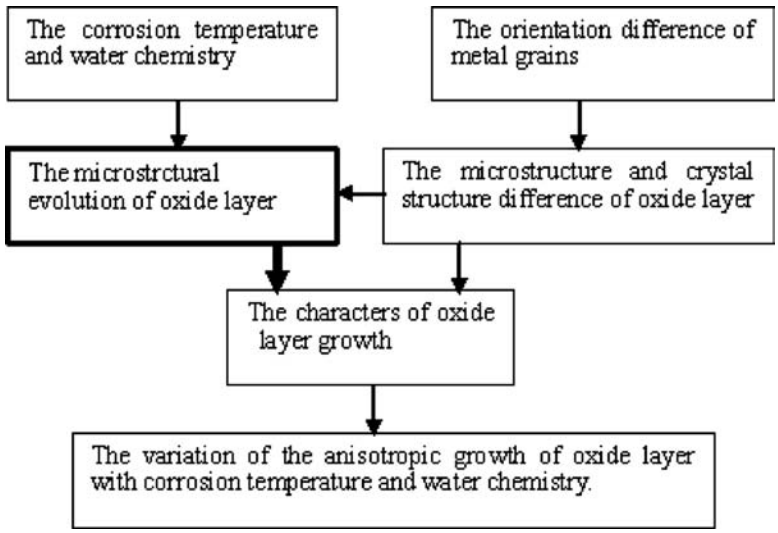


FIG. 16—*Schematic diagram showing the relationship among the corrosion temperature and water chemistry, crystal orientation of metal grains, and anisotropic growth of oxide layer.*

specimen after annealing at 600°C for 2 h are shown in Fig. 17. The textures of tubular specimens are very similar to those of sheet specimens. Such textures can be described as that the majority of the grains have their c-axis distributed within 20° around an axis tilted ±28° away from the ND of the sheet towards the TD. The textures become concentrated by grain growth after annealing at 820°C for 1 h as shown in Fig. 18. In this case, the majority of the grains have their c-axis distributed within 20° around an axis parallel to the ND of the sheet specimen, and the planes distributed in the range from $(01\bar{1})$ to $(\bar{1}2\bar{1}0)$ are parallel to the side planes around the sheet specimen as shown by RD and TD inverse pole figures in Fig. 18. Comparing the inverse pole figures of the textures (Figs. 17 and 18) to the inverse pole figures showing the relationship between the thickness of oxide layers and the metal grain orientations (Figs. 12 and 14), it is clear that the oxide layer on the normal plane of the sheet specimens corroded at 360°C in lithiated water becomes thicker than that on the side planes around the sheet specimens after a long time exposure. And the development of the nodular corrosion on the side planes of the specimens corroded at 500°C in superheated steam is easier than that on the normal plane of the specimens. This is a principle for the discussion on the relationship between the corrosion resistance and the textures of the specimens.

The weight gain versus exposure time for fine-grained and coarse-grained specimens corroded at 360°C in lithiated water is plotted together in Fig. 19. The data of fine-grained specimens are taken from Zhou et al. [8]. The weight gain for the fine-grained specimens shows a transition phenomenon after 100 days exposure, and the corrosion rate is accelerated markedly after the transition in comparison with the specimens corroded at 360°C in deionized water or at 400°C steam [8,14]. But this is not the case for coarse-grained specimens with no texture corroded in lithiated water at 360°C (Fig. 7). The reason for this is that the texture brings the crystal planes of the majority of the grains, on which the oxide layer grows faster after the transition, to be parallel to the normal plane of the specimens. Although the oxide layer on some grain surfaces is thicker than on others in coarse-grained specimens corroded in lithiated water, there is no transition phenomenon in the curve of weight gain versus exposure time since there is no texture.

The nodular corrosion resistance is improved by the increase of iron and chromium solid solution in the α−Zr matrix after increasing the annealing temperature in the alpha phase region [15] or irradiated in a reactor [16] to enhance the dissolution of small SPPs. Figure 20 shows the weight gain versus exposure time for Zircaloy-4 specimens corroded at 500°C in superheated steam after heat treatment at 600°C for 2 h or at 820°C for 1 h [9]. The nodular corrosion resistance is obviously improved by the increase of the annealing temperature in the alpha phase region, since the solid solution of iron and chromium alloying elements in the α−Zr matrix has been increased. The surface morphology of the specimens corroded at 500°C in superheated steam is also shown in Fig. 21 [9]. For the specimens annealed at 600°C, many nodules distribute on the surface of the specimen after 7 h exposure. For the specimens annealed at 820°C, there are no nodules on the normal plane but a very thick oxide layer developed from the nodules around the edges of the specimen after 90 h exposure. The nodules were completely eliminated on the normal plane of the specimens, but not on

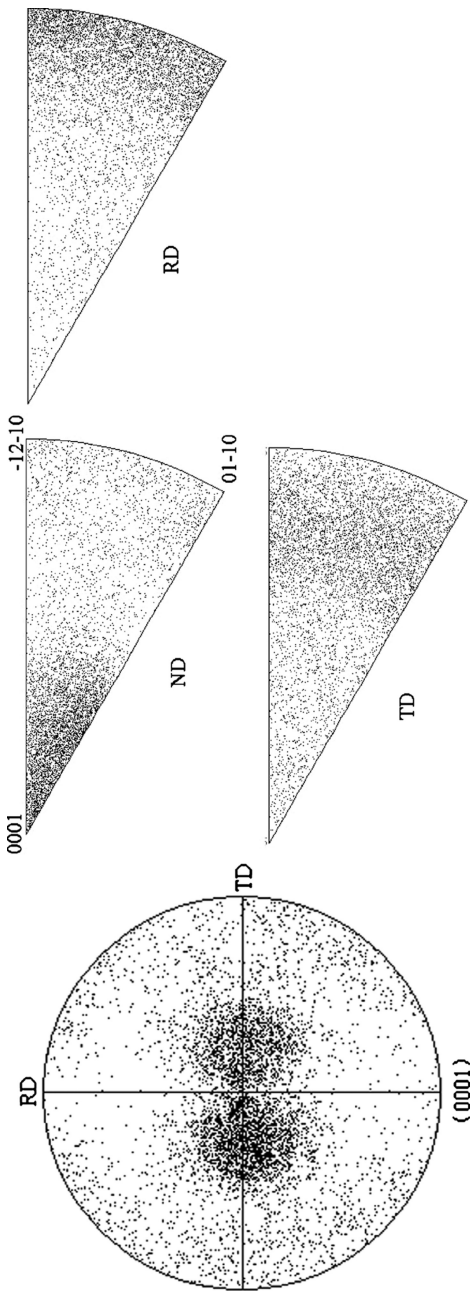


FIG. 17—*Recrystallization textures of the specimen annealed at 600°C for 2 h: (0001) pole figure; ND, RD, and TD inverse pole figures.*

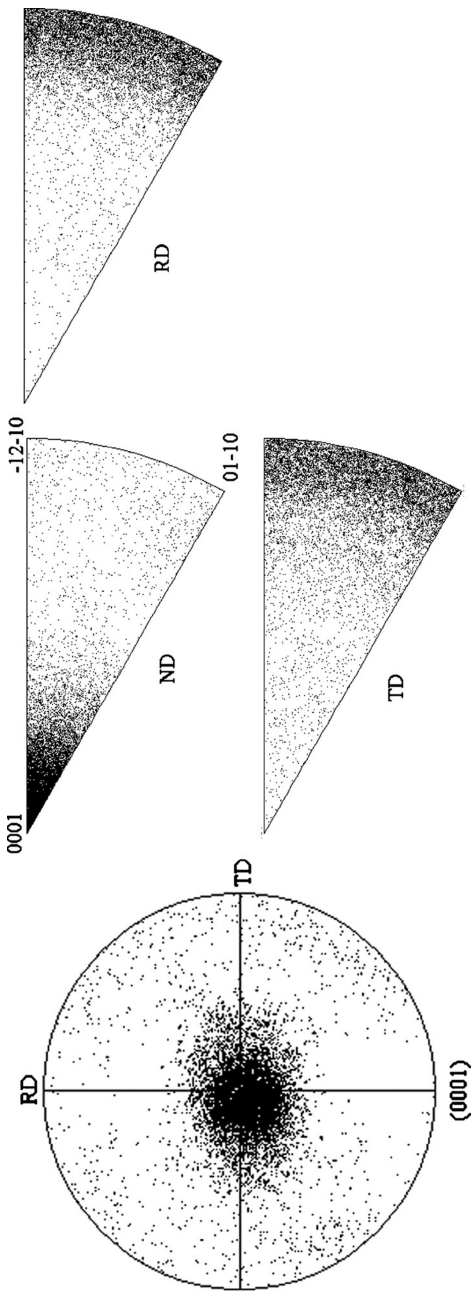


FIG. 18—*Recrystallization textures of the specimen annealed at 820°C for 1 h: (0001) pole figure; ND, RD, and TD inverse pole figures.*

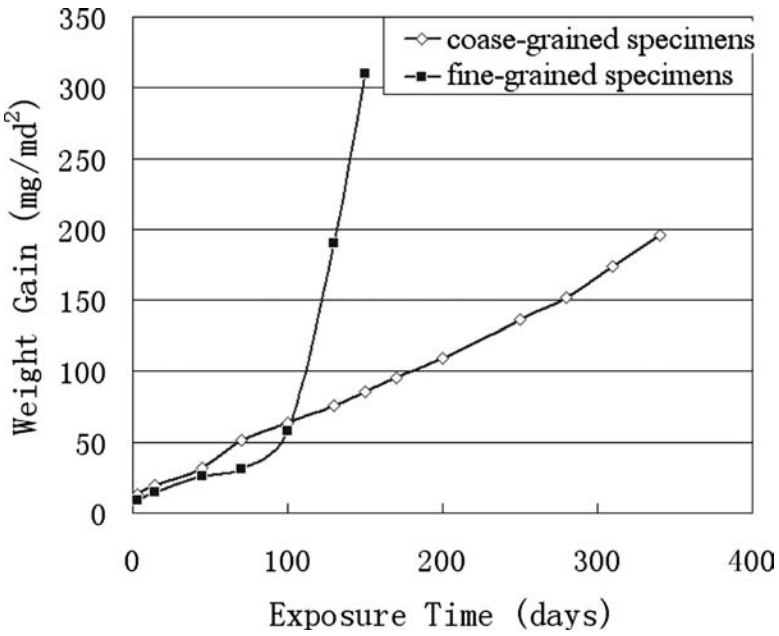


FIG. 19—*Weight gain versus exposure time for Zircaloy-4 fine-grained and coarse-grained specimens corroded at 360°C in lithiated water.*

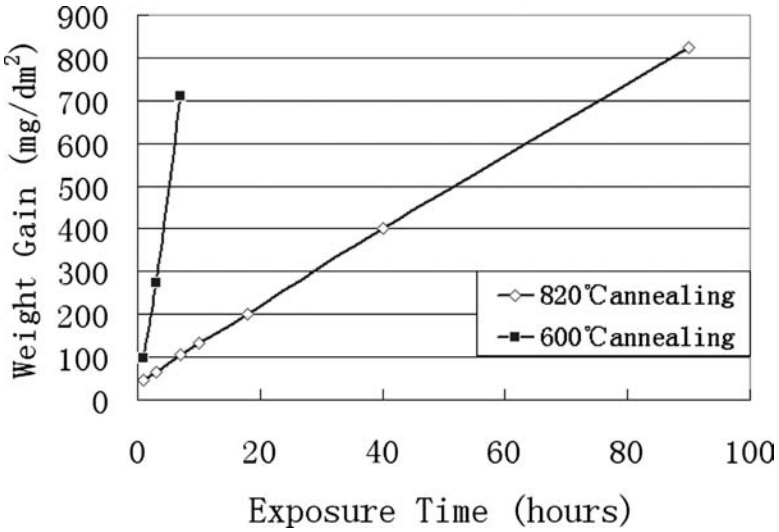


FIG. 20—*Weight gain versus exposure time during the corrosion tests at 500°C in superheated steam for Zircaloy-4 specimens annealed at 600°C for 2 h and at 820°C for 1 h.*

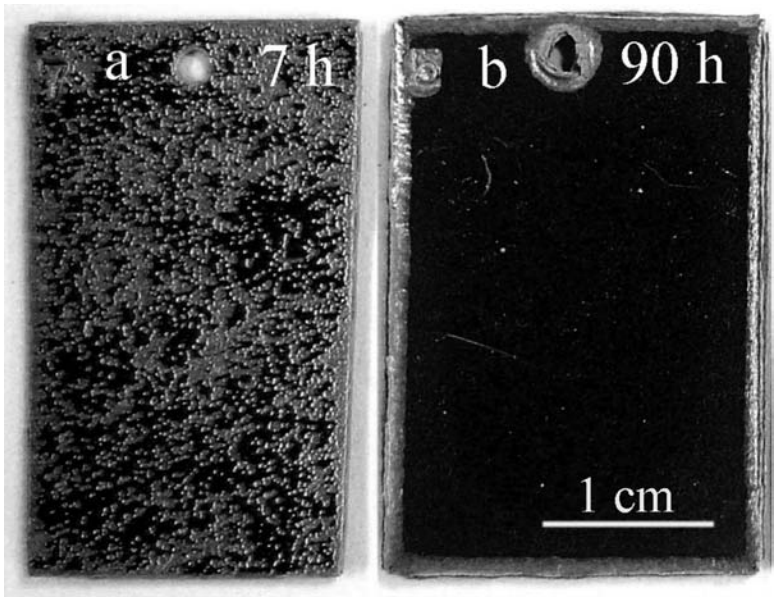


FIG. 21—*The morphology of Zircaloy-4 specimens corroded at 500°C in superheated steam: (*a*) Specimen annealed at 600°C for 2 h after 7 h exposure; (*b*) specimen annealed at 820°C for 1 h after 90 h exposure.*

the edges of the specimens. This phenomenon is attributed to the fact that the texture brings the different crystal planes on the different surface of the specimens. By comparing the texture of the specimens annealed at 820°C (Fig. 18) to the relationship between the oxide thickness and the grain surface orientations of the α−Zr matrix for the specimens corroded at 500°C (Fig. 12(*b*)), it can be seen that the normal plane of the specimens annealed at 820°C have a good resistance against nodular corrosion, but this is not the case for the side planes around the sheet specimens.

The corrosion behavior of irradiated Zircaloy was investigated by Cheng et al. [16]. The results showed that nodular corrosion as indicated by 520°C steam testing was completely eliminated after the tubular specimens had been irradiated in BWRs at a temperature near 288°C. But post-irradiation annealing at 650°C for 2 h caused a return of nodules to the specimen only on the edges, not on the tubular surface. This phenomenon is also attributed to the textures of the specimens because the textures of tubular specimens are very similar to that of sheet specimens.

Conclusions

The investigation of the relationship between the thickness of oxide layers and the grain orientations of the α−Zr matrix was performed using Zircaloy-4 coarse-grained specimens through corrosion tests at 500°C and at 400°C in superheated steam, and at 360°C in lithiated water and in deionized water for

long time exposure. In situ investigation of the epitaxial oxide layer formed on a thin specimen heated at 400°C in TEM was also carried out. The following conclusions have been obtained.

(1) Dot-like grains about 10 nm in size were formed on the surface of a relatively thin area around the hole of a thin specimen. The dot-like grains are monoclinic zirconium oxide ($m-ZrO_2$), and have an orientation relationship of $(001)_m//(0111)_{\alpha-Zr}$, $(111)_m//(1101)_{\alpha-Zr}$ with the $\alpha-Zr$ matrix. Long strip-like grains, probably a new kind of zirconium suboxide, were formed on the surface of a relatively thick area at a certain distance from the edge of the hole of a thin specimen. The strip-like grains have a bcc structure with a lattice parameter $a = 0.66$ nm, and have an orientation relationship of $(110)_{bcc}//(1010)_{\alpha-Zr}$, $[110]_{bcc}//[0001]_{\alpha-Zr}$ with the $\alpha-Zr$ matrix.

(2) The anisotropic growth of oxide layers was most prominent when the corrosion tests were carried out at 500°C in superheated steam in comparison with the corrosion tests at 400°C in superheated steam and at 360°C in deionized water. The thickest oxide layers were formed on those grains whose surface orientations were distributed around the planes from $(01\bar{1}0)$ to $(\bar{1}2\bar{1}0)$. The thicker oxide layers on those grains were further developed into nodular corrosion to form a lenticular shape observed on the sections as the exposure time lasted from 3 to 12 h.

(3) When the specimens were corroded in lithiated water at 360°C, the thickest oxide layers formed on those grains, whose surface orientations tilted from 15 to 30° away from the (0001) plane, but they were not in a lenticular shape.

(4) When the specimens were corroded in superheated steam at 400°C or in deionized water at 360°C, the difference of oxide layer thickness on different metal grain surfaces was less prominent. Some relatively thick oxide layers were observed on the surface orientation of metal grains distributed within 45° around the [0001] direction.

(5) The relationship between the anisotropic growth of oxide layers and the surface orientation of metal grains varies with the corrosion temperature and water chemistry for long time exposure, and it does not only depend on the surface orientation of the metal grains. In order to explain this phenomenon, it is suggested that the microstructural evolution of the oxide layers plays an important role in the growth of oxide layers at the later stage of oxidation.

(6) There is a relationship between the corrosion resistance and the textures of the specimens. This relationship varies with corrosion temperature and water chemistry, since the relationship between the anisotropic growth of oxide layers and the surface orientation of metal grains is also varied with corrosion temperature and water chemistry.

Acknowledgments

This project was financially supported by the National Nature Science Foundation of China (Grant Nos. 50871064 and 50971084), the National High Technology

Research and Development Program of China (Grant No. 2008AA031701), and the Shanghai Leading Academic Discipline Project (Grant No. S30107). The writers wish to acknowledge the Instrumental Analysis and Research Center of Shanghai University for help in the microstructural analysis.

References

[1] Pemsler, J. P., "Diffusion of Oxygen in Zirconium and Its Relation to Oxide and Corrosion," *J. Electrochem. Soc.*, Vol. 105, 1958, pp. 315–322.

[2] Bibb, A. E. and Fascia, J. R., "Aqueous Corrosion of Zr Single Crystals," *Trans. Metall. Soc. AIME*, Vol. 230, 1964, pp. 415–419.

[3] Wanklyn, J. N., "Corrosion of Zirconium Alloys," *ASTM Spec. Tech. Publ.*, Vol. 368, 1964, pp. 66.

[4] Wilson, J. C., "Anisotropy of Oxidation in Zr (Abstract of Paper Presented at the 15th Annual USAEC Corrosion Symposium)," ORNL-3970, 1966.

[5] Ploc, R. A., "Transmission Electron Microscopy of Thin (<200 nm) Thermally Formed ZrO_2 Films," *J. Nucl. Mater.*, Vol. 28, 1968, pp. 48–60.

[6] Cox, B., "Some Thoughts on the Mechanisms of In-Reactor Corrosion of Zirconium Alloys," *J. Nucl. Mater.*, Vol. 336, 2005, pp. 331–368.

[7] Kim, H. G., Kim, T. H., and Jeong, Y. H., "Oxidation Characteristics of Basal (0002) Plane and Prism (11–20) Plane in HCP Zr," *J. Nucl. Mater.*, Vol. 306, 2002, pp. 44–53.

[8] Zhou, B. X., Li, Q., Yao, M. Y., Liu, W. Q., and Chu, Y. L., "Effect of Water Chemistry and Composition on Microstructural Evolution of Oxide on Zr Alloys," *Zirconium in the Nuclear Industry: 15th International Symposium, ASTM-STP-1505*, Sunriver, OR, 2009, B. Kammenzind and M. Limback, Eds., ASTM International, West Conshohocken, PA, pp. 360–383.

[9] Zhou, B. X., Yao, M. Y., Li, Q., Xia, S., and Liu, W. Q., "Relationship Between Nodular Corrosion Resistance and Textures for Zircaloy-4 Strips," *J. Shanghai Univ.*, Vol. 14, 2008, pp. 441–445 (Natural Science Edition).

[10] Ge, T. S., "Metal Whiskers and the Theoretical Strength of Metals," *Crystal Defects and Metal Strength*, Vol. 2, Science Publishing House, Beijing, 1964, pp. 191–246, (in Chinese).

[11] Ramasubramanian, N., Precoanin, N., and Ling, V. C., "Lithium Uptake and the Accelerated Corrosion of Zirconium Alloys," *Zirconium in the Nuclear Industry: Eighth International Symposium, ASTM-STP-1023*, San Diego, CA, 1989, L. F. P. Van Swam and C. M. Eucken, Eds., ASTM International, West Conshohocken, PA, pp. 187–201.

[12] Pêcheur, D., Godlewski, J., Peybernes, J., Fayette, L., Noe, M., Frichet, A., and Kerrec, O., "Contribution to the Understanding of the Effect of the Water Chemistry on the Oxidation Kinetics of Zircaloy-4 Cladding," *Zirconium in the Nuclear Industry: 12th International Symposium, ASTM-STP-1354*, G. P. Sabol and G. D. Moan, Eds., Toronto, Canada, 2000, ASTM International, West Conshohocken, PA, pp. 793–811.

[13] Oskarsson, M., Ahlberg, E., and Pettersson, K., "Oxidation of Zircaloy-2 and Zircaloy-4 in Water and Lithiated Water at 360°C ," *J. Nucl. Mater.*, Vol. 295, 2001, pp. 97–108.

[14] Nikulina, A. V., Markelov, V. A., Peregud, M. M., Bibilashvili, Y. K., Kotrekhov, V. A., Lositsky, A. F., Kuzmenko, N. V., Shevnin, Y. P., Shamardin, V. K., Kobylyansky, G. P., and Novoselov, A. E., "Zirconium Alloy E635 as a Material for Fuel Rod

Cladding and Other Components of VVER and RBMK Cores," *Zirconium in the Nuclear Industry: 11th International Symposium, ASTM-STP-1295*, Garmisch-Partenkirchen, Germany, 1996, E. R. Bradley and G. P. Sable, Eds., ASTM International, West Conshohocken, PA, pp. 785–804.

[15] Zhou, B. X., Zhao, W. J., Miao, Z., Pan, S. F., Li, C., and Jiang, Y. R., "The Effect of Heat Treatments on the Corrosion Behavior of Zircaloy," *China Nuclear Science and Technology Report Nos.* CNIC-01074 and SINRE-0066, China Nuclear Information Centre Atomic Energy Press, Beijing, China, 1996.

[16] Cheng, B. C., Kruger, R. M., and Adamson, R. B., "Corrosion Behavior of Irradiated Zircaloy," *Zirconium in the Nuclear Industry: Tenth International Symposium, ASTM-STP-1245*, Baltimore, MD, 1994, A. M. Garde and E. R. Bradley, Eds., ASTM International, West Conshohocken, PA, pp. 400–418.

DISCUSSION

Question 1, P. Barberis, CEZUS:—1) During in-situ measurements, you find a cubic phase. Is it a sub-oxide (Zr_3O for example) or a zirconia phase (deformed tetragonal zirconia)? 2) Did you perform a chemical analysis (with EDX inside the TEM) of the "whiskers"? Is there no iron contamination?

Author's Response:—1) According to a video we acquired, the growing speed of this cubic phase is measured and roughly equal to 100 nm/min. According to the SAD pattern, a b.c.c. structure with lattice parameter of $a = 0.66$ nm is identified. This cubic phase might be an un-documented sub-oxide as we discussed in the text, but further investigation is needed to obtain more evidence.

2) Yes, we did a chemical analysis with EDX, and there is no obviously iron contamination on the whisker-like crystals. We have found some crystals caused by the contamination of iron on the surface of specimens after corrosion tests, but the morphology and the size of these crystals caused by iron contamination are quite different by comparing the whisker-like crystals. They are much bigger than that of whisker-like crystals. The morphology and an EDX analysis results for the crystals caused by the contamination of iron are shown in Fig.1 bellow.

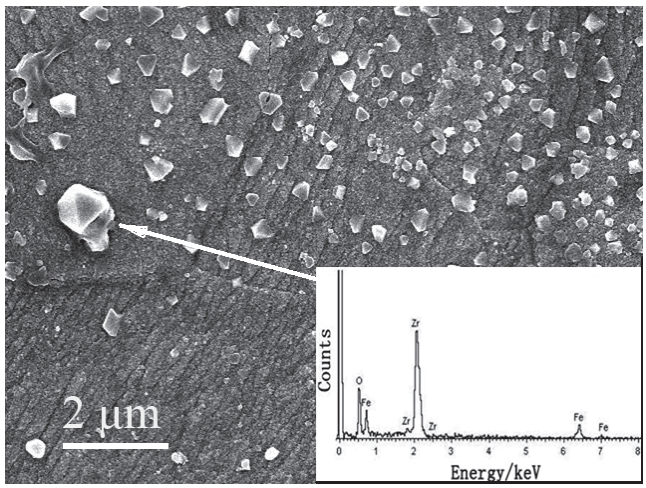


FIG. 1. The morphology of crystals caused by iron contamination on the surface of specimens corroded at 400°C in superheated steam after 280 days exposure.

Question 2, Philippe Bossis, CEA:—During in-situ TEM oxidation, was deformation of the metallic matrix observed?

Author's Response:—Yes, we have observed the deformation of the metallic matrix. When the oxide formed on the surface of the matrix, extinction contours drifting in a certain direction could be observed, and many dislocations could be also detected in the matrix between two cubic phases. Both of them were caused by the stress due to the formation of oxide on the surface of metallic matrix.

Question 3, Hans-Olof Andren, Chalmers Univ. of Tech.:—1) Can you really observe single vacancies with HRTEM? 2) How large were the SPPs in the very coarse grained materials?

Author's Response:—1) No, it is not possible to reveal a single vacancy with HRTEM at present moment. What we have observed is a cluster of vacancies including interstitial atoms, which looks like a cluster of amorphous in nano-scale.

2) The SPPs are quite large. They grew up to 0.5~0.8 μm in size, since specimens were annealed at 800°C for 10 hours to grow coarse grains. The information about SPPs has been added in the text.

Question 4, Anand Garde, Westinghouse Electric Company:—For commercial cladding materials, the extent of nodular corrosion in 500°C steam test strongly depend on the fabrication process history, typically represented by annealing parameter. Did you vary processing history to vary the extent of nodular corrosion in your test?

Author's Response:—No, we didn't vary processing history to vary the extent of nodular corrosion resistance (NCR) for coarse-grained Zircaloy-4 specimens in this research work, but we did that in the past for fine-grained Zircaloy-4 specimens. The results were described in reference [9] and [15], and a part of them is used to discuss the relationship between the NCR and the textures of the specimens in this paper.

Our opinion is that the main factor affecting the NCR for Zircaloy-4 materials is the level of solid solution contents of Fe and Cr alloying elements in α-Zr matrix, but not the size of SPPs. The NCR is improved obviously with the increase of solid solution contents of Fe and Cr alloying elements in α-Zr matrix. When Zircaloy-4 materials heated at a temperature between 600°C and 700°C after quenching from β phase during the fabrication processes, the NCR decreased as the increase of heating time. This phenomenon is attributed to the fact that the solid solution contents of Fe and Cr alloying elements in α-Zr matrix decreased due to the precipitation of SPPs, i.e., Fe and Cr alloying elements diffused out from solid solution in α-Zr matrix to form $Zr(Fe,Cr)_2$ SPPs. The size of SPPs increased and an accumulated annealing parameter *A* increased too during this heating process. Sometime people discussed NCR based on the factors of the size of SPPs and the accumulated annealing parameter *A,* and they thought that NCR decreased as the increase of SPPs size and of the accumulated annealing parameter. But this was not the case when Zircaloy-4 materials heated at a temperature between 800°C and 820°C in α phase region. According to Zr-rich corner of the system: Zr (1.4%Sn 0.1%O)-Fe, and Zr (1.4%Sn 0.1%O, 0.0036%Fe)-Cr given by Charquet et al (*Zirconium in the Nuclear Industry: Eighth Symposium, ASTM STP 1023, 1988, pp.405-422*), the solid solution contents of Fe and Cr in α-Zr matrix increase remarkably when Zircaloy-4 materials are heated at the temperature above 780°C. Some smaller SPPs dissolved into α-Zr matrix to increase the solid solution contents of Fe and Cr alloying elements and the larger SPPs further grew up during Zircaloy-4 materials heated at such temperature. In this case, NCR was improved considerably as shown in Fig. 20 and Fig. 21 of this paper, and the NCR was not degraded as the increase of SPPs size and of the accumulated annealing parameter. Therefore, the decisive factors affecting the NCR are solid solution contents of Fe and Cr alloying elements in α-Zr matrix, but not the size of SPPs and the level of accumulated annealing parameter.

Reprinted from JAI, Vol. 8, No. 9
doi:10.1520/JAI103246
Available online at www.astm.org/JAI

M. Preuss,[1] *P. Frankel,*[1] *S. Lozano-Perez,*[2] *D. Hudson,*[2]
E. Polatidis,[1] *N. Ni,*[2] *J. Wei,*[1] *C. English,*[1,2,3] *S. Storer,*[4]
K. B. Chong,[4] *M. Fitzpatrick,*[4] *P. Wang,*[1] *J. Smith,*[1]
C. Grovenor,[2] *G. Smith,*[2] *J. Sykes,*[2] *B. Cottis,*[1] *S. Lyon,*[1]
L. Hallstadius,[5] *R. J. Comstock,*[5] *A. Ambard,*[6] *and M. Blat-Yrieix*[6]

Studies Regarding Corrosion Mechanisms in Zirconium Alloys

ABSTRACT: Understanding the key corrosion mechanisms in a light water reactor primary water environment is critical to developing and exploiting improved zirconium alloy fuel cladding. In this paper, we report recent research highlights from a new collaborative research programme involving 3 U.K. universities and 5 partners from the nuclear industry. A major part of our strategy is to use the most advanced analytical tools to characterise the oxide and metal/oxide interface microstructure, residual stresses, as well as the transport properties of the oxide. These techniques include three-dimensional atom probe (3DAP), advanced transmission electron microscopy (TEM), synchrotron X-ray diffraction, Raman spectroscopy, and in situ electro-impedance spectroscopy. Synchrotron X-ray studies have enabled the characterisation of stresses, tetragonal phase fraction, and texture in the oxide as well as the stresses in the metal substrate. It was found that in the

Manuscript received July 9, 2010; accepted for publication July 11, 2011; published online August 2011.
[1] School of Materials, The Univ. of Manchester, Materials Performance Centre, Manchester, Lancashire M13 9PL, United Kingdom.
[2] Dept. of Materials, Univ. of Oxford, Oxford, OX1 3PH, United Kingdom.
[3] National Nuclear Laboratory, Sellafield, Seascale, Cumbria, CA20 1PG United Kingdom.
[4] Materials Engineering, The Open Univ., Milton Keynes, MK7 6AA United Kingdom.
[5] Westinghouse Electric, Vasteras/Pittsburgh, Sweden, USA.
[6] EDF, R&D, Moret sur Loing, 77818 France.

Cite as: Preuss, M., Frankel, P., Lozano-Perez, S., Hudson, D., Polatidis, E., Ni, N., Wei, J., English, C., Storer, S., Chong, K. B., Fitzpatrick, M., Wang, P., Smith, J., Grovenor, C., Smith, G., Sykes, J., Cottis, B., Lyon, S., Hallstadius, L., Comstock, R. J., Ambard, A. and Blat-Yrieix, M., "Studies Regarding Corrosion Mechanisms in Zirconium Alloys," *J. ASTM Intl.*, Vol. 8, No. 9. doi:10.1520/JAI103246.

Copyright © 2011 by ASTM International, 100 Barr Harbor Drive, PO Box C700, West Conshohocken, PA 19428-2959.

thick oxide (here, Optimized-ZIRLO, a trademark of the Westinghouse Electric Company, tested at 415C in steam) a significant stress profile can be observed, which cannot be explained by metal substrate creep alone but that local delamination of the oxide layers due to crack formation must also play an important role. It was also found that the oxide stresses in the monoclinic and tetragonal phases grown on Zircaloy-4 (autoclave testing at 360C) first relax during the pre-transition stage. Just before transition, the compressive stress in the monoclinic phase suddenly rises, which is interpreted as indirect evidence of significant tetragonal to monoclinic phase transformation taking place at this stage. TEM studies of pre- and post-transition oxides grown on ZIRLO, a trademark of the Westinghouse Electric Company, have used Fresnel contrast imaging to identify nano-sized pores along the columnar grain boundaries that form a network interconnected once the material goes through transition. The development of porosity during transition was further confirmed by in situ electrochemical impedance spectroscopy (EIS) studies. 3DAP analysis was used to identify a ZrO sub-oxide layer at the metal/oxide interface and to establish its three-dimensional morphology. It was possible to demonstrate that this sub-oxide structure develops with time and changes dramatically around transition. This observation was further confirmed by in situ EIS studies, which also suggest thinning of the sub-oxide/barrier layer around transition. Finally, 3DAP analysis was used to characterise segregation of alloying elements near the metal/oxide interface and to establish that the corroding metal near the interface (in this case ZIRLO) after 100 days at 360C displays a substantially different chemistry and microstructure compared to the base alloy with Fe segregating to the Zr/ZrO interface.

KEYWORDS: corrosion mechanisms, residual stress, sub-oxide, oxide porosity, corrosion kinetics transition

Introduction

Corrosion of zirconium alloys is an electrochemically driven process affected by the micromechanics, microstructure, and microchemistry in the metal, the oxide near the metal/oxide interface, as well as the water chemistry, irradiation, and time. Zirconium and its alloys are highly reactive and react at ambient temperatures with oxygen-containing environments (including deaerated water), becoming covered in an air-formed passive oxide film that is 2–4 nm thick. At higher temperatures this passive barrier oxide thickens, forming a crystalline oxide that is either cubic or tetragonal in structure [1]. Zirconium alloys initially display oxide growth rates that are more often closer to cubic than parabolic [2,3]. This is followed by a kinetic transition at which the corrosion kinetics first accelerate and then display a similar cubic/parabolic growth rate to that during the first stage. Such cyclic corrosion behaviour is repeated until enhanced, linear breakaway corrosion takes place [4]. To date, the mechanisms that lead to such oxidation kinetics are only poorly understood. Particular interest has been focused on understanding the key mechanisms operating during the transition

stage since delay in the onset of transition will improve the overall corrosion performance of a zirconium alloy. Since zirconium first forms a protective oxide layer, the point of transition is often associated with the formation of defects in the oxide structure near the metal/oxide interface [5–8]. Important from a micromechanical aspect are the large stresses that will build up in the oxide as it forms (Pilling–Bedworth ratio of about 1.56). Consequently, the preferential crystallite orientations during oxide growth are those that will minimise stress due to the volume change from zirconium to zirconium oxide, resulting in an oxide film formed of columnar ZrO_2 grains with preferred orientation [9]. It has beenreported previously that near the metal/oxide interface increased levels of tetragonal ZrO_2 are found [10–13] with some tetragonal ZrO_2 still being present further away [14]. It is noticeable that in some cases it is assumed that the tetragonal phase reaches levels as high as 40 % near the metal oxide interface, while other work shows far lower values. The stabilisation of this phase is due to a number of factors. For instance, tetragonal crystallites smaller than 25–30 nm can be stable over a broad pressure–temperature range [15,16]. In addition, significant compressive stresses in the oxide will also stabilise the tetragonal phase in the temperature range of interest here [17]. Some research has demonstrated that in order to stabilise tetragonal zirconia, stresses in the range of 2–4 GPa are necessary [18]. However, any of such studies were carried out on zirconia with a grain size in the range of many micrometers rather than nanometers. Consequently, it seems possible that the stresses to stabilise the tetragonal phase grown on zirconium during corrosion are significantly lower.

The effect of dopants has also been studied, and it has been suggested that Fe^{3+} [19] and Sn^{4+} [20,21] might stabilize the tetragonal phase while Nb^{5+} has the opposite effect [22]. By contrast, it has been suggested for zirconia ceramic that dopant levels are too low to explain the stabilisation of the tetragonal form, whereas they can play a major role in the destabilisation process [23].

It should be noted that there is still a high level of confusion about the existence of the tetragonal phase in the oxide grown on zirconium alloys, which is most likely related to the difficulties of measuring it. Since it is stress stabilised, creating a free surface might always destabilise some of the tetragonal ZrO_2, which is necessary for many analytical techniques. Therefore, transmission electron microscopy (TEM) analysis often either only identifies very small levels or fails to identify the tetragonal phase in the oxide near the metal/oxide interface [7,8]. It is also noticeable that any work using Raman spectroscopy tends to suggest significantly higher levels of tetragonal phase than data recorded by X-ray diffraction [7,13]. As the oxide is very strongly textured, conventional laboratory X-ray diffraction techniques often make it very difficult to undertake quantitative phase fraction analysis. It is also not clear if the standard equation of calculating the tetragonal phase fraction from Raman signals derived from stabilised zirconia [24] is still accurate when working with nano-sized and strongly textured zirconia.

It has been demonstrated that the large compressive stresses in the oxide can result in sufficiently high tensile stresses in the metal substrate for creep to occur [25]. It has also been predicted that such substrate creep deformation will result in a stress profile across the oxide layers [25,26]. With stresses falling

away in the oxide as the metal/oxide interface continues to move deeper into the substrate, a martensitic type phase transformation from tetragonal to monoclinic is expected to take place, which is associated with a 3%–5 % volume increase [27], inevitably generating microcracks in the oxide. However, it is currently not clear if the stresses in the oxide fall away quickly enough to result in the phase transformation taking place near the metal/oxide interface or only further away. It is clearly important to understand this, as in the first case this phase transformation could result in cracks providing a fast path through the rate-determining oxide layer at the metal/oxide interface, while in the latter case additional crack formation might be of less significance.

It has been shown that zirconium alloys with the best corrosion resistance tend to display the greatest continuity in the growth of columnar grains while poorer performing alloys exhibit imperfect development of columnar grains [9]. The repeated attempt to re-grow a columnar crystallite type oxide has been associated with the cyclic corrosion kinetics [4,14]. However, the effect of alloying elements or impurities on the effective growth of these columns has not been established and therefore we currently do not understand why certain alloys and environments enable more stable columnar growth, and hence slower corrosion kinetics, than others.

This demonstrates that despite considerable research efforts over 4 decades the precise mechanism of the process that causes the transition in oxidation kinetics remains unclear. From the point of developing future alloys to improve the possible burnup of fuel assemblies this is certainly very unsatisfactory, as alloy development remains driven empirically. In addition, only a more mechanistic understanding of the corrosion kinetics of zirconium alloys will enable predictions that are physically informed and hence provide sufficient confidence in taking fuel assemblies to increased burnup regimes.

The present paper brings together observation undertaken by a research consortium in the United Kingdom studying corrosion mechanisms in zirconium alloys. A particular aspect of this work is that it combines a range of the most advanced analytical tools to characterise the oxide and metal/oxide interface microstructures, residual stresses, as well as the transport properties of the oxide. In the first part of the paper, observations on thick oxides grown in steam at 415°C on ZIRLO[7] will be presented. The aim of this work was to characterise the residual stress and the tetragonal phase fraction profile from the metal/oxide interface toward the outer surface of the oxide and provide information on the oxide texture. This information was recorded by using high energy synchrotron X-ray diffraction. For the second part of the paper, samples were autoclave tested at 360°C in simulated primary water. In this case, samples were taken out from the autoclave before, during, and post-transition in order to describe the evolution of the metal/oxide interface and the oxide as the material goes through the transition of the corrosion kinetics. Detailed microstructure and stress characterisation of the oxide was carried out on these samples using a three-dimensional atom probe (3DAP), advanced TEM for the characterisation

[7] ZIRLO and Optimized-ZIRLO are trademarks of the Westinghouse Electric Company.

of the nanostructure, oxide porosity, and microchemistry variations, Raman spectroscopy, and synchrotron X-ray diffraction for stress and phase fraction analysis and impedance studies for studying oxide porosity. The two materials presented here were chosen purely from the point of view that they were available at the beginning of the project (ZIRLO tested at 415°C) or showed relatively early transition during autoclave testing at 360°C. As this is a report of work in progress, observations of a range of other alloys such as Optimized ZIRLO and a model zirconium alloy containing 1 % Nb will be compared with the results presented here in the near future. It should also be pointed out that the present work only focuses on autoclave performance and makes no attempt to compare with in-reactor performance.

Experimental Methods

Material and Autoclave Testing

The material characterised in the present study was provided by Westinghouse and had been thermomechanically processed using standard procedures. First, some initial investigations were carried out on recrystallised sheet Optimized ZIRLO samples that had been steam tested at 415°C for 600 days by Sandvik, Sweden, and had grown an oxide of up to 78 μm (Fig. 1). In the second phase,

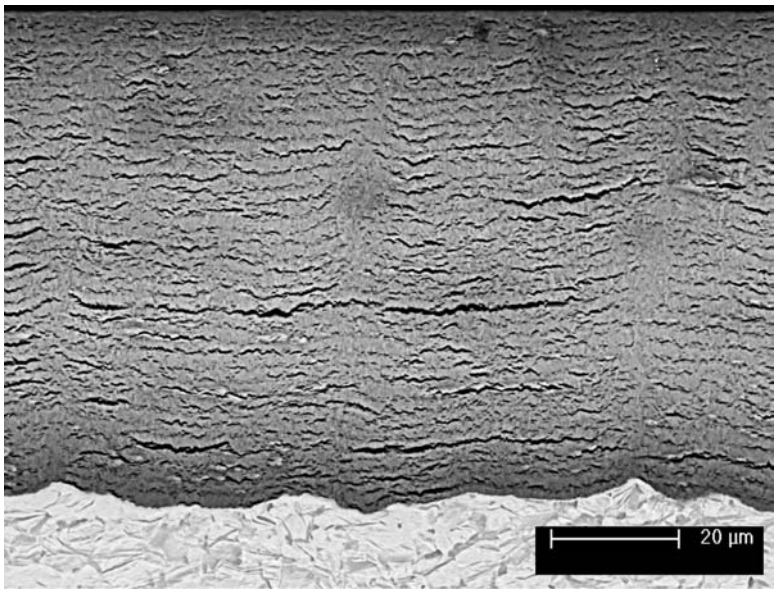


FIG. 1—*Cross-sectional scanning electron microscope images of the oxide (entire oxide thickness) and metal/oxide interface taken from the ZIRLO specimen revealing layers of oxide separated by bands of cracks parallel to the metal/oxide interface. Note, the metal appears bright grey and the oxide dark grey in the image.*

TABLE 1—*Measured chemical composition of alloys corrosion tested at 360°C in simulated primary water.*

Alloy	Zr	Fe, wt. %	Sn, wt. %	Nb, wt. %
Recrystallised ZIRLO sheet	Balance	0.1	0.9	0.9
Recrystallised ZIRLO tube	Balance	0.1	0.9	0.9
Recrystallised Zircaloy 4 sheet	Balance	0.2	1.2	…

material was received before corrosion testing and comprised sheet and tube material of a wide range of zirconium alloys. The work presented here focuses on recrystallised Zircaloy-4 (sheet) and recrystallised ZIRLO (sheet and tube), which was corrosion tested at EDF R&D, Moret sur Loing, France, at 360°C and 18 MPa in a static autoclave using simulated primary water chemistry (pure H_2O with additions of 2 ppm LiOH and 1000 ppm boric acid, deaeration). The chemical composition of each alloy was also determined by EDF and the concentrations of main alloying elements can be found in Table 1. The corrosion kinetics of these samples can be seen in Fig. 2. The main aim with this batch of samples was to study the early stage of corrosion, before, during, and after the first transition. By inserting sets of 4 samples of each alloy/condition into the autoclave about every 20 days over a period of 80 days, it was possible to obtain

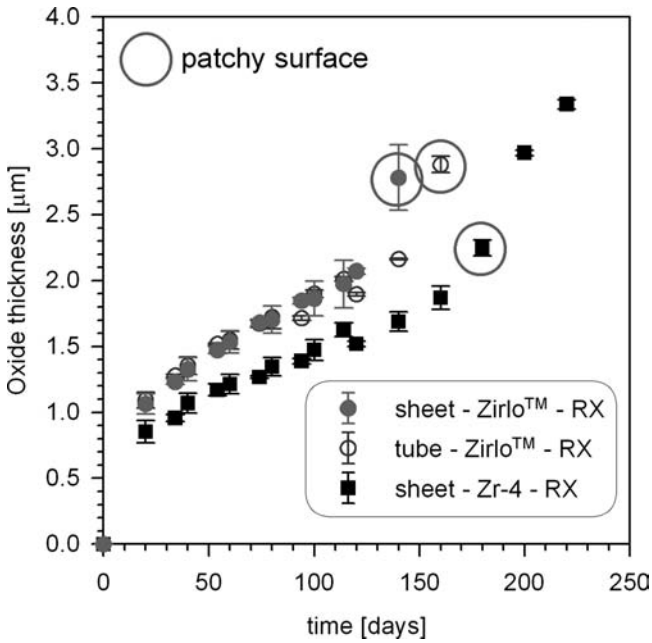


FIG. 2—*Corrosion kinetics of recrystallised Zircaloy-4 (sheet) and ZIRLO (sheet and tube) recorded during corrosion testing at 360°C in simulated primary water environment.*

data points with 20 days intervals while subsequently opening the autoclave only every 80 days to measure the weight gain. Once a set had gone through transition (according to the corrosion kinetics), all 5 sets of that particular alloy/condition were taken out of the autoclave, providing samples that describe the evolution of the oxide through the transition. Generally, samples that were in the process of going, or had just gone, through transition displayed a typical patchy oxide of lighter (region has already gone through transition) and darker regions (region has not gone through transition yet). For sheet Zircaloy-4, the first patchy samples were observed after 180 days, while sheet and tube ZIRLO displayed a patchy oxide after 140 and 160 days, respectively. In the case of tube ZIRLO, one sample that had been in the autoclave for 140 days (not through transition yet) was subsequently studied using in situ impedance measurements in a static autoclave under the same conditions as in the EDF research laboratory.

Electron Microscopy

Pores less than 10 nm in diameter can be effectively imaged in thin samples using Fresnel contrast [28], and this method is regarded as the only way to image voids smaller than 1/20 of the foil thickness when there is no associated strain field [29]. When the image is over-focused, black fringes appear around the periphery of a cavity and the cavity is white; when the image is under-focused, white fringes appear around the cavity and the cavity is black. The contrast originates from the difference in the inner potential of the matrix and the cavity, and depends on the thickness variations in the direction of the incident electron beam. Specimen surface craters can produce similar phase contrast [29], but this is minimised in the focused ion beam prepared TEM samples where an almost homogeneous thickness with very little surface roughness can be achieved. In this work, an FEI FIB 200 was used to prepare electron transparent samples with large areas of specimen with thickness below 100 nm, and Fresnel contrast imaging was undertaken in a Philips CM20.

3DAP

The 3DAP is a microscope that allows the creation of three-dimensional (3D) atom maps. These reconstructions can be interrogated to determine the nanoscale chemistry of the specimen material. The atom probe requires the fabrication of sharp, partially conductive needles so that the application of an electric potential generates a very high electric field at the needle apex. This potential is held just below that required, causing the ionization of atoms, and additional energy can be delivered in the form of a thermal pulse from a laser. As the field evaporation process is dependent upon temperature, this momentary increase in thermal energy raises the probability of an ionization event. The ions liberated from the sample are subsequently accelerated from the surface by the strong electric field toward a position-sensitive detector and identified by time-of-flight mass spectrometry. The standing voltage on the tip was varied

automatically in order to maintain an average evaporation rate of 5 ions for every 1000 laser pulses.

The instrument benefits from high spatial resolution, around 0.5 nm laterally and up to atomic resolution along the axis of the tip when analysing a metal matrix. The 3DAP also benefits from uniform chemical sensitivity across the whole mass-charge spectrum. An Imago Scientific Instruments LEAP 3000 X HR atom probe with a wide field of view was used in the current study [30].

One of the chief difficulties involved in such analysis is the preparation of very sharp needle like specimens with a metal–oxide interface at their very apex. A focussed ion beam (FIB) milling method in a Zeiss NVision dual beam FIB was used to prepare lift-out type specimens, which were then affixed to 2 μm silicon posts and milled to produce needles with end radii of the order of 100 nm. This process is described in more detail elsewhere [31,32]. At the final stage, a low energy ion beam was used to clean the surface of the specimen in order to minimise any surface contamination.

Synchrotron X-Ray Diffraction

The main purpose of the synchrotron X-ray diffraction experiments was to determine the residual stress profiles in the oxide and in the metal near the metal/oxide interface, the texture of the oxide, and the evolution of the tetragonal phase volume fraction from the metal/oxide interface toward the oxide surface. The two batches of samples required different approaches to undertake these measurements using synchrotron X-ray diffraction.

The samples tested for 600 days at 415°C in steam (thick oxide) were investigated on the materials science beam line ID11 at the European Synchrotron Radiation Facility (ESRF), Grenoble, France [33]. Samples produced for this experiment were strips 5 mm in width (x) and 1 mm high (thickness of the coupon—y) mounted in epoxy. The specimens were cut into 1 mm cross-sectional slices and subsequently ground and polished carefully to minimise the introduction of stresses from cutting. The experiment was carried out using a monochromatic focused beam with an energy of $\sim$40 keV, which allowed us to undertake measurements in transmission recording entire diffraction rings with an area detector. A spot size of $\sim 1.5 \times 4$ μm (in x and y directions) allowed spatially resolved mapping of the lattice spacing (here the $(1\bar{1}11)$ reflection of the monoclinic phase and the [101] reflection of the tetragonal phase were scanned) with position. By analysing horizontal or vertical sectors of the detector image it is possible to detect lattice spacing variations associated with the oxide growth direction and the direction parallel to the metal/oxide interface [34]. In order to convert these variations into strain it is necessary to determine strain-free lattice spacing [35]. Various methods were tried, including the measurements of oxide detached from the metal substrate. The most reliable result was achieved by using mechanically meaningful boundary conditions, i.e., the out-of-plane stress near the surface should be zero and that the two in-plane stresses should be equal. By measuring the out-of-plane and one in-plane strain it was then possible to identify strain-free lattice spacing for each sample. The elastic constants for converting strain to stress were calculated from single

crystal data of the monoclinic ZrO_2 phase by using an elastic self-consistent model and considering the texture that was determined during the experiment. More details on this analysis can be found in Ref [36]. For tetragonal ZrO_2, the same values were used, since measured elastic properties of chemically stabilised zirconia, such as in Ref [37], are not necessarily more accurate due to the chemical differences. It should be noted that these properties were determined for chemically stabilised tetragonal zirconia. By recording a number of diffraction rings, including relatively weak reflections of the tetragonal phase, it was also possible to determine the volume fraction of tetragonal phase as a function of position from the metal/oxide interface and relate it to the stress observations. In this case, the analysis was carried out using all diffraction rings undertaking a Rietveld analysis in the free available software package MAUD (Materials Analysis Using Diffraction), which then also took into consideration the texture effect.

The specimens tested at 360°C (thin oxide) were characterised on the EDDI beam line at BESSY, Berlin, Germany. EDDI is an energy dispersive beam line, which can be used for traditional $\sin^2\Psi$ stress analysis as, for instance, described in Ref [38]. In this case, the measurements are non-destructive, which has the advantage that samples can be put back into the autoclave after the measurement has been completed. An important requirement of a $\sin^2\Psi$ stress analysis is that the out-of-plane stress is zero, which is a reasonable assumption for relatively thin oxide layers. In order to obtain depth profiles, two different strategies can be chosen. First, when using a polychromatic beam, each individual diffraction peak from a spectrum achieves a different penetration depth; therefore, analysing a number of reflections can provide a profile from a single $\sin^2\Psi$ measurement procedure [39]. However, since each reflection has a different diffraction elastic constant, and some reflections might be strongly affected by so-called intergranular strains, it was found that such approach resulted in an unsatisfactory large data scatter for the present set of samples. The second approach was to measure the same reflection, but by changing the angle of the incident beam, changing the energy at which that reflection is measured and with it the penetration depth. This strategy reduced the scatter dramatically and provided a convoluted stress profile when using the $(1\bar{1}11)$ reflection of the monoclinic phase and the (101) reflection of the tetragonal phase. In addition, it was possible to analyse the $(101\bar{1}1)$ reflection of the zirconium substrate.

Raman Spectroscopy

The Raman measurements were carried out using an optical fibre probe energy dispersive Raman spectrometer operating at 400 nm and 150 mW. The relatively low intensity of the laser was chosen to avoid local heating occurring in the sample. The laser beam had a diameter of (0.8 ± 0.1) μm, and the penetration depth of the spectroscopy in this study was about 75 nm. The specimen was placed directly on a fully motorised stage of an optical microscope whose objective lens enables the laser beam to be focussed on a particular position. In this way it was possible to map areas in an automated manner. The spectral range extended from 200 to 850 cm^{-1}. A microcomputer control enabled averaged

Raman spectra to be obtained (over an acquisition time of 15 min), which were corrected for background noise based on a spectrum obtained without illumination. A statistical average of 50 spectra for each position from the metal/oxide interface was carried out in order to account for any material inhomogeneities. The residual stress was calculated by using [40,41]

$$\text{Raman} \quad \text{shift} = \Pi\sigma \tag{1}$$

where:

Π = piezo-spectroscopy constant, 1.69 cm^{-1}/GPa for zirconia, and
σ = stress, GPa.

The piezo-spectroscopy constant was obtained by undertaking an in situ uniaxial compression experiment on a standard monoclinic ZrO_2 sample. In the case of overlapping peaks, a deconvolution procedure was followed that is available in a commercial peak-fitting software package (GRAMS, Thermo Electron Corp, Philadelphia, PA), assuming mixed Gaussian and Lorentzian profiles. With a peak position accuracy of ± 0.05 cm^{-1}, the calculated stress uncertainty was ± 28 MPa. The tetragonal phase fraction (ZrO_2 %) was estimated by using [24]

$$ZrO_2\% = \frac{I(445_t)}{I(382_m) + I(445_t) + I(475_m)} \tag{2}$$

where:

I = intensity of a tetragonal peak at 445 cm^{-1} and the surrounding monoclinic peaks.

Even though it is common to use this equation in the context of oxide grown on zirconium alloys, it is not entirely clear if this equation is indeed valid for such cases. However, to date no alternative equation is available.

In Situ Electrochemical Impedance Spectroscopy

As mentioned earlier, a ZIRLO tube specimen that had been initially oxidised in an autoclave for 140 days at 360°C and 18 MPa was subsequently studied in situ in an autoclave under the same conditions by impedance spectroscopy.

The experiment was carried out inside a static autoclave with 1 L inner volume. The sample was welded to a zirconium wire and positioned close to a platinum plate counterelectrode. The reference electrode consisted of a high-temperature Pd/Pt reference electrode and simulated primary water as described earlier was used as the electrolyte. The electrolyte was deaerated with a gas mixture of 95 % N_2 and 5 % H_2 for 12 h prior to the experiment in order to reduce the oxygen content. "Mechanical" deaeration with nitrogen, inert gas sparging, or application of a vacuum will struggle to achieve dissolved oxygen concentrations below around 50–100 ppb. In order to obtain PWR (pressure water reactor) conditions of 1–2ppb O_2, chemical deaeration is required and this achieved by use of an excess of hydrogen. Note that the hydrogen level is chosen to approximate in-reactorconditions. The electrochemical impedance

measurements were obtained at the open circuit potential of the electrode and thus insofar as hydrogen affects the redox potential, this is accounted for during measurements. All electrochemical impedance spectroscopy (EIS) measurements were carried out using a Newton 4th Phase Sensitive Multimeter PSM1735. The frequency range used during the EIS measurements was between 100 kHz and 0.01 Hz and the amplitude of the ac perturbation was 100 mV (rms). The validity of the impedance spectra was ensured by checking the linearity condition, i.e., measuring the impedance spectra at signal amplitude between 10 and 100 mV (rms), and by checking the causality using a Kramers–-Kronigtransform test included in the ZView software used for undertaking the data analysis. Performing the same measurements on an additional sample ensured the reproducibility of the impedance spectra.

The recrystallised ZIRLO tube sample was tested in situ in the autoclave for 25 days, which took it to a total exposure of 165 days, and hence through transition (Fig. 2). The impedance spectra were recorded every 24 h for the duration of the experiment, and the resulting data were analysed with ZView (Scribner Associates). In order to interpret the impedance spectra, a physical model presenting the actual oxide has to be chosen, which considers the properties of the metal/oxide and oxide/electrolyte interfaces. This is achieved by representing the relative interfaces by different circuit elements to create an equivalent circuit for the measured system. As the model is based on our microscopy observations on similar samples it is described in the following section. In comparison to earlier measurements of this type [42], the present results are expected to benefit from measurements in a very high frequency range that should provide improvements when estimating the capacitance. The present study also consists of a two layer rather than a three layer structure. The present model also distinguishes itself by assuming that the inner layer stays dense and therefore a pure capacitance can describe its response.

Results

Long Term Steam Tested Specimens (415°C)

The residual stress profiles of the monoclinic oxide phase grown on Optimized-ZIRLO for the in-plane direction (parallel to the metal/oxide interface) and out-of-plane direction are plotted in Fig. 3. It can be noted that the in-plane compressive stress near the metal/oxide interface reaches about 1200 MPa, which are typical stress levels also reported by other researchers [43,44]. Near the interface the oxide displays a very steep stress gradient, which becomes shallower about 10 μm away from the interface (indicated by dashed line labelled with A). The diffraction data of the tetragonal phase were of insufficient quality to determine strains and calculate stresses. Figure 3 also includes the predicted stress profile if one considers creep elongation of the metal substrate according to the rates determined in Ref [25] for recrystallised Zircaloy-4 tested at 415°C in air. The calculation of the stress profile is based on the assumption that the oxide displays a biaxial stress field. The result of this rather simple model is a linear stress profile of the oxide as a function of distance from the metal/oxide

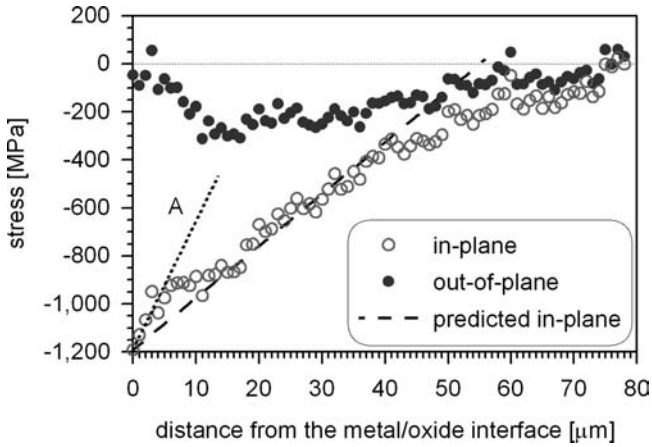


FIG. 3—*In-plane residual stresses as a function of distance from the metal/oxide interface for Optimized-ZIRLO tested for 600 days at 415°C. Measured by synchrotron X-ray diffraction at ID11, ESRF.*

interface. The comparison of the predicted and measured stress profiles will be discussed later.

Since for tetragonal phase fraction analysis the complete diffraction rings were used (in contrast to strain analysis where only certain directions of the diffraction rings are used), it was possible to analyse the volume fraction as a function of position from the metal/oxide interface. The analysis revealed that Optimized-ZIRLO displayed about 5 vol. % tetragonal phase near the metal/oxide interface, Fig. 4(*a*). As one moves away from the interface, the tetragonal volume fraction drops very rapidly and reaches about 2 vol. % at about 30 μm from the interface. Further away from the metal/oxide interface only a slight additional decrease of the tetragonal phase volume fraction is observed. In order to understand the role of oxide stress on the stabilisation of the metastable tetragonal phase, Fig. 4(*b*) plots the tetragonal phase fraction versus the in-plane stresses of the monoclinic phase (ideally one would plot it against the stresses in the tetragonal phase). As one would expect, there seems to be a strong correlation between stress and tetragonal phase fraction. Figure 4(*b*) also shows that the tetragonal phase fraction continues to decrease, as the oxide reaches 0 MPa in-plane stress in the monoclinic phase. However, at zero stress, some tetragonal phase was still detected, suggesting that some of the tetragonal phase is stabilised by the nano-grain size. These observations are in principle in good agreement with previously published work stating a phase fraction gradient in the oxide.

Finally, the ESRF synchrotron data were also used for texture analysis of the oxide, which revealed a strong (about 80 mrd—multiple of a random distribution) near-(002) fibre texture perpendicular to the metal/oxide interface (Fig. 5), which indicates that the main epitaxial growth direction of the oxide is most likely $(10\bar{4}\bar{1})$ or $(10\bar{6}\bar{1})$ as reported and predicted in Ref [45]. No significant

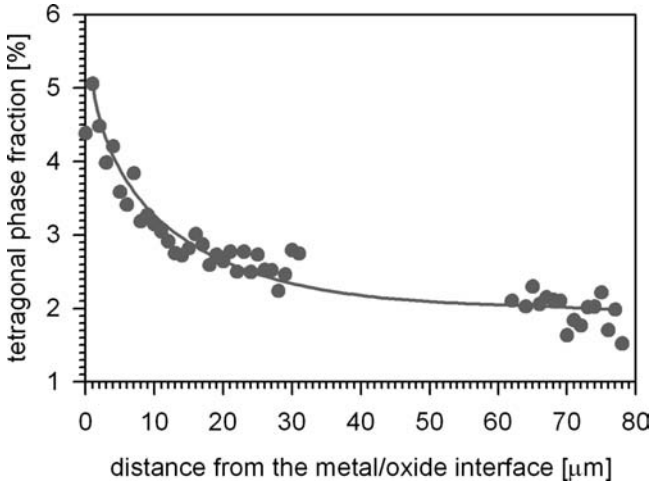


FIG. 4—*Volume fraction of tetragonal phase as a function of distance from the metal/oxide interface (a) and as a function of stress state (b) for Optimized-ZIRLO tested in steam at 415°C. Measured by synchrotron X-ray diffraction at ID11, ESRF.*

texture variation was found when comparing oxide grown during the early and late stage of the 415°C steam experiment.

Short Term Autoclave Tested Specimens (360°C)

The corrosion kinetics of the autoclave-tested material are presented in Fig. 2. The data suggest that recrystallised ZIRLO exhibits slightly faster corrosion kinetics in the pre-transition phase compared to Zircaloy-4. The pre-transition corrosion kinetics of all three samples displayed an exponent n of about 0.35–0.4 when applying the exponential growth function. The data also suggest that sheet ZIRLO goes first through transition (between 120 and 140 days) followed by tube ZIRLO (between 140 and 160 days) and sheet Zircaloy-4 (between 160 and 180 days). All samples were also inspected for the patchy surface appearance that indicates the beginning of the first transition. Samples that displayed such patchy oxide surface are highlighted with a circle in Fig. 2.

Residual Stress Analysis

As described earlier, the main interest of the short term autoclave-tested samples was to study in detail the moment when the oxide goes from a pre-transition to a post-transition state. Figure 6 displays the evolution of the in-plane through thickness stresses (here, direction of the original transverse rolling direction of the sheet) measured for the monoclinic and tetragonal oxide phases grown on recrystallised Zircaloy-4 as well as the in-plane stresses in the metal near the metal/oxide interface. In addition, the corrosion kinetics of Zircaloy-4 are displayed again in order to relate the stress evolution to the change of corrosion kinetics. The first measurement was recorded after 34 days

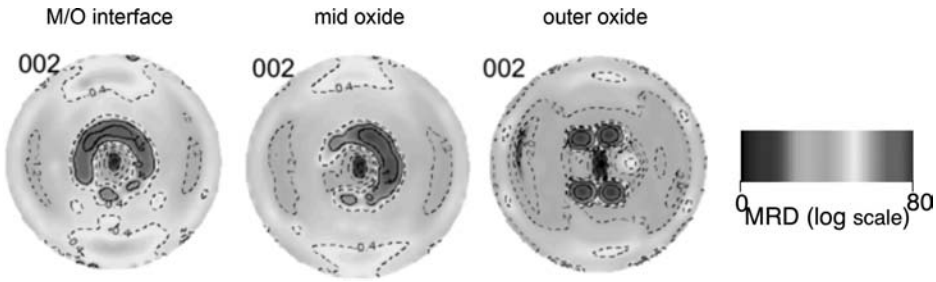


FIG. 5—*(002) pole figure of the monoclinic oxide phase grown on Optimized-ZIRLO during steam testing at 415°C. Measurements were recorded close to the metal/oxide interface, at mid-oxide thickness and near the oxide outer surface. Measured by synchrotron X-ray diffraction at ID11, ESRF.*

exposure and revealed compressive stresses of about 2.5 GPa in the tetragonal phase and about 1.3 GPa in the monoclinic phase. A very slight balancing tensile stress in the metal substrate of about 20 MPa was detected at this stage. Since the phase fraction of tetragonal oxide was unknown for these measurements it was difficult to check the stress balance, but assuming a reasonably low volume fraction of 5–20 vol. % tetragonal oxide phase, stresses in the metal should not exceed 10 MPa if one assumes that the stress field in the metal is constant. However, this might not be the case. As corrosion proceeded, the most pronounced change was detected in the tetragonal phase, reaching about 1.5 GPa compressive stress just before transition. The monoclinic phase also showed stress relaxation, although somewhat less significant. However, after 160 days exposure, i.e., the last data point before transition according to corrosion data and sample appearance, a sudden increase of compressive stress in the monoclinic phase was observed. Figure 6 suggests that the tensile stresses in the metal substrate first increased slightly toward transition but then dropped just before transition. It is possible that such an increase is related to the growth of the oxide thickness, requiring larger balancing tensile stresses in the metal substrate even though the stresses in the oxide relax. Around transition, both monoclinic and tetragonal phases seem to assume large compressive stresses again, which start relaxing again as corrosion proceeds further.

Microstructure and Chemical Analysis

A detailed microstructural characterisation of pre- and post-transition oxide was carried out on recrystallised ZIRLO and Zircaloy-4 sheet material using Raman spectroscopy and on recrystallised ZIRLO sheet material using TEM and 3DAP analysis.

First, Raman spectroscopy analysis was undertaken to record the evolution of the tetragonal phase fraction on the outer oxide surface as the material approaches transition, see Fig. 7. It should be remembered that a surface oxide was already formed before the material was inserted into the autoclave. This very early oxide seems to have high levels of tetragonal phase. Figure 7 suggests

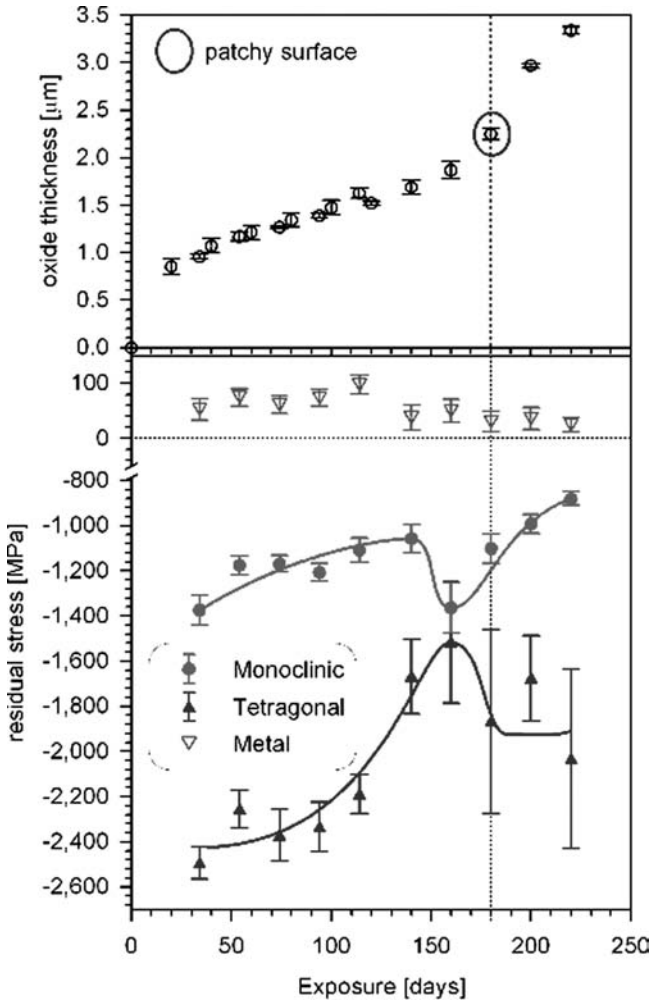


FIG. 6—*Evolution of through thickness in-plane oxide stresses as a function of exposure time in an autoclave at 360°C for recrystallised Zircaloy-4. Measured by synchrotron X-ray diffraction at EDDI, BESSY II.*

that the tetragonal phase fraction at the outer surface is about 15 % after 54 days for ZIRLO and 17.5 % after 80 days for Zircaloy-4. In both cases, the tetragonal phase fraction at the surface decreases as transition is approached. However, it seems that this change in tetragonal phase volume fraction is slower in Zircaloy-4 than ZIRLO.

In order to understand the ion and electron transport mechanisms through the oxide, particularly around transition, TEM analysis mainly concentrated on studying nano-sized porosity in the oxide near the metal/oxide interface. A particular focus was placed on identifying any interconnected porosity that might

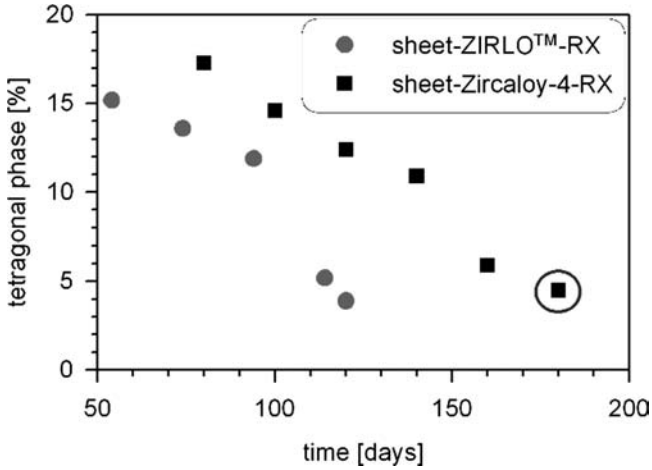


FIG. 7—*Tetragonal phase fraction measured from the top oxide surface grown on ZIRLO and Zircaloy-4 sheet material in the recrystallised condition as a function of time. Circles indicate the time when samples showed patchy surface. Measured by Raman spectroscopy.*

provide a fast diffusion path for oxidising species to the metal/oxide interface. It should be mentioned first that any observations and conclusions presented here are based on a large number of images and not only on the small number of images presented here. TEM analysis was carried out on recrystallised sheet ZIRLO samples exposed for 34, 100, 114 days (all pre-transition) and 140 days (post-transition). Data presented here focus on samples exposed for 100 and 140 days. Regardless of oxidation time, all samples studied by TEM revealed an innermost oxide layer that is almost perfectly dense apart from isolated nano-pores or discontinuous pores decorating the columnar grain boundaries running normal to the metal/oxide interface. In this "dense" part, connected porosity was only seen aligned in the direction parallel to the metal/oxide interface, forming flake like pores at the top of the columnar oxide. These features were previously observed in a pre-transition Zr-4 oxide [6]. At some distance away from the interface, the nano-pores start to be connected along the oxide growth direction, and the overall porosity increases. An overview TEM image of a pre-transition oxide sample exposed for 100 days can be seen in Fig. 8(*a*) and high magnification images at about 500 and 700 nm from the metal/oxide interface in Fig. 8(*b*), 8(*c*). First, vertical interconnected porosity was detected at ~500 nm away from the interface, while at 700 nm for the metal/oxide interface the porosity had increased slightly. The 140 day post-transition oxide (sample with patchy surface—TEM samples extracted from white, thicker oxide) is presented in Fig. 9(*a*) displaying substantially more cracks than the pre-transition oxide. The vertical interconnected pores closest to the metal/oxide interface were first found at 300–400 nm away from the interface—Fig. 9(*b*). This type of porosity becomes well developed at around 700 nm and further away from the metal/oxideinterface. The long chains of porosity along the columnar grain boundaries

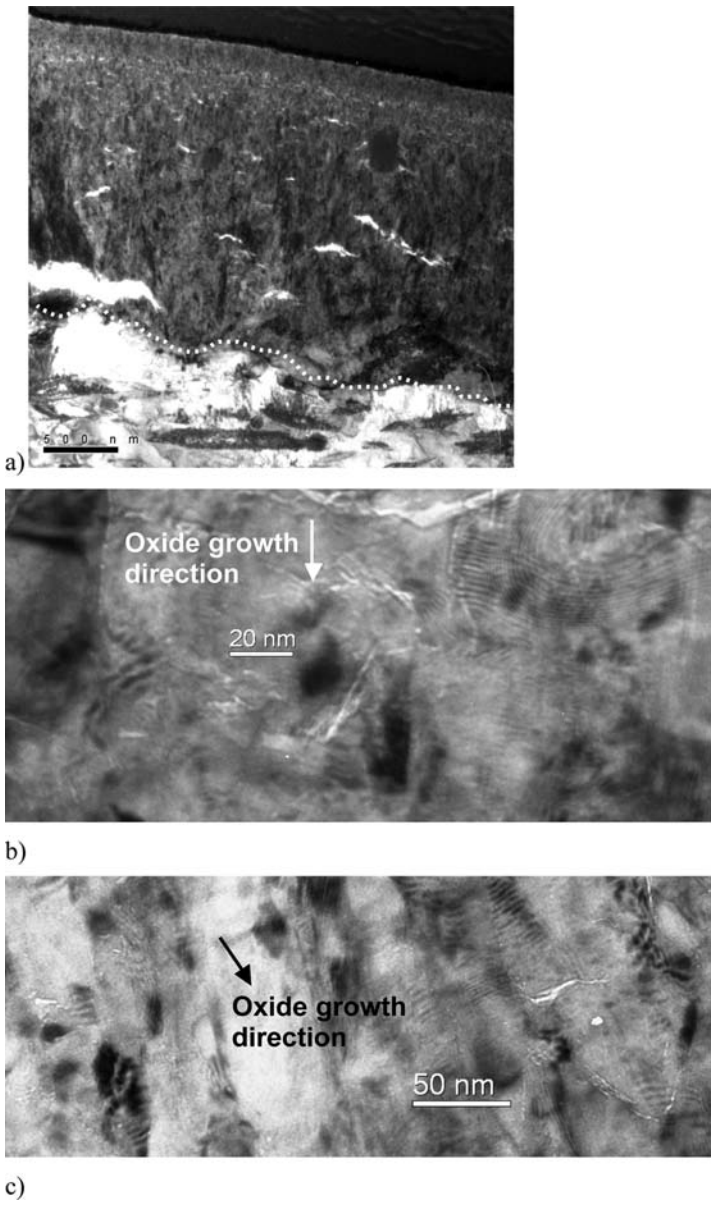


FIG. 8—*Typical TEM images of the oxide extracted from a ZIRLO sheet sample, recrystallised condition, after 100 days. Images provide (a) an overview of the whole 2 μm thick oxide layer, (b) nano-pores linked perpendicular to the metal/oxide interface at around 500 nm from the interface and (c) at 700 nm from the interface.*

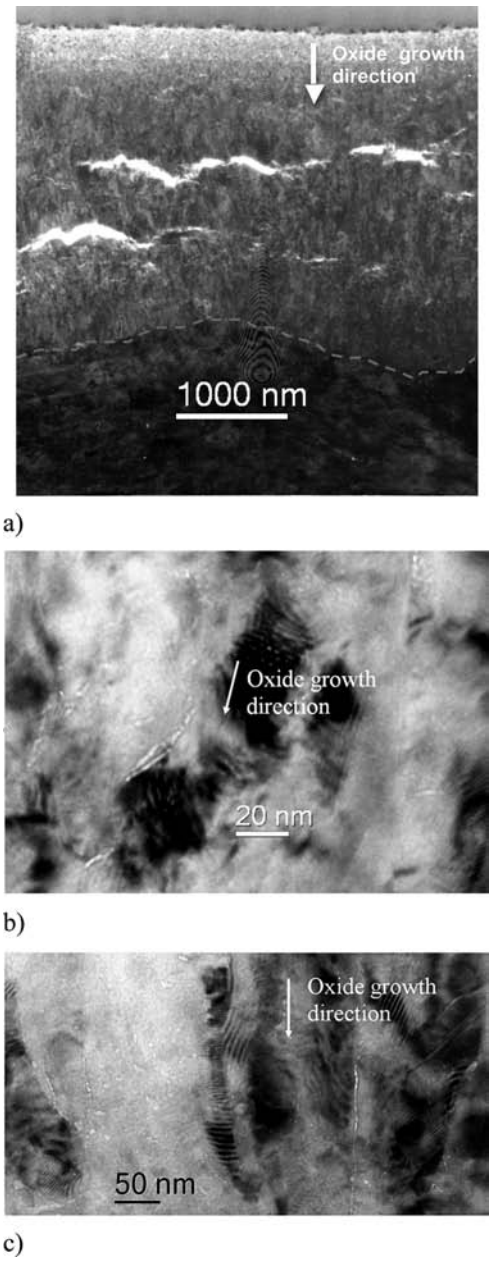


FIG. 9—*Typical TEM images of the oxide extracted from a ZIRLO sheet sample, recrystallised condition, after 140 days. The TEM foil was taken from a grey oxide area, i.e., this region had gone through transition. Images provide(a) an overview of the 2.7–3.1 μm thick oxide layer, (b) nano-pores linked perpendicular to the metal/oxide interface at around 350 nm from the interface and (c) at 700 nm from the interface.*

shown in Fig. 9(*c*) are generally absent in the entire columnar oxide region of the pre-transition oxide. In contrast, the pre-transition oxide only displayed such well-developed porosity at the tip of the columnar oxide region, which was at least 1.5 μm away from the metal/oxide interface. Figures 9(*a*) also show the more obvious cracks already mentioned earlier. TEM studies in the vicinity of early cracks did not reveal any predominance of cracks in such locations. Finally, both oxides displayed an outer layer of several hundred nanometres, which consists of nano-sized equiaxed grains and a high level of porosity as reported previously by Refs [8 and 46]. Since Raman spectroscopy indicated high levels of tetragonal phase during the early stage of corrosion at the outer surface, it seems reasonable to assume that these equiaxed grains were originally of tetragonal phase. The high porosity of the outer region could be explained by the tetragonal to monoclinic phase transformation taking place near the outer surface, as shown in Fig. 7, as the metal oxide interface moves inwards.

In summary, although the first connected porosity perpendicular to the metal/oxide interface seems to be seen at similar distance from the interface for pre- and post-transition oxides, the distance from the metal/oxide interface at which substantial porosity along columnar grains is found is significantly smaller in the early post-transition oxide than in the pre-transition oxide that is still 40 days away from transition, providing an easy path for the penetration of oxidising species.

Similar to the TEM analysis, 3DAP analysis was carried out on recrystallised sheet ZIRLO samples exposed for 34, 100, 114 days (all pre-transition) and 140 days (post-transition). It was of particular interest to identify a possible intermediate oxide layer and study chemical changes across the metal/oxide interface. For Zircaloy-4, a complex sub-oxide structure (ZrO) had been identified previously by 3DAP analysis and confirmed by chemical analysis in the TEM [32,47]. For this reason, particular focus was placed on the development of such sub-oxide structure in pre- and post-transition samples. Figure 10(*a*)10(*c*) displays typical interfacial layer morphologies for different exposure times by plotting the isosurface for 45 at. % oxygen (blue/light grey) and 55 at. % (red/dark grey). Consequently, the ZrO layer is located in-between the two isosurfaces and in this way it was possible to represent the complex 3D morphology of the interface layer. It can be seen that after relatively short autoclave testing —34 days, Fig. 10(*a*)—a simple, locally planar interface layer was observed with little separation between the two isosurfaces and no significant layer of intermediate composition. In contrast, after 100 days a complicated sandwich structure with an intermediate layer of ZrO was detected—Fig. 10(*b*). In general, this intermediate layer varied quite significantly from a few tens of nanometres to almost 100 nm. In the case of the post-transition sample (140 days, patchy surface and therefore very early stage of transition) it was found that a simple, locally planar, interface was present, again with no evidence of an interfacial sub-oxide layer. Line profiles of the zirconium and oxygen concentration across the metal/oxide interface are presented Fig. 11. These line scans were created by defining a 3D volume orientated such that it passes through the plane of the metal–oxide interface, and partitioning this volume at fixed finite intervals along the axis

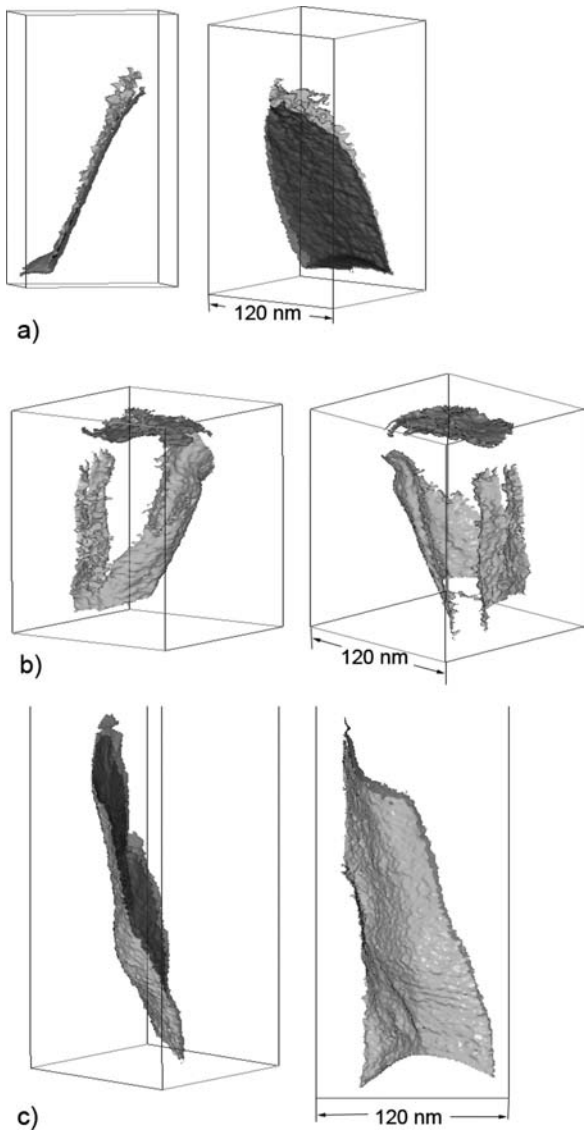


FIG. 10—*Representation of the metal/oxide interface in terms of possible sub-oxide layer recorded by 3DAP analysis. The isosurface of a constant concentration of oxygen is presented red (dark grey) for 55at. % oxygen concentration and blue (bright grey) for 45 at. % oxygen concentration. Interfaces are presented after (a) 34 days exposure (pre-transition), (b) 100 days exposure (pre-transition), and (c) 140 days (post-transition).*

perpendicular to the interface [48]. The composition of each sub-volume was then calculated and defines a point in Fig. 11. The cross-sectional area of such volume was about 1000 nm^2 when studying samples with an interlayer of complex morphology and an order of magnitude larger when studying samples with

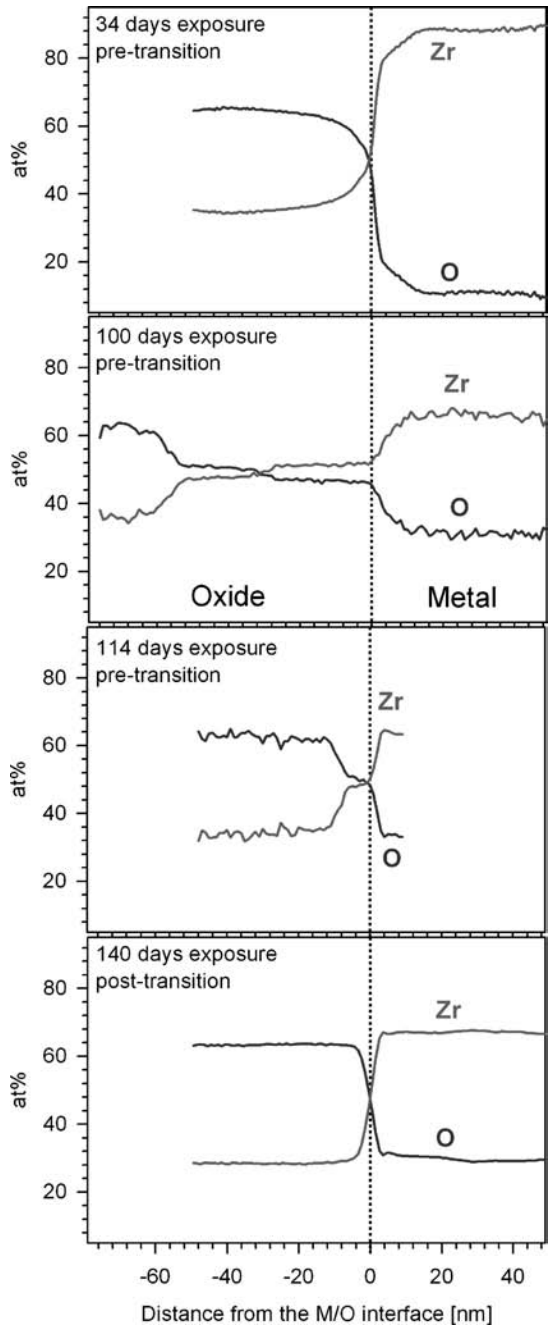


FIG. 11—*Zirconium and oxygen profile across the metal/oxide interface of corrosion tested recrystallised sheet ZIRLO after 34, 100, 114, and 140 days exposure measured by 3DAP analysis.*

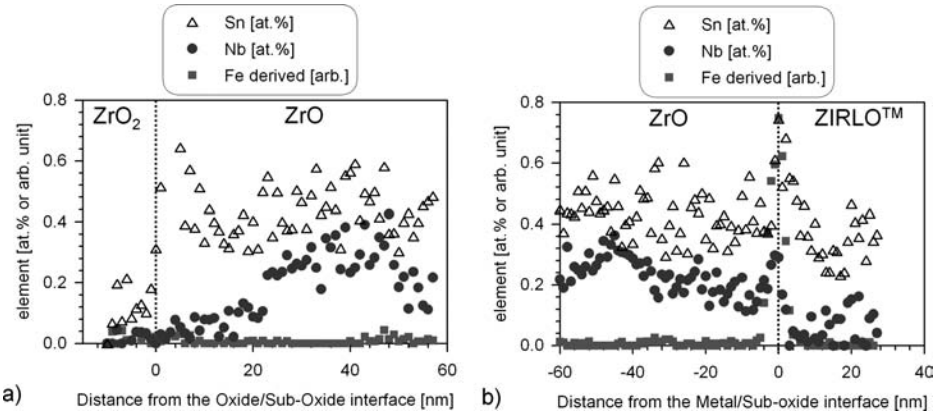


FIG. 12—*Sn, Nb, and Fe concentration profiles across (a) the oxide/sub-oxide interface (o/so interface about 60 nm from m/o interface) and (b) sub-oxide/metal interface (so/m interface about 60 nm from so/o interface) in 100 days corrosion tested recrystallised sheet ZIRLO recorded by 3DAP.*

a more planar interface. It can be seen that after 34 days of exposure the oxygen content on the metal side is still relatively low (Fig. 11(*a*)), but has increased after 100 days to a level similar to that expected of a saturated solid solution (Fig. 11(*b*)) [49]. At this stage an average width of about 50 nm for the ZrO intermediate layer was determined in the studied volume. Figure 11(*c*) suggests that around transition the sub-oxide layer has become thinner. Once the oxide is early post-transition, the profile indicates no sub-oxide layer similar to the sample exposed for 34 days (Fig. 11(*d*)). Attempts were also made to identify the crystal structure of the ZrO layer using TEM and synchrotron X-ray diffraction. Previous work found some ω-Zr in these regions [46]. However, in this case the phase contained about 60 at. % oxygen. Due to the very thin nature and complex shape of the layer, it was impossible to obtain any meaningful information to obtain the crystal structure in the present case.

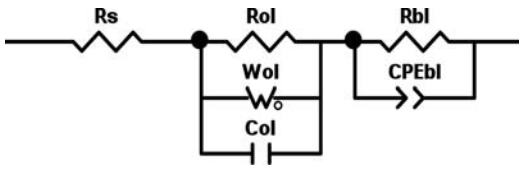


FIG. 13—*Model to describe the equivalent circuit and interpret the impedance spectra. Here R_s represents the solution resistance ($\Omega\ cm^2$), R_{ol} the outer layer oxide resistance ($\Omega\ cm^2$), W_{ol} is the Warburg resistance due to diffusion of the outer layer ($\Omega\ cm^2$), C_{ol} is the capacitance of the outer layer (F/cm^2), R_{bl} represents the resistance of the barrier layer($\Omega\ cm^2$), and CPE_{bl} is the constant phase element of the barrier layer due its capacitance ($S\ s^n$).*

A further analysis of chemical segregation at the interface is shown in Fig. 12(*a*), 12(*b*) for the sample exposed for 100 days displaying a significant sub-oxide layer. In the interface region, Fe clusters were detected resulting in the Fe spike seen in Fig. 12(*b*). The data suggest that Sn and Nb are accepted by the sub-oxide layer but rejected by the ZrO_2 oxide. The Nb content near the metal/oxide interface is low compared to the base matrix level. However, Nb-rich particles were also observed in such regions but were not included in this particular analysis. There is no obvious change in the average level of Sn in the sub-oxide layer compared to the metal substrate. Excess Sn solute is seen at interfacial regions, and this is most apparent at the ZrO_2–ZrO interface. Great care should be taken when discussing these profiles of alloying elements across the interfaces as the interpretation is at an early stage and inherent local chemistry variations might affect the profiles.

In Situ EIS Measurements

Several equivalent circuits have been proposed in the literature to study the corrosion mechanism of zirconium alloys. The majority of these equivalent circuits are based on the physical model that the zirconium oxide is uniform and non-porous [50]. Other models for the post-transition oxide are based on zirconium oxide having a porous non-protective layer formed on top of a protective barrier layer with varying stochiometry for each layer [42,46,51]. In the present work, the model used to describe the equivalent circuit and to interpret the impedance measurements is shown in Fig. 13, and is based on the TEM and 3DAP observations described earlier. It attempts to distinguish between an outer oxide layer that can develop porosity (ZrO_2) and an inner layer, which stays non-porous and may include a region of altered stochiometry ZrO. The equivalent circuit shown in Fig. 13 is comprised of a resistance R_s (the electrolyte resistance), a resistance R_{ol} in parallel with a capacitance C_{ol} (the resistive and capacitive properties of the presumably porous outer oxide, the double layer capacitance can be neglected in this case, because it is in series with the C_{ol}, when capacitances are in series configuration, the smallest capacitance dominate) and a Warburg impedance W_{ol} (the impedance attributed to the mass transfer through the outer layer), and finally a charge transfer resistance R_{bl} (a constant phase element CPE_{bl}, corresponding to the capacitive properties of the dense inner oxide layer, i.e., the barrier layer). By using such model, generally excellent fits of the impedance spectra could be achieved.

The evolution of the individual components in the equivalent circuit is presented in Fig. 14 as a function of exposure time. According to the model, the resistance of the outer oxide layer and the barrier layer first decrease until they reach a minimum between 150 and 155 days, which is in excellent agreement with the corrosion data shown in Fig. 2. While the reduction in resistance of the outer layer can be interpreted by an increase in porosity, also supported by the evolution of the Warburg impedance, a slight reduction of the barrier layer resistance would suggest that this layer becomes thinner toward the moment of transition before it grows again at the beginning of the post-transition phase. A similar interpretation can be obtained from the variation of the outer oxide and barrier layer

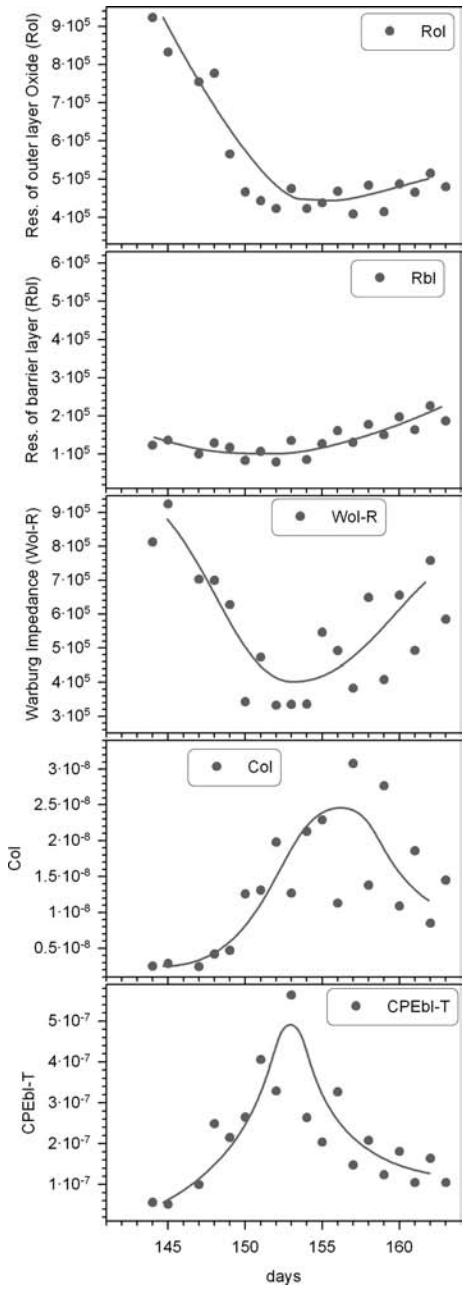


FIG. 14—*Evolution of the resistance of the ZrO_2 layer (a), the ZrO sub-oxide layer (b), of the Warburg impedance (c), of the capacitance of the ZrO_2 layer (d), and the ZrO sub-oxide layer (e) between 144 and 163 days determined by impedance measurements using the model shown in Fig. 13.*

capacitance. The capacitance profile of the outer oxide layer is fairly noisy but a slight delay in respect of the assumed transition time is noticeable. This might be related to the outer oxide layer further increasing in porosity while a new dense oxide layer is now growing at the interface. It can be noted that the phase angle of the CPE is close to 1 and therefore the CPE was treated as a capacitor.

Discussion

Oxide Stresses and the Metastable Tetragonal Oxide Phase

Even though the oxide layer closest to the metal interface is expected to be most important from a transport point of view [42], the stress profile in the thick oxide highlights the issue of stress relaxation taking place in the oxide as the metal/oxide interface moves inwards. At this stage it is interesting to identify possible oxide stress relaxation mechanisms. First, Blat-Yrieix *et al.* have demonstrated that the large compressive stresses in the oxide layer, even though the oxide layer is more than 100 times thinner than the metal substrate, can result in overall creep elongation of the entire corrosion coupon [25]. The effect of creep elongation, assuming average creep rates determined in Ref [25] for recrystallised Zircaloy-4, on stress relaxation of the oxide have been included in Fig. 3. It demonstrates that between 10 and 40 μm from the metal oxide interface stress relaxation in Optimized-ZIRLO might well have been dominated by this mechanism. However, closer to the interface the oxide displays a much steeper stress gradient (highlighted by the short dashed line A) suggesting that additional oxide stress relaxation mechanisms must be active (note, we mean stress relaxation in the previously formed oxide and not the oxide right at the interface). The formation of cracks between oxide layers, as clearly visible in Fig. 1, should result in partial delamination between layers reducing load transfer between oxide layers and hence a more rapid stress relaxation of the oxide layers. Indeed, if substrate creep alone was an active mechanism, the outer oxide should eventually display significant tensile stresses, which is clearly not the case in Fig. 3.

The stresses in the oxide on the Zircaloy-4 samples tested at 360°C are particularly interesting as they highlight a very significant stress evolution of both oxide phases as the first corroding oxide layer goes through transition (Fig. 6). Creep of the metal substrate (in slight tension) can possibly explain the early stress relaxation in both oxide phases. Contribution to stress relaxation of the oxide can also be expected from early crack formation in the oxide (well before transition) as indicated by the impedance work and discussed in the following paragraph. The sudden increase of the stress in the monoclinic phase, just before transition, seems to coincide with the comparatively low compressive stresses ($<$1.5 GPa) of the tetragonal phase. Such stresses seem sensible for the destabilisation of the tetragonal phase considering the small grain size. This martensitic phase transformation results in a volume increase and the new monoclinic crystals should contribute to an increase of the overall stresses in the monoclinic phase. Therefore, the stress variation provides an indirect proof of the onset of tetragonal to monoclinic phase transformation in the moment before transition. One would also expect that such local volume expansion

results in significant compatibility issues in the oxide and further crack formation or growth. Similar observations and line of thought have been previously put forward in Ref [7]. The only difference in their case was that it was assumed that the phase transformation is a result rather than a cause for transition in corrosion kinetics. It is indeed very difficult to say what came first. However, in the present work, we have clear indications that the sudden increase of stresses in the monoclinic phase happens just before transition. It should be kept in mind that the stress values provided here can only be average values and that on a grain to grain level there might be significant stress variations. Consequently, some tetragonal to monoclinic phase transformation might already take place at a stage well before transition and that it is a more continuous process. However, due to the limited grains that might fulfill the criteria for phase transformation at this stage, one would not probably expect to see any dramatic increase of the stress level in the monoclinic phase at an early stage. Once the mean stress level of the tetragonal phase has undercut the stress level for destabilisation, more significant phase transformation takes place in the oxide resulting in more extended crack formation and transition. The Raman data (Fig. 7) also suggest that such phase transformation happens from an early stage, although it should be remembered that these observations were undertaken on the surface and not close to the metal/oxide interface. However, the data observed at the outer surface in combination with the TEM images of an outer porous layer seem to demonstrate the potentially damaging effect of tetragonal to monoclinic phase transformation.

Porosity in the Oxide and the Metal/Oxide Interface

The TEM observations provide evidence of porosity along the grain boundaries of the columnar structured oxide grains. In contrast to the much more obvious cracks parallel to the metal/oxide interface, these pores have the potential for transport of oxidising species through a protective oxide. As discussed by other researchers, oxygen ion transport through the oxide is expected to be fastest along grain boundaries [13] and therefore any grain boundary porosity will be of great significance. However, the TEM observations also suggest that this porosity perpendicular to the interface only develops an interconnected network a few hundred nanometres from the interface regardless of whether the oxide was pre-transition or just post-transition. In the post-transition stage a much more pronounced network of linked up porosity is seen from about 700 nm from the interface, which suggests that the oxide becomes significantly more porous around transition and therefore changes the overall protective properties of the oxide. Supporting evidence for such increase of porosity is provided by the in situ impedance study. In this case, a tube shaped ZIRLO sample was taken through transition showing a very rapid decline of the outer oxide layer resistivity before reaching a trough and slowly increasing again. These data also demonstrate that the actual transition takes place over many days, with a gradual increase of porosity until it has reached a maximum and then the growth of a new more protective oxide becomes the dominant feature. It seems likely that there is a link between the cracks parallel to the metal/oxide interface and the pores along oxide

grain boundaries. Following the argument made in the previous paragraph, the cracks could contribute to the stress relaxation in the oxide, which might be sufficient to allow the pores to link up. However, no indication of increased levels of porosity in the vicinity of cracks was found during the TEM studies.

The 3DAP studies suggest that the metal/oxide interface changes quite dramatically as the oxide goes through transition and that the presence of a sub-oxide layer very much depends on the exposure time in respect to transition (Figs. 10 and 11). It is also noticeable that the decline of the sub-oxide layer seems to happen before the onset of transition, although such conclusions should be treated with great care as the volume studied by 3DAP is very small. However, the in situ impedance studies carried out on tube ZIRLO recrystallised seem to support the 3DAP observations since the resistance of the layer that does not develop any porosity (R_{bl}) displays a slight trough between 150 and 155 days (Fig. 14). Considering that the R_{bl} value only shows a very slight trough through transition while the sub-oxide layer disappears entirely, one can assume that the sub-oxide layer only plays a small part in the barrier layer and that it is mostly the most inner ZrO_2 layer that projects the metal. It is also interesting to note that after 34 days exposure, the oxygen content in the metal substrate is about 15 at. % while after 100 days it has reached a level of about 30 at. %, which is the saturation level of oxygen in zirconium [52]. This very high level of oxygen is still observed after transition and hence there is a noticeable difference of the metal substrate (for instance in strength) between the early stage of pre-transition corrosion and the early stage of post-transition corrosion. At this stage, the actual role of the sub-oxide is unclear. First, the transformation from ZrO to ZrO_2 should result in a smaller volume increase than Zr to ZrO_2. Hence, the sub-oxide should have the potential to reduce the stresses in the oxide or the mechanisms that lead to stress relaxation near the interface. The disappearance of the sub-oxide might, however, simply be a result of the enhanced corrosion kinetics around transition, providing insufficient time to build up such intermediate phase.

Particularly interesting also are the concentration profiles of Nb, Fe, and Sn across the metal/oxide interface recorded by 3DAP. First, high concentration levels of Fe effectively form an Fe monolayer (based on the 3D observation) at the metal/sub-oxide interface. The Nb content in the metal is low compared to values of unexposed material (around 0.6 wt. % Nb). It should be pointed out that in the present data set it was possible to range all of the Nb containing species, which is not always the case due to overlapping of a ZrH^{2+} and Nb^{2+} species. In summary, it is important to note that the metal close to the corroding interface has the potential to develop a significantly different alloy chemistry and second phase particles distribution compared to the base material. Small changes in base alloy chemistry have been shown to result in tremendous variations of previous corrosion performance.

Conclusions and Future Work

The present study has highlighted a number of mechanisms active during corrosion of zirconium alloys that might affect transition. It is clear that the

development of an improved mechanistic understanding of corrosion in zirconium, and in particular transition, requires a range of state-of-the-art analytical characterisation tools to be used on the same set of samples. It also seems clear that observations of stresses, porosity, or sub-oxides are very much time dependent and it is important that any observation is clearly stated against time to transition. In addition, following the evolution of the interface structure, phases and the stresses seems to be critical to identifying the mechanisms that lead to accelerated corrosion during transition. In the present work, the alloys tested at 360°C all displayed relatively similar corrosion behaviours. It will be important to confirm some of the time dependent observations for different alloys to improve confidence in the observations and interpretations given in the present paper. Autoclave corrosion tests at 360°C are still ongoing and some alloys, not presented here, have shown no indication of transition even after 360 days exposure. It will be important that these alloys are investigated to the same level of detail as presented here and that comparison of the oxide stresses, porosity, and sub-oxide structures is not only carried out around transition but also for exposure times when the alloys presented in this paper went through transition. It is hoped that such comparison will finally shed light on the question why time to transition can be so significantly different when comparing alloys. The main findings of the present work can be summarised as follows:

- The monoclinic oxide phase grown on Optimized-ZIRLO, steam tested at 415°C for 600 days, displayed a stress profile with the highest compressive stresses of about 1200 MPa near the metal/oxide interface while close to the outer surface the stresses seem to level out around zero stress. The profile can be partly explained by creep of the substrate, but it is clear that delamination of the oxide layers, near the metal/oxide interface, also plays an important role in the stress evolution.
- Phase fraction mapping of the tetragonal phase in steam tested material and the stress evolution of the oxide through the first transition tested at 360°C suggest that as corrosion proceeds, decreasing stresses in the oxide result in the destabilisation of the tetragonal phase. Particularly, the tetragonal phase seems to stress relief very substantially and when it reaches a stress level of about 1.5 GPa, significant destabilisation seems to take place, resulting in a sudden increase of compressive stress in the monoclinic phase. As this seems to be a comparatively sudden event just before transition, it suggests that indeed this phase transformation plays an important role in initiating the transition.
- The porosity of the oxide was studied by TEM and in situ EIS measurements. Both techniques indicate that during transition the porosity near the metal/oxide interface increases, providing a faster path for oxidising species. Particular attention was placed on identifying possible diffusion paths perpendicular to the metal/oxide interface, which was achieved by using Fresnel contrast in TEM. Nano-sized pores were found close to the metal oxide interface that, with time, link up and form a network about 700 nm from the metal/oxide interface. The development of such a network might be related to the aforementioned phase transformation, which should result in compatibility issues between the

transformed grain and their neighbourhood. The formation of the more obvious cracks parallel to the metal/oxide interface, which provide local delamination and hence stress relief, should also play a role as it enables the pores to link up in an otherwise compressive stress field. The in situ EIS measurements suggest that the average porosity steadily increases over at least 10 days until the growth of a new oxide becomes more dominant in the EIS measurements.

- Observations of sub-oxide with a ZrO stochiometry at the metal/oxide interface have been reported previously. However, the present work demonstrates that the appearance of the sub-oxide changes dramatically during pre- and post-transition. While it is absent during the very early stage of corrosion, the sub-oxide layer develops as the samples moves closer to transition. A particular difficulty of determining the sub-oxide thickness lies in its very ragged 3D morphology at this stage. In situ EIS studies and the 3DAP characterisation both indicate that the sub-oxide layer thickness decreases before transition. After transition, 3DAP analysis displays a complete absence of a sub-oxide structure, similar to the early pre-transition observations. However, the high level of oxygen build up in the metal substrate very near the interface during pre-transition remains after transition, demonstrating that oxygen levels in the metal near the interface differ significantly between early pre-transition and early post-transition. It is believed that the sub-oxide layer is only a small part of the inner layer that protects the metal.
- Finally, 3DAP analysis also enabled us to study segregation of alloying elements near the metal/oxideinterface. Very high levels of Fe were found at the metal/sub-oxide interface. In general, Sn and Nb seem to be rejected either from the ZrO_2 or from the ZrO. As a consequence, the actual metal substrate that is corroded displays a significantly different chemistry in addition to the high levels of oxygen after some time compared to the base material. Considering that very minor changes of an alloy can have fast effects on the corrosion performance of an alloy, this seems to be an important observation.

Acknowledgments

The writers would like to thank the Engineering and Physical Science Research Council (EPSRC) and MoD in the United Kingdom for funding the research as part of the Materials for Energy call (research code: EP/E036171/1). The project would not have been possible with the strong support of our project partners (in alphabetical order) EDF, National Nuclear Laboratory, Rolls-Royce, Serco, and Westinghouse, who have provided substantial in-kind and financial support. For the technical input we would particularly like to thank Antoine Ambard and Martine Blat-Yrieix from EDF and Bob Comstock and Lars Hallstadius from Westinghouse. The writers would like to thank the ESRF and BESSY II for providing the requested beam time and the experimental support by Caroline Curfs from ID11, ESRF and Manuela Klaus and Christoph Genzel from EDDI, BESSY

II. K.B.C. from the OU also acknowledges Queen Mary University for London for using their Raman Spectroscopy facility. M.E.F. is supported by a grant through The Open University from The Lloyd's Register Educational Trust, an independent charity working to achieve advances in transportation, science, engineering and technology education, training and research worldwide for the benefit of all.

References

[1] Ploc, R. A., "Physical Changes in Thin ZrO2 Films With Thickening," *International Conference on Electron Microscopy*, 1970, Grenoble.

[2] Arima, T., Moriyama, K., Gaja, N., Furuya, H., Idemitsu, K., and Inagaki, Y., "Oxidation Kinetics of Zircaloy-2 Between 450°C and 600°C in Oxidizing Atmosphere," *J.Nucl. Mater.*, Vol. 257, No. 1, 1998, pp. 67–77.

[3] Motta, A.T., Erwin, T., Delaire, O., Birtcher, R. C., Chu, Y. S., Maser, J., Mancini, D. C., and Lai, B., "Microstructural Characterisation of Oxides Formed on Model Zr Alloys Using Synchrotron Radiation," *15th International Symposium on Zirconium in the Nuclear Industry*, Sunriver, OR, 2006, *J. ASTM Int.*, Vol. 5, No. 3, paper ID JAI101257.

[4] Bryner, J. S., "The Cyclic Nature of Corrosion of Zircaloy-4 in 633 K Water," *J. Nucl. Mater.*, Vol. 82, No. 1, 1979, pp. 84–101.

[5] Cox, B., "Pore Structure in Oxide Films on Irradiated and Unirradiated Zirconium Alloys," *J. Nucl. Mater.*, Vol. 148, No. 3, 1987, pp. 332–343.

[6] Ni, N., *et al*., "Porosity in Oxides on Zirconium Fuel Cladding Alloys, and its Importance in Controlling Oxidation Rates," *Scr. Mater.*, Vol. 62, No. 8, 2010, pp. 564–567.

[7] Garzarolli, F., Seidel, H., Tricot, R., and Gros, J. P., "Oxide-Growth Mechanism on Zirconium Alloys," *Zirconium in the Nuclear Industry: Ninth International Symposium*, ASTM-STP 1132, 1991, Kobe, Japan, pp. 395–415.

[8] Beie, H. J., Mitwalsky, A., Garzarolli, F., Ruhmann, H., and Sell, H. J., "Examinations of the Corrosion Mechanism of Zirconium Alloys," *Zirconium in the Nuclear Industry: Tenth International Symposium*, ASTM STP 1245, 1994, Baltimore, MA, pp. 615–643.

[9] Yilmazbayhan, A., Breval, E., Motta, A. T., and Comstock, R. J., "Transmission Electron Microscopy Examination of Oxide Layers Formed on Zr Alloys," *J. Nucl. Mater.*, Vol. 349, No. 3, 2006, pp. 265–281.

[10] Cox, B., "Are zirconia corrosion films a form of Partially Stabilized Zirconia (PSZ)?," Report No. AECL 9382, Atomic Energy of Canada Ltd, Chalk River Nuclear Laboratories, Chalk River, ON, Canada, 1987.

[11] Godlewski, J., "How the Tetragonal Zirconia is Stabilized in the Oxide Scale that is Formed on a Zirconium Alloy Corroded at 400°C in Steam," *Zirconium in the Nuclear Industry: 10th International Symposium*, Philadelphia, PA, n, 1994, ASTM International, West Conshohocken, PA. 1994, pp. 663–683.

[12] Godlewski, J., Bouvier, P., Lucazeau, G., and Fayette, L., "Stress Distribution Measured by Raman Spectroscopy in Zirconia Films Formed by Oxidation of Zr-Based Alloys," *Zirconium in the Nuclear Industry: 12th International Symposium*, Toronto, 1999, ASTM International, West Conshohocken, PA., pp 877–900.

[13] Godlewski, J., Gros, J. P., Lambertin, M., Wadier, J. F., and Weidinger, H., "Raman-Spectroscopy Study of the Tetragonal-to-Monoclinic Transition in Zirconium-Oxide Scales and Determination of Overall Oxygen Diffusion by

Nuclear Microanalysis of O-18," *Zirconium in the Nuclear Industry: Ninth International Symposium*, Kobe, Japan, 1991, ASTM STP, Vol. 1132, pp. 416–434.

[14] Yilmazbayhan, A., Motta, A. T., Comstock, R. J., Sabol, G. P., Lai, B., and Cai, Z., "Structure of Zirconium Alloy Oxides Formed in Pure Water Studied With Synchrotron Radiation and Optical Microscopy: Relation to Corrosion Rate," *J. Nucl. Mater.*, Vol. 324, No. 1, 2004, pp. 6–22.

[15] Aldebert, P., and Traverse, J.-P., "Structure and Ionic Mobility of Zirconia at High Temperature," *J.Am. Ceram. Soc.*, Vol. 68, No. 1, 1985, pp. 34–40.

[16] BarbÈris, P., CorolleurThomas, G., Guinebretiere, R., MerleMejean, T., Mirgorodsky, A., and Quintard, P., "Raman Spectra of Tetragonal Zirconia: Powder to Zircaloy Oxide Frequency Shift," *J. Nucl. Mater.*, Vol. 288, No. 2-3, 2001, pp. 241–247.

[17] Bouvier, P., Godlewski, J., and Lucazeau, G., "A Raman Study of the Nanocrystallite Size Effect on the Pressure-Temperature Phase Diagram of Zirconia Grown by Zirconium-Based Alloys Oxidation," *J. Nucl.Mater.*, Vol. 300, No. 2-3, 2002, pp. 118–126.

[18] Block, S., Jornada, J. A. H., and Piermarini, G. J., "Pressure-Temperature Phase Diagram of Zirconia," *J. Am. Ceram. Soc.*, Vol. 68, No. 9, 1986, pp. 497–499.

[19] Ping, L., Chen, I. W., and James, E. P. P.-H., "Effect of Dopants on Zirconia Stabilization; an X-Ray Absorption Study: I, Trivalent Dopants," *J. Am. Ceram. Soc.*, Vol. 77, No. 1, 1994, pp. 118–128.

[20] Ping, L., Chen, I. W., and James, E. P. P.-H., "Effect of Dopants on Zirconia Stabilization; an X-Ray Absorption Study: II, Tetravalent Dopants," *J. Am. Ceram. Soc.*, Vol. 77, No. 5, 1994, pp. 1281–1288.

[21] Dae-Joon, K., Joo-Wung, J., and Hong-Lim,. L., "Effect of Tetravalent Dopants on Raman Spectra of Tetragonal Zirconia," *J. Am. Ceram. Soc.*, Vol. 80, No. 6, 1997, pp. 1453–1461.

[22] Dae-Joon, K., "Effect of Ta2O5, Nb2O5, and HfO2 Alloying on the Transformability of Y2O3-Stabilized Tetragonal ZrO2," *J. Am. Ceram. Soc.*, Vol. 73, No. 1, 1990, pp. 115–120.

[23] Lawson, S., "Environmental Degradation of Zirconia Ceramics," *J. Eur. Ceram. Soc.*, Vol. 15, No. 6, 1995, pp. 485–502.

[24] Clarke, D. R., and Adar, F., "Measurement of the Crystallographically Transformed Zone Produced by Fracture in Ceramics Containing Tetragonal Zirconia," *J. Am. Ceram. Soc.*, Vol. 65, No. 6, 1982, pp. 284–288.

[25] Blat-Yrieix, M., Ambard, A., Foct, F., Miquet, A., Beguin, S., and Cayet, N., "Towards a Better Understanding of Dimensional Changes in Zircaloy-4: What is the Impact Induced by Hydrides and Oxide Layer," *15th International Symposium on Zirconium in the Nuclear Industry*. Sunriver, OR, 2006, *J.ASTM Int.*, Vol. 5, No. 9, Paper ID JAI101321.

[26] Busser, V., Desquines, J., Fouquet, S., Baietto, M. C., and Mardon, J. P., "Modelling of Corrosion Induced Stresses During Zircaloy-4 Oxidation in Air," *Mater. Sci. Forum*, Vol. 595–598, 2008, pp. 419–427.

[27] Heuer, A. H., and Ruhle, M., "Overview 45—On the Nucleation of the Martensitic-Transformation in Zirconia," *Acta Metall.*, Vol. 33, No. 12, 1985, pp. 2101–2112.

[28] Ruhle, M. and Wilkens, M., "Defocusing Contrast of Cavities—1. Theory," *Cryst. Lattice Defects*, Vol. 6, No. 3, 1975, pp. 129–140.

[29] Jenkins, M. L., and Kirk, M. A., "Characterization of Radiation Damage by Transmission Electron Microscopy," *Series in Microscopy in Materials Science*, B. Cantor and M. J. Goringe, Eds., Institute of Physics Publishing, London, 2001, pp. 130–132.

[30] Kelly, T. F., and Larson, D. J., "Local Electrode Atom Probes," *Mater. Charact.*, Vol. 44, No. 1–2, pp. 59–85.
[31] Miller, M. K., Russell, K. F., and Thompson, G. B., "Strategies for Fabricating Atom Probe Specimens with a Dual Beam FIB," *Ultramicroscopy*, Vol. 102, No. 4, 2005, pp. 287–298.
[32] Hudson, D., *et al.*, "The Atomic Scale Structure and Chemistry of the Zircaloy-4 Metal-Oxide Interface," *14th International Conference on Environmental Degradation of Materials in Nuclear Power Systems—Water Reactors 2008*, American Nuclear Society, Virginia Beach, VA.
[33] Jensen, D. J., *et al.*, "X-Ray Microscopy in Four Dimensions," *Mater. Today*, Vol. 9, No. 1-2, pp. 18–25.
[34] Withers, P. J., *et al.*, "Residual Strain Measurement by Synchrotron Diffraction, in Ecrs 6," *Proceedings of the Sixth European Conference on Residual Stresses*, 2002, A. M. Dias *et al.*, Eds., Trans Tech, Zurich-Uetikon, 2002, pp. 1–10.
[35] Withers, P. J., *et al.*, "Methods for Obtaining the Strain-Free Lattice Parameter When Using Diffraction to Determine Residual Stress," *J. Appl. Crystallogr.*, Vol. 40, No. 5, 2007, pp. 891–904.
[36] Frankel, P., Polatidis, E., and Preuss, M., "Diffraction Constants of Monoclic Zirconia Calculated by Self Consistent Modelling," *J. Appl. Crystallogr.* (submitted).
[37] SelÁuk, A., and Atkinson, A., "Elastic Properties of Ceramic Oxides Used in Solid Oxide Fuel Cells (SOFC)," *J. Eur. Ceram. Soc.*, Vol. 17, No. 12, 1997, pp. 1523–1532.
[38] Noyan, I. C., and Cohen, J. B., Residual Stress, 1986.
[39] Genzel, C., *et al.*, "The Materials Science Synchrotron Beamline EDDI for Energy-Dispersive Diffraction Analysis," *Nucl. Instrum. Methods Phys. Res. A*, Vol. 578, No. 1, 2007, pp. 23–33.
[40] Ma, Q., and Clarke, D. R., "Piezospectroscopic Determination of Residual Stresses in Polycrystalline Aluminia," *J. Am. Ceram. Soc.*, Vol. 77, No. 2, 1994, pp. 298–302.
[41] Portu, G. D., *et al.*, "Measurement of Residual Stress Distributions in Al2O3/3Y-TZP Multilayered Composites by Fluorescence and Raman Microprobe Piezo-Spectroscopy," *Acta Mater.*, Vol. 53, No. 5, 2005, pp. 1511–1520.
[42] Wikmark, G., Rudling P., Lehtinen B., Lehtinen B., Hutchinson, B., Hutchinson, B., Oscarsson, A., and et Ahlberg, E., "The Importance of Oxide Morphology for the Oxidation Rate of Zirconium Alloys," *11th Symposium on Zirconium in the Nuclear Industry, Garmisch-Partenkirchen, ASTM-STP 1295*, 1997, ASTM International, West Conshohocken, PA, pp. 55–73.
[43] Roy, C., and Burgess, B., "A Study of the Stresses Generated in Zirconia Films During the Oxidation of Zirconium Alloys," *Oxid. Met.*, Vol. 2, No. 3, 1970, pp. 235–261.
[44] Petigny, N., Barberis, P., Lemaignan, C., Valot, C., and Lallemant, M., "In Situ XRD Analysis of the Oxide Layers Formed by Oxidation at 743 K on Zircaloy 4 and Zr-1NbO," *J. Nucl. Mater.*, Vol. 280, No. 3, 2000, pp. 318–330.
[45] Li, H., Glavicic, M. G., and Szpunar, J. A., "A Model of Texture Formation in ZrO2 films," *Mater. Sci. Eng., A*, Vol. 366, No. 1, 2004, pp. 164–174.
[46] Bossis, P., Lelièvre, G., Barberis, P., Iltis, X., Lefebvre, F., "Multi-Scale Characterization of the Metal-Oxide Interface of Zirconium Alloys," *Zirconium in the Nuclear Industry: 12th International Symposium*, ASTM-STP 1354, 2000, Vol. 1354, pp. 918–945.
[47] Wadman, B., Andren, H. O., and Falk, L. K. L., "Atom Probe Analysis of this Oxide Layer on Zircaloy Needles," *J. Phys. (Paris)*, Vol. 50, No. C8, pp. C8303–C8308.
[48] Miller, M. K., *et al.*, *Atom Probe Field Ion Microscopy*, Clarendon, Oxford, 1996.
[49] Banerjee, S., and Mukhopadhyay, P., *Phase Transformation: Examples from Titanium and Zirconium Alloys*, Pergamon, Oxford, 2007.

[50] Bardwell, J. A., and McKubre, M. C. H., "Ac Impedance Spectroscopy of the Anodic Film on Zirconium in Neutral Solution," *Electrochim. Acta*, Vol. 36, No. 3-4, 1991, pp. 647–653.
[51] Barberis, P., and Frichet, A., "Characterization of Zircaloy-4 Oxide Layers by Impedance Spectroscopy," *J. Nucl. Mater.*, Vol. 273, No. 2, 1999, pp. 182–191.
[52] Abriata, J., Garcés, J., and Versaci, R., "The O-Zr (Oxygen-Zirconium) System," *J. Phase Equilib.*, Vol. 7, No. 2, 1986, pp. 116–124.

Reprinted from JAI, Vol. 8, No. 9
doi:10.1520/JAI103550
Available online at www.astm.org/JAI

A. Ly,[1,2] *A. Ambard,*[1] *M. Blat-Yrieix,*[1] *L. Legras,*[1] *P. Frankel,*[3] *M. Preuss,*[3] *C. Curfs,*[4] *G. Parry,*[2] *and Y. Bréchet*[2]

Understanding Crack Formation at the Metal/Oxide Interface During Corrosion of Zircaloy-4 Using a Simple Mechanical Model*

ABSTRACT: It has been established in previous works that corrosion kinetics in primary water of various zirconium alloys are periodic. Each period is associated with a layer of cracks parallel to the metal-oxide interface. These observations have been made either in autoclave or in pile. This indicates that corrosion processes in autoclave and under irradiation are of similar nature though their absolute kinetics might be different. Taking advantage of this correlation between cracks and corrosion kinetics, the present work aims at identifying the main microstructural parameters controlling cracks appearance in the oxide layer under well-controlled conditions. In order to achieve this, Zircaloy-4 was heat-treated to obtain various metallurgical states (stress-relieved versus recrystallised with different grain sizes) followed by corrosion tests in primary water. The key metallurgical parameters for the various conditions have been analysed (texture, precipitate sizes and grain sizes and distributions) using electron microscopy and synchrotron X-ray diffraction techniques. Corrosion kinetics of the various Zircaloy-4 microstructures are distinct as expected from the literature. Crack morphology in the oxide layer has been analysed and quantified using a dual beam

Manuscript received November 5, 2010; accepted for publication July 5, 2011; published online August 2011.
[1]EDF R&D, MMC department, Route de Sens Ecuelles, 77818 Moret Sur Loing Cedex, France
[2]INPG SIMAP, 1130, rue de la Piscine - BP 75 - F-38402 St Martin D Heres Cedex, France
[3]Univ. of Manchester, School of Materials, Grosvenor St., Manchester M1 7HS, UK
[4]ESRF, ID11, 6 Rue Jules Horowitz – BP 220 –F- 38043 Grenoble Cedex 9, France
*16th International Symposium on Zirconium in the Nuclear Industry, 9th May 2010 – 13th May 2010, Chengdu, Sichuan Province, China

Cite as: Ly, A., Ambard, A., Blat-Yrieix, M., Legras, L., Frankel, P., Preuss, M., Curfs, C., Parry, G. and Bréchet, Y., "Understanding Crack Formation at the Metal/Oxide Interface During Corrosion of Zircaloy-4 Using a Simple Mechanical Model*," *J. ASTM Intl.*, Vol. 8, No. 9. doi:10.1520/JAI103550.

Copyright © 2011 by ASTM International, 100 Barr Harbor Drive, PO Box C700, West Conshohocken, PA 19428-2959.

scanning electron microscope/focused ion beam. Crack layers are evident even at small scale of observation. Three dimensional (3D) images of the oxide structure are presented. Cracks observed in this way are typically penny-shaped with a radius of about 100 nm. Near the metal-oxide interface, they are mainly found at the top of metal protrusions in the oxide. The roughness of the metal-oxide interface was measured. It does not exhibit any periodicity. The residual stresses in the oxide layers were measured by high energy (44 keV) synchrotron X-ray diffraction in transmission mode. Large compressive stresses (~ -1 GPa), changing with the metallurgical state and through the oxide scale thickness, were measured. The residual stresses in the oxide layers were measured by high energy (44 keV) synchrotron X-ray diffraction in transmission mode. Large compressive stresses (~ -1 GPa), changing with the metallurgical state and through the oxide scale thickness, were measured. A model of the oxide breaking at the point of transition has been developed. It is based on mechanical considerations and the existence of compressive stress in the oxide layer.

KEYWORDS: corrosion kinetics, zircaloy-4, stress and strain measurements, heat treatments, synchrotron x-ray diffraction, interface undulations, metal-oxide interface, fourier transform, transmission electron microscopy.

Introduction

Zirconium alloys are commonly used in pressurized water reactors (PWR) as fuel cladding tubes. Even though they are chemically very stable, they do corrode in primary water at typical operating temperatures and pressures. Previous works have shown that corrosion kinetics is periodic in primary water [1–5]. It has also been shown that the end of each period is associated with the appearance of a crack layer running parallel to the metal-oxide interface [3,4]. The increase of oxide thickness during one period is equal to the distance between two successive layers of cracks. This singularity is named transition thickness or transition in the following. The point at which transition occurs depends on the composition of the alloy [4].

The transition thickness and the cracks are related to long term corrosion kinetics (several years) at a given temperature. This has been established on layered oxides formed in autoclaves [4]. The layers of cracks are also commonly observed on in-reactor fuel rods (e.g, Ref [6].) suggesting thus, a common driving mechanism for zirconium alloy corrosion whether in autoclave or in-reactor. Therefore investigation of crack appearance is likely to be a key element in understanding the corrosion mechanism in zirconium alloys.

Furthermore, large stresses have been reported in oxide scales. They are assumed to result from the increase of molar volume during zirconia formation [7–9]. Even though such increase should generally result in very significant in-plane compressive stresses, it has also been predicted that the undulating metal-oxide interface might result in local out-of-plane tensile stresses in the oxide that may lead to cracking [10]. In fact, a plane, smooth metal-oxide

interface should generate no stresses perpendicular to itself and therefore should not lead to any transition. Therefore measurements of stresses in the oxide layer combined with measurements of the roughness of the metal-oxide interface should shed light on the mechanism of cracking and its relation to transition.

In the present work, the link between cracks and microstructure was studied. Composition was fixed by choosing Zircaloy-4 material. Various microstructures were elaborated through various heat treatments. The oxide stresses were measured using high energy synchrotron X-ray diffraction while the metal-oxide interface was characterized using a method, which was specially developed within the project. For the very first time, to the best of the authors knowledge, the oxide microstructure was characterised in 3D using a dual beam microscope (scanning electron microscope (SEM) combined with focused ion beam (FIB). The paper also describes the first steps of a new model that aims at correlating the mechanical interaction, stresses and crack formation.

Materials and Experimental Details

Material

The material used in the present study was Zircaloy-4 in the cold work stress relieved state that had been provided by AREVA. Its composition is given in Table 1. Various heat treatments were performed and are summarized in Table 2. The resulting microstructures are described in Sec. 3.1.

Material Characterization

For microstructural characterisation of the metal and the oxide, samples were first polished with diamond paste of 1 μm diameter. A combined mechanical-chemical polishing was then performed using colloidal silica mixed with H_2O_2. Specimens for optical metallography were slightly etched with HF-HNO_3. Specimens for electron backscattered diffraction (EBSD) were electrochemically etched in Struers A3 electrolyte at 8°C for about 1 min with a voltage drop of 18 V. Similar conditions were used to prepare transmission electron microscopy (TEM) specimens. In addition, a dual beam microscope was applied to obtain 3D images of the oxide. This was achieved by progressively removing thin slices of the material (here oxide) from the top surface of the sample using the FIB and imaging each new layer using the SEM.

Corrosion Testing

Specimens were rinsed in acetone then etched for 3 mins and washed in deionised water. All specimens were corroded in static autoclaves at 360°C and

TABLE 1—*Chemical composition of the alloy (%wt otherwise indicated).*

Sn	Fe	Cr	Ni	Si (ppm)	O (ppm)	C (ppm)
1.25	0.2	0.12	<0.01	70	1300	136

TABLE 2—*Microstructures identification and associated heat treatments.*

Stress Relieved Annealed (SRA)	Recovered	Recrystallised (RXA)	GG 1	GG 2
As received	500°C – 3 h	540°C – 2 h	540°C – 24 h 800°C – 0.25 h	540°C – 24 h 800°C – 1 h

Note: CG: Coarse Grains

18 MPa using deionised water with addition of boron acid and lithium hydroxide in such proportions that [B] = 1000 ppm and [Li] = 2.2 ppm were obtained. 30 cm^3/liter of hydrogen were added at ambient temperature. Weight gains were translated into oxide thicknesses using the classical equivalence 15 $mg.dm^{-2} \sim 1$ μm.

Oxide Characterization and Stress Measurements

The metal-oxide interface was characterized using SEM. Thirty pictures were taken with a characteristic length of about 30 μm. Oxide microstructure at a fine scale was examined using a FEG-SEM Supra 55 operating at 15 kV with a resolution of 1 nm for imaging and 20 nm for EBSD. Metal texture was measured using orientation distribution functions (ODF) by EBSD. It was checked on one sample (SRA) that despite low indexation factor (about 25 % of the points indexed), the ODF reconstructed from EBSD results was similar to that obtained from X-ray diffraction measurements.

Stresses in the oxide were measured at the ESRF ID11-beamline. Thin specimens (500 μm) were sliced from a tube perpendicularly to its axis. A metal-free oxide layer was used as a reference stress free oxide following a method proposed in Ref [11]. It was prepared by dissolving the metal of the specimen in a HF-HNO_3 mixture.

Monochromatic beam with an energy of 44 keV was used that enabled to record diffraction rings in transmission mode. The spot size was about 1.5 μm perpendicular to the metal/oxide interface and 5 μm parallel to the interface. The oxide was mapped using a step size of 0.5 μm perpendicularly to the metal-oxide interface and 4 μm along that interface. The analysis of the diffraction spectra is detailed in Sec. 3.6.

The main difficulty with this experiment was to align the specimen. The beam converges on the detector behind the specimen but, considering the distances between the detector and the lenses, the angle of convergence was very small. Thus, it resulted in an almost parallel beam in the specimen. LaB_6 powder was placed next to the specimen as a standard. It provided a reference spectrum required when using Fit2D[5] for distortion correction. Another difficulty was to locate the oxide with such a small probe size considering its thickness. Specimens were precisely aligned with the beam (eucentrism insurance) before diffraction spectra were acquired mapping a grid covering the oxide scale.

[5]Fit2D is a data post-treatment software provided by the ESRF.

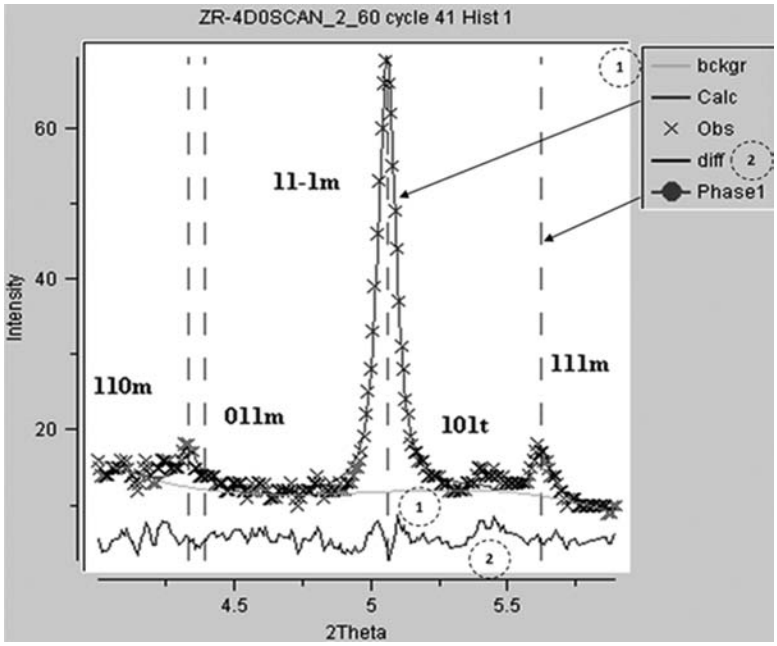


FIG. 1—*Example of a Rietveld refinement applied on the reference sample (3.6-μm thick). Phase 1 = Monoclinic zirconia. Obs = experimental data. Calc = GSAS Rietveld fitting. Tetragonal peak [101]t is ignored in the analysis of the spectrum.*

Measurements were made at ambient temperature. It should be stated that due to highly anisotropic dilatation coefficient of zirconia [12] high level of internal stresses can be generated in the oxide layer during cooling. The differential dilatation of metal and oxide should also be taken into account.

The diffraction rings were converted (Fit2D partitioning) into 1D diffractograms which were analysed using GSAS[6]. A Rietveld refinement was performed usually on three or four peaks of the monoclinic oxide phase (see Fig. 1). Strains were analysed using the $[11\text{-}1]_m$ reflection since it was the least sensitive to texture with the highest intensity.

Results

Alloys Microstructure

Micrographs of the various metallurgical states are shown Fig. 2. Precipitate diameter was measured using TEM (30 pictures in random locations). Laves phase $Zr(Fe,Cr)_2$ are predominant and grow with heat treatment. Table 3

[6]GSAS is a software useful in X-ray diffraction spectrum analysis freely available at ww.ccp14.ac.uk/solutions/gsas

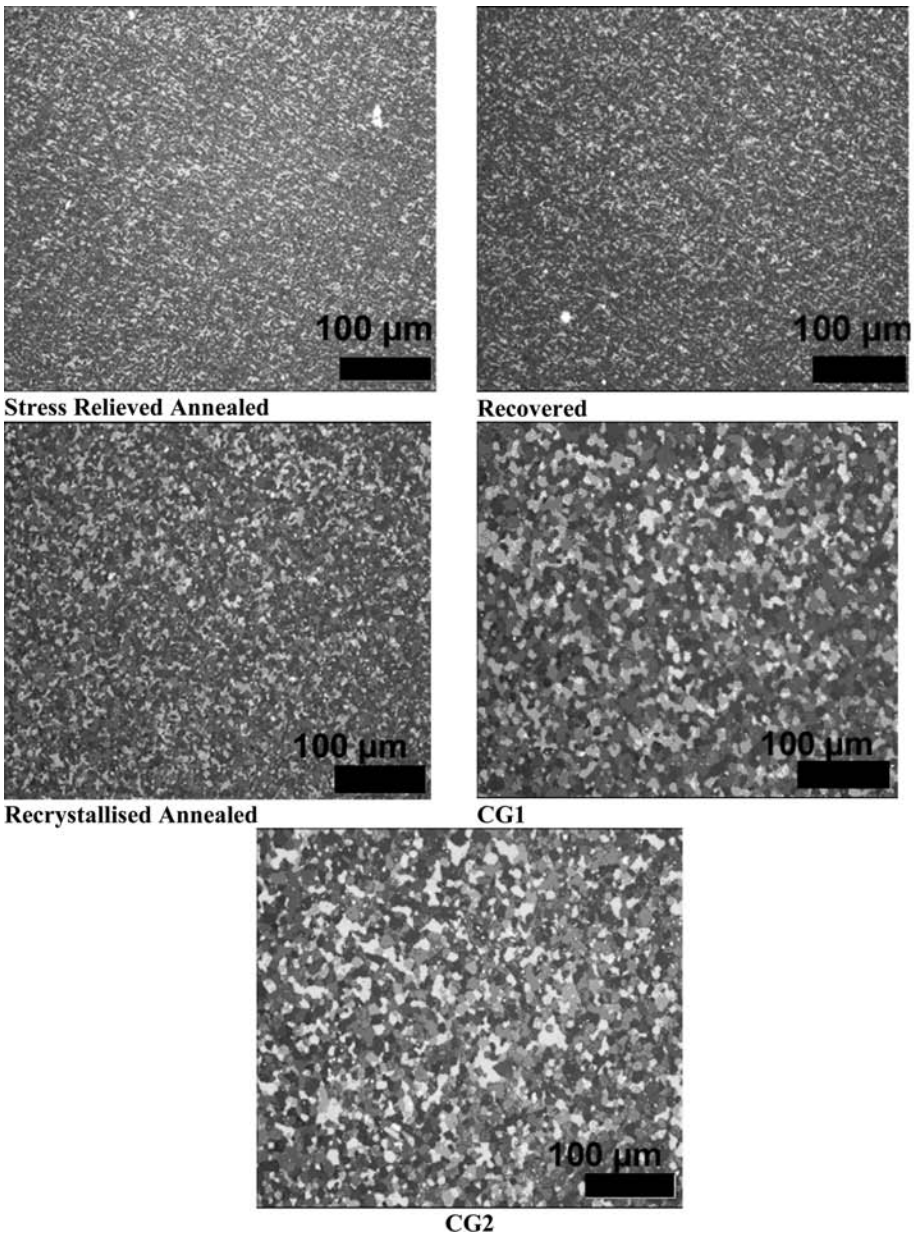


FIG. 2—*Microstructure of the various metallurgical states obtained after heat treatments (polarized light).*

TABLE 3—*Quantitative results gained from microstructure analysis.*

	Stress Relieved	Recovered	Recrystallised	GG1	GG2
Grain size (μm)	–	–	6	8	12
Hardness (Hv)	211 ± 5	199 ± 6	172 ± 6	166 ± 7	175 ± 8
Precipitate size (μm)	60 ± 21	112 ± 23	128 ± 27	144 ± 40	220 ± 60

gathers the grain diameter and Vickers microhardness measurements for all metallurgical states. The observed hardness values are typical for Zircaloy-4 alloys in stress relieved or recrystallised states. Table 3 also shows that hardness values of the three different recrystallised conditions stayed constant considering the standard deviations.

Grain size was not measured on the samples in the stress relieved and recovered samples condition since grains were too deformed and elongated along the rolling direction. In comparison., the recrystallised microstructures displayed typical equiaxed grain morphology.

Electron backscattered diffraction texture measurements are presented in the form of a partial ODF in Fig. 3(*a*), 3(*b*) and display the expected basal texture [13]. During recrystallisation, some grains grow at the expense of others, which is described qualitatively as a rotation of 30° around the *c*-axis. Texture of the recovered microstructure is similar to the stress relieved one whereas textures of CG1 and CG2 are similar to the recrystallised one with the 30° rotation around the *c*-axis.

Corrosion Kinetics

The corrosion kinetics of the five different Zircaloy-4 conditions are illustrated in Fig. 4. For all the microstructures, transition is followed by a new sub-parabolic growth except for the recrystallised conditions where the delayed transition in combination with the comparatively short corrosion time did not allow this to be established. Similar observations have been obtained previously in a number of alloys [3–6] including recrystallised alloys [14].

Sub-parabolic growth before transition is well reproduced using this kinetics law: $s_{ox} = k.t^b$ where s is the oxide thickness, t is the corrosion time, k is a constant and b is the order of the kinetics (parabolic if $b = 2$). The fitted parameters are given in Table 4 as well as the transition thicknesses. It appears clearly that the sub-parabolic kinetics does not depend on the metallurgical state.

Transition is analysed in terms of transition times since weight gain measurements are not sensitive enough to let us use transition thicknesses. It is clear that transition time depends on the metallurgical state.

Corrosion Kinetics Versus Microstructures

First of all there is no correlation between the sub-parabolic corrosion kinetics (regarding values of b and k) and any metallurgical parameter since they are not significantly affected by microstructural changes. Any correlation should thus

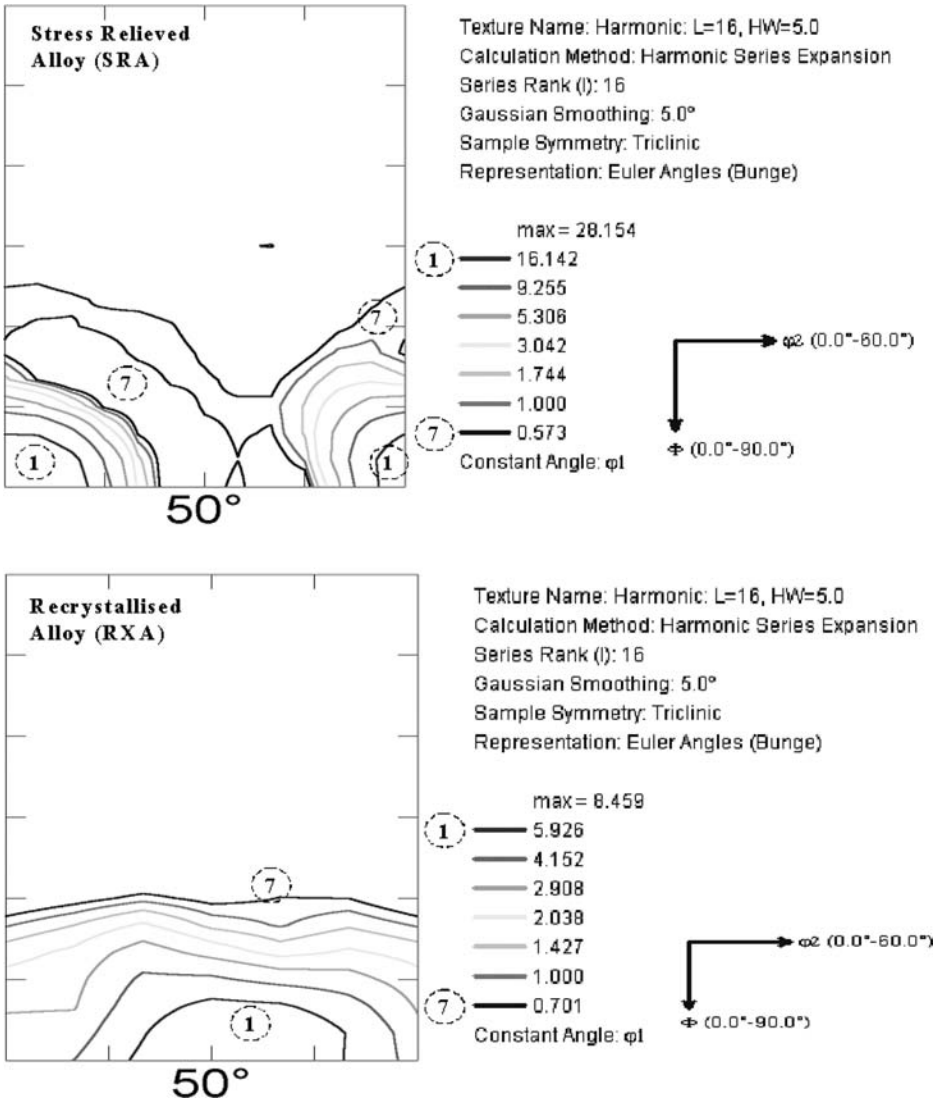


FIG. 3—*Rotation of 30° around the c-axis (marked Φ_2) after recrystallisation. ODF were obtained from EBSD reconstructed poles figures.*

be investigated through the transition times which are more sensitive. As shown in Fig. 5, it is not possible to find a monotonous (increasing or decreasing) correlation between transition times and microstructural parameters of the base metal. Nevertheless, it would be possible to draw a correlation between transition and a combined microstructural parameter. For example, as suggested in Fig. 4, one can correlate transition time to Vickers hardness up to recrystallisation (i.e., considering only the deformed microstructures) then link it to grain

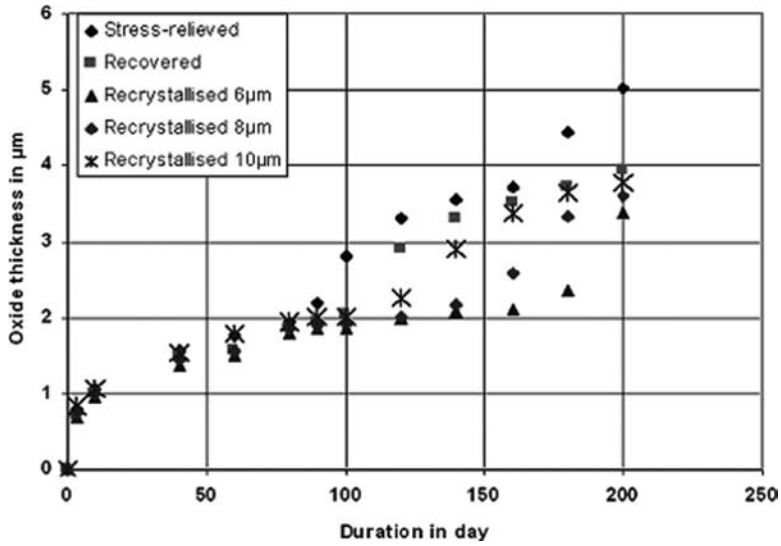


FIG. 4—*Corrosion kinetics of the five metallurgical states considered. Recrystallised 8 µm and 10 µm stand respectively for CG1 and CG2.*

size for recrystallised microstructures. In that case it decreases monotonously. A similar conclusion could be drawn if combining hardness and precipitate size once recrystallisation is completed.

As there is no direct correlation between the microstructural parameters and the corrosion kinetics via the transition time, the oxide microstructure was investigated.

Oxide Microstructure

The SEM examinations showed that cracks parallel to the metal-oxide interface appear at transition point, which is commonly observed [3, 4 and 6]. Figure 6 shows the oxide scale grown Zircaloy-4 in the recovered condition. A few cracks can be observed directly at the metal-oxide interface after 80 days of corrosion before transition (95 days). It means that transition is a sluggish phenomenon.

TABLE 4—*Synthesis of the corrosion kinetics results.*

	Stress Relieved	Recovered	Recrystallised	GG1	GG2
Transition time (days)	85	95	170	140	100
Transition thickness (μm)	2	2	2.1	2.1	2.1
2nd transition time (days)	170	190	–	–	–
2nd transition thick. (μm)	4	3.9	–	–	–
N	0.28	0.29	0.3	0.28	0.27
k (μm.d^{-n})	0.57	0.51	0.47	0.51	0.59

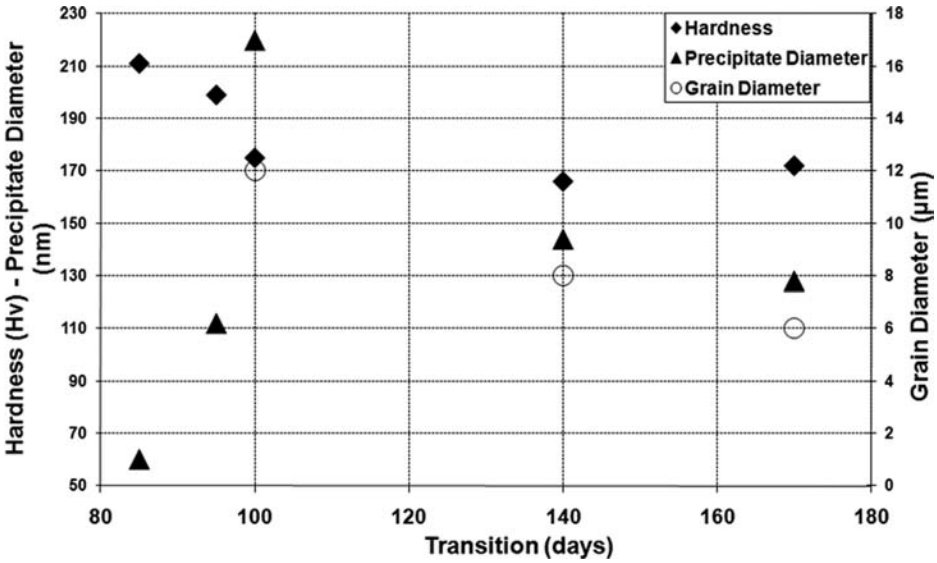


FIG. 5—*Plots of properties of metallurgical states versus transition time.*

Cracks seem to be preferentially located at the top of metal-oxide interface undulations. In order to obtain a clearer picture of the exact location of the cracks in respect to the undulating interface 3D images using the dual beam microscope were obtained. Resulting micrographs were reconstructed into a 3D volume and by creating an isosurface it was possible to highlight the cracks in such volume (Fig. 7).

Figure 7 displays a 3D image of the oxide grown on Zircaloy-4 in the stress relieved condition after 160 days of corrosion. The image reveals penny-shaped cracks with a diameter of around 100 nm. Near the interface, some are found at the top of the protrusions of the metal into the oxide. In the bulk oxide layer their distribution is not uniform. Their density increases in the region when the oxide went through transition. It is however remarkable that cracks are not only restricted to these regions but can be found everywhere in the oxide (indicated as "pores" in Fig. 7). This observation means that the transition (defined here as the crack appearance) stretches over a longer period than weight gains and Impedance Spectroscopy [3] suggest. By moving the frame so that the metal-oxide interface is parallel to the viewing axis, it is possible to evidence the parallelism between crack layers and metal-oxide interface. The Dual Beam imaging has thus confirmed the conclusions which have been assumed previously from the 2-D SEM micrographs. Furthermore pores or small cracks are clearly evidenced.

Metal-Oxide Interface

Since the metal-oxide interface undulation has been suggested to generate local tensile stresses in the oxide that sits on a metal protrusion [10] and cracks are indeed observed in this region, a detailed characterisation of the metal-oxide

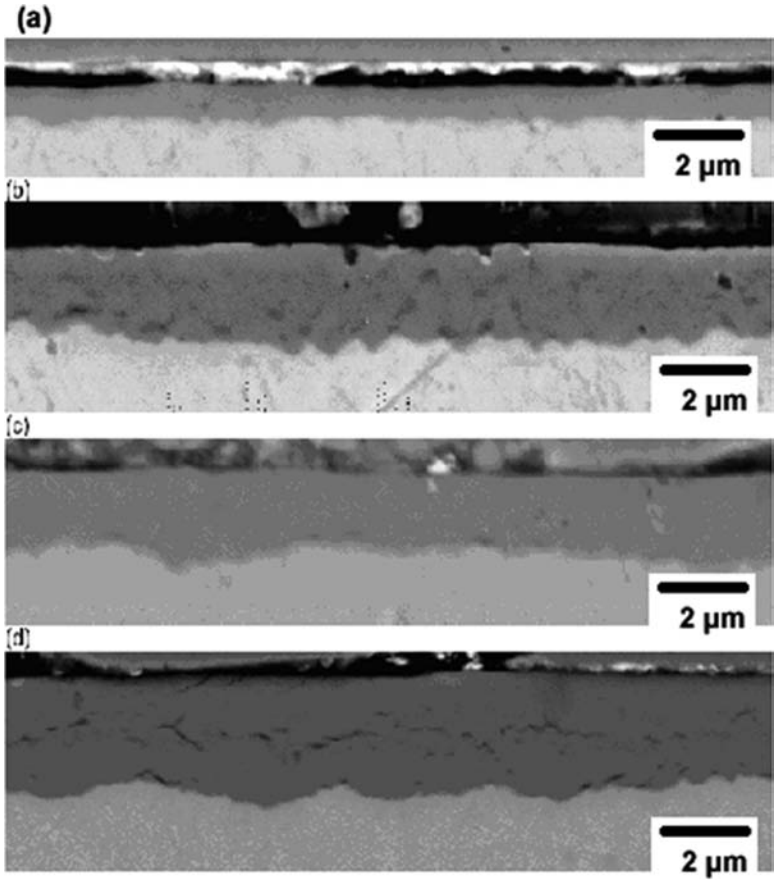


FIG. 6—*SEM oxide layers micrographs for a Recovered Zyrcaloy-4 after (a) three days (b) 80 days (c) 100 days (d) 160 days of corrosion. Base metal is light gray. Oxide layer is grey and cracks are imaged as dark segments. Transition occurs after 95 days according to weight gain measurements.*

interface undulation was carried out. The metal-oxide interface undulation was quantified by following a procedure based on Fourier transforms that has been developed by Ref [15]. The interface was first digitised using SEM micrographs. No periodicity could be inferred from the power spectrum density. The standard deviation of the interface undulation height has been plotted versus time on Fig. 8. It can be seen that it increases very slowly with corrosion time but does not show any sudden change around transition. Height variations are not significant between the various metallurgical states.

The summit curvature was also also analysed since it might affect the stress state above undulations. Following [16,17] the distribution of summit curvatures of any surface or profile could be quantified using a single dimensionless parameter ζ. ζ describes statistical properties of rough surfaces (such as summit

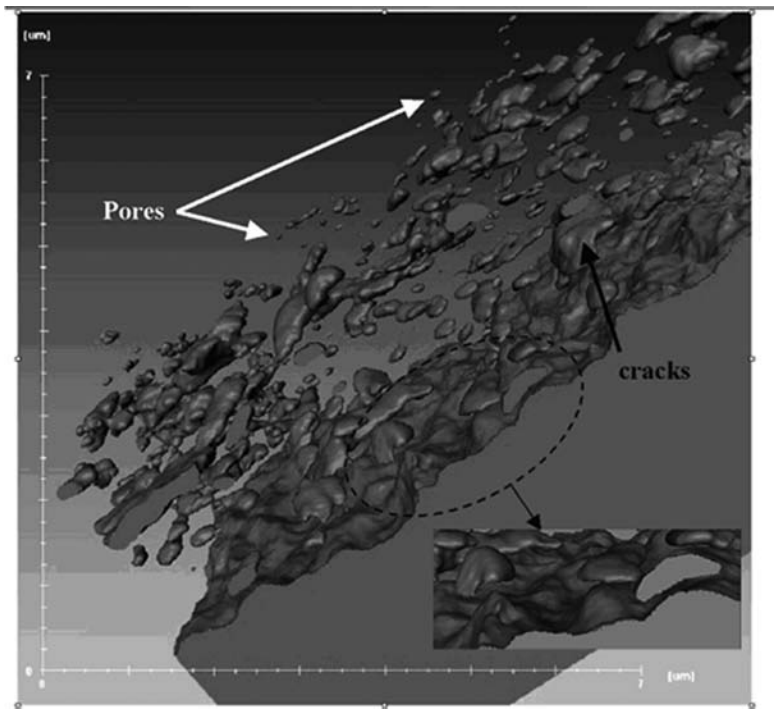


FIG. 7—*FIB analysis of as-received state after 160 days of corrosion. Base metal is on the right. Pores and cracks are imaged by removing virtually the oxide on the top of the metal. Insert on the right shows few cracks located above metal protrusion in the oxide.*

height or curvature distributions). It is also used here to deduce the properties of the surface (2D interface) from those of the profile (1D interface imaged in SEM). Assuming isotropy, the properties of the surface can be determined from those of the profile [15–17]. Figure 9 shows that there is no significant evolution of ζ below 200 days of corrosion. Thus the summit curvature do not change neither with corrosion time below 200 days nor with the metallurgical state. An increase of ζ was detected for longer corrosion times in Zircaloy-4 in the stress relieved condition. The main conclusion from this is that the metal-oxide interface roughness evolves slightly with corrosion time but shows no correlation with transition and is not affected by the metallurgical state of Zircaloy-4 (below 200 days). The modelling will thus consider that the interface is similar for all the metallurgical states. Integration of the modification of the summit curvature for larger times is postponed.

Stress Measurements

Oxide cracking is related to the residual stresses in the scale. Stresses have been computed from strains measured using transmission synchrotron X-ray diffraction by following the evolution of diffraction ring positions. The $(11\bar{1})$

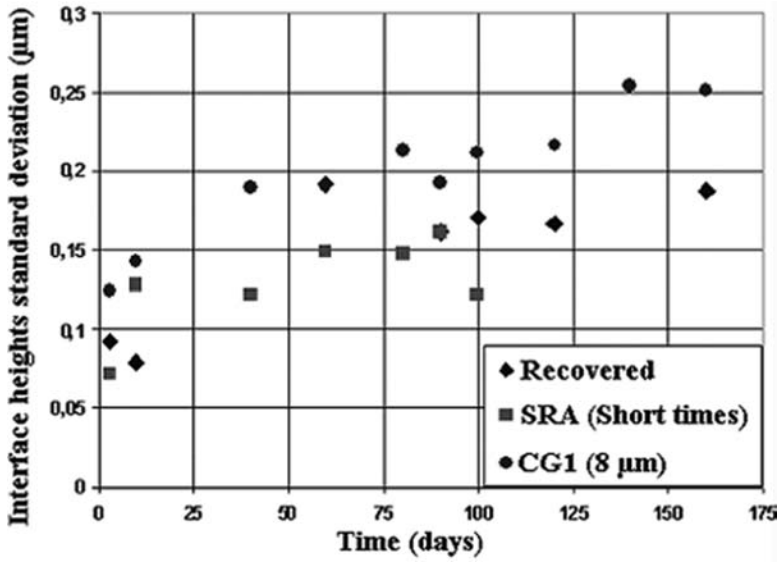


FIG. 8—*Variation of the interface heights standard deviation for three metallurgical states (Stress relieved, recovered and recrystallised CG1).*

monoclinic plane $((11\,1')_m)$ was selected for the strain analysis. Diffraction spectra were acquired on a 2-D CCD detector (Frelon type) in transmission mode. Each set of lattice planes generates a ring more or less continuous (intensity variations due to texture) which is in fact an ellipse in a stressed sample when

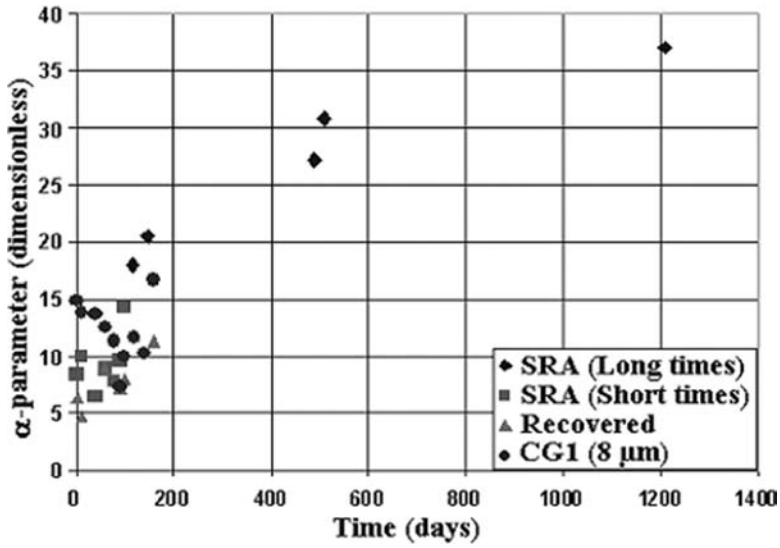


FIG. 9—*Variation of α with corrosion time. α values for time >200 days come from [14].*

examined carefully. In the stress-free reference sample $d^0_{11-1m} = 0.316398$ nm with a standard deviation of $9.7.10^{-5}$ nm, i.e., an error of 0.06 %. Considering an elastic isotropic Young modulus for zirconia (241 GPa [18]), it yields a precision of 150 MPa on stress values.

Hoop and radial stresses can be obtained by caking the 2D spectra in sections that correspond to the strain direction (here +/− 5°), then integrating the intensity along the radial direction to obtain classical 1D diffractograms. A Rietveld refinement was performed on the 1D profiles to obtain d_{11-1m} along each direction. This is done by using a set of softwares: Fit2D (for alignment corrections and "caking" the ring) and GSAS (for Rietveld Refinement). A Matlab routine has been written to identify directions of interest by fitting an ellipse on the $(11\,1')_m$ diffraction ring. Hoop stress in the oxide is known to be compressive [8, 19 and 20] while radial stress should be tensile above delayed oxidised zones [10,[19]] and compressive in the advanced ones with a mean value which might average to zero. It means that they respectively correspond to the larger and smaller distances on the elliptic (stressed) diffraction ring. The transformation of angular positions into Cartesian coordinates is illustrated onto Fig. 10.

In order to calculate stresses in the oxide, an assumption about the stress state is required. Three possibilities can be used:

- A biaxial stress state exist with the axial stress being zero due to the small sample thickness (0.5mm)
- A triaxial stress state with equal hoop and radial strains (transversal isotropy)
- A biaxial stress state exists with the radial stress being zero due to the thin oxide thickness (microns)

The third approach is clearly the most suitable one in a thin oxide which should not produce any out-of-plane stresses. In addition, FEM simulation has shown that cutting a sample to 0.5 mm thickness does only relief the stresses by

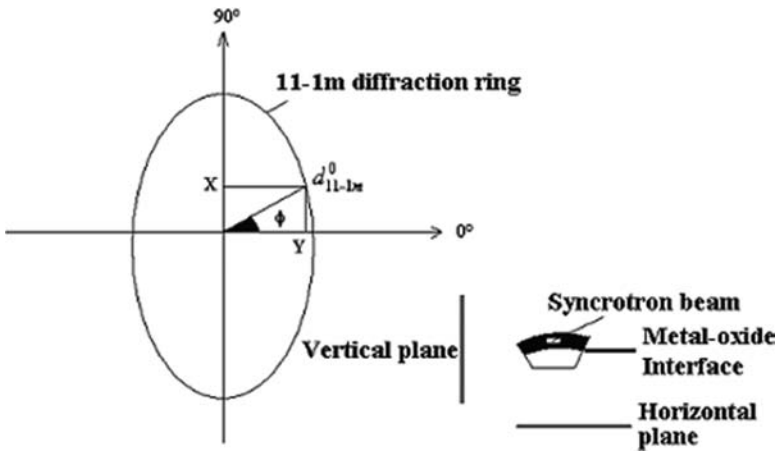


FIG. 10—*Transformation of diffraction ring angular coordinates into Cartesian coordinates for fitting* $X = d^0_{11-1m}\sin\varphi$ *et* $Y = d^0_{11-1m}\cos\varphi$.

10–20 %. The stiffness tensor used here was that of Parise [10,[19]] who used data from Ref [18]. It was assumed that hoop strains are equal to axial strains. Strain was calculated according to Eq 1

$$\varepsilon = \frac{d_{11-1m} - d^0_{11-1m}}{d^0_{11-1m}} \tag{1}$$

Stresses were derived as follows

$$\begin{array}{ccc} 0 & = & 385\varepsilon_r + 148.5\varepsilon_\theta + 95.5\varepsilon_z \\ \sigma_\theta & = & 148.5\varepsilon_r + 385\varepsilon_\theta + 95.5\varepsilon_z \\ \sigma_z & = & 95.5\varepsilon_r + 95.5\varepsilon_\theta + 229.5\varepsilon_z \end{array} \tag{2}$$

where the subscript r designates stress or strain in the radial direction, z in the axial direction and θ along the hoop direction. Stresses are expressed in MPa. Due to the symmetry of the rod, other components are zero.

The effects of microstructure, corrosion time and oxide thickness, to a smaller extent, were studied. Results can be summarised as follows:

- Stress decreases when moving away from the metal-oxide interface. Indeed, a 300 MPa decrease has been noticed on a 3.6-μm thick post-transition oxide. However, due to the beam size (1.5 μm) compared to the oxide thickness this result has to be confirmed on thicker oxide scales.
- Residual stresses in pre-transition oxide layer (only Recovered, CG1 and CG2) increase with decreasing transition time as shown in Table 5. Data are lacking for SRA due to poor data recorded on the specimen corrosion tested for 60 days but it is possible to interpolate a value considering that stress has been measured at 40 and 80 days. For the RXA state, no spectrum was usable.
- Residual stresses measured on a SRA specimen increase with corrosion time (and thickness) until transition where they decrease steeply (Fig. 11). That moment corresponds to increased crack formation in the oxide (experimentally observed by SEM) or to the maximum crack density according to the FIB-SEM examination.

The main conclusion of this section is that it is possible to correlate transition time (and thus thickness) with the hoop stress in the oxide. A brief commentary about the thermal stresses should be made here: as stated in §2.4 thermal stresses

TABLE 5—*Evolution of the mean hoop-stress in recovered, CG1 and CG2 Zircaloy-4 after 60 days of corrosion at 360°C. Data for SRA states are interpolated using results at 40 and 80 days. RXA data are lacking due to poor spectrum quality.*

Zircaloy-4 Microstructures	*SRA*a	Recovered	CG1	CG2
Transition time (days)	*85*	100	140	105
Oxide thickness (μm)		1.6	1.6	1.7
Residual hoop-stress (GPa)	*−1.18*	−1.25	−0.98	−1.33

[a]Inferred by interpolation.

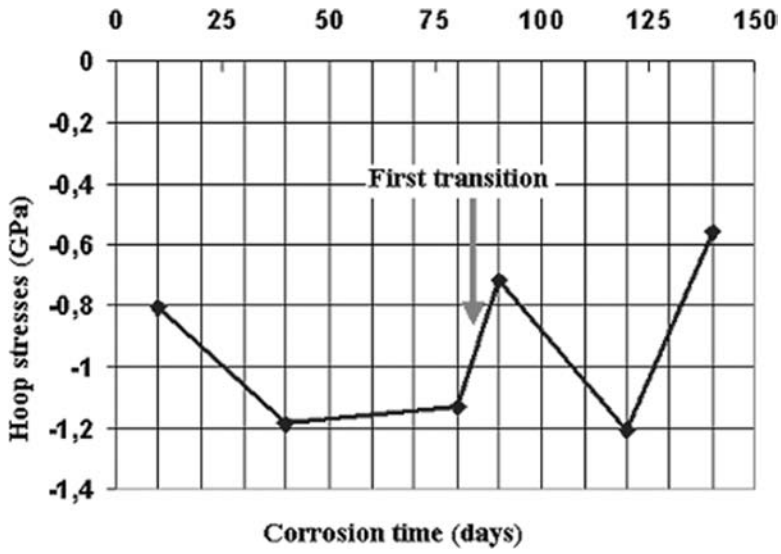


FIG. 11—*Stress evolution with corrosion time of SRA Zircaloy-4. Primary water 360°C. Each points is measured at the nearest point of the metal oxide interface.*

appear in the oxide layer during cooling. The level of these stresses is not known but we assume that they are of similar intensity for all the metallurgical states since the texture of the oxide is known to change very little with time and alloy [19,[20]]. The correlation of stress with transition which is established should still stand since the stresses measured are the sum of the thermal stresses and those generated by the swelling of the oxide. That opens the possibility to understand transition through the stress state in the oxide. Since layers of cracks are also associated to transitions, one obvious possibility would be to relate stress and cracks in the oxide layer, which requires modelling.

Modelling

An attempt to compute stresses in the oxide layer and relate them to cracking is presented in this section. As a starting point, the modelling is kept as simple as possible and analytical formulations are retained as far as possible.

Rough Estimation of the Transition Thickness

In a first approach, the order of magnitude of the transition thickness is identified. The basic idea of the modelling is to evaluate the stored elastic energy coming from the incompatibility strains between the metal and the oxide and to compare it to a critical energy. The incompatibility strains could originate from the Pilling-Bedworth ratio. Some energy could be dissipated in any inelastic phenomena occurring in the system (plastic deformation of the metal, creep of the oxide, phase change, cracking…). Dissipation is not taken into account in

this first step. When the elastic energy reaches a critical value, it is released through the formation of cracks parallel to the metal oxide interface. This facilitates the migration of oxidizing species close to the metal-oxide interface. It must be recalled that the exact mechanism which enhances diffusion through the oxide layer at the transition remains unexplained but some hypotheses exist. In Ref [21], the possible role of porosity is addressed. Enhanced diffusion along grain boundaries due to stress relieve could also be proposed.

Following Eshelby [22] metal (ε_m) and oxide (ε_o) deformations are related through an incompatibility equation which takes into account the Pilling-Bedworth ratio (ε^*). First of all, a metal layer of length L_0 is allowed to expand freely after oxidation. The length of the so formed oxide is equal to $L_0(1+\varepsilon^*)$. This layer is joined to another metal layer of length L_0. The metal layer expands (ε_m) while the oxide layer contracts (ε_o) so that their final lengths become equal. It leads to the following equality

$$L_0(1+\varepsilon_m) = L_0(1+\varepsilon^*)(1+\varepsilon_o) \tag{3}$$

By developing to the first order in deformation and dropping L_0, the equation becomes

$$\varepsilon^* + \varepsilon_o = \varepsilon_m \tag{4}$$

Stresses are assumed to be constant throughout the thickness of both the oxide scale (h) and the metal (gh) where g is a proportionality coefficient which should range between 1–10. In the following numerical evaluations, g is taken equal to one. The strain (ε^*) due to the Pilling-Bedworth ratio is taken to be constant and equal to 0.5 % in the plane of the metal-oxide interface [19].

The second equation is obtained by minimising the density of the stored elastic energy (W/h)

$$\frac{W}{h} = \frac{1}{2}\left(E_o\varepsilon_o^2 + gE_m\varepsilon_m^2\right) = \frac{1}{2}\left(\frac{\sigma_o^2}{E_o} + g\frac{\sigma_m^2}{E_m}\right) \tag{5}$$

Minimizing this equation relatively to the oxide deformation requires constitutive laws. The oxide is taken to be a purely elastic body with a modulus E_o equal to 281 GPa. In the metal, only an elastic constitutive law is considered (further refinements can be found in Ref [21]). Elastic modulus E_m is taken to be 78 GPa. Combining Eqs 3 and 4 and minimizing the elastic energy relatively to the oxide deformation allows to establish the following equalities

$$\varepsilon_o = -\frac{gE_m\varepsilon^*}{E_o + gE_m} \tag{6}$$

$$\left(\frac{W}{h}\right)_{min} = \frac{1}{2}\left(E_o\left(\frac{-gE_m\varepsilon^*}{E_o+gE_m}\right)^2 + gE_m\left(\frac{E_o\varepsilon^*}{E_o+gE_m}\right)^2\right) \tag{7}$$

Equation 7 shows that the total elastic energy W is proportional to the oxide thickness h since the density of the stored elastic energy (W/h) is constant. The transition thickness $h_c$is obtained by solving Eq 8

$$W(h_c) = 2\Gamma \tag{8}$$

where Γ is the energy required to nucleate a crack. Γ is assimilated to a surface energy and is taken equal to 1 $J.m^{-2}$. It must be pointed out that Eq 8 assumes weak points in the oxide layer for crack nucleation. In fact Parise *et al.* [10] have shown that the undulations of the metal-oxide interface concentrate stresses, especially the stress normal to the interface. The transition oxide thickness is thus given by

$$h_c = \Gamma\left(\frac{1}{2}E_o\left(-\frac{gE_m\varepsilon^*}{E_o+gE_m}\right)^2+\frac{1}{2}gE_m\left(\frac{E_o\varepsilon^*}{E_o+gE_m}\right)^2\right)^{-1} \tag{9}$$

A numerical evaluation gives $h_c \sim 2.6$ μm. A sensitivity study shows that changing elastic modulus of the oxide, or Γ, h_c ranges between 1 and 10 μm. As far as order of magnitude is considered, it is demonstrated that the model can capture the transition although it must be reconsidered to be able to predict precisely oxide breaking. This is the aim of the following approach in which it is tried to introduce the morphology of the metal-oxide interface.

Second Approach

Balint and Hutchinson [24,25] have developed a model to take into account undulations of metal-oxide interface. It has appeared that their model could be adapted to our problem. They describe the stress state resulting from a rough interface assumed to be periodic. The real interface is not periodic as stated before in Sec. 3.5 but it can be analysed as a weighted sum of periodic functions. Therefore one could consider, as a first approximation, to superpose all the stress states resulting from all the elementary periodic functions. First results of this method are given. It will plainly appear that further refinements are needed to get more precise results.

Modelling Approach—The system studied by Balint and Hutchinson is presented Fig. 12. It is made of an infinitely thick substrate (1), a binding layer (PtNiAl) [2], an alumina layer (3), and a protective zirconia layer (4). Each of these layers (i) is characterized by its thickness $h^{(i)}$ and mechanical properties (Young modulus E, Poisson ratio ν and thermal dilation coefficient α).

Undulations of the alumina layer (3) exert a variable pressure $p^{[2]}$ or $p^{[4]}$ on its neighbouring layers (2 or 4) depending on their amplitudes. They are characterized by a half wavelength (L) and initial amplitude (δ_0). Their shape changes due to metal creep. This phenomenon is hypothesized to be responsible of the small changes in metal-oxide interface roughness (Fig. 8). The stress state is assumed to be equibiaxial along directions x_1 and x_3 (radial and axial

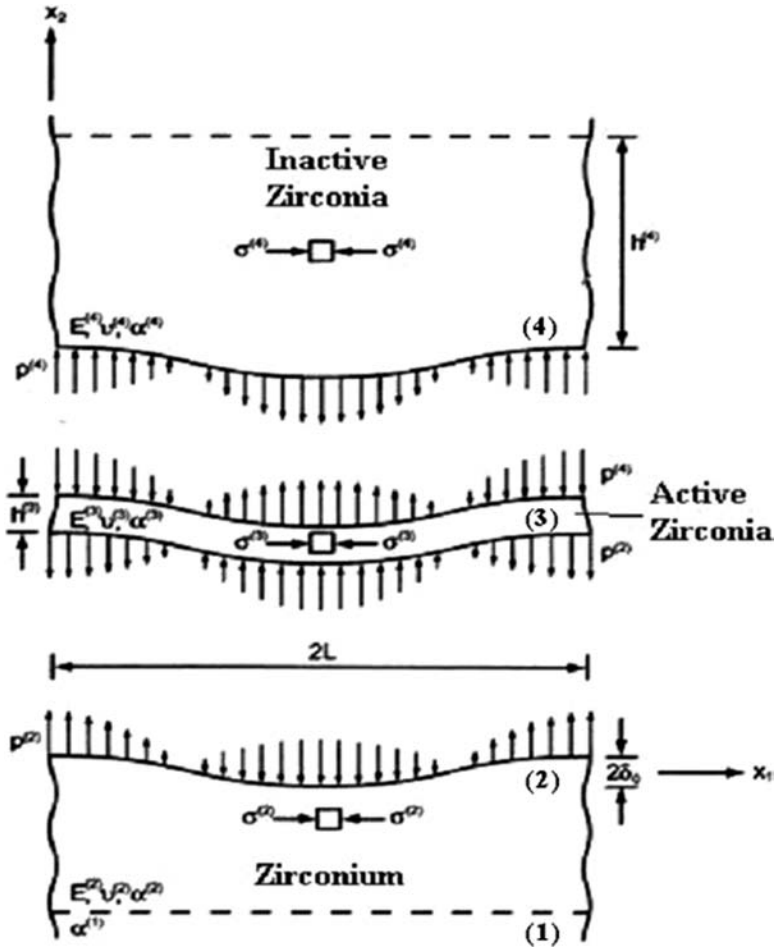


FIG. 12—*Descritption of the mechanical system of Balint and Hutchinson [21,22].*

direction considering a rod). Evolution of undulations ($\Delta\delta$), oxide stresses ($\Delta\sigma_{11}^{(3)}$) and oxide thickness h [3] are calculated by solving the following non linear differential equation system

$$\dot{Y}(t) = F(Y,t) \text{ with } Y = (\delta, h^{(3)}, \sigma_{11}^{(3)}) \tag{10}$$

where F is a function of material properties detailed in Refs [24,25], Y is a vector used to store the time solved variables and the "dot" denotes the first order time differentiation.

All these variables depend on the creep properties ($\epsilon_0^{\bullet(2)}$, $\sigma_0^{(2)}$ and $n^{(2)}$) respectively deformation rate,reference stress and Norton coefficient) of the layer (2). Pressure $p^{(2)}$ is computed from all of the variables after resolution.

TABLE 6—*Comparing undulations and stress relaxation characteristics of SRA and RXA alloys.*

Zircaloy-4	SRA		RXA	
n	2.61	2.61	4.7	4.7
$\dot{\varepsilon_0}(s^{-1})$	$6.60.10^{-4}$	$6.60.10^{-7}$	$6.60.10^{-4}$	$6.60.10^{-7}$
σ_0(MPa)	230	130	100	72
$\delta_0 + \delta$ (m)	$38.5.10^{-9}$	$30.3.10^{-9}$	$37.90.10^{-9}$	$30.9.10^{-9}$
$\sigma_{11}^{(3)}$(GPa)	−1.44	−1.98	−1.48	−1.95

Application to Zirconium/Zirconia System—The following modifications are needed to use the model for zirconium-zirconia system:

- Suppression of the first part (1) unnecessary in that case while part (2) will be attributed to zirconium and parts 3 and 4 to zirconia.
- Dummy separation of zirconia layer into two parts that allows the application of Von Karman plate theory in order to solve the ODE system in the undulating part (3) further called the active part in terms of undulations sensitivity. Indeed, for the Von Karman theory to be applicable, the $h^{(3)}/L$ ratio should be small: around 0.2 or less. Part (4) will be called the inactive part. Total oxide thickness is given by $h^{(3)} + h^{(4)}$.
- Due to the relatively "low" corrosion temperatures (360°C) elastic response is assumed for zirconia rather than viscoplastic one. Creep resulting from small oxide grain size could be taken into account at a later stage of modelling.

Experimentally breakaway occurs at oxide thickness around 2 μm. A 2-μm thick zirconia scale with a *purely sinusoidal* metal-oxide interface is assumed in the model. Undulations are assumed to have a 1 μm wavelength. So, considering the previous Von Karman theory limitation, the maximum active-part thickness will be 200 nm.

Analysing oxide breaking requires determination of stresses in the inactive part (4). This is done by solving the problem of an elastic band thick of $h^{(4)}$ along x_2-axis, infinite along the x_1-axis, submitted to a sinusoidal pressure $p^{(4)}$ on its lower face (see Fig. 12). Such a problem is solved through the stress function or Airy function [26]. This stress function is as follows

$$\Phi(x,y) = \cos(\alpha x)[C_1\ \cosh(\alpha y) + C_2 \sinh(\alpha y) + C_3 y \cosh(\alpha y) + C_4 y \sinh(\alpha y)] \quad (11)$$

With $\alpha = \Pi/L$ and *C1, C2, C3* and *C4* are constants

The following boundary conditions allow to determine the C_i constants:

- On the undulated lower face:
  $\sigma_{yy}(x,0) = -p^{(4)}\cos(\pi/Lx), \forall x$
  $\tau_{xy}(x,0) = 0, \forall x$
- On the straight, free, upper face:
  $\tau_{yy}(x,h^{(4)}) = 0, \forall x$
  $\tau_{xy}(x,h^{(4)}) = 0, \forall x$

Normal and shear stresses can be derived from the stress function

$$\sigma_{xx} = \frac{\partial^2 \Phi}{\partial^2 y} \quad \sigma_{yy} = \frac{\partial^2 \Phi}{\partial^2 x} \quad \tau_{xy} = \frac{\partial^2 \Phi}{\partial x \partial y} \quad (12) \tag{12}$$

The pressure $p^{(4)}$ at the dummy interface is obtained from elastic band deformations (ε_{yy}) and the undulation amplitudes (δ)

$$\delta = 1/2 \int_0^{h^{(4)}} (\varepsilon_{yy}(0,y) - \varepsilon_{yy}(L,y)) dy \tag{13}$$

Assuming a plane strain state, ε_{yy} is given by

$$\varepsilon_{yy} = \frac{1 + v^{Ox}}{E} [(1 - v^{Ox})\sigma_{yy} - v^{Ox}(\sigma_{xx} + \sigma_{11}^{(3)})] \tag{14}$$

In that equation $\sigma_{11}^{(3)}$is the compressive stress due to the Pilling-Bedworth ratio. It is given by the resolution of the differential equations system in the active zirconia part (3).

Assuming continuity of displacements between parts (3) and (4) [24], the undulation amplitude variation (δ) in the inactive part will be the same as the one calculated in the active part. Thus, $p^{(4)}$ is derived as follows

$$p^{(4)} = \frac{E^{(3)}}{1 - v^{(3)2}} \frac{\pi}{2} \frac{\delta}{L} \left(\frac{\sinh(\alpha h^{(4)}) + \alpha h^{(4)}}{\cosh(\alpha h^{(4)}) - 1} \right) \tag{15}$$

Considering a typical crack length observed near the metal-oxide interface and toughness values characteristic of ceramics, one can basically approximate breaking stress using Griffith criterion

$$K_{IC} = \sigma_{yy} \sqrt{\pi a} \tag{16}$$

where a is the half crack length

Results—For numerical applications, stress relieved (SRA) and recrystallised (RXA) Zircaloy-4 alloys are considered. Their creep properties ($\epsilon_0^{\bullet(2)}$, $\sigma_0^{(2)}$ and $n^{(2)}$) are taken from Refs [27,28]. The Pilling-Bedworth ratio is assumed to be the unique stress source in the oxide. The initial stress is a fixed parameter. It is taken as equal to −2 GPa on the basis of previous works reported in the literature [10,[20]] and previous measurements.

Active Zirconia Part

The undulation amplitude (δ) and oxide compressive stress ($\sigma_{11}^{(3)}$) are followed when considering an oxide thickness smaller than $h^{(3)}$. Table 6 shows that the microstructure affects neither the undulation amplitude nor the oxide stress. However, the creep properties seem to have a significant effect. Increasing the

TABLE 7—*Comparison of pressures at active/inactive zirconia interface for SRA and RXA Zircaloy-4.*

Zircaloy-4	SRA		RXA	
n	2.61	2.61	4.7	4.7
$\dot{\varepsilon_0}$ (s^{-1})	$6.60.10^{-4}$	$6.60.10^{-7}$	$6.60.10^{-4}$	$6.60.10^{-7}$
σ_0 (Mpa)	230	130	100	72
$p^{(4)}$ (Gpa)	12.36	9.72	12.16	9.91

strain rate and/or the reference stress enhance the undulation growth. This can be understood as facilitating creep can render the deformation easier; therefore favouring undulation growth. Evolutions are observed for long term corrosion in autoclaves (Fig. 8 and Ref [15]) but they are not so small.

Inactive Zirconia Part

This part of the oxide is used to analyse oxide cracking at the transition when $h^{(4)}$ equals 1.8 μm for Zircaloy-4. In Table 7 pressure $p^{[4]}$ at the dummy interface in zirconia is computed (using Eq 15).

From this table, it is clear that the calculated pressure values are unrealistically higher than the measured compressive stress in the oxide. Indeed, expected values are of the order of at most 2 GPa.

Such deviations may be due to the isotropic elastic behaviour taken for the inactive oxide part. It is porous and cracked which might induce some kind of plasticity. Furthermore the grain diameter is of such a small size that creep could be considered as an active deformation mechanism. They could also be ascribed to the fact that the mechanical properties used have been measured at a large scale (tensile specimen) whereas what matters in the process is the local behaviour (very near the interface). They could also be found in the unrealistic geometry of the metal oxide interface used in these calculations. It has been taken as periodic whereas it is non periodic [15] and the typical lengths are not of the right order of magnitude. Changing the interface morphology requires a change in the modelling method since the Von Karman theory as applied here might be no longer valid. In fact, the validity of Von Karman theory is limited by the ratio of the undulations height to the wavelength which shall not exceed 0.2.

Finally it should also be stated that the oxide growth is not modelled whereas, stress state in the oxide evolves with time as some measurements indicate (Fig. 11).

In order to analyse the cracking propensity in the oxide scale, stress distributions are needed. An example obtained for Zircaloy-4 in the stress relieved condition is given (Fig. 13). Stress maxima are clearly located just above the interface summits as calculated by Parise *et al.* [10].

Using a simple Griffith criterion Eq 16) and considering the characteristic toughness values of oxides, stress distributions can be analysed. Ceramics usually have toughness values ranging between 2 and 5 $MPa\sqrt{m}$ [29]. Considering a typical crack half-length of 300 nm, the breaking stress in mode I should be

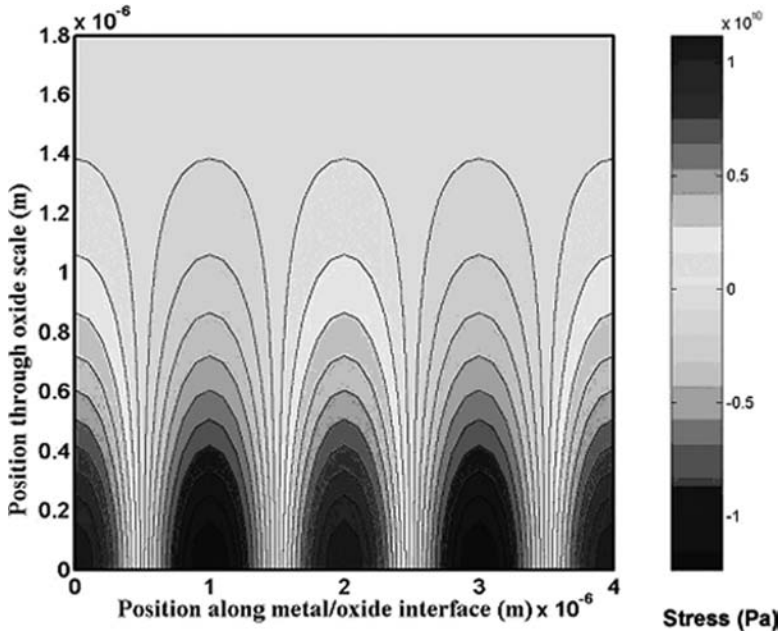


FIG. 13—*Metal/oxide interface normal (σ_{yy}) stress map for SRA ($n = 2{,}61$; $\dot{\varepsilon}_0 = 6{,}6.10^{-4}$ s^{-1}; $\sigma_0 = 230$ MPa).*

between 2 and 5 GPa. These values are much lower than stress values that have been computed near the interface summits. The scale would never keep its mechanical integrity with such stress levels. It shows that the modelling should be developed further. In particular the use of the Von Karman theory for plates should be reconsidered especially for large and high undulations. An obvious way of calculating stresses in the oxide while letting the interface evolves would be to use phase-field modelling [30].

Conclusion and Perspectives

In this paper the effect of Zircaloy-4 microstructure evolution has been presented. The main results show that:

- Transition time is the characteristic parameter of corrosion kinetics that is most sensitive to microstructure variation.
- There is no simple correlation between transition time and classical microstructural characteristics (grain size, precipitate, hardness).
- Undulations of the metal-oxide interface are not affected by microstructural changes on the time scale of the experiment (200 days) but they change on a longer time scale.
- There is a correlation between transition time and compressive hoop stress in the oxide layer. In pre-transition oxides, residual stress level depend on the substrate microstructure. It has been found that the

residual stresses are smaller when the material is recrystallised with small grain size. The transition time seems longest for the samples with the smallest residual stresses in the oxide during pre-transition. An explanation of such a correlation may be found in substrate mechanical properties. Assuming that initial oxide stress is constant whatever the metallurgical state of Zircaloy-4, a "soft" substrate that can release stress by creep will enable to minimise the oxide stresses and would thus delay transition. This hypothesis may be confirmed by measuring the elongation resulting from the oxidation on various substrates.

- Oxide compressive hoop stresses near the metal-oxide interface in SRA Zircaloy-4 increase with corrosion time until the transition where they are released. They re-increase after transition.

A simple model assuming that cracks in the oxide layer appear when the stored elastic energy is equal to a "surface" energy allow us to calculate the order of magnitude of the transition thickness.

A more elaborate model has led to unrealistic high values of the stresses in the oxide layer. Its merit lies in its analytical character. Further developments of modelling should take into account the local mechanical behaviour of oxide and metal, a realistic morphology of the metal-oxide interface and the stress evolution with the oxide growth. The current model shows that all these parameters have strong influences on the final result. Given the fact that transition thicknesses of various alloys are not so different (few hundred nanometres), it shows that the model cannot rely on assumptions that are crude. Further refinements like considering the whole relaxation processes, using FEM calculations to determine stresses in the inactive part and acquiring localised mechanical properties should be considered in the future.

References

[1] Griggs, B., Maffci, H. P., and Shannon, D., "Multiple Rate Transitions in the Aqueous Corrosion of Zircaloy," *J. Electrochem. Soc.*, Vol. 109, 1962, pp. 665–668.

[2] Bryner J. S., "The Cyclic Nature of Corrosion of Zircaloy-4 in 633 K Water," *J. Nucl. Mater.*, Vol. 82, 1979, pp. 84–101.

[3] Schefold, J., Lincot, D., Ambard, A., and Kerrec, O., "The Cyclic Nature of Corrosion of Zr and Zr-Sn in High Temperature Water (633K): A Long Term in Situ Impedance Spectroscopic Study," *J.Electrochem. Soc.*, Vol. 150, 2003, pp. B451–B461.

[4] Yilmazbayhan, A., Motta, A. T., Comstock, R. J., Sabol, G. P., Lai, B., and Cai, Z., "Structure of Zirconium Alloy oxides Formed in Pure Water Studied with Synchrotron Radiation and Optical Microscopy: Relation to Corrosion Rate," *J. Nucl. Mater.*, Vol. 324, 2004, pp. 6–22.

[5] Bouineau, V., Ambard, A., Bénier, G., Pêcheur, D., Godlewski, J., Fayette, L., and Duverneix, T., "ANew Model to Predict the Oxidation Kinetics of Zirconium Alloys in a Pressurized Water Reactor," *J. ASTM Int.*, Vol. 5, Paper No. JAI101312.

[6] Pilling, N. B. and Bedworth, R. E., "The Oxidation of Metals at High Temperatures," *Journal of the Institute of Metals*, Vol. 29, 1923, pp. 529–591.

[7] Roy, C. and Burgess, B., "A Study of the Stress Generated in Zirconia Films During the Oxidation of Zirconium Alloys," *Oxydation of Metals*, Vol. 2, 1970, pp. 235–261.
[8] Evans, H. E., Norfolk, D. J., and Swan, T., "Perturbation of Parabolic Kinetics Resulting From the Accumulation of the Stress in Protective Oxide Layers," *J. Electrochem. Soc.*, Vol. 125, 1978, pp. 1180–1184.
[9] Bossis, P., L. G., Barberis, P., Iltis, X., and Lefebvre, F., "Multi-Scale Characterization of the Metal-Oxide Interface of Zirconium Alloys," *Zirconium in the Nuclear Industry, ASTM-STP* 1354, G. P. Sabol and G. D. Moan, eds., ASTM International West Conshohocken, PA, 2000, pp. 918–945.
[10] Parise, M., Sicardy, O., and Cailletaud, G., "Modelling of the Mechanical Behavior of the Metal-Oxide System During Zr Alloy Oxidation," *J. Nucl. Mater.*, Vol. 256, 1998, pp. 35–46.
[11] Withers, P. J., Preuss, M., Steuwer A., and Pang, J. W., "Methods for Obtaining Strain-Free Lattice Parameter When Using Diffraction to Determine Residual Stress," *J. Appl. Crystallogr.*, Vol. 40, 2007, pp. 891–904.
[12] Touloukian, Y. S., Kirby, R. K., Taylor, R. E., and Lee, T. Y. R., *Thermophysical Properties of Matter: Thermal Expansion – Vol. 13*, Plenum Press, NY, 1975, p. 451.
[13] Tenckhoff, E., "Deformation Mechanisms, Texture and Anisotropy in Zirconium and Zircaloy," *ASTM Spec. Tech. Publ.*, Vol. 966, ASTM International, Philadelphia, PA, 1988.
[14] Thomazet, J., Dalmais, A., Bossis, D., Godlewski, J., Blat, M., and Miquet, A., "The Corrosion of the Alloy M5^{TM}: An Overview," *Proceedings of IAEA Technical Committee Meeting on Behaviour of High Corrosion Resistance Zr-Based Alloys*, Buenos Aires, Oct. 25–28, 2005.
[15] Ly, A., Ambard, A., and Bréchet, Y., "On the Evolution of Zirconium-Alloy/Zirconia Interface Morphology During a Corrosion Experiment in High Temperature Water," J. Nucl. Mater. (submitted).
[16] Nayak, P. R., "Random Process Model of Rough Surfaces," *J. Lubr. Technol.*, Vol. 93, 1971, pp. 398–407.
[17] Longuet-Higgins M. S., "Statistical Properties of an Isotropic Random Surface," *Philos. Trans. R.Soc. London, Ser. A*, Vol. A250, 1957, pp. 157–174.
[18] S-K. Chan, Y. Fang, M. Grimsditch, Z. Li, M. V. Nevitt, W. M. Robertson, and E. S. Zouboulis, "Temperature Dependence of the Elastic Moduli of Monoclinic Zirconia," *Journal of the American Ceramic Society*, Vol. 74, 1991, pp. 1742–1744.
[19] Parise, M., 1996, "Mécanismes de Corrosion des Alliages de Zirconium: Etude des Cinétiques Initiales d'Oxydation et du Comportement Mécanique du Système Métal-Oxyde," *Ph.D. thesis*, Ecole Nationale Supérieure des Mines de Paris, Paris.
[20] Petigny, N., Barberis, P., Lemaignan C., Valot Ch., and Lallemant, M., "In Situ XRD Analysis of the Oxide Layers Formed by Oxidation at 743K on Zircaloy-4 and Zr-1NbO," *J. Nucl. Mater.*, Vol. 280, 2000, pp. 318–330.
[21] Ni, N., Lozano-Perez, S., Jenkins, M. L., English, C., Smith, G. D. W., Sykes, J. M., and Grovenor, C. R. M, "Porosity in Oxides on Zirconium Fuel Cladding Alloys, and its Importance in Controlling Oxidation Rates," *Scr. Mater.*, Vol. 62, 2010, pp. 564–567.
[22] Eshelby, J., "The Determination of the Elastic Field of an Ellipsoidal Inclusion, and Related Problems," *Proc. R. Soc. London*, Vol. A241, 1957, pp. 376–396.
[23] Lamy, M., Ambard, A., Bréchet, Y., and Kerrec, O., "Coupling Corrosion and Plasticity: The Example of Zircaloy-4," *EUROMAT*, Rimini, Italy, June 10–14, 2001, Federation of European Materials Societies, Associazione Italiana di Metallurgia, Paper No. 747.

[24] Balint, D. S., Hutchinson, J. W., "Undulation Instability of a Compressed Elastic Film on a Nonlinear Creeping Substrate," *Acta Mater.*, Vol. 51, 2003, pp. 3965–3983.
[25] Balint, D. S. and Hutchinson, J. W., "An Analytical Model of Rumpling in Thermal Barrier Coatings," *J. Mech. Phys. Solids*, Vol. 53, 2005, pp. 949–973.
[26] Timoshenko, S., and Goodier, J. N., *Théorie de l'élasticité*, Librairie Polytechnique Ch. Béranger, Paris, 1961, p. 28.
[27] Robinet, P., 1995, Etude Expérimentale et Modélisation du Comportement Viscoplastique Anisotrope du Zircaloy-4 Dans Deux états Métallurgiques, Ph.D. thesis, Université de Franche-Comté.
[28] Delobelle, P., Robinet, P., Geyer, P., and Bouffioux, P., "A Model to Describe the Anisotropic Viscoplastic Behaviour of Zircaloy-4 Tubes," *J. Nucl. Mater.*, Vol. 238, 1996, pp. 135–162.
[29] Hauffe, K., *Oxidation of Metals*, Plenum Press, NY, 1965.
[30] Ammar, K., 2010, "Modelling and Simulation of Phase Transformation-Mechanics Coupling Using a Phase Field Method," Ph.D. thesis, Ecole nationale supérieure des mines de Paris.

IN PILE BEHAVIOUR

Reprinted from JAI, Vol. 7, No. 7
doi:10.1520/JAI102955
Available online at www.astm.org/JAI

F. Garzarolli,[1] *B. Cox,*[2] *and P. Rudling*[1]

Optimization of Zry-2 for High Burnups

ABSTRACT: Two major high burnup boiling water reactor (BWR) issues today are (1) shadow corrosion (hydrogen) induced fuel channel bowing and (2) accelerated hydrogen pickup fraction, HPUF of fuel claddings. Both these issues occur only at high burnups. Several factors impact the tendency for fuel channel bowing, the most recent one that is responsible for the current issue of difficulties to insert control rods is due to differences in hydrogen pickup of the different facing surfaces of the fuel channel. Accelerated HPUF of fuel cladding at high burnups may result in reducing fuel clad integrity during reactivity initiated accidents and cask drop accident during dry storage conditions. Some fuel vendors are now shifting from Zry-2 to Zry-4 in structural components to mitigate the fuel channel bowing issue. All BWR fuel vendors are also looking into new alloys (other than Zry-2 and Zry-4) for structural materials. However, one should keep in mind that it is imperative that a mechanistic understanding of the accelerated HPUF is developed to understand the accelerated HPUF tendency in Zry-2. Without such an understanding, it is not possible to rule out that accelerated HPUF can occur also for the new alloys under certain in-pile conditions. This paper summarizes the state of knowledge on the accelerated HPUF and provides suggestions on (1) the mechanism responsible for the accelerated HPUF of Zry-2 at high burnups and (2) how the currently used Zry-2 material for fuel rods and structural materials in BWRs can be modified to delay the accelerated HPUF at high burnups.

KEYWORDS: zirconium alloys, zirclaoy-2, zircaloy-4, corrosion, corrosion acceleration, hydriding, second phase particles, high burnup

Manuscript received January 8, 2010; accepted for publication May 3, 2010; published online July 2010.
[1] ANT International, Krongjutarvägen 2C, SE-730 50 Skultuna, Sweden.
[2] ANT International, Birch Street 89 Deep River, PO Box 1000, ON K0J1P0 Canada.

Cite as: Garzarolli, F., Cox, B. and Rudling, P., "Optimization of Zry-2 for High Burnups," *J. ASTM Intl.*, Vol. 7, No. 7. doi:10.1520/JAI102955.

Copyright © 2011 by ASTM International, 100 Barr Harbor Drive, PO Box C700, West Conshohocken, PA 19428-2959.

Introduction

Zry-2 was originally selected for boiling water reactor (BWR) fuel rod claddings, whereas for structural components of BWRs, Zry-4 and Zry-2 have been applied. Due to the relatively low operation temperature, the normal (uniform) corrosion rate of Zry-2/4 is rather low. The uniform oxide thickness is $< 20\,\mu$m, and the corrosion hydrogen pickup (HPU) has historically been rather low (typically < 100 ppm) even at high burnups. However, there are different types of excessive corrosion that may occur under certain circumstances. The boundary condition for the operation of BWR fuel rods such as, the exposure time, burnup, fuel duty, and water chemistry have changed over the years. The changing boundary conditions made it necessary to optimize the material condition in several steps.

In the early days, the manufacturing process did not include a billet beta-quench but process steps in the $(\alpha + \beta)$-phase field. This resulted in rather large intermetallic precipitates (second phase particle (SPP)). Components with such large SPP showed severe nodular corrosion (up to $250\,\mu$m at a burnup of 35 MWd/kgU) and severe spalling, e.g., Refs [1 and 2], To avoid excessive nodular corrosion and oxide spalling, a β-quenching step was introduced after the hot forging at the billet stage, and the process temperatures during the subsequent fabrication steps was limited to the α phase field.

Originally, contrary to structural components that were fully recrystallized (RX), the fuel rod cladding material was used in cold worked and stress relieved (CWSR) condition. A relatively high room temperature (RT)–yield strength (YS) was required to fulfill the ASME pressure vessel criterion.

In 1971, when pellet cladding interaction failures had been recognized, general electric (GE) (today global nuclear fuel (GNF)) pointed out that CWSR claddings showed a much higher variability and lower minimum ductility than fully RX claddings. In 1973 GE changed thus to RX claddings. Due to the lower YS of RX claddings, GE increased the wall thickness from 0.81 to 0.9 mm (for improved 7×7 design) [3]. Most of the other fuel vendors followed this change from CWSR to RX fuel claddings later on, although at least partly because of other reasons (the lower irradiation growth of RX than that of CWSR Zircaloy was one of the reasons) in the years up to 1983. Only AREVA, United States, still applies the CWSR condition for the Zry-2 fuel rod claddings.

In the early 1980s, chalk river unidentified deposits (CRUD) induced localized corrosion defects were observed in several BWRs having admiralty brass condensers and a filter-demineralizer condensate clean up system, resulting in rather high Cu contents in the reactor water. The evaluation of these defects showed that the root cause of the failures was heavy Cu rich CRUD, which deposited only on fuel rods that experienced a nodular corrosion coverage of $> 90\,\%$ [4]. To counteract these defects, *the nodular corrosion resistance was improved by optimization of the SPP size by GE* (by a tube shell heat treatment) and later in process heat treatment) [5]. Later on, also the other suppliers optimized their SPP size (ABB: L*å*g Korrosion (LK)2 and LK3; Siemens: low temperature process and particle growth parameter+).

In 1988, Graham et al. [6] proposed a controlled composition for Zircaloy-2 (CC Zry-2) to optimize the corrosion behaviour of Zry-2 further. In detail, they *proposed to restrict the Ni content of Zry-2 to the upper half of the ASTM specification to 0.058–0.078 % Ni*. Huang et al. [7] pointed out that the increased Ni content, which resulted in reduced corrosion in their laboratory tests, did not affect the HPU fraction (HPUF) at 360 and 420°C. The HPUF was between 53 % and 68 %, independent of the actual Ni content within the ASTM specification range.

State of Knowledge on the Acceleration of Corrosion and Hydrogen Pickup of Zry-2 at High Burnups

In 1995, Huang et al. [8] *reported* that after irradiation of *Zry-2 coupons with fine SPP* in a commercial BWR, *corrosion as well as the HPUF increased at high burnups* due to the irradiation induced SPP dissolution. This corrosion rate and HPUF increase was more pronounced for material with small SPP size (in the non-irradiated material). Also the "annealing-parameter," defined as $A = \Sigma t_i \exp(-40\,000/T_i)$, with t_i and T_i being the time and temperatures of the different annealing/fabrication steps, was shown to have a major impact on the corrosion rate and HPUF increase.

The reported results can be seen in Table 1.

In the late 1990s, Sihver and Hallstadius [9], Limbäck et al. [10], and Tägtström et al. [11] reported that uniform oxide formation and HPU of LK2 and LK2+ fuel cladding of ABB (today Westinghouse) accelerated at higher burnups, while the LK3 material was much less affected (Fig. 1). The reason for the different behaviours of the three different materials was proposed to be the initial SPP size, which is very small for LK2 (low *A*-parameter) and largest for LK3. The authors argued that a minimum SPP size is necessary to form a protective barrier layer, and if the SPPs are too small, e.g., due to fast dissolution of initially small SPPs, the barrier layer protectiveness will deteriorate, resulting in

TABLE 1—*Acceleration of corrosion and HPU after irradiation of Zry-2 with fine SPP sizes to high fluences. A fluence of 8.5×10^{21} corresponds to a burnup of about 40 MWd/kgU [8].*

Specimen	*A*-Parameter(h)	Fluence(n/cm^2), $E > 1$ MeV	Average SPP Size(nm)	Weight Gain(mg/dm^2)	HPUF(%)
3R	1.45×10^{-19}	0	42		
2R	7.40×10^{-20}	0	32		
1R	3.46×10^{-21}	0	25		
3R	1.45×10^{-19}	2.5×10^{21}		40	2
2R	7.40×10^{-20}	2.5×10^{21}		53	3
1R	3.46×10^{-21}	2.5×10^{21}		45	2
3R	1.45×10^{-19}	8.5×10^{21}		112	26
2R	7.40×10^{-20}	8.5×10^{21}		204	35
1R	3.46×10^{-21}	8.5×10^{21}		294	25

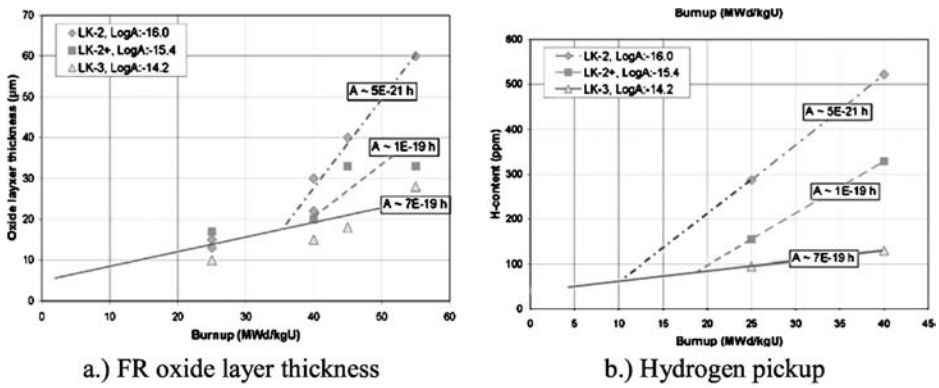


FIG. 1—*Late increased corrosion of LK Zry-2 claddings in Forsmark-3; data from Refs [9–11].*

increased corrosion rate. In addition, the Fe content of LK2 was rather low (about 0.11 %) and has been increased for LK2+ and LK3 to about 0.18 %. This Fe content increase may also play a role in delaying the accelerated corrosion and HPUF since increased Fe content increases SPP size with constant manufacturing process.

In 2001–2005, it became evident that HPUF increases above 50 MWd/kgU also in Japanese Step II [12] and Swedish LK3 [13] Zry-2 claddings (Fig. 2).

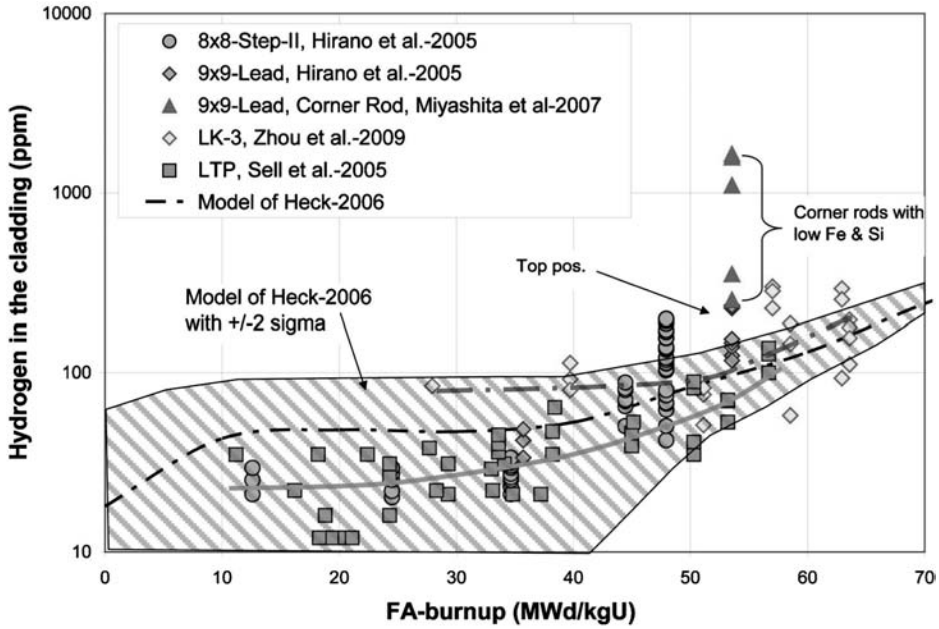


FIG. 2—*HPU of Zry-2 fuel rod claddings in BWR at high burnups [14–18].*

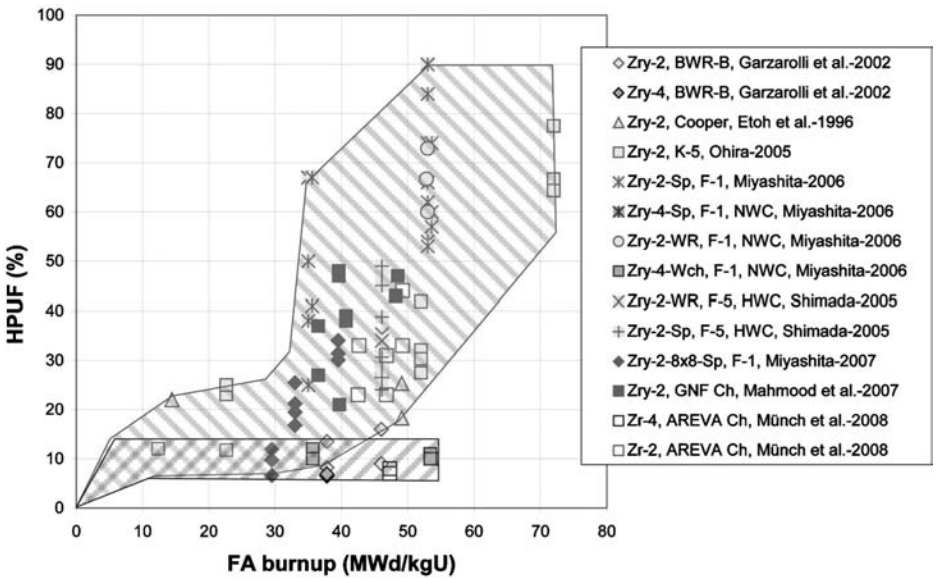


FIG. 3—*HPU of Zry-2 structural components in BWR at high burnups [15,19–25].*

Furthermore, in 2005–2008, it became evident that structural components fabricated from Zry-2 also experience a large acceleration of HPUF even at lower burnups (> 30–40 MWd/kgU) than the claddings, e.g., Refs [15, 19–22] (Fig. 3). Figure 3 clearly indicates that Zry-4 does not exhibit an acceleration of HPUF as observed for Zry-2. Zry-4, which is free of Ni, however, exhibits in most cases some nodular corrosion at burnups in excess of 20 MWd/kgU, which also contributes to the HPU. Actually, the hydrogen content in Zry-4 structural components may be significantly higher than that in Zry-2 structural components at least up to burnups of 30 MWd/kgU.

Since 2004 significant control blade (CB) friction was found in some BWRs with GNF Zry-2 fuel channels [26]. Investigations showed that the fuel channel bow is related to CB induced shadow corrosion (bow towards the CB) and manifests at high burnups. This phenomenon was not seen before when control cell core operation was done with high burnup fuel in the control cells. Increasing cycle length and power density made it necessary to increase the fraction of fresh reload assemblies, which made it necessary to locate a substantial amount of fresh fuel in control cell positions. The Zry-2 shadow corrosion induced bow occurred only at high burnups (> 30 MWd/kgU). The magnitude of Zry-2 shadow corrosion induced bow correlated with the insertion depth and the time of a CB during the early channel life. Post irradiation examinations of coupons from affected high burnups Zry-2 channels have shown thicker shadow corrosion oxide layers and higher HPU in the channel sections facing the control rod than in other sections not facing the control rod. The fact that the shadow corrosion forms at low burnup and that HPU is usually lower in areas with shadow corrosion formed at low burnup but results in Zry-2 channel bowing only at

high burnups indicates clearly that the acceleration of HPUF at high burnups is more pronounced in areas with thick porous shadow corrosion. Zry-4 channels have not shown such shadow corrosion induced channel bow, confirming that Zry-4 does not suffer from a late accelerated HPU [22].

Another important effect on the accelerated HPU at high burnups is the water chemistry. Limbäck et al. [27] summarized the performance experience for the cladding materials LK2, LK2+, and LK3, as deduced from Swedish BWRs and Kernkraftwerk Leibstadt, Leibstadt Nuclear Power Plant (KKL). These cladding materials differ in the SPP size. LK2 has the finest SPP size, LK2+ has a somewhat larger, and LK3 has the largest SPP size. The reported data indicate the lowest corrosion rate as well as the lowest scatter in corrosion data for LK3. The material LK2 appears to have the thickest oxide layers and the largest scatter in oxide layer thickness at high burnups. LK3 was furthermore reported to be superior with regard to HPU. Fuel rod elongation data indicate lower HPU for fuel rods with LK3 cladding than for the other cladding variants. Rod elongation is driven by a combination of irradiation growth and creep and HPU of the cladding. Contrary to the above conclusions, a different ranking was observed for the various LK variants in an irradiation experiment, performed in the time period of 1998–2000 in Kernkraftwerk Brunsbuttel, Brunsbüttel Nuclear Power Station (KKB) [28]. In this reactor, LK3 showed a thicker oxide than LK2+. At a burnup of 20 MWd/kgU, furthermore, no increased rod elongation was observed with LK2 in KKB up to 47 MWd/kgU as found in Swedish BWRs and KKL. The five cycle fuel rods measured in 1999 and the one, two, and three cycle fuel rods measured in 1998 all exhibited a low rod elongation, similar to the elongation of LK3. The rather low rod elongation values indicate that the HPU rate of LK2 cladding at high burnups is low in KKB, much lower than in the other reactors analyzed by [27]. *The different behaviours may be related to the difference of the water chemistry in the different reactors. The reactors can be separated into two groups based upon the water chemistry characteristics.*

- The first group is characterised by plants with very low Cu content. Water chemistry data for KKL were given in Ref [29]. According to these data, the coolant had a low RT electrical conductivity ($< 0.1\ \mu$S/cm) and low Fe and Cu contents but a significant Zn content. The Swedish BWRs also have low electrical coolant conductivities, low Fe and Cu contents, and at that time low Zn content.
- The second group is characterised by plants with medium Cu content. According to Ref [30], the conductivity in KKB was in the interesting time period of 0.11–0.16 μS/cm, Cu content of 5–20 parts per billion (ppb), and the Zn content of 2–10 ppb.

It is noteworthy that BWRs, operating with admiralty brass condensers and some Cu in the reactor water (thus, included in the second group mentioned above), all show lower tendency for HPU in Zry-2. Data from coupon irradiation in German BWRs, with medium Cu and low to medium Fe content and low to medium RT electrical conductivity, all show a relatively low HPUF (6–16 %) in spite of the rather high burnup (1372–1693 effective full power days ≈ 7.6–9.3×10^{21} n/cm^2 $\approx$ 38–46 MWd/kgU); see data points in Fig. 3 related to references "Zry-2, BWR-B, [23]" and "Zry-4, BWR-B, [23]." These

HPUF values of Zry-2 are furthermore the same as for Zry-4 and below the large scatter band for Zry-2 HPUF shown in Fig. 3. Also, the fuel rod cladding hydriding data generated in German BWRs, reported in Ref [17] included in Fig. 2, are lower than other data. So it is very likely that coolant elements such as Cu in the reactor water delays or even prevents the acceleration of HPU at high burnups.

Possible Reasons of the Acceleration of Hydrogen Pickup at High Burnups

This section has the objective to explain the mechanism behind the observed HPUF acceleration at high burnups. Knowledge of this mechanism is necessary to enable the reduction of such accelerated HPU at high burnups.

As will be pointed out in more detail later, Ni seems to play an important role for the accelerated HPU at high burnups. Contrary to Sn, which is soluble in the Zr matrix in the interesting range up to 1.5 %, the transition elements Fe, Cr, and Ni have a very low solubility in Zr metal and precipitate as $Zr(FeCr)_2$ and $Zr_2(FeNi)$ SPPs. There are many studies that show that SPPs dissolve in the metal under irradiation at the typical BWR operation temperature of 280–300°C, e.g., Refs [31–33]. Under irradiation at 280–300°C, the $Zr(FeCr)_2$ Laves phase becomes amorphous, loses most of its Fe, and becomes almost fully dissolved at a fast fluence of $> 1 \times 10^{22}$ n/cm^2 (corresponding to a burnup of about 50 MWd/kgU). The $Zr_2(FeNi)$-Zintel phase remains crystalline but loses most of its Fe and Ni and also becomes almost fully dissolved at $> 1 \times 10^{22}$ n/cm^2. This means that at a fast fluence of $> 1 \times 10^{22}$ n/cm^2, most of the Fe and Ni are in forced solution in the Zry metal matrix. Certainly, the burnup where most of the SPP are dissolved depends on the initial SPP size. For material lots with very fine SPPs, as in the case of LK2, an almost fully dissolution may occur already at burnups of 30 MWd/kgU [34]. The SPP dissolution behaviour depends on the temperature. In pressurised water reactor (PWR) fuel rod claddings, the temperature is so much higher that no or only very little dissolution occurs, e.g., Ref [35].

The HPUF should be governed mainly by the two following aspects.

- Since HPUF is determined by the cathodic reaction and the oxide thickness by the anodic reaction, the galvanic cell will control the whole process as a function of time. Cathodic and anodic areas will vary as a function of time and the variations in the effective areas of anodes and cathodes, which will change as a function of intermetallic corrosion and corrosion film formation. Unfortunately, measurements of these galvanic potentials of the different components of the system and the "effective" sizes of all the cathodes and anodes are largely missing.
- The other aspect is the question how H can enter into the metal since there is no reliable evidence for H atom diffusion through the ZrO_2 lattice [36,37]. Since the barrier layer of the oxide films is usually imperfect and probably contains a few flaws that penetrate right through to the oxide/metal interface, these oxide flaws are a probable route for H uptake [38]. Another possibility, often proposed, is that SPP bridging the barrier layer may act as windows, e.g., Refs [39–41]. However,

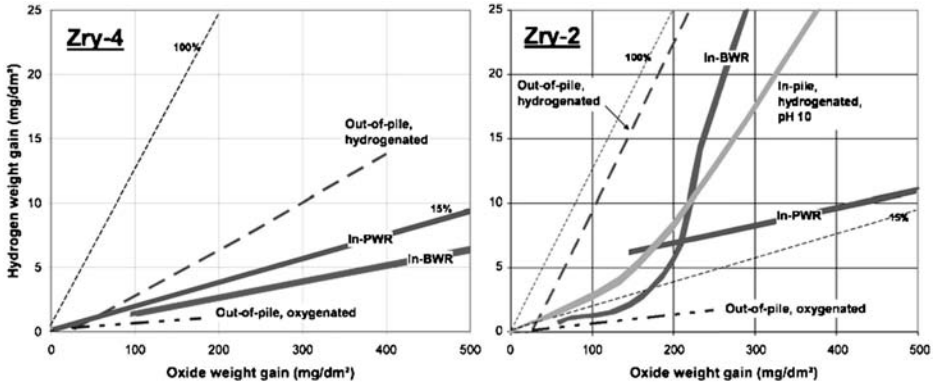


FIG. 4—*Time averaged HPUF of Zry-2 and Zry-4 in different environments; data from Refs [43–45].*

stainless steel particles embedded in the surface of Zry-4 guide tubes and covered with Ni were only able to pickup catalytic hydrogen[3] from the coolant during start up and only if these particles were not oxidized [42]. Thus, a hydrogen window of SPP bridging the barrier layer can only occur for SPPs that are not oxidized at the outer oxide barrier side.

The acceleration of the HPUF in BWRs at high burnups is seen only for Zircaloy-2 and not for Zircaloy-4. This indicates that Ni may play an important role for the HPUF acceleration (since Ni is contained in Zry-2 but not in Zry-4). In out-of-pile tests, high HPUF was only reported for oxygen free hydrogenated environments and again only for Zry-2, as can be seen from Fig. 4.

An acceleration of HPUF of Zry-2 is also reported in-pile at high burnups in hydrogenated environments without boric acid additions and rather low temperatures when oxide thickness exceeds 10–15 μm, e.g., Ref [43], and when the SPPs are largely dissolved by neutron irradiation. No acceleration of HPU is observed for Zry-2 in PWRs, which operate with boric acid (boric acid, contrary to LiOH, has too large molecules to enter into the porous Zr oxide layer; thus a *p*H gradient between the porous oxide and coolant will be established). Furthermore, PWR cladding temperatures are so high that a significant SPP dissolution may not occur.

Figure 5 shows how HPUF of Zircaloy varies with the corrosion conditions and the reduction-oxidation reaction (REDOX) potential. From this figure, the following key conclusions can be obtained.

- In out-of-pile oxygen, free hydrogenated water (REDOX potential of about −800 mV), Zry-2 HPUF is increased at medium oxide thickness values (after a rate transition of $> 2\,\mu$m). In this environment, the Ni in the Zintel SPP phase should be not oxidized (the REDOX is below the oxidation potential of Ni; see arrow in Fig. 5) and may bridge the barrier

[3] Pickup of hydrogen from the hydrogen molecules added to the coolant.

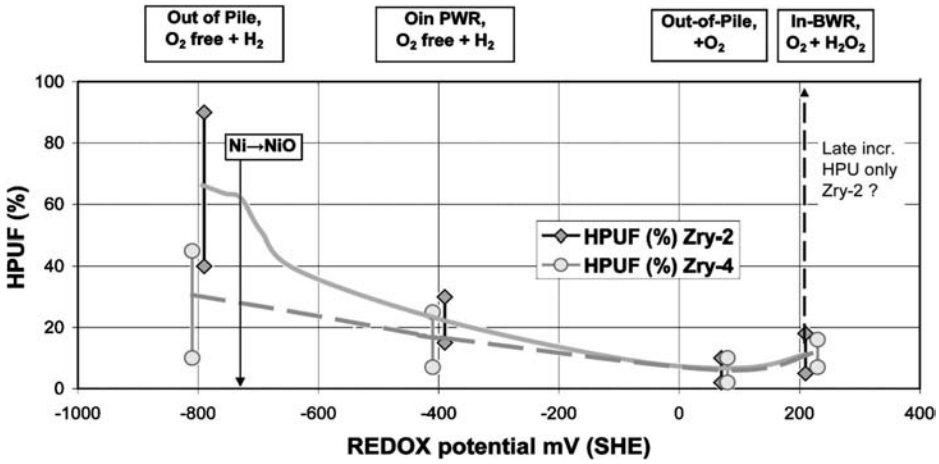


FIG. 5—*HPUF (in percent) and the effect of SPP size on increased corrosion phenomena in different high temperature water environments as a function of varying REDOX potential.*

layer and form a path for the corrosion hydrogen to enter the metal below the oxide layer.

- If oxygen is contained in the water, even in very small quantities, the REDOX potential increases and HPUF of Zry-2 coupons decreases significantly and becomes similar to that of Zry-4, which is clearly shown by the fact that in many corrosion tests in alleged oxygen free environments, no or only a very small difference was found between Zry-2 and Zry-4. Figure 5 shows that oxygen free hydrogenated water out-of-pile is the only environment in which Ni can be in metallic state at the oxide/water interface, while in the other environments, NiO should exist.
- If the Zr–Fe–Ni SPPs contain metallic Ni throughout the whole SPP, even a catalytic pickup of hydrogen from the coolant could be possible.
- In case of BWR conditions Ni could only remain metallic on the surface of the barrier layer if the REDOX potential in the outer porous would be significantly reduced, e.g., by corrosion hydrogen, radiolysis, and other processes. This reduction of corrosion potential could only occur if the bulk coolant (with high REDOX potential) is hindered to mix with the local environment at the barrier layer oxide/water interface (with low REDOX potential). Such hindrance can occur if the outer porous part of the oxide layer contains only very small pores and the total oxide thickness reaches a certain minimum value, which may happen at high burnups.

The position, where alloying elements oxidize in the Zr oxide layer, should be determined by the oxygen partial pressure within it. Oxidation is expected when the equilibrium oxygen pressure for the metal/oxide reaction of the alloying element is exceeded (Fig. 6). Cr should remain metallic only in the innermost part of the oxide barrier layer. Fe, Sn, and Ni should remain metallic over

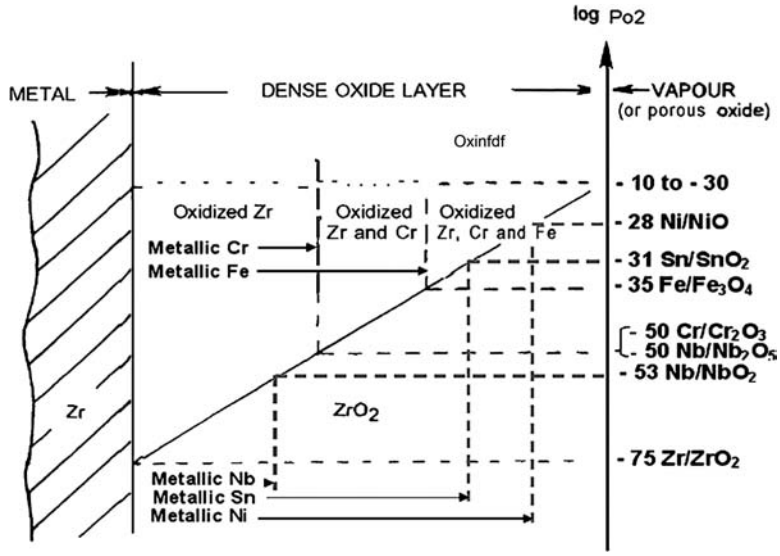


FIG. 6—*Stability domain of Zr, Fe, Cr, Ni, and Sn at the metallic state in the dense oxide layer versus the distance from the metal-oxide interface and corresponding value of the oxygen partial pressure, from Ref [46], modified.*

a major part of the barrier layer. Ni under oxygen free hydrogenated conditions may remain metallic even at the outer surface of the barrier layer. The oxygen potential at the outer surface is lowest under oxygen free out-reactor conditions, low in PWR, and highest under oxygenated water conditions in BWR. Thus, the fraction of the oxide layer in which the alloying elements exist still in metallic form should be different in the different environments.

During out-of-pile oxidation of zirconium alloys in oxygen free water and steam, most SPPs remain unoxidized when the Zr matrix around them oxidizes. The SPPs eventually oxidize later as their distance to the metal-oxide interface continues to grow. During the oxidation phase of the SPP, some of the alloying elements from the SPP may diffuse into the bulk of the oxide and change its local crystallography, but the diffusion distance is extremely small [47] due to the low thermal diffusion rate of the transition elements within the oxide.

The relatively noble Sn, which is uniformly distributed in the metal matrix, migrates to the ZrO_2 crystallite boundaries at the metal/oxide interface, forming here a thin Sn and later SnO_2 film or small crystals [48]. These authors showed that the max. Sn content at the oxide crystallite boundary is higher ($\leq 6\,\%$) in the oxide on Zry-4 with 1.4 % Sn than in a similar alloy with 0.65 % Sn ($\leq 3.8\,\%$ Sn). When after irradiation Fe and Ni are in forced Zr-alloy metal solution, both elements will also very likely concentrate at the oxide crystallite boundaries in the ZrO_2 film. The diffusion of these two species in hexagonal closed packed structure Zr metal is several orders higher than that of Sn, e.g., Ref [49]. Thus, their migration to the oxide crystallite boundaries should be even more pronounced than that of Sn. Consequently, metallic Fe–Ni bands should exist at oxide grain boundaries

at least in the inner part of the barrier layer when a highly irradiated Zry-2 matrix oxidizes. These metallic bands may oxidize or remain at least to some fraction metallic at the outer surface of the oxide barrier layer, depending on the REDOX potential at this position. Fe will always oxidize in a water environment, but Ni may stay metallic if the environment is hydrogenated and free of oxygen.

As already mentioned, a much higher HPUF was found for Zry-2 than for the Ni free Zry-2 and Zry-4 in out-of-pile tests in oxygen free hydrogenated water and steam, and under certain conditions, HPUF values close or even above 100 % could be reached, e.g., Ref [44]. The high HPUF very likely needs Zintel phase SPP that bridges the barrier layer. In case of the reported out-of-pile tests, e.g., Ref [44], the size of the SPP was very likely rather large. Unfortunately, no HPUF data from out-of-pile corrosion tests in fully oxygen free environments have been published for Zry-2 lots with widely varying SPP sizes. But it can be suggested that small SPPs typical for modern BWR claddings may not bridge the barrier layer and may thus not lead to an increased HPUF in out-of-pile tests. However, Ni rich metallic bands at the oxide grain boundaries of highly irradiated Zry-2 could well act as a path for hydrogen to enter the metal, as long as they are not fully oxidized at the outer surface of the barrier layer.

The microstructural differences in the oxide layer of BWR claddings with rather fine SPP are schematically shown in Fig. 7 for low and high burnups.

Figure 7(*a*) shows schematically the situation at low burnup with low corrosion rate and low HPUF. All SPPs in the Zry-2 matrix are in metallic form, and essentially no dissolution of the SPPs in the Zry-2 matrix has occurred. However, the SPPs incorporated in the growing oxide are slowly oxidized. The inner part of the columnar oxide at the metal/oxide interface constitutes the "barrier layer." The corrosion process is limited by the O^{2-} diffusion through the barrier layer. The small fraction of corrosion hydrogen is suggested to be picked up by the Zry-2 material through tiny defects in the barrier layer or other imperfections.

Figure 7(*b*) shows the situation at higher burnup when all the SPPs have been dissolved. Water molecules can easily penetrate the outer part of the oxide arriving at the barrier layer at which it dissociates into O^{2-} and H^{+}. The O^{2-} diffusion still occurs through the barrier layer with significant thickness, resulting in a moderate corrosion rate. The H^{+} is reduced at the outer part of the barrier layer by the electrons released from the ionization of the Zr atoms into Zr^{4+} at the metal/oxide interface. Due to the dissolution of the SPPs, it is hypothesized that Ni and Fe in solution are concentrated at the oxide grain boundaries (shown in Fig. 7(*b*) as red bands in the barrier layers). If the Ni/Fe ratio is high enough in the grain boundary and the oxidation potential at the outer part of the barrier layer is low enough, the Ni/Fe band may be metallic up to the interface to the porous layer and form a freeway of hydrogen transport into the Zry-2 matrix, thus resulting in a dramatic increase in HPUF.

As already pointed out, Ni could remain metallic on the surface of the barrier layer in case of BWR conditions only at high burnups if the outer porous part of the oxide layer has reached a significant thickness and the pores are very fine. At such conditions, an environment with high hydrogen concentration from the corrosion process can build up in the oxide. Under such circumstances, a potential gradient must exist over the porous outer part of the oxide

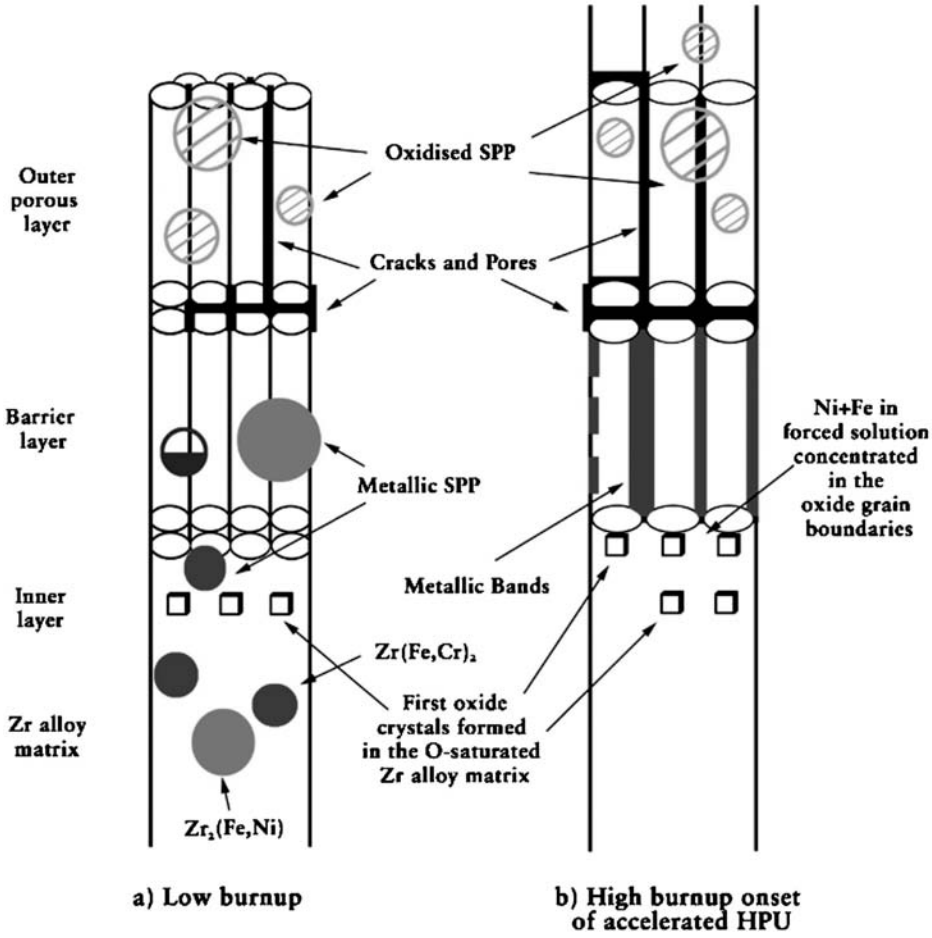


FIG. 7—*Schematics showing the material microstructure at (a) low burnup with low HPUF and (b) high burnup with high HPUF.*

(more positive at the outer part of the porous oxide), which should reduce the concentration of negatively charged ions, such as, e.g., the radiolytic product HO_2^-, at the inner part of the porous oxide layer. At the same time, the potential gradient will favour migration of H^+ to the inner oxide surface. Furthermore, in the outer porous part of the oxide layer, corrosion hydrogen will react with the oxygen from the BWR coolant by radiolysis, which may result in such a low REDOX potential at the barrier oxide layer/water interface that Ni remains metallic. Rishel et al. [50] reported that tetragonal Zr oxide (which is more abundant in the inner part of the oxide) increases the heterogeneous radiolysis significantly, which may increase the radiolysis in the inner part of the oxide.

The observation that the acceleration of HPU at high burnup starts under isothermal condition much earlier than under a high heat flux (fuel cladding)

can be explained by the increased mixing of the coolant within the oxide (with low REDOX potential) with that of the bulk coolant (with high REDOX potential) With such an increased mixing occurring in fuel rods, the higher REDOX potential in the outer porous oxide will delay the HPUF acceleration compared to the situation with structural components without surface heat flux.

Furthermore, the beneficial effect of Cu in the water on lowering the HPU at high burnup fits well with the observation that Cu makes the radiolysis more sluggish. Cu should thus reduce the radiolytic reaction of oxygen from the coolant with the corrosion hydrogen in the oxide pores and therefore increase the oxidation potential in the oxide. Cu, in addition, may cause nodular corrosion with large pores, which favours coolant mixing and increase the potential at the metal/oxide interface and as consequence delay the increased HPU.

Possibilities to Minimize Accelerated HPUF at High Burnups for Zry-2

In the following, the possibilities to minimize accelerated HPUF at high burnups for Zry-2 are discussed. If Ni is responsible for the late accelerated HPU, the absolute value may play an important effect. Therefore, an evaluation of the literature information on the effect of the actual Ni content (Fig. 8) and of the Ni/Fe ratio (Fig. 9) was performed. The figures reveal that not only the Ni content but also the Fe content has an effect. The Ni/Fe ratio turns out to correlate best with the late accelerated HPUF. The large effect of the Ni/Fe ratio probably reflects the fact that Ni in metallic Fe–Ni bands at the ZrO_2 grain boundaries can be oxidized

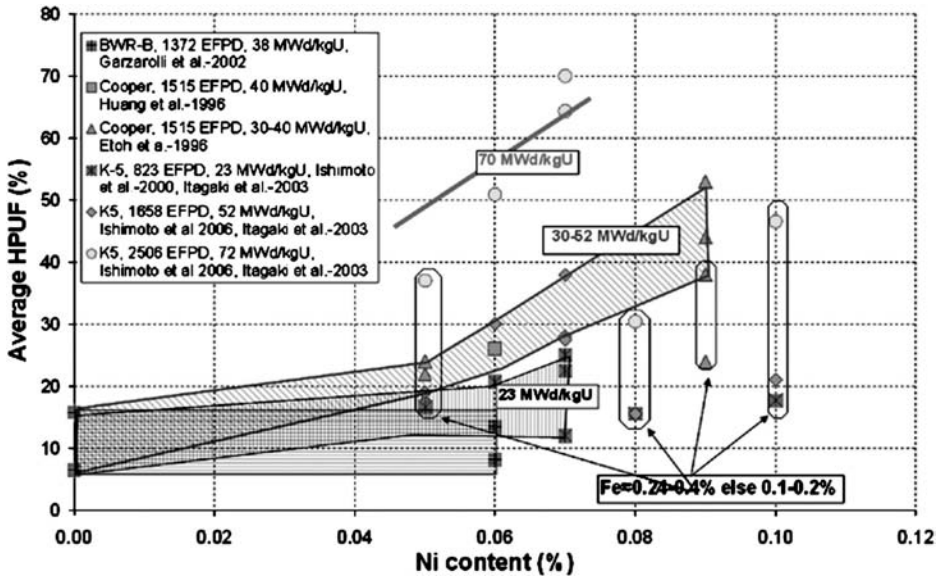


FIG. 8—*Correlation between Ni content of the Zry lot and the time averaged HPUF at high burnups under isothermal conditions. The ASTM specification of Ni content for Zry-2 is 0.05–0.08 wt % [8,23,24,51–53].*

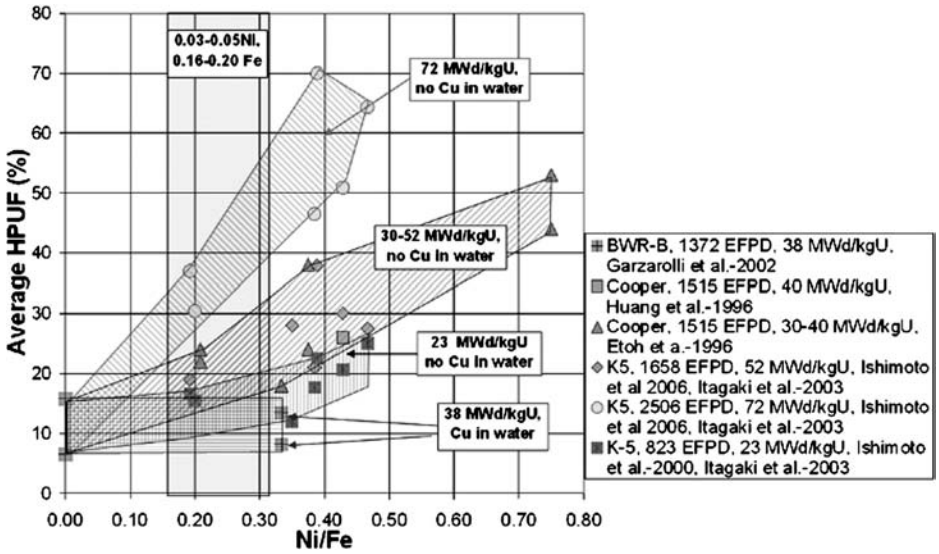


FIG. 9—*Correlation between the Ni/Fe content ratio of Zry and the time averaged HPUF at high burnups under isothermal conditions. The ASTM specification for Zry-2 allows a Ni/Fe ratio of 0.15–1.14 [8,23,24,51–53].*

not only to NiO but also to a Fe–Ni-spinel. However, it is hypothesized that the Fe–Ni-spinel is formed at even lower REDOX potential than NiO.

For an optimization of Zircaloy-2 for high burnups, obviously Ni should be limited to 0.05 %. Most of the old Zry-2 data are from lots with 0.04–0.05 % Ni. Today, the Ni content is usually at 0.06–0.07 % probably because high Ni is considered as beneficial for nodular corrosion resistance. Thus, we suggest that Ni should be limited to the lower ASTM range, 0.03–0.05 % instead of 0.06–0.08 %, to reduce the HPUF. Furthermore, Fe should be limited to the upper ASTM range of to 0.16–0.20 % instead of 0.07–0.20 %. This would result in a Ni/Fe ratio ranging from 0.15 to 0.22, which in turn would result in much lower HPUF, as can be seen from Fig. 9. To avoid an increase of the sensitivity to nodular corrosion, *Cr* should also be limited to the upper ASTM range, e.g., 0.1–0.15 % instead of 0.05–0.15 %.

Acknowledgments

The writers gratefully acknowledge the many helpful discussions on the effect of Ni on corrosion and SPP dissolution over the years with Dr. Ron Adamson.

References

[1] Garzarolli, F., Dietz, W., Franke, K. P., and Fricke, W., "Corrosion and Hydriding of Zry-2 and Other Zr Alloys in BWRs," *Proc. BNES Conf. on Effects of Environment on Material Properties in Nuclear Systems*, Bournemouth, UK, 1971, pp. 15–20.

[2] Cantonwine, P. A., "GNF Channel Performance and Success in Mitigating Channel Distortion and Cell Friction," *2008 Water Reactor Fuel Performance Meeting*, Seoul, Korea, October 2008.
[3] Proebstle, R. A., Baily, W. E., and Klepfer, H. H., "Current Trends in BWR Fuel Performance," *ANS-LWR Fuel Performance Conf.*, St. Charles, USA, 1977.
[4] Marlow, M. O., Armijo, J. S., Cheng, B., and Adamson, R. B., "Nuclear Fuel Cladding Localized Corrosion," *Proc. Int. ANS Topical Meeting on LWR Fuel Performance*, Orlando, FL, 1985, pp. 3.73–3.90.
[5] Williams, C. D., Marlowe, M. O., Plaza-Meyer, E., Proebstle, R. A., White, D. W., and Adamson, R. B., *Evolution of Processing of GE Fuel Clad Tubing for Corrosion Resistance in BWRs*, Jahrestagung Kerntechnik, Mannheim, Germany, 1996.
[6] Graham, R. A., Tosdale, J. P., and Finden, P. T., "Influence of Chemical Composition and Manufacturing Variables on Autoclave Corrosion of the Zircaloys," *ASTM Spec. Tech. Publ.*, Vol. 1023, 1989, pp. 334–345.
[7] Graham, R. A. and Eucken, C. M., "Controlled Composition Zry-2 Uniform Corrosion Resistance," *ASTM Spec. Tech. Publ.*, Vol. 1132, 1991, pp. 279–303.
[8] Huang, P. Y., Mahmood, S., and Adamson, R. B., "Effects of Thermo Mechanical Processing on In-Reactor Corrosion and Post Irradiation Mechanical Properties," *ASTM Spec. Tech. Publ.*, Vol. 1295, 1996, pp. 726–756.
[9] Sihver, L. and Hallstadius, L., "Zero-Failure Fuel," *Proc. ENS TOPFUEL 99, Topical Meeting on Nuclear Fuel*, Avignon, France, September 1999, pp. 396–406.
[10] Limbäck, M., Dahlbäck, M., Tägtström, P., Jourdain, P., Massih, A., Sihver, L., Andersson, T., and Witt, P., "Westinghouse Optimized BWR Cladding and Channel Materials," *TopFuel-2001*, Stockholm, Sweden, 2001.
[11] Tägtström, P., Andersson, T., Bergström, O., Dahlbäck, M., and Limbäck, M., "The Effect of Secondary Phase Particle Distribution on the In-Reactor Performance of BWR Cladding," *Enlarged Halden Progr. Meeting*, Loen, Norway, 1999.
[12] Hiroshi, H., Yoshiaki, T., Sachio, S., and Yoshinori, E., "Outside-in Failure of BWR Segment Rods During Power Ramp Tests," *Proc. ENS Top Fuel 2003*, Würzburg, Germany, March 16–19, 2003.
[13] Ledergerber, G., Limbäck, M., and Abolhassani, S., "Characterisation of High Burn-Up Fuel Irradiated in KKL," *Proc. Water Reactor Fuel Performance Meeting*, Kyoto, Japan, Oct. 2–6, 2005.
[14] Hirano, Y., Mozumi, Y., Kamimura, K., and Tsukuda, Y., "Irradiation Characteristics of BWR High Burnup 9×9 Lead Use Assemblies," *Int. Meeting on Water Reactor Fuel Performance*, Kyoto, Japan, October 2005.
[15] Miyashita, T., Nakae, N., Ogata, K., Baba, T., Kamimura, K., Matsumoto, T., and Kakiuchi, K., "Corrosion and Hydrogen Pick-up Behaviours of Cladding and Structural Components in BWR High Burnup 9×9 Lead Use Assemblies," *Proc. 2007 Intern. LWR Fuel Performance Meeting*, San Francisco, CA, 2007.
[16] Zhou, G., Hallstadius, L., Wright, J., Dahlback, M., Wetterholm, U., Lindquist, A., Valizadeh, S., Wikmark, G., and Brandes, L. P., "Corrosion and Hydrogen Uptake Behavior and Modeling for Modern BWR Cladding Materials at High Burnup," *Proceedings of Top Fuel 2009*, Paris, France, Sept. 6–10, 2009, Paper 2020.
[17] Sell, H. J., Trapp-Pritsching, S., and Garzarolli, F., "Effect of Alloying Elements and Impurities on In-BWR Corrosion of Zirconium Alloys," *ASTM Spec. Tech. Publ.*, Vol. 1467, 2005, pp. 404–417.
[18] Heck, C., "BWR Control Rod Drop Accident," *NRC RIA Workshop*, Bethesda, MD, 2006.
[19] Koichi, O., Jin, K., Noboru, I., Yasuyuki, O., and Shingo, Y., "Recent Experience and Development of BWR Fuel at NFI," *Proc. Water Reactor Fuel Performance Meeting*, Kyoto, Japan, Oct. 2–6, 2005.

[20] Sachio, S., Shinji, I., Toshio, M., Yoshiaki, I., and Akihiro, M., "Effect of Hydrogen Water Chemistry on Zircaloy-2 Fuel Cladding and Structure Material Performance," *Water Reactor Fuel Performance Meeting*, Kyoto, Japan, Oct. 2–6, 2005.
[21] Mahmood, S. T., Lin, Y.-P., Dubecky, M. A., Edsinger, K., and Mader, E. V., "Channel Bow in Boiling Water Reactors—Hot Cell Examination Results and Correlation to Measured Bow," *Proc. 2007 Intern. LWR Fuel Performance Meeting*, San Francisco, CA, 2007.
[22] Münch, C. J., Hoffmann, P. B., and Blavius, D., "Ursachenanalyse zur Erhöhten Biegung von Brennelementkästen [Reasons for Abnormal Fuel Channel Bowing]," *KTG Fachtag Brennelemente und Kernbauteile*, Karlsruhe, Germany 2008.
[23] Garzarolli, F., Ruhmann, H., and Van Swam, L., "Alternative Zr Alloys with Irradiation Resistant Precipitates for High Burnup Application," *ASTM Spec. Tech. Publ.*, Vol. 1423, 2002, pp. 119–132.
[24] Etoh, Y., Shimada, S., Yasuda, T., Ikeda, T., Adamson, R. B., Chen, J.-S. F., Ishii, Y., and Takei, K., "Development of New Zirconium Alloys for a BWR," *ASTM Spec. Tech. Publ.*, Vol. 1295, 1996, pp. 825–849.
[25] Miyashita, T., Nakae, N., Ogata, K., Baba, T., Kamimura, K., Matsumoto, T., and Kakiuchi, K., "Corrosion and Hydrogen Pick-up Behavior of Zircaloy Component of BWR High Burnup 9×9 Lead Use Assemblies," *Technical Meeting on High Burnup Fuel Experience and Economics*, Sofia, Bulgaria, Sept. 26–28, 2006.
[26] Schardt, J. F., Potts, G. A., and Stachowski, R., "Recent GNF Fuel Performance Experience," *KTG Fachtagung*, Karlsruhe, Germany, March 30–31, 2004.
[27] Limbäck, M., Kesterson, R. L., and Hallstadius, L. G., *Development of Alloys for High Duty LWR Operation*, Jahrestagung Kerntechnik, Berlin, 2003.
[28] Ketteler, M., Skusa, J., and Limbäck, M., *Operating Experience of Westinghouse Fuel Rod Cladding in KKB*, Jahrestagung Kerntechnik, Berlin, 2003.
[29] Blaser, W., "BWR Water Chemistry," *SVA-Advanced Water Chemistry and Material Behaviour Course*, Brugg-Windisch, Germany, April 21–23, 1999.
[30] Roßkamp M., "Copper Reduction in the Water-Steam Cycle of a BWR Plant by Applying Chitin," *VGB Konferenz Chemie im Kraftwerk*, ESSEN, Germany, 1998.
[31] Yang, W. J. S., Tucker, R. P., Cheng, B., and Adamson, R. B., "Precipitates in Zry: Identification and Effects of Irradiation and Thermal Treatment," *J. Nucl. Mater.*, Vol. 138, 1986, pp. 185–195.
[32] Griffiths, M., Gilbert, R. W., and Carpenter, C. J. C., "Phase Instability, Decomposition and Redistribution of Intermetallic Precipitates in Zry-2 and Zry4 During Neutron Irradiation," *J. Nucl. Mater.*, Vol. 150, 1987, pp. 53–66.
[33] Etoh, Y. and Shimada, S., "Neutron Irradiation Effects on Intermetallic Precipitates in Zry as a Function of Fluence," *J. Nucl. Mater.*, Vol. 200, 1993, pp. 59–69.
[34] Tägtström, P., Limbäck, M., Dahlbäck, M., Andersson, T., and Pettersson, H., "Effects of HPU and SPP Dissolution on In-Reactor Corrosion Performance of BWR Cladding," *ASTM Spec. Tech. Publ.*, Vol. 1423, 2002, pp. 96–118.
[35] Garzarolli, F., Goll, W., Seibold, A., and Ray, I., "Effect of In-PWR Irradiation on Size, Structure and Composition of Intermetallic Precipitates of Zr Alloys," *ASTM Spec. Tech. Publ.*, Vol. 1295, 1996, pp. 541–556.
[36] Elmoselhi, M. B., Warr, B. D., and McIntyre, S., "A Study of Hydrogen Uptake Mechanism in Zr Alloys," *ASTM Spec. Tech. Publ.*, Vol. 1245, 1994, pp. 62–79.
[37] Ramasubramanian, N., "Lithium and Boron Effects in the Corrosion Mechanism of Zirconium Alloys Under Coolant Chemistry Conditions," *Proc. Seventh Int. Conf. on Water Chemistry of Nuclear Reactor Systems*, Bournemouth, United Kingdom, 1996, Vol. 1, pp. 91–93.

[38] Cox, B. and Wong, Y.-M., "A Hydrogen Uptake Micro-Mechanism for Zr Alloys," *J. Nucl. Mater.*, Vol. 270, 1999, pp. 134–146.
[39] Isobe, T., Murai, T., and Mae, Y., "Anodic Protection Provided by Precipitates in Aqueous Corrosion of Zircaloy," *Proc. 11th Int. Symp. on Zr in the Nuclear Ind., ASTM STP 1295*, Garmisch-Partenkirchen, Germany, 1996, ASTM International, West Conshohocken, PA, pp. 203–217.
[40] Bossis, P., Lelievre, G., Barberis, P., Iltis, X., and LeFebvre, F., "Multi-Scale Characterisation of the Metal-Oxide Interface of Zirconium Alloys," *Proc. 12th Int. Symp. on Zr in the Nucl. Ind., ASTM STP 1354*, 2000, ASTM International, West Conshohocken, PA, pp. 918–940.
[41] Hatano, Y., Sugisaki, M., Kitano, K., and Hayashi, M., "Role of Intermetallic Precipitates in Hydrogen Transport Through Oxide Films on Zircaloy," *ASTM Spec. Tech. Publ.*, Vol. 1354, 2000, pp. 901–917.
[42] Pettersson, H., Bengtson, B., Andersson, T., Sell, H.-J., Hoffmann, P.-B., and Garzarolli, F., "Investigation of Increased Hydriding of Guide Tubes in Ringhals 2 During Cycle Startup," *International LWR Fuel Performance Meeting*, San Francisco, CA, 2007, Paper 1082.
[43] Urbanic, V. F., Cox, B., and Field, G. J., "Long Term Corrosion and Deuterium Uptake in CANDU-PHW Pressure Tubes," in *Zircnium in ASTM Spec. Tech. Publ.*, R. B. Adams and L. F. P. Van Swam, eds., American Society for Testing and Materials, Philadelphia, 1987.
[44] Hillner, E., "Hydrogen Absorption in Zircaloy During Aqueous Corrosion, Effect of Environment," *Report No.* WAPD.TM-411, 1964.
[45] Limbäck, M., Krammen, M., Rudling, P., Pati, S., and Garde, A., "Corrosion and Hydriding Performance of Zircaloy-2 and Zircaloy-4 Cladding Materials in PWRs," *Proceedings of the International Topical Meeting on LWR Fuel Performance*, West Palm Beach, FL, 1994, ANS, USA, p. 286.
[46] Pecheur, D., Lefebvre, F., Motta, A., Lemaignan, C., and Charquet, D., "Oxidation of Intermetallic Precipitates in Zircaloy-4: Impact of Irradiation," *ASTM Spec. Tech. Publ.*, Vol. 1245, 1994, pp. 687–708.
[47] Cox, B. and Sheikh, H. I., "Redistribution of the Alloying Elements During Zry-2 Oxidation," *J. Nucl. Mater.*, Vol. 249, 1997, pp. 17–32.
[48] Takeda, K. and Anada, H., "Mechanism of Corrosion Rate Degradation Due to Sn," *ASTM Spec. Tech. Publ.*, Vol. 1354, 2000, pp. 592–608.
[49] Tendler, R. and Abriata, J. P., "Atomic Size and Fast Diffusion of Metallic Impurities in Zr," *J. Nucl. Mater.*, Vol. 150, 1987, pp. 251–258.
[50] Rishel, D. M., Eklund, K. L., and Kammenzind, B. F., "In Situ EIS Measurements of Irradiated Zr-4 Post Transition Corrosion Kinetic Behaviour," *15th International Symposium on Zirconium in the Nuclear Industry*, Sunriver, OR, Canada, 2007.
[51] Ishimoto, S., Kubo, T., Adamson, R. B., Etoh, Y., Kunio, T. I., and Suzaswa, Y., "Development of New Zirconium Alloys for Ultra-High Burnup Fuel," *ANS Topical Meeting on Light Water Reactor Fuel Performance*, Park City, 2000.
[52] Itagaki, N., Kakiuchi, K., Yasuhiro, M., and Furuya, T., "Development of New High Corrosion Resistance Zr Alloy 'HiFi' for High Burnup BWR Fuel," *Topfuel-2003*, Würzburg, Germany.
[53] Ishimoto, S., Etoh, Y., Matsumoto, T., Lutz, D., and Takagi, A., "Improved Zr Alloy for High Burnup BWR Fuel," *TopFuel-2006*, Salamanca, Spain, 2006.

DISCUSSION

Question 1, P. Barberis, AREVA/CEZUS:—You recommend to lower Ni and increase Fe and Cr as much as possible within the ASTM specification, that is as close as possible to Zircaloy-4. Would you recommend to switch to Zircaloy-4 for the cladding? And for the structural components?

Author's Response:—We would not recommend to switch to Zry-4 for BWR fuel rod claddings. There is only a very limited experience with Zry-4 claddings in BWR and Zry-4 has a higher sensitivity to nodular corrosion, which played an important role for the CRUD induced fuel failures observed in the 1980ies. From early days experience it can be concluded that 0.03% Ni is enough to reduce the sensitivity to nodular corrosion in-BWR, contrary to out-reactor results in 500°C high pressure steam, which indicate a further reduction in nodular sensitivity by higher Ni contents. For structural compounds a large in-BWR experience exists for Zry-4 and nodular corrosion has here never led to any major problem.

Question 2, Arthur Motta, Penn State University, USA:—You propose that the acceleration of HPUF is caused by precipitation of metallic layers of Fe-Ni at the columnar oxide grain boundaries at high BU. a) Is there any experimental evidence of such phases in the literature? b) Theoretically speaking, how much Fe-Ni would one need to cause the observed acceleration of HPUF? A few monolayers?

Author's Response:—To our knowledge there is no experimental evidence and it will probably not be easy to prove this experimentally especially in case of highly irradiated coupons.

We think a few mono-layers metal at the oxide grain boundaries in the barrier layer should be effective for the proposed mechanism.

Question 3, A. D. Bachik, CNA:—We have fuel channels made of Zircaloy-4 with no Ni. However, we have high pick-up rate, up to 50%. Could you comment on that point?

Author's Response:—The hydrogen pickup fraction (HPUF) of Zry-4 depends very much on the environmental condition, the oxygen and hydrogen content as well as basic and acidic addition, and it may well reach values >50% in certain oxygen-free environments. However, under oxygenated conditions the HPUF of both Zry-2 and Zry-4 is only about 10%, which increases in case of Zry-2 at high burnup to values ≥100%. Values in excess of 100% indicate that some hydrogen is even picked up catalytically.

Question 4, Mirco Grosse, Karlsruhe Institute of Technology:—You have discussed the diffusion way of atomic hydrogen into the metal. Can you be sure that hydrogen diffuses as atoms but not as protons?

Author's Response:—It is usually assumed that during corrosion water molecules can easily penetrate the outer part of the oxide arriving at the "barrier layer" at which it dissociates into O^{2-} and H^{+}. The O^{2-} diffusion still occurs through the "barrier layer" with significant thickness resulting in a moderate corrosion rate.

The normal way of hydrogen ingress is through defects in the "barrier layer" (which results in rather low HPUF). Investigations have shown that the hydrogen solubility in ZrO_2 is extremely low. However, formation of the metal bands may result in a much easier way for hydrogen to get into the metal.

There are good reasons to assume that H^{+} is reduced at the outer part of the barrier layer by the electrons released from the ionization of the Zr atoms into Zr^{4+} at the metal/oxide interface, especially if metallic bands exist in the barrier layer. Nevertheless, if the potential drop over the barrier layer is high, e.g. under cathodic polarization, proton migration through the barrier layer may well play an important effect.

Reprinted from JAI, Vol. 8, No. 2
doi:10.1520/JAI103025
Available online at www.astm.org/JAI

S. Valizadeh,[1] *G. Ledergerber,*[2] *S. Abolhassani,*[3] *D. Jädernäs,*[4] *M. Dahlbäck,*[5] *E. V. Mader,*[6] *G. Zhou,*[5] *J. Wright,*[5] *and L. Hallstadius*[5]

Effects of Secondary Phase Particle Dissolution on the In-Reactor Performance of BWR Cladding

ABSTRACT: Although the complete mechanisms are not yet fully understood, it is well established that the secondary phase particle (SPP) size distribution and chemical composition have a crucial affects in the reactor corrosion rate and hydrogen uptake in boiling water reactor (BWR) cladding. To further study these effects, different selected fuel rod assemblies with standard LK3 cladding materials that have been irradiated in KernKraftwerk Leibstadt (KKL) for three, five, six, seven, and nine annual cycles were investigated using transmission electron microscopy (TEM). TEM analysis of the samples showed that the average size of SPPs increases as the small SPPs are dissolved during irradiation. After three cycles the Fe–Cr bearing SPPs have been identified as completely amorphous over the whole range of examined samples and the Fe–Ni bearing SPPs remained crystalline. The EDX analyses of several Fe–Ni bearing precipitates show that the Fe/Ni ratio stays more or less constant for the irradiated material at 1.5 to 1.6 and drops to about 1 after fast fluence of 17.9×10^{21} n/cm^2 (>1 MeV) for nine cycles

Manuscript received February 9, 2010; accepted for publication November 18, 2010; published online January 2011.

[1] Westinghouse Electric Sweden AB, SE-72163 Västerås, Sweden, e-mail: valizas@westinghouse.com
[2] Kernkraftwerk Leibstadt AG, CH-5325 Leibstadt, Switzerland.
[3] Paul Scherrer Institut, CH-5232 Villigen, Switzerland.
[4] Studsvik Nuclear AB, SE 611 82 Nyköping, Sweden.
[5] Westinghouse Electric Sweden AB, SE-72163 Västerås, Sweden.
[6] Electric Power Research Institute, Palo Alto, CA.

Cite as: Valizadeh, S., Ledergerber, G., Abolhassani, S., Jädernäs, D., Dahlbäck, M., Mader, E. V., Zhou, G., Wright, J. and Hallstadius, L., "Effects of Secondary Phase Particle Dissolution on the In-Reactor Performance of BWR Cladding," *J. ASTM Intl.*, Vol. 8, No. 2. doi:10.1520/JAI103025.

Copyright © 2011 by ASTM International, 100 Barr Harbor Drive, PO Box C700, West Conshohocken, PA 19428-2959.

sample. Results from this study confirms that the increased oxide thickness, the higher hydrogen content, and the accelerated growth of the rods at rod average burnup of 78 MWd/kgU goes along with a change in the appearance of SPPs by TEM.

KEYWORDS: zircaloy, corrosion, hydriding, second phase particle, radiation-induced dissolution

Introduction

The microstructure of Zr based alloys used in boiling water reactor (BWR) type nuclear reactor fuel rod claddings plays an important role in the material behavior during operation. It is of key importance to limit processes like oxidation, hydriding, and radiation-induced rod growth.

One important aspect of the Zircaloy chemistry specifications that remains to be clarified relates to the hydriding behavior. Recent hydriding data of irradiated Zircaloy-2 components showed that the probability of accelerated hydriding at burnup exceeding $\sim 45\,\mathrm{MWd/kgU}$ is an industry issue that needs further optimization of the alloy chemistry for hydriding resistance [1]. For improvement of Zircaloy chemistry corrosion and hydriding resistance the alloying elements, Sn, Fe, Cr, Ni, and O are added to zirconium, to improve the mechanical strength and corrosion resistance. Sn and O both have high solubility in zirconium and are added as solid solution strengthening elements. Fe, Cr, and Ni are added to increase the corrosion resistance in a reactor [2].

All three of these elements have very low solubility in the Zircaloy-2 matrix, with an estimated value of < 200 parts per million (ppm) total at temperatures $< 500^{\circ}\mathrm{C}$. In Zircaloy-2 the majority of these elements will precipitate out as second phase particles (SPP) in the forms of body centred tetragonal C16 $Zr_2(\mathrm{Ni,Fe})$ and hexagonal close packed or face centred cubic $\mathrm{Zr(Fe,Cr)}_2$ [3]. These intermetallic precipitates undergo size, number density, structural, and chemical changes during irradiation. It is known that the dissolution and depletion of the alloying elements, such as Fe, Ni, and Cr from intermetallic precipitate play a key role in the high burnup performance of Zircaloy-2. It is known that the neutrons irradiation changes the microstructure of Fe–Cr intermetallic and it becomes amorphous and progressively dissolved in Zircaloy-2 matrix, while Fe–Ni SPPs size decreases due to Fe dissolution. No evidence of amorphisation of the Fe–Ni bearing SPPs was found [3–6].

Huang et al. [7,8] showed that the fast neutron irradiation changes the SPPs' chemical compositions in zirconium matrix in terms of Fe/Ni and Fe/Cr ratios. The authors believed that the SPPs' dissolution increases dramatically the BWR corrosion and hydriding rates. The dissolution of the SPPs in turn, has substantial effect on the hydrogen pickup fraction. According to Kesterson et al. [9] the increasing volume associated with hydrogen pickup fraction during the corrosion could be the reason behind the fuel rod growth mechanisms. Furthermore, several studies indicated that growth is associated with the density of $c\rangle$ dislocation loops [10].

In view of the above, this work presents the results of the fast neutrons irradiation effect on the evolution of SPPs in irradiated Westinghouse Zircaloy-2 based LK3 cladding materials. The selected samples were taken from the fuel rod assemblies irradiated after three, five, six, seven, and nine cycles of operations. The nine cycles sample is selected from the two-life rods that have been irradiated up to ultra-high rod average burnups of 78 MWd/kgU.

All the samples have been extensively characterized in detail during the pool-side inspections, non destructive and destructive examinations in the framework of the second phase of the Fuel Performance Programme (FPP-2) [11].

Results from this study confirms that the increased oxide thickness, the higher hydrogen content and the accelerated growth of the rods at rod average burnup of 78 MWd/kgU goes along with a change in the appearance of the secondary phase particles characterized by transmission electron microscopy (TEM).

Materials

The Westinghouse LK3 clad material is a Zircaloy-2, based material with chemical composition within the ASTM Zircaloy-2 specification is represented in Table 1.

The heat treatment of the cladding materials is specified by the annealing parameter called cumulative annealing parameter A. The A is determined by

$$A = \sum_i t_i \cdot \exp(-Q/R \cdot T_i) \tag{1}$$

where:

i = different heat treatments,
t_i = annealing time (h),
T_i = temperature (K),
Q = activation energy = 63 000 cal/mol, and
R = molar gas constant (cal/mol K).

The Zircaloy-2 LK3 cladding material fabricated at accumulated annealing of $\log A$ value of −14,2, in accordance with Eq 1, by Sandvik Material Technology.

The fuel rods studied here were fabricated by Westinghouse Electric (former ABB Atom), Västerås, Sweden. The rods were irradiated in KKL reactor [12].

Microscopic Characterization

Sample Preparation—Ring-shaped samples were cut from the fuel rod and the cladding was defueled by submersion and heating in acid. Three millimeter samples were cut and subsequently ground and polished ending with a 3 μm silica suspension to remove most of the cold worked surface from cutting and grinding. The polished samples were then electrolytically thinned until electron

TABLE 1—*The chemical composition of standard Zircaloy-2 claddings and the nominal composition LK3 material.*

Element	Zr (wt %)	Sn (wt %)	Fe (wt %)	Cr (wt %)	Ni (wt %)	Fe + Cr + Ni	O (ppm)	C (ppm)	Si (ppm)
Standard Zry-2 (ASTM B3553)	Balance	1.20–1.70	0.07–0.20	0.05–0.15	0.03–0.08	0.18–0.38	1000–1400	max 120	max 270
Zry-2 Cladding	Balance	1.34	0.18	0.11	0.05	0.34	1320	70	130

transparent using a 10 % perchloric acid ($HClO_4$) in acetic acid solution at $T = 8°C$. The final foil thicknesses was around 100–200 nm. Therefore, the size and number density of precipitates analyzed by TEM are limited to maximum particle size of the order of 200 nm.

TEM Investigation on Unirradiated and Irradiated Samples—A field emission TEM model JEOL 2100F, operating at an accelerating voltage of typical 200 keV was used for the TEM analysis. The microscope is equipped with two charged coupled device cameras and a bright field scanning TEM (BF-STEM) detector, high angle annular dark field detector, electron energy loss spectrometer (EELS), and an energy dispersive X-ray detector (EDX). The TEM analysis was performed by Studsvik.

Material data regarding the samples selected for TEM analysis are summarized in Table 2. Note, the SPPs analysis of LK3 cladding sample irradiate after 3 cycles has been investigated earlier. The result is reported in more detail elsewhere [13]. In the present study these 3 cycles results are incorporated to the data obtained for 5, 6, 7 and 9 cycles. It is worth mentioning that the data are obtained on two different instruments, and the samples used to examine unirradiated state of the cladding are not of the same batch and the position of the specimen in the cladding wall are not identical, however taking all the above mentioned aspects into consideration the results are comparable.

SPP and Chemical Analysis—Images were acquired using the Bright Field Scanning TEM (BF-STEM) detector in order to determine the SPP density and size distribution. The chemical compositions of the SPPs were determined using the EDX detector either by acquiring one spectrum in each SPP to quantify the chemical composition of the SPP or by mapping X-ray line scans. The line scans were acquired to detect any diffusion of Ni, Fe or Cr out from the SPPs. At least 15 images were used for the quantification of SPPs. Two orthogonal diameter measurements were performed on each SPP and the average value was calculated. The degree of the crystallinity of the SPPs was determined by using selected area electron diffraction (SAED) pattern. Furthermore, the foil thickness was determined by using electron energy loss spectroscopy. This is done by dividing the electron mean free path in Zr by the logarithm of I/I_0 where I_0 is the integrated intensity under the zero loss peak and I is the integral of the whole spectrum. The number of particles measured was around 50–111 for each material, depending on the frequency of occurrence of the particles. The uncertainties are calculated with assuming a 3 % uncertainty in the foil volume determination and the relative error corresponding to counting SPPs size and distribution are set to $\sqrt{n}/n$ where n is the total number. See Table 3.

Post Irradiation Examinations of Oxide Thickness and Hydrogen Measurements—The hot cell examinations of oxide and hydrogen measurements on all samples were performed at Paul Scherrer Institute hot cell laboratories. The oxide thickness was measured after polishing with 4 μm paper. the variation of oxide thickness with orientation around the circumference of each

TABLE 2—*Description of all irradiated samples data after irradiation. The local fast fluence is given as a specimen fast fluence.*

Sample ID	Burnup Rod Average [MWd/kgU]	Number of Cycles	Specimen Fast Neutron Fluence [10^{21} n/cm^2] for $E > 1$ MeV	Rod Average Fast Neutron Fluence [10^{21} n/cm^2] for $E > 1$ MeV	Position of the Specimen Elevation [mm]
Unirradiated	...	...		...	
AEB070-E4 13	34.7	3	...	5.9	2011
AEB069-E4	51.1	5	10.7	8.7	2700
AEB068-E4	57.3	6	11.6	9.5	2700
AEB071-E4	57.4	7	11.7	9.7	2100
AGB108-G6	78.7	9	17.9	14.7	2100

TABLE 3—*Summary of TEM results of the SPPs analysis for unirradiated and irradiated samples.*

Rod ID	Fast Neutron Fluence at Specimen Elevation [10^{21} n/cm^2]	Position of the Specimen Elevation [mm]	Number of Cycles	SPP Diameter				SPP Density [10^{19} m^{-3}]	Number of SPPs	Analysed Volume [10^{-18} m^{-3}]
				Mean [nm]	Median [nm]	s [nm]	s_{mean} [nm]			
Unirradiated	0		0	42	30	32	3.0	6.4	111	1.7
AEB069-E4	10.7	2700	5	59	49	40	4.2	2.2	92	4.2
AEB068-E4	11.6	2700	6	60	52	26	2.6	1.5	100	6.9
AEB071-E4	11.8	2100	7	53	48	28	3.6	1.5	60	3.7
AGB108-G6	17.9	2100	9	80	75	34	5.0	1.0	47	4.9

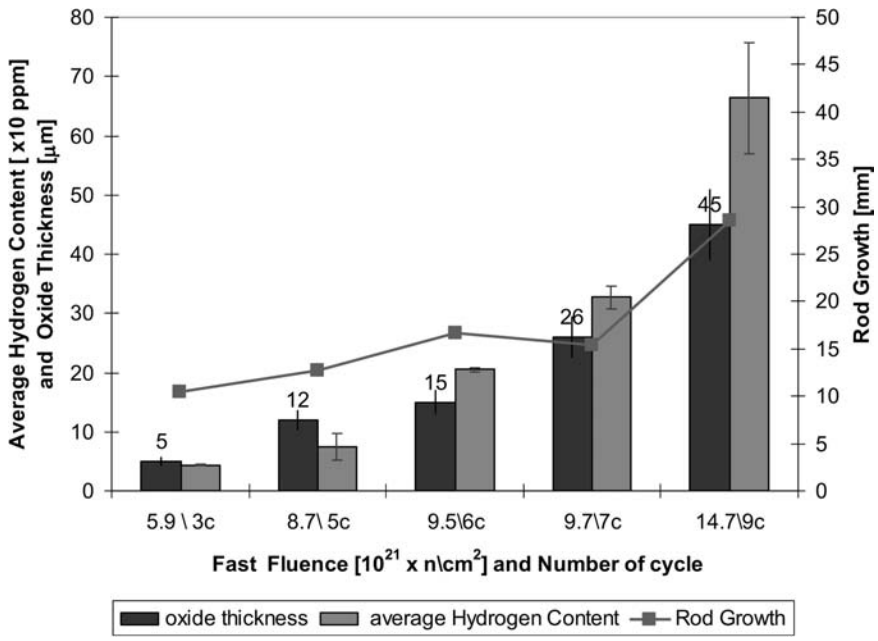


FIG. 1—*The hydrogen content and oxide thickness versus rod growth and accumulated rod average fast fluence for all irradiated samples after three, five, six, seven, and nine cycles.*

fuel rods segment were measured as average oxide thickness, the maximum measured oxide thickness and also the oxide thickness calculated from the remaining wall thickness. A Leica® TELATOM-4® microscope equipped with remote control system was used to examine the polished metallography samples.

The hydrogen concentration in metal of cladding was analyzed using hot gas extraction technique. The hot gas extraction technique allows a separation of the total hydrogen content of the sampling, in a contribution of the oxide layer and that of the metal. The procedure consists of heating the specimen up to 2000°C and to measure the release of the gas as a function of time. The amount of gas released at temperatures up to 500°C is associated to the hydrogen present in the oxide and the gas released at higher temperatures corresponds to hydrogen in the metal [14]. The Zircaloy cladding hydrogen pickup fraction in this study is defined as the fraction of hydrogen liberated by the oxidation reaction that is absorbed by the metal.

Results and Discussions

Oxide Thickness and Hydrogen Content Measurements

The results of hot cell examination of oxide and hydrogen content are summarized in Fig. 1.

The results clearly revealed that the hydrogen content and oxide thickness increase with increasing the fast fluence. It can be seen that LK3 cladding retains a good corrosion resistance up to a rod average fast fluence of 14.8×10^{21} n/cm^2 (> 1 MeV, corresponding to a rod average burnup of about 78 MWd/kgU).

It is known that the growth rate due to the effect of neutron irradiation on Zircaloy microstructure rapidly increases with fast neutron fluence of 1.8×10^{21} n/cm^2 (correspond to a burnup below ~ 10 MWd/kgU) [7,15,16]. Then, rod growth increases approximately linearly with fast fluence. This trend clearly is illustrated in Fig. 1. Moreover, rapid increase of hydrogen content after seven annual operation cycles, (correspond to rod average fast fluence of 9.7×10^{21} n/cm^2 (> 1 MeV), can clearly be observed. Comparison of the results presented for six and seven cycles in Fig. 1 demonstrates that in spite similar fast fluence values for both fuel rod specimens the oxide and hydrogen content of the seven cycle fuel rod increases due to longer residence time in the reactor.

SPP Characterization of Irradiated and Unirradiated Materials—The representative TEM images of the SPP distribution in the samples are presented in Fig. 2.

The radiation damage defects can be observed as black dots on all the irradiated samples which could interfere with the detection of very small precipitates. It is therefore difficult to consider without ambiguity the distribution of 10 nm particles in the matrix. It is worth noting that sample preparation of specimens can also create surface artefacts that sometimes make it difficult to differentiate between the defects caused by irradiation and the effects of specimen preparation. As an example of the artefact in some images a complex hydride character, i.e., created during the elctropolishing are labelled as "E" and "F." A large number of chemical analyses on different particles were performed in order to distinguish a SPP from a defect. Nevertheless, the contrast due to a precipitate remains often different from the defect. The typical bright field contrast images were used to determine the SPP density and size distribution for all irradiated samples. The results from TEM analyses on irradiated and unirradiated materials are shown in Table 3. The parameters σ and $\sigma_{\text{mean}} = \sigma/\sqrt{n-1}$ correspond to the standard deviation of the measured population and the standard deviation of the mean SPP diameter, respectively.

As seen in the table, the mean diameter of the SPPs in unirradiated sample is 42 nm whereas the sample after five, six, and seven annual operation cycles showed a mean SPP diameter of 53–60 nm. For the sample irradiated for nine annual cycles, the average SPP size has increased to 80 nm. The reason for large SPP average size for nine annual cycles sample can be explained by the fact that due to the high fast fluence the diameter of the large SPP particles has been reduced somewhat, but simultaneously the number density of visible small size SPP particles has significantly decreased; therefore the average particle size of SPPs shows an increasing mean diameter. All irradiated samples show a very clear drop of the total density of the SPPs compared to the unirradiated sample. The comparison of the results between the unirradiated sample and irradiated

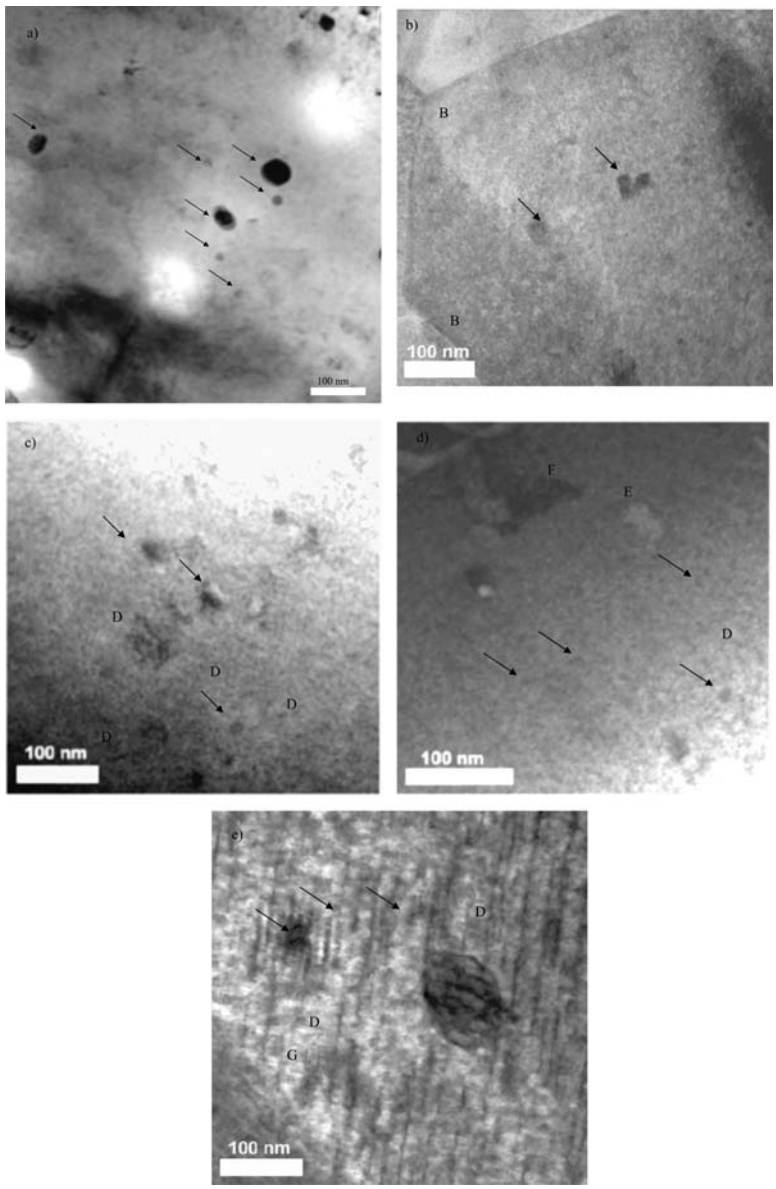


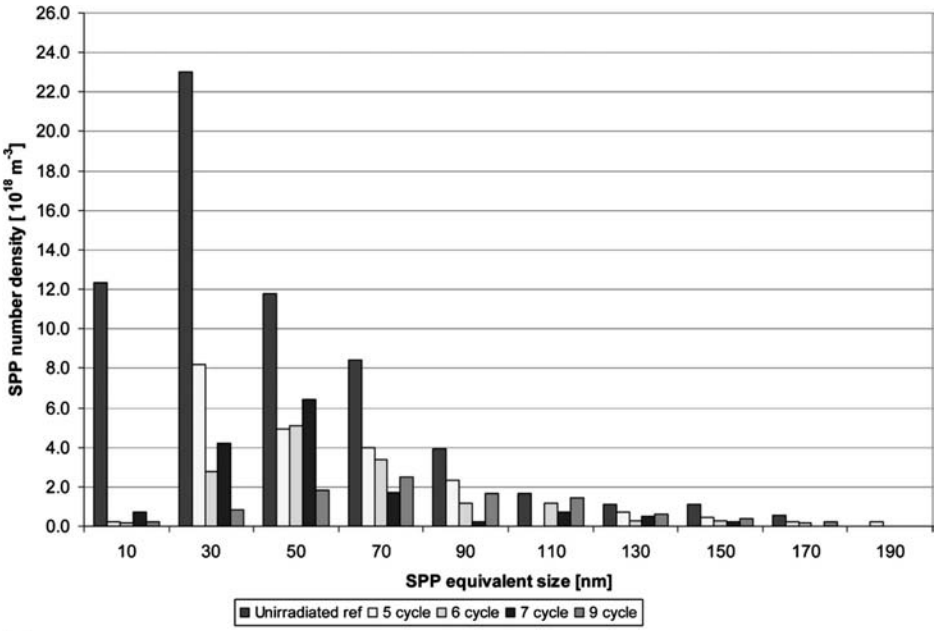
FIG. 2—*TEM micrograph showing the examination analysis of the SPPs on (a) unirradiated sample; (b) sample after five cycles of operation; (c) sample after six cycles of operation; (d) sample after seven annual cycles; and (e) the nine cycles samples. The SPPs are arrowed into the image. The grain boundaries are labelled as B. The defects with ⟨c⟩ dislocations are labelled as D. "E" and "F" representing the artefacts and complex hydride character created during the elctropolishing. Dislocations surrounding the stacking-fault is labelled as G.*

specimens up to the local fast fluence of 10.7×10^{21} n/cm^2 shows that all small SPPs < 30 nm were fully dissolved into the matrix. For the five, six, and seven cycles samples with local fast fluence from 10.7–11.8×10^{21} n/cm^2, the most probable SPP size is shifted towards a higher value meaning that the smaller particles have dissolved and very large particles are becoming smaller during irradiation. Finally for the local fast fluence between 11.8×10^{21} and 17.9×10^{21} n/cm^2 the most probable size is further shifted to higher SPP sizes.

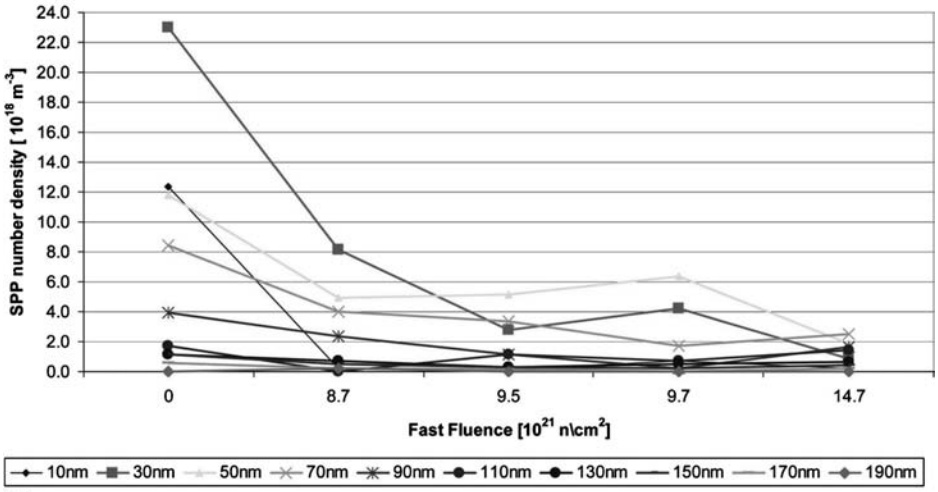
A comparison of the SPP size distribution for all irradiated and unirradiated samples as function of fast fluence and SPP density is provided in Fig. 3(*a*), 3(*b*). As seen in Fig. 3(*a*) for all irradiated samples small precipitates are partly dissolved and the size distribution of the precipitates turns into a continuous decrease of large size precipitates within 0–5 annual cycles (corresponds to local average fast fluence of 0–10.7×10^{21} n/cm^2). On the other hand a drastic reduction of SPP number density of the precipitates between the fast fluence of 10.7×10^{21} and 17.9×10^{21} n/cm^2 could be observed. Furthermore, an increase of the median of the precipitate size was also observed for the sample irradiated after nine annual cycles (correspond 17.9×10^{21} n/cm^2) in this table.

From Fig. 3(*b*) it can clearly be seen that the size distributions of the samples with six and seven cycles irradiation are similar. However, the number of precipitates below 70 nm is considerably reduced. After seven cycles a further reduction of the precipitate number density can be observed below about the 90 nm size. Interestingly, the class of 50 nm drops from 6×10^{18} to 2×10^{18}/m^3 for the nine cycle specimen.

SPP Chemical Analysis—The chemical analyses and size distribution of precipitate from all samples were calculated on the basis of 50–100 particles by EDX analysis. The results clearly showed that the SPPs chemical composition due to the increasing fast fluence varies considerably between the samples. It should be noted that the quantitative chemical and compositional analyses of the SPPs were difficult due to high background noise from the Zr matrix underneath the SPP as well as from the SPP itself. In general the elemental content of Fe and Cr decreased from the centre of the precipitate to the matrix. Most probably this could be due to the high signal from matrix at the edge of precipitate. For instance, for the unirradiated materials, the $Zr_2(Ni, Fe)$ particles indicates the presence of Cr but due to statistical variation a quantification of Cr was not achievable. The equivalent behavior was seen for the $Zr(Cr, Fe)_2$ particles. However, it is clear that the overall alloying element content of the precipitates decreases with the number of cycles in the reactor. This phenomenon is due to the continuous dissolution of alloying elements of the precipitates into the surrounding Zr matrix. As an example, although the ratio of Fe/Cr remains low from the beginning of irradiation (as shown for the material having with a fluence of 5.9×10^{21} n cm^2), the amount of alloying elements present in these precipitates was still very high and for large precipitates very close to the concentration in unirradiated precipitates. These types of precipitates showed much lower alloying element content for materials after high irradiation times.



(*a*)



(*b*)

FIG. 3—*(a) The precipitate size distribution of all irradiated and unirradiated samples as a function of operating cycles. The three cycles data are normalized values 13. (b) The SPP number density versus specimen fast fluence*

TABLE 4—*Summary of data for Fe/Ni and Fe/Cr ratios with the measured rod growth, and calculated hydrogen pickup fraction.*

Rod Identity	Number of Cycles	Rod Growth [mm]	Oxide Thickness [+m]	Rod Av. Metal H2 (ppm)	Hydrogen Pickup Fraction (%)	Fast Fluence [10^{21} n cm^2]	Average Fe\Ni			Avareage Fe\Cr	Number of Analysed Particles (EDX)
Uniradiated	0					0	max 2.1 min 1.6	1.9	0.8	max 1.1 min 0.7	39
AEB070-E4	3	10.5	5±2	44±2	12.8	5.9	max 1.3 min 0.9	1.5	0.2	max 0.4 min 0.1	15
AEB069-E4	5	12.7	12±2	75±22	12.7	8.7	max 4 min 0.8	1.5	0.2	max 0.4 min 0.1	42
AEB068-E4	6	16.6	15±3	205±4	23.2	9.5	max 4 min 0.8	1.5	0.1	max 0.3 min 0.1	45
AEB071-E4	7	15.34	26±4	327±19	25.6	9.7	max 4 min 0.8	1.6	0.1	max 0.4 min 0.1	40
AGB108-G6	9	28.5	45±7	664±94	30.0	17.9	max 2 min 0.5	1	0.2	max 0.5 min 0.1	33

The microchemistry variation of the analyzed SPP with respect to Fe/Ni and Fe/Cr is summarized in Table 4. The chemical composition of SPPs in unirradiated material consists of Cr–Fe particles with a Cr/Fe ratio of 0.8 and for Ni–Fe particles where the Ni/Fe ratio is measured to 1.9. The lowest Fe/Cr ratios in the table, i.e., for nine cycles sample with specimen fluence of 17.9×10^{21} n/cm^2, should be considered as an approximate value because of the EDX resolution. The EDX analyses of several Fe–Ni bearing precipitates show that the Fe/Ni ratio stays more or less constant for the irradiated samples at 1.5 to 1.6 and drops to about 1 after 17.9×10^{21} n/cm^2 for nine cycles of operation. The chemical analyses for irradiated samples showed the formation of high density Fe-depleted Cr-rich particles whereas Fe–Ni containing particles reveal a typical average ratio of Fe to Ni of about 1. It indicates that the Fe depletion of Fe–Ni SPPs is followed by a parallel Ni dissolution.

The Fe/Cr ratio drops immediately after irradiation and remains essentially identical for six and seven cycles samples, with similar number densities. EDX line scans across SPPs are shown in Fig. 4. The line scan from the sample after five cycles confirms the fact that the Fe is diffusing out of the Cr–Fe SPPs and that the Fe is retained to greater extent within the Ni–Fe particles. Analyses performed across a grain boundary close to a dissolved SPP do not show an increased Fe signal in the grain boundary, implying that Fe remains in the Zr matrix. The line scans across the six and seven annual cycles with almost similar accumulated fast fluence, Figs. 5 and 6, show that the Cr–Fe SPPs appear to have lost more Fe to the matrix, than in the five cycles sample (see Fig. 4). The analysis of Fe–Ni and Fe–Cr bearing SPPs for six and seven annual cycles indicates strong signals for both Ni and Cr and the elemental ratio of Fe/Ni of 1.5 and 1.6 were obtained for the six and seven samples, respectively (see Table 4). Figure 7 illustrates the line scan acquired for the sample irradiated after nine cycles with fast fluence of the 17.9×10^{21} n/cm^2. The line scan profile across the Fe–Cr SPP exhibits a gradual gradient of the Cr content compared to the Cr line profile observed for the sample irradiated between five and seven cycles with local accumulated fast fluence of 10.7×10^{21}–11.8×10^{21} n/cm^2. Furthermore, EDX analysis of the precipitate shows that the Fe/Cr ratio decreases with increasing the neutron fast fluence from 0.8 for unirradiated sample down to ~ 0.2 for all irradiated samples. As seen in Fig. 7 the line scan profile of the crystalline Fe–Ni precipitate type of SPP shows irregular shapes. The EDX analysis of $Zr(Cr, Fe)_2$ intermetallic precipitate from which Fe is diffusing into the matrix, confirm a Cr–Fe SPP particle with a contrast in the basal plane direction, i.e., perpendicular to the 0002-direction. This image may illustrate the nucleation of radiation-induced $\langle c \rangle$ loop dislocation, i.e., located on the basal plane. The chemical analysis of the small particle along these fringes showed a high Cr concentration content with Fe/Cr ratio of 0.1. A number of $\langle c \rangle$ dislocations together with dislocations surrounding the stacking-fault (labelled as G) are also found in the TEM image taken from the nine cycles sample (Fig. 2(*e*)). Details of the dislocation analysis will be published later.

As seen the Fe/Ni ratio subjected to the nine cycles sample reduces compared to the Fe/Ni ratio obtained for the unirradiated, five, six, and seven cycles

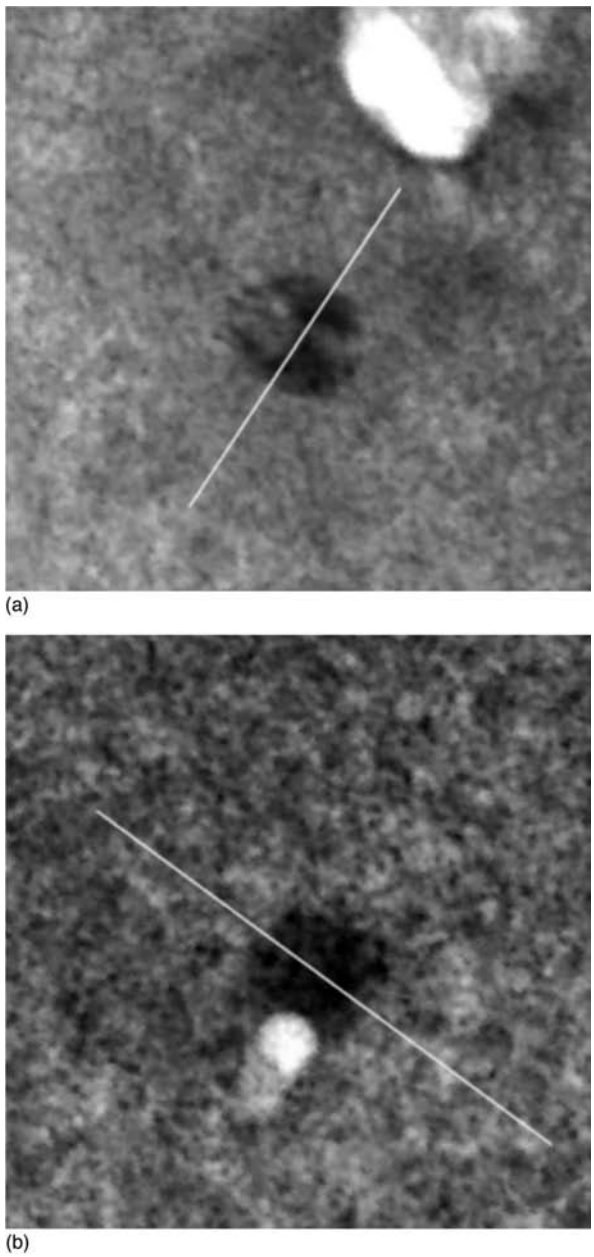


FIG. 4—*The line scan across SPP on the five cycles sample: (a) Image and line scan on two Ni–Fe SPPs. Very limited Fe might be observed diffusing out of SPP. (b) Line scan and images on Fe–Cr SPP show that Fe is diffusing out of SPP. Low Fe signal implies that a large part of Fe is already lost into the Zr matrix.*

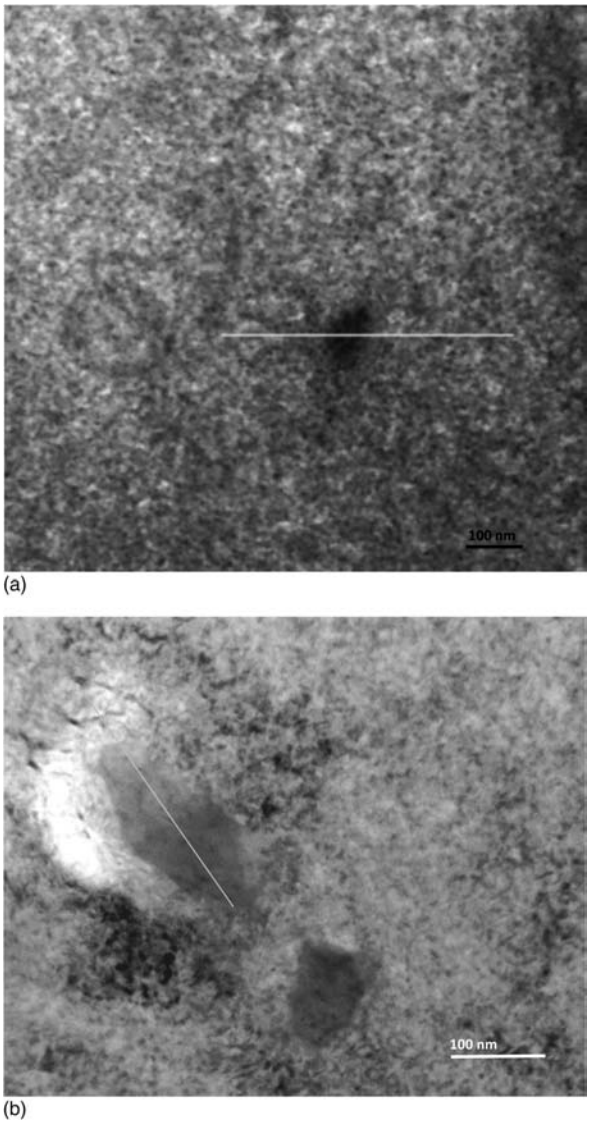


FIG. 5—*The line scans across the Fe–Cr SPP for the sample irradiated after six operation cycles: (a) Fe–Cr bearing SPP; (b) Fe–Ni bearing SPP.*

samples. An Fe/Ni ratio reduction could be evidence for the dissolution of $Zr_2(Ni, Fe)$ particles with Fe diffusing faster than Ni. Dissolution is far more obvious for $Zr(Cr, Fe)_2$ with high Cr concentration visibly surrounding these particles. This may be related to the fact that Cr has much slower diffusion rate in Zr matrix as compared with Fe and Ni.

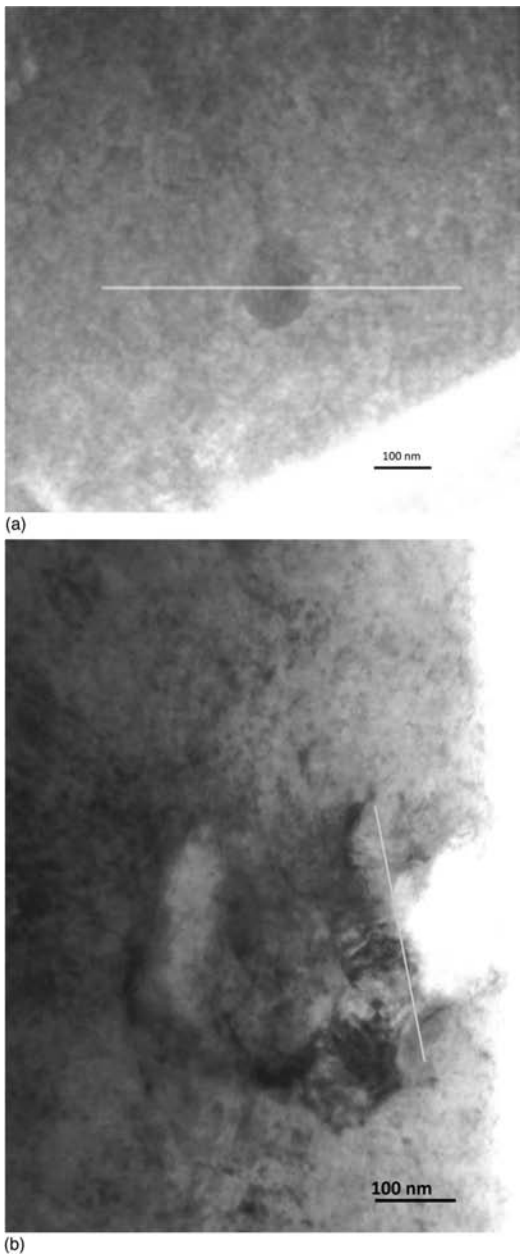


FIG. 6—*The line scans across the Fe–Cr SPP for irradiated sample after seven cycles: (a) Fe–Cr bearing SPP; (b) Fe–Ni bearing SPP.*

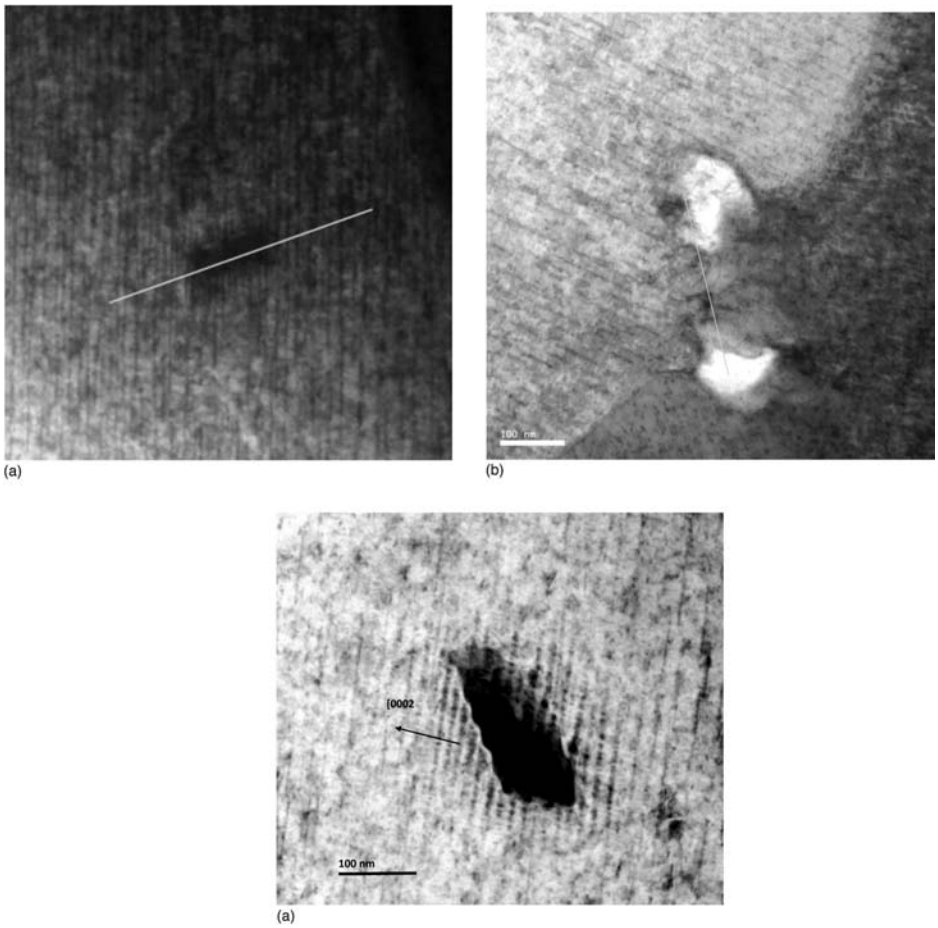


FIG. 7—*The line scan across the SPP on nine cycles sample. (a) The small Fe–Cr SPP type along these fringes showed a high Cr concentration with Fe/Cr ratio of 0.1. (b) The Fe–Ni SPP precipitate with Fe/Ni ratio of 1. Note that the Fe/Cr ratio value is associated with this SPP particle observed in this image. Note, the ratios in the Tables 3 show the SPPs average values, i.e., estimated for each sample. (c) The TEM image shows a radiation-induced ⟨c⟩-loop dislocation located on the basal plane direction, i.e., perpendicular to the 0002-direction.*

SPP Amorphisation—Bright field images with corresponding SAED of the Fe–Cr bearing SPP particle with Fe/Cr ratio on all four irradiated samples are shown in Fig. 8. The sample irradiated after five annual cycles exhibits a Fe/Cr ratio of 0.2. The concentration profile within the precipitates results in a duplex structure, e.g., crystalline core and amorphous periphery [17]. The amorphous transformation is understood to begin at the particle matrix interface and advances inwards until complete amorphisation is accomplished. Thus,

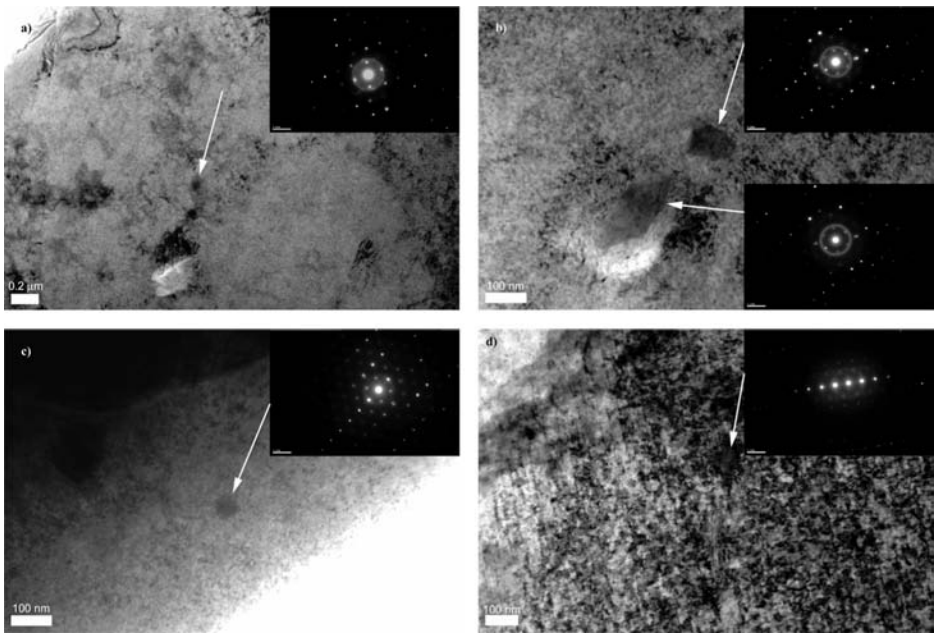


FIG. 8—*Bright field images and corresponding SAED patterns of Fe–Cr bearing precipitates for (a) five cycles sample with Fe/Cr=0.22; the SAED image Fe–Cr SPP reveals a duplex structure; (b) six cycles sample with Fe/Cr=0.12; (c) seven cycles sample with Fe/Cr=0.11; and (d) nine cycles sample with Fe/Cr=0.05. The SAED patterns of six cycles sample is fully amorphized SPPs.*

amorphization is correlated with Fe depletion, and may be caused by it. The diffraction patterns obtained by SAED for all respective samples revealed fully amorphous structures for SPPs.

Figure 9 shows the bright field images with corresponding SAED for the Fe–Ni particles with Fe/Ni ratio for all irradiated samples in this study. As seen in the images the Ni containing particles are still fully crystalline and no amorphous halos were observed for any of the samples. The Fe/Ni ratio was slightly decreased with increasing fast fluence without any transformation to amorphous structures. It should be noted that the Fe/Cr and Fe/Ni ratios are the values measured for that specific SPP particle in the image. The ratios in Table 4 present the average value of each specific SPPs. Chemical analysis and EDX line scans of SPPs presented in Figs. 5–7 show that the Fe–Ni bearing SPPs particle size decreases slightly with increasing the fast fluence. However, as expected, no evidence of amorphisation for the Fe–Ni bearing SPPs particle was found during this investigation. The reason is believed to be related to parallel dissolution of Fe and Ni into matrix, while Fe in Zr–Fe–Cr precipitates dissolves selectively due to the difference of diffusivity between Fe and Cr. It is known that the respective diffusivities of Fe and Ni in Zr are similar and greater by one to two orders than that of Cr [18].

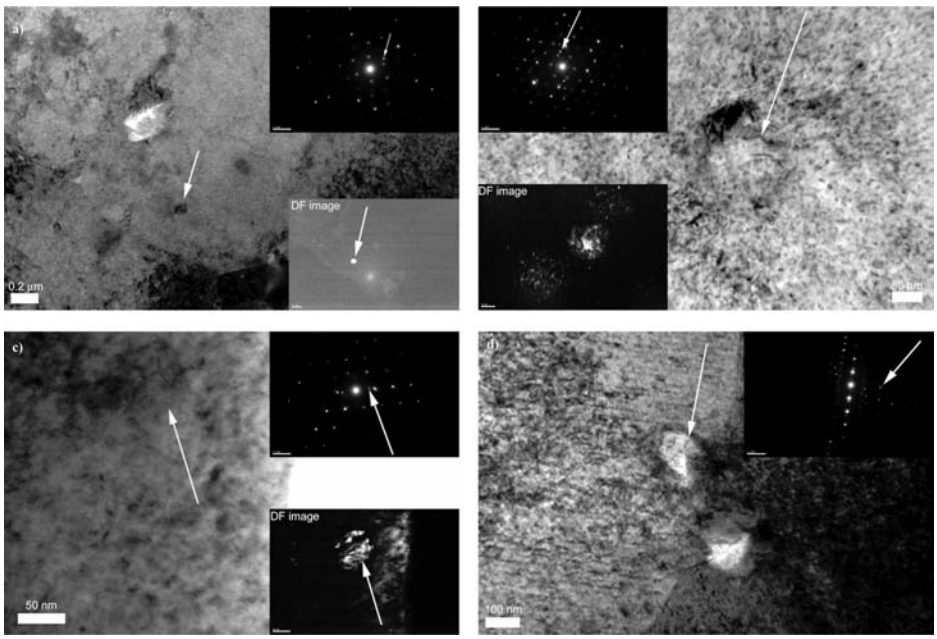


FIG. 9—*Bright field image with corresponding SAED patterns of Fe–Ni type SPP particle. All irradiated samples showed the crystalline Fe–Ni SPPs. (a) Five cycles sample with Fe Ni=1.5; (b) six cycles sample the Fe/Ni=1; (c) seven cycles sample with Fe/Ni=1.2; and (d) nine cycles sample showed crystalline Fe–Ni SPP with Fe/Ni ratio of 0.66. It should be noted that the Fe/Ni ratio is the value measured for this specific SPP particle in the image. The ratio in the Table 4 shows the average value estimation.*

Effect of SPP Size Distribution and Dissolution on Hydriding and Rod Growth Performance—The known mechanisms behind fuel rod growth include the fast neutron irradiation effect on the Zircaloy microstructure, the volume increase of the cladding as an effect of hydrogen pickup and the creep driven by swelling of the fuel, once the inner cladding wall is in hard contact with the fuel pellets and lead to pellet-cladding-mechanical-interaction. The precise growth mechanism associated with neutron irradiation of Zircaloy is not known, but a correlation of growth to microstructure evolution exists. The magnitude of irradiation growth is believed to be dominated by radiation-induced damage including dislocation density and SPPs size [6,7,10].

Also, it is known that the dissolution and depletion of the alloying elements, such as Fe, Ni, and Cr, from intermetallic precipitates play a crucial role in the high-burnup behavior of Zircaloy-2. Secondary phase particle dissolution throughout the Zr matrix is associated with the Fe and Cr concentration increases in the matrix surrounding the precipitate [7,15]. It is also believed that the dissolution of the $Zr(Cr,Fe)_2$ SPP affects the breakaway growth under irradiation [19]. But this hypothesis may not be consistent with the conclusion of this study. During the dissolution process Fe will diffuse into the matrix

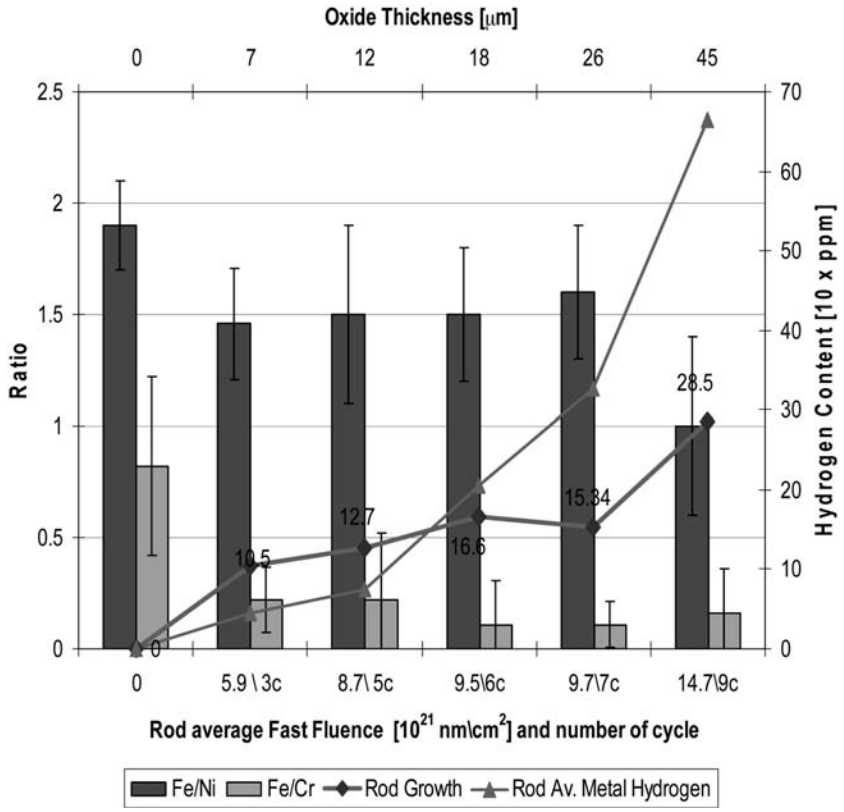


FIG. 10—*Rod growth behavior of the irradiated sample with respect to Fe/Cr and Fe/Ni ratios at the rod average fast neutron fluence (≥1 MeV) between* 5.9×10^{21}–14.7×10^{21} n/cm^2. *The error bar represents the standard deviations of the Fe/Cr and Fe/Ni ratios. Note that the x-axis represents the rod average fast fluence.*

without being replaced by another element, e.g., by vacancy exchange mechanism [10]. Consequently decreasing of the local Fe content may be associated with the nucleation and growth of ⟨*c*⟩ component dislocation loops. Several studies indicate that growth is associated with the density of ⟨*c*⟩ dislocation loops [10]. If the result of ⟨*c*⟩ loops formation would accelerate or breakaway growth this still need to investigated.

As shown in Fig. 1 the average hydrogen concentration increases after seven cycles of operation, leading to greater rod growth. Table 4 and Fig. 10 indicate that the high growth observed for nine cycles sample can be correlated with the chemical composition of SPP with respect to the different Fe/Ni ratios, compared to the 5, 6, and 7 cycles sample.

From these observations it can be concluded that indeed the cladding microstructure after irradiation has an influence on the growth behavior.

Comparing the EDX analysis, the results showed that the Fe/Cr ratio of the intermetallic $Zr(Cr, Fe)_2$ precipitates of the six cycles sample is slightly lower than that of the five cycles sample. The Fe/Ni ratio in the Ni bearing SPPs of the seven cycles sample is about 1,6 and decreasing to about one for the nine cycles sample. Thus, the significant Fe depletion, reflecting the decreasing Fe/Ni and Fe/Cr ratios, together with the decreasing number density of SPPs may cause the observed increase of the hydrogen pickup, leading to an increased rod growth rate—with increasing fast fluence (Fig. 10 and Table 4). The exact mechanism is, however, not yet understood.

Apart from the chemical composition of SPPs and the resulting matrix composition of dissolved elements, another factor influencing growth could be the anisotropic diffusion of the alloying elements into the matrix, i.e., atoms in solution could hypothetically interfere with the evolution of the dislocation structure.

M. Griffiths et al. [6,10] has shown that there is no obvious dependence of growth on SPPs size. The study showed that neutron irradiation causes dissolution and redistribution of the SPPs due to displacement cascades leading to the migration of the solute elements into the Zr matrix. Hypothetically, this could be the reason on how dissolution of SPPs influences corrosion properties. As shown in Fig. 1 and Table 4 the hydrogen pickup fractions as well as the corrosion rate appear to correlate to Fe/Cr and Fe/Ni ratios, which change continuously under irradiation conditions, together with the number density of SPPs.

The data presented in this work is consistent with a previously reported model regarding the cladding oxidation and exponential acceleration of the hydrogen pickup fraction under normal reactor conditions [16]. Results from this study confirm that the increased oxide thickness, the higher hydrogen content, and the accelerated growth of the rods at rod average burnup of 78 MWd/kgU go along with a change in the appearance of the secondary phase particles characterized by TEM.

Conclusions

The radiation-induced evolution of chemical composition and size distribution of SPP in Zircaloy-2 cladding material after three, five, six, seven, and nine annual cycles were studied. The following concluding remarks can be made:

- The SPP number density was found to decrease dramatically with fast neutron fluence after three cycles of operation (Fig. 3(*a*)).
- The SPP average size initially decreases during irradiation due to the dissolution of small, most probably Fe–Cr, SPPs. At the specimen fast fluence of 10.7×10^{21} n/cm^2 all SPPs with an initial diameter less than 30 nm had been fully dissolved.
- The Fe–Cr SPPs become amorphous at Fe/Cr ratios lower than about 0.2. This is followed by depletion of Cr from the SPPs and finally total dissolution. Amorphous and Cr-rich particles along with crystalline Fe–Ni particles are left after 78 MWd/kgU.
- A high number density of amorphous and Cr-rich particles along with crystalline Fe–Ni particles are seen after at fast fluence level of 17.9×10^{21}/cm^2.

- No amorphisation of Fe–Ni SPPs was found. The Fe–Ni SPPs decrease in size due to a parallel loss of Fe and Ni. No amorphisation could be found.
- At very high fluence, 17.9×10^{21} n cm^2, no preferential diffusion path for Fe could be established except for Cr, the apparent preferred diffusion occurred along the Zr basal planes (Fig. 7).
- The acceleration of the hydrogen pickup seems correlated with depletion of Fe from the $Zr_2(Fe, Ni)$ SPPs (see Table 4).
- The overall amount of alloying element in the remaining precipitates reduces with the fluence.

Acknowledgments

The writers would like thank the staff at PSI and Studsvik as well as Fuel Performance Program-Phase 2 (FPP-2) members for their very significant contributions.

References

[1] Rudling, P., Wikmark, G., Lehtinen, B., and Pettersson, H., "Impact of Second Phase Particles on BWR Zr-2 Corrosion and Hydriding Performance," *Zirconium in the Nuclear Industry: Twelfth International Symposium, ASTM STP 1354*, G. P. Sabol and G. D. Moan, Eds., Toronto, Canada, ASTM International, West Conshohocken, PA, 2000, pp. 678–706.

[2] Garzarolli, F., Schumann, R., and Steinberg, E., "Corrosion Optimised Zircaloy for Boiling Water Reactor (BWR) Fuel Elements, " *Zirconium in the Nuclear Industry: Eleventh International Symposium, ASTM STP 1295*, A. M. Garde and E. R. Bradley, Eds., Germany, Sept. 11–14, ASTM International, West Conshohocken, PA, 1996, pp. 709–723.

[3] Kruger, R. M. and Adamson, R. B., "Precipitate Behaviour in Zirconium-Based Alloys in BWRs," *J. Nucl. Mater.*, Vol. 205, 1993, pp. 242–250.

[4] Yang, W. J. S., Tucker, R. P., Cheng, B., Adamson, R. B., "Precipitate in Zircaloy: Identification and the Effects of Radiation and Thermal Treatment," *J. Nucl. Mater.*, Vol. 138(2–3), 1986, pp. 185–195.

[5] Fidleris, V., Turker, R. P., and Adamson, R. B., "An Overview of Microstructral and Experimental Factors that Effect the Irradiation Growth Behavior of Zirconium Alloys," *Zirconium in the Nuclear Industry: Seventh International Symposium, ASTM STP 939*, R. B. Adamson, L. F. P. Van Swam, and C. M. Eucken, Eds., ASTM International, West Conshohocken, PA, 1987, pp. 49–85.

[6] Griffiths, M., Mecke, J. F., and Winegar, J. E., "Evolution of Microstructure in Zirconium Alloys During Irradiation," *Zirconium in the Nuclear Industry: Eleventh International Symposium ASTM STP 1295*, E. R. Bradley and G. P. Sabol, Eds., Germany, Sept. 11–14, ASTM International, West Conshohokcen, PA, 1996, pp. 580–602.

[7] Huang, Y. P., Mahmood, S. T., and Adamson, R. B., "Effects of Thermo Mechanical Processing on In-Reactor Corrosion and Post Irradiation Mechanical Properties of Zircaloy-2," *Zirconium in the Nuclear Industry: Eleventh International Symposium, ASTM STP 1295*, E. R. Bradley and G. P. Sabol, Eds., ASTM International, West Conshohocken, PA, 1996, pp. 726–757.

[8] Tägtström, P., Limbäck, M., Dahlbäck, M., Andersson, T., and Pettersson, H., "Effects of Hydrogen Pickup and Second Phase Particle Dissolution on the In-Reactor Corrosion Performance of BWR Claddings," *Zirconium in the Nuclear Industry: Thirteenth International Symposium, ASTM STP 1423*, France, June 10–14, ASTM International, West Conshohocken, PA, 2001, pp. 96–118.

[9] Kesterson, R., King, S., and Comstock, R., "Impact of Hydrogen on Dimensional Stability of Fuel Assemblies," *Proceedings of the ANS International Topical Meeting on LWR Fuel Performance*, Park City, UT, Apr. 10–13, 2000.

[10] Griffiths, M., Gilbert, R. W., and Carpenter, G. J. C., "Phase Instability and Redistribution of Intermetallic Precipitates in Zircaloy-2 and Zircaloy-4 During Neutron Irradiation," *J. Nucl. Mater.*, Vol. 150, 1987, pp. 53–66.

[11] Ledergerber, G., Valizadeh, S., Wright, J., Hallstadius, L., Gavillet, D., and Abolhassani, S., "Fuel Performance Beyond Design—Exploring the Limits," *TopFuel September 2010 LWR Fuel Performance Meeting*, Orlando, FL, Sept. 26–29, 2010.

[12] Ledergerber, G., et al., "Burnup Increase and Power Update Operation History of KKL," *Proc. Intern. LWR Fuel Performance Meeting*, San Francisco, CA, Sept. 30–Oct. 3, 2007.

[13] Abolhassani, S., Gavillet, D., Groeschel, F., Jourdain, P., and Zwicky, H. U., "Recent Observations on the Evolution of the Secondary Phase Particles in Zircaloy-2 Under Irradiation in a BWR up to High Burn-Up," *Proc. of the Intern. Topical Meeting on Light-Water-Reactor Fuel Performance*, April 10–13, IAEA, Park City, UT, 2000, p. 470.

[14] Hermann, A., Wiese, H., Bühner, R., Steinmann, M., and Gerhardt, B. "Hydrogen Distribution Between Fuel Cladding Metal and Overlying Corrosion Layers," *Proceedings of the ANS International Topical Meeting on LWR Fuel Performance*, April 10–13, IAEA, Park City, UT, 2000, pp. 327–384.

[15] Adamson, R. B., "Effects of Neutron Irradiation on Microstructure and Properties of Zircaloy," *Zirconium in the Nuclear Industry: Twelfth International Symposium, ASTM STP 1354*, G. P. Sabol and G. D. Moan, Eds., Toronto, Canada, June 15–18, ASTM International, West Conshohocken, PA, 2000, pp. 15–31.

[16] Zhou, G., Wikmark, G., Hallstadius, L., Wright, J., Dahlback, M., Brandes, L. P., Wetterholm, U., Lindquist, A., Valizadeh, S., and Long, Y., "Corrosion and Hydrogen Uptake Behavior and Modeling for Modern BWR Cladding Materials at High Burnup," *2009 Water Reactor Fuel Performance Meeting*, Paris, France Sept. 6–10, 2009, pp. 23.

[17] Lefebvre, F. and Lemaignan, C., "Analysis with Heavy Ions of the Amorphisation Under Irradiation of Zr(Fe, Cr)2 Precipitates in Zircaloy-4," *J. Nucl. Mater.*, Vol. 171, 1990, pp. 223–229.

[18] Etoh, Y., Nonaka, Y., Kubo, T., Nomata, T. Hayashi, H., and Kitamura, M., "The Effect of Microstructure on the Corrosion Behavior of Zircaloy-2 in BWRs," *Zirconium in the Nuclear Industry: Twelfth International Symposium, ASTM STP 1354*, G. P. Sabol and G. D. Moan, Eds., Toronto, Canada, June 15–18, ASTM International, West Conshohocken, PA, 2000, pp. 658–677.

[19] Garde, A. M., "Enhancement of Aqueous Corrosion of Zricaloy-4 due to Hydride Precipitation at the Metal/Oxide Interface," *Zirconium in the Nuclear Industry: Ninth International Symposium, ASTM STP 1132*, C. M. Eucken and A. M. Garde, Eds., Japan, Nov. 5–8, ASTM International, West Conshohocken, PA, 1991, pp. 566–594.

DISCUSSION

Question 1, Ron Adamson:—1) What is the temperature(s) of the material? 2) Are you understanding that the relatively constant Fe//Ni ratio means that the SPP is not dissolving or Fe and Ni are diffusing out of the SPP at equal ratio? Did you mean the composition of the matrix?

Author's Response:—1) We did not measure the material Temperature. But the operating temperature at KernKraftwerk Leibstadt (KKL) is 286°C.

2) Yes we did measure the composition of the matrix. Also the EDX analyses of several Fe-Ni bearing precipitates show that the Fe/Ni ratio stays more or less constant for the irradiated material and drops to about 1 after specimen fast fluence of 17,9 × 1E21 n/cm^2. (>1 MeV). It indicates that the Fe depletion of Fe-Ni SPPs is followed by a parallel Ni dissolution into Zr-matrix.

Question 2, Artur Motta, Penn State University:—Concerning the evolution of SPP, we see a large depletion of 30 nm precipitates at 5 cycles. Do you think results might be affected by all inability to detect small precipitates? Were they detected by EDS?

Author's Response:—Your question addressing to different measurement values:

1) The SPP size and distribution and the number density using TEM imaging technique
2) Chemical analysis of SPP using TEM/EDS detector

For case 1: The radiation damage defects usually interfere with the detection of very small precipitates. It is therefore difficult to consider without ambiguity the distribution of 10 nm particles in the matrix. It is worth noting that sample preparation of specimens can also create surface artefacts that sometimes make it difficult to differentiate between the defects caused by irradiation and the effects of specimen preparation. In order to differentiate a SPP from a defect, chemical analysis is performed on a large number of particles before it can be claimed that they represent a precipitate. However, the comparison of the results between unirradiated sample and irradiated specimens up to the local fast fluence of 10,7 × 1E21 n/cm^2 shows that all small SPPs <30 nm were fully dissolved into the matrix. For the 5, 6 and 7 cycles samples with local fast fluence from 10,7 -11,8 × 1E21 n/cm^2, the most probable SPP size is shifted towards a higher value meaning that the smaller particles have dissolved and very large particles are becoming smaller during irradiation. This was one of the finding results presented in this work.

For case 2, The quantitative chemical and compositional analyses of the SPPs were difficult due to high background noise from the Zr matrix underneath of the SPP as well as from the SPP itself. In general the elemental content of Fe and Cr decreased from the centre of the precipitate to the matrix which is most probably could be due to the high signal from matrix at the edge of precipitate. For instance, for the unirradiated materials, the Zr2(Ni,Fe) particles indicates the presence of Cr but due to statistical variation a quantification of Cr was not achievable. The equivalent behaviour was seen for the Zr(Cr,Fe)2 particles. Poor sample preparation and artifact created during the elctropolishing has also crucial influence on EDS measurement. Otherwise the EDS diction limits is 0.1–1% with lateral resolution <0,2 nm.

Question 3, Zhongwen Yao, Queens University:—1) 1) Temperature effects? 2) Irradiation dose? 3) Why is there a one side peak of Ni in EDS measurement?

Author's Response:—1) Please see above.

2) Irradiation growth is very sensitive to metallurgical conditions and growth behavior varies from one Zircaloy material to another depending on the detailed chemical compositions and the microstructure evolved during fabrication processes as mentioned above. The important metallurgical factors are, (i) crystallographic texture, (ii) degree of cold working (ii) degree of recrystallization, (iii) grain size and morphology and (iv) chemical composition. The operational factors are temperature and fast neutron fluence. Fast neutrons (with energies $E \geq 1$ MeV) cause displacement of Zr atoms from their stable positions by collision. Generally to the conversion factor for the fast neutron fluence ($E \geq 1$ MeV) to displacement per atom is around 2 dpa for each 10^{25} neutron n/m^2 and in case of cladding tube it receive about 4 dpa per irradiation cycle, i.e., each Zr atom is displaced on average 4 times per cycle. In this paper we focused on fast fluence influences on SPP chemical, size and number of density changes. The Details of the dislocation analysis will be published later.

3) The reason is that the line scan is performed on two overlapping SPPs.

Question 4, Anand Garde, Westinghouse Electric:—For the 9-cycles Fe-Cr SPP dislocation micrograph what is the reason for the blank lines? Are they c+ a dislocations generated by Fe dissolution from the SPP?

Author's Response:—The authors believed that decreasing of the local Fe content may be associated with the nucleation and growth of ⟨c⟩ component dislocation loops. The black lines or fringes showing the ⟨c⟩ type of dislications. Several studies indicate that growth is associated with the density of ⟨c⟩ dislocation loops. The TEM image shows the radiation- induced ⟨c⟩-loop dislocation located on the basal plane direction i.e. perpendicular to the 0002-direction.

Question 5, J.-C. Brachet, CEA, France:—1) How many SPP have you analyzed for each condition you investigated? 2) You have presented the mean value Fe/Ni and Fe/Cr ratios evolution vs the BU. Perhaps it could be interesting to plot the results vs the remaining SPPs diameter (because of the initial size distribution of SPPs.)

Author's Response:—1) The number of SPP measured was around 50–111 for each material, depending on the frequency of occurrence of the particles.

2) To compare the SPP size distribution for all irradiated and unirradiated samples as function of fast fluence Figure 3a with the SPP equivalent size vs. SPP number density is plotted. This plot indicates that at fluence of 10,7 × 1E21 n/cm^2 all small SPPs <30 nm were fully dissolved into the matrix. It is also shows that for the 5, 6 and 7 cycles samples with local fast fluence from 10,7–11,8 × 1E21 n/cm^2, the most probable SPP size is shifted towards a higher value meaning that the smaller particles have dissolved and very large particles are becoming smaller during irradiation. After 7 cycles a further reduction of precipitate number density can be observed below about 90 nm size. Interesting the class of 50 nm drops from 6 × 1E18 to 2 × 1E18/m^3 for the 9 cycles specimen.

Instead of the plotting graph associated with the Fe/Ni and Fe/Cr data vs. BU, we add a table to show the uncertainties of the measurement, the number SPP i.e., analyzed by EDS, the average ratio Fe/Ni and Fe/Cr in different precipitate.

Reprinted from JAI, Vol. 8, No. 1
doi:10.1520/JAI102949
Available online at www.astm.org/JAI

P. Vizcaíno,[1,2] *A. V. Flores,*[2] *P. B. Bozzano,*[3] *A. D. Banchik,*[2] *R. A. Versaci,*[3] *and R. O. Ríos*[2]

Hydrogen Solubility and Microstructural Changes in Zircaloy-4 Due to Neutron Irradiation

ABSTRACT: The present work deals with two essential degradation mechanisms of zirconium alloys: Hydrogen behavior and microstructural transformations due to neutron irradiation. The studies were carried out by using samples taken from Zircaloy-4 components, which remained for 14 years in the Atucha I pressurized heavy water reactor, accumulating neutron fluences of up to $10^{22}\,\mathrm{neutrons/cm^2}$. A hydrogen/deuterium solubility increase was observed in both dissolution and precipitation processes. With the aim to follow this evolution with radiation damage recovery, the irradiated samples were annealed for different periods at 350 and $400^{\circ}\mathrm{C}$ in a differential scanning calorimeter (DSC). These temperatures were chosen to reproduce those reached by spent fuels in the early stages of the dry storage (DS). Between intervals, the terminal solid solubility temperatures in dissolution (TTSSd) and in precipitation (TTSSp) were determined. They were also determined after additional annealing at 500 and $600^{\circ}\mathrm{C}$, trying to simulate long periods at DS. The hydride morphology and the metallurgical state of the $\mathrm{Zr(Fe,Cr)_2}$ second-phase particles (SPPs) were followed between

Manuscript received January 6, 2010; accepted for publication October 1, 2010; published online November 2010.

[1] Ph.D., Centro Atómico Ezeiza (CAE), Comisión Nacional de Energía Atómica (CNEA), Buenos Aires B1802 AYA, Argentina and Carrera del Investigador del Consejo Nacional de Ciencia y Técnica (CONICET), Pres. J. González y Aragón No. 15, Buenos Aires B1802 AYA, Argentina (Corresponding author).
[2] LMFAE, CAE, CNEA, Pres. J. González y Aragón 15, Buenos Aires B1802 AYA, Argentina.
[3] UAM, CAC, CNEA, Av. General Paz 1449 (1650), Buenos Aires, Argentina.

Cite as: Vizcaíno, P., Flores, A. V., Bozzano, P. B., Banchik, A. D., Versaci, R. A. and Ríos, R. O., "Hydrogen Solubility and Microstructural Changes in Zircaloy-4 Due to Neutron Irradiation," *J. ASTM Intl.*, Vol. 8, No. 1. doi:10.1520/JAI102949.

Copyright © 2011 by ASTM International, 100 Barr Harbor Drive, PO Box C700, West Conshohocken, PA 19428-2959.

annealing by optical microscopy, analytical electron microscopy, synchrotron light X-ray diffraction[4] (SXRD), and DSC. As a brief summary, we found from the first to the last run of the annealing sequence an increase of $55^{\circ}C$ in TTSSd and $40^{\circ}C$ in TTSSp on average. The optical and transmission electron microscopies (TEM) indicate that in the material in the irradiated condition, exists a hydride size distribution of four orders of magnitude, from 10 nm to $100\,\mu m$, but biased to sizes smaller than $5\,\mu m$. A complete amorphisation of the SPPs was observed in high fluence samples by TEM and SXRD. Similar TEM observations made in irradiated samples annealed above $400^{\circ}C$ show a re-precipitation process of nano-SPPs forming clusters. The re-precipitation is affected by kinetics: The SPPs crystallization temperature, T_c, rises from 450 to $500^{\circ}C$ as the heating rate increases from 5 to $20^{\circ}C/min$. The measured heat of crystallization was $27.3 \pm 2.1\,kJ/mol\ (Fe + Cr)$.

KEYWORDS: Zircaloy-4, irradiation, hydrogen, SPPs, AEM, DSC

Introduction

Under the reactor operating conditions, zirconium components go through transformations that affect their original microstructural and thermodynamical properties. For Zircaloy-4 components, depending on the time in service and the irradiation conditions, two phenomena have significant consequences: Hydrogen uptake and second-phase particle (SPP) amorphisation/dissolution. Zircaloy-4 has been extensively used for fuel claddings, fuel channels, and other reactor internal components. In the case of the Atucha I reactor, the cooling channels, Zircaloy-4 tubular structural components about 6 m long, were designed to withstand the entire lifetime of the reactor. Inside the channels are placed fuel elements of 5.3 meters long. The fuel elements are cooled by a heavy water flow, which circulates from the bottom ($250^{\circ}C$) to the top of the reactor ($305^{\circ}C$). The channels are affected by a fast neutron flux ($E_n > 1\,MeV$), increasing from a nominal value of $1.35 \times 10^{13}\,neutrons/cm^2 \cdot s$ at the bottom to $1.69 \times 10^{13}\,neutrons/cm^2 \cdot s$ at the top, reaching a maximum value of $3.76 \times 10^{13}\,neutrons/cm^2 \cdot s$ at the centre of the channels.

These channels, depending on their position in the reactor core, can accumulate fluences of up to $10^{22}\,neutrons/cm^2$ after 10.3 effective full power years. These levels are similar to those reached by *high burn up* fuel claddings, for which other Zr-base alloys have recently replaced Zircaloy-4 [1,2]. Studies on cooling channels are meaningful from many points of view. The channels are structural components, which do not work under internal pressure or any other type of structural stress. The typical temperature of the cladding tubes in the reactor is about $350^{\circ}C$, at which many types of irradiation defects are annealed [3]. The temperature range of the cooling channels lies between 200–$235^{\circ}C$ (outer foil of the channels) and 260–$300^{\circ}C$ (internal tube), a difference that

[4]X-ray diffraction diagrams were obtained at the Brazilian Synchrotron (LNLS), Campinas, S. P., Brazil.

makes the defect recovery kinetics slower. The same is also valid for the amorphisation-dissolution kinetics of the $Zr(Fe, Cr)_2$ second-phase particles [4].

In the present context, a program oriented to determine the hydrogen solubility and microstructural transformations was carried out in LMFAE, CNEA[5], during the last decade. The most fruitful techniques were differential scanning calorimetry (DSC), analytical electron microscopy (AEM), and synchrotron light X-ray diffraction (SXRD) [5–8]. The aim of the present work is to summarize the results obtained from irradiated Zircaloy-4 taken from the cooling channels described above in relationship with hydride dissolution and precipitation, SPP amorphisation/dissolution, and the recovery of these conditions due to annealing processes.

Experimental

Unirradiated Zircaloy-4 Samples: Microstructure and Hydriding

For reference purposes, the hydrogen solubility was determined in unirradiated Zircaloy-4. The material was taken from a fully recrystallized Zircaloy-4 sheet with a grain size between 15 and 20 μm. The chemical composition is shown in Table 1.

Hydrogen was incorporated into the Zr matrix by the cathodic charge technique. Samples of $50 \times 10 \times 1.5\,mm^3$ were charged in an electrolytic cell containing a diluted aqueous solution of sulfuric acid at $80 \pm 2^{\circ}C$ in periods from 18 to 96 h. The current density was of $5\,mA/cm^2$. As a result, the hydride surface layers of a few microns up to 50 μm were obtained. The hydrogen was diffused and homogenized in the bulk with thermal annealing at 550°C during 3 h in air. Then, samples of $4 \times 4 \times 1.5\,mm^3$ were cut for DSC experiments. After the runs, the oxide layer was eliminated by mechanical polishing. The hydrogen content was measured by using a LECO RH-404 meter. We obtained the contents in the interval [50, 650] wppm, with an error of 4 %.

Irradiated Material Characterization and Sample Preparation

The irradiated material was taken from two Zircaloy-4 cooling channels removed from the Atucha I reactor. The channels consist of three concentric tubes of 6 m long and about 10 cm in diameter, having a 1.73 mm in the inner tube thickness and a 0.2 mm in the outer tube thickness (from now on we will call it foil 0.2). A 0.1 mm foil between both tubes isolates them. The channels were located one at the center of the reactor core (central channel (CC)) and one at the outer layer of the reactor (outer channel (OC)). The microstructure was fully recrystallized with a grain size of 20 ± 6 μm. The chemical composition is shown in Table 2.

[5]LMFAE: Laboratorio de Materiales de Fabricación de Aleaciones Especiales. CNEA: Comisión Nacional de Energía Atómica.

TABLE 1—*Chemical composition of the unirradiated Zircaloy–4 sheet.*

Alloying Elements (wt %)			Impurities (wppm)										
Sn	Fe	Cr	O	Ni	Hf	Al	Co	Cu	Mn	Mo	Ti	U	W
1.49	0.20	0.11	1100	49	99	39	18	30	36	8	3	1.5	25

Two rings were cut from the inner and outer tubes of the CC from a region close to the bottom of the reactor, called region R2CC. The inner ring remained in operation at 268°C while the outer (foil 0.2) at 205°C. The fast neutron ($E_n > 1$ MeV) fluence calculated for this region is 0.7×10^{22} neutrons/cm^2 [7,8]. Another ring was cut from the inner tube of the CC at the middle height of the channel, referred to as region R3CC. This material remained at 280°C. A fluence of 10^{22} neutrons/cm^2 was estimated for it. Finally, a fourth ring was cut from the inner tube of the OC at the middle height of the channel, called R3OC. This material also remained at 280°C, accumulating a neutron fluence of 0.4×10^{22} neutrons/cm^2.

The corrosion reaction between the zirconium and the heavy water releases deuterium (D), part of which is incorporated into the metal. In this way, the total equivalent hydrogen isotope concentration in wppm is given by $[H]_{eq} = [H] + 1/2^*[D]$, where [H] is the hydrogen content of the original material (about 15±5 wppm) and [D] is the deuterium content incorporated in service. The $[H]_{eq}$ contents were also measured with a LECO RH-404 m calibrated with deuterium gas. The $[H]_{eq}$ measured in this way are shown in Tables 3. The error for the concentration range of the samples is 4 wppm. Considering the uncertainty in the original material content we add to this value 5 wppm and, from the statistical error obtained in batches of similar hydrogen contents, another 6 wppm. Then, we estimate for $[H]_{eq}$ a global error of 15 wppm.

Samples for Differential Scanning Calorimeter Experiments—Twenty irradiated samples were prepared for DSC experiments. Particular attention was given to removing the oxide layer formed in service. The final shape of the irradiated samples was the same as the one already described in the Unirradiated Zircaloy-4 Samples: Microstructure and Hydriding section for unirradiated samples.

Samples for Synchrotron X-Ray Diffraction Experiments—Samples of $7 \times 7 \times 0.2$ mm^3 were prepared for synchrotron X-ray experiments. They were cut from the rings of the high fluence regions R2CC and R3CC as follows.

TABLE 2—*Chemical composition of the irradiated Zircaloy-4 CC and OC cooling channels.*

	Alloying Elements (wt %)			Impurities (wppm)
	Sn	Fe	Cr	Ni
CC	1.6	0.22	0.065	32
OC	1.6	0.21	0.07	41

TABLE 3—*Evolution of TTSSd and TTSSp in the samples of the batch R2CC (0.7×10^{22} neutrons/cm^2) with thermal annealing. The equivalent hydrogen contents are indicated.*

Samples		1	2	3	4	5	6
$[H]_{eq}$ (wppm)		63	80	···	79	62	68
T_{anneal} (°C)	Time (h)			TTSSd (°C)			
First run	0	246	244	246	250	251	251
350	1	273	267	278	277	276	280
400	7	292	291	294	296	296	302
500		296 (13 h)[a]	···	293 (1 h)	297 (3 h)	295 (1 h)	300 (1 h)
600		300 (7 h)	···	293 (2 h)	···	294 (1 h)	···
					TTSSp (°C)		
First run	0	205	205	205	207.0	206	205
350	1	211	204	209	211.3	208	209
400	7	···	211	206	217.9	216	208
500		222 (13 h)	···	219 (1 h)	222.4 (3h)	220 (1 h)	223 (1 h)
600		229 (7 h)	···	222 (2 h)	···	224 (1 h)	···

[a]Some of the samples were annealed at the same temperatures during different periods. These times are indicated on the right of TTSSd/TTSSp values.

TABLE 4—*Evolution of TTSSd and TTSSp in the samples of the batch R3CC (10^{22} neutrons/cm^2) with thermal annealing. The equivalent hydrogen contents are indicated.*

Samples		1	2	3	4
$[H]_{eq}$ (wppm)		84	147	···	···
T_{anneal} (°C)	Time (h)		TTSSd (°C)		
First run	0	253	259	269	274
350	1	308	320	308	304
400	15	335	361	333	343
600	1/12	330	363	329	337
			TTSSp (°C)		
First run	0	251	264	254	251
350	1	252	277	254	253
400	15	258	299	255	259
600	1/12	272	···	266	279

TABLE 5—*Evolution of TTSSd and TTSSp in the samples of the batch R3OC (0.4×10^{22}neutrons/cm^2) with thermal annealing. The equivalent hydrogen contents are indicated.*

Samples	1	2	T_{anneal} (°C)	3	4	5
$[H]_{eq}$ (wppm)	175	143		179	200	112
T_{anneal} (°C)	TTSSd (°C)			TTSSd (°C)		
First run	312 (0)	305 (0)	First run	313 (0 h)	310 (0 h)	302 (0 h)
420	331 (5 min)	312 (5 min)	350	319 (1 h)	325 (1 h)	300 (1 h)
600	366 (62 h)	363 (62 h)	400	366 (50 h)	363 (50 h)	331 (16 h)
			500	376 (6 h)	...	...
			600	...	...	331 (4 h)
	TTSSp (°C)			TTSSp (°C)		
First run	273 (0 h)	250 (0 h)	First run	278 (0 h)	265 (0 h)	254 (0 h)
420	279 (5 min)	273 (5 min)	350	292 (1 h)	282 (1 h)	253 (1 h)
600	336 (62 h)	306 (62 h)	400	327 (50 h)	319 (50 h)	253 (50 h)
			500	327 (6 h)	...	...
			600	...	318 (3 h)	278 (4 h)

(1) Three samples of the region R2CC (foil 0.2): one annealed 24 h at 600°C, one annealed 72 h at 600°C, and one preserved as-received.
(2) Four samples of the region R3CC: one annealed 24 h at 600°C, one annealed 72 h at 600°C, one annealed 72 h at 400°C, and one preserved as-received.
(3) For reference purposes, an unirradiated Zircaloy-4 sample was also prepared.

Samples for Analytical Electron Microscopy—Fifteen samples of the regions R2CC (foil 0.2) and R3CC were prepared for AEM. The R2CC samples were observed in the as-received condition and samples from R3CC were observed as-received, annealed 72 h at 400°C and 24 h at 600°C. The double jet technique was used, with a solution of 10 % of perchloric acid in methanol at −30°C.

Samples for Optical Microscopy—Three of the calorimetric samples were selected for optical microscopy: The samples 2 and 3 of the batch R3OC. Sample 2 was observed after the DSC program and sample 3, as-received, and after the DSC program. The sample 4 of the batch R3CC was observed as-received.

Calorimetry

Criteria for Temperatures of Terminal Solid Solubility in Dissolution and Temperatures of Terminal Solid Solubility in Precipitation Determinations—The DSC used to determine the temperatures of terminal solid solubility in dissolution (TTSSd) and in precipitation (TTSSp) is a thermal flux calorimeter, model DSC-60 by Shimadzu, which has been described elsewhere [6]. These

temperatures were measured at the peak temperature of the calorimetric curve, *pT*. This is one of the criteria commonly used for this aim [9–11]. These points are depicted in Fig. 1.

Differential Scanning Calorimetry Program—The thermal annealing and experimental runs for TTSSd and TTSSp determinations were both made at the DSC with the aim to observe the recovery effects on these temperatures. The choice of the annealing temperatures was made with the aim to simulate the dry storage (DS) conditions of spent fuel. During the first year at the DS, the fuel cladding remains at temperatures ranging from 350 to 400°C [12–14]. Taking this into account, both of these temperatures were included for the annealing. Even though an expression like the cumulative annealing parameter to choose equivalent temperature/time annealings would be useful to simulate long periods at these temperatures, it is not available for the irradiation damage [15]. Then, with the aim to assure a complete recovery of the radiation damage, the "equivalent" temperatures were selected as 500 and 600°C [7,8]. At the first DSC cycle (first run) all the samples were heated up to 350°C. The annealing sequence included an intermediate run, remaining 5 min at 400°C between the annealing at 400, 500, or 600°C. The experiments were made at a rate of ±20°C/min under a dynamic flow of 25 mL/min high purity N_2.

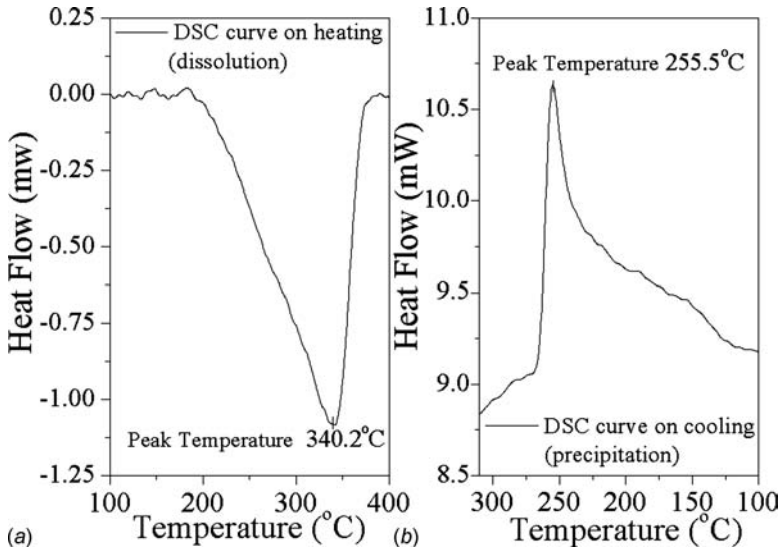


FIG. 1—*(a) DSC heating curve (dissolution) of a hydrided unirradiated Zircaloy-4 sample (132 wppm). (b) DSC cooling curve (precipitation) of the same sample. The maximum temperature reached in the experiment was 550°C. The points related with TTSSd and TTSSp determination are also indicated.*

Differential Scanning Calorimeter Studies on Re-Precipitation of the Amorphous Second-Phase Particles—The DSC used for these experiments is a thermal flux calorimeter DSC-Q200 by TA Instruments. The apparatus allows reaching 725°C as the maximum temperature.

The experiments were made under a N_2 dynamic atmosphere at heating rates of 5, 10, and 20°C/min. The heating ramps started after some min at 50°C, ending at 700°C.

X-Ray Diffraction Parameters

The diffraction diagrams were obtained at a powder diffraction line of the Brazilian synchrotron. The diffractometer was used in the $\theta-2\theta$ layout with a 0.05° step. The photon beam of 8.08 KeV defined a wavelength $\lambda = 1.542\,484$ Å ($\Delta\lambda = 0.000\,001$ Å). The number of photons per step fixed for the monitor was 280,000. The 2θ range was $20^\circ \leq 2\theta \leq 130^\circ$. The surface of the sample exposed to X-rays was the surface of the tubes. Owing to the fabrication texture, the normal to the surface exposed to the beam is close to the c-axis of the $\alpha-$Zr hexagonal cell [16].

Analytical Electron Microscopy

The transmission electron microscopy (TEM) analysis were carried out in a Philips CM 200 transmission electron microscope operated at 160/200 kV, with an energy dispersive X-ray Spectrometer EDAX DX-4. The measured parameter was the Fe/Cr ratio within the SPPs according to the Mott and Massey model [17].

Results

Hydrogen Solubility: Unirradiated Zircaloy-4

The dissolution curve obtained for unirradiated Zircaloy-4 was measured by using the pT criterion (see Fig. 2). The obtained solubility curve is

$$[\mathrm{H}] = 171\,687 \times \exp\Big(-4367/T(\mathrm{K})\Big) \tag{1}$$

The precipitation temperatures were also determined at pT. They were obtained by heating the samples up to 380, 420, 500, and 600°C. As it is observed in Fig. 2, hysteresis exists between the curves obtained cooling from 380/420°C with respect to the ones obtained cooling from 500/600°C. The solubility curves obtained in precipitation are

$$[\mathrm{H}]^{380} = 23\,324 \times \exp\Big(-2846/T(\mathrm{K})\Big), \text{ for } T_{\max} = 380^\circ\mathrm{C} \tag{2}$$

$$[\mathrm{H}]^{420} = 23\,623 \times \exp\Big(-2834/T(\mathrm{K})\Big), \text{ for } T_{\max} = 420^\circ\mathrm{C} \tag{3}$$

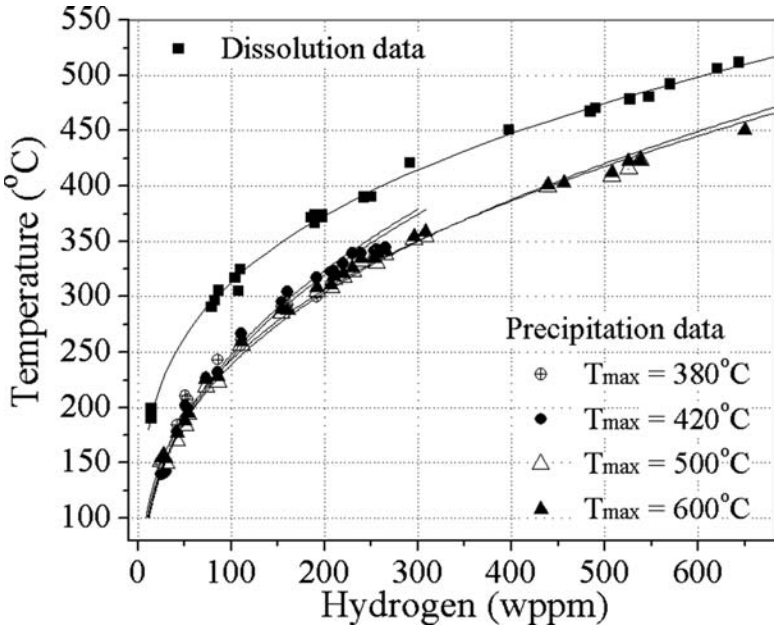


FIG. 2—*Hydrogen solubility curves for unirradiated Zircaloy-4. TTSSd and TTSSp were determined at the peak temperature, pT. TTSSp were determined by cooling from for four temperatures* (T_{max})*: 380, 420, 500, and 600°C.*

$$[\mathrm{H}]^{500} = 45\,913 \times \exp\Big(-3141/T(\mathrm{K})\Big), \text{ for } T_{max} = 500^{\circ}\mathrm{C} \tag{4}$$

$$[\mathrm{H}]^{600} = 57\,228 \times \exp\Big(-3282/T(\mathrm{K})\Big), \text{ for } T_{max} = 600^{\circ}\mathrm{C} \tag{5}$$

Hydrogen Solubility: Irradiated Zircaloy-4

The TTSSd evolution through the annealing sequence for the batch R2CC is shown in Table 3. The trend followed by the samples is similar, increasing TTSSd from 245 to around 300°C with time and annealing temperature. No significant changes are observed after annealing at 500 or 600°C. The increase in TTSSd after long annealing at 400°C is of about 40°C. Figure 3(*a*) shows the TTSSd average between the samples at a given annealing time at and 400°C plotted versus annealing time[6]. In Fig. 3(*b*) the evolution of the TTSSd average values to the unirradiated solvus line is shown.

[6]It is not strictly correct to plot TTSSd measured after annealings at different temperatures on the same time line. Yet, in the absence of an equivalent time for these annealing temperatures, it is a reader friendly way to show the data.

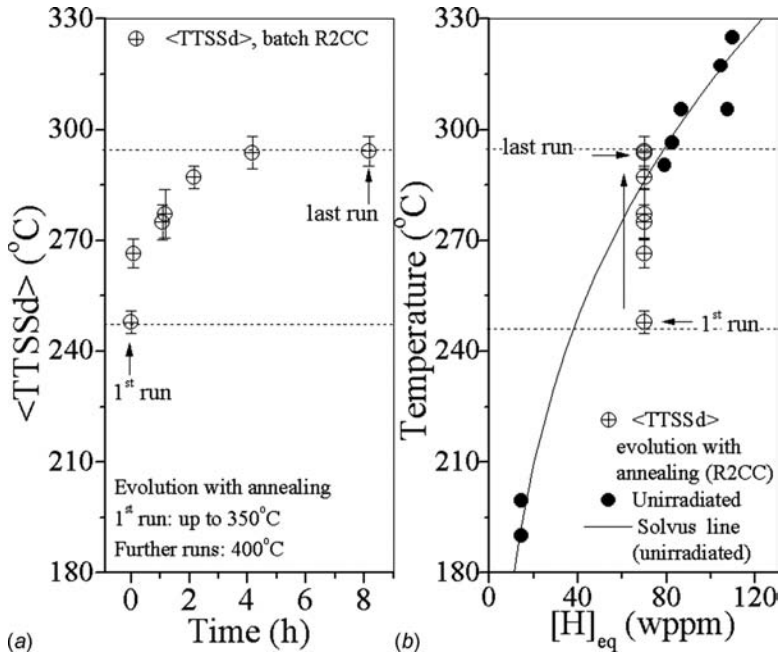


FIG. 3—*(a) Evolution of TTSSd average for the batch R2CC with annealing at 350 and 400°C. (b) TTSSd increase of the batch R2CC to the unirradiated solubility curve.*

Table 3 also shows the TTSSp values. The thermal annealing at 350 and 400°C produced a slight effect. The TTSSp increase does not surpass 10°C in all the samples of the batch. Considering the annealing sequence, an increase of about 20°C in average is observed.

Table 4 shows the TTSSd and TTSSp results for the batch R3CC. The change in the TTSSd for the whole batch from the first to the last run is of about 80°C and about 30°C, from the second to the last, i.e., after 5 min at 350°C. The higher increase in the TTSSd of sample 2 with respect to sample 1 can be attributed to the hydrogen contents: Sample 2 contains almost twice as much concentration as sample 1. In the TTSSp case, the annealing at 400°C has little effect, but the annealing at 500 or 600°C produced a significant increase.

Finally, the TTSSd and TTSSp evolution of the batch R3OC is shown in Table 5. Samples 1 and 2 were annealed for large periods at 600°C after a short annealing at 420°C. In both cases, the increase in the TTSSd surpasses 50°C. Samples 3 and 4 behaved similarly, showing an increase higher than 50°C after a long annealing at 400°C.

Again, as with samples 1 and 2 of the region R3CC, the higher final TTSSd values of samples 1–4 with respect to sample 5 could be understood comparing $[H]_{eq}$ of this batch: Sample 2 surpasses the content of sample 5 extensively while samples 1, 3, and 4 practically double the content of sample 5. The same behavior is observed for the TTSSp.

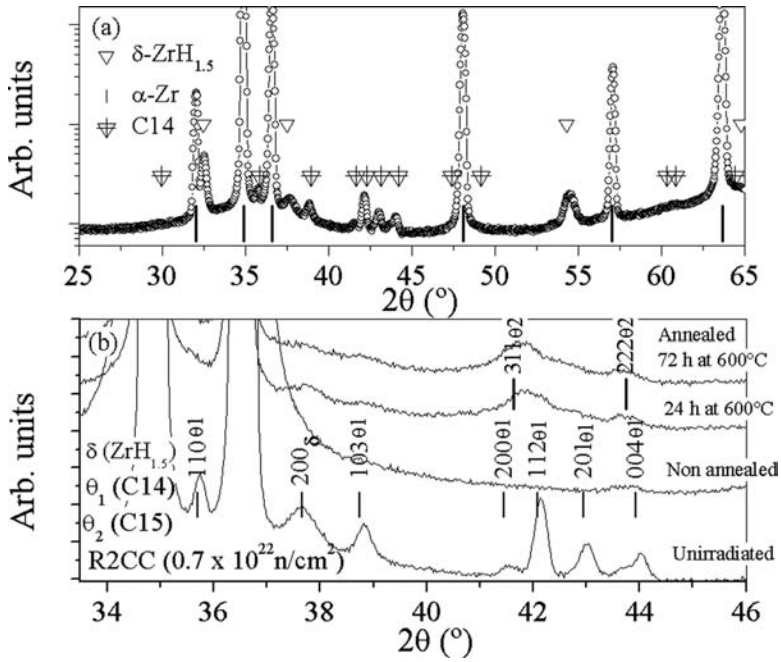


FIG. 4—*(a) Synchrotron X-ray diffraction diagram of a recrystallized Zircaloy-4 sheet. The most intense lines of the SPPs are indicated. (b) These intense lines are not observed in the non-annealed samples of region R2CC, but after the annealings at 600°C, two highly distorted peaks appeared.*

Synchrotron X-Ray Diffraction Data—Figure 4(*a*) shows the diagram obtained from a fully recrystallized Zircaloy-4 sheet taken from an unirradiated original cooling channel. Three phases were identified as: The $\alpha-$Zr phase, the C14 phase (θ-phase), both expected in Zircaloy-4, and the $\delta-$hydride phase due to additional hydrogen incorporation. The most intense peaks of C14: $(110)_\theta$, $(103)_\theta$, $(200)_\theta$, $(112)_\theta$, $(201)_\theta$, and $(004)_\theta$ were clearly resolved.

As it was shown in a previous work, the SPP lines (phase C14) of low fluence samples (10^{20} neutrons/cm^2) were observed in the diagrams of both the annealed and the non-annealed samples [5]. On the other hand, in the diagram of the high fluence samples of the region R2CC (foil 0.2) these peaks are not observed (see Fig. 4(*b*)). The same occurs in the diagram of the highest fluence samples of the region R3CC [5].

Finally, the high fluence R2CC samples annealed 24 and 72 h at 600°C show a wide peak at the position of the lines $(200)_\theta$, $(112)_\theta$, $(201)_\theta$, and $(004)_\theta$. The diagrams suggest that annealings at higher temperatures are needed for a complete recovery.

Analytical Electron Microscopy Data—Figure 5 shows the typical appearance of $Zr(Fe, Cr)_2$ SPPs in unirradiated Zircaloy-4. The size distribution of SPPs lies

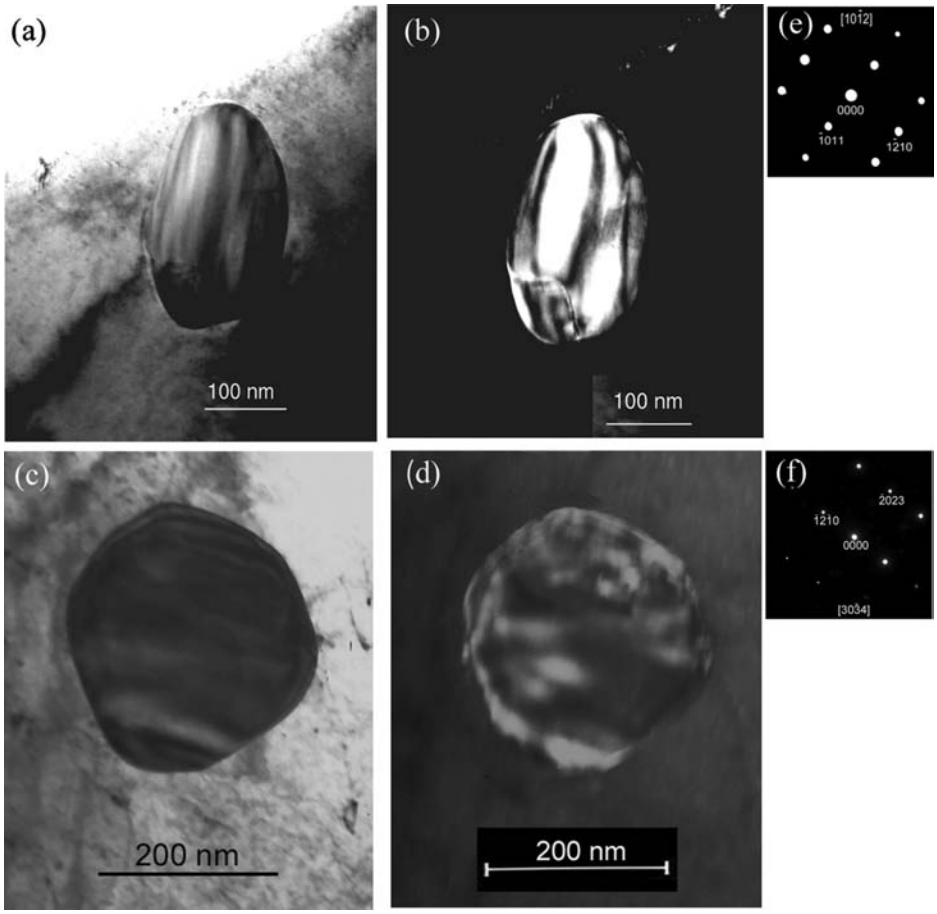


FIG. 5—$Zr(Fe,Cr)_2$ *second-phase particles of Zircaloy-4 in bright* (a) *and dark fields* (b) *showing a polytype band structure. [*(c) *and* (d)*] This polytype structure is not always observed [*(c) *bright field and* (d) *dark field)]. [*(e) *and* (f)*] The indexed electron diffraction patterns indicate hexagonal structure 20.*

between 0.2 and 0.5 μm. Previous works point out that about 20 % of these particles show a polytype band structure of hexagonal C14 (hcp) and cubic C15 (fcc) [18]. The particle in Fig. 5(*a*), 5(*b*) seems to have this band structure although the electron diffraction patterns indicate hexagonal structure (C14), in agreement with the X-ray diffraction data. This band structure is not observed in the particle in Fig. 5(*c*), 5(*d*). The energy dispersive spectrums (EDS) indicate that the relative concentration of Fe and Cr in the unirradiated particles is Fe: 65 at. % and Cr: 35 at. %, typical of unirradiated Zircaloy-4 SPPs [19].

Figure 6 shows the SPPs observed in the region R2CC (foil 0.2). Neither in the bright field (left) nor dark field (center) is a band structure observed. The dark field images show another distinctive feature: The boundaries are diffuse.

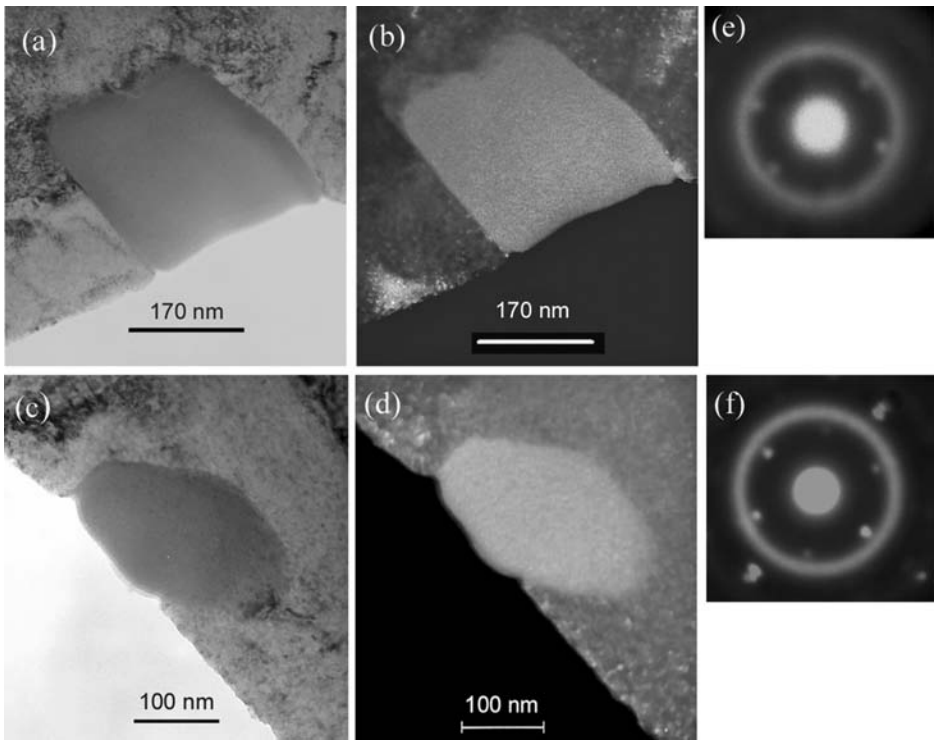


FIG. 6—*[(*a*) and (*c*)] Bright field of two SPPs: Polytype structure is not observed in irradiated particles. [(*b*) and (*d*)] Dark field images show diffuse dissolving boundaries. [(*e*) and (*f*)] Diffraction patterns show a diffuse ring instead of spots, indicating that SPPs are amorphous. Region R2CC (0.7×10^{22} neutrons/cm^2).*

Indeed, in Fig. 6(*b*), 6(*d*), both dark field images, the particles seem to be dissolving in the matrix. The most important characteristic is shown in the electron diffraction patterns (Fig. 6(*e*), 6(*f*)): The spots are replaced by diffuse rings that the SPPs are amorphous.

Figure 7 shows the SPPs of the highest fluence region R3CC (10^{22} neutrons/cm^2). They show diffuse boundaries still in bright field. Their size is smaller than the ones of region R2CC (typically 100 nm), suggesting that a fraction of the original SPPs were already dissolved. The radiation damage is clearly visible in the matrix and very small hydrides are observed too.

In the samples of the region R3CC annealed 24 h at 600°C, the SPP's morphology is completely different with respect to the non-annealed ones (see Fig. 8(*a*)8(*d*)). The very small SPPs of a few tens of nanometers are grouped in clusters, generally formed at the grain boundaries. The diffuse rings in the electron diffraction patterns of the irradiated samples were replaced by a discontinuous ring formed by several small spots, indicating that the SPPs are crystalline (see Fig. 8(*e*), 8(*f*)). The matrix is completely clean of defects and small hydrides are not observed.

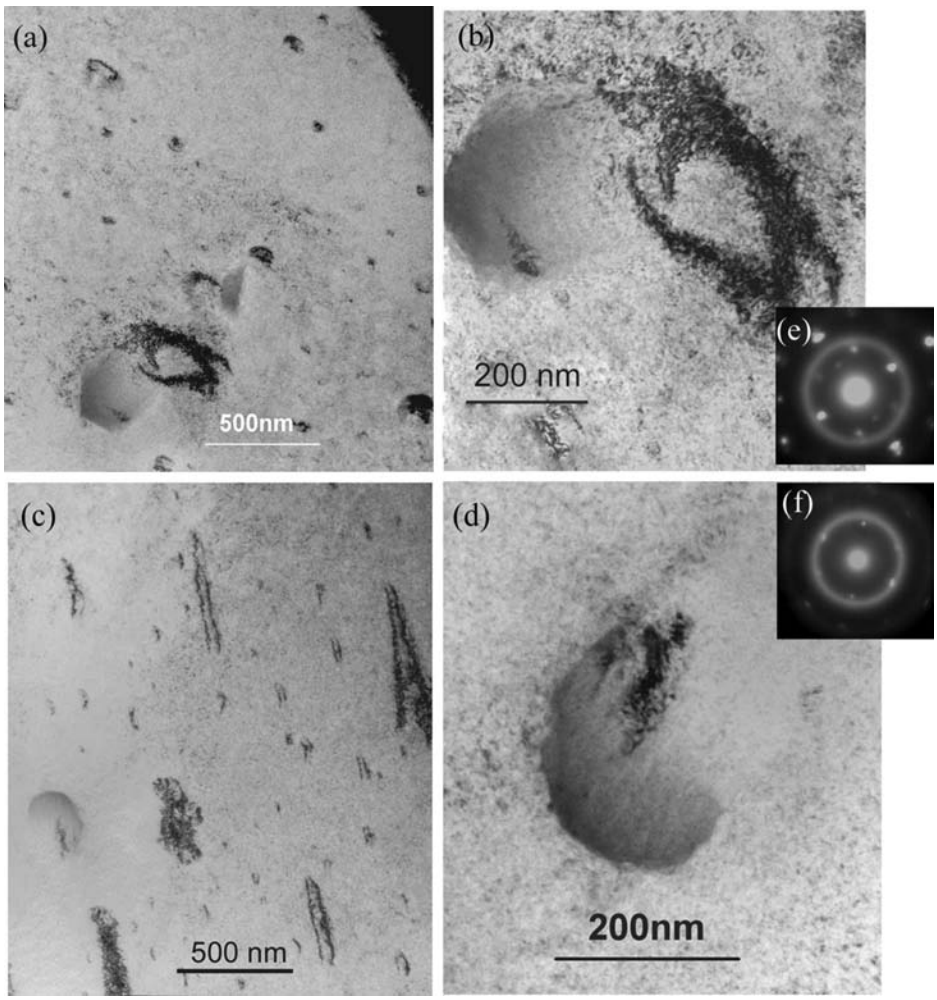


FIG. 7—*Bright field images:* (a) *A SPP with a hydride precipitated inside.* (b) *The SPP boundaries are diffuse, indicating that the dissolution is in progress. The matrix shows radiation damage.* (c) *A high density of hydrides that are smaller than 500 nm is observed.* (d) *On the left, a magnification of the SPP observed in* (c) *with a hydride precipitated inside. [*(e) *and* (f)*] Diffraction patterns indicate that the SPPs are amorphous. Region R3CC (*10^{22} *neutrons/cm*^{2}*).*

Discussion

Hydrogen Solubility: Baseline Correction and Criteria for Terminal Solid Solubility Temperatures in Dissolution Determinations

In previous works, the general behavior of TTSSd and ΔH_{solvus} in irradiated Zircaloy-4 was described and a significant solubility increase was found [6–8].

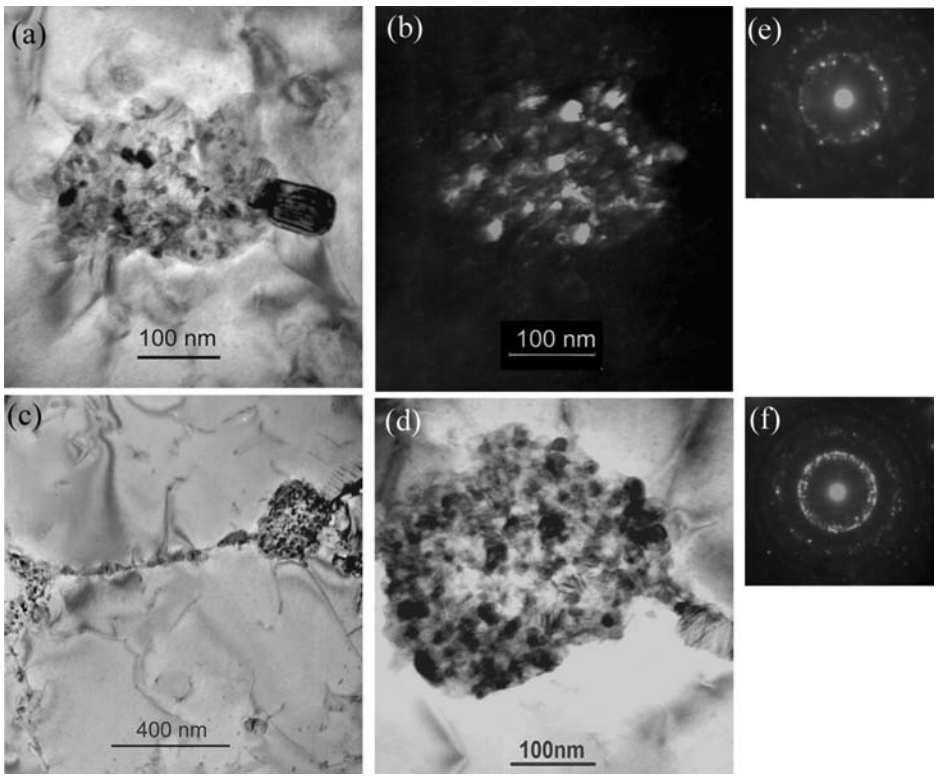


FIG. 8—*[(a) and (b)] Bright and dark field images of SPPs in the R3CC samples annealed 24 h at 600°C. [(c) and (d)] Clusters of nano-precipitates on a grain boundary. Their sizes are of a few tens of nanometers (bright field). [(e) and (f)] The spots observed around the rings in the diffraction patterns indicate that SPPs are crystalline.*

The DSC curves of Fig. 9(*a*) are a typical dissolutionsequence followed by an irradiated sample. This behavior was confirmed in the present work, but in addition, it was observed that this increase is hydrogen-dependant.

Recovery Phenomena Associated with Differential Scanning Calorimeter Runs—The DSC heating ramp starts the recovery processes, which take place simultaneously with the hydride dissolution, making TTSSd determinations difficult at the first run curve. Figure 9(*b*) shows three calorimetric curves (batch R2CC, sample 2): The first run, the second run (after 5 min at 350°C), and the last run curve (after 8 h at 400°C). The exothermic peak superimposed to the dissolution curve at the first run creates uncertainty about the real value of TTSSd. After, the curve has the typical shape of the hydride dissolution. Due to this, the accurateness of the first run values is low. An experimental error of 5–6°C was assumed.

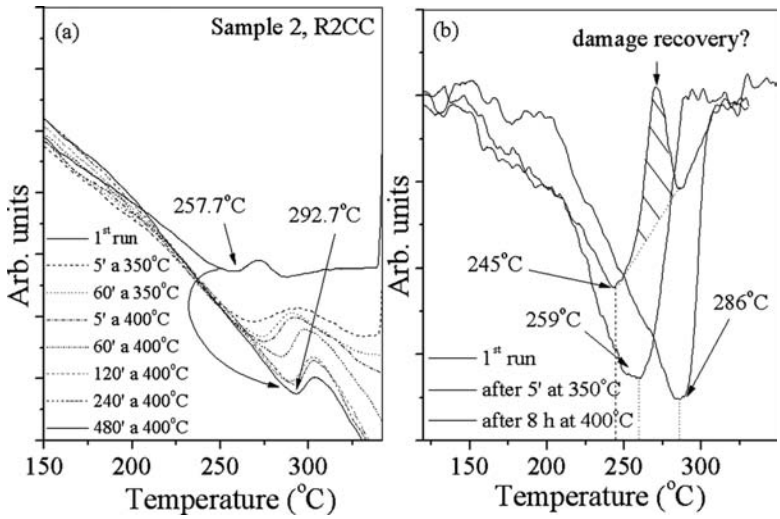


FIG. 9—*DSC heating curves sequence (sample 2, R2CC). (a) The peak shift's to higher temperatures after each annealing. (b) Baseline corrected curves. A recovery peak superimposed to the initial curve is observed. It is probably related with damage recovery.*

Considering the first run value as the most illustrative of the material under reactor-in conditions and, considering the value after the last annealing as the TTSSd of a completely recovered sample, we observe an average increase of 55°C for the whole set of samples. With the exception of a few samples, the observed increase in TTSSd varies from 40 to 60°C. The data in Tables 3 also indicates that the solubility increases monotonically with hydrogen content. The evolution with respect to the unirradiated Zircaloy-4 solubility curve is shown in Fig. 10. About 75 % of TTSSd values of the completely annealed samples lay between the error bands of hydrogen determinations.

Terminal Solid Solubility Temperatures in Precipitation Measurements: Peak Thickness Narrowing—The shift of the peak point of the DSC curve to higher temperatures during dissolution has a correlative behavior in precipitation. Figure 11 shows this for sample 6 of the region R2CC. In addition, a reduction of the peak width after each annealing at 350 or 400°C is observed, becoming sharper and tending to the typical narrow profile of unirradiated material. This narrowing suggests that the precipitation is a gradual process that starts before the peak (maximum of the DSC curve), i.e., at temperatures higher than the point at which TTSSp is usually determined. The last interpretation is apparently inconsistent with the criterion commonly used to determine TTSSp: *The peak temperature of the DSC cooling curve at which precipitation starts*, but the suitability of the criterion is not under discussion, the peak indicates the onset or at least the temperature at which precipitation becomes a massive phenomenon [10]. The observed behavior should be attributed to the non-equilibrium nature of the irradiated material: The irradiation defects that remain in the

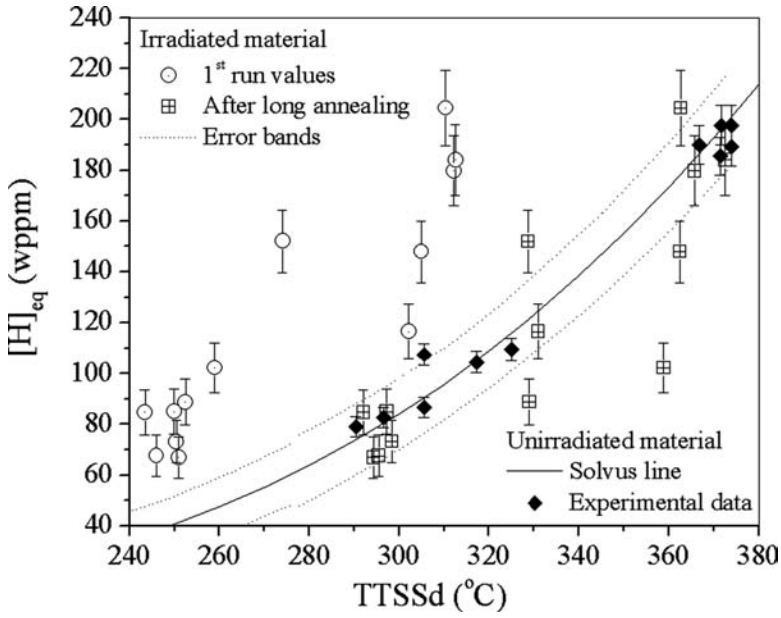


FIG. 10—*Dissolution data for irradiated Zircaloy-4. The first run and the last run value after long annealing are plotted. TTSSd of unirradiated Zircaloy-4 are also plotted. Both irradiated and unirradiated TTSSd values were determined at pT.*

matrix after the first run behave as nucleation sites for hydride precipitation where the hydrogen atoms are first trapped. Since the density of crystalline defects in the non-annealed sample is the highest of the annealing sequence, the density of hydride embryos after the first run should be the highest too. Thus, after the initial run and surely in the as-received material, a wide size distribution of hydrides is expected to be found with preponderance of small sizes.

The availability of nucleation sites could also explain the increase in the TTSSp differences, ΔTTSSp, from the first to the last run (recovered material), with the increment of the hydrogen bulk content. That dependency is more noticeable than for TTSSd differences, ΔTTSSd, which is natural: Being dissolution a process controlled by diffusion, it depends on hydride size distribution and not on nucleation site density (see Fig. 12). As it is observed in Tables 3, the general tendency of TTSSp is to increase with the annealing. However, whilst TTSSd increased monotonically with annealing in all the samples, TTSSp behaved differently in a few cases, remaining constant after the annealing at 350–400°C and increasing considerably after a further annealing at 600°C (samples 3–4 in Table 4 and sample 5 in Table 5). This behavior could be explained by considering a competition of two phenomena: The annihilation of the nucleation sites where there were hydrides before the previous dissolution process and the coalescence irradiation defects in larger clusters with thermal annealing, which can behave as new hydride nucleation sites. Then, the damage recovery implies an additional evolution in the nucleation sites for hydride

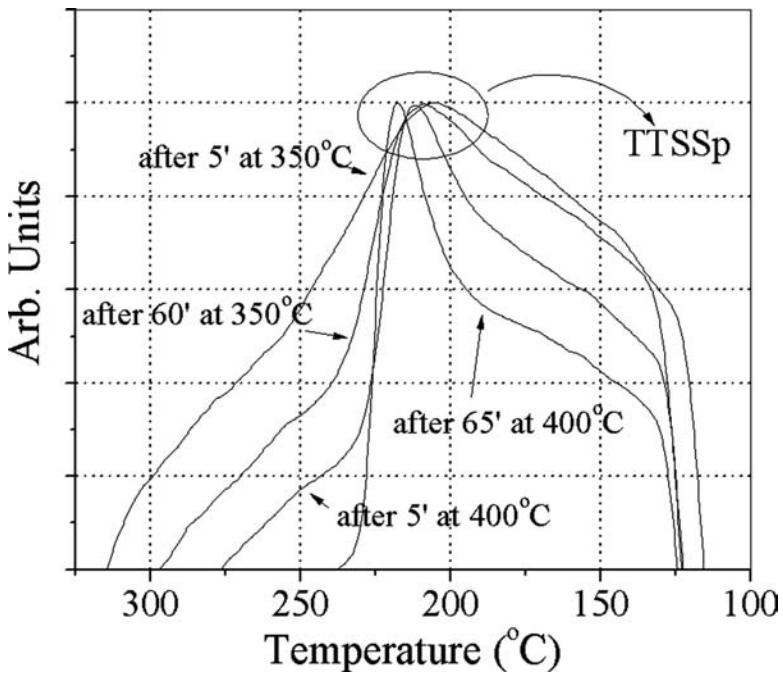


FIG. 11—*DSC cooling curves of sample 6 of the batch R2CC. A significant narrowing of the precipitation peak is observed after each thermal annealing.*

precipitation that is not present in an unirradiated matrix, which explains this non-uniformity in TTSSp values.

Hydride Size Distribution: Effects on the Hydrogen Solubility—Regarding the hydrogen trapping hypothesis verification, a high density of defects can be observed with TEM over the whole irradiated matrix. Figure 13 shows the irradiation defects that were identified as $\langle a \rangle$ loops (~ 10 nm) and $\langle c \rangle$ loops (100–180 nm), respectively, similar to the observed previously by R. Adamson in Zircaloy-4 [20]. Also, Fig. 13(*c*)13(*f*) shows a high density of very small hydrides precipitated parallel to the $\langle c \rangle$ loops and flanked by them. These hydrides show the typical orientation relation with the α–Zr matrix, i.e., $(\bar{1}1\bar{1})\delta // (0002)\alpha$ and $[110]\delta // [11\bar{2}0]$ are vacancy loops [20], this local absence of atoms and the consequent local expansion favors the hydride nucleation in these sites, whose orientation is close to the habit plane $(10\bar{1}7)\alpha$ of the δ–hydrides in Zircaloy-4. These observations give additional support to the hypothesis of hydrogen-defect interaction [9]. Although a direct verification of this hypothesis is not possible yet (hydrogen atoms could not be detected), it is possible to establish a chain of events, which, based on our hypothesis, determine the macroscopic consequences observed in the bulk: A solubility increase.

As pointed out in the Temperatures of Terminal Solid Solubility in Precipitation Measurements: Peak Thickness Narrowing section, the narrowing of the

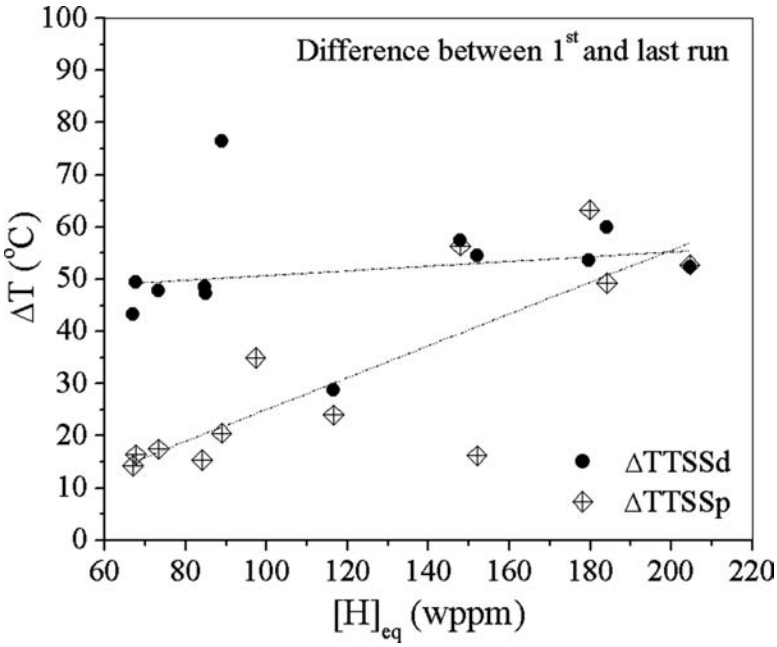


FIG. 12—*The TTSSd and TTSSp variation between the first and the last run (ΔTTSSd and ΔTTSSp, respectively) as a function of* $[H]_{eq}$. *ΔTTSSd depends moderately on* $[H]_{eq}$, *but ΔTTSSp dependence is remarkable.*

precipitation peak could relate the recovery of the radiation damage with a reduction of the availability of nucleation sites. If this assumption is correct, the as-received material should have the highest density of nucleation sites, and then, a hydride size distribution is biased to smaller values than the annealed material. Such a difference should affect the TTSSd determinations if this parameter is determined by a dynamic technique like DSC: Since hydride dissolution is controlled by diffusion, the time required to dissolve a large hydride is longer than the one to dissolve the same mass distributed in many small hydrides.

This phenomenon has been observed in the dissolution of $\beta-Mg_2Si$ in Al–-Mg–Si alloys [21]. Vermolen's dissolution model simulates successfully this process during a DSC run and predicts a solubility increase of about 50–60°C for the alloy composition 0.4 % Si, 0.45 % Mg, and 0.19 wt %, if the particle diameter is reduced roughly a third, from 1.76 to 0.67 μm [21–23].

Before starting a hydride size distribution analysis, it is convenient to make some considerations. First, hydrides are platelets. They can be recognized as individual objects by TEM, but not with optical microscopy, which show them as large chains formed by stacks of platelets. Although these composite objects conceptually cannot be considered as individual large plates, the local density of a chain/stack of hydrides is high and must slow down the dissolution kinetics compared with a finely dispersed distribution of individual platelets. Then, we

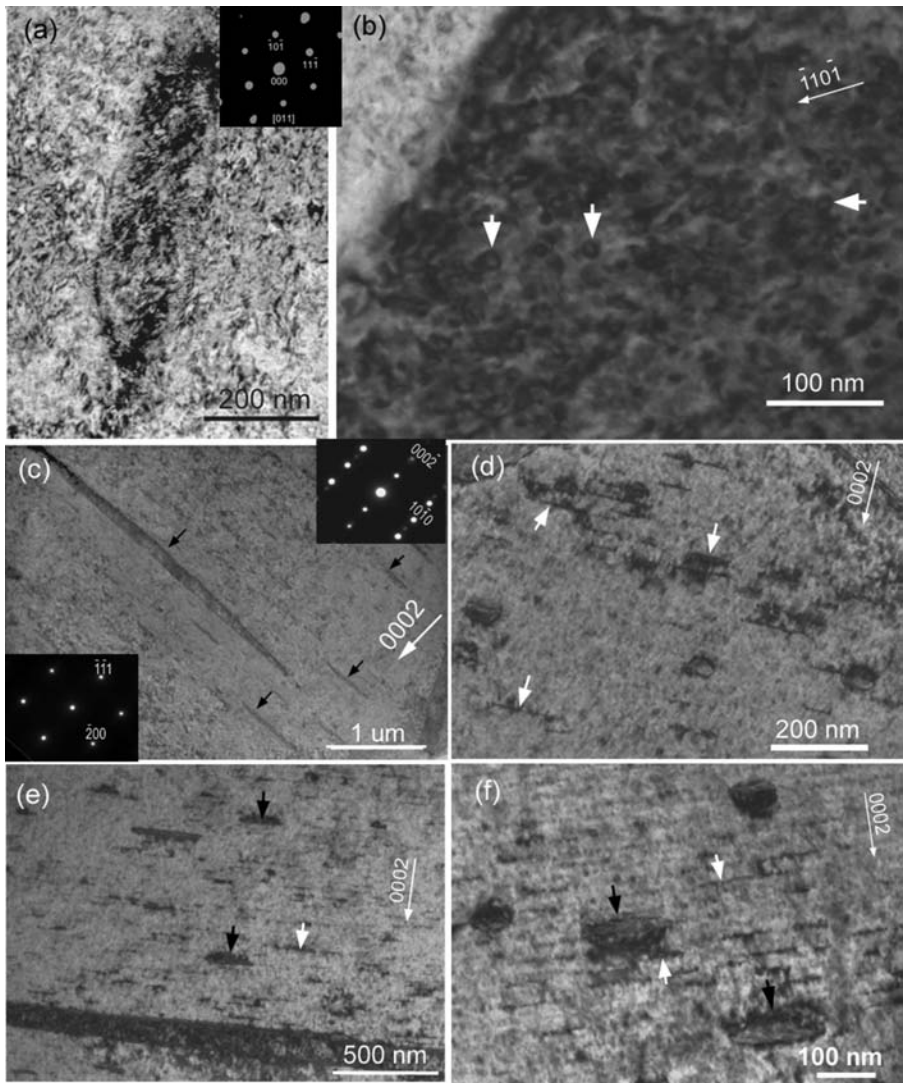


FIG. 13—*TEM images of ⟨a⟩ and ⟨c⟩ loops and hydrides observed in high fluence samples (region R3CC, 10^{22} neutrons/cm^2). (a) A hydride affected by irradiation damage and ⟨a⟩ loops are observed in bright field. The indexed diffraction diagram indicates cubic structure (δ-hydride). (b) Loops ⟨a⟩ microstructure observed close to the α−Zr/hydride interface (indicated by the white arrows). Zone axis =[12$\bar{1}$3]. (c) Hydrides parallel to the basal planes (black arrows). The selected area diffraction patterns of the α−Zr matrix and that of the large δ-hydride observed show the typical crystallographic relationship. Zone axis$_\alpha$=[11$\bar{2}$0] and zone axis$_\delta$=[011]. (d) ⟨c⟩ loops microstructure (white arrows) with sizes varying between 100 and 180 nm. [(e) and (f)] Hydrides are observed (black arrows) and ⟨c⟩ loops (white arrows) parallel to them. Zone axis =[12$\bar{2}$3].*

do not differentiate the nature of the hydrides observed by TEM from the one observed by optical microscopy. Another point is the surface/volume ratio of the hydrides, which is higher than the same ratio for spherical particles. This difference should attenuate the kinetic effect observed in the dissolution of spherical particles. Finally, still in unirradiated material a hydride size distribution that covers some tens of microns is observed. In this condition, the presence of long hydrides might compensate for the effect of the smaller ones. Summarizing, it would be probable that a ratio 3:1 like in the Al–Mg–Si would not be enough to explain the solubility increase in the irradiated material.

Figure 14 shows four optical micrographs of the DSC sample 4 of region R3CC as-received. On these micrographs, which cover an area of 6.1 mm^2, a

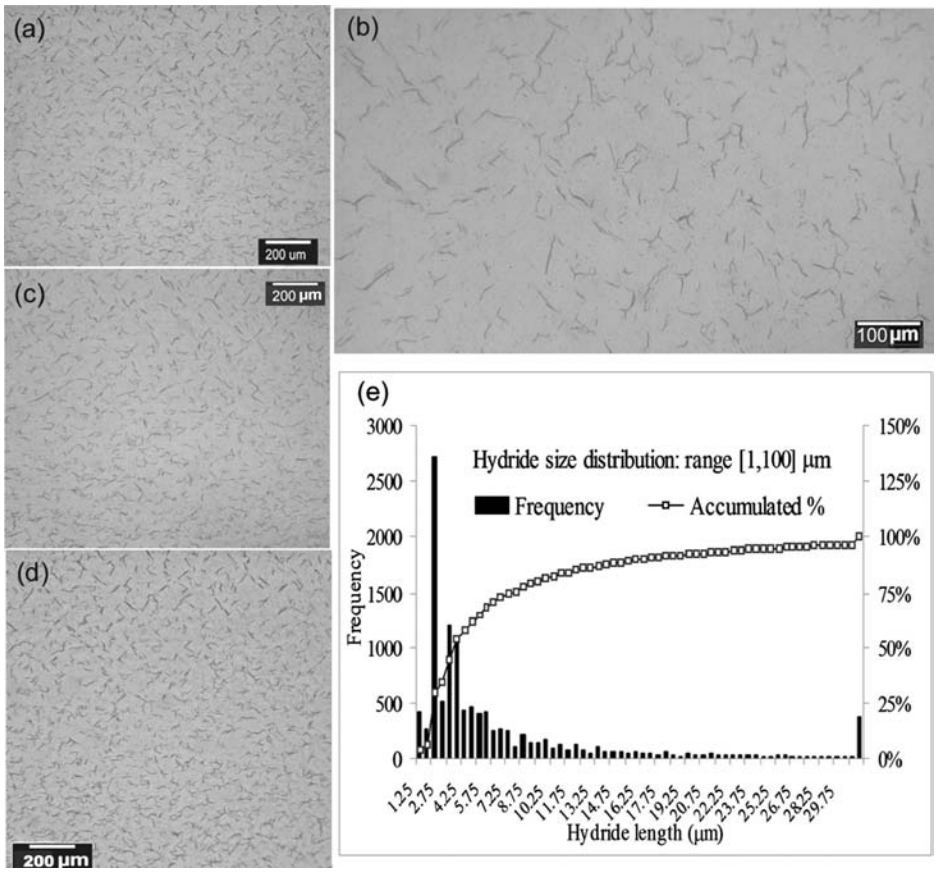


FIG. 14—*The optical microscope range: The observable size distribution lies between 1 and 60–70 µm. [(a) and (d)] The micrographs cover the whole profile of a DSC sample. (e) The histogram indicates a high concentration of hydrides smaller than 5 µm (maximum at 2.75 µm). Images correspond to sample 4 of R3CC before the DSC experiments.*

hydride counting and length determination was made by using the Sigma Scan[7] program.

The histogram also shown in Fig. 14 indicates that the size distribution is biased to small sizes. The maximum length frequency (2700 particles) is observed at 2.75 μm and 25 % of the detected hydrides are shorter than 5 μm. Only 10.5 % are longer than 20 μm. This distribution is not typical of unirradiated materials. In the present analysis 1 μm was taken as the lower length limit since smaller hydrides are seen as roughly spherical particles, which could be confused with a SPP. Thus, 1 μm was taken as the border between the optical and TEM fields.

Figures 7 and 13 and 15 show TEM micrographs of as-received samples of the region R3CC. The images show a significant density of very small hydrides, of about 100 nm. The histogram also observed in Fig. 15 was made over a whole set of 21 TEM micrographs analyzed with the Sigma Scan program. The hydride counting and length determinations were made over an area of 126 μm^2. Although the maximum frequency is at 25 nm, the size distribution is more homogeneous than the optical range one. In TEM range, 30 % of the observed hydrides are shorter than 100 nm.

If we consider now the intervals 10–1000 nm and 1–100 μm, which correspond to the TEM and optical ranges, respectively, we must face the problem of finding a way to integrate the data from two hydride populations, which coexist but cannot be observed simultaneously. A simple parameter to quantify the relative weight of these two populations is density. First, we define density as the ratio between the hydride lengths (particle size) of some interval and the total scanned area. The sum of the lengths of the detected hydrides in the optical range is 152.9 mm, so that, in this range the hydride density is $\rho_{optic} = 152.9\,mm/6.1\,mm^2 = 25.1\,mm^{-1}$. In the same range, the sum of the lengths shorter than 5 μm is 37.9 mm. Then their density is $\rho_{<5\,\mu m} = 6.2\,mm^{-1}$. On the other hand, the sum of the hydride lengths of the TEM range is 43.9 μm. Thus, the hydride density is $\rho_{TEM} = 43.9\,\mu m/126\,\mu m^2 = 0.35\,\mu m/\mu m^2 \equiv 348.9\,mm^{-1}$, and the ratio between both densities is $\rho_{TEM}/\rho_{optic} \sim 13$, which indicates a large preponderance of submicroscopic hydrides. However, it is possibly an overestimated value. The length as a parameter to characterize the hydride sizes shows limitations when dimensions are close to the extremes of the interval. A hydride length at the top of the optical range can be 1 μm in width while the submicroscopic hydrides at the bottom of the TEM range are of a few nanometers in width.

This problem could be solved by redefining density as the ratio between the area occupied by hydrides in the corresponding interval and the scanned area. This area in the optical range is $0.360\,mm^2$. The density will be then ρ_{optic} [area] $= 0.360\,mm^2/6.1\,mm^2 = 0.059$. In TEM range, the area occupied by hydrides is $0.986\,\mu m^2$. Thus, ρ_{TEM} [area] $= 0.986\,\mu m^2/126\,\mu m^2 = 0.078$. Then, the ratio between both ranges becomes $\rho_{TEM}/\rho_{optic} \sim 0.13$. The submicroscopic hydride density is 13 % of the hydrides observed in the optical field. Possibly

[7]SIGMA SCAN Pro 5.0. Aspire Software International.

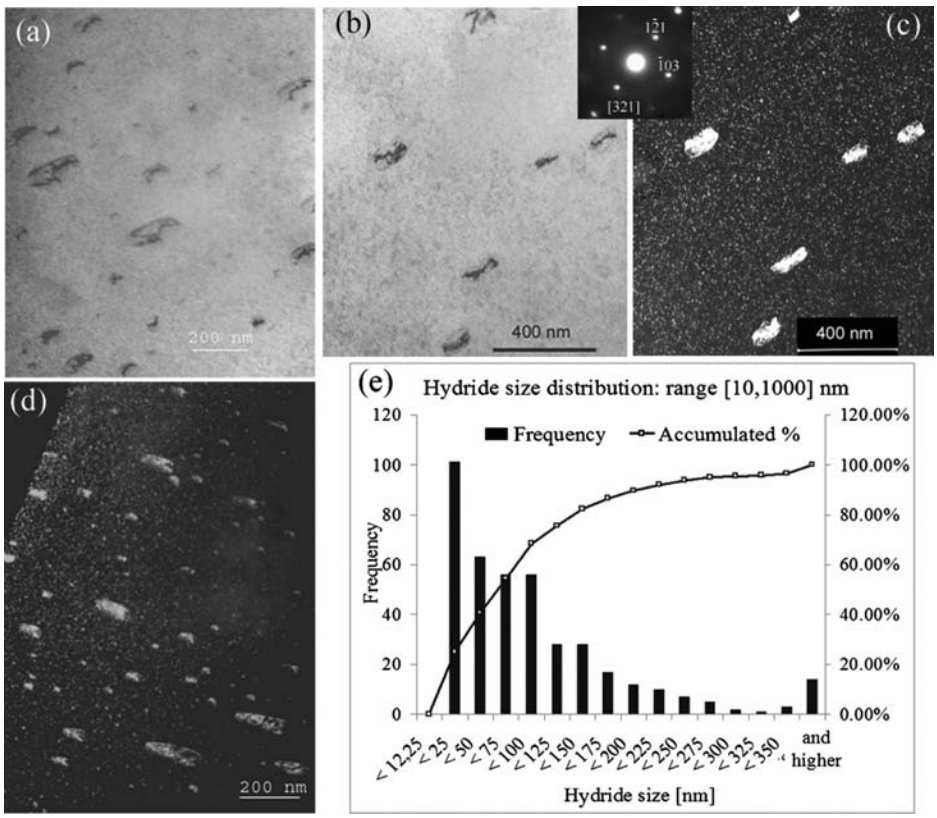


FIG. 15—*TEM range: A high density of submicroscopic hydrides is observed in the irradiated samples in a range from 10 nm up to 1 μm. [(a) and (b)] Hydrides of some tens of nm are observed (bright field). [(c) and (d)] Hydrides smaller than 200 nm are observed (dark field). The indexed electron diffraction patterns indicate γ-tetragonal hydrides. (e) The histogram shows a hydride size distribution biased to small sizes. The maximum frequency is observed at 20–30 nm (region R3CC).*

this is an underestimated value, since in the optical field the etchant used to reveal the hydrides affects much more hydride width than hydride length, and this does not occur in TEM samples. Yet, this last value is more reasonable than that which comes from the hydride length determination.

Summarizing the results of the statistical analysis, we can say that a non-negligible amount of submicroscopic hydrides higher than 13 % exists, which is not visible in the optical range. If we also consider that in the optical range 25 % of hydrides are shorter than 5 μm, a wide hydride size distribution exists, extended over four orders of magnitude, from 10 nm to 100 μm, biased to sizes shorter than 5 μm.

Finally, it must be said that the hydride lengths observed by TEM in samples of region R3CC annealed 24 h at 600°C are generally longer than 1 μm and

shorter hydrides were not observed like in unirradiated material. Then, in light of Vermolen's works, such a size distribution should be responsible for the hydrogen solubility increase in irradiated Zircaloy-4.

Second-Phase Particles: Amorphisation and Re-Precipitation

The SXRD diagrams allowed to identify the $Zr(Fe,Cr)_2$ SSPs in unirradiated Zircaloy-4 (see Fig. 4). Their crystalline structure corresponds to the hexagonal C14 phase, which is the structure of about 80 % of the SPPs. Although cubic C15 structure could not be detected, evidence of its possible presence as a polytype structure consisting of alternate packing of hexagonal C14 and cubic C15 layers is given in Fig. 5(*a*), 5(*b*) [18].

The SXRD of Fig. 4(*b*) of high fluence material proved for the bulk what was observed with TEM in each of the observed irradiated precipitates: A complete amorphisation in both batches of high fluence samples, R2CC, and R3CC.

Changes in the chemical composition were also observed. In unirradiated SPPs, the Fe/Cr ratio is close to 1.85, but when irradiated precipitates are considered, the Fe/Cr ratio presents significant variations according to the dose and the in situ temperature of the reactor. By operating the microscope in the nano probe mode (i.e., spot size 2.0 nm), 70 EDS spectrums were obtained from 13 different SPPs in the samples from the region R2CC (foil 0.2). A homogeneous Fe, Cr distribution within the SPPs was found, but we observed a spread distribution of the Fe/Cr ratio, between 0.8 and 2.0, showing the maximum frequency at 1.3, evidencing a Fe rejection. This rejection was slower than the one reported in the previous works [24], probably due to the relatively low temperature at which the outer foil remained in service (205°C). The composition change is also accompanied by a crystalline to amorphous phase transformation. A comparison between the foil 0.2 SPPs composition and unirradiated SPPs is shown in the histograms in Fig. 16.

On the other hand, the chemical composition in the high fluence samples of region R3CC was similar to the one observed in the previous works [24]. The EDS analysis made at the centre of 10 SPPs gave an average Fe/Cr ratio of 0.13, which means that Fe diffusion was driven by the higher irradiation temperature.

TEM observations made on samples of the region R3CC annealed 72 h at 400°C showed that the SPPs are still amorphous, which confirms the previous SXRD results [5], but the EDS analysis made at the centre of 10 SPPs gave an average Fe/Cr ratio of 0.4, suggesting the beginning of the amorphisation reversion process.

Finally, samples annealed 24 and 72 h at 600°C (from region R3CC) were characterized. The SXRD and also the TEM electron diffraction diagrams confirm the recrystalization of the amorphous SPPs. The EDS analysis made over 10 clusters such as those observed in Fig. 8 showed a Fe/Cr ratio of 1.5, close to the unirradiated SPPs.

All the data collected by the SXRD and TEM regarding the SPPs agree very well with predictions made by Motta and Lemaignan [25]. Our observations indicate that crystallization of amorphised SPPs starts above 400°C. From

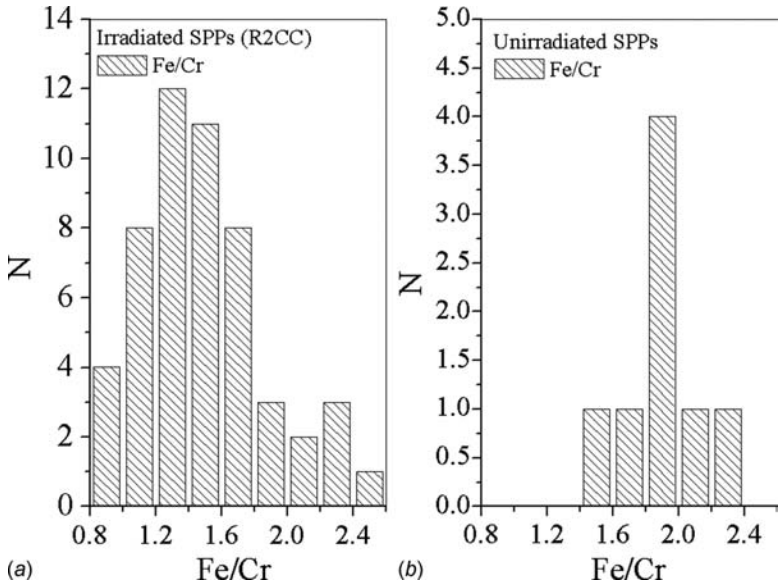


FIG. 16—*Histograms show the Fe/Cr ratio distribution measured over: (*a*) 70 irradiated SPPs of region R2CC and (*b*) 10 unirradiated SPPs of a Zircaloy-4 sheet. Data obtained from EDS.*

Motta's work, the critical temperature T_c above which amorphisation is precluded is about $0.3T_{\text{melting}}$. Being T_m of $ZrCr_2$ about 1630°C, this critical temperature is 490°C and the crystallization temperature should be around this value, considering that the SPPs condition is far from equilibrium and the reversion of the process should be affected by kinetics [26]. Thus, with the aim to determine the thermodynamic parameters of the process, four samples of the region R2CC were heated at the DSC at the rates 5, 10, and 20°C/min up to 700°C. The DSC first run curves showed an exothermic peak, which shifts to higher temperatures monotonically with the heating rate: 454°C at 5°C/min, 460°C at 10°C/min, and 497°C at 20°C/min. The enthalpy remained constant with the heating rate and the value 27.3 ± 2.1 kJ/mol (Fe + Cr) was determined for the crystallization process.

Conclusions

As a brief summary the following points can be underlined.

(1) After the annealing sequence, a TTSSd increased 55°C in average from the first to the last run, showing moderate dependence with the hydrogen content: From 40°C in the low hydrogen side of the interval (60–80 wppm) up to 60°C in the high hydrogen side (150–200 wppm).

(2) The precipitation temperature, TTSSp, increased 40°C in average from the first to the last run, but the tendency is strongly dependant on the

hydrogen content: From 15°C in the low hydrogen side of the interval (60–80 wppm) up to 65°C in the high hydrogen side (150–200 wppm).

(3) The optical and TEM observations show that in irradiated material there is a wide hydride size distribution, in the interval [10 nm, 100 μm]. A submicroscopic population higher than 13 % of the observed in the optical range was estimated. These observations give support to the hypothesized interaction between irradiation defects and hydrogen atoms as the cause of the observed solubility increase.

(4) The TEM and SXRD observations indicate a complete amorphisation of the SPPs in high fluence material. It was shown that Fe diffusion depends on the irradiation dose and also on temperature: The material that remained at 205°C showed a decrease in the Fe/Cr ratio, with a maximum frequency around 1.3, being the non-irratiated Fe/Cr ratio $\sim$ 1.85. But the SPPs that remained at 280°C showed a Fe/Cr ratio $\sim$ 0.13. Finally, the samples annealed 24 h at 600°C showed a Fe/Cr ratio $\sim$ 1.5, close to the unirradiated SPPs ratio. Based on the AEM, SXRD, and DSC data, we found that crystallization temperature is kinetic-dependant. T_c rises from 450 to 500°C increasing the heating rate from 5 to 20°C/min. The measured heat of crystallization was 27.3$\pm$2.1 kJ/mol (Fe + Cr).

Acknowledgments

The writers are thankful to Dr. Alfredo Tolley (CAB, CONICET) for the support given during the AEM analysis. The present work could not have been made without the collaboration of Rosa Samper, Walter C. Szieber, Alejandro Duarte, Gonzalo Zbihlei, and Leonardo Motillo (CNEA). The present work was supported by the Comisión Nacional de Eenergía Atómica and the Ministerio Nacional de Ciencia y Técnica from Argentina and also by the International Agency of Atomic Energy, in the framework of the SPAR II Project.

References

[1] Charit, I. and Murty, K. L., "Creep Behavior of Niobium-Modified Zirconium Alloys," *J. Nucl. Mater.*, Vol. 374, 2008, pp. 354–363.

[2] Duriez, C., Dupont, T., Schmet, B., and Enoch, F., "Zircaloy-4 and M5 High Temperature Oxidation and Nitriding in Air," *J. Nucl. Mater.*, Vol. 380, 2008, pp. 30–45.

[3] Anand, M. S., Mansel, W., Wallner, G., and Weck, W., "Effect of Alloying Elements on Recovery and Damage Rates in Zirconium," *J. Nucl. Mater.*, Vol. 126, 1984, pp. 144–151.

[4] Toffolon-Masclet, C., Guilbert, T., and Brachet, J. C., "Study of Secondary Intermetallic Phase Precipitation/Dissolution in Zr Alloys by High Temperature–High Sensitivity Calorimetry," *J. Nucl. Mater.*, Vol. 372(2–3), 2008, pp. 367–378.

[5] Vizcaíno, P., Banchik, A. D., and Abriata, J. P., "Synchrotron X-Ray Diffraction Evidences of the Amorphization/Dissolution of the Second Phase Particles (SPPs) in Neutron Irradiated Zircaloy-4," *Mater. Lett.*, Vol. 62, 2008, pp. 491–493.

[6] Vizcaíno, P., Banchik, A. D., and Abriata, J. P., "Hydrogen in Zircaloy-4: Effects of the Neutron Irradiation on the Hydride Formation," *J. Mater. Sci.*, Vol. 42, 2007, pp. 6633–6637.
[7] Vizcaíno, P., Banchik, A. D., and Abriata, J. P., "Hydride Phase Dissolution Enthalpy in Neutron Irradiated Zircaloy-4," *J. Nucl. Mater.*, Vol. 336(1), 2005, pp. 54–64.
[8] Vizcaíno, P., Banchik, A. D., and Abriata, J. P., "Solubility of Hydrogen in Zircaloy-4: Irradiation Induced Increase and Thermal Recovery," *J. Nucl. Mater.*, Vol. 304(2–3), 2002, pp. 96–106.
[9] McMinn, A., Darby, E. C., and Schofield, J. S. "Terminal Solid Solubility of Hydrogen in Zirconium Alloys," *Zirconium in the Nuclear Industry: 12th International Symposium, ASTM STP 1354*, G. P. Sabol, G. D. Moan, eds., ASTM International, West Conshohocken, PA, 2000, pp. 173–195.
[10] Pan, Z. L. and Puls, M. P., "Precipitation and Dissolution Peaks of Hydride in Zr-2.5Nb During Quasistatic Thermal Cycles," *J. Alloys Compd.*, Vol. 310, 2000, pp. 214–218.
[11] Khatamian, D. and Root, J. H., "Comparison of TSSD Results Obtained by Differential Scanning Calorimetry and Neutron Diffraction," *J. Nucl. Mater.*, Vol. 372(1), 2008, pp. 106–113.
[12] Goll, W., Spilker, H., and Toscano, E. H., "Short Time Creep and Rupture Test on High Burn up Fuel Rod Cladding," *J. Nucl. Mater.*, Vol. 289, 2001, pp. 247–253.
[13] Carpenter, J. C. and Watters, J. F., "Irradiation Damage Recovery in Some Zirconium Alloys", *Zirconium in Nuclear Applications ASTM STP 551*, American Society for Testing and Materials, 1974, pp. 400–415.
[14] Peeks, M., Garzarolli, F., and Goll, W., "Assessment of Dry Storage Performance of Spent LWR Fuel Assemblies with Increasing Burnup," *International Symposium on Storage of Spent Fuel From Power Reactors, IAEA-SM-352/39*, Nov. 9–13, 1998, IAEA and OECD Nuclear Agency, pp. 313–324.
[15] Erwin, K. T., Delaire, O., Motta, A. T., Chu, Y. S., Mancini, D. C., and Birtcher, R. C., "Observation of Second-Phase Particles in Bulk Zirconium Alloys Using Synchrotron Radiation," *J. Nucl. Mater.*, Vol. 294, 2001, pp. 299–304.
[16] Tenckhoff, E. "Review of Deformation Mechanism, Texture and Mechanical Anisotropy in Zirconium and Zirconium Base Alloys," *14th International Symposium of Zirconium in the Nuclear Industry, ASTM STP 1467*2006, P. Rudling and B. Kammendzind, eds., ASTM International, West Conshohocken, PA, pp. 25–52.
[17] Joy, D. C., Romig, A. D., and Goldstein, J. I., *Principles of Analytical Electron Microscopy*, Plenum Press, New York, 1986.
[18] Versaci, R. and Ipohorsky, M., "Polytype Structure of Intermetallic Precipitates in Zircaloy-4 Alloys," *J. Nucl. Mater.*, Vol. 80, 1979, pp. 180–183.
[19] Etoh, Y. and Shimada, S., "Neutron Irradiation Effects on Intermetallic Precipitates in Zircaloy as a Function of Fluence," *J. Nucl. Mater.*, Vol. 200, 1993, pp. 59–69.
[20] Adamson, R. B., "Effects of Neutron Irradiation on Microstructure and Properties of Zircaloy," *Zirconium in the Nuclear Industry, 12th International Symposium, ASTM STP 1354*, 2000, G. P. Sabol and G. D. Moan, eds., ASTM International, West Conshohocken, PA, pp. 15–31.
[21] Chen, S. P., Vossenberg, M. S., Vermolen, F. J., van der Langkruis, J., and van der Zwaag, S., "Dissolution of β Particles in an Al-Mg-Si Alloy During DSC Runs," *Mater. Sci. Eng., A*, Vol. 272, 1999, pp. 250–256.
[22] Vermolen, F. and Vuik, K., "A Numerical Method to Compute the Dissolution of Second Phases in Ternary Alloys," *J. Comput. Appl. Math.*, Vol. 93, 1998, pp. 123–143.

[23] Vermolen, F. J., Vuik, C., and van der Zwaag, S., "A Mathematical Model for the Dissolution of Stoichiometric Particles in Multi-Component Alloys," *Mater. Sci. Eng., A*, Vol. 328, 2002, pp. 14–25.

[24] Gilbon, D. and Simonot, C. "Effect of Irradiation on the Microstructure of Zircaloy-4," *Zirconium in the Nuclear Industry, Tenth International Symposium, ASMT STP 1245*, 1994, A. M. Garde and E. R. Bradley, eds., ASTM International, West Conshohocken, PA, pp. 521–548.

[25] Motta, A. and Lemaignan, C., "A Ballistic Mixing Model for the Amorphisation of Precipitates in Zircaloy Under Neutron Irradiation," *J. Nucl. Mater.*, Vol. 195, 1992, pp. 277–285.

[26] Yan, Z. J., He, S. R., Li, J. R., and Zhou, Y. H., "On the Crystallization Kinetics of $Zr_{60}Al_{15}Ni_{25}$ Amorphous Alloy," *J. Alloys Compd.*, Vol. 368, 2004, pp. 175–179.

DISCUSSION

Question 1, Young Suk Kim:—Please, comment why the TTSSd temperature increases upward by roughly 55°C after long annealing at 400°C. It seems to me that the TTSSd temperature should decrease to a lower temperature rather than increase upward.

Author's Response:—The increase of TTSSd in the irradiated material is related with the annihilation of defects created by neutron irradiation during post-irradiation annealing. This hypothesis originally proposed by T. Darby is supported by our present and previous measurements. The hypothesis assumes that there is an interaction between irradiation defects and hydrogen atoms which produce a trapping effect on these atoms. This effect reduces the amount of hydrogen atoms available to precipitate and then, the global hydride mass at room temperature. This process is assumed to occur while the material (Zircaloy-4) remains in service. After, during a DSC run, since the hydride mass is smaller than expected for the global hydrogen concentration of the sample, we obtain a TTSSd value that is smaller than the expected from an unirradiated sample with the same hydrogen content. Further annealing at 400°C, a temperature higher than the reactor operating temperature (250°C–280°C) produces a gradual recovery of the radiation damage. In fact, each run up to 350°C–400°C implies an annealing. In this way the 'traps' are removed, more hydrogen is free to precipitate and TTSSd tends to the unirradiated material expected value.

Question 2, Jean-Christophe Brachet:—1) In the DSC measurements on irradiated materials you have observed an exothermic peak during the first run at 275°C which could be attributed to the annealing of some irradiation defects and this peak is convoluted with the hydrides dissolution one. It could be interesting to perform the same measurement on irradiated samples (at the same fluence) without hydrogen inside the sample to be able to deconvolute this signal vs hydride dissolution and to check if it is really due to the behavior of the irradiated matrix. 2) Due to irradiation, the matrix solid solution is "supersaturated" by Fe (from the dissolution of the SPP's). Perhaps this could also influence the dissolution/precipitation sequences of hydrides. What is your opinion on this point?

Author's Response:—1) This is correct, the peak could be deconvoluted using a similar Zircaloy-4 sample with no hydrogen content. However, it is difficult to find a sample like this. In the present case the material was taken from cooling channels which remained at temperatures between 250°C to 280°C, and 200°C–230°C in the case of the foils which cover the channels. These temperatures are much lower than the ones of the fuel claddings (~350°C) and different kind of defects are expected. The hydrogen (deuterium in fact) is incorporated into the metal as a consequence of the corrosion reaction between the metal and the coolant. After 10 full power operating years, a period at which high neutron fluences are accumulated, the hydrogen content typically exceeds 100 wppm.

Maybe this study could be made using Zircaloy-2 taken from calandria tubes (CANDU reactors), since they remain at lower temperatures (60°C) and due to this, they have not a significant hydrogen pick up. Samples containing less than 25 ppm-H could be useful.

2) We observed a small hydride size distribution in the irradiated matrix with TEM. These hydrides are often observed next to or inside a SPP, which confirm the affinity between SPPs and hydrogen. However this is not the general case. However many small hydrides surrounded by ⟨c⟩ loops were observed frequently. Loops and hydrides are both similar in their length, between 100 and 200 nmts. Generally these small size hydride populations where mostly observed far away from the partially or totally dissolved SPPs, where the matrix is not supersaturated by Fe or at least Fe content is lower than surrounding a dissolving SPP. Thus, our observations don't support an evident relationship between the iron dissolved in the matrix and the hydrogen solubility.

Question 3, Ted Darby:—1) You used "peak temperature" on the DSC traces to determine TSS (as opposed to e.g. "Maximum slope temperature"). Please, comment as whether you believe peak temperature gives a good estimate of the solubility. 2) Annealing at relatively low temperature appeared to give significant recovery, implying predominantly ⟨a⟩ loop damage. Are TSS data available on the same material at higher fluences (with ⟨c⟩ loop damage)?

Author's Response:—1) In the last decade two experimental works arrived to different conclusions: Khatamian and Root using DSC and neutron diffraction as a contrasting technique concluded that the most representative point of TTSS is *pT*. In a previous work, Pan and Puls, performing a quasistatic study of hydride dissolution and measuring the Young modulus during heating runs concluded that *msT* is the most reliable temperature from a practical point of view of hydride dissolution. In my opinion the most physically clear paper is the Khatamian and Root one but, in any case, the reliability of the conclusion from any of both papers is strongly related with the accuracy of the contrasting technique: neutron diffraction cannot resolve precipitates smaller than a hundred of nanometers and internal friction (Pan's work) is capable to detect displacements of atoms to vacant sites in the lattice, that is, much smaller objects. I have determined recently TSS for Zr-2.5%Nb founding that pT values agree very well with Kathamian's ones. Theoretical studies ought to be made but so far the unique experimental evidence points to *pT* or *msT*. In the present context, since the best point to determine TSS on the trace is not completely clear yet, I made the choice seeking to maximize the experimental accuracy. From this point of view in irradiated material with low hydrogen contents (where the traces show higher noise than the unirradiated ones) pT is the best choice. The derivative of the DSC trace increases this noise and sometimes it is necessary to smooth the curve. I prefer to avoid the use of these mathematical tools if it is possible.

2) The samples accumulated fluences between 7×10^{21} n/cm^2 up to 10^{22} n/cm^2. These fluences are high and then both types of loops are present, as we observed with TEM. The annealing of many hours at 350°C and 400°C produced a significant recovery, which implies the growth and annihilation of the ⟨a⟩ loops but also the growth of the ⟨c⟩ loops.

From TEM observations it is clear that there is an interaction among ⟨c⟩ loops and hydrogen. Recent experiments studying in situ hydride precipitation under load at the Advanced Photon Source, Argonne, USA, show that precipitation starts at higher temperatures under load. Particularly, we observed that loading the sample in the direction where the texture is strong (tangential direction of a CANDU type pressure tube, at which most of the c poles of the grains are oriented) the hydrides precipitate copying the texture of the matrix: the intensity of the peak (111) of the hydrides is the highest in the direction at which the pole (0002) is intensified. Since the planes (111) of the hydrides are parallel to the (0002) of the matrix, the load expands the lattice splitting the basal planes favoring hydride nucleation/accommodation between them. This anticipates the onset of precipitation. In some sense the ⟨c⟩ loops, i. e., the absence of a disc of atoms in the basal planes, may be producing a similar local effect, becoming as sympathetic nucleation sites. In this context, the small hydride size population can be interpreted as a consequence of the presence of many small loops (100 to 200 nm) and hydrogen atoms in the material.

Similar irradiated samples annealed at 600°C show a matrix clean of defects without these small hydrides. In order to confirm the hypothesis we need to observe the intermediate stage, that is, the samples which were annealed many hours at 400°C. This work is in progress now.

Reprinted from JAI, Vol. 7, No. 9
doi:10.1520/JAI103030
Available online at www.astm.org/JAI

A. M. Garde,[1] *R. J. Comstock,*[2] *G. Pan,*[1] *R. Baranwal,*[1]
L. Hallstadius,[3] *T. Cook,*[4] *and F. Carrera*[5]

Advanced Zirconium Alloy for PWR Application

ABSTRACT: Westinghouse is evaluating several advanced zirconium-based alloys, designated collectively as AXIOM™, to achieve improved performance for more demanding fuel management schemes. There are five candidate AXIOM alloys currently being evaluated by Westinghouse. The in–pressurized water reactor (PWR) performance of one candidate alloy, X5A, is reviewed in this paper. The irradiation performance of X5A (previously identified as Alloy A) cladding that was fabricated using high-temperature processing (HTP) was published in 2002. Since then, the fabrication process of X5A was optimized by the use of a low-temperature process (LTP). Cladding tubes with the improved processing have been irradiated in two commercial PWRs (PWR A and PWR B) and in two test reactors (Test Reactor C and Test Reactor D). The irradiation performance of both versions (HTP X5A and LTP X5A) is reviewed in this paper with a primary emphasis on the current LTP cladding. After achieving an intermediate burnup in the range of 48–54 GWd/Metric Ton of Uranium (MTU) in PWR A, the average maximum oxide layer thickness for LTP X5A was about 23 μm or about 27 % lower than the oxide thickness on ZIRLO® clad fuel rods. In addition, the fuel rod axial growth strain for LTP X5A was about 50 % of ZIRLO rod growth. Lead fuel rod irradiation of LTP X5A in PWR B with burnup in the range of 47–53 GWd/MTU showed about 30 % lower corrosion relative to ZIRLO rods and a 7 % lower axial rod growth strain than ZIRLO. An irradiation experiment in Test Reactor C was designed to study breakaway irradiation

Manuscript received February 8, 2010; accepted for publication August 12, 2010; published online September 2010.
[1] Westinghouse Nuclear Fuel, Columbia, SC 29209.
[2] Westinghouse Research and Technology Unit, Pittsburgh, PA 15235.
[3] Westinghouse Sweden, Västerås, Sweden.
[4] Western Zirconium, Ogden, UT 84404.
[5] Westinghouse Specialty Metals Plant, Blairsville, PA 15717.

Cite as: Garde, A. M., Comstock, R. J., Pan, G., Baranwal, R., Hallstadius, L., Cook, T. and Carrera, F., "Advanced Zirconium Alloy for PWR Application," *J. ASTM Intl.*, Vol. 7, No. 9. doi:10.1520/JAI103030.

Copyright © 2011 by ASTM International, 100 Barr Harbor Drive, PO Box C700, West Conshohocken, PA 19428-2959.

growth (in the absence of waterside oxidation) of several alloys. LTP X5A cladding showed a growth strain of about 20 % that of ZIRLO cladding at a fluence of $16 \times 10^{25} n/m^2$. In Test Reactor D, at a burnup of about 44 GWd/MTU, HTP X5A had the same oxide thickness as ZIRLO. However, the post-irradiation hydrogen pick-up was 35 % lower for HTP X5A compared to ZIRLO. In addition to the irradiation experience, the supplemental out-reactor autoclave evaluation of X5A welds indicates adequate weld corrosion resistance. While additional in-PWR exposures are required along with post-irradiation examination, the results to date demonstrate that X5A is a promising alloy for future PWR application.

KEYWORDS: ZIRLO, alloy A, X5A, autoclave corrosion, in-PWR corrosion, in-PWR irradiation growth, hydrogen pick-up, weld corrosion resistance, in-PWR fuel performance, test reactor irradiation

Introduction

The in–pressurized water reactor (PWR) performance of several advanced zirconium alloys with dilute tin additions was reported in 2002 [1] where the irradiation performance of the alloys was compared to Low Tin Zircaloy (OPTIN), a low tin Zircaloy-4. All of the dilute alloy tubes were fabricated using high-temperature processing (HTP) that was similar to the process used for commercial Zircaloy-4 tubes. The as-fabricated microstructure for cladding tubes of the advanced alloys and OPTIN was partially recrystallized. Among the several advanced alloys that were evaluated, the alloy designated as Alloy A in Ref [1] was the most promising for combination of properties such as improved corrosion resistance in PWR water chemistry irradiation environment, good tube fabricability, and good ductility.

Alloy A has been renamed X5A and included as one of the candidate AXIOM alloys being developed by Westinghouse to achieve improved performance for both high-burnup and high-duty PWRs. Following the promising results from the initial in-PWR irradiation tests, an additional development activity focused on the following two areas: (a) The fabrication process of X5A was optimized through the use of a low-temperature process (LTP) appropriate for niobium-bearing alloys and based on the process optimization work completed on the Westinghouse cladding alloy, ZIRLO® [2], and (b) for the first time, X5A tubes were fabricated from a large commercial-sized ingot as all prior cladding tubes were made from small experimental-sized ingots. X5A cladding tubes of different pedigrees have been irradiated in two PWRs in the United States, two PWRs in Europe, and two test reactors in Europe. Previously unpublished X5A in-PWR performance data are presented in this paper. Also, the X5A performance is compared to that of the current Westinghouse commercial cladding material, stress-relief-annealed (SRA) ZIRLO.

Description of X5A Cladding Alloy

Chemistry

The alloying element compositions of X5A and ZIRLO are listed in Table 1. The major alloying elements in both X5A and ZIRLO are tin, niobium,

TABLE 1—*Zr cladding alloy chemical compositions, nominal weight percent.*

Alloy	Sn	Nb	Fe	Cr	Oxygen
X5A	0.5	0.3	0.35	0.25	0.15
ZIRLO	1.0	1.0	0.10	···	0.125

iron, and oxygen. X5A also contains chromium that is not present in ZIRLO.

As has been documented in a number of studies [2–4], a reduction of the tin content in zirconium-based alloys results in a reduction of cladding corrosion. This effect of tin has been reported for the Zircaloys [3] as well as niobium-bearing alloys such as ZIRLO [2,4]. However, the tin content in X5A was not reduced to zero due to the beneficial effect of tin on the mechanical strength (including creep resistance) of the alloy. The nominal tin level in X5A was selected to be 0.5 wt %, which is significantly lower than the 1.35 wt % in OPTIN [1] and 1.0 wt % in ZIRLO.

The iron and chromium levels in X5A were increased from the nominal concentrations of 0.2 and 0.1 wt %, respectively, in Zircaloy-4 to 0.35 % and 0.25 %, respectively. The higher level of iron in X5A was intended to further improve corrosion performance and decrease irradiation growth of the alloy [5]. The higher chromium addition was intended to improve the weld corrosion resistance of the alloy. The presence of tin, iron, and chromium in X5A is suggestive of a Zircaloy-4 type alloy but with composition changes (reduced tin and increased iron/chromium) in the direction of improved performance.

The final alloying addition to X5A was niobium due to the anticipated performance benefit (improved corrosion resistance with irradiation, lower H uptake, Second Phase Particle (SPP) stability after irradiation damage and superior ductility after irradiation) demonstrated by other niobium-bearing alloys [6]. The niobium concentration of 0.3 wt % was selected to be below the solubility limit of about 0.5 wt % for binary Zr–Nb alloys at 673 K [7] and to maintain good fabricability by keeping the total alloying additions low.

Processing

The fabrication of the original X5A cladding [1] used HTP, similar to that used for Zircaloy-4 (with minor modifications to treatment temperatures). The annealing parameter values were within the range appropriate for uniform corrosion resistance of PWR fuel cladding (2×10^{-18}–5×10^{-17} h) [8]. More recent development work from the process optimization of ZIRLO [2] identified the benefit of reduced annealing temperatures for niobium-bearing alloys. A similar cold-pilgering process using reduced annealing temperatures following beta quenching was utilized for the fabrication of X5A cladding produced from the commercial-sized ingot. The intermediate annealing temperature was the major processing difference between the HTP and LTP variants. The X5A cladding that was fabricated using this process modification is designated as LTP X5A.

As with the HTP X5A cladding, the final anneal of LTP X5A produced a partially recrystallized microstructure.

Microstructure

Transmission electron microscopy (TEM) was used to characterize the second phase particles that were present in the LTP X5A cladding. Representative micrographs of the second phase particles are shown in Fig. 1. The particle size was measured from TEM micrographs by measuring the diameter of a circle with an area that was equivalent to the projected area of the SPP. The average particle size was the average of the circle diameters and was about 90 nm for LTP X5A. A histogram of the particle size distribution is shown in Fig. 2. The uncertainty in average SPP size is about 10 nm as determined from measurements on multiple TEM foils. A comparable technique was used by a different laboratory to measure the particle size in HTP X5A from TEM micrographs. The average SPP size in HTP X5A was similar (90 nm) to that of LTP X5A. For comparison, the average particle size for ZIRLO is smaller, i.e., less than 80 nm [9] with typical values ranging from 50 to 60 nm. The smaller average SPP size in ZIRLO is due to the presence of beta-Nb particles that tend to be smaller than the Zr–Nb–Fe particles that are also present in ZIRLO. The absence of beta-Nb particles in X5A, as discussed below, results in an average particle size that is larger than the average size in ZIRLO.

Scanning Transmision Electron Microscopy-Energy Dispersive Spectrscopy (STEM-EDS) analysis was performed to characterize the chemistry of the second phase particles in LTP X5A. The presence of the zirconium matrix precluded the absolute determination of the particle composition. The dominant particle type contained iron and chromium with low levels of Nb (designated as Zr–Fe–Cr–(Nb)). Occasional particles containing higher concentrations of niobium along with iron and chromium (designated as Zr–Nb–Fe–Cr) were also detected in LTP X5A. The chemical analysis of the particles is shown graphically in Fig. 3 where the niobium content is plotted as a function of the iron plus chromium concentration. The figure shows the two types of particles with relatively constant ratios of Nb : (Fe + Cr). Chemical analysis was also performed on extraction replicas from HTP X5A where the SPPs were extracted from the matrix, thereby eliminating the zirconium matrix from the analysis. The average composition of the HTP X5A SPPs is plotted on Fig. 3 and is consistent with the Nb : (Fe + Cr) ratio of the Zr–Fe–Cr–(Nb) particles in LTP X5A. It is not known if the Zr–Nb–Fe–Cr particles were absent in HTP X5A or were dissolved during the preparation of the extraction replica. Interestingly, no beta-Nb particles were detected as the niobium segregated to second phase particles containing iron and chromium. This was in contrast to the second phase particles in ZIRLO, which consisted of both beta-Nb and Zr–Nb–Fe particles [9].

Ex-Reactor Autoclave Corrosion Testing

Ex-reactor autoclave corrosion tests of cladding specimens ($\sim$ 2.5 cm long) were performed in 633 K pure water, 633 K lithiated water (70 ppm lithium), and 700

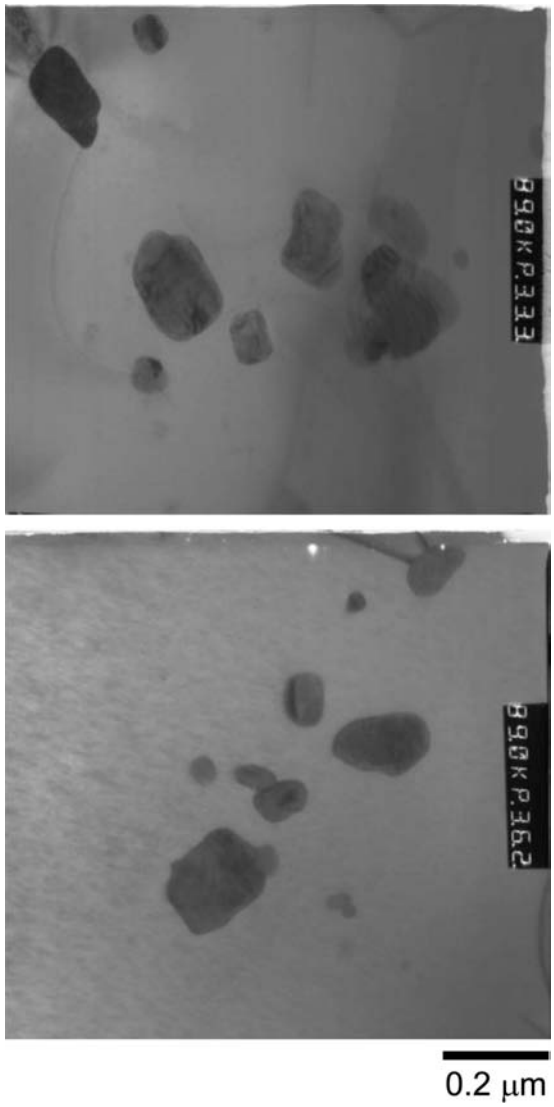


FIG. 1—*Representative TEM brightfield micrographs of second phase particles in LTP X5A.*

K steam. Both water tests were performed at saturation pressure, while the steam test operated at 10.3 MPa. Figure 4 plots the weight gain data as a function of exposure time for the LTP X5A, HTP X5A, and ZIRLO claddings exposed to 633 K pure water. After 84 days of exposure, all samples remain in the pre-transition corrosion kinetics with only small differences in weight gains. A prior comparison of post-transition corrosion rates from testing in 633 K pure water was previously shown to properly rank in-reactor corrosion performance [5].

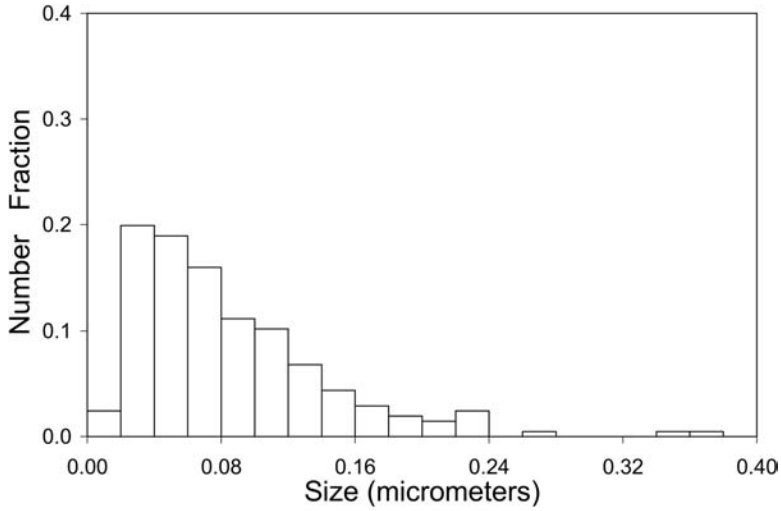


FIG. 2—*Histogram of second phase particle size distribution in LTP X5A.*

Longer term testing of X5A and ZIRLO to achieve post-transition corrosion rates is in progress.

Weight gain data for 633 K accelerated water autoclave test with 70 ppm lithium are presented in Fig. 5. HTP X5A exhibits accelerated corrosion during

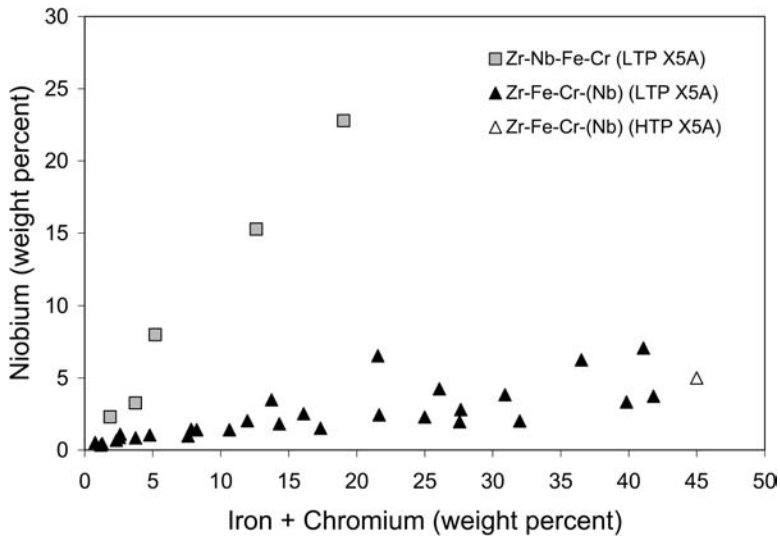


FIG. 3—*STEM-EDS analysis of SPPs in LTP X5A shows the presence of two particle types: Zr–Fe–Cr–(Nb) and Zr–Nb–Fe–Cr. Analysis of SPPs in HTP X5A shows the presence of Zr–Fe–Cr–(Nb) particles.*

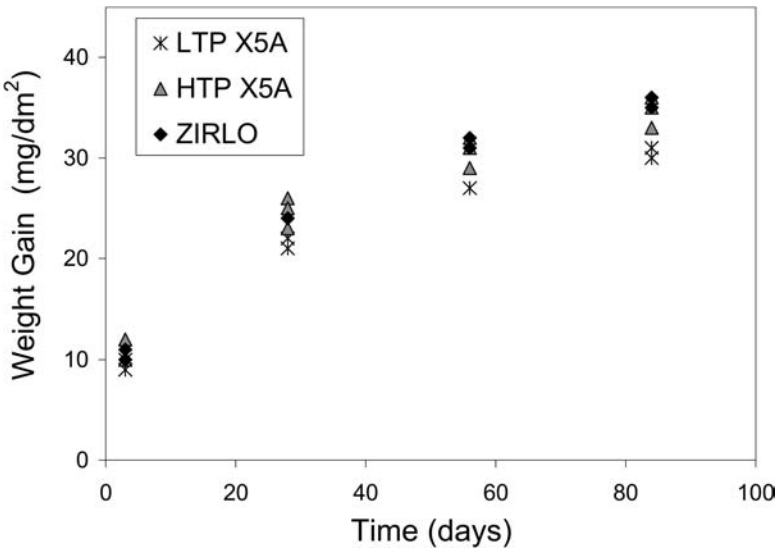


FIG. 4—*Weight gains as a function of time for LTP X5A, HTP X5A, and ZIRLO cladding samples exposed to 633 K pure water.*

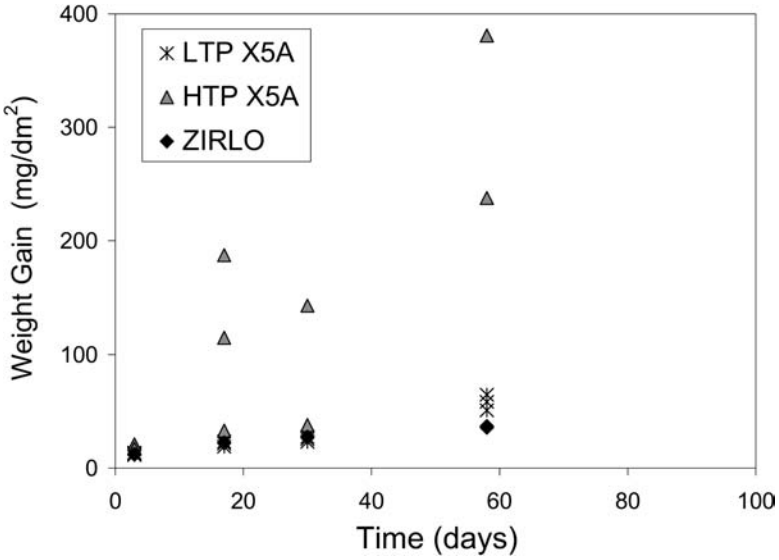


FIG. 5—*Weight gains as a function of time for LTP X5A, HTP X5A, and ZIRLO cladding samples exposed to 633 K water containing 70 ppm lithium.*

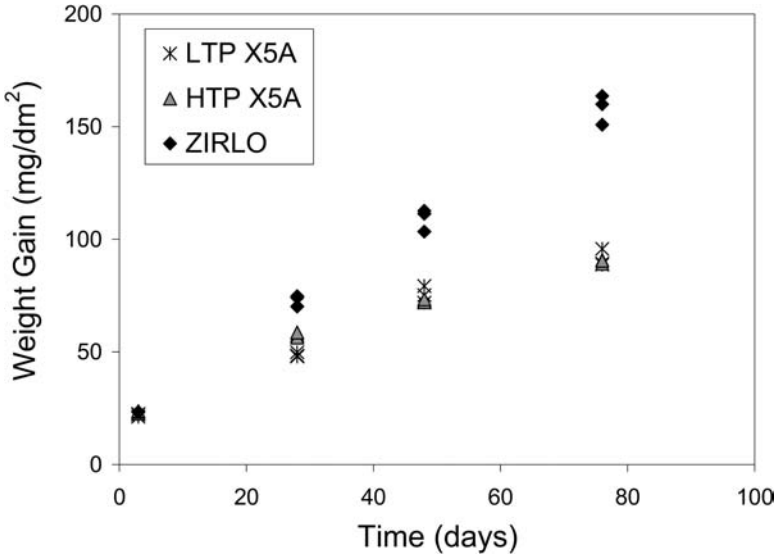


FIG. 6—*Weight gains as a function of time for LTP X5A, HTP X5A, and ZIRLO cladding samples exposed to 700 K steam.*

the 58-day exposure. The large scatter in the data points for HTP X5A in Fig. 5 implies a non-robust corrosion resistance for this variant in lithiated water environment. At the maximum exposure time of 58 days, the corrosion performance of ZIRLO is slightly better than that of LTP X5A.

The 700 K steam autoclave test results are shown in Fig. 6. After 76 days of exposure, the corrosion rates of the two versions of X5A are comparable and lower than the corrosion rate of ZIRLO.

Weld Corrosion Resistance

The corrosion resistance of laser welds that were made on LTP X5A sheet material was evaluated by autoclave tests in both 633 K water (84 days) and 700 K steam (132 days). The autoclaved specimens were destructively examined by metallography to measure the oxide layer thickness in both the base material and weld region. The metallographic results are presented in Table 2.

TABLE 2—*Metallographic measurement of oxide thickness of autoclaved weld specimens.*

	633 K Water		700 K Steam	
Specimen Type	56 days	84 days	48 days	132 days
LTP X5A (base)	2.1 μm	2.1 μm	6.2 μm	11.0 μm
LTP X5A (weld)	2.1 μm	2.8 μm	6.4 μm	13.8 μm
LTP X5A ratio (weld/base)	1.0	1.4	1.0	1.3

The heat input during welding changes the alpha phase microstructure in the non-weld region to the transformed beta-phase microstructure in the weld region. As a result of this microstructural change, the uniform corrosion resistance of the weld region is generally inferior to that of the base material. Thus, the ratio of oxide thickness in the weld region to that in the base material is expected to be greater than one. While the oxide thickness measurements in Table 2 follow this general trend, the slightly increased oxide in the weld region is acceptable as the corrosion at the end-plug location on a fuel rod is not design limiting.

In-Reactor Performance of X5A

Irradiation Performance in PWR A

PWR A is a 14×14 design reactor in the United States with 2-year irradiation cycles. The oxide thickness on the fuel rod cladding was measured by an eddy current technique. The accuracy of the eddy current oxide thickness measurement technique is estimated to be $+/-3\,\mu$m. A four pass composite circumferential average was used to determine *maximum average* oxide (average of maximum values measured on multiple traces). The measured oxide thickness values and axial growth strains for individual fuel rods with burnups are listed in Table 3.

A review of the oxide thickness data in Table 3 shows that after two cycles of irradiation and at a burnup of about 49 GWd/Metric Ton of Uranium (MTU), the oxide thickness on the LTP X5A, HTP X5A, and ZIRLO fuel claddings was 18, 27, and 33 μm, respectively. The rod growth data following two cycles are provided in Table 3. The growth of HTP X5A is higher than that of ZIRLO, while the rod growth of LTP X5A is about 50 % lower than that of ZIRLO.

After three cycles of irradiation, the oxide thickness on the LTP X5A, HTP X5A, and ZIRLO clad rods was measured on a second fuel assembly. The maximum average oxide thickness was 23, 31, and 32 μm, respectively. The irradiation power history of two- and three-cycle assemblies was different. Two-cycle assemblies had out-in core location sequence, while the three-cycle assemblies had out-in-out core location sequence. As a result, the burnup accumulation during different cycles was different. This power sequence difference may be a contributing factor for lower oxide thickness for ZIRLO after three-cycle exposure compared to the two-cycle exposure. The corrosion resistance of HTP X5A was comparable to ZIRLO, while the corrosion resistance improvement for LTP X5A relative to ZIRLO was about 27 %.

Irradiation Performance in PWR B

LTP X5A and ZIRLO clad fuel rods were irradiated in a European PWR of 17×17 XL Westinghouse design. This PWR operated with annual fuel cycles. Twenty-five ZIRLO and nine LTP X5A fuel rods were measured for oxide thickness and axial growth. The burnup range, oxide thickness range, and growth strain range following three cycles of irradiation are listed in Table 4.

TABLE 3—*Fuel rod cladding waterside oxide thickness and fuel rod axial growth strain after irradiation in PWR A.*

Alloy	Assembly	Irradiation Cycle	Rod Average Burnup GWd/MTU	Maximum Circumferential Average Oxide, μm	Percent Fuel Rod Axial Growth
LTP X5A	1	2	48.7	19	0.13
			48.1	17	0.14
			50.6	17	...
	2	3	51.3	25	...
			48.4	22	...
			53.7	22	...
			47.5	23	...
HTP X5A	1	2	51.1	25	...
			48.1	29	0.37
			45.2	21	0.42
	2	3	55.8	30	...
			56.7	34	...
			50.9	33	...
			51.8	27	...
ZIRLO	1	2	42.2	23	0.23
			48.0	32	0.30
			50.6	34	...
	2	3	47.5	27	...
			51.2	37	...
			51.0	30	...
			48.4	32	...

At burnup ranging from 45 to 53 GWd/MTU, the maximum average oxide thickness was about 21 μm for LTP X5A and was about 30 μm for ZIRLO. While both alloys have relatively thin oxide, the oxide thickness on LTP X5A was about 30 % lower. At the same burnup range, the rod growth was about 7 % lower for LTP X5A compared to ZIRLO.

TABLE 4—*Irradiation performance of LTP X5A and ZIRLO irradiated in PWR B.*

Clad Alloy	Fuel Rod Burnup Range, GWd/MTU	Maximum Oxide Thickness Range, μm	Rod Growth Range, %
LTP X5A	47.5–53.4	19–23	0.44–0.52
ZIRLO	45.5–53.4	25–30	0.45–0.60

TABLE 5—*Irradiation growth strain for LTP X5A and ZIRLO (two microstructures) irradiated in Test Reactor C to different fluence levels.*

	Irradiation Growth Strain (%) as Function of Fluence (10^{25} n/m^2, $E > 1$ MeV)				
Alloy, Microstructure	2.05	5.8	8.4	11.1	16.15
LTP X5A, partially recrystallized	0.06	0.095	0.14	0.155	0.285
ZIRLO, SRA	0.1	0.39	0.62	0.89	1.475
ZIRLO, recrystallized	0.075	0.1	0.125	0.16	0.46

Given the differences in PWR A and B and fuel rod designs, the relative oxide thickness values for X5A and ZIRLO are consistent. Oxide thickness for LTP X5A is lower than that for ZIRLO.

Irradiation Performance in Test Reactor C

The purpose of the experiment was to study breakaway irradiation growth of several zirconium-based alloys at high fluences, well beyond the discharge burnups of LWR fuel. The irradiation temperature ranged from 588 to 598 K. The temperature was constant for all specimens in the test holder. The listed temperature range is based on the temperature measurement uncertainty. Upon the completion of the program, the test materials had reached a fluence of 16×10^{25} n/m^2 ($E > 1$ MeV), equivalent to a burnup of about 75 GWd/MTU. The test materials did not contact water during irradiation, so there was no corrosion contribution due to hydrogen pick-up or oxide growth to the measured dimensional changes. The post-test growth strains for ZIRLO and LTP X5A irradiated in Test Reactor C are provided in Table 5.

A review of the irradiation growth data in Table 5 indicates that irradiation growth strain for partially recrystallized LTP X5A was much lower than that for SRA ZIRLO and slightly lower than that of recrystallized ZIRLO.

Irradiation Performance in Test Reactor D

In the PWR simulation loop (lithium, boron, and hydrogen additions to water) of Test Reactor D, segmented test fuel rods clad with HTP X5A and ZIRLO were irradiated to a burnup of about 44 GWd/MTU. The waterside oxide thickness was measured at several intermediate irradiation exposures and is presented in Fig. 7. The coolant temperature in Test Reactor D was 623 K.

A review of the data in Fig. 7 shows that the in-pile corrosion rate of HTP X5A is comparable to that of ZIRLO. After the completion of irradiation in Test Reactor D, the irradiated specimens were analyzed for hydrogen content to determine the hydrogen pick-up. Hydrogen analysis results are presented in Table 6.

A review of the data in Table 6 shows that the average hydrogen concentrations in HTP X5A and ZIRLO are 107 and 166 ppm, respectively. Test Reactor D

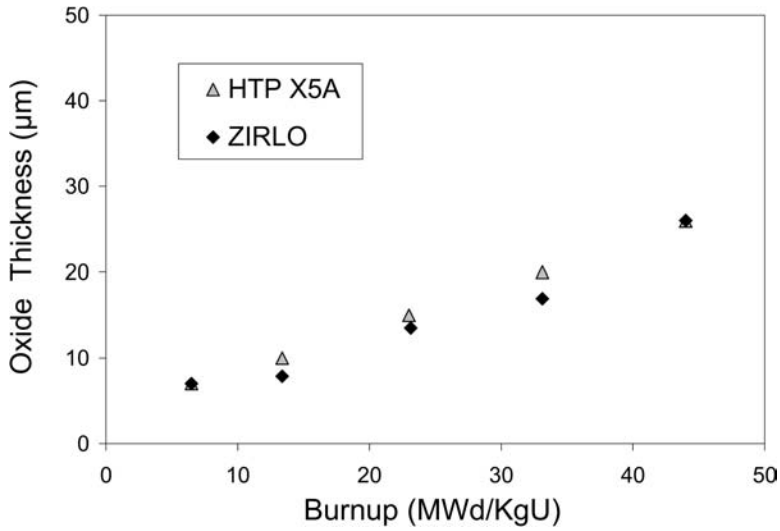


FIG. 7—*Oxide thickness as a function of burnup for ZIRLO and HTP X5A claddings irradiated in Test Reactor D.*

irradiation results show that although the waterside oxide thickness growth rates of HTP X5A and ZIRLO in the test reactor are comparable, the hydrogen pick-up for HTP X5A is about 35 % lower. The effect of low-temperature processing on hydrogen pick-up for X5A needs to be evaluated.

Discussion

All of the previously unpublished in-reactor corrosion data for LTP X5A, HTP X5A, and ZIRLO are presented in Figs. 8 and 9. The data trend in Fig. 8 shows that the in-reactor corrosion performances of ZIRLO and HTP X5A are comparable. With burnup in the range of 47–53 GWd/MTU, there is about 30 %

TABLE 6—*Measured hydrogen levels in HTP X5A and ZIRLO segmented test rods irradiated in Test Reactor D to a burnup of about 44 GWd/MTU.*

Segment Clad Alloy	Specimen Number	Measured Hydrogen, ppm
HTP X5A	1	103
	2	113
	3	90
	4	120
ZIRLO	1	234
	2	147
	3	133
	4	149

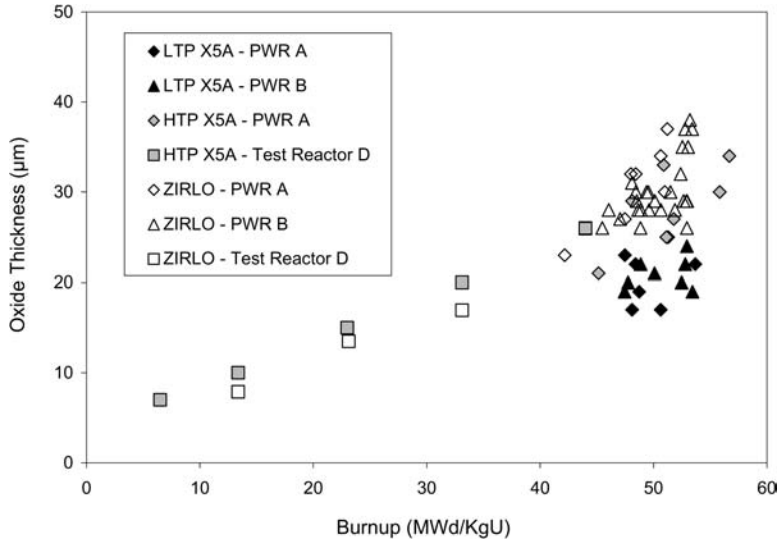


FIG. 8—*Measured oxide thickness for LTP X5A, HTP X5A, and ZIRLO as a function of burnup.*

improvement in corrosion resistance for LTP X5A compared to ZIRLO. The same level of corrosion resistance improvement is seen in Fig. 9 on the basis of modified fuel duty index (MFDI) considerations [10,11]. MFDI is defined [11] as FDI $+ b \times M_t$, where M_t = total mass evaporation, lb/ft^2, b is an empirical fit

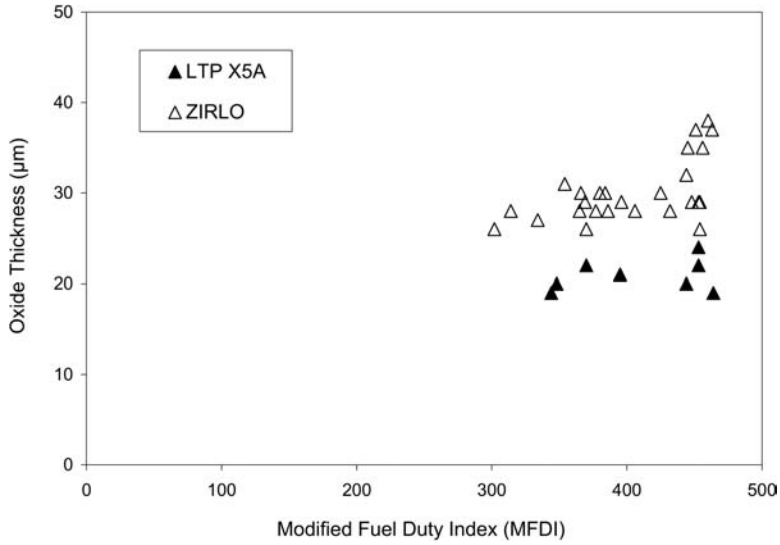


FIG. 9—*Measured oxide thickness for LTP X5A and ZIRLO clad fuel rods in PWR B as a function of MFDI.*

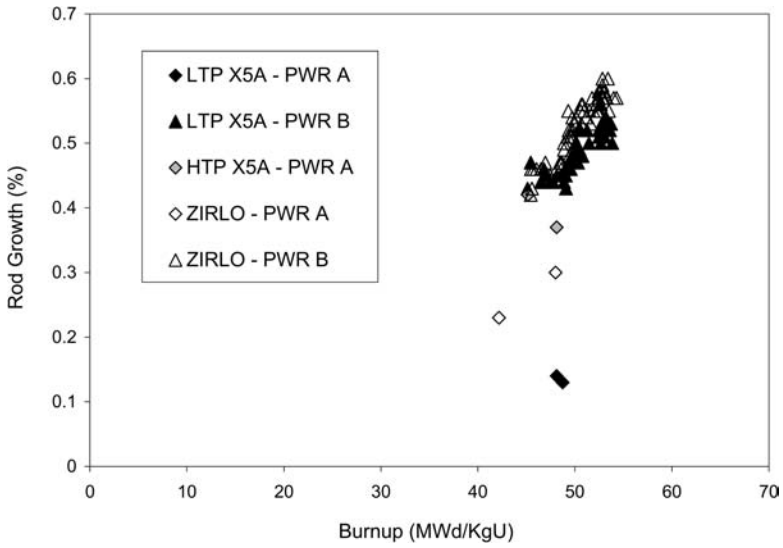


FIG. 10—*In-PWR fuel rod growth data for ZIRLO, HTP X5A, and LTP X5A clad fuel rods as a function of burnup.*

parameter, and FDI is defined as [10] $(T_{\text{avg}} - 580)/100 \times (Hrs/1000)^2$, where T_{avg} = time averaged oxide layer surface temperature, °F, and Hrs = total irradiation time in hours. Based on these data, X5A warrants further evaluation as a candidate for advanced cladding. Since the SPP size distribution and SPP chemical composition for HTP and LTP X5A were not measured in the same laboratory, it is not possible to attribute the difference in the corrosion resistance of the two variants to difference in SPP size distribution/composition. The available data are not sufficient to identify the reason for the superior corrosion resistance of LTP X5A. One postulated contributing cause could be the different levels of niobium level in the matrix due to lower intermediate anneal temperature for the LTP variant compared to the HTP variant.

In-PWR fuel rod growth data for the three alloys are presented in Fig. 10. Although there is scatter in the fuel rod growth data shown in Fig. 10, it appears that the fuel rod growth of HTP X5A is higher than ZIRLO and the growth strain of LTP X5A may be lower than that of ZIRLO. The possible reasons for the scatter in the fuel rod growth data are variations in the fuel rod design, pellet/cladding gap, differences in coolant temperatures, and pellet stack interactions with the cladding.

In addition to the properties discussed above (corrosion resistance, irradiation growth, hydrogen uptake, and weld corrosion resistance), other material properties necessary for satisfactory fuel performance and commercial implementation include mechanical strength, creep behavior, ductility, fabricability, loss of coolant accident performance, and wear resistance. Although such evaluations are yet to be completed, some expectations based on the available information are listed below. While the as-fabricated mechanical strength of X5A is

lower than that of ZIRLO due to the lower level of alloying elements, the mechanical properties of X5A exceed the design requirements. Moreover, irradiation hardening will increase the strength during PWR irradiation. The ductility and fabricability of X5A are expected to be satisfactory due to lower concentrations of alloying elements (Nb and Sn) in X5A. The fabricability improvement was noticed during tube fabrication, although the tube fabrication experience with X5A remains limited at this time.

A comparison of in-PWR corrosion resistance order of different alloys in Fig. 8 to the alloy corrosion resistance order for different autoclave conditions presented in Figs. 4–6 reveals that only 633 K water test condition shows the same ranking. It is worth noting that the 633 K water test data are still in pre-transition. The water test is continuing to confirm that the same trend continues in post-transition.

However, prior autoclave testing of ZIRLO and low tin Zircaloy-4 cladding revealed lower corrosion rates for low tin Zircaloy-4 in both 673 and 700 K steam [9]. The relative corrosion ranking from a 673 or 700 K steam test did not correlate to the relative in-PWR corrosion behavior of ZIRLO and low tin Zircaloy-4 [9].

Conclusions

(1) The in-PWR corrosion resistance of LTP X5A through a burnup of about 50 GWd/MTU is about 30 % lower than that of ZIRLO, while the in-PWR corrosion resistance of HTP X5A is comparable to that of ZIRLO. The absolute oxide thickness for all alloys remained low at this burnup level in these reactors.
(2) The in-PWR fuel rod growth of LTP X5A is lower than that of ZIRLO. The fuel rod growth of HTP X5A is comparable to that of ZIRLO.
(3) Based on the initial data, the in-PWR hydrogen pick-up of HTP X5A is about 35 % lower than that of ZIRLO.
(4) The weld corrosion resistance for X5A welds is adequate for potential in-PWR application.
(5) The reduction in the processing temperatures used for fabrication of X5A cladding improved the in-PWR performance of the alloy compared to the HTP variant.
(6) In-PWR results through a burnup of about 50 GWd/MTU demonstrate that X5A is a promising alloy for future PWR application. Additional in-PWR exposure of X5A is necessary to confirm its performance at high burnups.

References

[1] Garde, A. M., Smith, G. P., and Pirek, R. C., "In-PWR Irradiation Performance of Dilute Tin-Zirconium Advanced Alloys," *Zirconium in the Nuclear Industry: 13th International Symposium, ASTM STP 1423*, Annecy, France, June 10–14, 2001, G.

D. Moan and P. Rudling, Eds., ASTM International, West Conshohocken, PA, 2002, pp. 490–506.

[2] Yueh, H. K., Kesterson, R. L., Comstock, R. J., Shah, H. H., Colburn, D. J., Dahlback, M., and Hallstadius, L., "Improved ZIRLO™ Cladding Performance Through Chemistry and Process Modifications," *J. ASTM Int.*, Vol. 2, 2005, Paper ID JAI12344.

[3] Kilp, G., Thornburg, D. R., and Comstock, R. J., "Improvement in Zirconium Alloy Corrosion Resistance," *IAEA Technical Committee Meeting on Fundamental Aspects of Corrosion on Zirconium Base Alloys in Water Reactor Environments*, Portland, OR, September 11–15, 1989, IAEA, Vienna, 1990, p. 145, IWGFPT/34.

[4] Comstock, R. J., Schoenberger, G., and Sabol, G. P., "Influence of Processing Variables and Alloy Chemistry on the Corrosion Behavior of ZIRLO Nuclear Fuel Cladding," *Zirconium in the Nuclear Industry: 11th International Symposium, ASTM STP 1295*, Garmish-Partenkirchen, Germany, September 11–14, 1995, E. R. Bradley and G. P. Sabol, Eds., ASTM International, West Conshohocken, PA, 1996, pp. 710–725.

[5] Shishov, V. N., Peregud, M. M., Nikulina, A. V., Kon'kov, V. F., Novikov, V. V., Markelov, V. A., Khokhunova, T. N., Kobylyansky, G. P., Novoselov, A. E., Ostrovsky, Z. E., and Obukhov, A. V., "Structure-Phase State Corrosion and Irradiation Properties of Zr-Nb-Fe-Sn System Alloys," *J. ASTM Int.*, Vol. 5, No. 3, 2009, pp. 724–743, Paper ID JAI101127.

[6] Garde, A. M., Slagle, W. H., and Mitchell, D., "Hydrogen Pick-up Fraction for ZIRLO Cladding Corrosion and Resulting Impact on Cladding Integrity," *Proceedings of French Nuclears Energy Society (SFEN) Top Fuel 2009*, Sep. 6–10, 2009, Paris, France, Paper 2136.

[7] Hayes, E. T., "Zirconium Alloy Systems," *The Metallurgy of Zirconium*, B. Lustman and F. Kerze, Eds., McGraw Hill, New York, 1955, p. 467.

[8] Garzarolli, F., Steinberg, E., and Weidinger, H. G., *Microstructure and Corrosion Studies for Optimized PWR and BWR Zircaloy Cladding, ASTM STP 1023*, ASTM International, West Conshohocken, PA, 1989, pp. 202–212.

[9] Sabol, G. P., Comstock, R. J., Weiner, R. A., Larouere, P., and Stanutz, R. N., "In-Reactor Corrosion Performance of ZIRLO and Zircaloy-4," *Zirconium in the Nuclear Industry: Tenth International Symposium, ASTM STP 1245*, Baltimore, MD, june 21–24, 1993, A. M. Garde and E. R. Bradley, Eds., ASTM International, West Conshohocken, PA, 1994, pp. 724–744.

[10] Kaiser, R. S., Leech, W. J., and Casadei, A. L., "The Fuel Duty Index (FDI)—A New Measure of Fuel Rod Cladding Performance," *America Nuclear Society (ANS) Light Water Reactor Fuel Performance Conference*, Park City, UT, April 2000, p. 393.

[11] Leech, W. J. and Yueh, K., "The Fuel Duty Index, a Method to Assess Fuel Performance," *ENS Top Fuel Conference 2001*, May 27–31, 2001, Stockholm, Sweden, Paper P2-16.

DISCUSSION

Question 1, Ron Adamson, Zircology Plus:—Do you have any feel yet for the stability of the SPPs in the irradiation flux?

Author's Response:—The stability of SPPs after irradiation will be evaluated in the hot cell examinations planned in the future. It is anticipated that the niobium content of SPP will enhance stability of SPP under irradiation flux.

Question 2, Vladimir Markelov, VNIINM (Bochvar Inst):—What is the Li content you used for autoclave test?

Author's Response:—We conducted 633°K water autoclave test with 70 ppm Li addition.

Question 3, V. Shishov, Bochvar VNIINM, Moscow, Russia:—Have you measured elongation of the fuel rods or the free irradiation-induced growth?

Author's Response:—Elongation of fuel rods was measured in PWR A and PWR B. Irradiation induced growth (without the influence of pellet stack interaction or hydrogen charging of metal due to waterside corrosion) was measured in Test Reactor C.

Question 4, Xun Dai, Nuclear Power Institute of China:—You showed that new Zr alloys had enhanced PCI resistance. Is it about un-irradiated or irradiated material? New alloys have larger K_I-SCC than ZIRLO and Zircaloy-4?

Author's Response:—We have not yet measured PCI resistance of the advanced alloy in either un-irradiated or irradiated condition. The objective is to design an advanced alloy with K_I-scc higher than that for ZIRLO & Zircaloy-4.

Question 5, Yong Hwan Jeong, Korea Atomic Energy Research Institute:—Your new alloy (X5A) showed a good corrosion resistance compared to ZIRLO. Could you explain the reason for good corrosion resistance of new alloy in terms of alloying elements?

Author's Response:—The reasons for the better corrosion resistance of X5A compared to ZIRLO are primarily the lower tin content and also due to the higher levels of Fe and Cr.

Question 6, Bo Cheng, EPRI:—With substantially reduced Sn and Nb concentrations (both are solid solution strengthening elements), does the X5A alloy have sufficient initial strength to withstand the initial loading from the hold-down spring to prevent fuel assembly deformation?

Author's Response:—The advanced alloy X5A is currently evaluated for fuel cladding application for which it has adequate as-fabricated strength. Although it is not yet used for the thimble tubes, it is expected that it will have adequate strength for that application to withstand the assembly hold-down spring load. It is expected that neutron flux will introduce irradiation hardening early in irradiation exposure to increase the alloy strength.

Question 7, Michel Morel, CEZUS, AREVA:—Did you measure the creep rate under irradiation? What is expected with LTP X5A?

Author's Response:—The creep rate of LTP X5A under irradiation has not been measure yet. The creep rate of HTP X5A was measured and results were published in 2002 in ASTM STP 1423. The in-PWR creep rate of HTP X5A was comparable to that of p-RXA Zircaloy-4 (OPTIN). The effect of X5A processing on creep strength of the alloy has not been evaluated yet.

Reprinted from JAI, Vol. 8, No. 5
doi:10.1520/JAI103013
Available online at www.astm.org/JAI

V. Chabretou,[1] *P. B. Hoffmann,*[2] *S. Trapp-Pritsching,*[2]
G. Garner,[3] *P. Barberis,*[4] *V. Rebeyrolle,*[4] *and J. J. Vermoyal*[1]

Ultra Low Tin Quaternary Alloys PWR Performance—Impact of Tin Content on Corrosion Resistance, Irradiation Growth, and Mechanical Properties

ABSTRACT: The performance of Zr1NbSnFe alloys within the range of Sn 0–0.65 % and Fe 0.03–0.35 % were studied through irradiation of fuel rods in two pressurized water reactors (PWRs) operating with significantly different fuel management strategies. Material test rod irradiations have also been launched in order to determine irradiation growth and corrosion behaviour on tubes irradiated under conditions representative of guide tubes. Results show that the increase in tin content up to 0.3 % does not significantly change the corrosion resistance nor the hydrogen pick-up compared to Zr1Nb alloy, while ensuring a higher creep resistance and an improved dimensional stability. On the contrary, at 0.5 % Sn, the corrosion resistance can be significantly degraded under demanding conditions. The iron addition to the alloy can be considered as a second order parameter for both corrosion and creep properties.

KEYWORDS: PWR, corrosion, oxidation, hydrogen pick-up, irradiation creep, irradiation growth, zirconium alloys

Manuscript received February 2, 2010; accepted for publication April 10, 2011; published online June 2011.
[1] AREVA, AREVA NP SAS, 10 rue Juliette Récamier, F-69456 Lyon Cedex 06, France
[2] AREVA, AREVA NP GmbH, Paul-Gossen-Str. 100, D-91052 Erlangen, Germany
[3] AREVA, AREVA NP Inc., 3315 Old Forest Rd., Lynchburg, VA 24506-0935
[4] AREVA, AREVA NP/CEZUS Research Centre, Avenue Paul Girod, F-73403 Ugine, France

Cite as: Chabretou, V., Hoffmann, P. B., Trapp-Pritsching, S., Garner, G., Barberis, P., Rebeyrolle, V. and Vermoyal, J. J., "Ultra Low Tin Quaternary Alloys PWR Performance—Impact of Tin Content on Corrosion Resistance, Irradiation Growth, and Mechanical Properties," *J. ASTM Intl.*, Vol. 8, No. 5. doi:10.1520/JAI103013.

Copyright © 2011 by ASTM International, 100 Barr Harbor Drive, PO Box C700, West Conshohocken, PA 19428-2959.

Introduction

AREVA undertook an extensive R&D program to assess the performance of ultra low tin quaternary alloys Zr1NbSnFe. These alloys are an evolutionary development of M5™ obtained by the addition of small amounts of tin and iron. Tin is added to increase the irradiation creep strength and the beginning of life mechanical properties, but limited content is used to mitigate corrosion resistance degradation. The impact of iron, as said beneficial for corrosion behavior, is studied with a maximum content of 0.35 %. All these alloys are studied in the fully recrystallized annealed condition.

An exhaustive metallurgical characterization (microstructure, nature and composition of the second phase particles (SPP)) and detailed classical out-of-pile characterizations (mechanical properties, creep, and corrosion testing) were performed to complement the in-reactor performance data collected in the irradiation programs. This allowed for quantification of the degradation of corrosion resistance by the tin and, conversely, the beneficial impact of tin on the creep resistance.

As is generally the case in assessing material behaviour, Zr1NbSnFe alloys have been tested initially as cladding tubes in two European reactors (French and German), operating with significantly different fuel management strategies. Corrosion, fuel rod length changes and diametral creep data have been collected at fuel assembly burn up values up to 55 GWd/tU. The first irradiation program was completed after five annual cycles which included demanding operating conditions during the first two cycles. The fourth cycle of the second irradiation campaign is on going in a plant operating on 18-month cycles.

Specific irradiations of material test rods have also been launched in order to determine irradiation growth and corrosion behaviour on tubes irradiated under conditions representative of guide tubes. In particular, a free growth experiment on one of the ultra low tin quaternary alloys has achieved five cycles in a commercial PWR. Further in-pile demonstrations are on going to complete the irradiation program.

Post-irradiation examination studies are on going on fuel rods that have been extracted after different cycles and on material test rods irradiated in PWR.

This paper summarizes the experimental findings on the effect of the chemical composition, and in particular the tin content, on the Zr1NbSnFe alloys behaviour.

Materials and Experiments

Material

Zr1NbSnFe alloys within the range of Sn 0–0.65 % and Fe 0.03–0.35 % were manufactured in amounts ranging from laboratory scale to industrial size ingots. They were transformed into tubes, corresponding to fuel rod claddings, guide tubes and special tubes for experimental irradiation: Final tube wall thicknesses were from 0.4 to 0.7 mm. Those alloys are derived from M5™, with 1 %

Nb, controlled sulfur and oxygen additions, respectively of 20 and 1400 ppm, and with low tin and iron additions (see Table 1). These alloys were all processed with the same manufacturing route. In particular, the final dimension was obtained by four cold pilgering passes, and a low temperature process (characterized by intermediate and final annealings at a temperature lower than the 600°C monotectoid temperature) was applied. Fully recrystallized microstructures with fine grains and uniformly distributed precipitates were obtained.

Out-of-Pile Characterization Program

An exhaustive metallurgical characterization was carried out on the as-manufactured tubing samples. Microstructure was observed by optical and transmission electron microscopy (TEM). The nature and composition of the SPP were obtained by combining exams on thin foils and on extractive replicas with EDX. The textures were measured at mid thickness by X-ray diffraction.

Detailed classical out-of-pile characterizations were subsequently performed:

- Tensile tests were performed at room temperature, 315°C and 400°C;
- Biaxial creep tests were performed at 400°C during 240 h by internal pressure with hoop stresses of 130 MPa and 160 MPa;
- Corrosion tests were performed in steam at 415°C/10.5 MPa as well as in water at 360°C/18.6 MPa.

PWR Irradiation Program

First, as is classically the case, the materials have been irradiated as demo fuel rods in two European reactors operating with different fuel management strategies. Five annual cycles have been achieved in a German plant with a maximum fuel rod average burn up of 56 GWd/tU. In France, three 18-month cycles have been achieved with an estimated fuel assembly burn up of about 55 GWd/tU. A fourth cycle is currently on going. The main differences regarding irradiation conditions in these two plants is the maximum linear heat generation rate, which was higher during a certain duration in Germany compared to French

TABLE 1—*Nominal compositions of the studied alloys (in wt %).*

Alloy	Nb	Sn	Fe
M5™	1	< 100 ppm	0.035
Zr1Nb0.1Fe	1	< 100 ppm	0.1
Zr1Nb0.2Sn0.1Fe	1	0.2	0.1
Zr1Nb0.3Sn0.1Fe	1	0.3	0.1
Zr1Nb0.5Sn0.1Fe	1	0.5	0.1
Zr1Nb0.6Sn0.1Fe	1	0.6	0.1
Zr1Nb0.3Sn0.2Fe	1	0.3	0.2
Zr1Nb0.25Sn0.35Fe	1	0.25	0.35
Zr1Nb0.5Sn0.35Fe	1	0.5	0.35

irradiation. This means a higher neutron flux and metal temperature for the most demanding conditions.

On site visual inspections and measurements of oxide thicknesses, fuel rod lengths and diameters have been performed. On site oxide thicknesses are measured by Eddy Current. Rod lengths are deduced from the distances between nozzles and the lower and upper gaps, or can be obtained on extracted fuel rods by comparison with a standard. Fuel rod diameters are measured using linear voltage differential transformer transducers.

Fuel rods have been extracted after two and three cycles in France and after five cycles in Germany, and are or will be shipped to hot cells for characterizations.

Material test rods irradiations of many variants have also been launched in order to determine irradiation growth and corrosion behaviour. The test rods made of empty tubes are inserted in guide tubes of selected commercial fuel assemblies. Samples are located at axial positions where fast neutron fluence profile can be considered as almost constant. The specimens are designed in order to have a water flow inside and outside the test tubes thus avoiding a radial differential pressure over the samples. Second cycle assemblies are generally used to host the test rods during the irradiation program to achieve a rapid gain in fluence. The material behaviour of the test rods is followed-up by an annual evaluation of the length change by the measurement of the sample length with a depth gauge. A fluence of around $17E + 25\,\mathrm{n/m^2}$ has been reached in five cycles on Zr1Nb0.3Sn0.1Fe and M5™ (please note that fluences should be understood as fast fluences with $E > 1\,\mathrm{MeV}$).

Post-irradiation examinations in hot cells

Post-irradiation examinations (PIE) have been started and are still on going on 2-cycle fuel rods irradiated in the French power reactor. Non-destructive characterizations to measure length, diameter and oxide thickness show results in agreement with on site measurements (see below). Hydrogen content has been determined by hot vacuum extraction at the hottest span.

Hydrogen content has also been measured on a 0.5 % Sn tube segment (without fuel) that was placed as a free tube in a commercial plant.

Other destructive examinations, such as metallographies, mechanical tests, transmission electronic microscopy characterizations, are scheduled on the two-cycle fuel rods. Similar examinations will be performed after following cycles in the next years.

PIE of fuel rods irradiated five cycles in the German reactor are scheduled to start at the end of 2010.

Out-of-Pile Characterization Results

Microstructure

The microstructure of the cladding and guide tubes appears fully recrystallized as shown in Fig. 1. The grains are equiaxed, and their size does not depend on

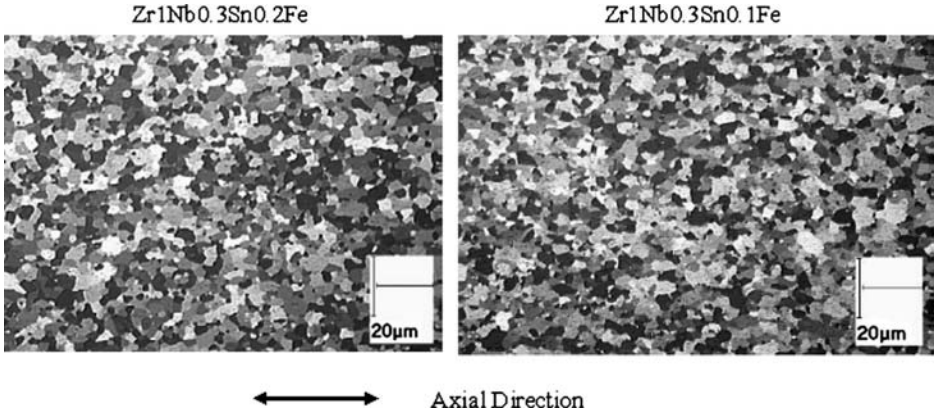


FIG. 1—*Optical micrographies on Zr1Nb0.3Sn0.1Fe and Zr1Nb0.3Sn0.2Fe tubes (polarised light).*

the alloy composition. The SPP appear homogeneously distributed. These results are confirmed by the TEM examinations (Fig. 2).

The nature and composition of the SPP was obtained by combining exams on thin foils (Fig. 2) and on extractive replicas with EDX. They are summarised in Table 2. The observed phases are the body centered cubic βNb, containing roughly 90 % Nb, the hexagonal C14 Laves phase $Zr(Nb,Fe)_2$, and for the highest iron content (0.35 %) some FCC $(Zr,Nb)_4Fe_2$ phase.

The SPP observed in TEM are those expected from the ternary Zr-Nb-Fe diagram [1] and computed at a temperature close to 600°C by THERMOCALC™ and the ZIRCOBASE (Table 2). It means that the equilibrium is reached on

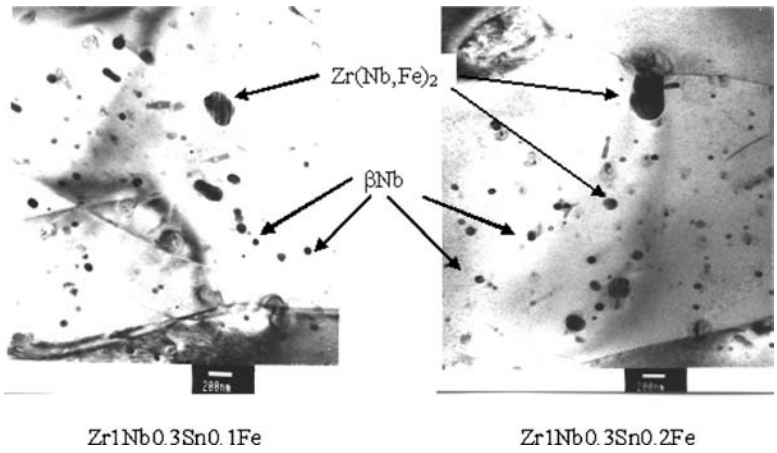


FIG. 2—*TEM examination—some Zr(Nb,Fe)2 and βNb are identified*

TABLE 2—*Nature and composition of the SPP. Comparison with thermodynamic computations (see text). The phase composition is given in at. %, while the alloy composition is given in wt % or ppm.*

	Computation				TEM + EDX		
Alloy	Phase Name and Molar Fraction	Zr	Fe	Nb	Zr	Fe	Nb
M5™	βNb 0.49 %	6.03	221 ppm	93.94	13	…	87
	$Zr(Nb,Fe)_2$ 0.22 %	40.72	26.08	33.2	37	26	37
Zr1Nb0.1Fe	$Zr(Nb,Fe)_2$ 0.62 %	40.7	26.1	33.2	37	26	37
	βNb 0.35 %	6.03	221 ppm	93.94	13	…	87
Zr1Nb0.5Sn0.35Fe	$Zr(Nb,Fe)_2$ 2.03 %	40.3	27.97	31.8	34.7	27.6	37.3
Zr1Nb0.25Sn0.35Fe	$Zr(Nb,Fe)_2$ 2.0 %	40.2	28.2	31.5	34.9	26.4	37.9
	$(Zr,Nb)_4Fe_2$				58.7	8.5	32.8
Zr1Nb0.5Sn0.1Fe	$Zr(Nb,Fe)_2$ 0.62 %	40.7	26.2	33.2	34.9	26.6	36.9
	βNb 0.40 %	5.9	221 ppm	94	12.1	1.1	86.4
Zr1Nb0.3Sn0.1Fe	$Zr(Nb,Fe)_2$ 0.62 %	40.7	26.1	33.2	35	26.3	37.2
	βNb 0.38 %	6	221 ppm	94	11.9	1.9	85.9
Zr1Nb0.3Sn0.2Fe	$Zr(Nb,Fe)_2$ 1.24 %	40.7	26.1	33.2	34.9	28.2	35.8
	βNb 0.16 %	6	221 ppm	94	11.3	1.4	86.6

these claddings. Some slight discrepancies are visible between the computed and measured compositions, mainly concerning the βNb phase which is computed slightly too rich in niobium. Despite some minor areas of needed improvement, ZIRCOBASE is already a powerful tool to predict and to adapt the manufacturing route in relation to the material and desired microstructure. In the present work, it is also observed that the tin content (in the investigated range) has no effect on the phase existence and stability. Increasing the iron content up to 0.1 and 0.35 %, respectively, leads to lower the Nb content in solid solution in αZr (computed values), and to the formation of LAVES phases and eventually $(Zr,Nb)_4Fe_2$ phase.

Texture

The texture was systematically measured at the mid thickness of the cladding. The (0002) and $(10\bar{1}0)$ pole figures of Zr1Nb0.2Sn0.1Fe are presented in Fig. 3, while the Kearns factors are given in Table 3. The (0002) pole figure shows two poles in the (radial, tangential) plane, orientated at about 30° from the radial direction. The $(10\bar{1}0)$ pole figure exhibits poles at about 20° from the axial directions. These features are representative of a recrystallized state, annealed at low temperature: The recrystallization is completed, while the grains could not grow significantly [2,3]. The pole figures for the other alloys are very similar.

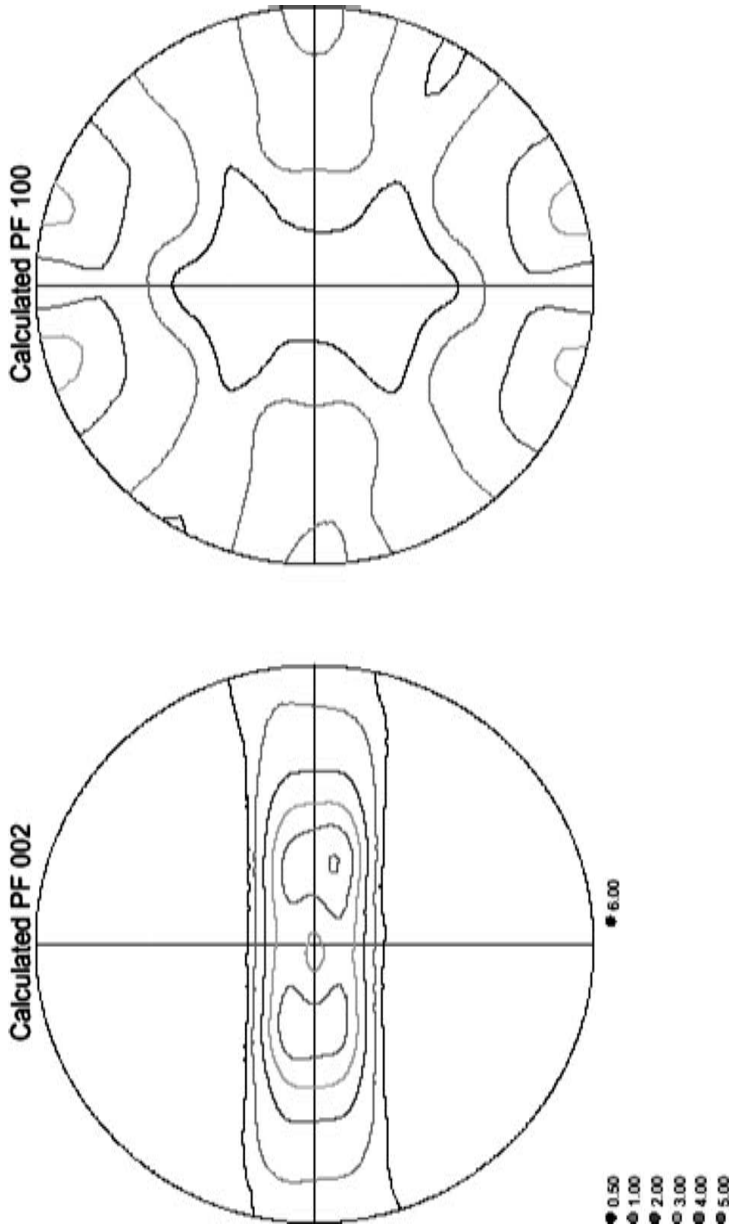


FIG. 3—*Pole figures for the Zr1Nb0.2Sn0.1Fe alloy.*

TABLE 3—*Kearns factors obtained at mid thickness.*

Mark	fN	fL	fT
Zr1Nb0.5Sn0.1Fe	0.617	0.07	0.313
Zr1Nb0.5Sn0.35Fe	0.595	0.078	0.327
Zr1Nb0.2Sn0.1Fe	0.625	0.069	0.306
Zr1Nb0.1Fe	0.594	0.087	0.319

The Kearns factors confirm the texture description given above, and stay within the measurement scattering without influence of the alloying elements.

Mechanical Properties and Creep

Tensile properties have been investigated at room temperature, at 315°C and at 400°C. The tin and iron contents do not significantly impact the yield and ultimate tensile strengths nor the elongation. Figure 4 is an example for tests performed at room temperature.

Creep tests have been performed at 400°C with internal pressure (hoop stresses of 130 MPa and 160 MPa). Results (Fig. 5) show that the tin content decreases the creep rate, with a gain on creep strain after 240h at 130 MPa of around 45 % for the tin content of 0.5 % and of about 10 % for the alloys with 0.3 % of tin compared to the reference material M5™. Results (Fig. 5) also indicate that the iron content slightly degrades the thermal creep strength. It is thought that this last effect is due to the slight reduction of the niobium content in solid solution when the iron level is raised. A saturation of the beneficial impact of tin can be deduced from Fig. 5: The lower the stress level, the lower is the Sn content for saturation.

Corrosion behaviour

Corrosion tests were performed in steam at 415°C/10.5 MPa as well as in water at 360°C/18.6 MPa.

At 415°C in steam, the kinetics first shows a parabolic behaviour (Fig. 6), and then a transition at about 50 days/4 μm toward a more or less linear kinetics. The tin content is detrimental, almost linearly (Fig. 7), while the iron has almost no effect (slightly beneficial when iron is increased up to 1000 ppm in M5™). In this kind of tests, the SRA Zircaloy-4 cladding used as reference has an intermediate behaviour (Fig. 6).

In this environment, the hydrogen pick-up increases with the tin content (Fig. 8), due to the higher oxidation rate, and classical and high Hydrogen Pick-Up Fractions (HPUF) are obtained (between 30 and 40 %).

In high temperature water (360°C), the oxidation kinetics appears linear after 200 days of exposure (Fig. 9). The presence of 0.3 % of tin has no impact on oxidation resistance compared to the reference (M5™), while 0.5 % of tin is significantly worse. The iron has no significant effect on oxidation (Fig. 10).

The evolution of measured hydrogen content versus oxide thickness is illustrated in Fig. 11. Figure 12 shows the HPUF for the different materials. The

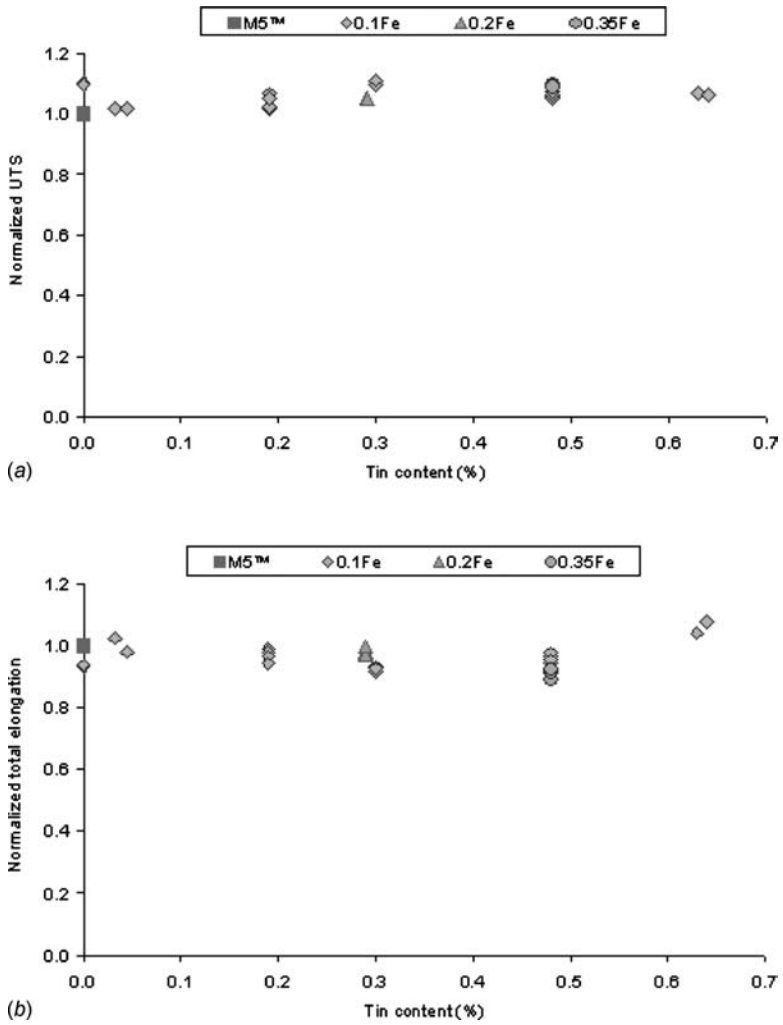


FIG. 4—*Tensile properties at RT as a function of the tin content—(a) UTS; (b) total elongation—Normalization to M5™.*

values range between 13 and 19 %. In this corrosion condition, tin has a detrimental impact whereas iron slightly improves the resistance to hydrogen pick-up. It is interesting to note that the HPUF for M5™ in this out-of-pile environment is slightly higher than values obtained from the large irradiation database from commercial plants, which is about 10 % [4]. We will discuss later the comparison between out-of-pile and in-pile condition, but this is noticeable that the hydrogen pick-up of M5™ in an irradiation environment is even lower than in an autoclave environment.

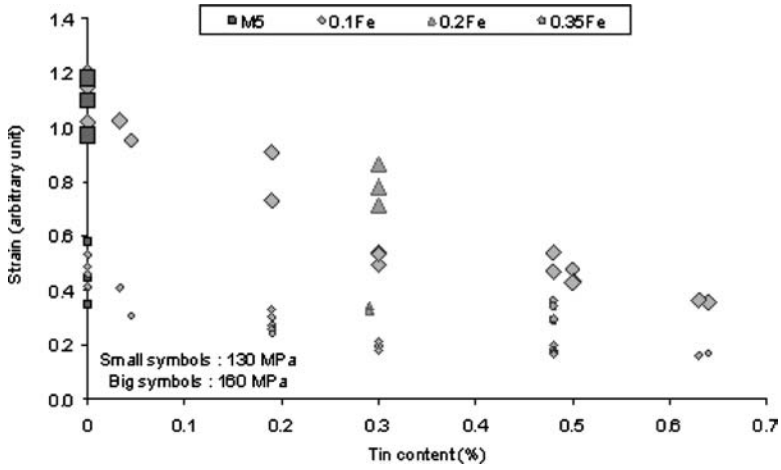


FIG. 5—*Biaxial creep results (internal pressure, 130 or 160 MPa, 240 h, 400°C)-Strain versus tin content.*

In Pile Results and Discussion

Free Growth on Material Test Rods

Stress free Zr1Nb0.3Sn0.1Fe and M5™ have been simultaneously irradiated through five cycles in a PWR. A maximum fluence of around $17E + 25\,\mathrm{n/m^2}$ has been reached.

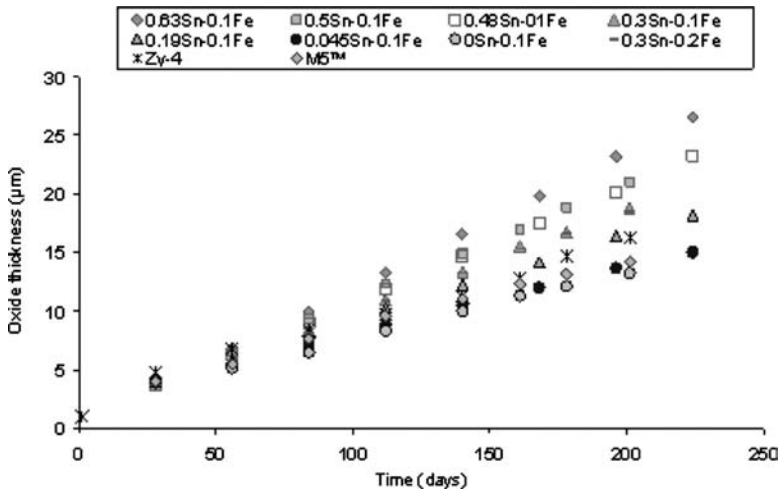


FIG. 6—*Corrosion kinetics in steam at 415°C.*

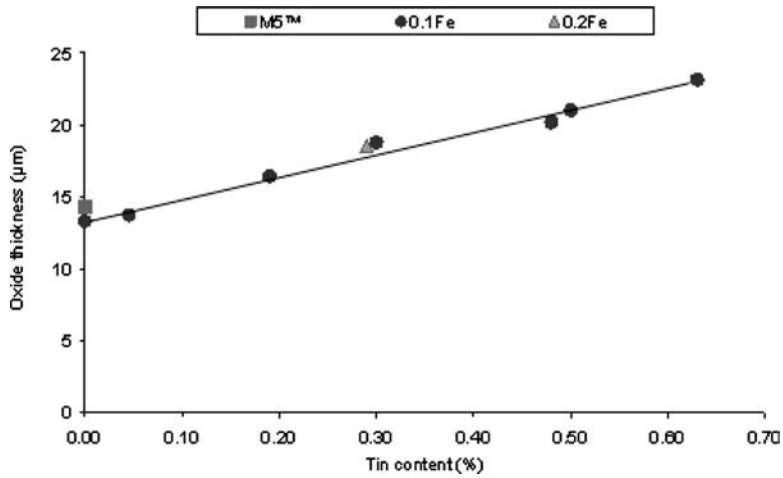


FIG. 7—*Oxide thickness versus tin content for corrosion tests in steam at 415°C after ~200 days.*

Elongations of the tubes are shown in Fig. 13. Previous results on M5™ from a similar experiment in another PWR are also included [5] and show good agreement between the two experiments. Low free growth elongation is measured on the Zr1Nb0.3Sn0.1Fe alloy, with very similar elongations to M5™ until a fluence of $14E + 25\,\mathrm{n/m^2}$. At higher fluences, elongations on the Zr1Nb0.3Sn0.1Fe alloy are a bit lower than those measured on M5™.

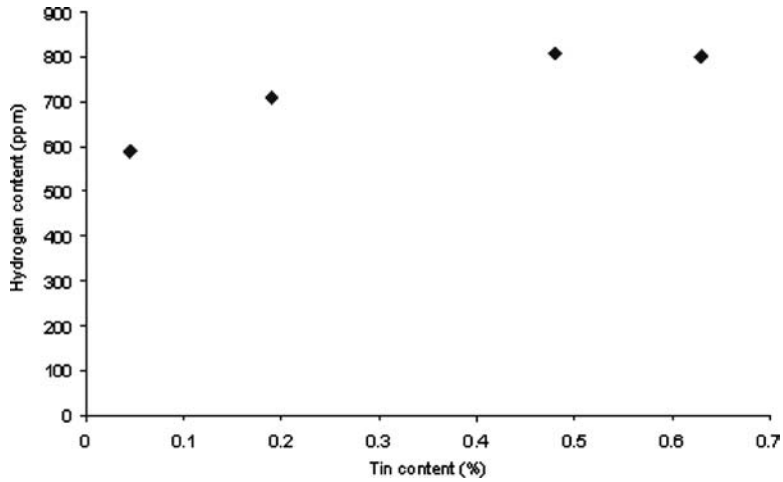


FIG. 8—*Hydrogen content versus tin content for corrosion tests in steam at 415°C after ~200 days on Zr1NbxSn0.1Fe.*

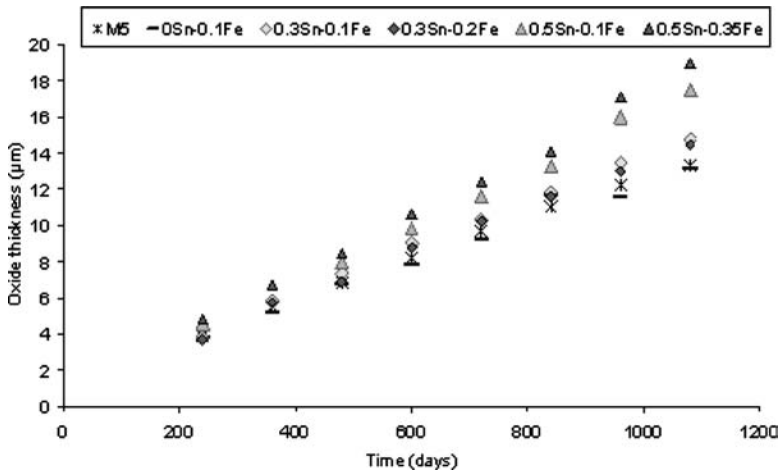


FIG. 9—*Corrosion kinetics in water at 360°C.*

Following the CASTA DIVA™ methodology described in Ref [6], the total elongation results from neutron irradiation-induced growth, hydride induced deformation and oxide induced strain. It is shown later on that the oxide thickness and hydrogen content do not vary significantly from the M5™ to the Zr1Nb0.3Sn0.1Fe. The neutron irradiation growth is likely not affected by the tin content for this quaternary alloy. Thus, the slight reduction observed on the Zr1Nb0.3Sn0.1Fe could be due to the lower creep induced by the oxide stresses.

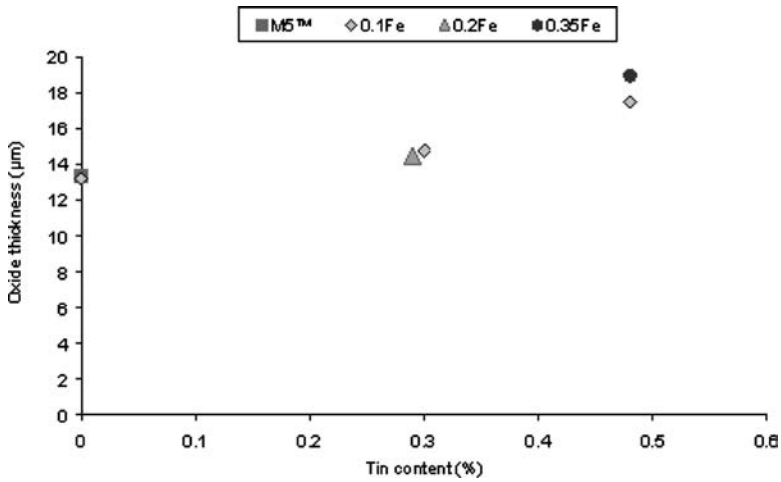


FIG. 10—*Oxide thickness versus tin content for corrosion tests in water at 360°C after 1080 days.*

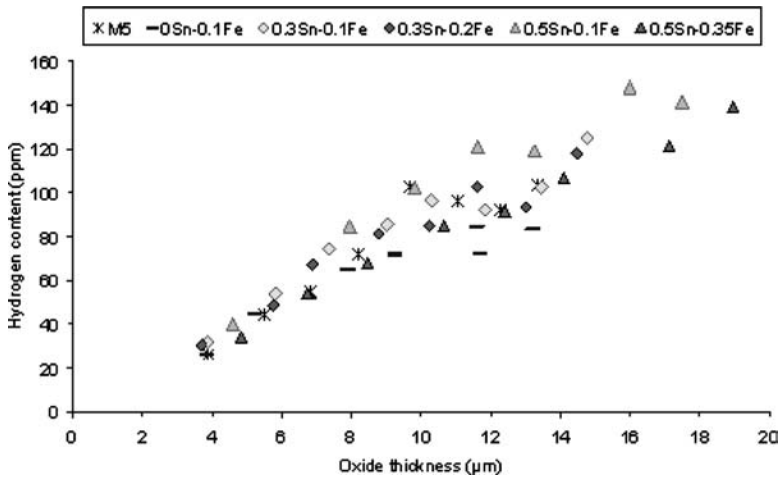


FIG. 11—*Hydrogen content versus oxide thickness for corrosion tests in water at 360°C.*

Fuel Rod Diameter Change

Fuel rod diameters have been measured following one to five cycles in a German PWR and after two cycles in a French PWR. The cladding creep resistance is improved when tin content increases (Fig. 14). If we take into account diametral changes not affected by the pellet-cladding contact, there is a diametral strain decrease of about 40 % for the highest tin content, compared to the reference M5™ (no tin), and of about 20 % for the 0.3 % Sn materials. The gain in irradiation diametral creep strength appears similar to what is measured in the standard thermal creep test (400°C – 130 MPa – 10 days). Nevertheless, no transfer

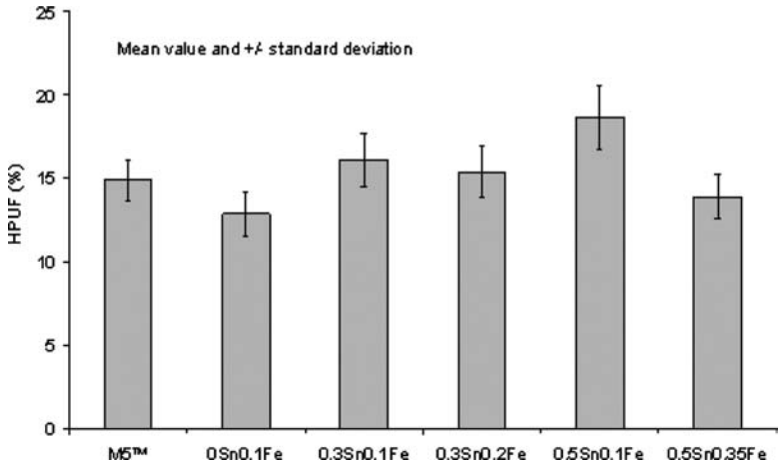


FIG. 12—*HPUF versus tin and iron content for corrosion tests in water at 360°C.*

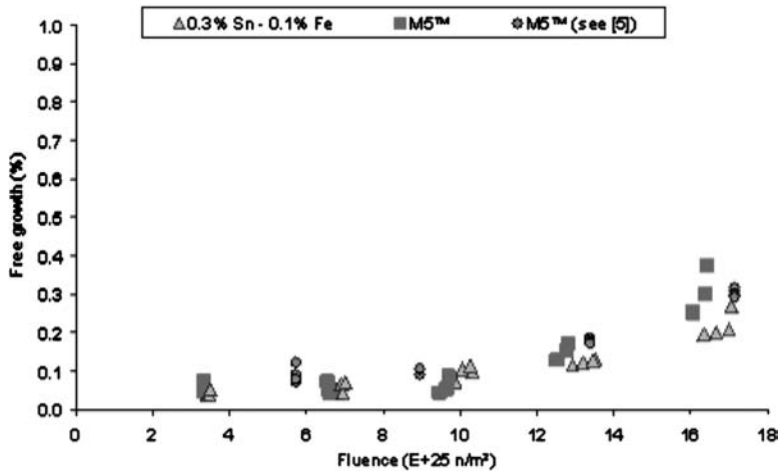


FIG. 13—*Tubes elongations by free growth.*

function based on physical mechanisms to calculate irradiation creep from thermal creep kinetics can be deduced considering that the activated systems are different for thermal and irradiation creep.

Under irradiation, no significant effect of iron is observed, whereas a slight deterioration was measured in thermal creep tests.

Tin being in solid solution as a substitute for zirconium acts as a strengthening element [7]. As observed in Table 2, it does not change the SPP nature or composition. It could decrease the secondary creep rate either by straining the zirconium lattice around the substitutional atoms and thus increasing the stress

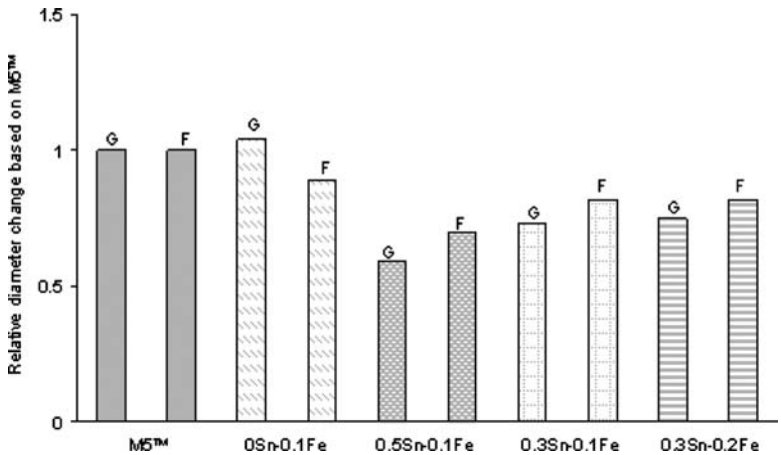


FIG. 14—*Fuel rod diameter changes before pellet-cladding contact (F: French PWR, G: German PWR).*

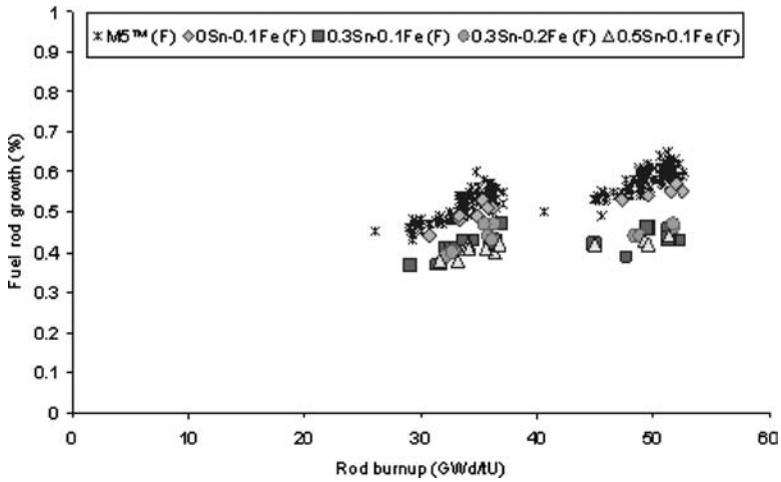


FIG. 15—*Fuel rod length versus burn up (French PWR).*

needed to move the dislocation, or by facilitating the dislocations dissociation [8]. The tin impact could also be related to a modification of the irradiation-induced defect structure or to the formation of very fine precipitates [9].

Fuel Rod Length Change

Fuel rod lengths have been measured following one to five cycles in a German PWR and following two and three cycles in a French PWR. The fuel rod length results are presented in Figs. 15 and 16. The addition of tin induces a reduction in the fuel rod length change, but there is no significant impact of iron content.

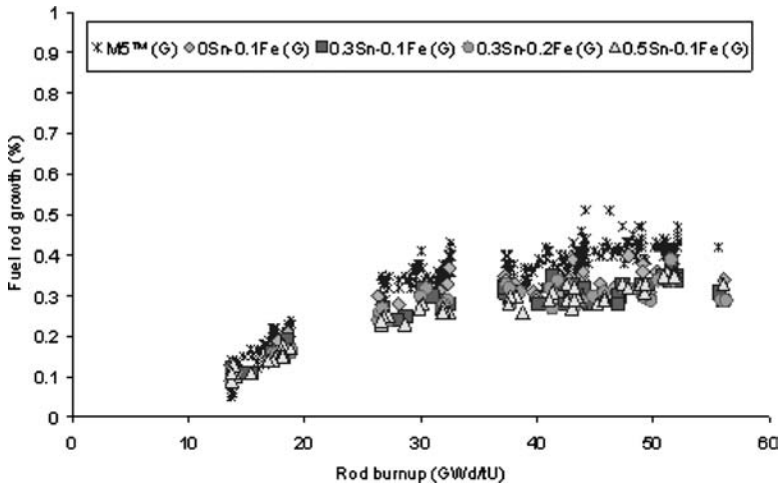


FIG. 16—*Fuel rod length versus burn up (German PWR).*

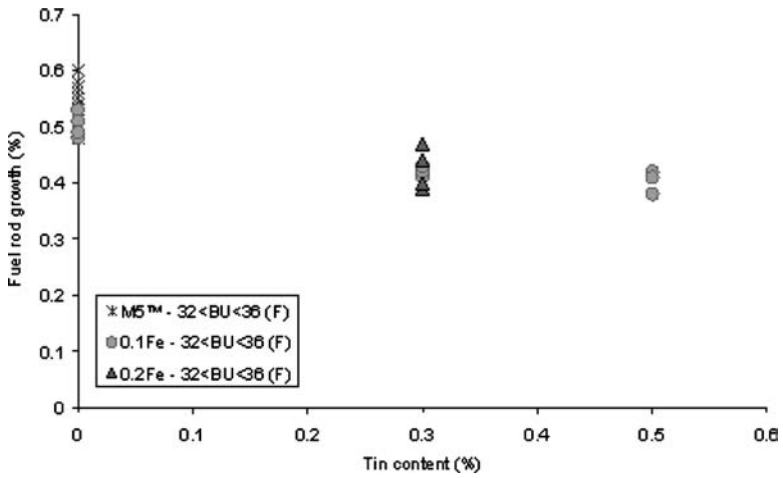


FIG. 17—*Fuel rod length between 32–36 GWd/tU versus tin content (French PWR).*

The axial fuel rod length changes are mainly the consequence of axial irradiation growth and diametral creep resultant deformation, which means that the cladding wall thickness and the internal pressure of the fuel rod are first order parameters. This is the explanation for the observed differences in irradiation performance between the rods irradiated in France and in Germany.

No difference in fuel rod length changes are observed between 0.3 and 0.5 % of tin (Fig. 17), whereas irradiation creep results show an improvement versus the tin content. Since the texture is similar for both materials (Table 3) and as there is no significant impact of tin on axial growth contribution (Fig. 13) at the considered burn up, it is suggested that tin impacts the activated systems and changes the anisotropy compared to reference material.

The effect of iron on fuel rod length changes appears negligible on both Zr1Nb and Zr1NbxSnFe materials.

Corrosion Resistance

Oxidation Resistance—Oxide thicknesses have been measured after 2, 3, 4, and 5 cycles in a German PWR and after 2 and 3 cycles in a French PWR. The average oxide thicknesses measured in the hottest span are presented in Fig. 18 for the fuel rods irradiated in a French PWR and Fig. 19 for the fuel rods irradiated in a German PWR.

In the French power plant, the impact of tin on oxide thickness can be observed after the end of the third cycle: At the current achieved burn up of 55 GWd/tU, 0.3 % of tin is slightly detrimental compared to M5™, whereas an addition of 0.5 % of tin leads to a more significant increase of oxidation rate. No significant impact of iron is detected.

On the other hand, there is a strong degradation of the oxidation resistance of the 0.5 % tin containing material in the high duty German power plant. On

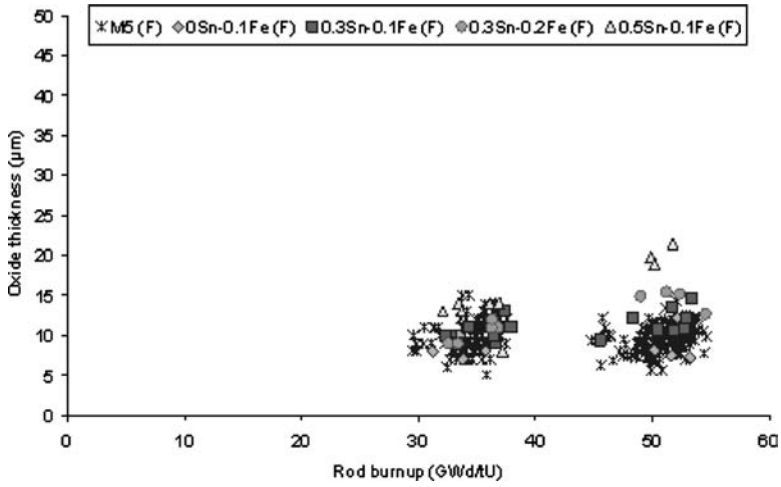


FIG. 18—*Oxide thickness versus burn up (French PWR). (a) Whole results; (b) zoom of (a).*

the Zr1Nb0.5Sn0.1Fe material, the oxide thickness reaches 90 μm at 55 GWd/tU while a maximum of around 30 μm is measured on the alloys with 0.3 % Sn. Figures 20 and 21 present the variation of the oxide thickness versus the axial location of the fuel rod for two different burns up. It seems that there is a breakaway for an oxide thickness close to 15–20 μm. It is interesting to note that this range of oxide thickness values also correspond to a slight oxidation increase for 0.3 % Sn material compared to the reference (M5™, see Fig. 19). A discussion about the origin of this breakaway is proposed later in this paper.

Regarding the iron impact, for both quaternary alloys with 0.3 % of tin and reference material (without Sn), an addition of iron is slightly beneficial for oxidation resistance. From a metallurgical point of view, the addition of Fe induces a decrease of Nb in solid solution and the formation of SPP Laves phases for both M5™ and quaternary alloys. It has been shown in the literature, for such Nb content, that the Nb decrease in solid solution is beneficial for the oxidation resistance [10].

The visual appearance of the material variants with tin addition varies from grey to white in the German plant, whereas M5™ is mostly grey and Zr1Nb0.1Fe is dark (Fig. 22). Variants with 0.3 % Sn show brighter appearance, and fuel rod cladding with 0.5 % Sn is white. Considering that the oxide thicknesses of M5™ and 0.3 % Sn are similar, the colors contrast likely results from the difference of alloying elements.

Discussion About 0.5 % Sn Material Oxidation Breakaway—The occurrence of an acceleration of the oxidation rate for Zr1Nb0.5Sn0.1Fe material at an oxide thickness of about 20 μm is in good agreement with the literature. For other quaternary alloys containing Sn contents of 0.7 and 1 % [11], there is a

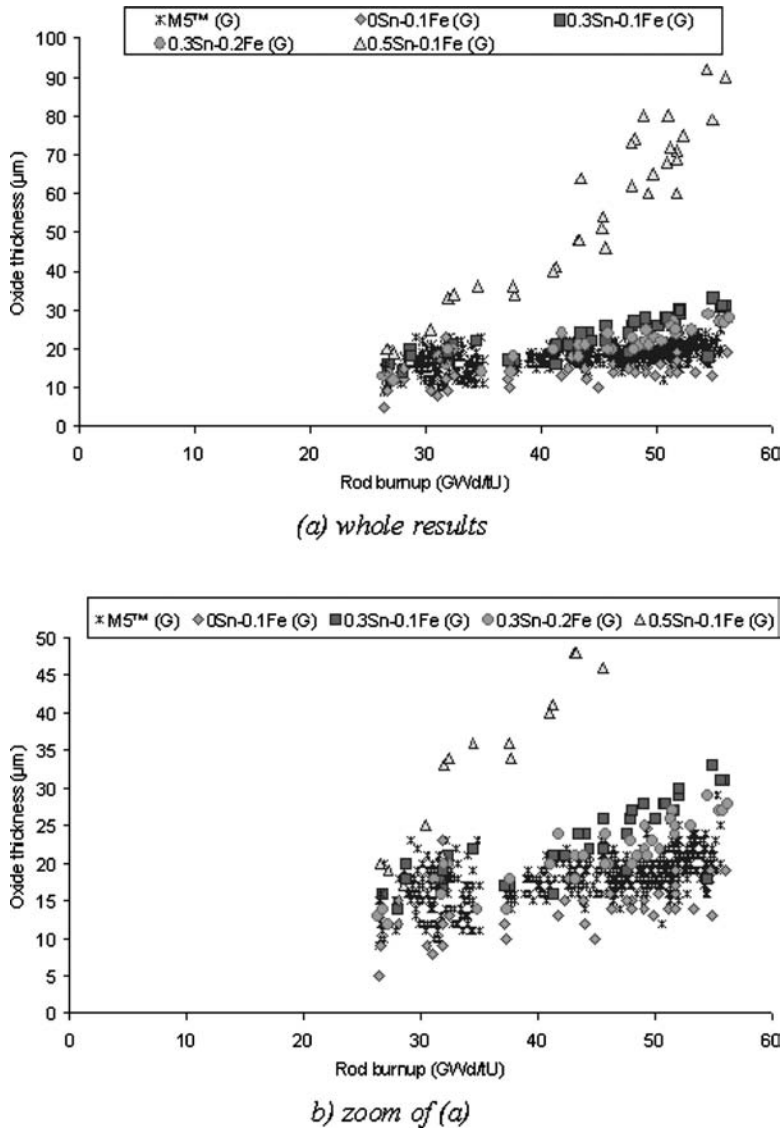


FIG. 19—*Oxide thickness versus burn up (German PWR).*

detectable increase of the oxidation rate which seems to depend on the irradiation conditions (different plants). For the two irradiation conditions discussed in the present paper, the main differences are the linear heat generation rates during the two first cycles, higher in the German plant compared to the French one. As a consequence, the metal/oxide interface temperature was a bit higher in the German plant compared to the French one. This can explain why the

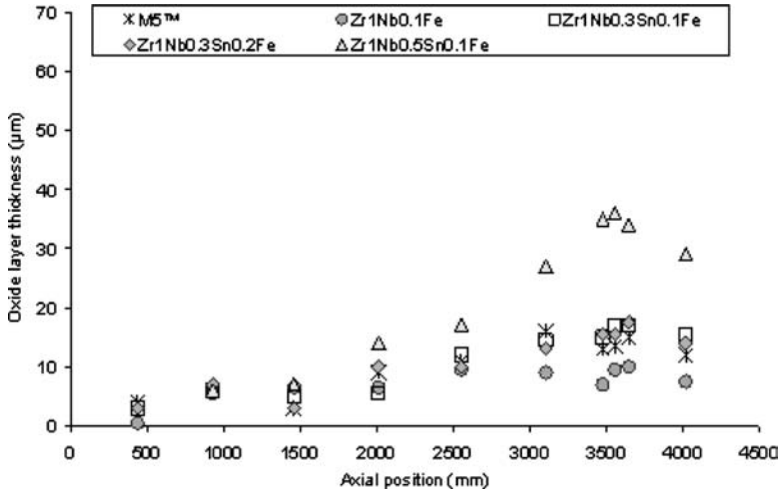


FIG. 20—*Oxide thickness versus axial position for burn up of about 37 GWd/tU (German PWR).*

"critical" oxide layer, if any, and then, the breakaway is reached for a lower burn up in this more demanding irradiation condition. Nevertheless, it is indisputable that the breakaway is not only related to a critical oxide thickness. The out-of-pile results presented in the previous part of this paper show that there is no significant modification of the oxidation rate for zirconia film after about 15–20 μm of film growth for a tin content of 0.5 %. It is highly probable that the

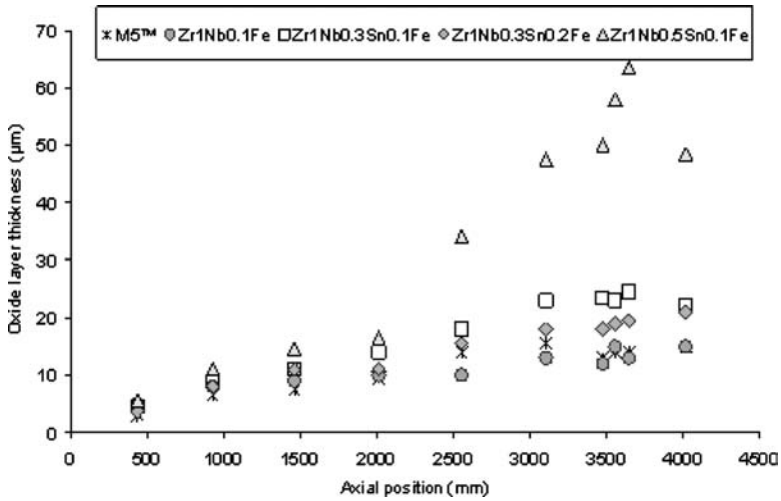


FIG. 21—*Oxide thickness versus axial position for burn up of about 44 GWd/tU (German PWR).*

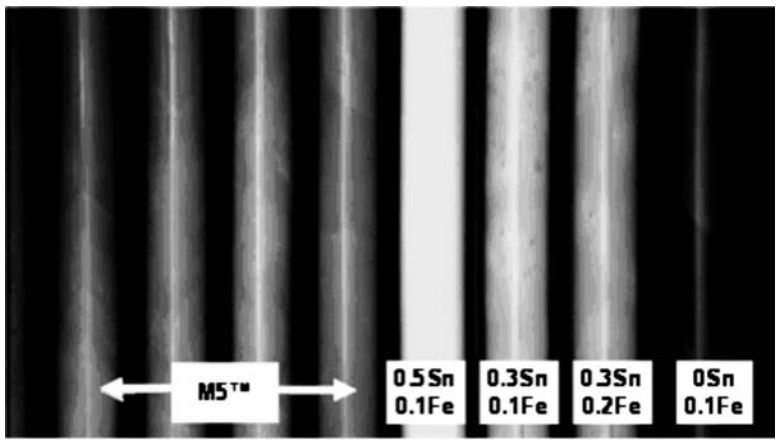


FIG. 22—*Visual appearance of the fuel rods irradiated five cycles in a German PWR.*

microstructural evolutions under irradiation are also involved in the oxidation breakaway mechanism.

Further Hot Cell Examinations (HCE) planned on extracted fuel rods from 2 to 5 cycles (in both plants) and on material test rods will give information to discuss this point taking into account what has been proposed to explain breakaway and accelerated corrosion, named "phase III," for Zircaloy-4.

On a metallurgical point of view, the main hypotheses under consideration to explain the onset of the corrosion acceleration are discussed in detail in the literature [12–16]. They are the following:

- Hydrides precipitation and accumulation at the metal oxide interface. Future metallographic examinations will look for evidence of this.
- Dissolution of the SPP (with the Fe depletion of the SPP and subsequently Fe enrichment in the Zr matrix): TEM investigations will be carried out to investigate the stability of the SPP and potential presence of Fe surrounding the SPP.
- Impact of tin content on the oxidation breakaway: In the literature [13], it is mentioned, for Zircaloy type alloys and in PWR environment that the oxide growth dependence is exponential with the Sn content, with a pre-exponential factor, which is first constant from 0 to 1.25 %, and then growing from 1.25 to 1.7 %. There is no direct comparison to Zircaloy-4 in the German plant in which this test was run since Zircaloy-4 was removed from this plant 15 years ago because it no longer met the corrosion requirements. Nevertheless, Fig. 23, showing the evolution of oxide thickness in a given burnup range versus the tin content of the considered alloy, indicates that the onset of the oxidation breakaway is between 0.3 and 0.5 % of tin. Thus, in the Zr1NbSnFe system, the critical Sn content for the degradation of the corrosion resistance is different and lower compared to Zircaloy type alloys. The

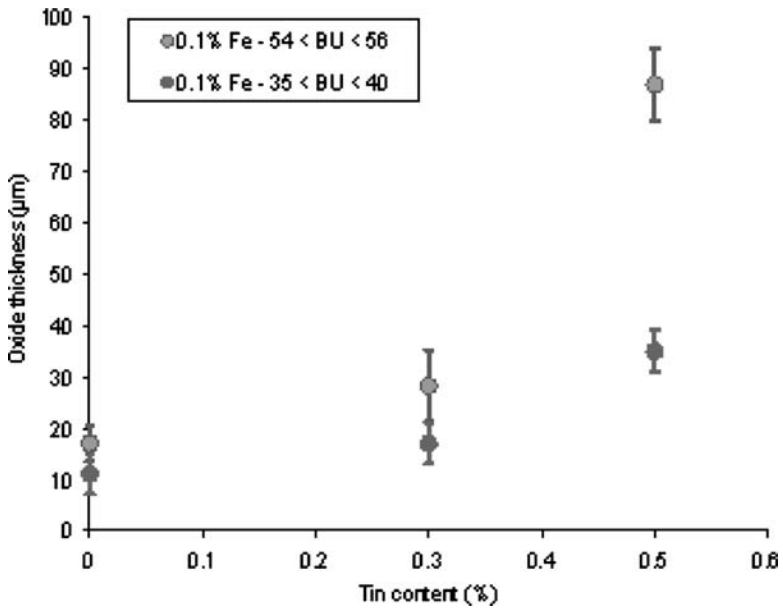


FIG. 23—*Impact of tin on oxide thickness (German plant).*

present work cannot fully explain the origin of this result but obviously the simultaneous presence of Nb and Sn in solid solution increases the sensitivity of the breakaway compared to Zircaloy-4, even if the oxidation resistance is significantly improved compared to this latter alloy. Again, future TEM investigations will give interesting information regarding the tin redistribution in the oxide layers as it was highlighted in Iltis et al. [14].

- Tetragonal zirconia at the metal oxide interface: Though regarded for several years as a promising parameter to explain the corrosion behaviour on zirconium alloys, it was shown that niobium-containing alloys exhibit lower tetragonal fraction at the interface than Zircaloys, despite their better corrosion resistance [15,16].
- Li impact: As the Li concentrations in the two plants are similar and correspond to very classical and low values compared to modified chemistry, the Li impact is judged very unlikely to explain the breakaway.

The comparison between out-of-pile corrosion tests and in-pile results leads to the classical conclusion that the out-of-pile results can only give partial information and identify materials that have low intrinsic corrosion resistance. Representative environment including irradiation is a prerequisite to assess the corrosion resistance of Zirconium alloys in a nuclear environment.

The irradiation feedback obtained in two PWRs with different fuel management shows that there is a degradation of the oxidation resistance for tin content between 0.3 and 0.5 %. In the high duty plant, the breakaway for the 0.5 %

Sn alloy used as a cladding material leads to a very high oxidation rate and the oxide thickness at a burn up of 55 GWd/tU is very close to the 100 μm criterion. Only a reduction in the linear heat generation rate in the last cycles could prevent exceeding this criterion.

Hydrogen Pick Up—Hydrogen content has been measured by hot extraction on fuel rod cladding tubes with 0.3 % Sn irradiated 2 cycles in a French PWR($\sim$36 GWd/tU). Average values of 68 ppm and 84 ppm respectively, have been obtained on the alloys with 0.1 % Fe and 0.2 % Fe. The hydrogen pick-up fraction is low, around 10–12 %, and close to that obtained for M5™. These first results on low tin material (0.3 % Sn) are promising but no conclusion can be drawn before gathering the values for high burn up in both plants.

Hydrogen determination has also been performed on material test rods irradiated inside guide tubes. A first result has been acquired on the alloy with 0.5 % Sn irradiated 5 cycles, at an equivalent burn up of 90 GWd/tU. A hydrogen content of around 230 ppm has been measured, which corresponds to a HPUF of around 20 %.

These first results seem to show that tin has no impact on hydrogen pick-up up to 0.3 %, and then degradation for higher values is observed.

There are few data available in the open literature on hydrogen pick-up for quaternary alloys. Very recent publication [17] for supposed 1 % tin material show very scattered values, between 8 and 40 % for the HPUF. In [17], the high HPUF values are assumed to be due to abnormal fuel management and handling damage to the waterside oxide layer. Nevertheless, the scatter remains quite high and it is not possible at the time to conclude about a potential degradation of the hydrogen pick-up resistance for tin contents higher than 0.5 %.

Conclusion

Ultra low tin quaternary alloys Zr1NbSnFe show improved diametral irradiation creep resistance correlated with the addition of tin. In addition, irradiation free growth results indicated no significant impact of tin, with a low free growth elongation on the Zr1Nb0.3Sn0.1Fe alloy similar to M5™. No significant impact of iron on dimensional stability is observed.

On the other hand, the addition of tin higher than 0.3 % induces a degradation of the oxidation resistance, strongly dependant of the irradiation conditions. For a tin content of 0.5 %, an important degradation of the oxidation behavior is observed on fuel rods irradiated in high duty conditions, with a breakaway that occurs at a low burn up of 25 GWd/tU and at an oxide thickness of around 20 μm. However, a material test sample made of Zr1Nb0.5Sn0.1Fe with a burnup of 90 GWd/tU did not show enhanced corrosion compared to the reference alloy. Therefore, for application as structural components Zr1NbSn0.1Fe alloys with 0.5 % Sn are a suitable option due to their higher creep resistance.

First results on hydrogen content also indicate a low hydrogen pick-up for alloys containing 0.3 % tin (HPUF around 10–12 %) but almost twice that was

measured on the 0.5 % tin material, although not irradiated under the same conditions. Final conclusion will be drawn when the values for high burn up and both plants will be available.

Further hot cell examinations on extracted fuel rods from two to five cycles and on material test rods are planned and will give information to discuss the mechanisms involved in the dimensional stability improvement and corrosion degradation due to tin addition.

Acknowledgments

AREVA is grateful to EnBW, Electricité De France and Kernkraftwerk Gösgen-Däniken for the irradiation of these materials. The authors would also like to acknowledge the effort of personnel at CEA for HCE.

References

[1] Barberis, P., Charquet, D., and Rebeyrolle, V., "Ternary Zr-Nb-Fe(O) System: Phase Diagram at 853K and Corrosion Behaviour in the Domain Nb<0.8%," *J. Nucl. Mater.*, Vol. 326, 2004, pp. 163–174.

[2] Bozzolo, N., Dewobroto, N., Grosdidier, T., Barberis, P., and Wagner, F., "Grain Growth Texture Evolution in Zirconium Zr702 and Commercially Pure Titanium T40," *Mater. Sci. Forum*, Vol. 467–470, No. 1, 2004, pp. 441–446.

[3] Dewobroto, N., Bozzolo, N., Barberis, P., and Wagner, F., "Experimental Investigations of Recrystallization Texture Development in Zirconium (Zr702)," *Mater. Sci. Forum*, Vols. 467–470, 2004, pp. 453–458.

[4] Kaczorowski, D., Chabretou, V., Thomazet, J., Hoffmann, P. B., Sell, H. J., and Garner, G., "Corrosion Behaviour of M5™: Experience Feedback and Understanding of Phenomenological Aspects," *Water Reactor Fuel Performance Meeting*, Seoul, Korea, October 19–23, 2008, Paper ID 8102.

[5] Bossis, P., Verhaeghe, B., Doriot, S., Gilbon, D., Chabretou, V., Dalmais, A., Mardon, J. P., Blat, M., and Miquet, A., "In PWR Comprehensive Study of High Burn-Up Corrosion and Growth Behavior of M5® and Recrystallized Low-Tin Zircaloy-4," *J. ASTM Int.*, Vol. 6(2), 2009, paper ID JAI101314.

[6] Barberis, P., Rebeyrolle, V., Vermoyal, J. J., Chabretou, V., and Vassault, J. P., "CASTA DIVA®: Experiments and Modelling of Oxide-Induced deformation in Nuclear Components," *J. ASTM Int.*, Vol. 5(5), 2009, paper ID JAI101124.

[7] Luton, M. J. and Jonas, J. J., "Solute Strengthening at High Temperatures in Zirconium-Tin alloys," *Can. Metall. Q.*, Vol. 11, 1972, pp. 79–90.

[8] Griffiths, M., "Microstructure Evolution in HCP Metals During Irradiation," *Philos. Mag. A*, Vol. 63, 1991, pp. 835–847.

[9] Garzarolli, F., Stehle, S., and Steinberg, E., "Behavior and Properties of Zircaloys in Power Reactors: A Short Review of Pertinent Aspects in LWR Fuel," *Zirconium in the Nuclear Industry: 11th International Symposium, ASTM STP 1295*, E.R. Bradley and G.P. Sabol, Eds., Garmisch-Partenkirchen, Germany, September 11–14, 1995, ASTM International, West Conshohocken, PA, pp. 12–32.

[10] Jeong, Y. H., Kim, H. G., and Kim, T. H., "Effect of Beta Phase, Precipitate and Nb-Concentration in Matrix on Corrosion and Oxide Characteristics of Zr-xNb Alloys," *J. Nucl. Mater.*, Vol. 317, 2003, pp. 1–12.

[11] Chapin, D., Wikmark, G., Maury, C., Therache, B., Claeys, M., Gutierrez, M. Q., and Ruiz, C. M., "Optimized-Zirlo Qualification Program for EDF Reactors," *Water Reactor Fuel Performance Meeting—Top Fuel*, Paris, France, September 6–10, 2009, SFEN, France.

[12] Bossis, P., Pecheur, D., Hanifi, K., Thomazet, J., and Blat, M., "Comparison of the high burn-up corrosion on M5 and low tin Zircaloy-4," *J. ASTM Int.*, Vol. 3(1), 2006, paper ID JAI12404.

[13] Garzarolli, F., Broy, Y., and Busch, R. A., "Comparison of the Long-Time Corrosion Behavior of Certain Zr Alloys in PWR, BWR and Laboratory Tests," *Zirconium in the Nuclear Industry: 11th International Symposium, ASTM STP 1295*, E.R. Bradley and G.P. Sabol, Eds., Garmisch-Partenkirchen, Germany, September 11–14, 1995, ASTM International, West Conshohocken, PA, pp. 850–864.

[14] Iltis, X., Lefebvre, F., and Lemaignan, C. "Microstructure Evolutions and Iron Redistribution in Zircaloy Oxide Layers: Comparative Effects of Neutron Irradiation Flux and Irradiation Damages," *Zirconium in the Nuclear Industry: 11th International Symposium, ASTM STP 1295*, E.R. Bradley and G.P. Sabol Eds., Garmisch-Partenkirchen, Germany, September 11–14, 1995, ASTM International, West Conshohocken, PA, pp. 242–264.

[15] Lin, J., Li, H., Szpunar, J. A., Bordoni, R., Olmedo, A. M., Villegas, M., and Maroto, A. J. G., "Analysis of Zirconium Oxide Formed During Oxidation at 623 K on Zr-2.5Nb and Zircaloy-4," *Mater. Sci. Eng., A*, Vol. 381, 2004, pp. 104–112.

[16] Petigny, N., Barberis, P., Lemaignan, C., Valot, C., and Lallemant, M., "In situ XRD Analysis of the Oxide Layers Formed by Oxidation at 743 K on Zircaloy 4 and Zr-1NbO," *J. Nucl. Mater.*, Vol. 280(3), 2000, pp. 318–330.

[17] Garde, A. M., Slagle, W. H., and Mitchell, D., "Hydrogen Pick-up Farction for Zirlo™ Cladding Corrosion and Resulting Impact on the Cladding Integrity," *Water Reactor Fuel Performance Meeting—Top Fuel 2009*, Paris, France, September 6–10, 2009, SFEN, France.

DISCUSSION

Question 1, Suresh K. Yagnik, EPRI:—The corrosion performance of the 0.5 Sn material was better inside the guide tube (no heat flux condition) compared to the fuel rod behavior. Is it due to heat flux effect?

Author's Response:—The better behaviour of the 0.5% Sn empty test sample irradiated inside a guide tube is attributed to the lower temperature of this test sample compared to the temperatures that are reached in the tubes irradiated as fuel rods. This is in agreement with the higher corrosion kinetics of the 0.5% Sn irradiated as fuel rods in the German plant correlated to the higher linear heat generation rates in this plant compared to the French ones.

Question 2, Vladimir Markelov, VNIINM:—1) What is the optimum content of Fe for this type of alloys in your opinion? 2) Did you have any problem with the manufacturing of the claddings from alloys with high Fe content?

Author's Response:—1) Concerning the composition impact on the product behaviour, this study shows that the Fe content is a second order parameter, Sn content being the first one. Moreover, the product behaviour also depends strongly on the irradiation conditions. Thus it is difficult to define a sole optimum Fe content.

For 0.5% Sn and 0.1% Fe material, corrosion resistance of fuel rods could be very low in demanding conditions. It is thought that an increase of Fe content won't be sufficient to recover sufficient corrosion resistance.

For quaternary alloys with 0.3% Sn or reference material (0% Sn), this study shows that an increase of iron content slightly improves the corrosion resistance (gain <5 μm for a maximum of 30 μm of oxide at ~55G Wd/t for 0.2% Fe), and does not impact fuel rod length and fuel rod diameter changes. Thus contents up to 0.1% Fe seems a good compromise for those alloys.

2) For content up to 0.2% Fe, no difficulties were found and the same manufacturing route as for the reference material (M5™) has been applied. But, for the highest Fe content, some manufacturing difficulties could indeed appear. See paper from A. Gaillac, P. Barberis and C. Lemaignan in this symposium.

Question 3, Ken Yueh, EPRI:—1) Were the tubing materials of the 0.5% Sn and 0.3% Sn manufactured the same way? 2) On the side where higher corrosion is shown for the 0.5% Sn material irradiated in the German plant, were corrosion data of 0.3% Sn material irradiated in the same German LTA program?

Author's Response:—1) Yes, the same manufacturing route was applied for all those alloys. It is the industrial manufacturing route that is applied for the M5™ tubes.

2) Concerning fuel rods irradiation in the German program, the irradiation took place in the same plant. A total of 4 LTAs (each containing all the different alloys) have been introduced. Similar results have been obtained whatever the fuel assembly is. The presented chart corresponds to the measurements performed on the 4 fuel assemblies.

Question 4, Arthur Motta, Penn State University:—1) For the unirradiated corrosion testing, what was the corrosion kinetics of the different alloys? Did you observe any breakaway in the corrosion rate? Did you determine the value of n ($w=At^n$)? 2) Is the difference in color in oxidation of 0.5 Sn caused by Sn or is it caused by the specific microstructure and heat treatment of these alloys?

Author's Response:—1) In primary like water and at 360°C, the corrosion kinetics is first parabolic and then linear. Those tests have been performed up to 1320 days (results up to 1080 days were available for the symposium). The oxidation resistance of the 0.3% Sn material is similar to the reference material up to ~1000 days, and then deterioration is observed. A content of 0.5% Sn significantly decreases the corrosion resistance. Fe content has no significant impact on the corrosion kinetics behaviour. No breakaway has been observed.

The n exponent has not been determined.

2) All materials are manufactured the same way (pilgering passes, intermediate and final heat treatments), leading in particular to a fully recrystallised microstructure. The colors contrast likely results from the difference of alloying elements (see appearance of 0.3 Sn material compared to reference whereas similar oxide thickness around 20-30 μm are measured). It should also be noted that the 0.5 Sn material exhibits an oxide thickness near 100 μm. This high oxide thickness compared to the other material could also contribute to the contrast.

Reprinted from JAI, Vol. 8, No. 1
doi:10.1520/JAI102941
Available online at www.astm.org/JAI

G. P. Kobylyansky,[1] *A. E. Novoselov,*[1] *A. V. Obukhov,*[1] *Z. E. Ostrovsky,*[1] *V. N. Shishov,*[2] *M. M. Peregud,*[2] *and V. A. Markelov*[2]

Radiation Damage of E635 Alloy Under High Dose Irradiation in the VVER-1000 and BOR-60 Reactors

ABSTRACT: Alloy E635 is used as a material for some parts of the water-water energy reactor (VVER)-1000 fuel assemblies (FAs). The evolution of structural components and redistribution of the elementary composition that occurred between the solid solution and phase precipitates in the E635 alloy were analyzed. The correlation between these changes and the irradiation-induced deformation of FA parts was determined. The common features of the E635 alloy's irradiation damageability was established as a result of the irradiation of model samples in the test reactor BOR-60 and the operation of products in the VVER-1000 reactor. The peculiarities of E365 alloy's irradiation damageability under high dose irradiation were revealed. The Laves phase ($Zr(Nb,Fe)_2$) particles were found to be the main type of secondary phase precipitates observed in the E635 alloy products with completely or partially recrystallized structures. Under irradiation, iron released from this phase causes a transformation of its crystalline structure, i.e., it changes from hexagonal-close-packed into body-centered-cubic with an Fe-enriched β-Nb phase. The Fe content in the particles decreases as the dose rises. The above transformations are not observed on those FA areas where the damage dose is low. Some bigger (up to 0.50 μ) precipitates of the $(Z,Nb)_2Fe$ phase with face-centered-cubic lattices were found in the material structure. Irradiation up to high damage doses results also in the appearance of

Manuscript received December 30, 2009; accepted for publication November 22, 2010; published online January 2011.
[1] JSC "SSC RIAR", Dimitrovgrad, Ulyanovsk Region 433510, Russia.
[2] JSC "Bochvar Institute", Moscow 123060, Russia.

Cite as: Kobylyansky, G. P., Novoselov, A. E., Obukhov, A. V., Ostrovsky, Z. E., Shishov, V. N., Peregud, M. M. and Markelov, V. A., "Radiation Damage of E635 Alloy Under High Dose Irradiation in the VVER-1000 and BOR-60 Reactors," *J. ASTM Intl.*, Vol. 8, No. 1. doi:10.1520/JAI102941.

Copyright © 2011 by ASTM International, 100 Barr Harbor Drive, PO Box C700, West Conshohocken, PA 19428-2959.

secondary fine-dispersed (up to ~5 in size) irradiation-induced precipitates. Practically no niobium is observed in the matrix, while all tin is in the solid solution and the Fe fraction in the matrix rises as the fluence becomes higher. The generation and formation of ⟨c⟩-dislocations occur only near the β-Nb precipitates (former Laves phases); ⟨a⟩-dislocations in the form of dislocation loops 10 nm in size and black dots are observed over the whole volume of recrystallized grains. On the whole, the changes in the structural-phase state of the FA parts tested in the VVER-1000 reactor correspond to the ideas about irradiation-induced damage in E635 alloy gained in experiments on irradiation of model samples in the BOR-60 reactor.

KEYWORDS: zirconium alloy E635, irradiation-induced growth, microstructure, radiation damages and phase composition, VVER-1000, BOR-60

Introduction

The behavior of zirconium-based items in nuclear reactors is determined, to a great extent, by the processes occurring in materials under irradiation. That is why the results of an electron-microscopic examination of the structure of these materials irradiated either in the VVER-1000 reactor as fuel assembly (FA) components or in the BOR-60 reactor as samples are of great interest. Irradiation of the samples in the BOR-60 reactor allows an accelerated (within time reasonable for researches) simulation of processes occurring in the materials under irradiation in commercial power reactors. Subsequent post-irradiation examinations of these samples show both the state of the material after certain irradiation stages and the main tendencies in its evolution. The comparison of the examination results of one and the same material (alloy E635), both after its operation in the commercial reactor and irradiation in the BOR-60, allows a more comprehensive study of the fundamental aspects of radiation damageability and behavior of E635 depending on various factors. The E635 alloy was earlier irradiated as samples and experimental items in test reactors, and as pilot items in power water-cooled reactors [1–3]. At present, it is successfully used as a structural material for the guide tubes (GTs), central tube (CT), and rigidity angles of the VVER-1000 FA of the new generation (alternative fuel assembly, FA-2) [4–6]. E635 is being tested as fuel rod cladding material for experimental assemblies.

Materials and Examination Techniques

The following E635 samples were selected for examinations: Fragments of structural components cut off from different areas of the VVER-1000 FA (fuel rod cladding, GT, CT, rigidity angle) and model samples in the form of plates and tube sections irradiated in the BOR-60 up to different damage doses (Table 1). The model samples were not submitted to any external stress.

Before irradiation in the BOR-60, the samples were autoclaved to have a protective film against possible penetration of H from the sodium coolant [7]. Before irradiation, the H mass fractions in the samples did not exceed 10 ppm.

TABLE 1—*Characteristics of objects under examination.*

Objects Under Examination	Place of Irradiation	Duration of Irradiation	Parameters of Irradiation	Coordinate of the Examined Area, mm[a]
Fuel rod claddings	Advanced FA, Unit 1, Balakovo NPP	3 years (21 086 effective h)	Bu = 39 MW · day/kgU; $T_{inlet} = 285^{\circ}$C; $T_{outlet} = 315^{\circ}$C; D ≈ 12 dpa[c]	80, 1890, 3260, 3690 (gas plenum)
GTs[b] and CT				100, 1900–2200, 3275, 3940
GTs[b]	FA-A, Unit 1, Kalinin NPP	4 years (25 968 effective h)	Bu = 44 MW · day/kgU;	1565
Rigidity angles			$T_{inlet} = 285^{\circ}$C; $T_{outlet} = 315^{\circ}$C; $F = 2,2 \times 10^{26}$ n/m^2; (D ≈ 18 dpa[c])	1565
Cladding tubes segments	BOR-60 reactor	Up to 43 720 h	$T_{irr} = 315 \div 345^{\circ}$C; $F \leq 13.5 \times 10^{26}$ n/m^2; (D ≤ 80 dpa);	...
Flat samples[d]		Up to 6 300 h	$T_{irr} \sim 320^{\circ}$C; $F = 3.8 \times 10^{26}$ n/m^2; D ≈ 23 dpa;	...

[a] From the bottom.
[b] $\sigma_z \leq |-65|$ MPa.
[c] Estimation (coordinates 1565–2200 mm) by data from Ref 11. At the core edges (coordinates 80–100 mm and 3260–3375 mm), the dose is ∼ two times lower; out of the core (coordinates ≥ 3690 mm) – it is two orders of magnitude lower.
[d] Parameters of irradiation resistance of these samples are published in Ref 7.

KOBYLYANSKY ETAL., doi:10.1520/JAI102941 829

The H content after irradiation did not exceed 50 ppm; as for the VVER-1000 FA material, it did not exceed 200 ppm.

The length of the flat samples was measured at a special measurement device by contact method using two linear displacement transducers (probes) that register the coordinates of the opposite sample edge surfaces into a personal computer. The length of the tube sections was measured by means of an indicating gage device with a scale interval of 0.002 mm. To evaluate the irradiation-induced growth (IIG), the reference was compared with the coordinates of scanning profiles of edge surfaces of the same plate samples and with readings of the indicating gage for tubular samples before and after irradiation. The IIG measurement error did not exceed ± 0.01 %.

Samples selected for transmission electron microscopy (TEM) were in the form of disks 3 mm in diameter. They were thinned at a TENUPOL-3 device by jet method. A 5 % solution of chloric acid in methanol was used as electrolyte; the operating voltage made up 38 V, the current was (130–150) mA, and the electrolyte temperature achieved -50°C. The thinned samples were examined at a JEM-2000FXII microscope at an accelerating voltage of 120 kV. The microstructure and phase composition of the samples were examined by TEM. The elementary composition of the matrix and secondary phase precipitates were determined by the method of energy-dispersion X-ray spectroscopy (EDS) using a LINK spectrometer. The obtained spectra were processed at the AN-10000 microanalyzer using RTS-2/FLS software. The elementary analysis of the secondary phase precipitates was done by extraction of carbon-varnished replicas.

In order to exclude the influence of sample radiation background on the value of niobium content in the matrix, we subtract a spectrum received from a hole from a matrix spectrum. In this case, we get rid of the additional peaks on the spectrum because of Nb isotopes' γ-emission. The error of Nb content in the E635 matrix evaluated by means of the X-ray energy dispersion analyzer is really high because of the small quantity of this element in the matrix.

Examination Results

Radiation Deformation

The E635-made VVER-1000 FA structural components have a high IIG resistance. After their operation for 4 years (the max fluence achieved was 2.2×10^{26} n/m^2 (herein after E > 0.1 MeV)), the elongation of the rigidity angles made up 0.1 %. The elongation of the GTs, which were under axial compressive load, made up 0.02 % on average. The growth of the tested fuel rods made up 0.2 % on average.

The strain of the model samples irradiated in the BOR-60 changed in the axial direction depending on neutron fluence (Fig. 1). It can be noted that regardless of the thermal treatment mode, the elongation of the samples is low up to high neutron fluence. There is a good correlation of the IIG values of VVER-1000 FA components and model samples irradiated in the BOR-60 at comparable irradiation doses. A slightly revealed accelerated growth appears at a neutron fluence higher than $\sim 7 \times 10^{26}$ n/m^2.

Microstructure, Phase, and Elementary Composition

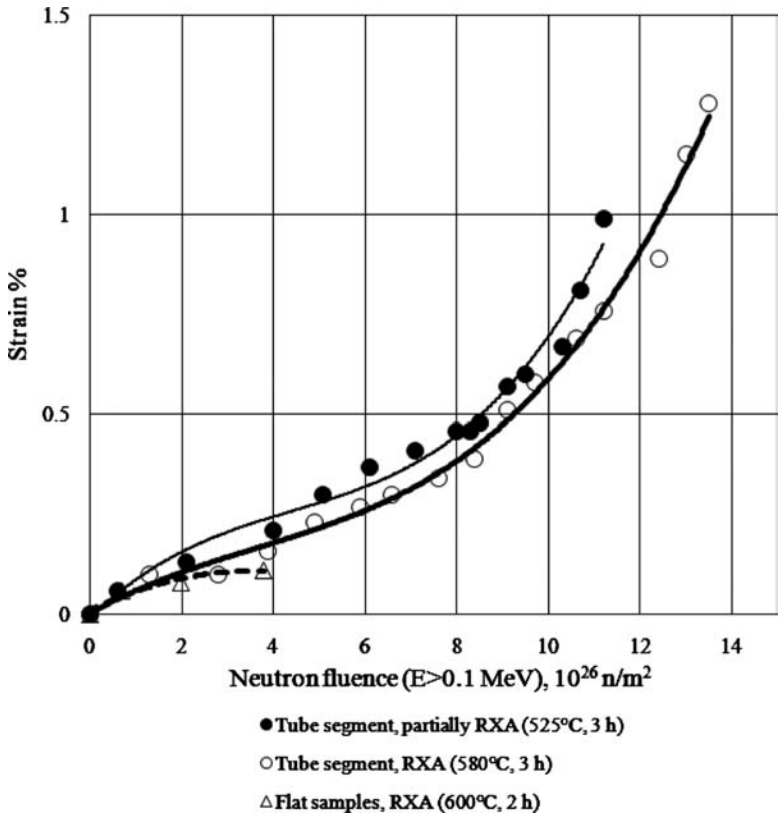


FIG. 1—*IIG strain of E635 samples versus neutron fluence at ~320°C.*

TEM examinations of the structure of the fuel rod claddings, rigidity angles, GTs, CT, and model samples irradiated in the BOR-60 showed that these E635-made objects had some similar peculiarities related to their final thermal treatment and the effect of irradiation on the evolution of secondary phase precipitates (Tables 2 and 3).

The microstructure of unirradiated alloy E635, both full and partially recrystallized, is shown in Fig. 2. The grain structure of the completely recrystallized material of the fuel rod claddings does not change significantly along its height. The material of the rigidity angles, GTs, and CT is not completely recrystallized. Globular precipitates of 80–140 nm were revealed in all examined materials. It should be noted that a good correlation of the globular precipitates' dimensions was observed in the fuel rod claddings, GTs, and CT as well as in model alloys. The smaller the precipitates' average size is, the higher is their concentration. Besides, a small amount of large particles (up to 500 nm) is found in the angles and flat samples (Fig. 3). Also, the presence of a fine-

TABLE 2—*General structure and secondary phases of examined objects from E635.*

Objects	Irradiation Conditions	Structure	Precipitates	Average Size, nm	Number Density, 10^{19} m^{-3}
Fuel rod claddings	VVER-1000; 3 years	100 % recrystallized; stable grain size along the length	Globular particles	80–110	$1.4 \div 3$
			Fine-dispersed plates	up to 5	1.5
Angles	VVER-1000; 4 years	50 % recrystallized	Globular particles	45	3.1
			Large particles	up to $500 \div 1000$	< 0.1
CT	VVER-1000; 3 years	75 % recrystallized	Globular particles	105–128	2.8–4.4
GT	VVER-1000; 3 years	75 % recrystallized	Globular particles	$110 \div 140$	$1.3 \div 3.2$
			Fine-dispersed plates	up to 5	1200
	VVER-1000; 4 years	75 % recrystallized	Globular particles	85	4.4
Flat samples	BOR-60; $T_{irr} \sim 320°C$; $F = 3.8 \times 10^{26}$ n/m^2	100 % recrystallized	Globular particles	112	1.3
			Large particles	up to 900	< 0.1
			Fine-dispersed plates	3	500
Tubes segments	BOR-60; $T_{irr} = 315 \div 345°C$; $F = 1.1 \times 10^{27}$ n/m^2	10–15 % recrystallized; ($0.5 \div 2\,\mu$m) and non-recrystallized ($\sim 0.25\,\mu$m) grains	Globular particles	105	$\sim 0.7 \div 10$
			Fine-dispersed plates	7	1200
			Thin plates	14	Low

TABLE 3—*Structure and phases in unirradiated E635 alloy.*

Structure	Precipitates	Average Size, nm	Number Density, 10^{19} m^{-3}	Composition, ±2 at%	Reference
Recrystallized annealing (RXA)	$Zr(Nb, Fe)_2$–Laves phase	100	2	Zr35-Nb35-Fe30	[10]
RXA		100	3–5	35Zr-35Nb-30Fe	[11]
RXA	$(ZrNb)_2Fe$–T-phase	300–1000	Low	60Zr-11Nb-29Fe	[11]
RXA	$Zr(Nb, Fe)_2$–Laves phase	95	3	34Zr-35Nb-31Fe	[7]
pRXA	$Zr(Nb, Fe)_2$–Laves phase	100	1.5		

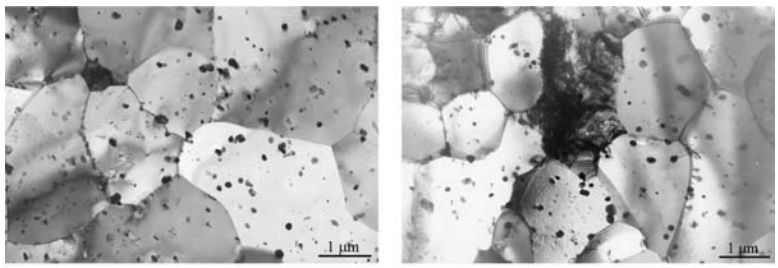


FIG. 2—*Typical microstructure in E635 tubes in (a) RXA (100 % recrystallization) and (b) parially recrystallized annealing (pRXA) (75 % recrystallization).*

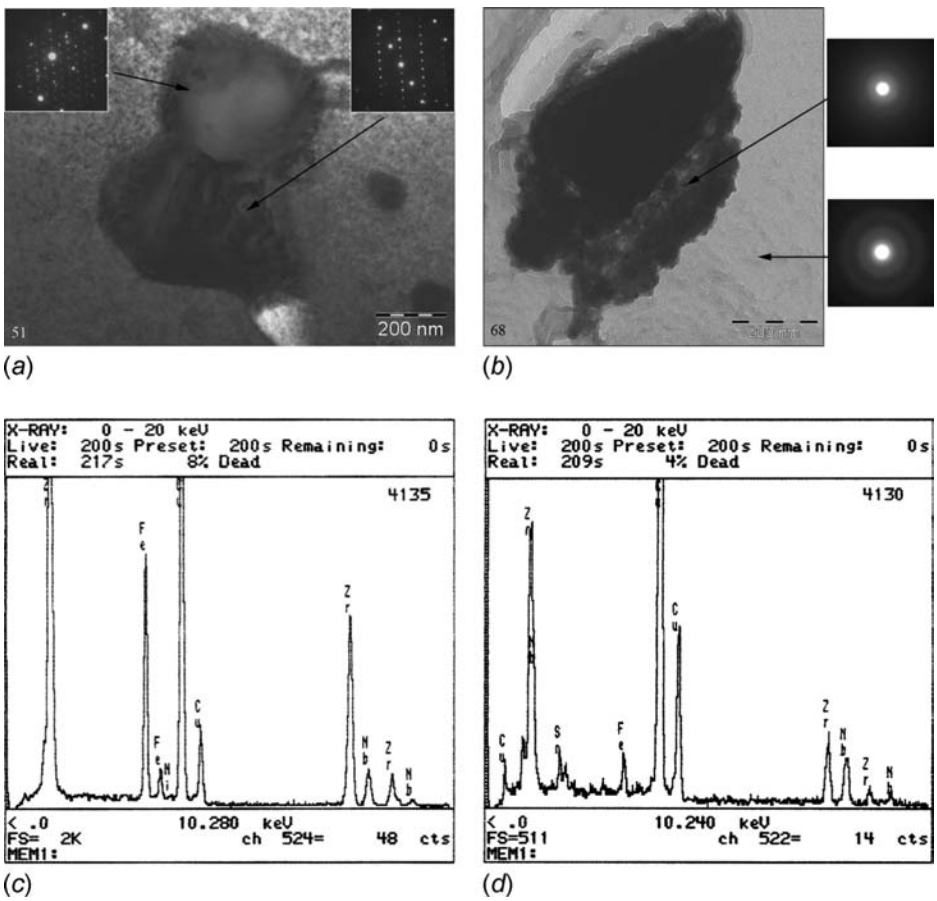
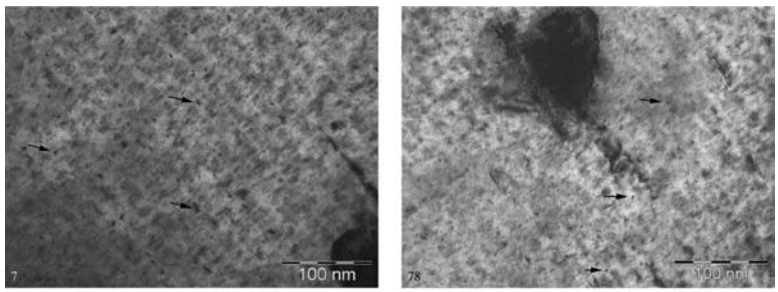


FIG. 3—*T-phase $(Zr,Nb)_2Fe$ (a) in the foil (flat sample) and (b) on the replica (rigidity angle); EDS-spectra from (c) a particle and (d) a flaked-away layer. The particle and the layer flaked away from it can be seen on the replica.*



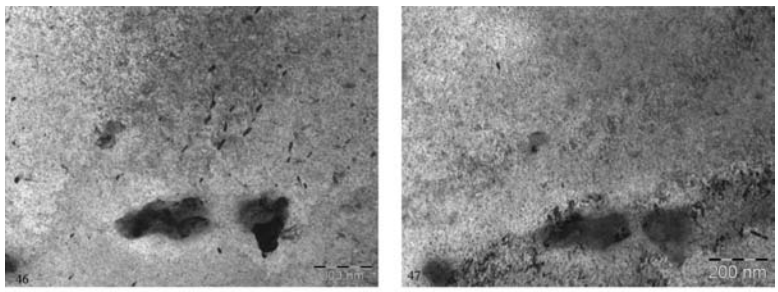
(*a*) (*b*)

FIG. 4—*Fine-dispersed precipitates (a) in the fuel rod cladding and (b) in a flat sample irradiated in BOR-60 up to a neutron fluence of* 3.8×10^{26} *n/m*^{2}.

dispersed irradiation-induced phase about 5 nm in size is observed practically in all objects under examination (except for the angles and CT) (Fig. 4). Under a significant increase of the neutron fluence (by about an order of magnitude), larger fine-dispersed particles are observed (Fig. 5).

The analysis of the diffraction pictures and the elementary composition of globular particles showed that before irradiation, these particles were Laves phase precipitates $Zr(Nb, Fe)_2$ with a hcp lattice and parameters $a = 0.53$ nm and $c = 0.87$ nm. Irradiation resulted in the redistribution of alloying elements between this phase and the matrix (Tables 4). The intensity of this redistribution depends on the irradiation conditions. It was noticed that at the fuel rod gas plenum and at the CT top, where the fluence is minimal, the globular precipitates were the Laves phase particles, the iron content being lower and the niobium content being higher as compared to the initial state (Fig. 6).

As the fluence rose, more and more iron was released and this process was accompanied by the conversion of the Laves phase hcp lattice into the body-centered one and the $\beta-$Nb phase containing a small amount of iron appeared. Here, one can observe the dependence of the iron content on the size of particles: The iron content is higher in larger particles. Mono-crystalline particles



(*a*) (*b*)

FIG. 5—*Another type of fine-dispersed precipitates at different [(a) and (b)] tilt angles in alloy E635 irradiated in BOR-60 up to a neutron fluence of* 1.1×10^{27} *n/m*^{2}.

TABLE 4—*Elementary composition of globular precipitates of objects under examination.*

Examined Objects	Irradiation Conditions	Area Coordinate, mm	Element Atomic Fraction, %		
			Zr	Nb	Fe
Fuel rod claddings	No irradiation	···	34	35	31
	VVER-1000; 3 years,	80	44.6±1.7	50.7±2	4.8±0.3
		1890	44.1±1.6	50.4±2	5.2±0.3
		3260	41.5±1.4	46.5±1.6	11.0±0.4
		3690 (gas plenum)	35.8±1.5	43.9±1.7	21.3±0.5
Angles	VVER-1000; 4 years	1565	47.5±1.6	45.6±1.7	1.9±0.3
CT	VVER-1000; 3 years	100	49.1±1.8	49.6±2	1.4±0.3
		2200	44.2±1.8	50.2±2	5.5±0.4
		3940	35.7±1.6	38.9±1.8	25.4±0.6
GT	VVER-1000; 3 years	1900	46.7±2	42.8±2	9.4±0.6
	VVER-1000; 4 years	1565	38.1±1.1	47.1±1.4	14.8±0.3
Flat samples	BOR-60; $T_{irr} \sim 320°C$; $F = 3.8 \times 10^{26}$ n/m^2	···	52.7±1.5	46.7±1.6	0.6±0.3
Tubes segments	BOR-60; $T_{irr} = 315 \div 345°C$;; $F = 1.1 \times 10^{27}$ n/m^2	···	51.3±1.1	47.4±1.2	1.40±0.14

TABLE 5—*Elementary composition of the solid solution matrix of the examined objects.*

Examined Component	Irradiation Conditions	Coordinate, mm	Mass Fraction, %		
			Nb	Fe	Sn
Sample	No irradiation	···	0.7	< 0.1	1.3
Fuel rod claddings	VVER-1000; 3 years	1890	0.18±0.29	0.32±0.06	1.35±0.14
		3690 (gas plenum)	0.31±0.35	0.23±0.06	1.48±0.2
Angles	VVER-1000; 4 years	1565 R	0.16±0.49	0.2±0.09	1.23±0.3
CT	VVER-1000; 3 years	100	0.89±0.33	0.3±0.06	1.21±0.19
		2200	0.18±0.27	0.41±0.06	0.99±0.17
		3940R	0.71±0.53	0.48±0.1	1.09±0.27
GT	VVER-1000; 3 years	1900	0.44±0.33	0.26±0.06	1.3±0.2
	VVER-1000; 4 years	1565	0.19±0.65	0.08±0.12	1.16±0.4
Flat samples	BOR-60; $T_{irr} \sim 320°C$; $F = 3.8 \times 10^{26}$ n/m^2	···	0	0.4±0.1	1.2±0.3
Tubes segments	BOR-60; $T_{irr} = 315 \div 345°C$; $F = 1.1 \times 10^{27}$ n/m^2	···	−0.3±0.4	0.28±0.08	1.4±0.27

KOBYLYANSKY ETAL., doi:10.1520/JAI102941 837

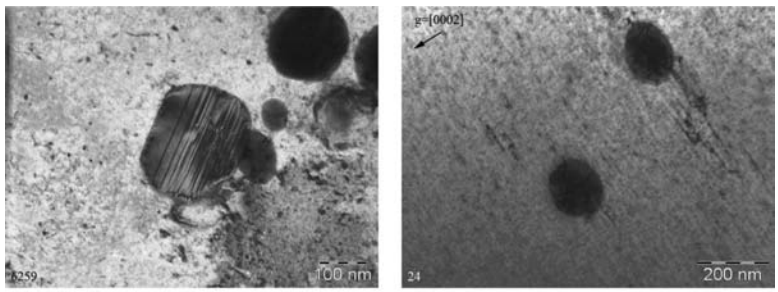


FIG. 6—*(a) Laves phase* $Zr(Nb,Fe)_2$ *precipitates in the fuel rod cladding material in the gas plenum area and (b) globular β-Nb precipitates in the flat sample irradiated in BOR-60 up to* 3.8×10^{26} *n/m*^{2}.

$Zr(Nb,Fe)_2$, in which thin parallel twins are observed, convert into polycrystalline precipitates $\beta-$Nb. In the gas plenum area, the particles' composition is the closest to that of one of the Laves phase and the precipitates preserve the twinning structure and mono-crystallinity (Fig. 6(*a*)).

The microdiffraction analysis of large particles (Fig. 3(*a*)) showed that this type of precipitates has the face-centered-cubic lattice with parameter $a = 1.21$ nm ($(Zr,Nb)_2Fe$, T-phase). A layer about 25 nm thick was revealed on the T-phase particles surfaces after irradiation. To investigate its features, a detailed examination of the elementary composition of both the layer and the precipitates' bulk was done along their transversal cross-section. The observations showed that when separating the replica from the sample, the layer exfoliated very often from the precipitates' bulk. Diffusion circles in the microdiffraction (MD) pictures of the flaked-away layer show its structure to be amorphous (Fig. 3(*b*)). Different MD pictures from both the layer and carbon substrate are given for comparison.

The elementary analysis showed that the layer contained 43 at % of zirconium, 53 at % of niobium, and 4 at % of iron (Fig. 3(*c*), 3(*d*)). At the same time, the evaluation of T-phase elements distribution over the cross-section showed that their concentration changed in the surface layers of the precipitates as compared to their center. The concentration of elements changes, as shown in Fig. 7, that presents the dependence of zirconium, niobium, and iron content in the composition "precipitate—layer—matrix." The concentration curve of the layer area shows clearly the drop of zirconium content, a prominent peak of niobium content, and the monotonous decrease of iron content up to its concentration in the matrix.

At a very high neutron fluence, the redistribution of elements between the matrix and the precipitates causes the generation of larger fine-dispersed precipitates, which have not been observed in E635 irradiated up to a lower neutron fluence (Fig. 5). These precipitates are thin plates ~ 14 nm in length located in different crystallographic planes. A part of precipitates of this type can be seen under a multi-beam diffraction when there is no strong active reflection

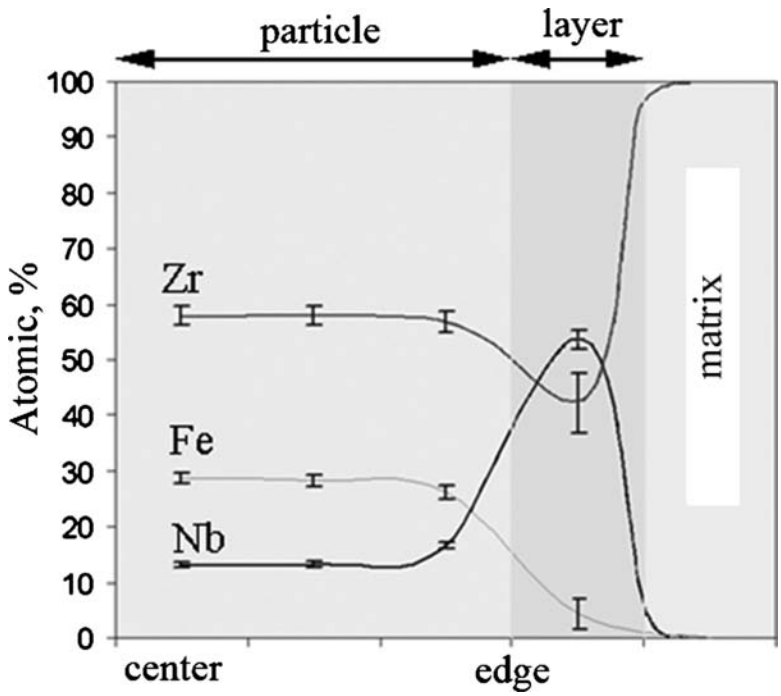


FIG. 7—*Schematic distribution curves of the T-phase elements and the layer and matrix surrounding it.*

and extinction contours are not practically observed. Under a favorable foil orientation, a part of the plates can be seen due to their diffraction contrast while contrast from others is weak or absent (Fig. 5(*a*)). If the foil tilt is changed, they are out of contrast (Fig. 5(*b*)).

Since the plates' dimensions were too small and there were no self-reflections during the diffraction examination, it was impossible to determine their elementary composition and crystalline structure.

Table 5 presents the summarized data on the composition and content of the matrix solid solution of the analyzed areas. The received values of Nb content in the matrix do have high uncertainties. First, it is due to the small content of this element, and second, to the background fluctuation from the irradiated sample in comparison with the background fluctuation on a spectrum from an unirradiated sample. However, the content of niobium decreased significantly, from 0.7 wt % of niobium before irradiation to practically zero (0.2 wt % in most cases). Due to the iron release from precipitates, the matrix became enriched with this element, the non-recrystallized areas being enriched more than the recrystallized ones. Irradiation did not cause any significant redistribution of tin in the matrix.

The examination of the dislocation structure of cladding active parts at different height levels showed that there were practically no ⟨c⟩-dislocations. Only

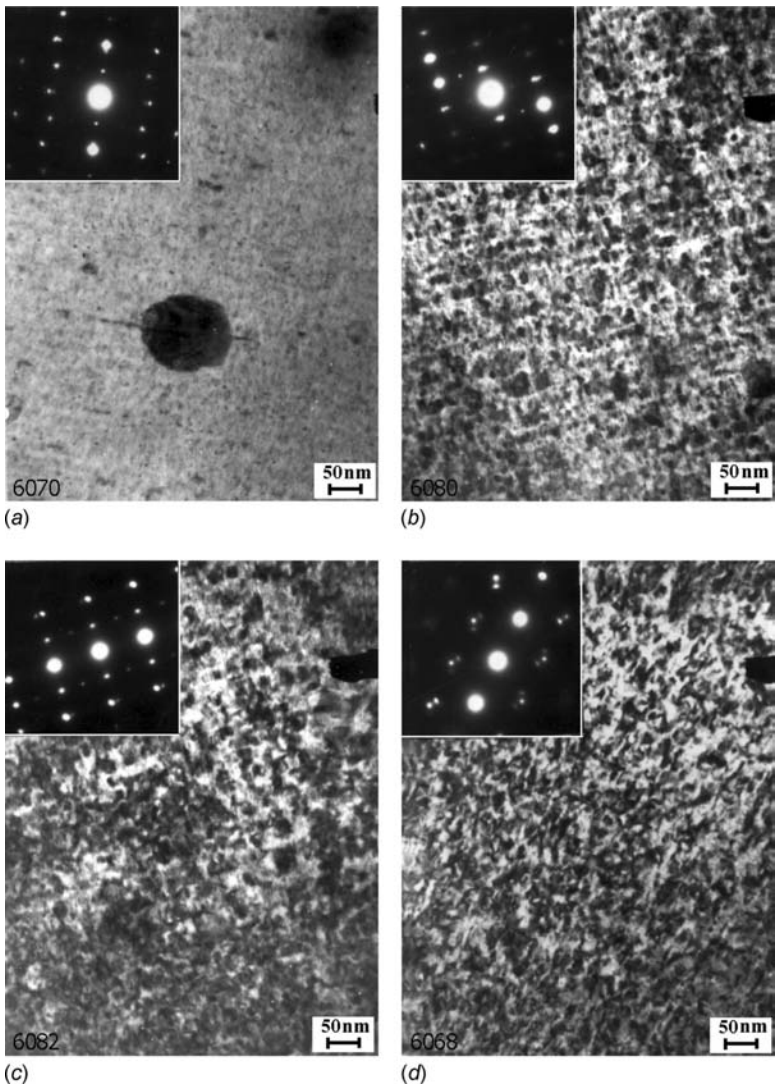


FIG. 8—*Dislocation structure of the fuel rod middle: (a) ⟨c⟩-dislocation loops near the secondary phase precipitates, foil plane (2$\bar{1}\bar{1}$0), vector* $\mathbf{g}=\pm 0002$*; (b) rows of dislocation loops, foil plane (2$\bar{1}\bar{1}$0), vector* $\mathbf{g}=\pm 01\bar{1}\bar{1}$*; (c) ⟨a⟩-dislocation loops, foil plane (2$\bar{1}\bar{1}$0), vector* $\mathbf{g}=\pm 01\bar{1}\bar{1}0$*; and (d) ⟨a⟩-dislocation loops, foil plane (0001), vector* $\mathbf{g}=\pm 10\bar{1}\bar{1}0$.

single dislocations up to 100 nm long were seen near the secondary phase precipitates; these dislocations were oriented parallel to the basal planes (Fig. 8(*a*)). If the foil orientation is prismatic and the actual vector is $\mathbf{g}=\pm 01\bar{1}1$, then rows of dislocation loops are observed that refer, mainly, to the $(\langle c+a\rangle)$ type and are located parallel to the basal planes (Fig. 8(*b*)). If vector **g** is changed

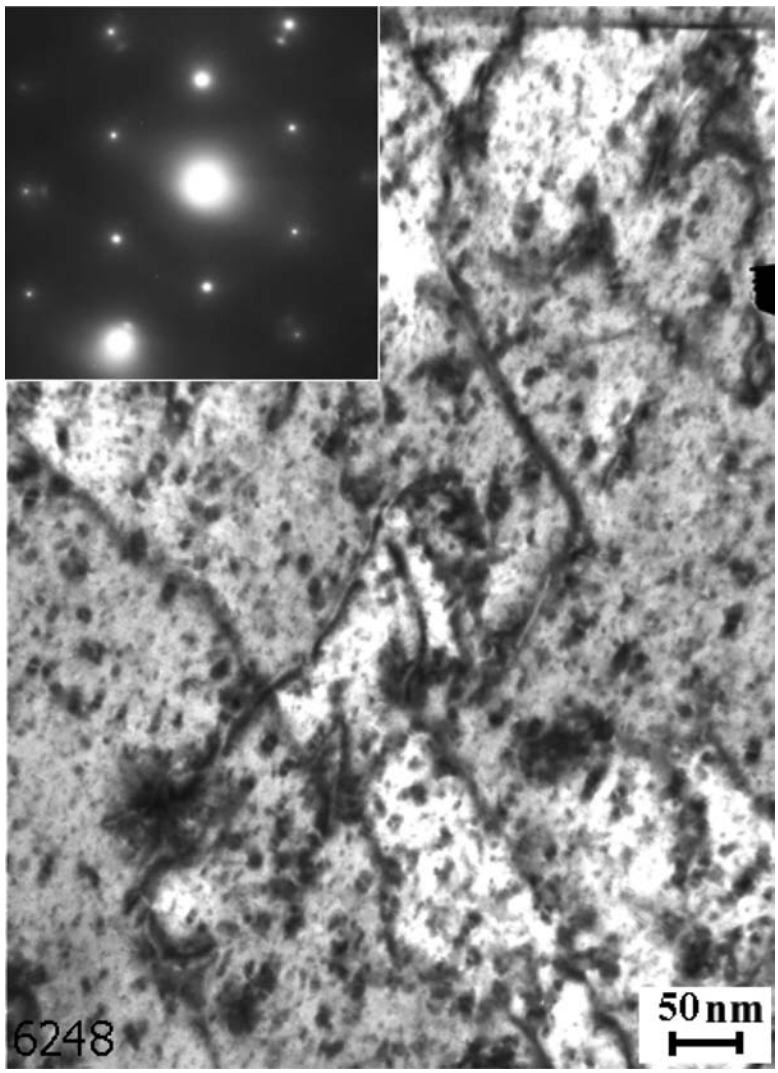


FIG. 9—*Dislocation structure in the fuel rod cladding gas plenum area.*

by $\mathbf{g} = \pm 01\bar{1}0$, the loops rows disappear and there is a chaotic distribution of loops interpreted as ⟨a⟩-dislocations (Fig. 8(*c*)). The latter are in contrast with foils in the basal orientation as well (Fig. 8(*d*)).

The E635 dislocation structure in the cladding gas plenum area (Fig. 9) differs from that of the fuel rod's active part. There are no ⟨c⟩-dislocations even near the secondary phase particles. When ⟨a⟩-dislocations can be seen, the initial linear dislocations and radiation defect clusters are observed mainly in the form of black dots or, sometimes, in the form of small dislocation loops no more than 15 nm in size. The linear dislocation density is $(1.1 \pm 0.3) \times 10^{14}\ \mathrm{m}^{-2}$.

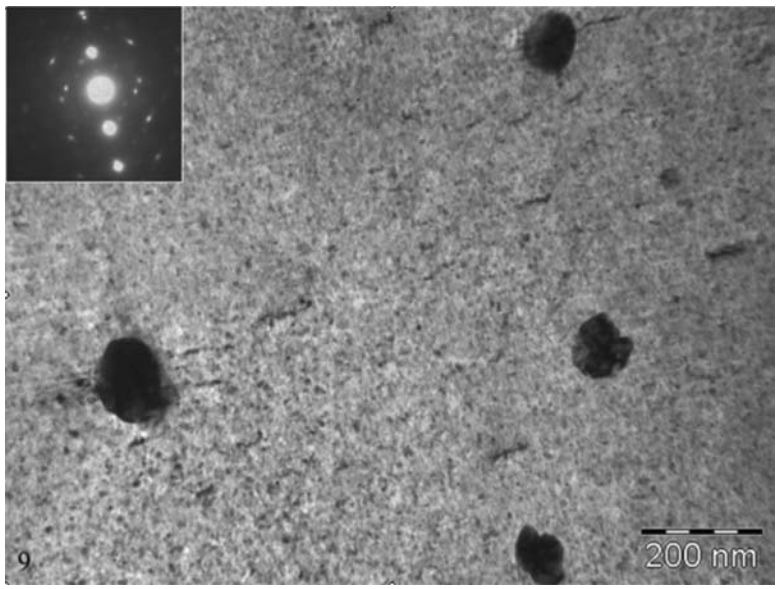


FIG. 10—*Dislocation structure of the GT middle. Reciprocal lattice section* $(10\bar{1}0)$*, vector* $\mathbf{g} = \pm 0002$.

In the GT middle, the size and concentration of ⟨a⟩-loops are practically the same as in the cladding of the fuel rod's active part. The average length and density of ⟨c⟩-dislocations are about twice less than in the fuel rod cladding (Figs. 10 and 8).

The examination of the dislocation structure at the GT top (Fig. 11) and the CT did not reveal any ⟨c⟩-dislocations. Rows of dislocation loops parallel to the basal planes were found in the grains with a prismatic orientation. As for grains with a basal orientation, ⟨a⟩-dislocation loops were observed. The average loop size achieved is 10–12 nm, and the concentration is $(4 \pm 1.3) \times 10^{22}$ m^{-3}.

Radiation defects found in the flat samples irradiated up to a fluence of 3.8×10^{26} n/m^2 were, mainly, dislocation loops 7.3 nm in size and with a concentration of 7.4×10^{22} m^{-3}. Linear ⟨c⟩-dislocations oriented parallel to the basal plane were observed, mainly near the secondary phase precipitates and, sometimes, in the matrix (Fig. 6(*b*)).

The structure of the alloy irradiated up to the maximal fluence has ⟨c⟩-dislocations not only near precipitates but also inside the matrix (Fig. 12(*a*)), the actual reflection being $\mathbf{g} = 0002$. In addition to the dislocations parallel to the basal planes, there are dislocations with other orientations. Perhaps they generated from the initial ones as a result of climbing. Radiation ⟨c⟩-dislocations appear both near some β–Nb precipitates and just in the matrix. Their density makes up 9×10^{13} m^{-2}, the average length achieved is 130 nm.

The grains with basal (Fig. 12(*b*)), prismatic (Fig. 12(*c*)), and pyramidal orientation have ⟨a⟩-dislocation loops. The average loop size in the basal-oriented grains makes up 8.4 nm; the concentration is 6.7×10^{22} m^{-3}. In grains with

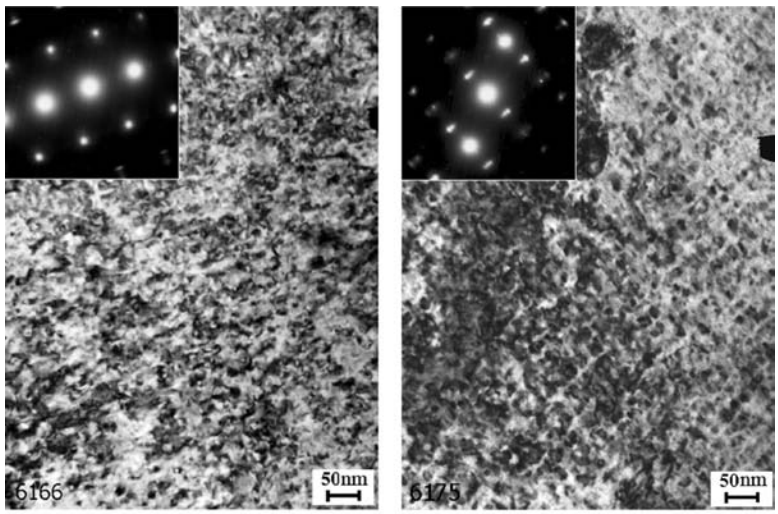


FIG. 11—*Dislocation structure of the GT top: (a) ⟨a⟩-dislocation loops, section (10$\bar{1}$0); (b) rows of dislocation loops, foil section (10$\bar{1}$0).*

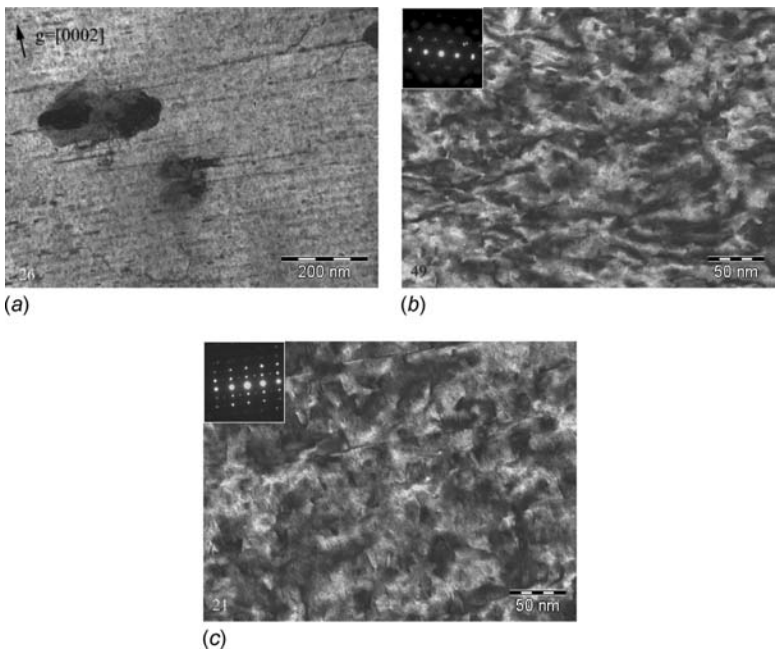


FIG. 12—*(a) ⟨c⟩-dislocations and [(b) and (c)] ⟨a⟩-dislocation loops in alloy E635 irradiated in BOR-60 up to 1.1 × 10^{27} n/m^2.*

prismatic and pyramidal orientations, the average loop size makes up 9.6 nm; the concentration is $4.3 \times 10^{22}\,m^{-3}$, the actual reflection being [01−10].

The characteristics of the dislocation structure of the examined E635 items are summarized in Table 6.

Discussions

The examination results show that whatever components of the VVER-1000 FA (fuel rod claddings, GTs, CTs, rigidity angle) or model samples (flat samples, tube segments) made of E635 alloy are examined, all of them possess a rather high resistance to radiation deformation. It confirms and supplements the previously obtained data [7–11]. It can be seen that the composition of alloying elements (Nb, Sn, Fe) of E635 causes, first of all, a low dependence of the IIG on neutron fluence up to extremely high values $13.5 \times 10^{26}\,m^{-2}$ (~ 80 dpa). An acceleration growth stage was observed to appear only at fluences higher than $\sim 7 \times 10^{26}\,n/m^2$. However, the rate of strain increment increased insignificantly. Since real water-cooled reactor core components need decades to achieve these neutron fluences, the above data are of interest from the viewpoint of an investigation of the basic trends in the evolution of the alloy's structural components and their correlation with dimensional changes under irradiation.

As can be seen from the TEM results, the E635 alloy's structure undergoes significant changes at temperatures typical for the operation of items at achievable neutron fluence ($F \leq 3.8 \times 10^{26}\,n/m^2$) during long-term FA operation in VVER-1000 reactors. The mechanism of these changes is the same for both VVER-1000 FA components and samples irradiated in the BOR-60. These changes are as follows.

- A specific dislocation structure appears in the form of dislocation loops of ⟨a⟩- and ⟨c + a⟩-type as well as a small amount of ⟨c⟩-dislocations near globular precipitates.
- Laves phase particles $Zr(Nb,Fe)_2$ (hcp) convert into β−Nb particles (bcc) due to the release of iron atoms into the matrix.
- A small amount ($< 1.5 \times 10^{22}\,m^{-3}$) of irradiation-induced fine-dispersed precipitates about 5 nm in size appears. Information about the appearance of fine-dispersed precipitates in Nb-containing zirconium alloys can be found in Refs [12 and 13]. However, at the comparable irradiation doses, the concentration of fine-dispersed precipitates in E635 is lower as compared to binary Zr-Nb alloys.
- After irradiation, the content of iron in the matrix increases and that of niobium decreases (practically to zero).
- The revealed large T-phase precipitates are effective sinks for niobium atoms from the matrix, while iron and zirconium release such particles and the concentration of these elements changes in the surface layers of precipitates as compare to their centers.

The absence of a large amount of ⟨c⟩-dislocations correlates well with the low dimensional changes of items under examination. According to the majority of IIG models (for instance [14,15], the IIG phenomenon may be related to

TABLE 6—*Parameters of irradiated E635 dislocation structure.*

Examined Component	Irradiation Conditions	Coordinate, mm	Dislocation Loops		⟨c⟩-Dislocations
			Average Size, nm	Concentration, 10^{22} m^{-3}	Density, m^{-2}
Fuel rod claddings	VVER-1000; 3 years	1890	10	4	Single, near SPP
		3690 (gas plenum)	10	4	No
Angles	VVER-1000; 4 years	1565	7	3	Single, near SPP
CT	VVER-1000; 3 years	100	9	3	Single, near SPP
		2200	9	3	Single, near SPP
		3940	9	3	No
GT	VVER-1000; 3 years	1900	10	4	Single
	VVER-1000; 4 years	1565	4	1.5	No
Flat samples	BOR-60; $T_{irr} \sim 320°C$; $F = 3.8 \times 10^{26}$ n/m^2	...	7	7	Single, near SPP
Tubes segments	BOR-60; $T_{irr} = 315 \div 345°C$; $F = 1.1 \times 10^{27}$ n/m^2		8	7	9×10^{13}

KOBYLYANSKY ETAL., doi:10.1520/JAI102941 845

the fact that ⟨c⟩-dislocations are formed in the basal planes of the crystalline lattice from one type of point defect (mainly, from vacancies), while ⟨a⟩-dislocation loops are formed in the prismatic planes from quite another type of defect (mainly, from interstitials). Under irradiation, directed flows of unlike defects interact asymmetrically (with the preference for interstitial atoms) with different sinks (dislocations, clusters, precipitates, grain boundaries, etc.). The disappearance of any point defect on these sinks controls the generation and evolution of dislocations with different Burgers vectors in the alloy structure. Some sinks, for instance, ⟨c⟩-dislocations and dislocation loops with different Burgers vectors (⟨a⟩− and ⟨c + a⟩), are anisotropic, and their characteristics change significantly as the damage dose rises. As a result, there is a growth in the atomic planes of the crystalline lattice in one direction, while in the other direction, the amount of atomic planes becomes less, i.e., the IIG mechanism is observed. Though the researchers have proposed quite a lot of models explaining the IIG of model samples and items made from Zr materials, of which the evolution can be found in Holt's paper [16], there is no a unique opinion about the mechanism of this phenomenon [17]. Probably, the low rate of IIG in E635 [2,18] is related to the fact that the composition of the solid solution in Fe and Nb provides a low activation self-diffusion energy [18,19] [that determines the movement of vacancies]. It slows down the generation of the ⟨c⟩-type dislocations being objects of many IIG models.

Mechanical stresses promote the appearance of fine-dispersed particles in alloy E635 at neutron fluences lower than in the unstressed material. As for unstressed rigidity angles, of which neutron fluence made up $2.2 \times 10^{26}\,\mathrm{n/m^2}$, no precipitates of this type were revealed, while in the GTs under compression stress and in fuel rod claddings with lower fluence, these precipitates were observed as well as in the unstressed model samples irradiated in the BOR-60 up to neutron fluence $\geq 3.8 \times 10^{26}\,\mathrm{n/m^2}$. A decrease in the niobium content in the matrix should not be necessarily accompanied by irradiation-enhanced precipitations. The portion of niobium can diffuse together with the Zr from the matrix in larger particles (β−Nb), leading to an increase in their size, the balance of this element observed in these particles being preserved. When in the reactor, the alloys are not in an equilibrium state because of a small duration of annealing during fabrication. Under irradiation, the niobium redistribution between the matrix and the particles is influenced by a limit of its solubility and a transition to a new equilibrium state.

The evaluation of the niobium content in the matrix showed that in the GT material, it decreased from $\sim 0.4\,\mathrm{wt\,\%}$ after a three-year operation to its complete or almost complete absence after a four-year operation. The same is typical for the fuel rod cladding matrix after a three-year operation.

Conclusions

The examination of the VVER-1000 FA components made from E635 alloy (fuel rod cladding, guide channels, CT, and rigidity angle) showed that during a three to four-year operation, significant structural changes are observed, which are

the generation of radiation defects in the form of dislocations and dislocation loops of different types, the transformation of both the phase and elementary composition of precipitates (hcp Laves phase–bcc $\beta-$Nb, change of the composition at the T-phase periphery), the appearance of irradiation-induced fine-dispersed particles, and the enrichment of the solid solution in iron and its depletion in niobium due to a redistribution of elements between the matrix and precipitates.

Mechanical stresses in the FA components promote the generation and evolution of irradiation-induced fine-dispersed particles under irradiation.

Insignificant dimensional changes of the E635 components (as compared to E110, of which the IIG strain is several times higher at high fluence [8,10,11,20]), correlate well with a small density of ⟨c⟩-dislocations (mainly, near precipitates); such correlations are observed for many zirconium-based alloys.

The mechanisms of irradiation damageability of the FA components during their operation in the VVER-1000 core correspond completely to processes that occurred in the E635 samples irradiated in the BOR-60 at comparable temperatures.

The data on irradiation damageability of model samples irradiated in the BOR-60 up to the highest damage dose $\sim$(66–80) dpa show no material degradation and can be used for both the estimation of changes in the VVER-1000 FA components under a long-term operation and the development of general models of irradiation damageability of zirconium alloys.

It is stated that as the damage dose rises, an increase in ⟨c⟩-type dislocations density and growth strain is observed. At a damage dose higher than $\sim$40 dpa, the rate of strain growth in E635 increases a bit, i.e., a stage of weak (as compared to other alloys) accelerated growth is observed.

References

[1] Nikulina, A. V., Markelov, V. A., Peregud, M. M., Voevodin, V. N., Panchenko, V. L., and Kobylyansky, and G. P., "Irradiation-Induced Microstructure Changes in Zr-1%Sn-1%Nb-0.4%Fe," *J. Nucl. Mater.*, Vol. 238, 1996, pp. 205–210.10.1520/JAI102941

[2] Nikulina, A. V., Markelov, V. A., Peregud, M. M., Bibilashvili, Yu. K., Kotrekhov, V. A., Lositsky, A. F., Kuzmenko, N. V., Shevnin, Yu. P., Shamardin, V. K., Kobylyansky, G. P., and Novoselov, A. E., "Zirconium Alloy E635 as a Material for Fuel Rod Cladding and Other Components of VVER and RBMK Cores," *Zirconium in the Nuclear Industry: 11th International. Symposium, STP 1295*, E. R. Bradley and G. P. Sabol, Eds., ASTM International, West Conshohocken, PA, 1996, pp. 785–804.

[3] Markelov, V. A., Nikulina, A. V., Gusev, A. Yu., Loguntsev, E. N., Panchenko, V. L., Pivovarova, N. A., and Kozlov, A. V., "Irradiation-Induced Structural Changes in the Tube Material of the Operating Channel Made of Zr-1.3Sn-1Nb-0.4Fe Alloy During Its Operation in the 1st Unit of the Ignalina NPP," *Issues of Nuclear Science and Engineering, Series: Material Science and New Materials*, Vol. 1(48), 1993, pp. 44–49.

[4] Markelov, V., Novikov, V., Nikulina, A., Kon'kov, V., Sablin, M., Shishov, V., Peregud, M., Tselischev, A., Novoselov, A., and Kobylyansky, G., "Application of E635

Alloy as Structural Components of WWER-1000 Fuel Assemblies," *Proceedings of the Sixth International Conference WWER Fuel Performance, Modeling, and Experimental Support*, Albena, Bulgaria, Sept. 19-23, 2005, pp. 188–193.

[5] Shishov, V. N., Markelov, V. A., Novikov, V. V., Nikulina, A. V., Kon'kov, V. F., Sablin, M. N., Peregud, M. M., Tselischev, A. V., Novoselov, A. E., Kobylyansky, G. P., Smirnov, V. P., and Markov, D. V., "Use and Improvement of E635 Alloy as Applied to Fuel Claddings and FA Structural Components of Water Cooled Reactors," *Proceedings of the 6th International Symposium on Contribution of Materials Investigation to Improve the Safety and Performance of LWRs*, Fontevraud, France, Sept. 18–22, 2006.

[6] Molchanov, V. L., Dolgov, A. B., Samoilov, O. B., Kaidalov, V. B., Romanov, A. I., Levanov, L. V., Petrov, I. V., and Aksenov, P. M., "Results of Development and Operation Experience of VVER-1000 Alternative FA," *Sixth International Conference on VVER Fuel Performance, Modeling and Experimental Support*, Albena Congress Center, Bulgaria, Sept. 19–23, 2005, Institute for Nuclear Research and Nuclear Energy, 2006, pp. 92–97.

[7] Kobylyansky, G. P., Novoselov, A. E., Ostrovsky, Z. E., Shishov, V. N., Obukhov, A. V., Shishin, V. Yu., Nikulina, A. V., Peregud, M. M., Mahmood, S. T., White, D. W., Lin, Y-P., and Dubecky, M. A., "Irradiation-Induced Growth and Microstructure of Recrystallized, Cold Worked and Quenched Zircaloy-2, NSF, and E635 Alloys," *15th International Symposium on Zirconium in the Nuclear Industry, STP 1505*, Sunriver, OR, June 24–28, B. Kammenzind and M. Limback, Eds., ASTM International, West Conshohocken, PA, 2009, pp. 564—582.

[8] Kobylyansky, G. P. and Novoselov, A. E., "Radiation Resistance of Zirconium and Zirconium-Based Alloys," *Reference Materials on Reactor Material Science*, V. A. Tsikanov, Ed., SSC RIAR, Dimitrovgrad, Russia, 1996.

[9] Kobylyansky, G. P., Shamardin, V. K., and Rogozyanov, A. Ya., "Peculiarities of Effect of Irradiation on Properties and Behavior of Zirconium Alloys," *Proc. Sixth Russian Conference on Reactor Material Science*, Dimitrovgrad, Russia, Sept. 11–15, Vol. 2, Part 1, 2001, pp. 303–322.

[10] Shishov, V. N., Peregud, M. M., Nikulina, A. V., Shebaldov, P. V., Tselishchev, A. V., Novoselov, A. E., Kobylyansky, G. P., Ostrovsky, Z. E., and Shamardin, V. K., "Influence of Zirconium Alloy Chemical Composition on Microstructure Formation and Irradiation Induced Growth," *13th International Symposium on Zirconium in the Nuclear Industry, STP 1423*, G. D. Moan and P. Rudling, Eds., Annecy, France, 2000, ASTM International, West Conshohocken, PA, pp. 758–779.

[11] Shishov, V. N., Peregud, M. M., Nikulina, A. V., Pimenov, Yu. V., Kobylyansky, G. P., Novoselov, A. E., Ostrovsky, Z. E., and Obukhov, A. V., "Influence of Structure–-Phase State of Nb Containing Zr Alloys on Irradiation Induced Growth" *14th International Symposium on Zirconium in the Nuclear Industry, STP 1467*, P. Rudling and B. Kammenzind, Eds., Stockholm, Sweden, ASTM International, West Conshohocken, PA, 2006, pp. 666–685.

[12] Doriot, S., Gilbon, D., Bechade J.-L., Mathon M.-H., Legras L., and Mardon J.-P., "Microstructural Stability of M5TM Alloy Irradiated up to High Neutron Fluences," *J. ASTM Int.*, Vol. 2, No. 7, 2005, pp. 175–201.

[13] Coleman, C. E., Gilbert, R. W., Carpenter, G. J. C., and Weatherly, G. C., "Precipitation in Zr-2.5 wt% Nb During Irradiation," *Phase Stability During Irradiation Symposium*, Pittsburg, Oct. 5–9, 1980, The Metallurgical Society of AIME, Littleton, CO, pp. 587–599.

[14] Holt, R. A., "Mechanisms of Irradiation Growth of Alfa-Zirconium Alloys," *J. Nucl. Mater.*, Vol. 159, 1988, pp. 310–338.

[15] Griffiths, M., "A Review of Microstructure Evolution in Zirconium Alloy During Irradiation," *J. Nucl. Mater.*, Vol. 159, 1988, pp. 190–218.

[16] Shishov, V. N., Nikulina, A. V., Markelov, V. A., Peregud, M. M., Kozlov, A. V., Averin, A. V., Kolbenkov, S. F., and Novoselov, A. E., "Influence of Neutron Irradiation on Dislocation Structure and Phase Composition of Zr-Base Alloys," *11th International Symposium on Zirconium in the Nuclear Industry, STP 1295*, E. R. Bradley and G. P. Sabol, Eds., Garmisch-Partenkirchen, Germany, ASTM International, West Conshohocken, PA, 1996, pp. 603–622.

[17] Holt, R. A., "In-Reactor Deformation of Zirconium Alloy Components," *J. ASTM Int.*, Vol. 5, No. 6, 2009, pp. 3–18.

[18] Hood, G. M., Zou, H., Gupta, D., and Schultz, R., "α-Zr Self-Diffusion Anisotropy," *J. Nucl. Mater.*, Vol. 223, 1995, pp. 122–125.

[19] Zou, H., Hood, G. M., Schultz, R., and Jackman, J. A., "The Solid Solubility of Fe in α-Zr: A Secondary Ion Mass Spectrometry Study," *J. Nucl. Mater.*, Vol. 210, 1994, pp. 239–243.

[20] Shebaldov, P. V., Peregud, M. M., Nikulina, A. V., Bibilashvili, Yu. K., Lositski, A. F., Kuzmenko, N. V., Belov, V. I., and Novoselov, A. E., "E110 Alloy Cladding Tube Properties and Their Interrelation with Alloy Structure-Phase Condition and Impurity Content," *12th International Symposium on Zirconium in the Nuclear Industry, STP 1354*, Toronto, Canada, G. P. Sabol and G. D. Moan, Eds., ASTM International, West Conshohocken, PA, 2000, pp. 545–558.

DISCUSSION

Question 1, S. Ishino, University of Tokyo:—I think the irradiation conditions for VVER fuel rod irradiations are different from those of BOR-60 irradiations. In VVER case, the specimens are irradiated in VVER water conditions, whereas in BOR-60 case, irradiation is performed probably in sodium coolant. The sodium inlet temperature might be higher than for VVER case. In VVER case, oxide is being formed by corrosion with some hydrogen uptake, while in BOR-60 case, no water side corrosion occurs. Do I understand correctly that although there are such differences, microstructural evolution is almost similar for both cases?

Author's Response:—In spite of the fact that sodium inlet temperature in the BOR-60 reactor is higher than in VVER case, temperature conditions for irradiation of specimens' material and VVER FA's elements are close thanks to the differences in heat removal conditions in these cases.

Your understanding is correct that while corrosion conditions are different, micro structural evolution is almost similar in both cases.

Question 2, Zhongwen Yao:—1) What is the nature of a type of a-loops and c-loops? 2) Can we check carefully the segregation of elements?

Author's Response:—1) Loops nature was not investigated in this work. The prevailing view in literature is that c-loops are vacancy loops and a-loops are chiefly interstitial loops.

2) Segregation of elements was not investigated in this work. This is an issue of a special separate study with the use of up-to-date sensitive instruments.

CREEP AND DEFORMATION

Reprinted from JAI, Vol. 8, No. 3
doi:10.1520/JAI103297
Available online at www.astm.org/JAI

John Paul Foster[1] *and Rita Baranwal*[2]

ZIRLO® Irradiation Creep Stress Dependence in Compression and Tension

ABSTRACT: Fuel operating margins in recent years have decreased due to increases in fuel duty. In response, Westinghouse has developed an improved version of Standard ZIRLO®, denoted as Optimized ZIRLO™. This paper is a continuation of a previous paper reported by Foster *et al.* in 2009, which presented methods used to develop Optimized ZIRLO from Standard ZIRLO. The previous paper only outlined the experimental methods used to determine irradiation creep. This paper presents the detailed methods used to determine in-reactor creep and growth. In additio n, in-reactor creep stress dependence in tension and compression will be evaluated. The results show that the: (1) In-reactor creep compliance is the same in tension and compression and (2) if total in-reactor strain is split into irradiation growth and creep components: (a) Deviatoric hoop stress component and/or the stress difference of hoop minis radial is the driving force for irradiation creep and (b) irradiation creep in tension is the same as compression. These are the first experimental results that explicitly demonstrate the relationship between irradiation creep (or alternately plastic deformation under a neutron flux) with the deviatoric hoop stress component and/or the stress difference of hoop minis radial.

KEYWORDS: irradiation creep, tubing, ZIRLO, stress

Introduction

Fuel operating margins in recent years have decreased due to increases in fuel duty. In response, Westinghouse has developed an improved version of Standard ZIRLO, denoted as Optimized ZIRLO. A previous paper 1 presented the

Manuscript received July 29, 2010; accepted for publication February 6, 2011; published online March 2011.
[1] Fellow Engineer, Westinghouse Electric Company, Columbia, SC 29250, e-mail: fosterjp@westinghouse.com
[2] Manager, Materials and Fuel Rod Design, Westinghouse Electric Company, Columbia, SC 29250.
ZIRLO® is a registered trademark of Westinghouse Electric Company, LLC.

Cite as: Foster, J. P. and Baranwal, R., "ZIRLO® Irradiation Creep Stress Dependence in Compression and Tension," *J. ASTM Intl.*, Vol. 8, No. 3. doi:10.1520/JAI103297.

Copyright © 2011 by ASTM International, 100 Barr Harbor Drive, PO Box C700, West Conshohocken, PA 19428-2959.

TABLE 1—*Material chemistry (weight %) and texture.*

Nb	Sn	Fe	f_{radial}	f_{hoop}	f_{axial}	Contractile Strain Ratio
1.01	1.02	0.10	0.60[a]	0.35[a]	0.05[a]	1.52

[a]The texture measurements were performed on different material lots.

methods used to develop Optimized ZIRLO from Standard ZIRLO. However, the previous paper only outlined the experimental methods used to determine the irradiation creep strains. The purpose of this paper is to document the methods used to determine both in-reactor creep and growth strains, and evaluate in-reactor creep in tension and compression.

Experimental

All of the testing was performed on stress relief annealed Standard ZIRLO (SRA STD ZIRLO). The chemical composition and texture are given in Table 1. The samples were tube sections 168 mm long with dimensions of 9.14 mm outside diameter (OD) × 0.57 mm wall. The irradiation growth samples had holes in the tubing to allow water to flood the samples.

The irradiation creep samples were internally pressurized with He gas at levels above and below system pressure so that the samples were in tension and compression, respectively. The samples were located inside the fuel assembly thimble tubes with segmented insert rods. The segmented insert rods consisted of spacers and the test samples. The spacers were used to locate the samples at axial positions above and below the core mid-plane where the fast flux is approximately constant. In addition, spacers were placed at the axial locations of the fuel rod spacer grids and intermediate flow mixing grids so that the samples were not subject to the flux depression associated with grids. As a result,

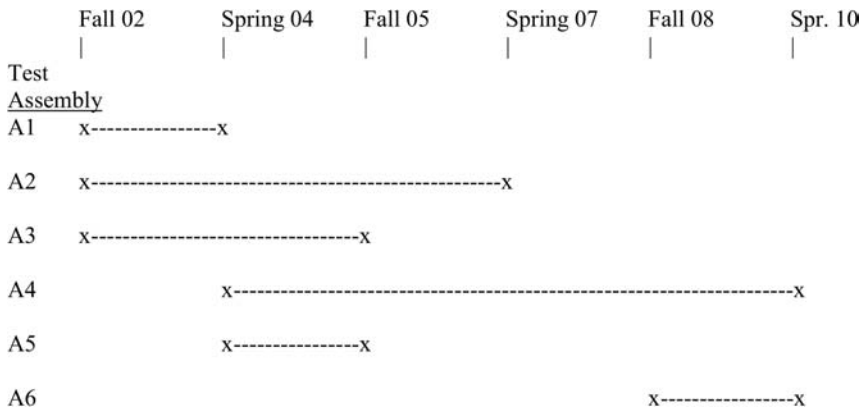


FIG. 1—*Irradiation schedule.*

the samples were located in free-standing axial positions in the constant fast flux location of the core.

Irradiation testing was initiated with three test assemblies in 2002 (see Fig. 1). Two additional test assemblies were subsequently inserted after the completion of one irradiation cycle, and one additional assembly was inserted in 2008. Each test assembly contains sister test samples and is irradiated for a fixed number of cycles so that the irradiation growth and creep can be monitored with increasing fast fluence. The test plan was to irradiate samples up to a maximum of four reactor cycles, which corresponds to an equivalent fuel burnup of about 81 GWd/MTU or a fast fluence of about 15×10^{21} n/cm^2 ($E > 1$ MeV). This paper presents results from some of the samples irradiated in Test Assemblies A1, A5, and A3.

The sample diameter and length was measured using a laser micrometer. The laser measurements were performed both prior to irradiation and after irradiation using the same facility. The diameter measurements were performed over an axial length of 75 mm relative to the sample axial mid-plane. The diameter accuracy of the measurement method was about $+/-0.37$ μm [1].

Data are available for three Test Assemblies. Two of the test assemblies were irradiated for one cycle and one was irradiated for two cycles. Test Assembly A1 was irradiated in Cycle 10, Test Assembly A5 was irradiated in Cycle 11, and Test Assembly A3 was irradiated for Cycles 10 and 11. The samples were irradiated in the temperature range of 302–312°C. Retrospective dosimetry measurements showed that there were no axial or radial fast flux gradients (Ref. [2] presents the Test Assembly A1 data for Cycle 10). The cycle-to-cycle fast fluxes are relatively constant and range between $9.3–9.7 \times 10^{13}$ n/cm^2 s ($E > 1$ MeV).

The sample stresses were calculated from the internal He gas temperature. The internal He gas temperature was determined from the calculated coolant temperature and the gamma heat generation rate. The coolant temperatures were calculated based on post-cycle inlet and outlet temperatures, and post-cycle fuel assembly powers. The gamma heat generation rate was determined using the $\Delta D/D_o$ data (with samples from the same ingot and lot) with two different types of internal mandrels. This is an indirect method of determining the gamma heat generation rate. The direct measurement method using thermocouples, which is performed in test reactors, could not be used. The samples contain internal mandrels to provide support in the event of sample collapse. Sample collapse has not been observed. The internal mandrels were placed concentrically inside the samples. Two types of internal mandrels were used. The types were solid cylinders and smaller diameter tubes. The solid cylinder and tube internal mandrels had significantly different mass values. The solid cylinder internal mandrel generated more heat than the tube internal mandrel. Further, the solid cylinder internal mandrel samples had a larger He gas gap between the internal mandrel OD and the sample ID, thereby reducing the heat flux and increasing the internal sample temperatures. The internal heat generation produces the gas internal temperature. The gas internal temperature, in turn, results in the internal gas pressure, which in turn with the coolant temperature determines the stresses. The $\Delta D/D_o$ in turn, depends on the hoop stress.

As a result, the measured $\Delta D/D_o$ is directly dependent on the gamma heat generation rate.

The method used to determine the gamma heat generation rate will be illustrated with the Test Assembly A1 data. Figure 2 presents the measured $\Delta D/D_o$ versus the deviatoric hoop stress component (the use of the deviatoric hoop stress component will be explained below). The deviatoric hoop stress component range of the data is from about −42 to +51 MPa (this corresponds to a hoop stress range of about −95 to +80 MPa). This range approximately envelopes the range of hoop stresses experienced by fuel rods during normal operation. Each marker in Fig. 2 represents one sample. Most of the stress levels include duplicate samples to confirm strain level consistency. Figure 2 shows that duplicate sample scatter is very small. Further, Fig. 2 shows that the data are very consistent from stress level-to-stress level.

The principal stresses were calculated using the thick-wall equations at the tube mid-wall [3]. The thick-wall equations were used because the tubing deviates about 7–8 % from the thin-wall approximation. The equations are

$$\sigma_\theta = [p_i - p_o][(a^2 \quad /(b^2 - a^2)][1 + 4b^2/(a+b)^2] - p_o \tag{1}$$

$$\sigma_r = [p_i - p_o][(a^2 \quad /(b^2 - a^2)][1 - 4b^2/(a+b)^2] - p_o \tag{2}$$

$$\sigma_z = [p_i - p_o][(a^2 \quad /(b^2 - a^2)] - p_o \tag{3}$$

where p_i and p_o are the internal and external pressures, and a and b are the inside and outside radii. The stress matrix may be separated into two parts. One part is the hydrostatic stress which causes elastic dilation. The hydrostatic stress is given by [3]

$$\sigma(\text{hydrostatic}) = (\sigma_\theta + \sigma_r + \sigma_z)/3 \tag{4}$$

The second part of the stress matrix is the deviatoric stress matrix which causes elastic distortion and plastic strain. The deviatoric hoop stress component, σ_θ (deviatoric), is 3

$$\sigma_\theta = \sigma_\theta(\text{deviatoric}) + \sigma(\text{hydrostatic}) \tag{5}$$

Figure 2 shows that the irradiation creep strain behavior is linear as a function of the deviatoric hoop stress component. Linear regression statistics were used to determine the gamma heat generation rate. The best fit of the data is given by the highest value of the R^2 coefficient. The hoop stress values were calculated for different gamma heat generation rates that enveloped the actual value. Figure 3 shows, for the Test Assembly A1 data, that a gamma heat rate of 1.42×10^{10} cal/h m^3 results in the highest value of the R^2 coefficient. This gamma heat generation rate was used to calculate the sample internal pressures and stresses. Figure 2 shows the Test Assembly A1 regression fit associated with the gamma heat generation rate. Similar calculations were also performed for Test Assemblies A5 and A3.

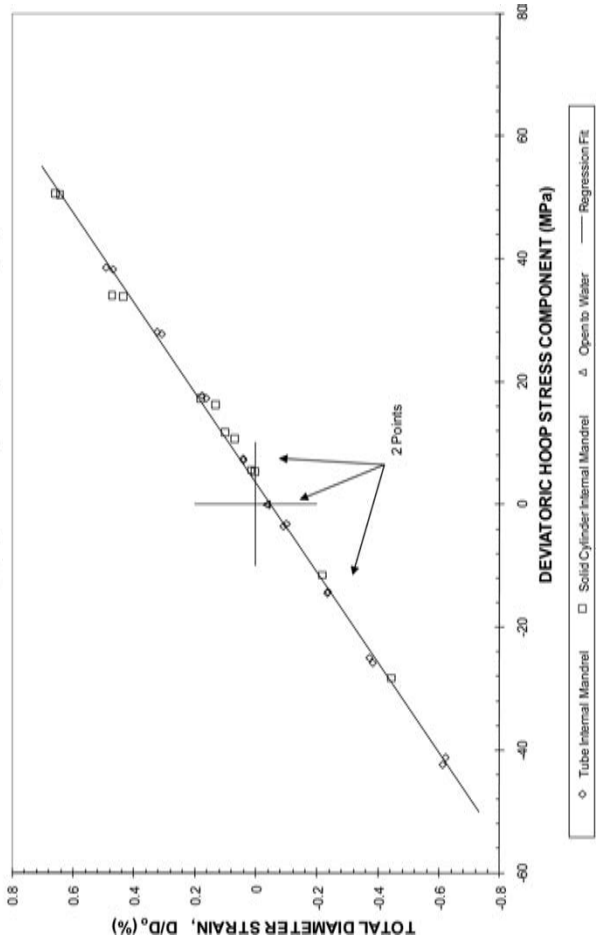


FIG. 2—*Total diameter strain versus deviatoric hoop stress component for Test Assembly A1 irradiated for one cycle (Cycle 10).*

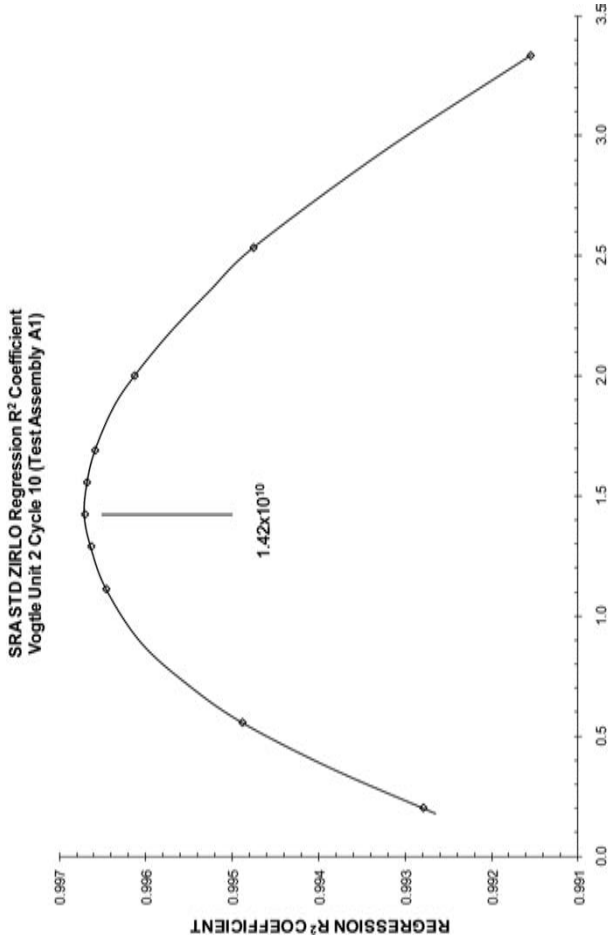


FIG. 3—*Regression R^2 coefficient versus the gamma heat generation rate for Test Assembly A1.*

Results and Discussion

The irradiation creep data will be presented using two representations. The first representation will be the total diameter strain versus the deviatoric hoop stress component. The second way will be to split the total diameter strain into irradiation growth and irradiation creep components according to

$$\Delta D/D_o = \Delta D/D_o(\text{irradiation growth}) + \Delta D/D_o(\text{irradiation creep}) \qquad (6)$$

and then evaluate the irradiation creep strain versus the deviatoric hoop stress component and the stress difference of hoop minis radial.

Figures 2,4, and 5 present the total diameter strain versus the deviatoric hoop stress component for Test Assemblies A1, A5, and A3, respectively. The total strain compliance is the slope of the data in Figs. 2,4, and 5. Figures 2,4, and 5 show that the data are linear over the entire stress range. Hence, the total strain compliance is the same in tension and compression. Note that every sample in Figs. 2,4, and 5 was subject to the exact same irradiation parameters (that is, the same power history, relative temperatures (and therefore stresses) and external pressures). Further, a comparison of Figs. 2 and 4 shows that total diameter strain versus the deviatoric hoop stress component data are approximately the same. This shows that the diameter strains are reproducible in different reactor cycles (that is, Cycles 10 and 11).

The second method is an evaluation of the diameter irradiation creep strain versus the deviatoric hoop stress component and the hoop stress minis the radial stress. In order to perform this evaluation, the irradiation growth must be determined. The irradiation growth strain method will be illustrated using the Test Assembly A1 data. Figure 6 presents the total diameter strain for Test Assembly A1 versus the pressure difference (that is, the internal/external pressure difference). Figure 6 shows that the total diameter strain versus the pressure difference is linear. Since the data are linear, the data were fit to a linear equation by regression analysis. The regression line crosses the total diameter strain axis at approximately the same strain as the two samples open to water (see Fig. 6). The regression fit $\Delta D/D_o$ was taken as the irradiation growth strain because the regression fit to 30 samples statistically is more accurate than using the two samples open to water.

Figure 7 presents the irradiation creep diameter strain versus the total hoop stress. The data are linear and were fit by linear regression. The result is reasonable for tension stresses (positive stresses) and compression stresses below a stress level of about −16 MPa. In the case of tension stresses, the irradiation creep diameter strains are positive, which is reasonable. In the case of compression stresses greater than −16 MPa, the irradiation creep diameter strains are negative, which is reasonable. However, in the total hoop stress region from 0 to −16 MPa (see the dashed line in Fig. 7), compression stresses result in positive irradiation creep diameter strains. Although this result is technically correct, the result is physically unreasonable. Therefore, the total hoop stress is not the driving force for irradiation creep. This unreasonableness is best illustrated by considering the irradiation creep diameter strain versus the pressure

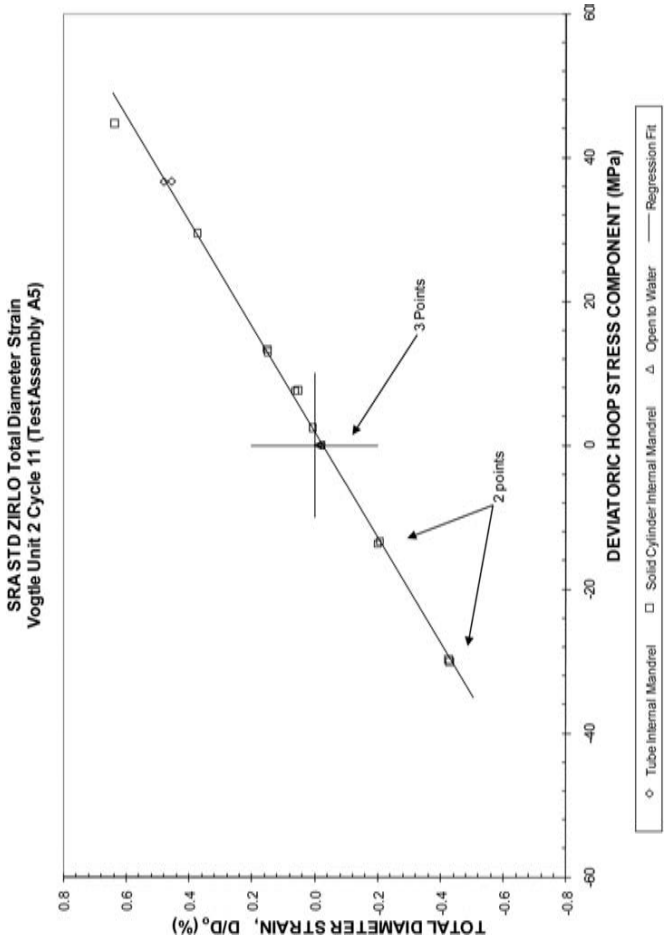


FIG. 4—*Total diameter strain for Test Assembly A5 irradiated for one cycle (Cycle 11).*

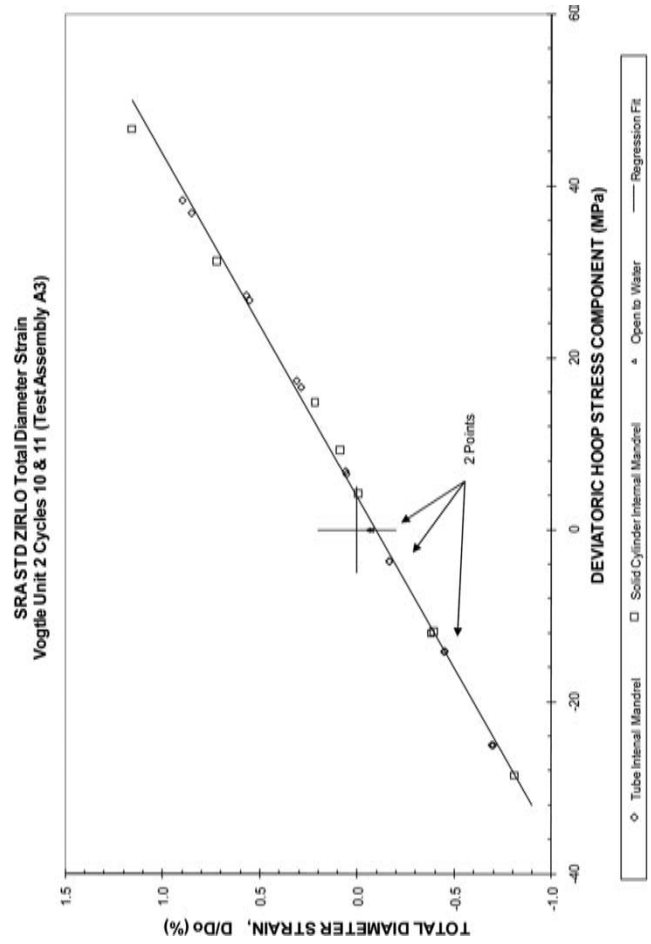


FIG. 5—*Total diameter strain versus deviatoric hoop stress component for Test Assembly A3 irradiated for two cycles (Cycles 10 and 11).*

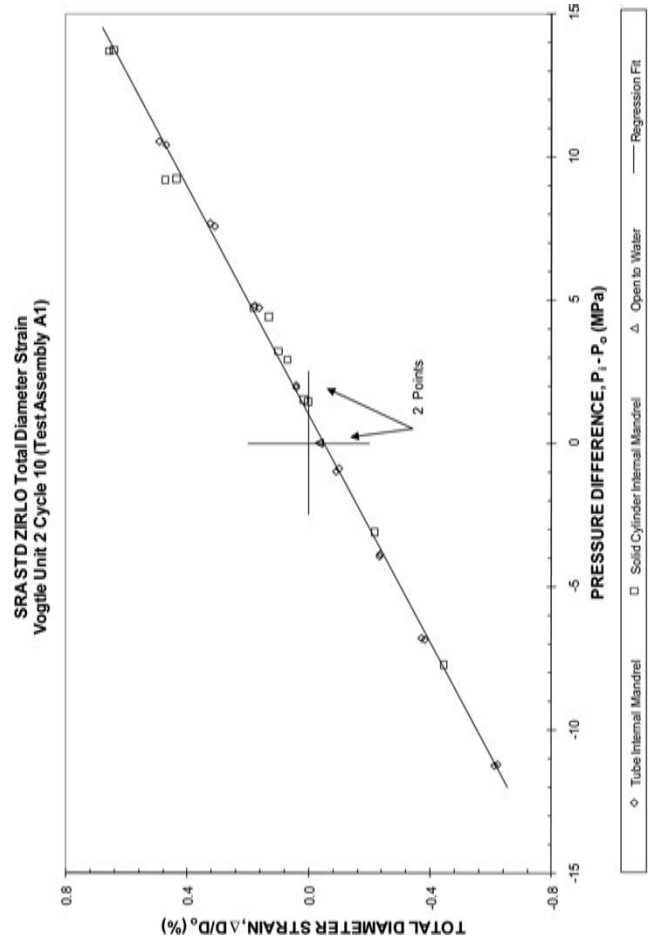


FIG. 6—*Total diameter strain versus the pressure difference for Test Assembly A1 irradiated for one cycle (Cycle 10).*

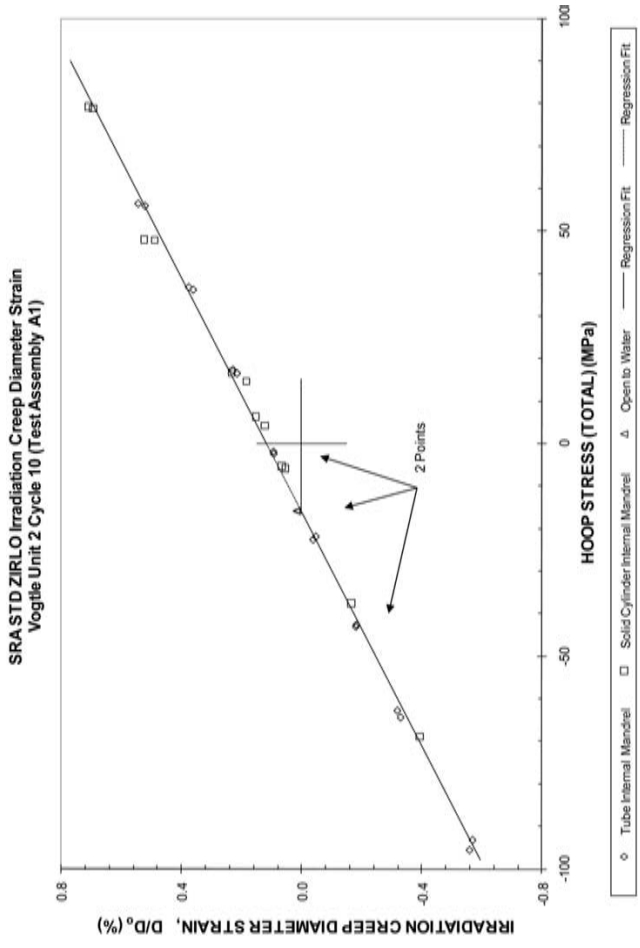


FIG. 7—*Irradiation creep diameter strain versus the total hoop stress for Test AssemblyA1 irradiated for one cycle (Cycle 10).*

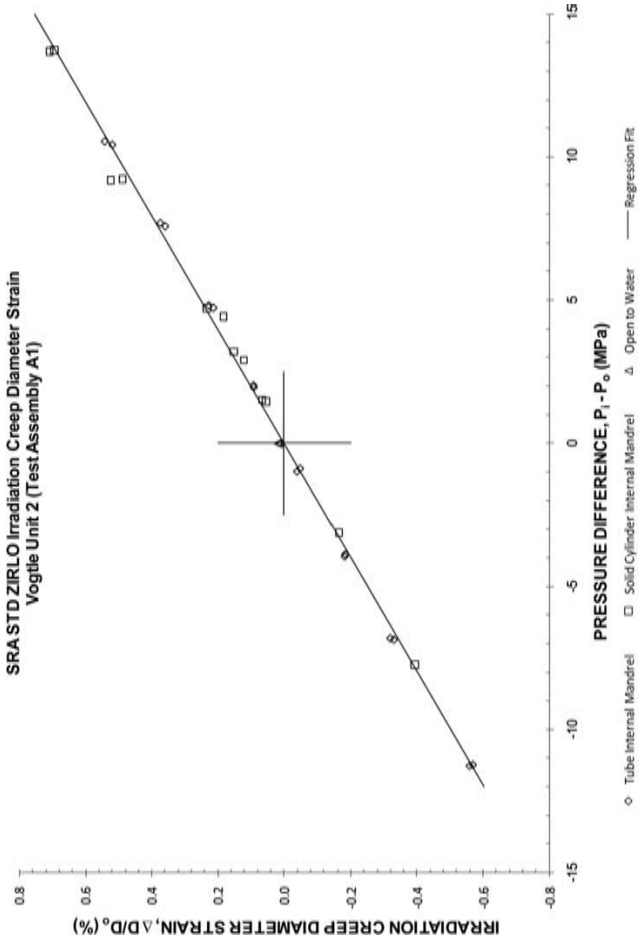


FIG. 8—*Irradiation creep diameter strain versus the pressure difference for Test Assembly A1 irradiated for one cycle (Cycle 10).*

difference, as shown by Fig. 8. Figure 8 shows for a positive pressure difference (that is, the internal pressure is greater than the external pressure) the irradiation creep diameter strain is positive. Figure 8 shows for a negative pressure difference (that is, the internal pressure is less than the external pressure) the irradiation creep diameter strain is negative. In addition, the regression fit passes through the point (0,0). These results are physically reasonable.

The following figures will present the irradiation creep diameter strain versus (1) the deviatoric hoop stress component and (2) the stress difference of hoop minis radial [4]. The deviatoric hoop stress component was selected because it describes the out-reactor plastic deformation strains (including creep) in metals and alloys. The hoop stress minis the radial stress was selected because it has been shown to describe the creep rupture time and diameter rupture strain of un-irradiated and post-irradiated Zr-4. Note that according to Fig. 8 the regression fits to the irradiation creep diameter strain versus each of these stress parameters is required to pass through the origin. The following figures will show that this requirement is satisfied by each of the selected stress parameters.

Figure 9 presents the irradiation creep diameter strain versus the deviatoric hoop stress for Test Assembly A1 that was irradiated for one cycle in Cycle 10. Note that every sample in Fig. 9 and all subsequent figures was subject to the exact same irradiation parameters (that is, the same power history, relative temperatures (and therefore stresses) and external pressures). The data are linear and were fit using linear regression. Note that the data and regression fit pass through the origin, and that the two samples open to water are at the origin. This result is physically reasonable. That is, tension stresses result in positive strains, and vice versa. Further, the diameter strain in tension is the same as in compression. For example, this result can be obtained by comparing the diameter strains at +40 and −40 MPa. Hence, irradiation creep in tension is the same as in compression.

Figure 10 presents the Test Assembly A1 irradiation creep diameter strain versus the stress difference of hoop minis radial. The results are the same as for the deviatoric hoop stress component. That is, the data are linear, were fit using linear regression, the data and regression fit pass through the origin and show that irradiation creep in tension and compression are the same.

Figures 11 and 12 present the irradiation creep diameter strain versus the deviatoric hoop stress component for Test Assembly A5 irradiated for one cycle in Cycle 11 and Test Assembly A3 irradiated for two cycles in Cycles 10 and 11, respectively. The results are the same as described for Fig. 9. That is, the data are linear, were fit using linear regression, the data and regression fit pass through the origin and show that irradiation creep in tension and compression are the same. Further, a comparison of Figs. 9 and 11 shows that the irradiation creep diameter strain versus deviatoric hoop stress component data are approximately the same. This shows that the diameter strains are reproducible in different reactor cycles (that is, Cycles 10 and 11).

Figures 13 and 14 present the Test Assemblies A5 and A3 irradiation creep diameter strain versus the stress difference of hoop minis radial. The results are the same as for the deviatoric hoop stress component. That is, the data are

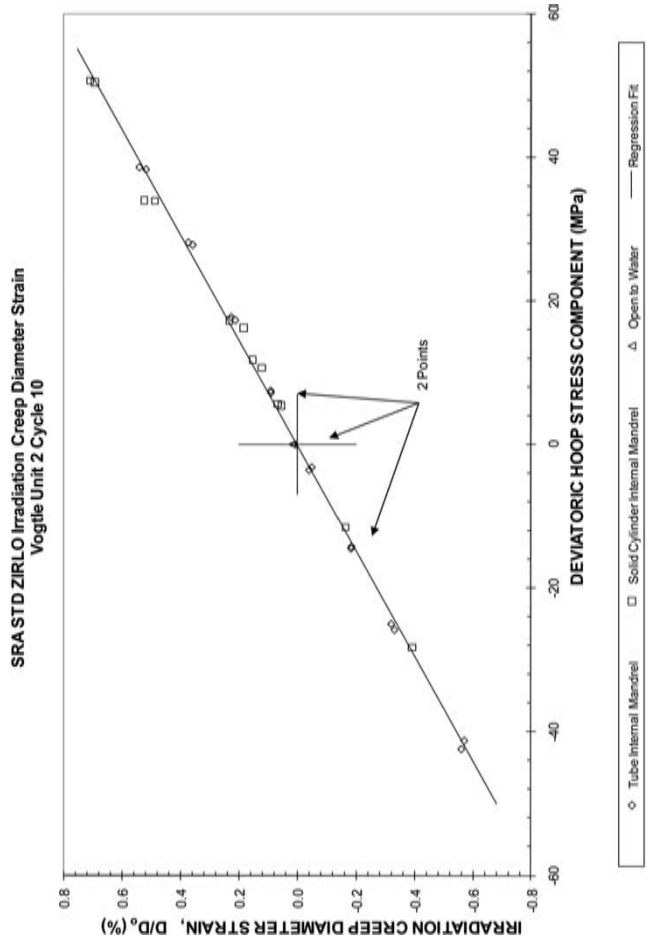


FIG. 9—*Irradiation creep diameter strain versus the deviatoric hoop stress component for Test Assembly A1 irradiated for one cycle (Cycle 10).*

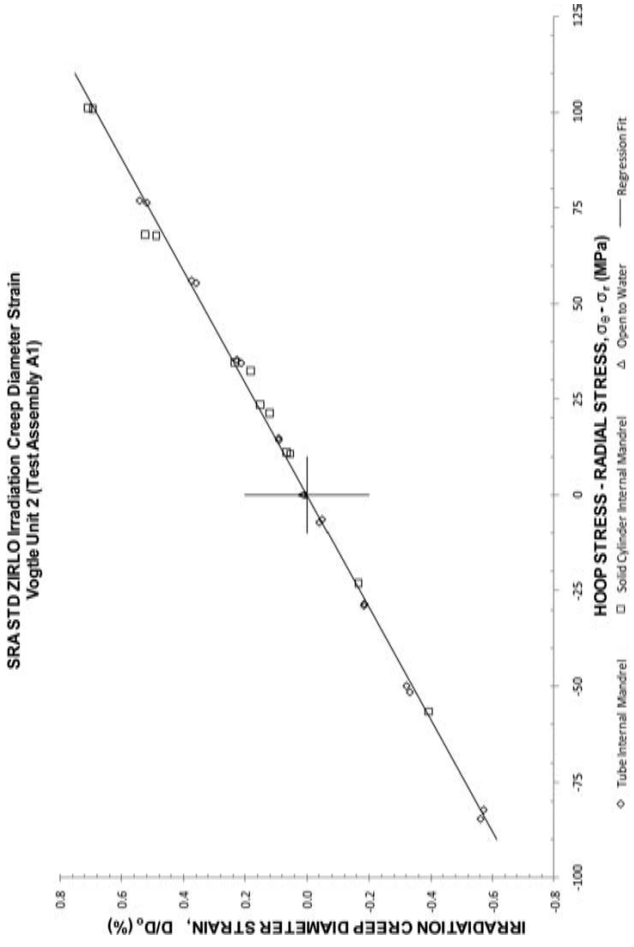


FIG. 10—*Irradiation creep diameter strain versus the stress difference of hoop minis radial for Test Assembly A1 irradiated for one cycle (Cycle 10).*

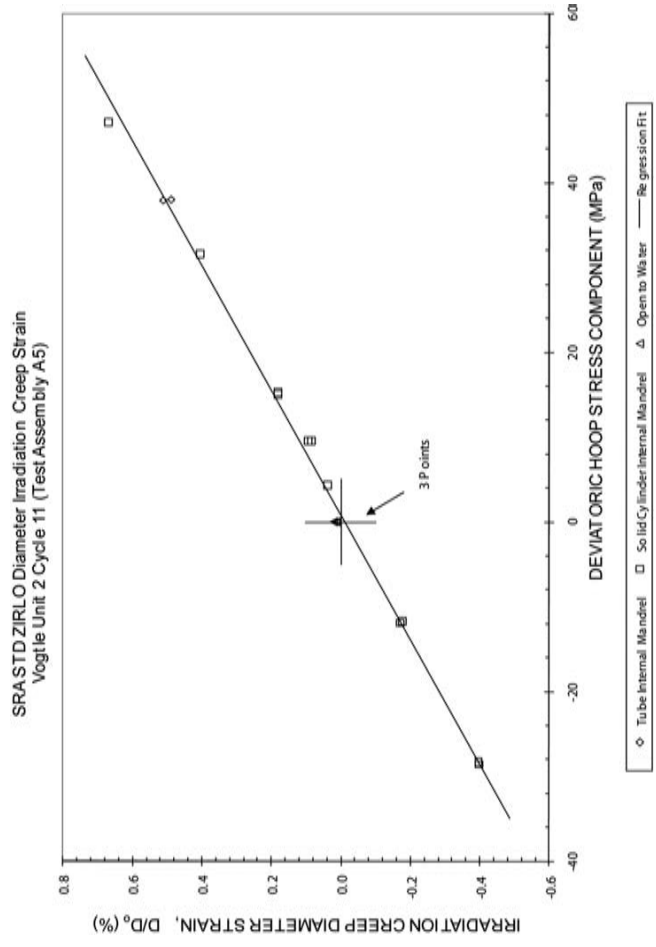


FIG. 11—*Irradiation creep diameter strain versus the deviatoric hoop stress component for Test Assembly A5 irradiated for one cycle (Cycle 11).*

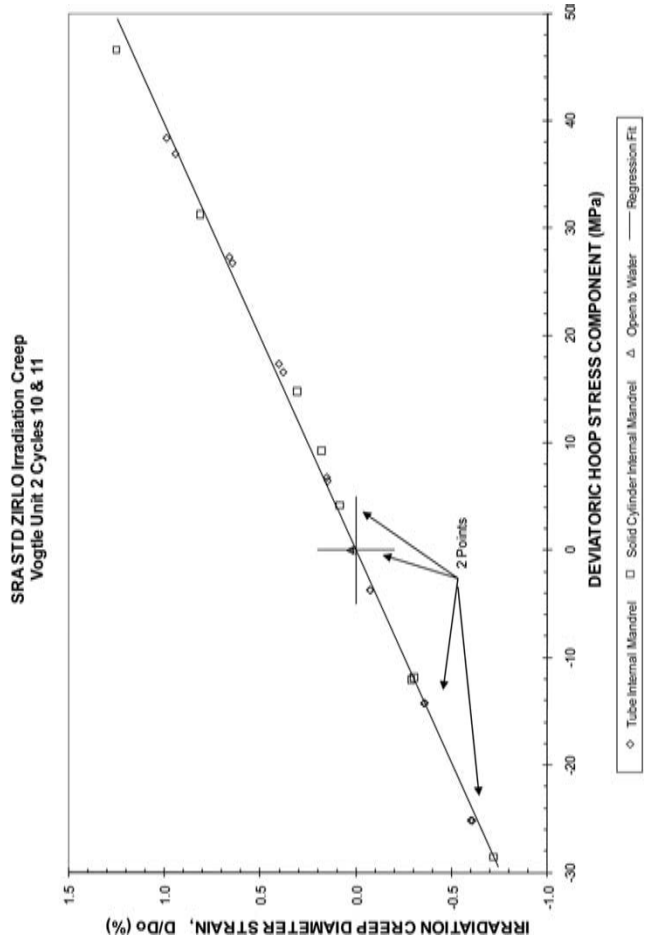


FIG. 12—*Irradiation creep diameter strain versus the deviatoric hoop stress component for Test Assembly A3 irradiated for two cycles (Cycles 10 and 11).*

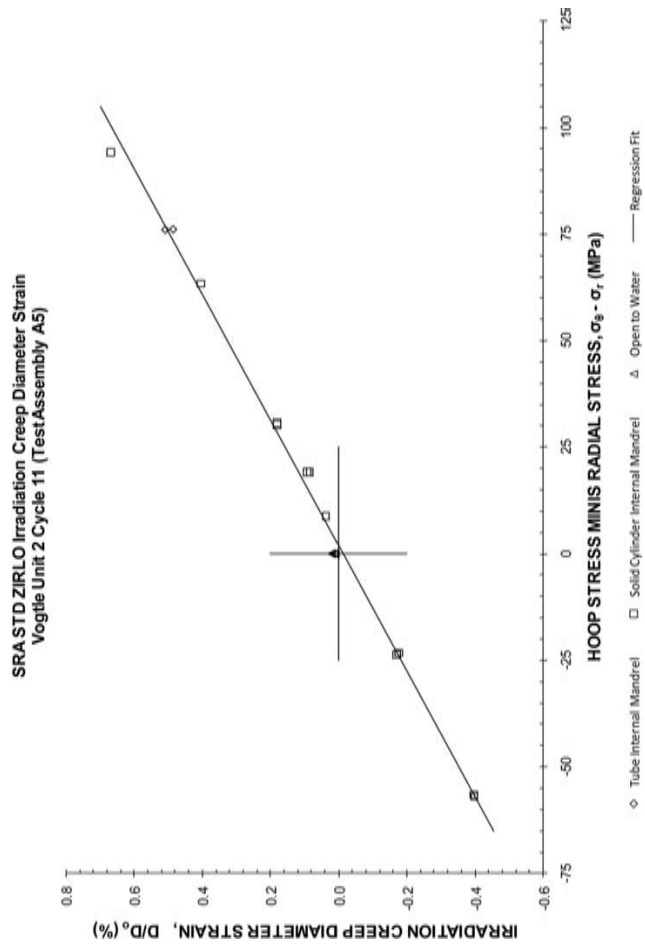


FIG. 13—*Irradiation creep diameter strain versus the stress difference of hoop minis radial for Test Assembly A5 irradiated for one cycle (Cycle 11).*

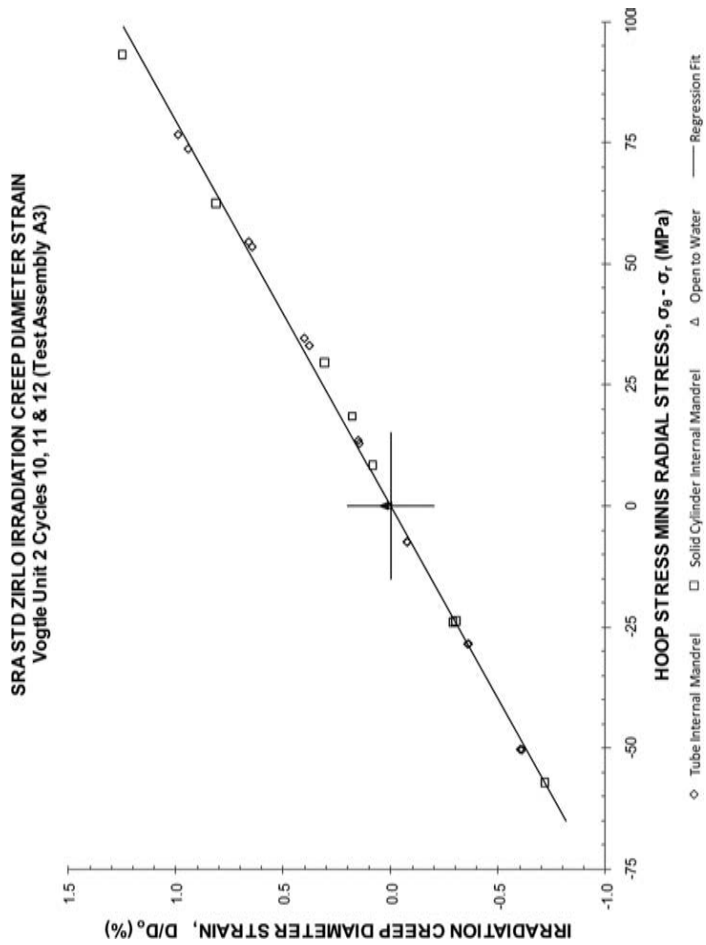


FIG. 14—*Irradiation creep diameter strain versus the stress difference of hoop minis radial for Test Assembly A3 irradiated for two cycles (Cycles 10 and 11).*

linear, were fit using linear regression, the data and regression fit pass through the origin and show that irradiation creep in tension and compression are the same.

Any statement regarding irradiation creep in tension versus compression needs to be qualified regarding the technical basis. This will be illustrated with the Test Assembly A1 data. Figures 9 and 10 show when the total diameter strain is split into irradiation growth and irradiation creep components, that irradiation creep in tension is the same as in compression. Consider Fig. 2, which presents the data as the total diameter strain versus the deviatoric hoop stress component. At stress levels of +40 and −40 MPa, note that the diameter strain in tension is less than the diameter strain in compression. Hence, for this representation, irradiation creep in tension is less than compression. On the other hand, consider Fig. 7. At stress levels of +50 and −50 MPa, note that irradiation creep diameter strain in tension is greater than in compression. Hence, for this representation irradiation creep in tension is greater than compression. As a result, any discussion of creep in tension versus compression needs to be qualified with the technical basis.

Conclusions

The following conclusions can be reached based on the results and discussion:

(1) In-reactor creep compliance is the same in tension and compression; and
(2) If total in-reactor strain is split into growth and creep components:
    (a) Deviatoric hoop stress component and/or the stress difference of hoop minis radial is the driving force for irradiation creep, and
    (b) Irradiation creep in tension is the same as compression.

These are the first experimental results that explicitly demonstrate the relationship between irradiation creep (or alternately plastic deformation under a neutron flux) with the deviatoric hoop stress component and/or the stress difference of hoop minis radial.

Acknowledgments

The coolant temperature analysis and sample temperature calculations were performed by John Killimayer and David Rumschlag/Westinghouse. Westinghouse is grateful to Southern Nuclear Operating Co. for irradiation of the test. The contributions of Richard Loftin, Ken Turnage, and the Vogtle site staff are greatly appreciated. The authors greatly appreciate the assistance of Nicolas Christodoulou/CNSC for technical assistance during all aspects of the program including design review, experimental measurement methods, evaluation and interpretation of the data while at AECL. The sample diameter, length and oxide thickness measurements were performed by Frank Butcher and Allan MacCormack/AECL. Manuscript discussions with Malcolm Griffiths and Grant Bickel/AECL are gratefully acknowledged.

References

[1] Foster, J. P., Yueh, H. K., and Comstock, R. J., "ZIRLO Cladding Improvement," *ASTM STP 1505*, B. Kammenzind and M. Limback, Eds., ASTM International, West Conshohocken, PA, 2009, pp. 457–469.

[2] Greenwood, L. R. and Foster, J. P., "Retrospective Reactor Dosimetry with Zirconium Alloy Samples in a PWR," *Proceedings of the 13th International Symposium on Reactor Dosimetry, State of the Art 2008 Reactor Dosimetry*, W. Voorbraak, L. Debarberis, P. D'Hondt, and J. Wagemans, Eds., Akersloot, The Netherlands, May 25–30, 2008, World Scientific Publishing Co., Singapore, 2009.

[3] Lin, T. H., *Theory of Inelastic Structures*, John Wiley and Sons, New York, 1968.

[4] Limon, R. and Lehmann, S., "A Creep Rupture Criterion for Zircaloy-4 Fuel Cladding Under Internal Pressure," *J. Nucl. Mater.*, Vol. 335, 2004, pp. 322–334.

DISCUSSION

Question 1, P. Barberis, AREVA:—1) Does the stress relate to mean stress or mid-wall stress? 2) Was the creep anisotropy measured (that is, the length change)? 3) Were the hydrogen (hydride) and oxide layer induced strains accounted for?

Author's Response:—1) The thick-wall equations for the hoop, radial and axial stresses are given in the paper. The reported hoop and radial stresses are the mid-wall values. The axial stress is not tube wall position dependent.

2) The length changes were measured on all samples. A separate paper is planned to describe the results.

3) The oxide thickness was measured on each sample and subtracted from the measured outside diameter (OD).

Question 2, David Dye, Imperial College:—The scatter in the data seems rather low, which is very promising from a modeler's point of view. What was the scatter in the 420 measurements per sample and what are the heat-to-heat and station-to-station variations?

Author's Response:—A statistical evaluation of the 420 OD measurements resulted in an OD measurement accuracy of +/– 0.11 μm as reported in the paper. The resulting experimental accuracy of (D – Do)/Do is smaller than can be presented on the Figures. Hence, no error bars are presented for the da. A separate paper is planned to describe the results.ta points.

All of the measurements presented in the paper were performed on the same heat (ingot) and material lot. Measurements have been performed on other material lots. A separate paper is planned to describe the results.

Question 3, Suresh Yagnik, EPRI:—1) The external pressure on your samples is the coolant pressure in the reactor, which varies through the cycle. How do you account for this in calculating the local stress at a given axial position for each sample? 2) How was each diametral strain datum deduced? 3) Did you consider any temperature drop within the stagnant gas layer over the gamma heating source inside the tube?

Author's Response:—1) The external pressure remains constant during the cycle. The pressure of 2250 psi in the pressurizer is continuously measured during the cycle and the variation is less than 1 psi. The local pressure in the fuel assembly is slightly higher and is a function of axial position. The stress of each sample was calculated using the local pressure (that is, the pressure in the fuel assembly at the axial position of the test sample).

2) OD measurements were performed around the tube circumference at the sample axial mid-plane and at locations of +/–.27, +/–2.54 and +/–3.81 mm relative to the axial mid-plane.

3) The reported average mid-wall tube temperatures presented in the paper are based on the calculated radial temperature profile. In the case of the samples with the solid cylinder internal mandrels, from the tube sample OD to the radial center the calculations include: the tube wall thickness, the He gas annulus and the internal mandrel wall thickness. In the case of the samples with the tube internal mandrels, from the tube sample OD to the radial center the calculations include: the tube wall thickness, the He gas annulus, the internal mandrel wall thickness and the He gas inside the tube internal mandrel. These calculations were performed for each sample.

Reprinted from JAI, Vol. 8, No. 3
doi:10.1520/JAI103770
Available online at www.astm.org/JAI

Margaret A. McGrath[1] *and Suresh Yagnik*[2]

Experimental Investigation of Irradiation Creep and Growth of Recrystallized Zircaloy-4 Guide Tubes Pre-Irradiated in PWR

ABSTRACT: Re-crystallized Zircaloy-4 guide tubes were irradiated in commercial pressurized water reactors (PWRs) at three different temperatures to fluences near 1×10^{22} n/cm^2 E>1 MeV (15 displacements per atom), resulting in moderate corrosion and three different hydrogen contents (approximately 135, 240, and 700 parts per million). Sections of the guide tubes were re-irradiated in the Halden reactor to assess the irradiation creep and growth behaviors. Three conditions were applied: Bellows-loaded axial compression creep; zero stress growth; and zero stress, zero flux (control specimens). The guide tube sections were re-irradiated under simulated PWR conditions by utilizing a pressurized light water loop operating with normal PWR water chemistry at approximately 320C. Axial length changes were measured in-reactor by linear variable differential transformers (LVDTs), and post-irradiation hot cell measurements were done to confirm the LVDT elongation measurements. After minor corrections were made to account for reactor testing variables, it was shown that the LVDT measurements were accurate, thus creep and growth or free growth rates were established for each guide tube section. Hot cell examinations were also performed to establish the state of corrosion of each specimen, including hydrogen content, both before and after the re-irradiation in the Halden reactor. The results showed that stress free irradiation growth was different for each specimen and correlated

Manuscript received January 15, 2011; accepted for publication January 31, 2011; published online March 2011.
[1] OECD Halden Reactor Project, Os Alle 5, P.O. Box 173, NO-1751 Halden, Norway, e-mail: maggs@hrp.no
[2] Electric Power Research Institute, Inc., 3412 Hillview Ave., Palo Alto, CA 94304-1338, e-mail: syagnik@epri.com

Cite as: McGrath, M. A. and Yagnik, S., "Experimental Investigation of Irradiation Creep and Growth of Recrystallized Zircaloy-4 Guide Tubes Pre-Irradiated in PWR," *J. ASTM Intl.*, Vol. 8, No. 3. doi:10.1520/JAI103770.

Copyright © 2011 by ASTM International, 100 Barr Harbor Drive, PO Box C700, West Conshohocken, PA 19428-2959.

qualitatively with the hydrogen content and commercial irradiation temperatures of the guide tubes. The higher hydrogen content, or higher commercial irradiation temperature, gave rise to higher subsequent growth rates. After subtracting the growth strain from the measured creep and growth strain values, the magnitude of creep and creep rates were essentially the same for all specimens: No effect of commercial reactor irradiation temperature or hydrogen content was observed. The results give important new data on irradiation creep and growth and on the correlation between hydrogen content and irradiation temperature on growth rates.

KEYWORDS: guide tube, irradiation creep, irradiation growth, Zircaloy-4

Introduction

Excessive creep and growth of zirconium alloy structural components during service can lead to the occurrence of incidents such as incomplete control rod insertion (IRI) in pressurized water reactors (PWRs) due to guide tube bowing or channel bow in boiling water reactors (BWRs). The phenomenon of IRI has had attention from the nuclear industry [1–6] and several national regulatory authorities, including the USNRC [7,8] because of potential safety implications as well as the economic implications. Although industry has implemented interim engineering and design solutions to address immediate concerns, fundamental understanding of how and why certain parameters affect the irradiation creep and growth of zirconium alloys is lacking.

Several factors have been identified that may influence both phenomena, including the presence of an axial force (compressive load), the material fabrication route, the state of hydriding and oxidation of the component in question as well as the operation temperature, and fast neutron fluence to which the material has been exposed [9]. In order to study the effect of some of these factors, the Nuclear Fuel Industry Research (NFIR) program commissioned an in-pile creep and growth test at the Halden reactor on pre-irradiated guide tube segments, offered by program members. This test was also to provide data regarding axial creep and growth *rates* for comparison with existing design and performance models of guide tubes in PWRs. The experimental approach used was a first of a kind in-pile test combining online, in situ length monitoring with axial compression of open-ended tube samples.

Guide tube segments were selected for testing on the basis of having different levels of oxidation/hydrogen pick-up from their respective base irradiations, but similar levels of fast neutron fluence, on the order $1 \times 10^{22}\,\mathrm{n\,cm^2}$ ($E > 1\,\mathrm{MeV}$). In-pile elongation data were subsequently obtained from nine guide tube specimens, over a period of five Halden reactor cycles, tested under prototypical PWR thermal-hydraulic and chemistry conditions with different axial load and neutron flux levels. Based on extensive material and specimen characterizations, an assessment of the creep and growth behavior of Zircaloy-4 guide tube material has been made.

Materials and Experimental Methods

Guide Tube Material

Six test specimens were made from guide tube segments provided by Westinghouse ($\bar{W}$), sectioned from different axial locations of guide tubes extracted from two different fuel assemblies that had exhibited IRI in a PWR in the United States. Another six test specimens were made from guide tube segments provided by EDF/Fragema (F), taken from the same axial position of different guide tubes all from the same fuel assembly irradiated for four cycles in a French PWR. A summary of the base irradiation conditions is given in Table 1.

All the guide tubes were re-crystallized Zry-4 (675°C for 2 h for the $\underline{W}$-guide tubes and 650°C for 3 h for the F-guide tubes), resulting in an ASTM grain size of 11 μm. The texture of the $\underline{W}$-guide tubes was: $F_r = 0.674$, $F_{\text{hoop}} = 0.277$, $F_z = 0.049$, whereas the texture of the F-guide tubes was: $F_r = 0.667$, $F_{\text{hoop}} = 0.241$, and $F_z = 0.092$.

The hydrogen content and oxide thickness of each test specimen was also determined and is reported later (Table 1), but in essence three different types of material were available for testing, the main differences between them being:

- $\underline{W}1$ Zry-4 with medium hydrogen content after base irradiation;
- $\underline{W}2$ Zry-4 with high hydrogen content after base irradiation; and
- F relatively high tin (1.49 wt%) Zry-4 with low hydrogen after base irradiation.

Test Rig and Instrumentation

A schematic of the test rig is shown in Fig. 1. The 12 guide tube specimen assemblies were supported on a test rig structure, housed in a pressure flask, distributed over four different axial locations, connected to one of the pressurized light water loop systems in the Halden reactor (Halden BWR (HBWR)). This arrangement enabled the test to be performed under PWR thermal-hydraulic and water chemistry conditions. The pressure flask was positioned in the reactor such that the lower half was located within the active core and the upper-half was above the core. The lower half of the flask was also surrounded by twelve highly enriched fuel rods or "booster rods" in order to provide a high fast neutron flux over six of the installed specimens (placed in Cluster 1 and Cluster 2). The other six specimens, in the upper-half of the flask, were outside of the fast flux region (in Cluster 3 and Cluster 4) and were thus only subjected to thermal effects.

Apart from fulfilling the objective of collecting basic irradiation creep and growth data for Zircaloy-4, placement of the different materials within the rig was also aimed at revealing any influence of hydrogen on creep and growth behavior. The segments were thus positioned in the four different axial clusters in the experimental test rig as follows:

- Cluster 1 (bottom): In order to investigate length changes due to irradiation creep and growth as well as thermal creep, specimens loaded in compression to 40 MPa of each material type were placed in the lower cluster in the high fast flux region of the test rig;

TABLE 1—*Summary of guide tube segment material characterization.*

			From Base Irradiation				Post HBWR		Increase After Six Cycles in HBWR	
Cluster	Halden ID	Material Type	Fluence ($E > 1$ MeV) (n cm^{-2})	Irradiation Temp (°C)	Oxide (μm)	H (ppm)	Oxide (μm)	H (ppm)	Oxide (μm)	H (ppm)
1	653-1	W1	1.05×10^{22}	307	6	250	19	362	13	112
	653-2	W2	1.00×10^{22}	321	18	600	31	850	13	250
	653-3	F	0.96×10^{22}	295–300	7	135	21	219	14	84
2	653-4	W1	1.05×10^{22}	307	6	225	22	340	16	115
	653-5	W2	1.00×10^{22}	321	21	800	36	888	15	88
	653-6	F	0.96×10^{22}	295–300	6	135	22	229	16	94
3	653-7	F	0.96×10^{22}	295–300	8	140	14	...	6	...
	653-8	W2	1.00×10^{22}	321	20	699	26	...	6	...
	653-9	F	0.96×10^{22}	295–300	8	142	14	...	6	...
4	653-10	W2	1.00×10^{22}	321	19	745	...	...	...	...
	653-11	F	0.96×10^{22}	295–300	7	141	...	...	...	...
	653-12	F	0.96×10^{22}	295–300	7	146	...	...	...	...

Note: Destructive PIE not performed on specimens from Cluster 4 due to lack of in-pile elongation data from these specimens.

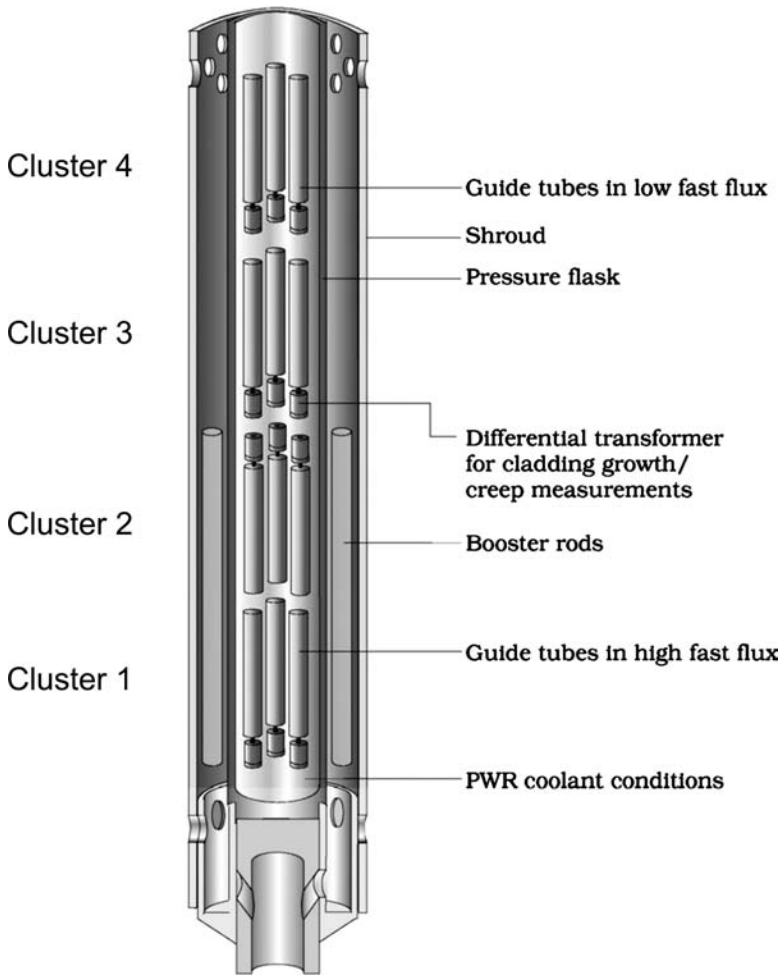


FIG. 1—*Schematic of the test rig layout.*

- Cluster 2 (lower-middle): In order to investigate length changes due to irradiation induced growth alone, unstressed samples of each material type were placed in the upper cluster in the high fast flux region of the test rig;
- Cluster 3 (upper-middle): In order to monitor any unexpected behavior due to the specimen assembly design, unstressed, control samples of *F* and W2 were placed in a cluster above the active core i.e., in the zero fast flux region of the test rig; and
- Cluster 4 (top): In order to provide data on thermal creep of guide tube material, compressive loads of 40, 60, and 80 MPa were applied to samples of *F* and W2 in a cluster above the active core, i.e., in the zero fast flux region of the test rig.

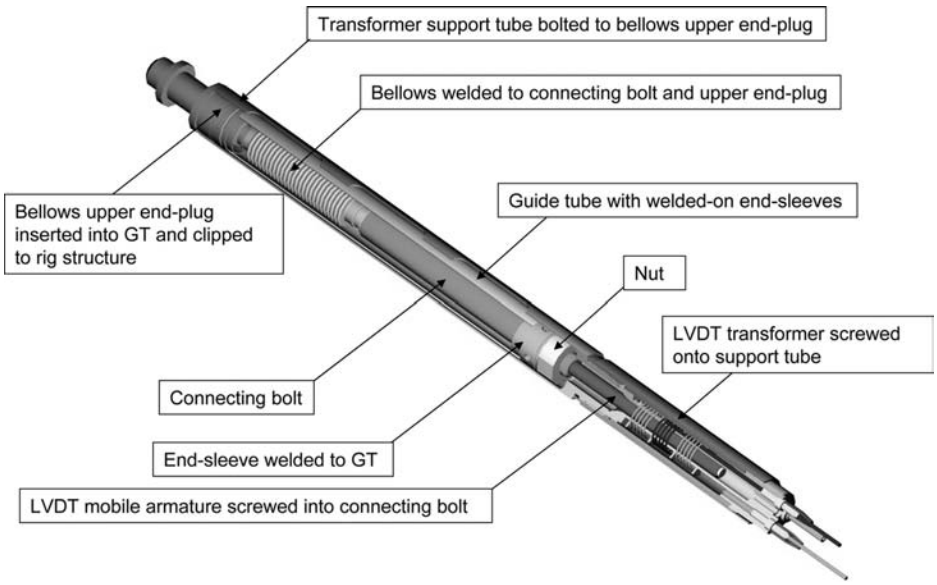


FIG. 2—*Isometric drawing of a guide tube specimen assembly with a bellows loading unit for applying a 40 MPa compressive load (as used in Cluster 1 and Cluster 4).*

The test rig structure also included coolant thermocouples, one placed at each cluster position and one each at the test section inlet and outlet. Other thermal-hydraulic conditions for the test were monitored by a pressure sensor and a flow meter in the loop system. The thermal neutron flux in the booster fuel region of the rig was monitored by two Va self-powered neutron detectors: One centered axially on Cluster 1 and the other on Cluster 2. From this, the HELIOS two-dimensional transport code [10] was used to model the experimental rig and calculate the fast neutron flux ($E > 1\,\text{MeV}$) at the guide tube specimens. Fluence monitor wires were also included in the rig to confirm the in-pile measurements, post irradiation.

Specimen Design and Instrumentation

The guide tube segments supplied for testing were approximately 400 mm long. Sections were cut from the middle of these segments, with a target length of 300 mm. This length was needed in order for the expected length changes from creep and growth to be detectable by the in-pile extensometry with good precision. For the specimens to be tested under load, the specimen assembly design is illustrated in Fig. 2. The design of the specimen assembly for testing without an applied load is illustrated in Fig. 3.

End-sleeves or end-plugs were welded to each end of the guide tube sections to allow for attachment of loading and/or extensometry devices. In both cases the end-fittings were machined with holes to allow for coolant flow through the inside of the guide tube specimens once the whole specimen assembly had been

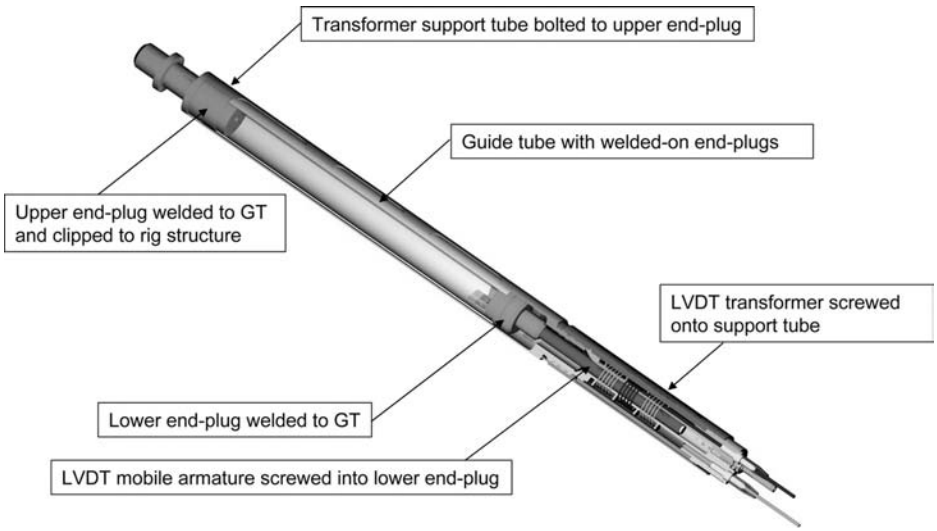


FIG. 3—*Isometric drawing of an un-stressed guide tube specimen assembly (as used in Cluster 2 and Cluster 3).*

assembled. In addition, after welding in place, the end faces of the end-sleeves were machined (dressed) as necessary in order to ensure their parallelism prior to applying the axial load to the guide tube specimens concerned. Profilometry was performed on each fabricated guide tube specimen, measuring between V-grooves machined into the end-fittings, to obtain accurate length measurements prior to irradiation in the Halden reactor as well as to determine any existing bow in the guide tube sections.

The loading units are best described as a "nut-and-bolt" arrangement. The "bolt" incorporates a sealed, pressurized stainless steel bellows with stainless steel end-plug welded to its upper end and a solid Zircaloy connecting bolt attached to its lower end (see Fig. 2). This bolt is inserted into the guide tube specimen (as shown in Fig. 2 where it has the end-sleeves welded to either end) and a stainless steel nut is screwed onto the protruding end of the connecting bolt. The guide tube specimen is thus located between the head of the bolt (actually the bellows' upper end-plug) and the "nut," with the bolt running through the center of the guide tube. The nut is tightened to put the bellows unit under slight tension at room temperature and pressure. Under operating conditions of coolant high temperature and pressure, the bellows unit tries to contract, thereby exerting a calculable compressive axial force on the guide tube, while in tension itself. The force generated by the bellows is equal to the product of the pressure differential acting on the sealed bellows and the bellows effective area. Any change in the spring rate or spring constant of the bellows, due to irradiation and temperature effects, is not a major concern here, as the bellows merely has to remain gas tight and experience a constant pressure differential in order to maintain its applied force. As the guide tube specimen

creeps and/or grows over time, the deflection of the bellows will change in order to accommodate this. As long as the bellows maximum deflection range in tension and compression is not exceeded, then the load it applies will remain essentially constant, given that its effective area does not significantly change.

All the guide tube test assemblies were fitted with an extensometer for monitoring length change online throughout the test. The extensometers utilize a linear variable differential transformer (LVDT) consisting of an outer transformer winding and a mobile armature (a stainless steel rod containing a magnetic core). The transformer is fixed relative to one end of the guide tube specimen, by attaching it to a stainless steel support tube (encasing the guide tube specimen), while the mobile armature is fixed relative to the other end of the guide tube specimen (see Figs. 2 and 3). Any length change in the guide tube specimen due to creep and growth during the irradiation results in a relative movement between the inner and outer parts of the LVDT; thus generating a millivolt signal that can be converted to mm by a pre-determined calibration factor.

The support tube for the outer transformer winding was made with slots to allow for flow of coolant past the outer surface of the guide tube specimens and the material selection was based on the support tube needing to be dimensionally stable throughout the experiment: A displacements per atom (dpa) of less than 3 was expected and the tube would be under insignificant loading, hence cold worked American Iron and Steel Institute 316 (a grade of stainless steel as designed by the Institute) was selected. The design allowed sufficient clearance between the guide tube and the support tube to avoid contact and restraint and the support tube was attached to one end of the guide tube specimen using Allen bolts, such that it could be easily removed at the end of the test.

In-Reactor Operation Conditions

The twelve guide tube specimen assemblies were operated in the Halden reactor for a total of six test cycles or 566 effective full power days. During the first reactor cycle (Cycle 0), manufacturing problems with the LVDTs led to failure of the signals such that the test rig was unloaded at the first available reactor outage and all the LVDTs and support tubes for the LVDT transformer were replaced. The test was re-started and successfully operated, generating elongation data for five subsequent reactor cycles (Cycle 1 through Cycle 5).

Time averaged values of the mean fast neutron flux and accumulated fast neutron fluence over each specimen cluster within the reactor active core for each reactor cycle are summarized in Table 2. A conversion factor between the fast neutron fluence accumulated by the specimens in the test rig and dpa of $1\,\text{dpa} = 6.6 \times 10^{20}\,\text{n}\,\text{cm}^{-2}$ ($E > 1\,\text{MeV}$) was determined using the HELIOS code.

The loop to which the pressure flask was connected operated with standard PWR water chemistry: 1000 ppm B and 3 ppm Li, giving a *p*H (at 25°C) of 7.1. The coolant flow, going both through the inside and past the outside of the tube specimens, was in the range 1.1 to $1.2\,\text{ms}^{-1}$, which was sufficient at the low gamma heating rate in the test rig for the temperature of the specimens to be considered equal to that of the surrounding coolant. Time averaged values of

TABLE 2—*Summary of in-reactor (HBWR) operation conditions.*

		Mean Fast Flux $E > 1$ MeV ($n\,cm^{-2}\,s^{-1}$)		Accumulated Fast Fluence $E > 1$ MeV ($10^{20}\,n\,cm^{-2}$)		Mean Coolant Temperature (°C)		
Cycle	Full Power Days	Cluster 1	Cluster 2	Cluster 1	Cluster 2	Cluster 1	Cluster 2	Cluster 3
0	109	2.9×10^{13}	3.3×10^{13}	2.66×10^{20}	2.95×10^{20}	312	313	313
1	97	3.0×10^{13}	3.2×10^{13}	2.51×10^{20}	2.65×10^{20}	318	321	319
2	92	2.9×10^{13}	3.3×10^{13}	2.26×10^{20}	2.57×10^{20}	318	322	320
3	83	2.6×10^{13}	2.6×10^{13}	1.88×10^{20}	1.86×10^{20}	318	321	319
4	93	2.6×10^{13}	2.6×10^{13}	2.04×10^{20}	2.04×10^{20}	318	321	320
5	92	3.3×10^{13}	3.4×10^{13}	2.55×10^{20}	2.64×10^{20}	317	322	324

Note: Data not given for Cluster 4 conditions due to lack of in-pile elongation data obtained from specimens placed there.

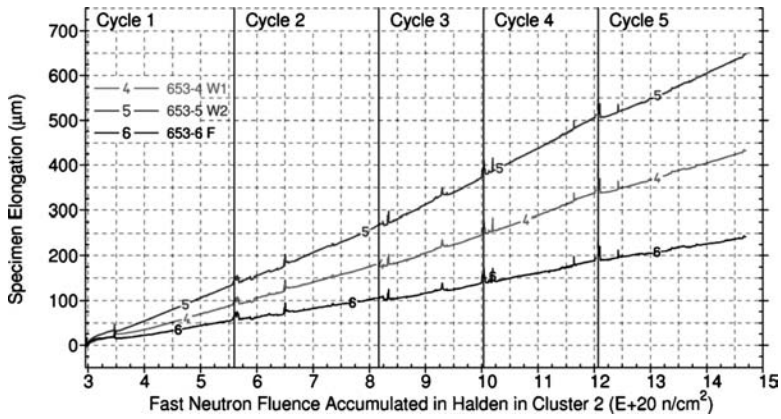


FIG. 4—*Specimen elongation of the three Cluster 2 free growth specimens (no compressive stress).*

the mean coolant temperature over each specimen cluster for each cycle are summarized in Table 2. The coolant pressure was maintained at 157–160 bar (16 MPa), keeping the compressive axial stress on the Cluster 1 specimens (via the installed bellows units) as specified at 40±1 MPa.

Results

In-Reactor Elongation Measurements

Elongation data were generated in situ via the LVDTs from the guide tube specimens over a period of five test reactor cycles (no data were collected from irradiation Cycle 0). The data are presented in the following sections by cluster.

Free Growth Specimens (Cluster 2)—The elongation signals from the specimens in Cluster 2 are shown as a function of fast neutron fluence in Fig. 4. These specimens were surrounded by booster fuel rods, generating a high fast neutron flux environment, but were not under an applied axial compressive load. Note that these specimens were also not under any hoop stress due to coolant from the test loop flowing both inside and outside of the guide tube sections.

The data can reasonably be described by a linear fit for the entire fast fluence increment and a best fit gradient, judged by eye, was put to the data to determine a growth rate for each specimen. These values are given in Table 3 (column 3), together with the net elongation accumulated by each specimen during the five cycles of irradiation over which the LVDT measurements were made (column 4).

Creep and Growth Specimens (Cluster 1)—The elongation signals from the specimens in Cluster 1 are shown as a function of fast neutron fluence in Fig. 5. These specimens were surrounded by booster fuel rods for a high fast neutron

TABLE 3—*Summary of length change measurements.*

Cluster	Halden Specimen ID	From In-Core LVDT Signals over Five Cycles: Stable Elongation Rate (μm/n cm^{-2})	From In-Core LVDT Signals over Five Cycles: Five-Cycle Specimen Elongation (μm)	From Out-of-Core Measurements: Five-Cycle LVDT Support Tube Elongation (μm)	From Out-of-Core Measurements: Six-Cycle Specimen Elongation Between V-Grooves (μm)
1 (in-flux creep and growth)	653-1	26×10^{-20} [a]	+150	−57	+80
	653-2	44×10^{-20} [a]	+350	−54	+220
	653-3	4×10^{-20} [b]	−85	−56	−310
2 (in-flux, free growth)	653-4	38×10^{-20} [c]	+435	−71	+450
	653-5	58×10^{-20} [c]	+640	−80	+730
	653-6	21×10^{-20} [c]	+245	−63	+220
3 (out-of-flux, unstressed)	653-7	0	+40	−70	−80
	653-8	0	+40	−40	−50
	653-9	0	+35	−41	−80

[a] Linear fit to LVDT data from middle of Cycle 3 onwards.
[b] Linear fit to LVDT data from Cycle 5 only.
[c] Linear fit to LVDT data from Cycle 1 through Cycle 5.

MCGRATH AND YAGNIK, doi:10.1520/JAI103770 885

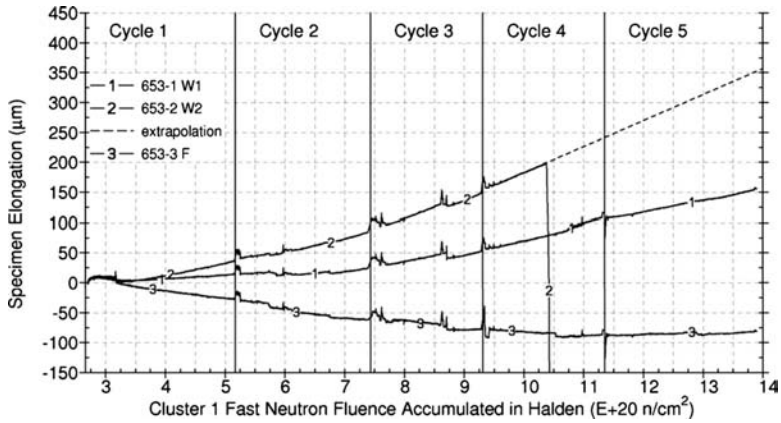


FIG. 5—*Specimen elongation of the three Cluster 1 creep and growth specimens (40 MPa compressive stress).*

flux as well as being placed under an axial compressive load by bellows loading units. The integrity of these units was tested out-of-pile at the end of the irradiation by pressure cycling the specimen in a small gas chamber and registering the response of the LVDT. This was done to confirm that the bellows were still gas tight and would therefore have delivered the planned axial stress to the specimens based on coolant loop pressure (see section Specimen Design and Instrumentation). Note that these specimens were not under any hoop stress while in the reactor due to coolant from the test loop flowing both inside and outside of the guide tube sections.

The data follow the shape of a curve as a function of dose, i.e., the creep and growth rate of the specimens is varying throughout the irradiation. This variation is attributed to the in-reactor creep of the specimens, assuming that the "underlying free growth" of the specimens would be linear as is the case for the un-stressed Cluster 2 specimens. Considering the competing effects of growth to elongate the specimens and creep to shrink the specimens, the specimen elongation curves indicate that the underlying creep rates are decreasing with progressive irradiation i.e., that the Cluster 1 guide tube specimens were still experiencing primary or transient creep during the period of irradiation in the HBWR. In fact for specimen 653-3, a low hydrogen *F*-segment, it appears that the rate of length change is dominated by transient compressive creep for most of the irradiation time. This suggests that the growth rate of this specimen was comparatively small, which is consistent with the data from the low hydrogen content *F*-specimen in free growth in Cluster 2 (specimen 653-6).

Estimates of stable creep and growth rate for each of the specimens in Cluster 1 were determined from a best fit gradient, judged by eye, put to the LVDT data from towards the end of the irradiation: From the middle of Cycle 3 for specimens 653-1 and 653-2 and from Cycle 5 alone for specimen 653-3. These values are given in Table 3 (column 3), together with the net elongation

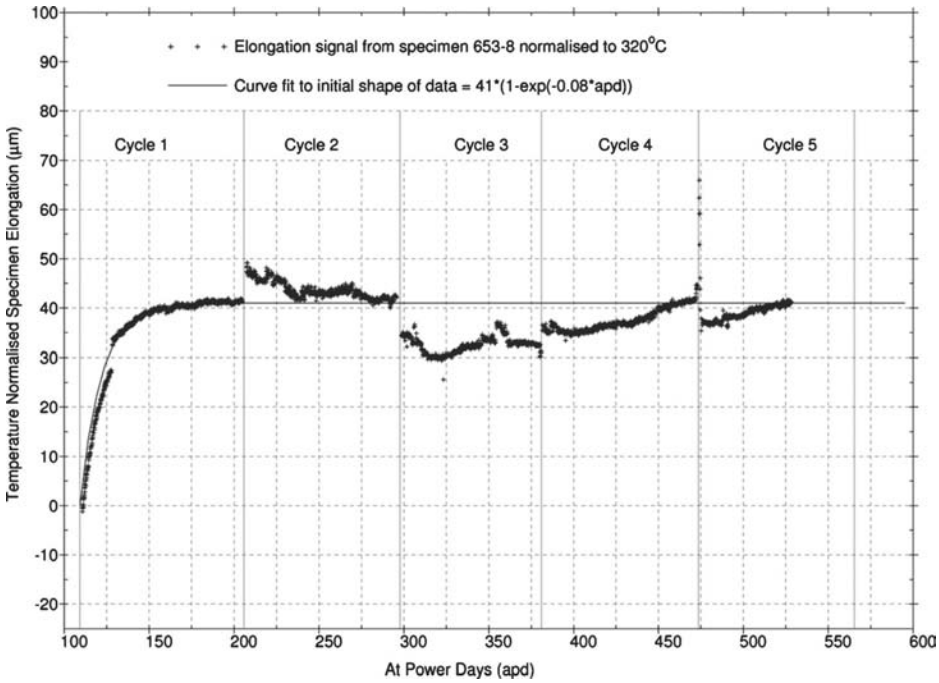


FIG. 6—*Specimen elongation of one of the three Cluster 3 control specimens (no compressive stress and no fast flux).*

accumulated by each specimen during the five cycles of irradiation over which the LVDT measurements were made (column 4).

Control Specimens (Cluster 3)—For the control specimens under zero fast flux and no applied axial or circumferential load, a typical specimen elongation signal is shown as a function of effective full power days in Fig. 6.

The LVDT elongation signals from all three control specimens exhibited an initial, parabolic-shaped, increase lasting about 100 days and reaching maxima of between 41 and 47 μm. Although smaller and less apparent, this initial parabolic increase is also shown to differing degrees by the elongation signals of the specimens in the other clusters. After reaching a maximum, the control specimen elongation signals essentially stopped changing with just a small variation in the order of 10–15 μm.

Because the control specimens were positioned in the test rig outside of the fast flux zone and had no applied load, they should not have exhibited any length change due either to creep (thermal or irradiation) or growth. However, the specimen assembly extensometry is made up of two parts: The LVDT mobile armature connected to the guide tube specimen and the LVDT outer transformer winding attached to the stainless steel support tube, which surrounds the guide tube (see Fig. 2). The specimen elongation signal generated in the

LVDT unit is the result of any relative movement of the mobile armature within the transformer winding. The parabolic length change recorded at the start of Cycle 1 has been attributed not to the control specimen guide tube specimens elongating, but rather to the stainless steel support tube *decreasing* in length. This assumption has been confirmed by length measurements made of the stainless steel support tubes before and after exposure in the reactor (see section Out-of-Reactor Elongation Measurements).

Thermal Creep Specimens (Cluster 4)—No reliable in situ elongation data were obtained from the LVDTs for these specimens. It was discovered during post irradiation examination (PIE) that the welds between the bellows and the upper end-plugs in these specimens had fractured at some point, resulting in the bellows no longer being gas tight. This in turn resulted in an unknown axial stress history being applied to these specimens.

Out-of-Reactor Elongation Measurements

Stainless Steel Support Tubes—After Cycle 0, new LVDT transformer support tubes were manufactured together with the new LVDTs for the re-loading of the experiment. The length of the new stainless steel support tubes were measured both before and after irradiation (Cycle 1 through Cycle 5) and the results are shown in column 5 of Table 3. All the support tubes showed a decrease in length regardless of position in the test rig indicating a temperature induced change rather than a flux effect. It has thus been assumed that the LVDT signals give an overestimate of the net elongation accumulated by each specimen during the irradiation period Cycle 1 through Cycle 5 on the order 40–80 μm. Note however that this overestimate from the LVDTs occurred entirely during Cycle 1, such that the best estimates of stable creep and growth rates, determined from LVDTs signals during Cycle 3 and onwards, are unaffected and thus remain valid without correction.

Guide Tube Specimens—Profilometry was performed prior to the start of the irradiation (Cycle 0) and after the final irradiation cycle (Cycle 5) to obtain accurate length change measurements of each guide tube specimen as well as determining the extent of any change in the bow of the specimens. The length determined is that between V-grooves machined into the specimen end-fittings. The results are shown in column 6 of Table 3. Note that these cannot be compared directly with the net length changes determined from the LVDT signal (column 4 in Table 3), as they relate to changes induced by six cycles of irradiation whereas the LVDT results relate to five cycles of irradiation. The data relating to bow are not included, but revealed no change in the slight levels of specimen bow that existed prior to the HBWR irradiation from the PWR irradiation.

Guide Tube Oxide Thickness

An eddy current probe was used to determine oxide thickness on the outer surface of each guide tube specimen just before the start of the irradiation (Cycle 0) and after the final irradiation cycle (Cycle 5). The results are given in Table 1.

The increase in oxide thickness during the experiment varies between the clusters as expected due to the different combinations of local coolant temperature and fast neutron flux that prevailed in each of the clusters. However, there is little variation in the results within a given cluster indicating that there is no differential oxidation between the three different types of guide tube (W1, W2, and *F*) tested within a cluster.

Guide Tube Hydrogen Content

Base irradiation hydrogen content was determined by melt extraction of small cross-sections cut from either end of the guide tube sections before the end-fitting were welded in place. Each cross-section was cut into a further three to six samples and the samples were cleaned and dried but the oxide was not removed, hence the results represent total hydrogen content of the base irradiated guide tube material. A similar procedure was used at the end of the irradiation in the Halden reactor, where cross-sections were taken from the ends and middle of the guide tube specimens from Cluster 1 and Cluster 2.

The results showed the guide tube specimens to have an axial gradient in hydrogen content from the base irradiations (more pronounced in the higher hydrogen content guide tubes). This axial hydrogen content gradient was maintained through the irradiation in Halden. Because of these hydrogen gradients, the most effective way to review the hydrogen content results was in a graphical fashion. The hydrogen contents determined from each sample, taken from a known relative axial position on the guide tube, were plotted as a function of axial position for each of the guide tube specimens. An example is shown in Fig. 7.

Hydrogen content for the specimens was thus determined as a mean axial value and hydrogen increase was determined by comparing the center axial position values before and after the HBWR irradiation obtained from the plotted data. The results are shown in Table 1. Five of the six guide tube sections studied showed approximately 100 ppm hydrogen pick-up (between 84 and 115 ppm), whereas one guide tube specimen (specimen 653-2) had an increase of 250 ppm hydrogen. The cause for this difference is not known.

The typical hydride distribution the guide tube specimens after irradiation in the Halden reactor is illustrated in Fig. 8 which shows randomly orientated hydrides even distributed through the wall-thickness.

Summary and Discussion

Nine guide tube specimens from two different manufacturing routes and with a range of starting hydrogen contents, from 135 to 800 ppm following different base irradiations, were successfully re-irradiated in the Halden reactor. Using different axial positions within a test rig structure and different loading conditions for the specimens, a test matrix was designed aimed at determining free growth as well as combined axial creep and growth. Unstressed control specimens were also included, positioned outside of the fast flux. Operating conditions were prototypical for PWR in terms of coolant temperature, pressure, and

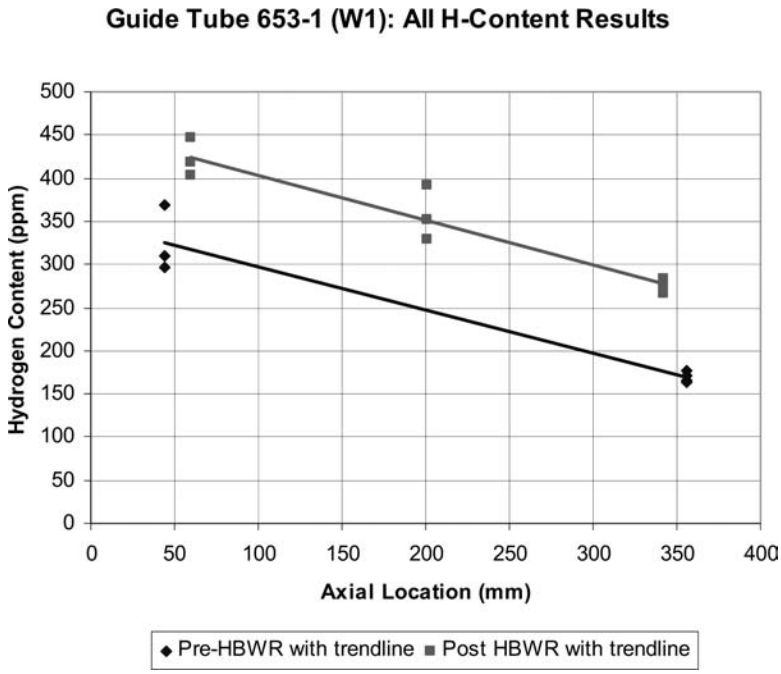


FIG. 7—*Hydrogen content data for one of the medium H-content, Westinghouse guide tube specimens (W1 type material, specimen 653-1 in Cluster 1).*

water chemistry. The irradiation lasted six reactor cycles, with guide tube specimen extensometry data collected over five cycles of irradiation, totaling 457 effective full power days, or an accumulated fast neutron fluence ($E > 1$ MeV) of 11–12 $\times 10^{20}$ n cm^{-2}.

The control specimens all showed an apparent elongation, whereas they should have showed no length change at all. Out-of-pile length measurements were made of the LVDT transformer support tubes-part of the specimen extensometry assembly-showing that they all decreased in length by similar amounts. This confirmed that the support tubes had contracted, which was unexpected when the material for the component was selected. From the design of the specimen assembly extensometry, it is known that a decrease in length of the support tube will have the same effect on the specimen elongation signal as if the guide tube specimen had elongated. The elongation signals of the control specimens each exhibited an initial parabolic increase, with net length increases accumulated over Cycles 1 to 5 of 40, 40, and 35 μm. These values compare well with the out-of-pile measured shrinkages of the support tubes for these specimen assemblies of 70, 40, and 40 μm, after their irradiation during Cycle 1 through Cycle 5. This supports the view that support tube shrinkage is the most probable explanation for the increase in the control specimen elongation signals.

The effect of these extensometry length changes has to be considered for all of the specimen assemblies. However, as indicated by the on-line signals for the

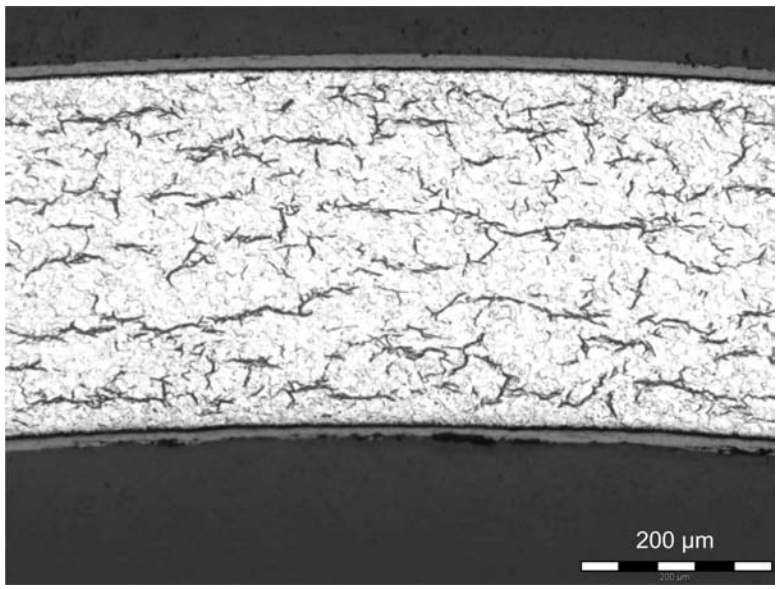


FIG. 8— *Optical micrograph prepared from specimen 653-4, showing the hydride distribution in the W1 type guide tube material after the HBWR irradiation.*

control specimens, the support tube contraction occurred only during the early stages of irradiation of the support tube (first ~ 60 days during Cycle 1), hence the specimen stable creep and growth rates, determined from the elongation signals later in the irradiation (Cycle 3 and onwards), would not have been affected and can thus be considered reliable. The specimen stable elongation rates (from column 3 in Table 3) have been converted to strain rates, based on the LVDT measurement spans for each specimen, and are given in Table 4. Note that these strain rates have not been corrected for hydrogen induced volume changes as a result of the hydrogen absorbed into the specimens during irradiation in the Halden reactor.

Out-of-core measurements were also made of all the guide tube specimens in order to evaluate the specimen in-pile elongation results. However, a direct comparison cannot be made because specimen elongation determined from the LVDTs relates to five cycles of irradiation (column 4 in Table 3) whereas specimen elongation determined by out-of-core measurement relates to six cycles of irradiation (column 6 in Table 3). However, for each of the three free growth specimens, where elongation was a linear function of fluence, a simple extrapolation of the five cycle LVDT data to the fluence accumulated over six cycles matches well with the out-of-pile measurements made for these specimens, taking into account the support tube shrinkage (column 5 in Table 3). For example, such an extrapolation is shown in Fig. 9 for free growth specimen 653-4 from Cluster 1. The net specimen elongation given by the LVDT from five cycles of irradiation is 435 μm. Extrapolating the specimen elongation from the LVDT linearly to zero fluence, i.e., to include Cycle 0, gives a net elongation of about

TABLE 4—*Summary of specimen strain rates.*

		Base Irradiation		Stable Creep and/or Growth Strain Rate	
Cluster	Halden Specimen ID	Hydrogen (ppm)	Temperature (°C)	(%/n cm^{-2})	(%/dpa)
1 (in-flux creep and growth)	653-1	250	307	8.4×10^{-23}	0.056
	653-2	600	321	14.2×10^{-23}	0.094
	653-3	135	295–300	1.3×10^{-23}	0.008
2 (in-flux, free growth)	653-4	225	307	12.2×10^{-23}	0.080
	653-5	800	321	18.6×10^{-23}	0.123
	653-6	135	295–300	6.7×10^{-23}	0.045

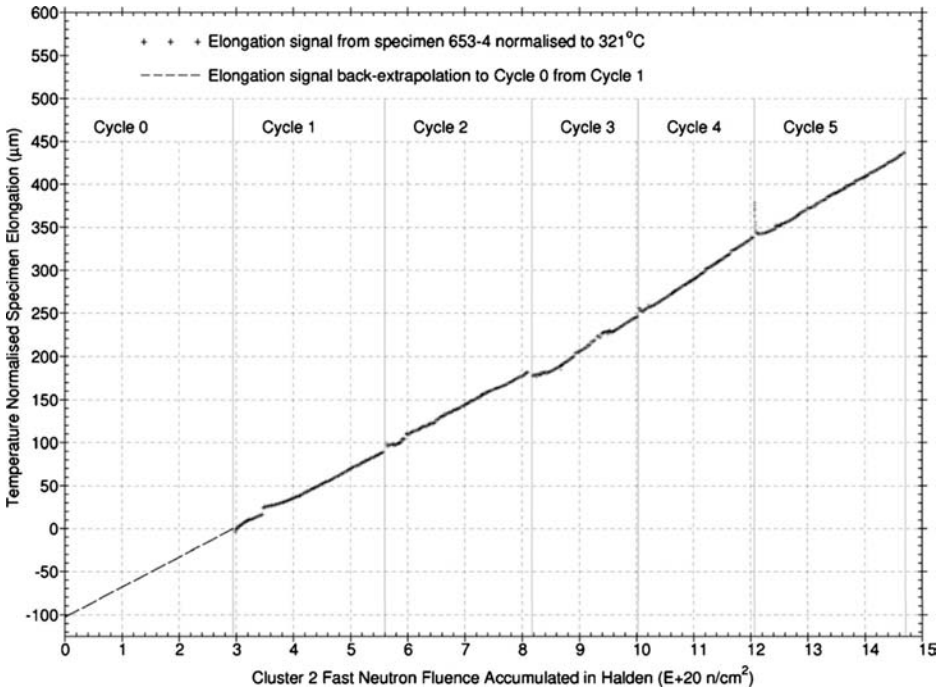


FIG. 9—*Specimen elongation of the free growth specimen 653-4 in Cluster 1 from LVDT data from Cycle 1 through Cycle 5 back-extrapolated for Cycle 0.*

535 μm. Removing the in-reactor overestimate generated by the LVDT support tube (during Cycle 1) for this specimen of 71 μm gives a six cycle net elongation of 464 μm. This compares well with the out-of-pile measured net specimen elongation (from six cycles of irradiation) of 450 μm.

Conclusions

The in-pile elongation data from the three free growth specimens in Cluster 2 indicated that these specimens were exhibiting essentially linear growth during the HBWR re-irradiation. A positive correlation is shown between hydrogen content as measured after base irradiation and stable growth rate. This is illustrated in Fig. 10. However, a correlation does not necessarily indicate a cause and other possibilities that could explain the differences in growth rate between the specimens need to be considered, such as differential oxidation or hydrogen uptake during the HBWR re-irradiation.

There is almost no difference in the amount of oxidation the three specimens underwent, with outer surface oxide layer increases of 16, 16, and 15 μm, respectively, in order of increasing growth rate. Comparison has also been made of the hydrogen content, at the axial mid-point, of each guide tube specimen from Cluster 2 (free growth) before and after the HBWR irradiation. Mean

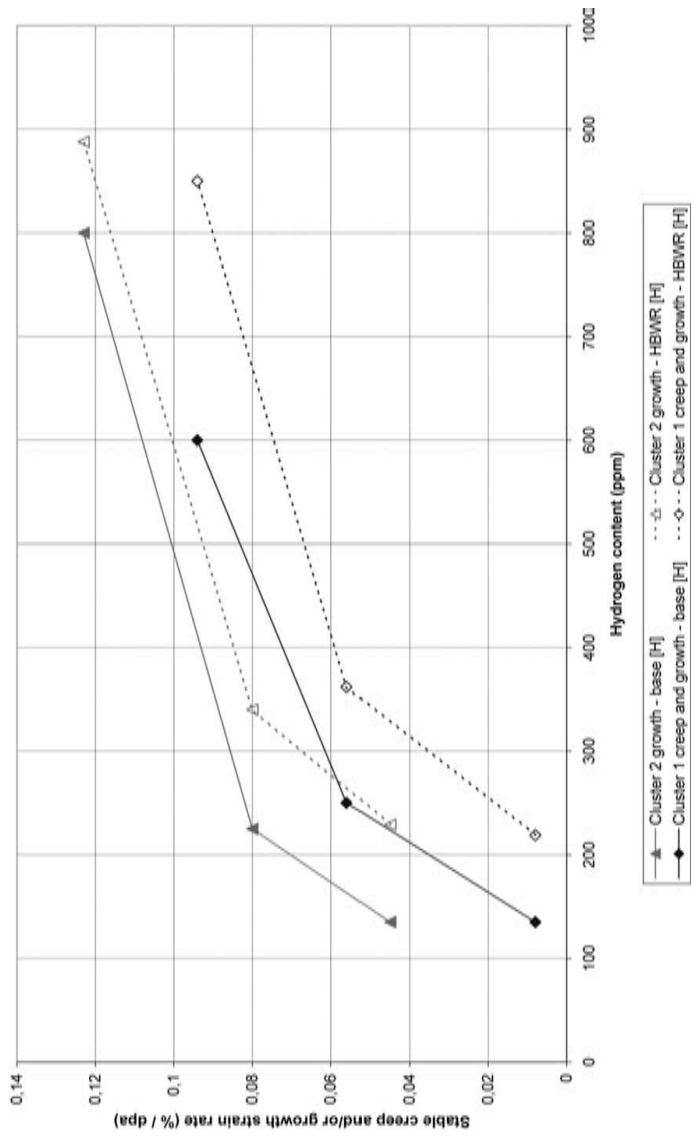


FIG. 10—*Specimen stable creep and/or growth rates plotted as a function of hydrogen content both at the end of the base irradiation (solid symbols) and at the end of the HBWR irradiation (outline symbols).*

axial values were chosen due to the hydrogen content axial gradient in the specimens induced during the base irradiation. In the order of increasing growth rate, the values were: 94, 88, and 115 ppm. In other words, the variation in hydrogen pick-up does not mirror the observed variation in growth rate, and Fig. 10 shows that the trend of increasing growth rate with base irradiation hydrogen content is paralleled for hydrogen content determined after the HBWR irradiation (compare the solid and outline triangles).

Differential oxidation or hydrogen uptake during the irradiation could thus be ruled out as the cause of the difference in growth rate. However, there was also a positive correlation between growth rate and base irradiation temperature. Substantiating a cause for either of these correlations is not considered in this paper, but is the subject of a further analysis and assessment carried within the NFIR program.

Comparing the online elongation results from the creep and growth specimens in Cluster 1 with their corresponding free growth specimens in Cluster 2 indicated that the underlying creep rates decreased with progressive irradiation. This illustrates, as could be expected, that the guide tube specimens experienced a primary or transient creep phase from the start of the HBWR irradiation. The creep and growth rates of two of the specimens did reach steady state around the middle of the irradiation, but not that of the low hydrogen specimen. This was attributed to the low hydrogen specimen exhibiting a relatively low growth rate (following the findings from the free growth specimens) such that its elongation would be dominated by creep due to the applied compressive load, hence continuing to exhibit a varying elongation rate and in fact a net contraction over the period of irradiation.

The stable creep and growth rates determined from the Cluster 1 specimens also show a positive correlation to hydrogen content, either as measured after base irradiation or after the HBWR irradiation (Fig. 10). Further, by comparing the Cluster 1 data in Fig. 10 with the Cluster 2 data, the distance between the two data sets in the Y-axis direction (comparing consistently either solid symbols or outline symbols) can be taken to be the underlying irradiation creep rate of the Cluster 1 specimens. In that this distance is near constant across the range of hydrogen content in the guide tube specimens, it has been deduced that there is little or no effect of hydrogen content on irradiation creep rate.

Acknowledgements

The work was carried out under the auspices of the EPRI-led NFIR Program. The authors acknowledge technical inputs from NFIR members and thank them for permission to publish the results.

References

[1] Andersson, T., Almberger, J., and Björnkvist, L., "A Decade of Assembly Bow Management at Ringhals," *Proceedings of the 2004 International Meeting on LWR Fuel Performance*, Orlando, FL, Sept. 19–22, American Nuclear Society, La Grange Park, IL, 2004.

[2] Willse, J. T. and Garner, G. L., "Recent Results from the Fuel Performance Improvement Program at Framatome Cogema Fuels," *An International Topical Meeting on Light Water Reactor Fuel Performance*, Park City, UT, Apr. 10–13, American Nuclear Society, La Grange Park, IL, 2000.

[3] Kesterson, R. L., King, S. J., and Comstock, R. J., "Impact of Hydrogen on Dimensional Stability of Fuel Assemblies," *An International Topical Meeting on Light Water Reactor Fuel Performance*,Park City, UT, Apr. 10–13, American Nuclear Society, La Grange Park, IL, 2000.

[4] West, J. P., Gautier, B., Esteve, B., and Ponticq, M., "Challenges for the Nuclear Fuel—A Utility Perspective," *An International Topical Meeting on Light Water Reactor Fuel Performance*, Park City, UT, Apr. 10–13, American Nuclear Society, La Grange Park, IL, 2000.

[5] Yang, R., Ozer, O., and Rosenbaum, H. S., "Current Challenges and Expectations of High Performance Fuel for the Millenium," *An International Topical Meeting on Light Water Reactor Fuel Performance*, Park City, UT, Apr. 10–13, American Nuclear Society, La Grange Park, IL, 2000.

[6] Seibold, A., Garzarolli, F., and Manzel, R., "Material Development for Siemens Fuel Elements," *An International Topical Meeting on Light Water Reactor Fuel Performance*, Park City, UT, Apr. 10–13, American Nuclear Society, La Grange Park, IL, 2000.

[7] 1996 USNRC Bulletin, 96-01, Control Rod Insertion Problems, http://www.nrc.gov/reading-rm/doc-collections/gen-comm/bulletins/1996/bl96001.html (Last accessed February 21, 2011).

[8] Chatterton, M. S., "Regulatory Perspectives on High Burnup Fuel Issues and Burnup Extension," *An International Topical Meeting on Light Water Reactor Fuel Performance*, Park City, UT, Apr. 10–13, American Nuclear Society, La Grange Park, IL, 2000.

[9] Franklin, D. G. and Adamson, R. B., "Implication of Zircaloy Creep and Growth to Light Water Reactor Performance," *J. Nucl. Mater.*, Vol. 159, 1988, pp. 12–21.

[10] HELIOS2 Generalized-Geometry Lattice Physics, http://www.studsvikscandpower.-com/products/helios2 (Last accessed February 21, 2011)

DISCUSSION

Question 1, Philippe Bossis, CEA, France:—Regarding the different hydrogen contents, there should be a significant difference in oxide thicknesses and remaining metal thicknesses. Did you take these respective thicknesses into account?

Author's Response:—On average the low, medium and high hydrogen content guide tubes had outer surface oxide thickness of 7, 6 and 20 μm respectively (at the start of the irradiation in the Halden reactor). The nominal inner/outer diameter of each guide tube section was 11.2/12 mm. Thus the differences in for example remaining metal thickness (assuming similar oxide thickness on inner as outer surface) were not so significant at 0.386, 0.388 and 0.360 mm respectively or 99%:100%:93%. No account was anyway taken.

Question 2, Joe Rashid, ANATECH, USA:—The dependence of growth rate (creep and growth) on base irradiation hydrogen content is non-linear, a factor of 3, whereas the hydrogen is a factor of 6 between the high and the low. Any explanation?

Author's Response:—I have no explanation, just an observation. The 2 "sets" of specimens (3 with no applied load and 3 with applied load) show the same trend: from the low to the medium hydrogen specimen, the increase in growth rate is larger than from the medium to the high hydrogen specimen. It may have something to do with the form of the hydrogen in the specimens: solid solution or hydrides. The hydrogen in the low content specimens may be present in solid solution only, whereas the other two specimens would have proportionally increasing amounts of hydrogen as hydride.

Question 3, Bo Cheng, EPRI, USA:—Your growth data are shown in μm (length). Would it be possible to show it also in % growth, so that it would be easier for designers? Also, since the thermal/fast neutron spectra in the Halden Reactor is quite different from that of power reactors (BWR & PWR), how should one use the data for application?

Author's Response:—In the paper, the growth rates are also given as %/dpa, which should allow the data to be compared with data from either power reactor or other research reactors.

Question 4, Malcolm Griffiths, AECL, Canada:—The hydrides will change the sink density in the material – have you considered the sink density and distribution of the hydrides for each specimen during testing and the effect this would have on point defect annihilation and therefore creep and growth?

Author's Response:—No, this has not been considered in this current presentation of the experimental results.

Question 5, Ron Adamson, Zircology Plus, USA:—If the growth strain is subtracted from the growth plus creep strain, it would appear that there is little if any effect of hydride content on irradiation creep. Can you comment on that observation and procedure?

Author's Response:—Assuming that a simple subtraction of the linear growth determined on one specimen from the creep and growth determined on the sibling specimen (similar hydrogen content) gives the underlying irradiation creep, then it is the case that these so determined creep rates are rather similar irrespective of the different hydrogen content of the specimens.

Question 6, John Foster, Westinghouse Electric Company, USA:—The observation that increasing hydrogen has no effect on irradiation creep is a reasonable result. Pol Bouffioux has previously reported for unirradiated Zr-4 that increasing hydrogen has no effect on the creep strain or strain rate. Assuming

that the creep mechanism is climb enhanced glide, the hydrides are not obstacles as sufficient point defects are thermally available to allow climb around hydrides. In the case of the irradiated samples, increased point defect concentrations due to neutron irradiation are available. As a result, hydrogen continues to not affect the creep strain or strain rate.

Reprinted from JAI, Vol. 7, No. 8
doi:10.1520/JAI103065
Available online at www.astm.org/JAI

S. Carassou,[1] *C. Duguay,*[2] *P. Yvon,*[3] *F. Rozenblum,*[3] *J. M. Cloué,*[4] *V. Chabretou,*[4] *C. Bernaudat,*[5] *B. Levasseur,*[5] *A. Maurice,*[5] *P. Bouffioux,*[6] *and K. Audic*[6]

REFLET Experiment in OSIRIS: Relaxation under Flux as a Method for Determining Creep Behavior of Zircaloy Assembly Components

ABSTRACT: A stress relaxation on bent-beam specimen irradiation campaign was performed in the French material testing reactor OSIRIS in order to screen different materials according to their in-flux behavior and to derive constitutive laws that are used to describe the in-reactor behavior of assembly components under axial stress. This paper presents the methodology used, with particular emphasis on the validation of the different hypotheses. The methodology is illustrated with the results obtained on an industrial Zircaloy-4 (Zy-4) alloy used in guide thimbles. As an illustration of the capability of the method, the parameters of simple creep behavior laws are adjusted to the relaxation results. The creep-law predictions are compared to results obtained previously in a creep experiment.

KEYWORDS: zirconium alloys, irradiation creep, relaxation

Manuscript received March 16, 2010; accepted for publication June 24, 2010; published online July 2010.

[1] Nuclear Energy Division, CEA Saclay, F-91191 Gif-sur-Yvette, France. (Corresponding author), e-mail: sebastien.carassou@cea.fr
[2] Nuclear Energy Division, CEA Cadarache, F-13108 Saint Paul Lez Durance Cedex, France.
[3] Nuclear Energy Division, CEA Saclay, F-91191 Gif-sur-Yvette, France.
[4] AREVA, AREVA NP SAS, 10 rue Juliette Récamier, F-69456 Lyon Cedex 6, France.
[5] SEPTEN, EDF, F-69628 Villeurbanne Cedex, France.
[6] DRD/MMC, EDF, Site des Renardières, 77818 Moret sur Loing Cedex, France.

Cite as: Carassou, S., Duguay, C., Yvon, P., Rozenblum, F., Cloué, J. M., Chabretou, V., Bernaudat, C., Levasseur, B., Maurice, A., Bouffioux, P. and Audic, K., "REFLET Experiment in OSIRIS: Relaxation under Flux as a Method for Determining Creep Behavior of Zircaloy Assembly Components," *J. ASTM Intl.*, Vol. 7, No. 8. doi:10.1520/JAI103065.

Copyright © 2011 by ASTM International, 100 Barr Harbor Drive, PO Box C700, West Conshohocken, PA 19428-2959.

Introduction

A precise knowledge of the mechanical behavior of a fuel assembly during its whole lifetime is a fundamental requirement for nuclear power plant operators, as well as assembly manufacturers. Thus, codes are developed and used to assess the dimensional changes of the assembly based on the evolution of its components as well as on the interaction with environment. Within this framework, separate-effect irradiations are performed in material testing reactors to derive material constitutive laws that are used in these codes. This paper presents such an experiment based on in-pile relaxation of bent specimens, with a focus on the methodology used to screen material viscoplastic behavior and to derive the governing creep-law.

Experimental Procedure

Materials and Specimens

The relaxation specimens are thin strips (0.21 mm in thickness, 50 mm in length, and 3 mm in width; see Fig. 1) that are machined by milling from guide tubes and cladding tubes, with the axial and radial directions of the tube corresponding respectively to the largest and the smallest dimension of the relaxation specimen. After machining, a heat treatment (50 h at 400°C) is applied in order to remove machining-induced stress and decrease the deflection that occurs in the specimen.

X-ray analysis performed on several specimens previously chemically stripped in order to reach different thicknesses showed that the depth of the specimen exhibiting a significant amount of hardening is lower than 10 μm.

Optical micrographs were performed both after the machining of the specimen and after heat treatment. It was confirmed (Fig. 2) that the heat treatment did not generate any grain size enhancement, especially near the hardening zone induced by the milling. The preparation of the sample is therefore assumed to have no significant influence on further mechanical behavior of the specimen.

Loading Device

The specimens are inserted in a three-point bending device, referred afterward in this study as a spool (see Fig. 1). Each spool allows bending four specimens with a given imposed deflection that induces an elastic stress-strain distribution. Furthermore, two locations are provided in each spool to permit stress-free irradiation of some specimens so that it is possible to bend specimens with or without initial irradiation damage. The maximum tensile stress $\sigma_{\max}$ in the bent specimen is given by Eq 1

$$\sigma_{\max} = \frac{6 \cdot E \cdot h \cdot (d_i - d_{r0})}{L^2} \tag{1}$$

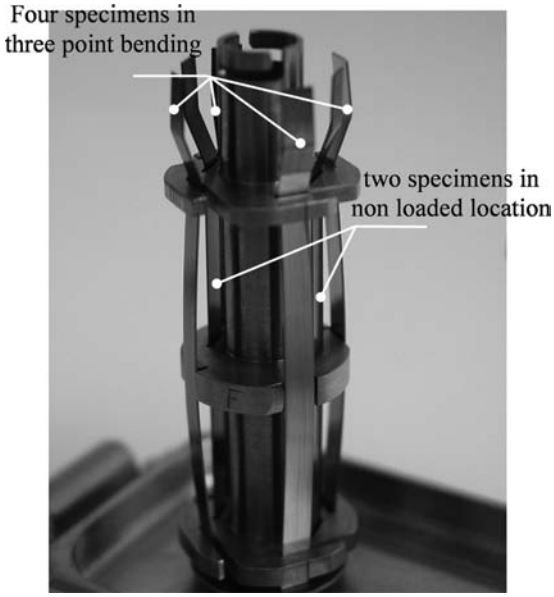


FIG. 1—*Specimens on loading device. Six specimens are inserted in a spool. Four of them are mechanically loaded (three points bending) and two of them are free of load. Eight spools are inserted in the irradiation device.*

where:

E = Young's modulus,
h = thickness of the strip,
L = distance between the two extreme bending points (35 mm),
d_i = imposed deflection ($d_i = 0.6$ mm, $d_i = 1$ mm, or $d_i = 2$ mm), and
d_{r0} = initial residual deflection of the strip.

The initial maximum stress values that are imposed in this study, depending on the spools, the initial deflection of the strip, and the test temperature, range approximately from 50 MPa (for $d_i = 0.6$ mm) to 80 MPa (for $d_i = 1$ mm). The deflection $d(l)$ in any axial location l between 0 and $L/2$ of the bent specimen is given by Eq 2

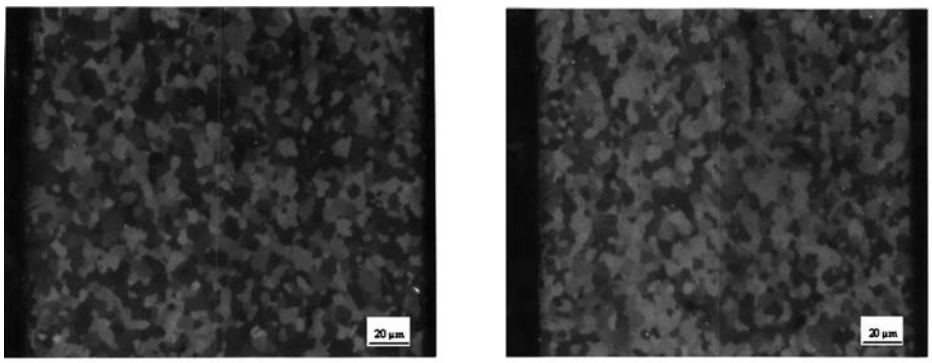
$$\frac{d(l)}{d_i} = \frac{3}{2}\frac{l}{L/2} - \frac{1}{2}\left(\frac{l}{L/2}\right)^3 \tag{2}$$

where:

l = axial location ($l = 0$ stands for an extreme bending point and $l = L/2$ stands for the central bending point).

Measurement Procedure and Quantification of the Stress Relaxation

The specimens are carefully removed from the spools, and placed in a laser measurement device (Fig. 3). The deflection of the specimen in an unloaded



a) Microstructure after machining

b) Microstructure after heat treatment (50h at 400°C, under vacuum)

FIG. 2—*Optical micrographs, on cross section, of a recrystallized Zy-4 specimen after machining and after heat treatment. No grain size enhancement is observed near the machined surfaces.*

configuration is then measured at 71 axial locations, providing the precise shape of the specimen (Fig. 4). This procedure, including removal and placement of the specimen in the measurement device, is repeated three times in order to account for uncertainty, and the mean value at each axial location is chosen.

The maximum deflection of the specimen in an unloaded configuration, referred further in this study as the residual deflection, is used to provide a quantification of the relaxation by the mean of the unrelaxed deflection ratio D_f (or relaxed deflection ratio R_f) defined by Eq 3

$$D_f = \frac{d_i - d_r}{d_i - d_{r0}} = 1 - \frac{d_r - d_{r0}}{d_i - d_{r0}} = 1 - R_f \tag{3}$$

where:

d_i and d_r = imposed deflection and the residual deflection, respectively.

Provided that some hypotheses that will be described further are fulfilled, the unrelaxed deflection ratio is equal to the unrelaxed stress ratio of the specimen

$$\frac{\sigma}{\sigma_0} = D_f \tag{4}$$

where:

σ = maximal stress in the specimen and

subscript 0 refers to the initial test conditions.

The uncertainties of the unrelaxed deflection ratio can be easily calculated using Eq 3, which leads to

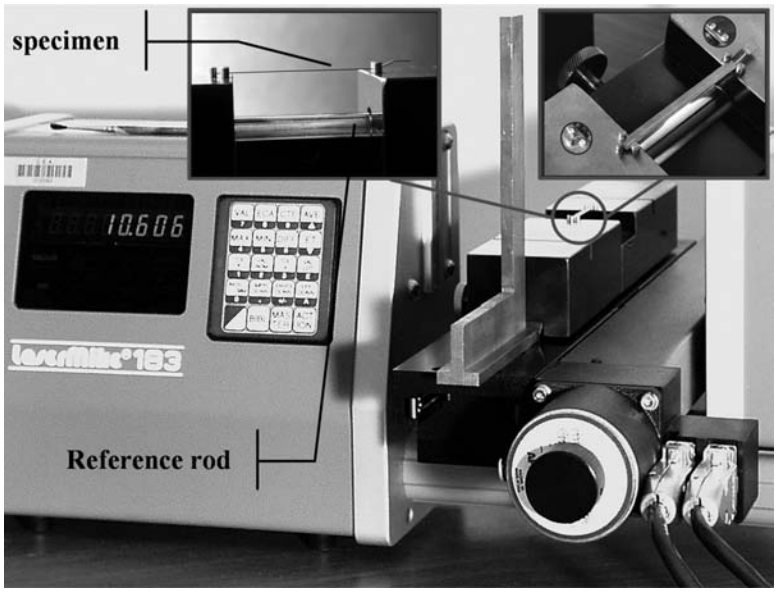


FIG. 3—*Laser measurement device (out of cell sample). The whole shape of the strip is assessed by measuring the distance between the strip and a reference rod on 71 different locations.*

$$\Delta(D_f) = \frac{2\Delta(d)}{d_i - d_{r0}} + (1 - D_f)\frac{\Delta(d) + \Delta(d_i)}{d_i - d_{r0}} \tag{5}$$

where:

$\Delta(d)$ = accuracy of any laser deflection measurement, assessed as 2 μm, and

$\Delta(d_i)$ = accuracy of the imposed deflection, assessed as 40 μm (depending on the uncertainty in the spool geometry and in the thickness of the strips).

Uncertainties are thus a function of the imposed deflection as well as the unrelaxed deflection ratio itself. As an example (see Table 1 for other values), for 1-mm imposed deflection d_i, the unrelaxed deflection ratio D_f is determined at $\pm 1.9 \times 10^{-2}$ for a value of 50×10^{-2}. For 0.6-mm imposed deflection and near-total relaxation, the unrelaxed deflection ratio is determined as $\pm 6.5 \times 10^{-2}$. It is important to notice that the biggest uncertainties are obtained for the lowest values of the unrelaxed ratio because in this case, uncertainties on the imposed deflection play a major role. In other words, when no residual deflection is measured, there is no relaxation whatever the value of the imposed deflection. But when the strip is totally relaxed, a poor knowledge of the imposed deflection value can lead to unrelaxed deflection ratio values misleadingly far from 0. This point has to be kept in mind when low unrelaxed deflection values are analyzed, as shown in Fig. 5.

In conjunction to the deflection, the apparent thickness of the strip is also measured. An evolution of these data is a clear evidence of any accidental

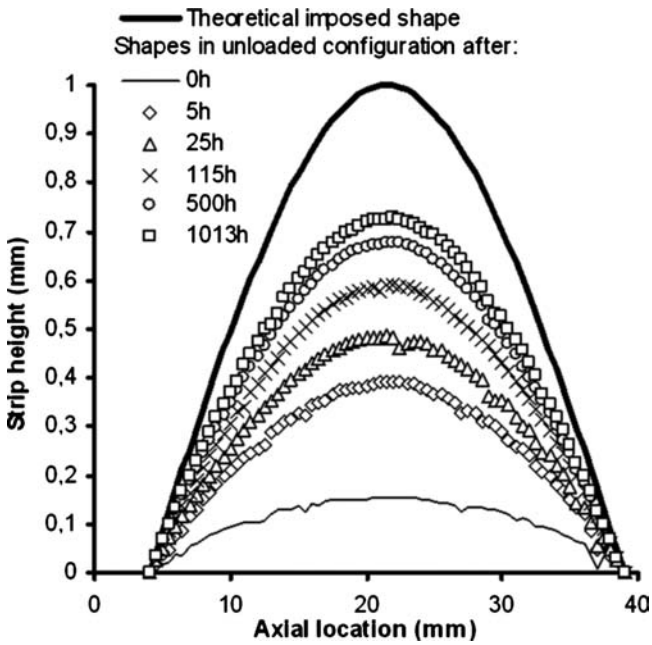


FIG. 4—*Measurements of a strip in unloaded configuration during relaxation. As viscoplastic deformation arises with relaxation, the strip tends to keep the imposed shape even in unloaded configuration.*

deformation of the delicate strip, which may be caused by rough remote handling, for instance. For the whole duration of the experiment, including 2500 remote handling operations (positioning of the strips on the spool or on the measurement device) on more than 80 strips, only five strips were damaged.

TABLE 1—*Uncertainties of unrelaxed deflection ratio D_f as a function of unrelaxed deflection ratio D_f and imposed deflection d_i.*

D_f, $D_f = D_f +/- \Delta/2$	ln (D_f)	$\Delta/2$ for $d_i = 1$ mm	$\Delta/2$ for $d_i = 0.6$ mm
1	0	5.00×10^{-03}	1.00×10^{-02}
0.61	−0.5	1.60×10^{-02}	3.20×10^{-02}
0.50	−0.7	1.90×10^{-02}	
			4.50×10^{-02}
0.14	−2	2.90×10^{-02}	5.80×10^{-02}
0.05	−3	3.10×10^{-02}	6.20×10^{-02}
0.02	−4	3.20×10^{-02}	6.40×10^{-02}
0.01	−5	3.20×10^{-02}	6.50×10^{-02}

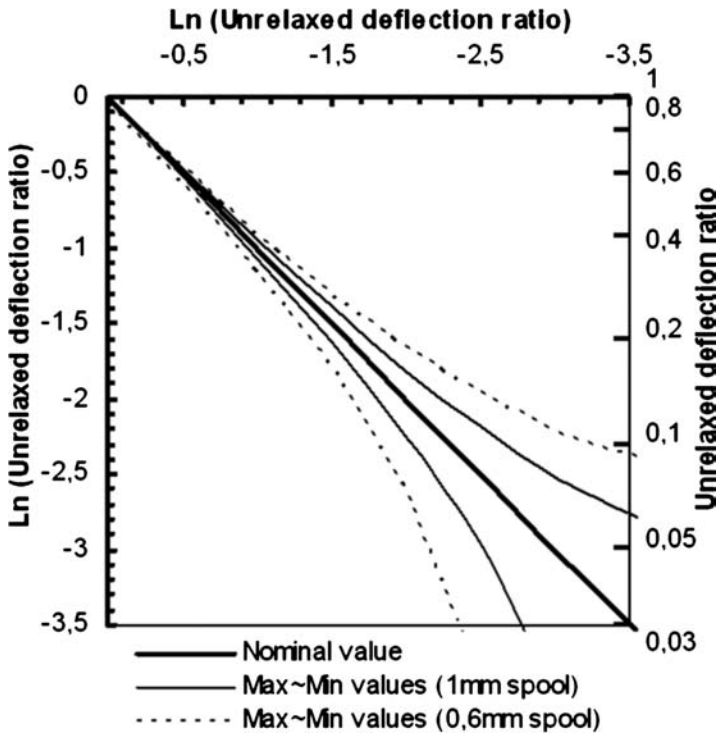


FIG. 5—*Uncertainties of unrelaxed deflection ratio for 1 and 0.6 mm imposed deflections.*

Irradiation Device

The irradiation relaxation experiments REFLET was carried out in the Chouca standard device for in-core irradiation of materials in OSIRIS, a stainless steel cask filled with static coolant medium NaK [1]. Eight spools are axially inserted in a sample holder placed in the Chouca device so that 32 stressed specimens and 16 nonstressed specimens can be irradiated together. The individual monitoring of the five heating zones of the furnace aids to minimize the axial thermal gradient originating from the neutron flux and γ-heating gradients. In order to minimize uncontrolled evolution with time of the local irradiation parameters (temperature and flux) on each specimen, the device is designed to allow the exact repeatability in angular and axial locations of the spools. The temperature is measured by sixteen thermocouples placed along eight axial levels and four angular locations. Copper detectors located at the mid-plane of each spool are used to measure the fast neutron fluences ($E > 1$ MeV) and irradiation damage productions.

Description of Hypothesis for Direct Quantitative Analysis

Stress relaxation of bent-beam specimens has been widely used to assess axial creep behavior under flux of zirconium alloys [2–4], as well as other materials,

including nickel alloys and stainless steels [5,6]. The main assumptions that have to be made in order to assess creep behavior from relaxation experiments are described in this section.

The aim of a relaxation test with no initial plastic deformation is to impose on a specimen a total strain field ε_t, initially fully elastic, as a constant with time (Eq 6)

$$\varepsilon_t = \varepsilon_{\text{vp}} + \varepsilon_e = \text{cte} \tag{6}$$

As viscoplasticity occurs, the elastic strain ε_e turns into viscoplastic strain ε_{vp}. This decrease of elastic strain leads to a stress decrease called "stress relaxation," as expressed by Eq 7, where E stands for the Young's modulus

$$\dot{\varepsilon}_{\text{vp}} = -\dot{\varepsilon}_e = -\frac{\dot{\sigma}}{E} \tag{7}$$

In most cases, when normalized specimens are used, the imposed strain field is homogeneous. In the case of bent-beam specimens, the initial stress and strain fields are not homogeneous and characterized by linear stress and strain gradients given by elasticity theory. Previous studies showed that the assumption of a linear stress and viscoplastic strain state all over the specimen (called in this study the "linearity assumption") permits the use of a single scalar value based on force [3], on radius [2,4], or on deflection [3] measurements to characterize the stress state in the specimen during relaxation. For instance, provided that the linearity assumption is fulfilled, Eq 4 can be used to assess the stress relaxation in each point of the specimen, as already done in Ref [3. In this case, the unrelaxed deflection ratio is equal to the unrelaxed stress ratio of an equivalent homogeneous specimen. An obvious consequence of the linearity assumption is that there is no effect of the initial imposed stress on the unrelaxed stress ratio of the material (because if there were an effect, the stress field inside the specimen would not remain linear during the test). We assume in this study that the converse proposal is true, that is, no effect of imposed deflection is the evidence that the linearity assumption is fulfilled.

In order to obtain relevant relaxation data, Eq 6 has to be fulfilled all along the relaxation test. In one study [2], for example, the authors applied a given shape to the bending specimen. In our case, however, the use of a three-point bending device only imposes the initial shape of the specimen through elasticity rules. Hence, in order to check that a pure relaxation test is really applied, we have to assume that global strains are constant throughout the test and throughout the specimen. This assumption will be called in this study the "constant-shape assumption."

Provided that the two previous assumptions are fulfilled, the experimental methodology described in this study is relevant to obtain material relaxation data. Those data also can be used to determine creep-law parameters, assuming that the creep rate is considered to be independent of the viscoplastic strain and only dependant on stress and time [2] (or, more precisely, as far as creep under flux is concerned, on fluence). This third assumption is called in this study the

"time hardening" assumption. For instance, the simple creep-law given in Eq 8, valid only for constant stress, is widely used to describe the primary creep stage or the steady creep state for some value of its parameters

$$\varepsilon_{vp} = \alpha(\sigma)^{n'}(t)^{p} \tag{8}$$

with

$$\alpha = A \exp\left(\frac{-Q}{T}\right)$$

where:

t = time,
T = temperature,
n' and p = material parameters,
Q = activation temperature, and
A = constant for a given neutron flux.

It is important to note that unless the value of p is equal to 1 (i.e., steady-state creep), the n' parameter in Eq 8 cannot be compared to the stress sensitivity parameter n defined in steady-state creep conditions and widely used for thermal creep studies (Ref [7, for example).

Assuming time hardening behavior, we can derive Eq 8 to get the strain-rate in variable stress conditions

$$\dot{\varepsilon}_{\mathrm{vp}} = \alpha p(\sigma)^{n'}(t)^{p-1} \tag{9}$$

and the substitution of Eq 9 into Eq 7 leads to Eq 10

$$\dot{\sigma} = -E\alpha p(\sigma)^{n'}(t)^{p-1} \tag{10}$$

The integration of Eq 10 leads to different solutions according to the value of the parameter n'

- For $n' \neq 1$, the integration of Eq 10 leads to

$$\left[\left(\frac{1}{1-n'}\right)(\sigma)^{1-n'}\right]_{\sigma_0}^{\sigma} = -Ep\alpha\left[\frac{1}{p}(t)^{p}\right]_{0}^{\Phi t}$$

and

$$(\sigma)^{1-n'} - (\sigma_0)^{1-n'} = -(1-n')E\alpha(t)^{p}$$

Thus

-

$$\frac{\sigma}{\sigma_0} = \left[1 - \frac{(1-n')E\alpha}{(\sigma_0)^{1-n'}}(t)^{p}\right]^{1/(1-n')} \tag{11}$$

TABLE 2—*Materials (chemical composition: wt %).*

Alloy	Denomination	Sn	O	Fe	Cr	Zr
RXA Zircaloy-4[a tbnb]	Thimble Guide tube reference (Zy4 RX ref)	1.29	0.13	0.21	0.11	Bal.
RXA Zircaloy-4[b]	Zy4 RX High Tin	1.47	0.13	0.20	0.11	Bal.
SR Zircaloy-4[a tbnb]	Cladding tube reference (Zy4 low tin SR)	1.27	0.13	0.21	0.11	Bal.

[a]Used for thermal studies.
[b]Used for irradiation.

In this case, the unrelaxed stress ratio depends on the initial stress value σ_0.

- For $n' = 1$ (note that in this case, an initial linear strain field remains linear during the whole relaxation), the integration of Eq 10 leads to

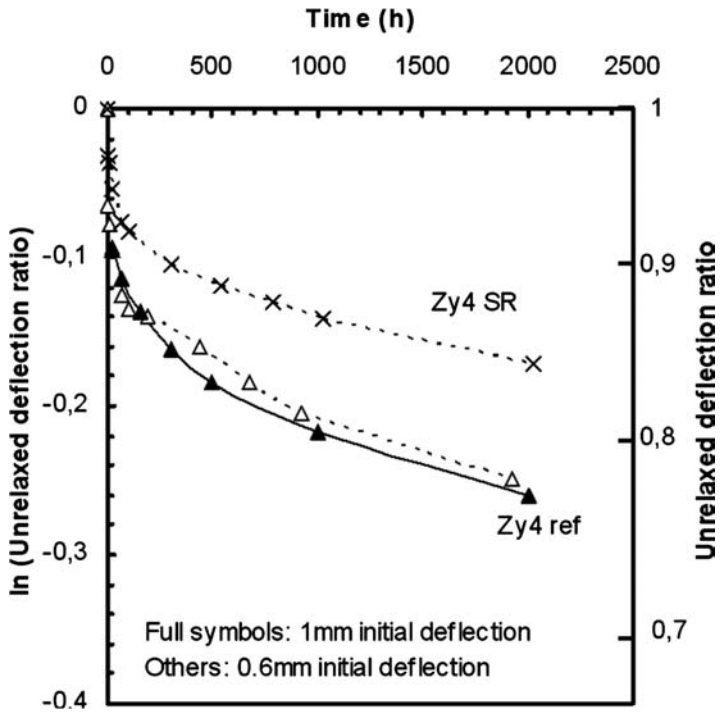


FIG. 6—*Thermal relaxation at 315°C of different Zy-4 specimens. The relaxation responses order the same way than the creep responses of the materials, evidencing the screening ability of the method.*

$$[\ln(\sigma)]_{\sigma_0}^{\sigma} = -Ep\alpha\left[\frac{1}{p}(t)^p\right]_0^{\Phi t}$$

and

$$\ln\left(\frac{\sigma}{\sigma_0}\right) = -E\alpha(t)^p \tag{12}$$

In this case, in accordance with the linearity assumption, we check that the relaxation rate does not depend on the initial stress value σ_0. Besides, Eq 12 shows that the case of a steady-state creep stage (i.e., if $p = 1$) is clearly visible for an unrelaxed stress ratio versus time curve plotted in logarithm scale.

Out-of-Pile Experiments

Introduction

Out-of-pile experiments were carried out with the dual objective to qualify the method and to provide reference data on materials to be submitted to irradiation.

Results of Out-of-Pile Tests

Thermal relaxations were performed at 315°C to qualify the method and also to provide reference data for material aiming to be submitted to irradiation (see Table 2 for chemical composition). The results are shown on Fig. 6. The effect of metallurgical state can be determined by comparing the responses of the Zy-4 in the stress relief state (Zy4 SR) and in the recrystallized state (Zy4 TG ref). The softening effect of the recrystallization on creep behavior [8] is also clearly visible in relaxation. The relaxation responses rank in the same way as the creep responses of the materials.

Discussion on Initial Stress Effect

All Zy-4 alloy tested at 315°C with two different initial deflections (Fig. 6), exhibited no imposed deflection effect. Thus, Eq 4 can be used, and the unrelaxed deflection ratio equals the unrelaxed stress ratio. According to Eq 9, the fulfilment of the linearity assumption suggests a value of n' close to unity. This result could be thought at the first sight to be in contradiction with stress sensitivity parameter values for thermal creep of zirconium alloys at those temperatures (n close to 4 [7]). Nevertheless, Fig. 6 does not exhibit any clear linear part so that no steady-state stage seems to occur. In those conditions, as explained previously, n and n' do not have the same meaning, and there is no contradiction between linearity assumption fulfilment (that was checked here only on a nonsteady-state stage) and stress sensitivity values of 4.

Discussion on the Shape of Strips

The device does not apply a constant global strain field in the specimens but only a maximal deflection value. The fulfilment of the previously exposed constant-shape

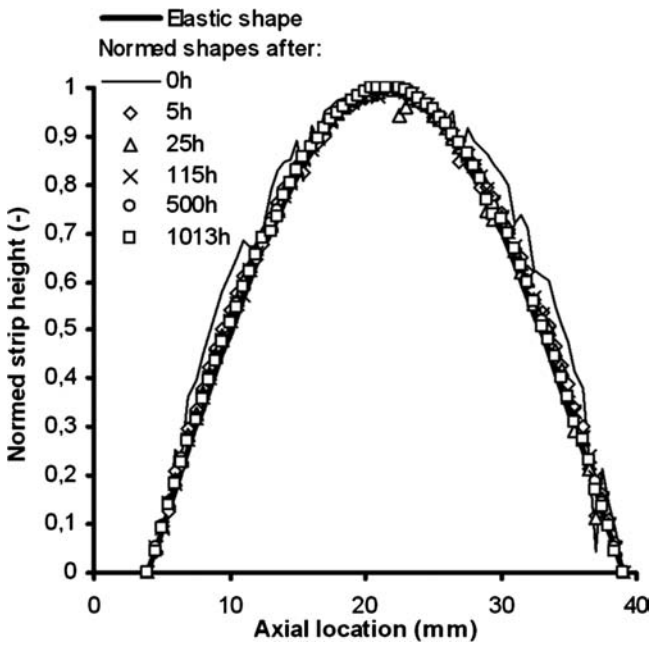


FIG. 7—*Normalized profiles during thermal relaxation at 315°C. The shape of the strip in unloaded configuration is coherent with linear strain field in this configuration. This is evidence that the imposed strain remains constant.*

assumption has then to be checked. As the device does not allow a measurement of the profile of the strips during relaxation in the loaded configuration (i.e., on the spools), the method exposed further has to be used: As a consequence of the superposition theorem, the difference between the strain field present in a strip at a given moment in the loaded configuration (i.e., on the spool) and the strain field of the same strip in the unloaded configuration (i.e., just after removal from the spool) is an elastic strain field. As a consequence, if the normalized profile of a strip in the unloaded configuration at a given moment matches with a profile induced by a linear total strain field such as described in Eq 2, then that was the case before the unloading of the strip. Hence, the profile of the strip in the spool at this moment is still given by Eq 2, as was the case at the beginning of relaxation. The constant-shape assumption is then fulfilled. Figure 7 shows the measured profiles in the unloaded configuration of a strip already shown in Fig. 4, normalized by their maximal value. All the profiles match very satisfactorily with the theoretical elastic profile, ensuring the fulfilment of the constant-shape assumption. This result has been verified for all the strips of the REFLET experiment.

Discussion on Stress and Strain-Rate Domain

Once the linearity assumption, as well as the constant-shape assumption, is fulfilled, Eq 7 can be used to assess the strain-rate domain reached during the

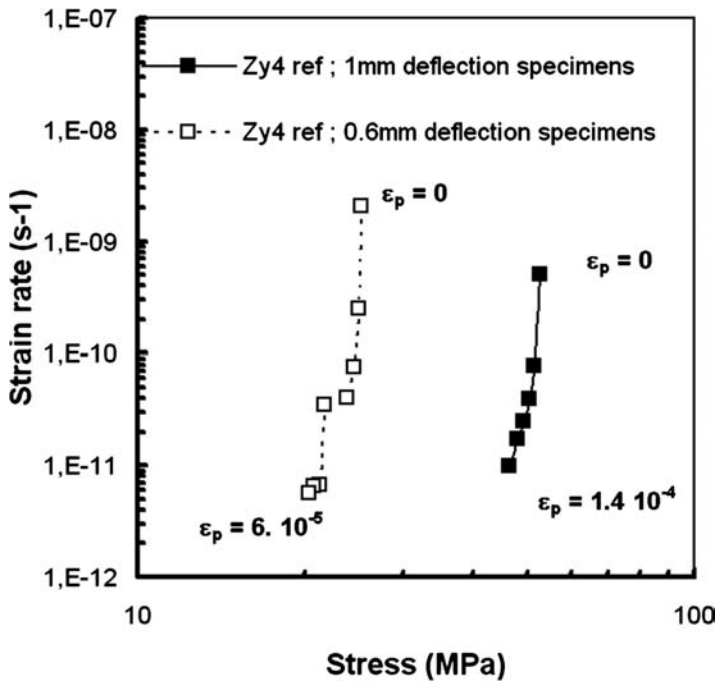


FIG. 8—*Strain-rate and stress domain during thermal relaxation at 315°C of RXA Zy-4.*

tests, as shown on Fig. 8. The strain-rates range from 10^{-8} to $10^{-10}\,s^{-1}$ for stresses ranging from 60 to 20 MPa. We can see that the two curves obtained for the two different initial deflections are distinct so that the strain-rate depends not only on the stress but also on the strain. This sensitivity to strain is considered as an evidence of a strain hardening behavior so that even if the curves on Fig. 6 are analytically determinate (i.e., the lack of influence of the initial deflection ensures that the results obtained on a bent strip are equal to those obtained on a homogeneous specimen), the time hardening assumption cannot be used to simply determine a creep behavior parameter directly from the relaxation response in the out-of-pile tests.

Conclusion on Out-of-Pile Experiments

Qualitatively, the ability of the method to screen material was qualified through its capability to determine the difference in creep behavior of different alloys at 315°C.

Quantitatively, the ability of the method to provide relevant data on relaxation can be checked following three steps. First, if the unrelaxed deflection ratio depends on the imposed deflection, the data cannot be used directly. In this case, to account for a structure effect, a smarter approach involving finite

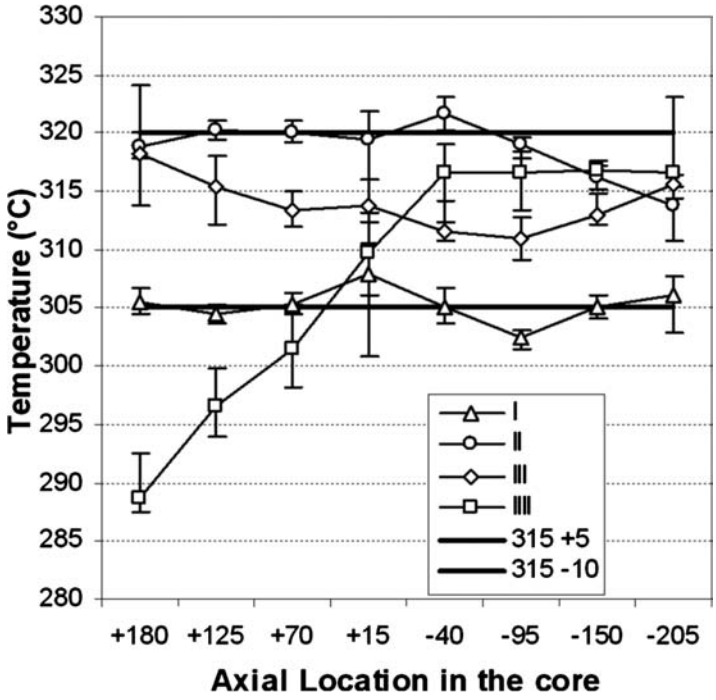


FIG. 9—*Mean temperature during six irradiation cycles (F177–F188) measured near the specimens as a function of axial location of the spool (numbers I–IIII refer to angular position of the specimen in the spool).*

element analysis, for instance, which has not been performed in this study, is needed to identify parameters of assumed constitutive equations. In the other case, the unrelaxed deflection ratio obtained can be considered to be the unrelaxed stress ratio of an equivalent homogeneous specimen. It is important to note that the fact that the initial deflection has no effect on the relaxation results is not in contradiction with stress sensitivity parameter values for thermal creep usually greater than one. Indeed, the stress sensitivity parameter is always obtained during the steady-state stage, which is not achieved in our out-of-pile study.

In a second step, the constant-shape assumption fulfilment can then be checked by analyzing the profile of the strips after relaxation in the unloaded configuration. This assumption was fulfilled for all the specimens tested during the out-of-pile study.

Finally, the "time hardening assumption" fulfilment, providing simple creep-law parameter identification through the relaxation response, can then be checked by comparing the strain-rates versus stress relationship for two different initial deflections. Obviously, this assumption is not fulfilled in the out-of-pile study dealing with thermal relaxation.

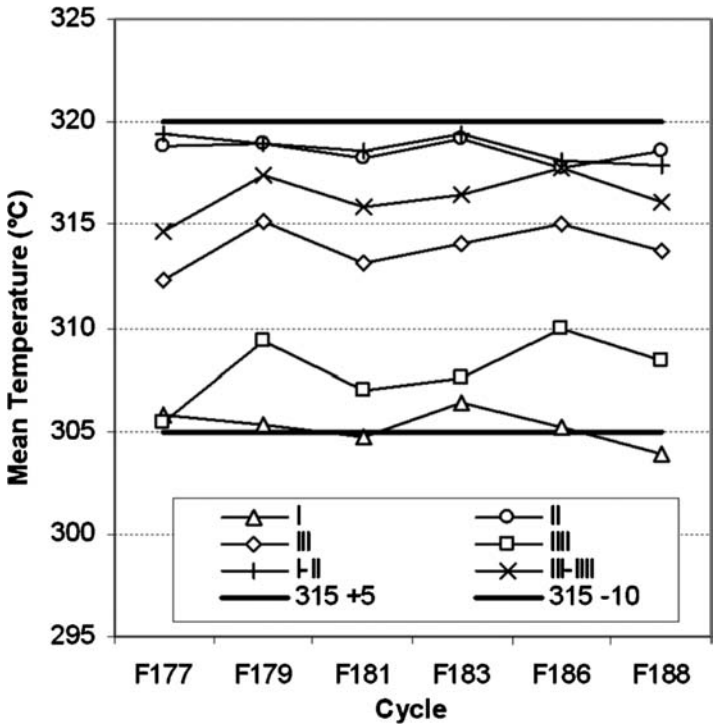


FIG. 10—*Evolution of the average temperature of different angular locations (for each cycle, the temperature are average on all the axial locations) during six irradiation cycles (numbers I–IIII refer to angular position of the specimen in the spool.*

In-Pile Experiments Results

Description of Irradiation Periods

The REFLET irradiation experiment took place in the OSIRIS material testing reactor from August 2000 (F166 cycle) to March 2006 (F209 cycle) in the location n° 24NE, which provides a neutronic flux of $1 \times 10^{18}\,\mathrm{n \cdot m^{-2} \cdot s^{-1}}$ ($E > 1$ MeV) at the maximum flux plane, with a local flux ranging from 80 % to 100 % of this value depending on the axial location. The maximum fluence accumulated by the specimens that were present during all the 18 irradiation phases, cumulating more than 5000 h of irradiation, is close to $20 \times 10^{24}\,\mathrm{n \cdot m^{-2}}$, which corresponds approximately to one annual PWR cycle.

The spatial temperature gradient that is obtained by the device-location-settings set is illustrated on Fig. 9, where the temperatures are averaged on a six-cycle duration basis. In our study, time stability of temperature for a given specimen is given more importance than the global constancy of the temperatures among different specimens, which has direct implications from an operational point of view. Hence, for one of the four angular positions available for the stressed specimens, the difference between the two most-distant specimens

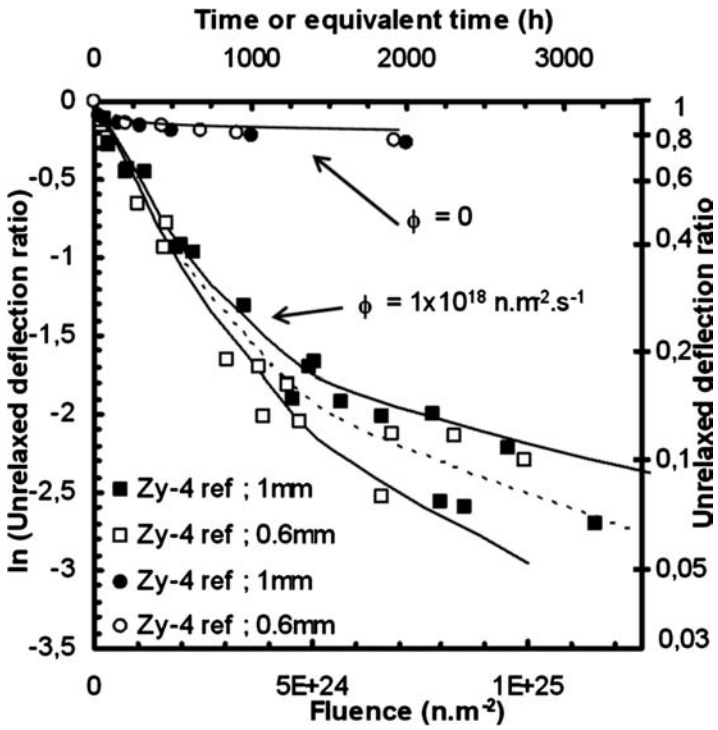


FIG. 11—*Evolution of the unrelaxed deflection ratio at 315°C of reference RXA Zy-4 as a function of time or fluence for two different imposed deflections (1 and 0.6 mm). For irradiated specimens, equivalent time refers to their measured fluence divided by the maximal flux* ($1\times10^{18}\, n\cdot m^{-2}\cdot s^{-1}$).

can be as high as 25°C. In this graph, the scatter bars are related to the maximum and minimum values monitored during all the duration of the survey, providing an indicator of the time stability of the temperatures (the monitoring frequency being the minute). As a consequence of the device surroundings (e.g., other experiments, core configuration, etc.), the time stability of the temperatures of the specimens depends on their location and especially on their angular position in the spool. The best regulation is obtained for the angular location *n*°II, exhibiting temperature stability close to 2°C at nearly any axial location. At every other locations, the time stability of the temperature remains roughly better than 5°C. At the scale of different cycles, the mean temperature of each location remains relatively constant (Fig. 10).

Qualitative Results and Comparison of Different Alloys

Figure 11 shows the unrelaxed deflection ratio as a function of fluence or equivalent time (i.e., fluence divided by the maximum flux) for the reference RXA(recrystallized) Zy-4 alloy and for the two imposed deflections. The comparison

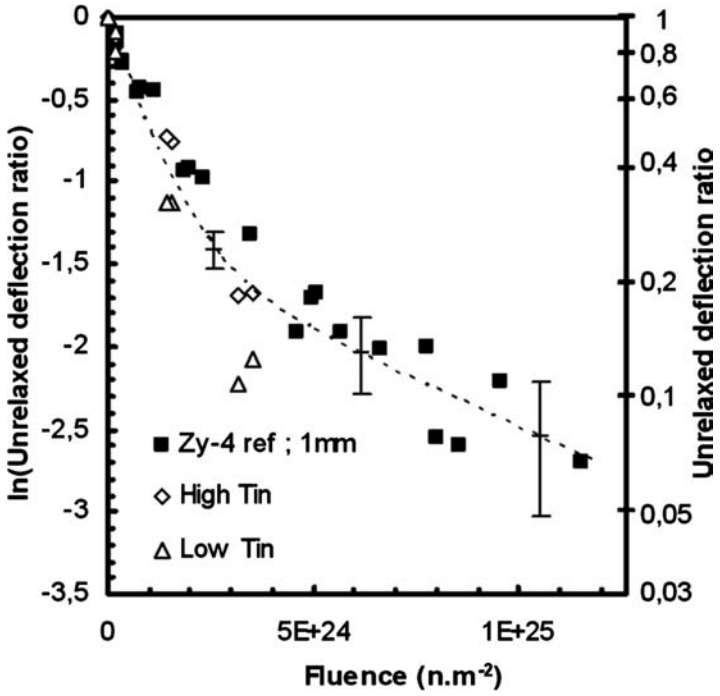


FIG. 12—*Unrelaxed deflection ratio as a function of fluence of RXA Zy-4 with different tin contents.*

with the thermal monitoring data illustrates the enhancement of the viscoplastic deformation induced by the irradiation. After 2000 h at 315°C without neutronic flux, the unrelaxed deflection ratio is about 0.8, compared with 0.1 at the same temperature under a constant flux of 1×10^{18} n · m^{-2} · s^{-1}.

It appears that the data obtained during the irradiation are more scattered than the data obtained during thermal relaxation. Nevertheless, taking into account the largest number of specimens, the intrinsic uncertainties of the irradiation experiment (homogeneity of the temperature for instance), and the measurement uncertainties that are higher for lowest unrelaxed deflection ratio, the repeatability of the data for a given deflection is quite satisfactory. Using Eq 5, we can plot for a 1 mm deflection the maximum value and minimum values (continuous lines) of an arbitrary reference curve (dotted line). Compared to uncertainties, there is no significant difference between the five specimens submitted to a 1 mm deflection and the three specimens submitted to 0.6 mm deflection. Thus, as explained previously, the unrelaxed deflection ratio can be considered as the unrelaxed stress ratio of an equivalent homogeneous specimen.

Figure 12 shows the unrelaxed deflection ratio as a function of fluence of RXA Zy-4 with different tin contents. The low tin grade exhibits an enhanced relaxation. The beneficial effect of tin content on the creep of zirconium alloys

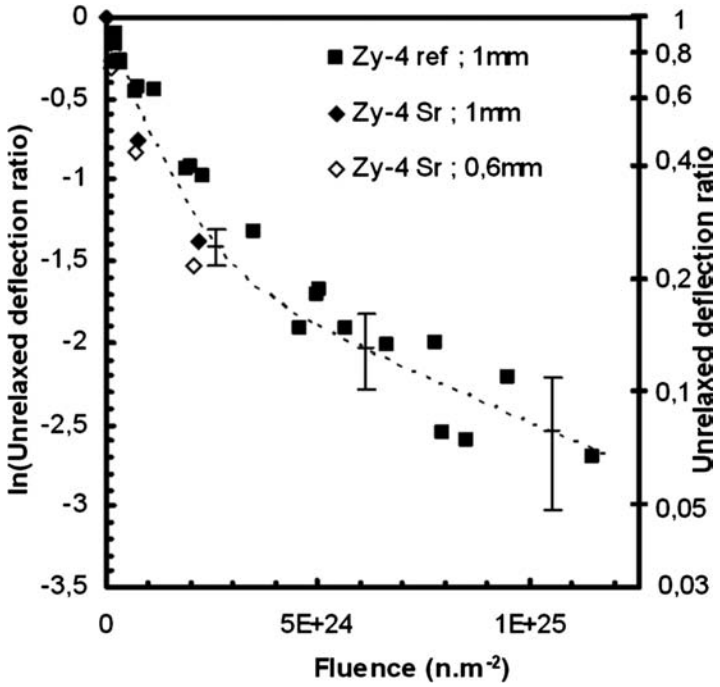


FIG. 13—*Unrelaxed deflection ratio as a function of fluence of Zy-4 in both recrystallized state and SR state.*

is already known for thermal creep [9]. Thus, Fig. 12 supports either an effect of tin on irradiation creep or a thermal component at the beginning of the relaxation.

Figure 13 shows the unrelaxed deflection ratio as a function of fluence of Zy-4 in both recrystallized state and SR state (specimens machined from the cladding tube reference material). No significant difference is observed for the same imposed deflection.

Figure 14 shows the unrelaxed deflection ratio as a function of fluence of RXA Zy-4 with prehydrided specimens with different initial hydrogen contents (0 ppm [H], 80 ppm [H], and 200 ppm [H] added). We can see a very strong effect of hydrogen, which enhances the relaxation. The same behavior is observed between 80 and 200 ppm. As the terminal solid solubility limit of hydrogen in the α phase of zirconium can be estimated close to 100 wt ppm at 315°C [10], this lack of difference suggests that only the solid solution of hydrogen has an effect on this enhancement of relaxation. This result is consistent with previous results where the softening effect of the solid solution of hydrogen was observed [11,12] and was attributed to a decrease of the dislocation pinning caused by interstitial atoms and/or to the enhancement of dislocation mobility [11].

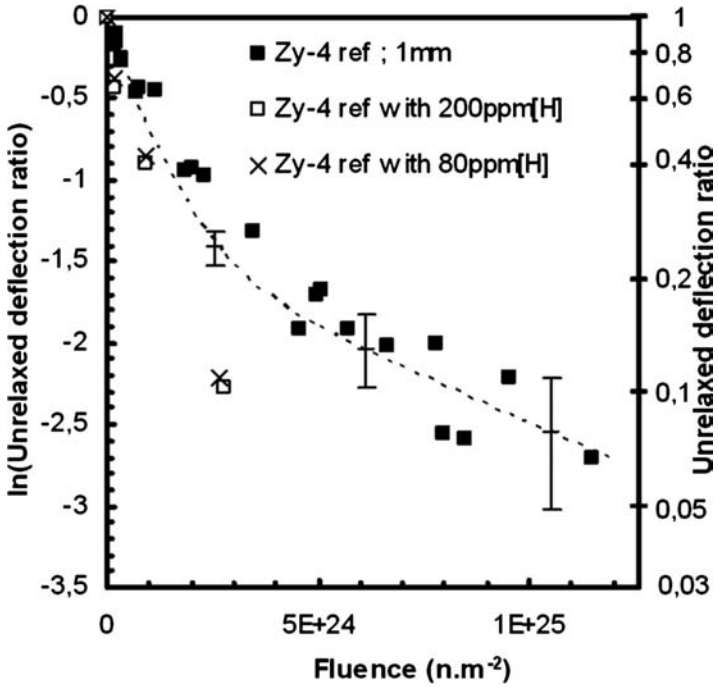


FIG. 14—*Unrelaxed deflection ratio as a function of fluence of RXA Zy-4 with different hydrogen contents.*

Effect of a Nonmonotonic Loading

A nonmonotonic loading was applied to some specimens by changing the configuration to which they were submitted during irradiation. Figure 15 shows the comparison of the unrelaxed deflection ratio between strips that were previously irradiated in a nonloaded configuration up to 8×10^{24} n · m^{-2}, then irradiated in a 1 mm deflection location, and strips that were previously irradiated in a 1 mm deflection location up to the same irradiation level (leading to an unrelaxed deflection ratio of 0.2), then placed in a 2 mm deflection location. For previously irradiated specimens, the origin of the x axis refers to the beginning of the second configuration of testing. The only difference between the two types of preirradiated specimens before the relaxation shown in this figure is the accumulated strains. The only difference between fresh material and preirradiated without deflection is the initial fluence. The good agreement between the two curves related to specimens preirradiated up to the same fluence with or without deflection shows that there is no effect of the previous strain accumulated before the beginning of relaxation, evidencing a mainly time hardening (or more precisely fluence hardening) behavior. On the other hand, the difference between the reference curve and the previously irradiated ones illustrates the hardening effect of accumulated fluence. It is worth noticing that as linear parts of the curves are related to the steady-state creep component, the

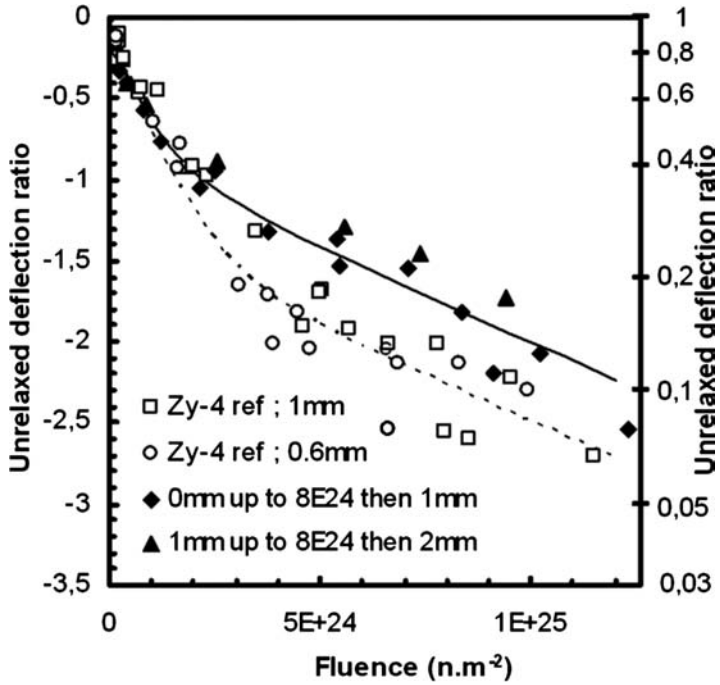


FIG. 15—*Unrelaxed deflection ratio as a function of fluence of RXA Zy-4 with different initial fluences and strains.*

steady-state for preirradiated material seems to occur at lower fluence (from the beginning of the test) than for fresh material. The strain-rate in steady-state appears to not be modified by preirradiation.

Quantitative Analysis

Validation of Hypothesis for Quantitative Analysis

The lack of effect of the imposed deflection was verified for the RXA Zy4 ref as shown in Fig. 11 so that the linearity assumption is fulfilled, as previously discussed. Figure 16 shows the normalized profiles of a strip during irradiation. As for thermal studies, the shape of the strip in an unloaded configuration is consistent with a linear strain field in this configuration. As a consequence, the "constant-shape" assumption is checked, ensuring that the total strain remains constant during relaxation. This assumption has also been checked on the specimen submitted to a nonmonotonic loading and was fulfilled in all cases.

Strain-Rate Determination

Since the linearity assumption, as well as the constant-shape assumption, is fulfilled, Eq 7 can be used to assess the strain-rate domain reached during the

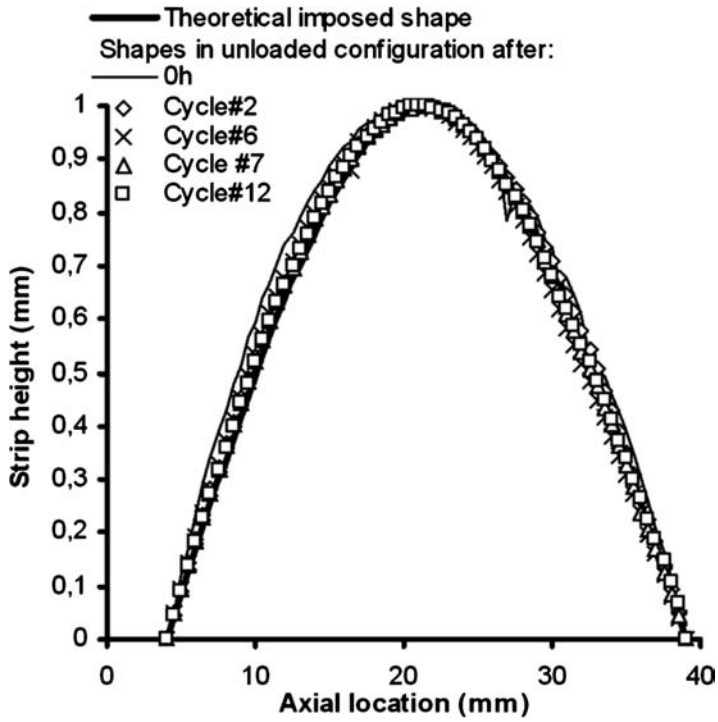


FIG. 16—*Normalized profiles during relaxation under flux at 315°C of reference RXA Zy4 alloy. The specimen was changed from a 1 mm imposed deflection to a 2 mm imposed deflection between cycle 6 and cycle 7 after a nearly total relaxation. In any configuration, the shape of the strip in unloaded configuration is coherent with linear strain field in this configuration. This is evidence that the total strain remains constant during relaxation even after the change of imposed deflection after relaxation.*

tests, as shown on Fig. 17. The curves corresponding to the two different imposed deflections coincide. Thus, contrary to the out-of-pile case, a relationship between stress and strain-rate that does not depend on the strain can be established. This result provides further evidence of a mainly fluence hardening type behavior.

Creep-Law Determination

In order to illustrate the potentiality of the method to characterize creep-law behavior, the parameters of the simple creep-law described in Eq 12 (referred hereafter as creep-law 1) were adjusted to the experimental unrelaxed deflection ratio obtained on the reference RXA Zy-4, as shown on Fig. 18. For more accuracy, the parameters were adjusted on the 1 mm deflection results. For each of the five specimens, the considered temperature is

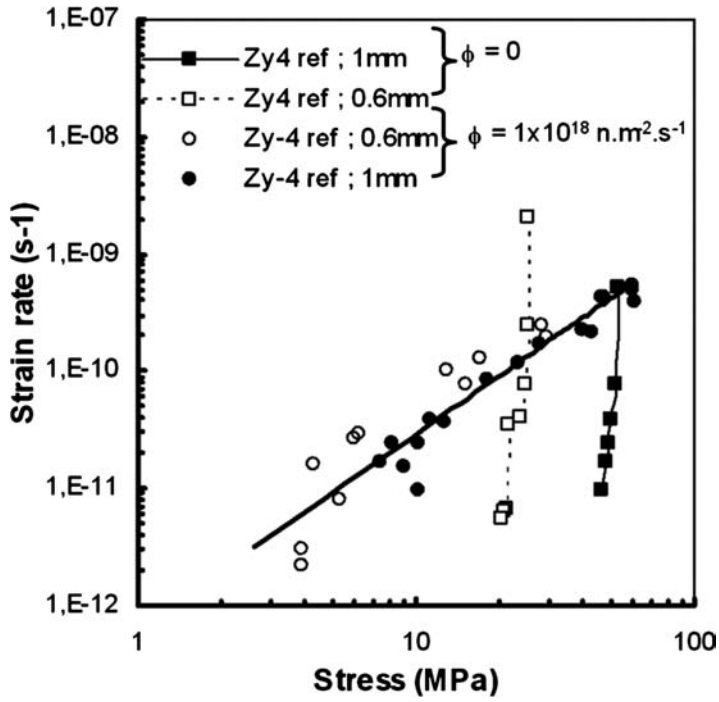


FIG. 17—*Strain-rate and stress domain during relaxation (with or without flux) at 315°C for reference RXA Zy-4 alloy for two initial imposed deflections.*

the average temperature during irradiation, ranging from 300 to 310°C. The values of the identified activation temperature, Q, that are compatible with experimental results range from $\sim$4500 to 8000 K. Considering the poor accuracy of this value, which has to be related with the small range of the temperature between specimens in this experiment, it was decided to fix the value at 5000 K, based on the value of 4722 obtained previously during the axial creep irradiation experiment FLETAN performed on the same material [13]. The other parameters are given in Fig. 18, where the good prediction of the model can be seen. Figure 19 shows the creep response obtained with Eq 8 compared to the creep experimental data obtained in Ref [13. Although the axial creep strains are of the same order of magnitude, they are slightly overestimated by the simple creep-law 1 adjusted on the relaxation results in the considered fluence domain. Quite logically, the steady-state that seems to occur in the relaxation response (linear part of Fig. 15) as well as in creep response (Fig. 19) is hardly described by this formulation, which may cause wrong predictions for extrapolated fluence. It is thus suitable to introduce both primary and secondary components in the creep expression. We choose for creep behavior an expression (referred hereafter as creep-law 2) close to that used in Ref [5]

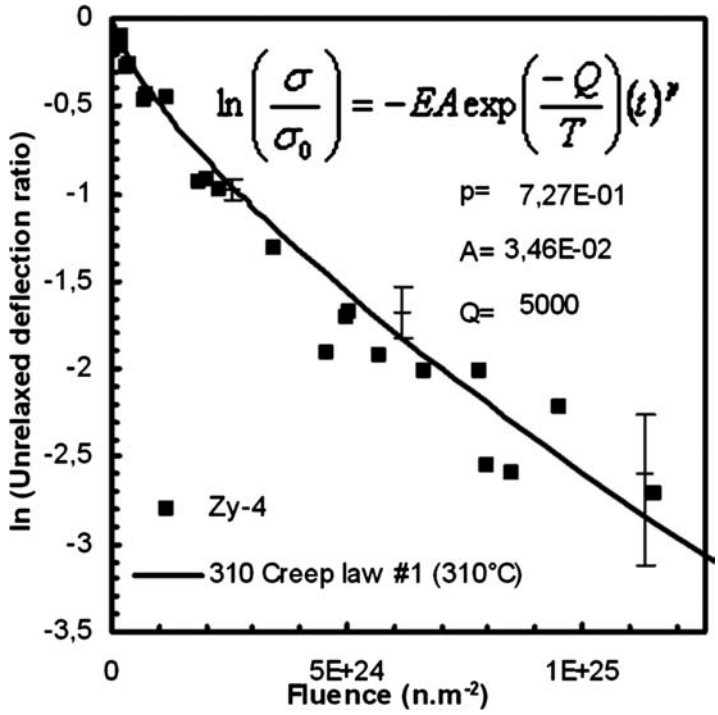


FIG. 18—*Identification of a simple Andrade law (with n=1) on fresh Zy-4-REFLET samples with 1 mm deflection.*

$$\varepsilon_{vp} = \exp\left(-\frac{Q}{T}\right) \cdot [B_1 \cdot \sigma \cdot \ln\left(1 + \omega(\Phi t)\right) + B_2 \cdot \sigma \cdot (\Phi t)] \tag{13}$$

Following the same reasoning than previously exposed, the relaxation behavior can then be described as follows:

$$\ln\left(\frac{\sigma}{\sigma_0}\right) = -E \exp\left(-\frac{Q}{T}\right) \cdot [B_1 \cdot \ln(1 + \omega \cdot \Phi_t) + B_2 \cdot \Phi_t] \tag{14}$$

where:

E = Young's modulus,
T = temperature,
Q = activation temperature,
Φ_t = fluence,
B_1 and ω = material parameters related to primary stage, and
B_2 = material parameter related to the secondary stage.

In order to discuss the potentiality of the method to derive creep-law from relaxation results, the parameters were adjusted using both Eqs 13 and 14, respectively, on the creep results obtained in Ref [13 (Fig. 20) and on the

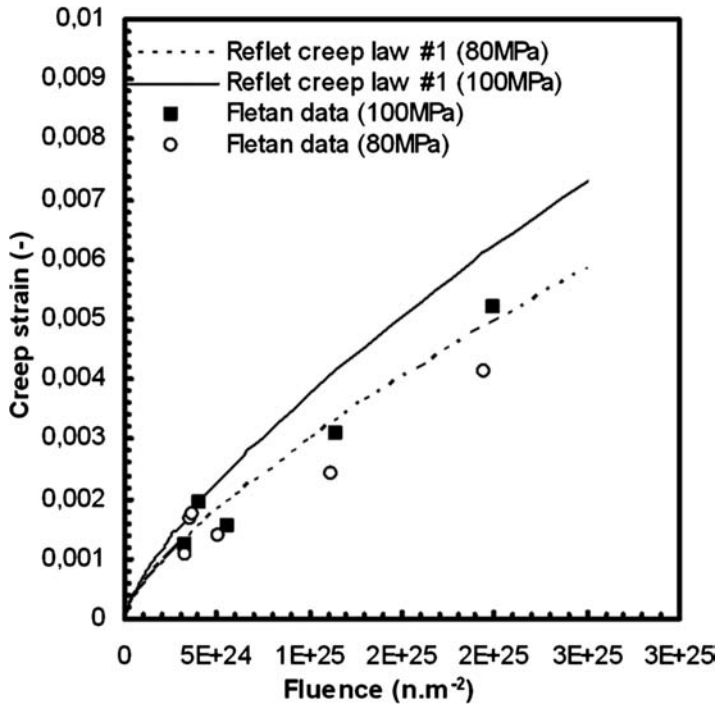


FIG. 19—*Creep response calculated with the creep-law 1 and comparison with previous results (data from FLETAN experiment).*

relaxation results obtained in this study (Fig. 21). In this example, the parameter related to the steady-state was determined from the creep strain-rate, considered mainly composed of secondary creep. The primary creep parameter was determined from the relaxation response mainly. Both relaxation and creep results are well reproduced with this kind of formulation. It is worth noticing that the relaxation response calculated with creep-law 2 identified this way is located between the fresh material and the preirradiated material with the same steady-state components (i.e., the slope of the linear part of the curve).

These results suggests that for some reasons that are not fully understood in this study but that are discussed further, the preliminary component of the creep-law may be overestimated when using relaxation results obtained on fresh material only. This overestimation could be correlated with the existence of a thermally induced viscoplastic strain component, depending not only on strains but also on fluence. The existence of such a component is suggested by Fig. 17, where a strain-rate of $5 \times 10^{-10}\,s^{-1}$ at the beginning of both out-of-pile and in-pile relaxation is obtained, showing that a thermal induced viscoplastic strain-rate is not negligible at the beginning of the in-pile relaxation. The effect of the fluence on this thermal component could explain the difference between the primary stage of both fresh and preirradiated materials as shown on Fig. 15, where the accumulated fluence before relaxation seems to increase the initial

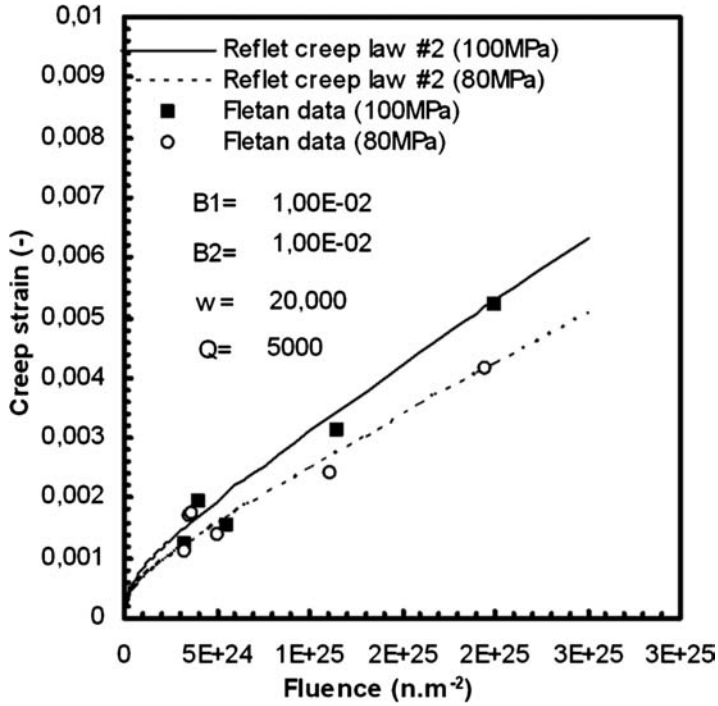


FIG. 20—*Creep response calculated with the creep-law 2. The parameters are identified on both creep and relaxation results.*

strain-rate but to decrease the global amount of the primary stage. On the other hand, in the FLETAN creep conditions, we conclude that the effect of such a thermal component can be neglected.

Discussion on Growth Component

An increase of the length of the strips could induce an artefact, through mechanical interaction between the spool and the strip. The relaxation process does not induce any dimensional change, but it has to be checked that there is no significant growth in our conditions.

There are three different components governing the growth of zirconium alloys [14]: The irradiation induced growth [15], the hydrogen uptake induced growth [16], and the oxidation induced growth [17,18]. As the experiment is performed in NaK, we do not expect any hydriding or corrosion of our specimens so that the only component that may occur is the irradiation induced growth. For RXA Zircaloys, the irradiation growth is divided into three stages: after the initial growth phase (below about $2 \times 10^{25}\,\mathrm{n \cdot m^{-2}}$ at temperatures close to 300°C), and the saturation phase (between about 2×10^{25} and $6\text{–}8 \times 10^{25}\,\mathrm{n \cdot m^{-2}}$ at those temperatures), a breakaway phase is observed [19], which is at fluences far above the fluence reached in our study. It was shown

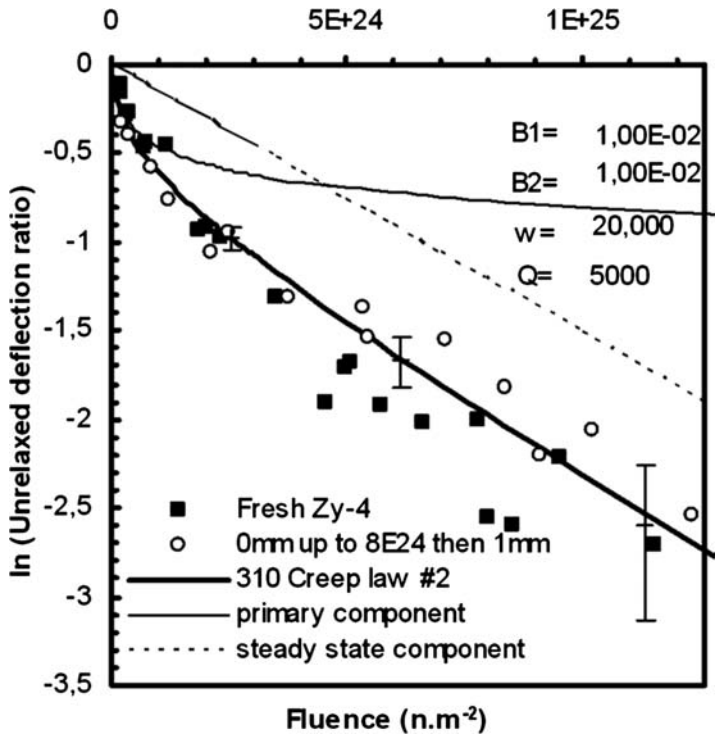


FIG. 21—*Rough identification of a creep-law composed by transient and steady-state components (creep-law 2). The parameters are identified on both creep and relaxation results.*

previously in Ref [13 that, on specimens irradiated in the same noncorroding environment (RXA Zircaloy-4 cladding tubes and RXA Zircaloy-4 specimens representative for thimble guide tubes), the free growth in the axial direction was about 0.2 % at 2×10^{25} n · m^{-2}. Such a small elongation is assumed to have no significant effect on the stress field applied by the spool on the strips.

Conclusion

It was shown that requirements needed to use the data obtained in this in-pile experiment as relaxation data obtained on homogeneous specimen are fulfilled. This result has been performed by the precise measurement of the shape of the strips, as well as the use of different initial imposed deflections.

Qualitatively, the REFLET experiment allows one to screen a large number of materials at once, which is a big asset compared to classical irradiation creep experiment. Indeed, more than 30 stressed specimens can be tested at once, whereas previous creep experiments performed in the same material testing reactor allowed less than five specimens to be loaded. For the simple shape of relaxation curves (i.e., curves that do not cross each other), it is possible to rank

the materials regarding their expected creep behavior, at least in the appropriate fluence and stress range.

Quantitatively, in the frame of the fulfilled requirements, this experiment provides advanced data that can be used for constitutive equation elaboration. In particular, the general relationship between strain-rate, stress, and strain can be experimentally established. Furthermore, it was shown by two different ways that, for in-pile tests, a time (or fluence) hardening assumption can be used. First, for in-pile tests, the strain-rate depends mainly on stress but not on strain, as it was confirmed by comparing the results obtained with two different imposed deflections. It is not the case for out-of-pile tests. Second, the in-pile relaxation on preirradiated materials does not depend on the possible deflection imposed during the preirradiation.

Since the time hardening assumption is fulfilled, it is possible to use directly the relaxation data to identify creep-law parameters. The comparison between creep results obtained in a previous experiment and a simple creep-law whose parameters are identified on relaxation test results is globally satisfactory as far as the stress and fluence range are compatible. Nevertheless, such a simple formulation cannot be easily extrapolated to higher fluences or stresses. It was thus shown that the identification of a more relevant formulation, with both primary and secondary components, is possible. The secondary component can be identified on the last points of relaxation, obtained on both fresh and preirradiated materials. The primary component seems to be more accurate when assessed on preirradiated material, which could be related to a thermal component of the viscoplastic strain, evolving with fluence.

Finally, the use of equations adapted to stress extrapolation is not studied here. It has to be kept in mind that the secondary component of the creep available with the REFLET experiment is related to the lowest stress values (i.e., the end of the relaxation), whereas the primary component reflects the highest stresses (i.e., the beginning of the relaxation). Thus, if stress extrapolation is an objective, the REFLET experiment has to be considered as complementary to more classical in-pile creep experiments, more devoted to the steady-state stage at higher stresses, and in which the primary stage is often inaccessible.

Acknowledgments

The writers want to thank all the people who made this experiment a success, through their expertise in the field of in-pile experiment monitoring or hot-cell remote handling.

References

[1] Auclair, M., Gosmain, L., Guimbal, P., Moulin, D., Roux, P., Sauder, C., and Villard, J. F., "CEDRIC Experiment: On Line Elongation Measurement of a High Temperature Specimen Under Driven Stress in the Osiris Reactor," *IGORR 2009*, Beijing, China, Oct. 28–30, 2009, http://www.igorr.com/home/liblocal/docs/IGORR2009%20-%20CEDRIC.pdf.

[2] Fraser, D. E., Ross-Ross, P. A., and Causey, A. R., "The Relation Between Stress-Relaxation and Creep for Some Zirconium Alloys During Neutron Irradiation," *J. Nucl. Mater.*, Vol. 46, No. 3, 1973, pp. 281–292.

[3] Morize, P., Baicry, J., and Mardon, J. P. "Effect of Irradiation at 588 K on Mechanical Properties and Deformation Behavior of Zirconium Alloy Strip," *Zirconium in the Nuclear Industry: Seventh International Symposium, ASTM STP 939*, Strasbourg, France, 1987, R. B. Adamson and L. F. P. Van Swam, Eds., ASTM International, West Conshohocken, PA, pp. 101–119.

[4] Causey, A. R., Butcher, F. J., and Donohue, S. A., "Measurement of Irradiation Creep of Zirconium Alloys Using Stress Relaxation," *J. Nucl. Mater.* Vol. 159, 1988, pp. 101–113.

[5] Foster, J. P., Gilbert, E. R., Bundec, K., and Porter, D. L., "Relationship Between In-Reactor Stress Relaxation and Irradiation Creep," *J. Nucl. Mater.*, Vol. 252, No. 1–2, 1998, pp. 89–97.

[6] Causey, A. R., Carpenter, G. J. C., and MacEwen, S. R., "In-Reactor Stress Relaxation of Selected Metals and Alloys at Low Temperatures," *J. Nucl. Mater.*, Vol. 90, No. 1–3, 1980, pp. 216–223.

[7] Ferrer, F., Barbu, A., Bretheau, T., Crepin, J., Willaime, F., and Charquet, D., "The Effect of Small Concentrations of Sulfur on the Plasticity of Zirconium Alloys at Intermediate Temperatures," *Zirconium in the Nuclear Industry: 13th International Symposium, ASTM STP 1423*, Annecy, France, 2002, G. D. Moan and P. Rudling, Eds., ASTM International, West Conshohocken, PA, pp. 863–885.

[8] Robinet, P., 1995, "Etude Expérimentale et Modélisation du Comportement Viscoplastique Anisotrope du Zircaloy-4 dans Deux États Métallurgiques [Experimental study and modelization of the anisotropic viscoplastic behaviour of zircaloy 4 in two metallurgical states]," °Ph.D. thesis, U.F.R. des Sciences et Technique de l'Université de Franche-Comté.

[9] McInteer, W. A., Baty, D. L., and Stein, K. O., "The Influence of Tin Content on the Thermal Creep of Zircaloy-4," *Zirconium in the Nuclear Industry: Eighth International Symposium, ASTM STP 1023*, San Diego, CA, 1989, ASTM International, West Conshohocken, PA, pp. 621–640.

[10] Kearns, J., "Terminal Solubility and Partitioning of Hydrogen in the Alpha Phase of Zirconium Zircaloy-2 and Zircaloy-4," *J. Nucl. Mater.*, Vol. 22, No. 3, 1967, pp. 292–303.

[11] Rupa, N., Clavel, M., Bouffioux, P., Domain, C., and Legris, A., "About the Mechanisms Governing the Hydrogen Effect on Viscoplasticity of Unirradiated Fully Annealed Zircaloy-4 Sheet," *Zirconium in the Nuclear Industry: 13th International Symposium, ASTM STP 1423*, Annecy, France, 2002, G. D. Moan and P. Rudling, Eds., ASTM International, West Conshohocken, PA, pp. 811–834.

[12] Le Saux, M., Besson, J., Carassou, S., Poussard, C., and Averty, X., "Behavior and Failure of Uniformly Hydrided Zircaloy-4 Fuel Claddings Between 25°C and 480°C Under Various Stress States, Including RIA Loading Conditions," *Eng. Failure Anal.*, Vol. 17, 2010, pp. 683–700.

[13] Yvon, P., Diz, J., and Ligneau, N., "Irradiation Creep and Growth of Guide Thimble Alloys," *Proceedings of the International Symposium Contribution of Materials Investigation to the Resolution of Problems Encountered in Pressurized Water Reactors Fontevraud IV*, Fontevraud, France, Sept. 14–18, 1998, Société Française de l'Energie Nucléaire, Paris, 1998, Vol. 2, pp. 1241–1252.

[14] Bossis, P., Verhaeghe, B., Doriot, S., Gilbon, D., Chabretou, V., Dalmais, A., Mardon, J. P., Blat, M., and Miquet, A., "In PWR Comprehensive Study of High Burn-up Corrosion and Growth Behavior of M5® and Recrystallized Low-Tin Zircaloy-

4," Sunriver, OR, 2009, *Zirconium in the Nuclear Industry: 15th International Symposium, ASTM STP 1505*, B. Kammenzind and M. Limback, Eds., ASTM International, West Conshohocken, PA, pp. 430–456.

[15] Fidleris, V., "The Irradiation Creep and Growth Phenomena," *J. Nucl. Mater.*, Vol. 159, 1988, pp. 22–42.

[16] King, S. J., Kesterson, R. L., Yueh, K. H., Comstock, R. J., Herwig, W. M., and Feguson, S. D., "Impact of Hydrogen on Dimensional Stability of ZIRLO Fuel Assemblies," *Zirconium in the Nuclear Industry: 13th International Symposium, ASTM STP 1423*, G. D. Moan and P. Rudling, Annecy, France, 2002, Eds., ASTM International, West Conshohocken, PA, pp. 471–489.

[17] Barberis, P., Vermoyal, J. J., Chabretou, V., and Rebeyrolle, V., "CASTA DIVA™: Experiments and Modelling Oxide Induced Deformation in Nuclear Components," *15th International Symposium, ASTM STP 1505*, Sunriver, OR, 2009, B. Kammenzind and M. Limback, Eds., ASTM International, West Conshohocken, PA, pp. 612–630.

[18] Blat-Yrieix, M., Ambard, A., Foct, F., Miquet, A., and Cayet, N., "Toward a Better Understanding of Dimensional Changes in Zircaloy-4: What is the Impact Induced by Hydrides and Oxide Layer?," *Zirconium in the Nuclear Industry: 15th International Symposium, ASTM STP 1505*, Sunriver, OR, 2009, B. Kammenzind and M. Limback, Eds., ASTM International, West Conshohocken, PA, pp. 594–607.

[19] Adamson, R. B., "Effects of Neutron Irradiation on Microstructure and Properties of Zircaloy," Toronto, Canada, 2000, *Zirconium in the Nuclear Industry: 12th International Symposium, ASTM STP 1354*, G. P. Sabol and G. D. Moan, Eds., ASTM International, West Conshohocken, PA, pp. 15–31.

DISCUSSION

Question 1, Joe Rashid, Anatech:—Applicability of time hardening versus strain hardening creep law to a given situation depends on whether you consider secondary creep only or a combination of primary and secondary. In the later case, you will find that time hardening ceases to be valid. Thermal creep, as compared to irradiation creep, has a strong primary creep component, and therefore, a strain hardening law would be more applicable.

Author's Response:—Strain or time hardening hypothesis deal with generalisation of a "classical creep formulation" (i.e. a strain or strain rate as a function of time and stress), that is **given only for a constant stress,** toward a "viscoplastic formulation", (i.e. a relationship between mechanical quantities, such as strain rate, stress, strain or internal variable, such as fluence) that is valid for any loading path.

As an example, during a creep test at a given value σ_1 of stress, we can change the stress from σ_1 to σ_2 at the time $\mathbf{t}_1$, and the corresponding strain ε_1.

If a viscoplastic formulation is not known, the strain rate value just after the stress change can't be given by the "classical creep formulation" only. The value of strain rate just after the stress change is usually considered to be included into two boundaries:

- The first one is the value of the strain rate given by the creep formulation used for σ_2 value, at time $\mathbf{t}_1$. This lower bound stands for "time hardening" behaviour.
- The second one is the value of the strain rate given by the creep formulation used for σ_2 value, at strain ε_1. This upper bound stands for "strain hardening" behaviour.

Obviously, for linear relationship between strain and time (secondary creep), both time hardening and strain hardening hypotheses lead to the same result.

So, I totally agree with the fact that, for secondary creep, using time hardening hypothesis (in order to use a classical creep law for non constant loading) leads to good results, but it is also the case for strain hardening hypothesis.

However, for non linear behaviour (primary creep, or a combination of primary and secondary creep), the use of the two hypotheses will lead to two different results. But we can't know *a priori* what hypothesis matches more the behaviour in non constant loading.

So, rather than "Applicability of time hardening versus strain hardening creep law to a given situation depends on whether you consider secondary creep only or a combination of primary and secondary." I would say "Applicability of time hardening versus strain hardening hypothesis depends on the **creep mechanisms involved**".

For instance, in our stress and temperature domains, zirconium alloy thermal creep is mainly related to dislocation gliding. It is therefore more than reasonable to assume a strong effect of the strain itself on the hardening of the material, by dislocation density raising effect. In this case, the strain rate has to be a function of the strain itself (at least), and a strain hardening is suitable.

But in our stress and temperature domains, irradiation creep is mainly assumed to be related to dislocation climbing, for instance by Stress Induced Preferred Absorption (SIPA) mechanism. Therefore, it is reasonable to assume that strain by itself does not harden the material, but time (or more precisely fluency) does. In this case, it is reasonable to assume time hardening, whatever the creep curve obtained.

In this paper, it has been shown that the relationship between stress and strain-rate does not depend on the strain for irradiation creep (Fig. 17), and depends for thermal creep (Fig. 8 and Fig. 17). This is an illustration with no creep test of time hardening applicability for irradiation creep, and time hardening non applicability for thermal creep.

Reprinted from JAI, Vol. 7, No. 9
doi:10.1520/JAI103006
Available online at www.astm.org/JAI

B. Bourdiliau,[1] *F. Onimus,*[2] *C. Cappelaere,*[1] *V. Pivetaud,*[1]
P. Bouffioux,[3] *V. Chabretou,*[4] *and A. Miquet*[5]

Impact of Irradiation Damage Recovery During Transportation on the Subsequent Room Temperature Tensile Behavior of Irradiated Zirconium Alloys

ABSTRACT: Zirconium alloys are commonly used in pressurized water reactor as fuel rod cladding tubes. After irradiation and cooling in pool, the spent nuclear fuel assemblies are either transported for wet storage to a devoted site or loaded in suitable casks for dry storage on a nuclear power plant site. During dry transportation or at the beginning of dry storage, at temperatures around 400C, the cladding experiences a creep deformation under the hoop stress induced by the internal pressure of the fuel rod. During creep, a recovery of the radiation damage can occur that can affect the subsequent mechanical properties. The mechanical behavior of the cladding has been investigated in laboratory on two neutron irradiated cladding materials: fully recrystallized Zr-1 % Nb and stress-relieved Zircaloy-4. Creep tests under internal pressure were conducted at 400 and 420C. After depressurization and cooling, ring tensile tests were carried out at room temperature. In addition, transmission electron microscopy observations have been performed after testing. The post-creep mechanical response exhibited a decrease of the

Manuscript received January 29, 2010; accepted for publication August 20, 2010; published online September 2010.
[1] DEN, Service d'Etudes des Matériaux Irradiés, CEA-Saclay, 91191 Gif-sur-Yvette, France.
[2] DEN, Service de Recherches Métallurgiques Appliquées, CEA-Saclay, 91191 Gif-sur-Yvette, France.
[3] EDF/R&D Les Renardières, Ecuelles, 77818 Moret sur Loing Cedex, France.
[4] AREVA, AREVA NP SAS, 10 Rue Juliette Récamier, 69456 Lyon Cedex 6, France.
[5] EDF/SEPTEN, 12-14 Av. Dutriévoz, 69628 Villeurbanne, France.

Cite as: Bourdiliau, B., Onimus, F., Cappelaere, C., Pivetaud, V., Bouffioux, P., Chabretou, V. and Miquet, A., "Impact of Irradiation Damage Recovery During Transportation on the Subsequent Room Temperature Tensile Behavior of Irradiated Zirconium Alloys," *J. ASTM Intl.*, Vol. 7, No. 9. doi:10.1520/JAI103006.

Copyright © 2011 by ASTM International, 100 Barr Harbor Drive, PO Box C700, West Conshohocken, PA 19428-2959.

strength compared to the as-irradiated material. This decrease is associated with a significant recovery of the ductility, which becomes close to the ductility of the unirradiated material. The transmission electron microscopy examinations, conducted on recrystallized Zr-1 % Nb ring samples, revealed that the radiation defects have been annealed. It was also observed that as for the unirradiated material, the deformation occurred homogeneously throughout the grains. No dislocation channeling was observed contrary to the as-irradiated material. These observations explain the recovery of the strength and of the ductility after post-irradiation creep that may also occur during dry transportation or at the beginning of dry storage.

KEYWORDS: ring tensile test, transmission electron microscopy, internal pressure creep test, heat treatment, deformation mechanisms, Zy-4, Zr-1 % Nb, spent nuclear fuel, transportation

Introduction

Zirconium alloys are commonly used in pressurized water reactors (PWRs) as fuel cladding tubes. After irradiation and cooling in the pool, the spent nuclear fuel assemblies (SNFA) are either transported for wet storage to a devoted site or loaded in suitable casks for dry storage on a nuclear power plant site. During dry shipment or at the beginning of dry storage, the cladding experiences creep deformation due both to the fuel rod inner pressure of the fission gas and to the significant temperature induced by the residual power of the fuel [1]. In order to guarantee the integrity of the cladding when retrieving the SNFA both after shipment and storage, it is essential to obtain a good knowledge of the effects of the transportation on the room temperature mechanical properties of the materials.

It has been shown in a previous study [2,3] that during a creep test, representative of transportation conditions, the recovery of the radiation damage occurs in addition to the creep deformation mechanisms. It has also been shown that the recovery of the irradiation damage is associated with the recovery of the hardening induced by irradiation, as demonstrated by transmission electron microscopy (TEM) observations and microhardness tests carried out at room temperature after heat treatments on as-irradiated zirconium alloys.

In order to have a better knowledge and understanding of the effect of post-irradiation creep testing on the subsequent room temperature mechanical properties of zirconium alloys, a thorough study has been done. This study is based on microhardness tests performed on the neutron irradiated zirconium alloys after creep testing and tensile tests carried on at room temperature on ring specimens, which were machined out of specimens after creep testing. In addition, on some of the tensile tests specimens, TEM observations have been performed after testing in order to obtain a better understanding of the deformation mechanisms in such testing conditions. The experimental results are presented in the first part of the paper. Then, in the last part, the results are discussed and interpreted in terms of microstructure and deformation mechanisms.

Materials and Experimental Details

Materials Studied

Two cladding materials have been studied: stress-relieved Zircaloy-4 and a recrystallized annealed Zr-1 % Nb alloy. The chemical compositions of the two alloys are given in Table 1. Information about the fabrication process may be found in Ref [4] for the Zy-4 cladding and in Ref [5] for the Zr-1 % Nb cladding. The texture of both alloys is detailed in Ref [6]. The materials have been irradiated from four to six PWR cycles and irradiation temperatures ranging from 300 to 350°C. After irradiation, the claddings have been cut and defueled in order to perform the mechanical tests. It has to be pointed out that in-reactor use induces hydriding of the cladding. The hydrides have mainly a circumferential orientation, which is representative of the spent fuel cladding material. For a same fluence, Zy-4 claddings have a higher hydrogen content than Zr-1 % Nb alloy.

Mechanical Testing

Creep Specimens—Four stress-relieved Zy-4 specimens irradiated for four PWR cycles have been tested under internal pressure during creep tests with an applied stress of 130 MPa, at temperatures from 380 to 420°C and times ranging from 1000 to 17 000 h. The creep tests were performed either in an internal pressure creep furnace with controlled internal gas pressure (hereafter called controlled gas pressure (CGP)) or as pre-pressurized samples (with internal gas pressure) in a furnace (called long term creep (LTC). The controlled internal pressure creep test (CGP) is performed at constant pressure, and at the end of the test, the specimen is depressurized before cooling. For the LTC test, the stress in the pre-pressurized specimen remains constant and gradually falls during cooling. The creep test conditions are given in Table 2.

Three recrystallized Zr-1 % Nb specimens irradiated from four to five PWR cycles have also been tested under internal pressure creep tests (in CGP or LTC conditions) with an applied stress of 130 MPa at temperatures from 400 to 420°C and for times ranging from 900 to 3300 h. The creep test conditions are given in Table 3.

Hardness Measurements—After the creep tests, 10 mm long sections of the specimens were cut, embedded into a resin, and then mechanically polished in a hot cell. Vickers microhardness experiments were carried out using a 200 g load along the z-direction of the tube (on the $r-\theta$ cross section of the tube).

TABLE 1—*Chemical composition of the alloys (wt %).*

Alloy	Metallurgical State	Sn	Fe	Cr	Nb	O	Zr
Zy-4	Stress-relieved	1.4	0.2	0.10	···	0.125	Bal.
Zr-1 % Nb	Recrystallized	···	0.02	···	1.0	0.125	Bal.

TABLE 2—*Testing conditions for the creep tests performed on the Zy-4 specimens. References to the tensile test specimens tested at room temperature are given in the last column. LTC: Long-term creep; CGP: Controlled gas pressure.*

Creep Specimen	Creep Test Type	Creep Temperature, °C	Creep stress, MPa	Creep Duration, h	Tensile Specimen
Zy4-1, four cycles	LTC	420	130	4974	Zy4-1a, Zy4-1b
Zy4-2, four cycles	CGP	420	130	1077	Zy4-2a, Zy4-2b
Zy4-3, four cycles	LTC	380	130	14 994	Zy4-3a, Zy4-3b
Zy4-4, four cycles	LTC	400	130	17 071	Zy4-4
Zy4-5 as-irradiated, four cycles	...	...	...	...	Zy4-5a, Zy4-5b
Zy4-6 non-irradiated	...	...	...	...	Zy4-6a, Zy4-6b

In order to provide correct statistical results, ten hardness measures were performed for each sample at room temperature.

Tensile Ring Specimens—Tensile ring specimens were also spark machined out of the cladding specimens (both Zy-4 and Zr-1 % Nb) after creep testing. The rings, cut out in the transverse section of the PWR cladding, were 3 mm long and 2 mm wide in the gauge length. Figure 1 shows an example of a tensile ring machined out of a LTC specimen. Two rings were cut out from a single creep specimen (except the Zy4-4 specimen) from each side of its symmetry axis. Moreover, two as-irradiated specimens and two unirradiated specimens were machined for both materials. The rings were then tested on an electromechanical tensile machine fitted with a LVDT sensor and a 50 kN load cell. The specimen was placed on its mandrel so that the sample legs were centered over the loading axis. The tensile test was displacement-controlled. All the tests were performed at room temperature with a strain rate of $3 \times 10^{-4}\,s^{-1}$. Several

TABLE 3—*Testing conditions for the creep tests performed on the Zr-1 % Nb specimens. References to the tensile test specimens tested at room temperature are given in the last column. LTC: Long-term creep; CGP: Controlled gas pressure.*

Creep Sample	Creep Test Type	Creep Temperature, °C	Creep Stress, MPa	Creep Duration, h	Tensile Specimen
ZrNb-1, five cycles	LTC	400	130	3301	ZrNb-1a, ZrNb-1b
ZrNb-2, four cycles	CGP	400	130	984	ZrNb-2a[a] , ZrNb-2b
ZrNb-3, four cycles	CGP	420	130	912	ZrNb-3a[a] , ZrNb-3b
ZrNb-4 as irradiated, six cycles	...	...	...	...	ZrNb-4a[a] , ZrNb-4b
ZrNb-5 non-irradiated	...	...	...	...	ZrNb-5a, ZrNb-5b

[a]Interrupted tests at UTS for TEM examination after testing.

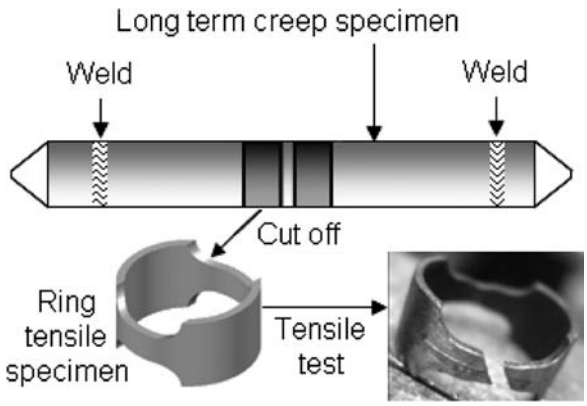


FIG. 1—*Example of a tensile ring machined out of a LTC specimen. The second ring was prepared the same way.*

conventional tensile properties are deduced from the tensile curves. The engineering stress is given as a function of the engineering strain: the yield stress (YS) (stress at 0.2 % plastic strain offset given in MPa), the ultimate tensile strength (UTS) (stress corresponding to the maximum force given in MPa), uniform elongation (UE) (plastic strain measured at maximum force, in percent), and total elongation (TE) (plastic strain at fracture, in percent). The stress-strain curves have been corrected from the overall testing machine stiffness, which is the result of the elastic deformation in the load line device and the mandrel stiffness. A Young modulus of $E = 100$ GPa at room temperature has been chosen in agreement with the values given by Northwood et al. [7].

Pictures of the ring specimens after testing were systematically taken. Some of these pictures are shown hereafter.

The non-irradiated Zr-1 % Nb alloy specimens were gaseously hydrided to 88 ppm in order to simulate the hydriding, which occurs in-reactor. In this way, the tensile tests measure the effect of irradiation, uncorrelated with the hydriding effect. In addition, in the case of the Zr-1 % Nb alloy, under each test condition, one ring was tested up to failure and a second one was stopped at UTS (indicated by footnotes in Table 3). From these specimens, thin foils have been taken in order to perform TEM observations of the as-deformed microstructure.

Transmission Electron Microscopy

TEM observations were carried out on neutron irradiated Zr-1 % Nb only previously tested to the UTS. The tests conditions of these samples are given in Table 3. No TEM examination has been conducted on Zy-4 due to its strongly cold-worked microstructure.

After testing, the legs of the ring specimens were cut and mechanically polished in hot cell. Thin foils were taken from the polished legs and electropolished in a glove box.

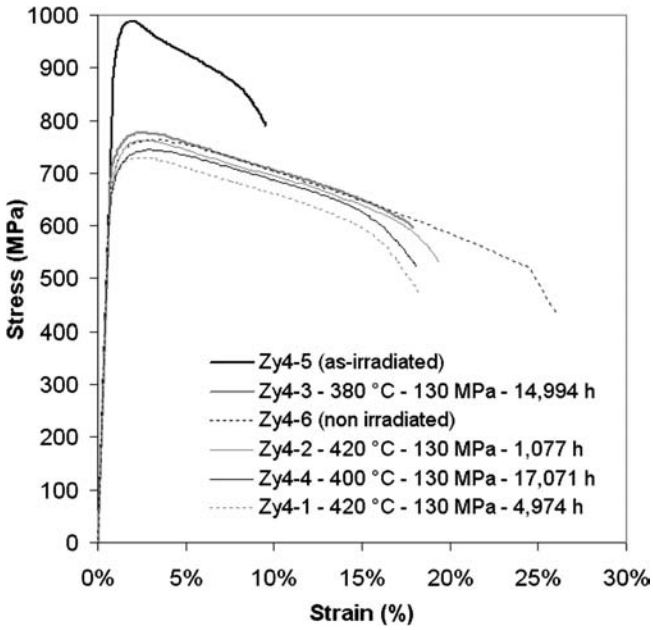


FIG. 2—*Engineering stress-strain curves obtained during ring tensile tests performed at room temperature on Zy-4 specimens after neutron irradiation and creep testing. Tensile tests on non-irradiated and as-irradiated Zy-4 specimens are also given.*

The TEM observations were performed on a Philips EM 430 operating at a 300 keV accelerating voltage. The study has been performed using a double tilt sample holder, conventional imaging of crystalline defects, and diffraction pattern indexing.

Experimental Results

Mechanical Tests

Zy-4 Specimens—The engineering stress-strain curves corresponding to the tests performed on Zy-4 are shown in Fig. 2. Conventional tensile properties deduced from the stress-strain curves are given in Table 4. On the basis of complementary testing, no significant span level effect has been observed on the mechanical properties.

When comparing the non-irradiated Zy-4 specimens and the as-irradiated specimens, Fig. 2 and Table 4 demonstrate that neutron radiation leads to a strong hardening (increase of the YS and UTS values) as well as to a reduction of the macroscopic ductility (decrease of the UE and TE values).

After creep testing, it can be seen in Fig. 2 and Table 4 that the YS as well as the UTS values has decreased compared to the as-irradiated behavior. It is also shown that after the creep testing, the UE as well as the TE values has

TABLE 4—*Conventional tensile mechanical properties deduced from the engineering stress-strain curves obtained for Zy-4 specimens (at room temperature).*

Ring Sample	Creep Temperature; Duration	YS, MPa	UTS, MPa	UE, %	TE, %
Zy4-1a	420°C; 4974 h	676	731	1.71	17.97
Zy4-1b		686	743	1.69	17.32
Zy4-2a	420°C; 1077 h	719	787	2.05	18.80
Zy4-2b		688	764	2.02	18.89
Zy4-3a	380°C; 14 994 h	722	778	1.94	17.31
Zy4-3b		722	788	1.49	15.89
Zy4-4	400°C; 17 071 h	674	745	2.16	17.59
Zy4-5a	As-irradiated	916	966	0.84	9.89
Zy4-5b		940	989	0.87	8.68
Zy4-6a	Non-irradiated	693	763	2.28	25.70
Zy4-6b		689	763	2.69	26.74

increased, proving that the creep test leads to a recovery of the ductility of the material.

However, it can be noticed in Fig. 2 and Table 4 that after creep testing, the room temperature tensile behavior remains different from the non-irradiated mechanical behavior. Indeed, the UE and TE values remain systematically lower than the values measured for the non-irradiated Zy-4, proving that the macroscopic ductility of the material was not fully recovered even after 4974 h at 420°C (specimen Zy4-1) or after 17 071 h at 400°C. On the other hand, the strength (YS and UTS) of the material can be fully recovered after creep testing and can even become lower than the YS and UTS values measured on the non-irradiated material.

It can also be noticed that when the creep temperature increases from 380 up to 420°C, the strength (YS and UTS) tends to a slight decrease. Increasing the duration of the creep test leads also to a slight decrease of the strength after creep. Concerning the UE and TE values, no obvious evolution with creep test temperature and duration can be observed.

The pictures of the ring specimens after tensile tests on the as-irradiated Zy-4 and on the Zy-4 after creep testing (Zy4-2) show that the failure occurs only on one leg by shearing and propagation of a crack, making a 45° angle with the tensile axis, which confirms a ductile fracture. Nevertheless, the necking of the gauge length of the ring remains limited for both specimens (Fig. 3). It is worth noticing that the as-irradiated specimen and the specimen after post-irradiation creep testing, exhibit a similar fracture morphology.

Zr-1 % Nb Specimens—The engineering stress-strain curves corresponding to the tests performed on the Zr-1 % Nb specimens are shown in Fig. 4, and the conventional tensile properties are given in Table 5. As for Zy-4, on the basis of

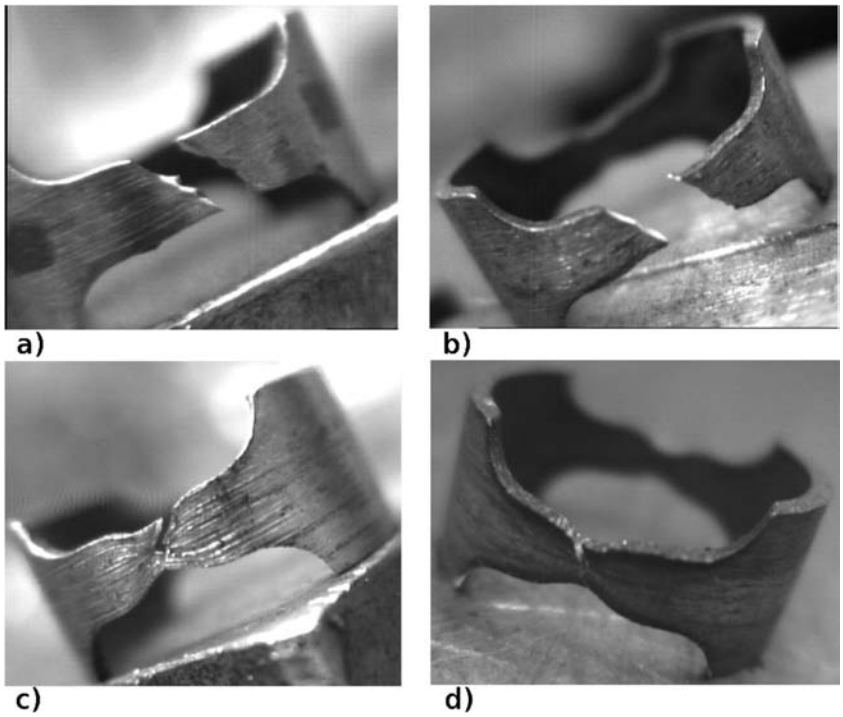


FIG. 3—*Pictures of the ring tensile test specimens after failure for* (a) *as-irradiated Zy-4 specimen (Zy4-5a),* (b) *creep tested Zy-4 specimen (Zy4-2a),* (c) *as-irradiated Zr-1 % Nb specimen (ZrNb-4b), and* (d) *creep tested Zr-1 % Nb specimen (ZrNb-1b).*

complementary testing, no significant span level effect has been observed on the mechanical properties.

Figure 4 and Table 5 show that, similar to Zy-4, neutron irradiation leads to a strong hardening, as shown by the increase of the YS and UTS values when comparing the non-irradiated and the as-irradiated specimens, and to a reduction of the macroscopic ductility (decrease of the UE and TE values). On the tensile curve of the as-irradiated ring tested up to failure, we can see a load drop just after the UTS. In addition, the tensile curve exhibits a sudden acceleration of the load decrease during the necking.

After post-irradiation creep, it can be seen in Fig. 4 and Table 5 that the YS as well as the UTS values of the Zr-1 % Nb specimens have decreased compared to the as-irradiated behavior, proving that a recovery of the radiation hardening has occurred during the creep test. It is also shown that, after the creeptest, the UE values have increased, proving that the post-irradiation creep test leads to a recovery of the ductility of the material.

However, it can be noticed that, when comparing the behavior after post-irradiation creep to the behavior before irradiation, the YS and UTS values after creep are still higher than the values measured before irradiation. The

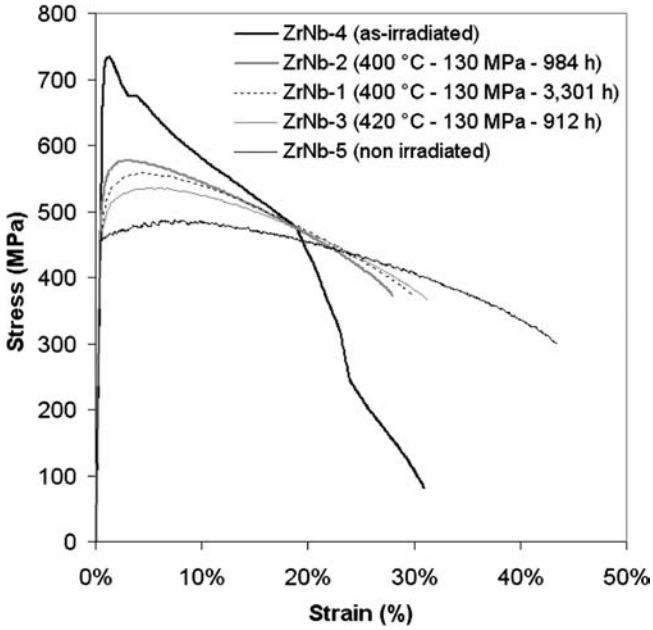


FIG. 4—*Engineering stress-strain curves obtained during ring tensile tests performed at room temperature on Zr-1 % Nb specimens after neutron irradiation and creep testing. Tensile tests on non-irradiated and as-irradiated Zr-1 % Nb specimens are also provided.*

macroscopic ductility also appears to be only partially recovered after creep: The UE and TE values remain lower than the values measured before irradiation. It is also worth noticing that the strain hardening behavior after post-irradiation creep is also very different from the strain hardening behavior before irradiation.

TABLE 5—*Mechanical properties obtained for Zr-1 % Nb specimens.*

Ring Sample	Creep Temperature; Duration	YS, MPa	UTS, MPa	UE, %	TE, %	UTS-YS, MPa
ZrNb-1a	400°C; 3301 h	470	555	5.01	27.17	85
ZrNb-1b		484	558	3.91	29.57	74
ZrNb-2a	400°C; 984 h	515	568	2.43[a]	...	53
ZrNb-2b		525	577	2.63	27.59	52
ZrNb-3a	420°C; 912 h	475	544	5.16[a]	...	69
ZrNb-3b		477	536	4.76	30.95	59
ZrNb-4a	As-irradiated	734	741	0.41[a]	...	7
ZrNb-4b		721	734	0.49	30.88	13
ZrNb-5a	Non-irradiated hydrided	460	498	9.26	42.74	38
ZrNb-5b		460	487	6.96	43.07	27

[a]Tests interrupted at UTS in order to provide samples for TEM observations.

Indeed, on the non-irradiated Zr-1 % Nb specimens, the strain hardening rate is low just after the onset of plastic flow and decreases slowly until reaching the maximum load. Whereas in the case of the Zr-1 % Nb after post-irradiation creep, the strain hardening remains high at the onset of plastic flow and decreases more quickly until reaching the maximum load. This change in the strain hardening behavior due to the post-irradiation creep test can be characterized by the difference between UTS and YS values. Table 5 shows indeed that the difference between UTS and YS values after post-irradiation creep is nearly twice the difference between the UTS and YS values measured on the non-irradiated specimens. This proves that the strain hardening after post-irradiation creep is higher than the strain hardening before irradiation.

It can also be noticed that when the creep temperature or the creep duration increases, the strength (YS and UTS values) slightly decreases and the ductility (UE and TE values) increases.

The pictures taken after the tensile test (Fig. 3) show that both the as-irradiated Zr-1 % Nb specimen and the Zr-1 % Nb specimen tested after post-irradiation creep show a significant necking. Strong shearing is observed as the crack shows a 45° angle with the tensile axis. The crack is close to 45° on one side of the reduced area and close to 135° on the other side due to a change of the crack propagation direction at the reduced area center. It is worth noticing that both specimens shown in Fig. 3 exhibit the same fracture morphology

Microhardness Measurements

Zy-4 Specimens—Table 6 displays the Vickers microhardness obtained on the Zy-4 specimens. Hardness values and measured UTS values were compared.

It can be seen in Table 6 that, when comparing the as-irradiated to the non-irradiated Zy-4 specimens, irradiation leads to a significant increase of the hardness linked to the radiation induced hardening observed during the tensile test. After creep testing, the hardness value decreases strongly because of the recovery of the radiation induced hardening. It can be seen that, as for the YS and

TABLE 6—*Microhardness values measured after post-irradiation creep tests on Zy-4 specimens compared to UTS values measured during tensile tests after post-irradiation creep tests.*

Tensile Sample	Creep Temperature; Duration	UTS, MPa	Microhardness, $kg \cdot mm^{-2}$
Zy4-1a	420°C; 4974 h	731	235±5
Zy4-1b	420°C; 4974 h	743	
Zy4-2a	420°C; 1077 h	787	244±3
Zy4-2b	420°C; 1077 h	764	
Zy4-5a	As-irradiated	966	300±8
Zy4-5b	As-irradiated	989	
Zy4-6a	Non-irradiated	763	244±3
Zy4-6b	Non-irradiated	763	

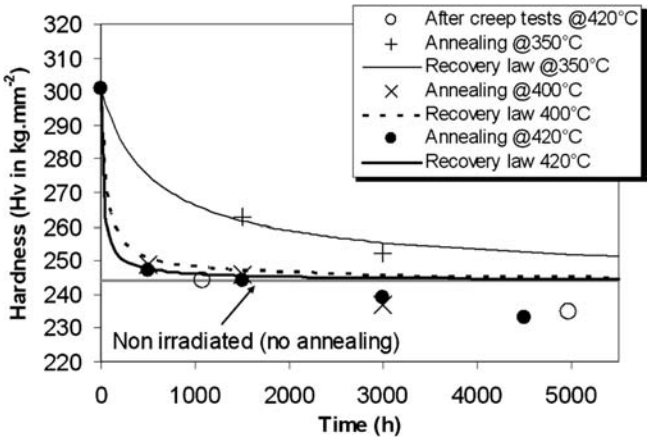


FIG. 5—*Comparison between the hardness evolution after post-irradiation creep tests and post-irradiation heat treatments performed on Zy-4 specimens at 350, 400, and 420°C. The recovery law is also shown.*

the UTS values, depending on the post-irradiation creep conditions, the hardness of the Zy-4 specimens can even become lower than the hardness of the non-irradiated Zy-4 specimen.

The hardness values measured after post-irradiation creep testing are also compared in Fig. 5 to the hardness evolution after post-irradiation heat treatments performed on Zy-4 at 350, 400, and 420°C. The empirical recovery law proposed in Refs [8 and 9] and adjusted in Ref [2] is also shown in Fig. 5. The recovered fraction of hardness, f, is defined in Eq 1

$$f = \frac{H_v^{AsI} - H_v(t)}{H_v^{AsI} - H_v^{NI}} \tag{1}$$

The values H_v^{AsI}, H_v^{NI}, and $H_v(t)$ used in Eq 1 are the as-irradiated hardness of the material, the non-irradiated hardness of the material, and the current hardness of the material, respectively, all along the heat treatment. According to Dollins [9], the hardness recovered fraction follows a chemical kinetics empirical law, expressed in Eq 2

$$\frac{df}{dt} = k(1-f)^n \tag{2}$$

In Eq 2, the coefficient k can be written as $k = k_0 \exp(-Q/k_B T)$, where k_B is the Boltzmann constant, T is the temperature of the heat treatment, Q is the activation energy of the recovery, and k_0 is a coefficient. The fitted values are $n = 2.3$, $k_o = 1.8 \times 10^8\ \mathrm{s}^{-1}$, and $Q = 1.800\ \mathrm{eV}$. Since in the empirical law the reference hardness value is the hardness before irradiation, the empirical law chosen here is therefore not able to reproduce the decrease of the hardness below its value before irradiation.

TABLE 7—*Microhardness values measured after post-irradiation creep tests on Zr-1 % Nb specimens compared to UTS values measured during tensile tests after post-irradiation creep tests.*

Tensile Sample	Creep Temperature; Duration	UTS, MPa	Microhardness, $kg \cdot mm^{-2}$
ZrNb-1a	400°C; 3301 h	555	195±5
ZrNb-1b	400°C; 3301 h	558	
ZrNb-2a	400°C; 984 h	568	189±5
ZrNb-2b	400°C; 984 h	577	
ZrNb-4b	As-irradiated	734	237±6
ZrNb-4a	As-irradiated	741	
ZrNb-5d	Non-irradiated	487	165±5
ZrNb-5c	Non-irradiated	498	

It can be seen in Fig. 5 that the hardness values measured after post-irradiation creep tests performed on Zy-4 specimens at 420°C during 1077 and 4974 h are in good agreement with the hardness measured after post-irradiation heat treatment performed at 420°C for similar duration showing that the effect of post-irradiation creep on the hardness of Zy-4 is the same as a post-irradiation heat treatment.

Zr-1 % Nb Specimens—The hardness values obtained on the Zr-1 % Nb specimens after post-irradiation creep performed at 400°C are given in Table 7 and compared to the UTS values. As for the Zy-4 specimens, the hardness values of the Zr-1 % Nb specimens follow the same evolution as the YS and UTS values. It can be seen in Table 7 that irradiation induces a strong hardening when comparing the hardness of the as-irradiated Zr-1 % Nb and the hardness of the non-irradiated Zr-1 % Nb specimens. As for the YS and UTS values, it can be seen that after post-irradiation creep, the hardness decreases due to the recovery of the radiation induced hardening. However, it can be observed that the hardness values after post-irradiation creep of Zr-1 % Nb specimens always remain higher than before irradiation.

The hardness values measured after post-irradiation creep tests performed at 400°C are also compared in Fig. 6 to the hardness evolution after post-irradiation heat treatments performed on a Zr-1 % Nb alloy at 350, 400, and 450°C. The empirical recovery law is also shown in Fig. 6. This law has been adjusted on the results obtained at 350 and 400°C. The values of the fitting parameters are $n = 3.1$, $k_o = 3.8 \times 10^2\ s^{-1}$, and $Q = 1.075$ eV. It can be noticed that the extrapolation of this law at 450°C overestimates the hardness recovery.

It can be observed in Fig. 6 that after post-irradiation creep performed at 400°C during 984 or 3301 h, the hardness of the Zr-1 % Nb specimens remains higher than the hardness measured after a post-irradiation heat treatment at 400°C lasting only 500 h. This proves that in the case of the Zr-1 % Nb specimens, post-irradiation creep and heat treatment have different effects on the hardness.

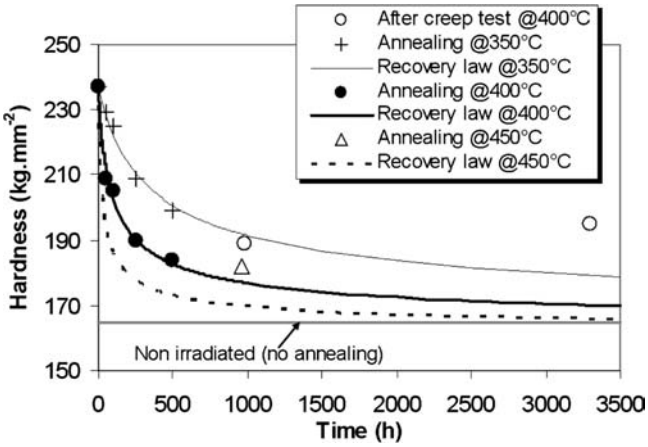


FIG. 6—*Comparison between the hardness evolution after post-irradiation creep tests and post-irradiation heat treatments performed on Zr-1 % Nb specimens at 350, 400, and 450°C. The recovery law is also shown.*

Correlation between Hardness and Ultimate Tensile Strength Values—Tables 6 show that the hardness and the UTS values follow the same evolution for Zy-4 and Zr-1 % Nb specimens. The change in UTS (with respect to the non-irradiated material) can therefore be plotted in Fig. 7 as a function of the change in hardness (with respect to the non-irradiated material) for both alloys. It can be observed in Fig. 7 that there is a linear relationship for all specimens between the change in UTS measured in the hoop direction and provided by the ring tensile tests and the change in Vickers hardness measured on the $r-\theta$ cross section of the tube. The proportionality coefficient is: $\Delta UTS = 3.485 \Delta H_v$ with ΔUTS in

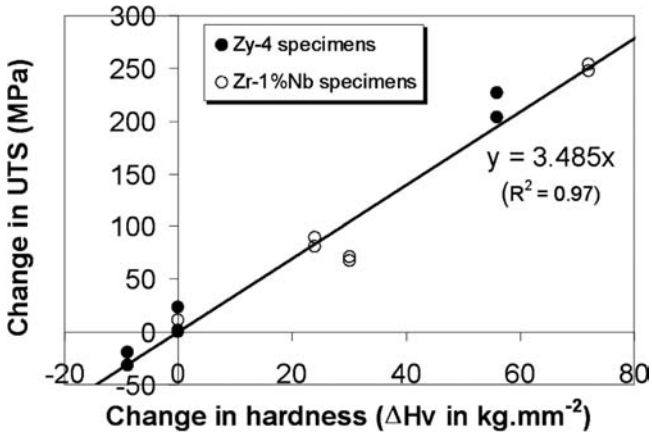


FIG. 7—*Correlation between the change in UTS and the change in hardness for both Zy-4 and Zr-1 % Nb specimens.*

MPa and ΔH_v in $kg \cdot mm^{-2}$ (or HV). This analysis is in agreement with the relationship obtained by Busby et al. [10] between hardness and YS in irradiated austenitic and ferritic steels. The good correlation obtained between UTS values and hardness values confirm that the two techniques provide a coherent quantification of the recovery state of the material after post-irradiation creep testing. In the following, these techniques are both used and compared to the TEM observations.

Results of the Transmission Electron Microscopy Observations on Zr-1 % Nb Samples

As-Irradiated Sample Observed after Tensile Testing—TEM examinations have been performed on the as-irradiated sample after tensile testing. TEM pictures of the microstructure obtained after deformation are given in Fig. 8. It can be observed that the microstructure exhibits cleared bands or so-called dislocation channels in numerous grains. The channeling plane has been analyzed using the method described in Refs [6 and 11]. It can be seen in Fig. 8(*a*) that the channeling plane corresponds to the basal plane. The deviation of the basal channels on the pyramidal or prism planes can also be observed in Fig. 8(*a*).

On the other hand, it can be seen that in several grains (Fig. 8(*b*)8(*d*)), the observed channels do not correspond to the basal plane. Indeed, the channels can be observed even when the basal plane is nearly perpendicular to the electron beam. The channeling planes have been analyzed and correspond to the prismatic planes. Moreover, it appears that contrary to the basal channels, which are only clearly observed when the basal plane nearly contains the electron beam, the prismatic channels can be observed for a wide tilt angle range, even when the electron beam is far from the prismatic plane. This can lead to a more ambiguous determination of the channeling plane.

Since the orientation of the tensile axis is known on the thin foil it is possible to compute the Schmid factors of the various slip systems for each grain observed. The basal and prismatic Schmid factors of the grains observed in Fig. 8 are given in Table 8. It can be seen in Table 8 that when the basal plane is well orientated for slip (high basal Schmid factor), basal channeling occurs. On the other hand, when the basal plane is not well orientated for slip (low basal Schmid factor), prismatic channeling occurs.

Samples Observed after Tensile Tests Following Creep Tests—TEM examinations have been performed after room temperature tensile tests following post-irradiation creep tests at 400 and 420°C under 130 MPa in internal pressure. It can be seen in Fig. 9 that the dislocation density observed after tensile tests is significant and that the dislocations appear to be tangled. No dislocation channel can be observed, in contrast to what occurs in the as-irradiated specimen, and the deformation is distributed homogeneously within the grains. It can also be noticed in Fig. 9 that the microstructures observed for the two creep tests conditions (400 and 420°C) are very similar.

In Fig. 9(*a*), where the grain is observed with the electron beam close to the $\langle c \rangle$ axis, two linear dislocation systems are clearly observed at 120° from each

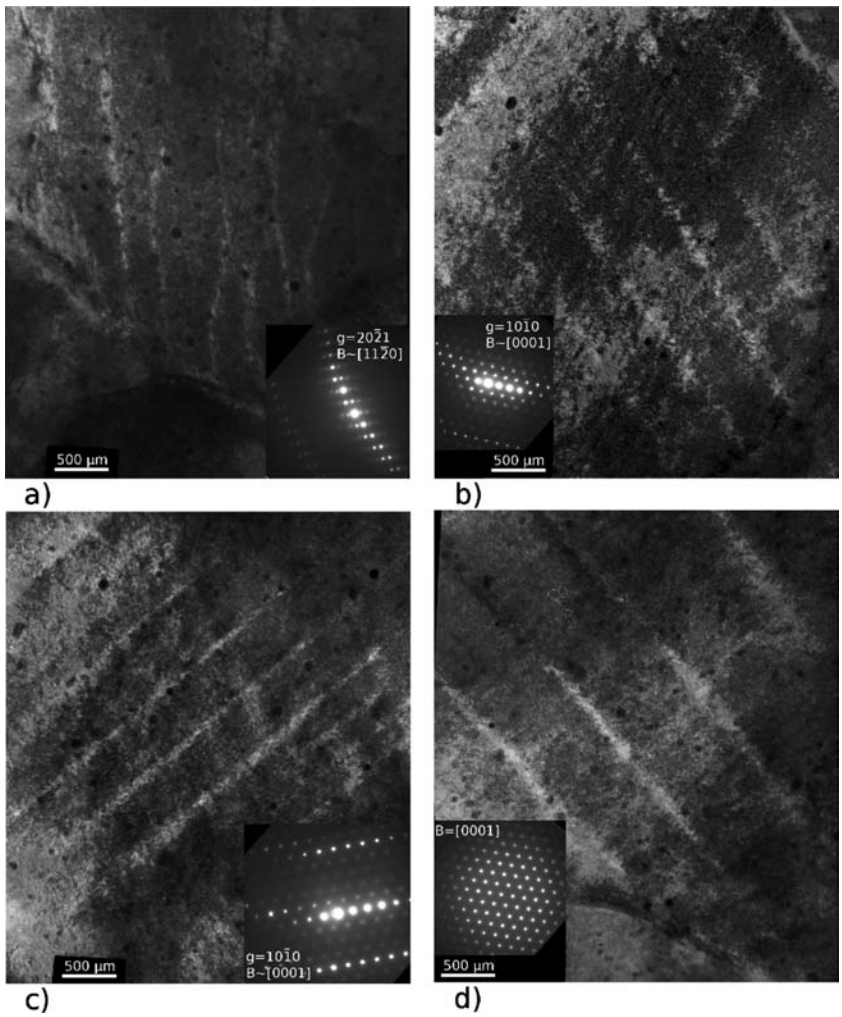


FIG. 8—*Pictures of the ZrNb-4a specimen microstructure: the channels appear as clear bands.* (a) *Basal channels in grain 1 observed with the electron beam close to the basal plane* ($B \approx [11\bar{2}0]$) *using the diffraction vector* $g=20\bar{2}1$. *[(*b*) and (*c*)] Prismatic channels in grains 2 and 3 observed with the electron beam close to the* $\langle c \rangle$ *axis* ($B \approx [0001]$) *using the diffraction vector* $g=10\bar{1}0$. (d) *Prismatic channels in grain 4 observed with the electron beam close to the* $\langle c \rangle$ *axis* ($B \approx [0001]$). *The picture has been observed in two beams condition close to the [0001] zone axis diffraction pattern shown on the picture.*

other. This shows that in that grain, prismatic slip is mainly activated. In Fig. 10(*a*), 10(*b*), the same area is shown using two different diffraction conditions. Nb-rich precipitates in the shape of needles are clearly observed in Fig. 10(*b*) without any contrast coming from the loops or the dislocations. The

TABLE 8—*Basal and prismatic Schmid factors for the four grains observed by TEM in Fig. 8. For basal slip, the maximum basal Schmid factor is always given. For prismatic slip, the prismatic Schmid factor corresponding to the activated slip system is given; when only basal channels are observed, the maximum prismatic Schmid factor is given.*

Grain Observed	Maximum Basal Schmid Factor	Prismatic Schmid Factor	Channeling Plane Observed
Grain 1 in Fig. 8(*a*)	0.4	0.12	Basal
Grain 2 in Fig. 8(*b*)	0.29	0.45	Prismatic
Grain 3 in Fig. 8(*c*)	0.16	0.47	Prismatic
Grain 4 in Fig. 8(*d*)	0.26	0.45	Prismatic

microstructure (size and density) of the needle-like precipitates appear to be similar to that observed in the as-irradiated Zr-1 % Nb alloy [12]. This suggests that both the creep test and the tensile test did not significantly affect the needle precipitates.

On the other hand, it turns out that it is very difficult to clearly distinguish dislocation loops after the tensile tests. As shown in Fig. 9 very few loops are clearly observed, and in addition, the small loop contrast can be mistaken for the contrast coming from the needle precipitates. This observation has to be compared to the TEM observations described in Ref [2] after post-irradiation creep tests. Indeed, after post-irradiation creep performed at 400°C under a 130 MPa applied stress, small $\langle a \rangle$ loops could still be observed with size and density in rather good agreement with the microstructure observed after heat treatments at 400°C. This proves that the tensile test performed after the post-irradiation creep test has strongly affected the remaining loops.

It can also be pointed out that the dislocations observed in Fig. 10(*a*) after tensile tests seem to be pinned on needle-like precipitates and/or on residual $\langle a \rangle$ loops.

Discussion

Discussion on the Behavior of the As-Irradiated Zr-1 % Nb Specimens

The TEM observations have shown that in the as-irradiated condition Zr-1 % Nb has a very high density of small $\langle a \rangle$ type dislocation loops induced by irradiation. This very high density of small dislocation loops that act as obstacles against dislocation motion explains the strong irradiation induced hardening measured through tensile and hardness tests.

It has been shown by TEM that the as-irradiated Zr-1 % Nb specimen tested at room temperature and interrupted at the UTS exhibits dislocation channels. This deformation mechanism consists of the clearing of the irradiation induced loops by gliding dislocations on only one slip system leading to the creation of a defect free zone that becomes a preferred area for further dislocations gliding [6,11]. This phenomenon leads to the localization of the plastic strain at the grain scale and to a softening at the microscopic scale. This mechanism, as well

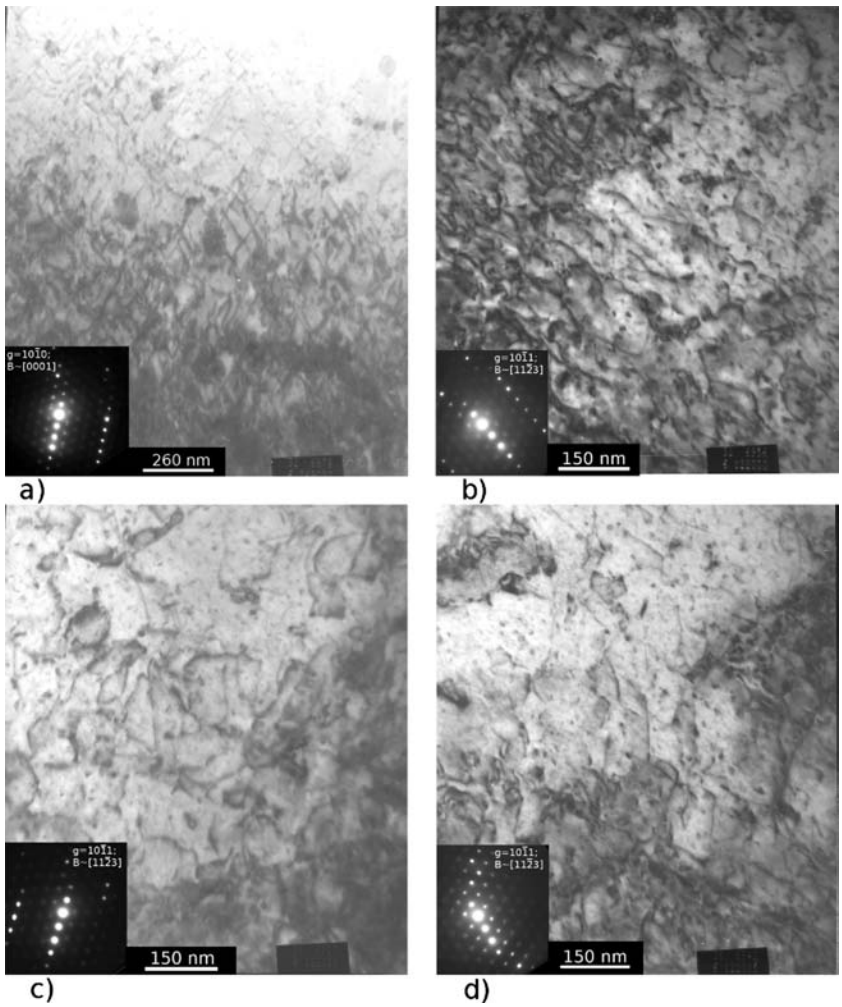


FIG. 9—*[(*a*) and (*b*)] Pictures of the ZrNb-2a specimen. [(*c*) and (*d*)] Pictures of the ZrNb-3a specimen. (*a*) Dislocations gliding in the prismatic plane observed with the electron beam close to the* $\langle c \rangle$ *axis* ($B \approx [0001]$) *using the diffraction vector* $g=10\bar{1}0$. (*b*) *Dislocations observed with the electron beam close to the* \langlec+a\rangle *direction* ($B \approx [11\bar{2}3]$) *using the diffraction vector* $g=10\bar{1}1$. (*c*) *Dislocations observed with the electron beam close to the* \langlec+a\rangle *direction* ($B \approx [11\bar{2}3]$) *using the diffraction vector* $g=10\bar{1}1$. (*d*) *Dislocations observed with the electron beam close to the* \langle-c+a\rangle *direction* ($B \approx [11\bar{2}3]$) *using the diffraction vector* $g=10\bar{1}1$.

as the fact that there is only one activated slip system, can explain the early localization of the plastic strain at the specimen scale which leads to the loss of macroscopic ductility observed after irradiation (decrease of the UE value) but the failure mode remaining ductile [13].

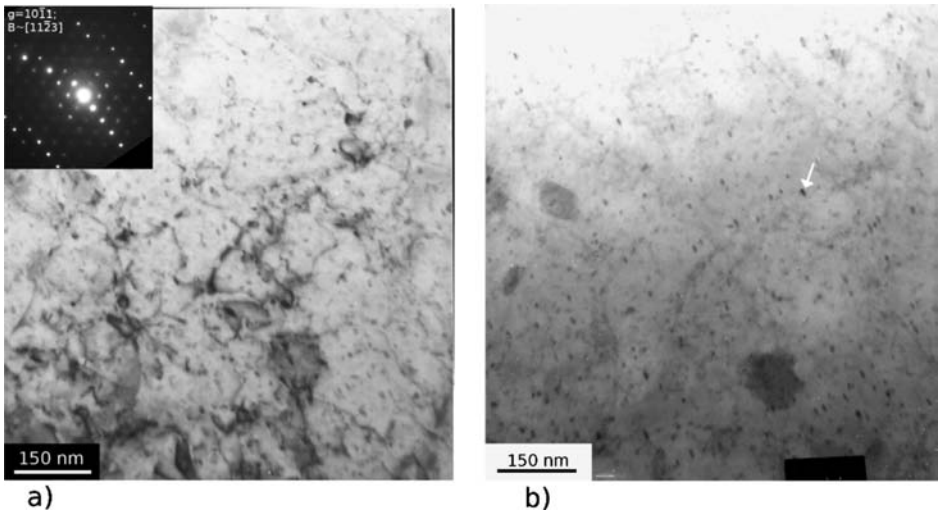


FIG. 10—*Pictures of the ZrNb-2a specimen. (*a*) Dislocations and needle precipitates observed with the electron beam close to the \langlec+a\rangle direction* ($B \approx [11\bar{2}3]$) *using the diffraction vector* $g=10\bar{1}1$. *(*b*) Needle precipitates observed in an out-of-contrast diffraction conditions (no lattice plane is in Bragg diffraction condition). An arrow shows one needle precipitate.*

Moreover, it has been shown that the observed dislocation channels correspond both to the basal and prismatic planes, proving that during ring tensile tests these two slip systems can be activated at room temperature. This observation has to be compared with the analysis of the post-irradiation deformation mechanisms at 350°C described in Refs [6 and 11]. It has been proven indeed through many TEM observations that for both transverse tensile tests and internal pressure tests performed at 350°C, the deformation occurs by a dislocation channeling mechanism. It has also been shown that up to the UTS only, basal channeling occurs. Only after the UTS prismatic, pyramidal as well as basal channels are observed on ring specimens tested at 350°C [11]. On the other hand, it has been shown that at 350°C when the grains are not properly orientated to allow basal slip, as they are for axial tensile tests, prismatic channels are observed. These deformation mechanisms are very different from the deformation mechanisms observed before irradiation. Before irradiation, indeed, the deformation occurs by way of homogeneous gliding of dislocations within the grains mainly by prismatic slip. The change in the principal slip system has been attributed to the difference in junction reactions between the loops and the dislocations gliding in the prismatic plane or the dislocations gliding in the basal plane [6]. Indeed, the irradiation induced loops can be easily swept up by the dislocation gliding in the basal plane since the junctions allow gliding which favors an easy dislocation channeling mechanism in the basal plane. On the other hand, the sweeping of loops by dislocations gliding in the prismatic plane is more difficult since the junctions are sessile explaining that the dislocation

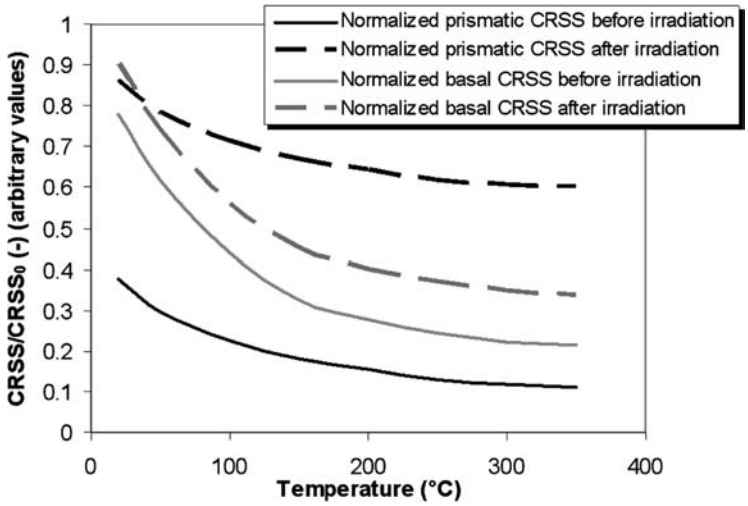


FIG. 11—*Schematic plot of the evolution of normalized prismatic and basal CRSS with temperature before and after irradiation. The values as well as the normalization coefficient $CRSS_0$ given in this plot are arbitrary.*

channeling mechanism in the prismatic plane is more difficult. However, the fact that at room temperature, for a ring test interrupted at the UTS, both basal channels and prismatic channels are observed can be understood if the evolution of the critical resolved shear stresses (CRSSs) of the various slip systems with temperature is taken into account. It has been shown by Akthar [14] that, while testing pure zirconium single-crystals at high temperature, the basal CRSS, which is higher than the prismatic CRSS, decreases quickly as a function of the temperature, whereas the prismatic CRSS decreases more slowly. A schematic plot of this evolution is proposed in Fig. 11 for polycrystalline Zr-1 % Nb at lower temperatures. On the other hand, it has been shown by Onchi [15] that the YS of both irradiated and unirradiated recrystallized Zy-2 decreases with the test temperature, the decrease being only slightly slower for the irradiated specimens between 20 and 300°C. This proves that the test temperature has only a small influence on the irradiation induced hardening. It can therefore be assumed that the evolution of both the basal and prismatic CRSS with irradiation only consists of a constant increment of the CRSS independent of the temperature, the increment of CRSS being much higher for prismatic slip than for basal slip [6,12]. A schematic plot, given in Fig. 11, using normalized CRSS with arbitrary values (the normalization coefficient $CRSS_0$ being arbitrary), explains the evolution of the CRSS with temperature and irradiation. As proposed on this schematic plot, a reversal of the prismatic and basal CRSS occurs with irradiation at 350°C, leading to a change of the easy glide slip system. On the other hand, at 20°C, no reversal of the CRSS occurs, but the basal and the prismatic CRSSs become very close to each other, therefore explaining that both basal and prismatic channels can be observed depending on the grain orientation.

Discussion on the Behavior of the Zr-1 % Nb Specimens after Post-Irradiation Creep

It has been shown [2] that during creep tests at 400 and 450°C, an annealing of the radiation induced loops occurs. The annealing of the radiation induced loops explains the recovery of the radiation hardening measured using tensile and hardness tests after post-irradiation creep. However, as shown in Fig. 4, after post-irradiation creep, the recovery of the hardening is only partial since the strength (or hardness) remains higher than for the non-irradiated material. This phenomenon has several origins. First, after 984 or 3301 h at 400°C, remaining loops can still be present in the material, the loop annealing being slow at this temperature. Second, the needle precipitates are also another source of residual hardening. Indeed, even after 960 h of post-irradiation heat treatment performed at 450°C, the hardness of the material is still not fully recovered (Fig. 6). In this condition, only very few large loops remain present in the material. These remaining loops cannot explain the residual hardening. The residual hardening is therefore due to the very small precipitates present in very high density in the material after irradiation [16], which can act as obstacles to dislocation motion. These two reasons can explain the residual hardening observed. Nevertheless, as it has been pointed out, after creep performed at 400°C for 984 or 3301 h, the hardness remains higher than the hardness measured after post-irradiation heat treatment performed at 400°C during 500 h only. This proves that the residual hardening cannot be explained only by the remaining loops and the needle precipitates that are both present in the case of the heat-treated material.

It has been proven [2] that during creep tests performed at 400°C with an applied stress of 130 MPa, in addition to the recovery of the radiation induced loops, the microstructure exhibits a high dislocation density, much higher than the dislocation density observed in the non-irradiated material for the same creep strain. It has been proposed that this high dislocation density is the result of dislocation multiplication due to the remaining loops that act as obstacles and therefore decrease the dislocation mean free path. The high density of small needle-like precipitates could also increase the dislocation multiplication. This higher dislocation density observed after post-irradiation creep performed at 400°C with an applied stress of 130 MPa could explain the higher residual hardening than observed after heat treatment only.

The TEM observations made after the ring tensile tests following the post-irradiation creep test have shown that the irradiation induced loops seem to have been fully cleared. This is in contrast to what was observed in the microstructure after post-irradiation creep, where remaining loops could still be seen. This can probably be explained by a homogeneous sweeping of loops by gliding dislocations as it is observed within the dislocation channels on the as-irradiated material.

It has been shown that the post-creep tensile deformation occurs homogeneously throughout the grain by dislocation glide, no channeling being observed. The easy glide system is the prismatic slip system as shown in Fig. 8(*a*). The deformation mechanisms are therefore similar to the deformation

mechanisms occurring for the non-irradiated material. This can explain why after post-irradiation creep, the material recovers its ductility. However, the dislocation density appears to be very high for this plastic strain level (2.43 % and 5.16 %). The high dislocation density already observed after creep test could explain these observations. Probably additional dislocation multiplication also occurs during the ring tensile test. Indeed, the high dislocation density, the remaining loops and the high density of needle-like precipitates decreases the mean free path along which the dislocations may glide. This could therefore lead to a high dislocation multiplication during the tensile test. This phenomenon could explain why the strain hardening is higher after post-irradiation creep compared to the non-irradiated material. The fact that the macroscopic ductility (UE and TE values) of the material remains lower than the macroscopic ductility of the non-irradiated material could also be explained by the high dislocation density. Indeed, the material is already strain-hardened, like a cold-worked material, its remaining strain hardening capability is therefore reduced.

Discussion on the Behavior of the Zy-4 Specimens after Post-Irradiation Creep

It is well known that non-irradiated stress-relieved Zy-4 exhibits a higher strength or hardness than non-irradiated recrystallized Zr-1 % Nb as confirmed by Tables 6 and 7. This can be explained because the two materials show different microstructures. Indeed, Zy-4 is a stress-relieved alloy with elongated grains that are very small (between 0.1 and 0.5 μm) in the transverse direction and with a very high dislocation density, whereas the Zr-1 % Nb alloy is a recrystallized alloy with larger equiaxial grains (5 μm) and a very low dislocation density. These two microstructural features can explain the higher non-irradiated strength of the Zy-4. This material also exhibits a lower ductility because of its strain-hardened state and therefore its lower strain hardening capability.

As for the Zr-1 % Nb alloy, strong irradiation induced hardening is also observed for Zy-4, the change in strength (YS and UTS) and hardness being similar for the two materials. Zy-4 specimens have not been examined by TEM in this study. The irradiation hardening is also likely explained by a high density of small irradiation induced $\langle a \rangle$ loops. After post-irradiation creep, the strength and hardness of the Zy-4 are probably recovered due to the annealing of the $\langle a \rangle$ loops. It has indeed been shown [1] that after 10 days at 470°C, a partial recovery of irradiation defects occurs, decreasing the number of $\langle a \rangle$ loops and increasing their size. Moreover, after creep, the strength (YS and UTS) and microhardness can become lower than the values measured for non-irradiated material, depending on the creep tests conditions. This phenomenon has already been observed after post-irradiation heat treatment. The fact that the strength or hardness can decrease below their initial non-irradiated values is probably due to the recovery of the dislocation network already present before irradiation and maybe due to a start of recrystallization. Indeed, it has been observed previously [1] that after 10 days of post-irradiation heat treatment at 520°C, the initial structure has evolved towards a structure of equiaxial grains with a low dislocation density. However, according to Dunlop et al. [17], even after 17 071 h at 400°C, the degree of

recrystallization might remain very low. The additional softening would therefore be mainly attributed to the annealing of the dislocation network. The fact that the effect of post-irradiation creep on Zy-4 is the same as the effect of a heat treatment alone, contrary to Zr-1 % Nb, can probably be attributed to the saturation of the dislocation density with plastic strain. Indeed, the dislocation density is already very high in the material, with the increase of the dislocation density during creep therefore not being significant. This also explains why the strain hardening behavior of the specimen after post-irradiation creep is similar to the strain hardening behavior of the non-irradiated material.

Conclusions

The effect of post-irradiation creep testing on the subsequent room temperature mechanical properties of zirconium alloys has been investigated and interpreted in terms of deformation mechanisms observed by TEM. It has been shown that for both stress-relieved Zy-4 and recrystallized Zr-1 % Nb alloys post-irradiation creep tests lead to the recovery of the strength of the material (decrease of the YS and UTS values towards its non-irradiated values) and to a recovery of the ductility of the material (increase of the UE and TE values towards its non-irradiated values). In the case of the Zr-1 % Nb, it has been shown that the recovery of the strength of the material is due to the irradiation loops annealing that occurs during the post-irradiation creep test. It has also been shown that the loss of macroscopic ductility of the as-irradiated material is due to the dislocation channeling mechanism that leads to an early localization of the plastic strain at the specimen scale.

On the other hand, after post-irradiation creep testing followed by a tensile test, no channeling is observed: the deformation occurs homogeneously throughout the grains, and the deformation mechanisms are similar to that of the non-irradiated material. These observations explain the recovery of the strength and ductility after post-irradiation creep. However, the coupling between the recovery of the mechanical properties and the hydrides reorientation has still to be investigated in order to obtain a full understanding of the mechanical behavior after dry transportation or dry storage.

References

[1] Cappelaere, C., Limon, R., Gilbon, D., Bredel, T., Rabouille, O., Bouffioux, P., and Mardon, J. P., "Impact of Irradiation Defects Annealing on Long-Term Thermal Creep of Irradiated Zircaloy-4 Cladding Tube," *Zirconium in the Nuclear Industry: 13th International Symposium, ASTM STP 1423*, Annecy, France, June 10–14, 2001, G. D. Moan and P. Rudling, Eds., ASTM International, West Conshohocken, PA, 2002, pp. 720–739.

[2] Ribis, J., Onimus, F., Béchade, J. L., Doriot, S., Cappelaere, C., Lemaignan, C., Barbu, A., and Rabouille, O., "Experimental and Modeling Approach of Irradiation Defects Recovery in Zirconium Alloys: Impact of an Applied Stress," *J. ASTM Int.*, Vol. 5, No. 3, 2008.

[3] Ribis, J., Onimus, F., Béchade, J.-L., Doriot, S., Barbu, A., Cappelaere, C., and Lemaignan, C., and , "Experimental Study and Numerical Modelling of the Irradiation Damage Recovery in Zirconium Alloys," *J. Nucl. Mater.* Vol. 403, 2010, pp. 135–146.

[4] Mardon, J.-P., Charquet, D., and Senevat, J., "Optimization of PWR Behavior of Stress-Relieved Zircaloy-4 Cladding Tubes by Improving the Manufacturing and Inspection Process," *Zirconium in the Nuclear Industry: Tenth International Symposium, ASTM STP 1245*, Baltimore, MD. June 21–24, 1993, A. M. Garde and E. R. Bradley, Eds., ASTM International, West Conshohocken, PA, 1994, pp. 329–348.

[5] Mardon, J.-P., Charquet, D., and Senevat, J., "Influence of composition and fabrication process on out-of-pile and in-pile properties of M5 Alloy," *Zirconium in the Nuclear Industry: 12th International Symposium, ASTM STP 1354*, Toronto, Canada, June 15–18, 1998, G. P. Sabol and G. D. Moan, Eds., ASTM International, West Conshohocken, PA, 2000, pp. 505–522.

[6] Onimus, F., Monnet, I., Béchade, J. L., Prioul, C., and Pilvin, P., "A Statistical TEM Investigation of Dislocation Channeling Mechanism in Neutron Irradiated Zirconium Alloys," *J. Nucl. Mater.*, Vol. 328, 2004, pp. 165–179.

[7] Northwood, D. O., London, I. M., and Bahen, L. E., "Elastic Constants of Zirconium Alloys," *J. Nucl. Mater.*, Vol. 55, 1975, pp. 299–310.

[8] Torimaru, T., "Changes in Mechanical Properties of Irradiated Zircaloy-2 Fuel Cladding Due to Short Term Annealing," *J. Nucl. Mater.*, Vol. 238, 1996, pp. 169–174.

[9] Dollins, C. C., "Post Irradiation Recovery of Irradiation Damage," *Radiat. Eff.*, Vol. 16, 1972, pp. 271–280.

[10] Busby, J. T., Hash, M. C., and Was, G. S., "The Relationship Between Hardness and Yield Stress in Irradiated Austenitic and Ferritic Steels," *J. Nucl. Mater.*, Vol. 336, 2005, pp. 267–278.

[11] Onimus, F., Béchade, J. L., Prioul, C., Pilvin, P., Monnet, I., Doriot, S., Verhaeghe, B., Gilbon, D., Robert, L., Legras, L., and Mardon, J. P., "Plastic Deformation of Irradiated Zirconium Alloys: TEM Investigations and Micro-Mechanical Modeling," *J. ASTM Int.*, Vol. 2, No. 8, 2005.

[12] Onimus, F. and Béchade, J. L., "A polycrystalline Modeling of the Mechanical Behavior of Neutron Irradiated Zirconium Alloys," *J. Nucl. Mater.*, Vol. 384, No. 2, 2009, pp. 163–174.

[13] Fregonese, M., Régnard, C., Rouillon, L., Magnin, T., Lefebvre, F., and Lemaignan, C., "Failure Mechanisms of Irradiated Zr Alloys Related to PCI: Activated Slip Systems, Localised Strains, and Iodine Induced Stress Corrosion Cracking," *Zirconium in the Nuclear Industry: 12th International Symposium, ASTM STP 1354*, Toronto, Canada, June 15–18, 1998, G. P. Sabol and G. D. Moan, Eds., ASTM International, West Conshohocken, PA, 2000, p. 377.

[14] Akhtar, A., "Basal Slip in Zirconium," *Acta Metall.*, Vol. 21, 1973, pp. 1–11.

[15] Onchi, T., Kayano, H., and Higashiguchi, Y., "The Inhomogeneous Deformation Behavior of Neutron Irradiated Zircaloy-2," *J. Nucl. Mater.*, Vol. 88, No. 2-3, 1980, pp. 226–235.

[16] Doriot, S., Gilbon, D., Béchade, J. L., Mathon, M. H., Legras, L., and Mardon, J. P., "Microstructural Stability of M5^{TM} Alloy Irradiated up to High Neutron Fluences," *J. ASTM Int.*, Vol. 2, No. 7, 2005.

[17] Dunlop, J. W. C., Bréchet, Y. J. M., Legras, L., and Zurob, H. S., "Modelling Isothermal and Non-Isothermal Recrystallisation Kinetics. Application to Zircaloy-4," *J. Nucl. Mater.*, Vol. 366, No. 1-2, 2007, pp. 178–186.

DISCUSSION

Question 1, Arthur Motta, Penn State Univ:—1) By performing a plane-strain test instead of a uniaxial test, might you have a non representative deformation and failure, and possibly activate different deformation mechanisms? 2) How does the microscopic channe lling develop into macroscopic deformation localisation? Is there any evidence of easier shear band formation from the channels?

Author's Response:—1) In a plane-strain test (such as a PSU test), the stress tensor is not the same as in the ring test. The resolved shear stress on the slip systems is also affected; this can lead to a change in the activation of the slip system. By having a strain equals to zero in the longitudinal direction, the prismatic slip systems would probably be more difficult to activate, and basal slip would be preferred.

2) According to previous TEM observations, dislocations channels develop and propagate from grain to grain before the ultimate tensile strength (UTS). Since the clearing of the loops inside the channels leads to a local microscopic strain softening, resulting in a decrease of the strain hardening capability that eventually yields to the development of an early macroscopic localisation.

Due to the dislocation channelling mechanism, the necking occurs earlier than on the non irradiated recrystallised alloy. Also, at the end of the test, macroscopic observations show that the necking is more pronounced and localised than on the non-irradiated recrystallised alloy.

Question 2, C. E. Coleman, AECL:—What are the proportions of the three contributions to the residual hardening? The strengthening by the β-Nb precipitates is especially interesting.

Author's Response:—We have not been able to separate clearly the three contributions. Irradiated recrystallised Zy-4 specimens could be used to distinguish the effect of the loops and β-Nb needles. Moreover, despite the high density of β-Nb precipitates, hardness tests show that their effect on the residual hardening remains limited.

Question 3, Jean-Christophe Brachet, CEA France:—Te deconvove the remaining loops, β-Nb needles … respective contributions on the residual hardening, you should irradiate a Zr 0.2%Nb alloy to have the same matrix without the β-Nb needles.

Author's Response:—Indeed, the Zr-0.2%Nb alloy could be more suitable to compare with Zr-1%Nb in order to study the effect of β-Nb needles.

Question 4, Ron Adamson, Zircology Plus:—Comment: As you know, I am pleased that you found prismatic plane channelling at room temperature, as we have seen this in the past

Did you observe any ⟨c⟩ component loops in these specimens? If no, can you comment on their possible effect on the residual hardening observed. I suspect no annealing of the ⟨c⟩ loops would have occurred under your conditions.

Author's Response:—Indeed, on the other specimens, I have observed that the ⟨c⟩ component loops seem to be more stable than the ⟨a⟩ component loops. No annealing of ⟨c⟩ component loops seems to occur.

The ⟨c⟩ component loops can also be an additional source of hardening, but however, due to their low density, it is believed their effect remains low.

Question 5, Malcolm Griffiths, AECL:—1) By changing the relative activity of the slip systems one might expect to see an effect on the anisotropy of yielding. Have you performed longitudinal tensile

tests to monitor the effect of irradiation on yield anisotropy? 2) By the same token creep anisotropy may be expected to change with irradiation. Are there any plans to perform tests in both directions and will this be published?

Author's Response:—1) Longitudinal tensile tests have also been performed at room temperature on non-irradiated and as-irradiated Zr-1%Nb. Only a slight reduction in the anisotropy of yielding (measured at 0.2% plastic strain) with irradiation is indeed observed.

2) Only few results on longitudinal creep test results are available at CEA. However, we have noticed that the ratio between longitudinal and hoop strain during internal pressure tests evolves toward a more isotropic behaviour after irradiation.

Reprinted from JAI, Vol. 7, No. 9
doi:10.1520/JAI103036
Available online at www.astm.org/JAI

Sheikh T. Mahmood,[1] Paul E. Cantonwine,[2] Yang-Pi Lin,[2] Douglas C. Crawford,[2] E. V. Mader,[3] and K. Edsinger[3]

Shadow Corrosion-Induced Bow of Zircaloy-2 Channels

ABSTRACT: For the past 10 years, the frequency of channel-control blade interference has been greater than before because of shadow corrosion-induced bow. Shadow corrosion-induced bow is caused by differential hydrogen concentration on channel sides adjacent to and away from the control blade. The differential hydrogen concentration is a result of increased shadow corrosion on the channel side adjacent to the control blade, hence the description of this mechanism as shadow corrosion-induced bow. Channel bow measurements and post-irradiation examinations (PIEs) confirmed that shadow corrosion-induced bow occurs independent of fluence gradient-induced bow. Specifically, bow of channels that experienced early-life control (i.e., shadow corrosion) was significantly greater than expected assuming only fluence gradient-induced bow. In addition, it was found that plants with smaller channel-to-channel gaps had greater channel bow, consistent with the gap dependence of shadow corrosion. PIE revealed that the elevated hydrogen concentrations in the metal were found only on those channel sides and elevations that experienced shadow corrosion. A model was developed that related this measured differential hydrogen to the observed channel bow that supports the increased volume of hydrides as the underlying cause. However, questions about the time/exposure dependence of shadow corrosion-induced bow remain. The PIE of shadow corrosion-induced bow at low exposure (one cycle) indicates that little shadow corrosion-induced bow occurs after the first cycle even though shadow corrosion is observed on the

Manuscript received February 8, 2010; accepted for publication August 23, 2010; published online September 2010.
[1] GE Vallecitos Nuclear Center, Global Nuclear Fuel, m/c V03, 6705 Vallecitos Rd., Sunol, CA 94586, E-mail: sheikh.mahmood@gnf.com
[2] Global Nuclear Fuel, 3901 Castle Hayne Rd., m/c H25, Wilmington, NC 28401.
[3] Electric Power Research Institute, 3420 Hillview Av., Palo Alto, CA 94304.

Cite as: Mahmood, S. T., Cantonwine, P. E., Lin, Y.-P., Crawford, D. C., Mader, E. V. and Edsinger, K., "Shadow Corrosion-Induced Bow of Zircaloy-2 Channels," *J. ASTM Intl.*, Vol. 7, No. 9. doi:10.1520/JAI103036.

Copyright © 2011 by ASTM International, 100 Barr Harbor Drive, PO Box C700, West Conshohocken, PA 19428-2959.

side adjacent to the control blade. The differentials in oxide thickness and hydrogen concentration between opposite channel sides are considerably less than those measured later in service lifetime (i.e., after additional cycles of operation). The data indicate that the larger differential hydrogen at high exposure/residence time is a result of a larger difference in oxide thickness and a corresponding increase in percent hydrogen pick up that developed at higher exposures/residence times.

KEYWORDS: Zircaloy-2, channel bow, shadow corrosion, shadow corrosion-induced bow

Introduction

In boiling water reactors (BWRs), fuel assemblies are placed inside channels, which provide a flow path for the coolant. The gap between some adjacent channels additionally provides path for the control blade. Excessive deformation of the channel, therefore, can result in the interference between the channel and the control blade motion (see Fig. 1). For the last 10 years, the interference between channels and control blades has complicated the operation of BWRs in plants using Zircaloy-2 channel material and cycle lengths of 18–24 months. Prior to 2000, channel distortion was attributed only to bow caused by differential growth due to a fluence gradient across the channel (i.e., the reactor core's flux gradient leads to higher accumulation of fluence on one side of the channel than the opposite side) and to bulge arising from irradiation creep induced by the channel inside-out pressure difference. These distortion mechanisms were effectively managed and accommodated during core design (e.g., by limiting the number of cycles in peripheral locations). Thus, when channel-control blade interference was noted starting in 2000, the observations were unexpected.

The unexpected interference was linked to bundles with control blade exposure early in the service life (i.e., close proximity exposure to stainless steel components of a control blade inserted during the initial period of in-reactor exposure). This link led to the suspicion of shadow corrosion being an important factor. The term shadow corrosion has been used to describe the enhanced in-reactor corrosion observed on zirconium alloys when the alloy is placed in close proximity to a dissimilar metal, such as stainless steel, and the affected surface often exhibits visual contrast shaped as the outline, or shadow, of the dissimilar metal component [1–4]. Shadow corrosion occurs on channels when control blades are inserted, particularly when inserted next to fresh bundles. Specifically, the hypothesis was that shadow corrosion between the channel and the control blade resulted in a thicker oxide on the control blade side (the side of the channel adjacent to the control blade) compared to the non-blade side (the side opposite from the control blade). These two sides will be referred to in this paper as the blade side and the non-blade side, respectively. Because hydrogen pick up (HPU) is generally proportional to oxide thickness, the shadow corrosion resulted in elevated HPU in the blade side of the channel relative to the non-blade side. Because hydrogen in Zircaloy causes a volume change on the order of 1 % per 1000 parts per million (ppm) [5,6], the increased hydrogen on

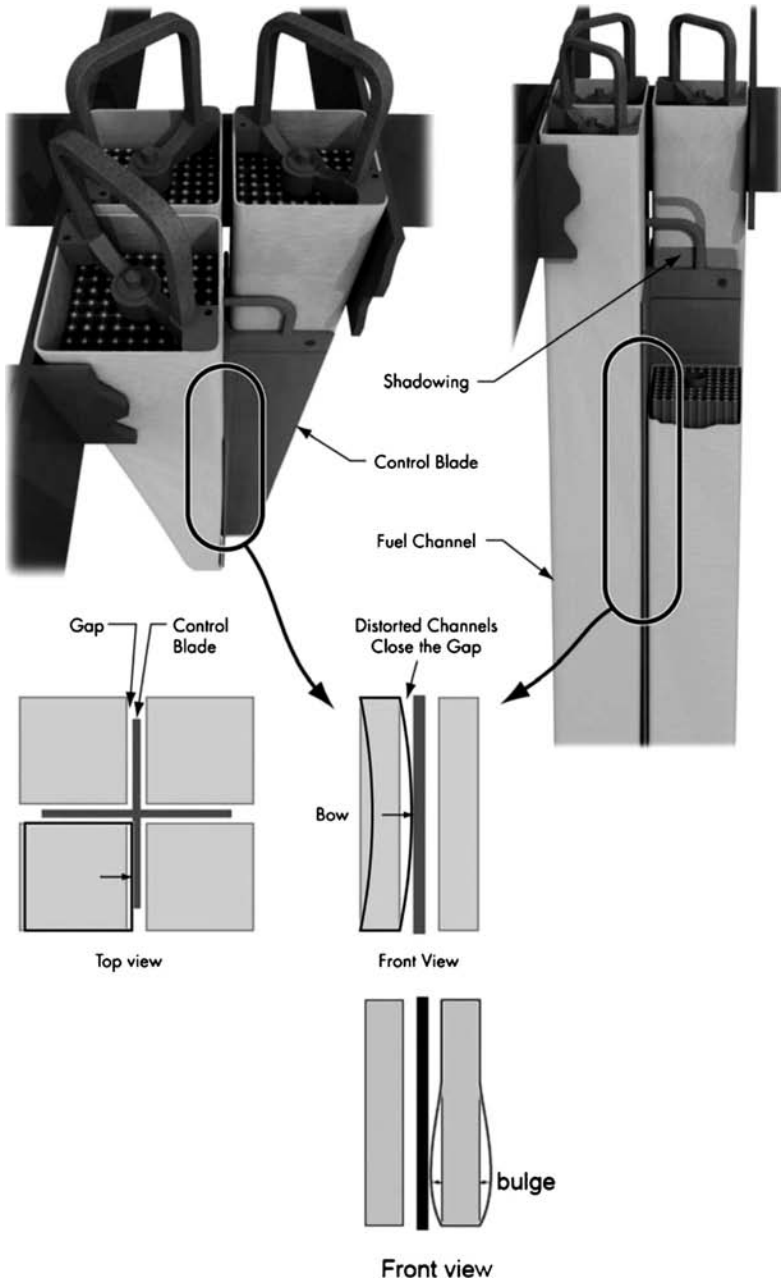


FIG. 1—*A BWR control cell with four bundles and a control blade. The bow and bulge conditions are exaggerated for illustration purposes.*

the blade side results in an increased length relative to the non-blade side, and the channel bows towards the blade. In analytic terms, this new channel bow mechanism is proportional to the product of the percent HPU and the oxide thickness differential (Δt)

$$\text{bow} \propto (\text{HPU})(\Delta t) \tag{1}$$

This hypothesis was confirmed in the post-irradiation examination (PIE) of coupons from several channels with varying degrees of bow and early-life control [7], and this new channel distortion mechanism was coined *shadow corrosion-induced bow*.

The purpose of this paper is to investigate more thoroughly the fundamental aspects of shadow corrosion-induced bow. The fundamental aspects are related to general and shadow corrosion kinetics that cause a difference in oxide thickness and the HPU behavior of the channel material under general and shadow corrosion conditions. Specifically, channel distortion data support the conclusion that shadow corrosion kinetics is a function of the distance between the host and shadow materials (i.e., the gap between a channel and a control blade). Shadow corrosion-induced bow also appears to have exposure dependence. That is, while shadow corrosion occurs early in life, the greatest distortion occurs late in life. The dependence of corrosion kinetics, HPU, and microstructure on this observation is discussed in this paper.

Effective Control Blade Exposure

Once the observations of channel-control blade interference were linked to early-life control, a metric called effective control blade exposure (ECBE) was developed to quantify the exposure that leads to shadow corrosion-induced bow [7]. This metric is based on a weighted summation of the product of the control blade insertion length (inches[4]) and insertion time (days) for each insertion applied, which is weighted such that the control blade insertion in the first 2 years is weighted more heavily than insertion in the third year or later. As an example, the control history of two bundles is shown in Fig. 2. These two bundles were controlled for similar amounts of time with similar insertion lengths. The bundle controlled earlier in life is more susceptible to shadow corrosion and subsequently to shadow corrosion-induced bow. Accordingly, the bundle controlled more early in life has an ECBE of 17 795 in. days, while the bundle controlled later in life has an ECBE of only 712 in. days. Initially, this metric was used to identify susceptible cells for monitoring during reactor operation. Subsequent channel surveillance and measurements confirmed the correlation of this metric to excessive channel bow.

[4]The ECBE is used as a metric for assessing the relative susceptibility to shadow corrosion. Throughout this paper, ECBE is expressed in in. days.

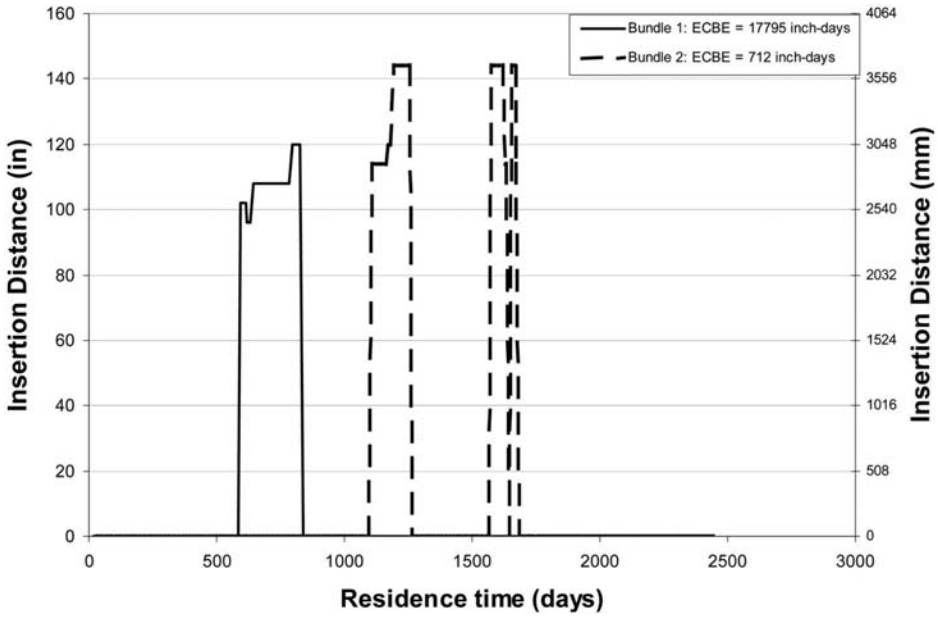


FIG. 2—*Examples of control history for two channels that have similar control blade insertion but at different times of control. Due to the weighting of the ECBE metric, the channel with early control has a higher ECBE.*

Observations of Shadow Corrosion-Induced Bow

Schematics of bulge and bow in channels are shown in Fig. 1. Channels will bulge out because of creep due to a pressure difference between the inside and the outside of the bundle. During operation, the magnitude of channel bulge is a function of both elastic and irradiation creep strains, where the elastic strains are present only under operating conditions and the irradiation creep strains increase with time and accumulated fluence. Although channel bulge can be a contributor to channel-control blade interference, it does not contribute to channel bow. Channel bow occurs when the length of one or two sides of the channel become longer than the opposing side(s). As already mentioned, there are two principal mechanisms for this type of channel distortion: Fluence gradient-induced bow and shadow corrosion-induced bow.

Channel distortion was measured at nine different reactor sites that included S-, C-, and D-lattice plants. From a channel distortion perspective, the main difference in these plants is the gap between the channel and the control blade. The nominal gap between the surfaces of the channel and the control blade in the S-lattice plant is 0.74 relative to the D-lattice plant and 0.83 for the C-lattice plant relative to the D-lattice plant. Thus, it was not unexpected that observations of channel-control blade interference occurred first in S-lattice plants then in C-lattice plants and finally in D-lattice plants. Measurements also have been made on two types of channels—designated 100T and 120T. The

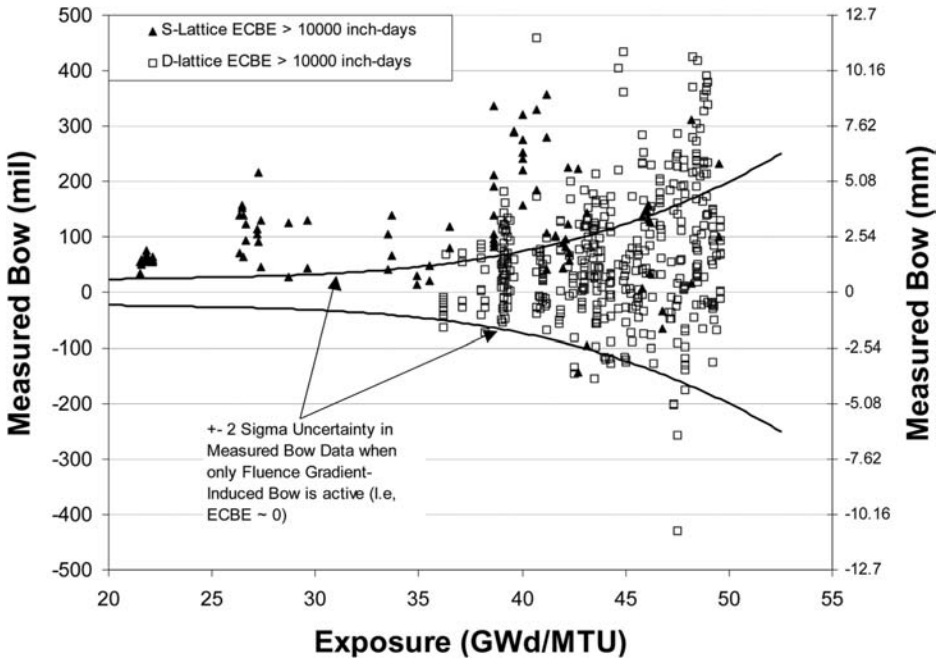


FIG. 3—*Measured channel bow of Zircaloy-2 channels from S- and D-lattice plants with significant early-life control (ECBE>10 000 in.ṡdays) compared to the ±2σ for channel bow with no early-life control.*

thinner 100T channel types are used in either C- or D-lattice plants, while the thicker 120T channel type is used in S- or C-lattice plants.

Channel distortion measurements were taken at each reactor site by a device that was inserted into the spent fuel pool. This device measures the total distortion at specific axial elevations relative to an undistorted channel. Because the total distortion includes bulge and bow, each is de-convoluted from the raw data. Channel bulge was found to behave as expected and is not discussed further herein. However, channel bow measurements from bundles with significant early-life control (ECBE $>$ 10 000′ in. $\cdot$ days) were statistically greater than the measured bow of low ECBE bundles where only fluence gradient-induced bow is active (see Fig. 3). Because the measured channel bow includes both fluence gradient-induced bow and shadow corrosion-induced bow, the portion caused by shadow corrosion-induced bow is quantified by subtracting out the predicted fluence gradient-induced bow based on irradiation growth correlation for Zircaloy-2.

The mean shadow corrosion-induced bow data for the 120T and 100T channel types are plotted in Fig. 4. For each channel type, the data indicate greater shadow corrosion-induced bow in plants with a smaller gap and less when the channel thickness increases. This indicates shadow corrosion increases as the gap decreases and that the hydrogen concentration decreases as the channel thickness increases. There is also an exposure dependence (see Fig. 5) that is of

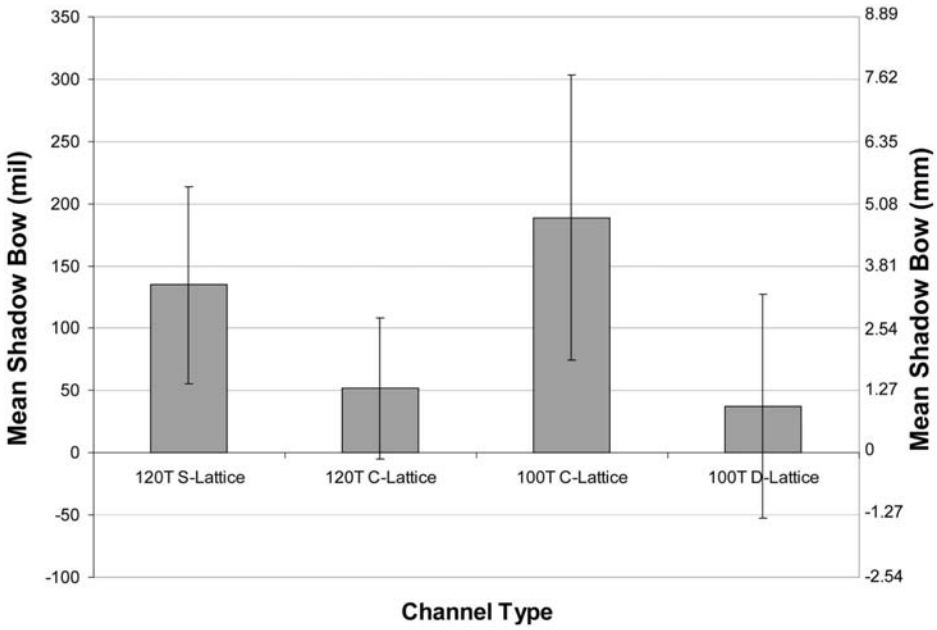


FIG. 4—*The mean shadow corrosion-induced bow for 120T and 100T channels with ECBE>10 000 in.*$\dot{s}$*days in S- and C-lattice and C- and D-lattice plants, respectively. The error bars represent the standard deviation in each channel type. Negative values indicate the measured bow was less than the predicted fluence gradient bow.*

interest; the shadow corrosion occurs at low exposure, typically in the first cycle of service, yet the maximum amount of shadow corrosion-induced bow occurs late in life at high exposure. The objective of the PIE presented below is to understand these observations.

Test Materials for Post-Irradiation Examination

Coupons of Zircaloy-2 channels were retrieved from four BWR plants (A–D) and transported to the Vallecitos Nuclear Center for PIE. The plants A–C are either C- or S-lattice plants, while the plant D is D-lattice plant. The coupon locations relative to the channel corners and the neighboring control blade are shown in Fig. 6. The nominal coupon dimensions were 13 mm high × 38 mm wide (0.5×1.5 in.^{2}). The actual dimensions varied from coupon to coupon due to difficulties involved in under-water cutting of the samples.

A total of 32 coupons was obtained from four three-cycle channels of Plant A (channels 1–4 in Table 1). The fuel assembly exposure associated with these channels was in the range of 36–41 GWd/MTU, and ECBE was in the range of 8000–22 000 in. days. The coupons were obtained from the 0.5, 1.4, 2.3, and 3 m (20, 55, 90, and 120 in.) elevations (above the channel bottom) of the non-blade side (side 2) and blade side (side 4) of these channels. Channels 1 and 2 were

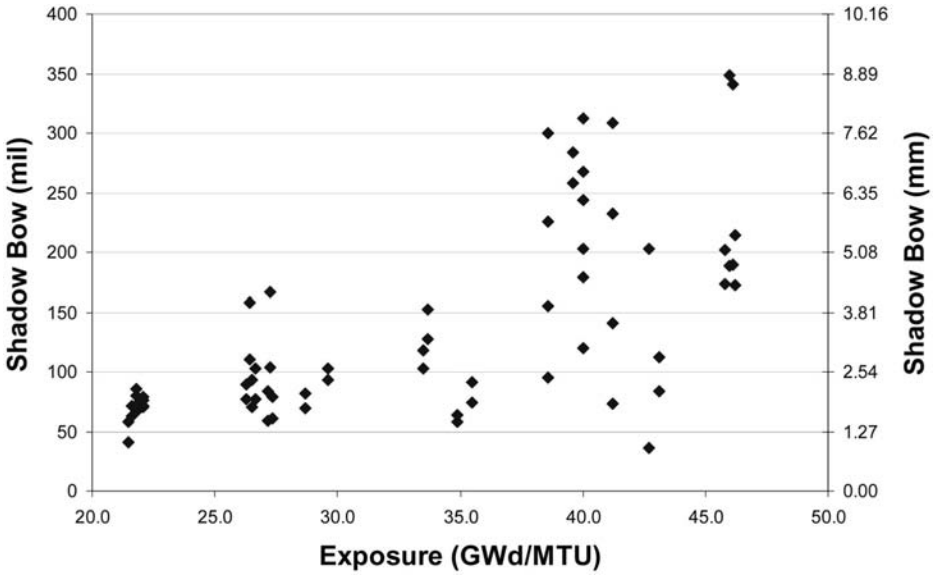


FIG. 5—*Shadow corrosion-induced bow of 120T channels in S-lattice plants showing greater bow at higher exposure (data only for ECBE>20 000 in.ṡdays).*

low bow channels with side 2 to side 4 maximum average bow of about 1.6 and 3 mm (61 and 119 mils), respectively, while channels 3 and 4 were high bow channels with side 2 to side 4 maximum average bow of about 7.4 and 8.5 mm (292 and 336 mils), respectively.

Coupons were also cut from the same elevations of sides 2 and 4 of a moderately controlled (ECBE = 14 025 in. · days) channel (channel 5 in Table 1) from Plant B with side 2 to side 4 maximum average bow of about 8 mm (314 mils). For comparison purposes, coupons were also sectioned from only the 0.5 m (20 in.) elevation of a non-controlled (ECBE = 0 in. · days) channel (channel 6 in Table 1) from Plant B. The measured bow of this channel was −0.8 mm (−30 mils), i.e., away from the control blade. The associated fuel assembly exposure of these channels was 48.2 and 47.9 GWd/MTU, respectively.

The coupons from the 0.5, 1.4, 2.3, and 3 m elevations of sides 2 and 4 of the heavily controlled channels (channels 7 and 8 in Table 1) from plant C were also retrieved. The associated fuel assembly exposure of these channels was 48.1 GWd/MTU, and channel ECBE was 27 112 in. days. The measured bow was 0.6 and 9.6 mm (25 mils and 376 mils), respectively.

At a later stage, coupons from the same four elevations of sides 2 and 4 of a heavily controlled single-cycle channel (channel 9 in Table 1) were also retrieved from plant A. The fuel assembly exposure and ECBE of this channel were 19.7 and 34 105 in. days, respectively. The measured side 2 to side 4 bow of this channel was 0.6 mm (22 mils).

The first occurrence of channel-control blade interference in a D-lattice plant was reported in Plant D. Coupons from sides 1 and 3 of two four-cycle

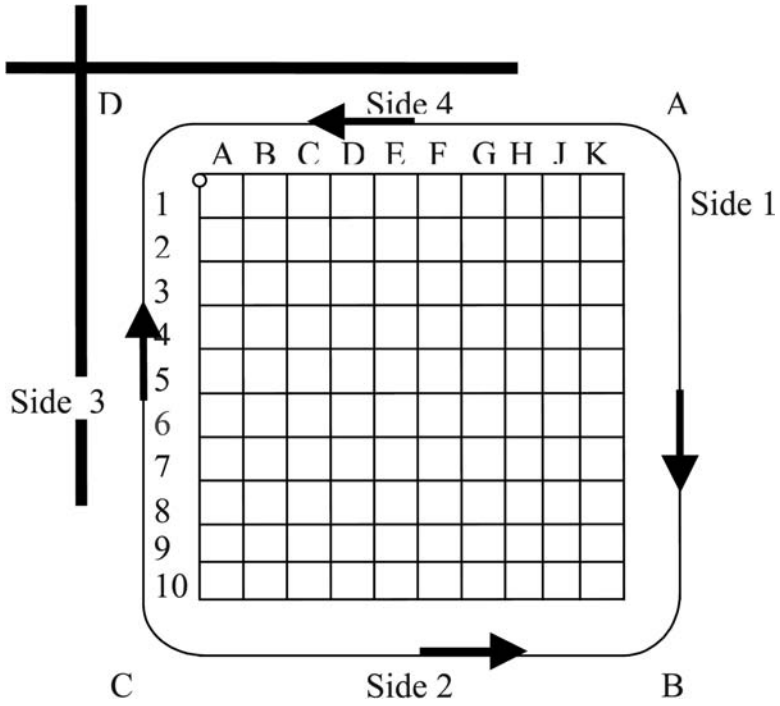


FIG. 6—*Location of channel coupons relative to channel corners and the neighboring control blade. Attempts were made to cut the channel coupons close to the channel corners that the arrows are pointing to.*

channels (channels 10 and 11 in Table 1) from this plant were also brought to the Vallecitos hot cells for PIE. The fuel assembly exposure, ECBE, and measured side 1 to side 3 bow of channel 10 were 43.9 GWd/MTU, 17 795 in. days, and 8.2 mm (323 mils), respectively. The coupons from channel 11 were brought as reference material because, although it had fuel assembly exposure of 42.9 GWd/MTU, its ECBE and measured bow were only 712 in. days and 0.7 mm (28 mils), respectively.

Experimental Procedure

Optical Metallography

Metallographic examinations were performed to measure the outer and inner surface oxide thicknesses and to characterize hydride distributions in the channel wall. Small sections from each of the coupons were sectioned using a slow speed diamond saw and mounted in Bakelite mounts using Caldofix epoxy. The epoxy was vacuum embedded and cured overnight in a 36°C oven. The mounted specimens were ground through FEPA 4000 grit SiC paper (5 μm) followed by polishing with 0.5 μm alumina slurry to examine transverse cross section of the

TABLE 1—*Plant, operational, and bow characteristics for channel coupons retrieved.*

Plant	Lattice Type	Channel ID	Channel Material	Exposure (GWd/MTU)	Number of Cycles	Residence Time (days)	ECBE (in. days)	Maximum Average Bow		Channel Side	Coupon Elevations			
											0.5 m	1.4 m	2.3 m	3.0 m
								mils	mm		20 in.	55 in.	90 in.	120 in.
A	S	1	Zircaloy-2	39.7	3	1486	8133	61	1.549	2	X	X	X	X
										4	X	X	X	X
		2	Zircaloy-2	36.5	3	1486	10 721	119	3.023	2	X	X	X	X
										4	X	X	X	X
		3	Zircaloy-2	39.6	3	1486	21 916	292	7.417	2	X	X	X	X
										4	X	X	X	X
		4	Zircaloy-2	40.7	3	1486	16 216	336	8.534	2	X	X	X	X
										4	X	X	X	X
B	S	5	Zircaloy-2	48.2	3	1882	14 025	314	7.976	2	X	X	X	X
										4	X	X	X	X
		6	Zircaloy-2	47.9	3	1882	0	−30	−0.762	2	X			
										4	X			
C	C	7	Zircaloy-2	48.1	3	2079	27 112	24.6	0.625	2	X	X	X	X
										4	X	X	X	X
		8	Zircaloy-2	48.1	3	2079	27 112	376.2	9.555	2	X	X	X	X
										4	X	X	X	X
A	S	9	Zircaloy-2	19.7	1	679	34 105	22	0.559	2	X	X	X	X
										4	X	X	X	X
D	D	10	Zircaloy-2	43.9	4	2401	17 795	323	8.204	1	X	X	X	X
										3	X	X	X	X
		11	Zircaloy-2	42.9	4	2401	712	28	0.711	1	X	X	X	X
										3	X	X	X	X

channel wall. The oxide thickness was measured at 20 randomly selected positions along the length (12.7 mm) of each of the metallographic samples. The oxide thickness data are reported as averages of these 20 measurements along with the corresponding standard deviations. After measuring oxide thicknesses in the as-polished condition using Bausch & Lomb Research Metallograph Model 42313650 with magnification in the range of 50×–500×, the sections were chemically polished using a solution of 10 mL glycerol, 10 mL HNO_3, and 2 mL HF. The specimens were then etched with an aqueous solution of 10 mL hydrogen peroxide, 10 mL HNO_3, and 2 mL HF to reveal zirconium hydride precipitates in the channel wall, which were then documented photographically.

Hydrogen Measurements

Hydrogen concentration in coupon sections next to the metallographic specimen locations was obtained using a LECO RH2 hydrogen analyzer, which employs an inert gas fusion method to release the hydrogen. The sample is melted in a graphite crucible containing a tin flux, and the evolved hydrogen is swept from the crucible with high purity nitrogen gas to a thermal conductivity detector. The change in the thermal conductivity of the gas stream is related to the hydrogen content through a series of calibration standards. In many cases, duplicate samples were used to check the reproducibility of the results. The method used distinguishes between hydrogen in the metal and that in the oxide. The results are reported as ppm by weight based on the weight of the specimen.

Results and Discussion

Oxide Thickness

Typical appearances of oxide cross-sections for low bow and high bow multicycle channels from plants A and B were shown previously [7]. Representative micrographs for the one-cycle channel (9) from plant A are shown in Fig. 7. Micrographs for high bow and low bow four-cycle channels from plant D are shown in Figs. 8 and 9, respectively. The results of metallographic oxide thickness measurements are summarized in Table 2. The results are presented in accordance with channel face. The oxide thickness data for the channel inner surface are shown in Figs. 10 and 11 for the non-blade and blade sides, respectively. Despite the considerable variation within each of Figs. 10 and 11, the general similarity between the two figures confirms the expectation that the inner surface corrosion was not affected by the orientation of the channel face relative to the control blade. For the channel outer surface, the oxide thickness data are shown in Figs. 12 and 13 for the non-blade and blade sides, respectively. These figures show that oxide on the blade side of the channel, Fig. 13, was generally thicker than oxide on the non-blade side of the channel, Fig. 12, and is consistent with the shadow corrosion effect from the control blade. The measured oxide thickness shown in Figs. 10–12 was not affected by shadow corrosion due to control blade exposure. However, the oxide thickness in Fig. 12 is for the

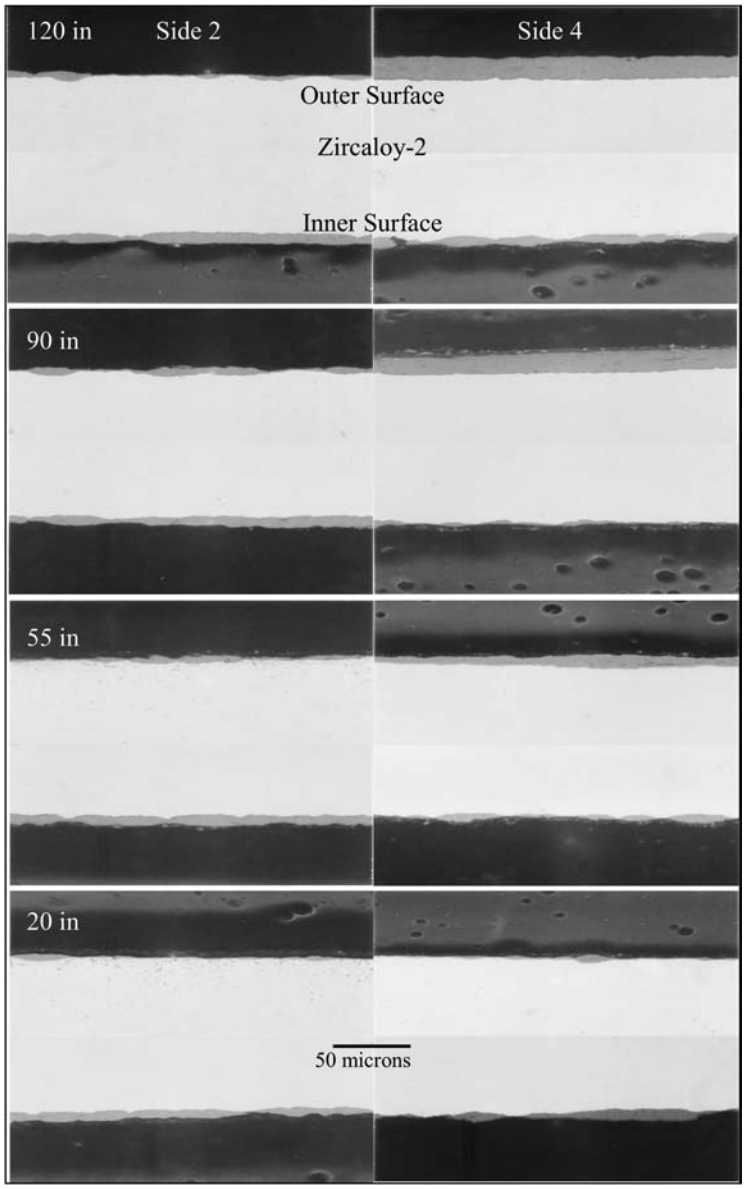


FIG. 7—*Inner and outer surface corrosion of single-cycle channel (channel 9) from Plant A (side 4 is the blade side and side 2 is the non-blade side).*

channel outer surface and is generally less than that in Figs. 10 and 11, which are for the inner surface. The greater corrosion on the inner surface compared to the corrosion on the outer surface of the non-blade side is consistent with the difference in water environments inside and outside of the channel (notable

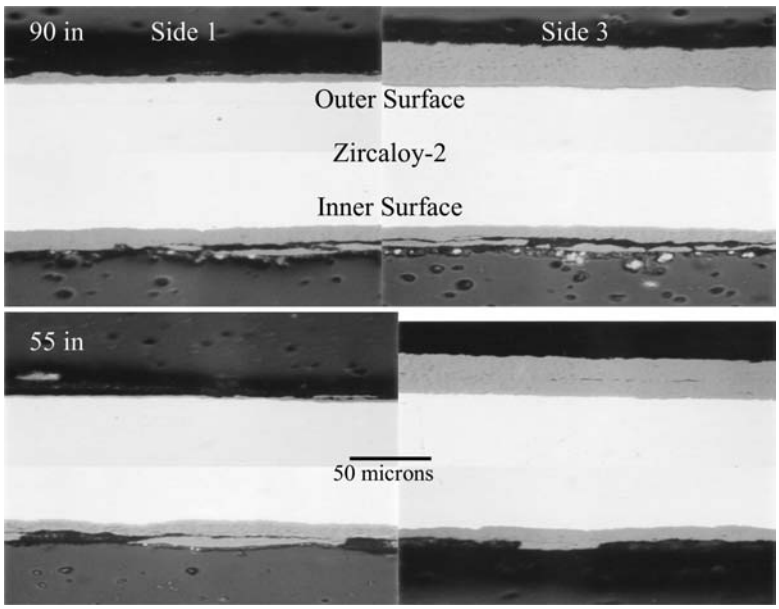


FIG. 8—*Inner and outer surface corrosion of channel 10 from Plant D (side 3 is the blade side and side 1 is the non-blade side).*

difference include higher concentration of radiolytic species and varying void fraction inside the channel).

Channel 7 is a notable exception to the general observation from Table 2 and Figs. 12 and 13 in that the oxide on the non-blade side of the channel was greater than the blade side. This channel and its companion, channel 8, were retrieved for hot cell examination because of markedly different channel bow performance despite very similar operational history. These two channels were part of a group of eight channels that had been located in core symmetric positions throughout the three cycles of operation, including identical exposure to control blade. Based on poolside dimensional measurements, channel 8 exhibited very similar characteristics as the other six channels in the group and showed significant channel bow. Channel 7 exhibited exceptionally low channel bow. The behavior of channel 7 was previously attributed to the placement next to an instrument tube during its first cycle of operation. The instrument tube's stainless steel casing is expected to be a potential source for shadow corrosion at the corner of sides 1 and 2 of the channel. The PIE included coupons from close to the corner of the channel. The greater oxide thickness on the non-blade side of the channel, especially near the corner, confirms a shadow corrosion effect from the instrument tube. However, the channel face on channel 7 exposed to the control blade exhibited little shadow corrosion, and the oxide thickness was similar to the oxide thickness on the non-blade side of channel 8. Thus, the presence of shadow corrosion from the instrument tube and the absence of control blade shadow corrosion are two notable characteristics of channel 7.

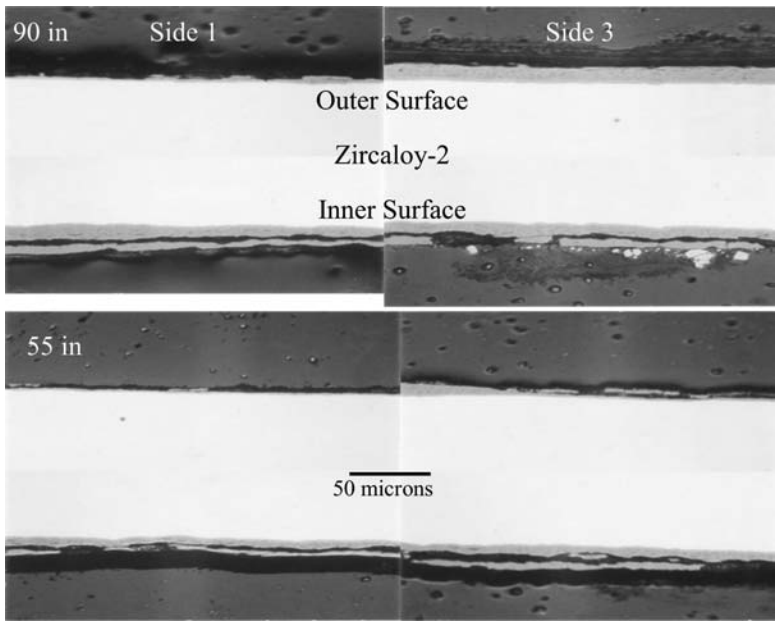


FIG. 9—*Inner and outer surface corrosion of channel 11 from Plant D (side 3 is the blade side and side 1 is the non-blade side).*

Hydrides and Hydrogen Concentration

Typical appearances of hydride morphology in low bow and high bow multi-cycle channels from plants A and B were shown previously [7]. Representative micrographs for the one-cycle channel (9) from plant A are shown in Fig. 14. Micrographs for high bow and low bow four-cycle channels from plant D are shown in Figs. 15 and 16, respectively. The amount of hydrides observed in each sample generally correlates with the measured hydrogen content. The results of hydrogen in metal are summarized in Table 3. In general, higher hydrogen concentrations were observed on the blade side of the channel compared to the non-blade side (see Fig. 17). The exceptions to the general trend are channels 6 and 7, which are not shown in Fig. 17. For channel 7, the greater hydrogen concentration on the non-blade side is consistent with the oxide thickness data, Table 2. For channel 6, data are available at only one axial elevation, the 20 in. location, and thus, it is not included in subsequent discussions.

The instrument used to measure hydrogen content has the ability to differentiate hydrogen in the metal and in the oxide. The hydrogen content in the oxide presented in Table 4 is derived by dividing the measured mass of hydrogen in the oxide by the weight of the measured sample. The hydrogen-in-oxide concentration is therefore a representation of the additional hydrogen concentration if the hydrogen in oxide is included in the evaluation of the overall

TABLE 2—*Summary of oxide thickness measurements.*

	Elevation		Average Oxide Thickness±Std. Dev. (μm)			
			Side away from CB		Side next to CB	
Channel ID	m	in.	Outer Surface	Inner Surface	Outer Surface	Inner Surface
1	3.0	120	10±5	13±4	15±4	15±5
	2.3	90	11±6	14±3	22±7	14±4
	1.4	55	12±6	15±5	26±6	16±4
	0.5	20	6±3	12±3	20±3	11±3
2	3.0	120	7±2	15±4	8±2	13±4
	2.3	90	8±3	14±3	24±4	13±4
	1.4	55	6±2	12±4	19±6	13±4
	0.5	20	3±1	9±2	17±6	8±3
3	3.0	120	12±4	13±4	29±3	17±4
	2.3	90	15±3	14±4	32±4	14±4
	1.4	55	14±3	14±3	30±7	15±4
	0.5	20	9±3	9±3	26±2	9±2
4	3.0	120	6±2	11±5	8±4	16±4
	2.3	90	6±2	12±4	30±6	15±5
	1.4	55	8±4	12±3	37±3	13±4
	0.5	20	10±5	9±3	37±6	9±3
5	3.0	123	6±3	16±6	33±3	19±5
	2.3	90	13±4	28±4	37±3	25±4
	1.4	55	8±5	26±4	26±3	23±4
	0.5	20	8±5	21±3	31±4	17±4
6	0.5	20	9±5	20±4	10±7	11±6
7	3.0	120			9±3	25±3
	2.3	90			7±5	24±3
	1.4	55	27±14	24±3	17±3	28±6
	0.5	20	11±3	25±5	11±3	31±3
8	3.0	120	11±2	26±3	28±3	26±3
	2.3	90	12±3	26±3	28±3	26±4
	1.4	55	8±2	26±4	64±2	33±3
	0.5	20	4±1	26±4	53±2	28±4
9	3.0	120	4±4	10±5	14±8	7±4
	2.3	90	4±2	8±4	21±5	7±5
	1.4	55	5±3	10±3	11±3	5±4
	0.5	20	3±2	11±5	5±3	8±4
10	3.0	120	7±2	15±4	14±3	19±4
	2.3	90	8±3	25±5	43±4	18±4
	1.4	55	5±2	24±4	42±5	18±3
	0.5	20	3±2	5±3	25±4	2±2

TABLE 2—*Continued*

	Elevation		Average Oxide Thickness±Std. Dev. (μm)			
			Side away from CB		Side next to CB	
Channel ID	m	in.	Outer Surface	Inner Surface	Outer Surface	Inner Surface
11	3.0	120	4±2	12±3	11±3	15±3
	2.3	90	5±3	15±3	16±3	18±4
	1.4	55	4±2	12±2	6±2	15±3
	0.5	20	3±2	2±2	3±2	3±2

hydrogen concentration in the sample. As shown in Fig. 17, with the exception of channel 9, the hydrogen concentration in the oxide is generally much less than in the metal, i.e., including the contribution of hydrogen in the oxide would not substantially increase the hydrogen content of the sample.

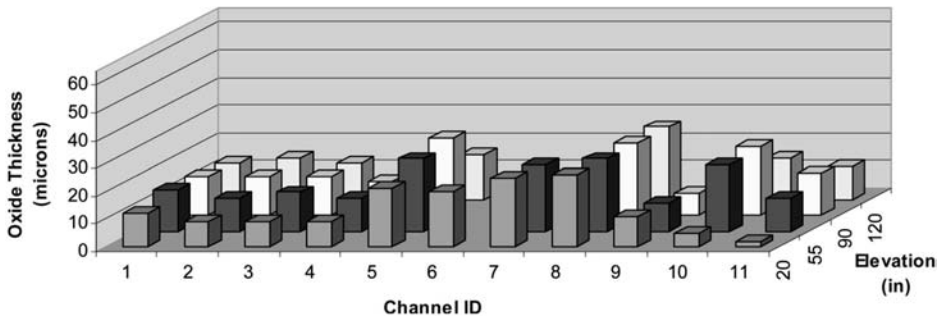


FIG. 10—*Inner surface oxide thickness on the non-blade side of the channels. The channel elevations of 20, 55, 90, and 120 in. correspond to 0.5, 1.4, 2.3, and 3.0 m, respectively.*

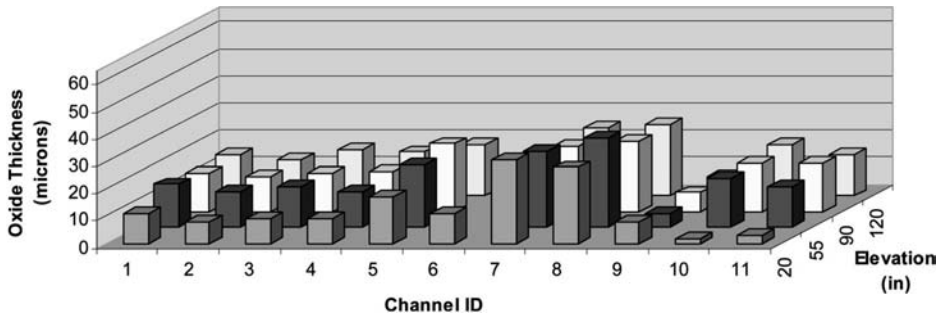


FIG. 11—*Inner surface oxide thickness on the blade side of the channels. The channel elevations of 20, 55, 90, and 120 in. correspond to 0.5, 1.4, 2.3, and 3.0 m, respectively.*

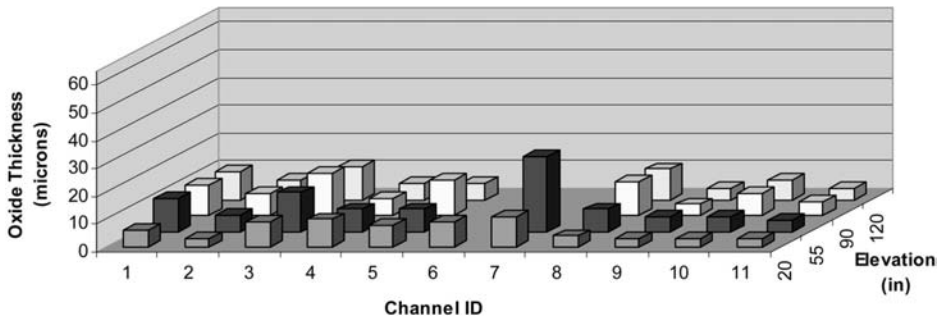


FIG. 12—*Outer surface oxide thickness on the non-blade side of the channels. The channel elevations of 20, 55, 90, and 120 in. correspond to 0.5, 1.4, 2.3, and 3.0 m, respectively.*

Hydrogen Pick up

The theoretical percentage of HPU at a given channel wall thickness, elevation, and side was calculated using Eq 2 using average hydrogen concentrations in the metal, and total oxide thickness (inside + outside) values, and assuming that the oxide was 100 % dense

$$\text{HPU} = \frac{3.11(H)t_m\rho_{\text{Zr}}}{t_T\rho_{\text{ZrO}_2}} \tag{2}$$

where:

H = average hydrogen concentration in the metal, in ppm,
t_m = metal thickness in mm,
t_T = total oxide thickness in microns, including inner and outer surfaces,
ρ_{Zr} = density of zirconium (6.5 g/cm^3), and
ρ_{ZrO_2} = density of zirconium oxide (5.6 g/cm^3).

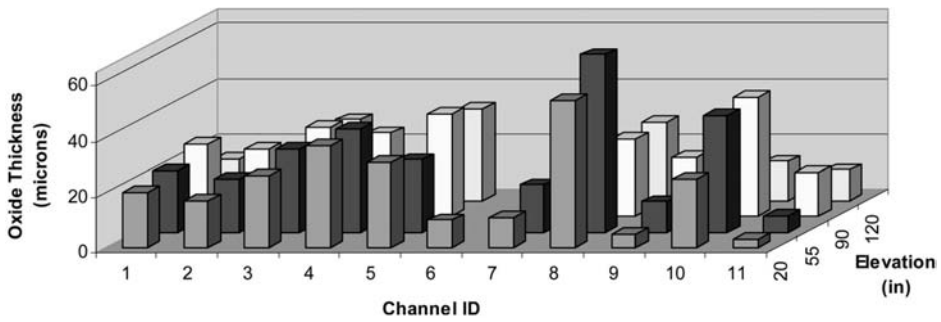


FIG. 13—*Outer surface oxide thickness on the blade side of the channels. The channel elevations of 20, 55, 90, and 120 in. correspond to 0.5, 1.4, 2.3, and 3.0 m, respectively.*

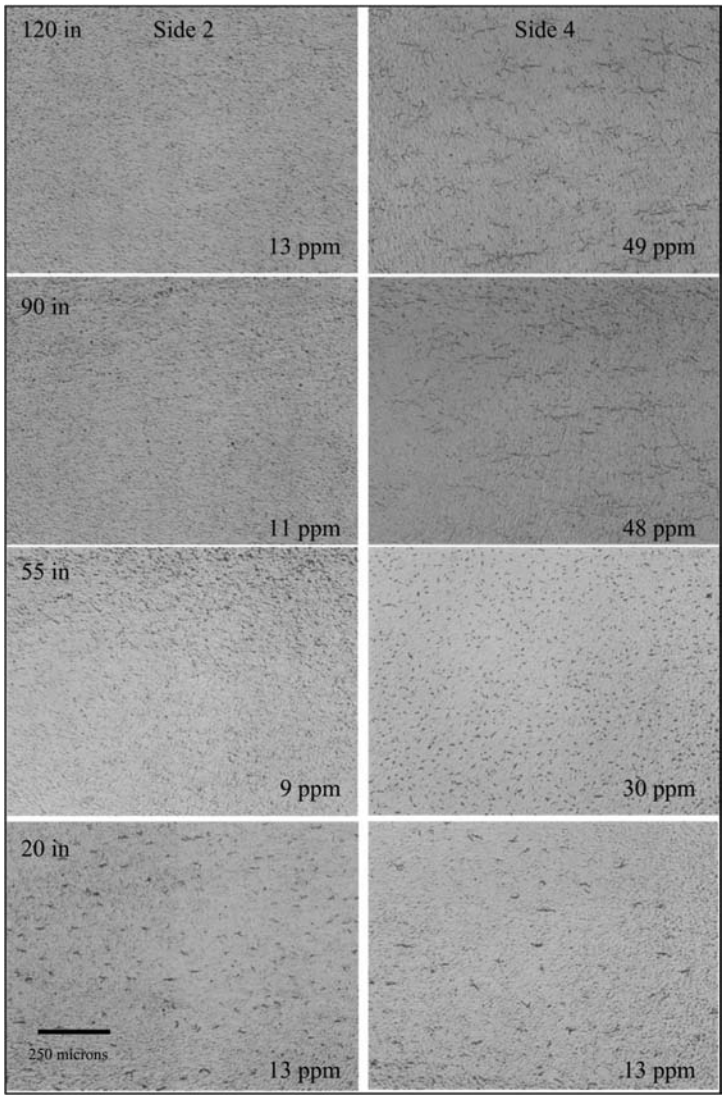


FIG. 14—*Hydrides in single-cycle channel (channel 9) from Plant A (side 4 is the blade side and side 2 is the non-blade side).*

Based on the measured oxide thickness and measured hydrogen content in the metal, the calculated percentage HPU is summarized in Table 5. In Fig. 18, the HPU percentage on the blade side is compared to the corresponding pick up percentage on the opposite, non-blade side. Table 5 and Fig. 18 show that the one-cycle channel (9) had the lowest HPU percentage and that the other multi-cycle channels exhibited a large variation in HPU percentage. The four-cycle channels (10 and 11) with the longest residence time show the highest HPU

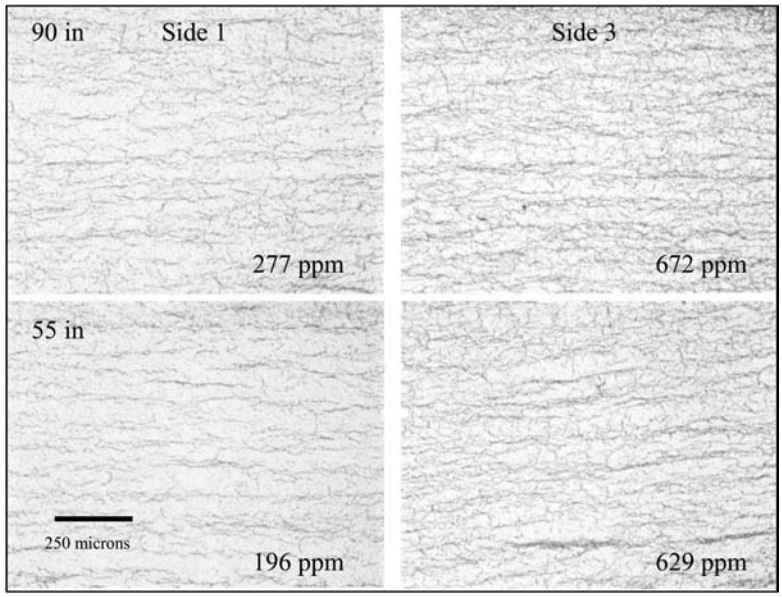


FIG. 15—*Hydrides in channel 10 from Plant D (side 3 is the blade side and side 1 is the non-blade side).*

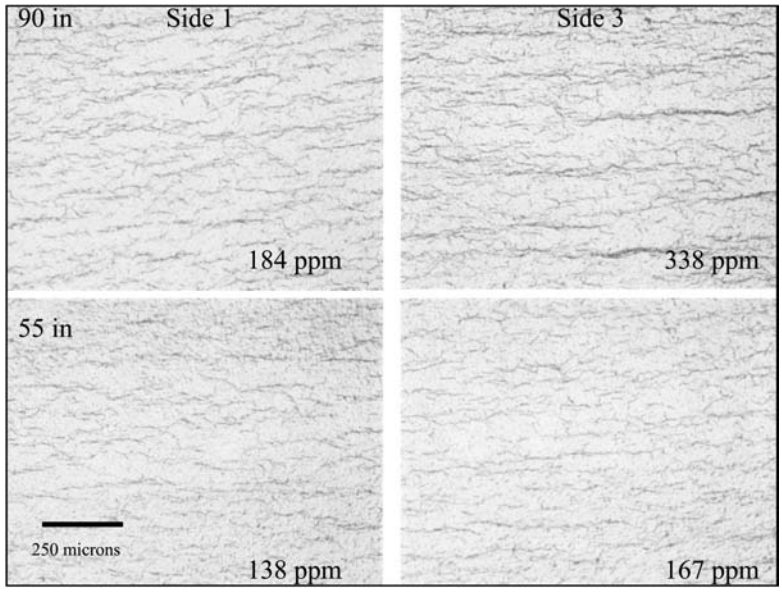


FIG. 16—*Hydrides in channel 11 from Plant D (side 3 is the blade side and side 1 is the non-blade side).*

TABLE 3—*Summary of measured hydrogen concentration in metal.*

	Elevation		Hydrogen Concentration (ppm)	
Channel ID	m	in.	Channel Side away from CB	Channel Side next to CB
1	3.0	120	85	102
	2.3	90	80	109
	1.4	55	77	105
	0.5	20	61	109
2	3.0	120	95	99
	2.3	90	74	206
	1.4	55	64	171
	0.5	20	51	169
3	3.0	120	200	355
	2.3	90	173	336
	1.4	55	159	319
	0.5	20	135	266
4	3.0	120	109	125
	2.3	90	91	244
	1.4	55	100	297
	0.5	20	118	308
5	3.0	123	179	337
	2.3	90	229	380
	1.4	55	208	375
	0.5	20	156	334
6	0.5	20	126	104
7	3.0	120		139
	2.3	90		156
	1.4	55	252	166
	0.5	20	154	107
8	3.0	120	165	198
	2.3	90	213	304
	1.4	55	171	418
	0.5	20	132	312
9	3.0	120	13	49
	2.3	90	11	48
	1.4	55	9	30
	0.5	20	13	13
10	3.0	120	193	300
	2.3	90	208	525
	1.4	55	170	500
	0.5	20	107	231
11	3.0	120	111	202
	2.3	90	158	268
	1.4	55	124	145
	0.5	20	83	76

percentage. However, for all the multi-cycle channels, the HPU percentage does not appear to be affected by the presence, or absence, of the control blade and is typically consistent between the two opposing channel sides. For the single-cycle channel (9), the pick up percentage on the blade side is twice that on the non-blade side, even though the values are low on both sides.

Shadow Corrosion-Induced Bow Model

A model for shadow corrosion-induced bow is derived first by rearranging relationship for HPU with the simplifying assumption that HPU is the same for both general and shadow corrosion and the differential hydrogen (ΔH) is $H_{\text{blade}} - H_{\text{non-blade}}$ such that

$$\Delta H = \frac{(\text{HPU})\Delta t_T \rho_{ZrO_2}}{3.11 t_m \rho_{Zr}} \tag{3}$$

where:

Δt_T = total blade side oxide thickness (inner + outer) minus the total non-blade side oxide thickness.

Theoretically, the precipitation of zirconium hydride causes a 1 % volume increase (ΔV) in Zircaloy when the hydrogen concentration is 1000 ppm. The theoretical consideration is based on assumptions that include the density and the stoichiometry of the zirconium hydride formed. If this volume increase is assumed to be isotropic, the corresponding linear strain increase (R_L) will be 0.33 % [5,6]. However, the experimental data suggest that the linear strain increase is lower [5,6].

Thus, the differential length (ΔL) between the blade side and the non-blade side is theoretically given by

$$\Delta L = \frac{R_L}{1000} \Delta H(L) \tag{4}$$

where:

L = length of the channel over which ΔH is relevant (assumed herein to be the full length of the channel) and

R_L is in units of in./in.

Channel bow can be approximated by

$$\text{bow} = \frac{L \Delta L}{8W} \tag{5}$$

where:

L = length of the channel that bows (i.e., the full length of the channel, 4.24 m or 167 in.) and

W = width of the channel, 0.14 m (5.518 in.).

Substituting Eq 4 into Eq 5 gives

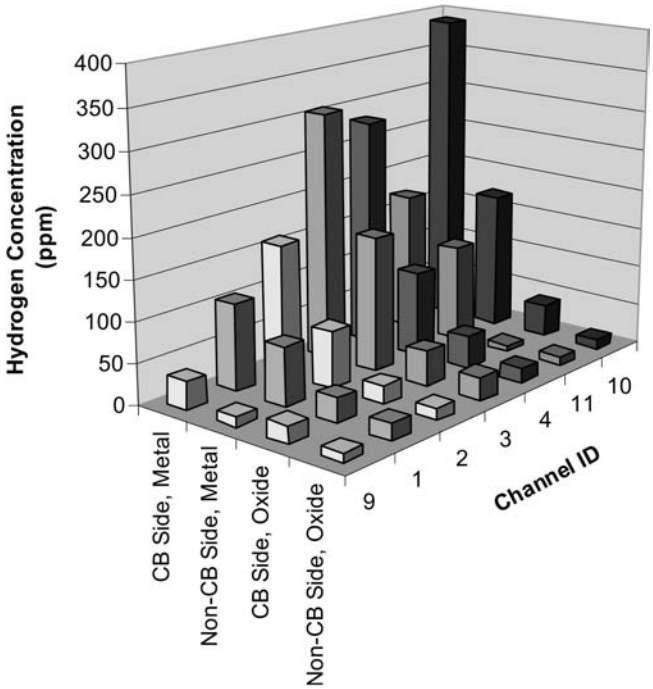


FIG. 17—*Comparison of hydrogen concentration in the metal and in the oxide (based on sample weight).*

$$\text{bow} = \frac{L^2}{8W}\frac{R_L}{1000}\Delta H \tag{6}$$

and substituting Eq 3 into Eq 6 gives

$$\text{bow} = \frac{L^2}{8W}\frac{R_L}{1000}\frac{(\text{HPU})\Delta t_T \rho_{\text{ZrO}_2}}{3.11 t_m \rho_{\text{Zr}}} \tag{7}$$

TABLE 4—*Comparison of concentration of hydrogen in the metal and in the oxide (based on sample weight).*

	Channel ID						
	9	1	2	3	4	11	10
	Average hydrogen concentration in metal (ppm)						
CB side	35	108	161	307	283	172	389
Non-CB side	12	73	71	167	104	119	170
	Average hydrogen concentration in oxide (ppm)						
CB side	22	31	22	43	40	8	40
Non-CB side	11	21	15	29	18	11	12

TABLE 5—*Summary of HPU percentage.*

	Elevation		HPU (%)		Avg. H Pick up (%)	
Channel ID	m	in.	Channel Side away from CB	Channel Side next to CB	Channel Side away from CB	Channel Side next to CB
1	3.0	120	25	23	21	21
	2.3	90	22	21		
	1.4	55	20	17		
	0.5	20	23	24		
2	3.0	120	30	26	27	37
	2.3	90	23	38		
	1.4	55	24	37		
	0.5	20	29	46		
3	3.0	120	55	42	47	48
	2.3	90	41	50		
	1.4	55	39	49		
	0.5	20	52	52		
4	3.0	120	44	29	39	38
	2.3	90	35	37		
	1.4	55	34	41		
	0.5	20	43	46		
5	3.0	123	53	58	40	56
	2.3	90	36	50		
	1.4	55	33	62		
	0.5	20	38	54		
7	3.0	120		31	30	26
	2.3	90		33		
	1.4	55	32	24		
	0.5	20	28	16		

TABLE 5—*Continued*

	Elevation		HPU (%)		Avg. H Pick up (%)	
Channel ID	m	in.	Channel Side away from CB	Channel Side next to CB	Channel Side away from CB	Channel Side next to CB
8	3.0	120	33	27	32	28
	2.3	90	35	35		
	1.4	55	32	27		
	0.5	20	28	24		
9	3.0	120	6	16	6	12
	2.3	90	6	12		
	1.4	55	4	13		
	0.5	20	6	7		
10	3.0	120	57	59	54	56
	2.3	90	41	56		
	1.4	55	37	53		
	0.5	20	79	55		
11	3.0	120	44	50	60	54
	2.3	90	52	50		
	1.4	55	51	44		
	0.5	20	93	74		

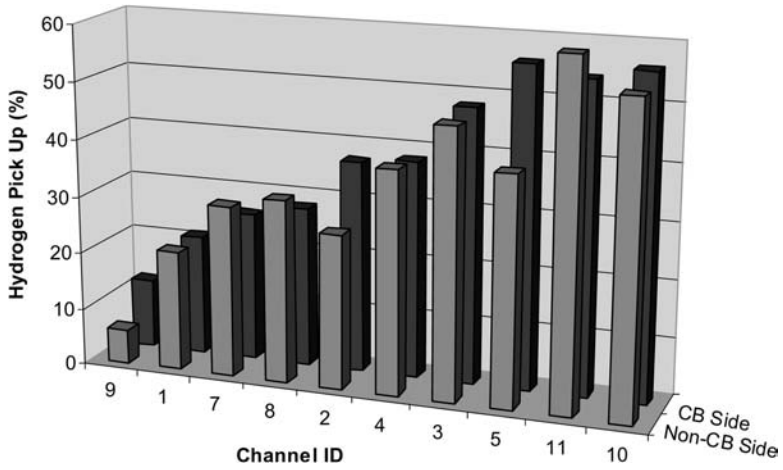


FIG. 18—*Comparison of HPU percentage between channel sides.*

This model of shadow corrosion-induced bow indicates that bow is a function of channel geometry (L, W, and t_m), material density (ρ_{Zr} and ρ_{ZrO_2}), HPU percent (HPU), and the difference in oxide thickness (Δt_T). One confirmation of this model is that it is consistent with the observations that shadow bow decreases as channel thickness increases (see Fig. 4). Because channel geometry and material density are independent of the corrosion process, the parameters that control the extent of shadow corrosion-induced bow are R_L, which is not well known, HPU and Δt_T.

In estimating the expected channel bow from measured hydrogen differential, the simplifying assumption is that the average measured hydrogen concentration on each channel side is representative of the average along the whole channel length. Table 6 shows the estimated bow due to the hydrogen differential based on the theoretical correlation and a best-fit correlation, the estimated bow due to the differential in fast-neutron fluence, the overall bow based on the theoretical and best-fit correlations, and the measured bow. The best-fit correlation was one that yielded a one-to-one correlation between the measured and the estimated total bow, as shown in Fig. 19. The linear correlations in Fig. 19 provide further confirmation that the measured channel bow is associated with the volume differential arising from the expansion of different amounts of hydrides between the blade side and the non-blade sides of the channel. The slopes of the two correlations in Fig. 19 are functions of R_L. It can be seen in Fig. 19 that the theoretical correlation ($R_L = 0.33\,\%$) yielded an over prediction of channel bow. The best fit to the present results was one based on a correlation of $R_L = 0.25\,\%$. The present correlation is in good agreement with a length increase of $\sim 0.23\,\%$ per 1000 ppm of hydrogen reported for growth of Zr-alloy PWR components [5,6]. The deviation of the observed correlations from the theoretical correlation is reasonable considering the uncertainties associated with the assumed hydride density and stoichiometry.

Plant Type Effect

The selected channels represented a wide range of channel bow performance resulting from a broad range of operational conditions in different plant types (Table 1). For the purpose of discussion on channel distortion due to bow, the main characteristic of interest is the difference in gap size between adjacent channels as shown in Figs. 3 and 4. Figure 3 shows that in the absence of contribution from the shadow corrosion mechanism (ECBE = 0), the large channel bow is generally observed at high exposures, associated with bow driven by fluence gradient. With contribution from the shadow corrosion mechanism, Fig. 3 shows that the onset of high channel bow occurs at lower exposures. Figure 4 shows that the S-lattice is the more susceptible to shadow corrosion-induced bow than the C-lattice and that the C-lattice is the more susceptible to shadow corrosion-induced bow than the D-lattice. The trend in susceptibility to shadow corrosion-induced channel bow is consistent with the S-lattice having the smallest gap and the D-lattice the greatest.

The distance between the control blade and the channel is a likely explanation for the behavior of channels 7 and 8. As noted earlier, channel 7 is different from the companion channel 8 in two important respects: First, there is shadow corrosion on the non-blade side (due to exposure to an instrument tube), and second, no shadow corrosion on the blade side. The absence of shadow corrosion is particularly notable since the companion channel 8 clearly shows shadow corrosion on the blade side and is typical of seven channels that operated in the same manner as channel 7 and showed very similar measured channel bow ($8.8 +/- 0.8$ mm or $348 +/- 33$ mil @ 1 sigma). The channels are from a C-lattice plant, where the interchannel gap is larger than in S-lattice plants and the control blade is more likely to lean on one of the adjacent channels. The most likely explanation for the lack of shadow in channel 7 is because the control blade was tilted away from the channel.

Corrosion and Hydriding Kinetics

Channel exposure (represented by the fuel assembly exposure) and channel residence time are parameters that affect the development of oxide on the non-blade side of the channel. On the blade side, exposure to the control blade, in terms of ECBE, is an additional factor that contributes to the development of the shadow corrosion. Figure 20 shows the average oxide thickness on the outer surface as a function of ECBE. (Channel 6 is excluded because of insufficient sampling.) The figure shows that the non-blade side behaved quite differently than the majority of the blade sides and is not sensitive to variation in ECBE. Most of the blade side shows an increase with ECBE as shown by the trend line that ignores two data points. These two data points correspond to channels 7 and 9, which, respectively, did not show elevated shadow corrosion thickness on the blade side and was low in assembly exposure. The correlation with ECBE thus works well for channels with high exposures (in the $\sim$ 36–48 GWd/MTU range) but cannot be applied to include low exposure channels.

TABLE 6—*Comparison of measured channel bow with estimated total channel bow using theoretical and experimental correlations for linear strain increase, R_L, due to hydride formation.*

Plant	Ch ID	Estimated Bow Due to H Differential, mm (mils)		Estimated Bow Due to Irradiation Growth, mm (mils)	Total Estimated Bow, mm (mils)		Measured Bow, mm (mils)
		Using Theoretical Correlation	Using Experimental Correlation		Using Theoretical Correlation	Using Experimental Correlation	
A	1	1.87 (74)	1.43 (56)	0.05 (2)	1.93 (76)	1.48 (58)	1.55 (61)
	2	4.82 (190)	3.67 (144)	1.42 (56)	6.24 (246)	5.09 (200)	3.02 (119)
	3	7.50 (295)	5.71 (225)	0.20 (8)	7.70 (303)	5.91 (233)	7.42 (292)
	4	9.54 (376)	7.25 (286)	0.48 (19)	10.02 (395)	7.74 (305)	8.53 (336)
B	5	8.79 (346)	6.68 (263)	0.08 (3)	8.86 (349)	6.76 (266)	7.98 (314)
C	7	−3.53 (−139)	−2.69 (−106)	3.71 (146)	0.18 (7)	1.02 (40)	0.64 (25)
	8	7.39 (291)	5.62 (221)	3.78 (149)	11.18 (440)	9.41 (370)	9.55 (376)
A	9	1.22 (48)	0.93 (37)	−0.25 (−10)	0.97 (38)	0.67 (27)	0.56 (22)
D	11	11.07 (436)	8.42 (332)	2.44 (96)	13.51 (532)	10.86 (428)	8.20 (323)
	10	2.49 (98)	1.89 (75)	−0.03 (−1)	2.46 (97)	1.87 (74)	0.71 (28)

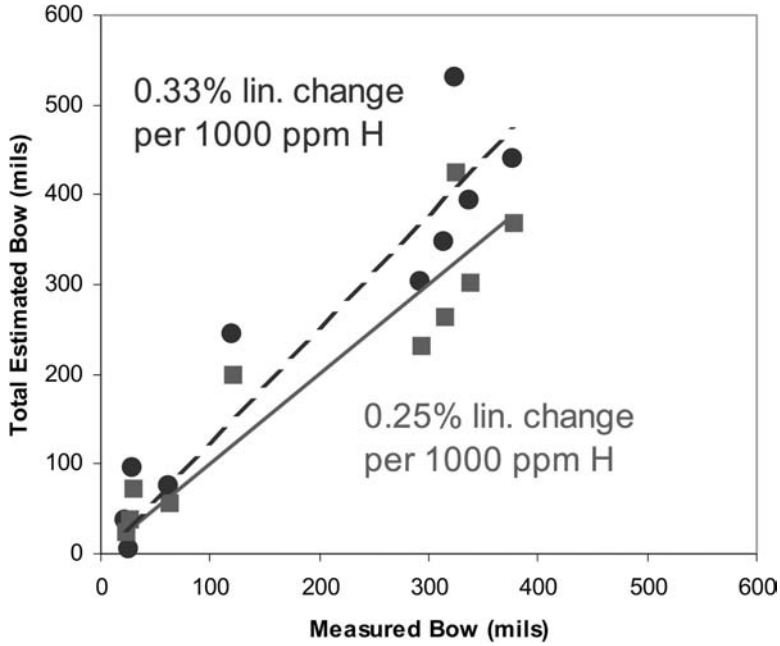


FIG. 19—*Comparison of the measured bow with estimated channel bow based on hydrogen differential and fluence gradient driven bow. Solid line is fitted line assuming 0.25 % linear change per 1000 ppm hydrogen and represents 1:1 correspondence between measured and predicted bow. The dashed line is based on 0.33 % linear change per 1000 ppm hydrogen.*

The correlation of outer surface oxide thickness with channel exposure is shown in Fig. 21. With the exception of two data points, the blade side shows a steady increase with exposure. The two exceptions are channels 7 and 11. The blade side of these two channels behaved like a non-blade side without showing increased oxide thickness due to shadow corrosion. As discussed above, channel 7 did not undergo shadow corrosion on the control blade side probably due to a tilted control blade; channel 11 did not show significant shadow corrosion on account of low ECBE. In contrast to the blade side, the outer surface oxide on the non-blade side shows a gradual increase with channel exposure. Figures 20 and 21 show that both exposure and ECBE are needed to account for the basic corrosion behavior of the blade side of channels. A similar assessment was made for residence time, which showed a similar trend as channel exposure except with greater scatter. Comparing the oxide thickness of the one-cycle with the multi-cycle channels, Fig. 21 shows that the outer surface oxide on the blade side continues to increase at a rate (exposure or time based) higher than on the non-blade side. That is, Δt_T is increasing with exposure, or time, even though the control blade is withdrawn later in life.

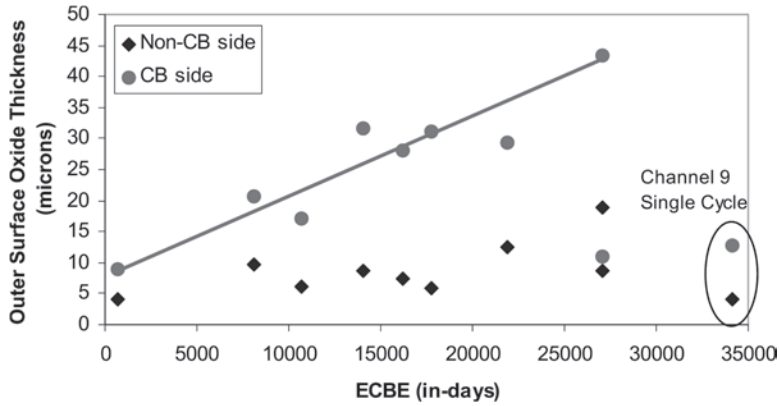


FIG. 20—*Average outer surface oxide thickness versus ECBE. The fitted line ignores two of the blade side data points.*

Hydrogen content also provided a better correlation with channel exposure than residence time. Figure 22 shows the average hydrogen content for the blade side and the non-blade side as a function of channel exposure. As with average outer surface oxide thickness, the hydrogen content on the non-blade side shows a gradual increase with channel exposure. On the blade side, the hydrogen content shows a more rapid increase with exposure. The exceptions are channels 7 and 11, which did not exhibit significant shadow corrosion, and channel 1, which had the lowest ECBE of the multi-cycle channels; in essence, the hydrogen content on the blade side of these three channels is consistent with the general trend for the non-blade side. The results from the present work indicate that the hydrogen concentration on the blade side increased at a higher rate than on the side not affected by shadow corrosion.

The HPU percentage generally increased with residence time or exposure of the channel. A comparison of the correlation with residence time or channel exposure indicated that the residence time provided the better correlation and the lowest and highest pick up percentages correspond to channels with the lowest and highest residence times, respectively, as shown in Fig. 23. As discussed earlier, Fig. 18 shows that there is little variation between the blade side and the non-blade side of the multi-cycle channels. For the single-cycle channel (9), despite the low values, the pick up percentage on the blade side is twice that on the non-blade side. Note the outer oxide thickness and the hydrogen concentration on the blade side were ~ 3 times those on the non-blade side, i.e., the pick up percentage for the shadow oxide would have to be even greater than the overall percentage, which included the contribution from inner surface corrosion. The present results (Table 5) suggest that shadow corrosion initially resulted in a higher percentage of HPU. This implication is in contrast with a previous report of lower HPU fraction for shadow corrosion [8]. With increased residence time

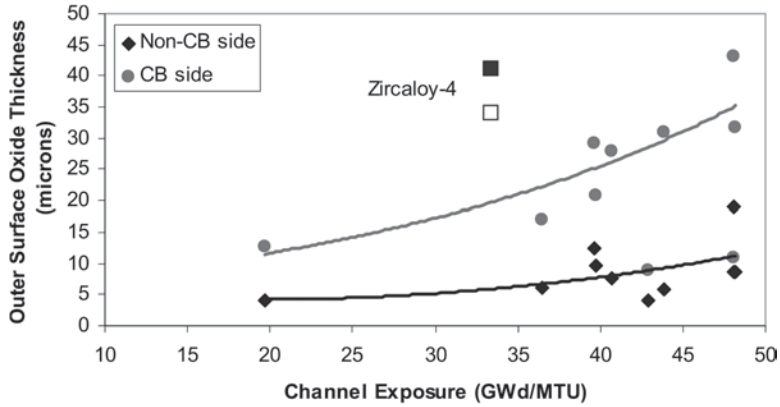


FIG. 21—*Average outer surface oxide thickness versus channel exposure. The fitted line ignores two of the blade side data points.*

(or channel exposure), this difference between channel sides with and without shadow corrosion diminishes as indicated by the trend lines in Fig. 23. Thus, the observed increase in the difference in hydrogen concentration with exposure (Fig. 22) is a result of the continued increase in the difference in oxide thickness (Fig. 21) with higher exposure.

Figures 21–23 also include data obtained from a Zircaloy-4 channel after 33.4 GWd/MTU exposure with ECBE = 30 896 in. · day [7]. The comparison of Zircaloy-2 and Zircaloy-4 is discussed in a later section.

Figures 21 and 22 both indicate that blade side oxide thickness and hydrogen concentration in the one-cycle channel were significantly lower than those in multi-cycle channels. The discussion above that the rates of corrosion and hydriding continue to increase at a higher rate on the blade side than on the

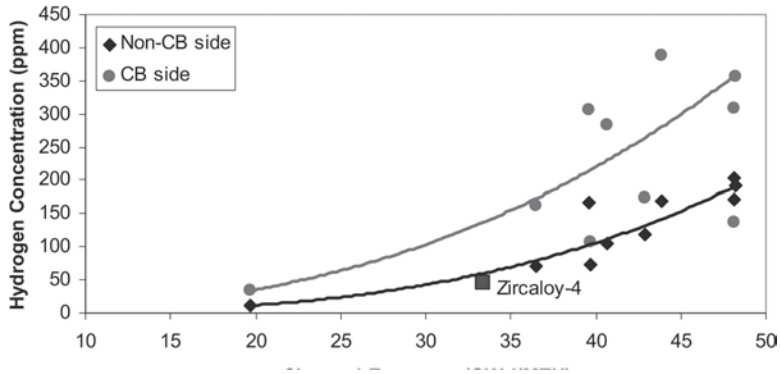


FIG. 22—*Hydrogen concentration versus channel exposure. The fitted line ignores two blade side data points (channels 7 and 11), which did not exhibit shadow corrosion.*

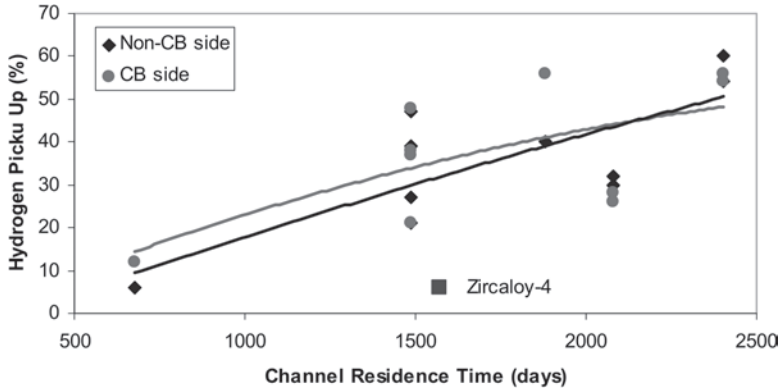


FIG. 23—*HPU versus channel residence time.*

non-blade side relies on one important assumption. The assumption is that the one-cycle channel (9) is representative of the channel condition after the initial setup of shadow corrosion on the blade side. In the examined one-cycle channel, the outer surface oxide thickness on the blade side is about three times that on the non-blade side, showing a clear presence of the shadow corrosion effect. However, the differential in oxide thickness (between opposite channel sides) is significantly less than those of multi-cycle channels that have lower ECBE. One source of uncertainty is that the inserted control blade might have leaned away from the channel, much like suspected for channel 7. In that case, the plant has a C-lattice and the larger interchannel gap implies a greater probability for the control blade to lean away from a channel, and oxide thickness measurements showed no indication of shadow corrosion on the control blade side. In the one-cycle channel, shadow corrosion on the blade side was clearly present. The channel is from plant A with the S-lattice, in which the small inter-channel gap means that the inserted control blade has lower probability to be tilted significantly away from any channel. The channel also had experienced considerable exposure to the control blade, with an ECBE value higher than any of the multi-cycle channels from the same plant. These are all conditions favorable for shadow corrosion, and therefore the examined one-cycle channel is expected to be representative of other channels with similar exposure and ECBE. On the basis that the behavior of the one-cycle channel is representative of the condition after the shadow corrosion was initially established, the present results indicate that the significant hydrogen differential responsible for channel bow in some of the multi-cycle channels, as well as the associated outer surface oxide differential, was developed after the initial shadow corrosion took place. In other words, the amount of channel exposure after the period of shadow corrosion is a factor that affects the build up of both oxide and hydrogen differential. The present results, Fig. 17, do not support an alternate hypothesis, in which most of the shadow corrosion oxide observed in multi-cycle channels was built up during the early-in-life exposure to the control blade and

that hydrogen trapped in the thick oxide was later released and absorbed into the channel's metal sides.

Additional Considerations

Shadow Corrosion Mechanism

Two types of mechanisms have been proposed to account for shadow corrosion that occurs on zirconium alloys when it is placed adjacent to a dissimilar material [1–4]. The first is a form of galvanic corrosion, and the second is that associated with the effects of beta-particles [3,9]. Recent investigations have provided more support for a galvanic-based mechanism that required the in-reactor radiation environment. For example, Lysell et al. [10] demonstrated that the potential difference between stainless steel (or Inconel) and Zircaloy is enhanced under irradiation. In another paper presented at this conference, Kim et al. [11] provided clarification on the significance of ultraviolet (UV) irradiation in changing the semi-conductance nature of the oxide formed on Zircaloy and on stainless steel or Inconel. In Kim's work, UV light was used to generate a greater difference in the corrosion potential of the Zircaloy and stainless (or Inconel) and hence higher galvanic current. The effect was found to be repeatable in these short-term laboratory tests and could be switched on or off in accordance with the presence or absence of the UV illumination. The observations are interpreted in terms of UV providing one of the necessary conditions, oxide conductivity, for the enhanced corrosion without inducing changes to the oxides.

In the reactor, zirconium oxide is expected to be sufficiently conducting, and enhanced corrosion or shadow corrosion can result from the increased corrosion potential difference between the inserted control blade and the Zircaloy channel. The present results suggest that after shadow corrosion has taken place on Zircaloy-2, the corrosion kinetics continues to remain different, i.e., higher than in channel not affected by shadow corrosion, even after the condition causing the shadow corrosion (i.e., control blade insertion) is no longer present. The results thus suggest that a persistent change to the oxide microstructure (such as grain size or morphology) was established during shadow corrosion. This appears to be an aspect of in-reactor shadow corrosion that cannot be simulated by out-reactor testing.

Hydrogen Absorption

The hydrogen absorption characteristics of Zircaloys are related to the corrosion behavior via the HPU percentage. Zircaloy composition and microstructure are known to affect its corrosion and hydriding behavior in a given environment. For HPU, it is also known that the characteristics of the oxide could be an important factor. In the one-cycle channel, the HPU percentage was low but was higher on the blade side than on the non-blade side. In multi-cycle channels, the pick up percentage was higher, and there was a variation between channels but

not between sides of a given channel (Fig. 18). The results indicate that the hydrogen absorption characteristics changed with exposure (or residence time). The consistency within each of the multi-cycle channels implies that the HPU percentage was related to the channel condition, specifically the microstructural condition, which is governed by the channel exposure and residence time.

In Zircaloys, the primary microstructural feature that affects corrosion is the presence of second phase particles (SPPs). The SPPs formed in Zircaloy-2 are $Zr(Fe, Cr)_2$ and $Zr_2(Fe, Ni)$, and the matrix is depleted in Fe, Cr, and Ni. In addition to irradiation damage, the main microstructural change in Zircaloys is radiation-induced dissolution of the SPPs. The result is a decrease in the number density of the SPPs and at sufficiently large fluences or irradiation times; the SPPs can become completely dissolved. The dissolution process in effect releases the alloying elements from the SPPs into the surrounding matrix [12–15]. The dissolution processes for the two types of SPP are different. For the $Zr(Fe, Cr)_2$ SPPs, the dissolution rate of Fe is faster than that of Cr, resulting in the SPP becoming enriched in Cr as the SPP dissolves. The Cr is eventually released from any Cr enriched SPPs or remnants [15]. In contrast, $Zr_2(Fe, Ni)$ SPPs appear to dissolve without appreciable change in the Fe/Ni ratio. With increased exposure or irradiation time, the Zircaloy-2 matrix, therefore, gradually becomes more concentrated with dissolved alloying elements, increasingly approaching the overall alloy composition.

In the corrosion process of Zircaloys, fresh oxide is formed at the interface by consuming the underlying metal. The state of the Zircaloy, therefore, affects the nature of the layer of fresh oxide that is in immediate contact with the metal. This layer of oxide may serve the purpose of acting as a barrier to the ingress of the corrosion generated hydrogen. The general increase in HPU percentage with channel exposure or time can be interpreted as a continuous change, or degradation, in the protectiveness of the interfacial oxide layer as the matrix and hence oxide composition evolve. As Fe, Cr, and Ni are all released into the matrix with irradiation, one or more of the three elements could potentially be responsible for the increased HPU percentage with irradiation. The behavior of Zircaloy-2 channels can be contrasted with that of Zircaloy-4 channels. In Figs. 21–23, the data for a Zircaloy-4 channel (33.4 GWd/MTU exposure with ECBE = 30 896 in. · days) [7] are also shown. In Fig. 21, it can be seen that the Zircaloy-4 channel had significantly thicker outer surface oxide than Zircaloy-2 channels at that exposure and that the thickness for the blade side (solid symbol) was slightly higher than for the non-blade side (open symbol). Despite the difference in oxide thickness, the overall hydrogen concentration for the Zircaloy-4 channel was low, and the hydrogen differential across the channel was quite small. The low hydrogen content in Zircaloy-4 is the result of the low HPU percentage (6 %), which was the same for both sides of the channel. The comparison of HPU percentage for Zircaloy-2 and Zircaloy-4 in Fig. 23 indicates that Zircaloy-4 does not appear to suffer from increasing HPU percentage with exposure. Similar results showing low HPU fraction in Zircaloy-4 but not in Zircaloy-2 at high exposures have been reported by Miyashita et al. [16]. The comparison of Zircaloy-2 with Zircaloy-4 behavior, therefore, leads to the conclusion that the release of Ni from SPPs could be a main contributing factor for the high pick up percentage in Zircaloy-2 at high exposures. In another paper in this

proceeding [17], the role of Ni in the acceleration of HPU in high burn up Zircaloy-2 has been discussed in terms of modification to the nature of the barrier layer in the oxide.

Summary and Conclusions

Poolside dimensional measurements of Zircaloy-2 channels have shown a wide range of bow behavior depending on the fuel assembly exposure, exposure to the control blade, and geometric factors in different reactors. Specifically, shadow corrosion-induced bow was found to be greatest in plants with the smallest channel-to-blade gap. In addition, although the conditions for shadow corrosion occurred at low exposure early in life, the full extent of shadow corrosion-induced bow is not observed until late in life at high exposure. Zircaloy-2 channel coupons from a number of plants and operational histories were retrieved and investigated in the hot cell with the aim of gaining better understanding of the mechanism responsible for shadow corrosion-induced channel bow.

Building on results from a previous investigation on channels from two S-lattice plants, the addition of data from C- and D-lattice plants and from a one-cycle channel further confirms the correlation of shadow corrosion-induced channel bow with differential hydrogen concentration across opposite channel sides. The best-fit linear dimensional change associated with hydride volume expansion was 0.25 % per 1000 ppm hydrogen, less than expected from theoretical isotropic considerations.

The kinetics of oxide growth and hydrogen accumulation is quite different for the blade side compared to the non-blade side. At low exposure, a differential in both oxide thickness and hydrogen content is established between opposite channel sides. The differential is, however, small compared with the differential that ultimately develops at higher exposure, as the rate of growth of oxide and accumulation of hydrogen is higher on the channel side affected by shadow corrosion. The large differential in hydrogen concentration that causes shadow corrosion-induced channel bow is therefore concluded to have been built up during channel exposure when the shadow corrosion condition no longer existed.

The HPU percentage appears to increase with channel residence time (and exposure), and the highest pick up percentage was observed in channels with the longest residence time. In the single-cycle channel, the HPU percentage was low and the channel side subjected to shadow corrosion shows a pick up percentage about twice that of the side unaffected by shadow corrosion. With increased exposure, the present results show that there is little difference in pick up percentage between channel sides affected or unaffected by shadow corrosion, although there is considerable scatter between the multi-cycle channels. The consistency in HPU percentages among opposing sides of a given multi-cycle channel are attributed to a HPU fraction that is independent of the corrosion mechanism but likely dependent on residence time and fluence. The variation of HPU percentage with time and fluence is considered to be associated with radiation-induced microstructural change, specifically, the dissolution of SPPs, a process that releases alloying elements into the matrix. Compared with HPU data for Zircaloy-4 channels, it is concluded that the release of Ni from the

dissolution of $Zr_2(Fe, Ni)$ SPPs in Zircaloy-2 may be the cause of high HPU fraction at high residence times.

Acknowledgments

The writers would like to thank Jerry Potts, Mark Dubecky, and Bob Rand for their significant contributions in the early stages of this work. The writers would also like to thank the GNF field inspection teams and personnel at a number of sites for the on-site channel measurements, and, in particular, utility personnel at the four plants for channel coupon sectioning and shipping support. The services provided by VNC hot cell team in performing non-destructive and destructive examinations/tests on the channel coupons are also acknowledged. The writers would also like to thank Dr. Ronald B. Adamson for many insightful discussions.

References

[1] Trowse, R. W., Sumerling, R., and Garlick, A., "Nodular Corrosion of Zircaloy-2 and Some Other Zirconium Alloys in Steam Generating Heavy Water Reactors and Related Environments," *Zirconium in the Nuclear Industry: Third Int. Symp, ASTM STP 633*, Quebec City, 1976, ASTM International, West Conshohocken, PA, 1977, p. 236.

[2] Sumerling, R., Garlick, A., Stuttard, A., Hartog, J. M., Trowse, F. W., and Sims, P., "Further Evidence of Zircaloy Corrosion in Fuel Elements Irradiated in a Steam Generating Heavy Water Reactor," *Zirconium in the Nuclear Industry: Fourth Int. Symp., ASTM-STP-681*, Stratford-upon-Avon, 1978, ASTM International, West Conshohocken, PA, 1979, p. 107.

[3] Chen, J. S. F. and Adamson, R. B., "Observations of Shadow Phenomena on Zirconium Alloys," *Proceedings of the International Topical Meeting on LWR Fuel Performance*, West Palm Beach, FL, 1994, American Nuclear Society, LaGrange Park, IL, 1994, pp. 309–317.

[4] Andersson, B., Limback, M., Wikmark, G., Hauso, E., Johnsen, T., Ballinger, R. G., and Nystrand, A.-C., "Test Reactor Studies of the Shadow Corrosion Phenomenon," *Zirconium in the Nuclear Industry: 13th International Symposium, ASTM STP 1423*, Annecy, 2001, G. D. Moan and P. Rudling, Eds., ASTM International, West Conshohocken, PA, 2002, pp. 583–615.

[5] Kesterson, R. L., King, S. J., and Comstock, R. J., "Impact of Hydrogen on Dimensional Stability of Fuel Assemblies," *Proc. ANS Light Water Reactor Fuel Performance Conference*, Park City, UT, 2000, American Nuclear Society, LaGrange Park, IL.

[6] King, S. J., Kesterson, R. L., Yueh, K. H., Comstock, R. J., Herwig, W. M., and Ferguson, S. D., "Impact of Hydrogen on Dimensional Stability of ZIRLO Fuel Assemblies," *13th ASTM Symposium on Zirconium in the Nuclear Industry, ASTM STP 1423*, Annecy, 2001, ASTM International, West Conshohocken, PA, 2002, p. 471.

[7] Mahmood, S. T., Lin, Y.-P., Dubecky, M. A., Edsinger, K., and Mader, E. V., "Channel Bow in Boiling Water Reactors—Hot Cell Examination Results and Correlation to Measured Bow," *LWR Fuel Performance Meeting/Top Fuel*, San Francisco, CA, September 2007, American Nuclear Society, LaGrange Park, IL.

[8] Adamson, R. B., Lutz, D. R., and Davies, J. H., "Hot Cell Observations of Shadow Corrosion Phenomena," *Proceedings Fachtagung der KTG-Fachgruppe, Brennelemente und Kernbautelle [Proceedings Symposium of Technical Meeting of the German*

Nuclear Society], Karlsruhe, Feb. 29–March 1, 2000, German Nuclear Society, Berlin, Germany, 2000.

[9] Lemaignan, C., "Impact of Beta Radioloysis and Transient Products on Irradiation-Enhanced Corrosion of Zr Alloys," *J. Nucl. Mater.*, Vol. 187, 1992, pp. 122–130.

[10] Lysell, G., Nystand, A.-C., and Ullberg, M., *On the Shadow Corrosion Mechanism for Zirconium Alloys*, ENS TOPFUEL, Stockholm, 2001, European Nuclear Society, Paper P2-13.

[11] Kim, Y., Rebak, R., Lin, Y. P., Lutz, D., Crawford, D., Kucuk, A., and Cheng, B., "Photoelectrochemical Investigation of Radiation Enhanced Shadow Corrosion Phenomenon," *Zirconium in the Nuclear Industry: 16th International Symposium*, Chengdu, China, ASTM International, West Conshohocken, PA, 2010.

[12] Griffiths, M., Gilbert, R. W., and Carpenter, C. J. C., "Phase Instability, Decomposition and Redistribution of Intermetallic Precipitates in Zircaloy-2 and -4 During Neutron Irradiation," *J. Nucl. Mater.*, Vol. 150, 1987, pp. 53–66.

[13] Yang, W. J. S., Tucker, R. P., Cheng, B., and Adamson, R. B., "Precipitates in Zircaloy: Identification and the Effects on Irradiation and Thermal Treatment," *J. Nucl. Mater.*, Vol. 138, 1986, pp. 185–195.

[14] Mahmood, S. T., Farkas, D. M., and Adamson, R. B., "Post Irradiation Characterization of Ultra-High-Fluence Zircaloy-2 Plate," *Zirconium in the Nuclear Industry; 12th International Symposium, ASTM STP 1354*, Toronto, 1998, ASTM International, West Conshohocken, PA, 2000, pp. 139–169.

[15] Takagawa, Y., Ishimoto, S., Etoh, Y., Kubo, T., Ogata, K., and Kubota, O., "The Correlation Between Microstructures and In-BWR Corrosion Behavior of Highly Irradiated Zr-Based Alloys," *Zirconium in the Nuclear Industry: 14th International Symposium, ASTM STP1467*, Stockholm, 2004, ASTM International, West Conshohocken, PA, 2006, p. 386.

[16] Miyashita, T., Nakae, N., Ogata, K., Baba, T., Kamimura, K., Matsumoto, T. and Kakiuchi, K., "Corrosion and Hydrogen Pick-up Behaviors of Cladding and Structural Components in BWR High Burnup 9×9 Lead Use Assemblies," *Proc. Intern. LWR Fuel Performance Meeting*, San Francisco, CA, 2007, American Nuclear Society, LaGrange Park, IL.

[17] Garzarolli, F., Cox, B., and Rudling, P., "Optimization of Zry-2 for High Burnups," *Zirconium in the Nuclear Industry; 16 International Symposium*, Chengdu, China, ASTM International, West Conshohocken, PA, 2010.

DISCUSSION

Question 1, M. Griffiths, AECL:—There were very significant density differences between the hydrides in the "shadowed" zones compared with non-"shadowed" zones. Were these hydrides present during service and if so then they are likely to affect the point defect mass transport. What is the relative density for the hydrides (no. of boundaries per unit length) in each case?

Author's Response:—In this paper, a wide range of hydrogen concentration is reported for channel sides with and without significant exposure to the control blade. For example, the hydrogen content on the non-shadow side ranged between 12 and 170 ppm. At the operating temperature of 561K, hydrides are expected above the solubility limit (~117 ppm, according to McMinn et al, ASTM STP 1354) especially on the sides affected by shadow corrosion. In Figure 19, a plot is shown comparing the estimated and measured channel bow. The bow measurements were conducted at room temperature, when most of the hydrogen is expected to be in the form of precipitated hydrides. The estimated channel bow is based on the measured hydrogen differential leading to volume and hence length differential; the estimate also includes contribution from fluence gradient driven bow. Figure 19 shows good linear correlation between measured and estimated bow, indicating that the basic premise of channel dimensional change due to volume change associated with hydride precipitation is valid. As shown in Figure 19, the best correlation between measured and estimated bow was obtained assuming linear increase of 0.25% per 1000 ppm of hydrogen. The estimation of channel bow is based on the differential in the average of the measured hydrogen concentrations on each side of the opposing channel sides and involved a number of other assumptions and inputs. These include the stoichiometry of the zirconium hydride, the density of the hydride and Zircaloy and isotropic volume expansion. The primary deduction from the linear correlation is that volume expansion due to hydride formation is a dominant factor in the shadow corrosion induced channel bow issue.

The number or area of interfaces between hydride and the alpha-zirconium is expected to be related to the amount of hydride present. The interaction of hydrogen with point defect mass transport is not a well-understood phenomenon and could potentially affect the growth of channels with a large amount of hydrides. However, potential contribution to channel bow (from differential growth of opposing channel sides) from this mechanism is not expected to be significant, since Figure 19 shows that shadow corrosion induced channel bow is dominated by the expansion due to hydride formation.

FAILURE MECHANISMS AND TRANSIENTS

Reprinted from JAI, Vol. 8, No. 2
doi:10.1520/JAI103156
Available online at www.astm.org/JAI

C. Duriez,[1] *S. Guilbert,*[1] *A. Stern,*[2] *C. Grandjean,*[1] *L. Bělovský,*[3] *and J. Desquines*[1]

Characterization of Oxygen Distribution in LOCA Situations

ABSTRACT: Oxygen distribution in the rod cladding tubes during a Loss of Coolant Accident (LOCA) situation is known to play a key role regarding the post-quench mechanical properties of fuel rods. Analytical solutions of the diffusion equations in the complex multilayer and multiphase systems describing the cladding material tube during high temperature oxidation are limited to stationary isothermal conditions. To address the problem of non-stationary transient LOCA situations, a numerical tool (named DIFFOX) has been developed. In the first part, the main assumptions and main features of the code are described. In parallel to the code development, an experimental program has been launched to provide a validation database as well as to input data for improvement of the code models. Zircaloy-4 cladding samples have been pre-oxidized at low temperature then vacuum annealed or steam oxidized at high temperature. Oxygen distribution profiles are investigated by Electron Probe Microanalysis. The ability of the code to describe the chemical reduction of the pre-oxide layer and oxygen diffusion into the metal during high temperature annealing is demonstrated. Regarding high temperature steam oxidation, the pre-oxide layers are observed to be either protective or not on a same given sample. While a good code to experimental data agreement is obtained in the first case, the growing of a high temperature oxide underneath the pre-oxide is not well reproduced by the code. The effect of hydrogen has also been investigated by performing small scale oxidation tests on 600 wppm hydrogen charged Zy-4 cladding. Samples have been

Manuscript received May 7, 2010; accepted for publication December 17, 2010; published online January 2011.
[1] IRSN/DPAM, BP3, Saint Paul-Lez-Durance 13115, France.
[2] Post-Doctorate, IRSN, BP3, Saint Paul-Lez-Durance 13115, France; currently at CEA/DEN-DANS/DMN/SEMI/LM2E, CEA/Saclay, Gif-Sur-Yvette 91191, France.
[3] ALIAS CZ, s.r.o., Bachova 1586/16, Praha 149 00, Czech Republic.

Cite as: Duriez, C., Guilbert, S., Stern, A., Grandjean, C., Bělovský, L. and Desquines, J., "Characterization of Oxygen Distribution in LOCA Situations," *J. ASTM Intl.*, Vol. 8, No. 2. doi:10.1520/JAI103156.

Copyright © 2011 by ASTM International, 100 Barr Harbor Drive, PO Box C700, West Conshohocken, PA 19428-2959.

long-term annealed for homogenization after oxidation. The main purpose of these experiments is to provide quantitative data on the modification of the α/α+β and α+β/β transus of the Zy4-O pseudo binary phase diagram induced by the presence of hydrogen. A variation of the transus locations deduced from these experiments is proposed.

KEYWORDS: LOCA, DIFFOX, oxygen diffusion, modeling, hydrogen, pre-oxide

Introduction

The French "Institut de Radioprotection et de Sûreté Nucléaire" (IRSN) launched in recent years a research program named Characterization and Investigation for Improved Calculation of LOCA Addressing the Determination and Evaluation of Safety (CYCLADES), aiming at improving the knowledge on fuel behavior during Loss of Coolant Accidents (LOCA). The IRSN's strategy is detailed in Ref [1. The CYCLADES program covers three main topics of interest for LOCA issues: Cladding mechanical behavior and failure conditions, axial fuel relocation, and the coolability of fuel rods after flow blockage. The present study addresses part of the research program on oxygen-induced cladding embrittlement, which mainly depends on oxygen distribution in the Zirconium β-phase [2–5]. The influence of oxygen content on cladding embrittlement is usually expressed using a single parameter: The Equivalent Cladding Reacted (ECR), which is directly related to the weight gain during the LOCA transient [3]. However the presence of the corrosion scale grown during normal operation was not taken into account in the original ECR criteria. This pre-existing oxide layer is potentially a source of oxygen for oxygen diffusion in the underlying metal. Actually, at elevated temperatures, partial or full dissolution of this pre-existing oxide layer is sometimes observed and its oxygen content moves inwards by diffusion. As a consequence of this dissolution process, significant oxygen embrittlement can be observed without any noticeable weight gain [6]. Furthermore, the hydrogen content as well as the cooling rate were recently demonstrated to play a key role in the oxygen distribution and consequently in cladding embrittlement [4,5,7,8]. It was thus decided to reach a better physical determination of the cladding embrittlement under LOCA conditions by relying on the oxygen distribution through the cladding wall rather than relying on the ECR parameter alone. The IRSN is developing the DIFFOX diffusion code in order to contribute to achieving this objective [9]. A similar approach is also adopted at the CEA [10].

The present paper focuses on the action plan established to obtain an accurate simulation of the oxygen distribution within the cladding thickness using the DIFFOX code in LOCA situations. This diffusion code will later be applied to the many configurations of interest for pressurized water reactor (PWR) LOCA safety issues. Three main subjects of interest are under investigation: The study of oxidation and oxide reduction kinetics at high temperatures, the study of hydrogen influence on oxygen distribution, and the study of oxygen

distribution under non-stationary cooling conditions. Only the two first topics are handled in this paper since the last one started being investigated too recently.

First, the paper describes the main assumptions for diffusion modeling in the DIFFOX code and associated numerical methods. Next, the test devices and experimental protocols supporting this study are presented. Then, experimental results relevant for oxidation and reduction kinetics are discussed and compared to open literature data. Particular attention is paid to oxygen concentration profiles obtained by Electron Probe Microanalysis (EPMA), which are compared to DIFFOX predicted distributions. Regarding the investigation on the influence of hydrogen on oxygen distribution, results obtained with 600 wppm hydrogen charged cladding samples are presented. The influence of hydrogen is mainly focused on measurements at thermodynamic equilibrium, which lead to new data on the Zy-4-O pseudo binary phase diagram for a hydrogen containing alloy.

The DIFFOX Diffusion Code

The development of the computer code DIFFOX started in early 2006 at the IRSN to calculate the Zircaloy oxidation in steam under LOCA conditions with the aim to predict the Zircaloy cladding embrittlement as a function of the oxygen and hydrogen contents (and distributions) in the cladding wall.

In view of a possible revision of the Emergency Core Cooling System acceptance criteria towards the use of the oxygen content in the "prior-β" phase as the leading parameter, it is important to be able to realistically calculate the transient oxygen profile in the metal layers. For that purpose, an advanced tool is necessary for the calculation of the oxygen diffusion in the different layers of an irradiated cladding under LOCA transient conditions. Such a tool should be able to reliably calculate

- the partial dissolution of thick corrosion layer(s) in the initial stage of the temperature transient (particularly below 1000°C),
- the more or less protective effect of the corrosion layer with respect to oxygen diffusion, and
- the influence of hydrogen absorbed during in-service operation on the oxygen solubility in the β phase.

The DIFFOX code issues partly from the PECLOX code by Hoffman et al. [11] and was subsequently modified at the IRSN in a private version for the simulation of two-sided oxidation by steam. It has then been largely reprogrammed and extended in the successive versions of the code under current development.

Main Features

The DIFFOX code considers a one-dimensional (1-D) system of reaction layers in finite cylindrical geometry among the physically possible combinations of the following layers.

$$ZrO_2,\ \alpha\text{–}Zr(\text{low } T \text{ or stabilized by O}),\ (\alpha+\beta)\text{–}Zr,\ \beta\text{–}Zr$$

The oxygen concentration profile is calculated in each reaction layer by solving the 1-D diffusion equation (second Fick law) in cylindrical coordinates

$$\frac{\partial C(r,t)}{\partial t} = \frac{1}{r} \cdot \frac{\partial}{\partial r}(r \cdot F_r) \tag{1}$$

where the left side is the oxygen accumulation and the right side is the space change of the diffusion flux F_r. The oxygen flux is assumed to be proportional to the oxygen gradient (first Fick law)

$$F_r = -D(T) \cdot \frac{\partial C(r,t)}{\partial r} \tag{2}$$

where:

$C(r,t)$ = oxygen concentration [kg/m^3],
$D(T)$ = oxygen diffusion coefficient as a function of temperature [m^2/s],
t = time [s], and
r = radius [m].

The movement of layer boundaries is derived from the mass balance of oxygen at the interface between two layers (Stefan equation)

$$\frac{\partial S}{\partial t} = \frac{F_+ - F_-}{2\pi S(C_+ - C_-)} \tag{3}$$

where:

S = interface position,
F_+ and F_- = oxygen fluxes, and
C_+ and C_- = oxygen concentrations respectively on each side of the interface.

The oxygen diffusion coefficients D are taken from literature for the single phase layers [12–16]. For the two-phase layer $(\alpha+\beta)$−Zr, an "equivalent" weighted D is deduced from a combination of values for the α and β phases.

The oxygen boundary concentrations were initially taken as the equilibrium values from the Zr-O and Zy-O phase diagrams found in the literature [12,17,18]. However, instantaneous equilibrium at boundaries appeared to be not applicable to transient conditions, particularly under cooling. A corrective approach has been introduced based on provisional assumptions on the limited increase or decrease of the oxygen boundary concentration during the temperature transient. This key question will be mainly addressed by specific experiments planned at the IRSN in late 2010 with controlled cooling prior to a final quench to freeze the oxygen concentration profile, which will be later determined by EPMA.

To predict the oxidation of hydrided specimens, oxygen boundary concentrations must also be known as a function of the hydrogen content. Only sparse data exist today for the oxygen solubility in β−Zr at 1200°C. Specific experiments have also been planned at the IRSN to provide the necessary

data required to allow a correct simulation of oxygen diffusion in hydrided material.

The above Eqs 1–3 are numerically solved using the implicit finite-difference method. A reaction layer is divided into N meshes with a variable width increasing from the boundaries towards the middle of the layer. The derivation of the finite-difference formulas leads to a system of linear equations with a tri-diagonal matrix. The numerical solution of the system of equations is obtained by Gauss elimination method.

Modeling of the Oxide in DIFFOX

The existing models for Zircaloy oxidation in LOCA conditions approximate the oxide as a homogeneous material in which the diffusion coefficient of oxygen only depends on temperature. This is acceptable for temperatures well above 1000°C where the oxide is in the tetragonal phase and the oxidation kinetic is parabolic. Such models, however, are no more sufficient in situations where the oxide has a more complicated structure, i.e., at temperatures below $\sim$ 1000°C or in case of a pre-existing oxide scale, such as a corrosion scale formed during reactor operation.

Although the monoclinic phase in ideal unstressed conditions is stable below 1200°C, the tetragonal phase is stabilized in the growing high temperature (HT) oxide through various mechanisms, especially near the oxide/metal interface. During the oxidation, the oxide scale is in a continuous transformation, including grain growth, phase transformation, porosity development, thickening. All these parameters influence the kinetics of the oxide growth.

There is a general agreement that during oxidation below $\sim$ 1000°C, the oxide is a mixture of monoclinic and tetragonal phases. It is agreed that the low temperature monoclinic phase dominates at low temperatures. The meta-stable tetragonal phase preferentially forms near the oxide/metal interface. The oxide layer, thus, can be virtually divided into several sub-layers.

In DIFFOX, the oxide model distinguishes up to three zones in the oxide layer, each with a distinct oxygen diffusion coefficient: Tetragonal sub-layer, bulk oxide, and pre-oxide (see Fig. 1). This allows to better simulate the effect of the pre-oxide as well as the oxide dissolution process.

This approach requires the knowledge of the oxygen diffusion coefficient in the different phases of oxide. The diffusion coefficients in the monoclinic ($m-Dx$) and tetragonal ($t-Dx$) phases were selected from the literature as a best estimate of the experimental data for a thermally grown oxide. Also required are the fractions of tetragonal alpha phase in both the bulk oxide (FTA) and the pre-oxide (FTAP) sub-layers. The $t-ZrO_2$ helps to simulate the cubic behavior of the kinetics below $\sim$ 1000°C, whereas the fractions FTA and FTAP allow the transition from the monoclinic to the tetragonal structure in the oxide as the temperature increases.

As experimental values of these functions were not found in the literature, they had to be determined empirically by fitting the package [$m-Dx$, $t-Dx$, $t-ZrO_2$, and FTAs] with the aim to obtain a good code-to-data agreement of the oxidation kinetics.

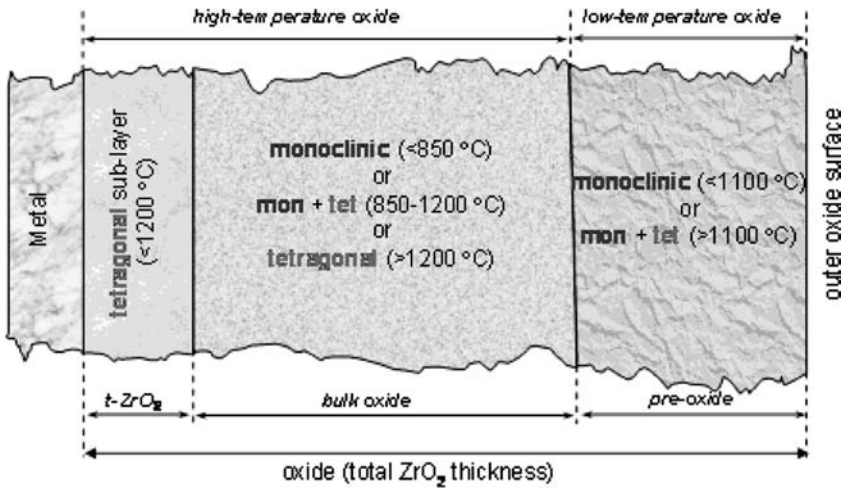


FIG. 1—*DIFFOX 1.2: Model of the oxide microstructure grown on Zircaloy cladding.*

Management of the Layer Systems (Sequences) and Possible Transitions Between Them

The earliest code version DIFFOX (one-sided oxidation only) was able to manage the basic layer sequences #1 to #4 only, including the transition between them

$$1 : \alpha\text{–Zr} + \text{ZrO}_2$$

$$2 : (\alpha + \beta)\text{–Zr} + \alpha\text{–Zr} + \text{ZrO}_2$$

$$3 : \beta\text{–Zr} + \alpha\text{–Zr} + \text{ZrO}_2$$

$$4 : \beta\text{–Zr} + (\alpha + \beta)\text{–Zr} + \alpha\text{–Zr} + \text{ZrO}_2$$

The implementation of the two-sided oxidation into the latest DIFFOX version increased the complexity of the code. The maximum number of simulated reaction layers within the cladding wall has increased up to seven

$$[\text{inner ZrO}_2 + \alpha\text{–Zr} + (\alpha + \beta)\text{–Zr} + \beta\text{–Zr} + (\alpha + \beta)\text{–Zr} + \alpha\text{–Zr} + \text{outer ZrO}_2]$$

The total number of simulated layer systems (sequences) exceeded 40 and the total number of the programmed transitions between the layer systems climbed over 100; most of them were tested. There is a considerable effort to cover all the possible layer sequences within DIFFOX that may physically form in a Zircaloy cladding. At present, some particular layer sequences still remain to be programmed.

Testing of the DIFFOX Code Capabilities

The early versions of the DIFFOX code were widely tested in the one-sided configuration in comparison with various experimental data found in the literature.

Under isothermal oxidation of as-received cladding, a reasonable agreement was obtained with Leistikow and Schanz's data [19] over the entire temperature range $\sim$ 650–1400°C for the growth of oxide and alpha layers thickness and weight gain. A fair agreement of O-profile prediction was obtained in comparison with the (few) available measurements.

Under transient oxidation, a reasonable agreement was obtained for most simple transients with heating and cooling through the α/β transus by modeling the $(\alpha+\beta)-$Zr and $\beta-$Zr layers' appearance and disappearance.

For a pre-oxidized cladding subsequently isothermally oxidized or heat treated under inert gas atmosphere in the 800–950°C temperature range, code predictions of the oxide thickness variation and oxygen concentration profile appeared in a fair agreement with partially available (proprietary) data. Oxygen diffusion from an initial corrosion layer in the underlying metal appears well predicted by the code.

The aim of testing the current DIFFOX version is to demonstrate the ability of the code to simulate both the two-sided oxidation and the oxidation of the inner cladding surface only. The test matrix is composed of a sub-set of all the possible layer sequences. It includes the ability of the code to treat both the as-received and the pre-oxidized cladding. All the reaction layers in the programmed layer sequences can appear or disappear according to the actual temperature, extent of the oxidation (consumption of the layer), or the availability of the oxygen flux at the cladding surfaces.

Experimental

Material and Equipments

The specimens used in this study were cut from low tin stress relieved annealed Zircaloy-4 industrial fuel cladding tubes provided by AREVA-NP. The composition of the alloy is given in Table 1. The outer diameter and wall thickness of the tubes are 9.5 mm and 570 μm, respectively. Open samples were used leading to two-sided oxidations.

For the low temperature pre-oxidation, 100 mm long cladding samples were pre-oxidized in a tubular resistive furnace in a pure oxygen flow at 500°C. For the HT oxidations, samples were oxidized in a vertical resistive furnace in a steam + argon flow and water-quenched by dropping into a water bath (Fig. 2).

TABLE 1—*Chemical composition of the Zy-4 batch used in this study.*

Sn (wt %)	Fe (wt %)	Cr (wt %)	O (wt %)	H (wt ppm)
1.30	0.21	0.10	0.12	10

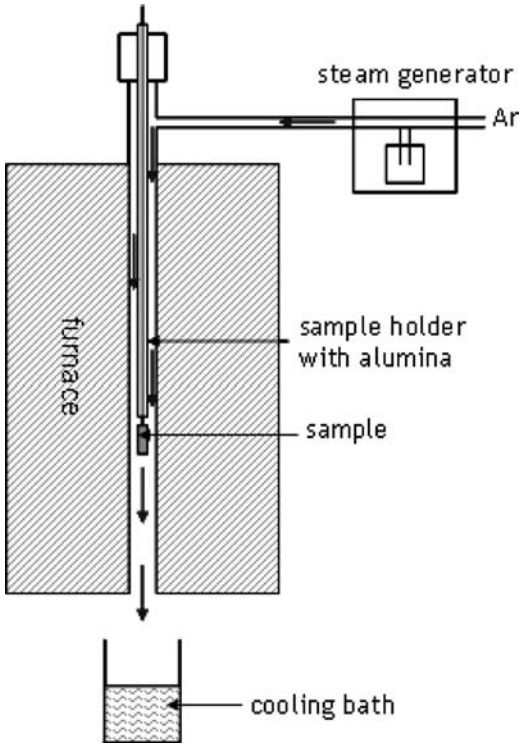


FIG. 2—*Vertical furnace used for the oxidation at high temperature under steam flow.*

The argon and steam flow rates were, respectively, $2\,\mathrm{NL}\cdot\mathrm{min}^{-1}$ and $100\,\mathrm{g}\cdot\mathrm{h}^{-1}$ (50 vol % Ar and 50 vol % steam).

To qualify the furnace and the oxidation protocol, results obtained in the laboratory at 900, 1000, 1100, and 1200°C on Zy-4 as-received cladding were compared to published data [8,20–23] (see Fig. 3). In this figure, the Cathcart–-Pawel (CP) correlation is reported for 1000, 1100, and 1200°C. At 900°C, the parabolic CP correlation is known to be no longer valid. Thus, a cubic law is fitted to the 900°C literature data. Our results are in good agreement with the published data, which confirms the relevance of the experimental protocol adopted for this study.

The weight and length of the samples were measured with an accuracy of 0.1 mg and 0.01 mm, respectively before and after oxidation or annealing.

After each step of the preparation protocol, metallographic cuts were inspected by optical microscopy (bright field and polarized light) and by scanning electron microscopy.

Radial oxygen concentration profiles and oxygen distribution maps were obtained by EPMA (CAMECA SX-100). Before the EPMA analysis, each sample was embedded in a conductive resin together with an as-received sample from the same Zy-4 batch. After mechanical polishing, a chemical etching with a fluohydric acid containing solution was carried out and samples were immediately

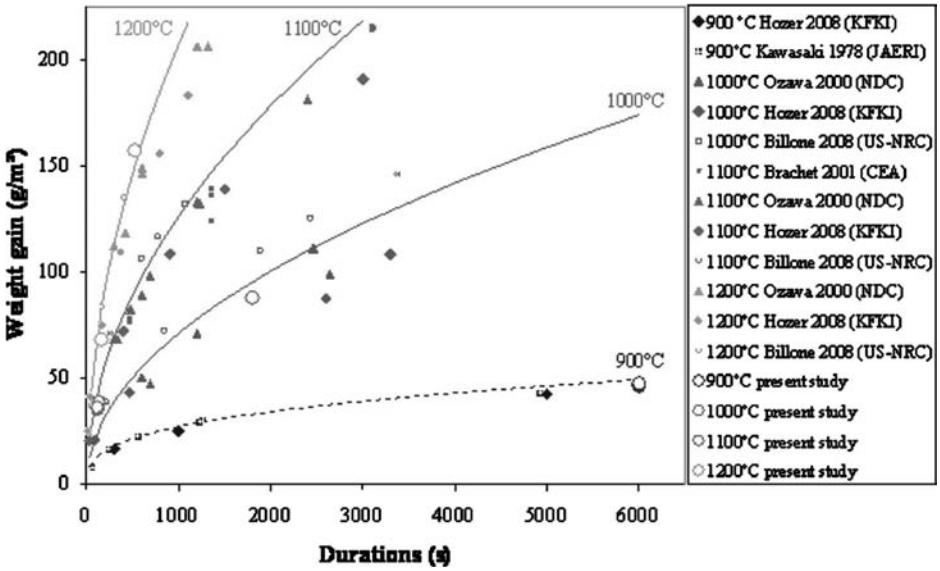


FIG. 3—*Weight gain as a function of heat treatment duration for steam oxidation of as-received samples from Refs 8, 13–16 and present results. Solid lines correspond to the CP correlation. The dotted line corresponds to a cubic law fitted to the experimental data.*

introduced inside the microprobe vacuum chamber. The oxygen $K\alpha$ line was measured with a W/Si multilayer synthetic crystal. Most of the profiles were performed along 200 μm long lines with a 1 μm stage displacement step. Maps were obtained from 100×200 or $100 \times 300\ \mu m^2$ surfaces with a stage displacement step of 1 μm.

Global hydrogen and oxygen contents were measured by the hot extraction technique (analyzer system JUWE ON/H-mat 286): The samples are melted in a graphite crucible with a carrier gas passing through. Hydrogen released from the sample is converted into H_2O and measured using a catharometric cell while oxygen converted to CO_2 by reaction with the graphite crucible is detected in an infrared absorption cell. Measurements are repeated at least three times on small pieces of few tens of milligrams for each sample.

Microhardness measurements were performed using a BUEHLER apparatus equipped with a Vickers diamond tip. A 100 g load was used. Four profiles were measured across a sample radius in the metal on each metallographic cut with 100 μm indentation step.

Steam Oxidation of Pre-Oxidized Versus Bare Samples

The DIFFOX code allows simulating the influence of a pre-existing oxide while distinguishing up to three zones within the oxide layer: A tetragonal sub-layer,

the bulk HT oxide, and, if present, the pre-existing low temperature oxide sublayer. The oxygen diffusion coefficients of the different zones are different depending on their monoclinic and tetragonal fractions. To validate the DIFFOX pre-oxide model and its ability to predict pre-oxide chemical reduction, two series of experiments were carried out on pre-oxidized samples; for the first series, samples were vacuum annealed at elevated temperature to study the separate effect of the dissolution of the pre-oxide layer; for the second series of tests, pre-oxidized samples were steam oxidized at high temperature. As-received samples were also steam oxidized in order to establish reference data on bare material. The temperature and duration (900°C, 6000 s) were chosen to better observe the elementary phenomena rather than to be representative of hypothetical LOCA conditions. The emphasis was placed on the reproducibility of the results, the tests being conducted using two to four different samples to repeat each experimental condition, and the analysis being performed at least on two metallographic cuts for each sample. Special attention was paid to the statistical analysis of measurements, specifically for oxide thickness determination. Mean values and standard deviation were calculated from 32 measurements (thickness measurements of the oxide and αZr(O) layers at eight different angular locations at both outer and inner surfaces on two different metallographic cuts).

Pre-Oxidation—Specimens were pre-oxidized in pure oxygen at 500°C for 10, 20, 30, 40, 50, and 60 days, leading to low temperature oxide layer mean thickness of 11.0 ± 1.7, 19.0 ± 1.3, 30.6 ± 2.8, 41.9 ± 2.4, 57.5 ± 1.9, and $68.8\pm3.5\,\mu$m, respectively. Pre-oxidized samples have a brown color, more or less uniform, except for the samples pre-oxidized for 10 days, which shows some regions having the black color characteristic of sub-stoichiometric zirconia. A high magnification examination of the oxide layer surface reveals, for a pre-oxide layer thickness of $30\,\mu$m and above, a network of regularly spaced cracks giving to the surface a snake skin aspect. On the optical micrographs, these cracks correspond to radially penetrating cracks nucleated at the outer surface of the samples. Such cracks have also been observed on Zy-4 fuel cladding tubes corroded in pressurized water reactors, but for thicker corrosion layers ($80–100\,\mu$m) [24]. Optical micrographs also reveal that the pre-oxidation layers are interspersed with many circumferential cracks periodically spaced in the radial direction, giving rise to a stratified structure (Fig. 4). The existence of a similar stratified microstructure has often been reported for in-reactor corrosion oxide grown on Zy-4 [24–26]. A typical radial spacing of about $2–3\,\mu$m between two strata is reported. Similarly, as for irradiated specimens, radially oriented veins are also observed in the micrographs. The veins' location usually corresponds to regions far from radially oriented cracks within the oxide. These features of circumferential and radial cracks and veins have strong similarities with PWR irradiated Zy-4 corrosion layers [24–26]. From this point of view, the pre-oxide layers of the present study are deemed representative of in-reactor corrosion. However, circumferentially oriented cracks are probably longer than for in-reactor corroded samples and with larger crack opening close to the metal/oxide interface, specifically for high pre-oxide thickness.

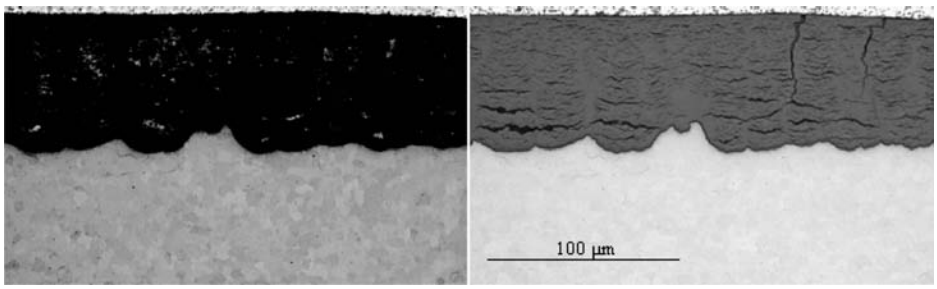


FIG. 4—*Optical micrographs of a 70 µm pre-oxide sample (left: In polarized light, right: In bright light).*

An examination of the optical micrographs in polarized light reveals an equiaxed grain structure in the metal. For all pre-oxidation durations, the metal is fully recrystallized, which is consistent with the recrystallizing kinetics provided by Bouffioux and Legras [27]. This is also confirmed by the Vickers microhardness values in the metal, which are lower than in the as-received cladding. Furthermore, the Vickers microhardness profiles are flat in the metal, indicating that there is no long-range (less than a few microns) diffusion of oxygen within the αZr layer during pre-oxidation. At last, pre-oxide layer thicknesses increase linearly with pre-oxidation duration and hydrogen content measurements show that the hydrogen pick-up increases with the pre-oxidation duration without exceeding 100 wppm for a 60 day pre-oxidation duration.

*High Temperature Steam Oxidation of Bare Samples (*900°C*, 6000 s)*—Post-test optical micrographs show a dense and uniform oxide layer (Fig. 5). The morphology of this compact oxide is typical of a pre-breakaway oxidation regime. The mean oxide layer thickness is $18.5 \pm 0.7\,\mu$m whereas the thickness of the αZr(O) layer revealed by the polishing is $34.5 \pm 1.0\,\mu$m. The hydrogen pick-up[4] during the steam oxidation is negligible (~ 5 wppm), which is also consistent with a pre-breakaway oxidation regime.

*High Temperature Vacuum Annealing of Pre-Oxidized Samples (*900°C*, 6000 s)*—The sample with an initial $10\,\mu$m pre-oxide layer has, after vacuum annealing, a metallic bronze color with small black islets (Fig. 6). On the metallographic cut, the remaining zirconia layer can barely be observed. The pre-oxide has been fully converted into metal, but memory of this formerly existing layer remains in the form of a stratified zone in the outer part of the αZr(O) region (Fig. 7). For 20 and $30\,\mu$m pre-oxide, part of the original zirconia layer remains at the outer surface after annealing, but similar with the $10\,\mu$m pre-oxide, a stratified metallic region appears beneath the oxide, showing that

[4]The hydrogen pick-up fractions are calculated as the ratio of the hydrogen incorporated in the metal to the hydrogen released by the $Zr + 2H_2O \rightarrow ZrO_2 + 2H_2$ reaction.

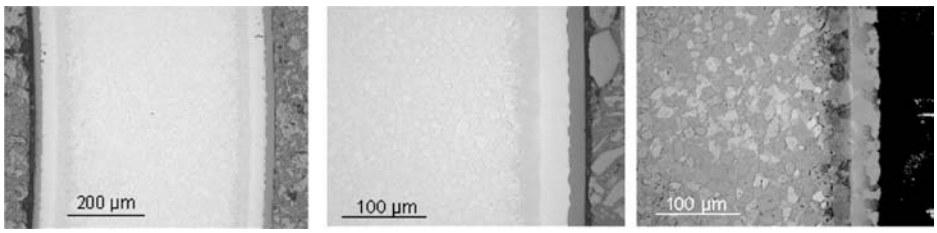


FIG. 5—*Optical micrographs of as-received samples subjected to steam oxidation at 900°C for 6000 s (in bright field for the two first micrographs and in polarized light for the last one).*

part of the oxide has been converted into metal. Macroscopically, the samples are bicolored, black, and bronze. For the 40 μm thick pre-oxide layer, the sample color is uniformly black after annealing but the same features as for the samples with 20–30 μm pre-oxide are observed on the optical micrographs. Finally, for the 60 and 70 μm pre-oxide, no conversion of the oxide into metal is evidenced, only partial reduction (in the chemical sense) is revealed by the black uniform color of the sample surface, typical of sub-stoichiometric zirconia. The thickness of the oxygen enriched αZr region formed by diffusion of oxygen from the pre-oxide is constant ($\sim 35\,\mu$m) whatever the pre-oxide initial thickness and equivalent to the αZr(O) thickness measured on bare samples directly subjected to HT steam oxidation. For a given alloy, a given temperature, and a given oxidation duration, the alpha layer thickness will depend only on the boundary

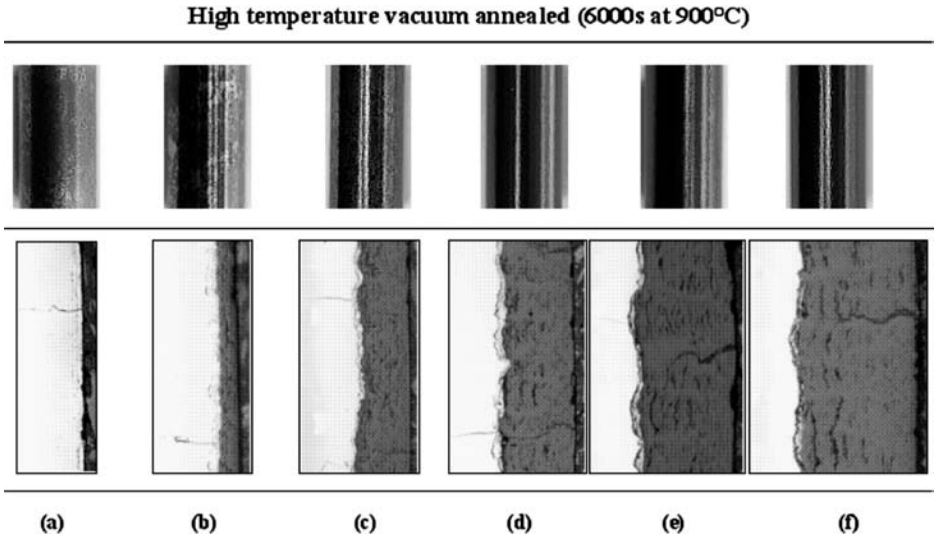


FIG. 6—*Photographs and optical micrographs of pre-oxidized samples after vacuum annealing at 900°C for 6000 s:* (a) *11.0 µm pre-oxide;* (b) *19.0 µm pre-oxide;* (c) *30.6 µm pre-oxide;* (d) *41.9 µm pre-oxide;* (e) *57.5 µm pre-oxide;* (f) *68.8 µm pre-oxide.*

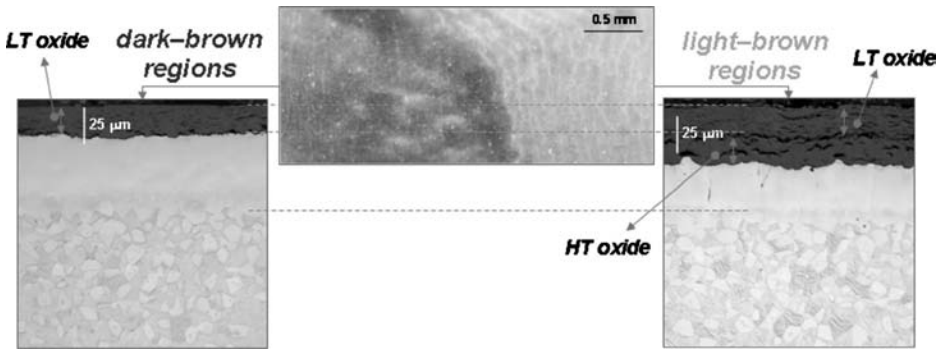


FIG. 7—*Surface photography and optical micrographs of 20 µm pre-oxidized and HT steam oxidized sample showing two kinds of regions: Left: Region with HT oxide. Right: Region without HT oxide.*

conditions, that is, the oxygen concentration in the metal at the $ZrO_2/\alpha Zr$ interface. Under vacuum conditions, the only oxygen source is the pre-oxide layer. As long as pre-oxide is present, the oxygen concentration in the metal at the metal/oxide interface is constant and given by the phase diagram.

*High Temperature Oxidation of Pre-Oxidized Samples (*900°C*, 6000 s)*—For comparison, samples having a 20 μm pre-oxide were oxidized in steam in the same experimental conditions. Samples are bicolored with coexistence of light brown and darker brown regions. An examination of their surface at high magnification reveals that the light brown regions are interspersed with a network of radial cracks whereas radial cracks are not visible in the darker regions (Fig. 7). Optical micrographs show that HT oxide has formed only in the regions where radial cracks are present. In the region with no HT oxide, thickness measurements indicate that the thickness of the pre-oxide has not decreased. In the region where a HT oxide has grown beneath the pre-oxide, the HT oxide thickness is about 20–25 μm, which is slightly higher than the HT oxide thickness formed by oxidation of bare samples in the same conditions. Where the HT oxide forms, the thickness of the αZr(O) layer is approximately uniform and lower compared to the regions without HT oxide. This is due to the inwards motion of the oxide-metal interface, which reduces the extent of the αZr(O) diffusion layer.

DIFFOX Validation—The DIFFOX code was evaluated in three different configurations: HT steam oxidation of as-received samples, vacuum annealing of 20 μm pre-oxidized samples, and HT steam oxidation of 20 μm pre-oxidized samples. Radial quantitative oxygen concentration profiles were measured by EPMA for each of these configurations and compared to calculated diffusion profiles.

Figure 8(*a*) shows that the O-profile is well predicted for as-received samples after steam oxidation. EPMA experimental profiles show that the oxygen

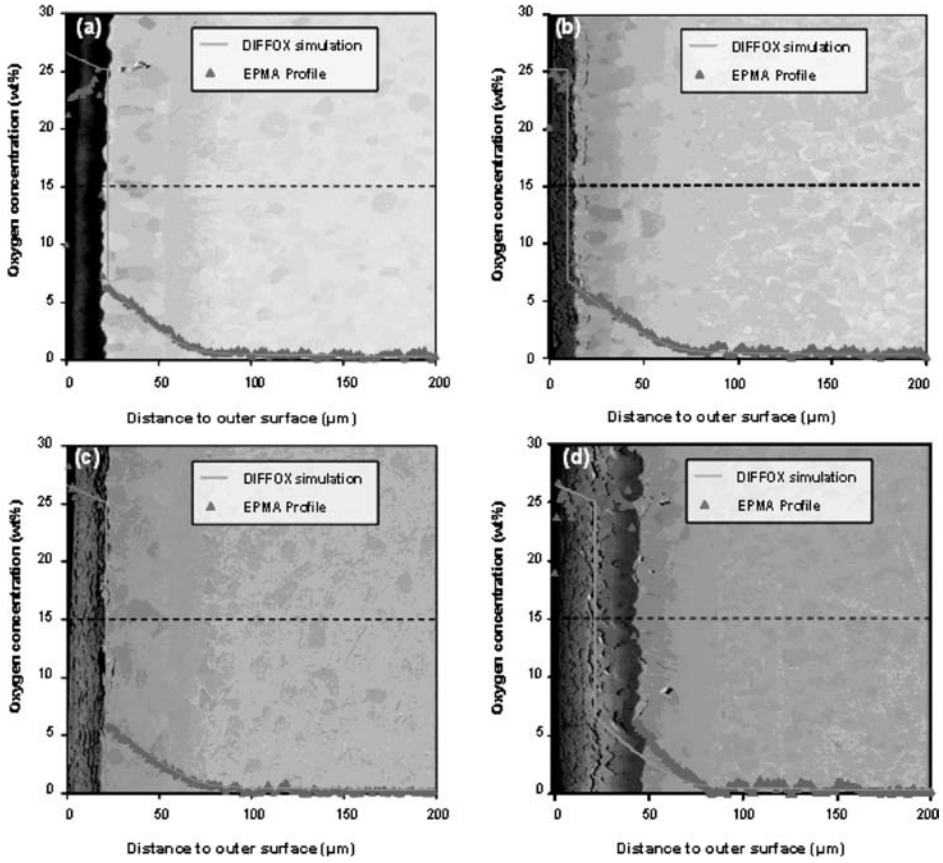


FIG. 8—*Code-to-data comparisons for* (a) *as-received sample after steam oxidation;* (b) *20 μm pre-oxidized sample after vacuum annealing; and [*(c) *and* (d)*] 20 μm pre-oxidized sample after steam oxidation:* (c) *Region without HT oxide;* (d) *region with HT oxide.*

enriched αZr region is ~ 70 μm thick, in good agreement with DIFFOX calculations. It is worthwhile noticing that on optical micrographs, the bright region corresponding to the oxygen enriched layer was only about 35 μm thick. It means that the polishing process reveals only the part of the α layer where the oxygen concentration exceeds a given threshold, estimated to be about 2 wt %.

Figure 8(*b*) shows the result for a 20 μm pre-oxide sample after vacuum annealing. A good code-to-data agreement is observed for the radial extension of the αZr(O) region and the oxide dissolution is well predicted (DIFFOX remaining pre-oxide thickness 10 μm versus 11.3±1.9 μm for experimental measurement).

Figure 8(*c*), 8(*d*) present the O-profile measured on pre-oxidized samples after steam oxidation in the region where the HT oxide has grown and in the region where the HT oxide was not formed, respectively. Where the pre-oxide is

not protective, the αZr(O) thickness is over-predicted and the growth of HT ZrO_2 is not predicted by DIFFOX. An explanation for the unprotectiveness of the pre-oxide layer is the strong difference in thermal expansion between the oxide and the metal, which may induce crack spreading and opening during the oxidation, particularly for thick pre-oxide layers. These phenomena would favor the percolation of steam, thus resulting in high weight gain and is not modeled in the current version of DIFFOX.

Effect of Hydrogen on the Oxygen Distribution After a LOCA

Hydrogen absorbed in Zr-based alloys during the in-reactor service can influence the oxygen distribution in the cladding after a LOCA transient because hydrogen is known to shift the $\beta/\alpha+\beta$ and $\alpha+\beta/\alpha$ transus of the Zr-O phase diagram towards low temperatures [4,5,28–30] (see Fig. 9). It also means that it increases the oxygen solubility in the βZr phase. However, experiments addressing this effect are scarce, specifically for temperatures above 1000°C. To take into account this hydrogen influence on the Zy4-O phase diagram in the DIFFOX code, it was deemed necessary to obtain complementary quantitative data relevant to this problem.

For that purpose, low tin Zircaloy-4 fuel cladding tubes pre-hydrided to ~ 600 ppm were pre-homogenized and detextured by short heating in the β domain, then oxidized at high temperature and long-term annealed under vacuum to achieve oxide dissolution and oxygen concentration homogenization to reach

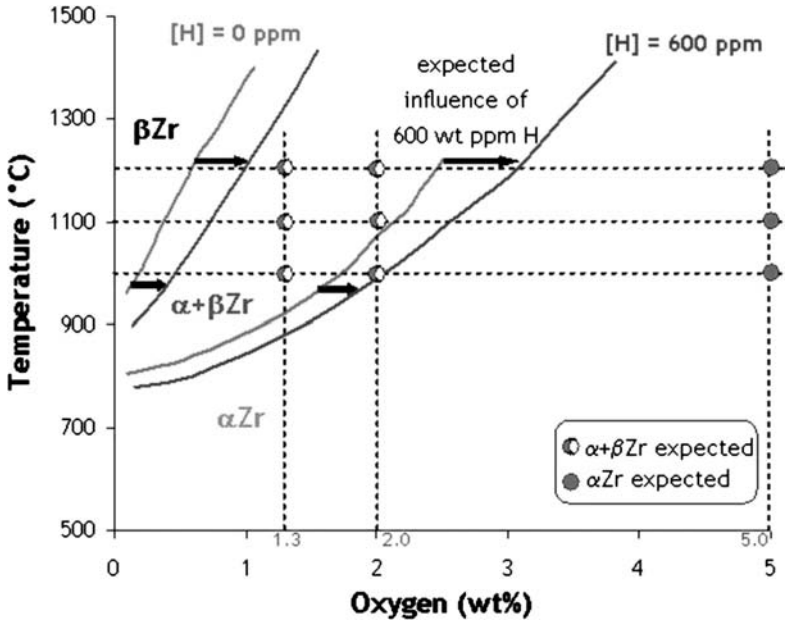


FIG. 9—*Sketch of the expected influence of hydrogen on the β/(α+β) and (α+β)/α transus of the Zy4-O phase diagram.*

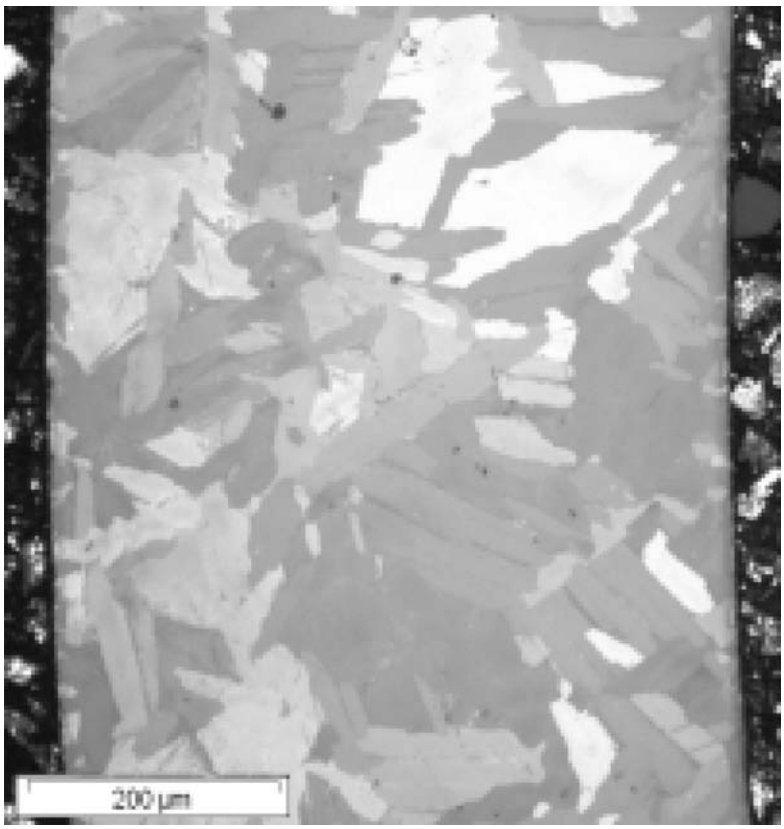


FIG. 10—*Sample #26 pre-hydrided at 600 wppm and loaded with 5.60 wt % oxygen. BSE image and oxygen profile measured by EPMA and calculated diffusion profile. Dotted lines indicate where the α/(α+β) and the (α+β)/β transus are measured on the experimental profile.*

thermodynamical equilibrium. Oxygen uptake was adjusted to fall either in the $\alpha + \beta$ or in the α domains of the Zy4-O phase diagram after homogenization [18,31]. Oxygen distributions were investigated by EPMA before and after the long-term homogenization. Before homogenization, assuming local thermodynamical equilibrium, oxygen profiles in the radial direction give access to the $\beta/\alpha + \beta$ and $\alpha + \beta/\alpha$ transus at the considered oxidation temperature; these limits are derived by measuring on the profile the oxygen concentrations at the interface between the α layer and the prior-β region, in the β side and in the α side, respectively (see Fig. 10). After homogenization, for bi-phased samples, the oxygen concentration measured in prior-β regions saturated with oxygen gives the oxygen solubility limit in the β-phase at the annealing temperature, that is, the $\beta/\alpha + \beta$ transus, while the oxygen concentration measured in α regions gives the $\alpha + \beta/\alpha$ transus. For mono-phased samples, an attempt to determine the α to β phase transformation temperature by calorimetry has been made. These experiments, not fully completed, are not discussed here.

The sample preparation protocol used is a four step process

(1) *Hydrogen loading* is performed on 50 cm long cladding segments by the electrolytic process at Electricité de France (EDF)-Les Renardières [32]. A 600 wppm concentration is targeted, corresponding to a typical Zircaloy-4 end-of-life hydrogen content. The total loading duration is 160 h (at room temperature), followed by 24 h annealing at 430°C. Tubes are cut into $\sim$ 16 cm long segments and samples for hydrogen content measurements (by hot extraction) are taken at each end, thus at four different locations of the 50 cm tubes. Values in the range of 574–640 wppm were obtained.

(2) *Pre-homogenization in the β* domain: Tubes are cut into 2 cm long samples, sealed under vacuum in quartz vials, heat-treated at 1050°C (thus in the βZr domain) for 5 min, and cooled down in the furnace by turning it off for full homogenization of the H concentration and isotropic texture. For each 2 cm segment, a small ring is cut after the β-treatment for H and O contents determination, both by hot extraction. Hydrogen and oxygen contents are thus determined individually for each sample to check the tightness of the vials. Metallographic examinations are also performed on a few samples and a typical microstructure obtained after the β heat treatment is shown in Fig. 11.

(3) *HT oxidation in steam:* For oxygen loading, two-sided oxidations are performed in the vertical furnace in flowing steam, at 1000, 1100, and 1200°C. The oxidation duration is adjusted to reach a given weight gain. Three different values of the weight gain were initially targeted corresponding to 1.3, 2, and 5 wt % mean oxygen content and chosen to fall after long-term annealing either within the $\alpha + \beta$ domain (1.3 and

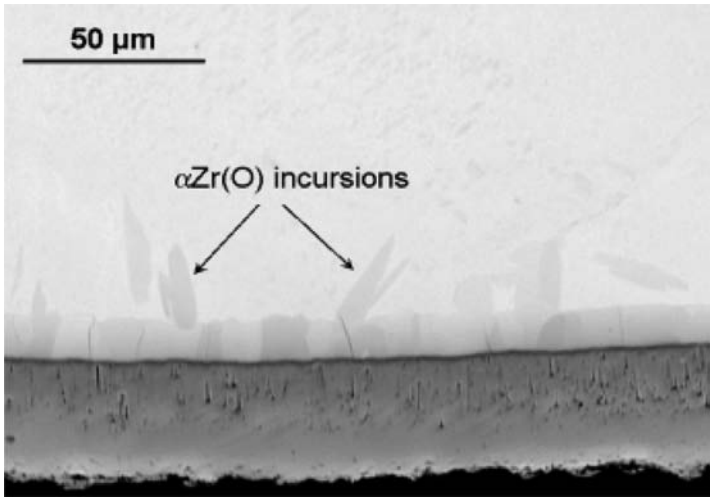


FIG. 11—*Polarized light optical micrograph of a pre-hydrided (600 wppm) Zy-4 sample after the pre-homogenization step in the β domain (5 min at 1050°C).*

2 wt%) or within the α domain (5 wt%) (cf. Fig. 9). Here, the expected effect of hydrogen on the location of the phase boundaries is taken into account. The CP correlation for Zy-4 HT steam oxidation was used for calculation of the oxidation times but it appeared that faster kinetics were observed with pre-hydrided samples, maybe because the electrolytic hydrogen loading induces a strong degradation of the surface state. Oxidation durations were thus adjusted to also account for this phenomenon. Finally, O-contents between 1.1 and 8 wt% have been obtained (see Table 2). Samples are water-quenched after HT oxidation. Post-quench hydrogen content is again measured for each sample by hot extraction. Hot extraction is here not effective for oxygen because the temperature of the hot extraction apparatus is below the melting point of zirconia. The microstructure of the samples is investigated by metallography.

(4) *HT homogenization*: Samples are individually sealed under vacuum in quartz vials and heat treated in the same vertical furnace, at 1000, 1100, or 1200°C. Annealing durations are 10 h at 1000°C and 3 h at 1100 and 1200°C (see Table 2). They were determined from previous experiments at the CEA [31]. When a bi-phased sample is expected, the vial is dropped into water and immediately broken to achieve fast quenching of the sample. For α mono-phase samples, cooling is performed by simply turning off the furnace. Hydrogen content is also systematically measured after the annealing. For oxygen loads above ~ 1.5 wt%, samples are extremely brittle after annealing, and it is thus difficult to avoid any loss of small fragments, specifically for quenched samples. Weight gain measurements may then be not consistent. Fortunately, hot extraction is here applicable for oxygen mean content determination because the oxide is fully reduced (in the chemical sense) after annealing. EPMA is used to check the homogeneity of the oxygen distribution and for quantitative determination of its concentration within each phase.

Results

The main results regarding the H and O global contents evolution through step 2 to 4 of the elaboration process are summarized on Table 2. The hydrogen content after the pre-homogenization at 1050°C annealing varies from sample to sample, which may be explained by the axial heterogeneity of the hydrogen distribution along the initial 50 cm long segment. Values are in the 542–787 wt ppm range, to be compared to the measurements performed by EDF at each end of the 16 cm long segments, which were in the 574–645 wt ppm range. The measurements are on 2 cm long segments, thus showing a higher scattering; however, they indicate that there is probably no significant variation of the hydrogen content during the 5 min vacuum annealing at 1050°C. Regarding oxygen, hot extraction data are here in good agreement with the weight gain results, showing that the uptake during this homogenization step is significant, generally on the order of 800–1000 wt ppm and up to 1500 wt ppm.

TABLE 2—*Oxygen and hydrogen global contents measured after pre-homogenization in the β-domain after steam oxidation and after homogenization.*

	After Step 2 (Annealing 5 min at 1050°C)			After Step 3 (HT Steam Oxidation)				After Step 4 (HT Homogenization)				
Sample Number	O (wt %) [a]	O (wt %) [b]	H (wppm)[b]	Toxid. (°C)	t (s)	O (wt %) [c]	H (wppm)[b]	T (°C), t (h)	O (wt %) [b]	H (wppm)[b]	Cooling[d]	Mono or Bi-Phased
9	0.198	0.217±0.031	772±38.9	1000	104	3.32	746±17.5	1200, 3	3.92±0.67	808±12.7	Q	αZr
11	0.207	0.236±0.152	696±15.7	1000	50	1.65	670±7.8	1200, 3	2.28±0.29	703±21.1	Q	$\alpha+\beta$
12	0.193	0.180±0.022	626±6.7	1000	50	3.10	649±5.1	1200, 3	3.82±0.28	621±14.8	Q	αZr
13	0.203	0.205±0.055	620±7.2	1000	40	2.90	626±15.9	1200, 3	3.80±0.01	607±30.4	Q	$\alpha+\beta$
14	0.198	0.222±0.041	631±17.6	1000	30	1.62	637±3.6	1100, 3	1.79±0.11	635±4.0	Q	$\alpha+\beta$
15	0.174	0.316±0.070	621±12.0	1000	30	1.78	623±2.6	1000, 10	1.54±0.29	720±29.5	Q	$\alpha+\beta$
16	0.213	0.281±0.002	609±7.5	1000	30	1.13	621±5.3	1000, 10	1.03±0.13	633±15.6	Q	$\alpha+\beta$
17	0.270	0.286±0.092	712±19.9	1100	40	3.92	684±3.5	1200, 3	4.32±0.34	683±57.4	N	αZr
18	0.274	0.233±0.03	658±16.3	1100	30	3.13	644±3.5	1100, 3	2.89±0.23	685±23.7	Q	αZr
19	0.274	0.232±0.034	641±3.2	1100	30	2.81	611±4.9	1200, 3	2.35±0.14	613±20.5	Q	$\alpha+\beta$
20	0.234	0.223±0.002	641±12.8	1100	30	2.46	623±4.5	1000, 10	···	903±21.1	Q	$\alpha+\beta$
21	0.229	0.199±0.037	639±7.2	1100	30	2.51	517±5.7	1000, 10	2.18±0.08	631±17.2	N	αZr
22	0.238	0.132±0.051	654±11.1	1100	30	2.52	631±8.1	1100, 3	2.39±0.22	675±10.7	Q	$\alpha+\beta$
23	0.218	0.240±0.119	643±15.2	1100	30	3.15	628±8.2	1100, 3	2.52±0.08	651±37.8	N	αZr
24	0.228	0.186±0.010	787±14.8	1200	100	6.81	737±17.2	1200, 3	4.68±0.30	717±29.4	N	αZr
25	0.229	0.172±0.003	661±15.9	1200	100	7.99	617±8.0	1200, 3	5.66±0.66	729±6.4	N	αZr
26	0.120	0.242±0.019	599±0.6	1200	60	5.60	···	1100, 3	3.26±0.12	603±21.1	N	αZr
27	0.209	0.243±0.088	570±1.4	1200	50	6.22	620±29.2	1100, 3	4.79±0.19	829±57.2	N	αZr
28	0.199	0.197±0.012	573±11.0	1200	40	6.24	645±6.1	1000, 10	4.45±0.31	825±113	N	αZr
29	0.192	0.144±0.001	562±4.0	1200	40	5.65	549±6.6	1000, 10	3.96±0.28	605±13.0	N	αZr
30	0.209	0.230±0.083	542±10.4	1200	40	5.89	523±6.5	1000, 10	4.19±0.10	673±48.3	N	αZr

[a]From weight gain, including the initial 0.14 wt % of the Zy-4 batch.
[b]Hot extraction. Uncertainties are the standard deviation over the measurements.
[c]From weight gain, including the oxygen already present after the β-treatment.
[d]Q = quenched, N = cooled into the furnace by turning it off.

After the HT steam oxidation, the hot extraction results show no significant H pick-up. Specifically, it means that the oxidation conditions are well controlled with a high enough steam flow rate to avoid local H_2O starvation and that no breakaway oxidation regime is encountered. This is confirmed by metallographs where a compact and adherent oxide layer is observed (see Fig. 12). It is worthwhile noticing on this figure that only the internal part of the oxide shows the typical columnar microstructure expected for zirconia scales grown on zirconium alloys by HT oxidation. The external part of the oxide layer has likely a fine grains structure and its surface is not smooth. It is believed that the degradation of the surface state of the cladding induced by the electrolytic hydrogen loading explains these features. Incidentally, a fine grains structure is in accordance with the fast oxidation kinetics observed. Another remarkable feature evidenced on Fig. 12 is the alpha incursions seen as elongated dark grains penetrating in the β domain. This three-dimensional effect, likely due to accelerated oxygen diffusion at grain boundaries [20], is not taken into account by the 1-D DIFFOX code and EPMA oxygen concentration profiles are thus acquired away from these incursions.

After the long-term annealing, strong dispersion of the H content measurements for a given sample is sometimes observed, as revealed by the rather high standard deviation values. Few samples seem to be affected by significant hydrogen pick-up during annealing. There is no obvious reason for such pick-up, and the explanation may be the following: Because of strong embrittlement, α grains are lost during sampling for hydrogen measurements, thus enhancing

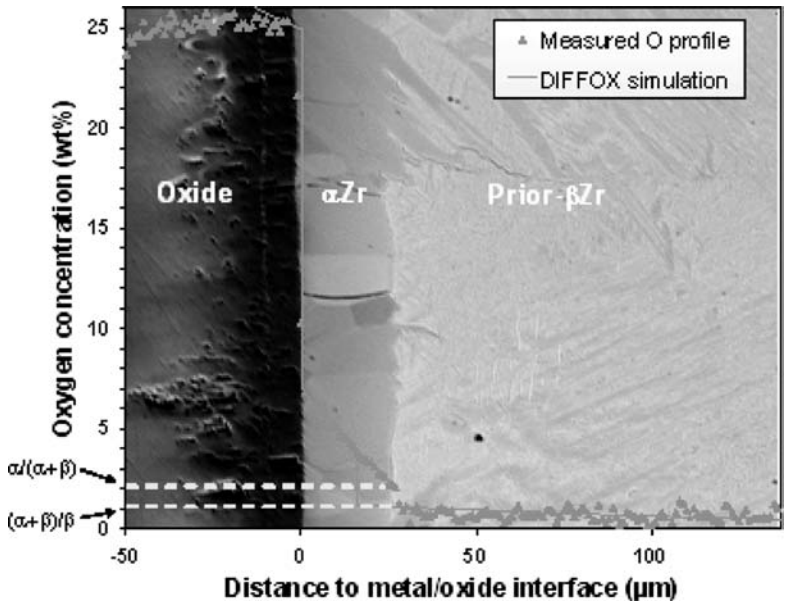


FIG. 12—*Backscattered electrons image of sample #13 oxidized for 40 s in steam at 1000°C.*

the β fraction, known to be strongly enriched with hydrogen (hydrogen partitioning [5]). Concerning the oxygen load, the hot extraction technique gives values rather consistent with the values determined by weight gain before the homogenization process. It means that there is no significant variation of the oxygen load during the long-term vacuum annealing. As the uncertainties are sometimes rather high for oxygen with the hot extraction method, it is preferable to retain the weight gain data as the reference value for the oxygen load.

EPMA Results

An example of an EPMA oxygen profile obtained after oxidation at 1200°C and quenching is given on Fig. 10. The profile is superimposed to a back-scattered electron (BSE) image of the region where it has been acquired and is compared to the oxygen diffusion profile calculated with the DIFFOX code. Underprediction of the αZr(O) layer thickness by the code is likely related to the hydrogen influence on oxygen solubility in the α and β phases, possibly also on the diffusion coefficients, still to be improved in DIFFOX modeling. The dotted lines in Fig. 10 show how experimental oxygen concentration profiles can be used to determine the $\beta/\alpha+\beta$ and $\alpha+\beta/\alpha$ transus, which are given by the oxygen concentrations close to the α/β interface in the β side and in the α side, respectively. It has to be pointed out that uncertainty associated to this method is rather large because the measurement has to be done close to the α/β interface; thus, it can be affected by the instrument's lateral resolution and averaging over a given area cannot be used. Table 3 gives the values determined in this approach. Each value is an average of values measured for all samples oxidized at a given temperature. Better accuracy is obtained when analyzing the homogenized bi-phased samples and measuring the oxygen concentration in O-saturated β regions and in equilibrated α regions. Samples 15 and 19 could not be used for metallography after homogenization because they were too brittle. Finally, six homogenized samples were investigated by EPMA, two for each annealing temperature. Oxygen, iron, and chromium maps as well as oxygen radial profiles were acquired. An example of results is presented in Fig. 13. Maps and profiles are used to check the homogeneity of the α and prior-β regions identified on the BSE images. Then, for each region, oxygen concentrations are accurately determined by point analysis. The electron beam is defocused to be less sensitive to short range fluctuations and five to 10 measurement points per phase, randomly distributed on the metallographic cut, are acquired and

TABLE 3—*Mean values of oxygen concentrations measured at the α/β boundary on EPMA oxygen radial profiles on the α side and on the β side.*

T (°C)	O in α (wt %)	O in β (wt %)
1000	2.16	0.44
1100	2.33	0.76
1200	3.27	1.02

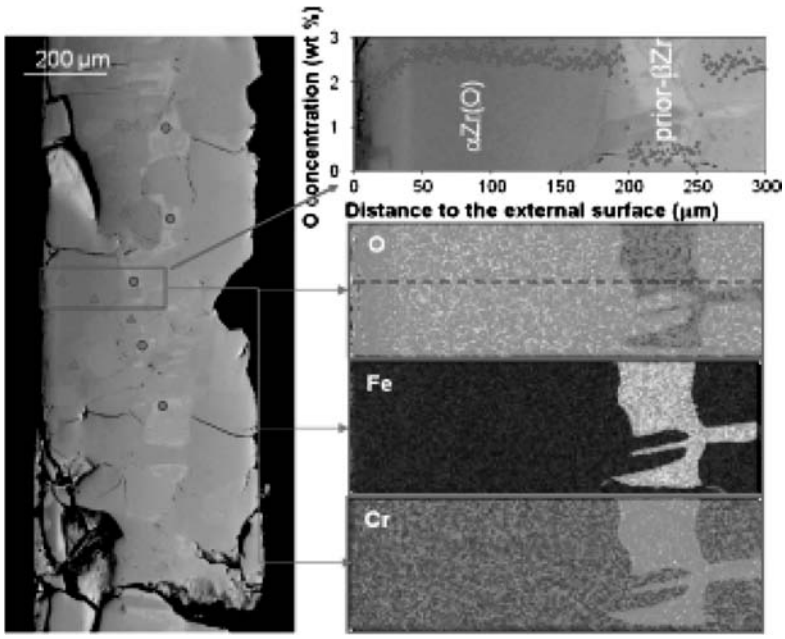


FIG. 13—*Sample #20 loaded with 2.46 wt % oxygen and homogenized at 1000°C. BSE image and oxygen, iron, and chromium EPMA maps. The line scanned for the oxygen concentration profile superimposed on the high magnification BSE image is indicated by the dotted line on the oxygen map. Locations of EPMA point analysis for quantitative determination of the oxygen content of the α and prior-β regions are indicated by triangles and circles, respectively.*

averaged. Edges affected by polishing problems are avoided. Results are given in Table 4 for each bi-phased sample investigated.

The concentration limit data points obtained in this work before and after the long-term homogenization for the $\beta/\alpha+\beta$ and $\alpha+\beta/\alpha$ transus are plotted on Fig. 14, which represents the Zy-4-rich portion of the Zy-4-O pseudo binary

TABLE 4—*Oxygen concentrations measured by EPMA on bi-phased homogenized samples. Each value is an average of 5 to 10 measurement points. Standard deviations are given.*

Sample Number	Annealing Temperature (K)	O in α (wt %)	O in β (wt %)
11	1200	2.41±0.14	0.9±0.24
13	1200	2.43±0.18	0.81±0.58
14	1100	2.11±0.20	1.01±0.10
16	1000	1.76±0.09	0.4±0.05
20	1000	2.46±0.17	0.52±0.08
22	1100	2.53±0.14	0.6±0.17

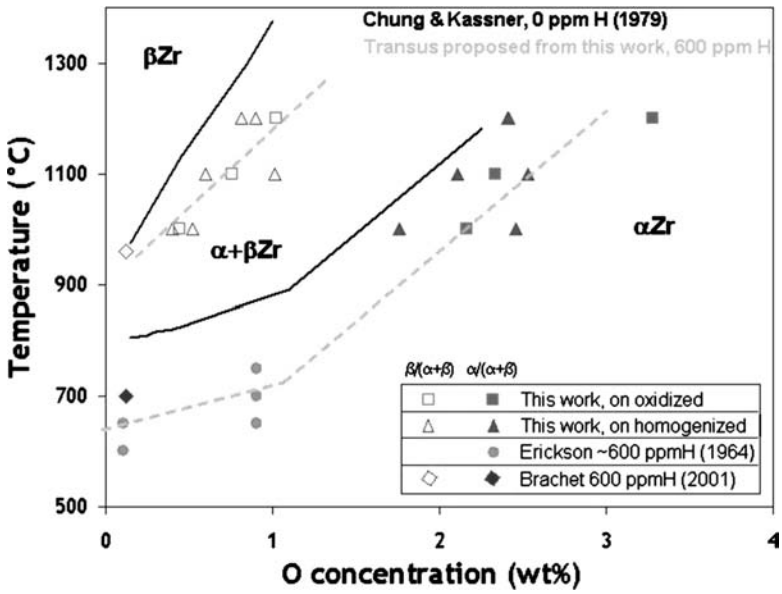


FIG. 14—*Zy-4-rich portion of the Zy-4-O pseudo binary phase diagram. Dotted lines are the β/α+β and the α+β/α transus proposed from this work for 600 wppm hydrogen loaded Zircaloy-4.*

phase diagram. The data plotted for non-homogenized cladding are average values over six samples oxidized at the same given temperature, while for homogenized samples, each individual value is plotted. Comparison is made with the Chung and Kassner limits for non-hydrided Zircaloy-4 [18]. Literature data obtained at low temperatures for the $\alpha + \beta/\alpha$ limit with ~ 600 wt ppm hydrogen loaded Zircaloy-4 are also plotted. The present study confirms in the investigated temperature range that the presence of hydrogen shifts the transus towards lower temperatures. The dotted lines show the $\beta/\alpha + \beta$ and $\alpha + \beta/\alpha$ transus proposed from this study. The $\beta/\alpha + \beta$ transus is obtained by linear regression on the values measured on homogenized bi-phased samples. For the $\alpha + \beta/\alpha$ limit, the dispersion of the data points is high, thus empirical fitting has been performed.

Conclusions

In the context of the LOCA safety criteria, the French IRSN is developing its own expertise regarding the characterization of cladding mechanical properties after a hypothetical LOCA scenario. More specifically, the oxygen distribution within the cladding wall and specially the oxygen concentration in the β phase are being investigated, as it plays a key role in the post-quench residual ductility of the cladding material. An analytical tool called DIFFOX has been developed to address the problem of the oxygen inward diffusion during a LOCA transient and is described in this paper. Moreover, an experimental program has been

launched at the IRSN to provide data that are necessary for further validation of the code.

Results obtained with low temperature pre-oxidized Zircaloy-4 having various pre-oxide thicknesses have been discussed. For vacuum annealing of these pre-oxidized samples, the ability of the code to predict a reduction of the pre-oxide layer and oxygen inward diffusion is demonstrated. For HT steam oxidation, a good code to experimental data agreement is obtained when the pre-oxide remains fully protective. However, when a HT oxide layer grows under the pre-oxide, the code fails to reproduce the experimentally obtained EPMA oxygen -profiles. An assumption is proposed to explain this phenomenon and improvement will be needed to better describe such cases, if it is confirmed that non-protectiveness of corrosion scales may correspond to real reactor situations.

Experiments have been also conducted with 600 ppm pre-hydrided Zircaloy-4 cladding to provide experimental oxygen diffusion profiles on hydrogen containing material. The objective was also to improve the knowledge regarding the effect of hydrogen on the $\alpha/\alpha+\beta$ and $\alpha+\beta/\beta$ transus of the Zy4-O pseudo binary phase diagram. Although the DIFFOX code in its latest version already takes into account the hydrogen effect (on the basis of literature data), the present study has demonstrated that improvements can be made. From new experimental data presented in this study, the position of the transus is proposed in this paper and will be implemented in the code and tested.

For the future, small scale tests with pre-oxidized and pre-hydrided cladding will be pursued to extend the IRSN database. Furthermore, experiments with controlled cooling rates before quenching are planned, aiming at providing "non-equilibrium" data on the oxygen concentrations at the α/β boundaries as well as to extend the DIFFOX comparison database to oxygen profiles representative of transient situations.

Acknowledgments

This work was conducted in the IRSN laboratory and Doris Drouan, Gaelle Montigny, and Anne-Lise Imbert took an important part in the investigations. The writers thank them sincerely. The writers are also grateful to EDF for his scientific and financial support.

References

[1] Barré, F., Grandjean, C., Petit, M., and Arreghini, F., "Fuel Behavior Under LOCA and RIA and Its Implication on the Current Safety Criteria," *Eurosafe Meeting*, Brussels, Belgium, 2009, European TSO Network.

[2] Sawatsky, A., "A Proposed Criterion for the Oxygen Embrittlement of Zircaloy-4 Fuel Cladding," *Zirconium in the Nuclear Industry: 4th International Symposium, ASTM STP 681*, J. H. Schemel and T. P. Papazoglou, Eds., 1979, ASTM International, West Conshohocken, PA.

[3] Chung, H. M., Garde, A. M., and Kassner, T. F., "Mechanical Properties of Zircaloy Containing Oxygen," *Report No*. ANL-77–10, Argonne National Laboratory, Argonne, IL, 1976.

[4] Brachet, J. C., Portier, L., Forgeron, T., Hivroz, J., Hamon, D., Guilbert, T., Bredel, T., Yvon, P., Mardon, J. P., and Jacques, P., "Influence of Hydrogen Content on the α/β Phase Transformation and on the Thermal-Mechanical Behavior of Zy-4, M4 and M5 Alloys During the First Phase of LOCA Transient," *Zirconium in the Nuclear Industry: 13th International Symposium, ASTM STP 1423*, Annecy, France, 2001, ASTM International, West Conshohocken, PA.

[5] Brachet, J. C., Vandenberghe-Maillot, V., Portier, L., Gilbon, D., Lesbros, A., Waeckel, N., and Mardon, J.-P., "Hydrogen Content, Preoxidation, and Cooling Scenario Effects on Post-Quench Microstructure and Mechanical Properties of Zircaloy-4 and M5 Alloys in LOCA Conditions," *Zirconium in Nuclear Industry: 15th International Symposium, ASTM STP 1505*, Sunriver, OR, 2008, ASTM International, West Conshohocken, PA.

[6] Vrtilkova, V., "Review of Recent Work at UJP PRAHA on the LOCA Embrittlement Criterion," *Sixth Plenary Meeting of the OECD/CSNI/SEGFSM*, Paris, France, 2005, OECD, Paris, France.

[7] Waeckel, N., "Fuel Safety Research at EDF," *FSRM Meeting*, Tokai, Japan, 2005, JAEA, Tokai, Japan.

[8] Billone, M., Yan, Y., Burtseva, T., and Daum, R., "Cladding Embrittlement During Postulated Loss-of-Coolant Accidents," *Report No.* NUREG-CR-6967, US-NRC, Washington, D.C., 2008.

[9] *DIFFOX Diffusion Code*. (under development).

[10] Corvalán-Moya, C., Desgranges, C., Toffolon-Masclet, C., Servant, C., and Brachet, J. C., "Numerical Modeling of Oxygen Diffusion in the Wall Thickness of Low-Tin Zircaloy-4 Fuel Cladding Tube During High Temperature (1100–1250°C) Steam Oxidation," *J. Nucl. Mater.*, Vol. 400, 2010, pp. 196–204.

[11] Hofmann, P., Neitzel, H. J., and Garcia, E. A., "Chemical Interactions of Zircaloy-4 Tubing with UO2 Fuel and Oxygen at Temperatures Between 900 and 2000°C (Experiments and PECLOX Code)," Report No. KfK 4422, Kernforschungszentrum Karhsruhe, Germany, 1988.

[12] Pawel, R. E., "Zirconium Metal-Water Oxidation Kinetics III.–Oxygen Diffusion in Oxide and Alpha Zircaloy Phases," Report No. ORNL/NUREG-5, US-NRC, Washington, D.C., 1976.

[13] Denis, A. and Garcia, E., "Diffusion in a Semi-Infinite System with a Moving Interface Considering Solvent Density Change: Application to the Oxidation of Zirconium," *J. Nucl. Mater.*, Vol. 96, 1981, pp. 127–140.

[14] Debuigne, J. and Lehr, P., *Mem. Sci. Rev. Metallurg*. Vol. 60, 1963, p. 911.

[15] Iglesias, F. C., Duncan, D. B., Sagat, S., and Sills, H. E., "Verification of the FROM Model for Zircaloy Oxidation During High Temperature Transient," *J. Nucl. Mater.*, Vol. 130, 1985, pp. 36–44.

[16] Perkins, R. A., "Oxygen Diffusion in a-Zircaloy," *J. Nucl. Mater.*, Vol. 68, 1977, pp. 148–160.

[17] Abriata, J. P., Garcés, J., and Versaci, R., "The O-Zr (Oxygen-Zirconium) System," *Bull. Alloy Phase Diagrams*, Vol. 7(2), 1986, pp. 116–124.

[18] Chung, H. M. and Kassner, T. F., "Pseudo-Binary Zircaloy-Oxygen Phase Diagram," *J. Nucl. Mater.*, Vol. 84, 1979, pp. 327–339.

[19] Leistikow, S. and Schanz, G., "Oxidation Kinetics and Related Phenomena of Zircaloy-4 Fuel Cladding Exposed to High Temperature Steam and Hydrogen-Steam Mixtures Under PWR Accident Conditions," *Nucl. Eng. Des.*, Vol. 103, 1987, pp. 65–84.

[20] Brachet, J. C., Pelchat, J., Hamon, D., and Maury, R., "Mechanical Behaviour at Room Temperature and Metallurgical Study of Low-Tin Zy-4 and M5™ (Zr-NbO)

Alloys After Oxidation at 1100°C and Quenching," *Proceedings of the Technical Committee Meeting*, Halden, Norway, 2001, Institutt for Energiteknikk, Halden, Norway.

[21] Hózer, Z., Gyori, C., Matus, L., and Horváth, M., "Ductile-to-Brittle Transition of Oxidised Zircaloy-4 and E110 Claddings," *J. Nucl. Mater.*, Vol. 373(1–3), 2008, pp. 415–423.

[22] Kawasaki, S., Furuta, T., and Suzuki, M., "Oxidation of Zircaloy-4 Under High Temperature Steam Atmosphere and Its Effect on Ductility of Cladding," *J. Nucl. Sci. Technol.*, Vol. 15(8), 1978, pp. 589–596.

[23] Ozawa, M., Takahashi, T., Homma, T., and Goto, K., "Behavior of Irradiated Zircaloy-4 Fuel Cladding Under Simulated LOCA Conditions," *Zirconium in the Nuclear Industry: 12th International Symposium, ASTM STP 1354*, G. P. Sabol and G. Moan, Eds., Toronto, Canada, 2000, ASTM International, West Conshohocken, PA.

[24] Bossis, P., Pêcheur, D., Hanifi, K., Thomazet, J., and Blat, M., "Comparison of the High Burn-Up Corrosion on M5 and Low Tin Zircaloy-4, Zirconium in the Nuclear Industry, 14th International Symposium," *ASTM Spec. Tech. Publ.*, Vol. 1467, 2006, pp. 494–524.

[25] Yilmazbayhan, A., Breval, E., Motta, A. T., and Comstock, R. J., "Transmission Electron Microscopy Examination of Oxide Layers Formed on Zr Alloys," *J. Nucl. Mater.*, Vol. 349(3), 2006, pp. 265–281.

[26] Busser, V., "Mécanismes d'endommagement de la couche d'oxyde des gaines de crayons combustible en situation accidentelle de type RIA," PhD Thesis, Institut National des Sciences Appliquées, Lyon, France, 2009.

[27] Bouffioux, P. and Legras, L., "Effect of Hydriding on the Residual Cold Work Recovery and Creep of Zircaloy-4 Cladding Tubes," *Light Water Reactor Fuel Performance*, Park City, 2000.

[28] Erickson, W. H. and Hardie, D., "The Influence of Alloying Elements on the Terminal Solubility of Hydrogen in a-Zirconium," *J. Nucl. Mater.*, Vol. 13(2), 1964, pp. 254–262.

[29] Yamanaka, S., Tanaka, T., and Miyake, M., "Effect of Oxygen on Hydrogen Solubility in Zirconium," *J. Nucl. Mater.*, Vol. 167, 1989, pp. 231–237.

[30] Moalem, M. and Olander, D. R., "The High-Temperature Solubility of Hydrogen in Pure and Oxygen-Containing Zircaloy," *J. Nucl. Mater.*, Vol. 178, 1991, pp. 61–72.

[31] Stern, A., "Comportements métallurgique et mécanique des matériaux de gainage du combustible REP oxydés à haute temperature," PhD Thesis, Ecole des Mines de Paris, France, 2007.

[32] Blat, M. and Noel, D., "Detrimental Role of Hydrogen on the Corrosion Rate of Zirconium Alloys," *11th International Conference on Zirconium in the Nuclear Industry, ASTM STP 1295*, E. R. Bradley and G. P. Sabol, Eds., Garmisch-Partenkirchen, Germany, 1995, ASTM International, West Conshohocken, PA.

DISCUSSION

Question 1, Mirco Grosse, Karlsruhe Institute of Technology, Germany:—1) Is there a possibility to change the oxidation correlation? Maybe, it is needed to apply the code to other alloys, i.e. Zr-Nb alloys. 2) Have you compared the DIFFOX code with other codes for instance with the mechanistic SVETCHA code from IBRAE Moscow?

Author's Response:—1) DIFFOX simulates the high-temperature oxidation of Zircaloy by solving a moving boundary problem at reaction layer interfaces under simultaneous calculation of the oxygen concentration profile in each layer. The code, thus, does not use any empirical correlation for the reaction layer growth deduced from measured kinetic data. Application of the current version of the code for Zr-alloys other than Zircaloy would require the material data such as oxygen concentrations at layer boundaries (in as-received and hydrided alloy) and oxygen diffusion coefficients, which are not openly available for other alloys than Zircaloy. Moreover, a possible effect of Nb would be ignored. However, according to the similar weight gain behavior of Zy-4 and M5 in the 1100-1200°C temperature range (see *Portier et al., Influence of Long Service Exposures on the Thermal-Mechanical Behavior of Zy-4 and M5 alloys in LOCA Conditions, 14th Symposium on Zirconium in the Nuclear Industry, Stockholm, June 2004*), significant differences may not be expected between Zy-4 and M5 for oxidation transients with a dominant isothermal oxidation phase in the 1100–1200°C temperature range.

2) Validation of DIFFOX through confrontation with experimental data rather than by comparison with other codes have been chosen. A code-to-code comparison at temperatures, where a continuous β-Zr layer exists (i.e. above ~970°C), would be possible and we expect to obtain similar results with other codes. A comparison over a whole transient including the heating/cooling phases requires the simulation of oxygen diffusion in the various layers appearing and/or disappearing during the transient.

Question 2, Pierre Barberis, AREVA, France:—Does the DIFFOX code rely on concentration or thermodynamic potential ? Is it coupled with a thermodynamic database?

Author's Response:—The code relies on concentration (see answer to M. Grosse's question). The code is not coupled to a thermodynamic database but it uses oxygen concentrations at layer boundaries taken from the Zy4-O phase diagram. The enhanced O-solubility in the alpha and beta layers due to absorbed hydrogen is taken into account. In transient conditions the oxygen boundary concentrations are allowed to deviate from the Zy4-O phase diagram (example for cooling: the O-concentration at the lower phase boundary in the alpha layer is prevented to decrease. This feature avoids unrealistic growth of the alpha layer).

Question 3, Arthur Motta, Penn State University, USA:—Could you clarify what in your view controls the formation of t-ZrO_2 layer at high temperature?

Author's Response:—In the DIFFOX code, the t-ZrO_2 sub-layer allows simulating the ~cubic reaction kinetics below ~1000°C. It has higher O-diffusion coefficient compared to m-ZrO_2, its thickness = f(T) was adjusted to get good code-to-data agreement. Formation at the metal-oxide interface of a tetragonal-rich zirconia sub-layer has been experimentally evidenced (see for example *J. Godlewski et al., Raman spectroscopy study of the tetragonal-to-monoclinic transition in zirconium oxide scales and determination of overall oxygen diffusion by nuclear microanalysis of O18, 9th Symposium on Zirconium in the Nuclear Industry, Kobe, November 1990)*, the t-ZrO_2 phase being stabilized at low temperature by stresses, grain size and substochiometry.

Question 4, Suresh K. Yagnik, EPRI, USA:—Your testing was obviously two-sided corrosion. Did you get into a situation either in low temp or high temp tests that the oxygen penetration from the OD was impacting the one from the ID side?

Author's Response:—Yes, for the long oxidation duration investigated at 900°C, outer oxygen diffusion is impacted by the inner one. This is implicitly taken into account by the DIFFOX code: oxygen concentration in the central region of the cladding wall is the result of oxygen fluxes coming from both the inner and outer surfaces.

Question 5, Zoltan Hozer, AEKI, Hungary:—Your model very well described the distribution of oxygen in the cladding. Can you simulate the transport and distribution of hydrogen with this model?

Author's Response:—The simulation of transport and distribution of hydrogen should be obtained by solving the diffusion equations of hydrogen in the multilayered system with moving boundaries as calculated at each time step by DIFFOX, providing that the required physical parameters (H diffusion coefficient and possibly boundary concentrations) were available in each layer.

Reprinted from JAI, Vol. 8, No. 1
doi:10.1520/JAI102954
Available online at www.astm.org/JAI

Masafumi Nakatsuka[1] *and Suresh Yagnik*[2]

Effect of Hydrides on Mechanical Properties and Failure Morphology of BWR Fuel Cladding at Very High Strain Rate

ABSTRACT: The data on the cladding mechanical response under rapid deformation are crucial for the safety assessment of LWR fuel rods for reactivity initiated accident (RIA) and for spent fuel shipping and storage cask-drop accidents. The reported data on the mechanical properties of the irradiated cladding under high strain rates, however, are very limited, and conventional axial tensile data measured at slow strain rates may not be directly applicable to RIA or drop impact analyses. The objective of this work was to obtain basic mechanical properties such as the stress-strain relationship, ductility, and the critical strain energy density (SED) of fuel cladding with various hydride morphologies at high deformation rate. A unique rapid burst test method was employed on open-end tube specimens, achieving a strain rate of $\sim$1 s^{-1} and specimen rupture in $\sim$10 ms. Unirradiated and irradiated Zry-2 fuel cladding specimens were tested from room temperature up to 350C. The mechanical properties data were assessed in terms of SED and failure strain, and failure morphologies were examined by optical and scanning electron microscopy. The tests performed at room temperature on unirradiated cladding with circumferential hydrides revealed that the failure elongation was unchanged or increased slightly with an increase the in hydrogen content up to $\sim$100 wt ppm but decreased drastically at $\sim$400 wt ppm to values approaching 0 %. A drastic reduction in failure strain occurred at a lower hydrogen concentration of $\sim$100 wt ppm for radial hydrides, compared to $\sim$200–400 wt ppm for the circumferential hydride

Manuscript received January 8, 2010; accepted for publication October 1, 2010; published online November 2010.

[1] Nippon Nuclear Fuel Development Co., Ltd., 2163 Narita-cho, Oarai-machi, Higashi-Ibaraki-gun, Ibaraki, 311-1313, Japan, e-mail: nakatsuka@nfd.co.jp
[2] Electric Power Research Institute, Inc., 3412 Hillview Av., Palo Alto, CA 94304-1338, e-mail: SYAGNIK@epri.com

Cite as: Nakatsuka, M. and Yagnik, S., "Effect of Hydrides on Mechanical Properties and Failure Morphology of BWR Fuel Cladding at Very High Strain Rate," *J. ASTM Intl.*, Vol. 8, No. 1. doi:10.1520/JAI102954.

Copyright © 2011 by ASTM International, 100 Barr Harbor Drive, PO Box C700, West Conshohocken, PA 19428-2959.

distribution. The fraction of specimen thickness occupied by the accumulated length of hydrides in radial direction was a better predictive indicator of specimen failure and ductility reduction than the total hydrogen content. In addition, the high strain rates did not seem to seriously impact stress-strain behavior when hydrogen content is >400 wt ppm. The data analyses revealed smaller values of the strain hardening exponent (*n*) compared to those from the conventional data for the slow strain rates, indicating that the plastic instability theory simply is not appropriate to evaluate the failure strain under RIA conditions.

KEYWORDS: fuel cladding tube, mechanical properties, high strain rate, circumferential, uniaxial tensile test

Introduction

During the postulated reactivity initiated accident (RIA), the rapid increase in pellet temperature causes pellet thermal expansion and swelling coupled with rapid expansion of accumulated fission gas [1–3]. This results in pellet cladding mechanical interaction (PCMI). For example, the temperature and strain rate during PCMI of RIAs are reported to be several tens to 100 %/s and the stress state is bi-axial in the case of cold-standby RIA in BWRs [4,5].

At high burnups, the decreased cladding ductility due to localized hydrides can lead to fuel failure. This so-called "hydride assisted PCMI" was identified as the key mechanism of fuel failure under RIA [6–8].

In RIA-simulation tests performed in NSRR or CABRI facilities [9,10], the energy deposition thresholds for the cladding failure were determined. The following characteristics of failed fuel cladding were noted: Hydrides that precipitate locally in a rim layer in the outer region of the high burnup cladding lead to a brittle fracture and the fracture surface is normal to the cladding surface. These characteristics suggest that the loss of ductility of fuel claddings played an important role in the failure because a fully ductile fuel cladding would not have failed, even if it experienced severe pressure from the fuel pellets during such power transients.

To understand the brittle failure mechanism of fuel claddings, the FEM analysis results based on the strain energy density (SED) of the cladding material were reported [11]. Localized necking instability theory of a plate with a surface flaw was also applied to the interpretation of the brittle failure behavior, and it was found that the thickness of the pre-existing hydride-embrittled rim layer reduced the overall ductility of cladding during RIA [12,13].

A detailed constitutive equation, i.e., the stress-strain relationship, for the material is an essential input for these analyses. Mechanical properties, such as strength and ductility, of a specimen are strongly dependent on stress state and loading direction in the specimen. Under the loading condition of PCMI, fuel cladding is subjected to almost equal bi-axial tensile stress in the hoop and axial directions [4,14]. However, since the fuel rods failed with radial crack and axial split under a RIA-simulated experiment [5], the hoop stress and strain play an important role in the failure process [15].

Although cladding response under the bi-axial stress state is essential for better understanding of the RIA situation, the approach in our study was not to replicate RIA conditions in the laboratory. Instead, we have pursued constitutive equation for the cladding material through a uniaxial hoop stress applied to the specimen and closely followed its stress-strain behavior.

The data available on detailed cladding mechanical response under rapid deformation, including discussion of the ductility and hydride morphology of the tubes, however, are very limited [16,17]. Further, conventional axial tensile data measured at slow strain rates [18] may not be applicable to RIA analysis. A test called the expansion-due-to-compression (EDC) test has been reported [19,20] in the open literature, wherein a short piece of cladding was circumferentially loaded in tension due to the expansion of a polymer pellet, axially compressed inside the tube. However, the EDC method has a limitation in obtaining the hoop stress-strain relationship without an additional numerical analysis. The ring tensile test with notched ring specimen has also been widely used [1,17,21–24], in which the stress state in the notched gauge section is non-uniform and depends on the sample geometry [25]. Generally, the specimen geometry [26] and stress states [27] are known to have a strong impact on the results of the mechanical tests. Although some investigators have conventional closed end burst testing to simulate PCMI, and ring tensile testing with plane strain condition are for predicting failure criteria, the experimental data from these tests are not directly applicable to obtain the constitutive equation.

We report here on a unique rapid burst tests performed on open-end tube specimens, where hoop stresses are applied directly from the internal pressure loading. In our study, a uniform hydriding was used to obtain fundamental dependency of the mechanical response to the hydrogen content at high deformation rate, and information on the tube embrittlement mechanism under the RIA condition was pursued.

Materials

Unirradiated

All the test specimens used were from the "8 × 8 type Zircaloy-2 fuel cladding," which satisfies ASTM B353 [28] specifications for nuclear fuel cladding application [29]. For the unirradiated specimens, no annealing after the final reduction during the processing of 71 % was applied. These specimens are designated as "as-cold-worked" (or ASC). The chemical composition of the specimens is given in Table 1.

The texture of these tube specimens was a bimodal distribution of basal poles with the maximum intensity at around ±30° from the radial toward the tangential directions. The Kearns' texture parameters [30] for axial, tangential, and radial directions were 0.021, 0.356, and 0.623, respectively. The elastic constants of the ASC material were computed on the basis of the X-ray diffraction intensity of the (0002) planes [31].

Irradiated

The irradiated test specimens were taken from available fuel rods, ZYF and ZYS, with low and intermediate burnups. Since it is also desirable to test

TABLE 1—*Chemical composition of the fuel cladding tubes.*

Test Materials	Sn(wt%)	Fe(wt%)	Cr(wt%)	Ni(wt%)	O(wt ppm)	N(wt ppm)	C(wt ppm)	H(wt ppm)
ASC (unirradiated)	1.53	0.14	0.10	0.05	1200	40	180	14
ZYF, ZYS (irradiated)	1.53	0.13	0.10	0.05	1100	35	85	13

TABLE 2—*Additional information for irradiated test materials.*

Fuel Rod	ZYF	ZYS
Cladding material[a]	Zircaloy-2	
Pellet material	UO_2	
Cladding OD and wall thickness (mm)	12.3; 0.86	12.5; 0.86
Number of irradiation cycles in a BWR (EFPD[b])	1 (210)	5 (1270)
Rod average burnup (GWd/t)	7.1	31.4
Estimated fast fluence (10^{25}; $E > 1$ MeV)	1.0	5.4

[a]See Table 1 for composition.
[b]Effective full power days.

specimens with various hydrogen contents (wt ppm) and distributions, both unirradiated and irradiated test specimens were additionally hydrogen charged in this study. The cladding for both ZYF and ZYS were fabricated by the same process as the ASC, but a recrystallization annealing treatment at 850 K for 2.5 h was applied. The chemical compositions of ZYF and ZYS are shown in Table 1.

The fuel rod ZYF cladding was retrieved from a BWR after one cycle irradiation, whereas the rod ZYS was irradiated for five cycles in the same reactor. To prepare the specimens, the fuel rods were cut to the length dimension and defueled by mechanical drilling of fuel pellets while preventing any mechanical damage to the cladding. Any adhering pellet material on the ID was removed by acid cleaning. No attempt was made to remove the thin and tightly adhering oxides on the OD.

The irradiation conditions together with neutron fluences are summarized in Table 2 [32]. The neutron fluence of the individual burst test specimens was calculated from the rod averaged values and the flux distribution profile along the rod length. The neutron fluence gradient along the specimen length was confirmed to be negligibe.

Figure z1 shows the typical hydride morphology of the intermediate burnup specimen from fuel rod ZYS after hydride charging. Mixed circumferential and radial orientation hydrides can be seen in this figure in as-etched and as-polished conditions. In some high burnup BWR fuel claddings, a combined radial and circumferential hydride morphology can be seen [33]. From a comparison of hydrides in the two photographs of the figure, it can be said that most hydrides formed in the irradiated and hydrogen charged specimens are transgranular and not intergranular.

Hydrogen Charging and Hydride Characterization

The cladding ductility is sensitive to the content and the orientation of hydrides. The irradiated cladding available for this investigation was of low and intermediate burnups as shown in Table 2. For typical BWR cladding, the hydrides are small and distribute uniformly at low burnup. The number density of hydrides increases with burnup, and they tend to populate at the outer periphery of the

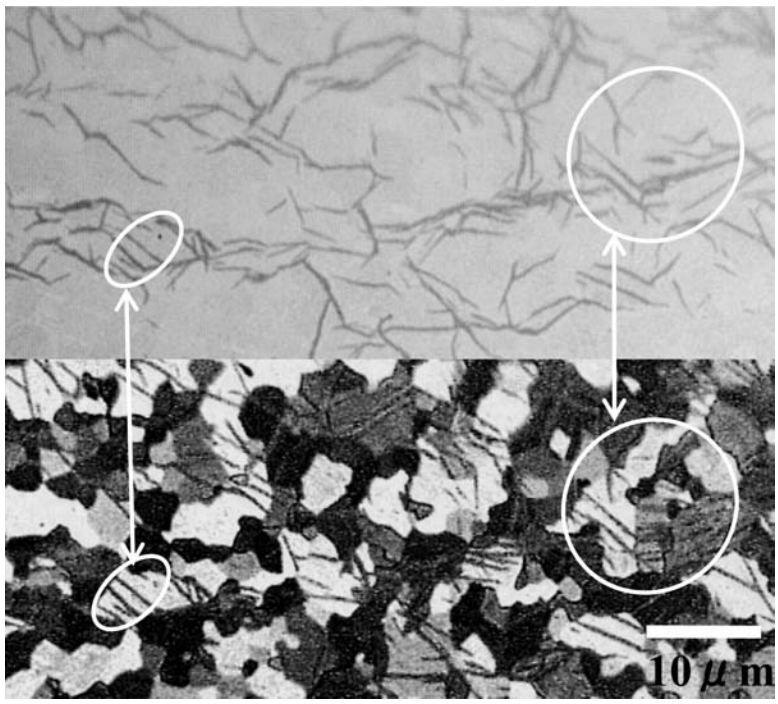


FIG. 1—*Hydrides (upper) and corresponding Zry grains (lower) in the same area (ZYS689, 212 wt ppm H).*

cladding [34]. At high burnup ($\sim$ 60 GWd/t), the morphology of hydrides is mixed radial and circumferential. It is difficult to simulate such a hydride morphology by out-reactor hydrogen charging method. Nevertheless, in this study hydrogen was charged into a number of test samples to represent higher burnups with either circumferential or radial hydrides.

The hydrogenation of the unirradiated specimen to form uniformly distributed circumferential hydrides was done in 3M LiOH aqueous solution at 350°C for times ranging from 12 to 24 h. For irradiated specimens, similar conditions and method was used in a hot cell but at somewhat lower temperature (330–340°C) and longer duration (18–42 h). The specimens are furnace cooled (20–30°C/h). To obtain specimens with radially oriented hydrides, the specimen tubes were internally pressurized by water at a constant pressure of 35 MPa in the furnace equipped with a cyclic temperature controller and a vessel for the mixed hydrogen gas environment. The temperature of the specimens was controlled cyclically between 330°C (603 K) and 180°C (453 K) to obtain completely radial hydrides.

For the information on the hydrogen distribution and location of radial hydride in the specimen, the composite metallographical images are presented in a three-dimensional view in Fig. 2. The left panel of the figure shows the

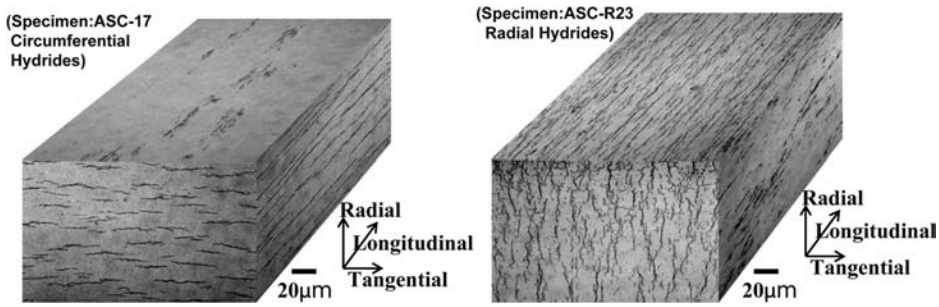


FIG. 2—*Typical hydrides morphologies in three dimensional representation for the specimens with circumferential and radial hydrides.*

specimen ASC-17 (115 wt ppm) with uniform circumferential hydrides, while the right figure shows specimen ASC-R23 (253 wt ppm) with the typical radial hydrides. These microphotographs show that hydriding forms thin and long platelets elongated in the longitudinal direction. The so-called circumferential hydrides (left figure) form platelets roughly in concentric circles. On the other hand, the so-called radial hydrides (right figure) form radially oriented plates.

The hydrogen concentrations for all the specimens after rapid burst testing were measured by the inert gas fusion thermal conductivity method by using a LECO apparatus and are summarized in Table 3. To confirm the uniformity of hydride distribution along the specimen length, cross section metallographic characterizations at and in the vicinity of the failure location were performed.

Experimental

Rapid Burst Test Method

To obtain the circumferential stress-strain relationship of the specimen under uniaxial stress state, an internal pressurization was applied to open-end tubular specimens in a rapid burst loading system [35]. The test system, shown schematically in Fig. 3, was designed to withstand high pressure and elevated temperature conditions. Unlike the conventional burst tests, where a constant volume pumping rate should be maintained [36] for the duration of the test, in this study, a high pressurization rate corresponding to the RIA condition was obtained by a piston which was driven by the release of stored energy through an oil pump and an actuator. The water was sealed inside the specimen not by welding but by O-rings at each end of the specimen so that no longitudinal (or axial) tensile stress could be induced in the tube specimen. The end plugs were fixed to the apparatus base so as to prevent internal pressure leakage during the test.

Test Procedure

For the intended rapid pressurization, a relatively short specimen length is desirable, as long as the specimens are long enough to avoid the end effects on the

TABLE 3—*Summary of the specimens, test conditions, and mechanical properties obtained in this study.*

Number	Specimen ID	Neutron Fluence ($E > 1$ MeV) ($\times 10^{25}$ m^{-2})	Hydride Type	Test Temperature (°C)	H. Content[a] (ppm)	Yield Stress[b] (MPa)	UTS[b] (MPa)	Uniform Strain (Plastic)[b] (%)	Failure Strain (Plastic)[c] (%)	Max. SED[b] (MJ/m^3)	Strain Hardening Exponent (Unit Less)	Constant K for True Stress (MPa)
1	ASC-37	0	Uni.[d]	RT	14	913	1028	1.6	7.3	81.1	0.067	1052
2	ASC-40	0	Uni.[d]	RT	15	887	1032	1.4	6.4	62.6	0.088	1068
3	ASC-16	0	Uni.[d]	RT	108	839	992	1.5	6.4	64.0	0.121	1017
4	ASC-17	0	Uni.[d]	RT	115	890	1010	1.6	5.4	60.4	0.057	1026
5	ASC-L28	0	Uni.[d]	RT	151	911	1034	1.5	8	84.9	0.082	1065
6	ASC-L27	0	Uni.[d]	RT	179	956	1031	1.2	5.3	52.8	0.050	1067
7	ASC-L26	0	Uni.[d]	RT	214	940	1032	0.8	1	15.5	0.075	1092
8	ASC-34	0	Uni.[d]	RT	303	948	964	0.4	0.5	16.2	···	···
9	ASC-32	0	Uni.[d]	RT	335	858	946	0.3	0.8	9.8	0.112	1063
10	ASC-28	0	Uni.[d]	RT	379	876	937	0.2	0.5	7.3	···	···
11	ASC-33	0	Uni.[d]	RT	382	824	947	0.6	0.7	9.9	···	···
12	ASC-29	0	Uni.[d]	RT	431	916	943	0.2	0.2	6.8	···	···
13	ASC-L39	0	Uni.[d]	RT	499	···	916	0	0	4.8	···	···
14	ASC-27	0	Uni.[d]	RT	528	914	946	0.2	0.5[e]	9.7	···	···
15	ASC-19	0	Uni.[d]	RT	871	···	838	0	0.2	4.3	···	···
16	ASC-18	0	Uni.[d]	RT	948	···	810	0	0.4	4.2	···	···
17	ASC-8	0	Uni.[d]	RT	1841	···	534	0.1	0.2	2.1	···	···
18	ASC-7	0	Uni.[d]	RT	1941	···	505	0.1	0.7	2.1	···	···
19	ASC-R31	0	Radial[f]	RT	53	872	1015	1.3	2.4	33.5	0.098	1035
20	ASC-R32	0	Radial[f]	RT	39	926	1019	1.4	2.8	24.6	0.061	1046
21	ASC-R52	0	Radial[d]	RT	30	···	856	0.1	0.5	4.8	···	···
22	ASC-R53	0	Radial[f]	RT	25	959	1006	0.9	1.3	17.6	0.034	1041

TABLE 3—*(Continued)*

Number	Specimen ID	Neutron Fluence ($E > 1$ MeV) ($\times 10^{25}$ m^{-2})	Hydride Type	Test Temperature (°C)	H. Content[a] (ppm)	Yield Stress[b] (MPa)	UTS[b] (MPa)	Uniform Strain (Plastic)[b] (%)	Failure Strain (Plastic)[c] (%)	Max. SED[b] (MJ/m^3)	Strain Hardening Exponent (Unit Less)	Constant K for True Stress (MPa)
23	ASC-R41	0	Radial[f]	RT	312	...	378	0.1	0.4	1.2	...	...
24	ASC-R42	0	Radial[f]	RT	108	...	507	0	0.3	1.4	...	...
25	ASC-R21	0	Radial[f]	RT	479	...	344	0	0.1	0.8	...	...
26	ASC-R23	0	Radial[f]	RT	253	...	422	0	0.5	3.6	...	...
27	ASC-101	0	Uni.[d]	350	48	725	732	...	8.2	...	0.041	775
28	ASC-102	0	Uni.[d]	250	43	735	797	1.9	11.7	> 80	0.064	816
29	ASC-103	0	Uni.[d]	150	47	779	894	1.8	4.9	65.1	0.066	892
30	ASC-104	0	Uni.[d]	RT	48	925	1015	1.2	3.3	58	0.046	1037
31	ASC-105	0	Uni.[d]	250	41	731	822	1.2	10.1	72	0.03	829
32	ASC-106	0	Uni.[d]	RT	12	835	1030	1.6	5.9	62.8	0.086	1021
33	ASC-118	0	Uni.[d]	300	12	685	785	3.5	7.4	> 80	0.065	785
34	ASC-119	0	Uni.[d]	350	12	640	720	1.9	9.9	> 80	0.049	720
35	ASC-120	0	Uni.[d]	250	12	711	813	2.4	9.1	98.4	0.053	813
36	ASC-121	0	Uni.[d]	200	12	753	840	2	8.2	80	0.048	843
37	ASC-122	0	Uni.[d]	150	12	791	873	1.5	7.2	57.8	0.037	877
38	ASC-L56D	0	Uni.[d]	150	176	851	883	0.8	8.6	56.6	0.023	913
39	ASC-L48	0	Uni.[d]	150	253	859	878	0.5	9.9	53.6	0.004	891
40	ASC-107	0	Uni.[d]	150	483	...	322	0	0.0	1.3	...	...
41	ASC-B2163	0	Uni.[d]	150	1209	738	762	0.2	0.8	5.1	...	...
42	ASC-W10U	0	Uni.[d]	250	281	774	794	1	9.4	80.6	0.013	817
43	ASC-106D	0	Uni.[d]	250	494	754	791	1.1	2.0	28.3	0.03	815
44	ASC-1301U	0	Uni.[d]	250	612	688	787	0.5	1.9	7.2	...	...

TABLE 3—*(Continued)*

Number	Specimen ID	Neutron Fluence ($E > 1$ MeV) ($\times 10^{25}$ m^{-2})	Hydride Type	Test Temperature (°C)	H. Content[a] (ppm)	Yield Stress[b] (MPa)	UTS[b] (MPa)	Uniform Strain (Plastic)[b] (%)	Failure Strain (Plastic)[c] (%)	Max. SED[b] (MJ/m^3)	Strain Hardening Exponent (Unit Less)	Constant K for True Stress (MPa)
45	ASC-L55D	0	Uni.[d]	300	285	629	742	1.6	12.4	54.2	0.084	756
46	ASC-1022	0	Uni.[d]	350	12	633	715	2.8	7.3	80.3	0.068	729
47	ASC-W10L	0	Uni.[d]	350	160	553	707	1.7	18.0	132.4	0.144	711
48	ASC-L50	0	Uni.[d]	350	282	604	712	1.9	10.5	93.9	0.11	731
49	ASC-2S2	0	Uni.[d]	150	300	855	871	1.7	8.8	75.2	0.021	904
50	ASC-2S4	0	Uni.[d]	150	257	825	890	1.4	8.3	67.2	0.045	913
51	ASC-2S8	0	Uni.[d]	250	389	765	803	1.1	9.1	71.4	0.029	828
52	ASC-2S14	0	Uni.[d]	250	353	744	791	1.0	1.1[b]	13.1	0.048	825
53	ASC-2S9	0	Uni.[d]	350	164	688	717	0.8	9.6	72.2	0.021	737
54	ASC-2S12	0	Uni.[d]	350	275	683	709	···	13.9	···	···	···
55	ASC-2S15	0	Uni.[d]	350	274	684	694	0.3	4.4	34.4	···	702
56	ZYF680	0.8	Uni.[d]	RT	28	1013	1034	1	2.2[b]	29.1	0.023	1075
57	ZYF681	0.8	Uni.[d]	RT	30	1039	1047	0.3	2.3[b]	28.7	···	1061
58	ZYF682	0.8	Uni.[d]	RT	293	···	701	···	···	4	···	···
59	ZYF683	0.9	Uni.[d]	RT	400	···	785	0.1	0.1[b]	5.1	···	···
60	ZYS685	6.2	Uni.[d]	RT	69	1075	1081	0.5	2.4	42.9	0.005	1115
61	ZYS686	6.1	Uni.[d]	RT	62	1061	1067	0.5	1.8	36.7	0.002	1099
62	ZYS687	6.5	Uni.[d]	RT	115	1070	1082	0.4	2.1	30.2	0.000	1104
63	ZYS688	6.5	Uni.[d]	RT	75	1080	1084	0.3	2.4	32.7	···	1110
64	ZYS689	6.5	Uni.[d]	RT	212	···	1057	···	1.1	···	···	···
65	ZYS702	6.7	Uni.[d]	150	47	996	1009	0.5	4.1	> 114	0.015	1046
66	ZYS700	6.9	Uni.[d]	250	46	860	866	0.3	10.9	> 99	0.002	884

TABLE 3—*(Continued)*

Number	Specimen ID	Neutron Fluence ($E > 1$ MeV) ($\times 10^{25}$ m^{-2})	Hydride Type	Test Temperature (°C)	H. Content[a] (ppm)	Yield Stress[b] (MPa)	UTS[b] (MPa)	Uniform Strain (Plastic)[b] (%)	Failure Strain (Plastic)[c] (%)	Max. SED[b] (MJ/m^3)	Strain Hardening Exponent (Unit Less)	Constant K for True Stress (MPa)
67	ZYS712	6.6	Uni.[d]	350	48	848	859	0.4	13.2	> 72	0.011	889
68	ZYS711	6.5	Uni.[g]	RT	162	1052	1058	0	5.1	21	⋯	1060
69	ZYS707	6.1	Uni.[d]	150	60	992	997	0.3	8	> 125	0.004	1028
70	ZYS709	5.9	Uni.[g]	150	187	975	991	0.8	7.1	> 127	0.016	1031
71	ZYS708	6	Uni.[g]	250	145	897	922	0.8	4.6	> 99	0.022	959
72	ZYS710	6.6	Uni.[a]	350	82	844	870	0.5	9.4	51	0.023	896

[a]By the inert gas fusion technique (LECO), values at maximum deformation of the specimen.
[b]Values are based on engineering stress-strain curves. (1 MN $\times$ m/m^3 = 1 MJ/m^3).
[c]Calculated failure strain based on the maximum opening width and diameter at the angle of 90° from the opening.
[d]Specimens with circumferential uniform hydride.
[e]Part of the specimen scattered. Failure strain based on engineering stress-strain curves.
[f]Specimens with radial hydride.
[g]Mixed circumferential and radial hydrides.

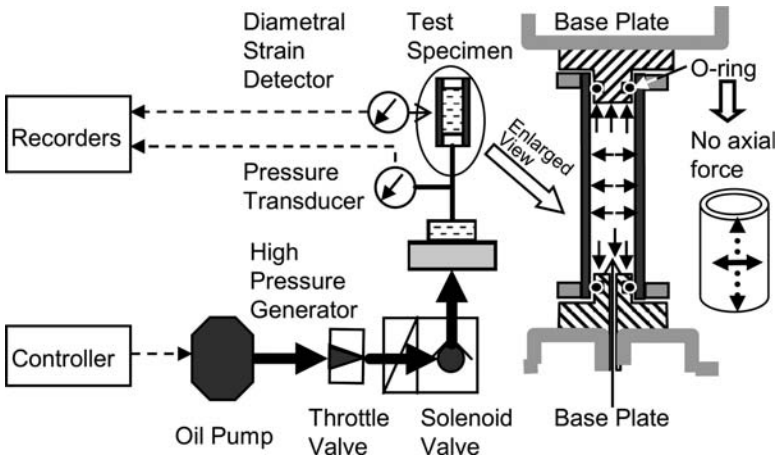


FIG. 3—*Schematic diagram of testing assembly for rapid internal pressurization burst test.*

results. Therefore, the tests to determine an optimum specimen length were performed by testing specimens of various lengths [35]. Based on the results, a specimen length of 60 mm (ratio of length to diameter: 5) was adopted throughout this study. The rapid pressurization typically ended within 10–20 ms depending on the ductility of the specimen being tested. This resulted in circumferential strain rates of roughly $1\,s^{-1}$. Considering the cold start-up RIA in BWRs and experimental limitation temperatures, the tests were performed at room temperature and at temperatures up to 350°C [5].

The outside diameter and wall thickness were measured for each specimen before the test. An eddy current strain detector was attached to the specimen OD approximately at the middle of the gage length where the burst failure normally occurred. Following the test, the failure strain and reduction in wall thickness was measured at positions 90° apart. For irradiated specimens, where some degree of ovality was expected due to cladding creep down in reactor, these measurements were taken at every 45° circumferential location.

Results

Definitions of Mechanical Properties

The nominal (engineering) hoop stress and nominal (engineering) hoop strain, hereafter σ_c and ϵ_c, are given by the following equations [37]:

$$\sigma_c = PR/t$$

$$\varepsilon z_c = d_i/D_o$$

where:

P = internal pressure at a certain lapsed time,
R = initial mean radius of the specimen,
t = initial average wall thickness,
d_i = diametral increment at a certain lapsed time, and
D_o = initial mean outer diameter.

By inserting the measured values of internal pressure and diametral change at a given lapsed time, the σ_c versus ϵ_c curve was generated for each test. The yield stress, σ_y, ultimate tensile strength, σ_u, and uniform elongation, ϵ_u, are all based on the nominal values, and are defined as the stress to induce 0.2 % plastic strain, stress at maximum value of the stress-strain curve, and the plastic strain for σ_u, respectively. The maximum SED, including the elastic region, is also based on the nominal values, and is given from the area under the σ_c versus ϵ_c curves up to the failure strains listed in Table 3. The failure strain or total elongation is given by the plastic strain at rupture on the curve. The Hollomon's equation is introduced to describe the plastic deformation of the specimen

$$\sigma = K{\epsilon_p}^n$$

where:

σ = true hoop stress,
K = strength coefficient,
n = strain hardening exponent (unit less), and
ϵ_p = plastic true hoop strain (unit less).

The true hoop stress, σ, is approximated by using the following expression [18]:

$$\sigma = \sigma_c(1 + \epsilon_c)^2$$

The true hoop strain, ϵ, is the natural logarithm of the ratio of the gage length at the moment of observation to the original gage length, then the true hoop strain, ϵ, and plastic true strain, ε_p, are given by

$$\varepsilon = \ln(1 + \epsilon_c)$$

$$\varepsilon z_p = \epsilon - \sigma/E$$

where:

E = Young′s modulus of the specimen.

Based on the above equations, the true and nominal values of hoop stress and hoop strain, plastic true strain, and strain hardening exponent can be calculated. Table 3 provides a complete set of test results obtained in this study. As strain hardening exponents, n, for irradiated specimens depends on plastic strain [38], the values in Table 3 are defined to be the average value of this parameter up to the failure strains.

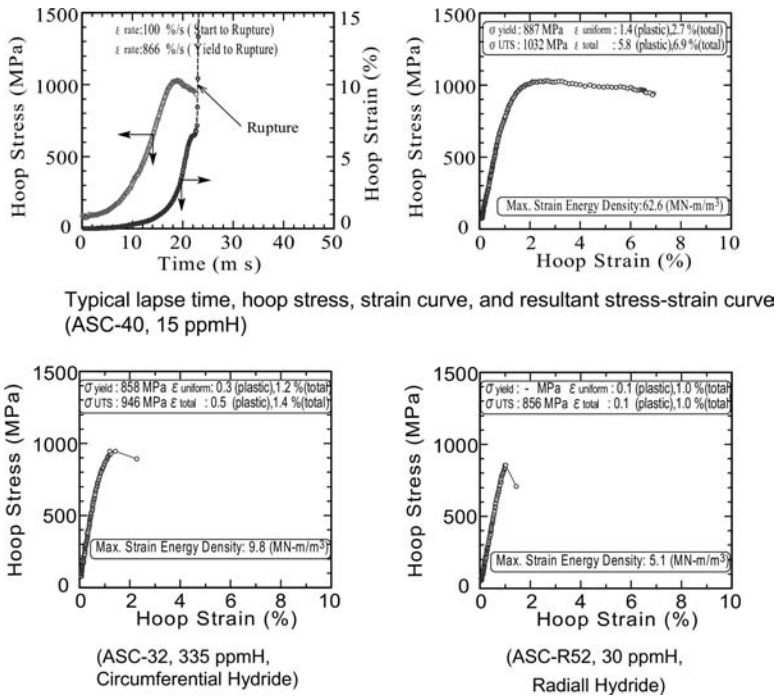


FIG. 4—*Typical stress-strain curves of the specimens with circumferential and radial hydrides tested at RT.*

Unirradiated Specimens

The specimens (No.1 through 18 in Table 3) with uniform circumferential hydride distribution were tested at room temperature. As an example, for a specimen with no hydrogen charging (ASC-40), the "hoop stress-hoop strain-lapse time" during pressurization, and the resultant nominal stress and nominal strain curves obtained from the stress-strain-time relationship is shown in Fig. 4 (upper panels). The bottom left plot of Fig. 4 shows the hoop stress-strain behavior for specimen ASC-32, with uniform circumferential hydrides at 335 wt ppm. The low strain failure of ASC-32 compared to the fairly ductile behavior of ASC-40 is obvious.

The fracture surfaces at the maximum deformation for another specimen (ASC-17 at 115 wt ppm hydrides) with typical circumferential hydrides are shown in the left panels of Fig. 5 at two different magnifications. Also shown is the corresponding cross section metallography from specimen ID to OD. In low magnification, the fracture surface of the ASC-17 is characterized by the shelf-like rough surface. The specimens designated with an R with radial hydride distribution were tested at room temperature (No.19 through 26 in Table 3). As an example, for the specimen ASC-R52 with 30 wt ppm radial hydrides, the hoop stress-strain curves is shown in the bottom right plot of Fig. 4. The typical

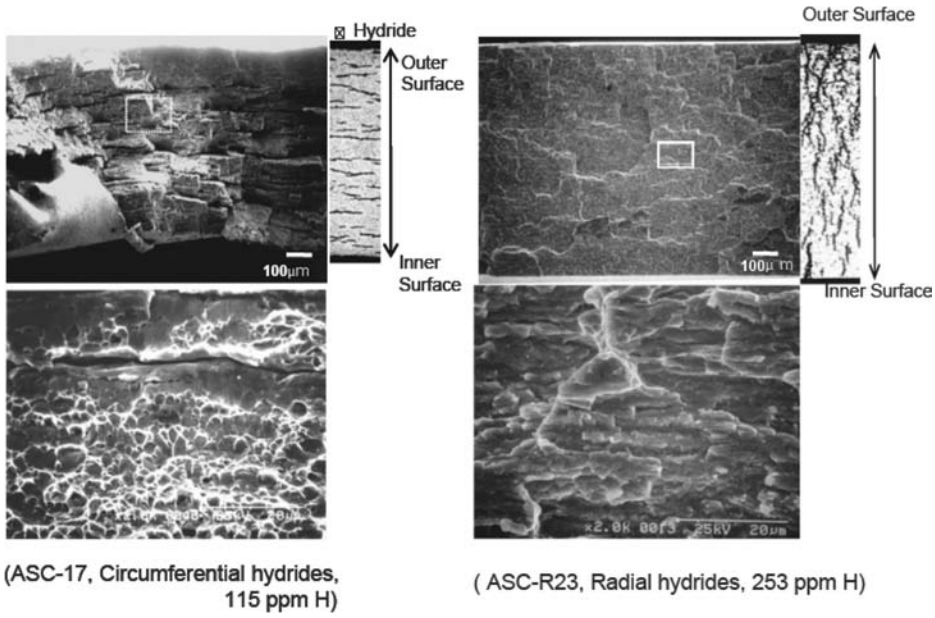


FIG. 5—*SEM images of fracture surface of the specimen after rapid burst test at RT.*

metallography of a specimen cross section and fracture surface of the specimen with radial hydrides are shown in the right of Fig. 5. Due to the difference in hydride distribution, a significant difference in fracture toughness is induced: Radial hydrides have a tendency to make a smoother fracture surface than circumferential hydride distributions.

ASC specimens were tested up to 350°C with and without hydrogen precharging. The hoop stress-strain, and resultant true hoop stress-plastic true strain (σ versus ϵ) curves of the non-hydrogen charged specimens are plotted in Fig. 6 at 25, 250, and 350°C. The data are also presented on logarithmic plots fitted to a Holloman type constitutive equation. Comparisons of the mean strain hardening exponents, n, from 25 to 350°C in the figure show that the test temperature dependence of n is not significant given relatively large scatter in n-values.

Irradiated Specimens

The specimens (No. 56 through 64 in Table 3) prepared from low burnup fuel rod (ZYF) and intermediate burnup fuel rod (ZYS) with and without additional hydrogenation were tested at room temperature only. The radial hydrides were not introduced in the irradiated specimens. Typical examples of stress-strain curves for both nominal and true values, true stress-plastic true strain curves, and mean strain hardening exponent for the typical as-irradiated specimens are shown in Fig. 7. The characteristic results for specimens with one cycle irradiation (ZYF) are failure strain, around 2 %, compared to 1.8–2.4 % for the five

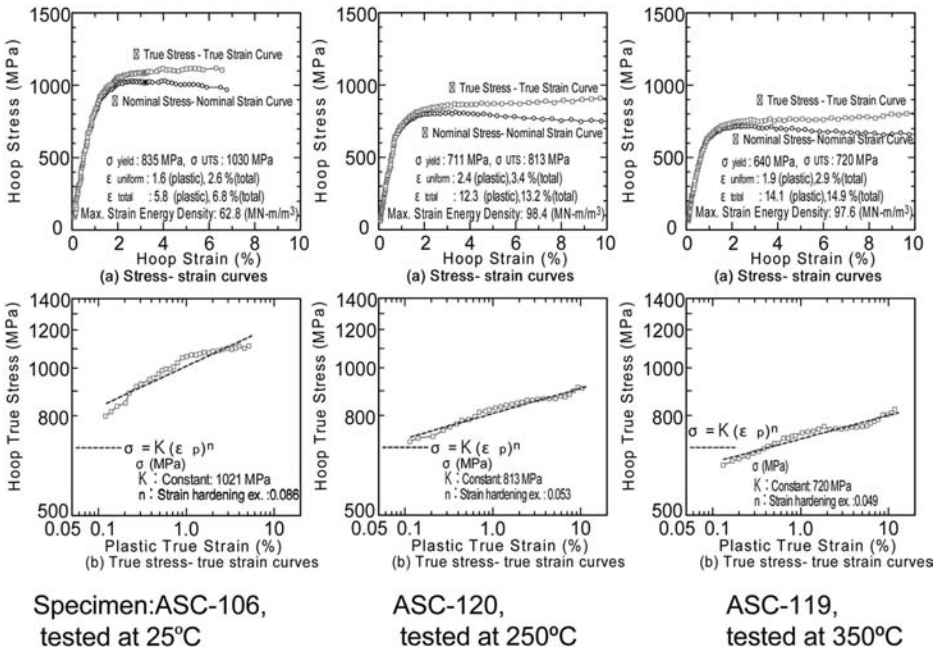


FIG. 6—*Effect of test temperature on stress-strain curves (specimens: −12 wt ppm H).*

cycles irradiated specimen (ZYS). For both specimens, very little work hardening was observed, i.e., the strain hardening exponent was very small, close to zero, as shown in Fig. 7.

The irradiated specimens from one cycle in a BWR and hydrogen charged failed within an elastic deformation range as exemplified in the right panels of Fig. 8. On the other hand, the ASC and hydrogen charged (unirradiated) specimens with almost the same hydrogen levels of around 300–400 wt ppm showed a small amount of plastic strain (see ASC-28, ASC-32, and ASC-33 in Table 3). These facts imply that the neutron irradiated material with hydrogen addition becomes more prone to failure than the unirradiated material containing the same level of hydrogen content. As shown in the two fractographs in Fig. 8, the unirradiated specimen (ASC-34) shows more ductile features compared to irradiated sample (ZYF-682) at comparable hydrogen levels. The fracture surface of the latter specimen is covered with clear brittle flat facets with Zircaloy grain size of around 5 μm.

The specimen outer surface appearance, metallography of specimen cross sections at the maximum deformation, and fracture surfaces of the specimens after burst failure are shown in Fig. 9. On the outer surface of the as-irradiated, i.e., no hydrogen charged specimen (ZYF-681), clear spiral type failure with localized shear deformation is observed. As shown in Fig. 9, the ductile dimples are observed on the fracture surface of the specimen with lower neutron fluence (ZYF-681), and a mixed ductile (dimples) and brittle (cleavage) fracture mode is observed for the higher neutron fluence (ZYS-685).

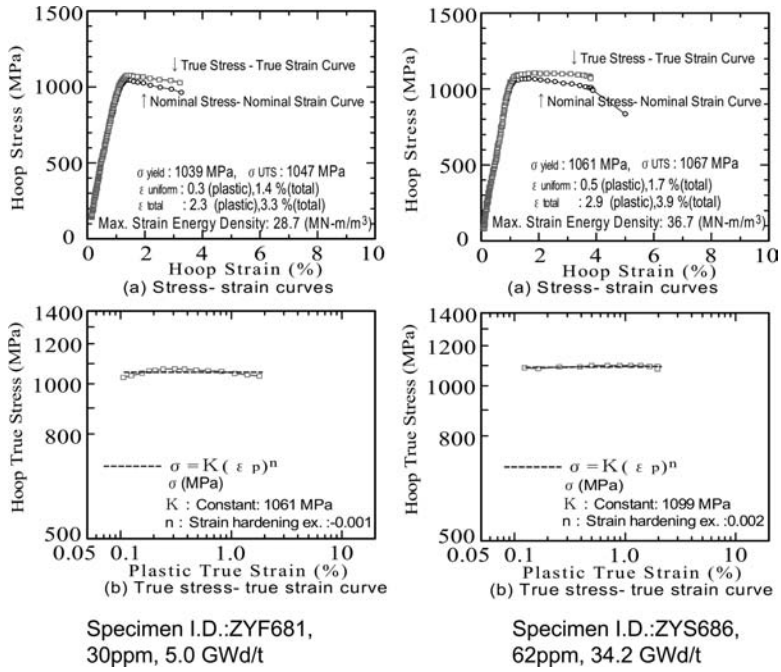


FIG. 7—*Stress-strain curves of the tubes with low and intermediated burnups tested at room temperature.*

The effect of the test temperatures up to 350°C was examined by using the ZYS specimens in in-cell hydrogen charged as well as as-irradiated conditions (No. 65 through 72 in Table 3). All the high temperature results, summarized in Table 3, showed ductile behavior with some amount of failure strains.

Discussion

Effects of Temperature and Hydrogen Concentration on Strength and Ductility

In Fig. 10(*a*), the effect of temperature on strength is compared for the unirradiated (hydrogen content lower than 180 wt ppm) and the irradiated specimens (hydrogen contents between 28 and 187 wt ppm). Both the yield stress and the ultimate tensile strength (UTS) decreased nearly linearly with an increase in the temperature. For the unirradiated specimens, the UTS is found to be slightly higher, $\sim 10\,\%$, than the yield stress. In the case of the irradiated specimens, however, there was little difference between the yield stress and the UTS due to the increase in yield strength by the neutron irradiation damage [39] and reduced strain hardening [40]. This is consistent with the low values of n, reported in the Irradiated Specimens section.

In Fig. 10(*a*), the solid squares are UTS values from burst tests at a lower strain rate ($\sim 0.5 \times 10^{-4}\,\mathrm{s}^{-1}$) for irradiated fuel cladding samples [41]. The small

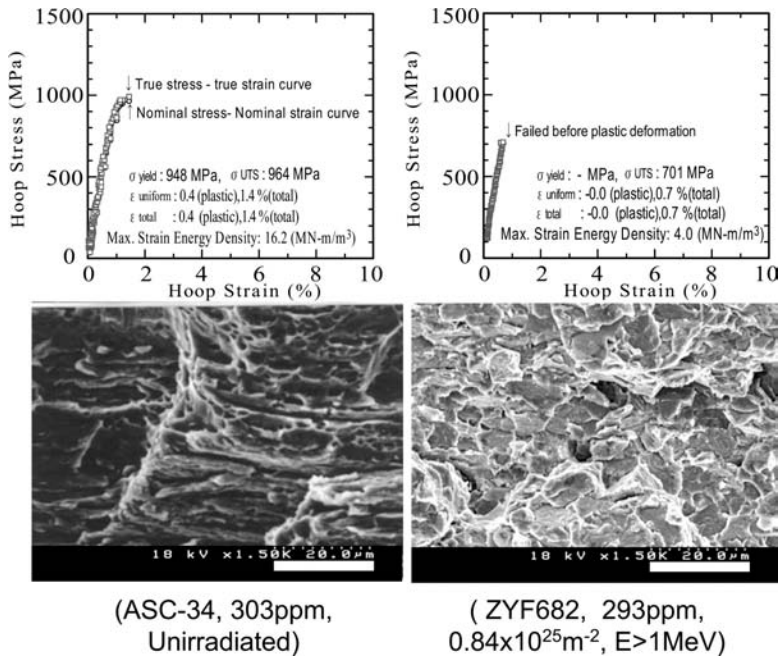


FIG. 8—*SEM images indicating significant effect of neutron fluence on the formation of cleavage planes in the fracture surfaces of the hydrogen charged specimens.*

open and solid circles are tensile test results, also at a lower strain rate ($\sim 10^{-4}\,s^{-1}$) for unirradiated guide tubes with around 1400–2000 wt ppm [41]. Due to the combined effects of slow strain rate, axial tension, and unirradiated materials, the strength (UTS and yield stress) are significantly lower than that for the burst tests. From the comparison of the data of this investigation and literature data, it is clear that the temperature dependence is almost identical regardless of the differences in hydrogen concentration levels. Even the large difference in strain rate implicit in the comparison showed no effect on the temperature dependence of strength.

In Fig. 10(*b*), the effect of hydrogen concentration, as circumferential hydrides, on the UTS is shown for the unirradiated specimens at different temperatures. The data obtained for the irradiated specimens at room temperature are also included. Generally, due to the higher elastic constants of zirconium hydride than Zircaloy [42], the UTS at room temperature increases with increasing hydrogen [22,43]. However, since zirconium hydride at room temperature is brittle and has low failure strength ~ 18 MPa [42] and its contribution of radial hydride fraction to strength is significant [44], it is reasonable that the UTS does not simply decrease with hydrogen content. Actually, a peak strength at −200 wt ppm was also reported in the literature [45].

In the case of the unirradiated specimens, a small reduction, by $\sim 20\,\%$, is seen at room temperature with an increase in hydrogen content from 200 to

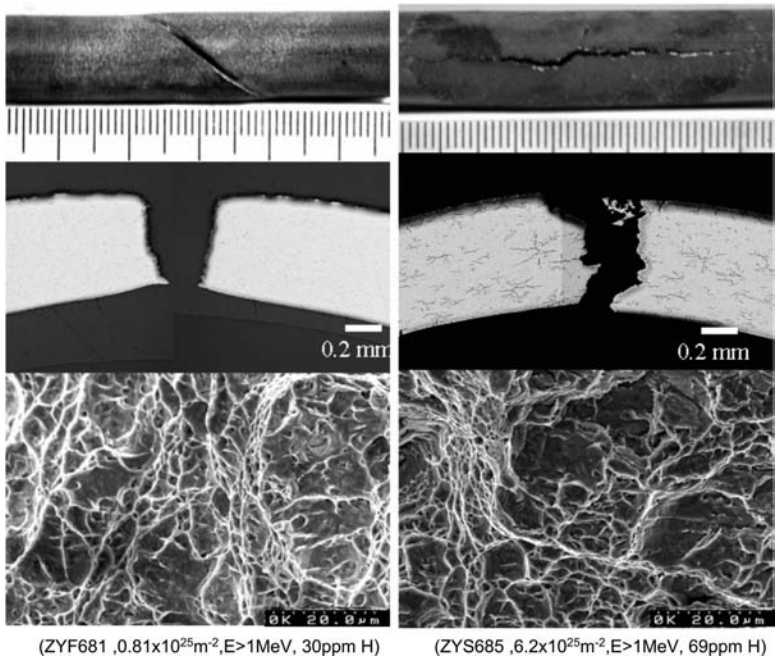


FIG. 9—*Photographs showing difference in fracture mode of the as-irradiated specimens with different neutron fluences.*

1000 wt ppm. However, very little or no reduction is seen above 150°C. The room temperature data for the irradiated specimens are not very different from those for the unirradiated specimens. These data show that hydrogen concentration up to around 600 wt ppm has little effect on the UTS of the tube specimens at the operating temperature of the fuel rods (about 350°C).

The literature data from the closed end burst test at room temperature (open circle) and 350°C (open triangle) for irradiated fuel cladding [41] are superimposed on the figure. From the comparison with these data, the hydrogen concentration dependence on strength is negligible except at room temperature. This implies that the strength of hydrides (circumferential uniform) at 150, 250 and 350°C should be no less than that of Zircaloy matrix, and the tube strength is mainly controlled by the alloy matrix.

The hydrogen concentration dependences of the failure elongation are shown in Fig. z11. The data are for mostly circumferential hydride distribution. The broken lines in these figures are intended as an indication of the rough trend of the observed behavior. Contrary to the small scatter on strength in Fig. 10, the elongation has large scatter band as shown in Fig. 11. This can be explained as follows: While failure elongation is determined by many factors such as plastic deformation mode, hydride morphology, and localized strain concentration during plastic deformation process, the failure strength depends on only two factors: Maximum pressure and area of specimen cross section.

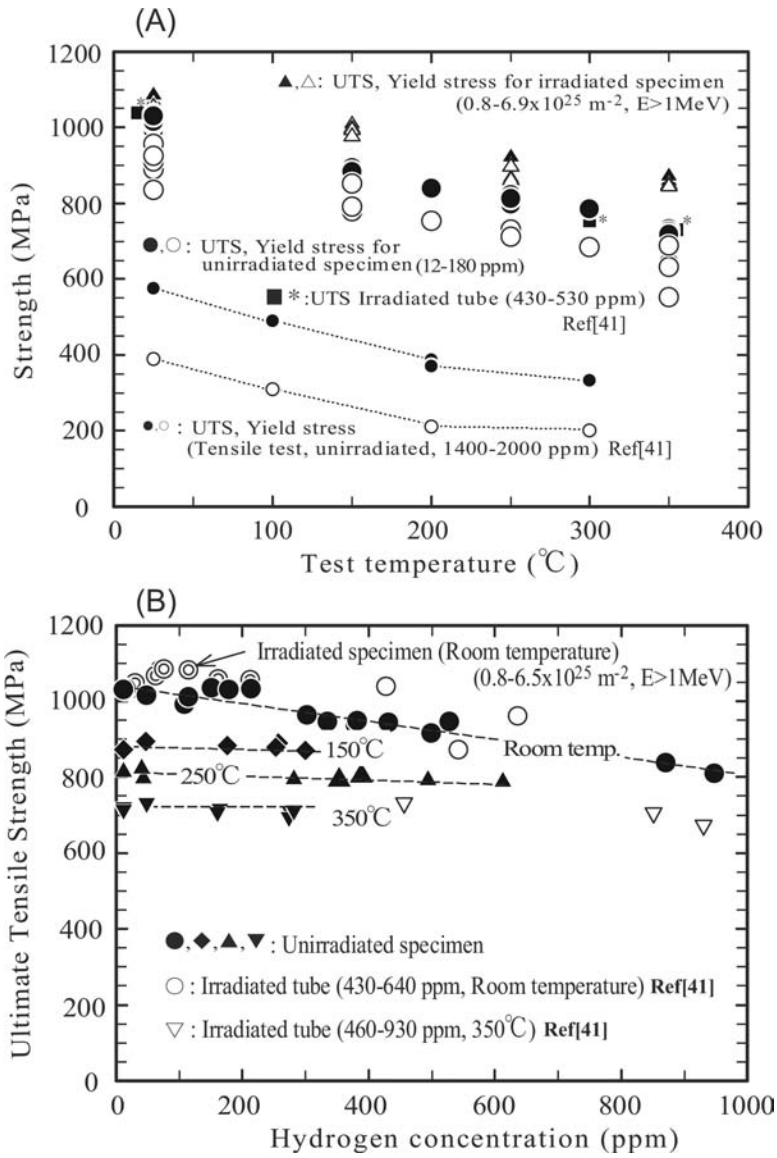


FIG. 10—*Effect of test temperature* (a*), and hydrogen concentration* (b*) on strength (hydride distribution: Circumferential uniform).*

The data at low temperatures (room temperature and 150°C) and higher temperatures (250 and 350°C) are presented on separate plots for greater clarity. At room temperature, in the case of the unirradiated material, no significant effect of hydrogen is seen up to ~ 200 wt ppm; there is then a sharp drop in the elongation from ~ 6% to less than 1 % with increase in hydrogen

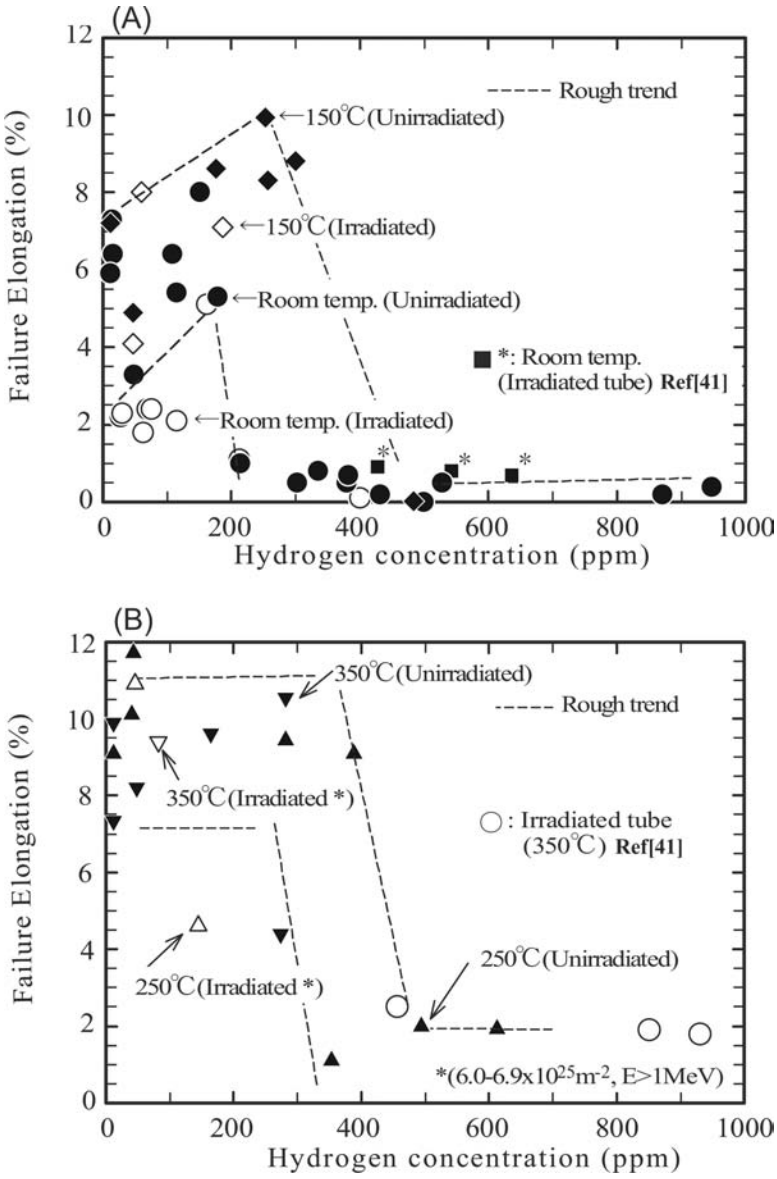


FIG. 11—*Hydrogen concentration dependence of failure elongation at low* (a) *and high* (b) *test temperatures (hydride distribution: Circumferential uniform).*

concentration. At 150°C, there is an increase initially from 8 to 10 % in elongation up to ~ 200 wt ppm followed by a sharp decrease to 0 % with an increase in hydrogen content. Initial plateau in failure elongation is followed by a sharp decrease at 250 and 350°C. A similar plateau was also observed in a previous

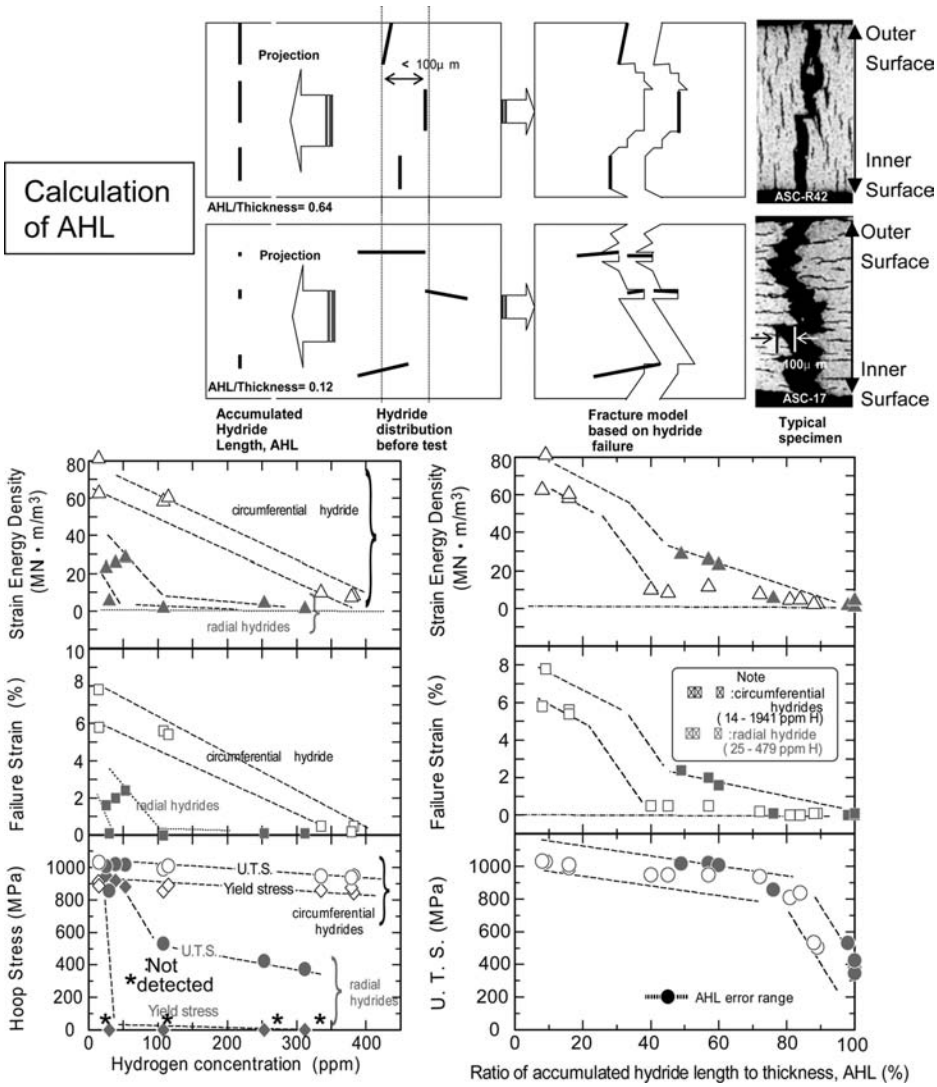


FIG. 12—*Effect of hydrogen concentration (lower left), AHL dependence (lower right), and illustrative representation of AHL (upper).*

investigation [46]. One possible interpretations of the behavior could be the many incipient cracks induced by the hydride cracking. In the case of the irradiated specimens, trends could not be established because of the limited data.

Effect of Hydride Orientation on Mechanical Properties

The results obtained at room temperature for the specimens with radial hydrides are compared with those of the specimens with circumferential

hydrides in Fig. 12 (lower left), which indicate a more significant reduction in the strength and ductility for the specimens with radial hydrides. To interpret this significant degradation in the mechanical properties with radial hydrides, a simple model is proposed in which the accumulated hydride length (AHL) that is projected to the specimen thickness (radial direction) controls the failure, as illustrated in the same Fig. 12 (upper panel). In the figure, the area to be analyzed is assumed to be the tube thickness by 100 μm in the circumferential direction, based on consideration of the spacing between hydrides in the metallographic images.

To calculate the hydride length and orientation, each hydride on the cross section image is copied on a transparent paper and is converted to the AHL for the unit area (tube thickness by 100 μm). The AHL obtained in this manner has the characteristic that its value increases as a function of hydrogen content and/or fraction of hydrides. The ratios of AHL to the specimen thickness were measured and depicted against the mechanical properties data in the bottom right of Fig. 12. In the figure, to avoid large scatter due to the superimposition of different materials data (unirradaited and irradiated specimens), only the results from unirradiated are analyzed.

It is seen from the figure that ductility is sensitive to the accumulated length of hydride in the specimen thickness direction (which is perpendicular to the main loading direction). For example, if 20 % of the thickness was covered by hydrides (i.e., AHL equals 20 %), ductility begins to decrease, whereas the strength starts to drop from AHL as high as 80 %, which consequently means that the strength is less sensitive to hydride orientation and/or content than ductility. Also, the mechanical properties plotted against the percent of AHL bring closer together the data from the tests performed on the specimens with circumferential and radial hydrides. This indicates that the AHL perpendicular to loading direction is a better criterion than the mean hydrogen content to describe the influence of hydrides on the mechanical properties. In Fig. 12, we can see slightly lower values of failure properties for a similar AHL in the presence of circumferential hydrides than in the presence of radial hydrides. This suggests that the proposed AHL criterion is not complete and other considerations such as hydride morphology and volume may also be important.

From these results, it can be concluded that the hydride orientation, with respect to stress direction, rather than the average hydrogen concentration, plays an important role in fuel cladding failure behavior. The result is consistent with the previously reported results obtained at lower strain rates [21,44].

Strain Hardening Exponent of Fuel Cladding Under Reactivity Initiated Accident Condition

The plastic deformability of the fuel cladding is one of the major considerations in the failure criteria under the strain controlled loading in the RIA situation. Since the strain controlled loading with the constant high strain rate is difficult to implement in separate effects laboratory experiments, the pressure controlled burst testing technique was employed as an alternative in this study.

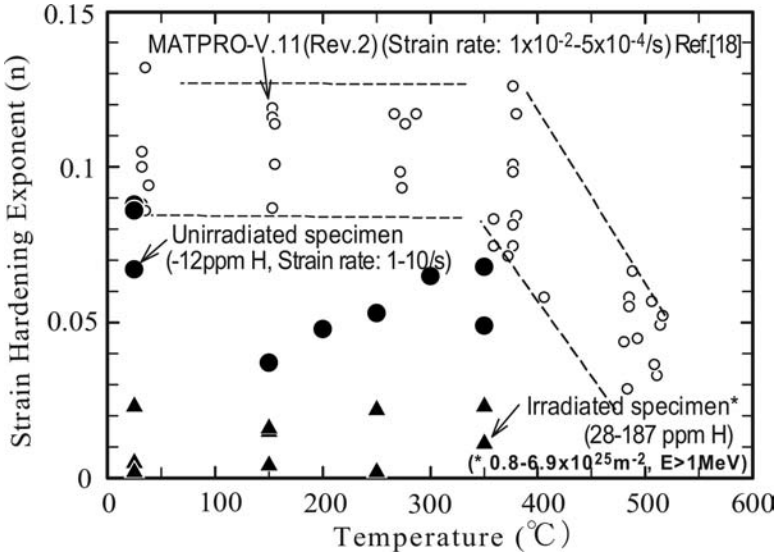


FIG. 13—*Effect of test temperature and strain rate on strain hardening exponent* (n).

As the failure elongation of the tube specimen can be evaluated from the strain hardening exponent (n) by using the plastic instability theory, it is is one of the most important material properties parameter. In this study, the n-value were obtained from the testing performed under high deformation rate loading conditions similar to those generated during a RIA incident, addressing an important lack of such data reported in the literature.

Our data on this exponent (n) for unirradiated as-received specimens are shown as a function of temperature in Fig. 13 and compared with similar data given in MATPRO, Rev. 2 [18]. The latter data were obtained from conventional testing under low strain rates (1.3×10^{-2}–$5 \times 10^{-4}\ s^{-1}$) and from longitudinal tension testing of the fuel cladding [18]. Since in this study a strain rate of around $1\ s^{-1}$ was applied, it can be said that such high strain rates reduce the n-value considerably. Another investigation [40] has also shown that the strain hardening rate of irradiated Zircaloy-2 plate decreased with the increase of strain rates.

The strain hardening in the circumferential direction is reported to be lower than that in the axial direction (Fig. 5 in [23, Fig. 7 in [39). Thus, a part of the reduction in n-value may be attributed to the loading direction, which is circumferential tensile in this study, compared to the axial tensile for MATPRO data. The strain rate dependence of the strain hardening ability has not been studied in detail. However, one can infer from the reduced failure strain (Fig. 4 in [35) that the increased stress or strain concentration at the tip of incipient crack of the specimen can likely accelerate the cracking rates during the high strain rate deformation that led a drop in the load-bearing ability and n-value.

The effect of neutron fluence on the exponent, n, obtained in this study is summarized in Fig. 14. The data for unirradiated and irradiated specimens in

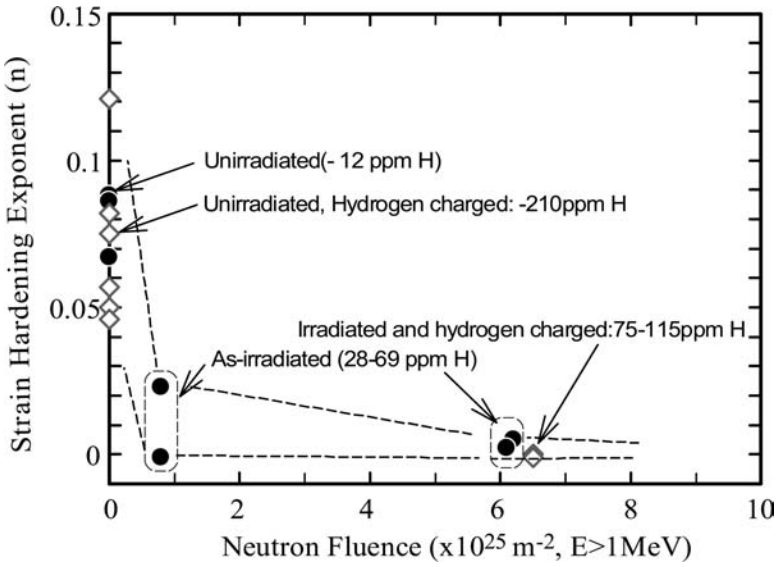


FIG. 14—*Effect of neutron fluence on strain hardening exponent (n) at room temperature.*

the as-received and hydrogen charged up to 200 wt ppm conditions are shown. Neutron irradiation reduces the n-values to less than 0.01 after 6×10^{25} nm^{-2} ($E > 1$ MeV), and most of the reduction is complete after even one cycle irradiation (0.8×10^{25} nm^{-2}, $E > 1$ MeV). Similar reduced strain hardening rate with neutron irradiation is also shown in [40. The data with hydrogen addition (open diamonds in Fig. 14) show the tendency that the strain hardening ability of both unirradiated and irradiated fuel cladding decreases as a function of the hydrogen content. From these results, it can be concluded that the plastic instability theory would be too conservative for the evaluation of failure strain under the RIA condition, because practically no strain hardening would be anticipated for irradiated materials with n-values lower than 0.01.

Effects of Temperature and Hydrogen Concentration on Strain Energy Density

The SED is regarded as one of the useful material parameters for the failure criteria of fuel rods under the RIA condition [11]. The maximum SED results for unirradiated, and irradiated cladding from the present investigation are shown in Fig. 15. The SED values for the irradiated material are lower than that for the unirradiated material at room temperature, while at 150–350°C no significant difference is seen. A large scatter is seen in this temperature range in the Fig. 15, as SED is the integrated value of stress multiplied by strain up to failure. Another index, fracture toughness, also shows a temperature-sensitive region at between 250 and 350°C [47].

The dependence of SED on hydrogen concentration, obtained in this study, is compared with the results formerly reported for an irradiated BWR fuel

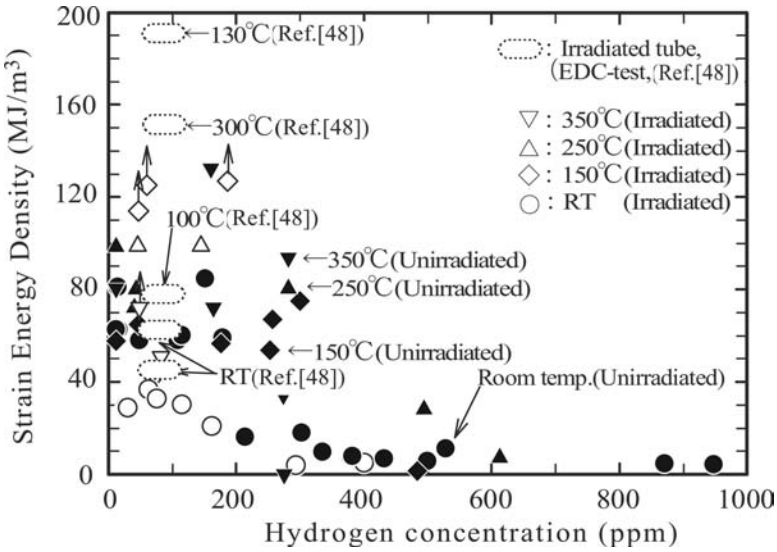


FIG. 15—*Effect of hydrogen concentration and test temperature on SED (hydride distribution: Circumferential uniform).*

cladding (40–42 GWd/t) with hydrogen concentration of around 60–130 wt ppm [48]. At room temperature, the SED obtained showed a relatively good agreement with [48 data. To clarify the relatively large scatter both in [48]. and in Fig. 15, additional tests remains to be explored in more depth.

Reduced Ductility of Irradiated Material

In the conventional data from the standard strain rate tests of around 10^{-4}/s to 10^{-2}/s, the ductility of fuel cladding is reduced with neutron irradiation (Figs. 4–12 in [49). There are many reasons for such ductility loss; irradiation hardening of Zircaloy matrix due to the accumulation of irradiation damage is one. Irradiation induced damage (Fig. 14 in [34) is swept out by the formation of dislocation channeling, which is induced by mobile dislocations such as slip or twins [50]. Therefore, the flow stress is rapidly reduced during the plastic deformation, resulting in a low strain hardening behavior [40].

As shown in Fig. 12, the fracture of hydrides in the specimen material also plays an important role in ductility loss. Considering both the transgranular hydrides observed in Fig. 1 and the rough surface in the right panel of Fig. 8, it is seen that the brittle fracture surface predominantly consists of transgranular quasi-cleavage facets induced by fracture of the hydride on or near the basal plane of $\alpha - Zr$, since the habit planes of the δ-phase Zr hydrides, which were precipitated within the α-phase Zr, are reported to be $(0001)_\alpha \parallel (111)_\delta$ [51].

More importantly, on the one hand, as can been seen on the right panel in Fig. 9, as-irradiated specimens with even as low a hydrogen concentration as 69 wt ppm failed to show the fracture surfaces of mixed quasi-cleavage facets and

ductile dimples. On the other hand, the fracture surfaces obtained from the axial tensile tests on irradiated tube specimen under slow strain rate are dominantly covered with ductile dimples [38]. Thus, this difference in the fracture morphology can be attributed to both the differences in the loading direction (axial or circumferential direction) and strain rate. The macroscopic failure mode for the axial and circumferential loading is shear [38] and axial split (Fig. 9), respectively.

Effect of Deformation Mode on Failure Elongation

Generally, the ductility of the material drops with the increase of neutron fluences. Contrary to that trend, the failure strain of the specimen ZYF-681 with low neutron fluence (0.81×10^{25} nm^{-2}; $E > 1$ MeV) was 2.3 %. Although this value is not large, it is almost the same as that for ZYS-685 with higher neutron fluence of 6.2×10^{25} nm^{-2}; $E > 1$ MeV. Comparisons of the outer surface appearance, cross sectional view, and fracture surfaces between the two specimens are made in Fig. 9. Both fracture surfaces are similar, but the surface of the lower neutron fluence specimen (ZYF) is completely covered with ductile dimples. This implies that the matrix ductility of ZYF will be slightly higher than that of ZYS. A clearer difference between the two specimens is the macroscopic deformation mode at failure; the typical spiral type failure for ZYF-681 and the zigzag axial split for ZYS-685. It has been reported that the macroscopic failure elongations are reduced with localized shear deformation compared to that with uniform deformation mode [38]. Accordingly, it can be said that ZYF-681 failed with axially localized through-thickness shear deformation at low diametric plastic deformation.

Conclusions

The present investigation and analysis produced complete sets of mechanical properties including nominal stress-strain, true stress-true strain, strength coefficient, and strain hardening exponent for irradiated and unirradiated materials Zircaloy-2 materials. The key conclusions are as follows.

(1) The unique experimental design of open-end rapid burst tests to impose a high strain rate of around 1 s^{-1} in the hoop direction is well-suited for a separate effects RIA test for unirradiated and irradiated fuel cladding materials. The methods for additional hydrogen charging with circumferential and radial hydrides have been developed.

(2) The mechanical properties of unirradiated cladding are as follows.
   (a) With an increase in hydrogen concentration at a given temperature and with an increase in temperature at a given hydrogen concentration, the yield stress and the ultimate tensile strength decreased gradually and nearly linearly. This was the case for both circumferential and radial uniform distributions of hydrides.
   (b) With an increase in hydrogen content up to $\sim$ 100 wt ppm, the failure elongation was nearly unchanged or increased slightly, but decreased drastically at $\sim$ 400 wt ppm to values approaching 0 %.

(c) Cracks propagated axially in a slight zigzag fashion which is attributed to cracking at hydride locations.
(d) The radial hydrides had a pronounced effect when compared to circumferential hydrides at comparable total hydrogen contents. A drastic reduction in failure strain and SED occurred at a hydrogen concentration of $\sim$ 100 wt ppm in the case of radial hydrides to be compared to $\sim$ 200–400 wt ppm for circumferential hydrides.
(e) The fraction of the specimen thickness occupied by the accumulated length of hydrides in the radial direction at fracture site is found to be a better indicator of the mechanical properties than hydrogen concentration.

(3) The mechanical properties of irradiated cladding are as follows.
(a) At room temperature, the failure strain for the low fluence material was nearly the same as for the intermediate fluence material. This is interpreted to be due to the different failure modes observed, i.e., a spiral mode for the low fluence material and an axial splitting for the intermediate fluence.
(b) The SED data obtained agree reasonably well with those reported in the literature.
(c) The values of the strain hardening exponent were extremely small indicating that the plastic instability theory is not appropriate to evaluate failure strain under RIA conditions.
(d) Most hydrides were observed to be transgranular, which led to fracture surface with transgranular quasi-cleavage facets.

Acknowledgments

The work was performed under the auspices of the EPRI-led NFIR Program. The writers acknowledge technical inputs from NFIR members and thank them for permission to publish the results. Many discussions with Drs. K. Ogata, N. Waeckel, and N. Ramasubramanian during the course of the experimental program were very useful and are thankfully acknowledged.

References

[1] Kim, J. H., Lee, M. H., Jeong, Y. H., and Lim, J. G., "Behavior of Zirconium Fuel Cladding Under Fast Pressurization Rates," *Nucl. Eng. Des.*, Vol. 238(6), 2008, pp. 1441–1447.
[2] Fuketa, T. et al, *26th Water Reactor Safety Information Meeting*, Bethesda, MD, October 26–28, 1998.
[3] Fuketa, T. *et al.*, *27th Water Reactor Safety Information Meeting*, Bethesda, MA, October 25–27, 1999.
[4] Suzuki, M., Saitou, H., and Fuketa, T., "RANNS Code Analysis on the Local Mechanical Conditions of Cladding of High Burnup Fuel Rods under PCMI in RIA-Simulated Experiments in NSRR," *J. Nucl. Sci. Technol.*, Vol. 43(9), 2006, pp. 1097–1104.

[5] Nakamura, T., Fuketa, T., Sugiyama, T., and Sasajima, H., "Failure Thresholds of High Burnup BWR Fuel Rods Under RIA Conditions," *J. Nucl. Sci. Technol.*, Vol. 41(1), 2004, pp. 37–43.

[6] Ichikawa, M., "High Burnup Fuel R&D in Japan," *IAEA Proceedings of a Technical CommitteeMmeeting*, San Carlos de Bariloche, Argentina, 1999, pp. 15–19.

[7] IAEA-TECDOC-1299, 2002, "Technical and Economic Limits to Fuel Burnup Extension," *Proceedings of a Technical Committee Meeting*, Argentina, November 1999, Viena.

[8] Schmitz, F. and Papin, J., "High Burnup Effects on Fuel Behaviour Under Accident Conditions: The Tests CABRI REP-Na," *J. Nucl. Mater.*, Vol. 270(1–2), 1999, pp. 55–64.

[9] Schmitz, F., Papin, J., Haessler, M., and Waeckel, N., "New Results from Pulse Tests in the CABRI Reactor," *Proceedings of the U.S. Nuclear Regulatory Commission, Twenty-Third Water Reactor Safety Information Meeting, NUREG/CP-0149*, Vol. 1, March 1996, USNRC, pp. 33–43.

[10] Fuketa, T., Ishijima, K., and Mori, Y., "New Results from the NSRR Experiments with High Burnup Fuel," *Proceedings of the U.S. Nuclear Regulatory Commission, Twenty-Third Water Reactor Safety Information Meeting, NUREG/CP-0149*, Vol. 1, 1996, USNRC, pp.45–63.

[11] Montgomery, O. R., Rashid, R. Y., Ozer, O. *et al.*, "Assessment of RIA-Simulation Experiments on Intermediate- and High Burnup Test Rod," *Nucl. Saf.*, Vol. 37(4), 1996, pp. 372.

[12] Link, M. T., Koss, A. D., and Motta, T. A., "On the Influence of an Embrittled RIM on the Ductility of Zircaloy Cladding," *ANS Topical Meeting*, Portland, 1997, p. 634.

[13] Udagawa, Y., Suzuki, M., Sugiyama, T., and Fuketa, T., "Stress Intensity Factor at the Tip of Cladding Incipient Crack in RIA-Simulating Experiments for High-Burnup PWR Fuels," *J. Nucl. Sci. Technol.*, Vol. 46(10), 2009, pp. 1012–1021.

[14] Suzuki, M., Saitou, H., and Fuketa, T., "Analysis on Split Failure of Cladding of High Burnup BWR Rods in Reactivity-Initiated Accident Conditions by RANNS Code," *Nucl. Eng. Des.*, Vol. 236(2), 2006, pp. 128–139.

[15] Jernkvist, L. O., Massih, A. R., and Rudling, P., "A Strain-Based Failure Criterion for Reactivity Initiated Accidents in Light Water Reactors," *SKI Report No.* 2004:32, August 2004.

[16] Glendening, A., Koss, D. A., Motta, A. T., Pierron, O. N., and Daum, R. S., "Failure of Hydrided Zircaloy-4 Under Equal-Biaxial and Plane-Strain Tensile Deformation," *J. ASTM Int.*, Vol. 2(6), 2005, pp. 833–850.

[17] Link, T. M., Koss, T. A., and Motta, A. T., "Failure of Zircaloy Cladding Under Transverse Plane-Strain Deformation," *Nucl. Eng. Des.*, Vol. 186, 1998, pp. 379–394.

[18] *MATPRO-Version 11 (Revision 2); NUREG/CR-0497, TREE-1280, Rev. 2*. (1981). A Handbook of Materials Properties for Use in the Analysis of Light Water Reactor Fuel Rod Behavior.

[19] Grigoriev, V., Jakobsson, R., and Schrire, D., "Experimental Evaluation of Critical Strain Energy Density for Irradiated Cladding Under Simulated RIA Conditions," *Proc. of ENS Topfuel 2001*, Stockholm, Sweden, May 2001.

[20] Dufourneaud, O., Varias, A. G., Grigoriev, V., Jakobsson, R., and Schrire, D. "Elastic-Plastic Deformation of a Nuclear Fuel Cladding Specimen Under the Internal Pressure of a Polymer Pellet," *Proc. of Fifth World Congress on Computational Mechanics*, Vienna, Austria, July 7–12, 2002.

[21] Daum, R. S., Majumbdar, S., Liu, W., and Billone, M. C., "Radial-Hydride Embrittlement of High-Burnup Zircaloy-4 Fuel Cladding," *J. Nucl. Sci. Technol.*, Vol. 43(9), 2006, pp. 1054–1067.

[22] Le Saux, M., Besson, J., Carassou, S., Poussard, C., and Averty, X., "Behavior and Failure of Uniformly Hydrided Zircaloy-4 Fuel Claddings Between 25°C and 480°C Under Various Stress States, Including RIA Loading Conditions," *Eng. Failure Anal.*, Vol. 17(3), 2010, pp. 683–700.

[23] Daum, R. S., Majumdar, S., Tsai, H., Bray, T. S., Koss, D. A., Motta, A. T., and Billone, M. C., "Mechanical Property Testing of Irradiated Zircaloy Cladding Under Reactor Transient Conditions," *ASTM Spec. Tech. Publ.*, Vol. 1418, 2002, pp. 195–210.

[24] Cazalis, B., Desquines, J., Poussard, C., Petit, M., Monerie, Y., Bernaudat, C., Yvon, P., and Averty, X., "The PROMETRA Program: Fuel Cladding Mechanical Behavior Under High Strain Rate," *Nucl. Technol.*, Vol. 157, 2007, pp. 215–229.

[25] OECD(NEA), "Nuclear Fuel Behaviour Under Rectivity-Initiated Accident (RIA) Conditions, State-of the Art Report," *Report No.* NEA/CSNI/R(2010)1, NEA No. 6874, NEA/CSNI/R(2010)1, 2010, ISBN 978-92-64-99113-2.

[26] Bates, D. W., Koss, D. A., and Motta, A. T., "Influence of Specimen Design on the Deformation and Failure of Zircaloy Cladding," *ANS Topical Meeting on LRW Fuel Performance*, April 10–13,, 2000, Park City, USA, pp. 296–305.

[27] Yunchang, F. and Koss, D. A., "The Influence of Multiaxial States of Stress on the Hydrogen Embrittlement of Zirconium Alloy Sheet," *Metall. Trans. A*, Vol. 16, 1985, pp. 675–681.

[28] ASTM B353-91, *Annual Book of ASTM Standards*, Vol. 02.04, ASTM International, West Conshohocken, PA, pp. 171–184.

[29] Yamamoto, H., "Manufacturing Process and Quality Control for Zircaloy Tubes," *Chemical Economy & Engineering Review*, Vol. 3(3), 1971, pp. 19.

[30] Kearns, J. J., "Thermal Expansion and Preferred Orientation in Zircaloy," *Report No.* WAPD-TM-472, Nov. 1, 1965.

[31] Rosenbaum, S. H., "Use of Pole Figure Data to Compute Elasticity Coefficient of Zirconium Sheet," *J. Nucl. Mater.*, Vol. 67, 1977, pp. 273.

[32] Ogata, K. *et al.*, "BWR Fuel Performance and Recent R&D Activities in Japan," *ANS Topical Meeting on LWR Fuel Performance*, Portland, 1997, March 2–6, p. 287.

[33] Shimada, S., Etoh, Y., and Hayashi, H., "A Metallographic and Fractographic Study of Outside-in Cracking Caused by Power Ramp Tests," *J. Nucl. Mater.*, Vol. 327(2–3), 2004, pp. 97–113.

[34] Hayashi, H., Ogata, K., Baba, K., Kamimura, K., "Research Program to Elucidate Outside-in Failure of High Burnup Fuel Cladding," *J. Nucl. Sci. Technol.*, Vol. 43(9), 2006, pp. 1128–1135.

[35] Nakatsuka, M. *et al.*, "Mechanical Properties of High Burnup BWR Fuel Cladding Tubes Under Simulated RIA Conditions," *Proc. 2004 Inter. Meeting on LWR Fuel Performance*, Orland, 2004, September 19–22, Paper 1017.

[36] ASTM B811-90, 1995, "Standard Specification for Wrought Zirconium Alloy Seamless Tubes for Nuclear Reactor Fuel Cladding," *Annual Book of ASTM Standards*, Vol. 02.04, ASTM International, West Conshohocken, PA, pp. 743–756.

[37] Pettersson, K. *et al.*, "Effect of Irradiation on the Strength, Ductility, and Defect Sensitivity of Fully Recrystallized Zircaloy Tube," *ASTM Spec. Tech. Publ.*, Vol. 681, 1979, pp. 155–173.

[38] Yasuda, T., Nakatsuka, M., and Yamashita, K., "Deformation and Fracture Properties of Neutron-Irradiated Recrystallized Zry-2 Cladding Under Uniaxial Tension," *ASTM STP 939*, R.B. Adamson and L. F. P. Van Swam, Eds., ASTM International, West Conshohocken, PA, 1987, pp. 734–747.

[39] Bement, A. L., "Effect of Cold Work and Neutron Irradiation on the Tensile Properties of Zircaloy," *Report No.* HW-74955, AT(45-1)-1350, April 1, 1963, Vol. 2.

[40] Onchi, T., Kayano, H., and Higashiguchi, Y., "Effect of Neutron Irradiation on Deformation Behavior of Zirconium," *J. Nucl. Sci. Technol.*, Vol. 14(5), 1977, pp. 359–369.

[41] Yagnik, K. S., Hermann, A., and Kuo, R.-C., "Ductility of Zircaloy-4 Fuel Cladding and Guide Tubes at High Fluences," *J. ASTM Int.*, Vol. 2(5), 2005,.

[42] Kuroda, M., Yoshioka, K., Yamanaka, S., Anada, H., Nagase, F., and Uetsuka, H., "Influence of Precipitated Hydride on the Fracture—Behavior of Zircaloy Fuel Cladding Tube," *J. Nucl. Sci. Technol.*, Vol. 37(8), 2000, pp. 670–675.

[43] Bai, J. M., Prioul, C., and Francois, D., "Hydride Embrittlement in Zircaloy-4 Plate: Part I, Influence of Microstructure on the Hydride Embrittlement in Zircaloy-4 at 20°C and 350°C," *Metall. Mater. Trans. A*, Vol. 25, 1994, pp. 1185–1197.

[44] Chu, H. S., Wu, S. K., Chien, K. F., and Kuo, R. C., "Effect of Radial Hydrides on the Axial and Hoop Mechanical Properties of Zircaloy-4 Cladding," *J. Nucl. Mater.*, Vol. 362, 2007, pp. 93–103.

[45] Nagase, F. and Fuketa, T., "Influence of Hydride Re-Orientation on BWR Cladding Rupture Under Accidental Conditions," *J. Nucl. Sci. Technol.*, Vol. 41(12), 2004, pp. 1211–1217.

[46] Nagase, F. and Fuketa, T., "Investigation of Hydride Rim Effect on Failure of Zircaloy-4 Cladding with Tube Burst Test," *J. Nucl. Sci. Technol.*, Vol. 42(1), 2005, pp. 58–65.

[47] Chung, H. M. and Kassner, T. F., "Cladding Metallurgy and Fracture Behavior During Reactivity-Initiated Accidents at High Burnup," *Nucl. Eng. Des.*, Vol. 186, 1998, pp. 411–427.

[48] Grigoriev, V. *et al.*, "Temperature Effect on BWR Cladding Failure Under Mechanically Simulated RIA Conditions," *Proceedings of Fuel Safety Research Specialists' Meeting, JAERI-Conf 2002–009*, March 4–5, 2002, pp. 97–106.

[49] Yamashita. K. *et al.*, "Effects of the Mechanical Properties of Recrystallized Zircloy-2 Cladding," *IAEA Specialists' Meeting on Post Irradiation Examination and Experience*, Tokyo, Japan, November 1984, Tokyo, Japan, pp.26–30.

[50] Garde, A. M., Smith, G. P., and Pirek, R. C., "Effects of Hydride Precipitate Localization and Neutron Fluence on the Ductility of Irradiated Zircaloy-4," *ASTM Spec. Tech. Publ.*, Vol. 1295, 1996, pp. 407–430.

[51] Une, K., Nogita, K., Ishimoto, S., and Ogata, K., "Crystallography of Zirconium Hydrides in Recrystallized Zircaloy-2 Fuel Cladding by Electron Backscatter Diffraction," *J. Nucl. Sci. Technol.*, Vol. 41(7), 2004, pp. 731–740.

DISCUSSION

Question 1, C. E. Coleman, Atomic Energy of Canada Limited, Canada:—Please comment on whether fixed-end loading would represent your stress state more fully. With fixed-end internal pressurization, texture strengthening is very large, especially if fr is high. Such loading would have consequence for both strength and ductility.

Author's Response:—The approach in this study was to perform uniaxial tensile test to obtain the constitutive equation of the test material. For application under bi-axial (or multi-axial) stress conditions, the texture hardening, as you pointed out, should be taken into account. While this effect can be significant for unirradiated Zircaloys, it decreases with the neutron fluence. Experimental and theoretical studies for irradiated Zircaloys (e.g., Nakatsuka et al.: J. Nucl. Sci. Tech., 24 [10], p. 832 (1987)., idem 24 [11], p. 906 (1987).) have shown almost equivalent strength as estimated from the Mises' equation for isotropic material.

Question 2, Arthur Motta, Penn State University, PA, USA:—1) Previous studies have not shown much effect of strain rate on failure strain. Have you performed tests at low strain rate for comparison? 2) You see very low levels of failure strain for low levels of H when tested at high temperature. Would not the hydrogen be in solution? 3) The special failures that you observe do not appear to be the representative of real loading.

Author's Response:—1) Yes, the results of the open end burst tests under strain rates ranging from 10^{-1} to 10^{3} %/s for unirradiated specimens (Nakatsuka, et al.: Proc. Int. Meeting on LWR Fuel Performance, Paper 1017 (2004).) showed that the failure strain of the specimens decreased significantly with the increase in strain rate.

2) The failure strains at each test temperature are discussed in terms of TSSD/TSSP in the paper, however no clear trend was found in our results.

3) The purpose of our investigation was to obtain constitutive equation of Zircaloy fuel cladding so that the results can be used as input data for the analysis under the real loading of fuel cladding in reactors.

Question 3, Johannes Bertsch, Paul Scherrer Institute, Villigen, Switzerland:—The failure strain is supposed to be measured rather globally. Do you have indications about a non-homogeneous strain distribution at failure, may be in dependence on the microstructure (radial/circumferential hydriding)? May it be that the measured strain rate has to be considered with respect to this potential inhomogeneity?

Author's Response:—In all the specimens that failed in ductile mode, local deformation or non-homogeneous strains with shear slippage were observed to various degrees. Generally, it seems that the slip in the specimen thickness direction (which results in thickness reduction) was dominant for unirradiated specimens. On the other hand for irradiated specimens, the slip is in the circumferential direction and forms shear bands oriented to around 45 degrees from the tube outer surface. Due to the practical difficulty in quantifying in-situ local deformation in the tube, local strain rate was not taken into account but average post-test diametral increment was considered.

Question 4, Young Suk Kim, KAERI, Yuseong-gu, Daejeon, Korea:—Please comment on a rapid decrease of the strain hardening coefficient above 300 or 350°C.

Author's Response:—In the temperatures range of 300 or 350°C in the conventional slow strain rates tests, hardening by the strain aging mechanism saturates and the thermal recovery of the dislocation

damage that is induced by the plastic deformation cannot be disregarded. Thus, around this temperature range, apparent activation energy for deformation decreases and consequently strain hardening is also decreased.

Question 5, Sébastien Carassou, CEA, France:—When testing a material in "stress-controlled" mode, the apparent ductility is lower than in "displacement–controlled" mode, due to plastic instability. Your testing is performed in "S-C" mode. However, RIA issues concern "D-C" mode (due to PCMI). So have you an idea or how to take this difference into account when using your data to address RIA issues?

Author's Response:—As you indicated, test results from this study can not be directly applied to predict the failure strain under RIA condition. However, constitutive equation obtained in this study should be applicable to other failure criteria such as the critical strain energy density or critical stress levels.

Reprinted from JAI, Vol. 7, No. 6
doi:10.1520/JAI102938
Available online at www.astm.org/JAI

Kan Sakamoto,[1] *Masafumi Nakatsuka,*[1] *and Toru Higuchi*[1]

Simulation of Outside-in Cracking in Boiling Water Reactor Fuel Cladding Tubes under Power Ramp

ABSTRACT: In power ramp tests, some high burn-up boiling water reactor (BWR) fuels failed by outside-in cracking. After detailed post irradiation examinations, it was deduced that fracture of radially oriented hydrides precipitated at the outer surface had resulted in the formation of incipient radial cracks that propagated towards the inner surface. Since crack propagation is a key process that dominates the outside-in failure, experimental data of outside-in cracking are obviously required. The objective of the present study is to evaluate the threshold conditions and the velocity of the outside-in cracking during a power ramp to assess the integrity of BWR fuels during a power ramp. In the experiments, by using unirradiated Zry-2 fuel cladding tubes, the outside-in cracking was examined both with and without the thermal gradient. Without the radial thermal gradient, there was no radial delayed hydride cracking in all experimental conditions examined. On the other hand, with the radial thermal gradient, the velocity of the outside-in cracking was significantly higher than that expected from the data obtained under the isothermal condition in our previous study. The threshold depth of the incipient crack was found to be $\sim$0.1 mm at the hoop stress of 300 MPa. It was suggested that the outside-in cracking during the power ram\p is strongly dependent on the distribution of dissolved hydrogen as a result of the thermal diffusion.

KEYWORDS: fuel cladding tube, delayed hydride cracking, Zry-2, high burn-up, hydrogen, hydride, outside-in failure, thermal gradient, thermal diffusion

Manuscript received December 26, 2009; accepted for publication April 27, 2010; published online June 2010.
[1] Nippon Nuclear Fuel Development Co., Ltd., 2163 Narita-cho, Oarai-machi, Ibaraki-ken 311-1313, Japan.

Cite as: Sakamoto, K., Nakatsuka, M. and Higuchi, T., "Simulation of Outside-in Cracking in Boiling Water Reactor Fuel Cladding Tubes under Power Ramp," *J. ASTM Intl.*, Vol. 7, No. 6. doi:10.1520/JAI102938.

Copyright © 2011 by ASTM International, 100 Barr Harbor Drive, PO Box C700, West Conshohocken, PA 19428-2959.

Introduction

The outside-in cracking of the high burn-up boiling water reactor (BWR) fuel cladding tubes is of practical and scientific interest. It has been indicated that the radial incipient crack on the outer surface would grow towards the inner surface of the fuel cladding tubes by the delayed hydride cracking (DHC) [1,2]. An important characteristic of the cracking during the outside-in failure is that the crack grows in the radial direction of the fuel cladding tube with the thermal gradient. An increase of the thermal gradient caused by the power ramp induces the thermal diffusion of hydrogen from the inner part to the outer part of the fuel cladding tubes. Therefore, the DHC occurs under the flow of hydrogen. Sagat et al. demonstrated using DHC tests in the axial direction [3] that a thermal gradient enhanced DHC. Their result implies that the thermal gradient is an important factor for the assessment of fuel integrity during the power ramp.

To assess the fuel integrity during the power ramp, the threshold condition for crack growth and the time to penetrate the cladding wall thickness are required. In the DHC process, those important factors are characterized by the threshold stress intensity factor for DHC K_{IH} and the velocity of crack growth V_{DHC}. Several studies have been conducted on DHC [3–13], but little attention has been given to the effect of thermal gradients and the flow of hydrogen. Therefore, we developed an experimental technique to simulate the outside-in cracking of the fuel cladding tubes during the power ramp. In previous studies, we developed the technique to produce the outer-surface radial incipient crack (ORIC) on the fuel cladding tubes [13] and measured the K_{IH} and V_{DHC} for radial DHC under isothermal condition [14]. Here, the isothermal condition means no thermal gradient in the radial direction of the fuel cladding tubes during DHC. We have also reported the development of the experimental technique for the test with the radial thermal gradient by using "power ramp simulator" [14,15].

In the present study, by using the power ramp simulator, we performed the radial DHC test with the radial thermal gradient to clarify the effect of the radial thermal gradient on the cracking in the outside-in failure during the power ramp.

Experimental Procedures

Making of Outer-Surface Radial Incipient Cracks

Unirradiated cold-worked Zry-2 BWR fuel cladding tubes (Zr-lined 8 × 8 type) were cut into sections 110 mm long and charged with hydrogen in the range of hydrogen concentration between ~100 and 300 ppm by corrosion in a LiOH solution at 563 K. The fuel cladding tubes were the same as those used in our previous studies [13–15]. The yield stress in the axial direction of the unirradiated cold-worked material was ~580 MPa at 523 K [14], which was slightly less than that of the irradiated materials (620 MPa at 523 K) [16]. The chemical composition of the tubes is shown in Table 1. By applying a cyclic compressive load with the corrosive solution (I_2/CH_3OH) [17], a radial incipient crack was formed on the outer surface of the fuel cladding tube (hereafter, this incipient

TABLE 1—*Chemical composition of specimens used (in mass percent).*

Sn	Fe	Cr	Ni	O	Zr
1.36	0.18	0.11	0.07	0.122	Bal.

crack will be described as ORIC). The cyclic compressive load was applied along ~5 mm in the axial direction and maintained less than ~0.1 kN to prohibit an undue plastic deformation around the ORICs. The shape of the ORICs was a semi-elliptical type having a long major axis in the axial direction. The maximum depths of ORICs were between 0.05 and 0.15 mm. Figure 1 shows a typical micrograph of ORIC. It can be confirmed that a very sharp radial crack was formed on the outer surface of the fuel cladding tube. The lengths of the ORICs

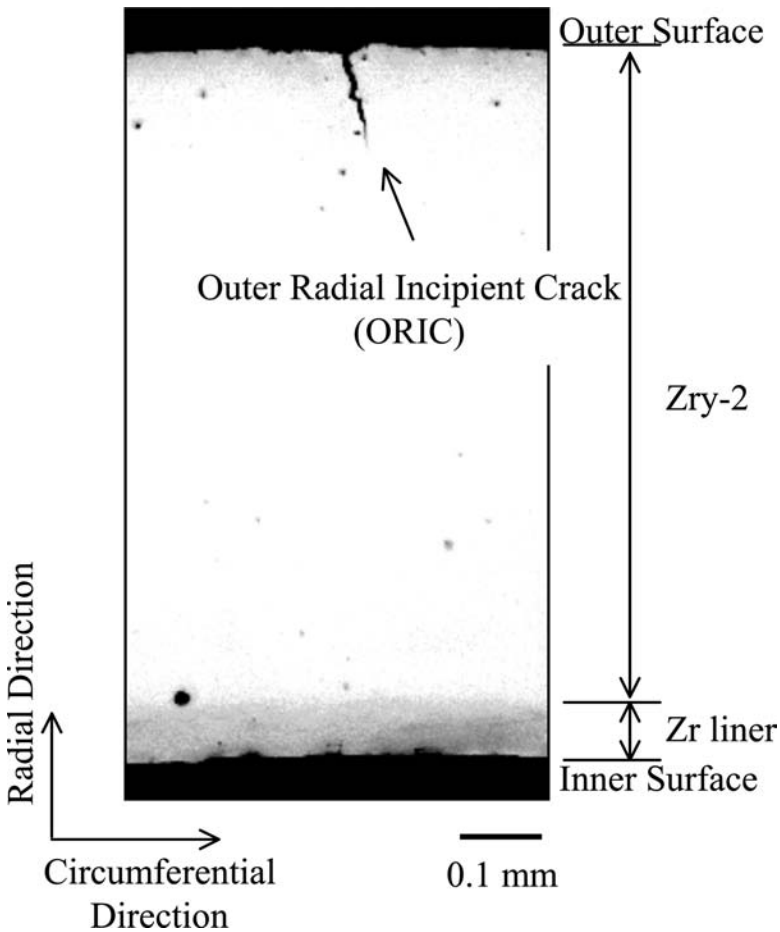


FIG. 1—*Micrograph of typical ORIC on the outer surface of fuel cladding tube (depth of ORIC was ~0.1 mm).*

were over 4 mm, so the depth to length ratio was less than 0.04, as has been already shown in the previous papers [13–15].

Radial Delayed Hydride Cracking Test with Radial Thermal Gradient

The specimen was assembled in the power ramp simulator [14,15,18]. The main components of the power ramp simulator are the internal heater, the coolant water system, and the water pump, as shown in Fig. 2. The middle of

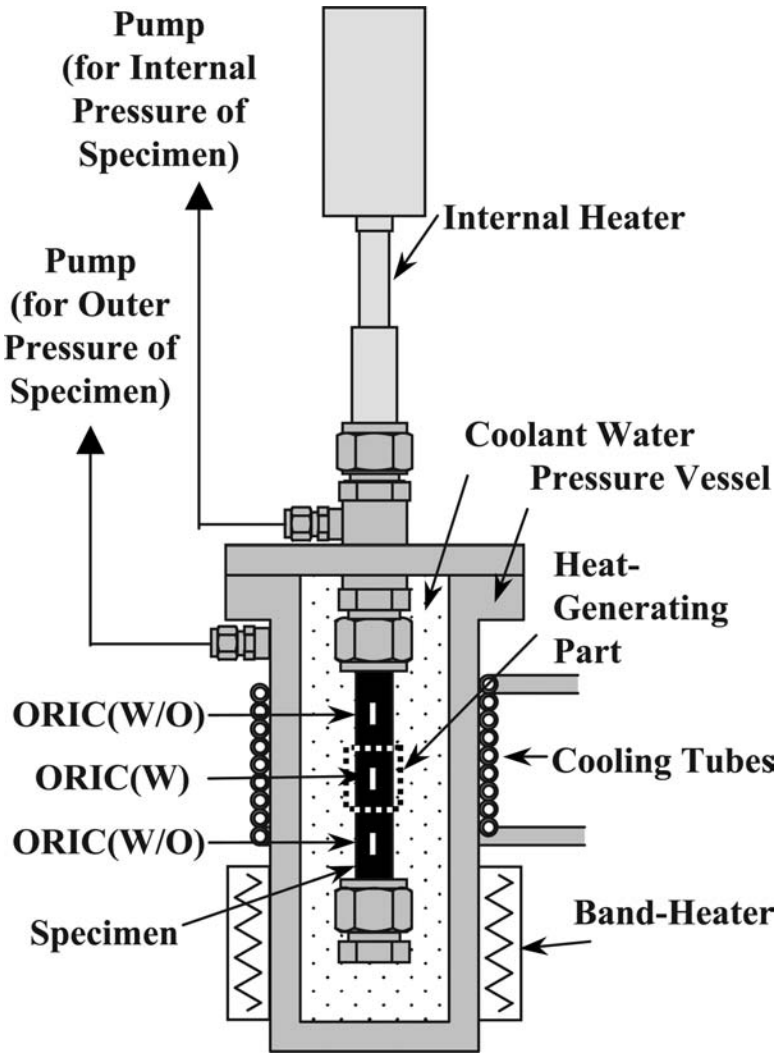


FIG. 2—*Schematic of experimental system, power ramp simulator, for radial DHC tests with radial thermal gradient (W/O: Without thermal gradient (non-heat-generating part); W: With thermal gradient (heat-generating part)).*

the specimen in the tube axial direction was heated by the internal heater that could generate a temperature difference up to ~65 K between the inner and the outer surfaces of the fuel cladding tubes used in the present study. To compare the radial cracking with and without the thermal gradient, the ORICs were formed at the heat-generating (with thermal gradient) and the non-heat-generating (without thermal gradient) parts of the specimen. The histories of the temperature at the outer surface of the specimen and the hoop stress are shown in Fig. 3. During the radial DHC test, the linear heat generation rate (LHGR) was maintained at 40kW/m (~60 K temperature difference between the inner and the outer surfaces). The hoop stress was increased up to 300 MPa ~0.5 h after the specimen temperature had stabilized at the DHC test temperature. During the DHC test, the temperature of the outer surface, T_{DHC}, and the hoop stress of the specimen, σ_θ, were 561 K and 300 MPa, respectively (Table 2). In order to examine the change of radial DHC with time, the duration of the DHC test t_{DHC} was varied from 0 to 1 h. After the radial DHC test, the fracture surface was observed by optical

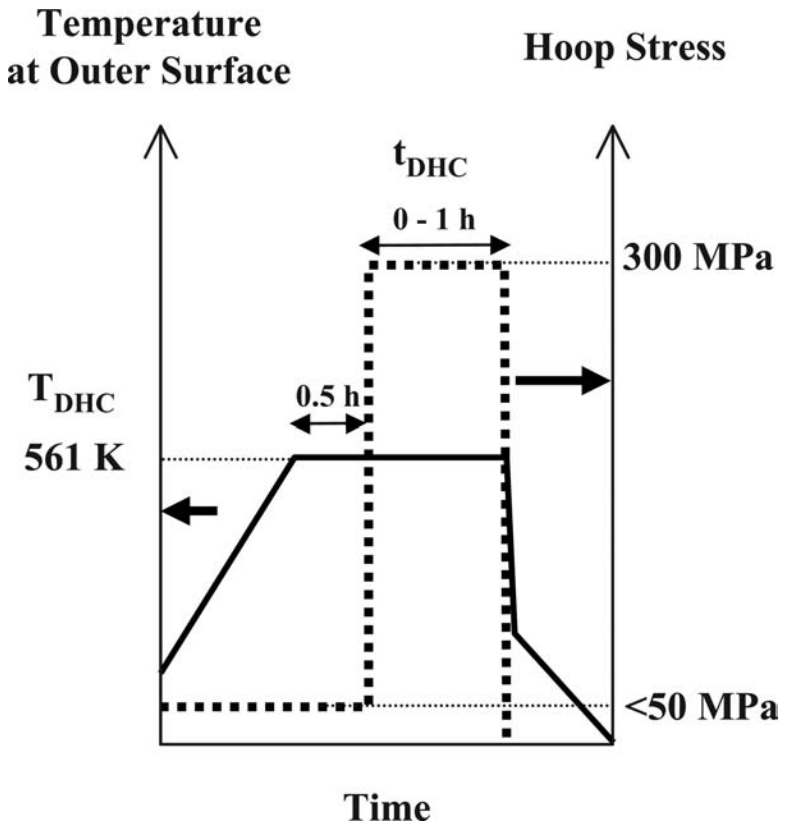


FIG. 3—*Schematic procedure used for radial DHC test with radial thermal gradient.*

TABLE 2—*Experimental conditions in radial DHC tests with radial thermal gradient.*

Specimen	T_{DHC} (K)	t_{DHC} (h)	Hoop Stress (MPa)	LHGR (kW/m)	Hydrogen Conc. (ppm)
TG01	561	0	300	40	236
TG02	561	0.25	300	40	187
TG03	561	0.5	300	40	367
TG04	561	1	300	40	352

microscopy (OM) and scanning electron microscopy (SEM) to measure the depths of ORIC and DHC crack.

Results

Typical micrographs of a crack after the radial DHC test with the radial thermal gradient are shown in Fig. 4. As can be seen in the optical micrograph (upper), the fracture surface was colored by oxidation since the radial DHC test was performed in water. In the SEM micrographs, the region that consisted of ORIC and DHC cracks was observed as a brittle fracture surface. Because the region of ORIC in the fracture surface was similar to that observed in a fatigue cracked fracture surface, we could separate the regions of ORIC and DHC crack in the SEM image of a fracture surface. By using the optical and the SEM micrographs, we calculated the depth of ORIC D_I and the depth of DHC crack D_{DHC}.

The change of the depth of DHC cracks with time is depicted in Fig. 5, which shows only the data obtained with the radial thermal gradient. No radial thermal gradient, there was no radial DHC in any of the tests examined in the present study. It was confirmed that there was no radial DHC before the increase of hoop stress because no DHC cracking was observed at $t_{DHC} = 0$ h. At $t_{DHC} = 0.25$ h the DHC crack depth extended to ~0.1–0.3 mm. The depth of DHC crack attained ~0.5 mm at $t_{DHC} = 0.5$ h, but no further significant extension was observed between $t_{DHC} = 0.5$ and 1.0 h. In terms of the depth of ORIC, it can be deduced that a threshold value of ORIC depth is needed for the radial DHC. The threshold depth of ORIC was around 0.1 mm, which should be attributed the threshold stress intensity factor for the radial DHC with the radial thermal gradient.

Discussion

Threshold Condition for Radial Delayed Hydride Cracking with Radial Thermal Gradient

As shown in Fig. 5, at a hoop stress of 300 MPa the threshold depth of ORIC for radial DHC was found to be ~0.1 mm. According to studies of DHC in the axial direction, this threshold depth of ORIC should be attributed to K_{IH}. Since the

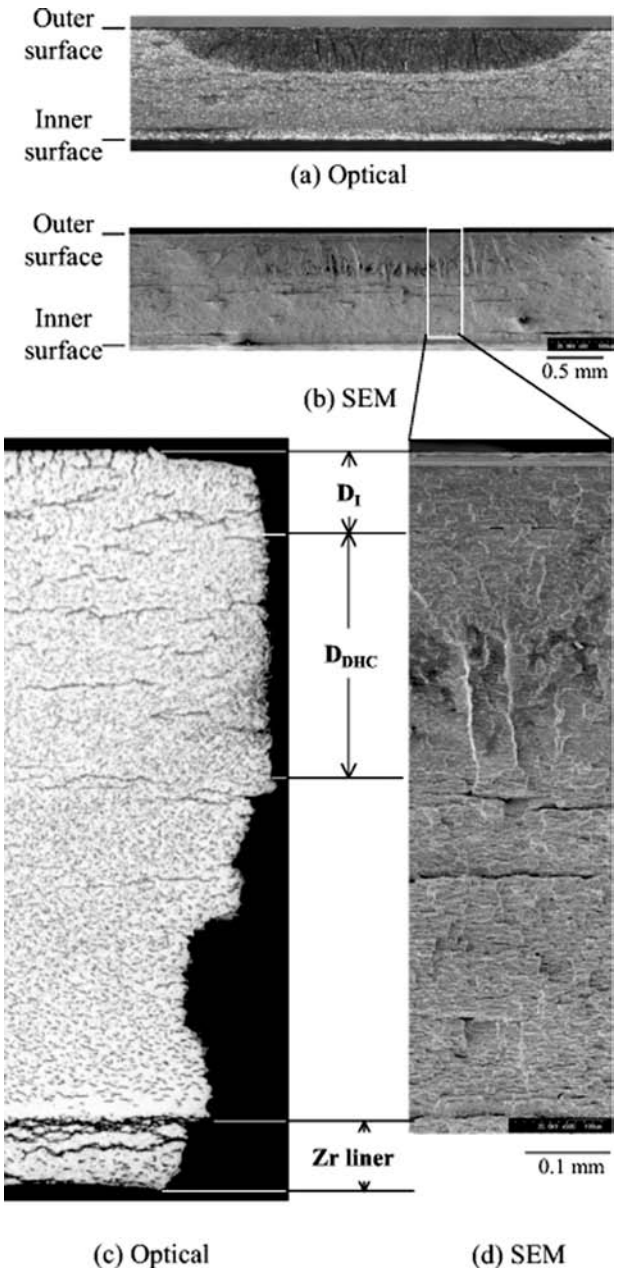


FIG. 4—*Micrographs of typical crack after radial DHC test with radial thermal gradient (LHGR=40 kW/m; T_{DHC}=561 K; t_{DHC}=0.25 h; hydrogen content=187 ppm; [(a), (b), and (d)] Radial-axial plane; (c) Radial-circumferential plane; D_I: Depth of ORIC; and D_{DHC}: Depth of DHC crack).*

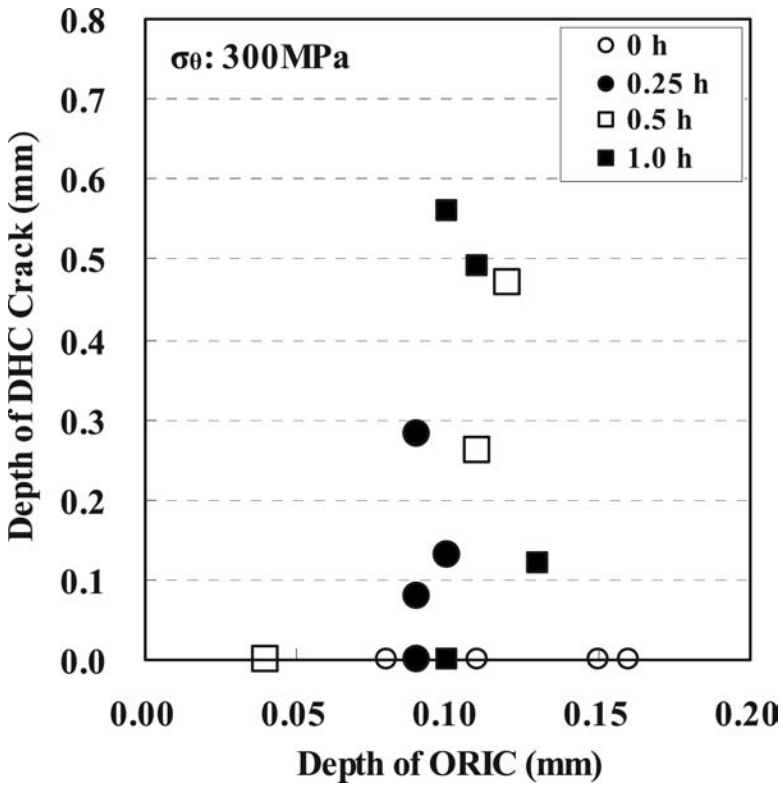


FIG. 5—*Extension of radial DHC crack with radial thermal gradient (LHGR=40 kW/m, T_{DHC}=561 K).*

specimens used in the present study did not meet the geometrical requirements for evaluation of K_I, strict values of K_I were not obtained. Hence, we made an approximate estimate of K_I using the following equation:

$$K_I = \sigma_\theta \sqrt{\pi D_I} \tag{1}$$

Here, σ_θ and D_I are the hoop stress in the fuel cladding tubes and the depth of ORIC, respectively. Because the depth-to-length ratio was small ($\sim$0.05), the values of K_I estimated by Eq 1 were reasonably close to those obtained from a detailed calculation assuming a semi-elliptical surface crack on the outer surface in Ref [19] (the difference in the values of K_I was less than 10 %). The plot of the average radial V_{DHC} versus K_I estimated from Eq 1 is shown in Fig. 6. Here, the average radial V_{DHC} is the average velocity of DHC cracking evaluated simply by $D_{\mathrm{DHC}}/t_{\mathrm{DHC}}$. At $t_{\mathrm{DHC}} = 0.25$ and 0.5 h, the maximum of the average radial V_{DHC} was $\sim 30 \times 10^{-8}$ m/s (1 mm/h). From the estimated K_I, the threshold K_I for radial DHC, K_{IH}, with the radial thermal gradient was found to be about 5 MPa $\cdot$ m$^{0.5}$ under the present experimental conditions, which was slightly

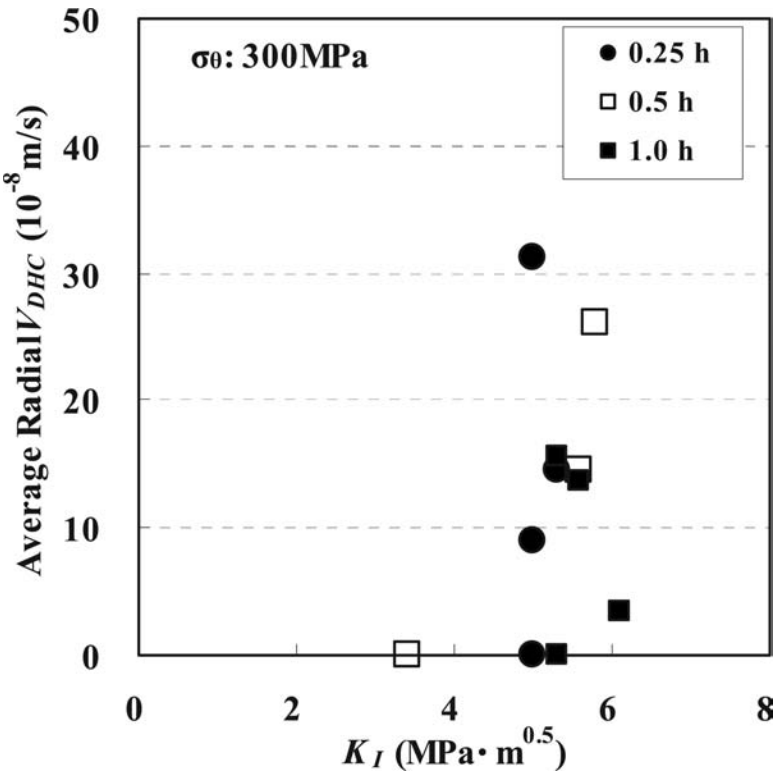


FIG. 6—*Average radial V_{DHC} with radial thermal gradient (LHGR=40 kW/m, T_{DHC}=561 K).*

higher than that observed in the isothermal radial DHC following cooling ($3.5\,\text{MPa}\cdot\text{m}^{0.5}$) that has been reported in the previous study [14]. In that previous study, the isothermal radial DHC tests were performed with similar histories of specimen temperature and hoop stress, but the specimens were heated up to the temperature 50 K higher than T_{DHC} and cooled down to T_{DHC} prior to applying the hoop stress. Therefore, "the isothermal condition" should be distinguished from "without thermal gradient."

The Predicted Relationship between D_I and the Hoop Stress

The relationship between D_I and the hoop stress conditions required to start radial DHC is shown in Fig. 7. In the micrographs of the failed rods in the power ramp test, numerous radial hydrides were found close to the outer surface of the fuel cladding tubes [1,2]. Those radial hydrides were considered to be incipient cracks for the outside-in failure. For instance, the length of the radial hydrides was ~0.1 mm in the case of the five-cycle irradiated segment rod that failed after a 22 min hold at 44.6 kW/m. By assuming the length of the radial hydrides is the same as D_I, the outside-in cracking requires the hoop stress of ~300 MPa.

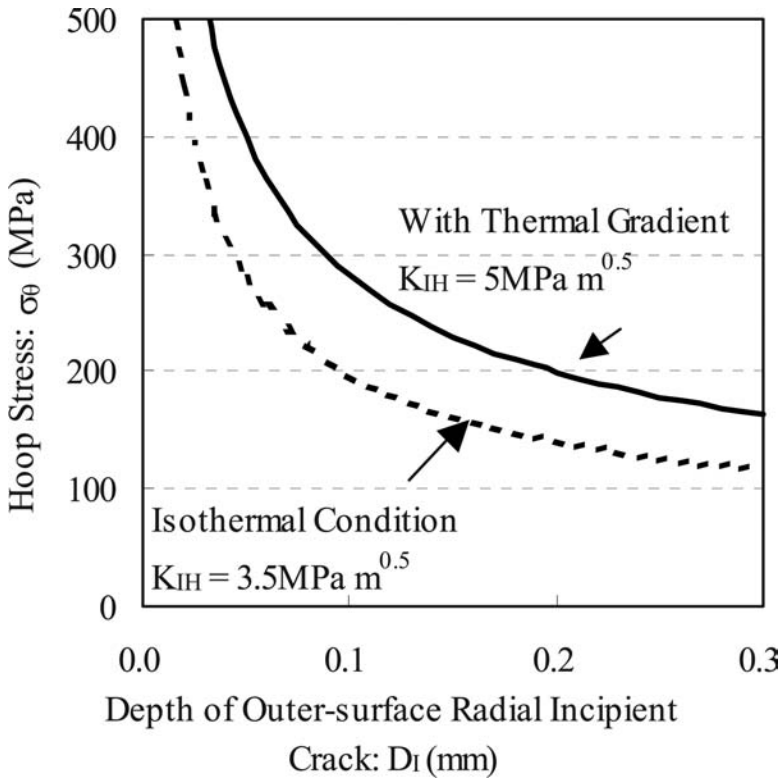


FIG. 7—*Relationship between D_I and hoop stress required for radial DHC.*

Velocity of Outside-in Delayed Hydride Cracking under Power Ramp

As has been shown in Figs. 5 and 6, between $t_{DHC} = 0$ and 0.25 h, the ORIC extended up to about 0.4 mm from the outer surface at the average radial V_{DHC} of $\sim 10 \times 10^{-8}$–30×10^{-8} m/s. Between $t_{DHC} = 0.25$ and 0.5 h, this outside-in cracking continued up to 0.6 mm in depth from the outer surface at the same average radial V_{DHC}. On the other hand, further DHC cracking can be considered to be suppressed between $t_{DHC} = 0.5$ and 1.0 h because the maximum value of depth of DHC crack at 1.0 h was nearly equal to that at 0.5 h, while the average radial V_{DHC} was reduced by half. Those results would indicate that the velocity of outside-in DHC cracking was approximately $\sim 10 \times 10^{-8}$–30×10^{-8} m/s. In Fig. 8 this velocity with the thermal gradient at $t_{DHC} = 0.25$ and 0.5 h is compared with the isothermal condition, which has been previously reported for the same materials by the present authors [14]. The representative temperature for the data with the thermal gradient was obtained by calculating the average temperature of the area where the outside-in cracking was observed. The important finding was that the radial V_{DHC} with the radial thermal gradient was significantly higher than that expected from the data obtained under the isothermal condition. Under the isothermal condition,

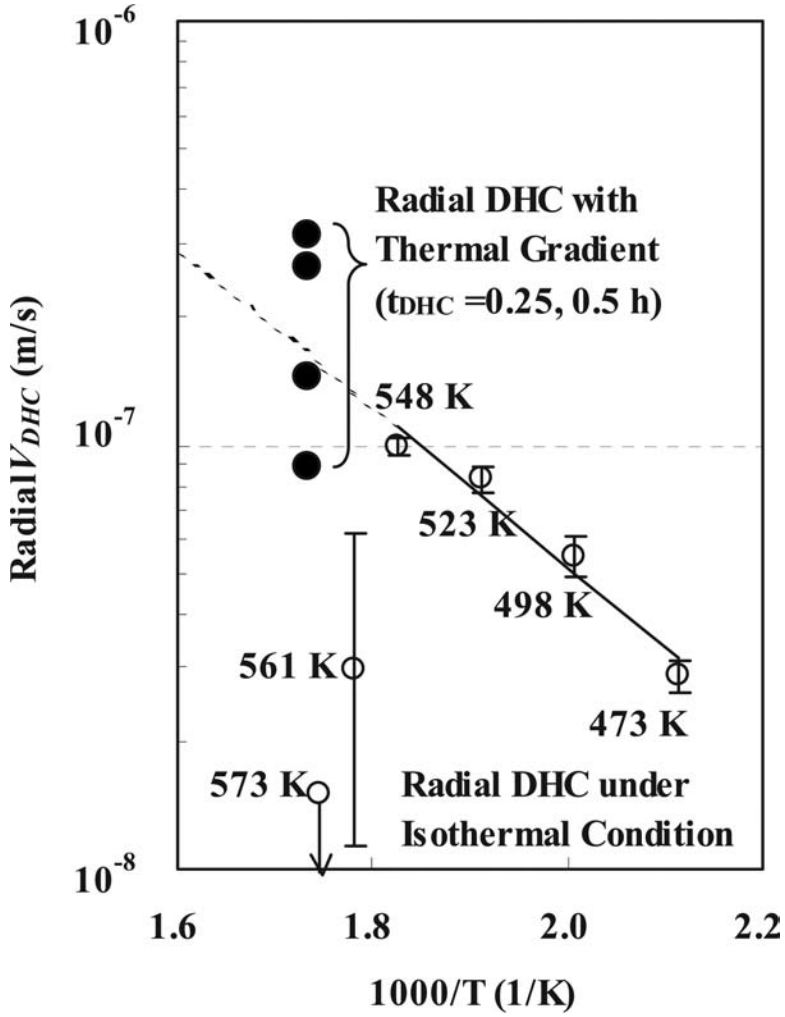


FIG. 8—*Effect of radial thermal gradient and isothermal conditions on radial V_{DHC} [14].*

the strong suppression of radial V_{DHC} was observed in the temperature range between 548 and 561 K, and at 573 K, no measurable radial DHC cracking was observed, which was called "critical temperature" [3]. However, there was no suppression of radial V_{DHC} by the thermal gradient at temperatures exceeding 571 K. Moreover, the maximum value of radial V_{DHC} with the thermal gradient approximately doubled the value expected from the temperature dependence for the isothermal condition between 473 and 548 K (shown as a dashed line in Fig. 8). As indicated in Ref [3], the thermal gradient accelerated the DHC cracking rate when the temperature at the crack tip was lower than that at the source of hydrogen: The ratio of crack velocity with the thermal gradient to that

without the thermal gradient increased with the value of thermal gradient, and this ratio became ~3 at the thermal gradient of 25 K/mm. In the present study, the ratio was ~2 when the thermal gradient was ~70 K/mm. Therefore, the acceleration effect of the thermal gradient on V_{DHC} was smaller than that expected from the data shown in Ref [3]. Further studies are obviously needed to clarify this difference in the effect of thermal gradient on the crack velocity, but a possible interpretation is that a relatively high thermal gradient in the present study would induce the saturation of the acceleration effect of the thermal gradient. To examine this saturation effect, the similar experimental study should be performed at lower thermal gradient.

Mechanism of Outside-in Cracking under Thermal Gradient

As mentioned above, the outside-in cracking rate is faster with the thermal gradient than that without thermal gradient (and also under the isothermal condition). A significant difference in the radial DHC with and without the thermal gradient is the radial distribution of dissolved hydrogen. In Zr-based alloys, it has been reported that by thermal diffusion of hydrogen, the hydrogen dissolved at a hotter region diffuses towards a colder region. In the case of the outside-in cracking of BWR fuel cladding tubes with a Zr liner, hydrides precipitated in the Zr liner and in the Zry-2 material around Zr liner would be a main source of the hydrogen. The dissolved hydrogen diffuses under the thermal and concentration gradients and its distribution can be evaluated by the following equation [19]:

$$J = -\frac{D_h C}{RT}\left(RT\frac{d\ln C}{dx} + \frac{Q^*}{T}\frac{dT}{dx}\right) \tag{2}$$

Here, J represents the flux of diffusing hydrogen, D_h is the diffusion coefficient of hydrogen, C is the concentration of dissolved hydrogen, R is the gas constant, Q^* is the heat of transport of hydrogen in Zr or Zry-2, and T is the temperature. By using Eq 2, we performed calculations of the distribution of dissolved hydrogen during the radial DHC test in a similar manner as has been reported in Ref [20]. In the calculations, the hydrogen solubilities in Zry-2 and Zr reported by Une and Ishimoto [21] and the diffusion coefficient of hydrogen in Zry-2 reported by Sawatzky [22] were used.

Calculation of Hydrogen Distribution—As an example of the results of calculations based on the experimental conditions in the present study, the concentration of dissolved hydrogen, C_{sol}, with the radial thermal gradient at t_{DHC} of 0.5 h is shown in Fig. 9, in which the terminal solid solubilities of hydrogen for dissolution and precipitation are expressed as TSSD and TSSP, respectively. As can be seen in Fig. 9, C_{sol} in the outer part of the fuel cladding tube is higher than TSSD, which means that the dissolved hydrogen can exist in the supersaturated state, which can enhance DHC significantly.

Effect of Supersaturated Hydrogen on Radial Delayed Hydride Cracking—In order to examine the relationship between the concentration of supersaturated

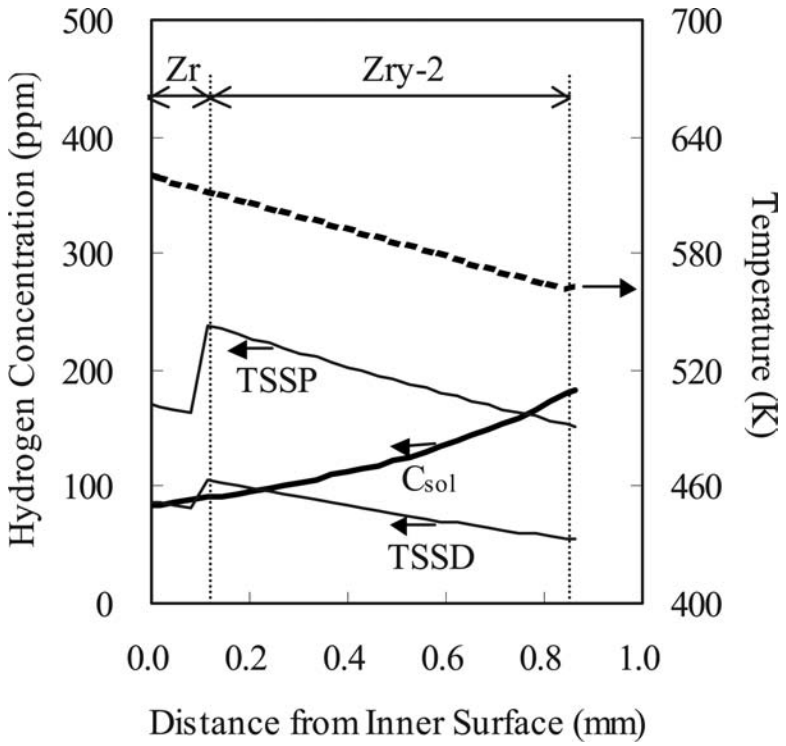


FIG. 9—*Radial distribution of dissolved hydrogen with radial thermal gradient at* t_{DHC}*=0.5 h (LHGR=40 kW/m, high hydrogen content).* C_{sol} *and TSSD(p) represent the concentrations of dissolved hydrogen and the terminal solid solubility of hydrogen for dissolution (precipitation), respectively.*

hydrogen and radial DHC, the radial DHC tests were performed with different concentrations of supersaturated hydrogen under isothermal conditions. The DHC tests under isothermal conditions were performed using the same procedure reported in the previous studies: the specimens were heated up to the maximum temperature T_{max} and cooled down to the DHC test temperature T_{DHC} prior to applying the hoop stress. In the present study, the concentration of supersaturated hydrogen could not be measured, so the difference of TSSD between at T_{max} and T_{DHC} was used to estimate the concentration of supersaturated hydrogen. As summarized in Table 3, the radial DHC tests were performed at T_{DHC} of 548 K with varying T_{max} between 568 and 598 K ($dT(=T_{max}$ and $T_{DHC})$ was 20–50 K). The relationship between dT and the radial V_{DHC} is shown in Fig. 10, in which filled squares and error bars represent the average and the range of four data points. The concentration threshold of supersaturated hydrogen for the radial DHC was confirmed to be between ~20 and 30 ppm.

Time Dependence of Distribution of Supersaturated Hydrogen—The time dependence of the concentration of supersaturated hydrogen is shown in Fig. 11,

TABLE 3—*Experimental conditions in radial DHC tests under isothermal conditions.*

Specimen	T_{DHC} (K)	T_{max} (K)	dT (K)	t_{DHC} (h)	Hoop Stress (MPa)
IT01	548	568	20	1	183
IT02	548	578	30	1	183
IT03	548	588	40	1	183
IT04	548	598	50	1	183

in which the concentration of supersaturated hydrogen is considered as the difference of hydrogen concentration between C_{sol} calculated and TSSD. Arrows represent the range where the radial cracking was observed in the radial DHC test for 0.25 and 0.5 h. As seen in Fig. 11, in the case of radial DHC cracking with the thermal gradient, the crack tip would be surrounded by the supersaturated hydrogen that could be the source of the hydrogen for the hydrides precipitated near the crack tip. This supply of supersaturated hydrogen near the crack tip would induce the acceleration of radial DHC. Near the inner surface of

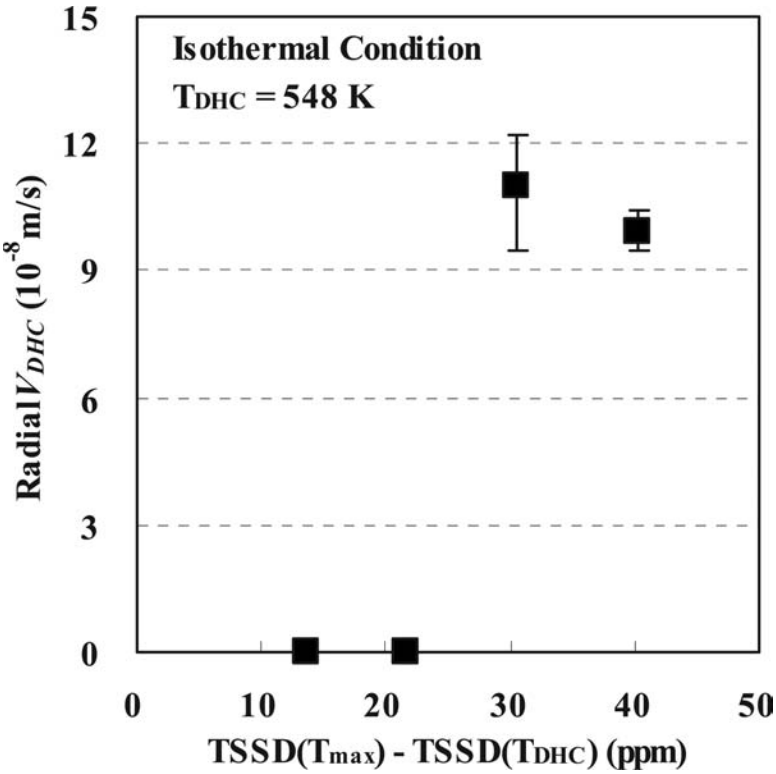


FIG. 10—*Dependence of radial V_{DHC} on the difference in TSSD at T_{max} and T_{DHC}.*

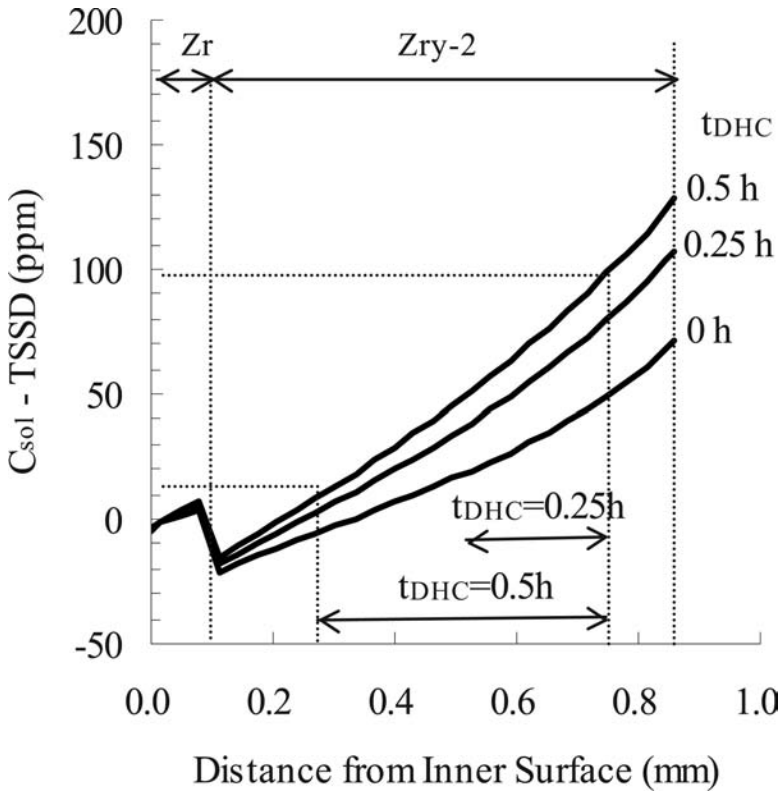


FIG. 11—*Radial distribution of dissolved hydrogen with radial thermal gradient up to* t_{DHC}*=0.5 h (LHGR=40 kW/m, high hydrogen content).*

the fuel cladding tube, there is a hydrogen-depleted zone where C_{sol} is lower than TSSD. This hydrogen-depleted zone was close to the depth at which the radial DHC was suppressed, as shown in Figs. 5 and 6. This agreement would also indicate that the radial DHC with the radial thermal gradient is strongly dependent on the distribution of hydrogen dissolved as a result of the thermal diffusion.

Conclusions

By using unirradiated Zry-2 fuel cladding tubes, outside-in cracking was examined both with and without thermal gradients. Without the radial thermal gradient, there was no radial DHC in any of the experimental conditions examined. On the other hand, with a radial thermal gradient, the velocity of the outside-in cracking was significantly higher than that expected from the data obtained under the isothermal conditions, and the threshold depth of the incipient crack was found to be ~0.1 mm at the hoop stress of 300 MPa. It was suggested that the outside-in cracking during the power ramp is strongly dependent on the distribution of dissolved hydrogen as a result of the thermal diffusion.

References

[1] Shimada, S., Etoh, E., Hayashi, H., and Tukuta, Y., "A Metallographic and Fractographic Study of Outside-in Cracking Caused by Power Ramp Tests," *J. Nucl. Mater.*, Vol. 327, 2004, pp. 97–113.

[2] Hayashi, H., Ogata, K., and Kamimura, K., "Outside-in Failure of High Burnup Fuel Cladding and Evaluation Tests of Mechanism," *Proceedings of the 2005 Water Reactor Fuel Performance Meeting*, Kyoto, Japan, Oct. 2–6, 2005, Atomic Energy of Japan, Tokyo, Japan.

[3] Sagat, S., Chow, C. K., Puls, M. P., and Coleman, C. E., "Delayed Hydride Cracking in Zirconium Alloys in a Temperature Gradient," *J. Nucl. Mater.*, Vol. 279, 2000, pp. 107–117.

[4] Sagat, S., Coleman, C. E., Griffiths, M., and Wilkins, B. J. S., "The Effect of Fluence and Irradiation Temperature on Delayed Hydride Cracking in Zr-2.5Nb," *Tenth International Symposium on Zr in the Nuclear Industry, ASTM STP 1245*, Baltimore, MD, 21–24 June 1993, A. M. Garde and E. R. Bradley, Eds., ASTM International, West Conshohocken, PA, 1994, pp. 35–61.

[5] Pan, Z. L., Lawrence, S. S., Davies, P. H., Griffiths, M., and Sagat, S., "Effect of Irradiation on the Fracture Properties of Zr-2.5Nb Pressure Tubes at the End of Design Life," *J. ASTM Int.*, Vol. 2, No. 9, 2005, pp. 759–782.

[6] Efsing, P. and Pettersson, K., "Delayed Hydride Cracking in Irradiated Zircaloy Cladding," *12th International Symposium on Zr in the Nuclear Industry, ASTM STP 1354*, Toronto, Canada, 15-18 June 1998, G. P. Sabol and G. D. Moan, Eds., ASTM International, West Conshohocken, PA, 2000, pp. 340–355.

[7] Grigoriev, V. and Jakaobsson, R., "Delayed Hydrogen Cracking Velocity and J-Integral Measurements on Irradiated BWR Cladding," *J. ASTM Int.*, Vol. 2, No. 8, 2005, pp. 711–728.

[8] Shek, G. K. and Graham, D. B., "Effects of Loading and Thermal Maneuvers on Delayed Hydride Cracking in Zr-2.5Nb Alloys," *Eighth International Symposium on Zr in the Nuclear Industry, ASTM STP 1023*, San Diego, CA, 19-23 June 1988, L. F. P. Van Swam and C. E. Eucken, Eds., ASTM International, West Conshohocken, PA, 1989, pp. 89–110.

[9] Kim, Y. S., Kwon, S. C., and Kim, S. S., "Crack Growth Pattern and Threshold Stress Intensity Factor, K_{IH}, of Zr-2.5Nb Alloy with the Notch Direction," *J. Nucl. Mater.*, Vol. 280, 2000, pp. 304–311.

[10] Simpson, L. A. and Clarke, C. F., "Application of the Potential-Drop Method to Measurement of Hydrogen-Induced Sub-Critical Crack Growth in Zirconium-2.5 wt% Niobium," *Report No.* AECL-5815, Whiteshell Nulcear Research Establishment, Pinawa, Manitoba, 1977.

[11] Huang, J. H. and Ho, C. S., "Subcritical Crack Growth Behaviour for Hydrided Zircaloy-4 Plate," *Mater. Chem. Phys.*, Vol. 47, 1997, pp. 184–192.

[12] Efsing, P. and Petterson, K., "The Influence of Temperature and Yield Strength on Delayed Hydride Cracking in Hydrided Zircaloy-2," *Eighth International Symposium on Zr in the Nuclear Industry, ASTM STP 1295*, Garmisch-Partenkirchen, Germany, 11-14 Sept. 1995, E. R. Bradley and G. P. Sabol, Eds., ASTM International, West Conshohocken, PA, 1996, pp. 394–404.

[13] Sakamoto, K. and Nakatsuka, M., "Development of Experimental Technique for Simulation of Radial Cracking of High Burnup Fuel Cladding Tubes," *Transactions of TopFuel2006, 2006 International Meeting on LWR Fuel Performance*, Salamanca, Spain, Oct. 22–26, 2006, European Nuclear Society, Brussels, Belgium.

[14] Sakamoto, K., Nakatsuka, M., and Higuchi, T., "Simulation of Cracking During Outside-in Type Failure of High Burn-up Fuel Cladding Tubes," *Proceedings of WRFPM2008, Water Reactor Fuel Performance Meeting in Seoul*, Seoul, South Korea Oct. 19–23, 2008, Korean Nuclear Society, Daejeon, Korea.
[15] Sakamoto, K., Nakatsuka, M., Higuchi, T., and Ito, K., "Role of Radial Temperature Gradient in Outside-in Type Failure of High Burn-up Fuel Cladding Tubes During Power Ramp Tests," *Proceedings of Top Fuel 2009*, Paris, France, Sep. 6–10, 2009, European Nuclear Society, Brussels, Belgium.
[16] Wappling, D., Massih, A. R., and Stahle, P., "A Model for Hydride-Induced Embrittlement in Zirconium-Based Alloys," *J. Nucl. Mater.*, Vol. 249, 1997, pp. 231–238.
[17] Nakatsuka, M. and Sakamoto, K., Patent Number (Japan) 4330964 (2005).
[18] Higuchi, T., Sakamoto, K., Etoh, Y., and Nakatsuka, M., "Power Ramp Test Simulation for Fuel Cladding Tubes by Using Internal Heating and Pressure," *Proceedings of WRFPM2008, Water Reactor Fuel Performance Meeting in Seoul*, Seoul, South Korea, Oct. 19–23, 2008, Korean Nuclear Society, Daejeon, Korea.
[19] Murakami, Y., *Stress Intensity Factors Handbook*, Pergamon Press, Oxford, 1987, Vol. 2, p. 751.
[20] Takagi, I., Shimada, S., Kawasaki, D., and Higashi, K., "A Simple Model for Hydrogen Re-Distribution in Zirconium-Lined Fuel Claddings," *J. Nucl. Sci. Technol.*, Vol. 39, No. 1, 2002, pp. 71–75.
[21] Une, K. and Ishimoto, S., "Dissolution and Precipitation Behavior of Hydrides in Zircaloy-2 and High Fe Zircaloy," *J. Nucl. Mater.*, Vol. 322, 2003, pp. 66–72.
[22] Sawatzky, A., "Hydrogen in Zircaloy-2: Its Distribution and Heat of Transport," *J. Nucl. Mater.*, Vol. 2, No. 4, 1960, pp. 321–328.

DISCUSSION

Question 1, Dr. V. Grigoriev, Studsvik:—This is, perhaps, more comment than question, you concluded from your work that there is no radial DHC without through wall thermal gradient. However, there are some observations that don't fit to such conclusion. In the experiments performed at Studsvik on radial DHC without any thermal gradients we observed radial cracking with all fractographic features that are typical for the DHC in cladding. Perhaps, thermal gradient can affect the DHC rather than to be a mandatory condition for the DHC.

Author's Response:—I agree with your comment that the thermal gradient can affect the DHC rather than to be a mandatory condition for the DHC.

The main difference of experimental conditions between in a "standard" DHC test and in the present study is the temperature history prior to DHC cracking. In the "standard" DHC test, specimens are overheated (~50 K above the DHC test temperature) to generate oversaturated hydrogen, which enhances DHC cracking significantly. On the other hand, in the present study there was no overheating treatment. The source of oversaturated hydrogen in the present study was dissolved hydrogen that diffused from inner (hotter) part of cladding as a result of the thermal diffusion.

We also performed the "standard" radial DHC test in the previous studies by using the same claddings, as shown in Fig. 8 (depicted as "radial DHC under isothermal condition"). In this "standard" radial DHC test, as similar to the radial DHC test performed in Studsvik, specimens were subjected to the overheating treatment and cracked by typical DHC in cladding. In this case, of course, thermal gradient is not a mandatory condition for the DHC. However, we also observed a strong effect of thermal gradient at higher temperature. The mechanism of this effect is not still clear but this result suggests that thermal gradient affects the DHC.

Question 2, Dr. Young Suk Kim, KAERI:—1) At what conditions did you obtain K_{IH} of 5 MPa $m^{0.5}$ for a cold worked Zircaloy-2 tube? (At what temperature?) Do you think that if the measured value of 5 MPa $m^{0.5}$ was obtained at 250 deg. C, do you think the same KIH can be effective even above 300 deg. C? 2) Above 300 deg. C, given that hydrogen diffusion is so fast and is not the limiting factor to control the crack growth rate, your conclusion that a temperature gradient enhances hydrogen diffusion, enhancing the crack growth rate is doubtful. Please comment on this.

Author's Response:—1) The present experimental study with radial thermal gradient was performed at the outer surface temperature of 288 deg. C and the hoop stress of 300 MPa. The temperature of Zry-2 tube was from 288 deg. C (at the outer surface) to 348 deg. C (at the inner surface). So, the obtained K_{IH} of 5 MPa $m^{0.5}$ for a cold worked Zircaloy-2 tube is also effective above 300 deg. C.

2) As you mentioned, the hydrogen diffusion is fast at higher temperature. Since we have not measured the activation energy for DHC (with radial thermal gradient), the limiting process has not been clarified. Now, we consider that the thermal gradient enhances preferential precipitation at the crack tip, whose temperature is lower than the source of dissolved hydrogen. However, it is clear that further studies are required to clarify the role of the thermal gradient in DHC process.

Question 3, Dr. Y. R. Rashid, ANATECH:—1) Have you compared the crack velocity in your DHC simulation to the power ramp rate to determine if the in-reactor crack extension process is simulated in the DHC experiment you conducted? 2) If the threshold crack length is 0.1mm at 300 MPa stress, as derived from a K_{IH} of 5 MPa $m^{0.5}$, have you verified this condition with the radial hydride lengths at the cladding OD and the actual stress these during the power ramp?

Author's Response:—1) In the power ramp tests in JMTR (Japan Materials Testing Reactor), four high burnup segment rods were failed by the outside-in manner. Failures of segment rods were detected after 22–149 min at 42.1–55.1 kW/m. The mechanism of the outside-in failure is now considered that 1) dissolved hydrogen diffuses towards outer part of claddings, 2) part of diffused hydrogen precipitates as radial hydrides on the outer surface of claddings, 3) a radial hydride fractures (to be an incipient radial crack at the outer surface of claddings) and 4) radial cracking towards the inner surface of claddings. In the power ramp tests in JMTR, the initiation of the incipient cracks was not detected, so the time and the velocity of radial cracking were not measured. Therefore, the durations to detection of failure would include the time for 1)–4). This implies that the time for radial cracking (DHC) would be less than 100 min. According to our DHC simulation by using unirradiated claddings, the predicted time for through-wall cracking is 30–100 min (for 0.5 mm cracking). Taking into account that the crack velocity for irradiated claddings is expected to be higher than that for unirradiated claddings owing to higher strength for irradiated claddings, we expect that the our DHC simulation can demonstrate the in-reactor crack extension process.

2) One of the failed segment rods, the radial hydrides having a length of 0.06 mm were found on the outer surface of the cladding. An evaluation of stress during the power ramp is not easy but the maximum stress during power ramp tests were expected to be higher than 300 MPa. According to K_{IH} of 5 MPa $m^{0.5}$, an incipient crack having a length of 0.06 mm requires the hoop stress of approximately 350 MPa to radial extension. Taking into account the uncertainty of evaluation of stress, the value of K_{IH} obtained in the present study is expected to be good accordance with the actual power ramp tests.

Reprinted from JAI, Vol. 7, No. 9
doi:10.1520/JAI102988
Available online at www.astm.org/JAI

V. Grigoriev,[1] *R. Jakobsson,*[2] *D. Schrire,*[3] *G. Ledergerber,*[4] *T. Sugiyama,*[5] *F. Nagase,*[5] *T. Fuketa,*[5] *L. Hallstadius,*[6] *and S. Valizadeh*[6]

RIA Failure of High Burnup Fuel Rod Irradiated in the Leibstadt Reactor: Out-of-Pile Mechanical Simulation and Comparison with Pulse Reactor Tests

ABSTRACT: A high burnup boiling water reactor fuel rod was subjected to reactivity initiation accident (RIA) tests in a research reactor. Two ramp tests were carried out under almost identical irradiation conditions, resulting in cladding failure in a room temperature test, while no failure was observed in a high temperature test. An adjacent segment of the same rod was used for mechanical expansion-due-to-compression (EDC) testing simulating the pellet-cladding mechanical interaction loadings on the cladding during an in-reactor RIA. The EDC tests show the existence of a transition temperature where an abrupt increase in the specimen hoop strain at failure occurs. Additional tests revealed that the transition temperature depends on hydrogen concentration. A possible effect of the rapid heating, which is a specific condition for an in-reactor RIA compared to the static heating in the EDC tests, was verified in the rapid heating/loading tests on unirradiated hydrided Zircaloy, when both loading and heating are performed simultaneously within 50–80 ms. It was shown that strain to failure is dependent on the

Manuscript received January 22, 2010; accepted for publication August 20, 2010; published online September 2010.
[1] Studsvik Nuclear AB, Nyköping 61182, Sweden, e-mail: slava.grigoriev@studsvik.se
[2] Studsvik Nuclear AB, Nyköping 61182, Sweden.
[3] Vattenfall Nuclear Fuel AB, Stockholm, 16287, Sweden.
[4] Kernkraftwerk Leibstadt AG, CH 5325 Leibstadt, Switzerland.
[5] Nuclear Safety Research Center, Japan Atomic Energy Agency, Tokai 319-1195, Japan.
[6] Westinghouse Electric Sweden AB, Västerås, 72163, Sweden.

Cite as: Grigoriev, V., Jakobsson, R., Schrire, D., Ledergerber, G., Sugiyama, T., Nagase, F., Fuketa, T., Hallstadius, L. and Valizadeh, S., "RIA Failure of High Burnup Fuel Rod Irradiated in the Leibstadt Reactor: Out-of-Pile Mechanical Simulation and Comparison with Pulse Reactor Tests," *J. ASTM Intl.*, Vol. 7, No. 9. doi:10.1520/JAI102988.

Copyright © 2011 by ASTM International, 100 Barr Harbor Drive, PO Box C700, West Conshohocken, PA 19428-2959.

instantaneous material temperature and is not affected by the pre-heating history. The results show good consistency between the EDC and in-reactor pulse test data. It is concluded that the EDC test can provide valuable information to predict the in-reactor RIA fuel failure.

KEYWORDS: BWR, high burnup, RIA failures, EDC mechanical testing, rapid heating, hydrogen

Introduction

A postulated reactivity initiation accident (RIA) in light water reactors (LWRs), rod ejection accident in pressurized water reactors (PWRs), or rod drop accident in boiling water reactors (BWRs) results in rapid heating (RH) of the fuel. The fuel pellets expand rapidly to come into contact with the cladding inner wall and push it from inside. If the cladding has reduced ductility due to irradiation hardening and hydrogen absorption during normal operation, it may fail due to the pellet-cladding mechanical interaction (PCMI). To prevent the PCMI failure, a limit of fuel enthalpy during an RIA should be defined in order to avoid the generation of mechanical forces. Since cladding strength and ductility are of fundamental importance to fuel rod survivability under the RIA, a number of mechanical test programs have been conducted to better understand the results obtained in research pulse reactor RIA tests. Most of the mechanical tests have therefore been focused on the embrittling effects in cladding related to waterside oxidation and hydrogen uptake. All tests were performed at strain rates that were much higher than those normally used in mechanical testing, in order to reproduce the PCMI-induced loading expected in the cladding under RIA conditions. However, the RH of the cladding was generally not simulated in the laboratory tests.

The present work is based on a comparison of the results from out-of-pile mechanical tests with the results from in-reactor RIA pulse tests performed on the same irradiated fuel rod. High burnup fuel irradiated in the Leibstadt BWR Nuclear Power Plant in Switzerland (KKL) has recently been subjected to simulated RIA tests in the Japanese Nuclear Safety Research Reactor (NSRR) within the framework of the Advanced LWR Fuel Performance and Safety Research Program (ALPS). In order to evaluate the temperature influence on transient fuel behaviour, the pulse irradiation tests were performed at room and operating temperatures representing cool zero power and hot zero power.

The fuel rod AEB072-E4 has been characterised in great detail utilizing non-destructive techniques in the spent fuel pool at KKL and at the Paul Scherer Institute (PSI) hot cell. Additionally, destructive examinations of the fuel and cladding materials were performed at the PSI and at the Studsvik hot cell laboratories within the framework of the Westinghouse–KKL–PSI Fuel Performance Programme (FPP) [1].

Samples of cladding from the same fuel rod, AEB072-E4, have also been used for the high strain rate mechanical testing technique called the expansion-due-to-compression (EDC) test. The EDC test was developed at Studsvik to simulate the PCMI loadings on the cladding during an in-reactor RIA [2]. To

TABLE 1—*Main characteristics of the fuel rod removed from the assembly AEB072.*

Fuel Rod	AEB072-E4		
Irradiation (cycles)	7		
Pellet enrichment (%)	4.46		
Rod average burnup (MWd/kg)	62.9		
Rod growth, pool/hot cell (%)	0.42/0.40		
Fission gas release (%)	1.1		
Cladding material	Zircaloy-2 (LK3 with liner)		
Rod average total hydrogen (ppm)	305		
Standard deviation	< 10%		
Radial hydride fraction (%)	7		
Segment	G	H	J
Position from BEP (mm)	2004–2007	2019–2219	2280–2730
Segment average burnup (MWd/kg)	72.3	71.8	68.6
Total hydrogen content (ppm)	329±23	318±46	295±9
Tests performed	DE[a]	EDC[b]	RIA[c]

[a] DE = destructive examinations.
[b] EDC = mechanical simulation of RIA by means of the out-of-pile EDC test.
[c] RIA = pulse irradiation RIA test performed in the NSRR.

evaluate an effect of burnup and, consequently, an effect of hydrogen content, additional EDC tests have also been performed on lower burnup fuel rods from the FPP (AEB068-E4, AEB069-E4) [1] and on the fuel rod 20461-J2 with the same type of cladding material irradiated in the Oskarshamn BWR in Sweden.

Experimental Details

Fuel Rod Characterisation

The fuel rods used in the present work were fabricated by Westinghouse Electric (formerly ABB Atom) in Västerås, Sweden, with the same pellet fabrication and the same type of cladding material (fully recrystallized Zircaloy-2, LK3 with zirconium liner). The LK3 cladding was fabricated by Sandvik Material Technology using a manufacturing process with $\log A = -14.2$, where A is the cumulative annealing parameter characterising the heat input to the cladding during the manufacturing process [3]. The irradiation conditions and irradiation history as well as the characterisation of the fuel and the cladding material of the fuel rods can be found in Table 1 and have been published elsewhere [1,4]. The position of the KKL rod used for both pulse irradiation RIA tests and for mechanical EDC testing is indicated in Fig. 1(*a*). The hot cell examination showed nearly no net creep down, and the diameter was found to be within the tolerances of the as-fabricated value. In the region with high burnup, no gap between the fuel and the cladding was visible (Fig. 1(*b*)). The average oxide thickness

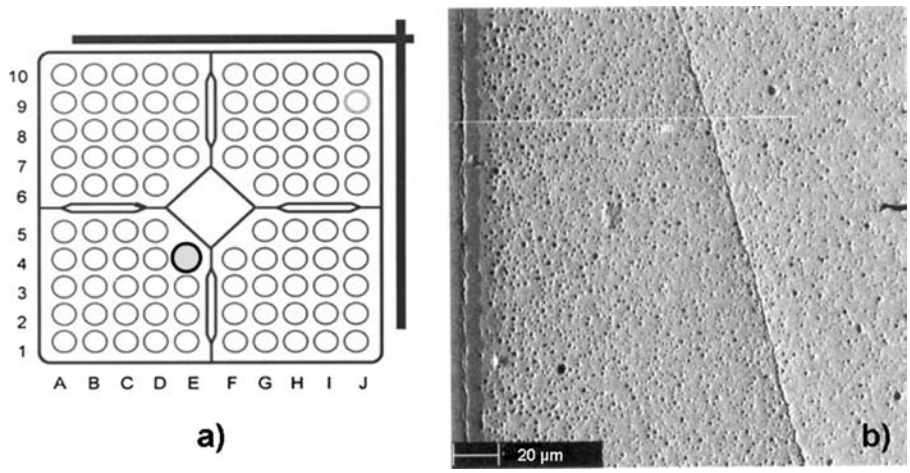


FIG. 1—*(a) Position in the fuel assembly of the rod AEB072-E4 used in the ALPS RIA experiments and in mechanical RIA simulation tests and (b) typical rim area of fuel pellet at midheight of the rod AEB072-E4; no gap is visible in the bound area at the interface between the pellet and cladding (on the left side of the photo).*

was 18 μm with a maximum of 23–24 μm. Typical power histories for nodes of the fuel rod segments used for in-reactor RIA tests and for mechanical EDC tests are shown in Fig. 2. The linear heat generation rate was, for the first two irradiation cycles, between 180 and 250 W/cm and declined gradually to 80–100 W/cm in the seventh cycle. The hydrogen hot gas extraction technique used at the PSI [5] allows measurement of the total hydrogen content of the segment,

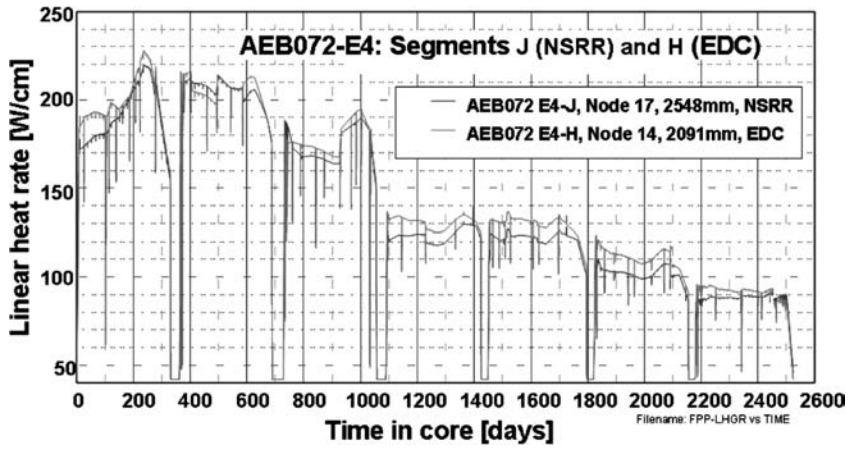


FIG. 2—*Power histories of the fuel segments used for RIA testing: Node 17 is the centre of the segment AEB072-E4-J tested in the NSRR, whereas Node 14 represents segment AEB072-E4-H used for mechanical EDC tests.*

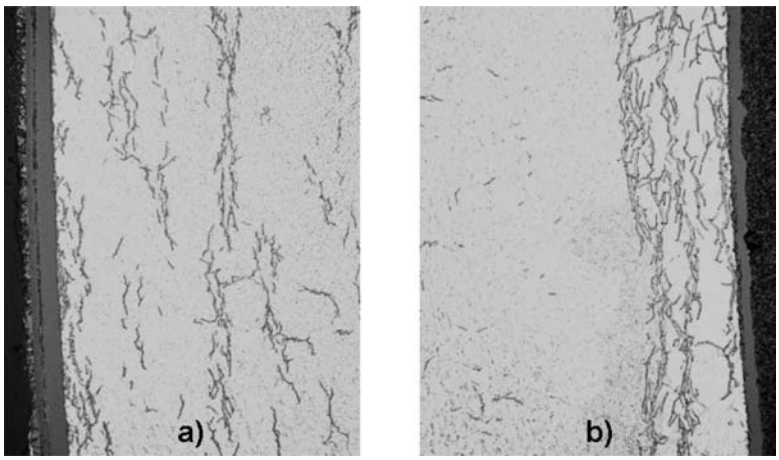


FIG. 3—*(a) Cladding of AEB072-E4 at midheight; hydrides near the outer diameter surface, oxide layer with the typical delaminating of crud layer; (b) Cladding on the fuel side with hydrides located in the liner. Average of the total hydrogen content is 329±23 ppm with 292±21 in the metal.*

separating the contribution of the oxide layer and that of the metal to the total value. The measurement series resulted in a value of about 90 % of hydrogen in the metal and about 10 % of hydrogen being released at lower temperatures, presumably from the oxide. The calculated average values of total hydrogen (metal plus oxide) in different segments of AEB072-E4 used for mechanical EDC and for in-reactor RIA tests are shown in Table 1. Within this examination campaign, an interlaboratory comparison between PSI and Studsvik was performed. Excellent agreement between the values obtained at Studsvik (180–202 wt ppm) and at PSI (207–208 wt ppm) has been found for samples 5 mm apart from each other on a rod irradiated for six cycles in KKL (AEB068-E4). Hydride morphology in the cladding material is shown on the photos taken from the polished and etched cladding ring samples at midheight of the rod (Fig. 3).

Out-of-Pile Mechanical Simulation of Reactivity Initiation Accident

In the EDC tests, a polymer pellet is axially compressed inside a 20 mm piece of the cladding, thereby providing hoop straining of the cladding specimen. Depending on the ductility of the cladding material, the specimen can be deformed without cracking up to 15–20 % of its hoop strain, or specimen failure is observed for embrittled cladding materials (Fig. 4). The loading is performed in a displacement-controlled mode, i.e., the displacement of the machine crosshead (2.9 mm) and the time interval for that displacement (80 ms) are defined before the test. The EDC technique is able to produce hoop strain rates in cladding samples up to 1000 % per second, i.e., high enough to simulate the strain rates of about 100 % per second, which are typical for a LWR RIA [6].

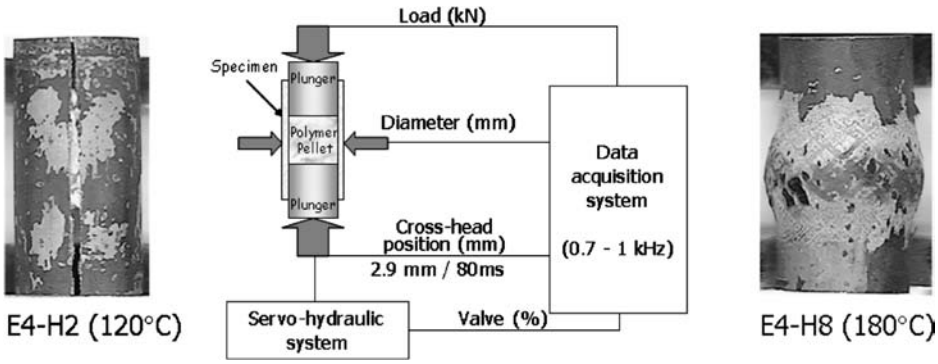


FIG. 4—*The schematic of the EDC test setup and an example of failed and non-failed specimen appearance after the EDC tests (Table 2, specimens E4-H2 and E4-H8).*

The EDC tests have been performed in air atmosphere on the AEB072-E4 fuel cladding material in a temperature interval ranging from 60–260°C. Four parameters; load, cross-head position, specimen diameter, and opening of a servo-hydraulic valve, are monitored once per millisecond by the data acquisition system (Fig. 4). Instantaneous values of specimen hoop strain are calculated from the increment of specimen diameter. The increment of diameter is measured at midlevel of the specimen using a Mitutoyo LSM 503 laser instrument. The detecting laser system registers the instantaneous value of specimen diameter with a frequency of 1600 Hz. Approximately every 2.5 ms, the specimen diameter is averaged and delivered at the output of the laser system, where that value is monitored once per millisecond by the data acquisition system.

A number of hydrogen hot extraction measurements, metallographic and fractographic examinations have also been performed on the specimens after the EDC tests. The main information about the EDC specimens and test results are summarised in Table 2.

Pulse Irradiation Tests in Research Reactor

The NSRR pulse irradiation RIA tests with the KKL fuel have been carried out at ambient temperature/atmospheric pressure condition (room temperature (RT) test, LS-1) and at High Temperature (290°C)/High Pressure (7 MPa) condition (HTHP test, LS-2). The characteristics of the NSRR test facilities and the re-fabricated rods as well as the design of NSRR RT and high temperature (HT) test capsules have been published in detail [7,8]. The hydrogen concentration in the test rod was determined by means of hydrogen hot gas extraction measurements on the cladding samples at both ends of each re-fabricated rod.

Both ramp tests were carried out under almost identical irradiation conditions (power pulse width of 4.4 ms). The HT test (LS-2) was carried out after heating the coolant and holding the target temperature for $\sim$ 1 h. The coolant pressure was the saturation pressure at the achieved temperature. Test fuel rod

TABLE 2—*Material characterisation and main results from the EDC tests.*

Rod	Burnup[a] (MWd/kgU)	Elevation (m)	Specimen ID	Hydrogen (ppm)	Test T°C	Failure	Strain at Failure (%)
AEB 072-E4 LK3/L (seven cycles)	63	2	E4-H0	371	60	Yes	1.2
			E4-H4	298	160	Yes	7.7
			E4-H8	253	180	No	···
			E4-H9	349	160	Yes	1.4
			E4-H1	320[a]	100	Yes	1.2
			E4-H2	320[a]	120	Yes	0.7
			E4-H3	320[a]	140	Yes	0.9
			E4-H5	320[a]	190	Yes	4.5
			E4-H6	320[a]	260	No	···
			E4-H7	320[a]	220	No	···
AEB 068-E4 LK3/L (six cycles)	58	2	E4-R1-1	200[a]	33	Yes	3.7[b]
			E4-R1-2	200[a]	33	Yes	1.9[b]
			E4-R	200[a]	280	No	···
AEB 069-E4 LK3/L (five cycles)	52	2	E4-Q1-1	90[a]	33	No	···
			E4-Q1-2	90[a]	33	Yes	16.2[b]
20461-J2 LK3/L (four cycles)	40	0.6	J2-4A	88	25	Yes	7
			J2-4B	99	25	Yes	6
			J2-4C	59	300	No	···
			J2-4D	78	25	Yes	8[b]
		2	J2-4E	129	130	No	···
			J2-4F	95	100	Yes	20
			J2-4G	195	300	No	···

[a] Estimated.
[b] Measured at specimen after test.

characteristics, test conditions, and the main results of the LS-1 and LS-2 tests are summarised in Table 3.

Experimental Results and Discussions

Pulse Irradiation Tests at Nuclear Safety Research Reactor

In the LS-1 test, the PCMI failure occurred when the fuel enthalpy reached 222 J/g [7]. According to the transient measurement, the cladding surface temperature remained below 30°C at the time of failure. At the same time, according to the RANNS code [9], the mid-wall cladding temperature reached ~ 80°C, while the inner surface temperature increased above 400°C. A long axial crack was generated in the cladding. The residual hoop strain of the cladding measured after the test was 0.8 %. The direction of fracture propagation in the outer region was radial, which suggests a brittle fracture (Fig. 5(*a*)). On the other hand, the slanted fracture in the inner region indicates a ductile fracture. These fracture modes were confirmed by a detailed observation of the cladding fracture surface in a scanning electron microscope (SEM). Image (c) from the cladding inner part shows a lot of small dimples all over the view, which is generally a feature of a ductile fracture (Fig. 5(*c*)). On the other hand, image (b) from the periphery shows not only small dimples but large craters with a smooth floor (Fig. 5(*b*)). The smooth floors could be generated by strain separation along the precipitated hydrides, which are observed as black lines at the cladding outer region in Fig. 5(*a*) or Fig. 3(*a*). The coexisting small dimples in image (b) may suggest that the matrix remained ductile, though the hydrides were brittle.

The LS-2 test resulted in non-failure [7]. Although cladding temperature data are not available, one could assume that the cladding surface temperature should be at least above an initial temperature of 283°C. The inner surface temperature estimated by means of the RANNS code could be expected, as a first approximation, to be above 600°C.

The results from tests LS-1 and LS-2 suggest that the failure limit increases with the temperature increase. In other words, the resistance of the cladding to PCMI failure possibly increases at higher temperatures where cladding ductility is higher.

Reactivity Initiation Accident Simulation by Means of the Expansion-Due-to-Compression Mechanical Testing

The EDC test data allow investigating the correlation between the occurrences of cladding failure under rapid loading (RL) typical for in-reactor RIA tests on one side and test parameters (temperature) and cladding properties (hydrogen concentration as a measure of material degradation) on the other side. The capacity of the cladding to survive under PCMI can then be characterised by the cladding hoop strain at failure measured on the specimen at test temperature. All mentioned parameters for the tested EDC specimens are included in Table 2. The maximum observed hoop strain obtained from the specimen diameter measured at failure is decreasing from 15 % to 20 % at 80–90 ppm of hydrogen

TABLE 3—*Fuel description, test conditions, and main results of the NSRR RIA tests.*

	ID for Test and Test Fuel Rod	
	LS-1	LS-2
Description of mother fuel rod		
Fuel type	10×10 BWR-UO_2 (Leibstadt)	
Clad outer/inner diameter (mm)	9.62/8.36	
Clad material	Zircaloy-2 (LK3) with Zr liner	
Pellet burnup (GWd/t)	69	
Description of test fuel rods		
Clad oxide thickness (μm)	25	25
Clad hydrogen content (ppm)	300	290
Pellet stack length (mm)	107	52
Rod internal gas	Helium of 0.1 MPa at $\sim$ 20°C	
Test conditions		
Power pulse width (ms)	4.4	
Initial coolant conditions (stagnant water)	17°C, 0.1 MPa	283°C, 6.6 MPa
Initial fuel enthalpy (20°C-based), H_0, J/g (cal/g)	...	70 (17)
Max. increase of fuel enthalpy, ΔH_{max}, J/g (cal/g)	469 (112)	371 (89)
Main results		
Enthalpy increase at failure, ΔH_{fail}, J/g (cal/g)	222 (53)	No failure
Key observations	PCMI failure All pellets fragmented Mechanical energy detected	PCMI-induced clad strain of 0.93 %

GRIGORIEV ET AL., doi:10.1520/JAI102988 1081

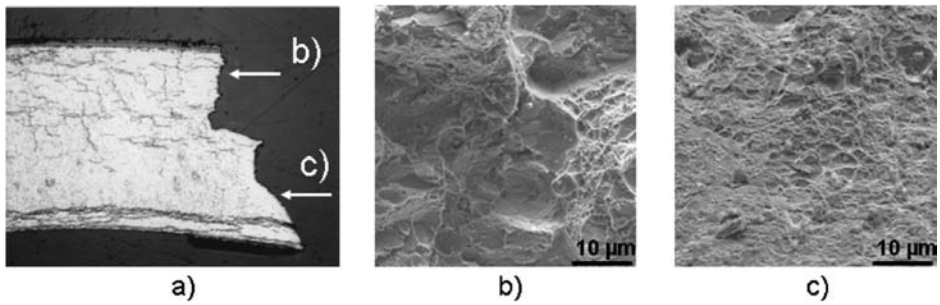


FIG. 5—*(a) Cladding metallographic picture at fracture of test LS-1; (b) SEM images of fracture surface at the outer region of the cladding; and (c) at the inner part of cladding thickness.*

to about 5 % at 400 ppm. A less pronounced correlation can be observed between the hoop strain at failure and the test temperature when only failed specimens are analysed. However, when both failed and non-failed specimens are included in the analysis, a very marked effect of the test temperature can be observed (Fig. 6). A sharp transition from a "lower shelf" with low cladding ductility to an "upper shelf" with large ductility is observed for fuel claddings with different hydrogen content as a result of burnup. The data in Fig. 6 clearly indicate that an increase in burnup from 40–63 MWd/kgU leads to an increase of transition temperature from 100–120 to 160–180°C. In addition to the shift in the transition temperature, the ductility (strain to failure) in the lower shelf is significantly lower in high burnup cladding. Nevertheless, even at the lowest

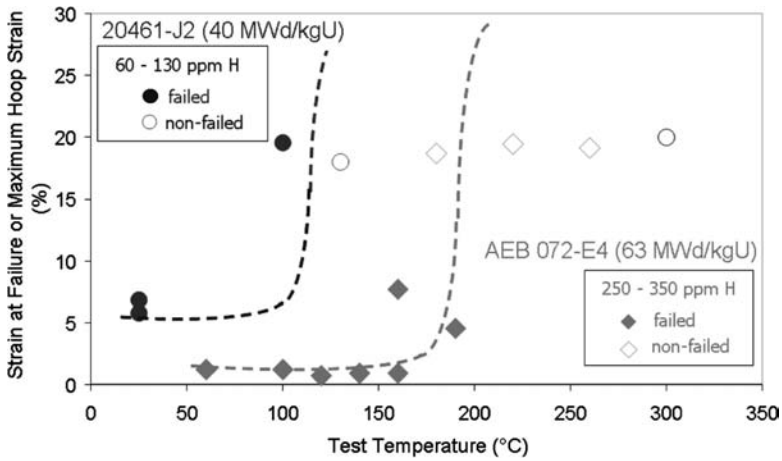


FIG. 6—*Temperature effect on cladding hoop strain observed in the EDC tests. Maximum hoop strain represents the strain at failure or maximum strain achieved for non-failed specimen.*

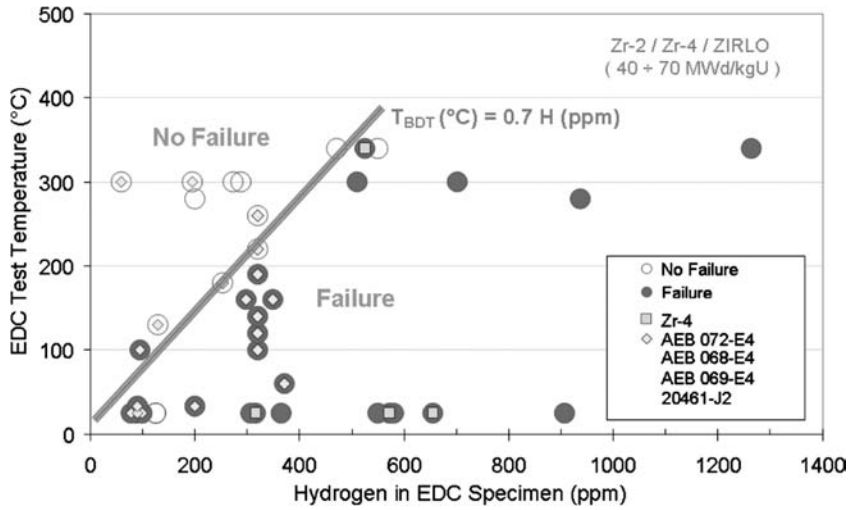


FIG. 7—*Effect of test temperature and hydrogen concentration on specimen failure in the EDC test.*

temperature, all the high burnup cladding specimens showed a total hoop strain at the level of 0.7–1.2 %.

Experimental data from the EDC tests (Table 2) mapped against test temperature and hydrogen concentration clearly indicate separate failure and non-failure regions (Fig. 7). All available EDC tests performed so far on different cladding materials (Zircaloy-2 LK2 and LK3, Zircaloy-4, and ZIRLO) after different burnup (40–70 MWd/kgU) in different reactors are collected in this diagram. There are two apparent areas of EDC specimen behaviour: Failed or brittle (filled circles) and non-failed or ductile (open circles). The boundary between those two areas or the brittle-ductile transition (BDT) corresponds to the relationship $T_{\mathrm{BDT}}\,(^{\circ}\mathrm{C}) = 0.7H$ (ppm), where T_{BDT} is the transition temperature and H is the hydrogen concentration in the cladding material. The rhombic symbols indicate the EDC test data from Table 2, and the square symbols show the data for Zircaloy-4 cladding [2].

Effect of Rapid Heating

Even though the loading of the cladding specimen is rapid in the EDC tests, the heating of the specimen is different compared to in-reactor RIA tests. To verify a possible effect of RH, which is a specific condition for in-reactor RIA experiments compared to the static heating (SH) typical for the EDC tests, RH/loading (RHL) tests have been performed at Studsvik on unirradiated hydrided ($\sim$ 500 ppm) Zircaloy plate material. The development of the RHL test was initiated and financed by the Electric Power Research Institute, including the delivery of hydrided plate material [10]. In the RHL test, a flat dog-bone specimen is heated by direct current, and the temperature is monitored by means of an

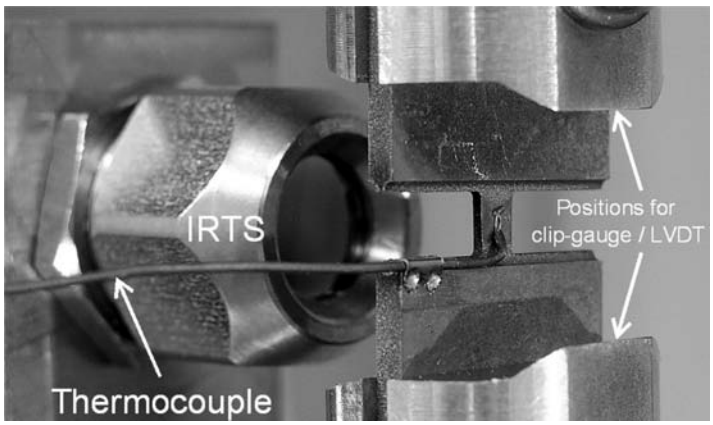


FIG. 8—*RHL specimen mounted in the grips of the testing machine. Grips allow the use of a clip-gauge for monitoring the specimen elongation. A thermocouple is welded to the specimen gauge length for temperature calibration measurements to compare the IRTS readings with the thermocouple data.*

infrared temperature sensor (IRTS) located close to the specimen and focused on the specimen gauge length surface (Fig. 8). To measure specimen elongation, a clip-gauge is mounted on the loading grips close to the specimen. The specimen is heated and simultaneously loaded to failure within 30–80 ms. All experiments were performed in open-air atmosphere. The load, specimen elongation (clip-gauge), and specimen temperature (IRTS) were monitored every millisecond. The temperature at the point of maximum load is used in the data analysis as the test temperature. A number of tests were performed after "static" heating in a conventional furnace when the specimen was held at the test temperature for 30–40 min before the RL. To increase an embrittling effect of hydriding, the hydrides in several specimens were re-oriented to correspond to the radial hydrides in fuel cladding. The procedure for hydride re-orientation consisted of heating the specimen to 400°C, loading in tension by 150 MPa, and slowly cooling down at the rate of 1.5°C/min under applied stress.

Some of the load-displacement curves from the RHL tests together with specimen appearance after fracture are shown in Fig. 9. Only specimens tested at low temperatures show a higher maximum load and lower displacement at failure compared to other specimens' behaviour. The load-displacement curves from the tests at 250–275°C are almost identical, despite the fact that specimens 06a-H and 06c-H had radial hydrides in their microstructure, while specimens 07b and 07f were not subjected to any hydride re-orientation, and thus contained predominantly tangential hydrides. Note that specimen 07b was tested after SH, while specimen 07f was tested under RH conditions. All specimens were tested under RL.

The observations from the RHL tests indicate that material properties, such as strength and ductility, depend on the material's instantaneous temperature

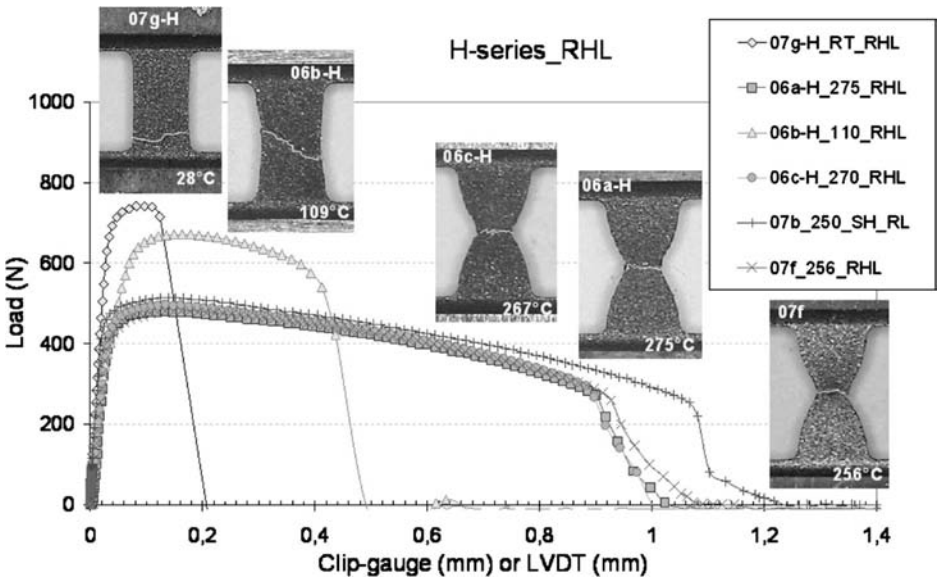


FIG. 9—*Load-displacement curves and specimen appearance after the RHL tests at different temperatures (re-oriented hydrides, H-series). The specimens 07b (SH) and 07f (RH) had original hydride morphology (no re-orientation procedure was applied) The linear variable differential transducer was used for specimen elongation measurements in the tests with SH. All specimens were tested under RL.*

or are very fast adapted to the actual temperature and are not affected by the applied heating time (rate of heating). There is no difference in material strength for specimens soaked at the test temperature during 30–40 min before loading (SH) and for specimens heated simultaneously with loading during 30–80 ms. The same conclusion is valid for the elongation. Specimens with radial hydrides show lower ductility at temperatures below ~ 100°C. This embrittling effect of radial hydrides is already diminished at temperatures of 250–270°C, assuming the occurrence of BDT under RL at temperatures somewhere between 100 and 250°C. This fits well to the BDT temperatures observed in the EDC tests for irradiated cladding materials (Figs. 6 and 7).

Comparison between the Expansion-Due-to-Compression and the Nuclear Safety Research Reactor Tests

Since the heating rate does not appear to affect the cladding strength and ductility, one can compare the effect of temperature in the EDC tests on fuel cladding AEB 072-E4 and in the NSRR RIA tests LS-1 and LS-2 performed on the same fuel rod segments. The cladding temperature in the LS-1 test at the moment of fracture varied from ~ 30°C at the outer surface of the cladding to slightly above 400°C at the inner surface of the cladding. It is known about the LS-2 test that

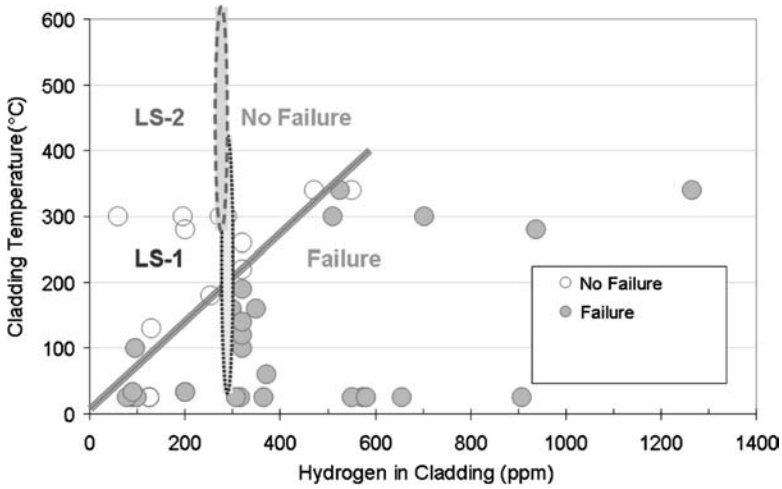


FIG. 10—*"Failed"-"not failed" map based on the EDC test data plotted in the coordinates "cladding temperature"-"hydrogen in cladding" and the data from the NSRR tests LS-1 and LS-2 located in the map.*

just before the ramp, the outer cladding surface temperature was about 280°C and that temperatures above 600°C could be expected at the inner cladding surface at the end of the in-reactor ramp. These temperature intervals can be indicated on the failure map based on the EDC test data (see Fig. 7) at a hydrogen concentration of about 300 ppm, which is the concentration defined for the AEB 072-E4-J cladding (Fig. 10). According to Fig. 10, different temperatures of the cladding wall in the LS-1 and LS-2 tests can explain different behaviours of the cladding in the ramp tests. The entire cladding thickness in the LS-2 test was in the "no failure" area, where a ductile behaviour of cladding is expected. In the LS-1 test, about half of the cladding thickness (outer part) was at temperatures where the cladding should experience a brittle fracture. In general, this is consistent with the fracture surface profile and the fractographical features observed for cladding failure in the LS-1 test (Fig. 5).

Fractographic examination of the EDC specimens clearly showed the change of fracture surface appearance with an increase of test temperature from 60 to 160°C (Fig. 11). Numerous dimples are observed at 160°C, while they could not be found at 60°C. Specimens AEB072-E4-H1 and AEB072-E4-H5 were examined by means of metallography, and both showed a slant fracture through the entire cladding wall thickness (Fig. 12). However, having the same macrotype of the slant fracture, the relief of the fracture surface appears to be smoother after fracture at 100°C (AEB072-E4-H1) and more irregular after fracture at 190°C (AEB072-E4-H5). Thus, we can see indications of more ductile behaviour (dimples and irregular macrosurface of fracture) at the temperatures close to the BDT.

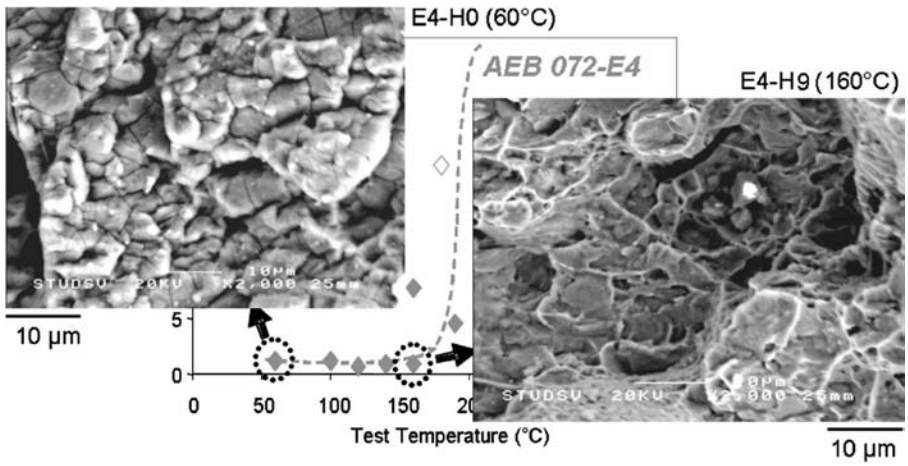


FIG. 11—*Different types of fractographic features observed at fracture surfaces of the EDC specimens AEB072-E4-H0 and AEB072-E4-H9 tested at different temperatures at the lower shelf of ductility (Table 2).*

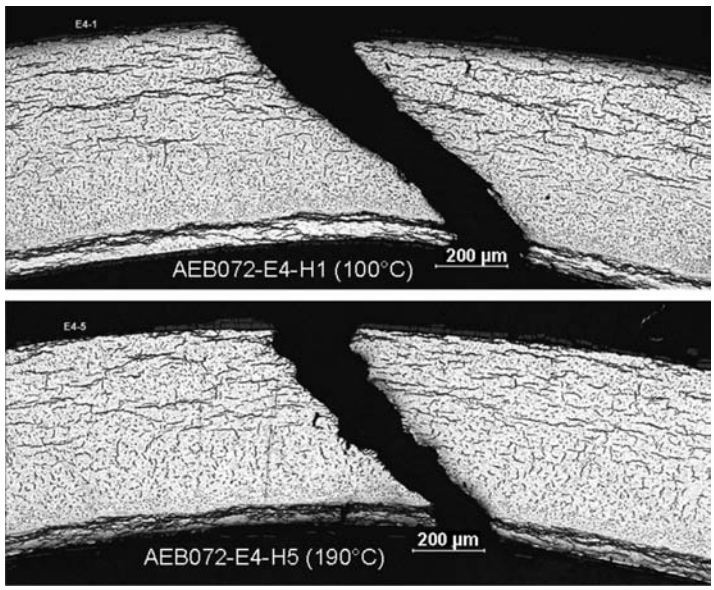


FIG. 12—*Cross-section metallography of the EDC specimens AEB072-E4-H1 and AEB072-E4-H5 tested at different temperatures (Table 2).*

Summary

A segment of a high burnup fuel rod (63 MWd/kg U rod average) irradiated at the Leibstadt BWR in Switzerland (KKL) has been subjected to simulated RIA tests in the Japanese Atomic Energy Agency, NSRR. In order to evaluate the temperature influence on transient fuel behaviour, the pulse irradiation tests were performed at ambient (test LS-1) and operating temperatures (test LS-2), representing cool zero power and hot zero power. Two ramp tests carried out under almost identical irradiation conditions resulted in specimen failure in the LS-1 test, while no failure was observed in the LS-2 test.

An adjacent segment of the same fuel rod has been subjected to high strain rate mechanical testing by means of the EDC test performed at Studsvik. The EDC tests performed at temperatures from 60 to 260°C show the existence of a transition temperature where an abrupt increase in the specimen hoop strain at failure occurs. Experimental data from the EDC tests mapped against test temperature and hydrogen concentration clearly indicate separate "failure" and "non-failure" regions. A simple relationship defining the transition temperature versus hydrogen concentration in the cladding has been obtained.

To verify a possible effect of RH, which is a specific condition for in-reactor RIA experiments compared to the SH typical of the EDC tests, the RHL tests have been performed on unirradiated hydrided (~ 500 ppm) Zircaloy plate material. The results from the RHL tests when both loading and heating are performed simultaneously and within 50–80 ms clearly indicate that strain to failure is dependent on the instantaneous material temperature and is not affected by the pre-heating history.

The results from the LS-1 and LS-2 RIA tests located in the failure map based on the EDC test data show good consistency between the EDC and in-reactor pulse test data. It is concluded that the failure of high burnup fuel under RIA conditions is mainly controlled by temperature and hydrogen concentration and that the EDC test can provide valuable information to predict fuel failure.

Acknowledgments

The writers are grateful to Vattenfall AB, OKG Aktiebolag, Barseback Kraft AB, Westinghouse Electric Sweden AB, and Studsvik AB, which sponsored the development of the EDC test and, together with Kernkraftwerk Leibstadt AG, the testing of irradiated cladding from the KKL fuel rods. The writers are grateful also to the Electric Power Research Institute, which initiated and sponsored the development of the RHL test and the testing of unirradiated hydrided Zircaloy plate material. Special thanks are due to Dr. Ken Yueh for continuing discussions and aid during the RHL development. The writers would also like to acknowledge Sousan Abholassani, Didier Gavillet, and Holger Wiese (PSI) as well as Roger Lundström and Sören Karlsson (Studsvik) for material characterisation.

References

[1] Ledergerber, G., Abolhassani, S., Limbäck, M., Lundmark, R., and Magnusson, K.-Å., "Characterization of High Burn up Fuel for Safety Related Fuel Testing," *J. Nucl. Sci. Technol.*, Vol. 43, No. 9, 2006, pp. 1006–1014.

[2] Grigoriev, V., Schrire, D., Jakobsson, R., Josefsson, B., and Jonasson, A., "Mechanical Testing of High Burnup PWR Cladding to Simulate RIA," *Proceedings of Annual Meeting on Nuclear Technology 2000: JAHRESTAGUNG KERTECHNIK*, Bonn, May 23–25, 2000, INFORUM GmbH, Germany, pp. 359–362. ISSN 0720-9207.

[3] Tägtström, P., Limbäck, M., Dahlbäck, M., Andersson, T., and Pettersson, H., "Effects of Hydrogen Pickup and Second Phase Particle Dissolution on the In-Reactor Corrosion Performance of BWR Claddings," *Zirconium in the Nuclear Industry: 13th International Symposium, ASTM-STP-1423*, 2002, G. D. Moan and P. Rudling, Eds., ASTM International, West Conshohocken, PA., pp. 96–118.

[4] Ledergerber, G., Kaufmann, W., Ritter, A., and Greiner, D., "Burnup Increase and Power Uprate–Operation History of KKL," *Proceedings Intern. LWR Fuel Performance Meeting*, San Francisco, CA, Sep. 30–Oct. 3, 2007, Paper 1036 American Nuclear Society, ANS.

[5] Hermann, A., Wiese, H., Bühner, R., Steinemann, M., and Bart, G., "Hydrogen Distribution Between Fuel Cladding Metal and Overlying Corrosion Layers," *Proceedings Int. Topical Meeting on LWR Fuel Performance*, Park City, 2000, American Nuclear Society, ANS, pp. 372–384, ISBN: 089448-656.

[6] NEA, "Nuclear Fuel Behaviour Under Reactivity-Initiated Accident (RIA) Conditions," *Report NEA No.* 6847, Nuclear Energy Agency, OECD, Paris, France, 2010, ISBN 978-92-64-99113-2.

[7] Sugiyama, T., Umeda, M., Fuketa, T., Sasajima, H., Udagawa, Y., and Nagase, F., "Failure of High Burnup Fuels Under Reactivity-Initiated Accident Conditions," *Ann. Nucl. Energy*, Vol. 36, 2009, pp. 380–385.

[8] Sugiyama, T., Umeda, M., Sasajima, H., Suzuki, M., and Fuketa, T., "Effect of Initial Coolant Temperature on Mechanical Fuel Failure Under Reactivity-Initiated Accident Conditions," *Proceedings of Top Fuel 2009*, Paris, France, Sept. 6–10, 2009, French Nuclear Energy Society, SFEN, Omnipress, Paper 2086.

[9] Suzuki, M., Sugiyama, T., Udagawa, Y., Nagase, F., and Fuketa, T., "Comparative Analysis on Behavior of High Burnup PWR Fuels Pulse-Irradiated in Reactivity-Initiated Accident Conditions," *Proceedings of Top Fuel 2009*, Paris, France, Sept. 6–10, 2009, French Nuclear Energy Scoiety, SFEN, Omnipress, Paper 2082.

[10] Yueh, K., "Rapid Heating and Loading Test," *US NRC Archive, ADAMS Accession Number ML090861034*, 2009.

DISCUSSION

Question 1, Joe Rashid, ANATECH:—The data you presented mixes two effects: radial hydrides and temperature. Similar simulations but without radial hydrides and at higher strain rates, would be closer to RIA.

Author's Response:—In the data presented, the mechanical simulations of RIA (EDC tests) have been performed on irradiated cladding with its existing hydride morphology. The wording "radial hydrides" in the paper is only used for the RHL unirradiated samples subjected to uniaxial tension and defines the hydride orientation, which is, relatively to the tension direction, similar to the orientation of radial hydrides in the cladding. The RHL tests have been mainly performed on the samples of hydrided plate material with their original hydride orientation (no radial hydrides). Only a limited number of the RHL samples were subjected to hydride re-orientation prior to the testing. Both the EDC and the RHL tests were performed at strain rates, which are similar to an in-reactor RIA: depending on test temperature the time to failure varied from 10 ms to 130 ms in the RHL tests and from 20 ms to 90 ms in the EDC tests. The LS-1 rod in the NSRR test failed at just under 10 ms.

Question 2, Ron Adamson, Zr+:—Could you comment on the comparison of the state of stress on the specimen in the EDC test and in the in-reactor RIA test? Does the difference affect any conclusions?

Author's Response:—This question has been under discussion since the first presentation of the EDC technique in 1999. Without doubts the in-reactor stress state of the cladding hardly possible to re-produce in out-of-pile mechanical tests. Besides specific details of in-reactor through-wall-thickness stress distribution caused by the presence of temperature gradient in the cladding it is usually claimed as the main difference that the cladding experiences a pure hoop straining in the EDC tests rather than a biaxial loading as in the in-reactor RIA. Indeed, an axial stress component is expected to be much weaker in the EDC specimen, where an axial tension is only present in the outer part of cladding thickness owing to specimen "ballooning" during the loading. However, an effect of stress state biaxiality on the material strain at failure is not so obvious. One could expect this effect to be more important in ductile materials, while for brittle failures an absolute value of the tensile stress appears to be the decisive factor. Such expectations are supported by the published data on biaxial burst tests performed on unirradiated and on irradiated cladding under different biaxiality ratios (published by U.S. Nuclear Regulatory Commission, April 2000, NUREG-IA-0199/ IPSN 01-16/NSI RRC 2241): circumferential elongation of unirradiated cladding is highly sensitive to the biaxiality ratio, while the sensitivity of irradiated cladding to this ratio is very low. This observation suggests that the conclusions made in the paper based on the EDC and/or RHL test data should not be greatly affected by the differences in the stress state under discussion. In fact, the measured residual strain in the LS-1 test was within the range of strains measured in the low temperature EDC tests on cladding samples from the same fuel rod.

Question 3, Bo Cheng, EPRI:—Your conclusion is that the RIA issue is only associated with the hydrogen content and the temperature. For current generation cladding, cladding hydriding resistance has been largely improved. If you can establish a hydrogen limit of <200 ppm, it appears that most BWR cladding will meeting this limit, and even PWR cladding, like M5, should also meet the limit. Is it possible that we can close out the RIA technical issue now?

Author's Response:—We believe that the data presented in the paper gives a new point of view on the RIA issue. More data are needed to prove that this point of view is valid for different cladding materials. For example, we need to know the effect of hydrogen concentration on transition temperature for each material under consideration. Presently, the RHL tests have been only performed on unirradiated materials and the conclusions should be confirmed on irradiated cladding. Thus, it seems to be early to

close out the RIA technical issue now. However, it appears that the most important cladding parameters controlling PCMI failure can be adequately determined using existing experimental techniques.

Question 4, Jean Desquines, IRSN:—Do you consider that there is any influence of the radial hydride content?

Author's Response:—We have only observed an embrittling effect of radial hydrides in the RHL tests performed at the temperatures below 150–200°C. At higher temperatures the fracture behavior was not dependent on the presence of radial hydrides. Keeping in mind the ring tension test data on cladding with purely radial hydride morphology, we might expect that the transition temperature is not strongly affected by the content of radial hydrides. If this is the case, we could assume that any influence of the radial hydride content would only be observed below the transition temperature indicated above.

Question 5, Artur Motta, Penn State University:—1) Did you observe an effect of strain rate on the ductility of the cladding? If so what was the effect, quantitatively?

Author's Response:—We have clearly observed an effect of strain rate in the RHL tests performed on the samples of hydrided unirradiated Zircaloy plate material (gauge length of 2 mm). In the tests performed at approximately 220°C the decrease of cross-head displacement rate from 13 mm/s to 0.0075 mm/s resulted in the increase of total elongation at fracture from 45 % to 55 % and in the decrease of the UTS from 450 MPa to 350 MPa.

Author Index

A

Abolhassani, S., 729-751
Alam, A. M., 523-542
Almer, J. D., 496-520
Ambard, A., 649-681, 682-707
Anantharaman, S. A., 349-369
Andersson, T., 595-617
Andrén, H.-O., 595-617
Aomi, M., 401-430
Audic, K., 899-927

B

Banchik, A. D., 754-781
Banerjee, S., 121-147
Banker, J. G., 3-16
Baranwal, R., 784-799, 853-873
Barberis, P., 244-266, 801-824
Bělovský, L., 993-1018
Bergin, S. G., 373-398
Bernaudat, C., 899-927
Bertsch, J., 523-542
Bickel, G. A., 327-346
Blat-Yrieix, M., 649-681, 682-707
Bouffioux, P., 899-927, 929-951
Bourdiliau, B., 929-951
Bozzano, P. B., 754-781
Bréchet, Y., 682-707
Buyers, A., 327-346

C

Cantonwine, P. E., 954-989
Cappelaere, C., 929-951
Carassou, S., 899-927
Carrera, F., 784-799
Chabretou, V., 801-824, 899-927, 929-951
Chakravartty, J. K., 121-147, 544-570
Cheadle, B. A., 67-88
Cheng, B., 91-116
Chong, K. B., 649-681
Ciurea, S., 595-617
Cloué, J.-M., 269-296, 899-927
Colas, K. B., 496-520
Coleman, C., 544-570
Combeau, H., 219-242
Comstock, R. J., 176-193, 649-681, 784-799
Cook, T., 784-799
Cottis, B., 649-681
Cox, B., 711-727
Crawford, D. C., 91-116, 954-989
Curfs, C., 682-707

D

Dahlbäck, M., 176-193, 595-617, 729-751
Daymond, M. R., 195-214, 496-520
Deshmukh, V., 349-369
Desquines, J., 993-1018
Dey, G. K., 349-369
Douchant, A., 327-346
Douglas, S., 327-346
Du, C. X., 620-646
Duguay, C., 899-927
Duriez, C., 993-1018

E

Edsinger, K., 954-989
Elliot, A. J., 373-398
English, C., 649-681
Etoh, Y., 401-430

F

Feaugas, X., 269-296
Fitzpatrick, M., 649-681
Flores, A. V., 754-781
Foster, J. P., 853-873
Frankel, P., 649-681, 682-707
Franklin, D. G., 17-36
Fuketa, T., 1073-1089

G

Gaillac, A., 244-266
Garde, A. M., 784-799
Garner, G., 801-824
Garzarolli, F., 711-727
Grandjean, C., 993-1018
Griffiths, M., 327-346
Grigoriev, V., 544-570, 1073-1089
Grosse, M., 575-589
Grovenor, C., 649-681
Guerin, P., 219-242
Guilbert, S., 993-1018

H

Hallstadius, L., 176-193, 595-617, 649-681, 729-751, 784-799, 1073-1089
Higuchi, T., 1054-1070
Hoffmann, P. B., 801-824
Holt, R. A., 195-214, 298-324
Hudson, D., 649-681

I

Inozemtsev, V., 544-570
Ito, K., 401-430
Ivermark, M., 150-172

J

Jädernäs, D., 729-751
Jakobsson, R., 1073-1089
Jardy, A., 219-242
Jha, S. K., 349-369

K

Kapoor, R., 121-147
Kerr, M., 496-520
Kim, Y.-J., 91-116
Kim, Y. S., 544-570
Kobayashi, T., 401-430
Kobylyansky, G. P., 827-849
Kubo, T., 433-463
Kucuk, A., 91-116
Kulkarni, R. V., 349-369

L

Lalgudi, R., 544-570
Leclerc, F., 219-242
Ledergerber, G., 729-751, 1073-1089
Legras, L., 682-707
Lemaignan, C., 244-266
Levasseur, B., 899-927
Li, Q., 466-493, 620-646
Li, W., 298-324
Liaqat Ali, K., 544-570
Lin, Y.-P., 91-116, 954-989
Lozano-Perez, S., 649-681
Lutz, D., 91-116
Ly, A., 682-707
Lyon, S., 649-681

M

Mader, E. V., 729-751, 954-989
Mahmood, S. T., 954-989
Makarevicius, V., 544-570
Mani Krishna, K. V., 349-369
Markelov, V. A., 544-570, 827-849
Matsunaga, J., 401-430
Maurice, A., 899-927

McGrath, M. A., 875-896
Miquet, A., 929-951
Miyamura, S., 401-430
Mizrahi, R., 544-570
Mosbrucker, P., 195-214
Motta, A. T., 496-520
Muta, H., 433-463

N

Nagase, F., 1073-1089
Nakatsuka, M., 1021-1051, 1054-1070
Neogy, S., 349-369
Ni, N., 649-681
Nordin, H. M., 373-398
Novoselov, A. E., 827-849

O

Obukhov, A. V., 827-849
Ogata, K., 433-463
Onimus, F., 929-951
Ostrovsky, Z. E., 827-849

P

Pan, G., 784-799
Parry, G., 682-707
Peng, J. C., 466-493, 620-646
Peregud, M. M., 827-849
Pilvin, P., 269-296
Pivetaud, V., 929-951
Polatidis, E., 649-681
Poquillon, D., 269-296
Preuss, M., 150-172, 176-193, 649-681, 682-707
Priser, M., 269-296

Q

Quinta da Fonseca, João, 176-193

R

Ramadasan, E., 349-369
Ramana Rao, S. V., 349-369
Rath, B. B., 349-369
Rautenberg, M., 269-296
Rebak, R., 91-116
Rebeyrolle, V., 219-242, 801-824
Revil-Baudard, M., 219-242
Ríos, R. O., 754-781
Robson, J., 150-172
Romero, J., 176-193
Roth, M., 544-570
Rozenblum, F., 899-927
Rudling, P., 711-727

S

Saibaba, N., 349-369
Sakamoto, K., 401-430, 1054-1070
Sarkar, A., 121-147
Schrire, D., 1073-1089
Shishov, V. N., 37-66, 827-849
Smith, G., 649-681
Smith, J., 649-681
Srivastava, D., 349-369
Stern, A., 993-1018
Storer, S., 649-681
Sugiyama, T., 1073-1089
Sykes, J., 649-681

T

Takagi, I., 401-430
Tejland, P., 595-617
Thuvander, M., 595-617
Tonpe, S., 349-369
Tracy, S., 298-324
Trapp-Pritsching, S., 801-824

U

Une, K., 401-430
Uno, M., 433-463

V

Vaibhaw, K., 349-369
Valance, S., 523-542
Valizadeh, S., 729-751, 1073-1089
Vermoyal, J. J., 801-824
Versaci, R. A., 754-781
Vizcaíno, P., 754-781

W

Wang, J. H., 466-493
Wang, P., 649-681
Wei, J., 649-681
Woo, O. T., 327-346
Wright, J., 729-751

X

Xia, S., 620-646
Xu, G., 620-646

Y

Yagnik, S., 875-896, 1021-1051
Yamanaka, S., 433-463
Yao, M. Y., 466-493, 620-646
Yvon, P., 899-927

Z

Zhou, B. X., 466-493, 620-646
Zhou, G., 729-751

Subject Index

A

AEM, 754-781
ageing, 349-369
alloy A, 784-799
anisotropic oxidation, 620-646
atom probe, 595-617

B

beta-quenching, 176-193
BOR-60, 827-849
BWR, 433-463, 1073-1089

C

channel bow, 954-989
characterization, 401-430
circumferential, 1021-1051
clad, 3-16
coarse grain, 620-646
cold pilgering, 244-266
corrosion, 17-36, 401-430, 620-646, 682-707, 729-751, 784-799, 801-824
corrosion control, 3-16
corrosion kinetics transition, 649-681
corrosion mechanisms, 649-681
creep, 269-296
creep anisotropy, 298-324
crystallographic texture, 298-324, 327-346

D

deformation, 17-36, 327-346
deformation mechanisms, 929-951
delayed hydride cracking, 433-463, 544-570, 1054-1070
deuterium ingress, 373-398
DIFFOX, 993-1018
diffusion, 401-430
dislocations, 37-66, 269-297
DSC, 754-781
ductile damage, 244-266

E

E110, 37-66
E635, 827-849
ECP, 91-116
EDC mechanical testing, 1073-1089
electron microscopy, 37-66
epitaxial oxide layer, 620-646
explosion clad, 3-16

F

FEM analyses, 433-463
fourier transform, 682-707
fuel cladding, 433-463, 523-542, 1021-1051, 1054-1070

G

galvanic corrosion, 91-116
grain thickness, 327-346
growth, 37-66, 784-800, 801-826, 827-850
guide tube, 875-896

H

HAADF, 595-617
heat exchangers, 3-16
heat treated pressure tube, 349-369
heat treatment, 682-707, 929-951
high burn-up, 1054-1070, 1073-1089

high strain rate, 1021-1051
hydride, 433-463, 496-520, 523-542, 1054-1070
hydriding, 729-751
hydrogen, 754-781, 993-1018, 1054-1070, 1073-1089
hydrogen absorption, 401-430
hydrogen diffusion, 433-463
hydrogen pick-up, 784-799, 801-824
hydrogen uptake, 575-589

I

impedance, 91-116
in-PWR corrosion, 784-799
in-PWR fuel performance, 784-799
in-PWR irradiation growth, 784-799
in situ observation, 433-463
interface undulations, 682-707
internal pressure creep test, 929-951
internal stresses, 195-214
irradiation, 37-66, 523-524, 754-781
irradiation creep, 327-346, 801-824, 853-873, 875-896, 899-927
irradiation-induced growth, 801-824, 827-849, 875-896

K

K_I dependence, 544-570

L

LOCA, 993-1018
low cycle fatigue, 244-266

M

M5™, 219-242, 244-268, 801-826
mechanical properties, 1021-1051
metal-oxide interface, 682-707
micromechanical approach, 269-296
microstructure, 37-66, 373-398, 401-430, 544-570, 827-849
modeling, 150-172, 219-242, 993-1018

N

neutron diffraction, 195-214
neutron radiography, 575-589

O

outside-in failure, 1054-1070
oxidation, 801-824
oxide crack, 595-617
oxide layer, 401-430
oxide porosity, 649-681
oxide void, 595-617
oxygen diffusion, 993-1018

P

PCI, 433-463
phase transformation, 176-194, 195-214
photoelectrochemistry, 91-116
PHWR, 349-369
pin-loading tension (PLT), 544-570
polycrystalline model, 298-324
precipitation kinetics, 150-172
pre-oxide, 993-1018
pressure tube, 373-398
pressure vessels, 3-16
PWR, 801-824

Q

quenching, 176-194, 195-216, 349-369

R

radiation damages and phase composition, 827-849
radiation-induced dissolution, 729-751
rapid heating, 1073-1089
relaxation, 269-296, 899-927
reorientation, 496-520, 523-542
residual stress, 649-681
RIA failures, 1073-1089
ring tensile test, 929-951

S

second phase particle, 37-66, 729-751
segregation, 219-242
shadow corrosion, 91-116, 954-989
shadow corrosion-induced bow, 954-989
simulation, 219-242
spent nuclear fuel, 929-951
SPP, 595-617, 754-781
strain broadening, 496-520
stress, 682-707, 853-873
sub-oxide, 595-617, 649-681
synchrotron X-ray diffraction, 150-172, 176-193, 496-520, 682-707

T

TEM, 269-296, 595-617
temperature dependence, 544-570
test reactor irradiation, 784-799
texture, 176-193, 195-214, 373-398, 620-646
thermal diffusion, 1054-1070
thermal gradient, 1054-1070
toughness, 244-266
transmission electron microscopy, 682-707, 620-646, 929-951
transportation, 929-951
transus temperature, 349-369
tubing, 853-873

U

uniaxial tensile test, 1021-1051

V

vacuum arc remelting, 219-242
variant selection, 176-193
VVER-1000, 827-849

W

weld corrosion resistance, 784-799

X

X5A, 784-799
X-ray diffraction, 195-214

Z

Zircaloy, 17-36, 729-751
Zircaloy-2, 176-193, 433-463, 523-542, 595-617, 954-989, 1054-1070
Zircaloy-4, 269-296, 620-646, 682-707, 754-781, 875-896, 929-951
Zircaloy-4 fuel cladding, 544-570
zirconium, 3-16, 195-214, 327-346
zirconium alloys, 150-172, 244-266, 401-430, 575-589, 801-824, 899-927
ZIRLO, 784-799, 853-873
Zr-1 % Nb, 929-951
Zr-2.5wt%Nb, 298-324, 349-369, 373-398
Zr alloys, 91-116
Zr–Nb–Fe–Sn alloys, 37-66, 801-826, 827-849

Cover Photo Courtesy of AREVA/ CEZUS Research Center

www.astm.org

ISBN: 978-0-8031-7515-0
Stock #: STP1529